VOLUME 12, NUMBERS 5–8, 1999

ISSN 0965-9773

SPECIAL VOLUME – PART B

THE FOURTH INTERNATIONAL CONFERENCE ON
NANOSTRUCTURED MATERIALS (NANO '98)
JUNE 14–19, 1998, STOCKHOLM, SWEDEN

NanoSTRUCTURED MATERIALS

Guest Editors: *Mamoun Muhammed*
K.V. Rao

Pergamon

Nano STRUCTURED MATERIALS

ISSN 0965-9773

(An Acta Metallurgica, Inc. Journal)

Editorial Office: Communications to the Editors and all manuscripts should be sent to Prof. Thomas Tsakalakos, *Nano*STRUCTURED MATERIALS, College of Engineering, PO Box 909, Brett and Bowser Roads, Piscataway, NJ 08855-0909, USA.

Publishing, Advertising and Subscription Offices: Elsevier Science Inc., 655 Avenue of the Americas, New York, NY 10010, USA, E-mail Address: ESUK.USA@ELSEVIER.COM; or Elsevier Science Ltd, The Boulevard, Langford Lane, Kidlington, Oxford, OX51GB, England.

Published 8 times per year in the months of February, March, May, June, August, September, October and November. Annual institutional subscription rate (1999): For customers in Europe, The CIS and Japan: NLG 1,704.00. For customers in all other countries: US$865.00. Special Nano 1998 Conference Optional Volume: For customers in Europe, The CIS and Japan: NLG 1,182.00. For customers in all other countries: US$600.00. Dutch Guilder prices exclude VAT. Non-VAT registered customers in the European Community will be charged the appropriate VAT in addition to the price listed. Prices include postage and insurance and are subject to change without notice.

For Advertising Orders & Inquiries: ***North & South America:*** Tino DeCarlo, Elsevier Science Inc., 655 Avenue of the Americas, New York, NY 10010-5107, USA. Tel: (212) 633-3815; Fax: (212) 633-3820; E-Mail: t.decarlo@elsevier.com ***International:*** Rachel Gresle-Farthing, Advertising Department, Elsevier Science, The Boulevard, Langford Lane, Kidlington, Oxford, OX5 1GB, United Kingdom. Tel: (+44) (0) 1865 843565; Fax: (+44) (0) 1865 843976; E-Mail: media@elsevier.co.uk ***Japan:*** Advertising Department, Elsevier Science K.K., Tel: (81) (3) 5561 5033; Fax: (81) (3) 5561 5047.

Any inquiry relating to subscriptions should be sent to:

The Americas: Elsevier Science Customer Support Department, P O Box 945, New York, NY 10010, USA [Tel: (+1) 212-633-3730/1-888 4ES-INFO. Fax: (+1) 212-633-3680. E-mail: usinfo-f@elsevier.com].
Japan: Elsevier Science Customer Support Department, 9-15 Higashi-Azabu 1-chome, Minato-ku, Tokyo 106, Japan [Tel: (+3) 5561-5033. Fax: (+3) 5561-5047. E-mail: kyf04035@niftyserve.or.jp].
Asia Pacific (excluding Japan): Elsevier Science (Singapore) Pte Ltd, No. 1 Temasek Avenue, 17-01, Millenia Tower, Singapore 039192. [Tel: (+65) 434-3727. Fax: (+65) 337-2230. E-mail: asiainfo@elsevier.com.sg].
Rest of the World: Elsevier Science Customer Service Department, P O Box 211, 10011 AE Amsterdam, The Netherlands, [Tel: (+31) 20-485-3757. Fax: (+31) 20-485-3432. E-mail: nlinfo-f@elsevier.nl]. For members of the TMS - $95.00. For members of co-operating societies of *Acta*METALLURGICA - $95.00. For members of sponsoring societies of *Acta*METALLURGICA - $95.00.

*Nano*STRUCTURED MATERIALS

Companion journal to
Acta MATERIALIA and *Scripta* MATERIALIA

Principal Editors

Thomas Tsakalakos*
Rutgers University

Bernard H. Kear
Rutgers University

Richard W. Siegel
Rensselaer Polytechnic Institute

SPECIAL VOLUME – Part B

The Fourth International Conference on Nanostructured Materials (NANO '98)
June 14–19, 1998, Stockholm, Sweden

Guest Editors:
Mamoun Muhammed and K.V. Rao
Royal Institute of Technology,
Stockholm, Sweden

* Deputy Editor: Professor William E. Mayo

PERGAMON

™ The paper used in this publication meets the minimum requirements of American National Standard for Information Sciences-Permanence of Paper for Printed Library Materials, ANSI Z39.48-1984

Printed in the USA

*Nano*STRUCTURED MATERIALS

(An Acta Metallurgica, Inc. Journal)

AIMS AND SCOPE

Advances in high performance materials for a variety of applications are now becoming increasingly dependent on our ability to control the size, distribution and morphology of their constituent grains or phases at the nanoscale level (less than 100 nm). Capabilities for synthesizing such nanostructured materials are becoming available, so that it is possible to produce the quantities of materials needed for prototype development and testing.

The primary mission of the journal for *Nano*STRUCTURED MATERIALS is to provide an international and interdisciplinary forum for the effective dissemination of scientific and technical information on synthesis, processing, theory, computational modeling, structure, properties, performance and applications of nanostructured materials. The materials of interest include metals, ceramics, polymers, semiconductors, superconductors, and magnetic, optical and electronic materials, and their composites. Synthesis routes of interest include chemical and physical vapor deposition, mechanical milling, gas phase pyrolysis and condensation, electrodeposition, cryochemical synthesis, laser pyrolysis, gel synthesis, and other methods with applications for structural materials, coatings, thin film devices, membranes, catalysts, sensors, etc.

The following are major areas of concentration of the journal:

- Clusters and cluster assembled materials;
- Ultrafine powders, thin films, coatings, multilayers, and fibrous materials;
- Structure and characterization of nanophases;
- Synthesis and processing of nanostructured materials: physical, chemical, mechanical, and biological methods;
- Properties: mechanical, electrical, optical, rheological, magnetic, etc.;
- Performance and applications: tribology, corrosion, etc.;
- Related fields such as: nanolithography, nanodevices, etc.

*Nano*STRUCTURED MATERIALS will rapidly publish research papers and regular invited review papers on scientific and technical issues in this rapidly evolving field. The journal will strive to maintain an international representation in published papers, and will, from time to time, co-sponsor regional, national and international meetings.

PREFACE

A remarkable group of almost 500 participants from 40 countries 'self-assembled' in Stockholm for the NANO'98 conference held during June 14-19, 1998. This international conference, with a considerably larger number of participants than in the past three meetings in this series, signified considerable maturity and significant growth in multidisciplinary scientific activity on a global scale.

The well-attended NANO'98 conference offered a "Smorgasbord" (in Swedish Smörgåsbord) of the latest exciting state-of-the-art developments in the field. In total, 572 papers were presented at the conference. There were plenary talks by two Nobel Laureates, 58 invited talks, and an equal number of oral contributory presentations. A unique feature of 'Invited Poster' session consisting of 41 presentations was introduced to highlight some of the novel contributions. This session was particularly appreciated both by the presenters and the participants because of the opportunity for extended informal discussions on specific topics. In addition, three poster-sessions were scheduled covering over 414 presentations, which were displayed till late in the evening. Pouring rain from the skies over Stockholm kept the participants indoors for extended discussions at the poster sessions with good attendance, despite the late hours.

From the contents of the presentations we see clear trends of exploiting the driving force of nanotechnology within the limits of imagination. Chemists are getting closer to post modern alchemy wherein dream materials are being modeled and synthesized almost at a molecular level. Physicists and materials scientists have engineered, atom by atom, features with increasing ease. The art of developing functionalized nanostructured materials exploiting unusual interfacial properties seems to have produced hitherto unknown man-made materials. The consequent natural lead to the world of self-assembled systems appears to bring the field closer to mimicking nature. Exploitations of the size-related properties of nanostructured materials include transparent-to-opaque ceramics, superplasticity, catalysts, and materials with enhanced mechanical properties (e.g. unusually hard material tools etc.), just to name a few. Complex tailored multilayer systems have produced value-added components of promise like the GMR heads, unusual soft and hard magnets, quantum dots, ...

A major effort by the conference Chairs was to ensure the participation of scientists from the "Eastern" countries and to encourage a significant amount of participation from students. It is pleasing to point out that over 90 students have participated in the conference and over 60 prominent scientists representing most of the "Eastern" countries have made important contributions during the conference.

It is a pleasure for us to thank the various individuals who have generously contributed their efforts and time to ensure the success of the conference. The conference chairs would like to thank the International and National Advisory Committees for their suggestions and support for the conference. We extend our special appreciation to the members of the Scientific Programme Committee, who struggled for three days in Stockholm reading through over 730 submitted abstracts in order to assemble the comprehensive programme. The local organizing committee, consisting of a significant number of graduate students and Post doctorals at the Royal Institute of Technology, has worked intensely with all the details of the conference. They also spent very many late nights after the conference to assemble and prepare the camera-ready format of the 400 manuscripts we received. In this, we are especially grateful to Professor Thomas Tsakalakos for his professional help and friendly assistance in finalizing the Proceedings. We specially thank Dr. Andrei Zagorodni for his committed and enthusiastic efforts in the formidable task of handling the manuscripts to finalize the proceedings. The

professional services of Stockholm Convention Bureau, Mrs. Britta Sjòblom in particular, is highly appreciated.

Generous financial support from several organizations has made it possible to hold the conference in Stockholm. We acknowledge and appreciate the support by the following organizations:
Royal Institute of Technology, Sweden
Swedish Consortium on Clusters and Ultrafine Particles, Sweden
Brinell Center, Royal Institute of Technology, Sweden
European Consortium for Nanophase Materials, Switzerland
Acta Metallurgica Inc., USA
Alps Electric Company, Japan
Canon Centre City, Sweden
Carl Tryggers Stiftelse, Sweden
Elsevier Science Inc., Switzerland
Finnair, Finland
The Office of Naval Research ONR, USA
European Research Office of the US Army, USARDSD-UK
Swedish Natural Science Research Council, NFR, Sweden
Swedish Research Council for Engineering Sciences, (TFR), Sweden
Swedish National Board for Industrial and Technical Development (NUTEK)
Swedish Royal Academy of Science, Nobel Committee for Physics, Sweden
Swedish Royal Academy of Science, Nobel Committee for Chemistry, Sweden

We gather from all the feedback we are constantly receiving through numerous letters, e-mails, and personal compliments, the NANO'98 conference held in Stockholm was highly appreciated. NANO'98 was an event to remember marked by outstanding performances from all the attendees, and the strong interactions among the different disciplines. It asserted a high promise and dynamism to this important field of science and technology. The outcome of NANO'98 is documented in the proceedings herewith.

Finally, we want to thank our families, Sunita, Charlotte, Alexandra, Jasmina and Marion who were truly supportive to us before, during, and in the aftermath of NANO'98.

STOCKHOLM, May 1999

Mamoun Muhammed
K.V. Rao

Professor Mamoun Muhammed
Materials Chemistry Division
Royal Institute of Technology
Brinellvägen 23, II
SE-100 44 Stockholm - Sweden

Tel+46-8-790 8158 Fax: +46-8-790 9072
Sec: +468-790 9072
email: mamoun@matchem.kth.se

SPECIAL VOLUME

The Fourth International Conference on Nanostructured Materials (NANO '98) June 14–19, 1998, Stockholm, Sweden

Contents – Part B

Pergamon

NanoStructured Materials, Vol. 12, pp. 601–604, 1999
Elsevier Science Ltd

0965-9773/99/$–see front matter

PII S0965-9773(99)00196-8

MAGNETIC NANOSTRUCTURES IN A GLASS CERAMIC CHARCTERIZED BY SMALL ANGLE NEUTRON SCATTERING

A. Wiedenmann[a)], U. Lembke[b)], A. Hoell[b)], R. Müller[c)], W. Schüppel[c)]
a) Hahn-Meitner Institut Berlin, Glienickerstrasse 100, D-14109 Berlin (Germany)
b) Universität Rostock, Fachbereich Physik, D-18051 Rostock (Germany)
c) Institut für Physikalische Hochtechnologie, Helmholtzweg 4, D-07743 Jena (Germany)

Abstract-- *Nanocrystalline magnetite Fe_3O_4 embedded in a non-magnetic matrix was formed by heat treatment of Ca-Si-B-Fe-oxide glass. Small Angle Neutron Scattering (SANS) revealed a bimodal volume size distribution for the nanocrystalline phase with maxima centred at radii of 2.5 nm and 10 nm, respectively. The magnetic scattering behaviour is characteristic for superparamagnetism of single-domain particles following the Langevin statistics. Both fractions of nanocrystals are composed by a superparamagnetic core surrounded by a non-magnetic surface layer. Magnetisation measurements indicate different thermal variation of the superparamagnetic moments in both fractions of nanocrystals. ©1999 Acta Metallurgica Inc.*

Introduction and Experimental

New nanosized spinel ferrites with interesting magnetic properties have been produced via the glass crystallisation method (1). A magnetic glass ceramic with a maximum value of the specific saturation magnetisation has been obtained by quenching the melt of composition 27.4 CaO - 42.8 SiO_2 - 6.1 B_2O_3 -23.7 Fe_2O_3 (mol %) and subsequent annealing in air at 700°C during 2 hours (1,2). From previous X-ray diffraction and TEM results the magnetic properties were attributed to the presence of nanosized magnetite, Fe_3O_4, formed during the heat treatment (2). The crystallisation process has been studied by small angle X-ray (SAXS) and neutron scattering (SANS) (3). The present SANS investigations were performed at the instrument V4 of the BER II reactor of the Hahn-Meitner Institute, Berlin (4). Applying a homogeneous magnetic field of 1 T perpendicular to the incoming neutrons of wavelength 0.6 nm allowed to study crystalline and magnetic microstructures separately. Background corrections and calibration to absolute values of differential scattering cross sections in cm^{-1} have been performed cell-by-cell for the area sensitive detector. Magnetisation isotherms have been measured between 298 K and 723 K using a vibrating sample magnetometer.

Results and Discussion

The two-dimensional SANS pattern measured at $\mu_0H = 1$ T present slightly elongated ellipses which result from the superposition of nuclear A(Q) and magnetic contributions B(Q) according to $I(Q)=A(Q)+B(Q)\sin^2\alpha$, where α is the angle between the horizontal external magnetic field $\boldsymbol{H}$ and the scattering vector $\boldsymbol{Q}$. Both contributions are plotted

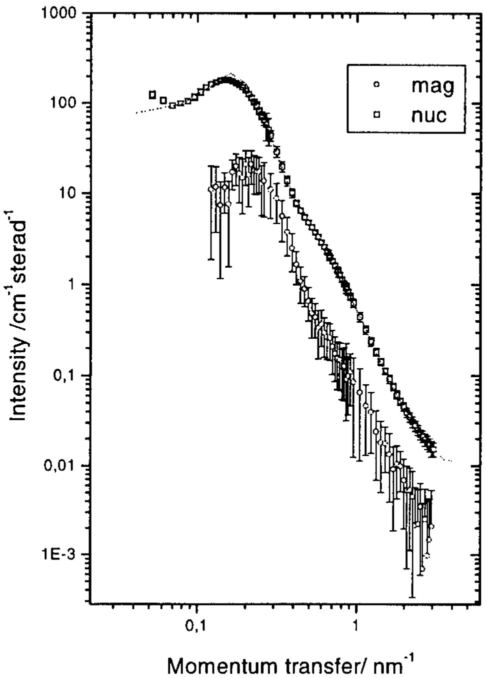

Figure 1: Nuclear and magnetic SANS contributions. Solid line: Fit with the size distribution of (Fig.2)

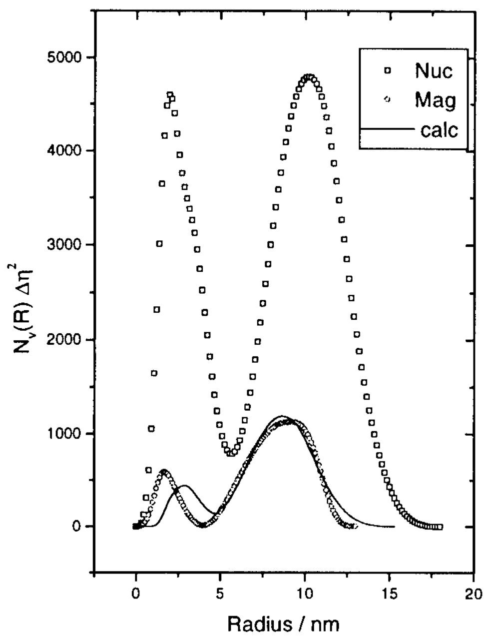

Figure 2: Volume distributions for nuclear and magnetic nanoparticles corresponding to Fig. 1. Solid line: Model calculation of D_{mag} for particles composed by a super-paramagnetic core and a non- magnetic surface

in Fig. 1 in double logarithmic scale. A(Q) scales well with the corresponding SAXS signal (3) and was therefore assigned to nuclear scattering contributions from Fe_3O_4 crystallites embedded in the glass matrix. The magnetic contribution B(Q) is nearly ten times smaller than A(Q) and shifted to higher Q values indicating that the magnetic inhomogeneities must be considerably smaller than the crystallites. The intensity maxima observed at low Q in both contributions are characteristic for interference effects in concentrated systems. Applying the Indirect Fourier transform method (5) the volume distributions of spherical particles D(R) = N(R) V(R) $\Delta\eta^2$, weighted by the nuclear and magnetic scattering contrast $\Delta\eta^2$ have been extracted from the contributions A(Q) and B(Q), respectively and plotted in Fig. 2. The volume distribution of the crystallites, $D_{nuc}(R)$, presents two well distinguished maxima centred at R_1 = 2.5 nm and R_2 = 10 nm, in good agreement with the results from a direct Fourier analysis of the SAXS curves (3). A similar bimodal volume distribution $D_{mag}(R)$ is found for the magnetic inhomogeneities which clearly shows that both fractions consist of magnetic particles. However, the maxima are shifted to lower values of R_1= 2.0 nm and R_2 = 8 nm, respectively

which suggests the presence of a nonmagnetic layer around the core of Fe_3O_4 with very similar values of the nuclear scattering length densities ($\eta_{Magnetite} \approx \eta_{Layer}$). In that case, the core-radius R' is related to the radius R of the crystallites by R' = a R - b. Assuming the same number densities N(R) for magnetic and crystalline particles the volume distributions of $D_{core}(R')$ and $D_{mag}(R')$ are obtained by $D_{core}(R') = (R'/R)^3 D_{nuc}(R)$ and $D_{mag}(R') = D_{core}(R')\ \Delta\eta_{mag}^2 / \Delta\eta_{nuc}^2$, respectively. For the present case of superparamagnetic particles the relative magnetisation $\sigma/\sigma_\infty = L(M(R')H / kT)$ is given by the Langevin function $L(x)=\coth(x)-1/x$, where the total particle moment, M(R'), depends on the size of the particles according to $M(R') = 4\,\pi\, R'^3\, m_0/3\ \Omega_{at}$. For non-interacting particles the magnetic scattering contrast has been derived for B(Q) in (6) as $\Delta\eta_{mag}^2 = (0.27\ m_0 10^{-12}\text{cm}/\mu_B\Omega_{at})^2\,(1\text{-}3L(x)/x)$, which depends on the core size R'. We emphasise that for a moment $m_0 = 3.72\ \mu_B$ and $\Omega_{at} = 0.0742\ \text{nm}^3$ per unit Fe_3O_4, at H = 1 T all particles with R' > 4 nm are magnetically saturated and exhibit maximum contrast ($x >> 3$, $L(x) = 1$), whereas small particles (with $x << 1$, $L(x) = x/3$) contribute to σ but not to D_{mag} (7). Good agreement with the observed curve of $D_{mag}(R')$ is obtained for the transformation parameters a = 0.85±0.05 and b = 0.5±0.4, for which the calculated distribution $D_{mag}(R')$ is reported as solid line in Fig. 2.
The volume fractions of the Fe_3O_4 particles and that of the magnetically active core can be estimated from integration of $D_{nuc}(R)$ and $D_{core}(R')$, respectively using $\Delta\eta = \eta_{Magnetite} - \eta_{glass} = 2.16\ 10^{10}\ \text{cm}^{-2}$. For Fe_3O_4 an overall volume fraction of 0.23 is obtained where 65% of the particles are larger than 5 nm. The volume fractions of the magnetic core are $f_1 = 0.05$ for small particles with R'< 5 nm and about $f_2 = 0.10$ for the second fraction of larger particles.

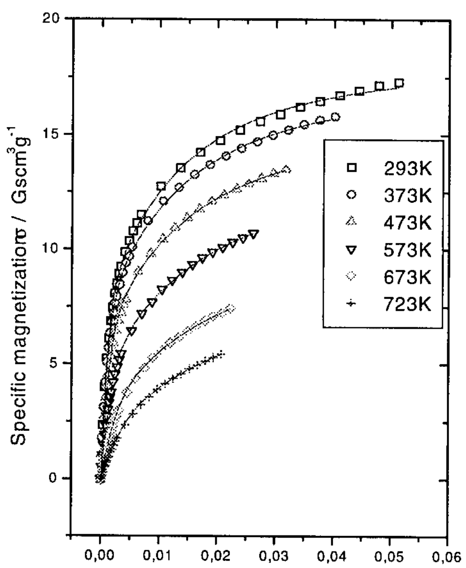

Figure.3: Magnetisation isotherms fitted by two Langevin functions for two fractions of nanocrystals

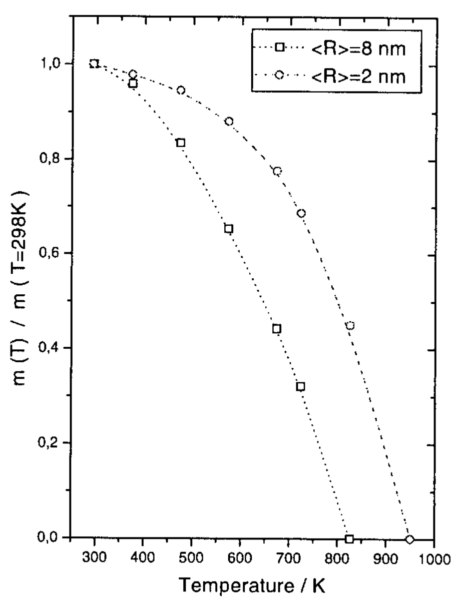

Figure 4: Thermal variation of magnetic moments for two fractions of nanocrystals with $T_{c1} \approx 950$K and $T_{c2} \approx 830$ K

These results allow to explain the variation of the specific magnetisation σ in an external field H measured at different temperatures between 293 K and 723 K is reported in Fig. 3 as a function of (H/T). For monodisperse superparamagnetic systems σ/σ_∞(H/T) should present one single master curve, which is not observed. Instead the curves of Fig. 3 are well described by two Langevin functions representing two fractions of superparamagnetic particles of different size. The solid lines in Fig. 3 represent fits with $\langle R_1 \rangle = 2$ nm and $\langle R_2 \rangle = 5$ nm and volume fractions of $f_1 = 0.09$ and $f_2 = 0.10$ with nearly identical moments $m_0 = 3.72 \pm 0.2\ \mu_B$ at 293 K. These values compare favourably with those of the SANS data. However, as shown in Fig. 4. the temperature variation of the spontaneous moment obtained from the fits in Fig. 3 are different for both fractions indicating different Curie-temperatures $T_{c1} \approx 950$ K and $T_{c2} \approx 830$ K. This analysis supports quantitatively the coarse model of a magnetic inactive layer formed around the magnetic nanocrystals during the crystallisation process. It shows that the size of the magnetic core is uniquely correlated with that of the whole particle. The thickness of the non-magnetic interface grows with increasing core-size.

The nature of the interface is not fully clear. Oxidation of Fe_3O_4 to antiferromagnetic Fe_2O_3 at the surface cannot be ruled out though no such crystallographic phase has been found in TEM or X-ray diffraction (1,2). More likely, the complicated structure of the cubic spinel might be strongly distorted at the growing zone. For the large fraction of surface atoms present in the extremely small particles, ferromagnetic and antiferromagnetic interactions are no longer completely balanced as in the bulk and the competition prevents long-range magnetic ordering, i.e. the spontaneous magnetic moment in the surface layer might be reduced to zero. This is supported by the thickness of about 1nm observed for the non-magnetic shell in the largest particles which is similar to the lattice parameter (0.8 nm) of the cubic spinel structure. The observed size dependence of the Curie-temperatures might then be ascribed to the sensitivity of the exchange couplings to variations of atomic distances.

In summary, SANS revealed a bimodal volume distribution of nanocrystalline magnetite Fe_3O_4 embedded in the glass ceramic where both fractions are composed by a superparamagnetic core surrounded by a non-magnetic surface layer.

References

1. Müller, R.,Schüppel,W., J. Magn. Magn. Mater. 1996, 155, 110-112
2. Hoell, A., Kranold, R., Lembke, U., Brückner, R., Müller, R., Görnert, P., Schüppel, A., Ber. Bunsenges. Phys.Chem.,1996, 100, 146-160
3. Lembke, U., Hoell, A., Kranold, R., Müller, R., Goerick, G., Gilles, R., Wiedenmann, A., submitted (1998) J. Appl. Phys.
4. Keiderling, U.,Wiedenmann, A., Physica B, 1995, 213&214, 895-897
5. Glatter, O., J. Appl. Cryst., 1980, 13, 7-11
6. Kohlbrecher, J., Wiedenmann, A., Wollenberger, H., Z. Physik, 1997, 104, 1-4
7. An additional magnetic contribution, see ref. (6), is expected for A(Q) with the contrast $\Delta\eta_{mag}^2 = 2\ (0.27\ m_0 10^{-12}\text{cm}\ m_0 / \mu_B\ \Omega_{at})^2\ L(x)/x$, which vanishes for large x, i.e. at large values of H. This weak magnetic contribution to A(Q) for small x corresponding to small particles is masked by the strong nuclear scattering contribution .

Pergamon

NanoStructured Materials, Vol. 12, pp. 605–608, 1999
Elsevier Science Ltd

0965-9773/99/$–see front matter

PII S0965-9773(99)00197-X

LOCAL ATOMIC CORRELATIONS OF BULK AMORPHOUS ZrTiCuNiBe ALLOYS

U. Gerold, A. Wiedenmann, R. Bellissent*, M.-P. Macht, H. Wollenberger
Hahn-Meitner-Institut, Berlin GmbH, Glienickerstr. 100, 14109 Berlin, Germany
* Laboratoire Léon Brillouin, C.E.Saclay (Paris), 91191 Gif-sur-Yvette Cedex, France

Abstract -- *Samples of bulk amorphous $Zr_{41}Ti_{14}Cu_{12.5}Ni_{10}Be_{22.5}$ and two related alloys have been heat treated in the supercooled liquid state and above the crystallization temperature. Wide angle neutron scattering experiments lead to very similar total structure factors S(Q) for both states. They show the characteristic modulations of amorphous material. The total pair correlation functions g(R) obtained by Fourier transformation of S(Q) exhibit three main groups of peaks corresponding to the coordination shells. For all samples and heat treatments the total coordination numbers for the first coordination shell are $Z=12 \pm 0.7$ indicating a dense packing of the atoms. By assigning pair correlations to the different maxima in g(R) partial coordination numbers of Be and Zr were estimated. ©1999 Acta Metallurgica Inc.*

Introduction and Experimental

$Zr_{41}Ti_{14}Cu_{12.5}Ni_{10}Be_{22.5}$ (alloy V) belongs to the bulk amorphous alloys which are rather stable against crystallization. Differential Scanning Calorimetry with a heating rate of 20 K/min revealed a wide temperature range for the supercooled liquid (SCL) state between the glass temperature $T_g = 625$ K and $T_{x1} = 705$ K where the first crystallization step occurs (1). For samples annealed in the SCL state, X-ray diffraction and transmission electron microscopy gave no significant evidence for crystalline phases (2,3) whereas small angle neutron scattering exhibits a pronounced scattering profile which was attributed to a decomposed nanoscaled microstructure (4). FIM/AP indicated anticorrelated fluctuations of Ti and Be concentrations (2) corresponding to compositions of $Zr_{41}Ti_{8.7}Cu_{12.5}Ni_{10}Be_{27.8}$ (alloy D1) and $Zr_{41}Ti_{16.5}Cu_{12.5}Ni_{10}Be_{20}$ (alloy D2). The present investigation aims to study the nature of atomic correlations in the as-quenched (a.q.), SCL and the partly crystallized state above T_{x1}.

Bulk ingots of the alloys V, D1 and D2 have been prepared by levitation melting, cut into cylindric samples of 11 mm height and 7 mm in diameter and submitted to different heat treatments in high vacuum ($p < 10^{-4}$Pa). The neutron scattering experiments have been performed at the instrument 7C2 at the LLB Saclay, France, using a wavelength of 0.0705 nm (5). Standard data reduction including background corrections and absolute calibration was performed in the Faber-Ziman formalism (6) leading to the total structure factor S(Q) as presented in Fig. 1a.

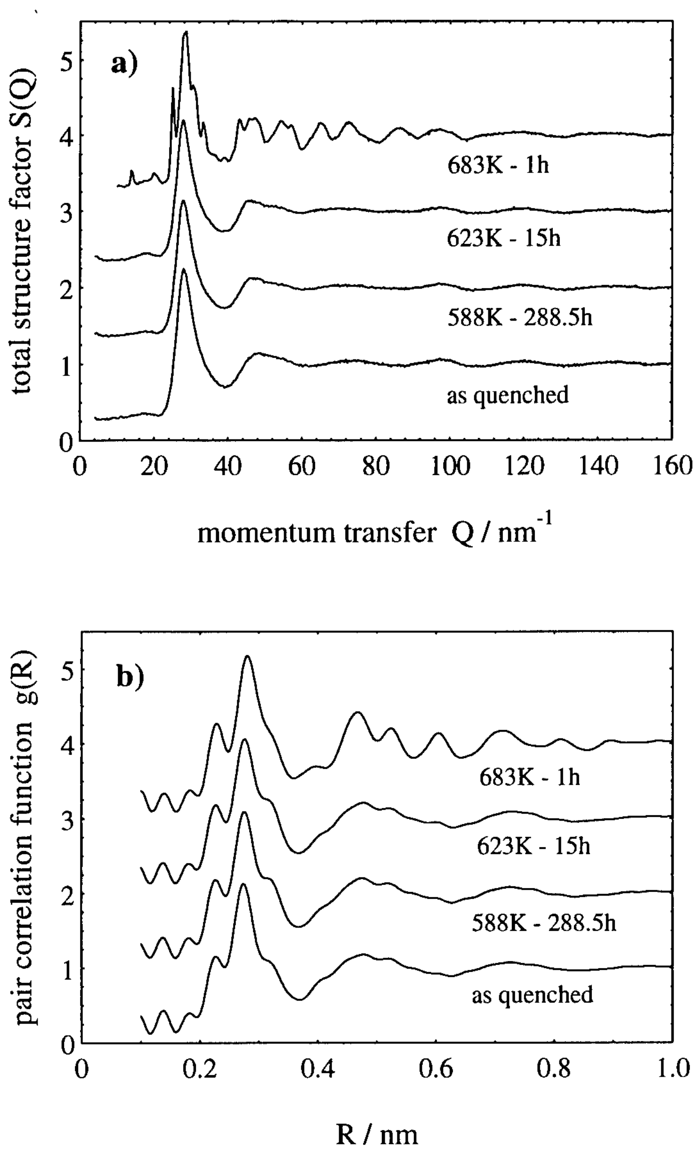

FIGURE 1: Total structure factor (a) and total pair correlation function (b) of $Zr_{41}Ti_{14}Cu_{12.5}Ni_{10}Be_{22.5}$ after different heat treatments. Curves above the bottom curve (as quenched) are shifted by 1, respectively.

Results and Discussion

The total structure factors S(Q) of the three investigated alloys are very similar presenting the characteristic modulations of amorphous materials. No structural change or relaxation between the a.q. and the SCL state was detected. Above T_{x1}, in addition to the diffuse scattering broadened Bragg reflections occur indicating partial crystallization. Fourier transformation of S(Q) leads to the total pair correlation function g(R), see Fig. 1b. Three main groups of peaks centered around 0.28nm, 0.5nm and 0.72nm are observed corresponding to first, second and third neighbour shells. Only for the first shell reliable values of the total coordination numbers Z are obtainied according to $Z = 4\pi\rho\int_0^{RM} R^2 g(R)dR$ (where RM=0.36nm is a cutoff radius of the first shell, and ρ is the atomic density) and reported in Table 1. For all samples and heat treatments Z = 12 ± 0.7 which is indicative for a very dense packing of the atoms in the amorphous state similar to that of the fcc lattice. For the first coordination shell g(R) is well described by three Gaussian profiles as shown in Fig. 2 leading to the positions R1 = (0.226±0.006)nm, R2 = (0.275±0.007)nm and R3 = (0.320±0.008)nm with only minor variations from sample to sample. The radii are very close to those of published data of pair correlations in binary and ternary systems (7,8) or to values derived from Goldsmith radii of the elements as indicated in Fig. 2. From the area of the Gaussians G(r) the partial coordination numbers are obtained according to $Z_{jk} = (4\pi\rho\, c_j / w_{jk}) \int R^2\, G(R)\, dR$ where $w_{jk}=c_jc_kb_jb_k/\langle b\rangle^2$ are the weighting factors and c_j the concentration of the ad-atom. Neglecting indissovable pair correlations with $w_{jk}<0.02$ the partial coordination numbers for Be at R1 (Be-Be, Be-Ni, Be-Cu), Zr at R2 (Zr-Be, Zr-Ni, Zr-Cu) and Zr-Zr at R3 as ad-atoms respectively are reported in Table 1. It should be noted that the observed values of Z(R2) and Z(R3) are certainly underestimated due to the negative contributions from the Zr-Ti correlations (with $w_{Zr\text{-}Ti} < 0$).
The estimation of the partial coordination numbers of only Zr and Be for the first shell is not sufficient for a detailed structural modelling. However, the low values $Z_{jk} \cong 2...4$ indicate the presence of polyhedra with rather low coordinations. Z_{jk} are definetly much lower than 6 expected for first nearest neighbours in the known crystalline hcp phases of Zr, Be or solid solutions with Ti, Ni and Cu and also than $Z_{Zr\text{-}Be}$ ("R2") in crystalline $ZrBe_2$. Latter phase has been identified in "V" by TEM (3) above T_{x1} beside a dominating fcc phase. No significant change of these partial coordination numbers occurs in the different annealing stages (alloy V) and samples with varying composition (alloys D1 and D2).

TABLE 1
Total and partial coordination numbers of heat treated amorphous alloys; for values of R1, R2 and R3 see text.

alloy	annealing temperature	Z	partial coordination number R1	R2	R3
$Zr_{41}Ti_{14}Cu_{12.5}Ni_{10}Be_{22.5}$ "V"	T ≤ Tg	12.1±0.2	1.93 ± 0.1	1.52 ± 0.11	3.46 ± 0.1
	T ≥ Tx	11.5±0.4	1.97 ± 0.8	1.52 ± 0.2	3.27 ± 0.8
$Zr_{41}Ti_{8.7}Cu_{12.5}Ni_{10}Be_{27.8}$ "D1"	T ≤ Tg	12.7±0.1	2.04 ± 0.09	2.20 ± 0.01	3.41 ± 0.04
	T ≥ Tx	12.0±0.1	3.26±0.01	2.42±0.01	2.26±0.01
$Zr_{41}Ti_{16.5}Cu_{12.5}Ni_{10}Be_{20}$ "D2"	T ≤ Tg	12.4±0.2	1.57 ± 0.02	1.13 ± 0.06	4.24 ± 0.15
	T ≥ Tx	12.5±0.1	1.62±0.01	0.91±0.01	4.75±0.01

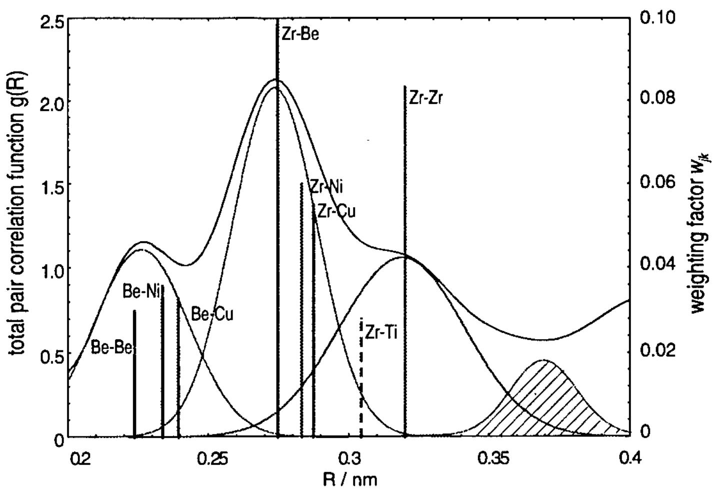

FIGURE 2: Total pair correlation function g(R) of $Zr_{41}Ti_{14}Cu_{12.5}Ni_{10}Be_{22.5}$ (as quenched state) with fitted gaussian functions and mean correlation distances of the relevant elemental correlations (height of bars indicates value of weighting factors, dashed bar = $w_{Zr\text{-}Ti} < 0$)

In summary, in the multicomponent amorphous alloy a dense random packing of the atoms with strong correlation up to third nearest neighbour shells is present. The total coordination number for the first neighbour shell was evaluated to Z = 12 ± 0.7 which is very close to the value expected for long-range ordered fcc structures. Local atomic arrangements are not in accordance with those of known crystalline phases.

Acknowledgment

This work was supported by the European Community via the "Human Capital and Mobility - Access to Large Scale Facilities" program (contract no. ERB CHGECT 920001).

References

1. Johnson, W.L. and Peker, A., *Applied Physics Letters*, 1993, 63, 2342.
2. Macht, M.-P., Wanderka, N., Wiedenmann, A.,Wollenberger, H., Wei, Q. Fecht, H.J. and Klose, S., *Materials Science Forum*, 1996, 225-227, 65.
3. Wanderka, N., Wei, Q., Doole, R., Jenkins, M., Friedrich, S., Macht, M.-P. and Wollenberger, H., *Materials Science Forum*, 1998, 269-272, 773.
4. Wiedenmann, A., Keiderling, U., Macht, M.-P. and Wollenberger, H., *Materials Science Forum*, 1996, 225-227, 71.
5. Ambroise, J.P., Bellissent-Funel, M.C. and Bellissent, R., *Revue de Physique Appliquée*, 1984, 19, 731.
6. Faber, T.E. and Ziman, J.M., *Philosophical Magazine*, 1965, 11, 153.
7. Steeb, S. and Lamparter, P., *Journal of Non-Crystalline Solids*, 1993, 156-158, 24.
8. Wagner, C.N.J., *Journal of Non-Crystalline Solids*, 1992, 150, 1.

Pergamon

NanoStructured Materials, Vol. 12, pp. 609–612, 1999
Elsevier Science Ltd

0965-9773/99/$–see front matter

PII S0965-9773(99)00198-1

NEW Gd-Al NANOPHASE OBTAINED BY CRYSTALLIZATION OF Gd_4Al_3 METALLIC GLASS

V. Petkov[1], T. Spassov[2], S. Suriñach[3] and M.D. Baró[3]
[1]Faculty of Physics, Sofia University, Sofia-1126, Bulgaria
[2]Faculty of Chemistry, Sofia University, Sofia-1126, Bulgaria
[3]Dept. Física, Universitat Autònoma de Barcelona, Bellaterra, E08193 (Barcelona), Spain

Abstract.- *Crystallization behaviour of Gd_4Al_3 metallic glass has been studied by X-ray diffraction and differential scanning calorimetry. It has been found that the crystallization of Gd_4Al_3 glass is a two-stage process with the first stage occurring at 710 K - 715 K and the second - at approximately 770 K. The product of the first stage in the crystallization of Gd_4Al_3 glass has been identified as a Gd_4Al_3 nanophase having a primitive tetragonal (t) lattice with parameters a = b =15.4893(8) Å, c = 5.3020(5) Å. Nanophase t-Gd_4Al_3 has been found to decompose into well-known tetragonal Gd_3Al_2 and cubic GdAl, which are the products of the second stage in the crystallization of Gd_4Al_3 glass. The kinetics of the crystallization of Gd_4Al_3 glass and the morphology of t-Gd_4Al_3 nanophase have also been briefly discussed.*

INTRODUCTION

It is well known that the rapid solidification technique allows large departures from equilibrium conditions resulting in extensions of solid solubility limits and formation of non equilibrium or metastable crystalline, quasicrystalline and amorphous alloys (1). Some time ago, a new class of amorphous alloys RE_4Al_3 (RE =Pr,Gd,Tb,Dy), which do not possess stable crystalline counterparts, was produced by this technique (2). Detailed X-ray diffraction studies have shown that the local atomic ordering in RE_4Al_3 glasses does not resemble the one occurring in RE_3Al_2 crystalline compounds which are closest to them in chemical composition (2,3). However, some similarities between the atomic arrangements in RE_4Al_3 glasses and REAl crystalline compounds, have been observed (3). These findings suggest that the crystallization of RE_4Al_3 glasses is quite likely to show some peculiar features with respect to its route and outcomes. On one hand one may expect that signatures of cubic REAL rather than of tetragonal RE_3Al_2 will first appear when RE_4Al_3 glass is heated at high enough temperatures. On the other hand, some rearrangement of the RE_4Al_3 disordered structure may be expected to take place at first and then both tetragonal RE_3Al_2 and cubic REAl to simultaneously emerge as a product of the crystallization process. Other scenarios are also possible. To clarify the situation we undertook a study on the crystallization behaviour of RE_4Al_3 glasses by employing differential scanning calorimetry (DSC) and X-ray diffraction (XRD). We concentrated our efforts on Gd_4Al_3 glass since, among all members of RE_4Al_3 series, it most clearly exhibited the peculiarities we address.

EXPERIMENTAL

Amorphous Gd_4Al_3 ribbons were prepared by rapid solidification on the surface of a rapidly spinning (45m/s) copper wheel under an argon atmosphere. Calorimetric measurements were carried out with Perkin-Elmer DSC7 on 5-10 mg of the material under pure argon atmosphere. XRD experiments were carried out on as-quenched and as-annealed samples to either confirm the amorphous state or to identify the outcomes of the crystallization process. No oxidation of the material was observed after the heat treatments. The XRD patterns were collected on an automated powder diffractometer (SIEMENS compatible) employing Co Kα radiation and scintillation registration

RESULTS

DSC curve for Gd_4Al_3 sample is shown in figure 1. As one can see in the figure the crystallization of Gd_4Al_3 metallic glass occurs as a broad exothermic effect where at least two peaks can be resolved. This observation suggests that the crystallization of Gd_4Al_3 glass is a two-stage process with the first stage occurring at 713 K (position of the first main peak in DSC data) and the second - at approximately 770 K (position of the second peak in DSC data). The overall enthalpy output of the crystallization has been estimated to be of the order of 105 ± 5 J/K. In order to establish the crystalline phases that appear during the different stages of crystallization we performed two kinds of heat treatments. The first, corresponding to the first stage of crystallization, was carried out at low temperatures (685-713K) and the second, corresponding to the second stage, at higher temperatures (715-800K).

The XRD patterns obtained from samples heat treated at low temperatures are presented in figure 2.

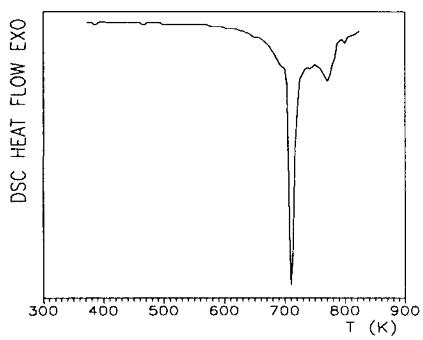

Figure 1. DSC curve of Gd_4Al_3 metallic glass (scan rate 20 K/min).

DISCUSSION

Analyses of the XRD patterns shown in figure 2 revealed that the product of the first step in the crystallization of Gd_4Al_3 glass is a new Gd-Al phase, Gd_4Al_3, that has not been reported so far. The phase has a primitive tetragonal (t) lattice with parameters a=b=15.4893(8) Å, c=5.3020(5) Å. All diffraction lines, observed and calculated, together with the corresponding Miller indexes and experimental intensities are listed in table 1.

The indexing has been performed with the help of the program TREOR (4). Ge standard (a_{Ge}= 5.6577(8) Å) has been used to account for possible instrumental aberrations. Analyzing figure 2 carefully one may notice that all Bragg lines present are considerably broadened, which indicates that the crystallites of t-Gd_4Al_3 are of relatively small size and/or are under considerable strain. The latter effect was discounted as contributing to the observe line broadening since the XRD lines fitted best with Lorenz-type functions (6). From the integral breadth of selected XRD lines, properly corrected for instrumental broadening, and applying the

formula of Sherrer (6, and refs. therein) we estimated the mean size of the crystallites constituting the bulk of t-Gd_4Al_3. It has been found that t-Gd_4Al_3 obtained by annealing of Gd_4Al_3 glass at 711 K, 713 K and 715 K is constituted (in bulk) of crystallites with a mean size of 70 Å, 80 Å and 90 Å, respectively

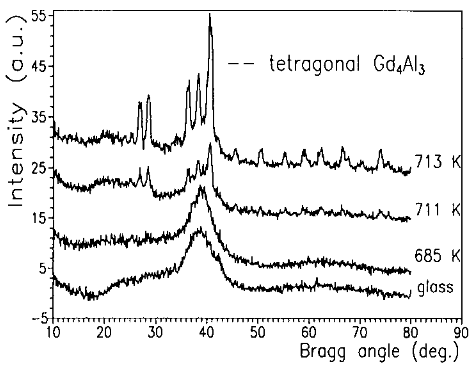

Figure 2. XRD patterns of the product of the first stage of the crystallization of Gd_4Al_3 metallic glass. The corresponding temperature of heat-treatment is indicated.

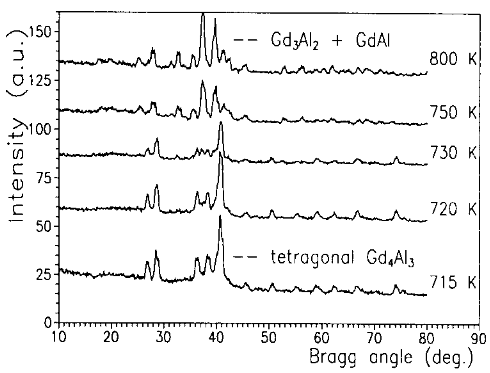

Figure 3. Reflection and transmission geometry XRD patterns of a Gd_4Al_3 sample annealed at 713 K

The size of the crystallites on the surface of the annealed ribbons, estimated on the basis of the XRD data collected in a reflection geometry, has been estimated to be of the order of 400 Å. As these estimates show, the newly observed t-Gd_4Al_3 phase can be unambiguously classified as a nanophase. Also, it obviously emerges and develops with different speeds on the surface and in the bulk of the annealed samples. However, it is worth noting that the newly obtained t-Gd_4Al_3 phase is a metastable Gd-Al phase. It starts to decompose into tetragonal Gd_3Al_2 and cubic GdAl when heated at temperatures higher than 720 K. The decomposition is complete at temperatures as high as 800 K as one can see in figure 3. This fact concours with the DSC results. Thus the crystallization of Gd_4Al_3 glass may be described as a sequence of phase transformations as follows. Up to temperatures of annealing of 685 K the glassy structure remains almost intact. No considerable differences between the XRD patterns of untreated and annealed glassy Gd_4Al_3 are observed (see figure 2, lower part). The correlation between the positions of the atoms constituting these glassy samples extends to interatomic distances no longer than 13 Å - 17 Å (2). When the temperature of annealing approaches 690 K -700 K (the onset of the first peak in the DSC data of figure 1) nanocrystallization takes place with the size of the emerging bulk crystallites being about 70 Å. The apparent activation energy of this event, as estimated by DSC data, is 326 kJ/mol. No substantial growth of t-Gd_4Al_3 nanocrystals is observed upon a further thermal treatment. Instead, a gradual decomposition into tetragonal Gd_3Al_2 and cubic GdAl takes place within the temperature range 720 K - 800 K.

CONCLUSION

Crystallization of Gd_4Al_3 glass is a two-stage process. The product of the first stage is a nanophase with tetragonal lattice and that of the second a mixture of tetragonal Gd_3Al_2 and

cubic GdAl. The reason for this peculiar behaviour is that the parent Gd_4Al_3 glass and the stable crystalline phases Gd_3Al_2 and GdAl are of neither the same chemical composition nor the same structure type. In conclusion, at first, an initial rearrangement of the glassy structure and nanocrystallization take place, followed by the emergence of the stable Gd_3Al_2 and GdAl as the final product of the crystallization.

TABLE 1.
Experimental and calculated positions, d, in Å, Miller indices (hkl) and observed intensities (I) of the XRD lines of the tetragonal Gd_4Al_3. The reliability of the indexing of the XRD lines (de Wolf factor (5)) is M(20) = 13.

Line Number	(hkl)	$d_{obs.}$	$d_{calc.}$	I
1	1 1 1	4.776	4.772	4
2	4 0 0	3.872	3.872	18
3	3 3 0	3.649	3.651	71
4	5 2 0	2.877	2.876	28
5	4 4 0	2.738	2.738	29
6	1 0 2	2.610	2.613	38
7	6 0 0	2.581	2.581	100
8	1 1 2		2.576	
9	2 1 2	2.475	2.476	7
10	6 0 1	2.321	2.321	7
11	4 2 2	2.105	2.105	13
12	8 0 0	1.936	1.936	8
13	6 6 0	1.824	1.825	13
14	8 1 1	1.806	1.806	5
15	6 3 2	1.740	1.741	3
16	8 4 0	1.731	1.732	11
17	7 5 1	1.704	1.704	3
18	3 2 3		1.634	
19	9 3 0	1.632	1.633	14
20	7 3 2	1.613	1.614	4
21	9 3 1	1.560	1.560	4
22	7 5 2	1.489	1.489	20
23	10 0 1		1.487	
24	9 5 1	1.447	1.447	4
25	9 3 2		1.390	
26	10 4 1	1.388	1.387	5
27	12 0 0	1.291	1.291	6
28	5 1 4	1.215	1.215	4
29	13 0 0	1.191	1.191	2
30	12 6 0		1.154	
31	11 5 2	1.153	1.154	4
32	12 6 1	1.128	1.128	4
33	6 4 4		1.128	

ACKNOWLEDGEMENTS

We thanks Dr. V. Skumryev, University of Sofia, Bulgaria for supplying the Gd_4Al_3 glassy samples.

REFERENCES

1. C. Surynarayana and E.N. Froes in *Rapidly quenched alloys*, Marcel Dekker, Inc.,1993, 737.
2. V. Petkov, A. Apostolov and V. Skumryev, *J. Non-Cryst. Sol.*, 1989, 108, 75.
3. V. Petkov, A. Apostolov and V. Skumryev, *J. Non-Cryst. Sol.*, 1989, 110, 184.
4. P.-E. Werner, L. Eriksson and M. Westdahl, *J. Appl. Cryst.*, 1985, 18, 367.
5. P.M. de Wolf, *J. Appl. Cryst.*, 1968, 1, 108.
6. Th.H. de Kieser, J.I. Langford, E.J. Mittemeer and A. Vogels, *J. Appl. Cryst.*, 1982, 15, 308.

Pergamon

NanoStructured Materials, Vol. 12, pp. 613–616, 1999
Elsevier Science Ltd

0965-9773/99/$–see front matter

PII S0965-9773(99)00199-3

BORON CONTAINING NANOPARTICLES AND THEIR CONTRIBUTION TO THE THEORY AND PRODUCTION OF NEW MATERIALS

I. Dragieva, Z. Stoynov and K. Klabunde[1]

Bulgarian Academy of Sciences, CLEPS, 1113 Sofia, Bulgaria
[1] Kansas State Univ., Depart. Chemistry, KS 66506, USA

Abstract-*The nanosized $Co_xB_yH_z$ particles synthesized by the two ('tea' and 'antigravity') methods based on borohydride reduction process have been subjected to additional compositional study in this work. For the particles obtained by 'antigravity' method, the estimated Co/B ratio is around 1.5, which may be due to the substitution of one boron by one hydrogen atom , considering its position as a nearest neighbor atom into cobalt atom surrounding. The compositional studies of particles in respect to boron and hydrogen content stand by such assumption. We suggest the hypothesis that the presence of two states of B 1s electron (as well as of C 1s, N 1s or O 1s) is responsible to the appearance of an amorphous structure in all materials produced and applied as amorphous materials. We suggest the hypothesis the nanocrystalline particles obtained by the 'antigravity' method, containing only 'odd' elements, posses predetermined on a quantum level unusual properties.* ***©1999 Acta Metallurgica Inc.***

INTRODUCTION

The reduction of dissolved metal salts with a solution of sodium or potasium borohydride is a method arousing increasing interest. The preparation of various metal (or alloy), boride (or mixed with hydrides and nitrides) and borate (or mixed with hydroxides) powder particles in the amorphous or crystalline (including nanosized) state is easy and technologically accessible. Different products are obtained and the differences in their properties indicate underestimation of the experimental conditions and equipment used. Several years ago a review appeared on the use of this process for preparation of amorphous monometallic and polymetallic nanoparticles and their application in practice (1).

In addition to the known variations of the process conditions (concentration of mixing solutions, temperature, pH value, pressure, vacum or protecting atmospheres) attention should be paid to the equipment and the design of reactors and apparatuses with special constructions. The nanosized $Co_xB_yH_z$ particles synthesized by the two ('tea' and 'antigravity') methods based on borohydride reduction process have been subjected to additional compositional study in this work.

EXPERIMENTAL

Nanoparticles with the composition $Co_xB_yH_z$ were synthesized from an aqueous solution of a cobalt salt which formed aqua-complex with well known structure using reduction with sodium borohydride at room temperature and a definite pH (or range of pH values) which did not allow the formation of borate shells around the particles (2). Since years work on this

process, using a 'tea' or 'Y' variant of the above method and a specially constructed and patented equipment, along with maintenance of precise control of technological parameters (1), an attempt has been made to change the hydrodynamics of the solutions being mixed (3). We have experimented with the multiplication of the nucleation process by changing the hydrodynamics of the solution and designing a special new apparatus for 'antigravity' method (3). The nanosized $Co_xB_yH_z$ particles synthesized by the two ('tea' and 'antigravity') methods based on borohydride reduction process have been subjected (3, 4) to compositional, structural and magnetic properties studies by means of various techniques.

RESULTS AND DISCUSSION

Data on the investigation of composition, structure and properties of CoxByHz particles obtained by two different ('tea' and 'antigravity') methods are presented in Table 1.

The cobalt to boron atomic ratio demonstrates an interesting fact. About 1.5 atoms of cobalt per boron atom correspond to sample obtained by the 'antigravity' method. In the case of amorphous sample prepared by the 'tea' method two atoms of cobalt per boron atom are found. The same ratio is obtained by chemical and gaseous analyses as mean values for the sample bulk, whereas the XPS data may be defined as surface values of this ratio.

The application of the new 'antigravity' method results in nanosized particles in which the BE (binding energy) of the B 1s electron in boron atoms is only one and has a higher value. This corresponds to the nuclei of the nearest-neighbor atoms coming closer to one another, which has also been estimated on the basis of XRD of these types of powder (a significant shrinkage of the

TABLE 1
Experimental Characteristics of Nanosized Metal Particles Obtained by Means of Two Different Apparatuses

Investigated parametres		Particles obtained by 'tea' method	Particles obtained by 'antigravity' method
Boron	(wt %)	6.02	6.83
Hydrogen	(wt %)	0.495	0.499
Binding energy of B 1s electrons	(eV)	188.5 ; 191.7	191.7
Ratio Co/B	by XPS	1.93	1.44
	by Chem. analysis	2.16	1.04
Shape	by TEM)	ball	angular
Structure	(by SAED, XRD)	amorphous	crystalline
Unit cell vol.	(Co_3B, $Å^3$)	149.792	148.917
Tap density	(g/cm^3)	0.5 – 0.73	0.9 – 1.1
Spec. surf. area	SSA (m^2/g)	9.86	3.25
Coercive force	H_c, (Oe)	60	900
Saturation magnetization	M_s,(emu/g)	32.6	59.6
Squareness	M_r/M_s	0.06	0.76

volume of the unit cell and all lattice parameters (2) to 2.43 %). The amorphous particles obtained under technologically precise conditions by the common, so-called 'tea' method, contain boron atoms whose 1s electrons are connected by two types of BE. Both states (BI 1s, 188.5 eV; BII 1s, 191.7 eV) can be quantitatively equal, especially in the magnetically disordered amorphous state. Both BEs of 1s boron electrons determine the amorphous structure of the nanosized particles. The single value for the BE of the boron 1s electrons fixes a nanocrystalline structure for particles obtained by the 'antigravity ' borohydride method. These particles have smaller cell volumes and lattice constant and considerably stronger magnetic properties, compared with the particles obtained by the 'tea' borohydride method.

For the particles obtained by 'antigravity' method the estimated Co/B ratio is around 1.5, which may be due to the substitution of one boron by one hydrogen atom, considering its position as a nearest neighbor atom into cobalt atom surrounding. The compositional studies of particles in respect to boron and hydrogen content (see Fig. 1 and Fig. 2) stand by such assumption.

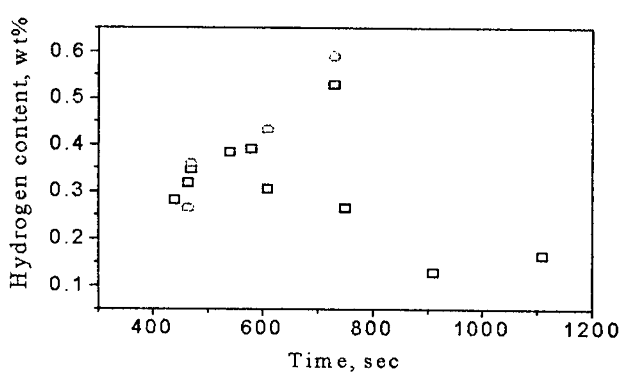

Figure 1. Influence of borohydride reduction time on hydrogen content in (□) amorphous and (○) nanocrystalline $Co_xB_yH_z$

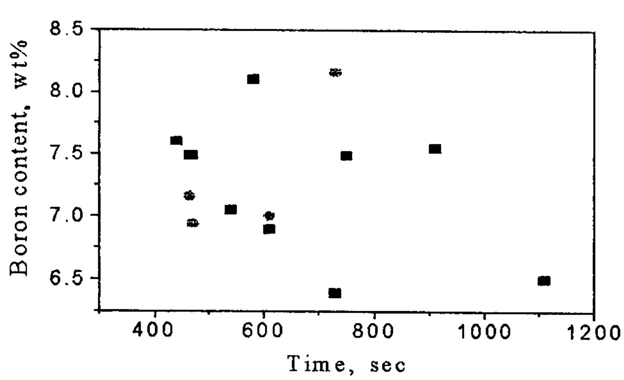

Figure 2. Influence of borohydride reduction time on boron content in (■) amorphous and (●) nanocrystalline $Co_xB_yH_z$ particles

The higher the rate of mixing of solutions, the higher is only the content of hydrogen direct bonded to the cobalt atoms and the higher are all magnetic parameters and evidently the more perfect is the structure of nanoparticles obtained by the 'antigravity' method (4).

CONCLUSION

The new type of reactor and the borohydride method offer opportunities for synthesis of crystalline nanoparticles whose size and chemical content are similar to that of known amorphous particles. The investigations perform uncover the realization of nanocrystalline state while simultaneously fixing the bond between atoms of the closest proximity. The comparative impedance and photon spectroscopy investigations of the state of boron atoms in amorphous materials (5) show that traditionally applied structural methods are not sensitive enough to the structural changes and properties of amorphous materials containing light elements, such as boron and hydrogen. Boron (and hydrogen) containing amorphous magnetic materials proved to be highly sensitive to the inductance (the imaginary part of the impedance) and its the time constant spectra proved to be highly sensitive to the nanostructural changes. The presence of two binding energies of B 1s electrons to boron nuclei is established irrespective of the shape, size, composition, and method of production of the amorphous materials - powders or ribbons (4, 5).

We suggest the hypothesis that the presence of two states of B 1s electron (as well as of C 1s, N 1s or O 1s) is responsible to the appearance of an amorphous structure in all materials produced and applied as amorphous materials. We suggest the hypothesis the nanocrystalline particles obtained by 'antigravity' method, containing only 'odd' elements, posses determined on quantum level unusual properties.

ACKNOWLEDGMENTS

This work has been accomplished with the partial financial support of the NSF-USA, Project INT-9727193 and the NSF-Bulgaria, Project X708.

REFERENCES

1. Dragieva, I., *Amorphous metal magnetic powders obtained by borohydride reduction process*, Dr. Sc. Thesis, 1992, Sofia, Bulgaria.
2. Dragieva, I., Mehandjiev, D., Lefterova, E., Stoycheva, M. and Stoynov, Z., *J. Magn. Magn. Mat.*, 1995, **140–144,** 457.
3. Dragieva, I., Mazdrakov, P. and Stanimirova, M., *IEEE Trans. Magnet.*, 1992, **MAG 28,** 3183.
4. Krastev, V., Stoycheva, M., Lefterova, E., Dragieva, I. and Stoynov, Z., *J. Alloys and Comp.*, 1996, **240,** 186.
5. Dragieva, I., Stoynov, Z., Nikolaeva, I. and Krastev, V., *J. Solid State Chem.*, 1997, **133,** 273.

Pergamon

NanoStructured Materials, Vol. 12, pp. 617–620, 1999
Elsevier Science Ltd

0965-9773/99/$–see front matter

PII S0965-9773(99)00200-7

NANOSTRUCTURE AND MICROHARDNESS OF $AL_{86}NI_{11}YB_3$ NANOCRYSTALLINE ALLOY

G.E Abrosimova, A.S.Aronin, Yu.V.Kir'janov
Institute of Solid State Physics RAS, Chernogolovka, Moscow distr., 142432, Russia

T.F.Gloriant, A.L.Greer
University of Cambridge, Department of Materials Science & Metallurgy
Pembroke Street, Cambridge CB2 3QZ, England

Abstract – *Nanocrystalline structure formation and properties of $Al_{86}Ni_{11}Yb_3$ alloy were studied by DSC, X-ray diffraction, transmission and high resolution electron microscopy and microhardness measurements. The nanocrystalline structure was produced by annealing of the amorphous alloy at 473 K for different times. It consists of Al nanocrystals dispersed in an amorphous matrix. The nanocrystal size is about 10 nm. The average grain size of the nanocrystals increases slightly with annealing time. The microhardness of the nanocrystalline structure is higher than that of the initial amorphous alloy. The microhardness increases to 4 GPa during the annealing. The fine structure of the nanocrystals and their mutual arrangement have been studied. ©1999 Acta Metallurgica Inc.*

INTRODUCTION

Light Al- and Mg-based nanocrystalline alloys produced by controlled crystallization of metallic glasses have generated considerable interest. This method was used for production of nanocrystalline alloys with high strength and ductility in some Al-TM-RE systems (TM = transition metal, RE = rare earth metal). The tensile strength at room temperature was found to be as high as 1.6 GPa combined with good bending ductility (1). Structure and properties of nanocrystalline alloys were reported for Al-Ni-RE (RE = Y, Nd, Ce) systems (2-4).

The aim of this paper was to study the nanocrystalline structure produced by crystallization of amorphous $Al_{86}Ni_{11}Yb_3$ alloy, structure evolution during the isothermal annealing, mechanical properties and structure/property correlations.

EXPERIMENTAL

Amorphous ribbons of $Al_{86}Ni_{11}Yb_3$ alloy were produced by melt quenching. The ribbons obtained were typically 3 mm wide and 40 μm thick. Differential scanning calorimeter (Perkin-Elmer DSC-7) was used for isothermal annealing and for investigation of crystallization kinetics. The heating rate was 20 and 40 K/min, isothermal annealing was carried out at 473 K

for 5, 15, 30, 45 and 60 min. An evaluation was made of the percentage volume fraction of nanocrystalline α-Al transformed during different annealing times using the enthalpy of formation calculated from the first DSC peak according to the method proposed in (5). The structures of as-prepared and annealed samples were studied by X-ray diffraction using a Siemens D-500 diffractometer and by transmission and high resolution electron microscopy using JEM-100CX and JEOL-4000 EX (U = 400 kV) electron microscopes. The sizes of the nanocrystals were determined from dark field TEM images. Vickers testers were used with a 0.2 N load for the microhardness measurements.

RESULTS AND DISCUSSION

According to diffraction data, the as-prepared samples were fully amorphous. The DSC curve of $Al_{86}Ni_{11}Yb_3$ alloy is shown in fig. 1a. The DSC trace shows three exothermic peaks. The first peak corresponds to primary crystallization of α-Al; this peak is spread over a large temperature range. The remaining peaks correspond to formation of intermetallic phases.

To study the structure and properties of $Al_{86}Ni_{11}Yb_3$ alloy, samples were annealed at 473 K for different times. Nanocrystalline α-Al was found to form during the annealing. Fig. 1b shows a set of X-ray diffraction patterns for the samples annealed for 5, 15, 30 and 60 min. The fraction of crystalline phase is seen to increase with the annealing time. Volume fraction of α-Al crystals in amorphous matrix was evaluated by investigation of the first DSC peak evolution after different steps of annealing. Fig. 2a shows the volume fraction of α-Al crystals in the amorphous matrix. The average grain size slightly increases during the annealing (fig. 2a). The dependence of microhardness on annealing time (fig. 2b) correlates with appropriate dependence of the volume fraction of α-Al crystals in amorphous matrix. Microhardness increases more than doubles, reaching 4 GPa during the annealing.

The structure of nanocrystalline alloys consists of two phases: Al crystals and amorphous matrix. In most cases the nanocrystals are arranged separately, they have no direct contact with each other. This structure is shown in fig. 3a. In some cases groups of nanocrystals can be observed, these nanocrystals border each other. Al nanocrystals, as a rule, are free from defects (fig.3a) (dislocations, stacking faults, microtwins), some nanocrystals consisted of twinned parts were observed in $Al_{86}Ni_{11}Yb_3$ alloy as well (fig. 3b).

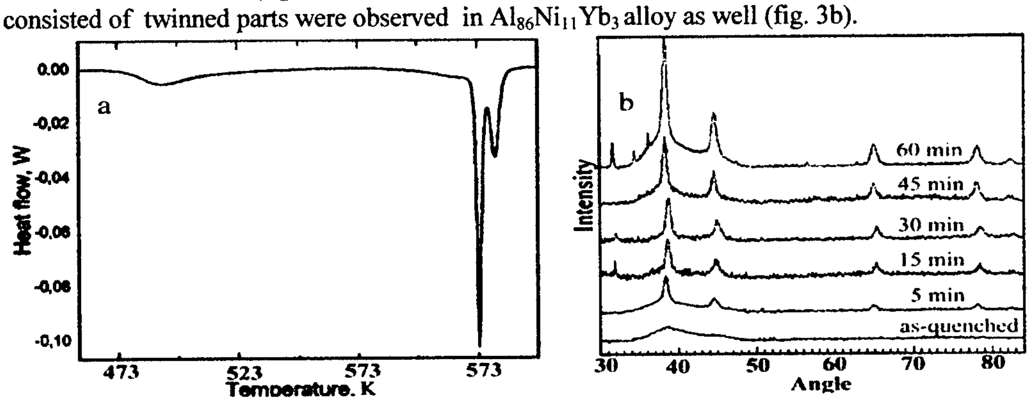

Fig.1. DSC curve (a) and evolution of X-ray diffraction spectra (b) of $Al_{86}Ni_{11}Yb_3$ alloy

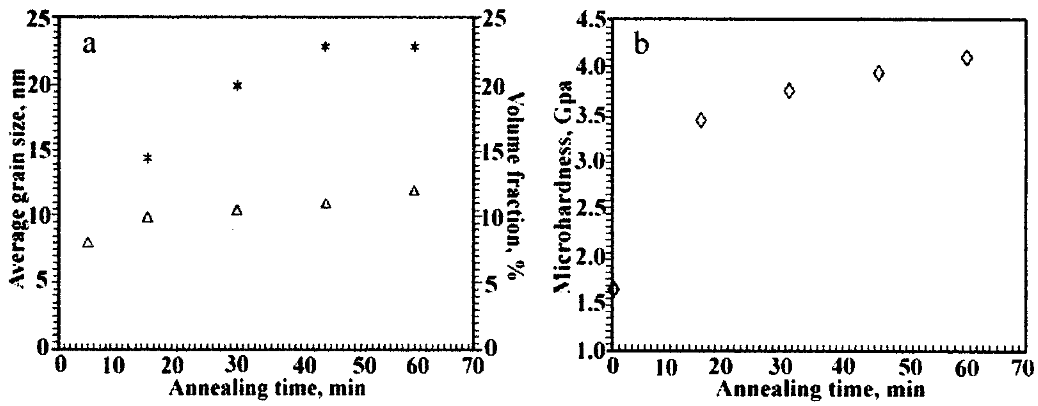

Fig. 2. The dependencies of average grain size (Δ), volume fraction (*) (a) and microhardness (b) of $Al_{86}Ni_{11}Yb_3$ alloy on the annealing duration

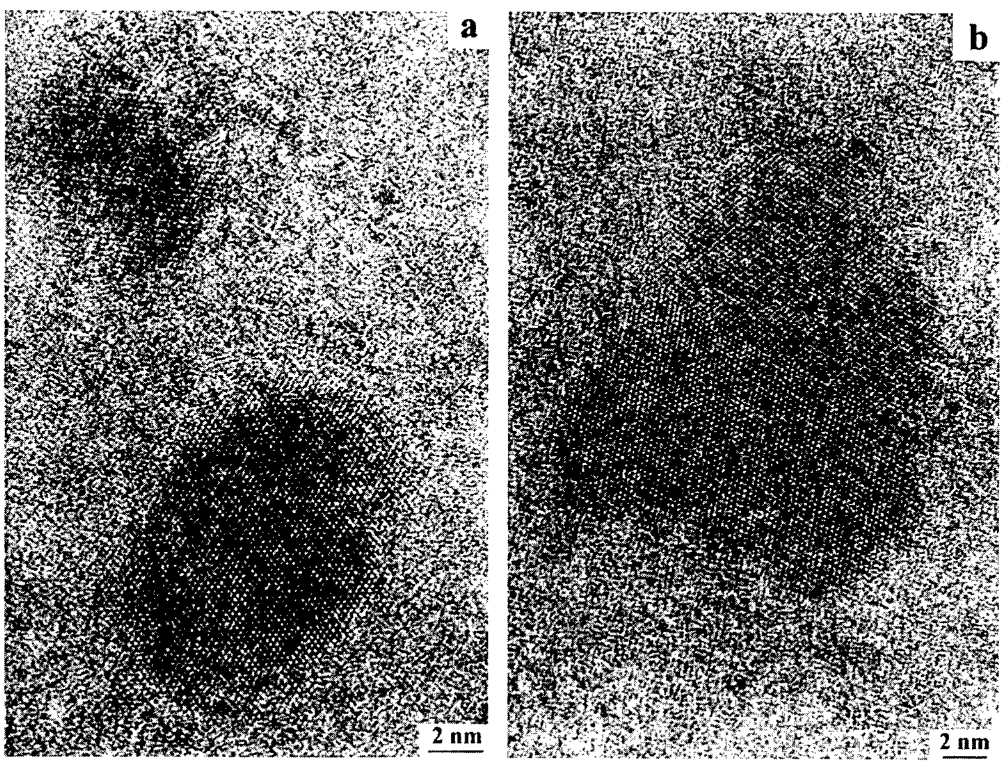

Fig. 3. HREM images of defect-free (a) and twinned (b) Al nanocrystals

The increase of microhardness during the annealing (together with the increasing of grain size and volume fraction of the nanocrystals) has been already observed (3,6). This dependence is generally related to a strengthening of the remaining amorphous matrix. The strengthening occurs due to enriching of amorphous matrix in Ni and Yb at the initial stage of crystallization when the nanocrystals form and grow. The chemical composition of amorphous matrix should be about $Al_{82}Ni_{14}Yb_4$ when it is considered that all atoms of Ni and Yb are located in the amorphous matrix (both components are insoluble in Al) and the volume fraction of Al nanocrystals is about 23% (fig. 2a). Increase of Ni and Yb concentrations in the amorphous matrix will lead to its strengthening. The similar situation was observed for Al-Ni-Y alloy and it was studied in detail in (3). Of course, defect-free nanocrystals of Al may also contribute to strengthening of the alloy. Unfortunately we don't know the microhardness value of the amorphous phase with the same chemical composition ($Al_{82}Ni_{14}Yb_4$) and we cannot make conclusions whether the defect-free nanocrystals significantly strengthen the alloy. This effect cannot be excluded from consideration for the moment. It should be noted that the dependence of microhardness on (Ni + Yb) concentration in amorphous matrix is more sharp than the dependence of microhardness on (Ni + Y) concentration in $Al_{86}Ni_{11.67}Y_{2.33}$ (3).

CONCLUSIONS

Primary crystallization of amorphous $Al_{86}Ni_{11}Yb_3$ alloy leads to the nanocrystalline structure formation. The average grain size of nanocrystalline structure is about 10 nm and slightly increases with annealing time increasing. Correlations between grain size, volume fraction of crystalline phase and microhardness were observed.

REFERENCES

1. Kim, Y.H., Inoue, A., Masumoto, T., *Materials Transactions. JIM,* 1991, 32, 331
2. Tsai, A., Kamiyama, T., Kawamura, Y., Inoue, A., Masumoto, T., *Acta Materialia*, 1997, 45, 1477
3. Zhong, Z.C., Jiang, X.Y., Greer, A.L., *Materials Science and Engineering*, 1997, A226-228, 531
4. Inoue, A., Ochiai, T., Horio, Y., Masumoto, T., *Materials Science and Engineering*, 1994, A179/A180, 649
5. Inoue, A., Tomioka, H., Masumoto, T., *Journal of Materials Science*, 1983, 18, 153
6. Choi, G.S., Kim, Y.H., Cho, H.K., Inoue, A., Masumoto, T., *Scripta Metals and Materials*., 1995, 33, 1301

Pergamon

NanoStructured Materials, Vol. 12, pp. 621–624, 1999
Elsevier Science Ltd

0965-9773/99/$–see front matter

PII S0965-9773(99)00201-9

PHASE TRANSFORMATIONS IN NANOCRYSTALLINE MECHANICALLY ALLOYED Ni-Mo POWDERS

D.Oleszak, V.K.Portnoy[1], H.Matyja
Dept.of Mater.Sci.& Eng., Warsaw University of Technology
Narbutta 85, 02-524 Warsaw, Poland
[1]Dept.of Chemistry, Moscow State University, Moscow, Russia

Abstract -- *The mechanical alloying process of Ni-20 at.% Mo powder mixture led to the formation of fcc Ni(Mo) solid solution, characterized by lattice parameter of 0.3612 nm, crystallite size 30 nm and lattice strain 0.8%. The synthesis in argon of Ni-43 at.% Mo alloy, both under high and low energy conditions, resulted in the formation of two-phase structure: amorphous + nanocrystalline Mo. The presence of oxygen during milling in air and with addition of ethanol, reduced the structure refinement and formation of Ni(Mo) solid solution. Moreover, the amorphous structure was not observed in this case.* ©1999 Acta Metallurgica Inc.

INTRODUCTION

Ni-Mo based alloys are widely used in the industry due to their good electrocatalytic properties. However, many investigations are aimed towards improving these properties. It can be achieved by changing the structure of the alloys from microcrystalline into nanocrystalline one (1-3). Among the possibilities of producing nanostructured materials is mechanical alloying (MA) technique. Recently it has been shown that introducing some amount of oxygen to the alloy microstructure, considerably improves its electrocatalytic properties (4). However, the influence of oxygen on phase transformations has not been studied yet.

The aim of this work was to investigate the phase transformations in the Ni-Mo alloys produced by high and low energy MA. The influence of milling environment (argon, air, ethanol) on phase transformations during low energy milling was studied as well.

EXPERIMENTAL

Powders of crystalline Ni and Mo with a purity of 99.9 % and particles sizes less than 100 μm were used for the experiments. The powders were mixed to give the desired Ni-20 and 43 at.% Mo. The MA processes were performed in a Fritsch P5 planetary ball mill rotating at a speed of 240 rpm and in low energy rotational mill. The ball-to-powder weight ratio was 10:1 and 40:1, respectively. Stainless steel vials and balls were used. All powder handling was performed in a glove box under argon atmosphere. X-ray diffraction (XRD) and differential scanning calorimetry (DSC) were employed as experimental techniques.

RESULTS AND DISCUSSION

Fig.1 shows a sequence of XRD patterns registered for Ni-20 at.% Mo powders after increasing MA time. The diffraction lines corresponding to the bcc Mo become weak and disappear after 50h of processing. However, even after prolonged milling the trace of the strongest Mo(110) line is visible. Simultaneously the fcc Ni lines become broad and shift to the low angle side of the spectrum with increasing milling time. This shift can be attributed to the increase of lattice parameter of the fcc Ni due to the dissolving of molybdenum atoms and formation of the fcc Ni(Mo) solid solution. The value of this lattice parameter calculated from the shift of Ni(311) line after 100h of MA reaches 0.3612 nm, compared with 0.3524 nm for pure fcc Ni.

The observed broadening of the diffraction lines after MA can be attributed to the refinement of crystal size and increase in internal strains. The minimum crystallite size and the maximum strain level of the fcc Ni(Mo) solid solution, calculated by Williamson-Hall method, are about 30 nm and 0.8%, respectively (Fig.2).

Heating in the DSC the sample after 50h MA up to 1000 K results in the increase of the Ni(Mo) crystallites size only. The decomposition of the fcc Ni(Mo) solid solution and formation of the equilibrium Ni_4Mo phase is not observed.

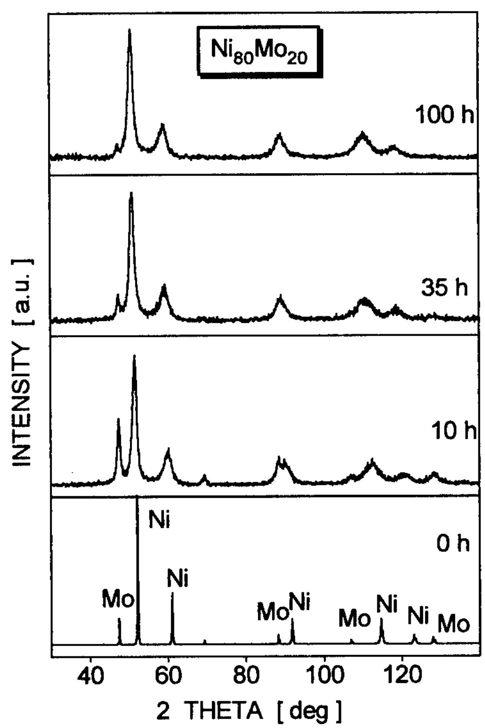

Fig.1. XRD patterns of Ni-20 at.% Mo alloy for increasing milling time.

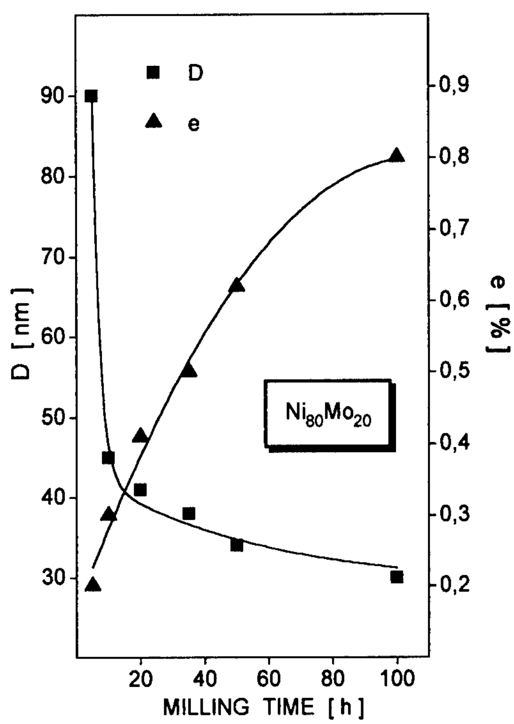

Fig.2. The dependence of average crystallite size and lattice strain in the fcc Ni(Mo) solid solution on processing time.

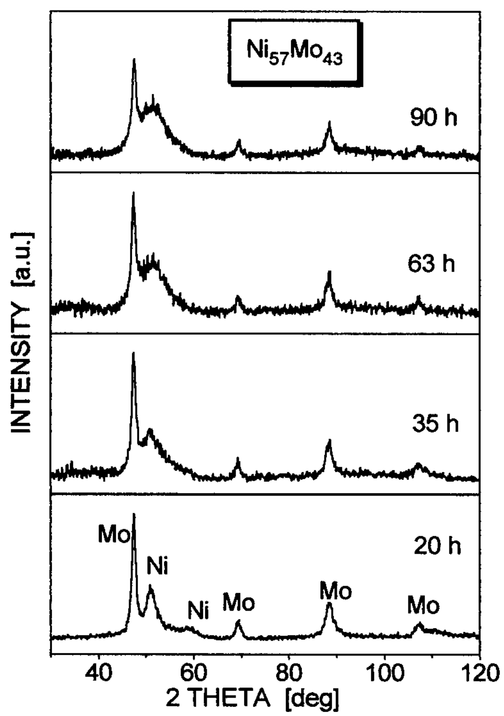

Fig.3. XRD patterns of Ni-43 at.%Mo alloy for increasing processing time.

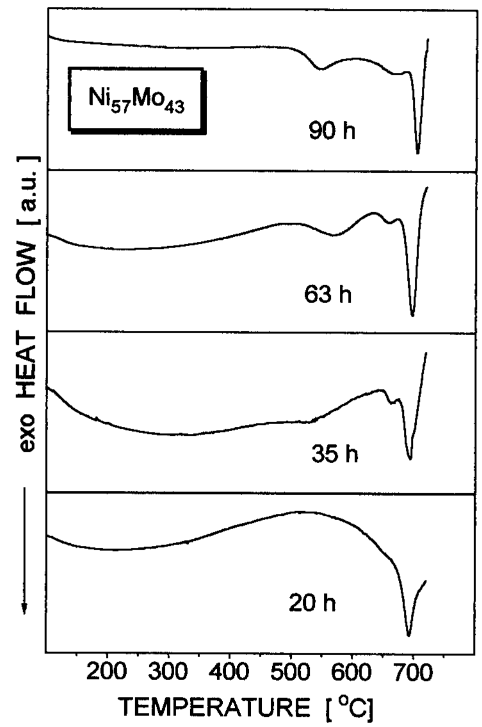

Fig.4. DSC curves registered for Ni-43 at.% Mo samples after various milling times.

XRD patterns registered for Ni-43 at.% Mo powders milled under argon in Fritsch device are shown in Fig.3 and one can conclude that starting powder mixture subjected to 63 h MA transforms into a two-phase structure: amorphous + residual nanocrystalline Mo. Prolonged milling up to 90 h does not introduce further changes into the microstructure obtained.

At the early stage of processing the formation of the fcc Ni(Mo) solid solution is observed. After 20 h MA the lattice parameter of Ni(Mo) increases up to 0.3609 nm, compared with 0.3524 for pure Ni. According to (5), the obtained value corresponds to about 21 at.% Mo soluted. The strong broadening of high angle diffraction lines does not allow for a precise measurements of the Ni(Mo) lattice parameter after long term MA.

The lattice parameter of Mo decreases to 0.3143 ± 0.0001 nm after 35 h MA, however, prolonged processing results in obtaining the value corresponding to that of starting pure Mo, i.e. 0.3148 nm. This behaviour can be attributed to the increase of vacancies density and their subsequent relaxation, when the crystallites size of Mo significantly decreases.

The average crystallites size of Ni(Mo) and Mo, calculated from the broadening of the diffraction lines, decreases upon 20 h milling down to 10 and 30 nm, respectively. However, the final crystallites size and lattice strain of Mo after 90 h of processing reaches 20 nm and 0.6%, respectively.

The observed exothermic effects at the DSC curves (Fig.4) are attributed to the crystallization processes of the synthesized amorphous phase.

The MA processes performed in a low energy rotational mill for the same composition of starting powder mixture (Ni-43 at.% Mo) under argon atmosphere result in the formation of structure very similar to that from Fritsch device, consisting of Mo nanocrystals (12 nm after 600h of milling) embedded in an amorphous matrix. Before amorphization, after 300h of milling, the lattice parameter of the fcc Ni(Mo) solid solution exhibits the value of 0.3555 nm.

Completely different behaviour of the same powder mixture subjected to milling is observed when the MA process is performed in air. The formation of the fcc Ni(Mo) solid solution is very limited. The value of lattice parameter increases up to 0.3528 nm only. Also the process of the refinement of microstructure is significantly reduced. The final Mo and Ni crystallites size after 600h of processing are 17 and 9 nm, respectively. Simultaneously there are no traces of amorphization of the alloy.

When ethanol is added to the powder mixture, the fcc Ni(Mo) solid solution is formed as well. This solid solution is characterized by the value of lattice parameter of 0.3532 nm, i.e. higher than for milling in air. The mean crystallite sizes obtained by Scherrer's formula for Mo and Ni(Mo) are 30 and 12 nm, repectively.

CONCLUSIONS

High energy MA of Ni-20 at.% Mo powder mixture under argon atmosphere resulted in the formation of the fcc Ni(Mo) solid solution with lattice parameter of 0.3612 nm. The minimum crystallite size and the maximum strain level of this solid solution were 30 nm and 0.8%, respectively.

Processing under the same conditions of Ni-43 at.% Mo mixture led to the formation of two-phase structure: amorphous + nanocrystalline Mo, which exhibited crystallite size and lattice strain of 20 nm and 0.6%, respectively.

Under low energy milling conditions, the formation of the fcc Ni(Mo) solid solution was also confirmed. However, the presence of oxygen (milling in air and with addition of ethanol) slowed down the solid solution formation and reduced the microstructure refinement.

ACKNOWLEDGEMENTS

The financial support of the Polish State Committee for Scientific Research under the contract No T08A 010 12 is gratefully acknowledged.

REFERENCES

1. Schulz, R., Huot, J.Y., Trudeau, M.L., Dignard-Bailey, L., Yan, Z.H., Jin, S., Lamarre, A., Ghali, E. and Van Neste, A., *J.Mater.Res.*, 9, 2998 (1994).
2. Rose, P., Banda, D.E., Cowlam, N. and Enzo, S., *Mater.Sci.Forum*, 179-181, 787 (1995).
3. Oleszak, D., Portnoy, V.K. and Matyja, H., *Phil.Mag.B*, 76, 639 (1997).
4. Alves, H., Ferreira, M. and Köster, U., *Mater.Sci.Forum*, 179-181, 449 (1995).
5. Kayser, C.F., *J.Mater.Sci.*, 24, 2677 (1989).

Pergamon

NanoStructured Materials, Vol. 12, pp. 625–628, 1999
Elsevier Science Ltd

0965-9773/99/$–see front matter

PII S0965-9773(99)00202-0

NANOCRYSTALLINE BCC SOLID SOLUTIONS OF Al–Fe-V SYSTEM PREPARED BY MECHANICAL ALLOYING

[a]V.I.Fadeeva, [a]V.K.Portnoy, [b]Yu.V.Baldokhin, [b]G.A.Kotchetov and [c]H.Matyja

[a]Dept. of Chem., Moscow State University, Russia
[b]Semionov Institute of Chemical Physic, RAN, Russia
[c]Dept. of Mat. Sci. & Eng., Warsaw University of Technology, Poland

Abstract *- Solid state reactions in $Al_{50}Fe_{50}$, $Al_{50}Fe_{45}V_5$ and $Al_{50}Fe_{25}V_{25}$ powder mixtures by mechanical alloying (MA) and following annealing were studied. MA was performedin the high energy planetary ball mill in an argon atmosphere. X-ray diffraction (XRD) and Mössbauer spectroscopy (MS) methods were used. It was established that the partially ordered solid solution of B2 type has been formed in the $Al_{50}Fe_{50}$ alloy and the BCC (A2) phase has been formed in the V containing alloys. According to MS one can conclude that the short range order of B2 type in the mechanically alloyed $Al_{50}Fe_{45}V_5$ and $Al_{50}Fe_{25}V_{25}$ alloys was presented too. MA phases were characterised by a crystallite size of 10 nm. Annealing at 750°C for 2h of mechanically alloyed $Al_{50}Fe_{50}$ and $Al_{50}Fe_{45}V_5$ resulted in the formation of completely ordered B2 phases. After annealing of the $Al_{50}Fe_{25}V_{25}$ alloy the A2 structure transformed in two phases – with B2 and $D8_a$ structure.* ©1999 Acta Metallurgica Inc.

INTRODUCTION

The study of the influence of transitional metal addition on the ordering of $Al_{50}Fe_{50-x}Me_x$ solid solution is relevant for the development of the technology of nanocrystalline intermetallic by MA method.

Formation of the ordered B2 phase by MA of the metal component mixture was found in Al-Fe-Ni system [1-3]. The strong tendency towards ordering of Al-Fe-Ni alloys can be explained by the large negative enthalpy value for the formation of the AlNi (B2) phase. Although of the B2 structure for mechanically alloyed $Al_{50}Fe_{50}$ has not been displayed by XRD, some DSC and MS results [4-5] indicated the local ordering of Al-Fe solid solutions.

EXPERIMENTAL

All samples were prepared using Al, Fe and V of a purity of 99.96% with the particle size of ~100 nm. The powders were mixed to give $Al_{50}Fe_{50}$, $Al_{50}Fe_{45}V_5$ and $Al_{50}Fe_{25}V_{25}$ initial compositions. MA was performed in a water cooled planetary ball mill in an argon atmosphere. Stainless vial and balls were used.

XRD investigations were performed on Philips-1830 and DRON-4 diffractometers using Cu K_α or Co K_α monochromatic radiation in step scanning mode with $\Delta(2\Theta)$=0.01, Δt =5 s for an analysis of (100) superlattice and the (110) fundamental line intensity for the long range order (LRO) definition. Lattice parameters were determined by the square fit with the angle correction function ($\Delta a = \pm\ 0.0001$ nm). Mean crystallite size D and average microstrains $<\varepsilon^2>^{1/2}$ were quantified by the Cauchy-Gauss method using (110) - (220) or (211) diffraction lines. The errors were estimated to be Δ D $\cong$ 10% and $\Delta<\varepsilon>\ \cong$ 15%.

Mössbauer measurements were carried out using and ^{57}Co (Cr) source. The processing of the MS results was performed by means of the software "NORMOS". There were determined isomer shift (δ) relative to α-Fe with an error of $\pm$0.02 mm/s and quadrupole splitting (Δ) with an error of $\pm$0.05 mm/s.

RESULTS AND DISCUSSION

Solid state reaction by MA of $Al_{50}Fe_{50}$ and $Al_{50}Fe_{50-x}V_x$ (x=5 and 25 at.%) powder mixtures resulted in the formation of BCC (A2) solid solutions (Fig.1). The diffraction lines of initial metals became weak already after 1h of MA and disappeared after 3h of MA..

Fig. 2 shows the evolution of the lattice parameters of the BCC phase during milling. The lattice parameter of the A2 phase in which all three components were dissolved of the alloy is larger than the α-Fe parameter and smaller than the V one. The parameter reached an almost constant value at the initial stage of the A2 phase formation and it was not significantly changed during following milling. The lattice parameter of the $Al_{50}Fe_{50}$ alloy decreased slightly down to 0.2907 nm after 6h of milling when the (100) superlattice line of B2 structure appeared in the X-ray diffraction pattern (Fig.1a). As the unit cell volume of the ordered AlFe phase is smaller then disordered one the mean lattice parameter of the solid solution may decrease during the ordered regions formation. After an annealing at 750° C during 2h the LRO parameter increased up to 0.8 and the lattice parameter was equal to 0.2902 nm that is close to the lattice parameter of completely ordered equilibrium AlFe (0.2896 nm [6]).

MS data indicated that the solid state reaction between the alloy components finished already after 4h of MA. It could be detected by the disappearance of the magnetic sextet corresponding to metallic iron. The sextet of $Al_{50}Fe_{25}V_{25}$ after 3h of milling was characterised by lower magnetic field (HMF = 31.7 T) in comparison to pure iron (HMF = 33.0 T). It may be

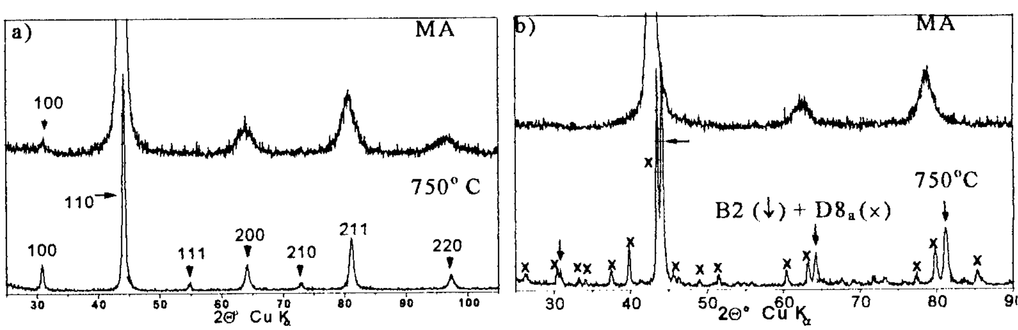

Fig.1 Diffraction pattern of $Al_{50}Fe_{50}$ (a) and $Al_{50}Fe_{25}V_{25}$ (b) alloys after 6 h of MA and annealing

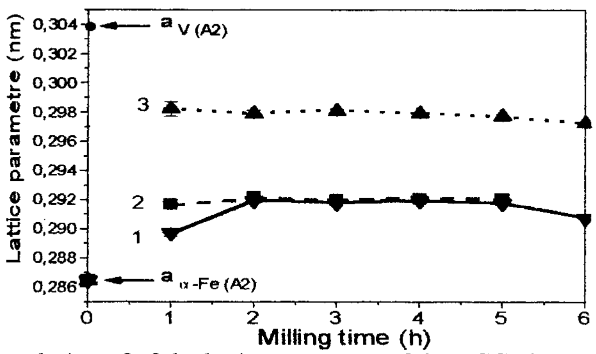

Fig.2 The evolution of of the lattice parameter of the BCC phase during MA of $Al_{50}Fe_{50}$ (1), $Al_{50}Fe_{45}V_5$ (2), Al50Fe25V25 (3)

associated with the insignificant dissolution of V and/or Al in α-Fe.

Fig. 3 shows that singlets and quadrupolar doublets are main components of the Mössbauer spectra. They characterise paramagnetic phases. The singlet is caracteristic of magnetic order forming at the symmetric environment of the Fe by 8 non magnetic Al atoms and this order takes place in the AlFe (B2) phase. The isomer shift (IS-1) for the AlFe singlet is equal to 0.28 mm /s [7] and it decreases down to 0.22 mm/s [8] under mechanical treatment. The IS-1 value for disordered $Al_{50}Fe_{50}$ solid solution was equal to 0.21-0.22 mm/s and increased up to 0.24 mm/s after 6 h of milling.The singlets for $Al_{50}Fe_{45}V_5$ and $Al_{50}Fe_{25}V_{25}$ alloys obtained after 6h of MA had IS-1 valuis equal to 0.18 and 0.14 mm/s respectively that is close with IS-1 0.15 mm/s for symmetric environment of Fe by V.

The change of the relation of the singlet area to the common spectrum (Q_s,%) depending on milling time is shown in Fig. 4. For $Al_{50}Fe_{50}$ and $Al_{50}Fe_{45}V_5$ alloys a monotonous growth of Q_s is observed that was indicated to the increas of the volume content of the ordered B2 regions. The singlet quota Q_s for the $Al_{50}Fe_{25}V_{25}$ alloy after 1h of milling equals ~33% and does not increase during further milling. The observed quadrupolar doublet is characteristic for a highly defected A2 phase formed by MA.

The crystallite sizes of the MA solid solution is equal to 10-15 nm and microstrains are ~1.2-%. Crystallites size and microstrains of the solid solutions changed insignificantly during MA. It can be associated with the simultaneous deformation and relaxation processes. The solid solution ordering promotes the microstrains relaxation.

The annealing of $Al_{50}Fe_{50}$ and $Al_{50}Fe_{45}V_5$ at 750° C resulted in an ordering of the solid solutions that corresponds to the A2→ B2 structural transformation. The LRO parameter

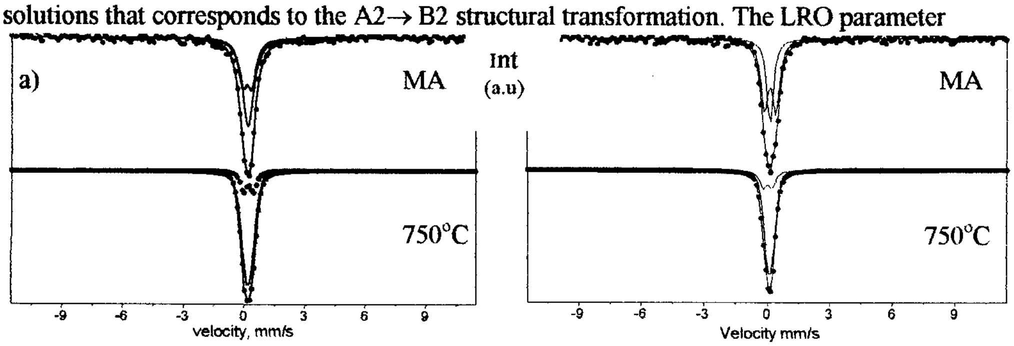

Fig.3 Mössbauer spectra of $Al_{50}Fe_{50}$ (a),and $Al_{50}Fe_{25}V_{25}$ (b) after MA and annealing

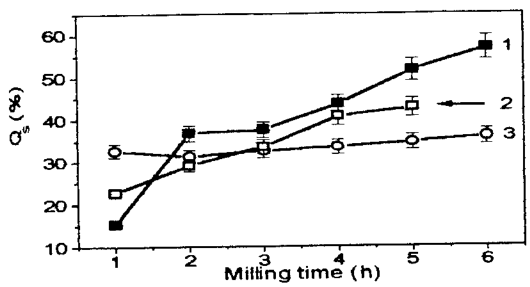

Fig.4 Relation of singlet area to common MS (Q_s%) for $Al_{50}Fe_{50}$ (1), $Al_{50}Fe_{45}V_5$ (2) and $Al_{50}Fe_{25}V_{25}$ alloys after different milling times

increased up to 0.83 for $Al_{50}Fe_{50}$ and up to 0.72 for $Al_{50}Fe_{45}V_5$. MS of annealed alloys mainly consisted of singlet components.

B2 and $D8_a$ phase formation was observed after the annealing of the MA $Al_{50}Fe_{25}V_{25}$ solid solution . The phase with the cubic $D8_a$ structure (a=1.1769 nm) is a ternary phase isostructural to the τ_2 phase in Al-Fe-Ti system [9]. Lattice parameter ratio of $D8_a$ to B2 in $Al_{50}Fe_{25}V_{25}$ alloy is equal to ≈ 4. This might indicate that the unit cell of the ternary phase is a superstructure relative to B2.

CONCLUSION

It was found that the BCC (A2) solid solution can be obtained by high energy ball milling of $Al_{50}Fe_{50}$ and $Al_{50}Fe_{50-x}V_x$ powder compositions. Long milling of $Al_{50}Fe_{50}$ alloy resulted in the partial ordering of the solid solution and the B2 phase formation. The addition of V into Al-Fe powder mixtures reduces the tendency to solid solution ordering although the short order of B2 type in $Al_{50}Fe_{50-x}V_x$ alloys was formed.

References

1. Gaffet, E., Nanostruct. Mat., 1995, 5, 393
2. Portnoy, V.K., Leonov, A.V., Fadeeva, V.I., Matyja, H., Mat.Sci.Forum, 1998, 269-272, 269
3. Cabrera, A.F., Fernández van Raap, M.B., Meyer, M. Rodrígez Torres,C., Mendoza-Zélis,L., Sánchez, F.H., Mat.Trans.,JIM, 1995, 36, 2, 357.
4. Yelsucov, E.P., Voronina, E.V., Barinov, V.A., J.of Magn. and Magn.Mat., 1992, 115, 271
5. Fadeeva, V.I., Leonov, A.V., Khodina, L.N., Mat.Sci.Forum, 1994, 179-181, 397.
6. Nat.Bur.Stand., (US), 1981, 25, Sec. 18.
7. Nasu, S., Gonzer, V., Preston, R.S., J.Physiq, 1980, 41, 385.
8. Clavaguera-Mora,M.T., Zhu, J., Meyer,M., Mendoza-Zélis,L., Sánchez,F.H., Clavaguera,N., Mat.Sci.Forum, 1997, 235-238, 541.
9. Palm, M., Inden, J., J. Phase Equil., 1995, 16, 209.

ACKNOWLEDGEMENTS

This work was supported by grant N7 T08D 043 10 of Warsaw University of Technology.

Pergamon

NanoStructured Materials, Vol. 12, pp. 629–632, 1999
Elsevier Science Ltd

0965-9773/99/$–see front matter

PII S0965-9773(99)00203-2

CHARACTERISATION OF THE MICROSTRUCTURE OF NANOPHASE Ni: A MOLECULAR DYNAMICS SIMULATION STUDY

H. Van Swygenhoven[1], M. Spaczér[1], A. Caro[2]
[1] Paul Scherrer Institute, CH-5232 Villigen PSI, Switzerland, helena.vs@psi.ch
[2] Centro Atómico Bariloche, 8400 Bariloche, Argentina, caro@cab.cnea.edu.ar

Abstract - The microstructure of computer generated Ni nanophase samples with mean grain sizes ranging from 3 to 12 nm is studied by means of atom energetics, coordination number, and local crystalline order. Two types of samples are considered: those with random crystallographic orientation, representing a sample with mainly high angle (HA) grain boundaries, and those with a limited misorientation, representing samples with mainly low angle (LA) grain boundaries. Overall density, grain boundary density and grain boundary excess enthalpy are discussed in terms of grain size and grain boundary type.

INTRODUCTION

The distinctive property of nanophase materials is the large number of grain boundaries compared to coarse grained polycrystals. The influence of these interfaces is crucial for mechanical properties; whilst in conventional models of plasticity interfaces represent obstacles for the deformation processes, contributing to the strengthening, in nanophase materials they are probably responsible for most of the observed plasticity. Peculiarities or differences in microstructure, such as the presence of a highly twinned structure [1] or the existence of dislocations in the grain boundaries [2] may play a major role in the deformation process and may cause the differences in mechanical behavior observed in samples with apparently the same microstructure when characterized only by density and mean grain size. Molecular dynamics computer simulations can help understanding the relationship between grain boundary structure and overall properties. In previous work we reported elastic and plastic deformation of Ni nanophase samples with mean grain sizes between 3.4 and 8.0 nm simulated at temperatures up to 500K [3-7] and emphasized the role of the grain boundary type in the deformation process.

The goal of the current work is to characterize the microstructure of the nanophase Ni samples with mean grain size between 3 and 12 nm, having mainly high angle grain boundaries or mainly low angle grain boundaries. The deformation mechanism of these samples is studied in an other contribution of the same authors in this conference.

SIMULATION METHOD

The atomic level structure of seven samples are investigated. Five of them are constructed by filling the simulation cell volume with nanograins nucleated at random location and with random crystallographic orientation, representing mainly high angle (HA) grain boundaries. Their mean grain sizes are 3.4, 5.2, 8.0, 10.0 and 12.0 nm. Samples Ni_3.4 and Ni_5.2 contain

approximately 100,000 atoms and 50 and 15 grains respectively, Ni_8.0 contains about 350,000 atoms, Ni_10.0 contains about 750,000 atoms and Ni_12.0 contains about 1.2 million atoms, all have 15 grains. Two other samples have the same grain location as for Ni_5.2, but the orientation of the grains, although still random, is restricted to a deviation angle between 3 and 17 degrees around the crystallographic <100> and <111> axis of grain 1. They are named Ni_5.2_100 and Ni_5.2_111, respectively; and represent a textured nanophase with mainly low angle (LA) grain boundaries. All samples are relaxed to a free enthalpy minimum at 300K, using a parallel molecular dynamics code with a tight-binding potential [8] in the Parrinello-Rahman approach and periodic boundary conditions. The characterization of the microstructure by calculating atomic energy and coordination number and by the local crystalline order in terms of a bond analysis technique described in [6,7]. Using this bond analysis, we define six categories of atoms: *perfect fcc*, atoms having a local fcc order till fourth neighbors, *good fcc*, atoms having a local fcc order till first neighbors, *perfect hcp*, atoms having a local hcp order till fourth neighbors, *good hcp* atoms having a local hcp order till first neighbors, atoms having other 12 coordinated combinations, and finally the non-12 coordinated atoms. Making a difference between atoms with a local fcc order up to both fourth and first neighbors helps us identifying fcc atoms which are close to the grain boundaries. The two classes of hcp atoms help us identifying eventually stacking faults inside the grains. They are especially useful for the analysis of the deformed samples. We define grain boundary as the ensemble of atoms having no local fcc surrounding. It is worth to mention that for other definitions of grain boundary such as non-fcc and non-hcp or non-12 coordinated the results remain qualitatively the same, only the absolute value of the results changes.

RESULTS AND DISCUSSION

Visual inspection of slices of the simulated samples revealed that (1) the interior of the grains in the HA and the LA samples are defect free (no hcp planes inside the grains), (2) small clusters of hcp atoms are present in the GB, the size of them being greater in the LA samples, (3) and that at the largest grain sizes the GB are less disordered and faceted boundaries appear. The sample densities (Fig. 1a) are calculated after relaxation of the sample to a free enthalpy minimum. The densities ranges from 95.2% of the theoretical density for a mean grain size of 3.4 nm towards 97% for a mean grain size of 12 nm. The LA samples have a slightly higher density (about 0.5%) then the HA sample with the same mean grain size. The density seems to be an intrinsic property related to grain boundary type and mean grain size, since hydrostatic pressure up to 10 GPa and 500K followed by relaxation could not increase the sample density. The simulated values correspond well with experimental values obtained by the inert gas condensation technique when powder is outgassed prior to compaction. For instance, a density of 97.6% is obtained for a n-Cu sample with a mean grain size of 10 nm [9]. We have also simulated a n-Cu with a mean grain size of 8 nm, and obtained a samples density of 97.2%. Fig. 1b shows the fraction of non-fcc (GB) atoms. When grain size decreases from 12 nm to 3.4 nm the fraction of GB atoms increases from 16 to 52%. When the GB volume is expressed following Palumbo et al [10] as

$$V_{IC} = 1 - \left[\frac{d-\Delta}{d}\right]$$

where d is the mean grain size and Δ the grain boundary width, then a grain boundary consisting of non-fcc atoms corresponds with a width of 0.7 nm in the HA case (about 2 lattice parameters) and a slightly lower value of 0.6 nm LA case.

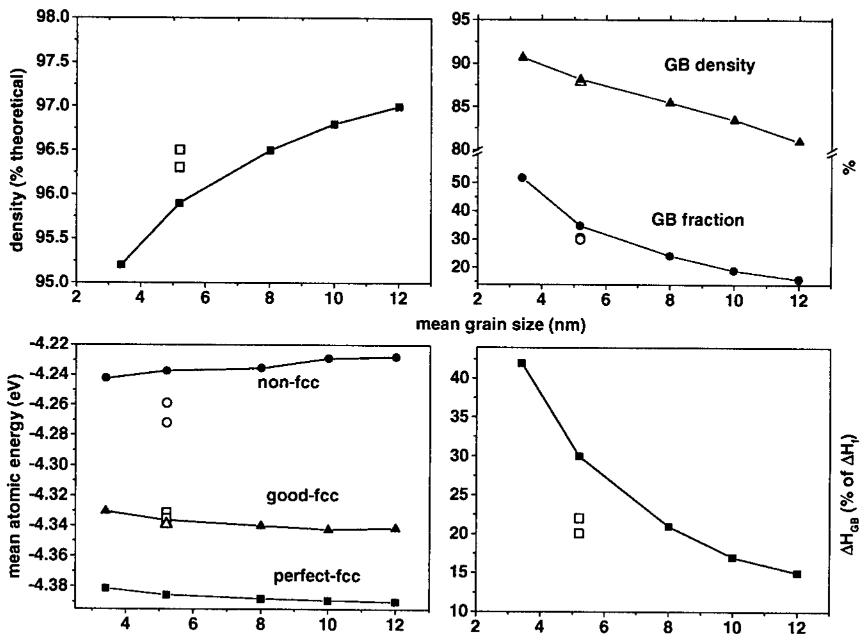

Fig.1 sample density (a), the grain boundary density and the % of atoms in the grain boundary (b), the mean atomic energy for perfect-fcc, good-fcc and non-fcc (c) the excess grain boundary enthalpy in the boundaries expressed as a fraction of the heat of fusion (d) as function of mean grain size. The full circles connected with lines are results for HA samples, the open circles are results for the LA samples.

Fig. 1b shows also the increasing grain boundary density increases with decreasing mean grain size to a value of 83%. For the LA samples the values are approximately the same. The GB density is calculated using the formula

$$\rho_{nano} = (\%fcc)\rho_{fcc} + (\%non-fcc)\rho_{non-fcc}$$

where $\rho_{non\text{-}fcc}$ is the GB density, ρ_{fcc} is the density inside the grain (set equal to the theoretical density), and ρ_{nano} the sample density. Analysis of the distribution of the coordination numbers indicates that at the larger grain sizes the fraction of overcoordinated atoms decreases, which could explain the reduced density. An average GB density mean of 85% was experimentally found in a Ni sample with a 20° twist angle in the (001) plane [11]. Fig. 1c shows the mean atomic energy of the perfect-fcc atoms (atoms well inside the grain), the good fcc atoms and the atoms in the GB. The mean atomic energy of the fcc atoms decreases slightly with increasing grain size, the value for the perfect fcc atoms reaches the perfect crystal energy (-4.3921 eV). In

the LA samples the mean energy of both classes is very similar to the mean energy of good-fcc in the HA. The mean energy of the grain boundary atoms on the contrary seems to increase slightly with increasing mean grain size, statistics on grain boundary orientations are however necessary to confirm this. The LA samples have less energy in the GB. In other words, whereas the mean energy per atom is approximately the same, the high angle sample has most of its excess energy in the grain boundaries, whilst in the low angle sample the energy is distributed among the boundary and the interior of the grain, as elastic distortions

Fig. 1d shows the excess enthalpy ΔH_{GB} expressed as a fraction of the heat of fusion. The excess enthalpy increases from 43% to 15%, when grain size is decreased from 12 nm to 3.4 nm. The excess enthalpy is lower in the LA sample then in the HA sample. DSC measurements of n-Ni with a mean grain size of 12 nm synthesized by mechanical attrition, showed a stored enthalpy in the grain boundaries of 25% of the heat of fusion [12].

CONCLUSIONS

Structural analysis on the atomic level of simulated nanophase samples with mainly high angle boundaries and of textured samples has been presented. We have shown that the sample density, the grain boundary density, the excess GB enthalpy are in good agreement with experimental measured values. It is also demonstrated that the presence of many LA grain boundaries have an important influence on the energy distribution in the sample. The samples will be used for the simulation of the mechanical properties (see contribution in the same issue) where it will be shown that not only the grain size, but also the grain boundary type play a crucial role in the plastic deformation process.

REFERENCES

1. P.G. Sanders, M. Rittner, E. Kiedaisch, J.R. Weertman, H. Kung, Y.C. Lu, Nanostruct. Mater., 1997, 9, 433
2. R.Z. Valiev, I.V. Alexandrov, W.A. Chiou, R.S. Mishra, A.K. Mukherjee, Mat. Sci. Forum, 1997, 235-238, 497
3. H. Van Swygenhoven and A. Caro,. Nanostruct. Mater., 1997, 9(1-8) 669
4. H. Van Swygenhoven and A. Caro, Mater. Res. Symp., 1997, 492
5. H. Van Swygenhoven and A. Caro. Appl. Phys. Lett., 1997, 71, 12
6. H. Van Swygenhoven, M. Spaczer, A. Caro, Proc. MRS Fall Meeting, 1997
7. H. Van Swygenhoven, M. Spaczer, A. Caro, Proc. TMS Fall Meeting, 1998
8. F. Cleri, V. Rosato, PRB 1993, 48(1) 22
9. P.G. Sanders, J.A. Eastman, J.R. Weertman, Acta Mater., 1997, 45(10) 4019
10. G. Palumbo, S.J. Thorpe, K.T. Aust, Scripta Metall., 1990, 24(7) 1347
11. M.R. Fitzsimmons, A. Roll, E. Burkel, K.E. Sickafus, M.A. Nastasi, G.S. Smith, R. Pynn, Nanostruct. Mater., 1995, 6 539
12. H.J. Fecht, Nanostruct. Mater., 1995, 6, 33

Pergamon

NanoStructured Materials, Vol. 12, pp. 633–636, 1999
Elsevier Science Ltd

0965-9773/99/$–see front matter

PII S0965-9773(99)00204-4

ORDERING OF NANOCRYSTALLINE FeAl PRODUCED BY CLUSTER CONDENSATION

K. Reimann and H.-E. Schaefer

Institut für Theoretische und Angewandte Physik, Universität Stuttgart, Pfaffenwaldring 57, 70550 Stuttgart, Germany,
e-mail: Klaus.Reimann@itap.physik.uni-stuttgart.de

Abstract — For studying the ordering kinetics of nanocrystalline $Fe_{50}Al_{50}$ *alloys the specimens were prepared by sputtering, crystallite condensation in an Ar atmosphere, and subsequent compaction (2–4 GPa) at room temperature. The lattice structure is B2 as in coarse grained FeAl but with a significantly lower degree* (≤ 0.5) *of order. The crystallite size is about 20* nm *and strains exceed 1.5 % in the* $\{110\}$ *direction and are higher than in nanocrystalline Fe. The ordering process takes place mainly in the temperature range from 400 to 500* K, *which is measured by the x-ray intensities of the superlattice reflections. This may indicate a higher vacancy diffusivity in the disordered than in the ordered state. The crystallite size remains smaller than 50* nm *even after annealing at* $0.8\,T_m$ *(melting temperature* $T_m = 1488$ K*) as evidenced by transmission electron microscopy. Furthermore the strains decrease during annealing. First results of magnetothermal analysis studies will be presented. ©1999 Acta Metallurgica Inc.*

Introduction

There are two techniques available to disorder the ordered B2 equilibrium structure of B2-FeAl: Ball milling and the technique of cluster condensation and compaction. In both techniques the disordering is connected to the nanocrystallisation process of the material. From the study of the ordering process information on the properties of atomic defects can be expected.

From the application point of view intermetallic aluminides may play a role because of their high-temperature strength and oxidation resistance. Atomic defects may substantially influence the mechanical properties (2) as, e.g., the yield stress anomaly in FeAl which can be attributed to the formation and migration of thermally formed vacancies (1). The brittleness at ambient temperature impedes the application. An increase in ductility may appear in a nanocrystalline structure if plastic deformation by grain boundary gliding plays a role.

Experimental

In order to prepare specimens of well defined composition a $Fe_{50}Al_{50}$ alloy target (purity 99.95+ %) was sputtered in 99.99999 % pure Ar gas of 4 mbar with a plasma current of 0.5–0.8 A at 320–400 V (fig. 1). The sputtered atoms condensate and agglomerate to nanocrystallites at a production rate of approx. 10 mg/h. They are collected and compacted at a 3–4 GPa uniaxial

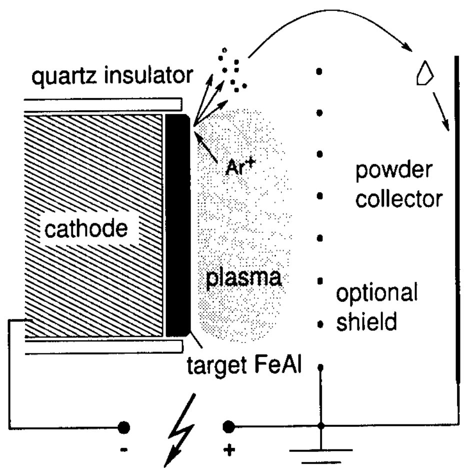

Figure 1: Schematic presentation of the production technique

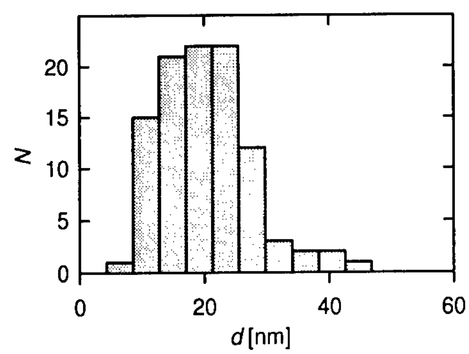

Figure 2: Histogram of the crystallite size distribution for nanocrystalline $Fe_{50}Al_{50}$ after annealing at 800 K for 70 min as determined from a dark field TEM micrograph. d is the mean diameter and N the number of crystallites.

pressure to discs. Magnetron sputtering which normally can increase the production rate was inefficient because the magnetic crystallites were predominantly retransferred to the sputter target. Within the limits of energy dispersive x-ray analysis (EDX) the composition of the nanocrystallites (50 ± 3 % (5)) is the same as that of the target.

An oxygen content of 0.3–0.4 wt% and a nitrogen content below 0.02 wt% was measured by hot extraction in a graphite crucible. The oxygen content increases after exposure to air up to 4 wt%. This behavior is due to the open porosity (relative mass density $\approx$80 %) and it shows that the oxygen is most probably located at the surfaces of the crystallites. No other impurities, especially no carbon, could be detected within the uncertainty limits ($\approx$1 wt%) of EDX.

A Siemens D500 diffractometer equipped with a secondary graphite monochromator was used to record the x-ray spectra. The profiles were fitted by Voigt functions taking into account the intensity factors and the Cu $K\alpha_{1,2}$ doublet structure (7).

The specimen were electrolytically thinned for TEM studies in a Tenupol-3 at a voltage of 30–90 V in a mixture of $HClO_4$ or HNO_3 and methanol.

A magnetothermal analysis was performed to determine the effective magnetic susceptibility by measuring the force on the specimen in a magnetic field gradient (average field 1.8 T) as described in (8).

Results

The crystallite size of 20 nm is, within the measuring uncertainty limits, constant up to 800 K as evidenced by transmission electron microscopy (TEM, see fig. 2). After annealing at 1150 K for 1 h anomalous grain growth occurs to about 50 nm. The crystallite growth may be initially impeded by interface pinning by oxide contamination or pores.

As shown in fig. 3 by two typical x-ray spectra nanocrystalline $Fe_{50}Al_{50}$ retains the B2 structure but the degree of order is lowered. The degree of order S is defined as $S = |p_{Fe/Fe} -$

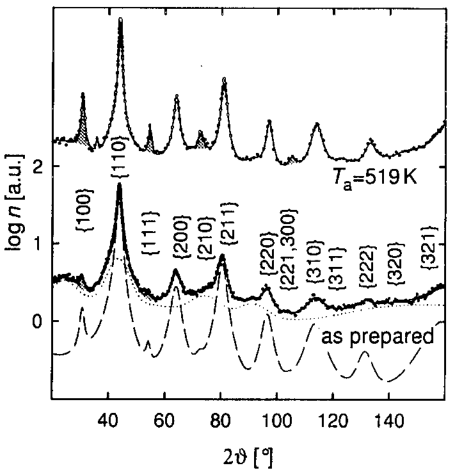

Figure 3: X-ray diffraction spectra of a specimen as prepared and annealed at 519 K for 59 min. Solid lines represent the fitted function, dotted lines the background, and dashed lines the reflection intensities. Note the increase in intensity of the superstructure reflections (gray shaded) which indicates ordering and the decrease of the linewidths which mainly corresponds to strain relaxation. The reflections are indexed according to the B2 structure.

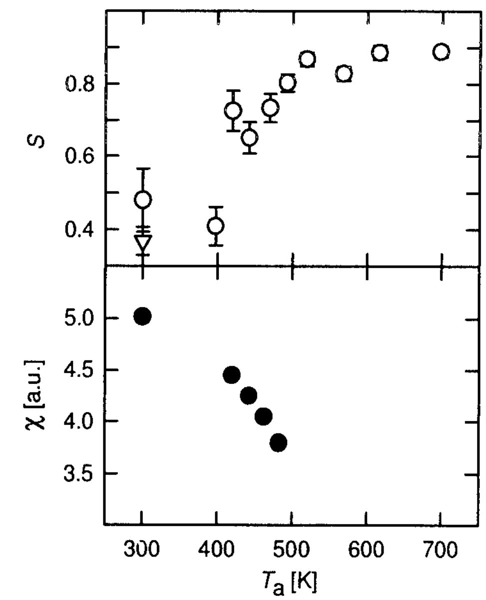

Figure 4: Order parameter S and the effective magnetic susceptibility χ (measured at 300 K) in dependence of of the annealing temperature T_a ($t_a \approx 1h$). Annealing time is approx. 1 h. Error bars indicate only the uncertainty due to the counting statistics of the x-ray spectra.

$p_{Fe/Al}|$ where $p_{X/y}$ are the probabilities for finding an X atom on the y sublattice. S can be obtained from the intensity of the superlattice reflections $\{100\}$, $\{111\}$ etc., where the $\{100\}$ reflection has the highest intensity. The small influence of vacancies from the preparation process on the intensities is neglected (11). The intensity of the superlattice reflections depends quadratically on S.

As fig. 4 shows, the raise of S with increasing annealing temperature T_a which signifies ordering occurs in the temperature range from $T_a \approx 400$ K to 500 K. In the same temperature range the strains determined by a Hall analysis (see details in (7)) decrease from the value $\langle \varepsilon^2_{\{110\}} \rangle^{1/2} \approx 1.7$ %, which is higher than in nanocrystalline Fe of similar crystallite size (6), to 0.8 %.

The effective magnetic susceptibility χ decreases in the same temperature interval (fig. 4). This decrease can be understood when the neighborhood of an Fe atom with partial coordination by Fe atoms in the disordered surrounding is changed into a full coordination by Al atoms upon ordering (12, 13). Disordered (A2, $S=0$) FeAl becomes ferromagnetic (14, 15).

Discussion and conclusion

In the disordered state of FeAl the concentration of antisite atoms on the opposite sublattices is high. For ordering these antisite atoms have to be removed to their propriate sublattices. This can be performed by the migration of vacancies which were specifically detected by saturation positron trapping in nanocrystalline FeAl (5). In ordered coarse grained FeAl long range vacancy migration has been directly observed in the temperature range of 650 K (16, 17). The ordering process in nanocrystalline FeAl, however, occurs at considerably lower temperatures at about 450 K. This can be understood by a lowering of the vacancy migration enthalpy in the disordered state (18, 19). In addition the high strains may facilitate vacancy migration.

We summarize that specimens of the nanocrystalline intermetallic compound $Fe_{50}Al_{50}$ are prepared by gas-phase condensation and compaction in a strongly disordered state. Ordering occurs at 450 K and is discussed in terms of an enhanced vacancy mobility in the disordered state.

Acknowledgements

The support of the Deutsche Forschungsgemeinschaft project Scha428/8-2 is appreciated. The authors would like to thank Prof. N. Karl for the possibility to collect the x-ray spectra, Dr. R. Lück, D. Lang and M. Scheffer for the magnetic measurements, M. Kelsch for the TEM micrographs, A. Weisshardt for the EDX analysis, and E. Grallath for the chemical analysis.

References

(1) H.-E. Schaefer, B. Damson, M. Weller, E. Arzt, and E. P. George, *phys. stat. sol. (a)*, 1997, 160, 531.
(2) K. Vedula, in J. H. Westbrook and R. L. Fleischer, eds., *Intermetallic Compounds*, vol. 2, chap. 9. John Wiley & Sons, Chichester, 1994, 199–209.
(3) G. Sauthoff, 1995, *Intermetallics*. VCH Verlagsgesellschaft, Weinheim.
(4) S. C. Deevi and V. K. Sikka, *Intermetallics*, 1996, 4, 357.
(5) B. Damson, 1995, diploma thesis, Universität Stuttgart.
(6) R. Dittmar, 1996, diploma thesis, Universität Stuttgart.
(7) K. Reimann and R. Würschum, *J. Appl. Phys.*, 1997, 81, 7186.
(8) H. Beißwenger and E. Wachtel, *Z. f. Metallkunde*, 1955, 46, 504.
(9) E. N. Maslen, A. G. Fox, and M. A. O'Keefe, in Wilson, ed., *International Tables for Crystallography*, vol. C, chap. 6.1–2. Published for the international Union of Crystallography by Kluver Academic Publishers, Dordrecht, Boston, London, 1992, 476–519.
(10) H. Xiao and I. Baker, *Acta metall. mater.*, 1994, 42, 1535.
(11) M. Kogachi, Y. Takeda, and T. Tanahashi, *Intermetallics*, 1995, 3, 129.
(12) G. P. Huffman and R. M. Fisher, *J. Appl. Phys.*, 1967, 38, 735.
(13) R. Hergt, E. Wieser, H. Gengnagel, and A. Gladun, *phys. stat. sol.*, 1970, 41, 255.
(14) C. Kuhrt and L. Schultz, *IEEE Trans. Magn.*, 1993, 29, 2667.
(15) A. Taylor and R. M. Jones, *J. Phys. Chem. Solids*, 1958, 6, 16.
(16) R. Würschum, C. Grupp, and H.-E. Schaefer, *Phys. Rev. Letters*, 1995, 75, 97.
(17) H.-E. Schaefer and K. Badura-Gergen, *Def. Diff. Forum*, 1997, 143–147, 193.
(18) L. A. Girifalco, *J. Phys. Chem. Solids*, 1964, 24, 323.
(19) J. P. Rivière and J. Grilhé, *phys. stat. sol. (a)*, 1974, 25, 429.

Pergamon

NanoStructured Materials, Vol. 12, pp. 637–640, 1999
Elsevier Science Ltd

0965-9773/99/\$–see front matter

PII S0965-9773(99)00205-6

CHARACTERISTICS OF NANOSTRUCTURED TiO_2 POWDERS SYNTHESIZED BY COMBUSTION FLAME-CHEMICAL VAPOR CONDENSATION PROCESS

B. K. Kim, G. G. Lee*, H. M. Park and N. J. Kim*****
Korea Institute of Machinery & Materials, 60 Sangnam-dong, Changwon, Korea
* Pukyong National University, 100 Yongdang-dong, Pusan, Korea
** Korea Research Institute of Standards & Science, 102 Yousong, Taejon, Korea
*** Pohang University of Science & Technology, San 31, Hyoja-dong, Pohang, Korea

Abstract—*Combustion Flame-Chemical Vapor Condensation(CF-CVC) process which can continuously produce nanostructured powders has been used to produce non-agglomerated TiO_2 powder. The synthesized powders are characterized for crystal structure, chemical composition, and particle size by using HRTEM, X-ray, TG-DTA, and SIMS. Nanostructured TiO_2 powders have mixed state of mostly anatase phase and small amount of rutile phase with particle size of about 20nm and 60~70nm, respectively. ©1999 Acta Metallurgica Inc.*

INTRODUCTION

Nanostructured powders with particle size under 20nm have shown great promise in the forming of advanced composites for application in tribological materials, high surface area supports for catalysis, high performance cutting tools, thermal barrier coatings, optoelectronic materials, gas sensors, and magnetic materials(1). The powders themselves have useful characteristics, such as a high degree of metastability, chemical reactivity, and low temperature sinterability(2). Recently, the Combustion Flame-Chemical Vapor Condensation(CF-CVC) process(3) has been developed for producing nanostructured ceramic powders which can not easily be produced by the Inert Gas Condensation(IGC) process, because of their high melting temperatures and/or low vapor pressures. This process involves the pyrolysis of metalorganic precursors instead of evaporation of solid metal source in the IGC process and can be synthesized nanostructured powders with no agglomeration, uniform particle size distribution, and high purity.

This paper reports on preliminary investigation of characteristics of nanostructured TiO_2 powders synthesized by CF-CVC process.

EXPERIMENT

Titanium(IV) ethoxide, $Ti(OC_2H_5)_4$, was used as starting metalorganic precursor to synthesize nanostructured TiO_2 powder. A schematic of the CF-CVC process is shown

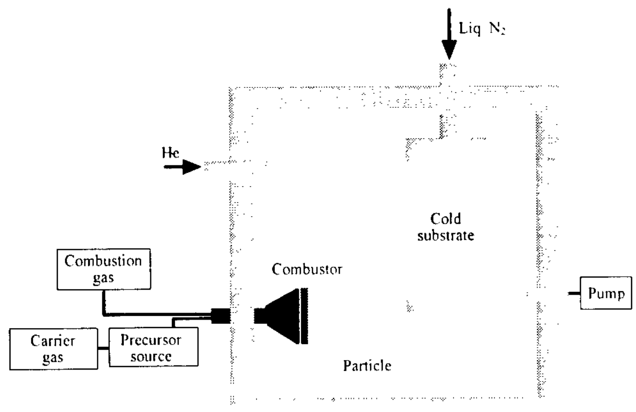

Figure 1. A schematic of CF-CVC process.

in figure 1. It mainly consists of a reaction chamber and precursor delivery system. Reaction chamber maintained at a dynamic He gas pressure of 20torr by high speed pumping and pyrolysis of metalorganic precursor/carrier gas stream was performed using a flat flame combustor. The temperature of the metalorganic precursor and carrier gas flow rate were maintained at 130℃ and 500cm^3/min., respectively. For the combustion heat source, H_2 and O_2 gases were feed into the combustor with flow rate of 2,100cm^3/min. and 2,700cm^3/min., respectively. The synthesized powders were characterized for crystal structure, volume fraction of phases, particle size, thermal stability, and chemical impurities by using XRD, HRTEM, TG-DTA and SIMS.

RESULTS AND DISCUSSION

Fig. 2 shows X-ray diffraction profile of synthesized TiO_2 powder collected on a rotating liquid N_2 cooled substrate. Intensities of anatase peaks are much stronger than those of rutile peaks. Comparison of primary peaks of anatase and rutile phases using the Spurr and Myers method(4) shows that synthesized TiO_2 powders consist of about

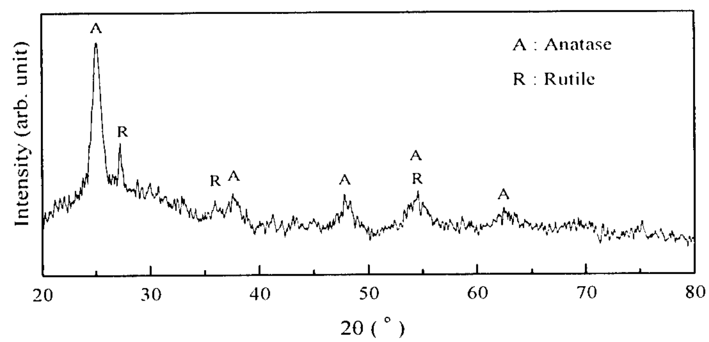

Figure 2. X-ray diffraction pattern of synthesized TiO_2 powder by CF-CVC process.

93.9 wt.% of anatase phase and 6.1 wt.% of rutile phase. The lattice parameter of the anatase phase determined by least square method using the program TREOR was as follows; a=3.775(2)Å, c=9.440(1)Å with tetragonal symmetry.

Figure 3(a) shows TEM micrograph of synthesized TiO_2 powders. As shown in figure, synthesized powders have mixed state of the large amount of fine spherical particles with about 20nm size, and small amount of coarse facetted particles with about 60~70nm size. Selected area diffraction (SAD) analysis of the powders shows the spotty ring pattern, which can be indexed based on anatase and rutile phases as shown in Fig. 3(b) and Table 1. Figure 3(c) shows interplanar spacings of the fine spherical particles calculated from the lattice fringe were a=3.75Å, c=9.51Å. This agrees well with the XRD results. Figure 3(d) shows microdiffraction pattern of the coarse facetted particles. These particles were identified as rutile phase with faces of (110) type planes. It knows that the fine spherical particles have metastable anatase phase, and coarse facetted particles have stable rutile phase.

Thermogravimetric(TG) examination of the synthesized powders showed a weight loss of 5% up to 1000°C, attributed the loss of absorbed water and organic residues from precursor. And a broad exothermic peak in DTA was observed about 675°C involving irreversible phase transformation from metastable anatase phase to stable rutile phase.

Table 1. Analysis of the spotty ring pattern shown in figure 3(b).

Ring No.	d-spacing (Å)	Phase
1	3.558	anatase (100)
2	2.530	rutile (101) and/or anatase (103)
3	2.132	rutile (111)
4	1.825	anatase (200)
5	1.657	anatase (211)
6	1.466	rutile (204) and/or anatase (002)
7	1.410	rutile (221)
8	1.259	anatase (215)
9	1.140	rutile (400)
10	0.968	rutile (421)

CONCLUSION

Nanostructured TiO_2 powder can be synthesized by Conbustion Flame-Chemical Vapor Condensation process. Syntheized TiO_2 powders consist of about 94% anatase phase with about 20nm particle size, and about 6% rutile phase with about 60~70nm particle size. Coarse rutile powder particles have facetted shape with face of (110) type planes.

ACKNOWLEDGMENTS

This research was sponsored by the Nano-Structure Technology Project of the Korea Ministry of Science and Technology.

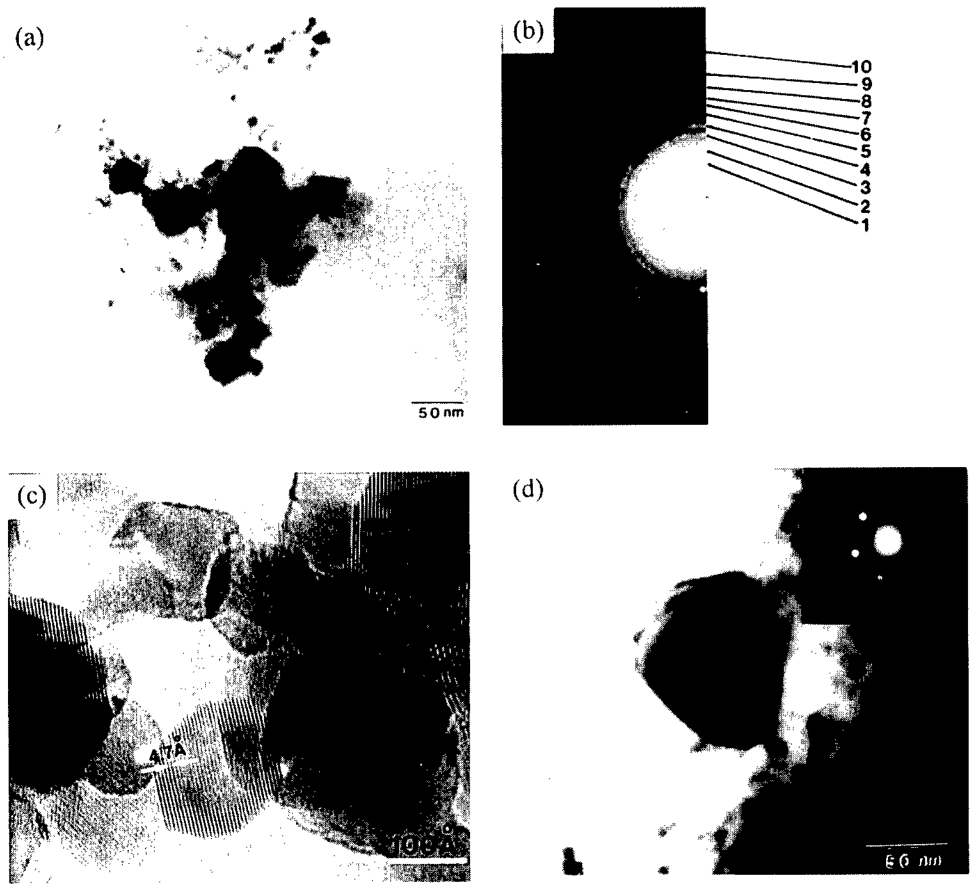

Figure 3. TEM micrograph(a), SAD pattern(b), lattice image of fine spherical particles(c), and microdiffraction pattern of the coarse facetted particles(d) of synthesized TiO_2 powder by CF-CVC process.

REFERENCES

1. Gleiter, H., *Progress in Materials Science*, 1989, 33, 223.
2. Ichinose, N., Ozaki, Y. and Kashu, S., *Superfine Particle Technology*, Springer-Verlag, London, 1988, p.1.
3. Chang, W., Skandan, G., Danforth, S.C., Kear, B.H. and Hahn, H., *Nanostructured Materials*, 1994, 4, 507.
4. Spurr, R.A. and Myers, H., *Analytical Chemistry*, 1957, 29, 760.

Pergamon

NanoStructured Materials, Vol. 12, pp. 641–644, 1999
Elsevier Science Ltd

0965-9773/99/$–see front matter

PII S0965-9773(99)00206-8

CHARACTERIZATION OF FERRITES SYNTHESIZED BY MECHANICAL ALLOYING AND SOFT CHEMISTRY

N. Millot[1], S. Begin Colin[2], P. Perriat[1], G. Le Caër[2], R. Welter[3], B. Malaman[3]
(1) L.R.R.S., U.M.R. 5613, BP 400, 21011 Dijon Cedex, FRANCE.
(2) L.S.G.2M., U.M.R. 7584, Ecole des Mines, 54042 Nancy Cedex, FRANCE.
(3) L.C.S.M., U.M.R. 7555, Université H.Poincaré, 54506 Vandoeuvre les Nancy,

Abstract --*For the purpose of comparing nanostructured materials prepared by different synthesis methods, nanocrystalline Fe-based spinels were synthesized using two different routes: soft chemistry and high-energy ball milling. The as-prepared powders were characterized notably by thermogravimetric analyses and ^{57}Fe Mössbauer spectrometry.*
©1999 Acta Metallurgica Inc.

INTRODUCTION

In the spinel structure of the titanomagnetite, $Fe_{2.5}Ti_{0.5}O_4$, investigated in the present work, tetrahedral (A) and octahedral (B) sites are occupied by the cations (1). When the ferrite contains some substitutional M cations, the cation distribution is not as simple as it is in magnetite at room and at low temperatures where all the Fe^{2+} ions are on B sites. In the case of titanium ferrite, the distribution of cations has been extensively studied (2,3,4,5). All the authors have found the Ti^{4+} cations residing on octahedral sites but the location of the Fe^{2+} cations is still controversial even when results are derived from the same technique. Moreover a change of the cation to anion ratio is possible in the spinel phase leading to a deviation δ from stoechiometry : $(Fe_{2.5}Ti_{0.5})_{1-\delta}O_4$. In any case the dispute may originate from differences in several experimental conditions and control parameters such as temperature, grain size, deviation from stoichiometry, method of synthesis...

To compare samples prepared by different methods, we have selected two routes, soft chemistry and mechanosynthesis, which lead to powder particles with nanometer-sized grains. Among the numerous methods of soft chemistry, the precipitation has been chosen (6,7). The second synthesis route is mechanosynthesis (8,9,10) which is a high energy ball milling process. The structure and properties of nanocrystalline ferrites are characterized mainly by Mössbauer spectrometry and by studing their oxidation behavior.

EXPERIMENTAL DETAILS

The processes of soft chemistry are described more precisely elsewhere (11). It involves two steps : precipitation in an aqueous solution followed by thermal annealing under

a reducing mixture of $N_2/H_2/H_2O$ gases. The different treatments eliminate remaining impurities and allow to reach a stoichiometric state ($\delta \approx 0$) (12).

Continuous grinding is performed in a planetary ball mill (Fritsch Pulverisette 7) with a powder to ball weight ratio R=1/40. The grinding tools are made of steel (Fe-13%Cr), the volume of the vial is approximately 45 cm^3 and seven balls of diameter $\varnothing \approx$ 13 mm are used. The powders mixture (Fe, α-Fe_2O_3, TiO_2) in stoichiometric proportions and balls are introduced in vials and sealed in a glove box under argon atmosphere.

The resulting powders are all characterized by ^{57}Fe Mössbauer spectrometry with a constant acceleration spectrometer and a $^{57}CoRh$ source. Their oxidation behavior is followed by thermogravimetry (SERARAM TAG 24).

RESULTS AND DISCUSSION

The mechanosynthesized spinel phase appears after 1h30 of grinding and all peaks on the XRD pattern are assigned to the spinel phase after 4 hours (10). Ground powders consist of aggregates of nanometric crystallites. The average size of aggregates is approximately 100-200 nm and the size of small crystallites in aggregates is about 15 nm as also confirmed by transmission electron microscopy. In contrast, powders prepared by soft chemistry are very well dispersed and homogeneous with a grain size of about 18 nm.

The oxidation behavior of both powders has been studied by thermogravimetry. The DTG curve displays one single peak for the powder obtained by soft chemistry (figure 1a) which can be attributed to the oxidation of Fe^{2+} only located in octahedral sites. For mechanosynthesized powders (figure 1b), two peaks are observed which means that some Fe^{2+} cations are in A sites.

The oxidation in the spinel phase leads to a weight gain of 4.1% for the powder obtained by soft chemistry and of 4.64% for the ball-milled powder. As the theoretical weight gain for a stoechiometric ferrite, 5.27%, is larger than the previous values, it means that there is already a significant oxidation of the Fe^{2+}cations at ambient temperature. From such studies, we deduce that δ, in $(Fe_{2.5}Ti_{0.5})_{1-\delta}O_4$, is about 0.040 and 0.022 in " soft chemistry " powders and in ground powders respectively.

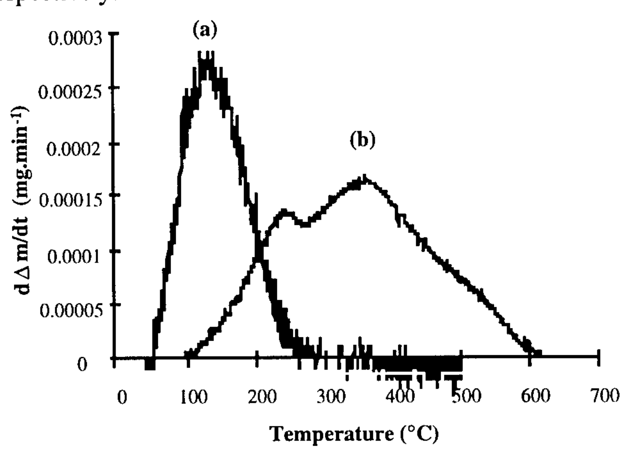

Figure 1 : DTG oxydation curves $d\Delta m/dt = f(T)$ of $Fe_{2.5}Ti_{0.5}O_4$ synthesized by a) soft chemistry, b) mechanosynthesis (4 hours, R=1/40, under argon)

This difference may be related to the agglomeration state of ground powders which limits the oxidation process at ambient temperature. The reactivity of the ground powder is smaller than that of the sample obtained by soft chemistry route.

Some Mössbauer spectra of the titanomagnetites synthesized by mechanical alloying and by soft chemistry are shown in figure 2. Both series of spectra are very different and very complex. Some information can nevertheless be extracted from undisputed features of the observed spectra. The spectrum of the spinel phase synthesized by soft chemistry (figure 2a) corresponds to the Mössbauer spectrum expected for a ferrimagnetic polycrystalline material with the superposition of more than two magnetic hyperfine sextets (13-14). Clear differences exist however with the spectrum published in litterature for a titanoferrite of the same composition (14). In particular, the hyperfine field of the outer sextet is much larger in our case H = 486 kG than it is for the titanomagnetite $Fe_{2.5}Ti_{0.5}O_4$ investigated by Melzer et al. H =447 kG (14). The outer sextet that we observe here cannot be associated with a titanomagnetite whose Ti content is x=0.50 even when taking into account the existence of deviations from stoechiometry. From the Ti content dependence of the hyperfine field, it is indeed mainly associated with a titanoferrite whose Ti content is less than at most x=0.10. The aforementioned Mössbauer characteristics are therefore accounted for by chemical composition variations inside each particle. The heterogeneities are then rather related to kinetic effects linked to partial oxidation of the iron cations occcuring when nanoparticles are studied in room conditions. Therefore whereas near the surface there are mainly iron Fe^{3+} cations, in the bulk of the particle the Fe^{2+} and titanium cations are predominant. The measured field H is indeed consistent with a Fe_2O_3 surface layer. Even if other Fe ions environments with a distribution of iron and titanium neighboring atoms contribute also to the observed spectrum, it is mainly in agreement with particles with a Ti-rich core and a Fe-rich shell. Mössbauer spectra of the mechanosynthesized titanomagnetite (figure 2b) are similarly difficult to analyze. The shape of the spectrum recorded at room temperature with four external lines, with a characteristic field of about 420 kG, and an intense asymmetric central doublet suggests that superparamagnetic relaxation takes place in the sample (15-16). The assumption of superparamagnetic relaxation, which is consistent with an average crystallite size of 15 nm, is confirmed by spectra recorded at 200 and 100 K (11). They show a progressive increase of the magnetically split part of the spectra when the temperature decreases. The latter increase is related to a distribution of grain sizes, classically broad in ground powders, which results in a distribution of blocking temperatures.

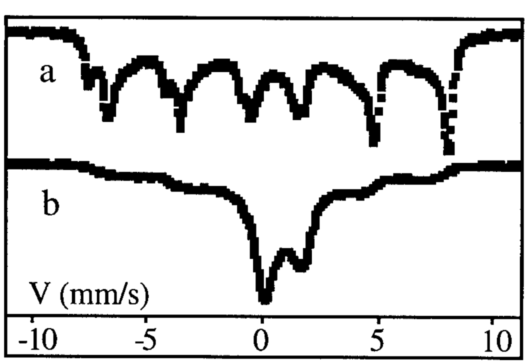

Figure 2 : ^{57}Fe room-temperature Mössbauer spectra of $Fe_{2.5}Ti_{0.5}O_4$ synthesized a) by soft chemistry, b) by high-energy ball milling.

Further, grain growth is induced by heat treatments under an argon atmosphere of ground powders at 1100K. The resulting Mössbauer spectrum is then similar to that of polycrystalline ferrites confirming the effect of grain size in nanoferrites [11]. The outer hyperfine field (H= 448 kG) corresponds to a titanomagnetite with a titanium content close to 0.5. This result confirms that in mechanosynthesized powders, the heterogneities of composition are not as important as they are in those obtained by soft chemistry.

CONCLUSIONS

In ferrites obtained by mechanosynthesis and by soft chemistry, the average crystallite size is about 15 nm, but whereas the ball-milled powders consist of aggregates, those obtained by soft chemistry are formed from isolated nanoparticles. Comparison of both ferrites show that oxidation phenomena occur thus at the surface of grains in the soft chemistry powders and lead to materials with a higher deviation from oxygen stoichiometry $\delta = 0.040$ in $(Fe_{2.5}Ti_{0.5})_{1-\delta}O_4$ than those formed from mechanical alloying $\delta = 0.022$. Mössbauer spectra agree with the previous conclusions on the differences in oxidation behaviour and in crystallite size distribution. They demonstrate that heterogeneities of titanium content exist in soft chemistry powders while a superparamagnetic behaviour is evidenced in mechanosynthesized ferrites at room temperature.

ACKNOWLEDGMENTS

The authors would like to thank P. Delcroix, Dr. F. Bernard and Dr. D. Aymes for their help in the experiments, Dr. B. Gillot for helpful discussions.

REFERENCES

(1) E.J. Verwey, E.L. Heilman, *J.Chem.Phys.*, 1947, **15**, 174.
(2) S. Akimoto, *J. Geomagn. Geoelec.*, 1954, **61**, 1.
(3) L. Néel, *Adv. Phys.*, 1955, **4**, 191.
(4) R. Chevalier, J. Bolfa, S. Mathiew, *Bull. Soc. Franc Min. Cris.*, 1955, **78**, 307.
(5) A. Trestman, S.E. Dorris, S. Kumarakrishnan, *J. Am. Ceram. Soc.*, 1983, **66**, 829.
(6) J.P. Jolivet, *De la solution à l'oxyde, InterEditions/CNRS Editions*, Paris, (1994).
(7) A. Rousset, F. Chassagneux, J. Paris, *J. Mater. Sci.*, 1986, **21**, 3111.
(8) C. C. Koch, *Annu. Rev. Mater. Sci.*, 1989, **19**, 121.
(9) V. V. Boldyrev, N. Z. Lyakhov, Pavlyukhin, E. V. Boldyreva, E. Y. Ivanov, E. G. Avvakumov, *Sov. Sci. Rev. B. Chem.*, 1990, **14**, 105.
(10) J. J. De Barbadillo, *Key Engineering Materials,* 1993, **77-78**, 187.
(11) N. Millot, S. Begin, P. Perriat, G. Le Caër, *J. Solid State Chem, 1998 in press.*
(12) D. Aymes, N. Millot, V. Nivoix, P. Perriat, *Solid State Ionics,* 1997, **101-103**, 261.
(13) H. Tanaka, M. Kono, *J. Geomagn. Geoelect.*, 1987, **39**, 463.
(14) K. Melzer, Z. Simsa, M. Lukaslak, J. Suwalski, *Cryst. Res. Technol.*, 1987, **22**, 132.
(15) V. U. Patil, R. G. Kulkarni, *Solid State Comm.*, 1979, **31**, 551.
(16) E. Tronc, J. P. Jolivet, *Materials Science Forum,* 1997, **235-238**, 659.

Pergamon

NanoStructured Materials, Vol. 12, pp. 645–648, 1999
Elsevier Science Ltd

0965-9773/99/$–see front matter

PII S0965-9773(99)00207-X

NEW HIGH PIEZOELECTRIC COUPLING PLuNT BINARY SYSTEM CERAMICS

A.Sternberg, L.Shebanovs, M.Antonova, M.Livinsh, J.Y.Yamashita*, I.Shorubalko, A.Spule,
Institute of Solid State Physics University of Latvia, e-mail:stern@latnet.lv
*Toshiba Corporation, Kawasaki, Japan

Abstract – *The new (1-x)$Pb(Lu_{1/2}Nb_{1/2})O_3$–x $PbTiO_3$ binary system ceramics in the interval 0<x<0.80 were obtained and the structural, dielectric and piezoelectric properties have been investigated. At room temperature the structure changes from monoclinic (x<0.38) (pseudo-cubic at x≈0.2) to tetragonal (x>0.49). The morphotropic region extends over the interval x=0.38-0.49, the concentration ratio M:T≅1 corresponds to x=0.41. The maximum values of the electromechanical coupling coefficients k_p=0.663, k_t = 0.481, k_{31}=0.355 of (1-x)PLuN-xPT ceramics were attained in compositions PLuNT 59/41 (T_m=353^{0}C) near the morphotropic phase boundary (MPB). The PLuNT system, having large values of electromechanical coupling and the highest T_m (>350^{0}C) among binary $Pb(B',B'')O_3$-PT perovskites may be favorable for piezoelectric sensors and actuators, and may have an interest as promising basis for thin film and single crystal performance. ©1999 Acta Metallurgica Inc.*

INTRODUCTION

Recently much attention has been paid to electromechanical (piezoelectric, electrostrictive) materials because of their promising application in electronics, ultrasound transduction, acoustic sensing, microelectromechanical systems (MEMS). An advanced approach is creating complex perovskites - binary, ternary and many-component systems, including lead-based $Pb(B',B'')O_3$ compounds, mainly being relaxors, and lead titanate $PbTiO_3$ (PT). Strong electromechanical coupling (k_p=0.76, k_t=0.56, k_{31}=0.46, k_{33}=0.79) has been reported by T.Yamamoto [1] in hot-pressed PSN-PT ceramic samples with a grain size ~1 μm and A.Kalvane [2]; by Y.Yamashita [3] in PSN-PMN-PT ternary ceramic material - k_p=0.72, k_{31}=0.45, k_{33}=0.77, the piezoelectric coefficient d_{33} reaching 640 pC/N. Another systems studied are PMNT [4], PSTT [5], PZN-PSN [6], PYbNT [7], PMTT [8], PINT [9] as well as multi-component systems PZN-PSN-PT [10], PMN-PT-$(Ba,Sr)TiO_3$ [11], PMN-PMT-PT [12].

Finally, ultrahigh strain levels up to 1.7% (under electrical bias 120 kV/cm) and k_{33} >0.9, d_{33} ≥ 2000 pC/N in PZN-PT (x=0.08 PT) single crystals grown by the flux technique are reported by S.E.Park [13] being the real ground for recently announced research breakthrough with relaxor-ferroelectric compounds. An essential advantage compared to conventional PZT compositions is the considerable ease to grow large complex perovskite single crystals [14].

The solid solution system (1-x)$Pb(Lu_{1/2}Nb_{1/2})O_3$–x$PbTiO_3$ was examined with the aim to investigate structural, dielectric and piezoelectric properties of ceramics, especially in morphotropic phase boundary (MPB) region.

EXPERIMENTAL

Twenty-five compositions were synthesized altogether with 10 mol.% intervals of the PT concentration and with 1 mol.% intervals near the MPB. According to X-ray data the MPB of the PLuNT powders is within the (1-X)/X interval of 49/51 - 59/41. Refined X-ray data of ceramics yielded the 59/41 - 60/40 morphotropic region with concentration M:T≅1.

All the compositions of PLuNT ceramics were obtained by solid phase reactions from oxides by following the wolframite precursor method.

Ceramics were synthesized and hot-pressed (temperature 950°C to 1130°C, pressure 25 MPa) in the interval $0<x<0.80$. To compensate the loss a 1 wt.% of excess PbO was used.

Crystallographic studies of the phase state and morphotropic phase transitions were made by X-ray diffraction maxima 200, 220, 222 analysis using a DRON-UM1 difractometer with Co K_α radiation, and Fe β filter. Capacitance and dielectric loss were measured on a HP4284 LCR instrument; the dielectric hysteresis loops were obtained by the Sawyer-Tower circuit in quasistatic regime. For the piezoelectric measurements the samples were poled at 125°C during 15 min. under applied field of 25 kV/cm and cooled under field to the room temperature. A HP4194 impedance analyzer was used to determine the electromechanical characteristics by the resonance-antiresonance method according [15].

More on technology and experimental technique is reported elsewhere [16].

RESULTS AND DISCUSSION

The following features of the PLuNT system can be revealed. Pure lutetium niobate (PLuN) has a pronounced long-range order in the B sublattice (the X-ray diffraction pattern contains superstructure maxima) and pseudo-monoclinic cell with linear parameters a=c=4.150 Å, b=4.119 Å and a monoclinic angle β=90.43° (Fig.1, Table 1), and a antiferroelectric - paraelectric (AFE-PE) phase transition at ~258°C, and absence of dielectric dispersion. As x is increased (the concentration of $PbTiO_3$ growing) the long-range ordering in the B sublattice gradually disappears - the I_{111}/I_{200} ratio changes from 0.919 (at x=0) to 0.054 (at x=0.3). With the growth of the content of $PbTiO_3$ the angle β proceeds through a minimum in the monoclinic part of the phase diagram. At x=0.2 the structure becomes pseudocubic, the angle β differs from 90° within the accuracy of measurement ±0.02° - Fig.1a, inset. Broadening of the phase transition and dielectric dispersion, characteristic features for ferroelectric relaxors, e.g., PMN, PLZT are observed within the concentration interval of $0<x<0.2$. The morphotropic region extends over the concentration interval x=0.38-0.49 shaded in Fig.1 (detected by appearance of the diffraction component of the relevant phase in the complex 200 profile); the conventional MPB where the concentration ratio tetragonal/monoclinic M:T≅1 corresponds to x=0.41. Position of the MPB changes by 1-2 mol.% depending on the amount of over-stoichiometric PbO in the synthesized PLuNT compound. E.g., if PbO is decreased from 1 wt.% to zero, concentration x corresponding to equal amounts of tetragonal and monoclinic phases changes from 0.41 (at 1 wt.% of PbO) to 0.39 (at 0 wt.% PbO).

Within the MPB interval, compared to the PZT system, a rather strong distortion of the unit cell $(c/a-1)\geq0.02$, $\beta\geq90.37°$) is maintained (Fig.1) and for this reason the PLuNT is a "hard" piezoelectric material.

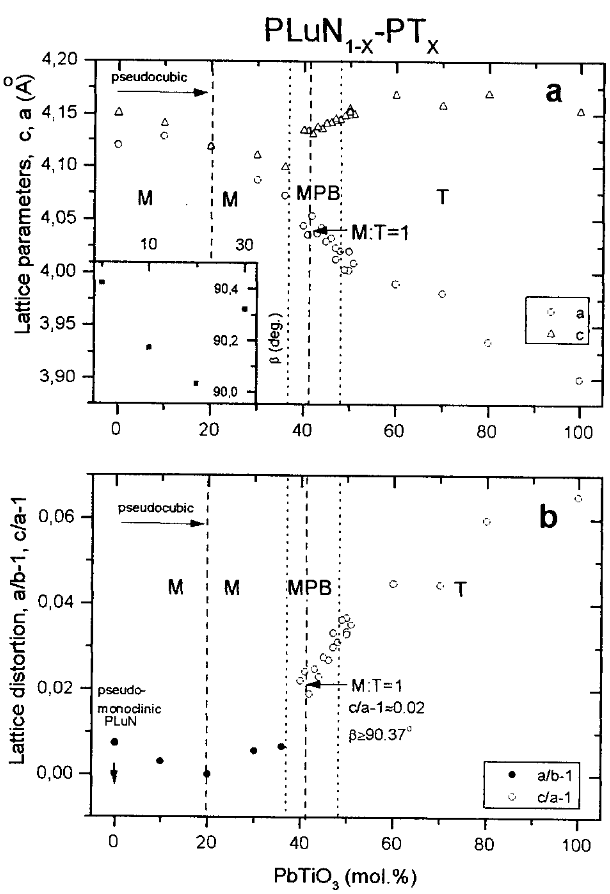

FIG.1. The phase diagram of the $PLuN_{1-X}PT_X$ system: lattice parameters (a) and distortion of the unit cell (b) vs. concentration (mol.%) of $PbTiO_3$. Inset (a) – concentration dependence of the monoclinic angle β.

The thermal dependence curves of the dielectric permittivity ε of (1-x)PLuN-xPT ceramics reveal the peak values of ε increasing with the increase of PT content and exceeding 25 000 in the MPB region. However, it still high enough (almost higher > 26 500) even at x=0.5. The lowest T_m is observed at x=0.10, however near the MPB T_m>350°C which is the highest value among known binary Pb(B',B'')O_3 - PT perovskites. The dependence $T_m(x)$ in the case of PLuNT is very similar to that of PYbNT [7]. Values of coercive field E_c=20 kV/cm and remanent polarization P_r = 38 μC/cm^2 (at T=20°C) are estimated for PLuNT 59/41 (MPB composition).

Coefficients of electromechanical coupling (k_p - planar mode, k_t - thickness mode) as functions of the PT concentration x in the (1-x)PLuN-xPT ceramic series reach maxima at x=0.41: k_p=0.663, k_t=0.481.

Structural and physical characteristics in PLuNT ceramics are summarized in Table 1.

ACKNOWLEDGMENT

The research was supported by Council of Science of Latvia and Dr.K.Hayashi of Hayashi Chemical Ltd., Kyoto, Japan.

TABLE 1. Physical and structural characteristics in PLuNT (1-X)/X ceramics at various content of lead titanate (mol.%).

$PbTiO_3$ (mol.%)	0	10	20	30	40	41	50	60	80
Perov-skite ratio, %	96	100	100	100	100	100	100	100	100
ρ, g/cm^3	8.80	8.79	8.69	8.51	8.42	8.44	8.16	8.24	7.76
T_m, °C	258	100	129	265	357	353	436	448	494
ε_{20}	126	750	2238	1429	1936	1228	713	477	198
tgδ	0.012	0.047	0.070	0.054	0.043	0.044	0.011	0.022	0.030
ε_{max}	580	3896	7311	17135	11800	25376	6060	8607	21500
ε_{20} (pol.)	119	590	1990	814	1005	1083		477	
k_p				0.385	0.518	0.663		0.197	
k_t				0.412	0.422	0.481			
k_{31}				0.209	0.282	0.355			
Phase	M	M	M	M	T+M	MPB	T	T	T
I_{111}/I_{200}	0.919	0.545	0.299	0.054	0	0	0	0	0

[1] T.Yamamoto and Y.Yamashita, *Proc. ISAF'96, (East Brunswick, NJ, U.S.A., Aug. 18-21), IEEE Catalog Number 96CH35948*, **2**, 573 (1996).

[2] A.Kalvane, M.Antonova, M.Livinsh, M.Kundzinsh, A.Spule, L.Shebanovs, and A.Sternberg, *Key Engineering Materials*, **132-136**, 1072-75 (1997).

[3] Y.Yamashita, K.Harada, T.Tao, and N.Ichinose, *Integrated Ferroelectrics* **13**, 9 (1996).

[4] Q.M.Zhang, J.Zhao, and L.E.Cross, *J.Appl.Phys.*, **79** [6] 3181-87 (1996).

[5] B.P.Burton and R.E.Cohen, *Phys.Rev.B*, **52** [2] 792-97 (1995).

[6] M.Dambekalne, I.Brante, M.Antonova, and A.Sternberg, *Ferroelectrics*, **131**, 67-73 (1992).

[7] T.Yamamoto and S.Ohashi, *Jpn.J.Appl.Phys.*, **34**, 5349-53 (1994).

[8] S.H.Lee, J.M.Jung, and S.W.Choi, *J.Korean Phys.Soc.*, **32**, S1013-S1015 (1998).

[9] E.F.Alberta and A.S.Bhalla, *J.Korean Phys.Soc.*, **32**, S1265-S1267 (1998).

[10] I.Pronin, T.Ajazbaev, N.Zaiceva, T.Shapligina, and V.Isupov, *Inorganic Materials*, **32** [10] 1247-49 (1996) (in Russian).

[11] S.M.Pilgrim, M.Masuda, and J.D.Prodey, *J.Am.Ceram.Soc.*, **79** [6] 1501-06 (1995).

[12] S.W.Choi, J.M.Jung, and A.Bhalla, *J.Korean Phys.Soc.*, **32**, S1282-S1285 (1998).

[13] S.E.Park, and T.R.Shrout, *J.Appl.Phys.* **82** (4), 1804-1811 (1997).

[14] T.Kobayashi, S.Shimanuki, S.Saitoh, and Y.Yamashita, *Jpn.J.Appl.Phys.*, **36**, 6035-6038 (1997).

[16] IEC Standard Publication 483, *Guide to Dynamic Measurements of Piezoelectric Ceramics with High Electromechanical Coupling* (1976).

[15] M. Antonova, L. Shebanovs, M. Livinsh, J. Y.Yamashita, A. Sternberg, I. Shorubalko, and A. Spule, submitted to *J.Am.Cer.Soc.* (1998).

Pergamon

NanoStructured Materials, Vol. 12, pp. 649–652, 1999
Elsevier Science Ltd

0965-9773/99/$–see front matter

PII S0965-9773(99)00208-1

NANOSTRUCTURED PRECIPITATES: EXPERIMENTAL VERSUS EXACT THEORETICAL SAXS PROFILES

V. Garrido[1], D. Crespo[1], E. Pineda[1,2], T. Pradell[2] & M. Capitán[3]

[1] Dept. Física Aplicada, Univ. Politècnica de Catalunya, Campus Nord, Modul B4, 08034-Barcelona, SPAIN, e-mail: crespo@benard.upc.es.

[2] ESAB, Univ. Politècnica de Catalunya, Urgell 187, 08036-Barcelona, SPAIN.

[3] European Synchrotron Research Facility, BP220 - F - 38043 Grenoble Cedex, FRANCE.

Abstract -- *Small Angle X-Ray Scattering is one of the few techniques suitable for the determination of the grain size distribution of nanostructured materials. A theoretical development has allowed us to determine the spatial self-correlation function of such systems and thus the scattering profile associated with the grain size distribution in the SAXS spectra without supposing any specific shape in the precipitates and taking into account their impingement. It has been tested in the primary crystallization of the amorphous $Fe_{73.5}Cu_1Nb_3Si_{17.5}B_5$ giving excellent agreement with the experimental data. ©1999 Acta Metallurgica Inc.*

INTRODUCTION

Microstructural characterization by Small Angle X-Ray Scattering (SAXS) is a powerful analysis technique for the description of the macroscopical properties of nanostructured materials. It is well known that the SAXS intensity of a structured system can be exactly computed (1), provided that the complete description of the system geometry (composition, shape and size of the particles) is available.

The inverse process, that is, the description of the microstructure of an unknown system, cannot be performed in general due to the fact that the scattering intensity function cannot be deconvolved uniquely. The usual deconvolution is performed by assuming that the system is composed of self-similar particles of known shape (2). The scattering function of the characteristic particle is then computed and the grain size distribution is optimized by fitting the theoretical SAXS spectrum to the experimental data.

The above procedure cannot be used with materials obtained by phase transformations driven by nucleation and growth kinetics, where the shape of the grown particles is unknown. In a recent paper (3,4) Garrido and Crespo have shown that the exact characteristic function of such a system can be exactly computed, provided that the grain size distribution is known, without making any assumption about the shape of the precipitates. Once the characteristic function has been obtained, the computation of the exact SAXS profile is straightforward, and comparison with the experimental data can be performed easily.

In this paper we show the application of this procedure to the primary crystallization of a FINEMET amorphous alloy of composition $Fe_{73.5}Cu_1Nb_3Si_{17.5}B_5$ by isothermal annealing. Experimental SAXS data, obtained at several stages of the transformation, is compared to the theoretical SAXS profile.

GENERALIZED SCATTERING INTENSITY FUNCTION

The procedure used in the calculation of the characteristic function of a nanostructured material is summarized in (4), and so we will only recall here the final results. Let $F(\vec{r},t)$ be the system global averaged self-correlation function and $X(t)$ the transformed volume fraction at time t. We have shown (3,4) that in the isotropic case the actual form of $F(\vec{r},t)$ with impingement is

$$F(r,t) = X^{-2}(t) \sum_{\gamma}\sum_{\beta} n_\gamma(t)\ n_\beta(t)\ V_\gamma\ V_\beta\ f_0\left(rL(t)/r_\beta r_\gamma\right) \quad [1]$$

where $V_\alpha = \frac{4}{3}\pi r_\alpha^3$ is the volume of an sphere of radius r_α, $n_\alpha(t)$ is the grain density of particles of volume V_α, $L(t) = \left(\dfrac{3\ V(t)}{4\pi\ N(t)}\right)^{1/3}$ is the scaling length, $V(t)$ is the total volume of the transformed phase, $N(t)$ is the total number of particles and

$$f_0\left(r/r_i\right) = \left[\ 1 - \frac{3}{4}\left(r/r_i\right) + \frac{1}{16}\left(r/r_i\right)^3\ \right]\Theta(2r_i - r) \quad [2]$$

is the self-correlation function of a sphere, $\Theta(x)$ being the Heaviside function.

The scattering intensity of a grain structure can be expressed (5) in terms of the scattering field function

$$\Psi(\vec{r},t) = \sum_{i=0}^{p} \varepsilon_i g_i(\vec{r},t) \quad [3]$$

where ε_i is the scattering amplitude of the i-th. phase and $g_i(\vec{r},t)$ is a bi-valued function which describes the geometry of the microstructure, being 1 inside the particles of the i-th. phase and 0 elsewhere. In terms of the characteristic function above defined, the scattering intensity is

$$I(\vec{q},t) = \int d\vec{r}\, e^{i\vec{q}\vec{r}} \langle \Psi^*(\vec{r},t)\Psi(\vec{0},t)\rangle =$$

$$= \left|[1-X(t)]\,\varepsilon_0 + X(t)\bar{\varepsilon}\right|^2 (2\pi)^3\delta(\vec{q}) + \left\{[1-X(t)]\left|\varepsilon_0 - \bar{\varepsilon}\right|^2 + \overline{\left|\varepsilon_i - \bar{\varepsilon}\right|^2}\right\} X(t)\, F(\vec{q},t) \quad [4]$$

$$F(\vec{q},t) = \int d\vec{r}\, e^{i\vec{q}\vec{r}} F(\vec{r},t) = X^{-2}(t)\ \frac{6\pi^2}{q^3} \sum_{\gamma}\sum_{\beta} n_\gamma(t)\ n_\beta(t)\ \overline{V_\gamma}\ \overline{V_\beta}\ J_{3/2}^2\left(\frac{q\ r_\beta\ r_\gamma}{L(t)}\right)$$

where the scattering amplitudes are thermally averaged, δ is the Dirac-delta distribution and $J_{3/2}(x)$ is the Bessel function of fractional order 3/2.

RESULTS

The isothermal nanocrystallization of Finemet exhibits two overlapped processes (6), as shown in Fig. 1. On the one hand a decaying calorimetric signal corresponding to the formation of Cu clusters. There is no temperature dependence on this signal in the range 430°C-550°C, indicating a very fast process of growth. Direct evidences from TEM images were also given by Hono (7).

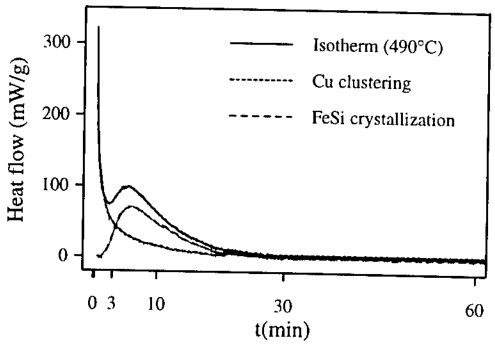

Figure 1 Isothermal DSC data.

On the other hand, following this first process but overlapped, an exothermic asymmetric calorimetric peak appears. This peak is related to the nanocrystalline precipitation of a Si depleted FeSi BCC phase with DO_3 ordering. The asymmetry is related to a diffusion controlled growth process with decreasing growth consequence of the accumulation of diffusing species in the matrix and known as soft impingement. The growth rate is given by (8)

$$\frac{dr}{dt} = \frac{D(T)}{r}\frac{\gamma - X(t)}{1 - X(t)} \qquad [5]$$

where γ accounts for the transformed fraction at the end of the primary precipitation and $D(T)$ is the diffusion coefficient of the slowest diffusing species, which in FINEMET corresponds to Nb. Nb is a well-known stabilizer of the amorphous phase and therefore a reduction of the nucleation rate should also be expected as transformation proceeds. We have taken (8)

$$I(T,\tau) = I_0(T)(1 - X(\tau)/\gamma) \qquad [6]$$

where τ is the time at which the nucleus forms, and $I_0(T)$ is the nucleation rate obtained for an undercooled liquid.

The grain size distribution along the transformation has been evaluated from these kinetic parameters by using the PKJMA model (9) giving the final distribution shown in figure 2. From this data the exact correlation functions are evaluated by using Equation (1). The addition of the SAXS profile corresponding to the nanocrystalline precipitates and the amorphous matrix are also shown in figure 2 after 10 and 60 minutes isothermal annealing at 490°C. It can be clearly seen that a second grain size distribution of smaller sizes has to be added in order to fit the SAXS profile at large q values. While introducing an extra grain size distribution with average size of about 2 nm, we can obtain a good fit of the experimental profile. The sizes of this phase agree with the measured sizes of the segregated Cu-clusters (7). Very small changes in the size of the clusters are found between the first minutes of isothermal annealing and the end of the nanocrystallization. However, although the relative intensities are obtained from the SAXS profile, it is not directly related to the number of clusters by unit volume because of the different absorption coefficients between the nanocrystalline precipitate and the Cu clusters.

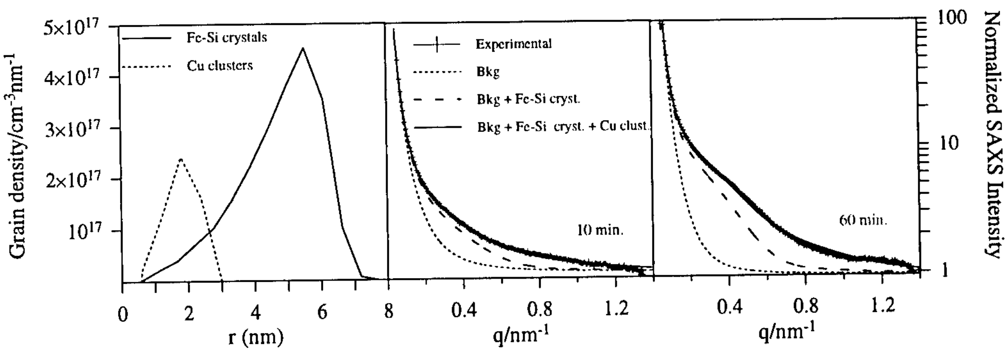

Figure 2 Computed grain size distribution at the end of the isothermal annealing at 490°C (left). Experimental and computed SAXS profile after 10 (center) and 60 (right) minutes.

CONCLUSIONS

In this paper we have presented a new method of calculating the scattering intensity function in systems underlying first order phase transitions. The grain size distributions used are obtained by the PKJMA model. The procedure has been applied to determine the SAXS profile associated with the grain size distribution appearing in the primary cristallization of the amorphous $Fe_{73.5}Cu_1Nb_3Si_{17.5}B_5$. Comparison with the experimental profile shows a discrepancy corresponding to an additional grain size distribution of smaller size. According to the DSC data and also to microstructural analysis, this grain population corresponds to the clusterization of the Cu present in the amorphous, which occurs previously to the primary crystallization.

This work was partially financed by DGICYT, grant PB94-1209, Generalitat de Catalunya 1997SGR 00039 and UPC, grant PR9505. SAXS measurements were performed at the European Synchrotron Research Facility at Grenoble, experiment HS-447.

REFERENCES

1. Guinier, A. and Fournet, G., *Small-angle scattering of X-rays*, John Wiley and Sons, New York, 1955.
2. Glatter, O., *J. Appl. Cryst.*, 1980, 13, 7.
3. Garrido, V. and Crespo, D., *Phys. Rev. E*, 1997, 56, 2781.
4. Garrido, V., and Crespo, D., *"Characteristic functions of nanostructured materials"*, in this volume.
5. Ohta, S., Ohta, T. and Kawasaki, K., *Physica*, 1987, 140A, 478.
6. Pradell, T., Clavaguera, N., Zhu, J. and Clavaguera-Mora, M.T., *J. Phys.: Condens. Matter* **7** 1995, 4129.
7. Hono, K., Hiraga, K., Wang,Q. and Sakurai, T., *Surface.Sci.* **266** 1992, 385.
8. Pradell, T., Crespo, D., Clavaguera, N. and Clavaguera-Mora, M.T. *J. of Phys: Condensed Matter* **10** 1998, 3833.
9. Crespo, D. , Pradell, T. , Clavaguera-Mora, M. T. and Clavaguera, N. , *Phys. Rev. B*, 1997, 55, 3435.

Pergamon

NanoStructured Materials, Vol. 12, pp. 653–656, 1999
Elsevier Science Ltd

0965-9773/99/$–see front matter

PII S0965-9773(99)00209-3

A DEPTH PROFILE STUDY OF THE STRUCTURE AND STRAIN DISTRIBUTION IN CHEMICALLY GROWN Cu FILMS ON AlN

L. J. Martínez-Miranda[1], Yiqun Li[1], G. M. Chow[2,3], and L. K. Kurihara[2,4]
[1]University of Maryland, Department of Materials and Nuclear Engineering, College Park, MD 20742 USA
[2]Naval Research Laboratory, Washington, DC 20375 USA
[3]Present address: National University of Singapore, Dept. of Materials Science, Kent Ridge, Singapore 119260
[4]Potomac Research International, MD 22030 USA

Abstract *-- We have studied Cu coatings grown on AlN substrates via a polyol deposition method using grazing incidence X-ray (GIXS) techniques and small angle scattering techniques to determine the dependence of film structure on depth as well as the presence of nanometer size structures in the films. Small angle measurements indicate the presence of ordered structures in the order of 4 nm close to the surface of the films. Depth studies using different X-ray energies in combination with the GIXS technique suggest the first 20 to 60 nm of the film correspond to a textured region, with strains ranging between +0.1% to -0.6%. The azimuthal ordering in the plane of the films depends on the sample deposition time and the substrate orientation. ©1999 Acta Metallurgica Inc.*

INTRODUCTION

The increased use of nanometer-scale advanced ceramic electronic elements depends on the careful control of the processing method used in developing such materials. Nanometer size particles, with sizes ranging between 1-100 nm have a number of potential electronic, magnetic and structural applications (1). These particles may have properties different from the bulk or micrometer-size samples of the same materials, due to confinement effects and the presence of a large number of interfaces. An understanding of how these properties (structural, electrical and mechanical) vary as a function of particle size and agglomeration is important to the development of any new applications.

We have recently studied the structural properties of metal coatings deposited using the polyol method (2,3). The metal precursors are dissolved in a polyol, such as ethylene glycol. The mixture is heated to reflux and the metals are precipitated out of solution. The precipitate is deposited on a ceramic substrate suspended inside the reflux for a specific amount of time. This substrate is placed either horizontally (H) with respect to the bottom of the solution container, near the bottom of the solution, or is suspended vertically (V) inside the solution. The resulting films have thicknesses that range between 2 and 4 μm.

Copper samples prepared using the method above exhibit structures that evolve both as a function of deposition time and substrate orientation. In this paper, we present evidence

of the presence of depth dependent texturing in Cu films deposited on AlN substrates. The texturing is observed in the near-surface region, and constitutes at least 20% of the sample thickness. It is associated with a distribution of lattice spacings and a strain field along the plane of the sample, which vary according to deposition time and substrate orientation.

EXPERIMENTAL

Depth-dependent measurements were performed at the National Synchrotron Light Source at Brookhaven National Laboratory, beamlines X22A and X22B, using 1.204Å and 1.554Å X-rays respectively. The beam was collimated to 2 mm^2, and had a resolution of $1.05 \times 10^{-3} q_0$. Samples prepared using 15, 20, 30, 45 and 90 minutes deposition time were studied using grazing incidence asymmetric Bragg diffraction (GIAB) in order to determine the evolution of the structure as a function of depth. In addition, the in-plane structure of samples prepared using 20 and 30 minutes deposition times was analyzed using grazing incidence X-ray scattering (GIXS). Scans were limited to the region near the (111) and (200) peaks of Cu, due to diffractometer size. A combination of small angle (SAXS) and GIXS techniques was used to ascertain the structure of the samples.

RESULTS AND DISCUSSION

Figure 1 shows the intensity of the Cu (111) peak as a function of incidence angle for samples prepared with a deposition time of approximately 90 minutes. The Cu(111) peak intensity increases at lower incidence angles for the sample grown on the vertical (V) substrate. The higher incidence angle observed for the H sample suggests either the existence of texturing, or a disordered, or chemically different top layer. These measurements also indicated the presence of copper oxide in some samples (3,4). The intensity of the oxide peak is small but finite at small incidence angles, below the critical angle, for the H sample, which suggests that for some samples there is a relatively higher concentration of oxide with respect to the metal near the surface of the sample, which may in part explain the observations of Figure 1.

Figure 2 shows a combined GIAB-SAXS measurement taken on the 45 minute deposition samples at glancing incidence (3). This measurement suggests that close to the

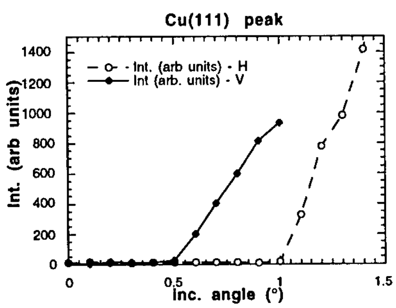

Figure 1. Cu (111) peak intensity as a function of incidence angle for a 90 minute deposition sample.

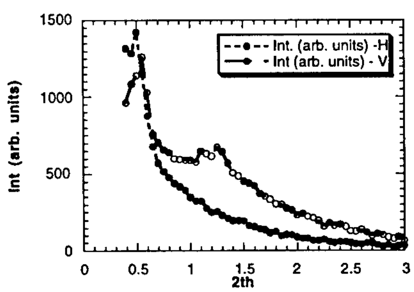

Figure 2. Small angle scan at glancing incidence angle ($\alpha = 0°$) for a sample prepared with a 45 minute deposition time (4).

surface of the V films, structures in the order of 4.3 nm are observed, whereas the (mostly) oxide layer in the H sample does not contain nanometer size particles. A depth study for the H sample shows that the low angle signal can be observed at higher incidence angles, corresponding to depths of approximately 500 nm inside the sample.

Figure 3 shows a scan taken on 45 and 15 minute reflux samples using 1.204Å X-rays. The measurements suggest these samples are textured. This same texturing is observed on 20 minute and 30 minute reflux samples. In contrast, scans taken on the same samples, as well as on the 20 and 30 minute samples using 1.5418Å X-rays indicate the structure of these samples is that of typical polycrystalline Cu. Cu has an absorption edge near 1.3Å. Near this wavelength, the absorption increases four-fold with respect to the absorption of Cu at 1.5418Å. As a result, the saturation depth at 1.2Å is in the order of 700 nm, compared to approximately 2 μm at 1.5418Å. Thus, the observed texturing exists in the top one tenth to one third of the samples.

In order to investigate the nature and origin of the textured region described above, we have studied the in-plane structure 20 and 30 minute films, using GIXS. Figures 4a - d show the in-plane GIXS contour scan of the Cu (200) on 20 and 30 minute samples grown on both a horizontal (Figures 4a, c) as well as a vertical (Figures 4 b, d) substrate respectively. The scans consist of a number of peaks, whose d-spacings correspond to strains ranging between +0.1% to -0.6%. A similar peak distribution is observed in the Cu (111) peaks (not shown). The in-plane azimuthal mapping of these peaks confirms the textured nature of these top layers. Figure 4 shows that the intensity and location of the different peaks depend on the azimuthal orientation of the sample with respect to the incoming beam.

The azimuthal distribution varies both as a function of metallization time as well as substrate orientation. The 20 minute H sample has an azimuthal distribution of approximately 20°, whereas the 20 minute V sample this distribution is approximately 80°, as seen in Figures 4a-b. This result is consistent with previous SEM observations that indicate that Cu crystallites deposited vertically consist of equiaxed particles (3). It also suggests that the horizontally prepared sample has in-plane texturing (a preferred azimuthal/stress orientation). This preferred orientation becomes less evident as the metallization time increases, as seen on the 30 minute samples (Figures 4c-d). The 30 minute samples show a broad azimuthal distribution, both for the H as well as for the interior regions of the V samples.

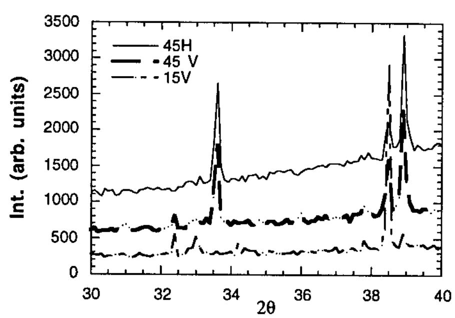

Figure 3. Diffraction scans on a 45V, 45H and 15V samples. Note the small (200) peak in the 15V sample, and the 200/111 texturing in all the samples.

CONCLUSIONS

We have presented the results of a depth profile structural study of Cu films prepared via a chemical route. Our results indicate the presence of nanometer size structures as well as textured regions in the upper 20% of the films. The center of the films show the structure of polycrystalline Copper. The results above suggest the process of aggregation and continuous film formation is a function of time primarily. Further analysis and studies are in progress.

This work was supported partially by a NSF grant No. ECS-9710789, and by NRL and ONR nanostructured materials programs. X-ray studies were performed at the National Synchrotron Light Source at Brookhaven National Laboratory, which is supported by the U. S. Department of Energy.

REFERENCES

1. L. M. Sheppard, Ceram. Bull, 1990, 69, 1881.
2. L. K. Kurihara, G. M. Chow, and P. E. Schoen, Nanostruct. Mater., 1995, 5, 607.
3. G. M. Chow, L. K. Kurihara, D. Ma, C. R. Feng, P. E. Schoen, and L. J. Martínez-Miranda, Appl. Phys. Lett., 1997, 70, 2315.
4. F. Fievet, F. Fievet-Vincent, J. P. Lagier, B. Dumont, and M. Figlarz, J. Mater. Chem., 1993, 3, 627.

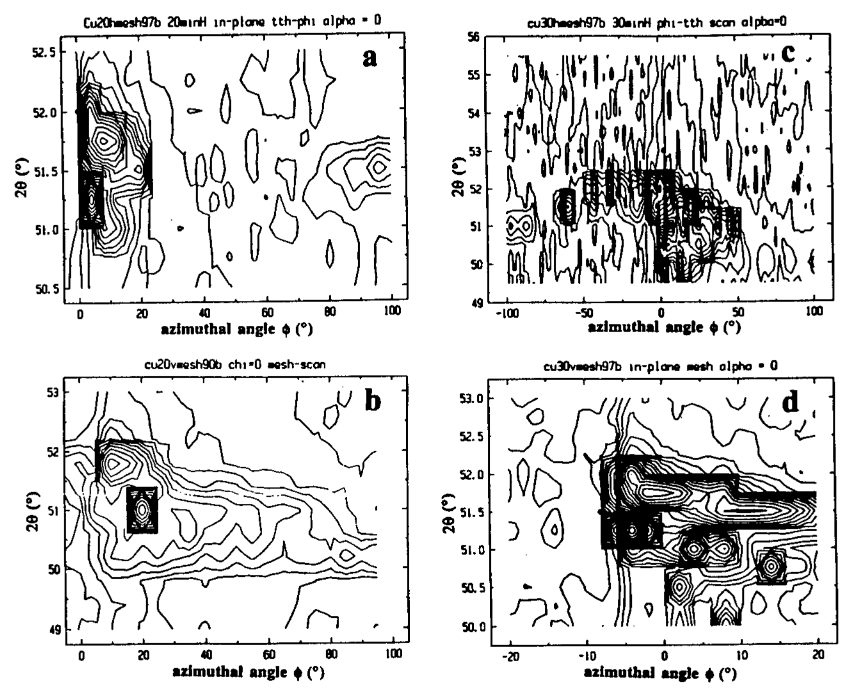

Figure 4. In-plane 2θ–φ contour maps of the Cu (200) at different deposition times and substrate orientations: a. 20 minute H; b. 20 minute V; c. 30 minute H; d. 30 minute V.

Pergamon

NanoStructured Materials, Vol. 12, pp. 657–660, 1999
Elsevier Science Ltd

0965-9773/99/$–see front matter

PII S0965-9773(99)00210-X

GRAIN SIZE MEASUREMENT OF NANOCRYSTALLINE GOLD BY X-RAY DIFFRACTION METHOD

T.Inami[1], M.Kobiyama[1], S.Okuda[2], H.Maeta[3] and H.Ohtsuka[3]

1.Faculty of Engineering, Ibaraki University, Nakanarusawa, Hitachi, Ibaraki, 316, Japan
2.Emeritus, University of Tsukuba,1455-29, Arakawa-oki, Ami-machi, Ibaraki,300-11, Japan
3.Department of Materials Science and Engineering, Japan Atomic Energy Research Institute, Tokai-mura, Ibaraki, 319, Japan

Abstract--*The X-ray diffraction profiles on nanocrystalline gold prepared by the gas deposition method were studied by Warren-Averbach and integral breadth analysis for the evaluation of grain sizes and internal strains. The grain size of as-prepared specimens, estimated by Warren-Averbach analysis, was in the range of 7 to 20nm. The thermal stability of these specimens was found to be quite high; when annealed for 1h, the grain size remained unchanged up to 770K and grew about twice at 1070K. The root mean square strain, estimated by integral breadth analysis, was in the range of* $0.8\text{-}2.3\times10^{-3}$ *and reduced to* $\sim3\times10^{-4}$ *after annealing at 870K and higher.* ©1999 *Acta Metallurgica Inc.*

INTRODUCTION

In evaluating mechanical properties and thermal stability of nanocrystalline materials, grain size and internal strain are very important factors. For nanocrystalline (hereafter, n-) Cu, Pd and Ag produced by the inert gas condensation and compaction method, abnormal grain growth was reported to occur even at room temperature(1). On the other hand, for n-Au prepared by the gas deposition method, the grain size was found to remain unchanged after annealing at 900K for 1min(2). In the gas deposition method(3) where nanosized particles produced in the evaporation chamber are transferred with He gas to the deposition chamber and deposited on a substrate to produce nanocrystalline film specimens, no compaction process is involved and many properties of the specimens could be quite different.

In the present work, the X-ray diffraction profiles on n-Au prepared by the gas deposition method were studied by two methods - Warren-Averbach and integral breadth analysis(4) - for the detailed evaluation of grain sizes and internal strains.

EXPERIMENTAL

Specimens of n-Au were prepared by the gas deposition method. The He gas pressures in the evaporation chamber and evaporation temperatures were ranging from 620-1200Torr and 1740-1860K, respectively. When depositing, the substrate temperature increased up to 340-400K. The sizes of specimens were $3\times25mm^2$ and their thicknesses were approximately 10-50μm. High purity Au(99.999mass%) was used as a starting material. After

TABLE 1
Grain Size and Root Mean Square Strain obtained by Warren-Averbach and Integral Breadth Analysis.

	preparation condition		W-A	IB	
No.	Pres.(Torr)	Temp.(K)	Size(nm)	Size(nm)	$<e^2>^{1/2} \times 10^3$
1	620	1810	15	27	1.2
2	630	1860	16	17	0.8
3	650	1740	9	12	1.5
4	650	1820	19	31	1.5
5	760	1780	12	19	2.3
6	1200	1830	7	11	1.8

removing from the substrate by a thin blade, the specimens were annealed in vacuum (less than 1×10^{-6}Torr) at various temperatures ranging from 670-1200K for 1h.

X-ray diffraction profiles were measured using the CuKα radiation at operating parameters of 40kV and 40mA. The profiles were recorded with a 2θ angular increment at 0.02° and a counting time of 4-10s. After removing Kα_2 peaks and instrumental broadenings, the crystal grain size and internal strain were determined by Warren-Averbach analysis. Measurements of integral breadths on the same diffraction profiles were also made. The combined relation may be arranged on the assumption of the grain size and strain line profiles being approximated by Cauchy and Gaussian function, respectively(4). From the slope and ordinate intercept in those linear plots, the size and strain parameters may be determined.

RESULTS AND DISCUSSION

In most diffraction profiles for the n-Au specimens measured in this works, the relative strengths of the 111 and 222 peaks were larger than other peaks and the 400 peak had a little strength. Some grains in those specimens seem to have preferred orientation of <111> normal to the specimen surface and to be elongated along the direction vertical to the surface as reported in previous work(5). With the exception of these grains, the other grains are considered to be almost isotropic. In this work, the grain sizes and internal strains were estimated by using 200, 220, 311, 331 and 420 peaks.

The results on as-prepared specimens by the Warren-Averbach (W-A) and integral breadth (IB)analysis are summarized in Table 1. The grain sizes obtained by W-A analysis are in the range of 7 to 20nm and rather small comparing with those obtained by IB analysis. This difference appears to arise from different averaging in analysis as mentioned by K.Reiman and R.Wurshum(6). When preparing under the conditions with evaporation temperatures >1800K and He gas pressures <700Torr, the specimens have relatively large grain size.

The dependence of grain size on annealing temperatures is shown in Fig.1(a) including the results of previous work (grain size; 7-11nm)(5). The grain sizes in most specimens remained unchanged up to ~770K and slightly increased at 870K. Above 1100K significant grain growth occurred. From these results, it can be said that the grain size of n-Au prepared by the gas deposition method is stable up to ~900K. This high thermal stability is in marked contrast with that of nanocrystalline pure metals prepared by the inert gas condensation and compaction method. However, the grain size in specimen(No.1)

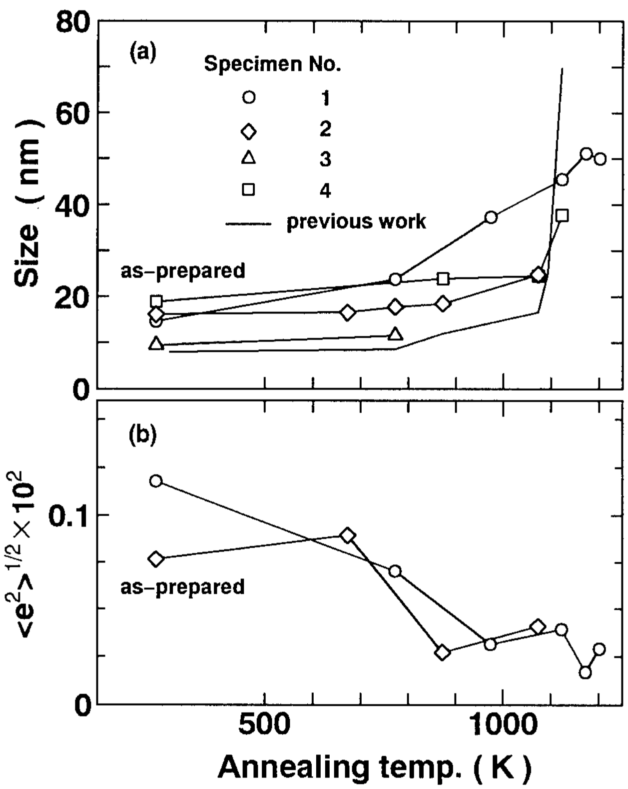

Fig.1 Grain size(a) and root mean square strain(b) as a function of annealing temperature. Annealing at each temperature was made for 1h in vacuum less than 1×10^{-5}Torr.

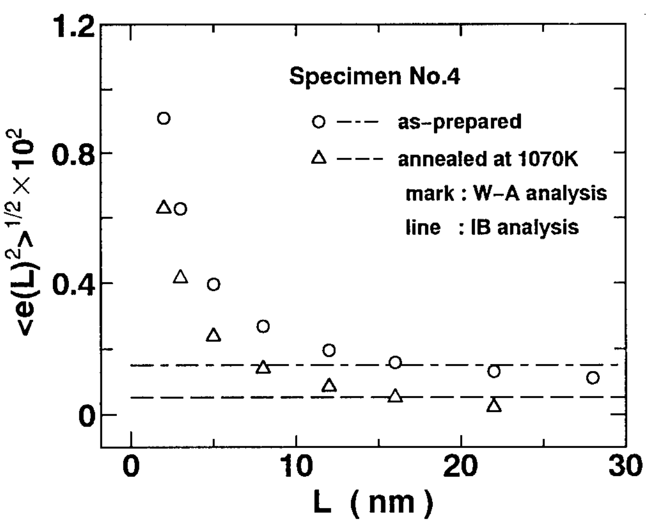

Fig.2 Root mean square strain as a function of L, the column length normal to the reflecting planes.

increased slightly at 770K and was more than 2 times of those of as-prepared after annealing at 970K. This specimen was prepared in almost same conditions (He gas pressure in the evaporation chamber and evaporation temperature) as the specimen(No.2). Both specimens have the same grain size, but their dependences of grain size on annealing temperatures are substantially different. Therefore, the thermal stability of n-Au specimens prepared by the gas deposition method seems to be controlled by other various preparation conditions.

The root mean square strain (rms strain) of W-A analysis are markedly reduced with increasing L, the column length normal to the reflection planes, as shown in Fig.2. These remarkable reduction of rms strain with L was reported for the pure niobium powder mechanically milled(7) and to be interpreted in terms of a strain localization(6). The difference between the rms strains obtained from W-A and IB analysis in this work is too large comparing with those other reports. Further studies on this point are now in progress. The rms strains of IB analysis in as-prepared specimens, summarized in Table 1, are in the range of $0.8\text{-}2.3\times10^{-3}$ and comparable to the observation for cluster-synthesized n-Pd. The rms strains seem to be large in the specimens produced in high He gas pressure in the evaporation chamber, that is, by high impinging speed. The dependence of rms strain on annealing temperatures is shown in Fig.1(b). In specimen(No.1) rms strains decrease with increasing annealing temperature, that is, grain growth. On the other hand, rms strain in specimen(No.2) reduces to 2.7×10^{-4} after annealing at 870K. But the grain size remains almost unchanged. Further work is now needed on this point.

CONCLUSIONS

The grain size and internal strains of n-Au prepared by the gas deposition method were studied by means of X-ray diffraction. The grain sizes of as-prepared specimens, estimated by Warren-Averbach analysis assuming to be isotropic grain, were in the range of 7- 20nm. The thermal stability of those specimens was found to be quite high; for annealings for 1h, the grain size remained unchanged up to 770K, grew about twice at 1070K. The root mean square strain, estimated by integral breadth analysis, was in the range of $0.8\text{-}2.3\times10^{-3}$ and reduced to $\sim3\times10^{-4}$ after annealing at 870K and higher.

ACKNOWLEDGEMENTS

This work was partly supported by Proposal-Based Advaned Industrial Technology R&D Program, NEDO.

REFERENCES

1. B.Gunther, A.Kumpmann and H.D.kunze: Scripta Metall. Mater., 27(1992), 833.
2. S.Okuda and F.Tang: Nanostruct. Mater., 6(1995), 585.
3. S.Kashuu, E.Fuchita, T.Manabe and C.Hayashi: Jpn. J. Appl. Phys., 23(1984), L910.
4. H.P.Klug and L.E.Alexander: *X-ray diffraction procedures for polycrystalline and amorphous materials*, 2nd edition, John Wily and Sons, New York, (1974), p.642.
5. T.Inami, S.Okuda, H.Maeta and H.Ohtsuka: Mater. Trans. JIM, in press
6. K.Reimann and R.Wurschum: J.Applied Physics, accepted, March 1997
7. S.K.Pradhan, T.Chakraborty, S.P.Sen Gupta, C.Suryanarayana, A.Frefer and F.H.Froes: Nanostruct. Mater., 5(1995),53.

Pergamon

NanoStructured Materials, Vol. 12, pp. 661–664, 1999
Elsevier Science Ltd

0965-9773/99/$–see front matter

PII S0965-9773(99)00211-1

ADHESION BETWEEN NANOPARTICLES

Y.Yao and A.R.Thölén
Experimental Physics
Chalmers University of Technology, S-41296 Göteborg, Sweden

Abstract *— A study of the contact and adhesion between particles with clean surfaces (free from oxide and other contamination) is important but increasingly more difficult to perform as the particle size is reduced to a nanoscale. A reproducible way of finding such contacts between a large number of nanoparticles has been developed. Cobalt particles within the size range 5-200 nm have been obtained by ageing a solution-treated Cu-2Co (w/o) alloy at 600-800°C, followed by the carbon film extraction technique. The dipole adhesion stress field was clearly observed in TEM. Convergent beam electron diffraction (CBED) proved that the free particles were likely to contact with a common interface , and they often orientated in the same direction. This work establishes a solid experimental base for computational image matching of the adhesion properties of nanoparticles. ©1999 Acta Metallurgica Inc.*

INTRODUCTION

Besides its fundamental theoretical interest, adhesion between nanoparticles is a basic and complicated phenomenon which has scarcely been interpreted on a microscopic scale. This issue is important, because one is subjected to it in many fabrication processes and applications of nanoparticles e.g. dry friction, electrical contact, deagglomeration and dispersion, pre-stage in nanosintering, etc. The adhesive effect makes handling even more difficult with a decreasing particle size.

Earlier investigations (1,2) have given both theoretically and experimentally a clear picture of the physics of two particles meeting and forming a contact. The balance between surface energy, grain boundary energy and elastic energy results in a minimized total energy of the system by forming a finite contact area. The contrast from the adhesion stress fields between particles has been calculated (2,3) by solving the Howie-Whelan equations for electron diffraction and detailed information on the contact zone can be studied and interpreted from the dipole stress field image. However, the performance of image matching was mostly hindered by the harsh requirements for TEM image quality often deteriorated by a tricky specimen

preparation, as well as by a lack of information on crystalline orientation and interface relationship from such small nanoregions.

In this paper we report on an extension of our earlier work on small metal particles. Co particles (5- 200 nm) precipitated and extracted from a Cu-2Co (w/o) alloy were used as the study material, and metallic contacting surfaces were achieved successfully by correctly selecting the electrolytes. We performed CBED to determine the orientation relationships of the adhered particles. This preliminary experimental work establishes a good starting point to image matching and simulation of the adhesion properties.

EXPERIMENTAL

The material used in this study was a Cu-2Co (w/o) alloy, which was first solution treated at 1000°C for 1h and then water quenched. The following ageing was conducted in the temperature range 600-800°C for 0.5-100 hours. This treatment results in the homogeneous precipitation of **fcc** cobalt particles in the size range 2–200 nm depending on the ageing conditions. The surface of the aged specimens were polished mechanically with diamond paste, and then briefly etched in an electrolyte of copper nitrate, nitric acid and methanol at 1V. The cobalt particles were collected by the conventional extraction replica technique described elsewhere (4). Conventional TEM observation and CBED were carried out using a JEOL 2000 FX microscope operating at 200 kV. The size of the defocused probe used was about 20 nm.

RESULTS AND DISCUSSION

So far, the studies of nanoparticle adhesion have mostly been performed on gas-evaporated particles, since this method can render clean surface contacts (oxide and contamination free). However, one difficulty with this method is the relative scarcity of particles which adhere to each other at room temperature. The adhesion stress is normally assumed to be somewhat recovered due to diffusion. As a comparison, the method of precipitate particles extracted by etching-evaporating carbon film-etching process can make particles meet freely at room temperature. The particle size can also be controlled by means of an appropriate design of the thermal treatment conditions. The particle size increases sharply with the temperature. There is a power-law behaviour between particle radius and ageing time until the particle size reaches a maximum value depending on temperature. The slope varies between 0.7 and 0.8 for the temperature interval 600-800°C, and presents a temperature-independent feature. It is also observed in TEM a critical particle size range for which spherical precipitates are transformed into faceted particles. For the present Cu-2Co (w/o) alloy, the average transition particle size is around 30-40 nm. This transformation certainly reflects the equilibrium state in terms of the interface energy and strain energies of cobalt precipitates in a copper matrix.

The cumbersome consequence of the electrolytic extraction method is the presence of oxide layer on the particles. It is imperative to determine the proper electrolytic agents. The best results were obtained by using a solution of $Cu(NO_3)_2$, HNO_3 and methanol. It is also essential to rapidly remove and rinse the specimen in both the polishing and replica-making

processes to minimise the oxidation. Surface-clean particles and metallic contact were here achieved successfully.

The typical TEM micrographs of cobalt contacting particles (Fig. 1) show dipole stress fields indicated by the arrows. The deviation of the incident beam direction from the zone axis was determined by $\varphi = r / L$ (where r is the radius of the ring where the Evald sphere intersects the zero order layer of the reciprocal lattice, L is the camera length). The particles A, B, C, D, E are basically orientated in the [110] direction though they deviate somewhat from the incident beam direction as shown in Table 1. In addition to [110] // [110], two other orientation relationships, [110] // [100] and [110] // [112], were also found. It is interesting to note that among the particles with the above orientation relationships, the contacting boundaries where the strain fringe image is strongly observed also contain certain interface relationships e.g. (111) // (111), (110) // (110) and (002) // (002). It is obvious that there is a tendency for free particles to contact preferentially along equivalent planes, and therefore, align with a common orientation in order to minimize the total surface energy of the system. Another interesting observation is that the contact is often formed near the corners where either a {111} facet and a {100} facet or two{111} facets meet. No doubt that at those points the local curvature radius is smaller and the surface energy is higher. Another factor in the first contact between cobalt particles is the magnetic attraction. This attraction could steer the first contact, however, the final contact is determined by the surface energy as forces emanating from the surface energy are much larger than the magnetic ones.

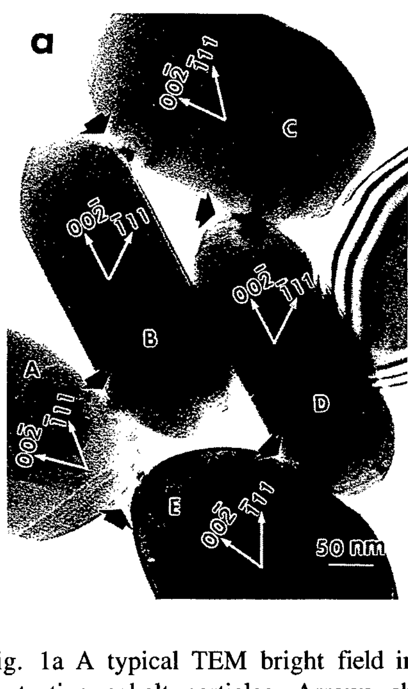

Fig. 1a A typical TEM bright field image of contacting cobalt particles. Arrows show the areas of dipole stress field fringes.

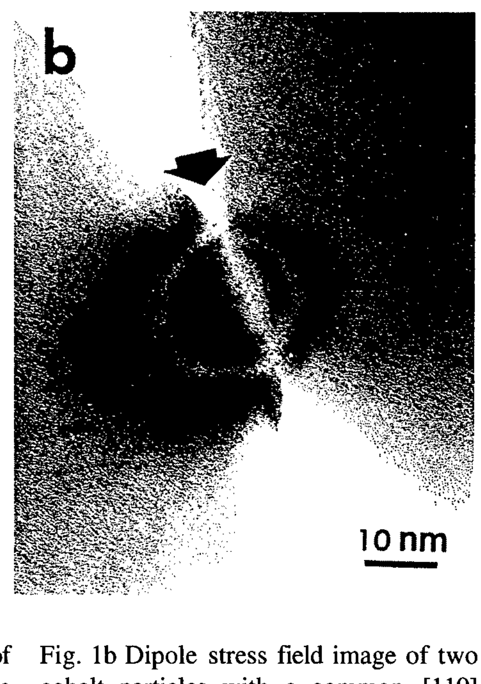

Fig. 1b Dipole stress field image of two cobalt particles with a common [110] orientation.

TABLE 1
Orientation and Interface Relationship of Particles in Fig. 1

Particle	Orientation	Deviation angle from zone axis(deg.)	Interface relationship
A	[110]	7.8	$(111)_A // (111)_B$, $(002)_A // (002)_E$
B	[110]	1.9	$(110)_B // (110)_D$
C	[110]	8.9	$(111)_C // (111)_B$
D	[110]	10.0	$(111)_D // (111)_C$
E	[110]	6.8	$(110)_E // (111)_D$

The previous investigation on the adhesion of faceted gold particles (5) has already revealed that two particles often adhere along identical planes. A recent study on nanosintering of Cu particles (6) has also pointed out the particle rotation to obtain the same orientation as the substrate. Therefore, it is reasonable to assume that the free particles are likely to adjust their mutual orientations spontaneously after adhering. Then, a final equilibrium configuration of contact should be in a minimum energetic state instead of in a random arrangement. These rearranging processes could be much faster than surface and self diffusion (6). The further understanding of the details of particle adhesion will be interpreted by modern TEM techniques i.e. HREM, EDX and EELS.

CONCLUSIONS

A method to make a large number of nano metal particles contact in a controlled way has been developed. TEM observations and CBED analysis on cobalt particles revealed that neighbouring particles do often adhere along identical planes, and the particles tend to align with a common low indexed zone axis or even with the same orientation. This investigation has formed a solid experimental basis for our next step of computer simulation to interpret the fine details of particle adhesion.

REFERENCES

1. Johnson, K.L., Kendall K., and Roberts, A.D., *Proc. R. Soc. Lond. A.*, 1971, 324, 301.
2. Easterling, K.E. and Thölén, A.R., *Acta. Met.*, 1972, 20, 1001.
3. Sethi, S.A. and Thölén, A.R., *Electron Microscopy*, EUREM 92, Granada, Spain, 1992, 2, 667.
4. Easterling, K.E. and Swann, P.R., *Acta Met.*, 1971, 19, 117.
5. Hansson, I. and Thölén, A.R., *Phil. Mag A*, 1978, 37, No4, 535.
6. Joanna, R. G., *Nanostructured Materials*, 1998, (in print).

Pergamon

NanoStructured Materials, Vol. 12, pp. 665–668, 1999
Elsevier Science Ltd

0965-9773/99/\$–see front matter

PII S0965-9773(99)00212-3

EXAFS STUDY ON NANOCRYSTALLINE $Fe_{40}Co_{10}Cu_{50}$ ALLOY PROCESSED BY MECHANICAL ALLOYING

Dong-Seok Yang, Yong-Goo Yoo and Seong-Cho Yu

Department of Physics, Chungbuk National University, Cheongju, 361-763, Korea.

abstracts -- Metastable $Fe_{40}Co_{10}Cu_{50}$ alloys were fabricated by mechanical alloying process from the mixed powder. The structural changes during mechanical alloying process and post heat treatment were examined by Fe, Co, and Cu K-edge EXAFS measurements. The EXAFS analysis verified that Fe and Co atoms diffused to the Cu matrix so that the metastable Fe-Co-Cu with fcc structure was formed by the mechanical alloying. Also we found that the metastable Fe-Co-Cu alloy was decomposed into Fe-Co alloy and Cu by annealing process. ©1999 Acta Metallurgica Inc.

INTRODUCTION

Recently mechanical alloying method has been studied extensively in order to manufacture new materials of metastable, amorphous and nanocrystalline state(1,2). The extended x-ray absorption fine structure (EXAFS) experiments have been done as a probe of the local structure of various states such as crystalline, amorphous and molecules for last two decades(3). Cocco(4) suggested that EXAFS was also useful to study the structural analysis for mechanically alloyed metastable alloys. Especially it has been shown that the mechanical alloying technique is useful method for alloy formation of the immiscibile systems such as Fe-Cu, Fe-Ag and Ag-Cu alloys. The miscibility of Fe-Cu system has been investigated clearly by Kirkland et al.(5) with x-ray diffraction and EXAFS, which were shown that the Fe atoms break into Cu matrix so that Fe-Cu alloys with fcc structure were formed by the high energy ball milling process. In this work, we studied the miscibility of mechanical alloyed Fe-Co-Cu systems, by the structural analysis which was conducted by the x-ray diffraction and EXAFS study.

EXPERIMENTAL

Mixtures of pure elements of Fe, Co, and Cu (80 mesh, 99.9 %) powders were mechanically alloyed by a high energy ball mill under an Ar atmosphere with the ball

to powder weight ratio of 20 : 1. The milling periods were 20, 40, 60, and 80 hours, respectively. The annealing for the 80 hours milled sample was done for one hour under an Ar atmosphere at 500 ℃. The structural change after milling for each period was examined by x-ray diffraction(XRD) pattern and EXAFS at room temperature. XRD patterns were measured using Mo $K\alpha$ radiation. EXAFS measurements were carried out in transmission set up at beamline, 3C1XAFS, of Pohang light source (PLS) in Pohang Accelerator Laboratory (PAL), Pohang, Korea. The radiation characteristics of PLS were the electron energy of the storage ring 2.0 GeV, the energy resolution ($\Delta\lambda/\lambda$), 2.0×10^{-4} at 10 KeV, the beam size 10×1 mm^2 (unfocused), and the photon flux 1.0×10^{9} photons/sec at 12 KeV. The maximum current was 120 mA. The EXAFS spectrum was measured at 300 K in a transmission mode. The absorption spectra were taken above K-edge of Fe (7.1 KeV), Co (7.8 KeV) and Cu (8.9 KeV).

RESULTS AND DISCUSSION

Figure 1 shows the XRD patterns of the mechanically alloyed $Fe_{40}Co_{10}Cu_{50}$ alloy for the indicated processing times. Initially the mixed powder of Fe, Co and Cu shows bcc-Fe peaks, hcp-Co peaks, fcc-Co peaks and fcc-Cu peaks in the XRD pattern. In 20 hours milling time, hcp-Co and fcc-Co peaks disappeared and in 80 hours milling time, hcp-Co, fcc-Co and the bcc-Fe peaks disappeared completely. From this figure we can see that Fe and Co crystalline phase has been broken but Cu crystalline phase remains. This indicates that metastable alloys were produced by mechanical milling process from the mixed powder. The structural orderness has been studied by the Fourier transform of the EXAFS spectra. EXAFS analysis provides information on both the short range (in first shell of Fourier transform) and the long range (higher shell than the second) order. Crystalline phase has both the short range and the long range order while amorphous phase has the short range order only. Unfortunately it was difficult to investigate the short range order of Fe, Co and Cu atom in the first shell because the interatomic distance, the backscattering amplitude and the phase shift for Fe, Co and Cu were similar each other, and three kind of atoms coexist in the first shell. However the higher shells show clearly the miscibility effect of Fe, Co and Cu because, for example, if Fe atom resides in the Cu matrix, the higher shells of the Fourier transform for Fe K- edge EXAFS spectrum should be resemble to the spectra of the pure copper.

Figures 2, 3 and 4 are the Fourier transformed spectra for Fe, Co and Cu K-edge spectra, respectively. In these figures, the peaks in higher shells are represented by r_3, r_4, r_5 for the third, the fourth, the fifth nearest neighbors of Fe and r_2', r_3', r_4' for the second, the third, the fourth nearest neighbor of Co and r_2'', r_3'', r_4'' for the second, the third, the fourth nearest neighbor of Cu.

As shown in figure 2, intensities of peaks at r_3, r_4, r_5 decreased with the increased milling time indicating that long range order was broken continuously due to

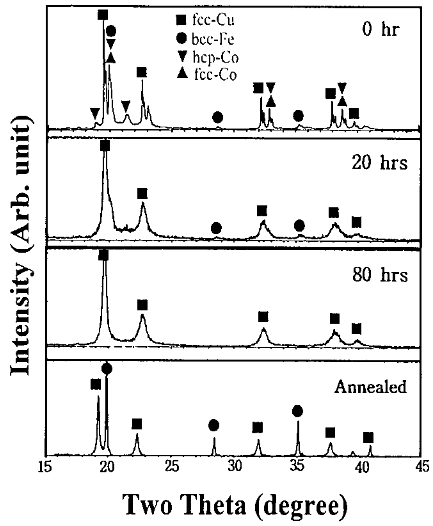

Fig. 1 XRD patterns of $Fe_{40}Co_{10}Cu_{50}$ alloys with processing periods.

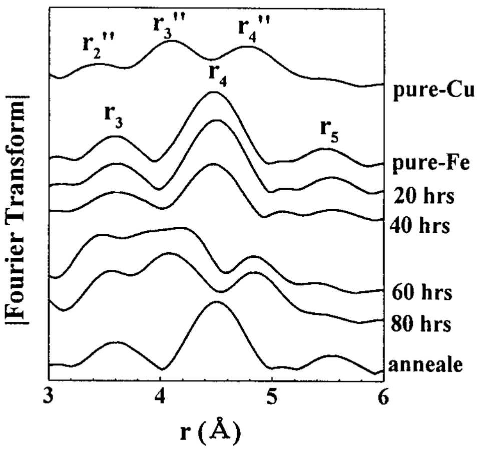

Fig. 2 Fourier transform of the Fe K-edge EXAFS spectra on $Fe_{40}Co_{10}Cu_{50}$ alloys with processing periods. The pure-Cu measured at the Cu K-edge was inserted to compare with the Fe spectra.

Fig. 3 Fourier transform of the Co K-edge EXAFS spectra on $Fe_{40}Co_{10}Cu_{50}$ alloys with processing periods. The pure-Fe and the pure-Cu measured at Fe and Cu of K-edge were inserted to compare with the Co spectra.

structural disorder. After 80 hours of milling process, r_3, r_4, r_5 peaks disappeared completely indicating the bcc-Fc structure was broken, but peaks corresponding to r_2'', r_3'', r_4'' of fcc-Cu structure appeared. This indicates that the structure around Fe atom has been transformed from bcc to fcc and supersaturated Fe-Co-Cu solid solution were formed by the mechanical alloying process. When the 80 hours milled sample was annealed, the peaks r_3, r_4, r_5 of bcc structure were recovered, indicating that Fe atoms in the metastable state of fcc structure were taken out. It showed that Fe and Cu were separated again.

Comparing the fcc peaks r_2', r_3', r_4' and r_2'', r_3'', r_4'' for Co and Cu in figure 3, the peak distances r_2', r_3', r_4' of Co were slightly shifted to the central atom due to the different atomic distance of Co and Cu atoms. The peak distance r_2', r_3', r_4' of Co decreased as the milling time increased. The peak positions of r_2', r_3', r_4' for 60 and 80 hours milled samples were shifted to the r_2'', r_3'', r_4'' peaks of Cu which means that most Co atoms diffused to the lattice of Cu. When the 80 hours milled sample was annealed, Co peaks were not recovered while the bcc peaks r_3, r_4, r_5 were created during the annealing process. This indicates that Co atoms in the metastable state were merged to Fe and formed supersaturated Fe-Co solid solution when it was annealed.

As shown in figure 4, peak positions of Cu structure were not changed during the milling process but intensity of each peak reduced with increasing processing time.

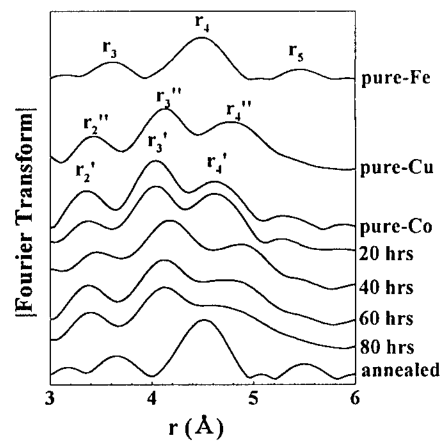

Fig. 3 Fourier transform of the Co K-edge EXAFS spectra on $Fe_{40}Co_{10}Cu_{50}$ alloys with processing periods. The pure-Fe and the pure-Cu measured at Fe and Cu of K-edge were inserted to compare with the Co spectra.

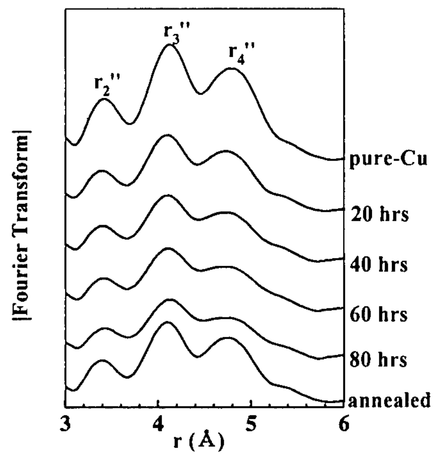

Fig. 4 Fourier transform of the Cu K-edge EXAFS spectra on $Fe_{40}Co_{10}Cu_{50}$ alloys with processing periods.

The reduction of the magnitude represents the loss of long range order due to the intrusion of Fe and Co atoms into Cu matrix. The peaks of the Fourier transformed spectra for the annealed specimen increased again so that the long range order of Cu was recovered by precipitation of Fe-Co bcc structure.

The EXAFS measurements were performed under the approval of the Korean Synchrotron Radiation User's Association. The research was supported by the Korean Ministry of Education Research Fund for Advanced Materials in 1997 and Korean Science and Engineering Fundation under grant No. 96-0702-05-01-3.

REFERENCES

1. T. Ambrose, A. Gavrin and C. L. Chien, *Journal of Magnetism and Magnetic Materials*, 1993, 124, 15.
2. Y. Chen, M. Bibole, R. Le Hazif, and G. Martin, *Physical Review B*, 1993, 48, 14.
3. D. S. Yang, D. R. Fazzini, T. I. Morrison, L. Troeger, G. Bunker, *Journal of Non-Crystalline Solids*, 1997, 210, 275.
4. G. Cocco, S. Enzo, N. T. Barrett and K. J. Roberts, *Physical Review B*, 1992, 45, 7066.
5. V. G. Harris, K. M. Kemner, B. N. Das, N. C. Koon, A. E. Ehrlich, J. P. Kirkland, J. C. Woicik, P. Crespo, A. Hernando, A. Garcia Escorial, *Physical Review B*, 1996, 54, 6929.

Pergamon

NanoStructured Materials, Vol. 12, pp. 669–672, 1999
Elsevier Science Ltd

0965-9773/99/$–see front matter

PII S0965-9773(99)00213-5

SELF-ORGANIZATION IN FERROFLUIDS PREPARED BY SONOCHEMICAL RADIATION METHOD

T. Prozorov [1], R. Prozorov[2], K. V. P. M. Shafi[1], A. Gedanken[1]

[1] Department of Chemistry, Bar-Ilan University, Ramat-Gan 52900, Israel.
[2] Department of Physics, Bar-Ilan University, Ramat-Gan 52900, Israel.

Abstract *-- We report on the sonochemical synthesis and aging of ferrofluids consisted of nanosized particles. TEM study reveals that nanoparticles in fresh liquids are round-shaped and have almost uniform particle size distribution centered around 10 nm. During aging, magnetic nanoparticles organize themselves in clusters of different shape, which depends mainly on the magnetic nature of metals in a particular ferrofluid. Magnetization measurements demonstrate the change of magnetic signal, as compare to the fresh ferrofluids. ©1999 Acta Metallurgica Inc.*

INTRODUCTION

Liquids containing small magnetic particles (ferrofluids) are of immense technological importance (1-3). Conventionally, such fluids are prepared in the presence of stabilizing agents (surfactants or dispersants) (4-7). However, the synthesis of ferrofluids is also possible without the surfactant additive (8). In the present work we report on self-organization during aging in sonochemically obtained ferrofluids, containing iron oxide (prepared with dispersant), and Co- and Cu- based ferrite nanoparticles (synthesized without surfactant).

EXPERIMENTAL

The ferrofluids were synthesized by using the sonochemical radiation (5,6). The synthesis was performed using the sonicator of Sonics and Materials, VC-600, Ti horn, 20 kHz, 100 W·cm^{-2} and immersion cooler with PT-100 sensor of Julabo (JU965089/1). In one case, stable magnetic fluid consisting of amorphous iron oxide nanoparticles was synthesized by ultrasound irradiation of a decalin solution of $Fe(CO)_5$ at 30^0 C for three hours in the presence of oleic acid as a solutions of $Co[CH_3(CH_2)_3CH(C_2H_5)CO_2]_2$ or $Cu[CH_3(CH_2)_3CH(C_2H_5)CO_2]_2$ and $Fe(CO)_5$ in decalin, which were sonochemically irradiated at -60^0 C for 4 hours. In this method the role of a stabilizing agent is played by the organic ligand $[CH_3(CH_2)_3CH(C_2H_5)CO_2]^-$. Varying the ratio between components in initial solution

yields cobalt or copper ferrite fluids of different stoichiometry, determined by EDAX analysis on a precipitated component. Magnetic measurements were conducted using a *Quantum Design* MPMS SQUID magnetometer at 40 *K* (when ferrofluid is frozen). TEM study was performed using the JEOL Instruments JEM-1200EX electron microscope (IEM 1200EX-3) on Formvar coated copper grids (200 mesh).

RESULTS AND DISCUSSION

TEM study of the fresh iron oxide ferrofluid shows that the material consists of round-shaped nanoparticles with the mean size of about 10 nm, Fig.1(a). Magnetization measurements performed on frozen liquids, Fig.2, are typical for superparamagnetic material, i. e., there is no saturation of magnetization at high fields as well as no noticeable hysteresis. After aging at room temperature for two months, magnetization of ferrofluidal iron oxide has increased as compare to a fresh liquid. The TEM study conducted on the aged material, revealed the formation of the acicular particles of 50×5 nm, Fig.1(b). Formation of the acicular particles in this case is naturally explained recalling that each nanoparticle is a magnetic dipole, so that interaction between two particles is anisotropic with maximal attraction along the dipole axis. Therefore, the diffusion assisted growth during the aging results in the formation of elongated particles. The increase of the magnetic signal is due to a larger magnetic moment of each particle, because the aggregate consists of oriented nanoparticles. Figure 2 demonstrates the increase of the magnetic signal of aged (b) colloid as compared to a fresh one (a).

TEM images of Cu-based ferrofluids synthesized without the surfactant additives, Fig.3(a)-4(a), demonstrate the initially rounded particles of the mean size of less than 8 nm. Aged for one week, the magnetic liquids begin to arrange in bigger clusters with the *lower* magnetization. The TEM study carried out after six more weeks revealed the formation of much larger round aggregates (Fig.3(b)) of the mean size of about 50 nm. The decrease of the magnetic signal may be explained considering disorientation of the elementary magnetic moments in aggregates, so the net magnetic moment is small.

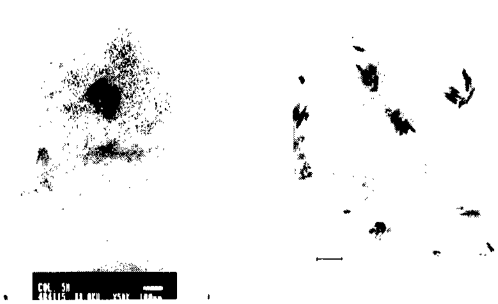

Figure 1. TEM images of the iron oxide ferrofluid: (a) fresh, (b) aged for two months

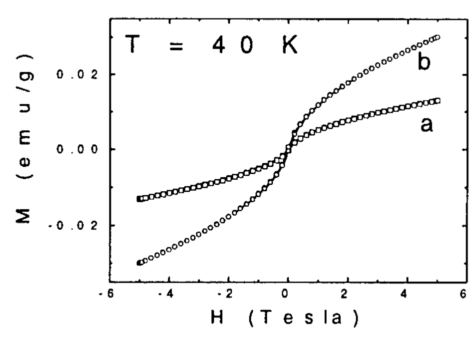

Figure 2. Magnetization loops for (a) fresh and (b) aged iron oxide ferrofluid.

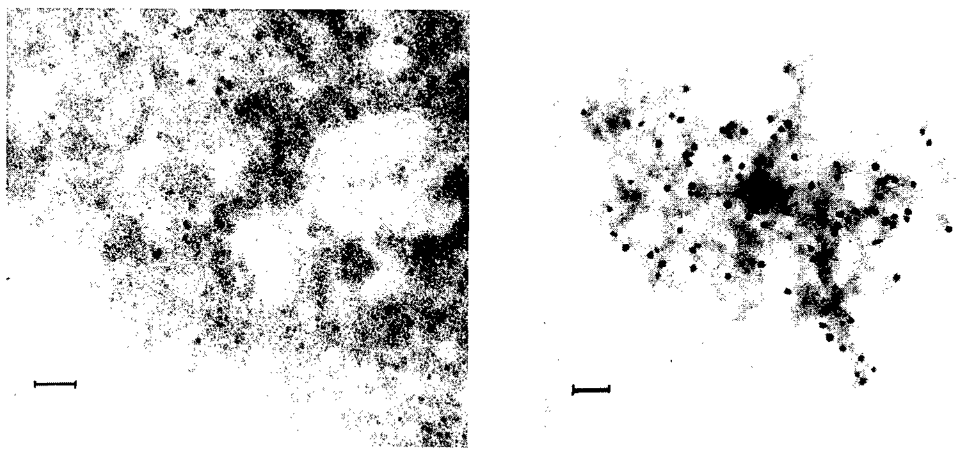

Figure 3. TEM images of (a) as prepared and (b) aged for two months Cu-based ferrofluids prepared without a dispersant

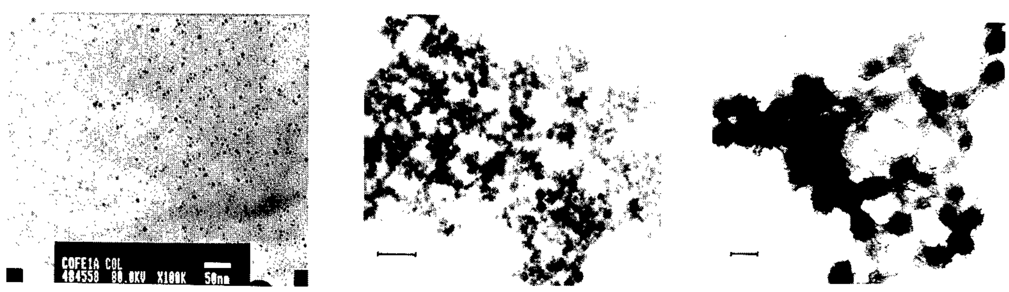

Figure 4. TEM images of (a) as prepared and (b) aged for one week and (c) aged for two months Co-based ferrofluids prepared without a dispersant

The assemblies formed in Co-based ferrofluids during aging form network-like structures, Fig. 4(b,c).

This difference in a geometry of clusters forming during aging can be explained by difference in the magnetic properties of components: the magnetic moment is the largest in the case of Fe-Co nanoparticles, intermediate in the case of Fe_2O_3 and smallest for Fe-Cu particles. The competition between surface and magnetic dipole energies is a driving force determines the clusters shape. Namely, weak magnetic interactions in Cu-based ferrofluids cannot prevent surface area minimization and result in round-shaped clusters. Intermediate-strength Fe_2O_3 results in separated, but elongated particles. The magnetic strongest Fe-Co based particles aggregate in a form of chains closing magnetic field inside the formation. Apparently, this behavior is a self-organizing process. Once appeared, the magnetic anisotropy assists the growth of the clusters in particular directions. The increase of a cluster size and corresponding change of its shape, amplify the anisotropy of magnetic interactions. Thus, there is a feedback through the strength of anisotropic magnetic interactions resulting in self-organization of a cluster growth.

SUMMARY

In conclusion, we have presented results implying self-organization of the cluster formation during aging in various ferrofluids. The driving force of a self-organizing growth is the anisotropic magnetic interactions between nanoparticles. Cluster size and shape depend on the strength of the magnetic interactions determined by the chemical composition of the ferrofluids.

REFERENCES

1. Raj, K. and Moskowitz, R., *J. Magn. Magn. Mater.*, 1990, 85, 233.
2. Berkovsky, B. M., Medvedev, V. F., and Krokov, M. S., *Magnetic Fluids: Engineering Applications*, Oxford Univ. Press, Oxford, 1993, p. 218.
3. Charles, S. W. and Popplewell, *J., IEEE Trans. Magn. Magn.*, 1980, 16, 172.
4. Rosensweig, R. E., *Ferrohydrodynamics*, Cambridge University Press, 1985.
5. Suslick, K. S., Fang, M., and Heyon, T., *J. Am. Chem. Soc.*, 1996, 118, 11960.
6. Shafi, K. V. P. M., Prozorov, R., and Gedanken, A., *J. Advanc. Mater.*, 1998, 8, *590.*
7. Shafi, K. V. P. M., Wisel, S., Prozorov, T. *et al.*, *Thin Solid Films*, 1998, 318, *38.*
8. Shafi, K. V. P. M. and Gedanken, A., 1998, *J. Amer. Chem. Soc.*, *In print.*

Pergamon

NanoStructured Materials, Vol. 12, pp. 673–676, 1999
Elsevier Science Ltd

0965-9773/99/$–see front matter

PII S0965-9773(99)00214-7

NEUTRON DIFFRACTION STUDIES OF CERIA-ZIRCONIA CATALYSTS PREPARED BY HIGH-ENERGY MECHANICAL MILLING

S. Enzo*, R. Frattini‡, F. Delogu*, A. Primavera† and A. Trovarelli†

*Istituto Nazionale di Fisica per la Materia e Dipartimento di Chimica dell'Università di Sassari, via Vienna 2, 07100 Sassari (Italy); enzo@micromat.dipchim.uniss.it

‡Istituto Nazionale di Fisica della Materia e Dipartimento di Chimica Fisica dell'Università di Venezia, Dorsoduro 2137, 30123 Venezia (Italy); frattini@unive.it

† Dipartimento di Scienze e Tecnologie Chimiche, Università di Udine, via Cotonificio 108, 33100 Udine (Italy); trovarelli@dstc.uniud.it

Abstract *The structural transformation occurring to a mixture of cubic CeO_2 and monoclinic ZrO_2 by High-energy Mechanical Milling (MM) has been followed by neutron diffraction. Rietveld analysis indicate that 9 hours of milling produce a tetragonal solid solution for Zr-rich composition and a nanocrystalline cubic solid solution for Ce-rich composition.*

INTRODUCTION

Materials containing ceria have been the subject of thorough investigation in the last years because of their usefulness in a broad range of applications in catalysis (1) due to their redox efficiency. The redox/catalytic properties of ceria are strongly enhanced if it is used as a component of binary/ternary solid solutions in combination with other transition metal or rare earth oxides (2), and among several different elements, the introduction of Zr into the lattice of CeO_2 is particularly effective in the enhancement of the overall performance of ceria in catalysts for auto exhaust treatment (3).

Usually these compounds for use in catalysis are prepared via a conventional coprecipitation from the corresponding salts or using a sol/gel route. Recently mechanical milling (MM) process has been employed to synthesize nanocrystalline Ce-ZrO_2 in a wide composition range, starting from powders of the individual oxides (4). The preliminary X-ray diffraction studies pointed out the formation of a cubic solid solution for CeO_2-rich samples, ($Ce_xZr_{1-x}O_2$, with $x>0.5$) and an increasing degree of tetragonality for higher ZrO_2 loading. Since it was reported that solid solutions having a cubic cell behave better than those of tetragonal symmetry (5), it is of importance to fully characterize the structural features of these materials.

The various reports on the structural transformations induced on oxides by MM are not reproduced in their main conclusions and a complete understanding of structural transformation occurring under mechanical milling is still missing (6-8). The reasons for these discrepancies can

be summarised as follows: i) the nature of end-products depends from the energetic conditions of the MM apparatus employed, such as oscillation frequency, number of colliding balls and their density, etc.; ii) X-ray diffraction data may not be suitably used to well distinguish between cubic and tetragonal structures, particularly when in a tetragonal structure the axial ratio c/a is close to $\sqrt{2}$ (t'' phase). Therefore, to better distinguish between cubic and tetragonal structure, and to calculate atomic coordinates, we have used neutron diffraction. This study reports preliminary neutron diffraction data of $Ce_xZr_{1-x}O_2$ (x = 0.8 and 0.2) solid solutions obtained by mechanical milling.

EXPERIMENTAL

CeO_2 (99.999%, surface area 7 m^2/g) was purchased from Aldrich. ZrO_2 was obtained by calcination of hydrous zirconia (MEL Chemicals) at 973 K (surface area 27 m^2/g). Preparation of the mixed oxides was carried out with a high-energy vibratory ball-mill (Spex 8000) at an oscillation frequency of 20 Hz and an amplitude of approx. 20 cm. Powders were loaded into a 50 ml ZrO_2 vial equipped with six Y-doped, high wear-resistant Zirconia balls (— 10 mm, Tosoh Corporation). The ball-to-powder ratio was 18/1 (i. e. 18 g of balls to 1 g of powder) and milling time ranged from 0.5 to 9 h.
The neutron diffraction measurements were made at ISIS neutron source RAL, Chilton (U.K.), on Liquid and Amorphous Diffractometer (LAD). The specimens were placed in thin walled vanadium tubes of 6 mm internal diameter. The data were analysed with the Rietveld code FULLPROF (9).

RESULTS AND DISCUSSION

Figure 1 shows the neutron diffraction patterns (data points) and the Rietveld fit (full lines) of 0.20 CeO_2+0.80 ZrO_2 specimen mechanically milled for 0 (parental mixture), 1 and 9 h, in a Q-range extended up to Q_{max} = 100 nm^{-1}. The pattern of parental mixture is well described by the contribution of three phases: the monoclinic and tetragonal forms of ZrO_2 and cubic CeO_2. As it concerns the peak broadening, the related U and W parameters (10) obtained from the fit for ZrO_2 monoclinic phase (1.256 and 0.012) are larger than those of CeO_2 (0.640 and 0.009 respectively) beyond the experimental uncertainty. Assuming, to a first crude approximation, that the peak broadening is of isotropic nature, this effect can be attributed mainly to internal strain rather than to crystallite finiteness. The lattice parameters found for all phases in the parental mixture agree well with those known from the literature. After 1 h of MM we note a pattern substantially changed at high-Q. However, the structure factor can still be described in terms of the three phases present in the parental mixture. In the specimen MM for 1 h, the relative content of the tetragonal phase is increased (49% vs 14% for parent specimen), as well as the peak broadening. In fact for tetragonal ZrO_2 U varies from 1.51 at 0 h to 5.01 at 1h until 6.33 after 9 h, suggesting again a predominant role of lattice strain. The lattice parameters of the tetragonal phase are slightly increased after 1 h of MM (a=0.3623 nm and c=0.5215 nm). On the other hand, the cubic CeO_2-based phase appears diminished; thus, the lattice parameter increase of the tetragonal phase is certainly due to the formation of a $Ce_xZr_{1-x}O_2$ solid solution.

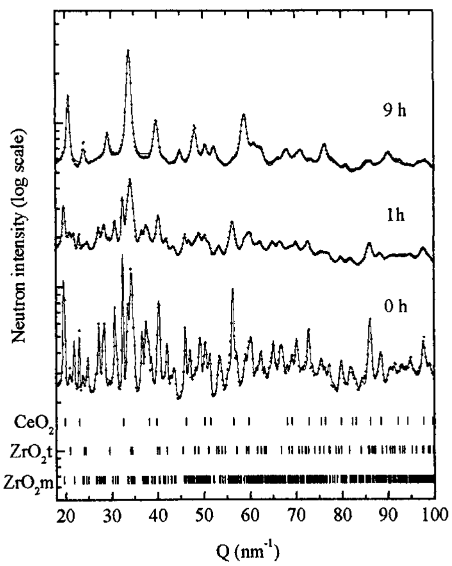

Figure 1. Neutron diffraction patterns (data points) and best fit (full lines) for the specimens with composition 0.20 CeO_2+0.80 ZrO_2 ball milled for the times indicated.

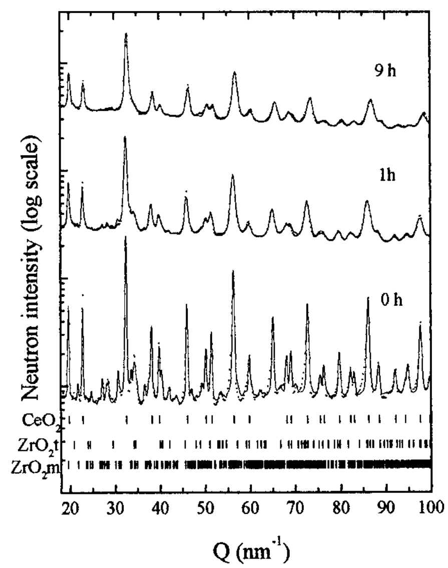

Figure 2. Neutron diffraction patterns and best fit for the specimens with composition 0.80 CeO_2+0.20 ZrO_2. Notation as in figure 1.

In the specimen MM for 9 h we observe one tetragonal $Ce_xZr_{1-x}O_2$ solid solution, even if we can not disregard completely the existence of some nanocrystalline fraction (below 10% wt) of the monoclinic form. In our refinement of the tetragonal phase we have adjusted the position z_O of oxygen atoms along the c axis in sites 4(d), which was determined to be $z_O = 0.045$. This means that, taken into account the simultaneously refined lattice parameters values a = 0.3652 nm and c = 0.5234 nm, the M-O (M = Zr, Ce) nearest neighbour distance is approx. 0.1844 nm. Similar value of z_O parameter was recently reported by Yashima et al. (11) on CeO_2-ZrO_2 solid solutions by neutron diffraction.

The neutron diffraction patterns of the specimens with composition 0.80 CeO_2+0.20 ZrO_2 are reported in figure 2 as data points and the relevant Rietveld fit as full lines. In the 0 h pattern the contribution of cubic CeO_2 is, of course, dominant. In the pattern left out, the 20% of zirconia is described again with a mixture of monoclinic and tetragonal forms. 1 h of ball milling makes the line of the monoclinic ZrO_2 phase to disappear almost entirely from the background and some weak peaks typical of the tetragonal phase can be hardly recognised. In the mean time the lattice parameter of the cubic phase appears increased slightly beyond the experimental uncertainty (a=0.5422 nm), which may be ascribed to a reductive process effected by the milling. Further milling for 9 h gives a pattern satisfactory fitted with one cubic phase having decreased lattice parameter (a=0.5376 nm) because of the insertion of smaller Zr cations.

Since it is known that non-stoichiometric (MM')-O_{2-y} solid solutions can occur by ball milling (where M,M' = Zr, Ce), we have checked that by plotting in figure 3 the lattice

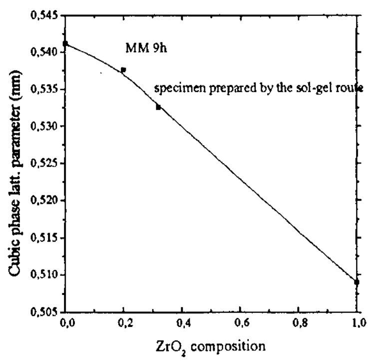

Figure 3 Lattice parameter of cubic phase vs ZrO_2 composition. Data at 0 and 1 are from literature, dashed line correspond to behaviour according to a Vegard law

parameter of the cubic phase vs ZrO_2 composition. Data at 0 and 1 are from the literature, so, the dashed line correspond to the regular behaviour according to a kind of Vegard law as it is often found in metallic binary systems. The lattice parameter of the cubic phase reported after 9 h of MM for the (0.80 CeO_2 + 0.20 ZrO_2) composition is above the dashed line, suggesting that reductive processes, increasing the size of cations, are effectively induced during formation of solid solutions. Whether this reduction is proper of the ball milling technique rather than of other methods of preparation, it must be ascertained with more data points on cubic single-phase systems.

ACKNOWLEDGEMENTS

The neutron scattering measurements were performed with the support ot the Science and Engineering Research Council (RB/8206) and the help of A.C. Hannon.

REFERENCES

1. A. Trovarelli, *Catal.Rev.-Sci.Eng.* 1996, 38, 439.
2.. P. Vidmar, P. Fornasiero, J. Kaspar, G. Gubitosa, and M. Graziani, *J. Catal,.* 1997 171, 160.
3. A. Trovarelli, C. de Leitenburg and G. Dolcetti, *CHEMTECH,* 1997, 6, 32.
4. A. Trovarelli, F. Zamar, J. Llorca, C. de Leitenburg, G. Dolcetti and J. Kiss, *J.Catal,.* 1997, 169, 490.
5. P. Fornasiero, R. Di Monte, G. Ranga Rao, J. Kaspar, S. Meriani, A. Trovarelli, and M. Graziani, *J. Catal.*, 1995, 151, 168.
6. J. E. Bailey , D. Lewis, Z. M. Libran, and L. J. Porter, *Trans. J. Brit. Ceram. Soc.*, 1972, 71, 25.
7. D. Michel, F. Faudot, E. Gaffet, L. Mazerolles, *J. Amer. Ceram. Soc.*, 1993, 76, 2884.
8. M. Qi and H. J. Fecht, *Mater. Sci. Forum,* 1998, 269-272, 187.
9. J. Rodriguez-Carvajal, *Physica B*, 1993, 192, 55.
10. S. Enzo, *Mater. Sci. Forum,* 1998, 269-272, 363.
11. M. Yashima,S. Sasaki, Y. Yamaguchi, M. Kakihana, M. Yoshimura and T. Mori, *Appl. Phys. Lett.*, 1988, 72, 182.

Pergamon

NanoStructured Materials, Vol. 12, pp. 677–680, 1999
Elsevier Science Ltd

0965-9773/99/$–see front matter

PII S0965-9773(99)00215-9

CORRELATION BETWEEN MICROSTRUCTURE AND SOFT-MAGNETIC PROPERTIES OF FeCuNbSiB BASED ALLOYS

A.M. Tonejc[1], N. Ramšak[2], A. Prodan[2], A. Tonejc[1], A. Khalladi[3], S. Suriñach[3], M.D. Baró[3]
[1]Faculty of Sciences, Department of Physics, Bijenička c. 32, POB 162, 10001 Zagreb, Croatia
[2]Institute Josef Štefan, Jamova 39, SI-1000 Ljubljana, Slovenia
[3]Dep. Física, Universitat Autònoma de Barcelona, E-08193 Bellaterrra, Spain

Abstract.- *In this work the influence of different heat treatments on the crystallization behaviour of soft magnetic alloys $Fe_{77.5}Cu_1Nb_3Si_{9.5}B_9$ was investigated using different techniques: transmission electron microscopy (TEM), electron diffraction (ED) and scanning tunneling microscopy (STM). From TEM and STM examination some evidence on nucleation and growth process was obtained. STM revealed atomic resolution in the nanocrystalline grain boundaries. The microstructural studies have been correlated with the results obtained by means of X-ray diffraction (XRD), differential scanning calorimetry (DSC) and thermogravimetry analysis (TGM) measurements. ©1999 Acta Metallurgica Inc.*

INTRODUCTION

Nanocrystalline materials produced by primary crystallization of amorphous alloys consist of fine crystalline grains embedded in the residual amorphous matrix (1). Since the grain sizes are smaller than the magnetic interaction lengths; the local magnetocrystalline anisotropy is averaged out by the exchange interactions. This, together with suitable magnetostrictive properties, leads to soft magnetic behavior superior to that of amorphous alloys, which means a higher magnetization and greater stability of properties on further annealing (2-5). These nanocrystalline materials are in a non-equilibrium state, therefore, their properties depend not only on the composition but also on the preparation conditions. Thus, identification of various phases during the nanocrystallization process, as well as a good insight into the corresponding nucleation and growth mechanisms, are some of the clues for a better understanding of the physical properties of these materials.

In the present work the dependence of the microstructure on the thermal annealing during the amorphous-to-nanocrystalline phase transition in rapidly quenched soft magnetic alloys was studied. A sample with composition $Fe_{77.5}Cu_1Nb_3Si_{9.5}B_9$ was subjected to different annealing treatments and then investigated by means of XRD, TEM, ED and STM. The results were correlated with DSC and TGM.

EXPERIMENTAL

Amorphous ribbons of nominal composition $Fe_{77.5}Cu_1Nb_3Si_{9.5}B_9$ were prepared by planar flow-casting (15 mm wide and 20 μm thick) (2). Structural analyses were performed by XRD

using CuKα radiation. The DSC and TGM measurements were conducted in a Perkin-Elmer DSC-7 and TGA-7 apparatus respectively (6). The foils were thinned by ion beam milling and analyzed in a JEOL JEM 2010 200kV. An Omicron UHV-STM system was used, operated in both constant current and constant height modes and at a pressure of about 10^{-10} mbar. After polishing and cleaning, the samples were introduced into the UHV chamber, where the surfaces were cleaned in-situ by a 500 eV Ar-ion gun for at least two hours before the investigation. For more details see Ref. (7-8).

RESULTS and DISCUSSION

It appears from the DSC scans that crystallization occurs in several exothermic events, the first one corresponding to the nanocrystallization process and the others to the formation of intermetallic phases. The overall crystallization enthalpy is 107±5 J/g. From the TGM the first fall corresponds to the ferro-paramagnetic transition of the amorphous alloy and is identified as the Curie temperature of the amorphous phase (558±2 K). The increase of the magnetization at the crystallization onset indicates the formation of some crystalline magnetic phase(s). In order to have stress-free samples, the as-quenched ribbon was relaxed by being pre-heated at 20 K/min till 700K.

The crystallization kinetics was studied by combining both constant heating rate and isothermal techniques. Upon increasing the heating rate, all the crystallization peaks were shifted to higher temperature. From the analysis of the TGM curves obtained at low heating rates it is clear that, parallel to the nanocrystallization process, new magnetic phases emerge in the same temperature range as the second exothermic event appears. The apparent activation energies calculated by the shift's peak method were 3.4±0.2 eV and 4.5±0.2 eV for the first and second exothermic event respectively.

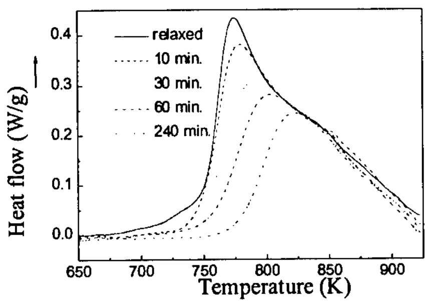

Fig. 1. DSC curves obtained during continuous heating (20 K/min) of the alloy in the relaxed state and after different times of annealing at 705 K.

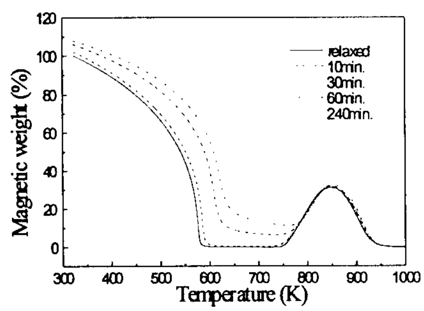

Fig. 2. Temperature dependence of the magnetization of the alloy studied in the relaxed state and after different times of annealing at 705 K.

From the isothermal DSC curves it is clear that the transformation to the nanophase microstructure involves nucleation and growth rather than coarsening of an existing microstructure. However, the isothermal DSC curves are not sufficiently accurate for detailed kinetic analysis. Assuming that the total enthalpy release (during the anneal and during the non-isothermal scan) is constant, the nanocrystalline fraction which occurs in the anneal can be evaluated by measuring the

residual area of the primary crystallization peak in non-isothermal DSC after anneals. The DSC curves obtained during continuous heating (20 K/min) of the alloy in the relaxed state and after different annealing times at 705 K are shown in Figure 1. The temperature dependence of magnetization of the alloy studied in the relaxed state and after different annealing times at 705 K is presented in Figure 2. The enhancement found in the Curie temperature of the amorphous matrix is supposed to be due to the interaction of the ferromagnetic particles with higher Curie temperature. Similar results were obtained in related alloys (9).

With increasing the annealing time, the diffraction peaks of the nanocrystalline phase emerge from the amorphous halos. They have been identified as an α-Fe(Si) solid solution. The relative intensity of the various peaks indicates no preferred orientation in the resulting crystalline phase. The crystallite size and the lattice parameter were determined from the XRD data (7). After long annealing times a steady value of 8.5±0.5 nm was found, independent of the annealing temperature. From the position of the lines in the XRD patterns the lattice parameter was evaluated. A strong decrease in the lattice parameter was observed. According to the dependence of the lattice parameter on composition (10), the Si content of the α-Fe(Si) grains in samples annealed at 705 K or 813 K for 4 h was obtained to range from 4 at% to 10 at%.

On the basis of TEM experiments and from the uniform distribution of spots in the nanocrystalline rings observed in ED patterns, it can be concluded that grains are uniformly distributed in the foils without any preferred orientation. The measured distribution of α-Fe(Si) nanoprecipitates in samples annealed at 705K during 20 and 30 min were fitted by a Γ function. The average grain sizes of these samples from the different annealing times used, were 4.8±0.4 and 5.3±0.4 nm respectively, in agreement with the values obtained from the XRD results (8). The overall distribution seems compatible with a process of nucleation.

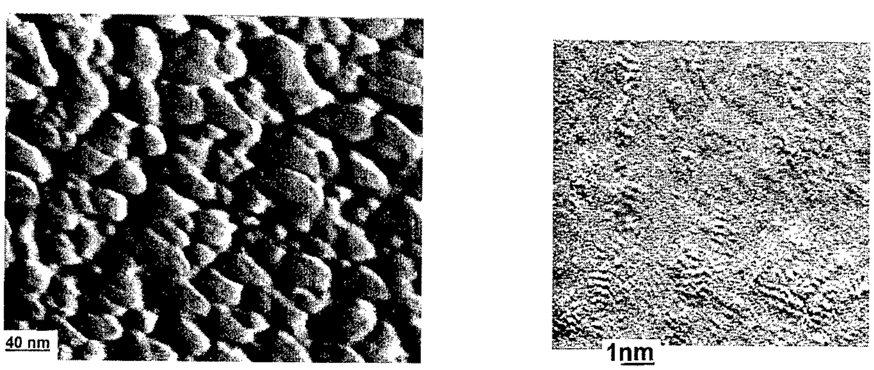

a) b)

Fig. 3. STM image of a sample annealed at 705 K for 10 min: a) region of (200 nm^2); b) region of (10 nm^2). (U_g=0.005 V, I_t=10 nA)

Constant current mode STM observations were also carried out. A partial atomic resolution was occasionally achieved. Figure 3a shows a constant current mode image of a part of (200 nm)^2 area of a sample, annealed at 705 K for 10 minutes, and Figure 3b a part of (10 nm)^2 enlargement of the lower-left corner of the same region. While the first shows a regular

distribution of grains, with grain sizes comparable to TEM and XRD results, a short-range ordered atomic distribution is evident in the second, where islands of different atomic groups with various diameter were observed. The STM image is one of the first results taken on this kind of samples and could be compared with high resolution electron microscopy (HRTEM) of other authors on related samples (7,11).

Structural features observed in STM images reveal that the concept of medium range order (MRO) could be applied to observed structural changes, which take place during the amorphous to nanocrystalline transformation in $Fe_{77.5}Cu_1Nb_3Si_{9.5}B_9$ alloy

CONCLUSION

The influence of different heat treatments on the crystallization behaviour of the soft magnetic alloys $Fe_{77.5}Cu_1Nb_3Si_{9.5}B_9$ was investigated by a few microscopic techniques, i.e. TEM, ED and STM, and correlated with the results obtained by XRD, DSC and TGM. From XRD, the mean crystallite sizes were determined and found to be in agreement with those obtained from the TEM and STM. It was also shown by DSC that the process of primary crystallization with the transformation to the nanophased microstructure involves nucleation and growth, in agreement with the overall grain size distributions, determined by TEM. The magnetization as a function of temperature shows a behaviour typical of a material containing two ferromagnetic phases. The enhancement in the Curie temperature of the amorphous matrix is supposed to be caused by an interaction of the ferromagnetic particles with higher Curie temperature. STM observations indicate that the structural changes observed support the concept of MRO during the amorphous to nanocrystalline transformation.

ACKNOWLEDGEMENTS

We thank Dr. G. Herzer, Vacuumschmelze GmbH, for providing the amorphous ribbons. Acknowledgements are due to CICYT (project No. MAT94-0290-C03-01) which partially supported this research and to the Autonomous University of Barcelona for providing a grant to A. Tonejc during her stay at the Department of Physics of UAB in Bellaterra and to the Ministries of Science and Technology of the Republics of Croatia and Slovenia for providing the needed financial support.

REFERENCES

1. Y. Yoshizawa and K. Yamauchi, *Mater. Trans. JIM*, 31, 307 (1990).
2. G. Herzer, *IEEE Trans. Mag.*, 30, 4800 (1994).
3. Hernando and T. Kulik, *Phys. Rev. B*, 51, 7064 (1994).
4. Slawska-Waniewska, J.S. Muñoz and P. Nowicki, *J. Magn. Magn. Mater.*, 160, 251 (1996).
5. N. Randrianontoandro, A. Slawska-Waniewska and J.M. Greneche, *Phys. Rev. B*, 56, 10797 (1997).
6. S. Suriñach, M. Enrech, A. Khalladi, J.S. Muñoz and M.D. Baró, *Mater. Sci. Forum*, 225-227, 345 (1996).
7. S. Suriñach, A. Otero, M.D. Baró, A.M. Tonejc and D. Bagovic, *Nanostruc. Mater.*, 6, 461 (1995).
8. A. Khalladi, Z. Tong, S. Suriñach, A.M. Tonejc, A. Tonejc and M.D. Baró, *Mater. Sci. Forum*, (in press).
9. A. Hernando, I. Navarro and P. Gorria, *Phys. Rev. B*, 51, 3281 (1995).
10. W.P. Pearson, *Handbook of Lattice Spacings and Structures of Metals*, Pergamon, Oxford, (1967).
11. K. Anazawa, Y. Hirotsu and Y. Ichinose, *J. Non-Cryst. Sol.*, 156-158, 196 (1993).

Pergamon

NanoStructured Materials, Vol. 12, pp. 681–684, 1999
Elsevier Science Ltd

0965-9773/99/$–see front matter

PII S0965-9773(99)00216-0

SELF-DIFFUSION IN HIGH-DENSITY NANOCRYSTALLINE Fe

H. Tanimoto[1], P. Farber[1,*], R. Würschum[1], R.Z. Valiev[2] and H.-E. Schaefer[1]
[1]Universität Stuttgart, Institut für Theoretische und Angewandte Physik,
Pfaffenwaldring 57, D-70550 Stuttgart, Germany
[2] Institute of Physics of Advanced Materials, Ufa State Aviation Technical University,
450000 Ufa, Russia
*now at : Max-Planck-Institut für Metallforschung, Institut für Physik, D-70506 Stuttgart,
Germany

Abstract *- In order to gain insight into the characteristic behavior of grain boundaries in nanocrystalline (n-) materials, high-density n-Fe specimens are prepared by compaction of gas-condensed nanocrystallites at elevated temperatures and the self-diffusion coefficients are measured by radiotracer techniques. The self-diffusion coefficients of n-Fe (relative density higher than 91 %) determined by assuming a type-C kinetics are similar to those extrapolated from high temperature data of conventional grain boundaries, suggesting that the grain boundaries in the high-density n-Fe are similar to those in conventional polycrystalline Fe.*

INTRODUCTION

Nanocrystalline (n-) materials are expected to exhibit properties modified with respect to conventional polycrystals owing to the much increased volume fraction of grain boundary (GB) regions (1). Especially, the enhanced atomic diffusion in n-materials due to the increased GBs is a key feature not only for understanding the macroscopic properties such as the plasticity and magnetism but also for the study of the interfacial structure. A recent ^{59}Fe diffusion study in high-density n-Pd shows that the interface diffusivity is similar to that expected for GB diffusion of conventional polycrystalline (poly-) metals from extrapolation of high-temperature data to lower temperatures (2). To gain insight into the diffusion phenomena as well as the interface structure in n-metals with cubic body-centered structure, a tracer-diffusion study is performed on n-Fe. Since porosity may greatly affect the apparent diffusion phenomena (3), we prepared high-density n-Fe specimens with density higher than 91 % of the poly-Fe value.

EXPERIMENTAL PROCEDURE

High density n-Fe specimens were prepared by compaction of inert-gas condensed nanocrystallites. The compaction at 403 K with a pressure of 3.1 GPa in a UHV system at a vacuum of 10^{-8} mbar yielded high-density n-Fe disks with a diameter of 8 mm and a thickness

of 0.15 mm. Figure 1 shows the variation of the relative density (ρ/ρ_c, ρ_c : bulk Fe density) with the mean grain size (d) of n-Fe disks, where ρ and d were determined by the Archimedes technique and from the broadening of x-ray diffraction peaks, respectively. The preparation of n-Fe specimens with lower ρ but smaller d was previously reported by compaction of gas-condensed nanocrystallites at 373-571 K with pressure of 1.4 GPa in vacuum of 10^{-7} mbar (4).

For the present diffusion studies, n-Fe specimens with ρ/ρ_c of 91 - 96 % and d of 19 - 38 nm were used. It is noted that no obvious change in the diffusion behavior was found in these ρ and d ranges. The ^{59}Fe radiotracer was deposited on the polished specimens by thermal evaporation and afterwards the specimens were annealed (diffusion annealing) in an evacuated glass vial. After sputter sectioning by Ar-ions, the radioactivity of the sputtered sections was counted in order to obtain the penetration depth profile of ^{59}Fe tracers (5).

RESULTS AND DISCUSSION

Figure 2 shows the ^{59}Fe penetration depth profiles normalized by the annealing time (t_d) for high-density n-Fe at different temperatures. In the present study, the annealing was conducted below 500 K, where the volume diffusion in the crystallites is expected to be negligibly small (see Fig.4). Therefore the self-diffusion coefficient (D_s) was determined by assuming a type-C diffusion kinetics (6), i.e. the data up to 100 nm were fitted by a Gaussian. In Fig. 2, with increasing diffusion annealing temperature, the depth profiles become curved. Similar curved depth profiles of ^{59}Fe tracers were reported in high-density n-Pd and were attributed to the incorporation of tracer atoms into the crystallites due to GB migration during the diffusion annealing (2). The grain growth during diffusion annealing was also found in the present n-Fe specimens. For example, d showed an increase from 31 nm to 60 nm and to >100 nm after diffusion annealing at 452 K for 148 h and at 499 K for 22 h, respectively. The self-diffusivities determined here represent lower limit because of the migration of GBs during annealing. In addition, D_s also depends on t_d. Figure 3 shows a decrease of D_s with increasing t_d at constant temperature observed for high-density n-Fe and submicro-crystalline (smc-) Fe, where smc-Fe

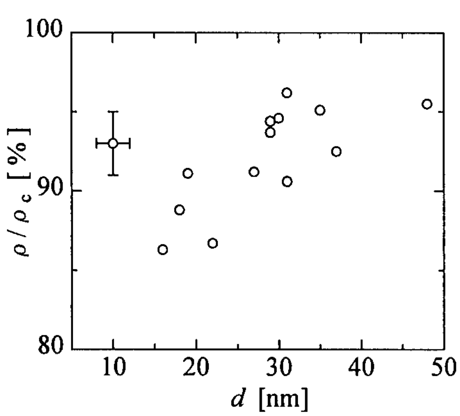

Fig. 1. Relative density ρ/ρ_c and mean grain size d of n-Fe specimens.

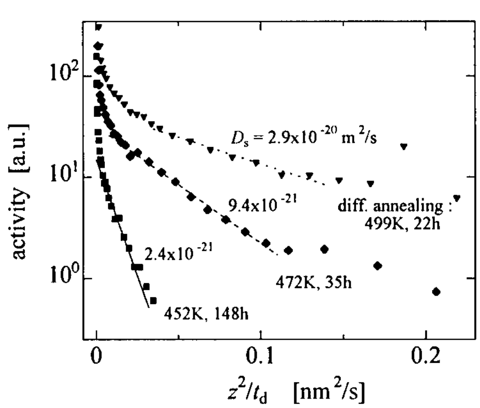

Fig. 2. ^{59}Fe depth profiles observed for high-density n-Fe specimens.

prepared by severe plastic deformation is considered to be fully dense. This suggests that a structural relaxation of the GBs in n- and smc-Fe occurs at rather low temperatures during diffusion annealing. For smc-Fe, however, the probable annealing out of dislocations also contributes to the decrease in the diffusivity. It is reported that a rapid structural relaxation at GBs in the n-metals takes place at slightly elevated temperatures (7). In the case of amorphous (a-) $Fe_{91}Zr_9$ alloy, a decrease in ^{59}Fe diffusivity with t_d at 633 K is attributed to the annealing out of excess free volume (8).

Figure 4 shows the Arrhenius plot of D_s of high-density n- and smc-Fe, together with the ^{59}Fe diffusion data reported for high-density n-Pd and the GB diffusion coefficient (D_{GB}) in conventional poly-Fe determined by the extrapolation of high temperature data (9). A good agreement in the $1/T$ dependence of D_s between fully dense smc-Fe and high-density n-Fe confirms that pores do not affect the present results on n-Fe. In addition, the self-diffusivities in high-density n-Fe are similar to those in conventional GB diffusion, but not as high as the diffusivities reported by earlier experiments (see references in (2)) where remnant pores might have behaved as a surface diffusion like path. The similarity in the diffusivities suggest that the behavior of GBs in high-density n-Fe is close to that in the conventional GBs as deduced from the ^{59}Fe diffusion study of high-density n-Pd (2). The ^{59}Fe diffusivities in a- and n-FeSiBNbCu alloys (Finemet) are much lower than D_s of high-density n-metals and it is believed that the dense packing of atoms in intergranular amorphous phases reduces the diffusivity (2).

It is worthwhile mentioning that at lower temperatures, the D_s values in n-Fe appear to be slightly higher than the extrapolated values for GBs in conventional poly-Fe. Recent molecular dynamic calculation and low-temperature diffusion studies on conventional GBs (12,13) conclude that the interstitial-type process with lower activation enthalpies plays a important role in addition to the conventional vacancy-type process at lower temperatures. On the other hand, the analogy of the time dependence between D_s in n-Fe and ^{59}Fe diffusivities in a-$Fe_{91}Zr_9$ leads to a view that GBs in n-metals just after preparation are loosely packed and

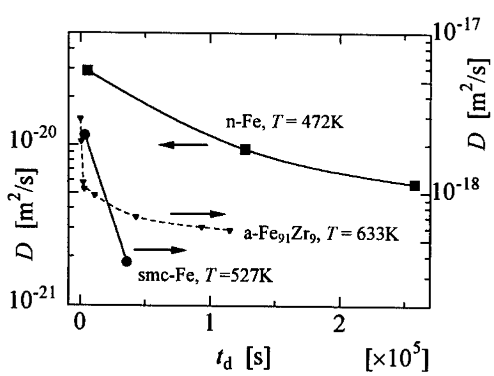

Fig. 3. Isothermal time-dependence of diffusivity in n-Fe, smc-Fe and a-$Fe_{91}Zr_9$ (8) due to structural relaxation.

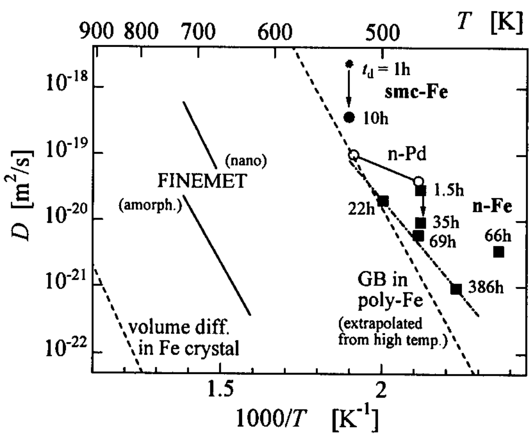

Fig. 4. Arrhenius plot of ^{59}Fe diffusion coefficients for n-metals, crystalline (c-) Fe (9), grain boundaries (GBs) in poly-Fe (10) and the Finemet alloys (11).

easily relax. The decrease of D_s in n-metals by annealing might reflect a disappearance of the excess free-volume in GBs with the equilibrium-like structure.

CONCLUSION

Self-diffusion studies were performed on high-density n-Fe specimens prepared by the compaction of gas-condensed nanocrystallites at elevated temperatures. The self-diffusion coefficients determined assuming a type C diffusion process are similar to or slightly higher than the values estimated for the conventional GB diffusion by extrapolating high temperature diffusion data to lower temperatures. The time-dependent decrease of the apparent self-diffusivities is probably due to structural relaxation of the interfaces and to interface migration effects. According to the measured D values, however, we presume that the nature of GBs in high-density n-Fe is similar to that in conventional poly-Fe.

ACKNOWLEDGMENTS

The authors are indebted to Prof. W. Frank and Dr. P. Scharwaechter for supporting the diffusion measurements. One of authors (H.T.) is indebted to the Ministry of Education, Science, Sports and Culture, Japan, and Max-Planck-Gesellschaft for financial support.

REFERENCES

1. M.L. Trudeau, V. Provenzano, R.D. Shull and J.Y. Ying (editors), Nanostructured Materials, 1995, 6.
2. R. Würschum, K. Reimann, S. Gruß, A. Kübler, P. Scharwaechter, W. Frank, O. Kruse, H.D. Carstanjen and H.-E. Schaefer, Phil. Mag., 1997, 76, 407.
3. B.S. Bokstein, H.D. Bröse, L.I. Trusov and T.P. Khvostantseva, Nanostructured Materials, 1995, 6, 873.
4. G.E Fougere, J.R. Weertman and R.W. Siegel, Nanostructured Materials, 1995, 5, 127.
5. K. Maier, Phys. Stat. Sol. (a), 1977, 44, 567.
6. L.G. Harrison, Trans. Faraday Soc., 1961, 57, 1191.
7. R. Birringer, C.E. Krill and M. Klingel, Phil. Mag. Lett., 1995, 72, 71.
8. H. Kronmüller, W. Frank and P. Scharwaechter, *Science and Technology of Rapid Solidification and Processing*, ed. by M.A. Otooni, Kluwer Academic Pub., 1995, p.271.
9. M. Lübbehusen and H. Mehrer, Acta Metall. Mater. 1990, 38, 283.
10. J. Bernardini, P. Gas, E.D. Hondros and M.P. Seah, Proc. Roy. Soc. London, 1982, A379, 159.
11. R. Würschum, P. Farber, R. Dittmar, P. Scharwaechter, W. Frank, and H.-E. Schaefer, Phys. Rev. Lett., 1997, 79, 4918.
12. Q. Ma and R.W. Balluffi, Acta Metall. Mater., 1993, 41, 133 ; Q. Ma, C.L. Liu, J.B. Adams and R.W. Balluffi, ibid, 1993, 41, 143.
13. T. Surholt and C. Herzig, Defect Diff. Forum, 1997, 143-147, 1391.

Pergamon

NanoStructured Materials, Vol. 12, pp. 685–688, 1999
Elsevier Science Ltd

0965-9773/99/$–see front matter

PII S0965-9773(99)00217-2

THERMAL EVOLUTION OF BALL MILLED NANOCRYSTALLINE IRON

E. Bonetti, L. Del Bianco, L. Pasquini, E. Sampaolesi
Dipartimento di Fisica, Università di Bologna and Istituto Nazionale per la Fisica della Materia, Viale Berti Pichat 6/2, I-40127 Bologna, Italy.

Abstract *– Mechanical spectroscopy and X-ray diffraction measurements were employed to investigate the thermally induced structural evolution of nanocrystalline iron, prepared by mechanical attrition through different ball milling equipment in different structural states. The evolution of the elastic modulus, grain size and microstrain as a function of temperature and after selected isothermal treatments indicates that the rearrangement of structural configuration at the interfaces may stabilise the nanostructure against grain growth.*
©1999 Acta Metallurgica Inc.

INTRODUCTION

The physical behaviour of nanocrystalline (nc) metals is in the bulk of cases strongly dependent on the grain size and on the atomic arrangement at the interfaces (1). On the other hand, these structural parameters are strictly correlated and depends on the selected synthesis route. Some examples, regarding nc-iron, include the different structural environments of the grain boundaries deduced by EXAFS and X-ray diffraction (XRD) in samples prepared by out of equilibrium and intrinsically equilibrium synthesis techniques (2,3), magnetic measurements revealing the presence of a specific magnetic phase at the interface after different ball milling treatments (4), different grain growth mechanisms depending on the thermal history (5). In this research, we have tried to investigate, by means of a combined mechanical spectroscopy and XRD study, the thermally induced structural evolution of nc-Fe prepared by mechanical attrition with two differently operating ball milling apparatus: a high energy shaker type equipment and a planetary mill.

EXPERIMENTAL

Nanocrystalline iron was prepared by ball milling, using 99.9 % pure Fe powders as starting material. Two different milling apparatus were employed: 1) a Spex mixer-mill model 8000, operating in argon atmosphere at room temperature; 2) a recently developed planetary mill, working in a vacuum of 10^{-4} Pa at a temperature of 210 K. The material was prepared by milling for 8 hours in the case of the Spex 8000 (Fe_SM), and for 65 hours in the case of the

planetary apparatus (Fe_PM). The powders were subsequently furnace annealed in flowing argon for 1 hour at selected temperatures in the range 470-820 K

XRD measurements were performed at room temperature by a Philips PW 1710 vertical powder diffractometer, using Cu-Kα radiation. The XRD spectra were analysed according to the Warren-Averbach line broadening method, in order to evaluate the volume weighted average grain size $\langle D \rangle_v$ and the root mean square lattice strain $\langle \varepsilon^2 \rangle^{1/2}$ (6).

Dynamic Young's modulus measurements as a function of temperature were carried out through a vibrating reed apparatus operating in the 10^2-10^4 Hz frequency range. Thin bar shaped specimens, suitable for mechanical spectroscopy, were obtained by cold consolidation of the milled powders under a uniaxial pressure of about 2 Gpa: for both powders, in spite of the different milling treatments, the average density of the compacted samples, as determined by archimedean method, was found to be about 95%.

RESULTS AND DISCUSSION

Figure 1a shows that two different stages can be clearly distinguished in the increase of Young's modulus with temperature, in the Fe_SM sample: a first increase, of about 15%, occurs between 470 K and 650 K, followed by a further stronger increase between 690 K and 790 K. It is noted in figure 1b that thermal treatments up to 620 K induce a strong reduction (about 60%) of the internal lattice strain without appreciable grain growth; for higher temperatures a marked increase of the mean grain size occurs up to the final value of 68 nm. The XRD results allow to correlate the observed modulus *vs.* temperature trend with a two-stage microstructure evolution characterised by a strong reduction of the internal stresses, supposed mainly localised at the grain boundaries (T>670 K), prior to the onset of a successive significant grain growth (T>670 K). Figures 2a,b show the results obtained for the Fe_PM sample: with respect to figure 1, it can be observed a monotonic and reduced modulus increase (about 10%) corresponding to a slower microstrain decrease and to a more gradual rise of the mean grain size up to about the same value of Fe_SM (66 nm). These results are consistent with Differential Scanning Calorimetry measurements performed on the same specimens (7) which reveal: i) a broad exothermic process in the entire temperature range (400-750 K) in the Fe_PM sample; ii) a two steps enthalpy release in the Fe_SM sample, well corresponding to the two temperature ranges of figure 1a. This behaviour is also in agreement with a study on the thermal stability of nanocrystalline Fe prepared by ball milling through a Spex 8000 pointing out two regimes of microstructure evolution, indicated as grain boundary structural relaxation and grain growth respectively (8).

In order to get insight into the grain boundary relaxation process and to investigate on its possible influence on grain growth, we carried out XRD measurements on the Fe_SM specimen subjected to the following kind of thermal treatments: the as-milled powders were annealed for 1 hour at 570 K, inducing a reduction of the microstrain of about 40% without substantial grain growth (fig. 1b). Then, the pre-annealed powders were subjected to subsequent 1-hour annealing at selected temperatures. The results, as shown in figure 3, indicate in the pre-annealed sample a slower increase of the grain size, which evolves towards average values significantly smaller (up to 40%) for annealing temperatures above 670 K.

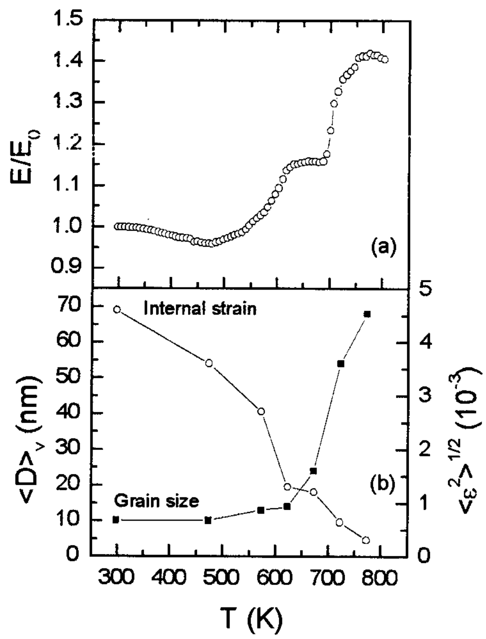

Figure 1 Fe_SM sample - (a) elastic modulus as a function of temperature; E_0 is the room-temperature modulus value (vibration frequency at 300 K ~ 1800 Hz). (b) grain size and lattice strain evolution with annealing temperature.

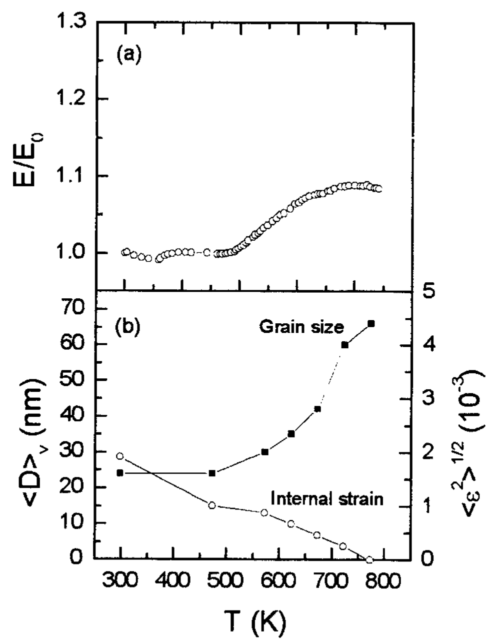

Figure 2 Fe_PM sample – (a) elastic modulus as a function of temperature; E_0 is identified as in fig. 1 (vibration frequency at 300 K ~ 1700 Hz). (b) grain size and lattice strain evolution with annealing temperature.

In particular, in the 670 - 720 K temperature range, the mean grain size strongly increases (about 130%) in the not pre-annealed sample, whereas no grain growth is experienced in the pre-annealed one. As regards the strain curves there are no significant differences in the monotonic reduction of lattice strain following the different thermal history.

These results indicate that low temperature annealing (570 K), inducing a partial relaxation of the interfacial structure, leads to a slowing down of the grain growth kinetics; probably this occurs because of a reduction of the grain boundary free energy which is the driving force for the grain growth process. To better clarify this point, we would like to remind a Mössbauer spectroscopy analysis (9), carried out at room temperature on Fe_SM samples after being annealed for 1 hour in the 570-670 K temperature range, as in the present work. This analysis, coupled to magnetisation measurements, showed that the relaxed grain boundary region gave origin to a well defined contribution to the Mössbauer spectrum (the hyperfine field was about 21 T), already visible after annealing at 570 K, with specific magnetic properties (4,9). In this framework, it may be considered that the pre-annealing stage at 570 K relaxes and stabilises the interfacial region which, in these conditions, inhibits the grain growth process, acting like a second *phase*.

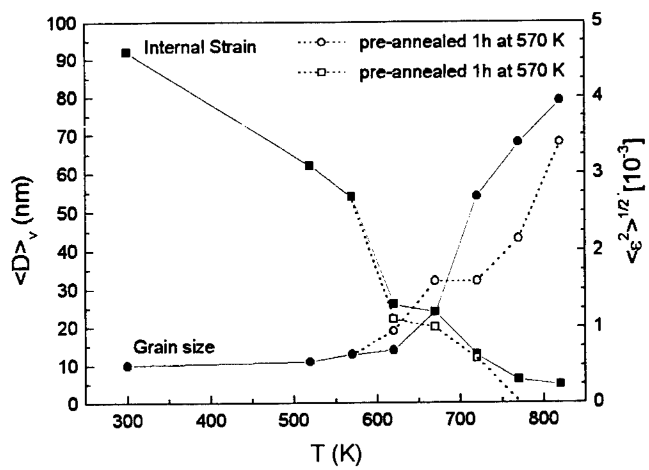

Figure 3 Grain size (circles) and lattice strain (squares) vs. temperature of annealing carried out on the Fe_SM powders as-milled (straight line) and pre-annealed at 570 K (dot line).

CONCLUSIONS

The experimental results clearly indicate that the synthesis of nc-Fe by equipment with different mechanical energy transfer (shaker and planetary mill) results in materials with different thermal stability against structural evolution. Moreover, it has been shown that, in samples prepared by the shaker mill, the grain growth process is slowed down by a pre-annealing at 570 K inducing the atomic reordering of the interfaces.

Acknowledgements - This work was carried out in the framework of a project PASS 97, sponsored by the Istituto Nazionale per la Fisica della Materia (INFM).

REFERENCES

1. See for review: *Proceedings of the Third International Conference on Nanostructured Materials*, Nanostr. Mater. 9 (1997).
2. A. Di Cicco, M. Berrettoni, S. Stizza, E. Bonetti, G. Cocco, Phys. Rev B 50, 12386 (1994).
3. N. Schlorke, J. Weissmüller, W. Dickenscheid, H. Gleiter, Nanostr. Mater. 6, 593 (1995).
4. L. Del Bianco, A. Hernando, E. Bonetti, E. Navarro, Phys. Rev B 56, 8894 (1997).
5. T.R. Malow, C.C. Koch, Acta Mater. 45, 2177 (1997).
6. S. Enzo, G. Fagherazzi, A. Benedetti, S. Polizzi, J. Appl. Cryst. 21, 536 (1988).
7. E. Sampaolesi, PhD Thesis, University of Bologna (1998).
8. H.J. Fetch, C. Moelle, Mat. Res. Soc. Symp. Proc. 457, 113 (1997).
9. L. Del Bianco, A. Hernando, E. Navarro, E. Bonetti, L. Pasquini, J. de Phys. III, in press.

Pergamon

NanoStructured Materials, Vol. 12, pp. 689–692, 1999
Elsevier Science Ltd

0965-9773/99/$–see front matter

PII S0965-9773(99)00218-4

LOW-TEMPERATURE ISOTHERMAL SINTERING AND MICROSTRUCTURAL CHARACTERIZATION OF NANOCRYSTALLINE ZIRCONIA CERAMICS USING SMALL ANGLE NEUTRON SCATTERING

U.Betz[1], A.Sturm[1], J.F.Loeffler[2], W.Wagner[2], A.Wiedenmann[3], H.Hahn[1]

[1] Darmstadt University of Technology, Department of Materials Science, Thin Films Division, Petersenstr. 23, 64287 Darmstadt, Germany

[2] Paul Scherrer Institute, CH-5232 Villigen PSI, Switzerland

[3] Hahn Meitner Institute, Glienicker Str. 100, D-1000 Berlin 39, Germany

Abstract -- *Nanocrystalline powders of zirconia, yttria and alumina were synthesized by Inert Gas Condensation and Chemical Vapor Condensation. Compacted samples of pure* ZrO_2 *and dispersion mixed* ZrO_2 + *14 wt.%* Al_2O_3 *and* ZrO_2 + *9 wt.%* Y_2O_3 *were pressureless sintered in vacuum at 1100 °C (≈ 0.4* T_m*) for 1, 2, 4 and 10 hours. Nearly full densities have been achieved in all of the three compositions with average grain sizes not exceeding 100 nm. Very small grain sizes of zirconia (< 30 nm) have been found for the composite due to a homogeneous distribution of alumina-phase particles hindering grain coarsening by pinning of the grain boundaries.*

Complementary to X-ray diffraction and scanning electron microscopy, the microstructural evolution of the n-ceramics was investigated by small angle neutron scattering. Irregularities during the densification of monoclinic zirconia were verified by the scattering curves and attributed to effects due to phase transformation. From the quantitative analysis of the scattering data pore-size-distributions of the materials were obtained.

INTRODUCTION

Nanocrystalline (n-)ceramics are known to be very promising materials which exhibit dramatic changes in properties due to a high interfacial area with respect to their coarse-grained counterparts. These properties are for example, excellent sinterability and formability, enhanced diffusion and ion-conductivity at moderate temperatures [1,2]. Since it has become possible to provide n-ceramic powders in sufficient quantity and quality in recent times, a special focus was put on the processing of these ceramics. One of the most challenging problems encountered during sintering was to maintain the grain size on the nanoscale in the final dense product.

The present paper deals with an investigation of the influence of yttria as a dopant and alumina as a second phase on the microstructure of n-zirconia during final stage sintering.

EXPERIMENTAL

Two common vapor phase condensation processes have been used to synthesize weakly agglomerated nanocrystalline oxide powders. Nanoparticles of zirconia and yttria were produced separately by the inert gas condensation and alumina by the chemical vapor condensation technique. Both methods are described in details elsewhere [3]. In order to achieve a homogeneous distribution of the additive-powders in n-zirconia the two compositions ZrO_2 + 9 wt.% Y_2O_3 and ZrO_2 + 14 wt.% Al_2O_3 were prepared by dispersion mixing in methanol. Thereby, the suspension has been stirred with a magnetic boat and simultaneously submitted to an ultrasonic bath for 2 hours. Drying by evaporating the alcohol provided the initial mixed n-powders. Compaction at room temperature of pure n-zirconia and the two compositions has been performed successively by applying 150 MPa uniaxially and 460 MPa isostatically resulting in compacts, typically 8 mm in diameter and 0.6 mm thick with relative green densities of about 50 %. The green bodies were sintered in vacuum (5 Pa) at 1100 °C for 1, 2, 4 to 10 h. The heating rate was 200 °C/h and cooling to room temperature was done in flowing oxygen.

Microstructural characterization of the n-ceramic discs has been carried out by using X-ray diffraction (XRD) with a Siemens D5000, scanning electron microscopy (SEM) with a Philips XL-30 FEG and small angle neutron scattering (SANS) at the V4 spectrometer at the BER II research reactor of the HMI (Berlin) using a wavelength λ of 0.906 nm. Besides, the densities of the ceramics were measured by immersion in water using the Archimedes' principle.

RESULTS AND DISCUSSION

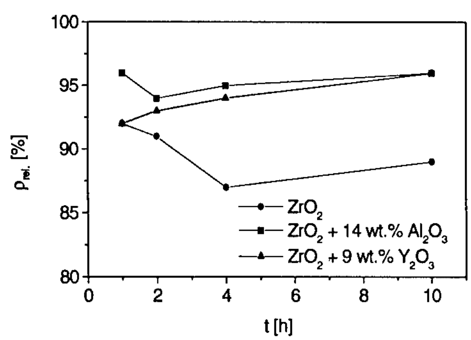

Fig.1: Relative densities of the three compositions as a function of the sintering time at 1100 °C.

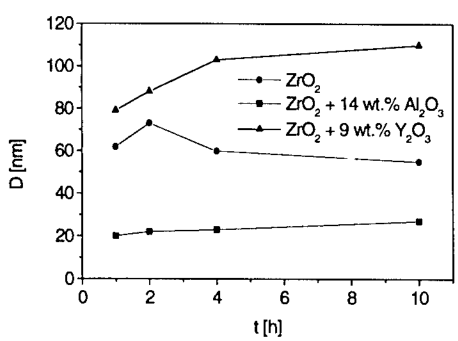

Fig.2: Static grain growth of the n-ceramics.

Average crystallite sizes were estimated from line broadening of XRD-lines using the Scherrer-formula. Grain sizes smaller than 10 nm in the case of alumina and zirconia and smaller than 20 nm for yttria have been calculated. After sintering phase evaluation of zirconia revealed the monoclinic structure in pure ZrO_2, the monoclinic with small amounts of the tetragonal phase in ZrO_2 + 14 wt.% Al_2O_3 and the tetragonal and cubic (< 35 vol.%) phase in ZrO_2 + 9 wt.% Y_2O_3. Fig.1 shows the densification behavior of the samples during isothermal final stage sintering at 1100 °C which is in the range of the grain size dependent monoclinic to tetragonal phase transformation (temperature) [4]. While consolidation of the yttria partially stabilized zirconia occurs in a typical manner by increasing the relative density from 91 to 96 % during the sintering time, pure ZrO_2 and ZrO_2 + 14 wt.% Al_2O_3 showed their maximum densities of 91 % and 96 % after 1 h at 1100 °C. The following density-drop of both systems can only be due to the creation of new voids during sintering. Most likely the martensitic phase transformation combined with the significant change in density is responsible for the nucleation of flaws in the zirconia matrix which is more pronounced in the pure ZrO_2 specimen. The average grain sizes as a function of sintering time are plotted in Fig.2. The suppression of grain growth during consolidation by pinning the grain boundaries with second phase particles was successful in the case of the composite ceramic where the grain size did not exceed 30 nm. The weak or non-agglomerated state of the as synthesised particles is an essential prerequisite for the homogeneous dispersion of alumina particles in

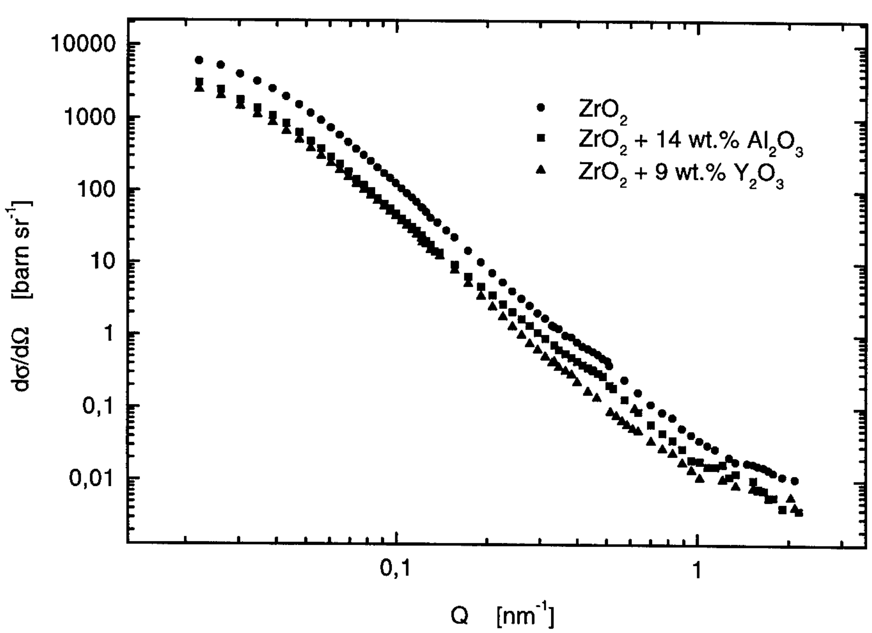

Fig.3: Scattering curves of the three compositions sintered at 1100 °C for 4 h.

the zirconia matrix. Grain sizes of the dense tetragonal zirconia were in the range of 100 nm.

The n-ceramics have also been examined by SANS. Scattering curves were obtained by correcting and averaging the recorded data of scattering-cross-sections which were always of radial symmetry. Fig.3 shows the scattering curves of the specimen sintered at 1100 °C for 4 h. Following a model of data evaluation for n-ceramics initially employed by Wagner et. al. [5] the main fraction of the differential scattering cross section $d\sigma/dQ$ is attributed to a polydispersed array of spherical particles causing the scattering of neutrons. By assuming a log-normal particle size distribution the experimental data can be fitted. SEM photos of the fracture surface of a 91 % dense ZrO_2 + 9 wt.% Y_2O_3 ceramic revealed that the closed pores in the size range of 10 to 70 nm were of spherical shape. Additionally, integration of the size distributions delivered the total volume of scattering particles. These values were in very good agreement with the total pore volume determined by the Archimedes' principle. This let to suggest that the main fraction of neutron scattering in final dense n-ceramics is due to log-normal size distributed closed pores of spherical shape. The curve of ZrO_2 + 9 wt.% Y_2O_3 in Fig.3 exhibits the typical features of n-ceramics. After the bend at low Q values the curve behaves linearly (Q^{-4}-regime) until incoherent scattering occurs at $Q > 1$ nm^{-1}. The shift to higher scattering intensities of ZrO_2 correlates to the lower density of the ceramic. In the case of the specimen containing the monoclinic phase an additional fraction of very small scattering particles at $Q > 0.3$ nm^{-1} is obvious. This behavior is attributed to the creation of new scattering volume during sintering and correlates with the suggestion that phase transformation effects induced the nucleation of voids.

CONCLUSION

Nearly full densities of ZrO_2 + 9 wt.% Y_2O_3 and ZrO_2 + 14 wt.% Al_2O_3 ceramics were achieved during sintering at 1100 °C, whereby the grain sizes of the zirconia containing alumina as a second phase revealed to be approximately 30 nm. Nevertheless, the consolidation of the specimen containing the monoclinic phase of zirconia showed abnormal densification behavior which was verified by SANS data showing an additional scattering fraction of small voids that arised from phase transformation effects during sintering.

References

[1] R.W.Siegel, NanoStructured Mat., 3, (1993), p.1
[2] H.Hahn, NanoStructured Mat., 2, (1993), p. 251
[3] H.Hahn, NanoStructured Mat., 9, (1997), p. 3
[4] R.C.Garvie, J. of Phys. Chem., Vol. 82, 2, (1978), pp. 218
[5] W.Wagner, R.S.Averback, H.Hahn, W.Petry, A.Wiedenmann, J. Mater. Res., 6, 10, (1991), p. 2193

Pergamon

NanoStructured Materials, Vol. 12, pp. 693–696, 1999
Elsevier Science Ltd

0965-9773/99/$–see front matter

PII S0965-9773(99)00219-6

Cu CLUSTERING STAGE BEFORE THE CRYSTALLIZATION IN Fe-Si-B-Nb-Cu AMORPHOUS ALLOYS

M. Ohnuma[1,2], K. Hono[1], H. Onodera[1], J.S. Pedersen[2] and S. Linderoth[2]
[1]National Research Institute for Metals, 1-2-1 Sengen, Tsukuba 305 Japan
[2]Risø National Laboratory, DK-4000 Roskilde, Denmark

Abstract *-- The Cu clustering stage before the crystallization of Fe-Si-B-Nb-Cu amorphous alloys have been studied by three dimensional atom probe (3DAP), small-angle neutron scattering (SANS) and high sensitive differential calorimetry (DSC). Cu clustering occurs prior to the onset of the primary crystallization reaction. The number of the clusters estimated by 3DAP is large enough to provide heterogeneous nucleation sites to all bcc/D0₃ Fe-Si crystals which appear at higher temperatures. This fact indicates that the distribution of nanocrystalline Fe-Si is strongly affected by that of the Cu-enriched clusters. The average diameter and interparticle distance of the Cu-enriched clusters have also been estimated by SANS. An exothermic reaction is observed above the Curie Temperature in the DSC curves of the Fe-Si-B-Nb-Cu alloys. The onset temperature of the exothermic reaction is shifted to lower temperature with increasing Cu content. ©1999 Acta Metallurgica Inc.*

INTRODUCTION

A nanocrystalline Fe-Si-B-Nb-Cu alloy, known as FINEMET, is a very fascinating soft magnetic material exhibiting excellent permeability while maintaining a high saturation magnetization [1]. This material is prepared by annealing a melt-spun $Fe_{73.5}Si_{13.5}B_9Nb_3Cu_1$ amorphous ribbon at the temperature range of 520 - 580°C. The microstructure produced by the primary crystallization reaction consists of nanoscale bcc/$D0_3$ Fe-Si grains embedded in the remaining amorphous matrix [2]. Atom probe field ion microscopy (APFIM) studies by Hono et al. [3,4] reported that Cu atoms form Cu-enriched clusters prior to the onset of the crystallization reaction, which suggested that Cu clustering stimulates the nucleation of bcc/$D0_3$ Fe-Si primary particles in the subsequent crystallization stage. From extended X-ray absorption fine structure (EXAFS) measurements, Ayers et al. [2] also reported that Cu atoms form clusters with near-fcc symmetry from very early stage in the heat treatment. Although earlier APFIM and EXAFS works convincingly showed presence of Cu-enriched clusters prior to the onset of crystallization reaction, no spatial information has been obtained by these techniques. In addition, the onset temperature of Cu clustering has not been determined yet. The aim of this paper is to clarify the spatial distribution, size and onset temperature of Cu-enriched clusters by three dimensional atom probe (3DAP) analysis, small-angle neutron scattering (SANS) and high sensitive differential calorimetry (DSC) in the annealing process before the crystallization of the Fe-Si-B-Nb-Cu amorphous alloys.

EXPERIMENTAL PROCEDURE

A melt-spun $Fe_{73.5}Si_{13.5}B_9Nb_3Cu_1$ amorphous ribbon was provided by Hitachi Metals Ltd. Heat treatments were performed at 400°C for 60 min in vacuum. Specimens for atom probe analysis were prepared by mechanically grinding the ribbon to a square rod followed by micro-electropolishing to a sharp needle shape specimen. These specimens were observed by field ion microscope (FIM) and then analyzed by the 3DAP. SANS was measured in a magnetic field of 0.3 T using the SANS instrument installed at the cold neutron source at Risø National Laboratory. DSC measurements for $Fe_{74.5-x}Si_{13.5}B_9Nb_3Cu_x$ (x=0, 0.5, 1, 1.5) were also performed using a high sensitive-type DSC. Although samples cannot be heated higher than 500°C in this type of DSC equipment, the high sensitivity is advantageous for studying Cu clustering because this may occur well below 500°C. The investigated samples were heated up to 450°C with a heating rate of 10 $Kmin^{-1}$ in a helium atmosphere.

RESULTS AND DISCUSSION

It has previously been shown [5] by DSC and TEM measurements that bcc/$D0_3$ Fe-Si crystal formation takes place at about 517°C (with a heating rate of 10 $Kmin^{-1}$). Figure 1 shows 3DAP elemental mapping of Cu and iso-concentration surface of 6 at.%Cu in a $Fe_{73.5}Si_{13.5}B_9Nb_3Cu_1$ melt-spun alloy annealed at 400°C for 60 min, which shows that the Cu atoms are clustering prior to the bcc/$D0_3$ Fe-Si crystal formation. The number of the Cu-enriched clusters is in the order of 10^{24} m^{-3}, which is large enough to provide heterogeneous nucleation sites to all bcc/$D0_3$ Fe-Si crystals. The structure of these clusters is unknown as a HREM image does not give a clear fringe contrast corresponding to a crystalline structure. Hono et al. [6] recently reported that most of the Fe-Si crystals are placed adjacent to Cu-enriched clusters, as observed by 3DAP in specimens annealed above 500°C. Accordingly, the distribution of Fe-Si nanocrystals is strongly affected by Cu-enriched clusters. The size of the clusters can be roughly estimated from Fig.1 to be less than about 3 nm. However, it is difficult to determine the average cluster size because of the restricted area. Small-angle neutron scattering has therefore been applied for obtaining the average cluster size.

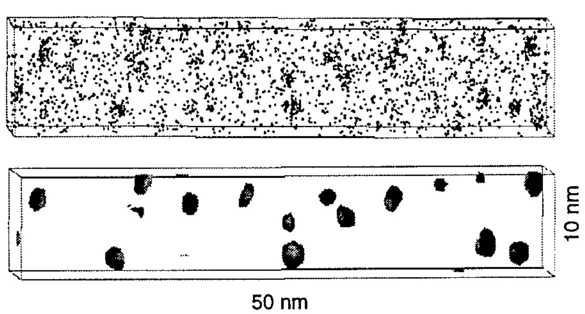

Fig.1 3DAP elemental mapping of Cu and iso-concentration surface of 6 at.%Cu in a $Fe_{73.5}Si_{13.5}B_9Nb_3Cu_1$ melt-spun alloy annealed at 400°C for 60 min.

Figure 2 shows SANS profiles for as-quenched $Fe_{73.5}Si_{13.5}B_9Nb_3Cu_1$ and annealed at 400°C for 60 min. Though the magnetic field of 0.3 T is not sufficiently strong to saturate the sample, the scattering parallel to the magnetic field mainly includes the nuclear component (Fig.2(b)) and the difference between the intensity perpendicular and parallel to the

magnetic field includes only the magnetic component (Fig.2(a)). No difference between as-quenched and annealed specimens exists in the scattering parallel to the magnetic field. However, the intensity for annealed specimens is apparently larger than for the as-quenched sample in the magnetic scattering as shown in Fig.2(a). On the basis of the concentration of Cu-enriched clusters obtained by atom probe experiments [4], the scattering contrast between matrix and clusters for the nuclear component is expected to be less than 5% relative to the scattering length density of the matrix. On the other hand, the scattering contrast for the magnetic component is large because the local magnetization in the Cu-enriched clusters is believed to be much smaller than in the matrix. The large difference between the scattering contrast for nuclear scattering and magnetic scattering explains why a difference can be obtained only for the magnetic scattering. A weak peak exists at around 1 nm^{-1}, implying that the interparticle distance between the clusters is about 6 nm. The average diameter of the Cu-enriched clusters is about 1.8 nm, as estimated by Guinier plots, assuming a spherical morphology. The uncertainty of the estimated diameter due to the interparticle interference is expected to be small because the peak is weak and the volume fraction of the Cu-enriched clusters is low, as shown in Fig.1. Kohlbrecher et al. [7] reported that precipitates of 1 nm radii have appeared in $Fe_{73.5}B_7Si_{15.5}Nb_3Cu_1$ alloy annealed at 450°C for 60 min on the basis of anomalous small-angle X-ray scattering experiments. They have reported that these precipitates are precursors of bcc/$D0_3$ Fe-Si and their concentration of iron is about 70-80 at.%. According to the result of APFIM [4] , the iron concentration of the Cu-enriched clusters in the alloy annealed at 450°C for 60 min is nearly 70 at.%. Thus, the precipitates with 1 nm size reported by Kohlbrecher et al. are suggested to be Cu-enriched clusters as the size shows very good agreement with the one obtained in this study.

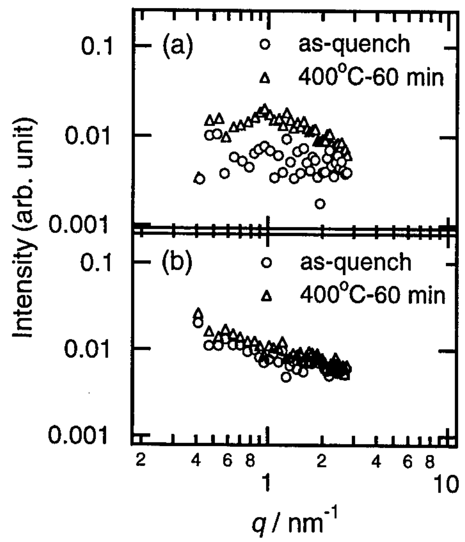

Fig.2 Small-angle neutron scattering profiles for as-quenched $Fe_{73.5}Si_{13.5}B_9Nb_3Cu_1$ and annealed at 400°C for 60 min in the field of 0.3 T. (a) The scattering intensity difference between perpendicular and parallel to the magnetic field, (b) The scattering intensity parallel to the magnetic field.

To evaluate the onset temperature of Cu-enriched cluster formation, we performed a DSC measurement using a high sensitive DSC equipment. Figure 3 shows the DSC signal for $Fe_{74.5-x}Si_{13.5}B_9Nb_3Cu_x$ (x=0, 0.5, 1, 1.5 at%) measured with a heating rate of 10 $Kmin^{-1}$. The DSC curves for as-quenched specimens exhibit excess exothermic signal in the range between the Curie temperature and 430°C compared with an alloy without Cu as shown in Fig.3(a). This exothermic reaction occurs apparently at a lower temperature than the temperature of bcc/$D0_3$ Fe-Si formation (~517°C [5]). Hence, this exothermic signal is believed to correspond to the formation of Cu-enriched clusters. The exothermic maximum and the onset

point are shifted to lower temperature with increasing Cu content. In the $Fe_{73.5}Si_{13.5}B_9Nb_3Cu_1$ alloy, the DSC curve starts to deviate from that of $Fe_{74.5}Si_{13.5}B_9Nb_3$ at around 350°C and the magnitude of the deviation reaches a maximum at around 400°C. This result implies that Cu clustering starts at around 350°C and continues up to about 430°C. Little difference between samples with different Cu content is observed for pre-annealed specimens (Fig.3(b)). This is because the Cu-enriched clusters have already formed during the pre-annealing.

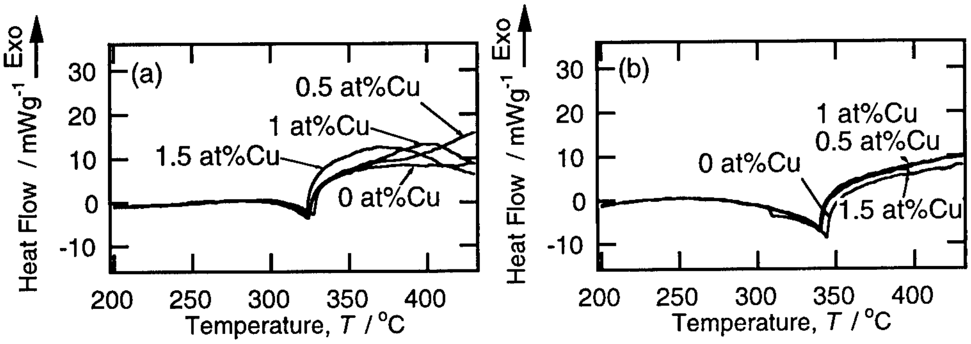

Fig.3 DSC signal for (a) as-quenched and (b) pre-annealed $Fe_{74.5-x}Si_{13.5}B_9Nb_3Cu_x$ (x=0, 0.5, 1, 1.5) ribbons with a heating rate of 10 $Kmin^{-1}$. Pre-annealing has been performed up to 450°C with a heating rate of 10 $Kmin^{-1}$.

CONCLUSIONS

The Cu clustering before the early crystallization stage of a $Fe_{73.5}Si_{13.5}B_9Nb_3Cu_1$ amorphous alloy has been investigated by 3DAP, SANS and DSC. It is concluded that:

(1) Cu clustering occurs prior to the onset of the primary crystallization reaction. The density of the clusters estimated by 3DAP is in the order of 10^{24} m^{-3}.

(2) The average diameter and interparticle distance of the Cu-enriched clusters estimated by SANS is about 1.8 nm and 6 nm, respectively.

(3) From the results of DSC measurements, Cu clustering is thought to occur at around 350°C and continue up to about 430°C in the $Fe_{73.5}Si_{13.5}B_9Nb_3Cu_1$ alloy.

REFERENCES

1. Y. Yoshizawa, S. Oguma and K. Yamauchi, J. Appl. Phys. **64**, 6044 (1988).
2. J. D. Ayers, V. G. Harris, J. A. Sprague, W. T. Elam and H. N. Jones, Acta metall. mater. **46**, 1861 (1998).
3. K. Hono, K. Hiraga, Q. Wang, A. Inoue and T. Sakurai, Acta metall. mater. **40**, 2137 (1992).
4. K. Hono, Y. Zhang, A. Inoue, and T. Sakurai, Mater.Trans, JIM., **36**, 909(1995).
5. Y. Yoshizawa and K. Yamauchi, Mater. Trans. JIM, **21**, 307 (1990).
6. K. Hono, M. Ohnuma, D. H. Ping, and H. Onodera, Acta metall. mater., to be published.
7. J. Kohlbrecher, A. Wiedenmann, H. Wollenberger, N. Mattern and G. Goerigk, NanoStructured Mat., **6**, 449(1995)

Pergamon

NanoStructured Materials, Vol. 12, pp. 697–700, 1999
Elsevier Science Ltd

0965-9773/99/$–see front matter

PII S0965-9773(99)00220-2

HIGH RESOLUTION STUDIES OF METALLIC NANOCOMPOSITE MATERIALS

P.J. Warren, D.J. Larson, C. Weston, A.Cerezo, A.K. Petford-Long, G.D.W. Smith and B. Cantor
Department of Materials, University of Oxford,
Parks Road, Oxford OX1 3PH, U.K.

Abstract *-- This paper briefly presents examples from current research involving metallic nanocrystalline materials within the Department of Materials, University of Oxford. The paper focuses on local variations in chemistry within nanoscale microstructures. The materials under investigation include 1) electrodeposited single phase nanocrystalline nickel; 2) rapidly solidified amorphous nanocrystalline AlYNi; 3) sputter deposited Cu-Co multilayer films. ©1999 Acta Metallurgica Inc.*

INTRODUCTION

An ability to design on the nanometre scale must be accompanied by an ability to characterize on the nanometre scale if we are to understand, or even just verify, the effect of our macroscopic manipulation of nanostructured materials. This paper briefly presents examples from current research involving metallic nanocrystalline materials within our department. The common thread between each material problem discussed is the desire to understand how local variations in chemistry on the nanometre scale are related to processing parameters.

The research projects discussed below involved numerous different processing techniques for producing nanostructured materials: electrodeposition of single phase nanocrystalline nickel[1]; single-roller rapid solidification (melt-spinning) of an amorphous Al-Y-Ni alloy followed by partial annealing to form Al nanocrystals in an amorphous matrix[2]; sputter deposition of a multilayer film (MLF) of alternating 2nm layers of Cu and Co[3,4]. In each case process parameters were varied to control the size, shape and distribution of the nanocrystals or layers and the changes in microstructure were quantified. Structural information was determined mainly by transmission electron microscopy(TEM) and high resolution electron microscopy(HREM). Compositional analysis by energy dispersive X-ray spectroscopy, however, was generally not possible due to the three dimensional microstructure morphologies. Instead compositional analysis of these microstructures was achieved by using specialist three dimensional atom probe(3DAP) techniques developed within the department[5]. 3DAP analysis consists of controlled field evaporation of individual atoms from the end of a very sharp needle-shaped specimen. Each atom is projected approximately radially from the end of the needle towards a single-atom-sensitive detector. The radial projection achieves direct magnification of typically x1million while the time-of-flight from the specimen to the detector enables accurate

identification of all ions according to their mass-to-charge ratio. The instrumentation is currently capable of collecting about 1million atoms in 24hrs, which corresponds to a volume typically 25x25x30nm^3.

RESULTS & DISCUSSION

Electro-deposited Nanocrystalline Ni

One of the main questions concerning single phase nanocrystalline materials is whether the material really is pure and hence whether the observed properties, such as inverse Hall-Petch effect, really are due to the nanocrystalline structure rather than unidentified impurities. Pulsed-electroplating has been used with a variety of organic additives to produce nanocrystalline Ni deposits up to 1mm thick. 3DAP analysis of 30nm grain size material was used to show that there was no trapping of (organic) impurities at the grain boundary visible in Figure 1. Grain misorientation was detected qualitatively by the difference in viewing angle necesary to observe

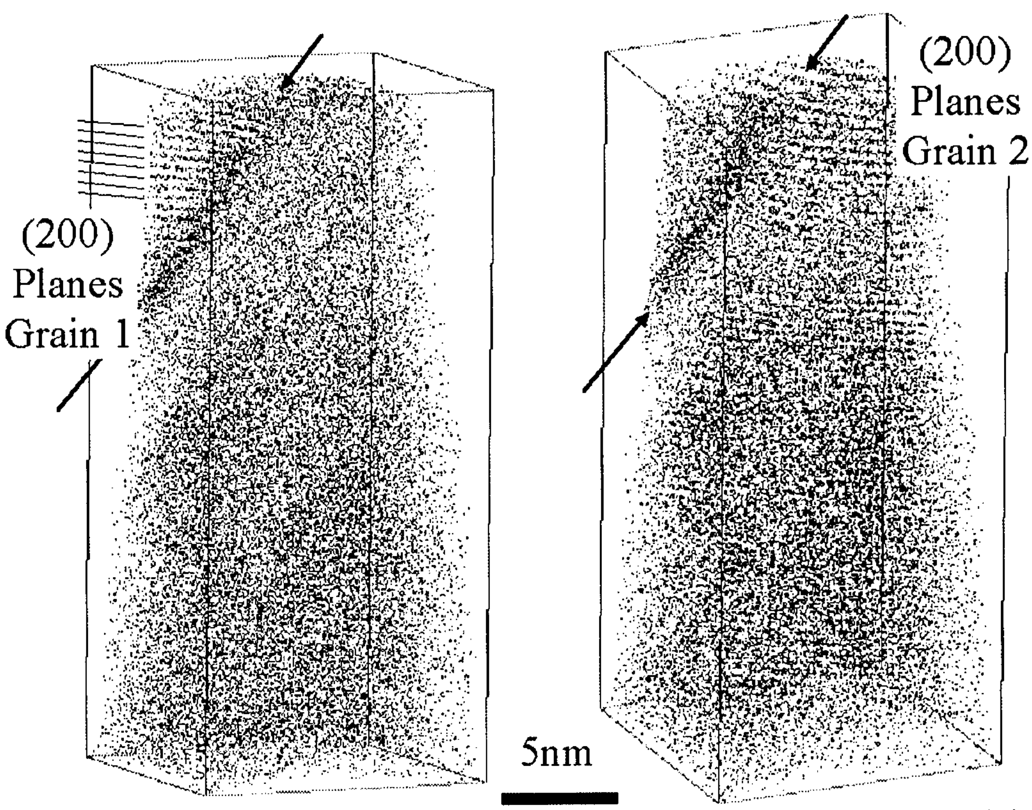

Figure 1. Position of atoms within a 3DAP analysis of electrodeposited nanocrystalline nickel. Due to the misorientation between grains the (200) planes are only visible when viewed at different tilts. No impurity atoms were detected at the grain boundary.

atomic planes either side of the grain boundary. Chemically this analysis showed the material to be 99.88% Ni with very low levels of N, O and C species, but more importantly these atoms were distributed evenly and not associated with the grain boundary. Extracting crystal structure information from 3DAP data has only recently become possible[6] and this exicting new technique is still being developed.

Rapidly solidified AlYNi nanocomposite alloys

Nanocomposite materials consist of nanosized particles embedded in a matrix, therefore the difference in chemistry between the particle and matrix is very important in determining how the microstructure forms. There is a large family of nanocomposite materials that are produced by controlled partial crystallization of an amorphous precursor to form a uniform distribution of primary nanocrystals embedded in a solute-rich amorphous matrix[7]. The changes in local chemistry during crystallization are critical in determining the size, distribution and stability of these systems. Virtually the only technique able to quantify chemical variations in this category of materials is atom probe. Hono[8] has used atom probe techniqes to detect diffusional solute pile-up in numerous alloy systems, which is an important mechanism for limiting growth of these nanocrystals. At Oxford a range of Al-Y-Ni alloys exhibiting this behaviour have been studied and the crystallization behaviour determined[2]. Further studies of are in progress.

Sputter deposited Cu-Co mulit-layer films

Another category of materials under investigation are multi-layer films. These materials have large commercial potential in the magnetic recording industry. For many years these materials have proved particularly difficult to analyse by 3DAP due to difficulties in specimen preparation however recently focussed ion beam machining has been used to sucessfully produce needle specimens from thin film materials[3,4]. Figure 2 shows a 3DAP analysis of a sputtered Cu-Co multi-layer film. This analysis clearly exemplifies the power of 3DAP analysis for the quantification of nanoscale variations in chemistry in complex metallic microstructures.

CONCLUSION

Three diverse examples of current research into metallic nanocystalline materials within our department have been discussed briefly. Each material problem has been presented in terms of the local variations in chemistry affecting the microstructural evolution. The technique of three dimension atom probe analysis has been shown to have made significant progress in quantifying local variations in chemistry within these materials.

REFERENCES

[1] Erb. U, *Nanostructured Materials*, 1995, 6, 533

[2] Gogebakan, M., Warren, P.J. and Cantor, B., *Mat.Sci.Eng.*, 1997, A226-8, 168

[3] Larson, D.J., Petford-Long, A.K., Foord, D.T., Cerezo, A., Anthony, T.C. and Smith, G.D.W., *Applied Physics Letters*, (submitted)
[4] Larson, D.J., Foord, D.T., Petford-Long, A.K., Anthony, T.C., Rozdilsky, I.D., Cerezo, A., and Smith, G.D.W., *Ultramicroscopy*, (submitted)
[5] Cerezo, A., Godfrey, T.J., Sijbrandij, S.J., Smith, G.D.W. and Warren, P.J., *Rev.Sci.Instrum.*, 1998, 69(1), 49
[6] Warren, P.J., Cerezo, A. and Smith, G.D.W., Ultramicroscopy, 1998, (in press)
[7] Tsai, A.P., Kamiyama, T., Kawamura, Y., Inoue, A. and Masumoto, T., *Acta Materialia,* 1997, 45, 1477
[8] Hono, K., Zhang, Y., Inoue, A., and Sakurai, T., *Mat.Trans.JIM*, 1995, 36, 909

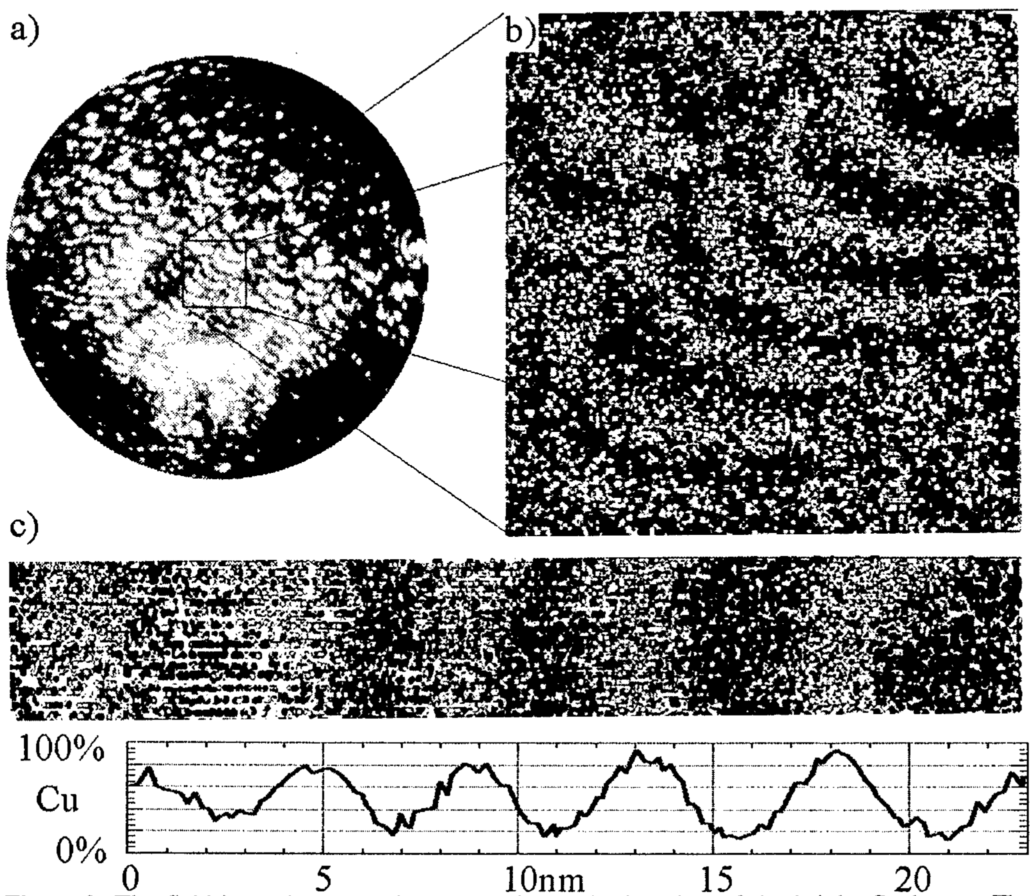

Figure 2. The field ion microscope image (a) shows the location of the bright Co layers. The atom map (b) shows the Co and Co atoms. The layers are very curved within each columnar grain, yet they join up across the grains as would be expected given the sputter deposition route. Viewing a sub-set in depth cross-section(c) shows (111) planes which are continous across the Cu/Co layers and the fluctuations in Co and Cu varying from 90%Co to 95% Cu.

Pergamon

NanoStructured Materials, Vol. 12, pp. 701–704, 1999
Elsevier Science Ltd

0965-9773/99/$–see front matter

PII S0965-9773(99)00221-4

SINTERING BEHAVIOUR OF NANOCRYSTALLINE Y_2O_3

Patricie Merkert, Horst Hahn and Jürgen Rödel
Darmstadt Technical University, Materials Science Department, 64287 Darmstadt, Germany

Abstract— *Sintering behaviour of nanocrystalline yttria with a grain size of 25 nm was investigated. Pellets of 10 mm diameter were pressed uniaxially at 60 MPa and subsequently cold isostatically pressed at 200 MPa. Sintering studies were performed at temperatures between 1200°-1300°C for 10-960 min to obtain densities from 60-100% theoretical density. The grain size was measured by the linear intercept method as a function of density. Sintering paths of nanocrystalline yttria were obtained and are discussed in comparison to microcrystalline yttria. Rapid coarsening at low temperatures and densities occurs in nanocrystalline yttria. Also differential sintering is observed. At later stages coarsening and densification occur simultaneously. ©1999 Acta Metallurgica Inc.*

Introduction

Mechanical properties of nanocrystalline oxides are of interest for the understanding of basic mechanisms and for applications of these materials. A prerequisite for measurements of fracture strength is the production of homogeneous bulk materials with small defects. Nanocrystalline oxides show a good sinterability, however in pure single phase materials grain growth into the micrometer regime occurs [1-3]. Therefore, the knowledge of the sintering mechanisms is essential for understanding bulk properties such as fracture strength and fracture toughness.

Experimental Methods

Commercial nanocrystalline yttria powder (NanoTek® Yttrium Oxide) with an initial grain size of 25 nm was first pressed uniaxially at 60 MPa and subsequently cold isostatically pressed at 200 MPa into pellets with a diameter of 10 mm. Sintering experiments were carried out between 1200°-1300°C for 10-960 min. (Table 1) in air. The density was determined using Archimedes methode. The grain size was measured on polished and subsequently thermally etched surfaces by high resolution scanning electron microscopy (HRSEM) by the linear intercept method over at least 300 intercepts. Polycrystalline yttria (Chempur) with a grain size of 0.5 μm was sintered at 1600°-1750°C for comparison. Pore size distributions were measured by nitrogen adsorption.

TABLE 1
Sintering conditions and results in air

[redacted]					
T [°C]	t [min]	rel. ρ [%]	T [°C]	t [min]	rel. ρ [%]
green body	-	54	green body	-	57
1200	10	60	1600	10	65
1200	340	65	1600	120	70
1200	960	70	1600	960	75
1300	40	80	1750	70	80
1300	230	90	1750	200	85
1300	450	95	1750	600	90

Results and Discussion

As can be seen from Table 1 densities between 60 to 95 % of the theoretical density (th.d.) were achieved for nanocrystalline yttria at ½ of the melting point. However, strong coarsening occurs during sintering. Even before significant densification (ρ<65-70% th.d.) an increase of fivefold the initial grain size is observed (Fig. 1 and 2a, b). At near full density the average grains have grown by a factor of 35 into the micrometer range as can be seen in Fig. 1 and 2c. Additionally, in these pellets porous regions were found (Fig. 2c) which indicates the occurrence of differential sintering. Polycrystalline yttria also coarsens during sintering but the relative increase of the grain size is much lower than for nanocrystalline yttria and porous regions can not be found in the almost dense bodies.
Since a large amount of very large pores (d>500 nm) were found in porous pellets pore size distribution measurements could not be carried out. The presence of the large pores complicates or even prevents densification to final density [1].

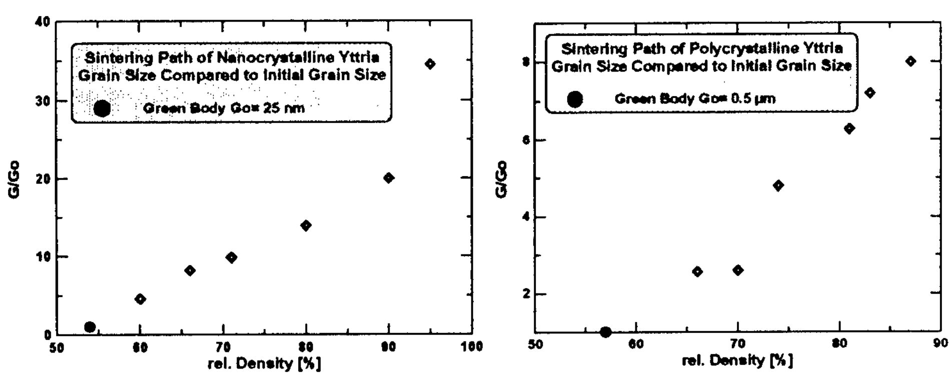

Fig. 1: Sintering path of nano- (left figure) and polycrystalline (right figure) yttria:

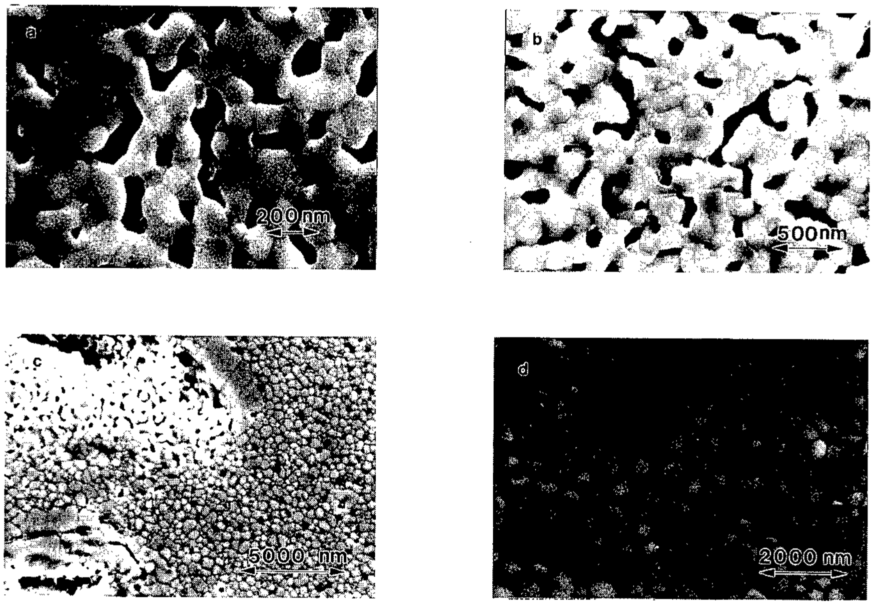

Fig.2: High resolution scanning electron micrographs of a) 60 % dense nano-yttria, b) 65 % dense nano-yttria, c) 95% dense nano-yttria, d) porous region in 90% dense nano yttria.

In the green body a large fraction of pores up to 200 nm (Fig. 3) was observed which indicates that agglomerates in the same range were present in the powders. Most likely these agglomerates are introduced by the post oxidation step of the inert gas synthesis. The slow increase of the density up to 70% th.d. can be explained assuming that the agglomerates have a higher density than the remaining parts. This assumption is plausible because agglomeration occurs at elevated temperatures during the post-oxidation of the nanoparticles [4] while consolidation is performed at room temperature. Therefore, the agglomerates sinter to full density before the remaining bulk material starts to densify.

Sintering models from Cannon, as quoted by N. Shaw [5], and Riedel [6] define a relative coarsening / densification ratio, Γ, which describes the densification and coarsening behaviour of a material in the intermediate and final stage. If Γ is large grain growth will predominate and almost no densification will occur; if Γ is small the material will densify with little grain growth. In our case Γ is rather large, since coarsening occurs early in the sintering process above 75% th.d.. Γ can be expressed by $\delta D_S/\omega D_B$, where δ is the depth of surface diffusion, D_S the surface diffusion coefficient, ω the grain boundary width and D_B the grain boundary diffusion coefficient. Since the diffusion coefficient for both nano- and polycrystalline materials should be the identical sintering of nanocrystalline materials cannot be predicted simply by using measurements on microcrystalline materials and neglecting effects due to agglomerates and differential sintering.

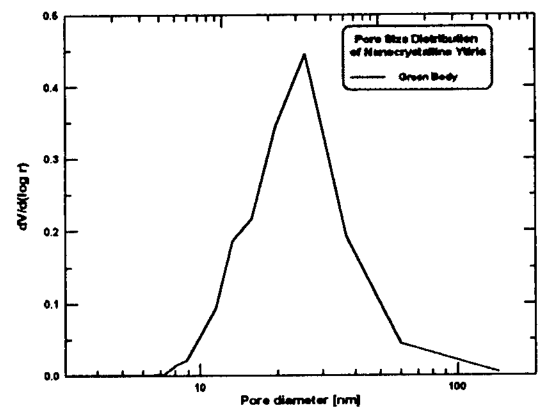

Fig. 3: Pore size distribution of a green body of nanocrystalline yttria.

However, it has been shown recently that other gas phase techniques are available which provide nanopowders with less agglomeration and consequently, sintering paths should be possible which result in less grain growth during densification. Nevertheless, it will not be possible to suppress grain growth completely during pressureless sintering and in single phase ceramics grain sizes will grow larger than 50 nm. In order to further reduce grain growth additions of nanoparticles of a second phase are necessary [7].

Conclusions and Outlook

Sintering paths of nano- and polycrystalline yttria were obtained. The presence of a significant amount of agglomerates in the nanocrystalline bulk material results in grain coarsening at low temperatures and high porosities in the sintered ceramic. Sintering models of Riedel and Cannon predict a large relative coarsening/densification ratio Γ.

A homogeneous green body could lead to a reduction in the coarsening rate in the initial and intermediate stage of sintering. Additionally, hot pressing could be used to enhance the driving force for sintering while reducing the tendency for grain growth.

References

1. Averback,, R.S., Höfler, H.J., Hahn, H. and Logas, J.C., *Nanostructured Materials*, 1, 173, 1992.
2. Chen, P.-L. and Chen, I-W., *J.Am.Cerm.Soc.*, 80, [3], 637, 1997.
3. Hahn, H., *Nanostructured Materials*, 2, 251,1993.
4. Skandan, G., Foster, C.M., Frase, H., Ali, M.N., Parker, J.C. and Hahn, H., *Nanostructured Materials*, 1, 313,1992.
5. Shaw, N.J, *powder metallurgy international*, 21, No.6, 25, 1989.
6. Svoboda, J. and Riedel, H., *Acta mater.*, 40, No.11, 2829,1992.
7. Srdic, V.V., Winterer, M. and Hahn, H., *J.Am.Cerm.Soc.*, submitted 1998.

Pergamon

NanoStructured Materials, Vol. 12, pp. 705–708, 1999
Elsevier Science Ltd

0965-9773/99/$–see front matter

PII S0965-9773(99)00222-6

NONEQULIBRIUM PHASE TRANSITION OF $Nd_3(Fe,Ti)_{29}$ COMPOUND DURING MECHANICAL MILLING

S.L. Tang, Z.Q. Jin, S.Y. Zhang and Y.W. Du
National Laboratory of Solid State Microstructures and Department of Physics, Nanjing University, Nanjing 210093, P.R. China

Abstract -- *A nonequilibrium phase transition has been found during mechanical milling of monoclinic $Nd_3(Fe,Ti)_{29}$ compound. The transition process and the mechanically milled products have been investigated by X-ray diffraction and AC initial susceptibility. The results show that mechanical milling results in the transformation of $Nd_3(Fe,Ti)_{29}$ compound into a nanostructure during the early stage of milling, and then generates it to decompose to the hexagonal $TbCu_7$-type $Nd(Fe,Ti)_7$ disorder phase and α-Fe(Ti), and finally transforms the material to a mixture of the amorphous phase and α-Fe(Ti). The structure of mechanically milled $Nd(Fe,Ti)_7$ phase is similar to but not exactly identical with that of annealed $Nd(Fe,Ti)_7$ phase. The magnetic-ordering transition of the former is broader than that of the later. The broadening of the magnetic-ordering transition can be attributed to the effect of the nanostructure, and the inhomogeneity of the concentration of $Nd(Fe,Ti)_7$ phase.*

INTRODUCTION

Since it is found that the formation of amorphous materials by the milling of Y-Co intermetallic compounds, mechanical milling as well as mechanical alloying (1) have been widely used to synthesize metastable phase, especially amorphous and nanocryatalline phase of intermetallic compounds. Since the amorphous state has a higher free energy than the crystalline state, there must be a way of storing mechanical energy in the material during the milling process. In principle, there are three possibilities, namely in the form of atomic(chemical) disorder, lattice defects, and grain boundaries. Most theoretical work speculates that the atomic disorder is the main source of energy storage (2). Experimentally, atomic disorder during the early stage of mechanical milling is really detected in Co_2Ge (3) compound by measuring magnetic properties.

The work of Smith (4) on the studies of milled Sm_2Fe_{17} compound indicated that Sm_2Fe_{17} decompose into a mixture of an amorphous and a α-Fe phase and expected that intermetallics with $Nd_3(Fe,Ti)_{29}$-type structure would undergo phase separation during mechanical milling. However, the separation process was not clear. In this paper, the intermetallic compound Nd3(Fe,Ti)29 has been chosen as the basic subject of investigation. The aims of the investigation is to gain a full understanding of the separation process and to assess whether there is a metastable intermediate phase during milling process.

EXPERIMENTAL PROCEDURE

The $Nd_3(Fe,Ti)_{29}$-type $Nd_3Fe_{27.5}Ti_{1.5}$ compound was prepared by melting the constituent metals in a magneto-controlled arc furnace under high-purity argon atmosphere. The purities of starting materials were 99.9% Nd and Ti, 99.8% Fe. The arc-melted button wrapped in Mo foil were sealed in an evacuated quartz tube. It was annealed at 1100 °C for 48 h. Mechanical milling was carried out in a high-energy ball mill. Loading and sealing of the vial and all subsequent powder handling were carried out in a high purity argon filled glove box. Structures of powders were examined by X-ray diffraction with Cu K_α radiation. The AC magnetic susceptibility measurements were carried out with the heating rate of 15 °C/min at 2 Oe magnetic field.

RESULTS AND DISCUSSION

Figure 1 shows the X-ray diffraction patterns of the $Nd_3(Fe,Ti)_{29}$ compound after various periods of milling. The X-ray pattern of the 6 h milled $Nd_3(Fe,Ti)_{29}$ after annealing at 650 °C for 30 min is also given at the top in Fig. 1(marked as NF). The NF X-ray pattern can be identified as the main phase of disordered $TbCu_7$-type $Nd(Fe,Ti)_7$ phase and α-Fe(Ti) with a small amount of Nd-rich phase stabilized by oxygen (5). The pattern of the unmilled material (0 h) is identified as the phase having the monoclinic $Nd_3(Fe,Ti)_{29}$ structure and a very small amount of α-Fe in substantial agreement with literatures (6). It is clearly seen that during mechanical milling the intensity of reflections decreases gradually and all peaks become broader with increasing milling time. When millled for 1 h, X-ray diffraction patterns remain unchanged as the starting compound and X-ray diffraction lines broaden. After 3 h of milling, comparing the X-ray pattern with that of the $Nd(Fe,Ti)_7$ phase, it is found that apart from the peak of α-Fe(Ti) the diffraction pattern is very close to the characteristic of the $TbCu_7$ structure (some feature diffraction lines of 3-29 phase, e.g. (322), almost disappear), implying that the $Nd_3(Fe,Ti)_{29}$ compound decompose to the disordered $Nd(Fe,Ti)_7$ phase and α-Fe(Ti) solid solution. The milled material is completely transformed to a mixture of α-Fe(Ti) solid solution and the amorphous phase after 6 h of milling.

The temperature dependence of the AC susceptibility of the $Nd_3(Fe,Ti)_{29}$ compound after various periods of milling as well as the 6 h milled sample after annealing at 650 °C for 30 min (marked as NF) is shown in Fig. 2. In the curve of the unmilled material (0 h) a magnetic-ordering transition exhibits at about 151-154 °C, which corresponds to the result reported by (6). For the 1 h milled sample, a broad magnetic-ordering transition appears in the curves. The transition starting (T_s) and ending temperature (T_e) span over a wide temperature range (134-164 °C). Compared with the unmilled sample, it is easy to discern that the irregular nanometersized $Nd_3(Fe,Ti)_{29}$ compounds lead to broaden of the magnetic-ordering transition. When the milling time is shorter than 3 h, the transition starting and ending temperature continuously increasse and is more and more close to that of $Nd(Fe,Ti)_7$ with increasing the milling time, characteristic temperatures of the transition starting and ending are summarized in Table 1. After 6 h of milling the magnetic order transition disappears, implying the complete decomposition of disorder $Nd(Fe, Ti)_7$ phase.

The combination of the results of X-ray diffraction and the AC susceptibility after different

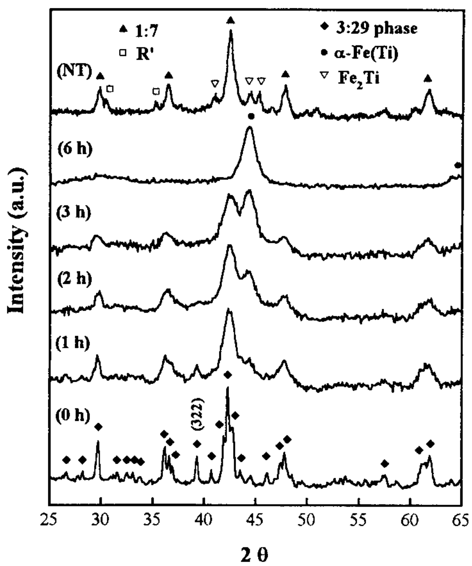

Fig. 1. X-ray-diffraction patterns of the $Nd_3(Fe,Ti)_{29}$ compound after various periods of milling as well as the 6 h milled sample after annealing at 650 °C for 30 min (marked as NF), (R'=Nd-rich phase).

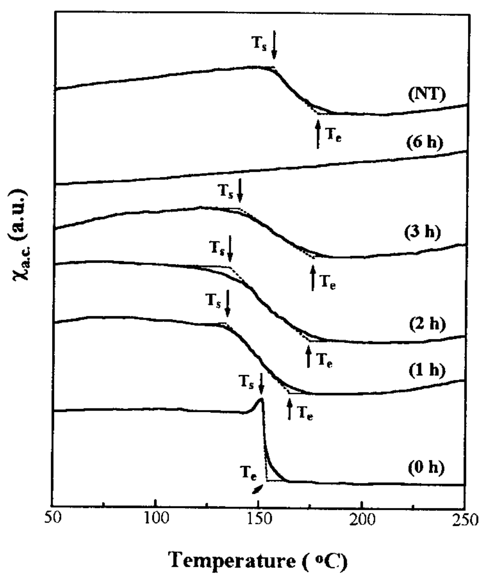

Fig. 2. Temperature dependence of the AC magnetic susceptibility of the $Nd_3(Fe,Ti)_{29}$ compound after various periods of milling as well as the 6 h milled sample after annealing at 650 °C for 30 min (marked as NF).

milling times gives a picture of the mechanical milling process. The process of mechanical milling of $Nd_3(Fe,Ti)_{29}$ compound can be divided into three stages.

The first stage is for milling time up to 1 h. In this period, the material remains in the same structure as the starting compound and X-ray diffraction line broadening shows that the average crystallite size decreases strongly and strain and distortion within the crystallites increases.

The second stage takes place during the milling time of more than 1 h and less than 3 h. In this period, X-ray diffraction patterns show that the material substantially transforms from the $Nd_3(Fe,Ti)_{29}$ phase to a mixture of the disorder $Nd(Fe, Ti)_7$ phase and α-Fe(Ti).

The changes in the temperature dependence of AC magnetic susceptibility of the material after various periods of milling give more detailed information about the process during the intermediate stage of milling. It is clearly observed from Fig. 2 that the magnetic-ordering transition of the $Nd(Fe, Ti)_7$ phase and the $Nd_3(Fe,Ti)_{29}$ phase broaden. There are two main factors which might bring about the broadening of the magnetic-ordering transition. One is the combined effect of the nanocrystalline, and another factor is inhomogeneity of the concentration. Due to the fact that the temperature of the powders is low during the mechanical milling (The peak temperature during the collision is not more than 30 °C-40 °C above the average processing temperature (7)) and the diffuse of the atoms is very difficult, it is likely that the $Nd(Fe, Ti)_7$ phase formed by the decomposition of $Nd_3(Fe, Ti)_{29}$ phase deviates beyond the stoichiometric composition and has concentration fluctuations. Therefore, the exchange integral, which determines the Curie temperature, will vary in the different concentration

TABLE 1
The starting (T_s) and ending temperature (T_e) of magnetic-ordering transition of $Nd_3(Fe, Ti)_{29}$ phase under different conditions.

Temperature	0 h	1 h	2 h	3 h	NT
T_s(°C)	151	134	136	141	155
T_e(°C)	154	164	174	175	178

regions. This leads to a broad transition in ac susceptibility vs temperature curve. During mechanical milling of Co_2Ge compound, it has been reported that the different number of the Co atoms in the different local environment leads the broadening of magnetic-ordering transition (3). Comparing the 3 h milled sample with NF sample, it can be seen that the magnetic-ordering transition of the former is broader than that of the later. This may be attributed to finer grain size and larger concentration fluctuations for $Nd(Fe, Ti)_7$ phase obtained by 3 h of milling.

The third stage takes place after 3 h of milling. In this period, the disordered $Nd(Fe, Ti)_7$ phase amorphizes and the material is transformed into a mixture of the amorphous phase and α-Fe(Ti).

CONCLUSION

Starting from the intermetallic compound $Nd_3(Fe,Ti)_{29}$, mechanical milling generates the compound to decompose to the disorder $Nd(Fe,Ti)_7$ phase and α-Fe(Ti) in the early stage and finally transforms the material to the mixture of the amorphous phase and α-Fe(Ti). The process of mechanical milling can be divided into three steps. The first step is the grain-fine process. In this step, the X-ray diffraction patterns of the milled samples reveal the same structure as the original compound. The second step is that the $Nd_3(Fe,Ti)_{29}$ compound decompose to the disorder $Nd(Fe,Ti)_7$ phase and α-Fe(Ti). The decomposition is a continuous process as can be seen from the AC susceptibility vs temperature curves. The last step is the amorphization of the disorder $Nd(Fe,Ti)_7$ phase.

The authors acknowledge the financial support from NMS and NSFC projects.

REFERENCES

1. Schultz, L., Wcker, J. and Hellstern, E., Journal of Applied Physics, 1987, 61, 3583.
2. Massobrio, C., Pontikis, V. and Martin, G., Physics Review Letters, 1989, 62, 1142.
3. Zhou, G.F. and Bakker, H., Physics Review B, 1993, 48, 13383.
4. Smith, P.A.I. and McCormick, P.G., Scripta Metallurgica et Materialia, 1992, 26, 485.
5. Ramesh, R., Chen, J.K. and Thomas, G., Journal of Applied Physics, 1987, 61, 2993.
6. Fuerst, C.D., Pinkerton, F.E. and Herbst, J.F., Journal of Magnetism and Magnetic Materials, 1994, 129, L115.
7. Schwarz, R.B. and Koch, C.C., Applied Physics Letters, 1986, 49, 146.

Pergamon

NanoStructured Materials, Vol. 12, pp. 709–712, 1999
Elsevier Science Ltd

0965-9773/99/$–see front matter

PII S0965-9773(99)00223-8

NANOSTRUCTURES FROM SEVERE PLASTIC DEFORMATION AND MECHANISMS OF LARGE-STRAIN WORK HARDENING

I.V. Alexandrov and R.Z. Valiev
Institute of Physics of Advanced Materials,
Ufa State Aviation Technical University, K. Marksa 12, 450000 Ufa, Russia

Abstract *– Results of experimental investigations of structure evolution processes during processing of nanostructured materials by severe plastic deformation techniques are presented. The obtained results are analyzed on the basis of recent approaches, developed to explain mechanisms of work hardening at large plastic deformations.*

INTRODUCTION

Investigations of recent years have shown that methods of the so-called severe plastic deformation (SPD) conducted under applied high pressure provide fabrication of bulk nanostructured samples from various materials (1,2). The obtained samples are characterized not only by the small grain size but also the specific defect structure, as well as enhanced physical and mechanical properties. Severe plastic deformation techniques were used to process a nanostructured state in a number of pure metals (Cu, Ni and Fe) and different alloys (1,2). However, till the present time mechanisms, which lead to formation of the nanostructured state during SPD, are not clear. From the other hand, there are a great number of publications devoted to investigation of structure evolution and behavior of metals during large plastic deformation at a true strain value of γ>1 (3-9).

The purpose of the present work was to reveal peculiarities of structure evolution during formation of the nanostructured state by SPD and to analyze the data obtained on the basis of the results of investigation of metals subjected to large strains.

PROCESSING

SPD was realized at room temperature using techniques of torsion straining under applied high pressure and equal-channel angular (ECA) pressing (1). During SPD, the disk type samples, up to 20 mm in diameter and 0.3-1 mm in thickness, were subjected to shear straining under conditions of applied pressure of several GPa. A shear displacement value depended on the distance from a rotation axis and the number of rotations. One rotation, for the analyzed part of structure remote from the rotation axis to a distance of r=2 mm, corresponded to a strain degree (γ) of 2, (10). During ECA pressing the cylinder shape samples, having 20 mm in diameter and 80 mm length, were passed several times through two, crossing under an angle of 90°, channels with equal crossing sections. With that, each pass corresponded to the

additional deformation degree γ, being approximately equal to 1 (2).

EXPERIMENTAL RESULTS

TEM investigation results showed that formation of low angle cell structure occurs at the initial stages of the SPD process ($\gamma \approx 2$) in pure metals, independent of their crystal lattice type. In Cu an average size of cells with wide boundaries is 0.3-0.4 μm (Figure 1a). Similar structures were observed in Fe as well (10).

A mixture of cell and grain structures forms in the intermediate stage of SPD ($\gamma \approx 4$). A mean cell size slightly decreases as compared to the previous stage. Volume fractions of cell and grain structures are essentially determined also by a character of passes during ECA pressing and a value of the applied pressure at torsion.

A uniform equiaxed grain structure having a grain size of about 100-200 nm (Figure 1b) can be produced on the final stage of SPD ($\gamma > 10$) if optimal regimes which provide the material with a uniform shear deformation are realized (1,2). The development of mainly high angle grain boundaries in this case is confirmed by the data of the electron diffraction (11) and HREM (12). The characteristic features of the given structure are the existence of high internal stresses that is confirmed by the bending extinction contours observed inside of a grain body and the presence of extrinsic grain boundary defects of high density (until 1 nm^{-1}) (12).

X-ray analysis results show that X-ray patterns of the studied metals undergo essential changes during SPD. With increasing a strain value the broadening (Figure 2) and the fraction of the Lorenz component in the function, which describes a profile of X-ray peaks, increase. Changes in integral intensities and centroid positions of X-ray peaks, and a gradual growth of the diffusive background take place as well (13,14).

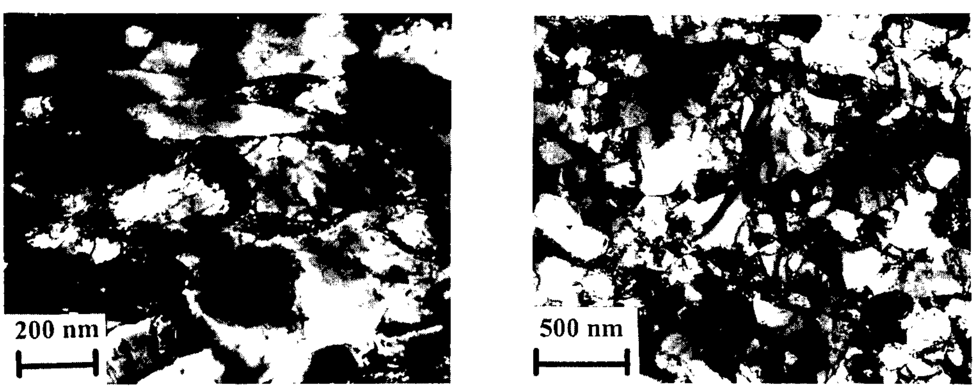

a b

Figure 1. A typical microstructure of pure Cu after SPD with $\gamma \approx 2$ (a) and $\gamma \approx 10$ (b).

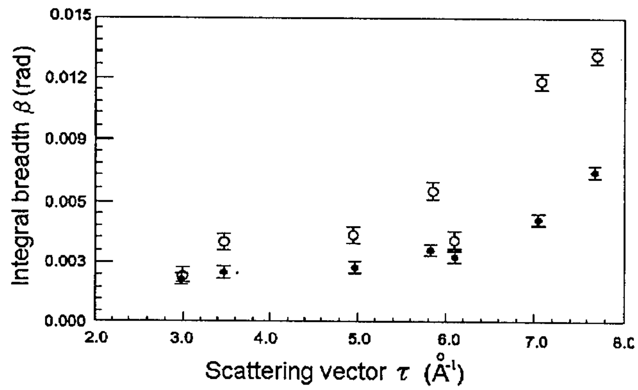

Figure 2. Dependence of an integral breadth of X-ray peaks β on a scattering vector τ for Cu: coarse-grained (•) and a nanostructured one (o).

The revealed changes in the profile of X-ray patterns reflect a decrease in a size of grains-crystallites, presence of elastic distortions in a crystal lattice, and also a change in the preferred grain orientations.

Interpretation of the obtained X-ray experimental results by means of computer simulation method allowed us to come to the conclusion that a typical view of X-ray peaks depends on both the ultrafine size of grains-crystallites and the specific defect structure of nanostructured metals produced by SPD techniques (15).

The X-ray studies also revealed elevated values of both static and dynamic atomic displacements, and decreased (until 22-23%) values of Debye temperature in nanostructured Cu and Ni (13,14).

DISCUSSION

The analysis of results of the conducted investigations in pure metals showed that an increase a SPD degree leads to a gradual transformation of the low angle cell structure to the equiaxed grain nanostructure with high angle grain boundaries. Similar results obtained at investigation of Fe (10) were interpreted by rearrangement and annihilation of dislocations having opposite signs. The excess dislocations of the same sign being concentrated at grain boundaries create long range stress fields resulting in enhanced atomic displacements. So, the obtained nanostructure is characterized both by the ultrafine grains and the specific defect structure. The process of nanostructured state formation in the case of shear deformation realization is completing at γ, close to 10, for the both considered techniques of SPD.

Recent investigations of work hardening in pure metals (6-9) subjected to large strains in stages IV ($\gamma \approx 1.5$) and V ($\gamma \approx 4$-5) show a sharp change in the deformation behavior. This change is caused by transformation of thick polarized dipolar walls to thin polarized tilt walls, consisting of edge dislocations. As a result, a misorientation angle between neighboring cells increases. Furthermore, high angle grain boundaries may be formed in structure.

During SPD at $\gamma > 5$ the evolution of structure continues. Due to that nanostructures having high angle grain boundaries and specific defect structure can be formed, and the high applied

pressure contributes to this (10).

The obtained results showed that the process of nanostructure formation during SPD is rather complex and its mechanisms require further investigations.

CONCLUSION

The provided experimental investigations testify that during SPD there occurs transformation of the low angle cell structure to the high angle grain one. This process results in formation of the nanostructured state. The obtained results are in conformity with modern ideas of structure evolution at large strains in stages IV and V, but require further development for SPD conducted at larger γ and high imposed pressures.

REFERENCES

1. Valiev, R.Z., Korznikov, A.V. and Mulyukov, R.R., *Mater. Sci. Eng.*, 1993, A168, 141.
2. *Ultrafine-grained materials prepared by severe plastic deformation*, ed. Valiev, R.Z., Annales de Chimie. Science des Materiaux, 1996, 21, 369.
3. Smirnova, N.A., Levit, V.I., Piljugin, V.I., Kuznetsov, R.I., Davydova, L.S. and Sazonova, V.A., *Phys. Met. Met.*, 1986, 61, 1170.
4. Rybin, V.V., *Large plastic deformations and fracture of metals,* Metallurgiya Publ., Moscow, 1986, p.279.
5. Sevillano, J.G., Aernoudt, E. *Mater. Sci. Engin.*, 1987, A86, 35.
6. Zehetbauer, M. and Seumer, V., *Acta Metall. Mater.*, 1993, 41, 577.
7. Zehetbauer, M., *Acta Metall. Mater.*, 1993, 41, 589.
8. Müller, M., Zehetbauer, M., Borbély, A. and Ungár, T., *Scr. Mater.*, 1996, 35, 1461.
9. Ungár, T. and Zehetbauer, M., *Scr. Metall. Mater.*, 1996, 35, 1467.
10. Valiev, R.Z., Ivanisenko, Yu.V., Rauch, E.F. and Baudelet, B., *Acta Metall. Mater.*, 1996, 44, 4705.
11. Mishin, O.V., Gertsman, V.Yu., Valiev, R.Z., and Gottstein, G., *Scr. Metall. Mater.*, 1996, 35, 873.
12. Valiev, R. Z. and Musalimov, R. Sh., *Phys. Met. Met.* 1994, 78, 666.
13. Zhang, K., Alexandrov, I.V., Valiev, R.Z. and Lu, K., *J. Appl. Phys.*, 1996, 21, 407.
14. Zhang, K., Alexandrov, I.V., Kilmametov, A.R., Valiev, R.Z. and Lu, K., *J. Phys. D: Appl. Phys.*, 1997, 30, 3008.
15. Alexandrov, I.V. and Valiev, R.Z., *Phil. Mag.*, 1996, B73, 861.

Pergamon

NanoStructured Materials, Vol. 12, pp. 713–718, 1999
Elsevier Science Ltd

0965-9773/99/\$–see front matter

PII S0965-9773(99)00224-X

THE NATURE OF FERROELECTRIC ORDER IN FINITE SYSTEMS

Pushan Ayyub, Soma Chattopadhyay, K. Sheshadri and Rangan Lahiri
Tata Institute of Fundamental Research, Homi Bhabha Road, Mumbai 400 005, India.

Abstract -- *The ferroelectric phase transition in the technologically important perovskite-type (ABO_3) systems is strongly affected by a reduction in the particle size below ≈ 100 nm. With decreasing size, there is a monotonic reduction in the T_C, and in the off-center displacement of the B-ion. Thus, there is a size-induced structural distortion that reverts the crystal to its high-symmetry paraelectric phase (which is normally stable only above T_C) even at room temperature. We briefly review our data on nanocrystalline ferroelectric $PbTiO_3$ and antiferroelectric $PbZrO_3$, and present a simple microscopic model for structural transitions in displacive ferroelectrics. We show that a competition between the elastic energy spent in displacing the central (B) ion and energy gain due to dipolar ordering, leads naturally to a first order transition from the paraelectric to the ferroelectric phase. The transition may occur either with decreasing temperature (for a fixed size) or with decreasing size (at a fixed temperature). The model is in good agreement with our data on nanocrystalline $PbTiO_3$.*

INTRODUCTION

A ferroelectric is a system which exhibits a spontaneous dielectric polarization (when $T<T_C$, the Curie temperature) that can be reversed by the application of an electric field. Conventionally, a ferroelectric is termed "displacive" when the elementary dipoles strictly vanish in the paraelectric phase, and "order-disorder" when they are non-vanishing but thermally average out to zero in the paraelectric phase. More rigorously, one may distinguish the two types of systems on the basis of the dynamics of their phase transition and the nature of the soft mode involved, whether propagating or diffusive (1).

Ferroelectrics and piezoelectrics have current and potential applications in sensors, nano-robotic and micro-electromechanical devices (2). Interest in these systems is growing rapidly because the high dielectric constant of a ferroelectric can be utilized in dynamic random access memories, whereas its capacity for being polarized in opposite directions makes it an attractive candidate for non-volatile random access memories. An important motivation for studying particle size effects in ferroelectrics is to determine the ultimate level to which a device based on such systems can be miniaturized. Also, from the point of view of basic physics, it is no less interesting to investigate size effects in systems showing long range, cooperative order.

In this paper, we briefly describe our experimental results on a typical ferroelectric ($PbTiO_3$) and a typical antiferroelectric ($PbZrO_3$). We then present a microscopic model which helps us to understand the nature of size-induced changes in displacive ferroelectrics. We have

selected $PbTiO_3$ as a test system, but the results should apply to other displacive systems as well. We also make certain predictions about order-disorder ferroelectrics, which appear to be consistent with the data available for such systems. In the present work, we restrict ourselves to the description of quasi-free ferroelectric nanoparticles. The system is assumed to consist of loosely aggregated, un-clamped particles which are not electrically isolated. Under these conditions, we can ignore the effects of external strain and depolarization.

The experimental study of size effects in ferroelectrics has a long history (3,4), but it has gained momentum in recent years due to the development of advanced synthetic techniques. Using the phenomenological Landau-Devonshire theory, Zhong *et al.* (5) have shown that the ferroelectric T_C should decrease with decreasing size, ultimately leading to a ferroelectric to paraelectric phase transition. This agrees with the observed size dependence of the T_C in sub-micron $PbTiO_3$ particles from measurements of the specific heat (6) and Raman mode-softening (7). Similar results were also obtained for $BaTiO_3$ (8). Shih *et al.* (9) have considered the effect of incorporating the depolarization energy in the Landau free energy density.

EXPERIMENTAL RESULTS

Phase-pure ultrafine particles of $PbTiO_3$ and $PbZrO_3$ with different average size (between 20-200 nm) were synthesized using wet chemical techniques such as co-precipitation and sol-gel. The coherently diffracting domain size (d_{XRD}) was calculated from a line shape analysis of the (111) x-ray diffraction (XRD) peak using the Scherrer equation. The equivalent spherical diameter of the particles was determined from the specific surface area measured by the gas adsorption (BET) method. The size, shape and size distribution were also studied from scanning electron micrographs. However, since ferroelectric phenomena in perovskites and other *displacive* systems are controlled by lattice vibrational mechanisms, we expect that of the three "sizes" measured by us, the one most relevant to the problem is d_{XRD}. So, all further references to "particle size" should be taken to imply d_{XRD}.

To obtain a complete and consistent understanding, the phase transition in the small solid ensemble was studied by three complementary techniques: measurement of the dielectric response vs. temperature, measurement of the temperature dependence of the tetragonal or ferroelectric distortion (c/a), and differential scanning calorimetry (DSC). XRD measurements were also made at temperatures down to 15 K to confirm that the large change observed in c/a at room temperature is an inherent particle size effect.

Size Effects in Ferroelectric $PbTiO_3$

The classical displacive ferroelectric $PbTiO_3$ has excellent dielectric, pyroelectric and piezoelectric properties. In the ferroelectric phase, it has a tetragonal perovskite structure (a = 0.3899 nm, c = 0.4153 nm, c/a = 1.065) at room temperature, and transforms to a cubic paraelectric phase ($a = c$ = 0.396 nm) above T_C = 763K.

Figure 1 shows the variation of the tetragonal distortion ($c/a - 1$) with particle size at room temperature. The dimensions of the unit cell do not change down to ≈ 150 nm, below which c decreases and a increases with decreasing size. The resulting reduction in the

tetragonal distortion is especially rapid below ≈ 60 nm. On extrapolating the data, we find that $c/a \rightarrow 1$, as $d_{XRD} \rightarrow 7$ nm, *i.e.*, ferroelectric order cannot be sustained below this critical size. The dielectric, thermal and structural (variable temperature XRD) data all indicate that the ferroelectric T_C decreases monotonically with decreasing particle size (10).

The observed decrease in the tetragonal distortion with a reduction in particle size appears to be a manifestation of a more general phenomenon. Earlier studies have shown that in a large number of partially covalent oxides, the crystal lattice tends to transform into a structure of higher symmetry when the particle size becomes smaller (11). In certain systems (e.g., Fe_2O_3 and Al_2O_3), the size-induced distortion is large enough to actually produce a crystallographic transition to a high-symmetry structure (12). In others (such as in the present case), there may be a gradual reduction in an asymmetry parameter ($c/a - 1$) with decreasing size. There is also a marked broadening of the transition peak (in dielectric and thermal measurements) below 60nm, and an increasing deviation from the usual Curie-Weiss Law, both of which can be explained in terms of a diffuse phase transition model (10).

Size Effects in Antiferroelectric $PbZrO_3$

$PbZrO_3$ is orthorhombic at 300K (a = 0.824 nm, b = 1.176 nm, c = 0.588 nm) with eight formula units per crystallographic unit cell. This structure is derived from a cubic perovskite prototype (the high-temperature paraelectric phase) by *antiparallel* displacements of the Pb ions along one of the original [110] directions - which becomes the a-axis of the orthorhombic phase. If the displacements of the Pb ions are ignored (so as to compare the unit cells of the paraelectric and the ferroelectric phases), we obtain a pseudo-tetragonal unit cell in the ordered phase, whose lattice constants (a_T, c_T) are related to the real orthorhombic unit cell (a, b, c) through: $a_T = a/\sqrt{2}$, and $c_T = c/2$. $PbZrO_3$ shows a strong dielectric anomaly at $T_C \approx 500$K.

Figure 2 shows the variation of pseudo-tetragonal distortion (c_T/a_T) with particle size. The crystallographic unit cell remains relatively undistorted down to ≈ 100 nm, below which there is an increasing tendency for it to attain the cubic structure. This behavior of antiferroelectric $PbZrO_3$ is very similar to that of the ferroelectrics $PbTiO_3$ and $BaTiO_3$. Extrapolation from our data implies that the crystal structure would become perfectly cubic below a size of 23 nm (13). The monotonic reduction in the T_C with decreasing particle size is shown in the inset.

Size Effects in Order-Disorder Ferroelectrics

While nanoparticles of *displacive* systems such as $PbZrO_3$ and $PbTiO_3$ were found to show certain essential similarities, their behavior differs from that of a typical *order-disorder* system such as $NaNO_2$ (14). In the latter case, very little change in T_C is observed down to 5 nm, whereas displacive systems start showing deviations in the T_C at sizes as large as 100 nm. This clearly underscores the importance of the size-induced *structural distortions* in the nanoparticles of the displacive systems. The other obvious difference in the two types of system is that the thermal (as well as dielectric) phase transition is not at all observed in nanoparticles of displacive systems with a size below ≈ 25 nm, while even 5 nm $NaNO_2$ nanoparticles exhibit a clear transition peak.

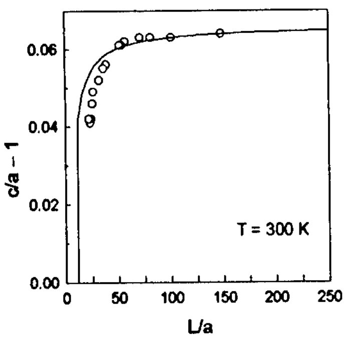

Fig.1. The tetragonal distortion ($c/a - 1$) In $PbTiO_3$ plotted as a function of the reduced system size (L = particle size, a = lattice constant) at 300K. The solid line represents a fit with the theory.

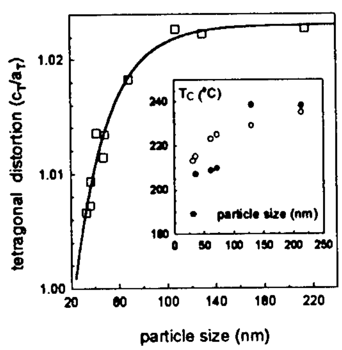

Fig.2. Size dependence of the tetragonal distortion in $PbZrO_3$ at 300K. The solid line is an empirical fit. Inset shows the variation in T_C with size (filled dots - DSC data, open dots - dielectric data).

SIZE EFFECTS IN FERROELECTRICS: A SIMPLE MICROSCOPIC MODEL

Evidently, a decrease in the size of a displacive ferroelectric or antiferroelectric system (of the type ABO_3) is accompanied by a monotonic decrease in the ferroelectric T_C, the temperature at which the high symmetry paraelectric structure transforms to a low symmetry phase in which the B ions no longer occupy the centrosymmetric positions in the BO_6 octahedra. If the particle size is made sufficiently small, the ferroelectric system reverts to the paraelectric phase, however low the temperature. Thus, our experimental results suggest that the ferroelectric to paraelectric transition can be made to occur as a function of increasing temperature or decreasing size. We now present a simple microscopic model which naturally leads to a size-induced structural phase transition of the first order.

The displacement of the centrosymmetric B-ion to an off-centric position at the ferroelectric T_C, is accompanied by a distortion in the cubic (paraelectric) unit cell to one of lower symmetry, e.g., a tetragonal one with sides $a \times a \times c$. The experimentally measured tetragonal distortion ($c/a - 1$) scales with the order parameter. Obviously, the displacement (d) of each such ion requires some energy, and the system would undergo a ferrodistortive transition only when it gains a *larger* amount of energy from the interaction of the resulting dipoles, aligned in some particular fashion.

The dipolar interaction energy, $\sim Jzd^2$, of the stable ordered phase, should be comparable to kT, where z is the coordination number. Therefore, the displacement (d) should be at least $\sqrt{(kT/Jz)}$, for dipolar alignment to occur. This argument immediately implies that it is possible to drive the transition by varying either the temperature, or the system size (which controls the

average value of z). Thus, our model describes the temperature-driven transition in the bulk, as well as the size-driven transition in finite systems.

We describe phenomenologically the interaction energy between the nearest neighbour dipoles by $\sim J d_i d_j \alpha_i \alpha_j$, where $\alpha = \pm 1$ is an Ising variable, which accounts for the fact that the central ion can be displaced in two opposite directions. J is positive for ferroelectrics and negative for antiferroelectrics. The effective Hamiltonian for the problem is thus the sum of an elastic part and an Ising part. From symmetry considerations, we obtain:

$$H = \sum_i \left(\frac{1}{2}\lambda_2 d_i^2 + \frac{1}{4}\lambda_4 d_i^4\right) - J\sum_{i,j} d_i d_j \alpha_i \alpha_j \qquad [1]$$

This Hamiltonian is solved by treating the Ising variable via an inhomogeneous mean-field theory (IMFT) and the displacement variable within a saddle point approximation. To bring out the difference between sites in the bulk and those near the surface of the finite system, the IMFT is carried out with *open* boundary conditions to study the size-driven transition and *periodic* boundary conditions to obtain the bulk transition. Finally, we obtain the free energy density in the form: $F(d) = E(d) + I(d)$, where the elastic part, $E(d)$, is given by:

$$E(d) = \frac{1}{2}\lambda_2 d^2 + \frac{1}{4}\lambda_4 d^4 \qquad [2]$$

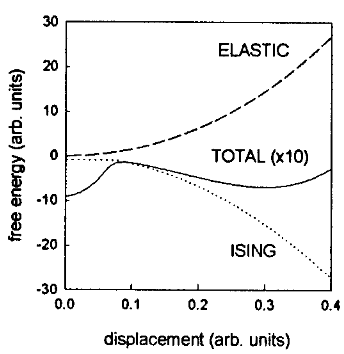

Fig.3. A schematic view of the nature of the different contributions (elastic energy and Ising energy) to the free energy. Note that the total energy has two minima.

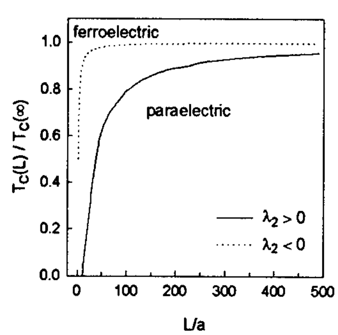

Fig.4. Ferroelectric phase diagram (temperature-size) predicted by our model. The solid and dotted lines represent displacive and order-disorder systems, respectively.

and the Ising part, $I(d)$, is given by:

$$I(d) = \frac{1}{2} Jzm^2 d^2 - T \ln 2 \cosh(\frac{Jzmd^2}{kT}) \qquad [3]$$

Here m ≡ <α> = tanh (Jzd^2m/T). The saddle point values of d, obtained by minimizing $F(d)$, are $d = 0$ and $d = d_0 = \sqrt{[(Jzm^2 - \lambda_2)/\lambda_4]}$. The nature of the variations of $E(d)$ and $I(d)$, and the presence of the two minima in $F(d)$ are shown schematically in Fig.3. Clearly, it is this two-minima structure of the free energy that is responsible for the first order ferroelectric ($d = d_0$) to paraelectric ($d = 0$) transition.

The model parameters (λ_2, λ_4, and J) were determined, in the case of $PbTiO_3$, from our experimental data. The phase diagram of the system (in the temperature-size plane) may now be plotted (Fig.4) by calculating $d_0(T)$ for each L from $d_0 = \sqrt{[(Jz(L)m^2 - \lambda_2)/\lambda_4]}$. The phase boundary for displacive systems (λ_2>0, solid line) represents first order transitions for all T>0. Thus, our theory predicts a suppression in T_C with reducing size. In systems with $\lambda_2 < 0$ (which usually describes order-disorder ferroelectrics), size effects are greatly suppressed, as shown by the dotted curve in Fig.4. One would require to study very small particles at temperatures close to T_C, to observe such effects. This is also in agreement with experimental observations. Thus, the observed size effects in ferroelectrics appear mainly to arise from a lower average coordination number for the atoms close to the surface of a nanoparticle.

References

1. Lines, M. E. and Glass, A. M., *Principles and Applications of Ferroelectrics and Related Materials*, Clarendon Press, Oxford, 1977, p. 10.
2. Francombe, M. H., in *Physics of Thin Films: Mechanic and Dielectric Properties*, eds Francombe, M. H. and Vossen, J. L., Academic, San Diego, 1993, pp. 225-300.
3. Anliker, M., Brugger, H. R. and Känzig, W., *Helv. Phys. Acta*, 1954, 27, 99.
4. Känzig, W., *Phys. Rev.*, 1955, 98, 549.
5. Zhong, W. L., Wang, Y. G., Zhang, P. L. and Qu, B. D., *Phys. Rev. B*, 1994, 50, 698.
6. Zhong, W. L., Jiang, B., Zhang, P. L., Ma, J. M., Cheng, H. M., Yang, Z. H. and Li, L. X. *J. Phys.: Condens. Matter*, 1993, 5, 2619.
7. Ishikawa, K., Yoshikawa, K. and Okada, N., *Phys. Rev. B*, 1988, 37, 5852.
8. Uchino, K., Sadanaga, E. and Hirose, T. *J. Am Ceram. Soc.*, 1989, 72, 1555.
9. Shih, W. Y., Shih. W-H. and Aksay, I. A., *Phys. Rev. B*, 1994, 50, 15575.
10. Chattopadhyay,S., Ayyub,P., Palkar,V.R. and Multani,M.S., *Phys. Rev. B*, 1995, 52, 13177.
11. Ayyub, P., in *Frontiers in Materials Modelling and Design*, eds. Kumar, V., Sengupta, S. and Raj, B., Springer Verlag, Heidelberg, 1997.
12. Ayyub, P., Palkar, V. R., Chattopadhyay, S. and Multani, M. S., *Phys. Rev. B*, 1995, 51, 6135.
13. Chattopadhyay, S., Ayyub, P., Palkar, V.R., Gurjar, A.V., Wankar, R.M. and Multani M.S., *J. Phys.: Condensed Matter*, 1997, 9, 8135.
14. Marquardt, P. and Gleiter, H., *Phys. Rev. Lett.*, 1982, 48, 1423.

Pergamon

NanoStructured Materials, Vol. 12, pp. 719–724, 1999
Elsevier Science Ltd

0965-9773/99/$–see front matter

PII S0965-9773(99)00225-1

HEAVY-FERMION BEHAVIOR IN $CeAl_2$ NANOPARTICLES

Y. Y. Chen[1], Y.D. Yao[1,2], T.K. Lee[1], W.C. Liu[1], H.C. Chang[1], K.Y. Lin[2], Y.S. Lin[2], Z.C. Wang[3] and W. H. Li[3]

1 Institute of Physics, Academia Sinica, Taipei, Taiwan, ROC
2 Department of Physics, Fu-Jen University, Taipei, Taiwan, ROC
3 Department of Physics, National Central University, Taiwan, ROC

Abstract--*In order to examine the quantum size effects on the heavy-fermion behavior in $CeAl_2$, we have performed measurements of the low-temperature specific heats for $CeAl_2$ nanoparticles with average particle size 80Å for temperature down to 80mK. For 80Å - nanoparticles the magnitude of γ of $CeAl_2$ can be as high as 3600mJ/ K^2 f.u. at T=80mK with $T_K \approx 0.65K$. Compared with the sharp anti-ferromagnetic order (T_N=3.8K) in bulk $CeAl_2$ only a blurred peak at same temperatures is observed in $CeAl_2$ nanoparticles. Due to the suppression of the long-range magnetic order by the limited geometric size and the less degeneracy of the density of states of conduction electrons $D(\varepsilon_F)$ the enhanced heavy-fermion behavior (in terms of γ) and the disappearance of magnetic order in $CeAl_2$ nanoparticles are attributed to the quantum size effects in nanoparticles. ©1999 Acta Metallurgica Inc.*

INTRODUCTION

About two decades ago nanoparticles were widely studied by scientists and mechanical engineers mostly for the reason of their general physical properties and engineering applications (1-4). Lately due to more interesting basic physical properties found in nanoparticles, such as the quantum size effects, the research on nanoparticles again becomes an important field (5-7). There is no doubt that the physical properties of nanoparticles can be affected directly by the confinement of limited geometric sizes. In this report these quantum size effects on magnetic interactions, such as crystal field effect, RKKY interaction and Kondo behavior were examined by thermodynamic measurements on bulk $CeAl_2$ and 80Å-$CeAl_2$ nanoparticles.

EXPERIMENTAL DETAILS

$CeAl_2$ nanoparticles were fabricated on a liquid-nitrogen-cooled cold trap by thermal evaporation of bulk $CeAl_2$ in He atmosphere (99.99%) of 0.1 torr. The structures and phase purities of bulk $CeAl_2$ and nanoparticles were examined by powder X-ray diffraction in Fig. 1.

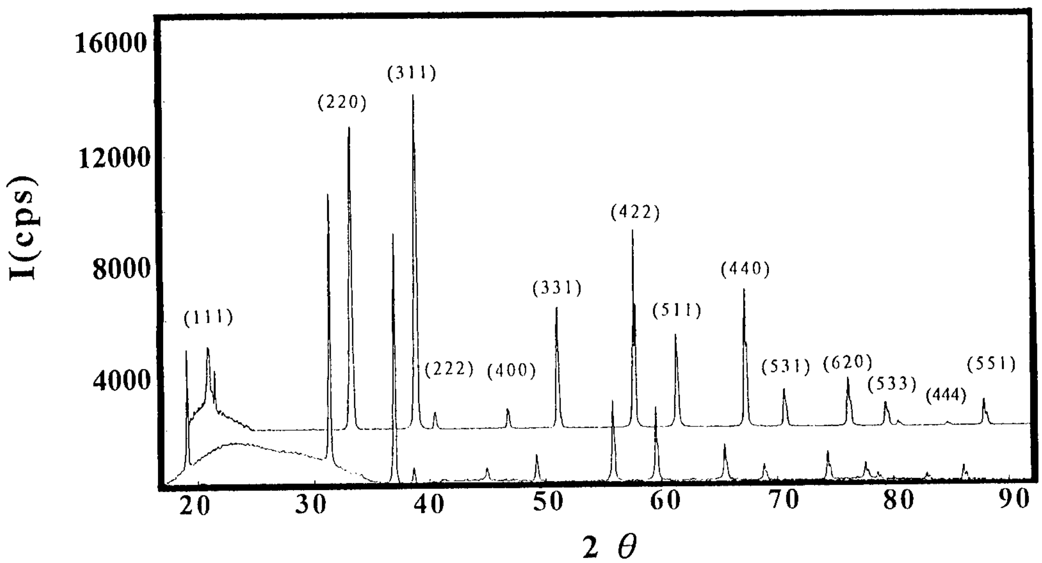

Fig. 1 The X-ray diffraction spectra of 80Å-$CeAl_2$ nanoparticles (bottom) and bulk $CeAl_2$ (top). The top one is slightly shifted to right for easy observation. The broad peaks seen at $2\theta \approx 22°$ and at 45° are from the grease used in sample attachment.

In bulk $CeAl_2$ the single phase of cubic Laves structure with lattice constant a= 8.06Å is determined and is consistent with that of early reports (8); in 80Å-$CeAl_2$ the X-ray diffraction shows the same structure as that of the bulk except a slight (≈0.37%) lattice expansion with a= 8.09Å. No second phase is detected for either specimen. A couple of different batches of 80Å-$CeAl_2$ were prepared, some of them showed no visible Ce oxidation (Fig. 1) whereas some ones did show minor CeO_2 phase (main diffraction peak at 2θ =28.56° for Cu Kα line). Although all the measurements in the report were done on our best quality specimens in Fig. 1, but due to the limitation of X-ray diffraction resolution it is possible that a very light layer of Ce oxidation especially on surface of nanoparticle is not detected.

The 80Å of average diameter of $CeAl_2$ nanoparticles was calculated from the distribution of particle sizes obtained by transmission electron microscopy (TEM). For specific heat measurements an assemble of $CeAl_2$ nanoparticles was collected and was very lightly pressed into a pellet with a pressure much less than the strength that can possibly transform $CeAl_2$ nanoparticles into a bulk. After being pressed no visible change on the color of nanoparticles is observed and the density of the pellet is estimated about 10-15% of the bulk by re-melting a pellet of nanoparticles into a bulk. The measurements of specific heat were performed using a thermal-relaxation micro-calorimeter which was described in an early report (9).

RESULTS AND ANALYSIS

The specific heat C(T) for bulk $CeAl_2$ is plotted as C/T versus T in Fig. 2. In bulk $CeAl_2$

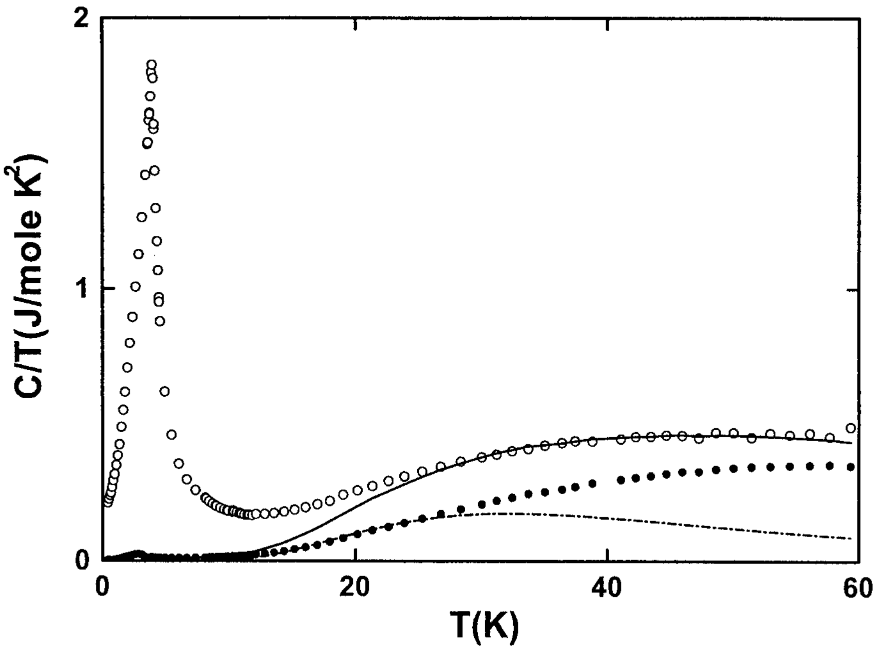

Fig. 2 The specific heat data, plotted as C/T versus T, for bulk $CeAl_2$ (open circles) and $LaAl_2$ (closed circles). The specific heat of $LaAl_2$ represents the contribution of lattice phonons. The peak at 3.2K in $LaAl_2$ corresponds to a superconducting transition. The dot-dashed line represents the theoretical specific heat due to the crystal field with T_{CF}= 110 K. The solid line is the sum of contributions of lattice phonons and the crystal field.

an anti-ferromagnetic order peaked at 3.8K is observed and a broad maximum centered at 35K over the background of lattice phonons is attributed to the contribution of a crystal field. Since for temperatures below T_N the anti-ferromagnetic specific heat is proportional to T^3, the low-temperature specific heat is fit to equation $C = \gamma T + a T^3$ with a value of $\gamma \approx$150mJ/ mole K^2. The magnitude of γ is only about one sixth of the single ion value 900 mJ/ mole K^2 calculated from equation ($T_0 = \pi R/6\gamma$, T_K=1.29 T_0) for Kondo temperature T_K=5K (10). An explanation for this observation was given by C.D. Bredl etc (10) who asserted that only a small fraction of the conduction band states is involved in the Kondo effect and works on weakening of the magnetic moments. We account for the specific heat of bulk $CeAl_2$ by the contributions of lattice phonons C_{ph}, magnetic correlation C_m and crystal field C_{cry}(the six-fold degeneracy of Ce^{3+} with J=5/2 splits into a quartet Γ_8 and a doublet Γ_7 in the cubic symmetry). To estimate the contribution of specific heat of lattice phonons, an iso-structure non-magnetic $LaAl_2$ is measured and shown as closed circles in Fig.2. After the subtraction of lattice phonons the specific heat of $CeAl_2$ fits well to that of a magnetic contribution C_m and a crystal field C_{cry} with T_{CF} =110K. The entropy integrated from C_m reaches Rln2 at T=17K. The specific heat C(T) for 80Å-$CeAl_2$ is plotted as C/T versus T in Fig. 3. In nanoparticles the sharp anti-ferromagnetic transition peak seen in $CeAl_2$ bulk is no longer observed, instead only a small blurred bump is found at same temperature region. An observation of a linear term with

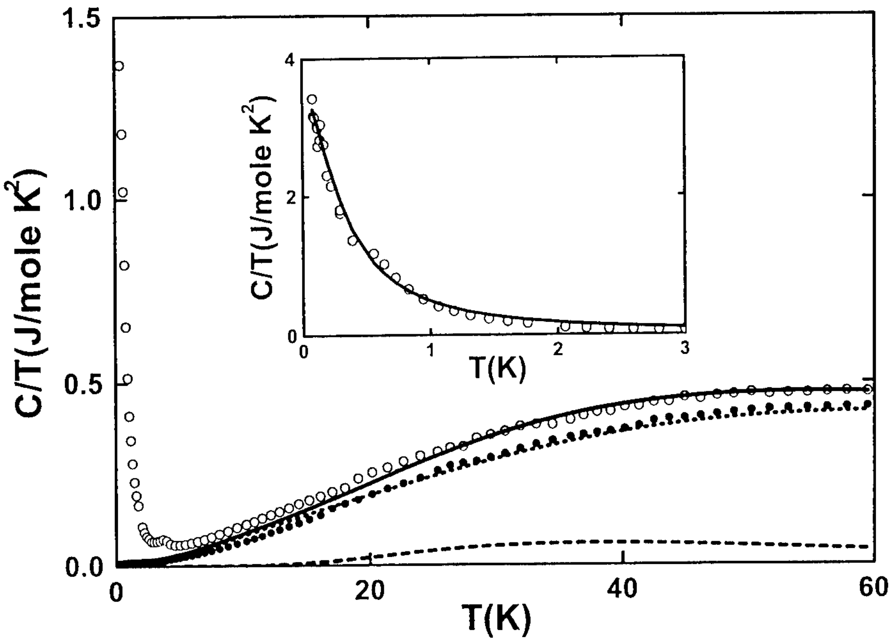

Fig. 3 The specific heat data, plotted as C/T versus T for 80Å-$CeAl_2$ nanoparticles (open circles) and 80Å-$LaAl_2$ (closed circles). The dotted line represents the specific heat of lattice phonons calculated for 80Å-$CeAl_2$ and the dashed line represents the 40% of specific heat of crystal field with T_{CF} = 130K. The solid line is the sum of all above various contributions. In inset the low temperature region is shown and the solid line is the fit for a 40% specific heat of Kondo anomaly with T_K = 0.65K.

a value of γ as high as 3600mJ/ mole K^2 as $T \rightarrow 0$ indicates a characteristic Fermi-liquid behavior (see inset in Fig. 3). This γ is about twenty-four times of its bulk value ($\approx$150mJ/ mole K^2). The small blurred bump at 3.8K (with an equivalent entropy about $\approx$1.5% of Rln2) is due to a residual anti-ferromagnetic transition as seen in the bulk as the long-range RKKY interaction is suppressed by the limited geometric size and the smaller $D(\varepsilon_F)$. After the subtraction of lattice phonons taken from 80Å-$LaAl_2$, the specific heat at high temperatures fits to a 40% of the contribution of crystal field with T_{CF}= 130K, while the specific heat at low temperatures fits to a 40% of Kondo anomaly with T_K = 0.65K. The smaller Kondo temperature $T_K \approx \varepsilon_F \exp(-1/JD(\varepsilon_F))$ of nanoparticles in comparison to 5K of the bulk is conceptually acceptable if nanoparticle exhibits a smaller value of $D(\varepsilon_F)$ owing to the electronic quantum size effect. Using the model treating small particles by Baltes and Hilf (9,11) a theoretical calculation for lattice phonon of 80Å-$LaAl_2$ is shown as dotted line in Fig. 3. The calculated result with sound velocity v=1950 m/s (corresponding to a Debye temperature θ_D= 212K) fits well to the experimental data of 80Å-$LaAl_2$. The smaller value of Debye temperature θ_D =212K of lattice phonon as compared to 325K of the bulk is due to the phonon softening in nanoparticles. Since the crystal field is very dependent on the inter-distance of Ce ions, the 20% increase of crystal field might be related to the 0.37% of lattice expansion in nanoparticles. This consequence is qualitatively consistent with the earlier pressurized resistivity

measurements of $CeAl_2$ made by M. Nicoas-Francillon etc. (8) in which the crystal field indeed decreases with the lattice compression by external pressures. Although the value of γ is as large as 3600mJ/ mole K^2 for $T \rightarrow 0$, it is only about 40% of 9000mJ/ mole K^2 of the theoretical value for T_K=0.65K expected by the model of V.T. Rajain (12). The magnitude of entropy integrated from the Kondo anomaly C_m is about 40% of Rln2. The reduced γ and entropy reflect the possibility that there are only 40% magnetic Ce ions left in 80Å-$CeAl_2$ nanoparticles and the rest of 60% of Ce ions are non-magnetic. The possible existence of non-magnetic Ce in the form of CeO_2 can account 5-10% non-magnetic Ce ions. Since the surface ions in nanoparticle occupy a large fraction of its volume, and usually have different magnetic behavior from that of core ions, this might account for the rest of the loss of magnetic Ce ions.

CONCLUSION

We have found a very large value of γ in 80Å-$CeAl_2$ nanoparticles and observed the quantum size effects in affecting the physical properties of heavy fermion compound. The linear coefficient of specific heat γ increases from 150mJ/ mole K^2 for the bulk material to a magnitude as large as 3600mJ/ mole K^2 for $T \rightarrow 0$ in 80Å-$CeAl_2$ nanoparticles. It is shown that the existing heavy-fermion behavior is revealed after the suppression of the long-range RKKY interaction. In addition to the 40% of crystal field fit to the high-temperature specific heat, the magnitude of the entropy below the Kondo anomaly is only about 40% of the theoretical value of Rln2; indicating the loss of 60% of magnetic Ce ions presumably on the surfaces of nanoparticles. The smaller T_K in nanoparticles as compared to 5K of the bulk is qualitatively acceptable owing to a smaller value of $D(\varepsilon_F)$ in nanoparticles. A conclusion is made that $CeAl_2$ can become a heavy fermion compound if its magnetic order can be suppressed properly by the quantum size effects.

ACKNOWLEDGMENTS

We would like to thank Professor J.C. Ho and Jon Lawrence for their very helpful discussions and continuing interest and support for our work. Professor H.M. Lin for helping determine the size of nanoparticles by TEM. This work was supported by the National Council of the Republic of China under Grants No. NSC87-2732-M-001-007.

REFERENCES

1 H.E. Schaefer and R. Wurschum, Phys. Lett. A 119, 370 (1987).
2 J. Rupp and R. Birringer, Phys.Rev. B 36, 7888 (1987).
3 X. .Zhu, R. Birringer, U. Herr, and H.Glecter, Phys. Rev. B 35, 9085 (1987).
4 R. F. Marzke and W.S. Glaunsinger, Solid State Commun. 18, 1025 (1976).
5 W. . Halperin, Rev. Mod. Phys. 58, 533 (1986).
6 Y. Y. Chen, Y.D. Yao, S.H. Lin, W.J. Cheng, H.M. Lin and C.Y. Tung,

Proceedingofthe21[st]International Conference on Low Temperature Physics, 2369 (1996).
7 Y. Volokitin, J. Sinzig, L.J. de Jongh, G. Schmid, M.N. Vargaftik, I.I. Moiseev, Nature 384, 621 (1996)
8 M.Nicolas-Francillon, A. Percheron, J.C. Achard, O.Gorochov, B. Cornut , D.Jerome and B.Coqblin, Solid State Commun. 11, 845 (1972).
9 Y..Y. Chen, Y.D. Yao, S.S. Hsiao, S.U. Jen, B.T. Lin, H.M. Lin and C.Y. Tung, Phys. Rev. B 52, 9364 (1995).
10 C. D. Bredl, F.Steglich and K.D. Schotte, Z. Physick B 29, 327 (1978).
11 G. .H. Comsa, D. Heitkamp and H.S. Rade, Solid State Commun. 24, 547 (1977).
12 V.T. Rajan, Phys.Rev. Lett. 51, 309 (1983).

Pergamon

NanoStructured Materials, Vol. 12, pp. 725–730, 1999
Elsevier Science Ltd

0965-9773/99/$–see front matter

PII S0965-9773(99)00226-3

OPTICAL PROPERTIES OF SQUARE LATTICES OF GOLD NANOPARTICLES

G.A. Niklasson*, P.A. Bobbert# and H.G. Craighead§
*Department of Materials Science, The Ångström Laboratory, Uppsala University, P.O. Box 534, S-75121 Uppsala, Sweden
#Department of Applied Physics, Eindhoven University of Technology, P.O. Box 513, NL-5600 MB Eindhoven, The Netherlands
§ School of Applied and Engineering Physics, Cornell University, Ithaca, NY 14853, U.S.A.

Abstract--*We reanalyse optical measurements on two-dimensional lattices of ultrafine gold particles, produced by electron beam lithography. The spectra exhibit a distinct absorption peak due to the localized plasma resonance of the conduction electrons in the particles. The theoretical modeling used rigorous solutions, in the long-wavelength limit, for the polarizability of oblate spheroids and truncated spheres on a substrate. The dipole-dipole interactions between the particles in the square lattice were taken into account. We find good agreement between experimental and theoretical absorption peak positions for the case of oblate spheroids, but not for truncated spheres. Peak widths and minimum transmittances also show satisfactory agreement with theory. ©1999 Acta Metallurgica Inc.*

INTRODUCTION

The optical properties of discontinuous metal films has been an active research field for a long time (1). Because of the disordered arrangement of the metal particles on the substrate surface, rigorous comparisons between theory and experiments have been difficult to carry out. The use of lithographic techniques for producing regular arrays of small metal particles on a substrate gives a system that is easier to describe theoretically. In 1984, two of us presented results of optical transmittance measurements on square lattices of gold particles with diameters in the range from 13 to 35 nm, with a lattice constant of 50 nm (2,3). For these small sizes, the optical absorption is dominated by the dipolar contribution. Later studies on lithographically produced arrays of metal particles have mainly employed larger particles (4-6). In some of these works the quadrupolar absorption peak was observed (5,6). Recently, Gotschy et al. (7) have produced arrays of particles with sizes as small as 40 nm, approaching our earlier work. They show that the absorption peak wavelength and its width may be tailored by varying particle size and separation. This may be of considerable interest for optical applications (7). However, a rigorous comparison of theory and optical experiments for the case of two-dimensional arrays of metallic nanoparticles appears not to have been carried out.

In this paper we reanalyse our previous measurements and compare them to a rigorous theory for the optical response of small metal particles on a surface, developed by

Vlieger and co-workers (8-11). In order to get a good agreement with experiment, it is of vital importance to take into account the multipolar interactions of the particles and their images in the substrate.

EXPERIMENTS

We first briefly review our previous experiments. The samples were produced by electron-beam lithography carried out in a Philips 400T electron microscope interfaced to a computer for pattern generation. We used 3 mm diameter sapphire discs as substrates. They were first coated with a thin (≈60 nm) layer of polymethylmethacrylate (PMMA), which was deposited from solution by spinning and subsequently baked. To prevent charging during electron-beam writing, the PMMA was coated by about 10 nm aluminium. The pattern was defined by exposing certain areas of the resist to the electron beam. The exposure time was of the order of 1 msec per point. The largest area that could be written without translating the sample was 15 x 15 μm. We produced several 15 x 15 μm arrays on the same substrate, but with different exposure times, thereby varying the particle sizes. After beam writing, the exposed areas were removed in a cellosolve-methanol solution. Subsequently, the sample was transferred to an evaporation system and gold was deposited from an electron beam source. Finally, the remaining resist was dissolved in an acetone bath, leaving small gold particles in the exposed areas. In order to obtain a more uniform and more rounded particle shape, the samples were subjected to a mild anneal at around 400 K for a few minutes. Our samples had a lattice constant of 50 nm.

The particles in the samples were characterized by scanning electron microscopy using secondary electron imaging. To avoid charging, a thin carbon film was evaporated onto the sample. Figure 1 shows an electron micrograph of an array of gold particles. It is seen that the particles have an approximately circular cross section, when viewed from the normal direction. The lattices are very regular with few vacancies, typically 3 percent. The spot size used in the electron microscopy investigations was nominally 5 nm. It is clear that particle sizes can be overestimated on the micrographs, because of signal from beam spots impinging close to the edges of the particles. Therefore we estimate the real particle sizes as the measured ones minus half the spot size, i.e. $d = d_{meas} - 2.5 \pm 2.5$ nm. In order to obtain information on the three-dimensional shape of the particles, we performed electron microscopy at a tilt angle of 60 degrees (2). The particles appear to be flattened. By modeling the particles as oblate spheroids, we obtained ratios between the major and minor axes in the range of 1.5±0.2 (2). The analysis is difficult, though, being based on small differences near the limit of resolution. We have prepared samples with very uniform particle sizes. The estimated values of d are the major axes of the particles; they were in the range 13 nm to 35 nm. The size distribution displayed a geometric standard deviation of only 1.10 to 1.15 .

The optical measurements were carried out in a conventional optical microscope. A small aperture was focussed onto the sample so that light from a tungsten lamp source was incident only on a portion of the particle array. The light transmitted through the sample was collected by an optical fiber bundle positioned under the microscope stage, and then transferred to a grating spectrometer and an optical multichannel analyzer. The transmittance signal from the particle array was recorded in the wavelength range 400 nm to 750 nm. After recording each spectrum, a reference measurement was performed on an area of bare sapphire substrate close to the sample array. Uncertainties arise from the instability of the lamp and problems associated with focussing on the sample and reference areas. We estimate the absolute level of transmittance to be accurate within ±0.02, with relative errors in a spectrum much smaller.

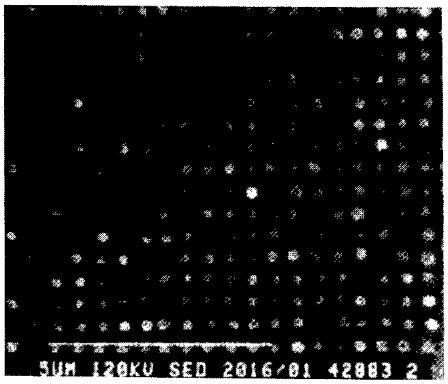

Fig. 1. Electron micrograph of a gold particle array with a lattice constant of 50 nm. The bar denotes 500 nm.

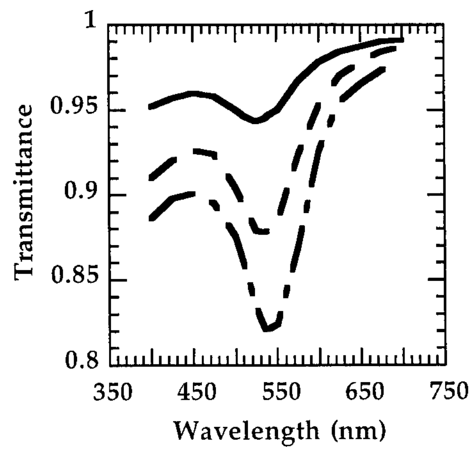

Fig. 2. Measured transmittance of three gold particle arrays. The particle major axes were 22 (full curve), 26 (dashed curve) and 28 nm (dash-dotted curve).

In figure 2 we present the effect of particle size on the transmittance for three samples. The main feature of the spectra is the localized plasmon absorption peak (1) centered at a wavelength of 525 nm to 540 nm. The transmittance decreases and the minimum is shifted towards longer wavelengths as the particle size increases.

THEORY

The polarisability of a free ellipsoid much smaller than the wavelength, can in the case of an electric field in direction j, be written as (1)

$$\alpha_j = (V\varepsilon_m/4\pi)\ [\ (\varepsilon-\varepsilon_m)\ /\ (L_j\varepsilon+(1-L_j)\varepsilon_m)] \qquad [1]$$

where V is the volume of the ellipsoid, ε and ε_m are the dielectric functions of the ellipsoid and the ambient, respectively, and L_j is the depolarization factor. A triplet of depolarisation factors describe the shape of the ellipsoid, and their sum is unity. For a sphere L=1/3. Eq. [1] gives rise to an absorption peak when $\varepsilon = (1\text{-}1/L_j)\ \varepsilon_m$. The simple expression above is modified by two effects in the case of an array of particles on a substrate. They are the interactions between a particle and its image in the substrate, and the interactions between the particles (with associated images) in the array. In a simplified picture, the interaction terms can be written as additional contributions to an "effective" depolarisation factor (12). The most important effect is a shift of the localized plasmon absorption peak.

The first effect is treated by the general theory of Vlieger et al. (9-11), for particles much smaller than the wavelength, and situated at a surface. The particle-substrate problem has been solved for the cases of truncated spheres (9,10) and oblate and prolate spheroids (11). A homogeneous electric field is incident from the ambient medium. In the quasistatic limit,

the Laplace equation has to be solved in the ambient, in the substrate, in the particle and in the image region in the substrate. In the case of the truncated sphere, the electrical potential is expanded into multipoles located at the centre of the sphere and image multipoles at the image of the centre with respect to the substrate surface. The use of multipoles makes it easy to satisfy the boundary conditions at the spherical surface, which lead to an infinite set of linear inhomogeneous equations for the multipole coefficients. A technique for solving these equations is given in ref. (9,10). One takes into account the N first equations to obtain the N first multipole coefficients. Subsequently the polarizabilities are calculated numerically. They are proportional to the dipole coefficients, but include contributions from the N first multipoles. Bobbert and Vlieger (11) have employed a similar method for the case of a spheroid on a substrate, by introducing spheroidal multipoles. In our calculations we have included all multipoles up to N=16. Haarmans and Bedeaux (12) have investigated the convergence for the case of a metal sphere on a transparent substrate. For low coverages they find that 15 to 19 multipoles are necessary to obtain an accuracy of 10^{-5}.

The multipolar interactions between the particles in an array have been treated in detail by Haarmans and Bedeaux (12). Because of the low particle coverage of our samples, we only took into account dipole-dipole interactions between the metal particles in our computations. All interaction effects are included in the electrical surface susceptibilities introduced by Bedeaux and Vlieger (13). For normally incident light, the transmittance is expressed in terms of the parallel surface susceptibility, γ, which is related to the parallel polarisability, $\alpha_{//}$, which is of the form of eq. [1] (12,13). The transmittance amplitude becomes

$$t = 2 / (1 + n_s - i(\omega/c)\gamma) \quad , \qquad [2]$$

where n_s denotes the refractive index of the substrate.

RESULTS

We analyze the optical spectra in terms of three important parameters, namely the wavelength of the transmittance minimum, the transmittance value at the minimum and the peak width. The peak halfwidth was determined from the long-wavelength side of the transmittance minimum, where the spectrum is unaffected by interband transitions in the gold particles. The theoretical calculations used the bulk dielectric functions of gold (14) and sapphire (15). The free electron part of the dielectric function of gold was modified to take into account scattering of electrons from the boundary of the particles. This gives a contribution to the relaxation time, τ, of the electrons according to (16)

$$\tau^{-1} = \tau_{bulk}^{-1} + v_F/S, \qquad [3]$$

where v_F is the Fermi velocity and S is the mean free path of the electrons. The mean free path of an electron in a metallic spheroid has been derived by Kraus and Schatz (17). We use their quantum mechanical result, which suggests that we may write S = 0.43 d. It should be noted that it is the relaxation time that determines the width of the absorption peak.

In figure 3 we compare experimental and theoretical values of the peak position. In the calculations we used oblate spheroids and truncated spheres with axial ratios in the range permitted by the experimental data. The peak clearly shifts to longer wavelengths as the axial

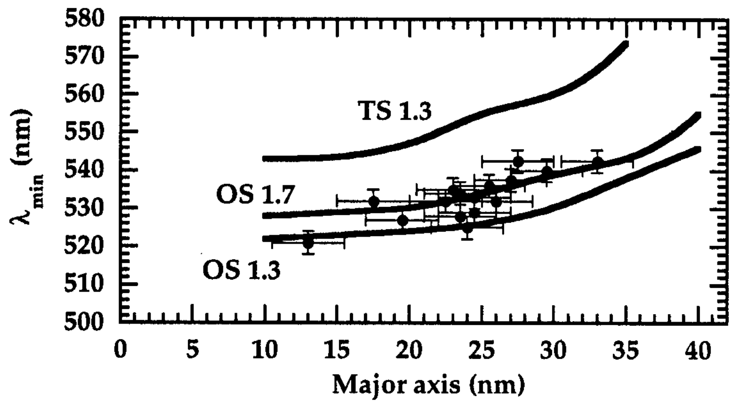

Fig. 3. Position of the transmittance dip for gold arrays as a function of particle major axis. Experimental values are given by dots with error bars. Theoretical calculations (full curves) are for oblate spheroids (OS) and truncated spheres (TS) with axial ratios as given in the figure.

ratio increases. It is seen that computations for truncated spheres are in strong disagreement with the experiments. On the other hand computed peak positions for oblate spheroids with axial ratios between 1.3 and 1.7 are in good agreement with the experiments. We conclude that our slightly flattened particles can be described as oblate spheroids.

Figure 4a and 4b show the peak width and the minimum value of the transmittance, respectively, as a function of major axis. The peak width is in fair agreement with theory, using the relaxation time of the free electrons from eq. [3]. The slightly enhanced experimental values can be ascribed to additional scattering from defects and grain boundaries in the particles. The experimental values of the minimum transmittance are above the theoretical predictions. However, in most cases the disagreement is not serious taking into account the uncertainties in the measurement.

CONCLUSIONS

The optical transmittance of lithographically produced arrays of gold nanoparticles were shown to be in good agreement with theoretical calculations for oblate spheroids in a quadratic lattice. The agreement, in contrast to earlier modeling (3), was due to an improved treatment of the interactions between the particles and their images in the substrate (11). The present model should be of great value for tailoring the optical response of lithographic arrays. We note that theoretical improvements continue to appear (12) and should be tested against well-designed experiments.

ACKNOWLEDGMENTS

This work was financially supported by the Swedish Natural Science Research Council. The experimental work was carried out at Bell Laboratories, Holmdel, N.J. in 1983-1984. We appreciate valuable discussions with D. Bedeaux, J. Vlieger, P.F. Liao and M.B. Stern and the assistance of P.M. Mankievich and J.E. Sweeney.

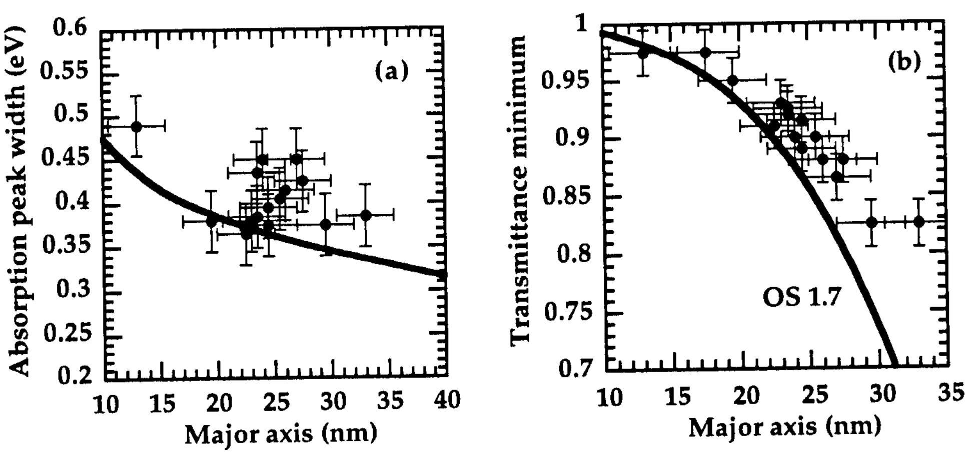

Fig. 4. Absorption peak width (a) and value of transmittance at the minimum (b) for gold arrays as a function of particle major axis. Experimental values are given by dots with error bars, while theoretical calculations for oblate spheroids (axial ratio 1.7 in (b)) are given by full curves.

REFERENCES

1. Abeles, F., Borensztein, Y. and Lopez-Rios, T., *Festkörperprobleme,* 1984, 24, 93.
2. Niklasson, G.A. and Craighead, H.G., *Appl. Phys. Lett.,* 1984, 44, 1134.
3. Niklasson, G.A. and Craighead, H.G., *Thin Solid Films,* 1985, 125, 165.
4. Buncick, M.C., Warmack, R.J. and Ferrell, T.L, *J. Opt. Soc. Am. B,* 1987, 4, 927.
5. Acker, W.P, Schlicht, B., Chang, R.K. and Barber, P.W., *Opt. Lett.,* 1987, 12, 465.
6. Russell, B.K., Mantovani, J.G., Andersson, V.E., Warmack, R.J. and Ferrell, T.L, *Phys. Rev. B,* 1987, 35, 2151.
7. Gotschy, W., Vonmetz, K., Leitner,A. and Aussenegg, F.R, *Appl. Phys. B,* 1996, 63, 381; *Opt. Lett.,* 1996, 21, 1099.
8. Bobbert, P.A. and Vlieger, J., *Physica A,* 1986, 137, 209.
9. Wind, M.M, Vlieger, J. and Bedeaux, D., *Physica A,* 1987, 141, 33.
10. Wind, M.M, Bobbert, P.A., Vlieger, J. and Bedeaux, D., *Physica A,* 1987, 143, 164.
11. Bobbert, P.A. and Vlieger, J., *Physica A,* 1987, 147, 115.
12. Haarmans, M.T. and Bedeaux, D., *Thin Solid Films,* 1993, 224, 117; *Thin Solid Films,* 1995, 258, 213.
13. Bedeaux, D. and Vlieger, J., *Physica,* 1973, 67, 55.
14. Johnson, P.B. and Christy, R.W., *Phys.Rev. B,* 1972, 6, 4370.
15. Malitson, I.H., *J. Opt. Soc. Am.,* 1962, 52, 1377.
16. Doyle, W.T., *Phys. Rev.,* 1958, 111, 1067.
17. Kraus, W.A. and Schatz, G.C., *Chem. Phys. Lett.,* 1983, 99, 353.

Pergamon

NanoStructured Materials, Vol. 12, pp. 731–736, 1999
Elsevier Science Ltd

0965-9773/99/$–see front matter

PII S0965-9773(99)00227-5

CHARACTERIZATION OF SILICON NANOCRYSTALS AND PHOTOLUMINESCENCE QUENCHING IN SOLUTION

Igor N. Germanenko, Shoutian Li, Stuart J. Silvers and M. Samy El-Shall*
Department of Chemistry
Virginia Commonwealth University
Richmond, VA 23284-2006

***Abstract**: Weblike aggregates of coalesced Si nanocrystals are prepared by the Laser Vaporization-Controlled Condensation (LVCC) method. Upon excitation with visible or UV light, the Si nanocrystals show red photoluminescence whose multiexponential time decays are characterized by lifetimes that range from 20 - 80 μs, depending on the emission wavelength. This red emission can be quenched with electron acceptors like 1,4-dinitrobenzene and WO_3 nanoparticles. The quenching rate constants obtained from a Stern-Volmer analysis are 7.65×10^6 $(Ms)^{-1}$ and 14.1×10^6 $(Ms)^{-1}$ for 1,4-dinitrobenzene and WO_3 nanoparticles, respectively. The quenching mechanism appears to proceed via an electron transfer from the CB band of the Si nanocrystals to the quenchers. ©1999 Acta Metallurgica Inc.*

INTRODUCTION

Since the remarkable discovery of photoluminescence (PL) from porous Si, great interest has grown in the synthesis and properties of Si nanocrystals because they are believed to be the luminescent centers in porous Si (1). Research in this area is motivated by the possibility of designing Si-based nanostructured materials that possess novel electronic and optical properties that can be used in new devices for optical communication.

In a recent study, we investigated the physical, optical and PL properties of Si nanocrystals prepared by a Laser Vaporization Controlled Condensation (LVCC) technique (2). The weblike aggregates of coalesced Si nanocrystals, passivated by a SiO_x barrier layer, exhibit red PL upon excitation with visible or UV light. This emission is characterized by a multiexponential decay having lifetimes that depend on emission wavelength.

Although many different mechanisms have been proposed to explain the visible PL from porous Si and Si nanocrystals (1,3), most of the PL properties of Si nanocrystals can be explained by the quantum confinement mechanism (1-3). According to an extended version of this mechanism, the larger band gap in Si nanocrystals is attributed to quantum confined Si structures where recombination of electrons and holes occurs in surface states (4). Therefore, a more fundamental understanding of the mechanism can be obtained by investigating the electron and hole transfer pathways accessible to Si nanocrystals. Recent studies have examined the quenching of PL from porous Si by small solvent molecules and organic electron donors and acceptors (5,6). Both energy and electron transfer mechanisms have been proposed

to explain the PL quenching. No prior studies have reported the quenching of PL from Si nanocrystals by other nanoparticles.

In this paper, we report on the quenching of PL from Si nanocrystals by 1,4-dinitrobenzene molecules and by WO_3 nanoparticles. The results provide evidence for an electron transfer pathway from the CB of the Si to the 1,4-dinitrobenzene molecules and the WO_3 nanocrystals and support a PL model which involves surface states in quantum confined Si nanocrystals.

EXPERIMENTAL

The Si and WO_3 nanoparticles were prepared by the LVCC method which has been described in several publications (2). The method is based on coupling laser vaporization of metals with controlled condensation from the vapor. Here, we offer only a brief description. The metal atomic vapor was generated by pulsed laser vaporization using the second harmonic (532nm) of a Nd:YAG laser (15 – 30 mJ/pulse). The tungsten and Si targets, with a stated purity of 99.99%, were obtained from Aldrich and Dow Corning, respectively. For the synthesis of WO_3 the chamber was filled with O_2 at a pressure of 800 torr which acted as a carrier as well as a reactive gas. For the synthesis of Si nanocrystals, the chamber was filled with He (99.999%) at a pressure of 800 torr. The SEM micrographs of the as-deposited Si particles on glass substrates reveal highly organized weblike structures with individual particles about 10 nm in diameter (2). However, from the correlation of the Raman shift of the allowed optical phonon of microcrystalline Si with size, the particle size of our sample can be estimated as 4-5 nm in diameter (2). This suggests that particles smaller than those detected by the SEM may be present in our sample.

For the quenching measurements, colloid stock solutions of Si, 1,4-dinitrobenzene and WO_3 nanoparticles in methanol with concentrations of 0.9 mg/mL, 0.042 M and 0.13 mg/mL, respectively, were used. The excitation wavelength was the third harmonic of a Nd:YAG laser (355 nm, photon power density $\approx$ 70 mW/cm^2). To 1 mL of the Si stock solution in a quartz cuvette, successive amounts of 1,4-dinitrobenzene or WO_3 stock solution were added. WO_3 nanoparticles do not emit light upon excitation with 355 nm. Suspended Si nanoparticles in methanol emit red light and the luminescence was dispersed by a SPEX 1 m spectrometer equipped with an EMI 9558 photomultiplier (S20 photocathode). An OG590 filter was used to block the laser light and the blue emission from the surface oxide layer of the Si nanoparticles. For dispersed luminescence spectra the photomultiplier output was processed by a PAR Model 162 boxcar averager and recorded by a computer. Time-resolved decays were averaged by a LeCroy 9350 oscilloscope and fit by a computer.

RESULTS AND DISCUSSION

The UV-vis absorption and the dispersed luminescence spectra obtained with 355 nm pulsed laser excitation of the suspended Si nanocrystals in methanol are shown in Figure 1. The Si nanocrystals show red photoluminescence under UV light excitation. The PL decays of this red emission are multiexponential and the lifetimes of the photoluminescence are emission wavelength dependent, increasing from short emission wavelength to long emission wavelength. We fit the PL decays with the stretch exponential model (7):

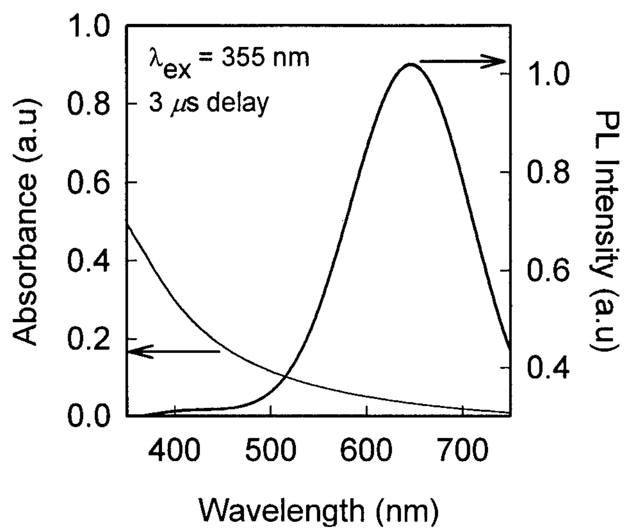

Figure 1. The UV-vis absorption and the PL spectra of the Si nanocrystals in methanol.

$$I(t) = I_0\left(\frac{\tau}{t}\right)^{1-\beta}\exp\left(-\left(\frac{t}{\tau}\right)^{\beta}\right) \tag{1}$$

This decay law is characteristic for systems in which the emitting centers with the decay time τ undergo quenching associated with random walks in the fractal space. The scaling factor β is used to approximate the kinetics of the process (7). We have found that this function gives good fits to the experimental data across the entire spectral range. Figure 2-a shows the PL decays of Si

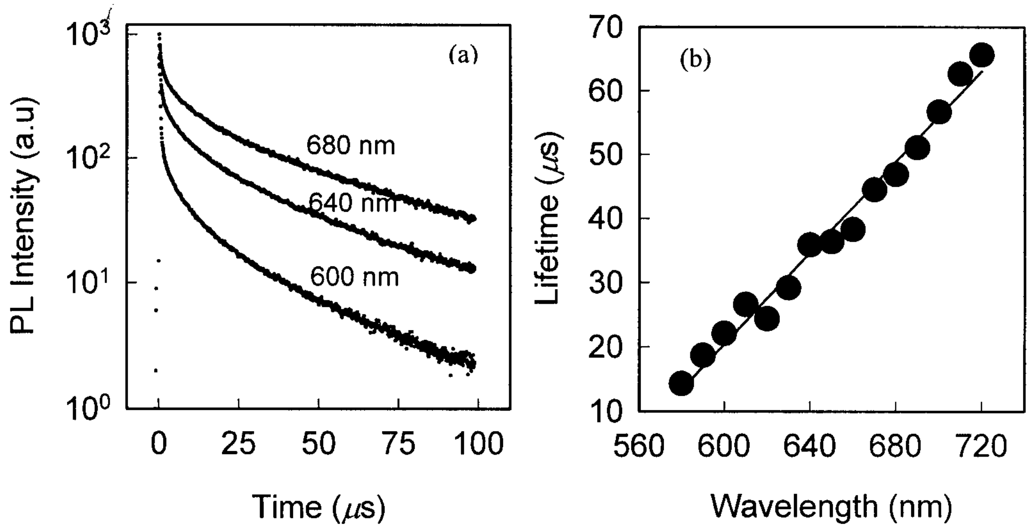

Figure 2. (a) PL decays of Si nanocrystals in methanol at three different emission wavelengths. (b) Lifetime dependence on the emission wavelength.

nanocrystals in methanol solutions monitored at three different emission wavelengths; while Figure 2-b shows the dependence of the lifetime on the emission wavelength.

Upon the addition of successive aliquots of the 1,4-dinitrobenzene or the suspended WO_3 nanoparticle solution into the suspended Si nanoparticles in methanol, a systematic decrease in the PL intensity with increasing 1,4-dinitrobenzene or WO_3 concentration was observed. However, this decrease in the PL intensity may not be used as evidence of quenching because 1,4-dinitrobenzene and the WO_3 nanoparticles absorb the 355 nm laser light. The time-resolved PL decay shows a clear decrease in the lifetime of the red emission from the Si nanocrystals with the addition of 1,4-dinitrobenzene or the WO_3 nanoparticles. Figure 3-a shows the PL decay of Si nanoparticles at an emission wavelength of 640 nm as a function of the concentration of 1,4-dinitrobenzene, while Figure 3-b shows the PL decay of Si nanoparticles at an emission wavelength of 660 nm as a function of the concentration of WO_3 nanoparticles in the methanol solution.

The quenching data follows Stern-Volmer kinetics according to (8):

$$1/\tau = 1/\tau_0 + k_q\,[Q] \qquad (2)$$

where τ is the lifetime with quenchers and τ_0 is the lifetime without quenchers. The Stern-Volmer plots for 1,4-dinitrobenzene and WO_3 nanoparticles are shown in Figures 4-a and 4-b, respectively. From the slopes of these plots, the quenching rate constant for the 1,4-dinitrobenzene is $k_q = 7.65 \times 10^6\,(\mathrm{mol/L})^{-1}\mathrm{s}^{-1}$ and for the WO_3 nanoparticles is $k_q = 14.1 \times 10^6\,(\mathrm{mol/L})^{-1}\mathrm{s}^{-1}$.

The quenching of the PL from the Si nanoparticles by 1,4-dinitrobenzene and WO_3 nanoparticles can be understood as an electron transfer process from Si to 1,4-dinitrobenzene and WO_3. The electron transfer is only possible when the electrode potential of the CB of Si nanoparticles is above that of a quencher so that no energy barrier exists. The CB position of bulk Si is –0.7 V against the NHE (6). Due to the quantum size effect, the band gap of our Si nanoparticles increases from 1.1 eV to 1.78 eV (2). Experiments support the calculation that as

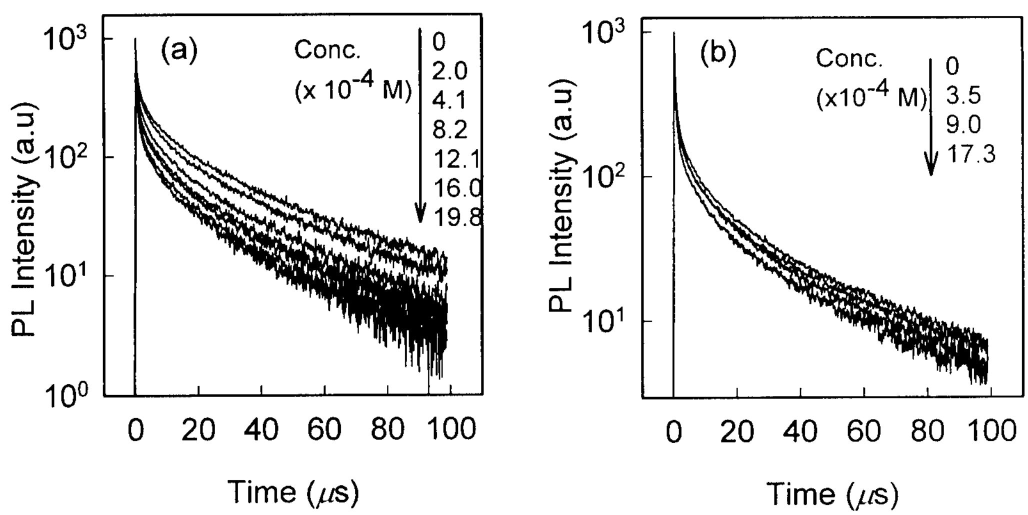

Figure 3. The PL decays (λ_{ex}=355 nm) of Si nanoparticles as a function of the concentration of (a) 1,4-dinitrobenzene (λ_{em}=640 nm) and (b) WO_3 nanoparticles (λ_{em}=660 nm).

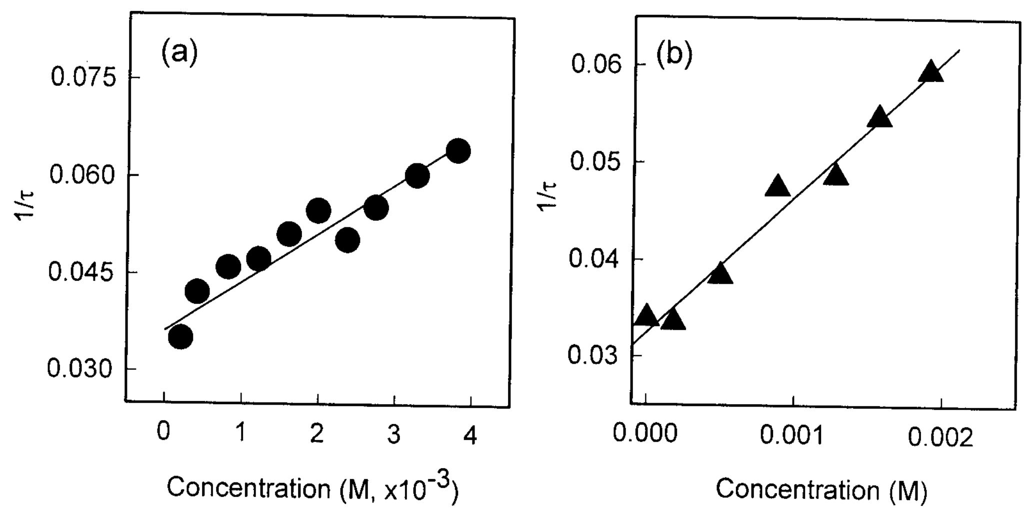

Figure 4. Stern-Volmer plots for (a) 1,4-dinitrobenzene and (b) WO_3 nanoparticles as quenchers of the PL from the Si nanocrystals.

the band gap opens, the shift in the VB should be twice as large as the shift in the CB (6). Thus, the CB position of our Si nanoparticles should be –0.93 V against the NHE. The CB position of bulk WO_3 is –0.17 V against the NHE[9]. The band gap of bulk WO_3 is 2.8 eV[10]. From the UV-vis absorption spectrum, we obtained a band gap for WO_3 nanoparticles of 3.35 eV[11], which is 0.55 eV larger than the bulk value. Thus, the CB position of WO_3 nanoparticles should be -0.35 V against the NHE. The electrode potential of 1,4-dinitrobenzene is –0.80 V against the NHE[6]. The relative energy positions of the CB and VB of Si and WO_3 nanoparticles are shown in Scheme 1.

CONCLUSIONS

The Si nanocrystals prepared by the LVCC method emit red light when excited by UV light. The multiexponential PL time decays are characterized by lifetimes on the order of tens of microseconds, depending on the emission wavelength. This red emission can be quenched by electron acceptors such as 1,4-dinitrobenzene and WO_3 nanoparticles. The quenching rate

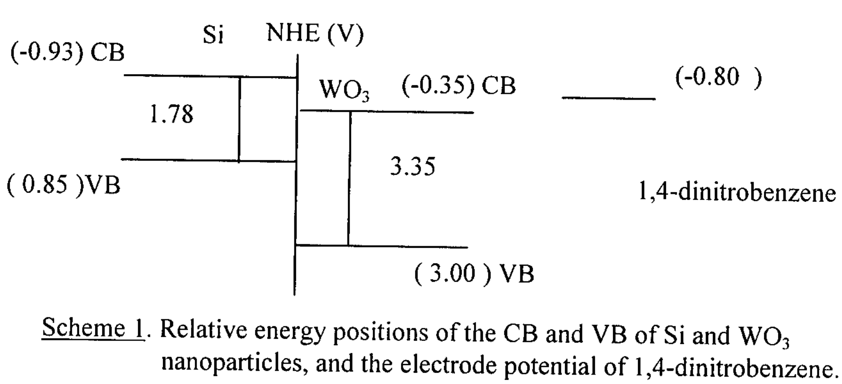

Scheme 1. Relative energy positions of the CB and VB of Si and WO_3 nanoparticles, and the electrode potential of 1,4-dinitrobenzene.

constants obtained from a Stern-Volmer analysis are 7.65×10^6 $(Ms)^{-1}$ and 14.1×10^6 $(Ms)^{-1}$ for 1,4-dinitrobenzene and WO_3 nanoparticles, respectively. The quenching mechanism appears to proceed via an electron transfer from the CB band of Si nanocrystals to the quenchers.

ACKNOWLEDGMENT

The authors gratefully acknowledge financial support from the NASA Microgravity Materials Science Program (Grant NAG8-1276).

REFERENCES

1. See for example: Canham, L. T. (a) *Appl. Phys. Lett.* 57, 1046, 1990; (b) Wilson, W. L.; Szajowski, P. F.; Brus, L. E. *Science* 262, 1242, 1993; (c) Brus, L. J. *Phys. Chem.* 98, 3575, 1994; (d) Kanemitsu, Y. *Phys. Rev. B* 49, 16845, 1994; (e) Brus, L Szajowski, P. F.; Wilson, W. L.; Harris, T.D.; Schuppler, S.; Citrin, P. H. *J. Am. Chem. Soc.* 117, 2915, 1995; (f) Prokes, S. M. in "Nanometerials: Synthesis, Properties and Applications", Edelstein, A. S.; Cammarata, R. C., Eds.; Institute of Physics Publishing, Bristol and Philadelphia, 1996, Chap. 17, 439-457.
2. Li, S.; Silvers, S. J.; El-Shall, M. S. J. Phys. Chem. 101, 1794,1997.
3. (a) Hill, N.; Whaley, K. *Phys. Rev. Lett.* 75, 1130, 1995; (b) Delerue, C.; Allan, G.; Lannoo, M. *Phys. Rev. B* 48, 11024,1993; (c) Wang, L.; Zunger, A. *J. Phys. Chem.* 98, 2158, 1994; (d) Takagahara, T.; Takeda, K. *Phys. Rev. B* 46, 15578, 1993; (e) Proot, J.; Delerue, C.; Allan, G. *Appl. Phys. Lett.* 61, 1948, 1992.
4. (a) Koch, F.; Petrova-Koch, V.; Muschik, T.; Nikolov, A.; Gavrilenko, V. *Mater. Res. Soc. Symp. Proc.* 283, 197, 1993; (b) Fauchet, P. et al., *Mater. Res. Soc. Symp. Proc.* 298, 271, 1993.
5. (a) Song, J. H.; Sailor, M. J. *J. Am. Chem. Soc.* 119, 7381,1997; (b) Ko, M. C.; Meyer, G. J. *Chem. Mater.* 8, 2686, 1996; (c) Fisher, D. L.; Harper, J.; Sailor, M. J. *J. Am. Chem. Soc.* 117, 7846, 1995.
6. Rehm, J. M.; McLendon, G. L.; Fauchet, P. M. *J. Am. Chem. Soc.* 118, 4490, 1996.
7. (a) Kanemitsu, Y. *Phys. Rev. B* 48, 12357, 1993. (b) Gaponenko, S. V.; Petrov, E. P.; Woggon, U.; Wind, O.; Klingshirn, C.; Xie, Y. H.; Germanenko, I. N.; Stupak, A. P. *J. Luminescence* 70, 346, 1996.
8. Turro, N. J. *Modern Molecular Photochemistry*, University Science Books: Mill Valley, CA, 1991.
9. Tennakone, K.; Lleperuma, O.A.; Bandara, J. M. S.; Kiridena, W. C. B. *Semicond. Sci. Tech.* 7, 423, 1992.
10. Strehlow, W. H.; Cook, E. L. *J. Phys. Chem. Ref. Data*, 2, 163, 1973.
11. Li, S.; Germanenko, I. N.; El-Shall, M. S. *J. Phys. Chem.*, 102, 7319, 1998.

Pergamon

NanoStructured Materials, Vol. 12, pp. 737–740, 1999
Elsevier Science Ltd

0965-9773/99/$–see front matter

PII S0965-9773(99)00228-7

MAGNETIC STRUCTURE EVOLUTION IN MECHANICALLY MILLED NANOSTRUCTURED $ZnFe_2O_4$ PARTICLES

J.Z. Jiang[1], P. Wynn[2], S. Mørup[1], T. Okada[3], and F.J. Berry[2]
[1]Department of Physics, Building 307, Technical University of Denmark, DK-2800 Lyngby, Denmark.
[2] Department of Chemistry, The Open University, Milton Keynes, MK7 6AA, UK.
[3] Magnetic Materials Laboratory, The Institute of Physical and Chemical Research, RIKEN 351-01 Wako, Saitama, Japan.

Abstract – Nanostructured partially-inverted $ZnFe_2O_4$ particles have been prepared from bulk $ZnFe_2O_4$ by high-energy ball milling in an open container. The grain size reduction, cation site distributions, and the evolution of magnetic structures have been studied by x-ray diffraction with Rietveld structure refinements, transmission electron microscopy, and Mössbauer spectroscopy. It is found that a change of magnetic structure from an antiferromagnetic to a ferrimagnetic (or ferromagnetic) structure occurs in the milled samples. This change is correlated with the redistribution of the cations, Zn and Fe, in the A and B sublattices.

INTRODUCTION

Zinc ferrite, $ZnFe_2O_4$, is usually considered to have a normal spinel structure with zinc cations in the tetrahedral, A, sites and iron cations in the octahedral, B, sites. It is antiferromagnetic with a Néel temperature of approximately 10 K. However, the magnetic structure can be altered by developing a non-equilibrium state with some iron cations in the A-sites. The site occupancy is often depicted in the chemical formula as $(Zn_{1-\delta}Fe_{\delta})[Zn_{\delta}Fe_{2-\delta}]O_4$, where round and square brackets denote the A and B sites, respectively, and δ is the inversion parameter. Partially-inverted $ZnFe_2O_4$, i.e., $\delta > 0$, can be achieved by several methods including sol-gel (1), quenching (2), sputtering (3) and co-precipitation methods (4). Here we report a study of nanostructured $ZnFe_2O_4$ particles prepared by high-energy ball milling in an open container from bulk $ZnFe_2O_4$ and the grain size reduction, cation site distributions, and the evolution of magnetic structures.

EXPERIMENTAL

$ZnFe_2O_4$ was synthesized in the polycrystalline form by a solid state reaction from a mixture of α-Fe_2O_3 (99.95%) and ZnO (99.9%) with a Zn:Fe ratio of 1:2. The single phase ($ZnFe_2O_4$, Franklinite, JCPDS 22-1012) nature of the starting material was confirmed by x-ray

powder diffraction analysis. Contamination of the material was found by chemical analysis to be below 0.2 %. For the preparation of nanostructured $ZnFe_2O_4$ samples, *dry* milling (i.e., no organic surfactant used during milling.) was carried out in an *open* container (i.e., the valves on the lid were open during milling in air) using a planetary ball mill (Fritsch Pulverisetter 5), with hardened stainless steel vials and balls (5). The milling intensity was 200 rotations per minute, and a ball-to-powder weight ratio of 20:1 was chosen. The milling was interrupted after selected times to remove small amounts of powder for analysis. The composition of the samples (after the longest milling time of 50 hours) was examined by scanning electron microscopy with an energy dispersive x-ray analysis facility. It was found that the contamination with Cr, originating from the abrasion of the vial and balls, was less than 1 wt.%. All samples were examined by x-ray powder diffraction (XRD) in Bragg-Brentano geometry with a Philips PW 1820/3711 diffractometer using Cu Kα radiation. The data were collected in the 2θ range from 10 to 130° with a step size of 0.02° and a counting time of 25 seconds per step. Rietveld structure refinements were used to identify the crystal structure, the lattice constant, and the cation occupancies in A and B sites. Transmission electron microscopy (TEM) measurements for selected samples were carried out using a Philips EM430 TEM. Mössbauer spectroscopy was performed with a conventional constant acceleration spectrometer with a source of 50 mCi ^{57}Co in a Rh matrix. Isomer shifts are given relative to that of α-Fe at room temperature. A closed-cycle helium cryostat, a nitrogen cryostat, and an electromagnet were used for low temperature and in-field Mössbauer measurements.

RESULTS AND DISCUSSION

By comparing the XRD patterns for the milled samples with that for the starting $ZnFe_2O_4$ material, it was found that positions of the reflection peaks for the milled samples were almost the same as the corresponding peaks for bulk $ZnFe_2O_4$. This implies that the basic structure of the milled samples is still identical to the $ZnFe_2O_4$ phase (JCPDS 22-1012). This was confirmed by Rietveld structure refinements. No decomposition process, $ZnFe_2O_4 \rightarrow ZnO + \alpha\text{-}Fe_2O_3$, which can be induced by heat treatment at elevated temperatures around 500 °C (6), was observed in the milled samples. The average grain size, d, and the root-mean square (rms) atomic-level strain, $\langle\varepsilon^2\rangle^{1/2}$, within particles were estimated from the diffraction line broadening (7). These parameters, together with the lattice constant, the inversion parameter, and the R value, obtained by Rietveld structure refinements, as a function of milling time are listed in table 1. As the milling time increases, the average grain size initially drops rapidly from about 100 nm (after 10 min.) to 15 nm (after 14 h), and remains unchanged with further milling time up to 50 h. Initially, the strain rapidly increases and then slowly decreases after milling times longer than 7 h. Similar behavior for average grain size vs. milling time has also been observed in other systems (5, 8). In the early stage of ball milling, the atomic-level strain increases due to the increasing defect density and the grain size is rapidly reduced. With increasing milling time the lattice constant decreases, but the inversion parameter increases and the Fe and Zn ions seem to be randomly distributed in the A and B sites in samples milled longer than 14 h. The correlation between lattice parameter and the degree of inversion observed is consistent with the results reported for partially-inverted $ZnFe_2O_4$ particles prepared by the co-precipitation method (4). TEM measurements of the sample milled for 50 h revealed $ZnFe_2O_4$ particles with

TABLE 1
The Average Grain Size, d, and the Root-Mean Square (rms) Atomic-Level Strain, $<\varepsilon^2>^{1/2}$, the Lattice Constant, a, the Inversion Parameter, δ, and the R Value for the $ZnFe_2O_4$ Samples After Different Milling Times.

Milling Time	d (nm)	$<\varepsilon^2>^{1/2}$ (%)	a (Å)	δ	R (%)
10 min.	100(5)	0.1(1)	8.435(1)	0.05(2)	7.12
3 h	43(5)	0.9(1)	8.436(2)	0.27(2)	3.34
7 h	28(3)	1.1(1)	8.433(1)	0.49(2)	2.41
14 h	15(2)	0.8(1)	8.432(1)	0.64(2)	2.21
29 h	13(2)	0.6(1)	8.431(2)	0.67(2)	2.17
50 h	14(2)	0.5(1)	8.428(1)	0.66(2)	2.20

an average size of approximately 13 nm. Well-defined lattice images for grains were obtained and no amorphous phase was observed.

Figure 1 shows the Mössbauer spectra obtained at 80 and 295 K of the $ZnFe_2O_4$ samples after different milling times together with the spectra obtained in a magnetic field for the sample milled for 50 h. At 295 K, only a paramagnetic doublet with an isomer shift (0.35(1) mm/s) and a quadrupole splitting (0.40(2) mm/s) was observed in the samples milled for 10 min. and 3 h. In the sample milled for 7 h, the doublet becomes broad and a sextet with a small hyperfine magnetic field and broad lines together with a doublet were used to fit the spectrum. The sextet component becomes significant in the sample milled for 14 h and has approximately 50 % of the total resonant area in the spectra for the samples milled for 29 h and 50 h. In addition, in the samples milled for 29 h and 50 h, the lines of the doublet are very broad. At 80 K, a sextet component is clearly observed in all samples except for the sample milled for 10 min. and the longer the milling time, the more sextet component is formed. In the samples milled for 29 h and 50 h, almost no paramagnetic component was detected, indicating that the materials are in a magnetic state although the paramagnetic-to-antiferromagnetic transition occurs at approximately 10 K for the normal $ZnFe_2O_4$ spinel phase. This demonstrates that the magnetic structure of $ZnFe_2O_4$ can easily be altered by mechanical milling. In order to clarify the origin of the doublet (observed at 295 K) and the magnetic structure in the sample milled for 50 h, in-field Mössbauer measurements were recorded at 295 K and 80 K, as also shown in Fig. 1. For a ferro- or ferri-magnetic material the relative intensities of lines of 2 and 5 and the relative area of the magnetic component (for small particles) would increase when a magnetic field perpendicular to the gamma ray direction is applied. In contrast, for an antiferromagnetic material, no polarization effect and no enhancement of the sextet component are expected. We find both the polarization effect and the enhancement of the sextet component in the in-field spectra. These results lead us to the conclusion that the material milled for 50 h is ferrimagnetic or ferromagnetic and not antiferromagnetic as the bulk material and the doublet is not due to a paramagnetic phase but to superparamagnetic particles. A significant fraction of the grains are in a superparamagnetic state at 295 K. This means that the paramagnetic-to-magnetic transition temperature for the milled samples is higher than 295 K, which is much larger than 10 K for the normal $ZnFe_2O_4$ spinel phase.

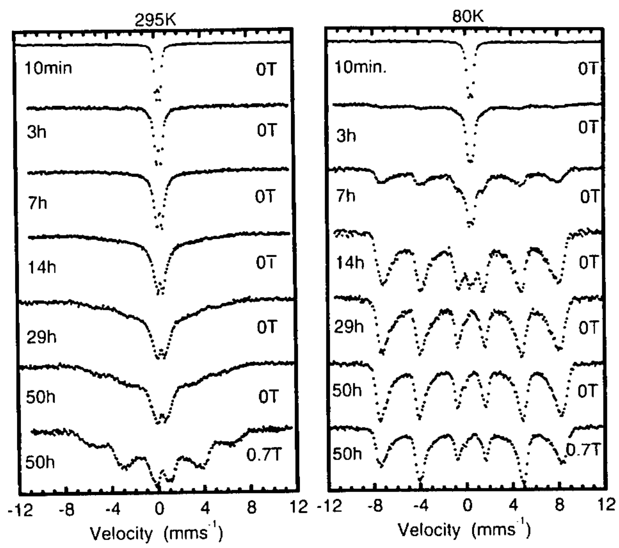

Fig. 1 The Mössbauer spectra recorded at 80 and 295 K for the $ZnFe_2O_4$ samples after different milling times together with the spectra for the sample milled for 50 h in a magnetic field.

ACKNOWLEDGMENTS

This work has been supported by the Danish Technical Research Council and by the European Commission Sokrates Student Mobility Programme (PW).

REFERENCES

1 S.J. Teichner, G.A. Nicolaon, M.A. Vicarini, and G.E.E. Grades, Adv. Colloid Interface Sci. **5**, 245 (1976); H.H. Hamdeh, J.C. Ho, S.A. Oliver, R.J. Willey, J. Kramer, Y.Y. Chen, S.H. Lin, Y.D. Yao, M. Daturi, and G. Busca, IEEE Trans. Magn. **31**, 3808 (1995).
2 K. Tanaka, Y. Nakahara, K. hirao, N. Soga, J. Magn. Magn. Mater. **131**, 120 (1994).
3 J.Chen, G. Srinivasan, S. Hunter, V.S. Babu, and M.S. Seehra, J. Magn. Magn. Mater. **146**, 291 (1995).
4 T. Sato, K. Haneda, M. Seki, and T. Lijima, Appl. Phys. A **50**, 13 (1990); T. Kamiyama, K. Haneda, T. Sato, S. Ikeda, and H. Asano, Solid State Commun. **18**, 563 (1992); and B. Jeyadevan, K. Tohji, and K. Nakatsuka, J. Appl. Phys. **76**, 6325 (1994).
5 J.Z. Jiang, Y.X. Zhou, S. Mørup, C.B. Koch, Nanostructured Mater. **7**, 401 (1996).
6 K. Tkacova, V. Sepelak, N. Stevulova, and V.V. Boldyrev, J. Solid State Chemistry **123**, 100 (1996).
7 G.K. Williamson and W.H. Hall, Acta Matall. **1**, 22 (1953).
8 J.Z. Jiang, C. Gente, R. Bormann, Mater. Sci. Eng. A **242**, 268 (1998); and J.Z. Jiang. R. Lin, S. Mørup, K. Nielsen, F.W. Poulsen, F.J. Berry, and R. Clausen, Phys. Rev. B**55**, 11 (1997).

Pergamon

NanoStructured Materials, Vol. 12, pp. 741–749, 1999
Elsevier Science Ltd

0965-9773/99/$–see front matter

PII S0965-9773(99)00229-9

HIGH-STRENGTH BULK NANOCRYSTALLINE ALLOYS CONTAINING COMPOUND AND AMORPHOUS PHASES

Akihisa Inoue and Cang Fan*

Institute for Materials Research, Tohoku University, Sendai 980-8577, Japan
* Inoue superliquid glass project, ERATO, Japan Science and Technology Corporation (JST), Sendai 982-0807, Japan

Abstract--Partial crystallization of cast bulk amorphous alloys in Zr-Al-Cu-Pd and Zr-Al-Cu-Pd-Fe systems was found to cause bulk nanocrystalline alloys with high tensile strength (σ_f). The nanostructure alloys consist of nanoscale bct- Zr_2(Cu, Pd) surrounded by the remaining amorphous phase. The crystallization of a ternary $Zr_{60}Al_{10}Cu_{30}$ amorphous alloy occurs by the simultaneous precipitation of Zr_2Cu and Zr_2Al phases with large particle sizes of 400 to 500 nm and hence the addition of Pd is essential for formation of the nanostructure. The Pd has much larger negative heats of mixing against Zr and the resulting Zr-Pd atomic pair seems to act as preferential nucleation sites leading to the precipitation of Zr_2(Cu, Pd). The nanostructure alloys in the cast cylinder of 4 to 5 mm in diameter keep good ductility in the volume fraction (V_f) range of the compound below 30 to 40 %. ©1999 Acta Metallurgica Inc.

INTRODUCTION

Recently, nanocrystalline alloys have attracted increasing interest because of the achievement of novel characteristics which had not been obtained for conventional crystalline and amorphous phases (1). As novel characteristics, one can list up hard magnetism, soft magnetism, high strength, high sensitive magnetostriction and high catalytic property (1). However, the nanocrystalline alloys exhibiting these useful characteristics have been obtained by partial crystallization of melt-spun amorphous alloys. There had been no data on a bulk nanocrystalline alloy of crystalline and remaining amorphous phases exhibiting useful characteristics. This is presumably because bulk amorphous alloys in Mg-Ln-TM, Ln-Al-TM, Zr-Al-TM, Pd-Cu-Ni-P and Fe-(Al, Ga)-(P, C, B, Si) (Ln=lanthanide metal, TM=transition metal) systems crystallize through a single exothermic reaction, accompanying the simultaneous precipitation of multiple phases more than three kinds of compounds (2,3). That is, the crystallization mode has been thought to cause the appearance of a wide supercooled liquid region before crystallization resulting from the increase of the stability against crystallization. The high glass-forming ability as well as the high thermal stability of the supercooled liquid has been reported to be obtained for the alloys which satisfy the following three empirical rules (2,3), i.e., (I) multicomponent alloy system consisting of more than three

elements, (II) significant difference in atomic size ratios above about 12% among their constituent elements, and (III) negative heats of mixing among their elements. If inhomogeneous nucleation sites are introduced in the supercooled liquid by deviating from the three empirical rules, the crystallization mode of the amorphous alloys is expected to change from the single stage to the multistage type leading to the precipitation of a primary crystalline phase. It has previously been reported that the primary crystallization mode is one of the necessary criteria for formation of a nanocrystalline phase from an amorphous phase (1). Consequently, we examined the possibility of forming a cast bulk amorphous alloy or a melt-spun amorphous alloy ribbon with a wide supercooled liquid region in which the crystallization takes place by the primary precipitation mode. As a result, we have found that Zr-Al-Cu alloys containing Ag, Pd, Au or Pt element which deviates from the three empirical rules can be made into an amorphous phase even in a bulk form (4,5). Furthermore, it was found that the resulting bulk amorphous alloys exhibited improved mechanical properties as compared with bulk amorphous single phase alloys. This paper is intended to present the nanocrystallization behavior and mechanical properties of the melt-spun amorphous Zr-Al-Cu-M (M=Pd or Au) alloys as well as the mechanical properties of the bulk amorphous alloys and to investigate the effectiveness of the additional M elements on the formation of the nanocrystalline structure and the improvement of their mechanical properties.

BASIC CONCEPT OF SYNTHESIZING BULK NANOCRYSTALLINE ALLOYS

It has previously been reported (1) that nanocrystallization including a remaining amorphous phase for metallic amorphous alloys requires the following factors; (I) two-stage crystallization process, (II) existence of preferential nucleation sites, (II) the retardation of growth reaction, and (IV) increase in the thermal stability of the remaining amorphous phase. Ordinary bulk amorphous alloys with a wide supercooled liquid region before crystallization in Mg-, Ln-, Zr-, Pd-, Fe- and Co-based systems crystallize through a single exothermic peak and do not satisfy the above-described conditions (2,3). In order to fabricate a bulk amorphous alloy with the above-described conditions, we have tried to deviate from the three empirical rules for achievement of high glass-forming ability for the multicomponent bulk amorphous alloys. We evaluated the influence of additional elements of Ti, Nb, Ag, Pd, Au and Pt on the crystallization behavior and fundamental properties of Zr-Al-Ni-Cu bulk amorphous alloys. These additional elements can be divided to the following three types; (I) soluble type against Zr for Ti and Nb (6), (II) immiscible type against Ni and Cu for Ag (6), and (III) preferential bonding type against Zr for Pd, Au and Pt (6). The addition of these elements deviates from the three empirical rules for the achievement of highly stable supercooled liquid and is expected to give preferential nucleation sites in the supercooled liquid, leading to the formation of nanostructure through the change into the two-stage crystallization.

NANOCRYSTALLINE Zr-Al-Cu-M (M=Pd, Au or Pt) ALLOYS

The heat of mixing between Zr and M elements is in the range of -74 to -100 kJ/atom and the absolute values are much larger than those for the other atomic pairs of Zr-Al, Zr-Ni and Zr-Cu (7). The addition of the M elements to Zr-Al-Ni-Cu amorphous alloys is presumed to

cause the change from the homogeneously mixed state of the constituent elements to the preferential generation of Zr-M atomic pair in the amorphous structure. The increase in the degree of the inhomogeneity seems to give rise to preferential nucleation sites which are necessary for the formation of the nanocrystalline structure.

Figure 1 shows the DSC curves of melt-spun $Zr_{60}Cu_{30}Al_{10}$ and $Zr_{60}Cu_{20}Pd_{10}Al_{10}$ amorphous alloys. An extra exothermic peak is observed at the higher temperature side for the Pd-containing alloys. The crystallization mode changes to a second-stage type in the maintenance of the supercooled liquid region by the addition of 10%Pd. The X-ray diffraction patterns of the 0%Pd and 10%Pd alloys annealed at the temperatures between T_g and T_x are shown in Fig. 2. The X-ray diffraction pattern of the 0%Pd alloy consists of Zr_2Cu and Zr_2Al phases and the peak intensity is also significant. Besides, no appreciable broad peak due to the existence of an amorphous phase is seen, indicating that the crystallization is completed by a single stage reaction of Am $\rightarrow$ Zr_2Cu + Zr_2Al and the grain sizes of their crystalline phases are rather large. On the other hand, the 10%Pd-containing alloy consists of amorphous and Zr_2Cu phases in the annealed state at 726 K. Besides, the peak of the Zr_2Cu phase is broad and has weak intensity, indicating that the Zr_2Cu phase has very fine grain sizes. In order to confirm the formation of the nanostructure consisting of amorphous + Zr_2Cu phases, the TEM images and selected-area electron diffraction patterns of the 10%Pd alloy annealed for various times at 726 K are shown in Fig. 3. The Zr_2Cu phase precipitates homogeneously from the amorphous matrix and the V_f appears to increase with increasing annealing time. The particle size is measured to be about 10 nm for 1.8 ks, 20 nm for 2.4 ks and 25 nm for 3.6 ks. The interparticle spacing appears to be as small as about 1nm. A halo ring due to an amorphous phase remains in the electron diffraction patterns, indicating clearly the formation of the nanostructure consisting of Zr_2Cu and amorphous phases. The grain size of the 0%Pd alloy was about 400 to 500 nm for Zr_2Cu and for Zr_2Al for

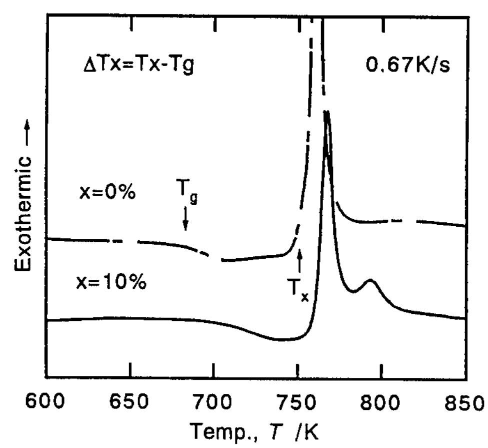

Fig. 1 Change in the DSC curves of melt-spun amorphous $Zr_{60}Al_{10}Cu_{30-x}Pd_x$ (x=0 and 10 at%) alloys with Pd content.

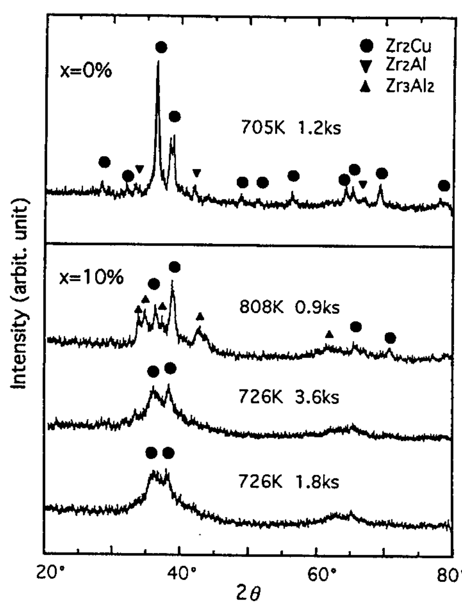

Fig. 2 X-ray diffraction patterns of melt-spun amorphous $Zr_{60}Al_{10}Cu_{30-x}Pd_x$ (x=0 and 10 at %) alloys annealed in different conditions.

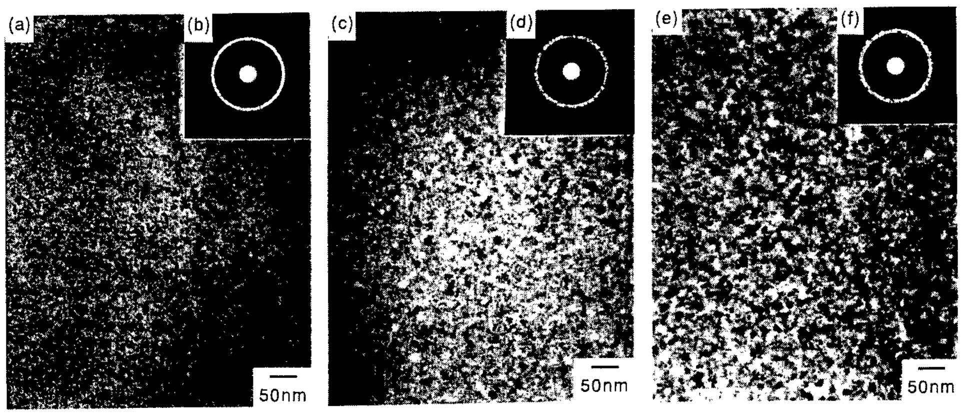

Fig. 3 Bright-field electron micrographs and selected-area electron diffraction patterns of melt-spun amorphous $Zr_{60}Al_{10}Cu_{20}Pd_{10}$ alloy annealed at 726 K for 1.8, 2.4 and 3.6 ks.

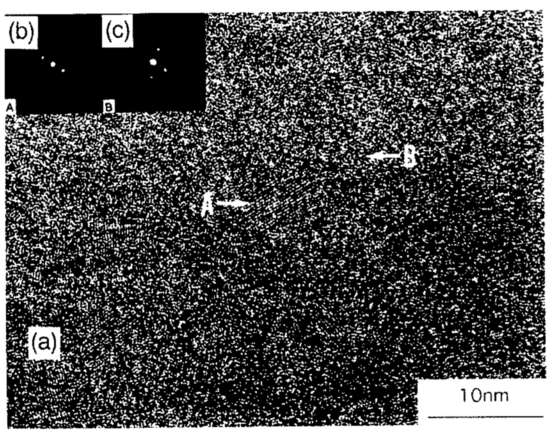

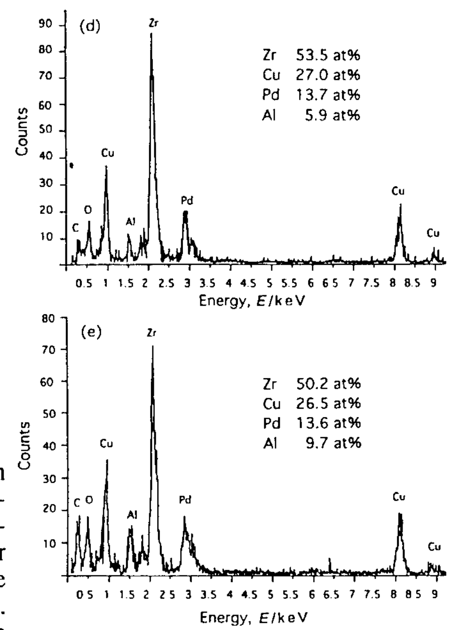

Fig. 4 High-resolution TEM image and nanobeam EDX spectroscopy profiles taken from the amorphous and compound phases in melt-spun amorphous $Zr_{60}Al_{10}Cu_{20}Pd_{10}$ alloy annealed at 726 K for 1.2 ks. The diffraction patterns (b) and (c) were taken from the regions A and B, respectively, in (a). The EDX profiles (d) and (e) were also taken from the regions A and B, respectively.

the $Zr_{60}Cu_{30}Al_{10}$ alloy annealed for 1.2 ks at 705 K. The contrast results indicate that the addition of Pd is important for the formation of the nanostructure. In order to investigate the role of Pd in the formation of the nanostructure, we examined the distribution of the constituent elements in the nanoscale Zr_2Cu and amorphous phases by the high-resolution TEM image and nanobeam EDX analysis methods. Figure 4 shows the high-resolution TEM image of the 10%Pd alloy annealed for 1.2 ks at 726 K and the analytical compositions in the regions A and

B obtained by nanobeam EDX spectroscopy. In the high-resolution TEM image, fringe contrast regions with a size of about 6nm disperse homogeneously in the amorphous phase characterized by the featureless modulated contrast region. The nanobeam EDX analyses indicate that the Al element is always enriched into the remaining amorphous phase, though no distinct redistribution of the other constituent elements is recognized. Considering that the equilibrium phase diagram in the Cu-Pd system (6) is soluble type over the whole composition range, the additional Pd element appears to be dissolved into the Zr_2Cu phase and the chemical formula of the precipitates is represented by Zr_2(Cu, Pd) (4). The enrichment of Al into the remaining amorphous phase is also supported from the experimental result that a Zr_3Al_2 phase precipitates from the remaining amorphous phase. The thermal stability of the remaining amorphous phase with enriched Al concentrations increases, leading to the residual existence of the remaining amorphous phase even in the higher temperature range. Besides, the necessity of the redistribution of Al elements seems to be the reason for the suppression of grain growth of the Zr_2(Cu, Pd) phase.

Very surprisingly, the 10%Pd nanostructure alloy remains ductile in the wide V_f range up to 75 % and can be bent through 180 degrees without fracture. We measured mechanical properties for the ductile samples. Figure 5 shows the changes in σ_f, Hv and E with V_f of Zr_2(Cu, Pd) for the melt-spun $Zr_{60}Cu_{20}Pd_{10}Al_{10}$ alloy. As the V_f increases up to 75 %, these properties increase almost linearly from 1650 to 1950 MPa for σ_f, from 505 to 605 for Hv and from 52.2 to 62.7 GPa for E. In order to confirm the good ductile nature for the 75%V_f sample, we observed the tensile fracture surface of the 0%V_f and 75%V_f samples. In comparison with the 0%V_f sample, the smooth region caused by shear sliding was enlarged for the 75%V_f sample, indicating that the 75%V_f sample keeps good plastic deformability before the adiabatic final fracture.

A similar two-stage crystallization behavior in which an extra exothermic peak appears at the higher temperature side in the maintenance of the wide supercooled liquid region is also recognized for melt-spun $Zr_{60}Cu_{30-x}Au_xAl_{10}$ (x=5, 8 and 10 at%) alloys. The σ_f, Hv and E values also increase almost linearly from 1740 to 2030 MPa, 500 to 610 and 52.2 to 74.4 GPa, respectively, with increasing V_f to 75 %. The longer annealing treatment to increase further V_f causes the disappearance of the remaining amorphous phase, accompanying the distinct grain growth of the constituent phases. The σ_f decreases drastically for the crystallized samples without remaining amorphous phase. The good correspondence between the increase in σ_f and the formation of the nanostructure by the residual existence of the remaining amorphous phase indicates that the achievements of the high σ_f and good bending ductility are attributable to the existence of

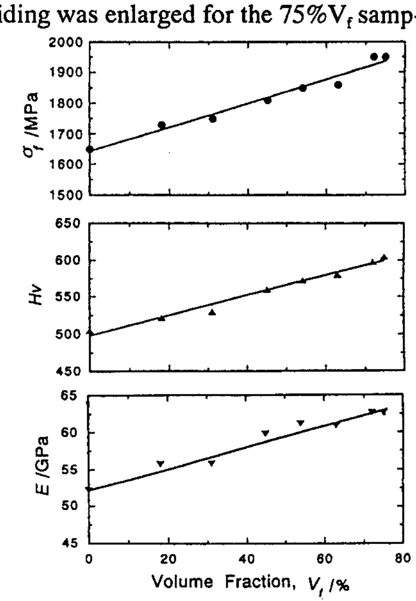

Fig. 5 Changes in the tensile fracture strength (σ_f), Vickers hardness (Hv) and Young's modulus (E) with V_f of Zr_2Cu phase for melt-spun amorphous $Zr_{60}Al_{10}Cu_{20}Pd_{10}$ alloy.

the remaining amorphous phase exhibiting the glass transition phenomenon. Furthermore, the linear increases in σ_f, Hv and E as a function of V_f also indicate that the change in the mechanical properties is interpreted by the simple mixture rule consisting of Zr_2(Cu, M) and amorphous phases.

BULK NANOCRYSTALLINE ALLOYS

We have confirmed that the $Zr_{60}Cu_{20}Pd_{10}Al_{10}$ and $Zr_{60}Cu_{15}Pd_{10}Al_{10}Fe_5$ alloys can be made as an amorphous phase to cylindrical bulk forms with diameters up to 4 and 6 mm by copper mold casting, respectively, as shown in Fig. 6. The tensile test specimen with a gauge dimension of ϕ2.0mm x 10mm and a total length of 45 mm was made from the cast bulk amorphous alloy by mechanical cutting. Figure 7 shows the changes in σ_f, E and fracture elongation (ε_f) including elastic elongation with V_f for the cast bulk $Zr_{60}Cu_{20}Pd_{10}Al_{10}$ and $Zr_{60}Cu_{15}Pd_{10}Al_{10}Fe_5$ cylinders. The σ_f and E increase almost linearly from 1760 to 1880 MPa and 81.0 to 89.5 GPa, respectively, in the V_f range up to 40 % for the former alloy and from 1750 to 1850MPa and 81.1 to 88.0 GPa in the V_f range up to 30 % for the latter alloy. The ε_f also tends to increase slightly from 2.1 to 2.3 % in the wide V_f ranges. With further increasing V_f, the σ_f and ε_f decrease significantly because of the loss of ductility for the remaining amorphous phase. Figure 8 shows the changes in the tensile fracture appearance and fracture surface structure with V_f for the Zr-Cu-Pd-Al cylinders. The fracture takes place along the maximum shear plane which is declined by about 45 degrees to the direction of tensile load in the V_f range up to 40 % and the fracture surface consists mainly of a well-developed vein pattern. There is no appreciable change in the fracture surface appearance in the V_f range up to 40%. However, the samples with V_f above 40% fracture along the plane which is perpendicular to the direction of tensile load and a shell-like pattern typical for embrittled amorphous alloys is observed in the fracture surface. The features of the tensile fracture mode and fracture surface structure are the same as those for the $Zr_{60}Cu_{20}Pd_{10}Al_{10}$ alloy. It is thus concluded that bulk nanocrystalline alloys with improved tensile strength are formed for the Zr-based systems containing Pd by the partial crystallization treatment in the supercooled liquid region.

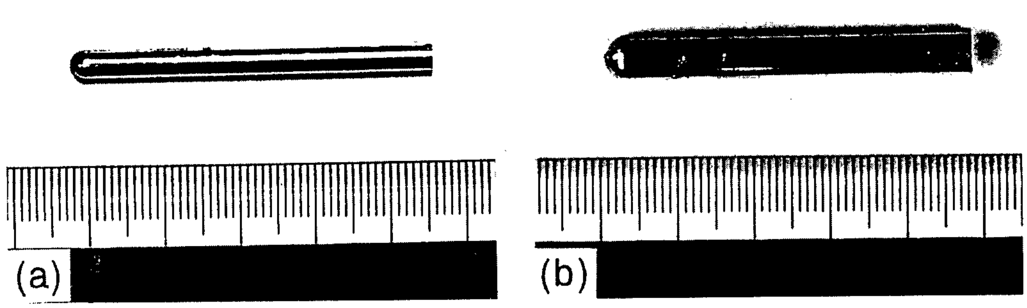

Fig. 6 Outer morphology of the cast bulk amorphous $Zr_{60}Al_{10}Cu_{20}Pd_{10}$ and $Zr_{60}Al_{10}Cu_{15}Pd_{10}Fe_5$ alloys with diameter of 4 and 6 mm, respectively.

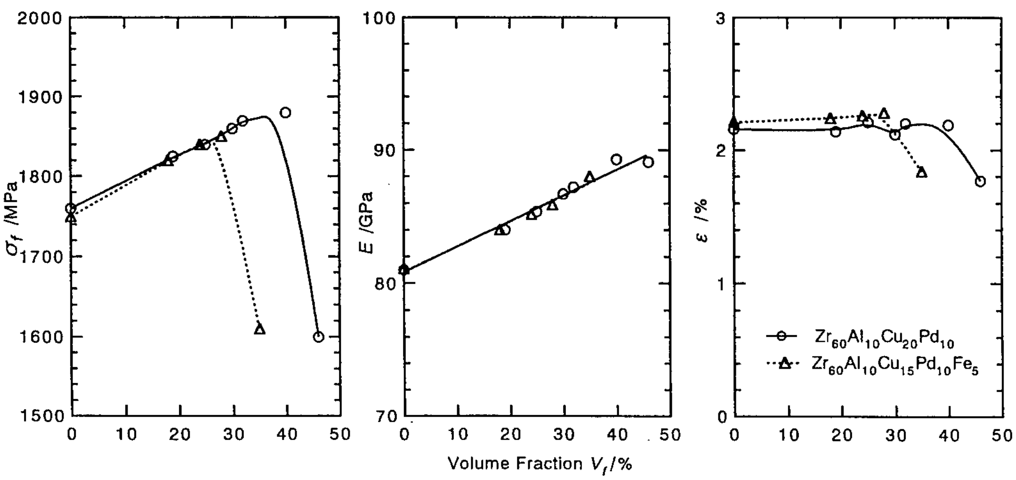

Fig. 7 Changes in the σ_f, E and ε with V_f of the Zr_2Cu for cast bulk amorphous $Zr_{60}Al_{10}Cu_{20}Pd_{10}$ and $Zr_{60}Al_{10}Cu_{15}Pd_{10}Fe_5$ alloys.

Here, it is important to discuss the reason why the Pd- and Au-containing alloys can contain the nanoscale $Zr_2(Cu, Pd)$ or $Zr_2(Cu, Au)$ phase in coexistence with the remaining amorphous phase. The grain size of the Zr_2Cu type compound is in the range of 400 to 500 nm for the Zr-Cu-Al alloy and decreases to about 5 nm for the Pd- and Au-containing alloys. In order to evaluate the crystallization behavior, the DSC curves were obtained for the three kinds of alloys subjected to various isothermal annealing treatments. The data were analyzed in the framework of the Johnson-Mehl-Avrami relation (8) which can be applied to the present crystallized structure. The data in the crystallized fraction between 0.2 to 0.8 have a good linear relation in the plot of ln{-ln(1-y)} versus ln(t). Here, y is the crystallization fraction and t is the annealing time which does not include an incubation time. The gradient of the linear relation corresponds to the Avrami exponent (n-value)(9). The n value is in the range of 3.3 to 3.4 for the Zr-Al-Cu alloy, 3.4 to 3.6 for the Zr-Al-Cu-Pd alloy and 3.2 to 3.3 for the Zr-Al-Au-

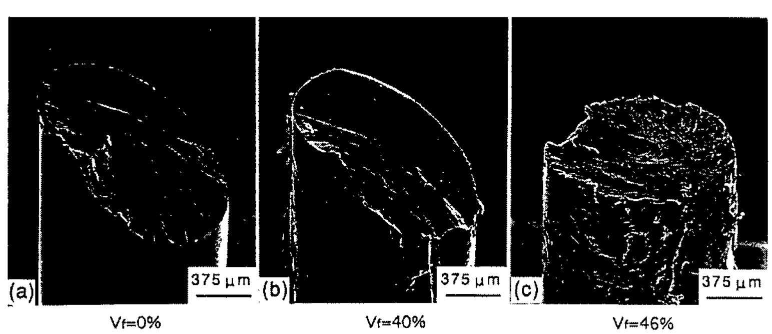

Fig. 8 Tensile fracture surface appearance of the cast bulk amorphous $Zr_{60}Al_{10}Cu_{20}Pd_{10}$ alloy. (a) V_f=0%, (b) V_f=40%, and (c) V_f=46%.

Cu alloy. These n-values indicate that the Zr-Al-Cu ternary amorphous alloy crystallizes in the polymorphic mode with a decreasing nucleation rate while the crystallization of the Pd- and Au-containing amorphous alloys takes place by the diffusion-controlled growth mechanism in which the precipitates growing from small dimensions have an increasing nucleation rate (10). Thus, the nucleation rate of the Pd- and Au-containing alloys is in good contrast to that for the Zr-Al-Cu alloy. Furthermore, we evaluate the activation energy for crystallization by the two different methods using the Arrhenius and the Kissinger (11) plots. The activation energy (E_c) obtained by the Arrhenius method is 2.0eV for the Zr-Al-Cu alloy, 3.6eV for the Zr-Al-Pd-Cu alloy and 3.8eV for the Zr-Al-Au-Cu alloy, indicating that the E_c values of the Pd-containing alloys are much larger than that for the Zr-Al-Cu alloy. The similar significant difference in E_c between the Pd-containing alloys and the Zr-Al-Cu alloy is also recognized in the use of the Kissinger analysis. The significant difference indicates that the crystallization of the Zr-Al-Cu amorphous alloys becomes difficult by the addition of Pd. Considering that the nucleation of the Zr_2Cu phase becomes easy by the addition of Pd, the increase in E_c is concluded to result for the retardation of the growth reaction of the Zr_2(Cu, M) phase.

Based on the above-described experimental data, a schematic illustration of the formation process of nanocrystalline Zr_2(Cu, Pd) phase surrounded by the remaining amorphous phase upon isothermal annealing is shown in Fig. 9. The addition of Pd into the Zr-Al-Cu alloy induces preferential cluster of Zr-Pd pair because of the much larger negative heats of mixing (7) and the Zr-Pd atomic cluster seems to act as preferential nucleation sites of Zr_2(Cu, Pd) phase. However, the subsequent growth reaction of the Zr_2(Cu, Pd) phase is sluggish because of the necessity of the redistribution of Al element into the remaining amorphous phase, the increase in the thermal stability of the remaining amorphous phase and the enrichment of Al element at the amorphous/Zr_2(Cu, Pd) interface. The simultaneous satisfaction of the ease of cr-

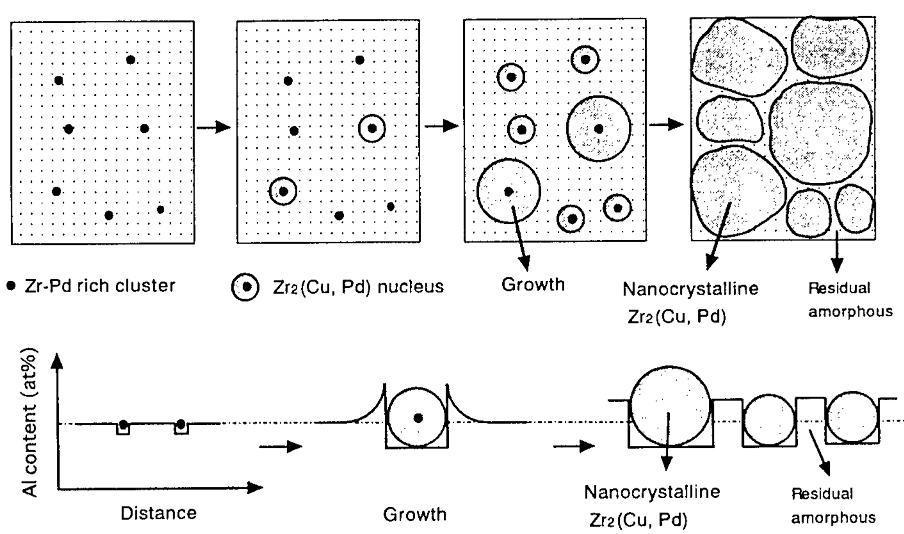

Fig. 9 Schematic illustrations showing the formation process of nanocrystalline Zr_2(Cu, Pd) phase surrounded by residual amorphous phase and showing the change in the Al concentration in the Zr_2(Cu, Pd) and remaining amorphous phases during isothermal annealing.

ystal nucleation, the retardation of crystal growth and the increase in the stability of the remaining amorphous phase against crystallization by the addition of Pd or Au is concluded to be the reason for the achievement of the nanocrystallization for the Zr-based bulk amorphous alloys.

Finally, it is important to discuss the reason why the nanostructure alloys consisting of $75\%V_f$ and $25\%V_f$ of $Zr_2(Cu, Pd)$ and remaining amorphous phases exhibit high tensile strength combined with good bending ductility. It was pointed out that the remaining amorphous phase in coexistence with $Zr_2(Cu, Pd)$ exhibits the glass transition and supercooled liquid region. Besides, the annealing treatment was performed by heating in the supercooled liquid region, followed by water quenching. Consequently, the remaining amorphous phase can contain again the free volumes by the water quenching treatment from the supercooled liquid. The reentrance of free volumes is thought to give the maintenance of good ductility to the remaining amorphous phase. The critical V_f leading to the ductile/brittle transition is considerably higher for the melt-spun ribbon samples than for the cast bulk samples. The difference is presumably because the ribbon samples have a higher cooling rate during water quenching from the supercooled liquid and can contain a larger amount of free volumes as compared with the bulk amorphous alloys with lower cooling rates.

CONCLUSIONS

In conclusion, the bulk nanocrystalline alloys have the following features; (I) The structure can be regarded as a new type of mixture consisting of nanoscale compound grains and amorphous intergranular phase, and (II) The deformation of the mixed phase alloys by bending or tensile stress occurs by sliding in the amorphous intergranular phase. Consequently, this is the first synthesis of high-strength and high-ductility alloys via amorphous intergranular sliding among intermetallic compounds at room temperature.

REFERENCES

1. A. Inoue, *Bulletin Japan Inst. Metals*, 1997, 36, 926.
2. A. Inoue, *Mater. Trans., JIM*, 1995, 36, 866.
3. A. Inoue, *Mater. Sci. Forum*, 1995, 691, 179-182.
4. C. Fan and A. Inoue, *Mater. Trans., JIM*, 1997, 38, 1040.
5. C. Fan, A. Takeuchi and A. Inoue, *Mater. Trans., JIM*, 1999, 40, in press.
6. T. B. Massalski, *Binary Alloy Phase Diagrams*, 2nd ed., ASM, Materials Park, Ohio, 1990.
7. F. R. de Boer, R, Boom, W. C. M. Mattens, A. R. Miedema and A. K. Niessen, *Cohesion in Metals*, Vol. 1, Nouth-Holland, Amsterda, 1988.
8. W. A. Johnson and R.F. Mehl, *Trans. AIME*, 1939, 135, 416.
9. F. S. Ham, *J. Appl. Phys.*, 1959, 30, 1518.
10. Christian, J. W., *The Theory of Transformations in Metals and Alloys*, Pergamon Press, Oxford, 1975, p. 542.
11. H. E. Kissinger, *Anal. Chem.* 1957, 29, 1702-1706.

Pergamon

NanoStructured Materials, Vol. 12, pp. 751–756, 1999
Elsevier Science Ltd

0965-9773/99/$–see front matter

PII S0965-9773(99)00230-5

MECHANICAL PROPERTY OF HIGH DENSITY NANOCRYSTALLINE GOLD PREPARED BY GAS DEPOSITION METHOD

H. Tanimoto*, S. Sakai and H. Mizubayashi
Institute of Material Science, University of Tsukuba, Tsukuba, Ibaraki 305-8573, Japan
*Now at: Universität Stuttgart, Institut für Theoretische und Angewandte Physik,
Paffenwaldring 57, 70550 Stuttgart, Germany

Abstract – *High density nanocrystalline gold (n-Au) specimens were prepared by the gas deposition method. The Young's modulus of n-Au is higher than* $0.94E_{crys}$, *suggesting* $E_{GB}/E_{crys} \approx 0.7$ *to 0.8, where* E_{GB} *and* E_{crys} *denote the Young's modulus of the grain boundary region and bulk-Au, respectively. Plastic deformation process at 300K in n-Au is governed not only by mean grain size but also by strain rate. The deformation map is proposed.*
©1999 Acta Metallurgica Inc.

INTRODUCTION

Atomic structures in grain boundary (GB) regions in nanocrystalline (n-) materials may, in general, differ much from those found in conventional polycrystalline materials (bulk materials, hereafter), and a volume fraction of the GB regions increases with decreasing grain size. Thus the properties of n-materials are expected to reflect much those of the GB regions (1,2). In n-metals, the mechanical property may be sensitive to that of the GB regions as well as grain size, d. Since the early days of n-metals research, much attention has been devoted to the mechanical properties, where the Hall-Petch relation predicts an increase in strength in proportion with $(1/d)^{0.5}$ and on the other hand, a decrease in elastic moduli is expected because of an increased fraction of atoms in grain boundaries. Most reports on Vickers microhardness tests indicate an increase in the Vickers microhardness, H_v, with increasing $(1/d)^{0.5}$ in the grain size range from about 10 nm to 100 nm and saturation or a decrease of H_v in the range of smaller grain sizes (3-12). For the elastic property, the pioneering works report a drastic decrease in the elastic moduli of n-metals ((3-6, 13-15), and see Table 1 in (16)). However, the combination of the increase in H_v with increasing $(1/d)^{0.5}$ and the drastic decrease in the elastic moduli brings a strange view that dislocations under high stress can be trapped by very soft GB. To clarify this issue, we carried out both the elasticity and the plasticity measurements on n-Au.

EXPERIMENTAL

Nanocrystalline gold (n-Au) specimens were prepared by the gas deposition method (see (16,17)). Table 1 compiles the density and the mean grain size, d, of n-Au specimens. The

TABLE 1
Density of Nanocrystalline Au Specimens (bulk-Au : 19.32 g/cm^3)

measurement method	sample	density (g/cm^3)
Archimedes' method	n-Au (60 nm)	$20.1\ ^{+0.6}_{-1.4}$
shape and weight	n-Au (20-60 nm)	19.3 ± 0.8

density was evaluated by the Archimedes' method and/or from mass and shape. The density of n-Au specimens shows good agreement with that reported for bulk Au. TEM observations made for some n-Au specimens indicate no detectable pore. *d* was estimated from X-ray diffraction profiles and the Scherrer's method. The mean lattice spacing observed for n-Au specimens shows good agreement with that reported for bulk Au. Evaluation for contamination of n-Au specimens during preparation was conducted by thermal desorption for gaseous elements and by EPMA for heavy elements. H_2O and a small amount of H_2 are detected, where the amount of H_2O can be explained when we assume that the specimen surface is covered by monolayer of H_2O. In contrast, EPMA indicates no detectable contamination by heavy elements. See (16) for the apparatuses for elastic and plastic measurements.

RESULTS AND DISCUSSION

Figure 1 shows the dependence of the Young's modulus, *E*, of n-Au specimens on the measuring temperature, *T*, where we plotted the data evaluated from tensile test for three n-Au specimens, that from vibrating reed measurement on a n-Au specimen and *E* reported for bulk-Au. Below about 200 K, the *E* vs *T* data observed for n-Au specimens is very similar to

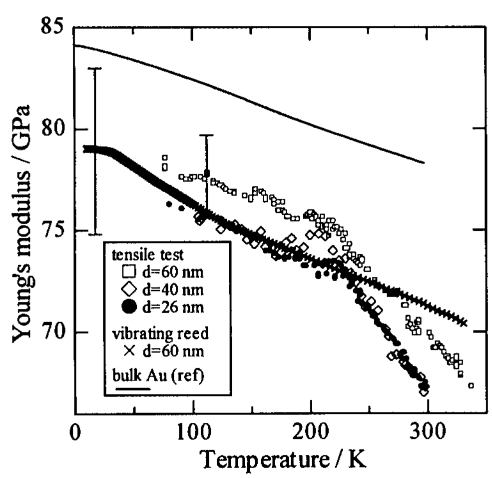

Fig. 1. *E* vs. *T* observed in n-Au specimens (see text).

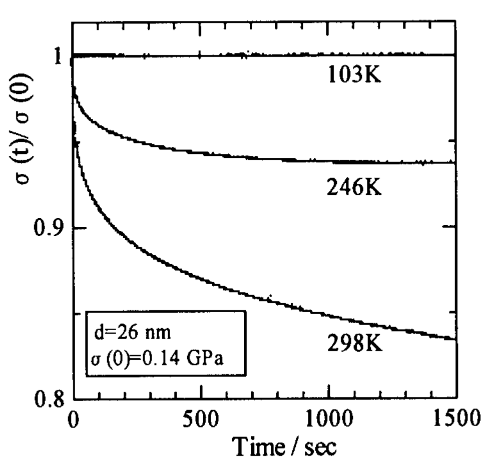

Fig. 2. An example of stress relaxation in a n-Au specimen.

TABLE 2
The Young's Modulus of n-Au Samples

method	n-Au		bulk-Au
	grain size (nm)	E (GPa)	E (GPa)
tensile test	60	79.5±2(80 K) *	84 (80 K)*
	26-40	77.5±2(80 K) *	
vibrating reed	60	79.0±4 (20 K)	84 (20 K)

* after the subtraction of the modulus defect of -1GPa.

that of bulk-Au except that E of n-Au specimens is lower by several percents than of bulk-Au. Within the experimental accuracy, E found in tensile tests and vibrating reed measurements shows good agreement with each other. For tensile tests, E of n-Au specimens tends to decrease with decreasing d. The E data found in the present work are listed in Table 2, where the modulus defect associated with the internal friction peaks below 100K (see (16) for details) is subtracted.

As seen in Fig. 1 and Table 2, E found in low T in the n-Au specimens is higher than 94 % of bulk Au. E observed at RT in high-density n-Cu and n-Pd specimens (18) is also higher than 85 % of bulk counterpart. It is considered that the anelastic process at RT (14) is partly responsible for the relatively lower values found in (18). E of n-Au specimens listed in Table 2 will be discussed below. We suppose that a n-Au sample is composed of the GB region with the effective thickness t_{GB} and the remaining crystalline region with the mean diameter (d - t_{GB}), where volume fractions of the regions are counted as ($1 - R_{cry}$) and R_{cry} with $R_{cry}=[(d - t_{GB})/d\,]^3$, respectively. We further assume that the Young's modulus E_{cry} of the inner crystallite region is the same to that in bulk Au, and the Young's modulus E_{GB} in the grain boundary region can be defined. Then under rule of thumb, we evaluate E of a n-Au specimen as a composite material under the condition that the stresses are uniform while the strains are additive. For the experimental values, we evaluate E for the n-Au specimens with d=33 (as the mean value for 26 to 40) nm and for the n-Au specimens with d=60 nm listed in Table 2. Although a recent molecular dynamics simulation for n-Cu (19) suggests t_{GB} in n-Cu being about 1 nm, the E vs. d data found in n-Au appears to be explained for t_{GB} being 2 to 3 nm, where E_{GB}/E_{crys} is evaluated as 0.7 to 0.8. The present ratio of E_{GB}/E_{crys} being 0.7 to 0.8 is similar to the ratio between the amorphous and crystalline states for alloys, but is much higher than the values estimated in the pioneering works (3-6, 13-15).

In Fig. 1, above about 200 K, E of n-Au specimens observed in tensile tests shows a rapid decrease with increasing temperature. The similar dependence of E on T is again observed in the vibrating reed measurements except that its slope becomes steeper above about 250 K with a smaller decreasing rate, suggesting that the anelastic process above about 200 K is a thermally activated relaxation with a non-linear relaxation strength. This is more clearly displayed in Figure 2 which shows an example of the stress relaxation measurements on tensile tests in the elastic range. Stress relaxation is not detected at 103 K, but is found above about 200 K. The stress relaxation is not of a single relaxation, but is accelerated as a whole with increasing T. On the other hand, the 20 MeV proton irradiation experiments at low temperatures indicate that dislocations are not responsible for the anelastic process above about

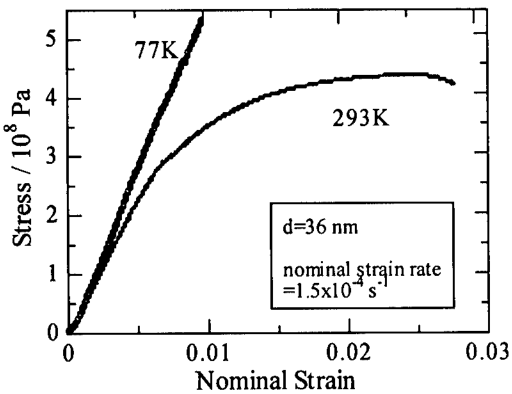

Fig. 3. Examples of tensile tests on a n-Au specimen.

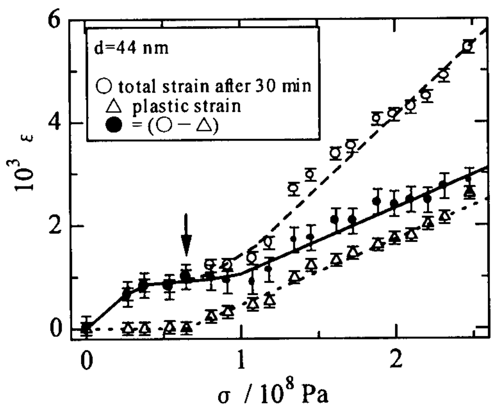

Fig. 4. Creep tests under a given stress made at RT in n-Au specimens.

200 K in n-Au (17). After these results, we surmise that a certain atomic process in the grain boundary region is responsible for the anelastic process above 200 K.

Figure 3 shows tensile tests at 77 and 293 K on a n-Au specimen, where the linear elasticity is found at 77 K in a wide strain range below 1 %, but at 293 K plastic deformation starts at strain of about 0.5 %. In tensile test at 300K, n-Au specimens show a fracture strain of 1.5-3%, and the yield stress and tensile strength are about 3 times as large as those in annealed bulk-Au specimens. However, the plastic deformation process in n-Au depends on strain rate. Figure 4 shows the results of creep tests under a given stress observed for n-Au specimens at RT. Plastic strain reveals above a threshold stress (see the arrow in Fig. 4), and shows a linear increase with stress beyond the threshold stress. Recoverable strain (anelastic strain) shows a complicated change with stress. We further measured the stress dependence of the strain rate at the steady state on stress with the results shown in Figure 5. In Fig. 5, the linear relationship between the strain rate and stress is found in the stress range indicated by arrows 1 (threshold) and 2 (upper limit), suggesting the Coble-type creep (20).

In contrast, for short term tests, an increase in Vickers microhardness, H_v, with decreasing d is observed. Figure 6 shows the Hall-Petch plot for the results of tests performed at RT with indentation load of 10 gf and loading time of 10 s. Thickness and d of the n-Au specimens used are 10 to 60 μm and 15 to 60 nm, respectively, and the indentation was made more than twenty times for every n-Au specimen. Although the number of data points are limited, the present results appear to be explained by the Hall-Petch relation. The results shown in Fig. 3 to 6 indicate that the preferable deformation process varies with d, strain rate and T. Above about 200 K, plastic deformation of n-Au is mainly governed by two different manners; slow process by creep associated with GB and rapid process by such as dislocation motion. In Figure 7, we schematically depict the deformation map in n-Au at RT, where the lower and upper bounds of $1/(d)^{0.5}$ are assumed to correspond with coarse grained Au and n-Au with $d \approx 10$ nm, respectively. The line AB denotes the Hall-Petch relation expected in short term tests and the line BD depicts an increasing role of the Coble creep with decreasing strain rate. Along the line CD, the yield stress shows an increase with increasing $1/(d)^{0.5}$ at first and

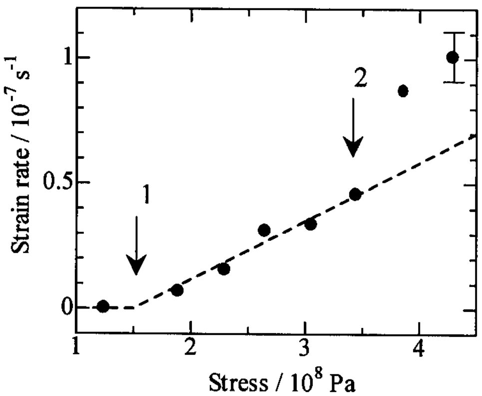

Fig. 5. Strain rate found in the steady state creep on the stress-control tests which were conducted at RT for n-Au specimens with $d \approx 36$ nm. See text.

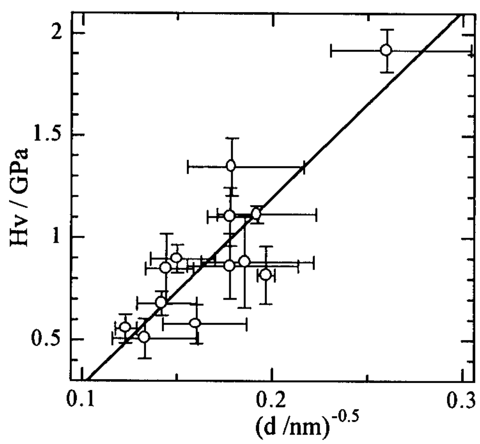

Fig. 6. The H_V vs. $(d)^{0.5}$ data observed at RT for n-Au specimens. The solid line shows a gradient k=9.2 GPa/nm$^{0.5}$. See text.

then turns to decrease with increasing role of the Coble creep for higher $1/(d)^{0.5}$. Since the present experimental range is limited, the further speculation is premature. However, it is noted that the role of creep on the plastic deformation behavior of n-metal is stirring up many interests [21-24]. To clarify the origin for the elastic and plastic properties of n-Au, the further work is now in progress.

CONCLUSION

The Young's modulus of high-density n-Au specimens with mean grain size of 26 to 60

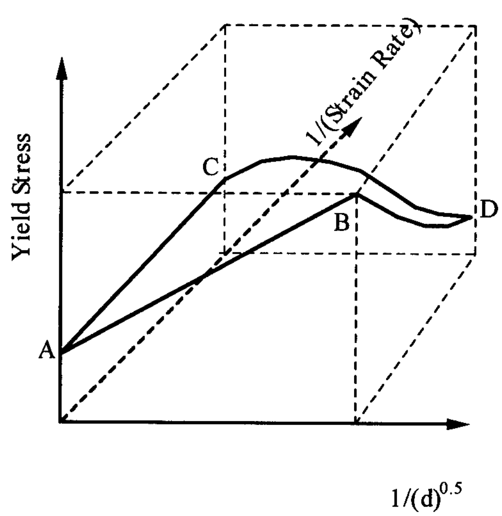

Fig. 7. A schematic drawing for the dependence of the yield or flow stress near RT on the inverse of the deformation rate and $(1/d)^{0.5}$ supposed for n-Au.

nm is higher than 95 % of that in bulk Au. For plasticity near RT, the Hall-Petch relationship is observed for n-Au specimens with mean grain size of 15 to 60 nm in the Vickers microhardness tests with holding time of 10 s. In contrast, plastic deformation with low strain rate proceeds through the Coble-type creep, indicating that the preferable plastic deformation process in n-Au is governed by mean grain size, strain rate and temperature.

Acknowledgement--The authors would like to thank Prof. E. Kita for his invaluable help on the course of experiments. This work is partly supported by Tsukuba Advanced Research Alliance at University of Tsukuba.

References

1. R. Birringer, U. Herr, and H. Gleiter, Phys. Lett., 102A, 365(1984).
2. H. Gleiter, Prog. Mater. Sci., 33, 223(1989).
3. G.W. Nieman, J.R. Weertman and R.W. Siegel, Scripta Metall., 23, 2013(1989).
4. G.W. Nieman, J.R. Weertman and R.W. Siegel, Nanostruct. Mater., 1, 185(1992).
5. J.R. Weertman, Mat. Sci. Engning., A166, 161(1993).
6. N.P. Kobelev, Ya.M. Soifer, R.A. Andrievski and B. Gunther, Nanostruct. Mater., 2, 537(1993).
7. A. Kumpmann, B. Gunther and H.-D. Kunze, in *Mechanical Properties and Deformation Behavior of Materials Having Ultra-Fine Microstructures*, Edited by M. Nastasi et al. (Kluwer Academic Pub., Amsterdam, 1993), p. 309.
8. J.R. Weertman and P.G. Sanders, Solid State Phenomena, 35-36, 249(1994).
9. R.W. Siegel, Nanostruct. Mater., 4, 121(1994).
10. R.W. Siegel and G.E. Fougere, Nanostruct. Mater., 6, 205(1995) .
11. X.Y. Qin, X.J. Wu and L.D. Zhang, Nanostruct. Mater., 5, 101(1995).
12. E. Bonetti, L. Pasquini and E. Sampolesi, Nanostruct. Mater., 9, 611(1997).
13. D. Korn, A. Morsch, R. Birringer, W. Arnold and H. Gleiter, J. Phys. (Paris), 49, C5-769(1988).
14. M. Weller, J. Diehl and H.-E. Schaefer, Phil. Mag. A, 63, 527(1991).
15. P.G. Sanders, A.B. Witney, J.R. Weertman, R.Z. Valiev and R.W. Siegel, Mat. Sci. Engng., A 204, 7(1995).
16. S. Sakai, H. Tanimoto and H. Mizubayashi, Acta Mater., submitted.
17. H. Tanimoto, H. Mizubayashi, H. Fujita and S. Okuda, J. Phys. IV (Paris), 6, C8-1999 (1996) .
18. P.G. Sanders, J.A. Eastman and J.R. Weertman, Acta Mater., 45, 4019(1997).
19. S.R. Phillpot, D. Wolf and H. Gleiter, J. Appl. Phys., 78, 847(1995).
20. R. Rai and M.F. Ashby, Met. Trans., 2, 1113(1971).
21. R.Z. Vliev, Mater. Sci. Engng., A 234-236, 59(1997).
22. P. Sanders, C.J. Youngdahl and J.R. Weertman, Mater. Sci. Engng., A 237, 77(1997).
23. N. Wing, Z. Wang, K.T. Aust and U. Erb, Mater. Sci. Engng., A 237, 150(1997).
24. M.N. Rittner, J.R. Weertman, J.A. Eastman, K.B. Yoder and D.S. Stone, Mater. Sci. Engng., A 234-236, 185(1997).

Pergamon

NanoStructured Materials, Vol. 12, pp. 757–762, 1999
Elsevier Science Ltd

0965-9773/99/$–see front matter

PII S0965-9773(99)00231-7

COLLECTIVE GLASS STATE IN A MAGNETIC NANOPARTICLE SYSTEM

J.L. Dormann[1†], D. Fiorani[2], R. Cherkaoui[1], L. Spinu[1], F. Lucari[3], F. D'Orazio[3], M. Noguès[1], E. Tronc[4], J.P. Jolivet[4], A. Garcia[2]

[1]LMOV, CNRS-Université de Versailles, 78035 Versailles cedex, France
[2]ICMAT, CNR, C.P. 10, 00016 Monterotondo Stazione, Roma, Italy
[3]INFM, Dip. Di Fisica, Università, 67100 L'Aquila, Italy
[4]LCMC, CNRS-Université Pierre et Marie Curie, 75252 Paris cedex 05, France

Abstract -- *Studies of static and dynamic properties of γ-Fe_2O_3 particle (5 nm) assemblies reveal the existence of three magnetic regimes with increasing strength of the interparticle interactions: pure superparamagnetic for very weak interactions, modified superparamagnetic for weak-medium interactions, and collective for strong interactions. The last presents a low-temperature state similar to the spin-glass state, but the glass transition shows distinct features. ©1999 Acta Metallurgica Inc.*

INTRODUCTION

Since Néel's pioneering work [1] some fifty years ago, the properties of ferromagnetic fine grains have been widely investigated [2], with both technological and academic motivations. However, the basic effects of the interparticle interactions are still debated. The problem is extremely complex, in particular because of the complexity of the real nanoparticle assemblies, with disordered arrangement, volume distribution, and easy axes in random orientation.

If the interactions are negligible, pure superparamagnetic relaxation occurs. With decreasing temperature, a collection of blocking processes occurs according to the distribution of the anisotropy energy barriers of the particles and the characteristic time, τ_m, of the measurement. The dynamical properties [3-5] are well described by the Néel-Brown model [2]. If the interactions become appreciable, the blocking processes are no longer independent. However, if the interactions are not too strong, one can still define the energy for an individual particle [2,6]. Due to the interaction-induced modifications, this energy presents a multivalley structure with many secondary minima superimposed on two main minima (in uniaxial symmetry). In the Néel-Brown model, the relaxation time is stated as depending only of the potential values at the minima and the saddle point, independently of the possible pathways, so this model is still valid, and the properties are well described [3-6] using our model [2,6] accounting for the interaction effect, which leads to a net increase of the energy barrier with respect to the noninteracting case. If the interactions are sufficiently strong [5,7-9], the relaxation processes become so correlated that the dynamics cannot be described by any adaptation of the

superparamagnetic model. The set of the individual energy double-wells has been replaced by a multivalley energy structure of the whole assembly. The nature and the properties of this collective regime are discussed. In particular the existence of a low-temperature spin-glass (SG)-like state, possibly with a thermodynamic phase transition, is debated. SG-like order has been suggested on the basis of the observation [5,8] of some dynamical properties similar to those of spin glasses, i.e., critical slowing down of the relaxation time at finite temperature, aging effect in the relaxation of the zero-field-cooled magnetisation. However, the last is not specific of canonical spin glasses and no definitive proof of the occurrence of a phase transition has yet been provided.

In this context, with the aim of clarifying the similarities to the spin-glass state, we report studies of static and dynamic properties of γ-Fe_2O_3 particles particle assemblies with the same size distribution and varying interparticle distance.

EXPERIMENTAL

The samples were prepared from a stock cationic aqueous sol of γ-Fe_2O_3 particles (ClO_4^- counterions, pH~2), practically free from aggregation, prepared according to references 9 and 11. Samples IF and IN were obtained by adding a given sol fraction into a variable volume of an aqueous solution of polyvinylic alcohol (PVA) with controlled pH and drying the mixture in air. Sample Floc was obtained by flocculating the sol at pH 8 and dispersing the precipitate in PVA. Sample Powder was obtained by drying the precipitate over P_2O_5. The particles are spheroidal, with average diameter $D = (6<V>/\pi)^{1/3} = 4.7$ nm where $<V>$ is the mean of the volume distribution, log normal in type, as deduced by transmission electron microscopy. The average centre-to-centre distance d_{cc} between neighbouring particles is ca. 21 nm and 7.3 nm in samples IN and IF, respectively, as deduced from the particle volume fraction of 0.007 and 0.196. d_{cc} is estimated at ca 6.8 nm in sample Floc. It is slightly larger than D in sample Powder, due to the remaining adsorbed water layer (~5 wt %).

Mössbauer spectra (4.2–300 K) were recorded using a conventional spectrometer. Ac-susceptibility (χ_{ac}) measurements at 1 Oe were performed in the 5–10^4 Hz frequency (ν) range with a commercial susceptometer. Field-cooled (M_{FC}) and zero-field-cooled (M_{ZFC}) magnetisations (5–300 K, 1–100 Oe) were measured using a SQUID magnetometer. M_{ZFC} relaxation (10 Oe) was measured for two waiting times (250 or 3600 s) before applying the field. Samples IF, IN and Floc were thick-film-shaped and all measurements were performed with the applied field parallel to the sample plane in order to minimize the demagnetising field.

RESULTS AND DISCUSSION

Mössbauer spectra of samples IN and Powder are shown in Figs.1a and 1b, respectively. Samples IF and Floc yield features similar to those observed for sample IN. For these three samples, the spectral evolution can roughly be described in terms of a quadrupole doublet and a magnetically-split pattern in temperature-dependent proportions. This is typical of superparamagnetic relaxation with a distribution of relaxation times τ. The doublet arises from the

superparamagnetic particles (τ shorter than the lower limit of the τ_m window) and the magnetic pattern results from the blocked particles (τ longer than the upper limit of the measuring time,τ_m,window).

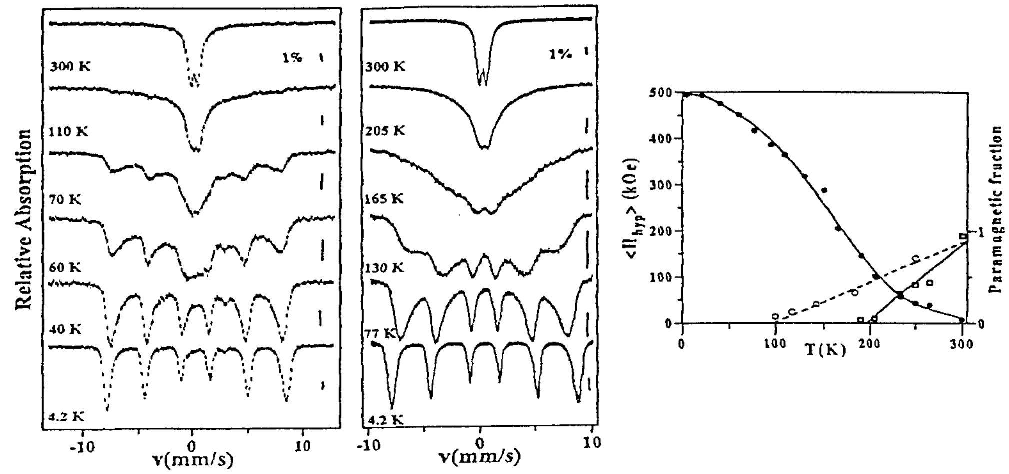

Fig.1. Mössbauer spectra of (a) sample IN; (b) Powder. (c) Average hyperfine field and superparamagnetic fraction vs temperature in sample Powder (--) and IN (- - -) (temperature scaling factor of 1.67). Lines as visual aid.

The spectra were analysed with a simple model [11] including a broadened single line accounting for the intermediate τ values. Good fits allowed us to determine T_B as a function of V for $\tau_m \sim 10^{-8}$ s. For sample Powder, the spectral evolution is completely different. No coexistence of the before-mentioned patterns is observed and perturbed spectra prevail in the intermediate temperature range. We modelled the spectra using a hyperfine-field (H_{hyp}) distribution. The variation of the average is shown in Fig.1c. The non-magnetically split components ($H_{hyp} < \sim 50$ kOe) can be modelled by a broadened singlet and/or a superparamagnetic doublet, detected above 165–190 K and 190–205 K, respectively. At 300 K, only the doublet remains. The variation of the superparamagnetic fraction is shown in Fig. 1c. The data relative to sample IN have been included with a temperature scaling factor of 1.67 for the sake of comparison.

According to the superparamagnetic model [2], the temperature T_{max} of the maximum of the real part (χ'_{ac}) of χ_{ac} is the blocking temperature T_B of a particle with volume $V_c = R\langle V^2\rangle/\langle V\rangle$, for $\tau_m = 1/\nu$. The R value (~1–2) depends essentially on the width of the V distribution, so it can be taken the same (1.3) in the four samples. The resulting $\log_{10}\tau_m$ vs $1/T_B$ variations, including Mössbauer data, are shown in Fig.2a. For sample IF, the Néel-Brown model [2] is quantitatively verified with $E_{Ba}/k = 555$ K and $\eta_r = 0.3$, where E_{Ba} is the energy barrier, k is Boltzmann's constant, and η_r the reduced damping constant. The E_{Ba} value is well consistent with a previous study [13] of IF-type samples with varying particle size, which showed that the energy barrier for the noninteracting particle comes mainly from the surface anisotropy (anisotropy constant of 0.05±0.01 erg/cm^2). For samples IN and Floc, the data can still be described by the Néel-Brown model with the energy barrier increasing according to our model

[2,6]. Assuming a close-packed arrangement, we find an increase per nearest neighbour, due to nearest-neighbour interactions, equal to $E_{B1}/k \sim 80$ K (IN) and 125 K (Floc).

For sample Powder, T_{max} is much higher than for the other samples. Its variation with ν is much weaker and cannot be described by the Néel-Brown model including any interaction term

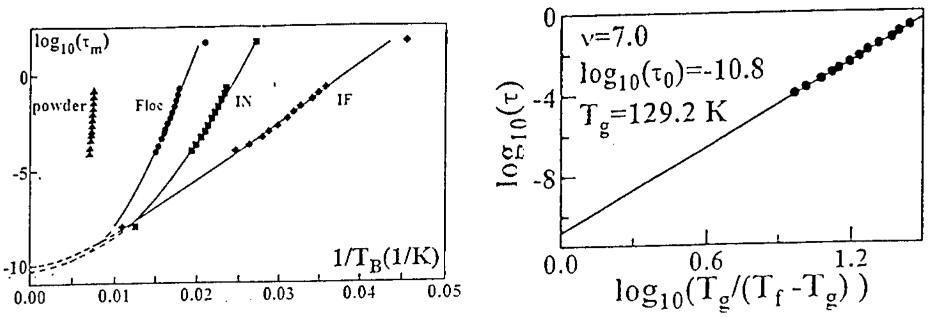

Fig. 2 a) Thermal variation of the relaxation time. Fits with the superparamagnetic model; b) ac susceptibility as a function of the frequency in sample Powder. Inset: thermal variation of the relaxation time according to a power law.

A dynamic scaling analysis according to a power law $\tau = \tau_0\, [T_g/(T_{max}-T_g)]^z$ yielded a good fit (Fig.2b) for $T_g = 129.2\pm0.3$ K, $\tau_0 = 10^{-10.7\pm0.2}$ s and $z = 7.0\pm0.3$, the last being similar to the exponent reported [14] for spin glasses and obtained by Monte-Carlo simulations. This suggests a homogeneous dynamical process, i.e. a collective freezing of particle moments, similar to the spin freezing in SG showing a phase transition. T_{max} is no longer a blocking temperature, but a freezing temperature. These features allow us to interpret [16] the thermal evolution of the Mössbauer spectra (Figs.1b,1c), in a way similar to that used for Au-3%Fe [15], by scaling the temperature by a factor of 0.12. Because of the ferrimagnetic order and very high Curie temperature inside the particle, and because of the H_{hyp} variations are too large to be solely due to surface effects, we can rule out a static explanation. In SG, a wide spectrum of relaxation times, τ, occurs below T_g [14]. Then it is likely that the observed spectral shapes are mainly due to relaxation between different energy valleys, leading to perturbed spectra, when τ is inside the τ_m window ($\sim 5\times10^{-10} - 2\times10^{-7}$ s, but dependent on the relaxation process), which can be modelled using a H_{hyp} distribution. Above T_g the up-down relaxation appears. The singlet and doublet in temperature-dependent proportions indicate a τ distribution. This contrasts with spin glasses and is related to the superparamagnetic state, different from the paramagnetic one, because of its inherent τ distribution. However, this distribution is narrower than in the other samples (blocking process), as revealed (Fig. 1c) by the faster temperature variation of the superparamagnetic fraction. This means that the transition to superparamagnetism keeps the memory of the collective state, as expected.

A static critical scaling with the same critical temperature as the critical slowing down of the relaxation time would be a definitive proof of a phase transition. In spin glasses, this is provided by the power-law divergence of the nonlinear susceptibility, χ_{nl}, on approaching T_g, because χ_{nl} is directly related [14] to the spin-glass order parameter. At $T > T_g$, χ_{nl} is given by $\chi_{nl} = 1 - M/(\chi_0 H)$ where the magnetisation M can be expanded in odd powers of the field H, as $M = (\chi_0 H) - a_3(T)(\chi_0 H)^3 + a_5(T)(\chi_0 H)^5 - \ldots$, and χ_0 is the linear susceptibility, which follows

a Curie or a Curie-Weiss law. The a coefficients exhibit a critical behaviour with power-law divergence at T_g (e.g. $a_3 \sim [T_g/(T-T_g)]^\gamma$). For a paramagnet, the a coefficients are temperature independent. For an assembly of fine particles in the superparamagnetic regime, $\chi_0 = \chi_{sp} = C_{sp}/(T-\theta_{sp})$, where C_{sp} and θ_{sp} are the superparamagnetic Curie constant and temperature, respectively, which depend

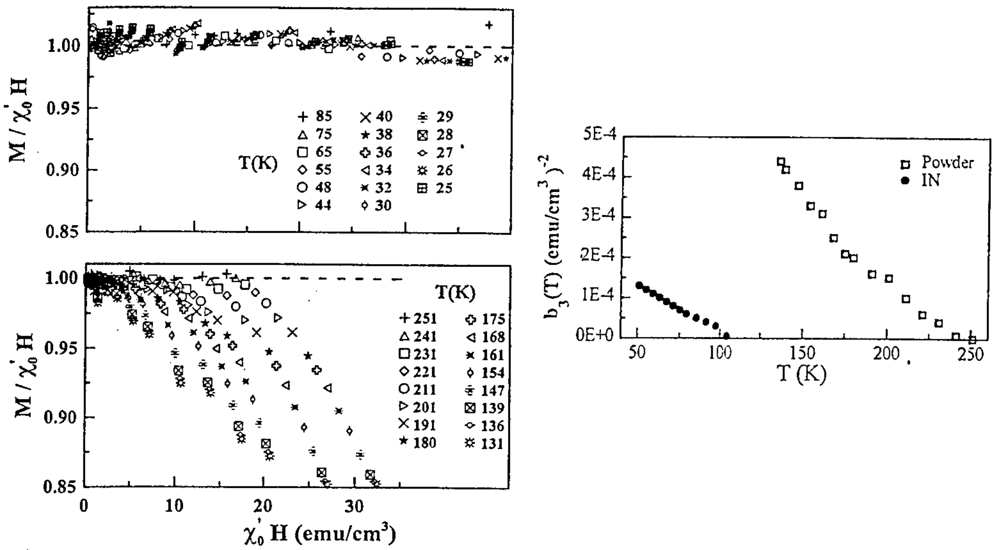

Fig.3. $M/(\chi_0'H)$ vs $(\chi_0'H)$ (see text) for samples IF (a) and Powder (b). Thermal variation of the nonlinear term b_3 in the field expansion of the magnetisation in samples IN and Powder (c).

on the sample parameters [2]. This formula is valid for uniaxial particles, provided that the susceptibility is field independent. This is not verified in any of our samples, probably because of the complex magnetic state of the surface. Very good fits to the experimental data were obtained for $\chi_0' = \chi_{sp} = C_{sp}/(T-\theta_{sp}+aH)$, where a is a constant characteristic of the particle. Thus, we expanded M as $M = (\chi_0'H) - b_3(T)(\chi_0'H)^3 + b_5(T)(\chi_0'H)^5 - ....$ and considered the $M/(\chi_0'H)$ vs $(\chi_0'H)$ variation at different temperatures. In the absence of nonlinear effects, we expect $M/(\chi_0'H) \sim 1$ over the range of validity of the χ_{sp} formula. The analysis was performed for M_{FC} and M_{ZFC} measured at different fields and temperatures above the M_{ZFC}-peak temperature. The results [5] show no difference between the two processes. For sample IF (Fig. 3a), the data for all fields and all temperatures are on a unique curve, which corresponds to $M/(\chi_0'H) \sim 1$, as expected for (quasi-)noninteracting particles. For sample Powder (Fig. 3b), the data do not overlap and strongly deviate from $M/(\chi_0'H) = 1$. The deviations are much weaker for sample IN. The thermal variation of b_3 is shown in Fig. 3c (b_5 is much smaller and its thermal variation is much weaker). The increase of the nonlinear effects from sample IF to IN and Powder clearly indicates growing interparticle correlations. The clear effect in the latter sample supports a low-temperature collective state. However, the increase of b_3, quasi-linear, is much smaller than in canonical spin glasses [14].

At $T < T_g$, the SG dynamics is characterized [18] by extremely low relaxation processes which make the dynamics dependent on the total age of the system, as revealed for instance by

aging effects on the relaxation of M_{ZFC}. In sample IF, at all investigated temperatures the relaxation of M_{ZFC} [5] follows a logarithmic variation, without any waiting-time effect, in accordance with a heterogeneous blocking process. In sample Powder, the relaxation presents a non-logarithmic time variation, with significant aging effects. An intermediate behaviour with much weaker aging effects is observed for Sample IN. Although the observed features are weaker than in SG, they give evidence of a change from independent to correlated relaxation processes on moving from sample IF to IN to Powder. However, such a dynamics in fine particles, also observed in other systems [5,8], does not imply a SG-type transition.

In summary, for the first time the existence of three magnetic regimes, purely individual, individual influenced by the interactions, and collective, has been revealed in an assembly of nanoparticles with interparticle interactions of varying strength. All studied static and dynamic properties of the collective regime indicate a low-temperature state similar to the spin-glass state, but the glass transition shows distinct features, in particular no χ_{nl} divergence, due to the specific properties of the high-temperature precursor state, superparamagnetic.

† Deceased 6 June 1998

References

1. Néel, L., *Ann. Géophys.* 5, 99, 1949.
2. Dormann, J.L., Fiorani, D., and Tronc, E., *Advances in Chemical Physics* 98, 283, 1997.
3. Dormann, J.L., D'Orazio, F., Lucari, F., Tronc, E., Prené, P., Jolivet, J.P., Fiorani, D., Cherkaoui, R., and Noguès M., *Phys.l Rev. B* 53, 14291, 1996.
4. Dormann, J.L., Spinu, L., Tronc, E., Jolivet, J.P., Lucari, F., D'Orazio, F., Fiorani, D., *J. Magn. Magn. Mater.* 183, L255, 1998.
5. Dormann, J.L., Cherkaoui, R., Spinu, L., Nogues, M., Lucari, F., D'Orazio, F., Fiorani, D., Garcia, A., Tronc, E., Jolivet, J.P., *J. Magn. Magn. Mater.* 187, L139, 1998.
6. Dormann, J.L., Bessais, L., Fiorani, D., *J. Phys. C: Solid State Physics* 21, 2015, 1988.
7. Mamiya, H., Nakatami, I., Furubayashi, T., *Phys. Rev. Lett.* 80, 177, 1998.
8. Jonsson, T., Nordlab, P., Svedlinh, P., *Phys. Rev. B* 57, 497, 1998.
9. Djurberg, C., Jonsson, T., Svedlinh, P., Nordlab, P., Hansen, M.F., Bødker, F., Mørup, S., *Phys. Rev. Lett.* 79, 5154, 1997.
10. Tronc, E., Jolivet J.P., *Magnetic Properties of Fine Particles*, Dormann, J.L., Fiorani, D. , eds., North-Holland, Amsterdam, 1992, p. 199.
11. Vayssières, L., Chanéac, C., Tronc, E., Jolivet J.P., *J. Colloid Interface Sci.*, in press.
12. Tronc, E., Prené, P., Jolivet, J.P., D'Orazio, F., Lucari, F., Fiorani, D., Godinho, M., Cherkaoui, R., Noguès, M., Dormann, J.L., *Hyperfine Interact.* 95,129, 1995.
13. Dormann, J.L., D'Orazio, F., Lucari, F., Spinu, L., Tronc, E., Prené, P., Jolivet J.P., Fiorani, D., *Materials Science Forum*, 235-238, 669, 1997.
14. See e.g. Fischer, K.H., Herz, J.A., *Spin Glasses*, Cambridge Univ. Press, Cambridge, 1991; Binder, K., Young, A.P., *Rev. Mod. Phys.* 58, 80, 1986.
15. Meyer, C., Hartmann-Boutron, F., Gros, Y., Campbell, I.A., *J. Magn. Magn. Mater.* 46, 254, 1985.

Pergamon

NanoStructured Materials, Vol. 12, pp. 763–768, 1999
Elsevier Science Ltd

0965-9773/99/$–see front matter

PII S0965-9773(99)00232-9

NANOSCALE CHARACTERIZATION OF MAGNETIC NANOPARTICLES

Y. Jin, C. L. Dennis, and S. A. Majetich
Department of Physics, Carnegie Mellon University, Pittsburgh, PA, 15213, USA

Abstract *-- A new technique for determining the magnetization direction of individual nanoparticles using the Foucault method of Lorentz microscopy is described. Experimental images for isolated $SmCo_5$ nanoparticles as a function of the objective aperture shift direction are shown. In preparation for studies of interparticle coupling using this approach, preliminary results describing the preparation of ordered arrays of magnetic nanoparticles are presented. Here nonmagnetic nanorods of uniform size are shown to self-assemble into arrays, which can be fixed in a silica matrix and heated to transform the rods into a ferrimagnetic phase.*

INTRODUCTION

While scientists have studied the physics and chemistry of magnetic nanoparticles for many years, theories have focused on isolated individual particles (1-4) while experiments have concentrated on disordered assemblies of particles which often have substantial size distributions and significant interparticle interactions (5-7). Here we report two results which will enable future experiments to better bridge the gap between theory and experiment: 1) the ability to determine the magnetization direction of individual nanoparticles using Lorentz microscopy, and 2) the preparation of self-assembled magnetic nanoparticle arrays, in which interactions occur but are more readily modeled because of the ordering.

SINGLE PARTICLE MAGNETIZATION DIRECTION

We have developed a method using Lorentz microscopy to uniquely determine the magnetization direction in $SmCo_5$ nanoparticles as small as 5 nm. With the tremendous strides being made in micromagnetics calculations (3,4), there is renewed interest in magnetic measurements on single particles. Several groups have performed experiments on individual nanoparticles using magnetic microscopies (8-10), or small numbers of magnetic nanoparticles using microSQUID methods (11,12). The advantage of the microscopy methods is the ability to readily determine the direction of the magnetic moment for a large number of particles.

An electron passing through a magnetic particle is deflected by a Lorentz force due to its magnetic field. Because TEM specimens are very thin and the deflection is small, conventional (bright field) electron micrographs are still possible. However, with slight modifications evidence of the magnetic deflection, and therefore information about the magnetization structure of the sample, can be obtained. In the Foucault method of Lorentz microscopy the objective

aperture is slightly shifted to block electrons with similar deflections. The aperture is at the back focal plane of the objective lens, and without magnetic deflection all electrons ideally pass through the same point in this plane. Compared with a conventional image, the Lorentz image shows dark regions in areas with similar in-plane magnetization components. The in-plane magnetization structure is revealed from analysis of images for different aperture shift directions.

Lorentz microscopy is standard for thin films but has received considerably less attention in the fine particle community. The Foucault method has previously been applied to larger, needle shaped γ-Fe_2O_3 particles (8), and the Fresnel method has been used to investigate 50-100 nm Co precipitates in Co-Au thin films (10). Here we build on this work, extending the Foucault method to the smallest particles to date, and noting some differences in the images in extremely small spherical particles, due to the small magnitude of the electron deflection.

Details of the procedure for generating ball milled $SmCo_5$ nanoparticles and dispersing them in a thermoplastic matrix have been reported elsewhere (13). TEM samples were prepared using standard ultramicrotomy sectioning techniques. Foucault Lorentz microscopy was carried out in a JEM-120CX transmission electron microscope equipped with a Lorentz pole piece. Particles were examined under bright field conditions, and then the objective aperture was shifted to cut off part of the electron beam. Images and diffraction patterns for the same fields of view were recorded for a series of different aperture shift directions. The aperture shift angles θ_A were found from the diffraction patterns and corrected for rotation, relative to the bright field image.

A single $SmCo_5$ particle is shown in bright field and Lorentz images for different aperture shift angles in Figure 1. The most notable feature of the Lorentz images is the appearance of a pair of dark lobes on either side of the particle. These lobes rotate with the aperture shift angle, θ_A (14). In addition, for a range of shift angles the center of the particle darkens, reaching minimum intensity at a shift angle θ_A * (14).

The dark lobes arise when the aperture shift blocks electrons which have passed through the fringe field of the particle. The orientation of the dark lobes rotates with the aperture shift angle and not twice as fast because the back focal plane contains the Fourier transform of the object wavefunction. Just as in single slit diffraction, electrons passing through the particle along a line at an angle θ are spread out in a line at an angle $\theta\pm\pi/2$ in the back focal plane. When the aperture is shifted at an angle θ_A, dark lobes appear in the image at $\theta_A\pm\pi/2$. These lobes are arcs because a range of fringe fields have a substantial component in this direction.

The appearance of the dark center with intensity maximized for a unique value of θ_A can be explained solely from the Lorentz deflection. All electrons are deflected in the same direction while passing through the particle, but those going through the center are deflected most. This creates a unique aperture shift angle θ_A* to reverse contrast in the particle interior, and causes the center of the particle to darken first. After accounting for image inversion by the lens, the true orientation of the particle magnetic moment, θ_M, is given by

$$\theta_M = \theta_A^* + \pi/2. \quad (1)$$

The particle in Figure 1 therefore has the in-plane component of its magnetic moment directed at approximately 55° relative to the vertical.

Lorentz microscopy images of $SmCo_5$ nanoparticles 15-50 nm in diameter behave like tiny dipoles, which is not surprising considering they are well below the theoretical limit for monodomain particles (2 μm). It is possible to uniquely determine their magnetic moment directions from images under different aperture shift directions, focusing on the angle which leads to a dark interior in each particle, rather than on the orientation of the prominent dark lobes

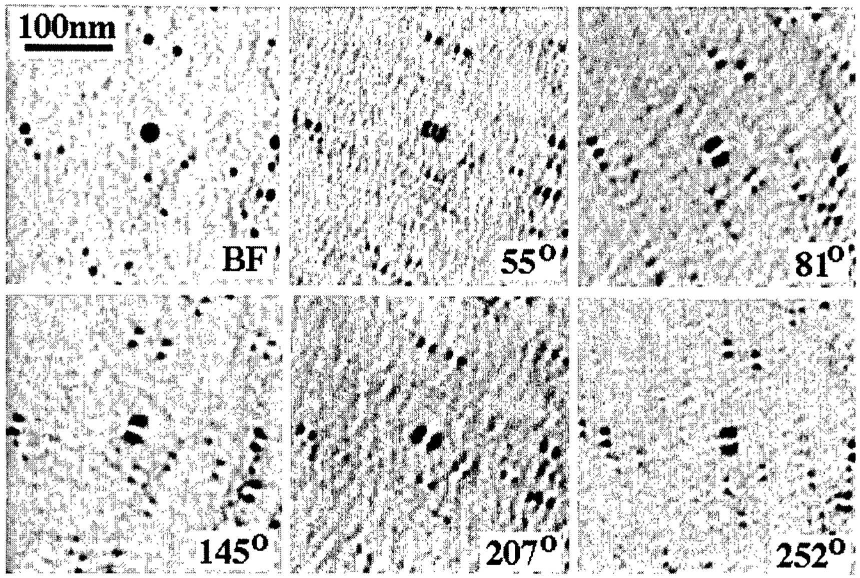

Fig. 1. Bright field image of a 20 nm diameter $SmCo_5$ nanoparticle (Upper Left), and Lorentz images of the same particle for different aperture shift angles.

which appear on either side. The different procedure for interpreting the images arises because in nanostructured materials the magnitude of the Lorentz deflection is small relative to the intensity distribution of the electrons in the back focal plane of the electron microscope.

SELF-ASSEMBLED ARRAYS OF MAGNETIC NANOPARTICLES

Successful self-assembly of nanoparticle arrays (15-17) depends on the ability to prepare monodisperse particles and to balance the interparticle forces so that ordered structures form spontaneously. Compared to other self-assembling systems, magnetic nanoparticles have an additional magnetostatic force, which favors the formation of magnetically aligned chains of magnetic dipoles, rather than two- or three-dimensional structures.

The previously reported fine particle magnet arrays have been made by lithographic methods (18-21), by a scanning tunneling microscope (STM) (12), or by electrodeposition of metals in the cylindrical pores of anodized aluminum (22). The lithographic approach has been used to make nearly perfect arrays, but extending this technology to the nanometer scale has been extremely difficult. The STM approach can form very small structures, but is slow and not readily adapted to fabricating large quantities. Self-assembly can produce nanostructures and is scaleable for the production of large quantities at low cost. If successful, the most obvious application would be in magnetic data storage. However, the production of magnetic nanoparticle arrays is in its infancy, and much must be learned about the process of self-assembly.

To make magnetic arrays we first prepared nonmagnetic arrays and then transformed them into a magnetic phase once the particles were solidified in a matrix. Randomly oriented needle-like γ-Fe_2O_3 particles are used in magnetic tapes, but they are poor candidates for forming

nanorod arrays because they, and their "nonmagnetic" precursors, γ-FeOOH, are not uniform in size, and form irregular lath-like structures (23) rather than rods. However, slow hydrolysis of $FeCl_3$ at pH 2 and below (24,25) generates uniform rods of β-FeOOH, which self-assemble to form smectic liquid crystals called Schiller layers. A schematic of the Schiller layer structure deduced from light scattering studies and optical microscopy (24) is shown in Fig. 2a. Characteristic iridescence with colors ranging from pink to blue occurs because the separation between layers of rods is on the order of a wavelength of light. Schiller layers are readily distinguishable from the brownish orange disordered slurries of β-FeOOH nanorods.

Schiller layers were prepared by centrifuging the solution until iridescence was seen in the deposited sediment, and then most of the supernatant was removed. The acid catalyzed reaction of tetraethylorthosilicate (TEOS) in a mixture of ethanol and water at 50 °C was used to form a SiO_2 matrix around the particles. Iridescence remained, but the color changed upon addition of the TEOS, suggesting a contraction of the interlayer spacing. Solid samples were sectioned with a diamond knife in a microtomy device to prepare specimens for TEM.

To make ferrimagnetic γ-Fe_2O_3, the antiferromagnetic β-FeOOH arrays were slowly heated (1°C/min., up to 240-260 °C) in an inert atmosphere and then exposed to H_2 overnight. The particle phase was monitored through x-ray and electron diffraction. Without the silica coating this reaction does not preserve the rod-like shape of the original particles, but generates spherical α-Fe_2O_3, and then reduction to Fe_3O_4, due to dissolution of the more soluble β-FeOOH followed by nucleation of α-Fe_2O_3 (26).

Figure 2b illustrates the range of structures present in the Schiller layers embedded in silica. In the upper left hand corner is a section where the order has been preserved and the particles are oriented with their long axis normal to the page. The unusual square superlattice arises from the tetragonal crystal structure of the β-FeOOH, which leads to faceted nanorods that pack most closely with this structure. Spherical nanoparticles tend to form hexagonal close

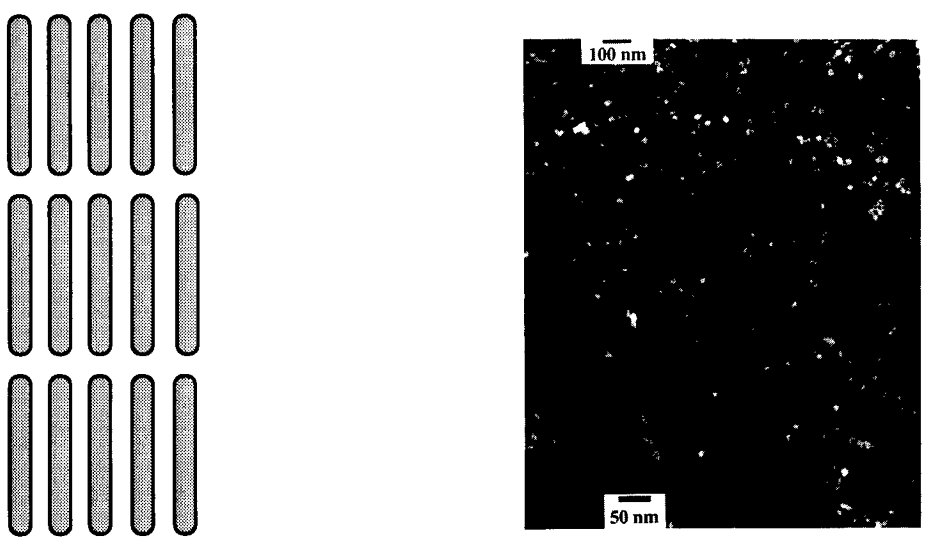

Fig. 2. Left: Schematic of Schiller layers; **Right:** TEM of Schiller layers embedded in silica; the inset shows a magnification of the ordered region in the upper left.

packed or face centered cubic crystal structures, which are closest packing arrangements for spheres. The central region of Figure 2b shows what appear to be layers of small particles oriented on their sides. The effect of the silica and heating in the current protocol is to decouple the layers and to introduce additional disorder, factors which should be minimized. While bulk magnetic measurements include contributions from both ordered and disordered particles, preliminary data from SQUID magnetometry shows that the heat treated samples are no longer antiferromagnetic and have a small ferro- or ferrimagnetic component, as well as a significant paramagnetic component from residual Fe^{3+} trapped in the silica matrix.

CONCLUSIONS

The magnetization direction of individual $SmCo_5$ nanoparticles 15-50 nm in diameter is determined using the Foucault method of Lorentz microscopy. While the observation method is similar to that used previously, for these very small particles the interpretation of the images is different. The experimental data can be understood in terms of a model which accounts for both the Fourier transform of the image in the back focal plane on the electron microscope and the Lorentz deflection of the electrons by the sample.

The degree of ordering is currently lower in the heat treated silica coated samples, relative to that for samples embedded in polymer resins at room temperature. However, the silica is necessary to withstand the temperature required for the phase transformation, which was determined by differential thermal analysis (DTA). Future work will concentrate on improving the degree of order by minimizing the stress applied to pores within the silica matrix during the drying process.

ACKNOWLEDGMENTS

Support from the National Science Foundation under grants DMR-9258308 and DMR 9500313, and assistance from M. Grant are gratefully acknowledged.

REFERENCES

1. Stoner, E. C., and Wohlfarth, E. P., *Phil. Trans. Roy. Soc. London*, 1948, A240, 599; Brown, W. F., Jr., *J. Appl. Phys.*, 1958, 29, 470.
2. Aharoni, A., *J. Appl. Phys.*, 1959, 30, 70S.
3. Zhu, J. G., and Bertram, H. N., *IEEE Trans. Mag.*, 1991, 27, 3553.
4. Braun, H. B., and Bertram, H. N., *J. Appl. Phys.*, 1994, 75, 4609.
5. Luborsky, F. E., *J. Appl. Phys.*, 1961, 32, 171S.
6. Kneller, E., *Magnetism and Metallurgy*, eds. A. Berkowitz and E. Kneller, Academic Press, New York, p. 366, 1969.
7. Chen, J. P., Lee, K. M., Sorensen, C. M., Klabunde, K. J., and Hadjipanayis, G. C., *J. Appl. Phys.* 1994, 75, 5876.
8. Salling,C., Schultz, S., McFayden, I., and Ozaki, M., *IEEE Trans. Mag.* , 1993, 27, 5184; Lederman, M., Gibson, G. A., and Schultz, S.,*J. Appl. Phys.,* 1993, 73, 6961.
9. Shi, J., Gider, S., Babcock, K., and Awschalom, D., *Science* , 1996, 271, 937.

10. Hütten, A., Bernardi, J., Nelson, C., and Thomas, G., *phys. stat. sol. (a),* 1995, 150, 171.
11. Wernsdorfer, W., Hasselbach, K., Mailly, D., Barbara,B., Benoit, A., Thomas, L., and Suran, G., *J. Magn. Magn. Mater.*, 1995, 145, 33.
12. Kent, A. D., Shaw, T. M., von Molnar, S., and Awschalom, D. D., *Science* , 1993, 262, 1249.
13. Majetich, S. A., and Kirkpatrick, E. M. *IEEE Trans. Mag.,* 1997, 33, 3721; Jin, Y.,Majetich, S. A., and Giri, A., *MRS. Symp. Proceedings*, 1998, 501, 103.
14. Jin, Y., and Majetich, S. A., (under submission).
15. Andres, R. P., Bielefeld, J. D., Henderson, J. I., Janes, D. B., Kolagunta, V. R., Kubiak, C. P., Mahoney, W. J., and Osifchin, R. G., *Science* ,1996, 273, 1690.
16. Harfenist, S. A., Wang, Z. L., Alvarez, M. M., Vezmar, I., and Whetten, R. L., *J. Phys. Chem.,* 1996, 100, 13904.
17. Bowden, N., Terfort, A., Carbeck, J., and Whitesides, G. M., *Science* 1997, 276, 233.
18. Pardavi-Horvath, M., *IEEE Trans. Mag.*, 1994, 30, 124.
19. Chou, S. Y., Krauss, P. R., and Kong, L. *J. Appl. Phys.* , 1996, 79, 6101.
20. Hehn, M., Ounadjela, K., Bucher, J.-P., Rousseau, F., Decanini, D., Bartenlian, B. , and Chappert, C. , *Science* , 1996, 272, 1782.
21. Fernandez, A., Bedrosian, P. J., Baker, S. L., Vernon, S. P., and Kania, D. R., *IEEE Trans. Mag.*, 1996, 32, 4472.
22. Al-Mawlawi, D. , Liu, C. Z., and Moskovits, M., *J. Mater. Res.* 1994, 9, 1014.
23. Schwertmann, U., and Cornell, R. M., *Iron Oxides in the Laboratory*, VCH Pub. Co., New York, 1991, p. 12.
24. Maeda, Y., and Hachisu, S., *Colloids and Surfaces* , 1983, 6, 1.
25. Zocher, H., and Heller, W., *Z. Anorg. Chem.* , 1930, 186, 75; Zocher, H., and Török, C., *Acta Cryst.* 1967, 22, 751.
26. Matijevic, E., and Scheiner, P., *J. Colloid and Interface Sci.* 1978, 63, 509.

Pergamon

NanoStructured Materials, Vol. 12, pp. 769–774, 1999
Elsevier Science Ltd

0965-9773/99/$–see front matter

PII S0965-9773(99)00233-0

GRAIN SIZE DEPENDENCE OF REMANENCE ENHANCEMENT AND COERCIVITY IN NANOCRYSTALLINE ND-FE-B-POWDERS

V. Neu[1], **L. Schultz, H.-D. Bauer**
IFW Dresden, Helmholtzstr. 20, D-01069 Dresden, Germany

Abstract *A detailed investigation of the grain size dependence of the magnetic properties has been performed for intensively milled, nanocrystalline single-phase Nd-Fe-B-powder. These powders were prepared with grain sizes in the range of 20-90 nm by controlled annealing. Phase evolution and microstructure have been studied by means of X-ray diffraction, including Rietveld analysis, and transmission electron microscopy. The reduced remanence of the isotropic powders is clearly above the Stoner-Wohlfarth limit and shows the typical grain size dependence expected for exchange-coupled nanograins. The coercive field of our samples remains almost constant at a value of* $\mu_0 H_c = 1\,\mathrm{T}$ *in contradiction to earlier experimental studies on rapidly quenched ribbons, where a pronounced drop in* H_c *is reported for grain sizes below 40 nm. We, therefore, support the findings of more recent micromagnetic calculations which predict an improvement of the magnetic properties of exchange-coupled nanocrystalline Nd-Fe-B-powders by a further decrease in grain size.* ©1999 *Acta Metallurgica Inc.*

Introduction

The reduced remanence $\alpha = M_r/M_s$ of an isotropic nanocrystalline permanent magnet material with uniaxial magnetocrystalline anisotropy exhibits values above 0.5, which is the Stoner-Wohlfarth limit for the above mentioned condition in the non-coupled case, when exchange-coupling between adjacent grains contributes to a considerable amount to the remanent magnetization. Hereby, M_r and M_s denote remanent and saturation magnetization, respectively. The enhancement originates from a small region around the grain boundaries where the magnetization vectors deviate from the local easy axis due to the exchange coupling across the grain boundary. The length scale of this boundary region is determined by the exchange correlation length $\delta = \sqrt{A/K_u}$, where A is the exchange constant and K_u an uniaxial anisotropy constant. For $Nd_2Fe_{14}B$ this value is $\delta = 1.3$ nm and the coupled grain boundary region extends to roughly $\pi \cdot \delta \approx 4.3$ nm. Due to the short range characteristic of the coupling an assembly of nanocrystalline $Nd_2Fe_{14}B$ grains shows an enhanced remanence only if the average grain size is below some 10 nm in diameter. Rapidly quenched, exchange-coupled single-phase $Nd_2Fe_{14}B$ has been developed soon after the discovery of this effect (1) and a systematic study on the grain size dependence of the magnetic properties has been performed (2). The reduced remanence α increases with decreasing grain size in agreement with the considerations sketched above and with results derived from micromagnetic calculations (3). The first report on remanence-enhanced single-phase $Nd_2Fe_{14}B$ prepared by intensive milling has been given in (4). In this paper we present a detailed investigation on the grain size dependence of the magnetic

properties for this kind of material. Thus, we studied the phase evolution of the 2:14:1 structure of an intensively milled master alloy upon annealing. The amount of residual α-Fe in this material has been quantified by Rietveld analysis and allows a correction of the magnetic data for this contribution. The average grain size was determined by both, X-ray diffraction (XRD) using Rietveld analysis, and by means of transmission electron microscopy (TEM).

Experimental

A stoichiometric $Nd_2Fe_{14}B$ alloy ($Nd_{11.8}Fe_{82.3}B_{5.9}$) and a Co-containing alloy with composition $Nd_{11.8}Fe_{66.2}Co_{14.7}Nb_{0.8}Ga_{0.6}B_{5.9}$ have been arc-melted using high purity initial materials (99.9% or better) and homogenized under Argon for 96 h at 1050°C. The resulting ingots were single-phase polycrystals with structural and intrinsic magnetic properties comparable to known data (5, 6). Milling the ingots with a Spex mill for 35 h results in a decomposition of the 2:14:1 structure and leads to a mixture of nanocrystalline Fe and an amorphous phase. A subsequent heat treatment at temperatures T_A between 600 and 800°C under vacuum results in the formation of 2:14:1 nanocrystals and a small amount of α-Fe. This residual Fe is due to wear debris and due to a small loss of Nd caused by oxydation. X-ray data have been taken with Co-K_α radiation in the angular range between 25° and 105°, using a step size of 0.03°. All diffraction patterns could be fitted to satisfaction assuming two phases, the 2:14:1 structure and α-Fe, whereby the phase ratio is given by the refined scaling factor. The crystal structure parameters have been constrained to known data (5), except for the lattice parameters. These have been refined to account for homogeneous atomic level strain. Profile shape and profile width have been determined by the fit procedure, too, and a subsequent integral breadth method allowed the separation of average grain size and inhomogeneous atomic level strain. Details to the fitting technique, instrumental broadening correction and integral breadth method are given in (7). The heat treated powders have been loosely mixed with epoxy resin and have been measured in a vibrating sample magnetometer (VSM) at room temperature and fields $\mu_0 H$ up to 8 T. The magnetic and the crystallographic behavior of the powders is isotropic, as a result of the roughly spherical shape of the particles, consisting of randomly distributed nanocrystalline grains. The hysteresis loops have, therefore, been de-sheared with a demagnetizing factor of 0.3. The magnetic data given here refer to the volume of the magnetic material in the bonded sample and have been calculated using the theoretical density of 7.6 g/cm^3.

Results

Fig. 1 shows the X-ray diffraction pattern of intensively milled $Nd_2Fe_{14}B$ after a heat treatment at 700°C. Additionally, the calculated patterns from the Rietveld refinement are plotted, distinguishing between the 2:14:1 phase and α-Fe. The so-calculated amount of α-Fe (3.2 Vol.%) has been verified by a magneto-balance experiment. The microstructural data (Vol.% of α-Fe, average grain size and inhomogeneous lattice strain of the 2:14:1-phase) were given for $Nd_2Fe_{14}B$ as a function of T_A (Fig. 2). With increasing temperature the phase transformation improves, as can be seen from the decrease in α-Fe, whereas the diameter of the $Nd_2Fe_{14}B$-grains increases. Although annealing at 620°C leads to almost single-phase $Nd_2Fe_{14}B$, at this

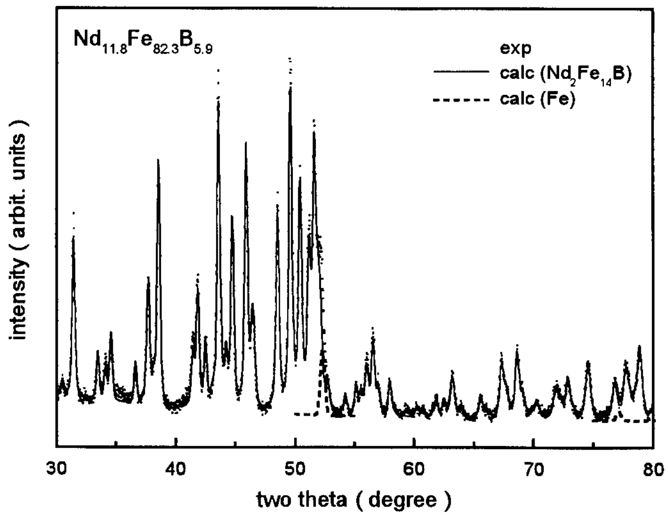

Fig. 1. Part of a measured X-ray pattern (▪) together with the fitted Rietveld curves for the 2:14:1-phase (—) and α-Fe (---).

temperature the 2:14:1-grains still exhibit considerable inhomogeneous strain and the lattice parameters deviate from those of the coarse grain starting ingot. With increasing T_A strain decreases drastically (Fig. 2b) and the lattice parameters approach the equilibrium values (not shown here). In this behavior, mechanically milled and annealed samples differ from rapidly quenched ribbons where often a strain free grain is assumed (2). A bright field transmission electron micrograph of a $Nd_2Fe_{14}B$-sample annealed at 750°C and with rather large grains is seen in Fig. 3a together with the accompanying grain size histogram. The volume-weighted average grain size D_V = 46 nm compares well with D_{XRD} = 54 nm derived from the X-ray experiment. Whereas the smallest grain sizes achievable with the simple ternary alloy is 30 nm, annealing the Co-containing powder at 620°C leads to an almost completely crystallized sample with an average grain diameter of only 19 nm (Fig. 3b). Again, the volume-weighted average D_V = 21 nm compares well with the X-ray result (D_{XRD} = 21 nm). Our X-ray approach, combining Rietveld analysis with a subsequent integral breadth technique, is therefore an appropriate method to derive quantitatively

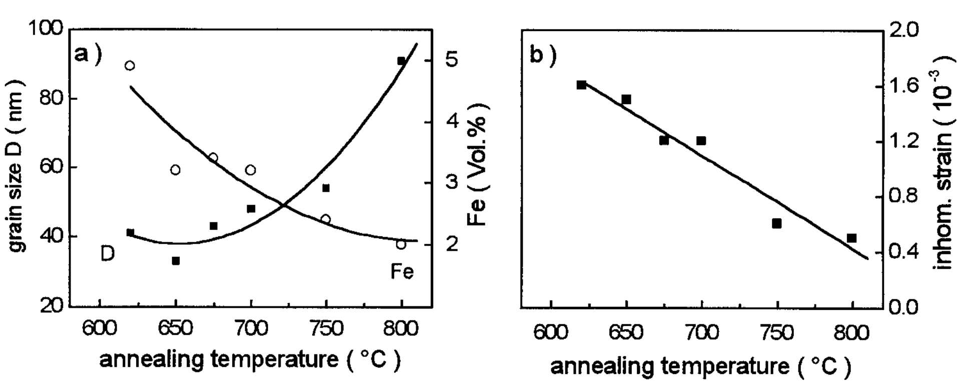

Fig. 2. (a) Average grain size (▪) and residual amount of α-Fe (o), and (b) inhomogeneous atomic level strain of intensively milled $Nd_2Fe_{14}B$ as a function of the annealing temperature.

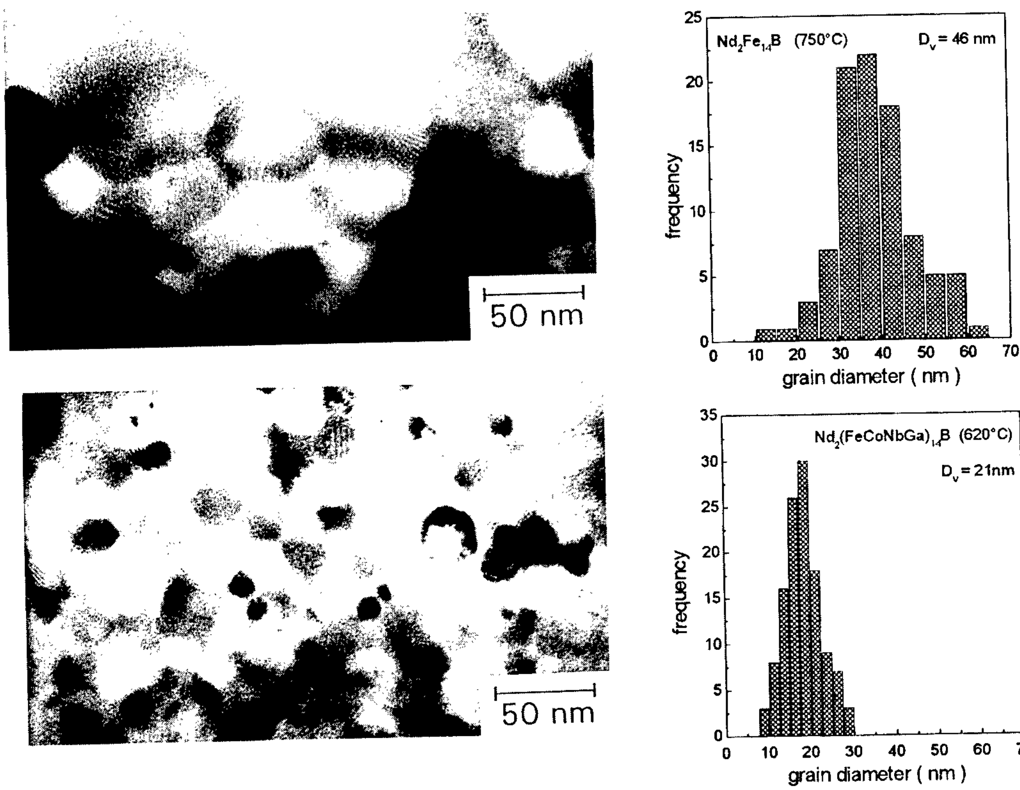

Fig. 3. Transmission electron micrograph of intensively milled $Nd_2Fe_{14}B$ annealed at 750°C (a) and of $Nd_2(FeCoNbGa)_{14}B$ annealed at 620°C (b). For the accompanying grain size histograms several pictures of each sample have been evaluated.

correct grain sizes in the range between 20 and 50 nm.

The magnetic data as a function of T_A are summarized for both compositions in Fig.4. Typically at higher temperatures the grain growth of the 2:14:1 nanocrystals reduces the coercivity. For low T_A coercivity drops due to an incomplete phase transformation and, therefore, low amount of hard magnetic phase. This behavior is consistent with our results on the microstructural evolution (Fig. 2). In order to study the influence of grain size on the reduced remanence α and on the coercivity of a single-phase material, we selected several samples in the grain size range of 20 to 50 nm and corrected the remanence values for the contribution of the residual α-Fe. These samples are encircled in Fig. 4. The correction takes into account the differences in the coupling behavior of nanocrystalline 2:14:1 on one hand and α-Fe-grains embedded in a 2:14:1-grain-matrix on the other hand (7). The Co-containing sample exhibits a slightly higher exchange correlation length $\delta = 1.4$ nm, but the anisotropy field $\mu_0 H_A$ is comparable to that of the simple ternary compound (6). The reduced remanence α is plotted as a function of the reduced grain size D/δ in Fig. 5. The values are clearly above 0.5 and show an increase with decreasing grain size as expected for exchange-coupled grains. Additionally, α is

compared with a theoretical prediction, where the effect of exchange coupling between adjacent grains has been calculated with a semianalytical model (8). In both cases the grain size dependence is in good agreement with experimental (2) and micromagnetic data (3, 9, 10).

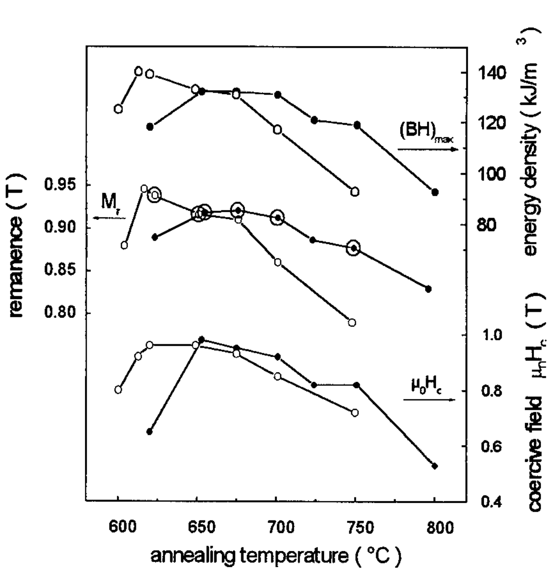

Fig. 4. Magnetic properties of intensively milled $Nd_2Fe_{14}B$ (•) and $Nd_2(FeCoNbGa)_{14}B$ (o) as a function of the annealing temperature.

The coercivity of these samples is plotted in Fig.6 and is more or less constant at a level of $\mu_0H_c \approx 1\,T$, down to the smallest grain size of 21 nm. In this behavior the samples differ from the predictions in (3) and from the experimental observations on rapidly quenched Nd-Fe-B (2) which show a drop in coercivity when grain size is reduced below 30-40 nm. We,also, prepared samples at the low temperature end of our annealing series (Fig. 4), which combine a small grain size with a decreasing coercivity, but our microstructural investigations indicate, that these samples contain a considerable amount of α-Fe. As this can dominate the magnetic properties (4), these samples are not included in our comparison. More recent micromagnetic calculations by Rave and Ramstöck (9) result in an increasing coercivity with decreasing grain size down to a critical limit which is determined by the exchange correlation length and is in the order of 6-9 nm for $Nd_2Fe_{14}B$. In a review article on rapidly quenched Nd-Fe-B Davies *et al.* (11) report an increasing coercivity with decreasing grain size for several $Nd_{11.9}Fe_{82.3-x}Ga_xB_{5.9}$ compositions and mention a similar observation for a simple ternary alloy, too. Our experimental data are more consistent with

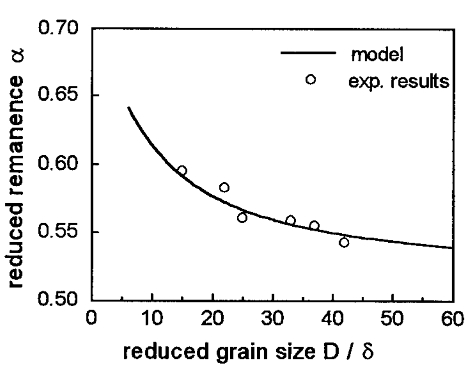

Fig. 5. Reduced remanence as function of reduced grain size for single-phase Nd-Fe-B.

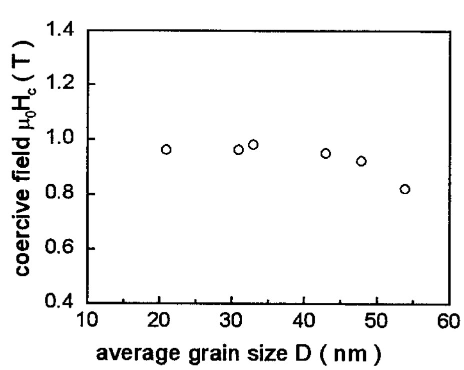

Fig. 6. Coercive field as a function of grain size for single-phase Nd-Fe-B.

these later findings and encourage the search for even smaller grain sizes below 20 nm, as we still expect an improvement in both remanence and coercivity.

Conclusions

The magnetic performance of exchange-coupled, nanocrystalline Nd-Fe-B-powders prepared by intensive milling and an additional heat treatment is remarkably superior to comparable isotropic powders with a Nd-rich grain boundary phase. Although the coercive field is reduced roughly by a factor of 2, with $\mu_0 H_c \approx 1\,\mathrm{T}$ it is high enough for most permanent magnet applications and the user benefits from the increase in remanence and energy density. The reduced remanence of intensively milled $Nd_2Fe_{14}B$ increases with decreasing grain size and is in good quantitative agreement with data reported in literature. The coercivity remains nearly constant in the range from 20 to 50 nm in consistence with more recent micromagnetic calculations (9). Simple ternary $Nd_2Fe_{14}B$-powders with optimum microstructure ($D \approx 30\,\mathrm{nm}$) exhibit a remanence of $M_r = 0.92$ T and an energy density of $(BH)_{\max} = 132$ kJ/m^3. Optimum annealing conditions for an intensively milled Co-containing alloy lead to an even smaller grain size of 21 nm and result in a further improved remanence of $M_r = 0.95$ T together with an energy density of $(BH)_{\max} = 140$ kJ/m^3. With a saturation magnetization of 1.51 T for this compound the reduced remanence is 20 % above the Stoner-Wohlfarth limit of non-coupled isotropic powders.

Acknowledgment

Financial support by the German BMBF and by the DFG is gratefully acknowledged. We would like to thank N. Mattern for help with the Rietveld analysis and S. Wirth for careful reading of the manuscript.

References

1. Clemente, G.B., Keen, J.E. and Bradley, J.P., *J. Appl. Phys.* 63, 1988, 3507.
2. Manaf, A., Leonowicz, M., Davies, H.A. and Buckley, R.A., *J. Appl. Phys.* 70, 1991, 6366.
3. Schrefl, T., Fidler, J., Kronmüller, H., *Phys. Rev.* B49, 1994, 6100.
4. Neu, V., Dunlop, J.B., Schultz, L., in: Missell, F.P. *et al.* (Eds), *Proc. 9th Int. Symp. on Magnetic Anisotropy and Coercivity in RE-TM Alloys*, São Paolo, 1996, 337.
5. Herbst, J.F., Croat, J.J., Pinkerton, F.E. and Yelon, W.B., *Phys. Rev.* B 29, 1984, 4176.
6. Xie, J.Q., Wu, C.H., Chuang, Y.C., *J. Magn. Magn. Mat.* 75, 1988, 361.
7. Neu, V., Dissertation, Technische Universität Dresden, 1998.
8. Neu, V., Hubert, A., Schultz, L., *J. Magn. Magn. Mat.* (submitted).
9. Rave, W., Ramstöck, K., *J. Magn. Magn. Mat.* 171, 1997, 69.
10. Fischer, R., Schrefl, T., Kronmüller, H., Fidler, J., *J. Magn. Magn. Mat.* 153, 1996, 35.
11. Davies, H.A., Liu, J.F. and Mendoza, G. in: Missell, F.P. *et al.* (Eds), *Proc. 9th Int. Symp. on Magnetic Anisotropy and Coercivity in RE-TM Alloys*, São Paolo, 1996, 251.

Pergamon

NanoStructured Materials, Vol. 12, pp. 775–778, 1999
Elsevier Science Ltd

0965-9773/99/$–see front matter

PII S0965-9773(99)00234-2

GIANT MAGNETO-IMPEDANCE EFFECT IN NANOCRYSTALLINE RIBBONS

H. Chiriac, T.-A. Óvári, and C.S. Marinescu
National Institute of R&D for Technical Physics, 47 Mangeron Blvd., 6600 Iaşi 3, Romania

Abstract – *Results on the GMI response of $Fe_{73.5}Cu_1Nb_3Si_{13.5}B_9$, $Fe_{90}Hf_7B_3$, and $Fe_{90}Zr_7B_3$ nanocrystalline ribbons are reported. The obtained results are compared with those obtained for CoFeSiB amorphous ribbons, using the MI ratio, defined as $\Delta Z/Z = [Z(H_{dc} = 0) - Z(H_{dc} = 1\ kA \cdot m^{-1})]/Z(H_{dc} = 0)$. The most sensitive GMI response is given by $Fe_{90}Zr_7B_3$ nanocrystalline ribbons – about 30%. A sensitivity of about 25% has been observed in $Fe_{90}Hf_7B_3$ nanocrystalline ribbons, which is comparable to that of CoFeSiB amorphous ones, while for $Fe_{73.5}Cu_1Nb_3Si_{13.5}B_9$ ones, the maximum MI ratio reaches only 10%. The results are explained in terms of differences in the electrical resistivities of the samples investigated, as well as by taking into account the local anisotropy distributions in each case. One of the main goals of this paper is to discuss the role of good soft magnetic properties on the magnitude and sensitivity of the GMI effect. ©1999 Acta Metallurgica Inc.*

INTRODUCTION

The giant magneto-impedance (GMI) effect consists of a large variation of the high frequency impedance of a magnetic conductor, when it is subjected to a small dc magnetic field. This effect was found appropriate for sensor applications, the most sensitive GMI response being reported in soft magnetic materials with very small negative magnetostriction, such as cold-drawn $Co_{68.15}Fe_{4.35}Si_{12.5}B_{15}$ amorphous wires (1).

A material that displays a large and sensitive GMI effect, has to comply as much as possible with the following two conditions: (i) - it has to display good soft magnetic properties, i.e. high permeability and low coercive force, and (ii) - it has to have an appropriate domain structure, usually a transverse one for ribbons (in-plane, transverse to the ribbon axis and to the applied dc field as well), and a circumferential one for wires. In the real case, it is difficult to obtain materials in which both conditions are fully accomplished. However, $Co_{68.15}Fe_{4.35}Si_{12.5}B_{15}$ amorphous wires, ribbons, and glass-covered wires, are close to the ideal case due to their small negative magnetostriction ($\lambda_S \approx -1 \times 10^{-7}$), which simultaneously ensures good soft magnetic properties and the formation of a favorable domain structure, due to the magnetomechanical coupling between internal stresses and magnetostriction.

The aim of the paper is to analyze the influence of soft magnetic properties on the sensitivity and magnitude of the GMI response. Thus, we investigated the GMI response of Fe-based nanocrystalline ribbons, and we compared the obtained results with those measured on as-cast CoFeSiB amorphous ribbons.

EXPERIMENT

$Co_{68.15}Fe_{4.35}Si_{12.5}B_{15}$ and Fe-based amorphous ribbons ($Fe_{73.5}Cu_1Nb_3Si_{13.5}B_9$, $Fe_{90}Hf_7B_3$, and $Fe_{90}Zr_7B_3$) have been prepared by rapid quenching from the melt. The Fe-based amorphous ribbons have been properly annealed (1h at 550°C, in vacuum) in order to obtain the nanocrystalline state. For the experimental investigations, we used ribbons with 18 μm in thickness and 320 μm in width. All samples investigated were 40 mm in length.

GMI measurements were performed using a driving ac current with the maximum value of 15 mA and frequencies up to 1 MHz, with a digital oscilloscope, coupled to a computer which allowed automatic frequency control, data acquisition and processing. The maximum value of the axial dc magnetic field H_{dc} for these measurements was 1 kA·m^{-1}. This value allows the samples to be saturated in the axial direction and Z to remain constant at a given frequency of the ac current. The changes in resistivity for the Fe-based ribbons have been continuously monitored during annealing.

RESULTS AND DISCUSSION

In order to analyze the GMI effect in the materials mentioned above, we use a convenient quantity that contains information about its sensitivity. The MI ratio is usually employed for such reasons, but different authors defined it in different ways (2, 3), and consequently, a unitary comparison basis for previously reported results is missing. We defined the MI ratio as $\Delta Z/Z = [Z(H_{dc} = 0) - Z(H_{dc} = 1\ \mathrm{kA\cdot m^{-1}})]/Z(H_{dc} = 0)$, in which Z is the impedance, and H_{dc} the applied dc magnetic field, its maximum value being 1 kA·m^{-1}. $\Delta Z/Z$ contains information about the sensitivity of the GMI effect, since it indicates the behavior of Z at two extreme values of the axial field H_{dc}. For $H_{dc} = 0$, the behavior of Z is affected only by the frequency of the ac driving current, f, through the skin effect that occurs at high frequencies, as well as through the changes that occur in the dynamics of magnetization in the transverse direction. 1 kA·m^{-1} is the maximum value of the applied dc field, chosen in order to saturate the sample in the axial direction, and consequently to damp the transverse magnetization processes that occur due to the alternating transverse field generated by the ac driving current. The dynamics of magnetization in the transverse direction – domain wall movements or spin rotations – has a decisive role on the sensitivity of the GMI effect, since it affects the magnitude of the skin effect, through the transverse permeability, $\mu_\perp$, according to $\delta_m = (\rho/\pi f\mu_\perp)^{1/2}$, where ρ is the resistivity and δ_m the magnetic penetration depth.

Figure 1 illustrates the frequency dependence of the MI ratio, $\Delta Z/Z$, for the Fe-based nanocrystalline ribbons and for the CoFeSiB amorphous ribbon. One observes that the most sensitive GMI effect is obtained in the $Fe_{90}Zr_7B_3$ nanocrystalline ribbon, that displays a maximum MI ratio of 30%, followed by the amorphous CoFeSiB ribbon with a maximum MI ratio of 26%, and the nanocrystalline $Fe_{90}Hf_7B_3$ ribbon with a maximum MI ratio of 25%. The smallest GMI effect is observed in the $Fe_{73.5}Cu_1Nb_3Si_{13.5}B_9$ nanocrystalline ribbon, in which the maximim MI ratio reaches slightly above 10%. The differences in the values of $\Delta Z/Z$ for nanocrystalline ribbons with different compositions can be mainly attributed to the differences in the electrical resistivities of these alloys.

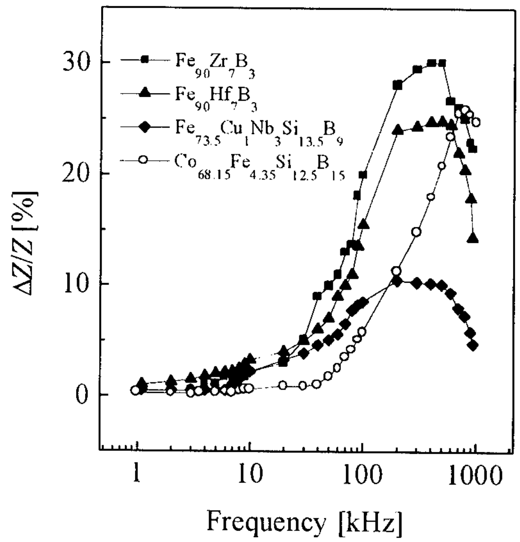

Figure 1. Frequency dependence of the MI ratio for Fe-based nanocrystalline ribbons and for the Co-based amorphous one; the maximum frequency of the ac driving current is 1 MHz.

Figure 2 shows the dependence of ρ on the annealing temperature for the Fe-based ribbons, starting from the as-cast amorphous state, after different stages of annealing. One observes that after the nanocrystalline phase formation - annealing at 550°C - the $Fe_{90}Hf_7B_3$ and $Fe_{90}Zr_7B_3$ ribbons have smaller values of ρ as compared to the $Fe_{73.5}Cu_1Nb_3Si_{13.5}B_9$ one, according to the existence of α-FeSi crystalline grains in the $Fe_{73.5}Cu_1Nb_3Si_{13.5}B_9$ nanocrystalline ribbon and α-Fe crystalline grains with a smaller resistivity in the $Fe_{90}Hf_7B_3$ and $Fe_{90}Zr_7B_3$ ones. The values of ρ in the nanocrystalline state are important as concerns the GMI effect, since δ_m is proportional to its square root. Thus, a smaller ρ corresponds to a smaller δ_m at the same frequency, and consequently, to a larger value of Z. For the Co-based amorphous ribbon, $\rho = 1.1 \times 10^{-6}$ Ω·m, being larger than those of nanocrystalline FeZrB and FeHfB ones, but their GMI response is almost similar. This fact is explained by considering its transverse domain structure, which at lower frequencies favors the transverse magnetization processes achieved through domain wall movements (3). Consequently, for this ribbon, $\mu_\perp$ is sensitive to H_{dc} and to the increase of frequency, resulting in a sensitive GMI response through the same mechanism of the skin effect. On the other hand, the macroscopic magnetostriction is vanishing in the nanocrystalline ribbons, the formation of a favorable domain structure being obstructed. The magnetization process on the transverse direction is achieved through spin rotations, although they occur easily due to their excellent soft magnetic properties. Thus, the values of $\mu_\perp$ at high frequencies, where spin rotations also occur in the amorphous ribbon, are larger in the nanocrystalline ribbons than in the amorphous one.

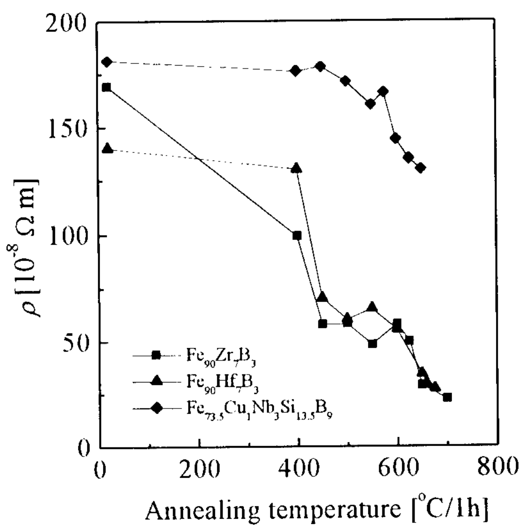

Figure 2. Dependence of the electrical resistivity on the annealing temperature for the $Fe_{73.5}Cu_1Nb_3Si_{13.5}B_9$, $Fe_{90}Hf_7B_3$, and $Fe_{90}Zr_7B_3$ ribbons.

CONCLUSION

The magnitude of the GMI effect in the analyzed samples is determined by two major factors, that differentiate their GMI responses, both affecting the impedance through the magnetic penetration depth: (i) – the differences in their electrical resistivities, and (ii) – the differences in their transverse permeabilities, that arise from the differences in the dynamics of magnetization in the transverse direction. The existence of an appropriate domain structure, results in a sensitive GMI effect, even in the absence of outstanding soft magnetic properties, while its absence is well compensated by good soft magnetic properties, like the case of Fe-based nanocrystalline soft magnetic materials, their response being comparable or even larger than that of as-cast amorphous ribbons.

References

1. Panina, L.V., Mohri, K., Bushida, K., and Noda, M., *Journal of Applied Physics*, 1994, 76, 6198.
2. Knobel, M., Sánchez, M.L., Gómez-Polo, C., Marín, P., Vázquez, M., and Hernando, A., *Journal of Applied Physics*, 1996, 79, 1646.
3. Chiriac, H., Vinai, F., Óvári, T.-A., Marinescu, C.S., Barariu, F., and Tiberto, P., *Materials Science and Engineering A*, 1997, 226-228, 646.

Pergamon

NanoStructured Materials, Vol. 12, pp. 779–782, 1999
Elsevier Science Ltd

0965-9773/99/\$–see front matter

PII S0965-9773(99)00235-4

MEASUREMENT OF MECHANICAL PROPERTIES OF NANOSCALED FERRITES USING ATOMIC FORCE MICROSCOPY AT ULTRASONIC FREQUENCIES

E. Kester, U. Rabe, L. Presmanes*, Ph. Tailhades*, and W. Arnold
Fraunhofer Institute for Nondestructive Testing (IZFP), Bldg. 37, University
D-66123 Saarbrücken, Germany
*Laboratoire de Chimie des Matériaux Inorganiques, Université Paul Sabatier
118 Route de Narbonne, F-31062 Toulouse Cedex, France

Abstract *To measure local elasticity by Atomic Force Acoustic Microscopy (AFAM), the sample placed in a commerical AFM is insonified by ultrasonic waves or the cantilever is oscillated at ultrasonic frequencies. In contact with the specimen, the cantilever-tip system vibrates out-of-plane and its resonances are measured. A quantitative model based on linear tip-sample force shows that the stiffness of the specimen can be derived from the shift of the contact resonance frequencies relative to resonance frequencies of the free cantilever. We report AFAM results with a well-known material, silicon single-crystal oriented in <100> direction, to prove the consistence of the local measurement of elasticiy. Then, in thin films of magnetite Fe_3O_4 and maghemite γFe_2O_3 with spinel structure, the influence of the deviation from the stoichiometry on the elasticity for a given grain size is determined.*

1. INTRODUCTION

Thin films of nanoscaled ferrites with spinel structure can be used in magneto-optic and magnetic recording systems. Their technological future depends largely on the control of their preparation and their nanostructure. Previous research has shown that the coercivity, one of the characteristics most in demand, is not only correlated with the chemical composition, but also with the grain size (1), the quenching temperature, and the cation distribution (2). To understand the coercivity as a function of the nanostructure, it has been demonstrated by theoretical simulation (3), XPS spectroscopy, and X-ray diffraction (4) that the coercivity is related to the chemical gradients induced by the thermal evolution. It is also influenced by mechanical gradients. This will lead to a variation of the elastic moduli on a nanoscale. In order to measure the elastic properties locally, a new Atomic Force Acoustic Microscope (AFAM) is used. In this microscope, one exploits the resonance frequencies of the cantilever of the AFM as they depend on the local contact stiffness. We report AFAM results on a well-known silicon single-crystal to prove the consistency of the measurements. Then, on thin films of magnetite Fe_3O_4 and maghemite γFe_2O_3 with spinel structure, the influence of the deviation from the stoichiometry on the elasticity for a given grain size is determined.

2. MEASUREMENT TECHNIQUE

A modified commercial AFM (Dimension 3000, Digital Instruments, S. Barbara, Ca.) is used (Fig.1). A frequency generator provides a stable sine wave excitation signal in the frequency range between 75 kHz and 3 MHz which is applied to a piezoelectric transducer integrated in the cantilever holder. Likewise, the sample may be insonified. With both techniques, the eigenmodes of the cantilever can be excited which has been described earlier (5-8). The cantilever vibrations are measured with a fast optical beam-deflection sensor (5) and they are fed to a heterodyne down-converter which also receives a reference signal at the excitation frequency. Both the signal and the reference inputs are mixed down to a fixed 20 kHz intermediate output and are evaluated by a standard lock-in amplifier. Its analog DC output is fed to a digital oscilloscope. The generator and the oscilloscope are connected to a computer. By aid of a Labview program (9) the excitation frequency is changed stepwise, the lock-in output at the given frequency is read, and the amplitude of the cantilever is displayed.

At the beginning of an experiment, the resonances of the freely oscillating cantilever are determined. When the cantilever is in contact with the sample vibrating at ultrasonic frequencies, the tip-sample interaction is highly nonlinear. For very small vibration amplitudes of the cantilever around its equilibrium position, however, the tip-sample interaction can be expanded linearly (6). It is represented by a linear spring with k* the spring constant equivalent to the negative derivative of the tip-sample force in the equilibrium position. The resonances of the cantilever in contact are shifted by Δf relative to the free ones (Fig. 2) allowing one to measure k* quantitatively. Damping, whose effects are reported elsewhere (10), is neglected. The cantilever is assumed to be parallel with the sample surface

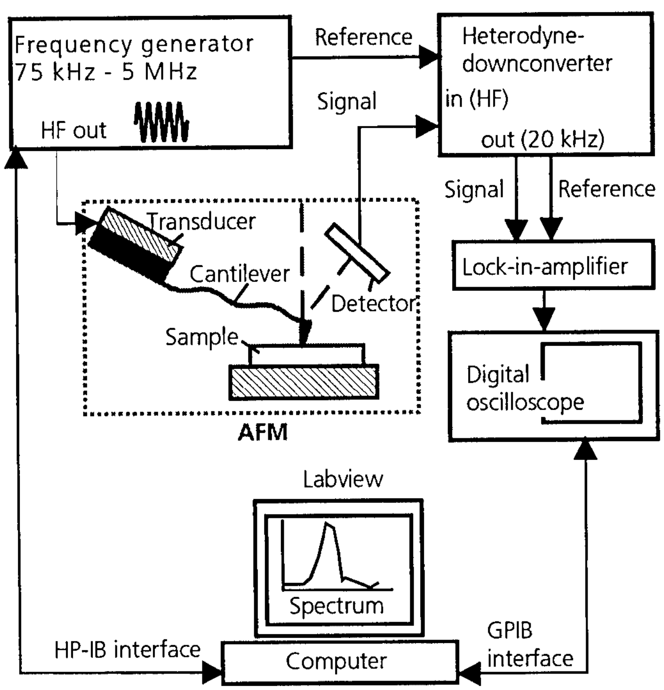

Figure 1: AFAM set-up

and lateral forces are taken into account assuming that the lateral contact stiffness equals the vertical stiffness k*(11-13). The Young's modulus of the sample is calculated using Herztian contact theory. To achieve a tip-sample interaction where contact forces dominate, the cantilever is pressed onto the surface with sufficient static load i.e. 800 - 1000 nN. Other forces in the contact (14) play a minor role.

3. MATERIALS

A silicon single-crystal oriented in <100> direction and fabricated by micromachining techniques was examined (15). To remove oxides, it was cleaned using sequential ultrasonic baths of acetone and methanol for 5 min at each step following a 10 min etch in 50% HF (16). Then, thin films of ferrites whose synthesis is a two-stage process are examined. Nanopowders of magnetite and maghemite are prepared by soft chemistry, compacted, sintered, and shaped in thin films by RF sputtering. The grain size and the thickness of the thin films are 70 and 200 nm, respectively (17).

4. EXPERIMENTAL RESULTS AND DISCUSSIONS

In the case of Si-crystal oriented in <100> direction, the Young's modulus calculated from the shift of the two first resonances and taking into account the normal force between the tip and the sample is $1.2 \pm 0.6 \times 10^{11}$ Pa. It is in good agreement with the known value of 1.3×10^{11} Pa (16).

When the same experimental conditions with the cantilever radius r [nm]: $30 < r < 50$, spring constant $k_c = 38$ N/m, second free resonance $f_2 = 908$ kHz, are adjusted, the shift of the second contact resonance on the magnetite film is larger than on the maghemite film (Fig. 2). This means that maghemite is softer than magnetite. The calculated Young's modulus of magnetite and maghemite are $1.2 \pm 0.2 \times 10^{11}$ and $0.6 \pm 0.2 \times 10^{11}$ Pa, respectively.

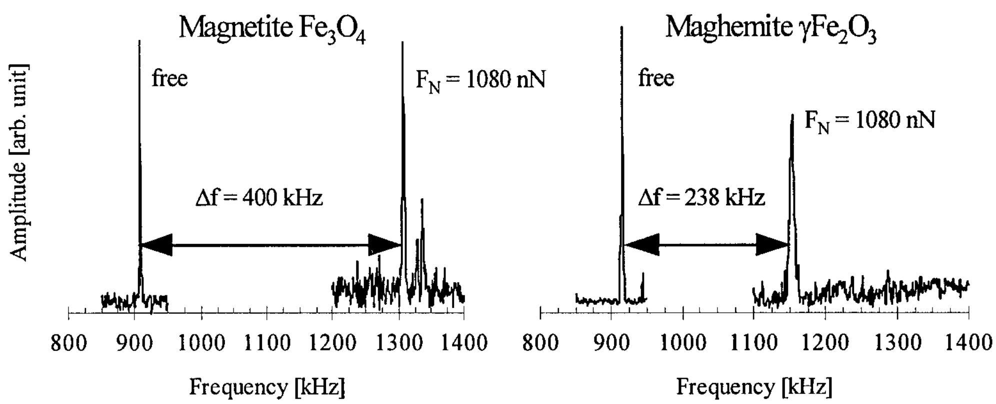

Figure 2: Shift Δf of the second contact resonance for magnetite and for maghemite at a static load $F_N = 1080$ nN.

Having the same crystalline structure and the same grain size, magnetite and maghemite only differ in stoichiometry. Indeed, maghemite results from the complete oxidation of the Fe2+ cations initially present in maghemite. In the material, the oxidation proceeds by the fixation of new oxygen ions which is associated with the simultaneous creation of new unit cells in which the oxygen sites are occupied and the cation sites are not. Thus the resulting maghemite can be seen as magnetite with cation vacancies. These cation vacancies would soften the material. That is exactly proved by our AFAM measurements.

5. CONCLUSION

The AFAM technique is a sensitive method for the quantitative measurement of local elasticity, here on a scale of 50 nm. On a silicon single-crystal oriented in <100> direction, the results are in good agreement with the value reported in the literature. In nanoscaled thin films of ferrites with a grain size of about 70 nm, we were able to detect the difference of the elasticity caused by the deviation from the stoichiometry improving chemical and physical understanding of nanoscaled ferrites.

6. ACKNOWLEDGEMENTS

One of us (E.K.) was supported by a stipend from the EU within the HCM program. It is a pleasure to thank J.D. Niepce, University of Dijon for helpful discussions and a critical reading of the manuscript.

7. REFERENCES

(1) Koch, A.J. and Becker, J.J., J. Appl. Phys., 1968, 39, 1261
(2) Kester, E., Gillot, B., and Tailhades, Ph., Mat. Chem. Physics, 1997, 51, 258
(3) Perriat, P., Domenichini, B., and Gillot, B., J. Phys. Chem. Solids, 1996, 57, 1641
(4) Kester, E. and Gillot, B., J. Phys. Chem. Solids, 1998, to be published
(5) Rabe, U. and Arnold W., Appl. Phys. Lett. 1994, 64 1493
(6) Rabe, U., Janser, K., and Arnold, W., Rev. Sci. Instr., 1996, 67, 3281
(7) Yamanaka, K. and Nakano S. Jpn. J. Appl. Phys., 1996, 35, 3787
(8) Cretin, B. and Vairac P., Appl. Phys. Lett. 1997, 71, 2082
(9) Labview, Version , National Instruments, Austin, Tx, USA
(10) Turner, J.A., Hirsekorn, S., Rabe, U., and Arnold, W., J. App. Phys., 1997, 82, 966
(11) Mazeran, P.E. and Lubet, J.L., Trib. Lett. 1997, 3, 125
(12) Wright, O. and Nishiguchi N., App. Phys. Lett. 1997, 71, 626
(13) Rabe U., Turner J., and W. Arnold, Appl. Phys. A, 1998, S66, 277
(14) Burnham N., Colton R. J., and Pollock, H.M., Nanotechnology, 1993, 4, 64
(15) Wolter, O., Bayer, Th., and Geschner, J., J. Vac. Sci. Technol., 1991, B9-2, 1353
(16) Kulatov, M.A., J. Cryst. Growth, 1996, 158, 261
(17) Bouet, L., Tailhades, Ph., and Rousset, A., J. Mag. Mater., 1996, 153, 389

Pergamon

NanoStructured Materials, Vol. 12, pp. 783–788, 1999
Elsevier Science Ltd

0965-9773/99/$–see front matter

PII S0965-9773(99)00236-6

OPTIMIZING NANOFABRICATED SUBSTRATES FOR SURFACE ENHANCED RAMAN SCATTERING

L. Gunnarsson, S. Petronis, B. Kasemo, H. Xu, J. Bjerneld and M. Käll
Department of Applied Physics,
Chalmers University of Technology, 412 96 Göteborg, Sweden,

Abstract *- Recently, Surface Enhanced Raman Scattering (SERS) has been used to record vibrational spectra from individual molecules adsorbed on colloidal silver particles. For specific particle dimensions an enormous enhancement, by a factor of 10^{14}, was achieved.*

In this work we intend to investigate the size and geometry dependence of the SERS effect on supported particles, by manufacturing artificial structures by modern nanofabrication techniques. Arrays of 100-200 nm silver particles of different shapes were prepared on a Si wafer by electron beam lithography, and were characterized by scanning electron microscopy. Preliminary Raman scattering experiments were performed with Rhodamin 6G (R6G) as a test molecule. Enhancement of the Raman signal was observed on all nanofabricated silver patterns, compared to the signals on a uniform silver film or on the (oxidized) Si surface.
©1999 Acta Metallurgica Inc.

INTRODUCTION

The enhancement of Raman scattering by rough metallic surfaces and microscopic metal domains has been known for more than two decades (1, 2). The intensity of the SERS signal is frequently enhanced by a factor 10^5-10^6. The theory of the SERS phenomenon has focused on classical *electromagnetic* considerations, which show that a curved metal surface gives rise to an enhanced field when the incident or scattered light are in resonance with localized surface plasmons.

Recently much larger enhancement factors, in the range 10^{14}-10^{15}, have been observed for dye molecules adsorbed on colloidal silver particles of specific dimensions (3,4). This giant enhancement allowed the recording of Raman vibrational spectra from a *single* molecule for the first time. Since Raman scattering measurements provides highly resolved vibrational information, single-molecule detection by SERS is expected to extend and complement fluorescence studies. Recent work at our department have shown that the results of Nie and Emory (4) can be extended to a wide variety of more complex biomolecules (5).

Only a small portion of the silver colloids - "hot particles" - gave rise to the giant enhancement, indicating that the size and shape of the particles are of great importance. Imaging of the colloids revealed that the "hot particles" had a size of 110-120 nm in diameter.

In this study we investigate the size and shape dependence of the SERS phenomenon by fabricating arrays of silver particles by modern micro- and nanofabrication methods extensively used for microelectronics purposes, as well as catalysis (6) and biomaterials (7) research. The fabrication technique is well developed and both the shape, size and arrangement of the features can be readily controlled. The minimum size attainable at present is

approximately 20 nm. By systematically controlling the geometry of the arrays and performing Raman scattering measurements we hope to establish the relation between the giant Raman enhancement and the dimensional aspects of the particles.

MATERIALS AND METHODS

Nanofabrication

All the nanofabrication in this work has been performed at the Swedish Nanometer Laboratory at Chalmers University of Technology.

For the measurements 5 μm x 5 μm and 10 μm x 10 μm arrays of silver particles on a Si(100) surface were prepared, with varied size, shape and separation of the particles. Within each array all the silver particles had a constant shape, size and separation. Three particle shapes (circular, triangular and square), two particle sizes (100 nm and 200 nm), and ten different particle separations (ranging from 10 nm to 500 nm) were prepared. For reference we prepared 100 x 50 μm^2 areas of uniformly deposited Ag films on each substrate.

The fabrication technique used in this work is based on electron beam lithography (EBL) and the so-called lift-off procedure. First an electron-sensitive polymer (resist) layer is spin-coated on a clean silicon wafer. The resist is exposed in an electron beam lithography machine (JEOL JBX5D-II, 50 keV) which draws a prescribed pattern in the resist with a focused electron beam. At the exposed areas the resist is removed by a suitable solvent/developer. The sample is then placed in a thin film vapor-deposition system (AVAC HVC 600) where (in this work) a 30 nm thick silver layer is deposited through the polymer mask (the exposed and developed resist). The last manufacturing step is to remove the polymer mask as well as the deposited film on top of the mask in a solvent that removes the unexposed resist.

For the smaller patterns (separation and size <150 nm) we used a double-layer resist system (see Table 1). In this case two different layers of electron sensitive resists are spin-coated on the clean wafer. By under-developing the top layer and over-developing the bottom layer an undercut in the polymer film is achieved which facilitates the lift-off procedure. The resulting patterns have been analyzed in a Scanning Electron Microscope (SEM) JEOL JSM-6301F.

TABLE 1
Resist Systems Used for Nanofabrication

Resist systems	**ZEP7000B-97**	**ZEP520/PMGI**	**PMMA 350/180**
Bottom layer	-	PGMI-SF7	180 k MWt PMMA
Top layer	ZEP7000B-97 : chlorobenzene 1:1	ZEP520 : chlorobenzene 1:2	350 k MWt PMMA
Comments	fast exposure, resolution 100 nm	medium exposure, resolution 30 nm	slow exposure, resolution 30 nm

Adsorption and Raman spectroscopy of R6G molecules.

The R6G molecules were adsorbed by depositing a 10 μl droplet of R6G solution (10^{-9}, 10^{-7} or 10^{-5} M) on the nanopatterned surfaces and drying it in air. This resulted in a fairly homogeneous coverage of the sample area. Large conglomerates of R6G were observed on a few occasions but these sample areas were avoided in the SERS experiments.

For the Raman experiments we used single grating spectrometers (Dilor) equipped with holographic notch filters and CCD camera detection. The measurements were performed in back-scattering geometry, using confocal optics for illumination and collection of the Raman scattered light. This resulted in a spatial resolution (laser spot size) of the order 2-3 μm. The excitation wavelength was either 5245 Å or 6328 Å and the power at the sample was kept below 8 mW. The spectrometers slits were set to give an frequency resolution of 5 -10 cm^{-1}.

RESULTS AND DISCUSSION

Nanofabrication

Fig. 1 shows SEM pictures of some typical nanofabricated silver patterns. We have manufactured 100 and 200 nm sized circular, triangular and square silver particles at all different separations mentioned in the previous section. The thickness of the silver particles is 30 nm.

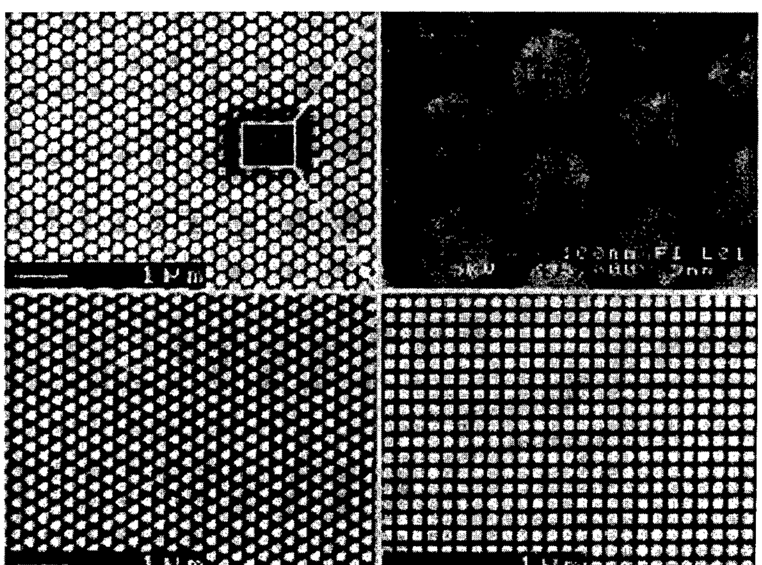

Fig. 1 SEM pictures of different patterns: 200 nm circular, triangular and square particles, separated by 100 nm. The thickness of the silver particles is 30 nm. The dark area in the top left picture is caused by the intensive scan by the e-beam in the SEM when the magnified top right picture was collected.

The smaller the separation the harder it is to get a perfect pattern and there were often some parts at the edges of the array where silver flakes remained. Since the spot area of the laser beam is as small as 2-3 μm this has no consequence for the SERS measurements, where non-perfect areas can be avoided. A closer look at the squares and triangles reveals that the corners are slightly rounded. This is due to the finite diameter of the electron beam (~10 nm), which also results in a small increase of the patterned size and in a decreased separation compared to the nominal one.

As already mentioned, two different excitation wavelengths, 5145 Å and 6328 Å, was used. Of these, the most suitable for Raman spectroscopy of R6G is 5145 Å, since this wavelength is close to being in resonance with an electronic transition of the molecule and thus yields an additional resonance enhancement of the Raman signal. In addition, theoretical considerations indicate a much larger surface enhancement for this wavelength compared to the red laser excitation at 6328 Å (8). On the other hand, the strong optical absorption at 5145 Å also gives rise to an intense fluorescence background, which decreases the signal to noise ratio (S/N). This is not the case for 6328 Å excitation.

Measurements were performed with 5145 Å excitation for a 10^{-9} M solution of R6G molecules adsorbed on a set of samples with arrays of circular, triangular, and square silver particles, 100 and 200 nm in size and separated by 10, 50, 100, 150 and 200 nm. On each sample there was also a reference silver area.

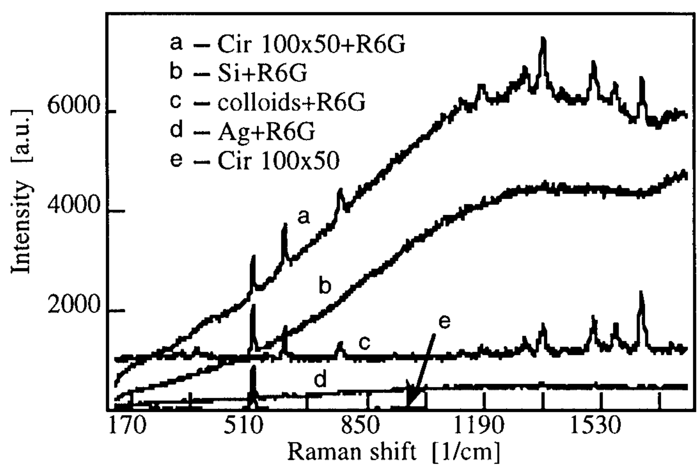

Fig. 2 Raman spectra obtained with 5145 Å excitation. a) R6G molecules adsorbed on a nanofabricated pattern array of 100 nm circular particles separated by 50 nm. The spectra looked almost the same for R6G molecule adsorbed on all different patterns, b) R6G molecules adsorbed directly on the Si surface, c) R6G molecules adsorbed on colloidal silver particles in solution, d) R6G molecules adsorbed on a uniform silver film, and e) a nanofabricated pattern (same as in b) but with no R6G molecules adsorbed.

In Fig. 2 we give examples of the Raman spectra obtained and it is clear that the nanofabricated patterns are highly efficient SERS substrates. Whereas R6G adsorbed to smooth Si and Ag surfaces only give rise to fluorescence, and no visible Raman scattering; the spectrum obtained from R6G adsorbed to an array of 100 nm circular silver particles, separated by 50 nm, exhibits a strong Raman contribution. The magnitude of this Raman scattering is similar to what is observed in colloidal SERS measurements. A more quantitative comparison can not yet be made.

A comparison between the R6G fluorescence intensity observed for the smooth silicon and silver surfaces, indicates that the metal surface quenches the fluorescence to some extent. It may thus be advantageous to deposit the Ag arrays on a metal film (e.g. aluminum). Work in this direction is in progress and will be reported elsewhere.

We obtained more or less the same SERS efficiency for all the different particle arrays, which is why no specific details are revealed about the geometry dependence of the SERS effect from these measurements. In order to obtain further information on this issue, a new set of samples were prepared for measurements with 6328 Å excitation. In this case we used 200 nm sized silver particles (again circular, triangular and square) and the inter-particle separation 100, 200, 300, 400, and 500 nm. Some of the results are shown in Fig. 3.

As expected from the discussion above the R6G Raman intensities observed were many orders of magnitude lower than for the green (5145 Å) excitation, and we were forced to use the highest power (8 mW) and a higher R6G concentration, 10^{-5} M, in order to detect any signal from the R6G molecules at all.

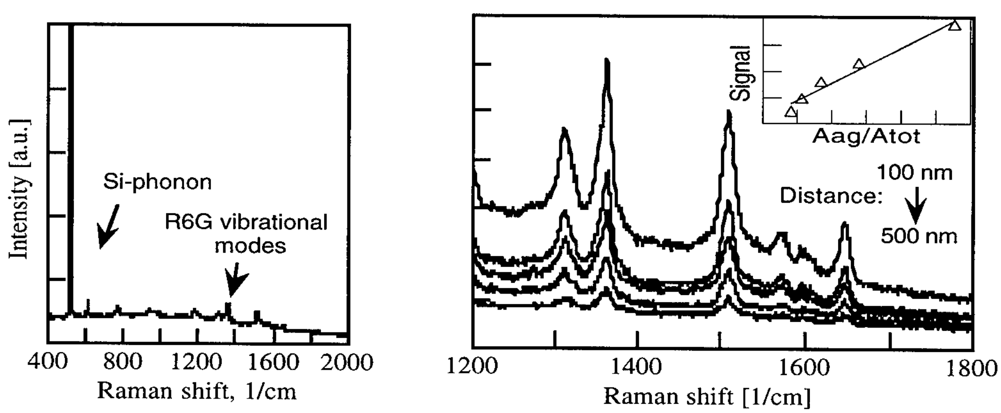

Fig. 3 Raman spectra from obtained with 6238 Å excitation. The left hand picture shows the spectrum of R6G adsorbed on an array of 200 nm triangular Ag particles 100 nm apart. The Raman signals from the R6G vibrational modes are very weak compared to the signals from the Si phonons. In the right hand picture the Raman signals of R6G molecules adsorbed on arrays of 200 nm triangular Ag particles, separated by 100, 200, 300, 400 and 500 nm are shown. In the inset the peak height versus the ratio of silver and total area of the array is plotted.

Nevertheless, the nanofabricated patterns also in this case yield an enhancement of the Raman signal of R6G which is not seen from the Si surface or a uniform silver film. Also, the intensity of the R6G signals clearly decreases with increasing separation between the particles as can be seen in the right side of Fig. 3, where the spectra from R6G molecules adsorbed on arrays of 200 nm triangles at five different separations are shown. R6G molecules adsorbed on a uniform silver-film did not give rise to any observable Raman shifts. The origin of this decrease of the signal is still unclear. The peak height seems to be proportional to the silver area or similarly to the number of silver particles in the laser spot area, as shown in the inset of Fig 3. Further results (not shown) from the same measurements indicates that the triangular particles give rise to a higher enhancement than the circular and square ones, but more measurements are required to confirm this.

SUMMARY

The preliminary nature of these data is emphasized. However, we demonstrate that the nanofabrication approach is a promising one to explore the giant Raman enhancement. For future work more detailed characterization of the particle microstructures is required, smaller particle sizes and separations should be explored, and the R6G deposition technique can be improved.

REFERENCES

1. M. Moskovits, *Reviews of Modern Physics* **57**, 783 (1985).
2. F. J. García-Vidal, J. B. Pendry, *Physical Review Letters* **77**, 1163 (1996).
3. K. Kneipp, Y. Wang, H. Kneipp, L. T. Perelman, I. Itzkan, R. R. Dasari, M. S. Feld, *Physical Review Letters* **78**, 1667 (1997).
4. S. Nie, S. R. Emory, *Science* **275**, 1102 (1997).
5. H. Xu, J. Bjerneld and M. Käll et al., *to be published*
6. K. Wong, S. Johansson, and B. Kasemo, *Faraday Discussions* **105**, 237 (1996).
7. J. Gold, Doctoral Thesis, Chalmers University of Technology and Göteborg University (1996)
8. Privat communication with Prof. J. B. Pendry, Imperial College of Science and Technology, London

Pergamon

NanoStructured Materials, Vol. 12, pp. 789–796, 1999
Elsevier Science Ltd

0965-9773/99/$–see front matter

PII S0965-9773(99)00237-8

LAYER-BY-LAYER SELF-ASSEMBLY: THE CONTRIBUTION OF HYDROPHOBIC INTERACTIONS

N. A. Kotov
Department of Chemistry, Oklahoma State University, Stillwater, OK, 74078, USA,
kotov@okway.okstate.edu

ABSTRACT *-- The layer-by-layer (LBL) adsorption of polyelectrolytes and other compounds is considered to be the result of electrostatic attraction between ionic side-groups of a polymer backbone to oppositely charged groups located on the surface of a substrate. The energy of electrostatic attraction, transformation of ionic atmosphere and the hydration shell around a polyelectrolyte chain during the self-assembly were estimated on the basis of available theoretical and experimental data for aqueous polyelectrolyte solutions. The analysis revealed that both ionic and hydrophobic interactions must be taken into account considering LBL multilayer formation. By using new data on adsorption of proteins, dyes, polymers, and nanoparticles it was demonstrated that the proposed approach to LBL explained a number of experimental observations that were difficult to rationalize in the framework of a pure electrostatic mechanism. ©1999 Acta Metallurgica Inc.*

1. INTRODUCTION

Self-assembly of polyelectrolytes (PE) has recently developed into a viable alternative to Langmuir-Blodgett technique, spin-coating, in-situ polymerization and other methods of preparation of organic and hybrid nanostructures. This technique was initially proposed for the layer-by-layer (LBL) adsorption of oppositely charged polymeric molecules(1) and later it has been extended to the self-assembly of biological compounds (2-5), conducting polymers(6), zirconium phosphate(7), dyes(8,9,14), metal nanoparticles(7,10-13), semiconductor quantum dots(15), alumosilicates(16-20), and graphite oxide(21). The layer-by-layer deposition is particularly attractive for its exceptional simplicity. Typically it consists of four consecutive steps: 1) adsorption of a positive component, 2) washing, 3) adsorption of a negative component, and 4) final washing. These steps can be repeated in a cyclic fashion for automatic film production. A trade-off for the ease of preparation is structural imperfection. As compared to LB films, the polyelectrolyte films produced by this method are substantially less ordered. Nevertheless, they can find numerous application as very interesting composite materials. Both organic-inorganic superlattices(7,8, 10-21), protein assemblies(3-5), new optical, and electronic coatings(8-21) can be constructed on their basis.

The driving force of the layer-by-layer self-assembly of polyelectrolytes is perceived to be solely electrostatic attraction of oppositely charged groups. Indeed, in most cases, alternation of positively and negatively charges species is required for the process to be successful. On the

other hand, LBL assemblies can be considered as a special case of polyelectrolyte complexes(22), for which the importance of short-range hydrophobic interactions is a well established fact(23, 24). Hence, it would be quite appropriate to look into the effect of hydrophobic interactions in LBL. Besides ionic and hydrophobic forces, other types of attractive interactions may take part in the sequential adsorption of polymer layers. In one of the recent publications(25) it was demonstrated that quite weak charge transfer interactions may also result in the formation of multilayers.

The starting point of this research was inability of the classical electrostatic approach to explain a number of experimental facts. 1) Positively charged myoglobin and lysozyme do not self-assemble on negatively charged alumosilicate, while no difficulties in building up multilayers of these proteins is encountered by using negatively charged polymers(4). 2) Positively charged protonated forms of polyaniline and polypyrrole can be prepared both in aqueous and in polar organic media, for example in dimethylacetamide (DMA). Their solubility in water is much lower than that in DMA. Nevertheless, aqueous solutions are the preferred media for the LBL self-assembly(6). 3) The dependence of surface density of negatively charged nanoparticles adsorbed on poly(dimethyldiallammonium chloride), PDDA, goes through a sharp maximum being negligibly small both for very highly and very weakly charged particles(15). This finding indicates that, a high charge *per se* does not necessarily ensure efficient self-assembly. 4) The dependence of the thickness of the adsorbed polyelectrolyte layer on the degree of quaternization (charge) has a fairly complex shape with peaks and valleys which can hardly be rationalized assuming monotonous increase of electrostatic attraction of an adsorbate to the substrate with greater number of NR_4^+ groups(26).

It is clear that the attraction of oppositely charged PE side groups represents a quite powerful, but not the only type of intermolecular interactions between the polyelectrolyte molecules. The others include ion-dipole, dipole-dipole, and Van-der-Waals interactions and may involve the molecules of solvent and hydrocarbon chains of the polyelectrolytes. Here, a thermodynamic analysis of PE LBL self assembly have been attempted in order to assess energies of the electrostatic and other contributions.

2. THE GIBBS FREE ENERGY OF FILM FORMATION

2.1. Model.

PE(+) and PE(-) notations will be used for positively and negatively charged polyelectrolytes respectively. Layer-by-layer self-assembly can be regarded as a process of adsorption of PE(+) on a layer of PE(-) present on a substrate:

PE(+)	------>	PE(+)	(1)
(in aqueous solution)		(adsorbed on PE(-))	

The goal of the analysis below is to find an estimate for the Gibbs free energy of reaction 1, ΔG_{SA}.

A hydrated ion can be represented as a charged core and a layer of partially immobilized water molecules around it (hydration shell)(26). The number of H_2O units bound in the hydration layer can vary from 1 to 14 depending on a charge and a diameter of an ion. Outside the hydration shell, electrostatically attracted oppositely charged ions form an ionic atmosphere.

Their concentration reaches a maximum at the border of the shell and quickly falls down to zero as the distance to the central ion increases.

Reaction 1 can be considered as an ion exchange process which effectively results in the replacement of aqueous media around PE(+) with PE(-). Thermodynamically, this process can be divided into several steps: removal of the ionic atmosphere around PE(+) and PE(-), partial removal of the first hydration shell around PE(+) and PE(-), and formation of PE(+)/PE(-) film. Accordingly, the change in the free Gibbs energy of reaction 1, ΔG_{SA}, can be divided into several contributions:

- (1) transformation of the *ionic atmosphere* of the PE(+) molecule in solution, ΔG_{atm+};
- (2) transformation of the *hydration shell* around PE(+), ΔG_{hyd+};
- (3) transformation of the *ionic atmosphere* around PE(-), ΔG_{atm-};
- (4) transformation of the *hydration shell* around PE(-), ΔG_{hyd-};
- (5) electrostatic interaction of opposite charges in PE(+) and PE(-) upon adsorption, $\Delta G_{+/-} = \Delta H_{+/-} - T\, \Delta S_{SS}$;
- (6) hydrophobic interaction of organic parts of PE molecules, ΔG_{org};

ΔG_{atm+} and ΔG_{atm-} represent ion-ion interactions between the polyelectrolyte chains and supporting electrolyte, ΔG_{hyd+} and ΔG_{hyd-} represent ion-dipole interactions with molecules of water. $\Delta H_{+/-}$ is a thermodynamic parameter considered to be primarily responsible for the LBL self-assembly. It represents electrostatic attraction of charged headgroups of oppositely charged polyelectrolytes.

Coulombic attraction of two PE chains also results in a change of degrees of freedom due to the transition to a solid state expressed as ΔS_{SS}. Combined with $\Delta H_{+/-}$, it yields the free energy of the polymer-polymer electrostatic attraction $\Delta G_{+/-}$.

ΔG_{org} is a cumulative representation of hydrogen binding in shells of structured water around hydrocarbon parts of PEs and the short-range Van-der-Waals forces between all atoms in the system. It has a large contribution of entropic nature originating from the liberation of structured of water molecules when hydrophobic parts of PE chains make a contact (hydrophobic interactions).

2.2. Energy of the ionic atmosphere

The energy of ionic atmosphere and conformation of PE strongly depend on ionic strength. Here only the case of a low ionic strength (≈0.01M) is considered. 0.01 M ionic strength corresponds to a typical concentration of both PE(+) or PE(-) used for LBL(1-22). Under these conditions, a highly charged macromolecule acquires an extended conformation approaching a free uncoiled chain, which mathematically can be approximated as a rigid rod.

The thermodynamics of electrostatic interactions between polyelectrolytes in water at low concentrations can be described quite well by using the Poisson-Boltzmann formalism. In Ref. 27 the PB equation was numerically solved for various patterns of charge distribution along the PE chain and for various ionic strength. The energy necessary to relocate ions electrostatically attracted to cylindrical polyelectrolyte chain from the ionic atmosphere to the infinity, or the energy of ionic atmosphere, E_{atm}, was calculated to be 3.34 kcal/mol = 14 kJ/mole for a typical PE at 0.01 M ionic strength. The contribution of the ionic atmosphere restructuring to ΔG_{SA} directly depends on E_{atm}. Upon adsorption to a substrate, a cylindrical ionic cloud around PE(+)

transforms into a collective double electric layer of a charged plane. The lower limit of the Gibbs energy associated with this restructuring can be found by assuming the charged plane to be composed of polyelectrolyte molecules that lost the ionic atmosphere only on one hemisphere adjacent to the substrate. The other half of the ionic atmosphere facing the solution is retained, therefore

$$\Delta G_{atm+} > E_{atm}/2 = 7 \text{ kJ/mol.} \tag{2}$$

Energy expenditures for the destruction of the ionic atmosphere of adsorbed negative polyelectrolyte PE(-) can be appraised in the same fashion,

$$\Delta G_{atm-} > E_{atm}/2 = 7 \text{ kJ/mol.} \tag{3}$$

2.3. Energy of the hydration shell

Adsorption of PE(+) onto PE(-) is analogous to the transfer of ions from an aqueous medium into an organic one. The environment in PE complexes is quite hydrophobic. The average dielectric constant inside them was reported to be $\varepsilon^{\text{PE complex}} = 5.5$ (28). The energy required to replace solvent molecules in the solvation shell can be estimated from the free energy of ion transfer from water to a solvent of an appropriate polarity, ΔG_{tr}. One can safely assume that the internal dielectric constant of LBL films $\varepsilon^{\text{PE complex}} < 32.6$, which is the dielectric constant of methanol. Since ΔG_{tr} increases for more hydrophobic solvents, the energy of the partial destruction of the organic hydration shell ΔG_{hyd+} and ΔG_{hyd-} will be larger than ΔG_{tr} of corresponding ions from water to methanol. For poly(dimethyldiallylammonium bromide) chain, the charged groups are quaternary ammonium bases. The free energy of $N(CH_3)_4^+$ transfer from water to CH_3OH was reported to be 6 kJ mole, and thus

$$\Delta G_{hyd+} > 6 \text{ kJ/mol} \tag{4}$$

A similar procedure can be applied to ionic groups of PE(-). Usually, negatively charged polyelectrolytes used in the self-assembly bear -COOH or $-SO_3H$ groups ionizable to $-COO^-$ and $-SO_3^-$ respectively. For simplicity, lets assume that we have polyacrilic acid, which was shown to form multilayers with PDDA. The transfer energy data for CH_3COO^- ion for the water - methanol pair yields ΔG_{tr}=16 kJ/mol. Therefore, $\Delta G_{hyd-} > \Delta G_{tr}(CH_3COO^-) = 16$ kJ/mol

$$\Delta G_{hyd-} > 16 \text{ kJ/mol} \tag{5}$$

2.4. Electrostatic interaction of two polyelectrolyte chains

Covalent bonds between the monomer units do not allow the charged side groups of the PE to attain a minimum energy conformation achievable for regular supporting electrolyte, while the lower polarity in PE(+)/PE(-) causes $\Delta H_{+/-}$ to become more negative as compared to the low molecular weight ionic atmosphere.

Most of the counterions around polyelectrolytes are concentrated within few nm around the PE chain (condensation effect) (28). In all layer-by-layer self-assembled structures, including multilayers of proteins, alumosilicates, and nanoparticles, thickness of a single polymer layer was determined to be 2-5 nm (1-22, 29). This enables consideration of the radial distribution of charges around PE(+), of buffer salt ions in solution and that of ionic side groups around a PE(+) molecule surrounded by PE(-) as qualitatively similar. This approximation removes constraints on ion positions imposed by the covalent bonds between charged groups. Therefore, $\Delta H_{+/-} > \Delta H_{el}$

$^{\text{free ions}}$, where $\Delta H_{el}^{\text{ free ions}}$ is the energy of the ionic atmosphere of a low molecular weight salt in a media corresponding to the bulk of the PE complex.

The energy of two interacting objects whose charge is arbitrary distributed in space is inversely proportional to the dielectric constant:

$$\Delta H_{el}^{\text{ pair}} = (1/4\pi\varepsilon\varepsilon_0)\int(q_+(x, y, z)\, q_-(x, y, z)/r^2)d(x, y, z) \qquad (6),$$

where q_+ and q_- can be considered as a collection of point charges located on PE(+) and PE(-) respectively. The difference in shapes and charge distributions between different objects does not disturb the universal nature of $\Delta H_{el} \sim 1/\varepsilon$ proportionality, which is applicable both to point charges and to charge cylinders, because the mentioned differences would affect only the term under the integral sign in eq. 5, while $(1/4\pi\varepsilon\varepsilon_0)$ will remain unchanged. This fact helps to assess $\Delta H_{el}^{\text{ free ions}}$ by relating it to the energy of ionic atmosphere in water, ΔH_{atm}

$$\Delta H_{el}^{\text{ free ions}}/\, \Delta H_{atm} = \varepsilon^{\text{solution}}/\varepsilon^{\text{ PE complex}} \qquad (7).$$

ΔH_{atm} of a polyelectrolyte at ionic strength 0.01 M was calculated in Ref. 27 and was found to be equal to -0.32 kcal/mol = -1.3 kJ/mol.

$$\Delta H_{el}^{\text{ free ions}} = (\varepsilon^{\text{solution}}/\varepsilon^{\text{ PE complex}})\Delta H_{atm} = (78/5.5)\bullet(-1.3)\text{ kJ/mol} = -18.4\text{ kJ/mol} \qquad (8)$$

Since $\Delta H_{el}^{\text{ free ions}}$ is always more negative than $\Delta H_{+/-}$, the interaction energy between positive and negative polyelectrolytes in LBL films can be estimated by an inequality:

$$\Delta H_{+/-} > \Delta H_{el}^{\text{ free ions}} > -18.4\text{ kJ/mol} \qquad (9)$$

2.5. Entropy

The entropy change for LBL self-assembly includes the contributions from (1) the release of ions from the solvation shell, (2) the reorientation of water previously oriented by charged headgroups of PE, (3) the destruction of a shell of water molecules around hydrophobic parts of PE, (4) the loss of mobility of polyelectrolyte chains, ΔS_{SS}. Entropy contributions (1) and (2) have been taken into consideration when ΔG_{atm+}, ΔG_{atm-}, ΔG_{hyd-}, ΔG_{hyd+} were estimated. Entropy (3) is accounted in the hydrophobic interactions discussed below. In fact, the increase of entropy upon hydrocarbon chain contact is responsible for 85% of ΔG_{org} (32). At the moment, ΔS_{SS} needs to be assessed and it is sufficient to establish

$$\Delta S_{SS} < 0 \qquad (10)$$

which is obviously true due to the loss of the degrees of freedom associated with the rotation and bending of polymer chains upon formation of a solid film. In general, the absolute value of ΔS_{SS} is not supposed to make a principal contribution to ΔG_{SA} (-10 J/mol•K $< \Delta S_{SS} < 0$) (30-31) because polyelectrolytes in PE complexes were found to be in an amorphous disorganized state (1-22).

2.6. Calculation of ΔG_{SA}

The ΔG_{SA} of adsorption of PE(+) on PE(-) can be expressed as

$$\Delta G_{SA} = \Delta G_{atm+} + \Delta G_{hyd+} + \Delta G_{org} + \Delta G_{atm-} + \Delta G_{hyd-} + \Delta H_{+/-} - T\Delta S_{SS} \qquad (11)$$

By using expression 2, 3, 4, 5, 9, and 10 one can obtain:

$$\Delta G_{SA} = \Delta G_{atm+} + \Delta G_{hyd+} + \Delta G_{org} + \Delta G_{atm-} + \Delta G_{hyd-} + \Delta H_{+/-} - T\Delta S_{SS} > 7\text{ kJ/mol} +$$

$$+ 6\text{ kJ/mol} + \Delta G_{org} + 7\text{ kJ/mole} + 16\text{ kJ/mole} + (-18.4\text{ kJ/mol}) - 0 \qquad (12)$$

$$\Delta G_{SA} > 17.6\text{ kJ/mol} + \Delta G_{org} \qquad (13)$$

Thus, one can see that the energy of ion-ion interactions in PE(+)/PE(-) film, $\Delta H_{+/-}$ (eq. 8), cannot

compensate for the positive contributions to ΔG_{SA}. The required negative contribution to ΔG_{SA} must come from ΔG_{org}, which describes hydrophobic interactions

How strong the hydrophobic interactions are? The energy of hydrophobic interaction between two $-CH_2-$ groups was found to be -7.5 kJ/mol (32). Since there are eight of $-CH_2-$ groups in each dimethyldiallylammonium unit, the value of ΔG_{org} is likely to be contained in the following interval

$$-60 \text{ kJ/mol} < \Delta G_{org} < -7.5 \text{ kJ/mol} \quad (14)$$

The comparison of eq. 14. with eqs. 2, 3, 4, 5, 9, and 10 demonstrates that the energy of hydrophobic interactions is at least comparable to the input of ion-ion ($\Delta H_{+/-}$, ΔG_{atm+}, and ΔG_{atm-}) and ion-dipole (ΔG_{hyd+}, ΔG_{hyd-}) interactions.

3. CORRELATION WITH EXPERIMENTAL DATA

Ref. 26 presents experimental data on polyelectrolyte multilayer build-up in the presence of large concentrations of low molecular weight salt (NaCl). Na^+ and Cl^- ions screen electrostatic forces between the substrate and the polyelectrolyte in solution which is supposed to decrease the amount of adsorbed material to zero. Conversely, a substantial increase of the polyelectrolyte layer thickness has been observed(34) experimentally, which clearly indicates participation of nonelectrostatic component in polyelectrolyte binding.

Many proteins, for example myoglobin or lysozyme, readily form multilayers on oppositely charged polymers, such as poly(styrenesulfonate), PSS(4). When negatively charged PSS is replaced with negatively charged alumosilicate sheets (montmorillonite), the formation of multilayers does not occur(4). Protein-alumosilicates complexes are not "cemented" by short-range charge-independent interactions due to a quite hydrophilic surface of alumosilicates. The loose electrostatic aggregates between alumosilicate and protein can be easily destroyed during the subsequent rinsing with water. Conversely, strong hydrophobic forces present in protein-polyelectrolyte multilayers make these complexes exceptionally stable.

The average particle density of negatively charged CdS nanocrystallites versus their surface charge as they are being adsorbed on a layer of PDDA have a maximum for relatively weakly charged particles. The nanoparticles were stabilized by a mixed layer of thiolactic acid (TLA) and ethanthiol (ET) whose ratio controls long-range electrostatic attraction ($-COO^-$ groups of TLA) and short-range hydrophobic forces ($-CH_2-CH_3$ moieties of ET). The details of experimental procedure can be found in Ref. 22. Precipitous decline of particle density with *the increase* of electrostatic attraction to the substrates indicates that there exist an optimum ratio between the number of hydrophobic and charged groups in order for the self-assembly to occur. The point of maximum surface density of nanoparticles corresponds to the optimum combination of electrostatic attraction and binding to the polyelectrolyte via hydrophobic interactions, which makes the adsorbed layer thermodynamically more preferable than a dissolved state.

The significance of hydrophobic forces can be also seen in recent results on LBL self-assembly of cationic and anionic dyes on PDDA, PSS and poly(ethyleneimine), PEI (5). It was observed that large dye molecules, for example, Congo Red, tetraphenylporphinetetrasulfonic acid, and $\alpha,\beta,\gamma,\delta$-tetrakis(1-N-methylpyridyl)porphine tetrakis(*p*-toluenesulfonate), TMPyP, have a greater tendency to self-assemble than smaller ones. Methylviologen was observed not to

adsorb on PSS despite the fact that it has twice as high positive charge density per atom as TMPyP. The situation here is identical to the case of highly charged CdS nanoparticles: a dye molecule must have properly balanced hydrophilic and hydrophobic properties in order to self-assemble. If the a molecule is too hydrophilic, *i.e.* it is small and highly charged it will not form a thermodynamically stable complex with polyelectrolyte (ΔG_{org} in eq. 13 is not negative enough to make $\Delta G_{SA}<0$).

4. CONCLUSION

The thermodynamics of the self-assembly process has been evaluated. It was demonstrated that strong electrostatic attraction of opposite charges located on a substrate and on a substance to be assembled does not guarantee the formation of multilayers. Along with pure electrostatic forces, hydrophobic interactions, restructuring of the solvation shell and the ionic atmosphere have been considered. Short-range hydrophobic forces can be identified as one of the important factors determining the ability of a compound to self-assemble via LBL technique. They should be considered as the driving force of layer-by-layer adsorption. Results on the preparation of LBL films of proteins, alumosilicates, dyes, polymers and nanoparticles confirm significance of hydrophobic interactions.

5. ACKNOWLEDGEMENT

The author would like to thank Oklahoma State University Research Foundation, Center for Laser and Photonics Research (CLPR), Center for Sensors and Sensor Technologies (CSST), and NSF-EPSCoR program for the financial support of this research.

6. BIBLIOGRAPHY

1. Decher, G., Hong, J. D., Schmitt, J. *Thin Solid Films*, **1992**, *210/211*, 831.
2. Lvov, Y., Haas, H., Decher, G., Möhwald, H., Mikhailov, A., Mtchedlishvily, B., Morgunova, E., Vainstein, B. *Langmuir*, **1994**, *10*, 4232-4236.
3. Lvov, Y., Ariga, K., Kunitake, T. *Chem. Lett.*, **1994**, 2323-2326.
4. Lvov, Y., Ariga, K., Ichinose, I., Kunitake, T. *J. Am. Chem. Soc.*, **1995**, *117*, 6117.
5. Ariga, K., Lvov, Y.; Ichinose, I., Kunitake, T; *J. Am. Chem. Soc.*, **1997**, *119*, 2224.
6. Ferreira, M.,Cheung, J. H., Rubner, M. F. *Thin Solid Films*, **1994**, *244*, 806.
7. Keller, S. W., Kim, H. N., Mallouk, T.E. *J. Am. Chem. Soc.*, **1994**, *116*, 8817.
8. Ichinoze I., Fujiyoshi, K., Mizuki, S., Lvov, Y., Kunitake T. *Chem. Lett.*, **1996**, 257.
9. Wischerhoff, E., Laschewsky, A., Mayer, B. *Proceedings of European Conference on Organized Films*, ECOF 6, Sheffield UK, 11-14 Sept **1996**, 3.15.
10. Feldheim, D. L.; Crabar, K. C.; Natan, M. J.; Mallouk, T. E., *J. Am. Chem. Soc.*, **1996**, *118*, 7640.
11. Schmitt, J., Decher, G.; Dressik, W. J.; Branduo, S. L. Geer, R. E.; Shashidhal, R.; Calvert,

J. M., *Adv. Mater.*, **1997**, *9*, 61.

12. Freeman, R. G., Grabar, K. C., Allison, K. J., Bright, R. M., Davis, J. A., Guthrie, A. P., Hommer, M. B., Jackson, M. A., Smith, P. C., Walter, D. G., Natan, M. J. *Science,* **1995**, *267*, 1629.
13. Grabar, K. C.; Freeman, R. G.; Hommer, M. B.; Natan, M. J. *Analytical Chemistry*, **1995**, *67*, 735.
14. Cooper T. M., Campbell, A. L.,Crane, R. L. , *Langmuir*, **1995**, *11*, 2713.
15. Kotov, N. A., Dékány, I., Fendler, J. H. *J. Phys. Chem.,* **1995**, *99*, 13065.
16. Kleinfeld, E.R., Ferguson, G.S. *Chem. Mater.*, **1995**, *7*, 2327.
17. Kleinfeld, E.R., Ferguson, G.S. *Science*, **1994**, *265*, 370.
18. Kleinfeld, E.R., Ferguson, G.S., *Mat. Res. Soc. Symp. Proc.* **1995**, *369*, 697.
19. Lvov, Y.; Ariga, K.; Ichinose, I.; Kunitake, T. *Langmuir*, **1996**, *12*, 3038.
20. Kotov, N. A., Haraszti, T., Turi, L., Zavala, G., Geer, R. E., Dékány, I., Fendler J. H. *J. Am. Chem. Soc.,***1997,** 119 (29), 6821.
21. Kotov, N. A.; Dékány, I.; Fendler, J. H. *Advan. Mater.*, **1996**, *8*, 637.
22. Laschewsky, A., Mayer, B., Wischerhoff, E., Arys, X., Jonas, A., *Ber. Bunseng. Phys. Chem.*, **1996**, 100, 1033.
23. Philipp, B., Dautzenberg, H., Linow, K.-J., Kötz, J., Dawydoff, W. *Prog. Polym. Sci.*, **1989**, *14*, 91 an references therein.
24. Mikulik, J., Vinklarek, Z., Vondruska, M., *Collect. Czech. Chem. Commun.,* **1993,** 58, 713 and referencies therein.
25. Shimazaki, Y.; Mitsuishi, M.; Ito, S.; Yamamoto, M.; *Langmuir*, **1997**, *13*, 1385.
26. Hoogeveen, N. G, Cohen Stuart M. A. C., Fleer, G. J., Bohmer, M. R. *Langmuir*, **1996**, 12, 3675.
26. Marcus,Y. *Pure Appl. Chem.*, **1987**, *59*, 1093
27. Sharp, K. A. *Biopolymers*, **1995**, *36*, 227.
28. Rice, S. A., Nagasawa, M., Morawetz H., *Polyelectrolyte Solutions. A Theoretical Introduction., An International Series of Monographs and Textbooks*, Eds., N.O.Kaplan, H.A. Sheraga, Academic Press, London, New York, 1961, p.318.
29. Hong, J.D.; Lowack, K.; Schmitt, J.; Decher, G. *Prog. Coll. Pol. Sci.* **1993**, 93, 98 and ref. therein.
30. Chatterjee, S.K., Chhabra, M., Nigam, S., *Pure Appl. Chem.*, **1995**, A32(1), 157.
31. Chaterjee, S. K., Rajabi, F. H., Faharani, B. V., Chatterjee N. *Polym. Comm.*, **1991**, 32, 15, 473.
32. Israelachvili, J. *Intermolecular & Surface Forces*, Academic Press, 1992.
33. Hoogeveen, N., Cohen Stuart M. A., Fleer, G. J., *J. Coll. Interface Sci.*, **1996,** 182, 133.
34. Lvov, Y., Decher, G., Möhwald, H., *Langmuir,* **1993**, 9, 481.

Pergamon

NanoStructured Materials, Vol. 12, pp. 797–800, 1999
Elsevier Science Ltd

0965-9773/99/$–see front matter

PII S0965-9773(99)00238-X

NANOSTRUCTURAL STATE AND MAGNETISM OF RFe_2H_X HYDRIDES OBTAINED BY HYDROGEN-INDUCED AMORPHIZATION

A.Ye.Yermakov, N.K.Zajkov, N.V.Mushnikov, V.S.Gaviko, V.V.Serikov, N.M.Kleinerman
Institute of Metal Physics, Ural Branch of the Russian Academy of Sciences,
620219 Ekaterinburg, Russia

Abstract – *The magnetic properties and the structure of hydrogen-amorphized RFe_2H_x compounds (R=Y, Gd-Er) have been studied. During hydrogen-induced amorphization (HIA) the structure of RFe_2 compounds is likely to be decomposed into the areas enriched in R, exchange-uncoupled with Fe, and those enriched in Fe. At least two exchange coupling constants differing by order of magnitude have to be assumed to describe the temperature dependence of the magnetization. From the magnetization measurements the characteristic size of the structural components is estimated to be of the order of a few nanometers. HIA causes noticeable increase of the Fe-magnetic moment and the Fe-Fe exchange interaction, and a decrease of the R-Fe exchange interaction in comparison with analogous crystalline hydrides. The magnetic state of amorphous hydrides is non-uniform and for R=Tb...Er a canted magnetic structure in the R-sublattice is formed owing to a high local uniaxial anisotropy and a low R-Fe exchange interaction. ©1999 Acta Metallurgica Inc.*

INTRODUCTION

The reaction of rare-earth intermetallics RM_2 (R- 4f-, M-3d-metal) with gaseous hydrogen, as is known, results in the formation of an isostructural hydride of the approximate RM_2H_4 composition where hydrogen atoms occupy interstitials sites of 2R-2M and 1R-3M types. Due to the high mobility and affinity of H atoms to R-metals environments of 3R-M and 4R types can be formed at elevated temperatures, which was considered as a driving force for hydrogen-induced amorphization (HIA) (1). Amorphization under hydrogenation was first observed in $CeFe_2$(2). Further it was shown that most of the RM_2 compounds can be amorphized under hydrogenation (1).

Taking the $PrNi_2$-H system (3) as an example it was shown that when the hydrogenation temperature decreases from 1150 to 630 K a gradual transition from a completely decomposed system (PrH_2+Ni) to the amorphous state takes place in the compound. The amorphous state can be considered as an extremely distorted lattice where the bonds between the metal atoms are broken. In this case the driving force for amorphization is twice the excess of the Pr-H bond energy compared to the metal-metal bond energy. In this work the model of a heterophase nanostructure of RFe_2H_x hydrides obtained by HIA is proposed.

EXPERIMENTAL DETAILS

Hydrogenation of RFe_2 alloys was carried out by high purity gaseous hydrogen. Changes in the crystal structure detected by X-ray diffraction Cr K_α radiation. The magnetic measurements were carried out using a vibrating sample magnetometer in a magnetic field up to 20 kOe.

RESULTS

Amorphization can be considered as an intermediate state between the formation of crystalline RFe_2H_x hydride and the decomposition into more stable RH_2 and α-Fe phases at high temperatures (of the order of 750-800 K).

When the hydrogenation temperature increases the amount of the amorphous phase grows while the RFe_2H_x crystalline phase decreases gradually. The shape and the position of the amorphous halo change with the hydrogenation temperature, as shawn in Fig.1. Two phases, HoH_2 and amorphous matrix usually coexist in the sample (curves 2,3, Fig.1) and there are no traces of α-Fe.

Mössbauer studies show that the mean hyperfine field on Fe increases considerably in the amorphous hydride $GdFe_2H_x$ in comparison to the parent $GdFe_2$ phase, and the distribution function broadens due to the fluctuation of local interatomic distances and local environment of Fe (4). The mean hyperfine filed B_{hf} grows from 23.3 T for the initial compound to 33.4 T for the amorphous sample and, hence, it is possible to assume an increase of μ_{Fe} (μ - magnetic moment) upon the HIA from 1.53 to 2.2 μ_B. The latter is typical of pure Fe.

In Table 1 a comparison of the magnetic properties of amorphous and the crystalline hydrides preceding the amorphous state are given. As can be seen from Table 1 in all amorphous hydrides the temperature of magnetization compensation decreases considerably which indicates the weakening of the R-Fe intersublattice exchange interaction.

The temperature dependence of the magnetization of the amorphous hydride measured by conventional method together with $\mu_{Fe}(T)$ determined from Mössbauer studies allows us to obtain $\mu_R(T)$. The temperature dependence of magnetic moment of the R-sublattice in amorphous $GdFe_2H_x$ (5) is shown in Fig.2. According to the molecular field model this dependence is given by the Brillouin function B_J including the intersublattice exchange interaction constant n_{RFe} (we neglect the weaker R-R exchange interaction). As can be seen from Fig.2, the experimental dependences $\mu_R(T)$ are best described by B_J with two parameters n_{RFe} differing in an order of magnitude.

Magnetostriction of $TbFe_2H_{2.5}$ hydride is main isotropic and therefore, has an exchange character as compared to the anisotropic magnetostriction in the initial $TbFe_2$ (6,7). This again points to a considerable weakening of the intersublattice exchange interaction and, correspondingly, to a severe deformation of the magnetic structure in the field.

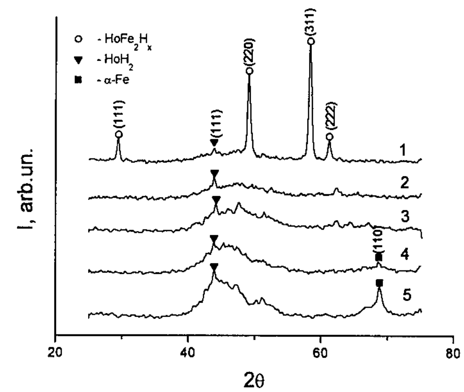

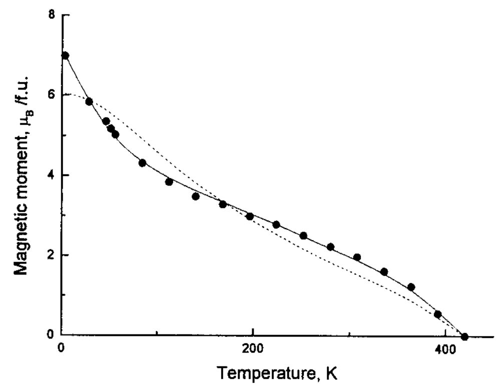

Fig.1. X-ray diffraction patterns of the $HoFe_2H_x$ compounds obtained under different heat treatment conditions. T(°C): 1-200, 2-230, 3-250, 4-310, 5-350.

Fig.2. Temperature dependence of the magnetic moment of the Gd sublattice in $GdFe_2H_x$. Circles - experimental data, dashed line - B_J with one n_{GdFe} and solid line - B_J with two parameters (2.4 and 23.5 T f.u./μ_B).

DISCUSSION

As can be seen from Fig.1, the wide halo of the amorphous matrix is located at angles corresponding to the position of most intensive lines of the HoH_2 phase. Similarly for all amorphous RFe_2H_x hydrides studied the amorphous halo is always located at the angles of the intensive lines of the RH_2 phase. Comparing the X-ray diffraction pattern of the amorphous RFe_2H_x hydride with that of the amorphous RFe_2 obtained, for example, by mechanical grinding (6) we can notice their essential difference. In the latter systems the amorphous matrix halo is located near the most intensive initial crystal lattice lines. Thus, hydrides obtained by HIA method have «RH_2-like» nearest neighboring. An analysis of the magnetic moment values shows (5) that the amorphous matrix is enriched by iron, at the expense of R atoms bonded with hydrogen forming RH_2 phase. The $\mu_R(T)$ dependence is essentially non-brillouin. However it can be describe well by the superposition of two Brillouin function B_J having different n_{RFe} values, with approximately equal weight ratios (Fig.2). It is reasonable to assume that the smaller exchange constant reflects the exchange interaction on the boundary between RH_2-type precipitations and Fe-enriched amorphous phase with stronger exchange interaction. In this case, as the contribution of the areas with two different R-Fe interactions are nearly the same, we can expect the characteristic size of the structural components to be of the order of 1 nm.

Finally, let us point out that the magnetic nature of the objects under investigation is rather complicated. In the R-sublattice a noncollinear magnetic ordering is observed for R=Tb..Er (7). The amorphization reduces the R-Fe intersublattice exchange interaction considerably and at least two intersublattice constant values are required to describe the

TABLE 1

Magnetic Properties of Crystalline (c) and Amorphous (*am*) Hydrides. T_{comp}- magnetization compensation temperature , T_c- Curie temperature, μ_S- spontaneous magnetic moment.

Compound	T_{comp}, K	T_c, K	μ_S, μ_B/f.u.
c-YFe_2H_4	-	306	3.66
am-$YFe_2H_{3.6}$	-	398	3.90
c-$GdFe_2H_4$	110	388	4.10
am-$GdFe_2H_{3.4}$	50	420	1.64
c-$TbFe_2H_{4.2}$	160	303	4.18
am-$TbFe_2H_{2.5}$	50	400	0.18
c-$DyFe_2H_4$	150	385	4.9
am-$DyFe_2H_{3.6}$	30	395	0.46
c-$HoFe_2H_{4.5}$	60	387	2.35
am-$HoFe_2H_{4.1}$	30	343	0.93
c-$ErFe_2H_{3.7}$	42	280	5.60
am-$ErFe_2H_{4.1}$	15	380	0.5

temperature dependence of the magnetization. Heterogeneous exchange interaction effects in amorphous hydrides were attributed to the formation of the heterophase nanocomposite.

References

1. Aoki, K. and Masumoto, T., *Journal of Alloys and Compounds*, 1993, 194, 251.
2. Buschow, K.H.J., *Solid State Communications*, 1976, 19, 421.
3. Irodova, A.V., Lavrova, O.A., Laskova, G.V., Parshin, P.P. and Shilov, A.L., *Fizika Tverdogo Tela*, 1996, 38, 277 (*in Russian*).
4. Mushnikov, N.V., Zajkov, N.K., Serikov, V.V., Kleinerman, N.M., Gaviko, V.S. and Yermakov, A.Ye., *Journal of Magnetism and Magnetic Materials*, 1997, 167, 93.
5. Zajkov, N.K., Mushnikov, N.V., Gaviko, V.S. and Ermakov, A.E., *Physics of the Solid State*, 1997, 39, 810.
6. Yermakov, A.Ye., Mushnikov, N.V., Zajkov, N.K., Gaviko, V.S. and Barinov, V.A., *Philosophical Magazine B*, 1993, 68, 883.
7. Zajkov, N.K., Mushnikov, N.V., and Yermakov, A.Ye., *The Physics of Metals and Metallography*, 1995, 79, 387.

Pergamon

NanoStructured Materials, Vol. 12, pp. 801–806, 1999
Elsevier Science Ltd

0965-9773/99/$–see front matter

PII S0965-9773(99)00239-1

MICROSTRUCTURE AND HARDNESS OF A NANOSTRUCTURED Fe-40Al at% ALLOY

X. Amils, J. Nogués, S. Suriñach, J. S. Muñoz, L.Lutterotti* and M.D. Baró

Departament de Fisica, Universitat Autonoma de Barcelona, E-08193, Bellaterra , Spain.
*Dipartimento di Ingegneria dei Materiali, Università di Trento, 38050 Mesiano, Italy

Abstract.- Microstructural changes induced by ball milling under different conditions and posterior annealing in Fe-40Al at% B2 alloys have been studied. High speed milling results in more disordered samples and milling media contamination, which affects the thermal reordering. The microhardness is closely correlated to the concentration of antisite defects of the samples. ©1999 Acta Metallurgica Inc.

INTRODUCTION

High-energy ball milling of metallic and intermetallic powders can induce microstructural changes, phase transformations and complex defect structures (1). These non-equilibrium structures can potentially overcome some of the typical shortcomings of intermetallic compounds, including poor room temperature ductility and low high-temperature strength, while keeping advantages over traditional alloys: higher yield and flow stresses, excellent corrosion behaviour and, in the case of B2 Al based alloys a low density (2). However, the microstructure of the milling products is very sensitive to the grinding conditions and may be unpredictably affected by unwanted contamination from the milling media and atmosphere. The high reactivity often associated to the extremely reduced grain size requires a particularly careful handling of these materials.

In this work we present a comparative study of Fe-40Al at% powder ball-milled under different conditions and their thermal reordering. Results on the long-range reordering, recrystallization and recovery of planar defects, were obtained, together with evidences of possible effects from contaminants. Microhardness testing indicated the strong dependence of hardness on the concentration of lattice defects for this class of alloys.

EXPERIMENTAL

The initial Fe-40Al at% gas-atomized powder was an ordered B2 phase with particle size of 50 to 200 μm. The powder was ball-milled in a planetary mill (Fritsch P7) in agate vials using zirconia balls with a ball to powder weight ratio equal to 4. Two series of powders were prepared, at "LOW" and "HIGH" speed ball-milling conditions, corresponding to 250 and 450 rpm rotating speed respectively. Both, LOW and HIGH speed powders were ball-milled for 72 hours, and were then subdivided into a number of specimens to be used for heat treatments. They were annealed, following the indications of differential scanning calorimetry and thermomagnetogravimetric results (3), for 1 hour at 403, 523, 673 and 973 K. Annealings were

performed under argon atmosphere fluxed into a tubular furnace after its chamber was evacuated down to 10^{-5} mbar to eliminate possible oxidizing species.

X-ray diffraction (XRD) analyses were carried out using a wide-angle diffractometer with Cu $K\alpha$ radiation. The microstructural parameters: lattice parameter (a_o), antisite probability of Fe atoms in Al site (w_{Fe}), r.m.s microstrain ($\sqrt{\langle e^2 \rangle}$) and effective crystallite size ($\langle D \rangle$) were obtained from a full pattern XRD Rietveld fitting procedure (4). It is worth noting that for Fe-40Al at% alloys the w_{Fe} values range from 0.6 for a completely disordered A2 structure to 0.2 for a completely ordered B2 alloy.

Microhardness tests were carried out for the different as milled and annealed powders, which were mounted in an epoxy cold resin and polished down to 0.3 μm. The Vickers indentation tests were performed with an Anton Paar MHT-10 device with a load of 0.1 N on single powder particles. It is noteworthy that each presented microhardness value is the average of at least 5 measurements.

Energy dispersive X-ray analysis (EDXS) was performed in a Cambridge Stereoscan 200 scanning electron microscope (SEM).

RESULTS

The XRD structural parameters obtained for the unmilled, as milled at LOW and HIGH speed and subsequently annealed powders are shown in table 1 and 2 respectively (note that the estimated statistical errors are shown in brackets).

The width of the XRD peaks broadens when increasing the milling time. This is due to the reduction of the crystallite size and the increase in microstrains (3). Simultaneously, the intensity of the superlattice reflections decreases, becoming undetectable after 72h of milling (3). Both as milled samples present a w_{Fe} value very close to 0.6 (table 1 and 2), suggesting that a nearly complete disorder has been achieved (3).

The LOW speed as milled powder shows smaller $\sqrt{\langle e^2 \rangle}$, and slightly larger $\langle D \rangle$ values (table 1) than the HIGH speed as milled one (table 2). The lattice parameter exhibits a significant increase for both as milled powders with a relative expansion of 0.8% for the LOW speed powder and of 0.5% for the HIGH speed one. This indicates the creation of antisite disorder during milling, i.e. both Fe and Al atoms are able to substitute each other's lattice (5,6). Moreover, the XRD data of the as milled at HIGH speed powder reveal not only peaks of the FeAl phase, but also low intensity reflections characteristic of Fe_3Al phase. Although the peak around 26.5° can be identified as the Fe_3Al (111) fundamental reflection, it can also be indexed as the agate (SiO_2, (101)) strongest diffraction peak. Note that SiO_2 contamination was confirmed by EDXS analysis. Rietveld calculations indicate that SiO_2 and/or Fe_3Al concentration are below 1 wt%.

When annealing the disordered powders the reordering of the alloy is induced. The LOW speed sample annealed at 523 K achieves a w_{Fe} value close to 0.2, indicating that the reordering process is nearly fully accomplished. Nevertheless, the recrystallisation is still at a very early stage. At this temperature the annihilation of line defects in the material, as can be seen in table 1 from the microstrain values, has just started (6). Annealing at 973K is required for a complete reordering and recovery of the alloy (table 1). Moreover, the calculated lattice parameter shows a large reduction for the lowest annealing temperature (403K) and it slowly reaches the value of the original unmilled powder for the highest annealing temperature (973K) (table 1).

The traces of SiO_2 and Fe_3Al are still visible in the HIGH speed ball milled powder even when the samples are annealed at different temperatures, remaining below 1 wt%. The lattice parameter shows a continuous decrease with the annealing temperature, comparable to that of

the LOW speed powder (table 1 and 2). Contrarily, after annealing at 523 K the w_{Fe} value remains large, indicating that the reordering is just half completed (table 2). Moreover, the reordering and recrystallization of the HIGH speed sample is not completed even at the highest annealing temperature (table 2).

It is noteworthy that the XRD patterns of the HIGH speed as milled powder, annealed at 673 K or 973 K, can be better fitted considering two distributions with different crystallite sizes, rather than a single one. The larger crystallite size component for the sample annealed at 673 K is around 47 wt% ($\langle D_1 \rangle$ = 28 nm, $\langle D_2 \rangle$ = 13 nm), increasing up to 56 wt% ($\langle D_1 \rangle$ = 65 nm, $\langle D_2 \rangle$ = 17 nm) when the powder is annealed at 973 K. The microstructural parameters displayed for these samples are average values calculated from the two crystallite size distributions (table 2).

As shown in figure 1, the microhardness values of the LOW speed powders present a continuous decrease as the annealing temperature is increased, ranging from 8.9 GPa for the as milled powder, to 5.6 GPa for the sample annealed at 973 K, which is very close to the value obtained for the unmilled powder (5.3 GPa). The microhardness value for the HIGH speed as milled powder is slightly smaller than the LOW speed one (figure 1). Nevertheless, when the powder is annealed at 403 K the microhardness increases up to 10.6 GPa, decreasing to 8.0 GPa for higher annealing temperatures.

TABLE 1
Structural Parameters LOW Speed Powder

Annealing temperature (K)	a_0 (nm)	$\langle D \rangle$ (nm)	$\sqrt{\langle e^2 \rangle} \cdot 10^3$	w_{Fe}
unmilled	0.28980(2)	207(9)	0.56(3)	0.20(1)
as milled	0.2917(1)	13(2)	6.4(1)	0.54(5)
403	0.2907(1)	14(2)	5.4(1)	0.46(3)
523	0.2902(1)	18(3)	4.5(1)	0.23(2)
673	0.2898(1)	26(4)	1.1(2)	0.22(3)
973	0.28972(2)	49(3)	0.49(3)	0.20(1)

TABLE 2
Structural Parameters HIGH Speed Powder

Annealing temperature (K)	a_0 (nm)	$\langle D \rangle$ (nm)	$\sqrt{\langle e^2 \rangle} \cdot 10^3$	w_{Fe}
unmilled	0.28980(2)	207(9)	0.56(3)	0.20(1)
as milled	0.2912(1)	12(1)	7.4(1)	0.54(1)
403	0.2907(1)	12(1)	7.2(1)	0.50(2)
523	0.2901(1)	13(3)	5.3(2)	0.40(1)
673	0.28971(2)	20(1)	4.0(2)	0.31(1)
973	0.28954(2)	44(4)	2.4(3)	0.30(2)

DISCUSSION

The larger microstrain and the slightly smaller $\langle D \rangle$ values obtained for the HIGH speed as milled powder, when compared to the LOW speed one, are due to the higher energetic milling conditions. These conditions are probably the cause of the contamination from the agate (SiO_2) vial. In addition, they may also induce a slight Al oxidation and a concomitant Fe enrichment of the FeAl phase composition, leading to the formation of small amounts of Fe_3Al.

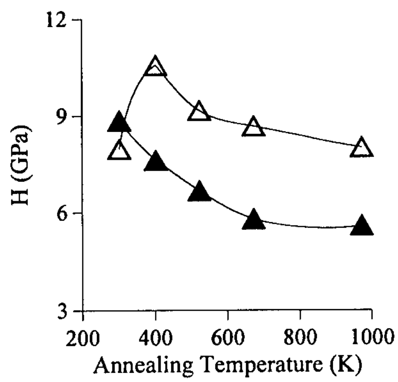

Figure 1. Dependence of the microhardness, H, on the annealing temperature for LOW (▲) and HIGH (Δ) speeds ball-milled Fe-40Al at% powders annealed at different temperatures.

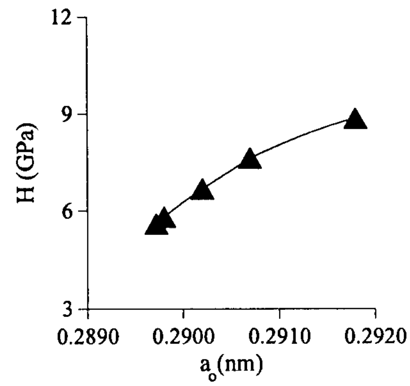

Figure 2. Dependence of the microhardness, H, on the lattice parameter for LOW (▲) speed ball-milled Fe-40Al at% powders annealed at different temperatures.

Note that in both curves the error bars are smaller than the symbol size and that curves joining experimental points are just a guide to the eye.

The difference of lattice parameters between the as milled at HIGH and LOW speed powders, may be related to this change in FeAl composition (5). However, this lattice contraction can also be associated, in part, with the crumbling down of the crystal structure when very high concentration of point defects is introduced (7).

The thermal reordering process of the LOW and HIGH speed ball-milled powders does not follow the same route. The LOW speed ball-milled powder is completely reordered and recrystallized after the annealing at 973 K (table 1). At this temperature the HIGH speed ball-milled powder presents a complex crystallite size distribution and remains partially disordered (table 2). The presence of more than one crystallite component has been previously reported in other mechanically alloyed systems, such as TiAl (8,9).

The differences in the reordering and recrystallization process can be caused by the SiO_2 powder contamination and by the large microstrain observed in the HIGH speed as milled powder. Both aspects can hinder the complete recovery and the recrystallization of the HIGH speed ball-milled powder (10). Finally, the different lattice parameter values observed in the LOW and HIGH speed ball-milled powders when annealed at 973 K, may be related to the previously discussed slight Al oxidation and the accompanying Fe enrichment of the FeAl phase.

The mechanical properties of the Fe-40Al at% powders can be explained considering the microstructure parameters obtained from XRD measurements. Microhardness values of the ball-milled powders are larger than the ones obtained for the unmilled sample. This increase is related to the different defect structures which are induced during the milling (point, dislocation or planar defects) and to the strain hardening they produce. When the ball-milled powders are thermally treated these defects are progressively annealed out and the microhardness values show a significant decrease (figure 1).

As shown in figure 2, the observed lattice expansion, i.e. antisite defects, induces an important microhardness increase. The relation between the microhardness and the point defects concentration has been previously reported for FeAl samples quenched from different temperatures at different cooling rates (11-14), these alloys retained a high concentration of vacancies, which produce a strong strengthening.

The interaction of point defects with moving dislocations leads to a power law dependence of the yield strength on the defect concentration (15,16). Following this approach, a similar relation between microhardness, H, and the square root of defect concentration can be obtained (16):

$$H = H_o + 6\gamma\mu\ c^{1/2} \quad [1]$$

where c is the defect concentration, antisite defect (w_{Fe}) in the present case, γ is a coefficient which is lower than unity and depends on the strength of the interaction, μ is the shear modulus and H_o is the microhardness at zero defect concentration. The microhardness values of the LOW speed powder annealed at different temperatures can be fitted through least square analysis to a straight line when they are plotted as a function of the square root of w_{Fe}. Considering the slope of the calculated straight line and assuming a shear modulus value around 100 GPa (17), the γ coefficient in equation [1] has been estimated to be around 0.0015. This value is in good agreement with the expected from a weak interaction between dislocations and antisite atoms (15). However, the γ coefficient values have been found to be larger in FeAl quenched alloys, suggesting that vacancies could have stronger interactions with dislocation (11).
The microhardness peak observed in the reordering process of the HIGH speed ball-milled powders is probably due to the transition from deformation by single dislocations, characteristic of a completely disordered lattice, to superlattice dislocations. The deformation transition has been already reported for heavily ball-milled Fe_3Al (2) and Ni_3Al powders (1). In our case, the partial reordering induced at the lowest annealing temperature can produce the transition from single to superlattice dislocations. The continuous decrease at higher annealing temperatures is associated with the annihilation of the different defects. The larger microhardness values measured for the HIGH speed ball-milled powders can be explained on the bases of the partial disorder still observed in the HIGH speed annealed powder and on the contamination by the ball-milling media.

CONCLUSIONS

Fe-40Al at% ball-milling has been carried out at two different rotating speeds ("LOW" and "HIGH"). XRD measurements indicate that ball-milling for 72 hours under both conditions induces the disordering and the nanocrystallization of the alloy. The microstructural parameters calculated for the HIGH speed as milled powder show a disordered structure, with larger microstrain and slightly smaller crystallite size values than the ones obtained at LOW speed. In addition the HIGH speed ball-milled powder presents a low concentration of SiO_2 and Fe_3Al phases (< 1wt%), which remain even after annealing.
The reordering of the LOW speed powder is nearly completed at 523 K, but at this stage the recrystallization has barely started. The recovery of the line and planar defects is fully achieved with the treatment at the highest temperature (973 K). The annealing of the HIGH speed powder at 523 K induces only a partial reordering of the alloy. The full recovery of the HIGH speed powder is not accomplished even at the highest annealing temperature (973 K). At high annealing temperatures, at least two different crystallite size distributions are needed to fit the XRD peaks. The milling media contamination introduced in the HIGH speed ball-milled powder, by the agate vial, causes the hindering of the reordering and recrystallization processes.
The disordering and nanocrystallization processes produce the strengthening of the alloy. The microhardness values for the reordering process of the LOW speed ball-milled powder show a monotonic decrease. A strong correlation between lattice parameter, i.e. antisite defects, and

microhardness values has been found, implying the interaction between moving dislocations and antisite atoms.
Finally, the HIGH speed annealed powder shows a maximum in the microhardness curve vs. annealing temperature at 403 K, which can be associated with a transition in the deformation mechanism from single dislocations to superlattice dislocations at the initial reordering stage of the alloy.

ACKNOWLEDGEMENTS

We wish to thank S. Gialanella for providing the FeAl powders and for his useful discussions. We want to acknowledge the financial support of the CICYT (contract # MAT94-0290-C03-01) and the EEC (contract # CHRX-CT93-0324). X. Amils and J. Nogués thank the Spanish MEC for their fellowships.

REFERENCES

(1) C.C. Koch, *Materials Science Technology*, Eds. R.W. Cahn, P. Haasen and E.J. Kramer, VCH, Weinheim, p. 193 (1991).
(2) N. S. Stoloff, Mat. Res. Soc. Symp. Proc., 39, 3 (1985).
(3) S. Gialanella, L. Lutterotti, M.D. Baró, X. Amils, S. Suriñach, P. Delcroix and G. Le Caër, Acta Mater., in press (1998).
(4) L. Lutterotti and S. Gialanella, Acta Mater., 46, 101 (1998).
(5) A. Taylor and R.M. Jones, J. Phys. Chem. Solids, 6, 16 (1958).
(6) X. Amils, J. Nogués, S. Suriñach, M.D. Baró, L. Lutterotti and S. Gialanella, Mat. Sci. For., 269-272, 637 (1998).
(7) L.Lutterotti and S. Gialanella, Acta Mater., 46, 101 (1998).
(8) M. Oehring, T. Klassen and R. Bormann, J. Mater. Res., 8, 2819 (1993).
(9) L. Lutterotti and S. Gialanella, Mat. Sci. For., 269-272, 373 (1998).
(10) M.D. Baró, S. Suriñach, J. Malagelada, M.T. Clavaguera-Mora, S. Gialanella and R.W. Cahn, Acta Metall. Mater., 41,1065 (1993).
(11) Y.A. Chang, L.M. Pike, C.T. Liu, A.R. Bilbrey and D.S. Stone, Intermetallics, 1, 107 (1993).
(12) M.A. Morris, S. Gunther and D.G. Morris, Mat. Sci. For., 269-272, 631 (1998).
(13) P. Nagpal and I. Baker, Met. Trans. A, 21A, 2281 (1990).
(14) Y. Yang and I. Baker, Intermatallics, 6, 167 (1998).
(15) R.L. Fleischer, *The Strengthening of Metals*, Ed. D. Peckner, Reinhold, London, p. 93 (1964).
(16) J.P. Hirth and J. Lothe, *Theory of dislocations*, John Wiley and Sons Inc., New York, p. 681 (1982).
(17) A. Wolfenden and M. Marmouche, J. Metals, 35, 684 (1983).

Pergamon

NanoStructured Materials, Vol. 12, pp. 807–810, 1999
Elsevier Science Ltd

0965-9773/99/$–see front matter

PII S0965-9773(99)00240-8

HARDNESS OF COMPOSITIONALLY NANO-MODULATED TiN FILMS

E.Kusano, M.Kitagawa, A.Satoh, T.Kobayashi, H.Nanto, and A.Kinbara
Kanazawa Institute of Technology, AMS R&D Center
Yatsukaho, Matto, Ishikawa, Japan
e-mail:kusano@neptune.kanazawa-it.ac.jp

Abstract--*Compositionally nano-modulated films have been deposited by a reactive gas flow rate modulation sputtering using a Ti target and N_2 gas. The explored modulation periods ranged from 6.7nm to 80nm. The thickness of the modulated layer was 400nm. A TiO_2/Ti underlayer with a thickness of 100nm was deposited for the entire sample films. By the X-ray diffraction measurements, it was found that films consisted of polycrystalline Ti and TiN mixtures for the periods longer than 10nm and of monolithic TiN for the periods of 6.7nm and 8nm. The X-ray photoelectron spectroscopy results for the film with a modulation period of 80nm showed that the N concentration in metallic layers was about 30% and that of the nitrided layers was about 45%. The maximum hardness of 11.2GPa was obtained at a modulation period of 10nm for an indenter load of 2.94mN by nanoindentation. This value is larger than that obtained for a monolithic TiN film (8.4GPa).* ©*1999 Acta Metallurgica Inc.*

INTRODUCTION

It has been reported that the hardness of coatings can be enhanced by using nano-laminated multilayer structures (1-3). The mechanisms involved in the hardness enhancement have been described by the effects based on the difference in mechanical properties of two alternatively laminated films. Since the interface seems to play an important role in an enhancement of the properties, it is expected that the films with stronger lamination, with a large number of repeated layers, provide better tribological properties. A compositionally modulated multilayer film without any abrupt interfaces is one of the films of this type. It has been reported that the hardness of the TiN/Ti nano-modulated films deposited by a reactive gas flow rate modulation sputtering yield a maximum hardness for an optimized modulation period (4). The modulation sputtering is the method to obtain ompositionally gradient multilayered film by using a combination of a metal cathode and a reactive gas (5). In this study, hardness enhancement for compositionally nano-modulated TiN multilayer coatings has been studied in conjunction with the film structures. In addition, to estimate elastic and plastic properties of the nano-laminated films, the ratio of the dissipated energy to the loaded energy during the nanoindentation process has been obtained.

EXPERIMENTAL

Film preparation

The sputtering apparatus used in this experiment was a batch type sputtering machine L-100S-FH(ANELVA corp.). The target was a 75mm diameter Ti (99.98%). The discharge current was kept at 0.4A throughout the deposition runs. The working gases were Ar(99.9999%) and N_2(99.9999%). The argon partial pressure was kept at 0.4Pa throughout the deposition runs. Nitorogen flow rate was changed to the desired values by a computer-controlled mass flow controller (Type FC-770AC, Nippon Aera) to obtain sinusoidal compositional-distribution. Total pressure was measured with a BARATRON TYPE690 capacitance manometer (MKS).

The thickness of the modulated layer was 500nm including a 100nm TiO_2/Ti underlayer which was deposited to prevent adhesive failure that had been observed for a compositionally nano-modulated TiN multilayer film deposited directly onto the substrate in a preparatory experiment. Substrates used for the deposition were aluminosilicate glass. The flow control patterns of N_2 to obtain a film with a compositional modulation were determined based on the hysteresis curve in deposition rate or Ti emission intensity with the increase and decrease of the N_2 gas flow rate in the range of 0 to 2sccm. The maximum flow rate of N_2 to deposit the nitride layer was 1sccm. The minimum flow rate of N_2 to deposit the metallic layer was 0.25sccm.

Film Estimation

Film composition depth profiles were obtained by X-ray photoelectron spectroscopy (XPS) using the PHI ESCA-5600Ci. The Ar^+ ion beam with an incident angle of 45° was also used for etching. The average etching rate during the XPS measurement was 1.7nm/min for an Ar^+ beam with energy of 4.0kV and with a beam current of 6.5nA. The film structure was examined by X-ray diffraction (XRD) using RINT Ultima type diffractmeter (Rigaku).

Film hardness was measured with a nanoindentation tester ENT-1040 (Elionix Inc.). The test loads ranged from 2.94 to 4.90mN for all measurements. Hardness values were obtained from a maximum displacement under an applied load and were an average of 5 measurement runs. The stylus used for the measurement was a triangular diamond pyramid with the angle of 115°. The ratio of the dissipated energy to the applied energy during the indentation was also obtained from the load-displacement curve during the loading/unloading process. The difference of the energies loaded and put back during the indentation process is the energy used to cause the plastic deformation or dissipated through the sample film.

RESULTS AND DISCUSSION

Figure 1 shows XRD measurement results as a function of the modulation period. It was found that films consisted of polycrystalline Ti and TiN mixtures for modulation periods

longer than 10nm and of monolithic TiN for modulation periods of 6.7nm and 8nm (not shown in the figure).

Figure 2 shows the XPS depth profiles obtained for the film with a modulation period of 80nm. The results showed that the film consisted of a multilayer without abrupt interfaces and that the N concentration in metallic layers was about 30% and that of the nitrided layers was about 45% for the film with a modulation period of 80nm.

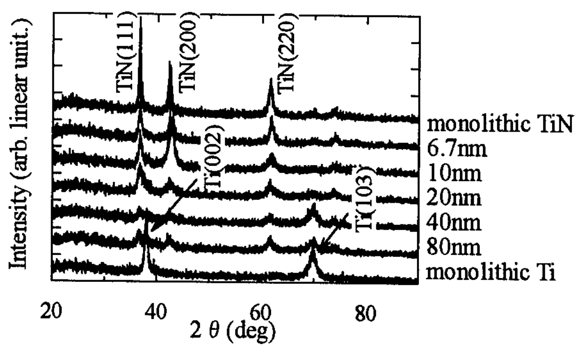

FIG.1 XRD results for compositionally nano-modulated TiN films with modulation periods from 6.7 to 80nm and for monolithic Ti and TiN films.

Figure 3 shows the film hardness as a function of modulation period for the stylus load from 2.94 to 9.80mN. The hardness shows its maximum for the modulation period of 10nm for all stylus loads. The stylus load of 2.94mN yielded the maximum of 11.2GPa for the film with the period of 10nm. This value is 1.3 times larger than that obtained for the monolithic TiN film. The modulation period that yields the maximum hardness is in good agreement with those reported previously (1-4). The hardness measurement results shows that the hardness of the nano-modulated film strongly depends its modulation period. The young's modulus also showed a maximum for the films with a modulation period of 10nm. The value was about 230GPa for a stylus load of 2.94mN.

Figure 4 shows the changes in the ratio of the dissipated energy to loaded energy during the loading/unloading process of the nanoindentation, as a function of the modulation period for the maximum stylus load of 2.94mN. The ratio showed a minimum of 26% for the

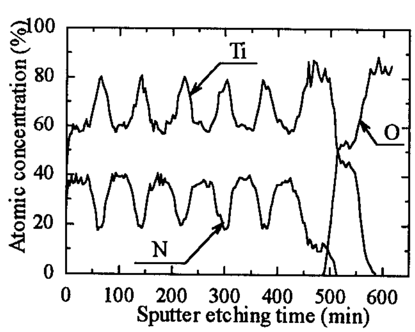

FIG.2 XPS depth profile for the compositionally nano-modulated TiN film with a modulation period of 80nm.

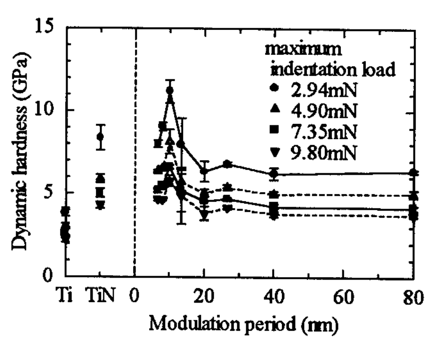

FIG.3 Hardness of compositionally nano-modulated TiN films as a function of modulation period and of monolithic Ti and TiN films.

film with a modulation period of 8nm and was about 39% for the films with modulation periods longer than 30nm. The results imply that the film with the modulation period of 8nm is most elastic, assuming that the most of the energy dissipated is used for plastic deformation. The sharp minimum shows that the compositionally modulation affects strongly elastic and plastic behavior of the film.

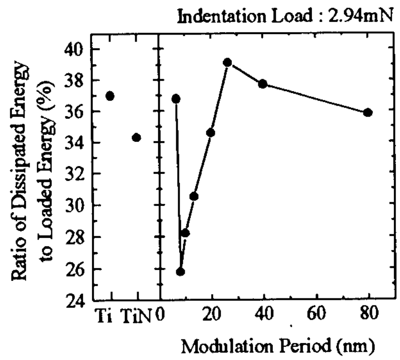

FIG.4 Ratio of the dissipated to the loaded energy during the loading/unloading process of nanoindentation for compositionally nano-modulated films as a function of the modulation period and for monolithic Ti and TiN films.

CONCLUSION

Compositionally nano-modulated films have been deposited by a reactive gas flow rate modulation sputtering using a Ti target and N_2 gas. The maximum hardness of 11.2GPa was obtained at a modulation period of 10nm for an indenter load of 2.94mN. This value is larger than that obtained for a monolithic TiN film (8.4GPa). The ratio of the dissipated energy to the loaded energy during the indentation showed a minimum of 26% for the film with a modulation period of 8nm and was about 40% for the films with modulation periods longer than 30nm. For compositionally nano-modulated TiN films, the film hardness as well as the energy dissipated during a loading/unloading process of the indentation depends on the modulation period.

ACKNOWREDGEMENTS

The financial support for the Advanced Materials Science R&D Center of Kanazawa Institute of Technology from the Ministry of Education, Science and Culture of Japan is highly appreciated.

REFERENCES

1. Helmersson, U., Todorova, S., Barnett, S.A., Sundgren, J.-E., Markett, L.C., and Greene, J.E., *J.Appl.Phys.*, 62, 481, 1987
2. Shinn, M., Hultman, L., and Barnett, S.A., *J.Mater.Res.*, 7, 901, 1992
3. Chu, X., Barnett, S.A., Wong, M.S., and Sproul, W.D., *Surf.Coat.Technol.*, 57, 13,1993
4. Kusano, E., Kinbara, A., Kondo, I., *J.Non-Crystalline Solids*, 218, 58, 1997
5. Kusano, E., Kitagawa, M., Nanto, H., Kinbara, A., *J.Vac.Sci.Technol. A*, in presss

Pergamon

NanoStructured Materials, Vol. 12, pp. 811–816, 1999
Elsevier Science Ltd

0965-9773/99/$–see front matter

PII S0965-9773(99)00241-X

MEASUREMENT OF ELASTIC AND ANELASTIC PROPERTIES OF NANOCRYSTALLINE METALS

M. J. Lang[1,4], M. Duarte-Dominguez[1,4], R. Birringer[2,4], R. Hempelmann[3,4], H. Natter[3,4] and W. Arnold[1,4]

[1]Fraunhofer-Institut für zerstörungsfreie Prüfverfahren (IZFP), [2]Technische Physik, [3]Physikalische Chemie und [4]SFB 277, Universität, D-66123 Saarbrücken, Germany

Abstract -- *Due to their high content in nanocrystalline materials, the grain boundaries are expected to contribute significantly to the elastic and anelastic properties of the bulk material. Thus nanocrystalline materials lend themselves to the study of grain boundary contributions to absorption and dispersion of ultrasonic waves. We have examined nanocrystalline Pd and Cu. They exhibit an anomalously large absorption which varies linearly with frequency. ©1999 Acta Metallurgica Inc.*

1. INTRODUCTION

In polycrystalline materials, a number of effects contribute to the attenuation of ultrasonic waves (1, 2). For large grain sizes (> 10 μm) scattering dominates, but dislocation and phonon interactions and thermoelastic relaxation might also be of importance (3). Scattering arises from grain boundaries and phase interfaces. Interaction with phonons is caused by the perturbation of the distribution of thermal phonons by the dynamic stress field and the its subsequent relaxation. Source for thermal relaxation is the heat flow between inhomogeneously strained regions. The damped vibration of dislocation lines in the alternating stress-field of ultrasonic waves leads to relaxational, resonance, and hysteretic type absorption mechanisms, as described by the Granato-Lücke-theory (4) and its extensions. For nanocrystalline metals (nc-metals) recent ultrasonic measurements (5-8) show a significantly increased attenuation compared to polycrystalline (pc) metals of the same composition. It is expected that the large number of grain boundaries in nc-metals with their disordered structure are to some extent responsible for this increased attenuation. In order to attribute the observed attenuation behaviour to the microstructural features of nc-metals, extended measurements are required. Here, the dependence of attenuation and phase velocity on frequency, polarization, temperature and amplitude are examined and compared to existing and proposed models of anelasticity mechanisms.

2. EXPERIMENTAL

Samples of nanocrystalline palladium, copper, and nickel were prepared by pulsed electrodeposition (9) and inert gas condensation (10). Their grain sizes range from 12 to 60 nm.

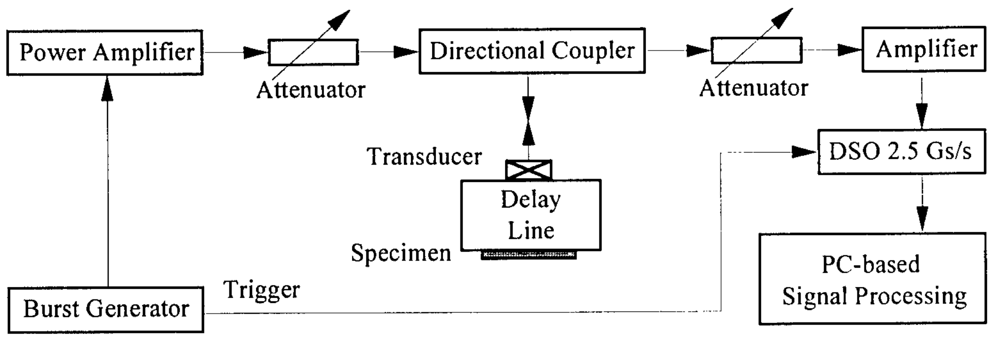

Fig. 1: Experimental set-up

Polycrystalline specimens with grain sizes larger than 15 μm were used for reference. Longitudinal and transverse waves of frequencies from 20 to 100 MHz were generated, either as tone-bursts or broad-band pulses. The ultrasonic pulses were fed into the specimen via buffer rods, either solid or liquid. For measurements at temperatures between 10 and 300 K, transducer assemblies with adapted thermal and acoustical mismatch were built. To eliminate the influence of possible nonlinearities in the rf-electronics, a balanced technique was adopted to maintain a constant receiver input (Fig.1). The intensity of the ultrasonic waves was varied by 40 dB. From the received signals and delay times, the absorption and dispersion was determined. The amplitude decay was determined either in the time or in the Fourier domain from the magnitudes of the signals (11). Corrections for partial reflection at the buffer/specimen interface were taken into account. Delay times were measured by time-domain autocorrelation or Fourier-domain normalized magnitude spectra (12). Corrections for phase shift associated with bonding layers were performed. Acoustic microscopy was used to determine the residual pore distribution of the samples, and to measure the Rayleigh wave velocity in nc-Ni at room temperature at 1 GHz. Atomic force microscopy was utilized to measure surface topography.

3. RESULTS AND DISCUSSION

For nc-Cu and nc-Pd the attenuation coefficient α increases linearly with frequency f, both for longitudinal waves (subscript l) (Figs. 2, 4) and for transverse waves (subscript t) (Fig. 6). Furthermore, within the accuracy of the measurement (± 10 m/s), no change in phase velocity v was observed (Figs. 3, 5, 7). The polycrystalline reference materials exhibit much lower attenuation coefficients. They vary with powers of 2 (pc-Pd) to 4 (pc-Cu) of the frequency (Figs. 2, 4, 6). The phase velocity for pc-Cu slightly decreases with increasing frequency, whereas for pc-Pd v_l fluctuates around a given value (Figs. 3, 5). Comparison with the corresponding grain sizes shows that the attenuation behaviour of the pc-specimen is governed by Rayleigh- (pc-Cu) and stochastic (pc-Pd) scattering, taking into account a distribution of grain sizes. Since for nc-specimen a pronounced dependence of α on some power of frequency was not observed, we conclude that scattering cannot be the main source of attenuation.

Varying the intensity of the incident ultrasonic wave, α is found to decrease at very small amplitudes, the effect being more pronounced for nc-Cu than for pc-Cu (Fig. 8). In examining nc-Pd at different frequencies, a similar behaviour was observed (Fig. 9). The amplitude

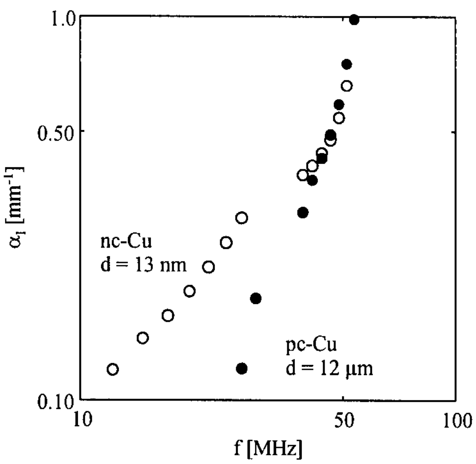

Fig. 2: US attenuation as a function of frequency for nc-Cu and pc-Cu (long. waves, RT)

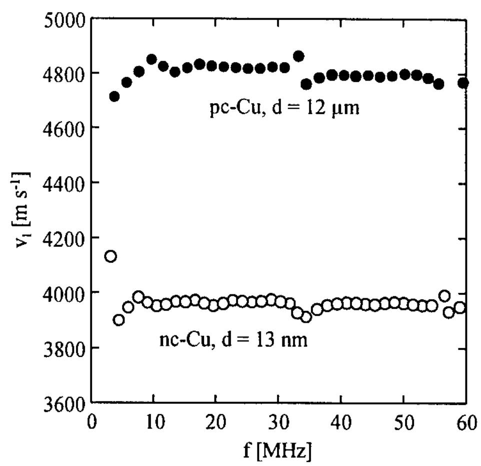

Fig. 3: Dispersion of sound velocity in nc-Cu and pc-Cu (longitudinal waves, RT)

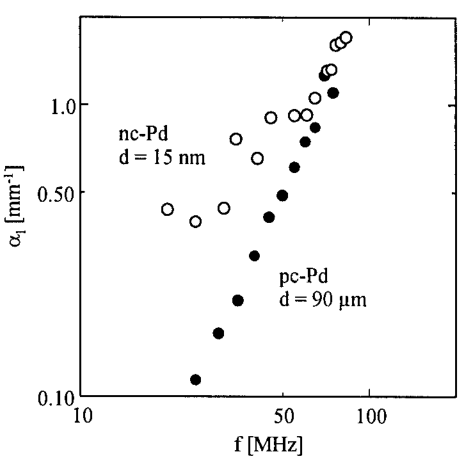

Fig. 4: US attenuation as a function of frequency for nc-Pd and pc-Pd (long. waves, RT)

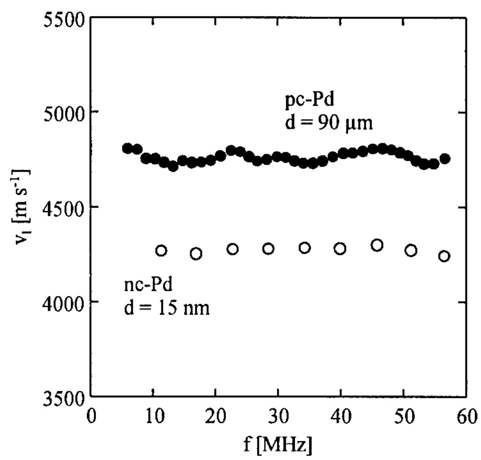

Fig. 5: Dispersion of sound velocity in nc-Pd and pc-Pd (longitudinal waves, RT)

dependence of α together with a linear frequency dependence hints to the presence of a hysteretic absorption mechanism. It is found that for nc-Pd the attenuation does not decrease significantly with decreasing temperatures and there is a large residual attenuation at low temperatures in comparison to pc-Pd (Fig. 10). Fig. 11 displays the velocity as a function of temperature for pc-Pd and nc-Pd. Note that the velocity in nc-Pd increases with decreasing temperature whereas it remains constant in pc-Pd within the accuracy of the experiment. In Table 1 values for dynamic elastic moduli, as calculated from the velocities, are presented. The moduli of nc-samples are smaller than those of pc-material, as found earlier (13).

Possible contributions to attenuation in nc-metals are listed in Table 2. For f = 50 MHz, the values for the corresponding attenuation are calculated for nc-Cu, grain size d = 100 nm, porosity 3%, pore diameter 1.5 μm, and RT. From the attenuation and velocity data, it can be

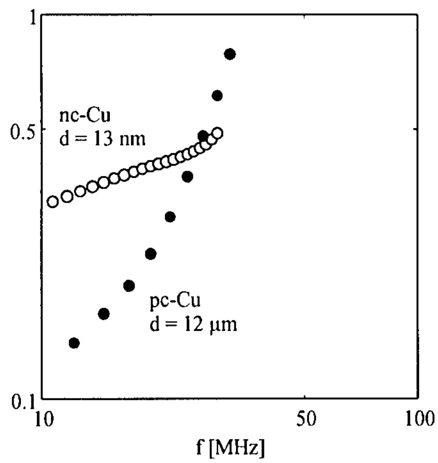

Fig. 6: US attenuation as a function of frequency for nc-Cu and pc-Cu (trans. waves, RT)

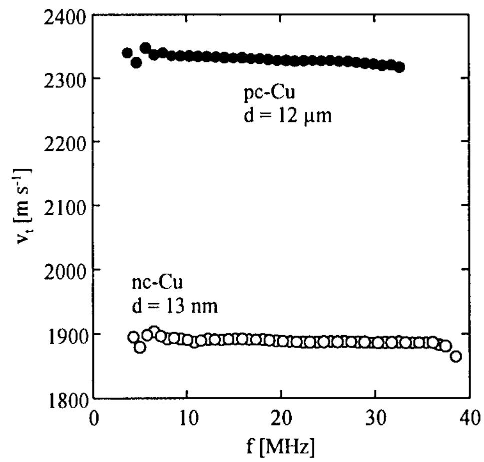

Fig. 7: Dispersion of sound velocity in nc-Cu and pc-Cu (transverse waves, RT)

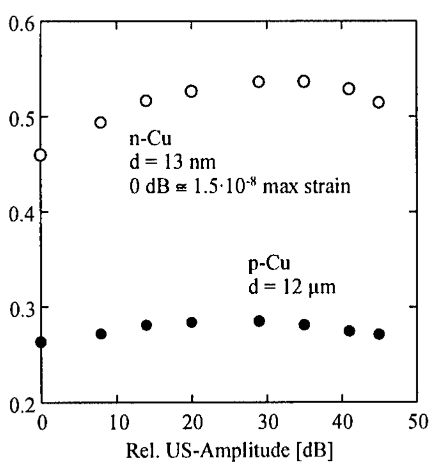

Fig. 8: Attenuation as a function of ultrasonic amplitude for nc-Cu and pc-Cu (20 MHz, RT)

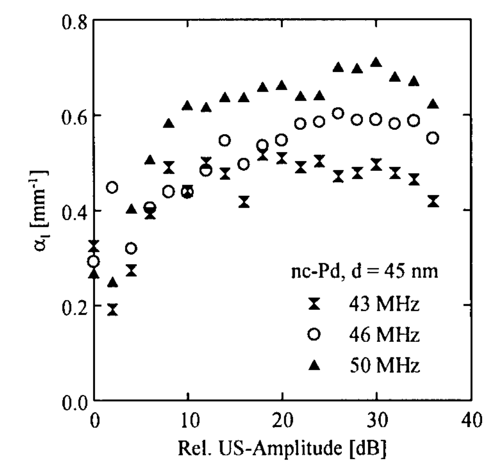

Fig. 9: Attenuation as a function of ultrasound amplitude for nc-Pd (RT)

concluded, that the attenuation exhibited by nc-Cu and nc-Pd cannot be attributed to presently known mechanisms alone. Since in the examined nc-metals attenuation is almost temperature independent, thermally activated absorption mechanisms can play only a minor rôle. The temperature dependence of the velocity in nc-Pd is also of interest. From experiments in crystals and glasses, it is known that the thermal phonon bath leads to a decrease of v with increasing T and the temperature dependence $v \propto (1\text{-const.}T^4)$ for low temperatures (17). The absolute magnitude depends on the Grüneisen constant and the thermal expansion (18). It might be that the effect is enlarged in nanocrystalline materials due to contributions of the grain boundaries and grain surfaces to the phonon density of states, in accordance with the observation of an enhanced thermal expansion (19).

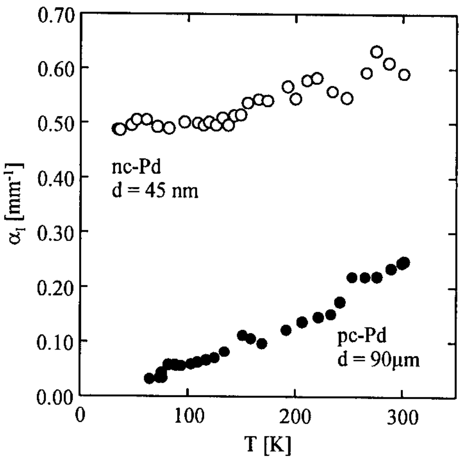

Fig. 10: Temperature dependence of attenuation in nc-Pd and pc-Pd (45 MHz)

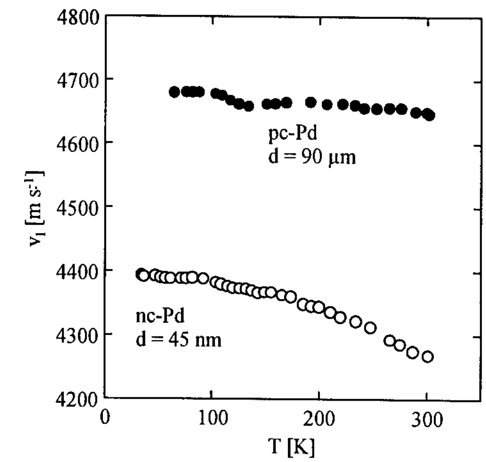

Fig. 11: Temperature dependence of sound velocity in nc-Pd and pc-Pd (45 MHz)

TABLE 1
Sound Velocities and Dynamic Elastic Moduli (f = 25 MHz, RT)

	v_l [m·s^{-1}]	v_t [m·s^{-1}]	v_{rayl} [m·s^{-1}]	E modulus	G modulus
pc-Pd	4765	1787		123.0	
nc-Pd	4066	1888		115.5	42.5
pc-Cu	4817	2327		129.8	48.3
nc-Cu	3966	1888		86.9	32.1
pc-Ni	5662	3253	2722	236.1	94.2
nc-Ni	5600	2881	2101	194.8	73.8

TABLE 2
Contributions to Attenuation in nc-Copper (f = 50 MHz, assumed grain size d = 100 nm, RT)

anelasticity mechanism	proportionality to d and f	estimated value
scattering (14, 15)		
$d/\lambda \ll 1$: Rayleigh scattering	$\alpha_{sr} \sim d^3 f^4$ $v = v_0$ - const. $d^2 f^2$	for grains: $\alpha_{sg} \cong 2 \cdot 10^{-6}$ mm^{-1} for pores: $\alpha_{sp} \cong 2 \cdot 10^{-2}$ mm^{-1}
$d/\lambda \cong 1$: stochastic scattering	$\alpha_{ss} \sim d^3 f^2$	
phonon interaction (1)	$\alpha_p \sim f^2$	$\alpha_p \cong 1.5 \cdot 10^{-2}$ mm^{-1}
thermoelastic relaxation (16)		
homogeneous material	$\alpha_p \sim f^2$	$\alpha_{trw} \cong 1.5 \cdot 10^{-3}$ mm^{-1}
nanocrystalline material	$\alpha_p \sim d^2 f^2$	$\alpha_{trc} \cong 1.5 \cdot 10^{-4}$ mm^{-1}

4. CONCLUSION

Ultrasonic methods were applied to the measurement of attenuation and sound velocity in nanocrystalline metals. The results indicate the presence of an athermal hysteretic damping mechanism in these materials. Models with such characteristics have been proposed in the case of dislocation absorption (20) and also for the absorption of seismic waves in rocks (21). In our view the latter can be applied to the situation studied by us. Hysteretic absorption of seismic waves takes places by the movement of parts of the rock structure over small distances induced by the strain wave, and hence is amplitude dependent. It is tempting to invoke such a mechanism in nc-metals by assuming that parts of the grain boundaries are mobile. The applicability of such a model to nc-metals has to be checked against further measurements. It should be mentioned that it is also possible to invoke a more classical relaxation mechanism as source of the anelastic behaviour of the grain boundaries by assuming a very broad distribution of barrier heights and relaxation times (22).

5. ACKNOWLEDGEMENT

We thank the "Deutsche Forschungsgemeinschaft" for financial support within the "SFB 277 Nanocrystalline Materials" and R. Hotz and R. Siems for enlightening discussions

6. REFERENCES

1. Truell, R., Elbaum, C., Chick, B., *Ultrason. Methods in Sol. State Phys.*, Acad., NY, 1969
2. De Batist, R., *Internal Friction of Structural Defects in Cryst. Solids*, North Holland, 1972
3. Goebbels, K., *Research Techniques in NDT*, R. S. Sharpe ed., Academic Press, 1980, 87
4. Granato, A., and Lücke, K., J. Appl. Phys., 1956, 27, 583
5. Korn, D., Morsch, A., Birringer, R., Arnold, W., Gleiter, H., *J. de Phys.*, 1988, C549, 769
6. Reszat, J., Diplomathesis, University of Saarbrücken, Department of Material Science, 1996
7. Weller, M., Diehl, J., Seeger, and Schaefer, H. E., *Phil. Mag.*, 1991, A63, 527
8. Zhang, X. R., Qin, X. Y. , Cheng, G. S., Zhang, L. D., in *Proc. Ultrason. Sym.*, 1996, 515
9. Natter, H., Krajewski, T., and Hempelmann, R., *Ber. Bunseng. Phys. Chem.*, 1996, 55, 100
10. Birringer, R., Herr, U., and Gleiter, H., *Trans. Jpn. Inst. Met.*, 1987, 27 Suppl., 43
11. Papadakis, E. P., Fowler, K. A., and Lynnworth, L. C., *J. Acoust. Soc. Am*, 1973, 53, 1336
12. Pialucha, T., Guyott, C. C. H., and Cawley, P., *Ultrasonics*, 1989, 27, 270
13. Nieman, G. W., Weertman, J. R., and Siegel, R. W., *J. Mater. Res.*, 1991, 6, 1012
14. Papadakis, E. P. , *J. Acoust. Soc. Am.* 1965, 37, 711
15. Hirsekorn, S., *Materialprüfung* 1989, 31, 357
16. Nowick, A. S., Berry, B. S., *Anelastic Relaxation in Cryst. Solids*, Acad., NY, 1972
17. Kittel, C., *Introduction to Solid State Physics*, Wiley, N.Y., 1971
18. Alers, G., in *Physical Acoustics*, Mason W. P. ed., Academic NY, 1966, 4, 277
19. Birringer, R., *Proc. NATO ASI Nanophase Materals*, G. C. Haddjipanayis, Siegel R. W., eds., Kluwer Dodrecht, 1994, 260, 157
20. Gremaud, G. *J. de Phys.*, 1987, C8-48, 15
21. McCall, K. R., and Guyer, R. A., *J. Geophys. Res.*, 1994, 99, 23 887
22. Siems, R., and Hotz, R., *private communication*

Pergamon

NanoStructured Materials, Vol. 12, pp. 817–820, 1999
Elsevier Science Ltd

0965-9773/99/$–see front matter

PII S0965-9773(99)00242-1

MAGNETOELASTICITY AND INTERNAL STRAINS IN NANOCRYSTALLINE NICKEL

E. Bonetti, E.G. Campari, L. Pasquini, E. Sampaolesi, G. Scipione
Dipartimento di Fisica, Università di Bologna, and Istituto Nazionale per la Fisica della Materia, viale Berti-Pichat 6/2, 40127 Bologna, Italy

Abstract: *The magnetic field dependence of the dynamic elastic modulus (ΔE effect) was studied in ball-milled nanocrystalline Nickel, as a function of the milling times and annealing treatments. The analysis of the crystallite size and internal strains has been performed as well by Fourier analysis of the X-ray spectra. A correlation between ΔE and the lattice strain calculated by X-ray analysis is observed, suggesting that the magnetic anisotropy is mainly determined by the internal strains. ©1999 Acta Metallurgica Inc.*

INTRODUCTION

A full characterisation of the microstructure is of crucial importance to understand the physical properties of nanocrystalline (nc) solids. In nc-magnetic materials, magnetic and magnetomechanical measurements can be employed, in addition to more traditional techniques such as electron microscopy and X-ray or neutron diffraction, to get information on the grain size, internal stresses, grain boundary structure and internal porosity. For example, in nc-Ni, the internal strains, due to magnetoelastic coupling, strongly affect the magnetic behaviour (1), so that the material's properties can be controlled to some extent by moderate thermal treatments. In this paper, we report on the magnetic field dependence of the elastic modulus (ΔE effect) in nc-Ni prepared by ball milling. The ΔE was studied in dependence of the milling time and annealing treatments; a correlation with X-ray analysis is presented.

EXPERIMENTAL

Nanocrystalline Nickel powders were produced by mechanical attrition using 99.9% pure Ni powders (3-7 μm size) as starting materials. The synthesis apparatus is an original planetary mill which can perform in vacuum or in controlled atmosphere; the temperature can be also varied by means of a liquid N_2 circuit (2). All the nc-powders were prepared in a vacuum of 10^{-4} Pa at a temperature of 220 K for selected milling times (10, 20, 40, 65, 90 h); the ball to powder ratio was 10:1. Thin bar-shaped samples were obtained by consolidation of the ball-milled powders under a uniaxial pressure of 2 GPa at room temperature. The resulting specimens have a rectangular section of 5x15 mm^2 and a thickness of 0.8 mm. The milling process introduced a little Fe contamination < 1% even in the long-milled specimens, as determined by energy-dispersive X-ray analysis in a scanning electron microscope.

X-ray diffraction measurements were performed through a Philips PW 1710 vertical powder diffractometer, using Ni-filtered Cu-K_α radiation with a graphite monochromator in the diffracted beam. The X-ray diffraction patterns were analysed according to the Warren-Averbach (WA) line broadening method, in order to evaluate the crystallite dimension $<D>$ and the lattice strain $<\varepsilon^2>^{1/2}$ (3), which was also calculated by the Vogel, Haase and Hosemann (VHH) method (4).

The dynamic elastic modulus (proportional to the square of the resonance frequency) was measured by the vibrating reed technique, as a function of external magnetic field. The magnetic field dependence, known as *ΔE effect*, is usually quantified by the dimensionless ratio $(E_s\text{-}E_0)/E_0$, where E_s and E_0 are the moduli at saturation and in the demagnetised state (zero field), respectively. Such a ratio depends on material's constants and microstructure trough the relation (5):

$$\frac{E_s - E_0}{E_0} = c\frac{\lambda_s^{\ 2} E_s}{K_{eff}}$$

where λ_s is the saturation magnetostriction, K_{eff} is an effective anisotropy constant, weighted sum of the magnetocrystalline and stress anisotropy, and c is a numerical constant. In the limit of high internal stresses σ_i, K_{eff} becomes equal to the stress anisotropy $(3/2)\lambda_s\sigma_i$, and one obtains (5):

$$\frac{E_s - E_0}{E_0} = \frac{2\lambda_s E_s}{5\sigma_i} = \frac{2\lambda_s}{5\varepsilon_i}$$

where ε_i are the internal strains. So the measure of the *ΔE effect* provides an alternative tool for the estimation of the internal strains in ferromagnetic materials. In this paper, the ΔE magnitude is calculated replacing E_s with $E_{max} \equiv E$ (850 Oe); the measurements are made at room temperature.

RESULTS AND DISCUSSION

The grain size, lattice strain, and ΔE magnitude on as-consolidated specimens, as a function of the milling time, are reported in Table 1. The ΔE magnitude measured on nc-specimens is very small (0.5×10^{-2} , compared to 10^{-1} of well-annealed coarse-grained (cg) Ni), and shows a rough correspondence with the strain values. Both these facts are expected when the stress anisotropy $(3/2)\lambda_s E_s \varepsilon_i$ is comparable or much larger than the magnetocrystalline anisotropy K. For cg-Ni at room temperature, one gets an estimate lower limit strain of 0.6×10^{-3}; for nc-Ni this value could also be lower due to a possible decrease of the effective K, as predicted by random anisotropy model (6), so that the approximation of high internal strains should be valid for as-consolidated specimens. The severe mechanical deformation during milling introduces high internal stresses which pin the magnetisation vector thereby reducing the ΔE. A rather small ΔE is obtained also on a cg-sample prepared by compaction of un-milled powders, most likely due to stresses originating from the cold-consolidation itself.

After heating up to 680 K (heating rate = 4 K / minute), the un-milled specimen exhibits a fairly high ΔE, while in nc-samples, despite a significant relative variation, ΔE is still rather small, about 10^{-2} (see Figure 1); in nc-sample, appreciable grain growth occurs, and the lattice strain is decreased by an order of magnitude (Table 1).

TABLE 1
WA area-weighted grain size $\langle D\rangle_{aw}$, root mean square lattice strain $\langle\varepsilon^2\rangle^{1/2}$, and ΔE, in as-consolidated nc-Ni specimens

Milling time (h)	$\langle D\rangle_{aw}$ (nm)	$\langle\varepsilon^2\rangle^{1/2}$ (10^{-3})	ΔE (10^{-2})
0	$> 10^3$	0.5	0.96
10	31	1.0	0.42
20	23	1.2	0.46
40	18	2.1	0.23
65	15	1.9	0.18
90	15	1.7	0.39
0[a]	$> 10^3$	< 0.1	5.1
65[a]	30	0.2	1.2

a: after 680 K heating (4 K / min)

In order to analyse the relationship between internal strains and ΔE magnitude in the nano-regime, we performed successive annealing steps of 1 hour on a 65 h milled specimen. After each annealing, the X-ray spectra and the ΔE (Figure 2) were measured. All the data are presented together in Figure 3, where the inverse ΔE magnitude is reported, since, according to Eq. (2), it is proportional to the internal strains for high strain level.

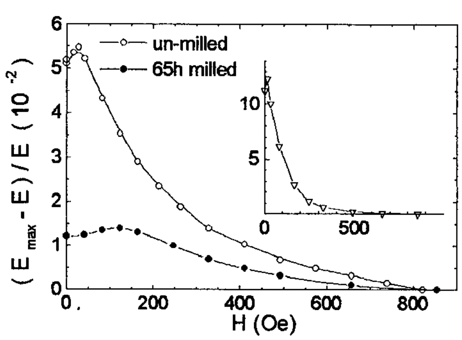

Figure 1: ΔE measured at room temperature on 65 h- and un-milled specimens after heating up to 680 K (at 4 K / min). The inset shows the results on a cg-Ni sheet after heating up to 1300 K

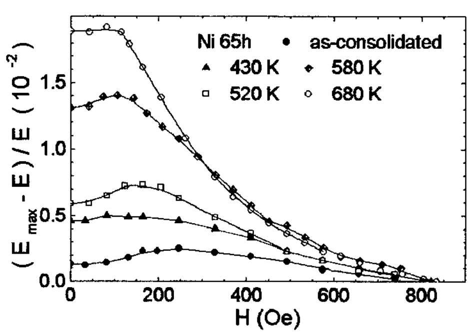

Figure 2: ΔE measured at room temperature on a 65 h milled specimen, as-consolidated and after successive 1 hour annealing steps at the temperatures indicated.

A large relative variation of the ΔE magnitude at annealing temperatures $\leq$ 520 K, which reflects a parallel strong decrease of the lattice strain is observed, the grain size being almost constant. The relation between internal strains and ΔE can be exploited further by plotting the internal strains calculated through Eq. (2) (assuming the value $\lambda_s=3\times10^{-5}$ of cg-Ni) *vs.* the strain value determined from X-ray (Figure 4). Even if a linear approximation is not able to fit all points within experimental error, there is a clear correlation between the two data sets. It should also be noticed that the strains calculated through Eq. (2) are 2-3 times larger than those derived from X-ray analysis.

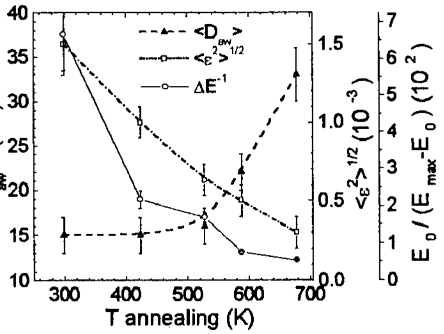

Figure 3: grain size (WA, area weighted), lattice strain (VHH method), and inverse ΔE magnitude on a 65 h-milled specimen, as a function of the annealing temperature

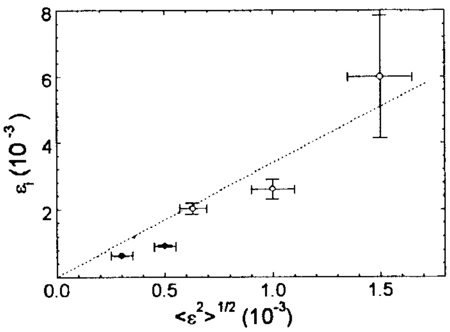

Figure 4: relationship between the internal strains ε_i, calculated through ΔE using Eq. (2), and the strains $<\varepsilon^2>^{1/2}$, determined by X-ray analysis.

CONCLUDING REMARKS

The data on nc-samples as a function of the milling time and annealing temperature show that a clear correlation between ΔE and the internal strains exist in nc-samples. It is difficult to perform a quantitative analysis, also because the milling or annealing modify the grain size, so that changes in the effective magnetocrystalline anisotropy may occur as well. The observation that strains calculated through ΔE making use of Eq. (2) are higher than those furnished by X-ray analysis, points to a localisation of internal strains. In fact, localised strains are effective in increasing the stress anisotropy, and from ΔE measurements one gets such localised strain value; conversely, X-ray methods yield a strain value averaged over the whole sample volume, which is clearly lower. Also the persistence of relatively small ΔE values after 1 h annealing at 680 K (see Table 1 and Figures 2-3), when almost no strain is detected from X-ray, may be due to localised strain centres, likely at the grain interfaces, which can not be annihilated by moderate annealing treatments, without the occurrence of extensive grain growth.

REFERENCES

(1) H. Kisker, H. Kronmuller, H.-E. Schaefer, T. Suzuki, J. Appl. Phys. **79**, 5143 (1996)
(2) E. Bonetti, L. Pasquini, E. Sampaolesi, Mater Sci. For. **269-272**, 999, (1998)
(3) S. Enzo, G. Fagherazzi, A. Benedetti, S. Polizzi, J. Appl. Cryst. **21**, 536 (1988)
(4) W. Vogel, J. Haase and R. Hosemann, Z. Naturforsch. Teil A **29**, 1152 (1974)
(5) R.M. Bozorth, Ferromagnetism, D. Van Nostrand, New York, (1951)
(6) G. Herzer, IEEE Trans. Magn. **26**, 1397 (1990)

Pergamon

NanoStructured Materials, Vol. 12, pp. 821–824, 1999
Elsevier Science Ltd

0965-9773/99/$–see front matter

PII S0965-9773(99)00243-3

SELF-ASSEMBLED SINGLE ELECTRON TUNNELING DEVICES WITH ORGANIC TUNNEL BARRIERS

S.H.M. Persson[1,3], L. Olofsson[1], L. Gunnarsson[2] and E. Olsson[4]

[1]Department of Microelectronics and Nanoscience,
[2]Department of Applied Physics,
[3]Department of Microwave technology
[4]Department of Experimental Physics, Microscopy and Microanalysis
Chalmers University of Technology, S-412 96 Göteborg, Sweden

Abstract -- Self assembling techniques were used to fabricate single-electron tunneling (SET) devices with organic tunnel junctions. The process involves angle evaporation of two gold electrodes. They have separations of less than 10 nm and were covered with a self-assembled monolayer of 1,8-octanedithiol. The active part of the SET device is a alkylthiol stabilised gold cluster which is captured in the small gap, when the substrate is immersed in a colloidal solution. This technique allows us to make well-defined structures by chemical synthesis which are much smaller than what can be made by traditional lithography. The current-voltage characteristic of the SET devices shows a prominent Coulomb blockade at room temperature, a Coulomb staircase and gate effect at 4.2 K. *©1999 Acta Metallurgica Inc.*

INTRODUCTION

As the size of electronic devices decreases down to the nanometer range it will be possible to observe and utilise single electron tunneling[1] and quantum effects in electronics at room temperature. However, using traditional lithography methods such as electron beam lithography the smallest feature size is limited to approximately 10 nm.

In this limit, size-variations corresponding to atomic layers are unavoidable. These variations are nevertheless critical to the performance of the device. Size control is therefore essential for uniformity and reproducibility of nano-scale electronics. Chemical synthesis offers the possibility to make very small well-defined structures with precise size control. Nanoscale structures can be built atom by atom to form the active part of the device. The electrodes which connect the active part to the electrical leads are less sensitive to size variations and can therefore be made by conventional lithographic techniques.

There are several problems related to miniaturisation of electronics to the nanometer scale. One problem is the alignment of several nanometer-scaled features on the same chip. A process which uses self-assembly circumvents this problem. It would be advantageous if the active part has a very high probability to be captured in the right position, but once it is there no further particles can be attached.

Recent reports on the creation of nanocrystals of metals and semiconductors offers new possibilities for manufacturing of nanoscale transistors. Klein et al.[2] have made a single electron transistor using CdSe clusters. The CdSe clusters are chemisorbed in the gap between two gold electrodes, which are covered by a self-assembled monolayer (SAM) of 1,6-hexanedithiol. They are able to change the number of electrons on the cluster by applying a voltage to the underlying substrate. Bezryadin et al.[3] used electrostatic forces to trap palladium particles between platinum electrodes. Sato et al.[4] have used a self-assembly method to make a multiple junction device, with single electron transistor behaviour at 4.2 K.

In this paper we report on our experimental studies on self-assembled devices. In the fabrication of these devices we have used a method similar to Klein et al.[2] to capture gold clusters in an electrode gap that is smaller than 10 nm. The tunneling characteristics indicate that only one cluster is captured between the gold electrodes.

EXPERIMENTAL

The lithographic patterning of the devices [see Figure 1(a).] was made in three steps. The first is photolithographical to define the contact pads on an oxidised silicon wafer by deposition of 20 nm NiCr and 80 nm Au. The second is a lift-off process with an electron beam patterned two-layer resist to define a gate electrode. This step was not included on all samples. The bottom resist layer is a 140 nm thick copolymer and the top layer is 60 nm thick PMMA. The gate electrode is made by evaporation of four layers: NiCr (40 Å), Au (100 Å), Al (100 Å), and Al_xO_y(20 Å). The aluminium is oxidised in the evaporation chamber before Al_xO_y is evaporated. The top electrodes are made of 40 + 40 Å NiCr and 100 + 100 Å Au, evaporated with the substrate tilted at two different angles. The angles are adjusted to give a gap of approximately 10 nm. There is a third lateral electrode with a 30 to 40 nm distance from the gap electrodes.

The chemical synthesis of the gold particles follows the scheme used by Brust et al.[5]. The size of the particles was controlled by the molar ratio between gold and alkylthiol molecules[6]. Alkanethiol molecules cover the whole surface of the particles. This prevents agglomeration and make the particles stable. Whetten et al.[7] showed that it is possible to make monodisperse clusters, by aggregation of large particles and separation by filtering in several steps. We have observed sizes in a range from 2 to 6 nm with transmission electron microscope.

The substrate was, after the angle evaporation of the gap, placed in a container with 1,8-octanedithiol dissolved in hexane for 1 to 24 h, where a SAM is formed on the gold surfaces. It was thereafter rinsed in hexane and directly put into a hexane solution of gold particles for 12-24 hours.

TEM samples were prepared by evaporating a few nm gold on graphite films, forming a granular film with distances between grains of the same order as the electrode gap. These were immersed in the same solutions as the devices.

RESULTS AND DISCUSSION

Figure 1(b) show particles adsorbed on the evaporated granular gold film. The gold grains are covered with 1,8-octanedithiol and there exist several gaps that have the same width as the

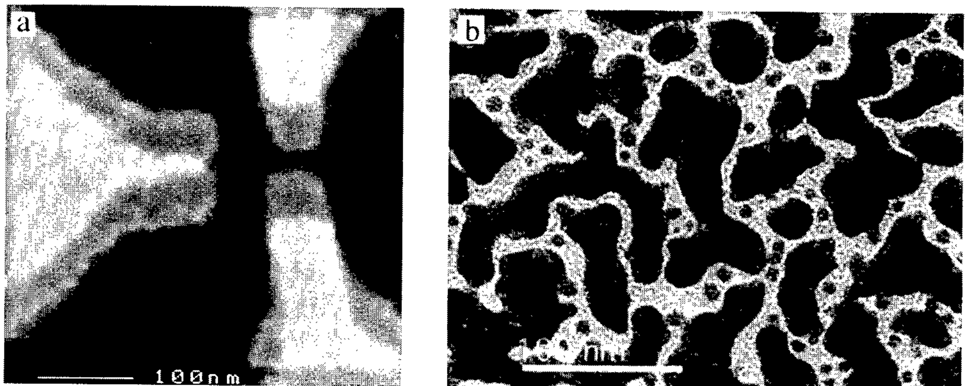

FIGURE 1. (a) Scanning electron microscope image of a device without clusters, showing two electrodes with a 10 nm gap, one lateral gate and one bottom gate.
(b) TEM image of an evaporated granular gold film, seen as large irregular grains, with small round clusters captured in the gaps between grains of evaporated gold.

electrode gap. We observe that there are few particles adsorbed and that they are positioned in the grooves and in the gaps between the largeer evaporated grains.

Terrill et al.[8] have studied alkanethiol stabilised particles on flat surfaces with STM and found that particles stick to steps and edges on the surface. The particles are mobile on the surface without electrostatic forces[9] and move to a position were the attractive forces are strongest. We assume that van der Waals forces attract particles to the surface and that the interaction is stronger in the gap where the particle is surrounded by the alkanedithiol covered electrodes, compared to a flat surface. The mobility of the particle and the stronger attractive force in the gap give a higher probability for capturing a particle in the gap, i.e., the alkylthiol shell prevents the particles from being stuck anywhere on the surface and keep them mobile until they are trapped. A chemisorption would result in an electrode surface that is more or less completely covered with particles. Electrons would then have larger probability for tunneling in several different current paths, through many adsorbed particles between the electrodes.

The current voltage characteristics were recorded by applying a symmetric voltage over two (typically 100 MΩ) bias resistors and measuring the current and the voltage over the device. The IV-characteristics at room temperature and at 4.2 K are shown in figure 2(a). The Coulomb gap and the staircase are characteristic of tunneling through a small double junction system and it can be modelled analytically or by Monte-Carlo simulations[10]. We can therefore assume that we have captured one or a few particles in the gap when we observe the Coulomb staircase. Figure 2(b) shows the IV curve for one device with different gate voltages applied to the lateral gate. We can see that the steps were shifted and the Coulomb gap is decreased. The device was destroyed when higher gate voltages was applied and we were not able to observe periodic modulation nor finite zero-bias conductance. The IV characteristic of a double junction system can be reproduced by Monte-Carlo simulations and the capacitances and resistances of the junctions can be estimated. These values are comparable with the self-capacitance of a sphere $C_0 = 4\pi e_0 e_r r = 0.4$ aF for a particle with radius $r = 2$ nm and dielectric constant $\varepsilon_r = 2$. These values are reasonable and indicate that the particle diameter should be in the range of 2-4 nm.

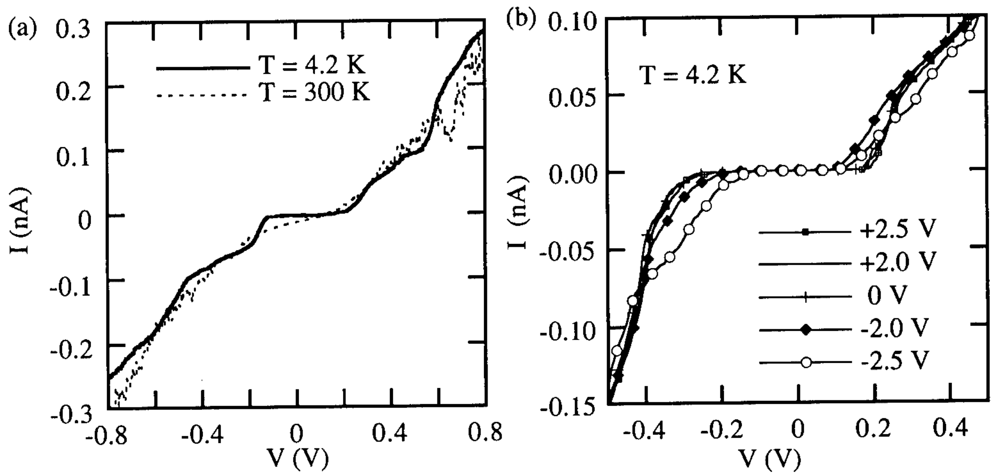

FIGURE 2. Current voltage characteristics: (a) at room temperature and 4.2 K and (b) as a function of voltage applied to the lateral gate

SUMMARY

We have used 1-dodecanethiol stabilised gold clusters which self-assemble in the gap between two electrodes. The reason for this is that the weak interaction forces between the particle and substrate are stronger there. With this method it could be possible to realise a single electron tunneling transistor operating at room temperature. We have observed Coulomb blockade in a self-assembled device at room temperature. The blockade voltage for the devices are approximately 0.2 V. The current voltage characteristics are modulated as a function of applied voltage to the lateral gate electrode at T = 4.2 K.

This work was supported by the Swedish Research Council for Engineering Science (TFR) and the Foundation for Strategic Research (SSF).

REFERENCES

1 *See references in* Single Charge Tunneling. H. Grabert, and M.H. Devoret, Eds. NATO ASI series B 294, Plenum, New York 1992.
2 D.L. Klein, R. Roth, et al., Nature 1997,. 389: 699-701.
3 A. Bezryadin, C. Dekker and G. Schmid. Appl. phys. Lett., 1997, 71, 1273-1275.
4 T. Sato, H. Ahmed, et al., J. Appl. Phys., 1997, 82, 696-701.
5 M. Brust, M. Walker, et al. J. Chem. Soc., Chem. Commun.. 1994. 801-802.
6 D.V. Leff, P.C. Ohara, et al. 1995. J. Phys. Chem, 99, 7036-7041.
7 R.L. Whetten et al. Adv. Mater. 1996, 8, 428-433.
8 R.H. Terrill et al. J. Am. Chem. Soc. 1995, 117, 12537-12548.
9 T. Sato, D. Brown and B.F.G. Johnson. Chem Commun., 1997, 1007-1008.
10. S.H.M. Persson, L. Olofsson, L. Hedberg et. al. Annals New York Acad. Sci. 1998, vol 852, 188-196.

Pergamon

NanoStructured Materials, Vol. 12, pp. 825–828, 1999
Elsevier Science Ltd

0965-9773/99/\$–see front matter

PII S0965-9773(99)00244-5

NANOCRYSTALLINE SOFT MAGNETIC Fe-M-B (M = Zr, Hf, Nb), Fe-M-O (M = Zr, Hf, RARE EARTH) ALLOYS AND THEIR APPLICATIONS

A. Makino[a], A. Inoue[b] and T. Masumoto[c]

[a] Central Research Laboratory, Alps Electric Co., Ltd., Nagaoka 940-8572, Japan
[b] Institute for Materials Research, Tohoku University, Sendai 980-8577, Japan
[c] The Research Institute of Electric and Magnetic Materials, Sendai 982-0807, Japan

Abstract — *New soft magnetic nanocrystalline materials in Fe-M-B (M = Zr, Hf, Nb) and Fe-M-O (M = Zr, Hf, rare earth) systems have been fabricated by use of partial crystallization of melt-spun amorphous phase and sputtering-induced partial crystallization, respectively. These alloys have a mixed structure of nano-scale α-Fe grains and an amorphous phase containing large amounts of M, B and M, O, respectively. This structural property should be a dominant factor for achieving good soft magnetic properties in both alloys. The Fe-M-B ribbons with high Fe content about 90 % exhibit high magnetic flux density of 1.5 to 1.8 T, good soft magnetic properties and very low core losses at low frequency. On the other hand, the soft magnetic Fe-M-O films with high O content of 10 to 35 at.% show high permeability at high frequency above 100 MHz because of their high electrical resistively of 6 to 23 μΩm much higher than those of other conventional soft magnetic alloy films. The Fe-M-B ribbons should be more suitable for low frequency applications such as power transformers and choke coils for active filters for power supplies and so on. The Fe-M-O films should be useful for high frequency applications such as thin-film inductors and transformers for micro switching converters for portable electric equipment and others. ©1999 Acta Metallurgica Inc.*

INTRODUCTION

Since an amorphous phase in Pd-Si, Fe-P-C and (Fe, Co, Ni)-Si-B systems have been found to be useful as a precursor to prepare a nanocrystalline structure upon crystallization (1), a great effort has been devoted to the development of a new type of high-functional material or high-strength by utilizing the formation of crystallization-induced nanostructure. In a soft magnetic field, it has been found in 1988 that the crystallization of Fe-Si-B amorphous alloys containing Nb and Cu causes the formation of a nanoscale bcc structure and the bcc alloys exhibit good soft magnetic properties of 1.2 to 1.4 T for saturation magnetization (B_s) and high effective permeability (μ_e) (2). Although the good soft magnetic properties are obtained for the nanoscale bcc $Fe_{73.5}Si_{13.5}B_9Nb_3Cu_1$, the relatively low Fe concentration leads to the limitation of B_s less than 1.4 T and hence the development of a new soft magnetic alloy with high B_s above 1.5 T has strongly been desired because the simultaneous achievement of both properties enables

the extension of application fields.

We tried to synthesize a nanocrystalline soft magnetic material with high B_s, and have developed nanocrystalline Fe-M-B (M = Zr, Hf or Nb) alloys with high B_s more than 1.5 T as well as good soft magnetic properties (3). And then we have found that dissolution of a large amount of oxygen into the remaining amorphous phase is effective for a drastic increase in electrical resistivity of sputtered Fe-Hf-O, Fe-Zr-O and Fe-rare earth elements-O films, leading to the achievement of good high-frequency permeability in the high frequency range of 1 to 100 MHz (4). This paper aims to review our recent results on two kinds of the nanocrystalline soft magnetic materials and their engineering applications.

MATERIALS PROCESSING

Fe-M-B alloys "NANOPERM®" with 15 mm in width and 15-20 μm in thickness was obtained by crystallizing an amorphous phase produced by single roller melt-spinning method. The crystallizing was carried out by keeping the samples at 793-923 K for 60-1800 s. Fe-M-O films with 2-3 μm in thickness were deposited onto indirectly water-cooled glass substrates by an rf reactive sputtering technique in a mixed atmosphere of pure argon and oxygen. The deposition was performed in no magnetic field or a static magnetic field to induce in-plane uniaxial magnetic anisotropy. The films were subjected to annealing for 10.8 ks under a uniaxial magnetic field (uniaxial field annealing, UFA) of 160 kA/m at lower temperatures than crystallization temperature of an amorphous phase in an evacuated atmosphere below 10^{-3} Pa.

STRUCTURE AND PROPERTIES

Figure 1 shows typical examples of the structure for (a) crystallized F-M-B ribbon (NANOPERM®) and (b) as-deposited Fe-M-O film. Both alloys have a similar structure composed of nano-scale α-Fe grains and an amorphous phase with high Curie temperatures (T_c) because of large amounts of M and B, or M and O elements, respectively (4, 5). Good soft magnetic properties should be achieved mainly by the achievement of the decreased apparent anisotropy caused by the nano-scale α-Fe grains smaller than the domain wall size and easy magnetic coupling between the grains through the amorphous phase with high T_c. The B_s value lager than 1.5 T results from a high volume fraction of α-Fe phase for NANOPERM®. High ρ valves of the Fe-M-O films result from the existence of the amorphous phase with large amounts of M and O elements (4).

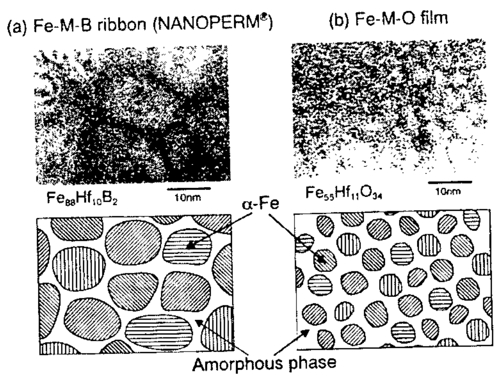

Figure 1. High resolution TEM images and schematic illustration of microstructure for (a) Fe-M-B ribbon (NANOPERM®) and (b) Fe-M-O film.

Magnetic properties of Fe-M-B ribbons "NANOPERM®" are summarized in Table 1. NANOPERM® with nearly zero-magnetostriction (λ_s) exhibits high B_s values of 1.5-1.8 T, high μ_e at 1kHz of 30000 to 51000 and low core losses (W) at 1.4 T and 50 Hz of 0.11 to 0.21 W/kg. It is to be noted that these

Table 1. Magnetic properties of Fe-M-B ribbons (NANOPERM®) and Fe-B-Si amorphous alloy.

	B_s (T)	μ_e*	H_c (A/m)	λ_s (10^{-6})	W** (W/kg)
$Fe_{90}Zr_7B_3$	1.70	30,000	5.8	-1.1	0.21
$Fe_{90}V_1Zr_6B_3$	1.75	30,000	4.6	-0.3	0.11
$Fe_{89}Hf_7B_4$	1.59	32,000	4.5	-1.2	0.14
$Fe_{84}Nb_7B_9$	1.52	51,000	4.8	0.2	0.14
$Fe_{78}B_{13}Si_9$ (amor.)	1.56	10,000	3.5	27	0.28

* 1 kHz
** 1.4 T, 50 Hz

Table 2. Magnetic properties of Fe-M-O films and other soft magnetic films.

	B_s (T)	H_c (A/m)	ρ ($\mu\Omega$m)	Structure
$Fe_{55}Hf_{11}O_{34}$	1.2	154	9.1	amor.+bcc
$Fe_{61}Hf_{13}O_{26}$	1.2	73	6.3	amor.+bcc
$Co_{44.3}Fe_{19.1}Hf_{14.5}O_{22.1}$	1.1	185	15.1	amor.+bcc
$Fe_{65}Zr_9O_{26}$	1.3	211	6.6	amor.+bcc
$Fe_{68}Y_{22}O_{10}$	0.9	207	22.6	amor.+bcc
$Fe_{67}Dy_7O_{26}$	1.3	322	9.3	amor.+bcc
$Fe_{72}Al_{10}Si_{18}$	1.1	40	1.3	bcc
$Ni_{81}Fe_{19}$	0.8	24	0.2	fcc
$Co_{83}Ta_{11}Hf_6$	0.8	33	1.7	amorphous

values are superior to those of $Fe_{78}B_{13}Si_9$ amorphous alloy.

The relation between B_s and μ_e at 1kHz for NANOPERM® and the conventional soft magnetic materials is shown Figure 2. It is seen that NANOPERM® is the best for achievement of B_s and μ_e in all the materials.

Figure 3 shows the frequency dependence of the real part of permeability (μ') and the quality factor (Q = μ'/ μ", μ" is the complex part of permeability) for the Fe-M-O films. As the ordinary metallic films such as Fe-Al-Si, Ni-Fe and Co based amorphous alloys have low electrical resistively (ρ) smaller than 2 $\mu\Omega$m, the μ' drastically decreases at the frequency below 100 MHz where the eddy current loss become relatively large. On the contrary, nanocrystalline Fe-M-O films with high ρ valves larger than 6 $\mu\Omega$m, as shown in Table 2, exhibit superior μ frequency characteristics, and moreover, the Q valves of the films is much higher than those of the ordinary ones.

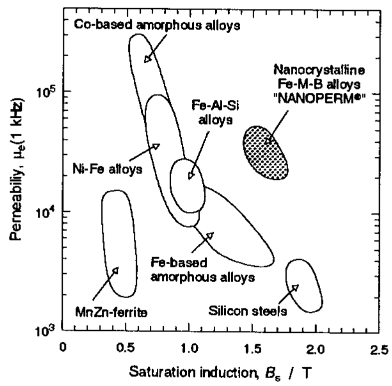

Figure 2. Relation between B_s and μ_e at 1 kHz for Fe-M-B ribbons (NANOPERM®) and conventional soft magnetic materials.

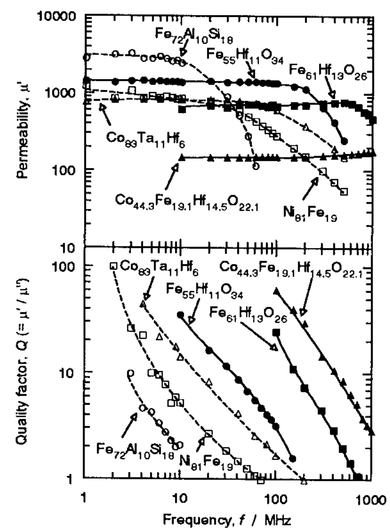

Figure 3. Frequency dependence of μ' and Q for Fe-Hf-O and Co-Fe-Hf-O films compared with other soft magnetic films.

APPLICATIONS

Figure 4 summarizes expected application fields for NANOPERM® together with the

magnetic characteristics which are required for their applications. As the application fields, one can list up the power transformers, data communication interface components, electro-magnetic interference (EMI) prevention components, magnetic heads, sensors, magnetic shielding and reactors.

As applications of the Fe-M-O films, micro switching converters, high density recording heads, noise filters and others used at high frequencies are now under investigation. For an example of the applications, Figures 5(a) and 5(b) show a schematic illustration of a planar inductor for micro switching converters and the frequency dependence of Q value of a planer Cu coil using each magnetic films, respectively (6). The inductor is made up of a planar coil sandwiched with two magnetic films faced each other as shown in Fig 5(a). In the case of the inductor, we use the one side of Cu coil as a conductor. As can be seen in Fig. 5(b), an inductor using the Fe-Hf-O film shows a maximum. The Q value of 12.3 at 6 MHz and extremely high value of 21.8 at 20 MHz is obtained for an inductor using Co-Fe-Hf-O film. Therefore, these planar inductors using the Fe-Hf-O and the Co-Fe-Hf-O films enables higher frequency operating and higher efficiency than the inductor using the Co-Ta-Hf amorphous films for the microswitching converters owing to the low loss characteristics of the magnetic films.

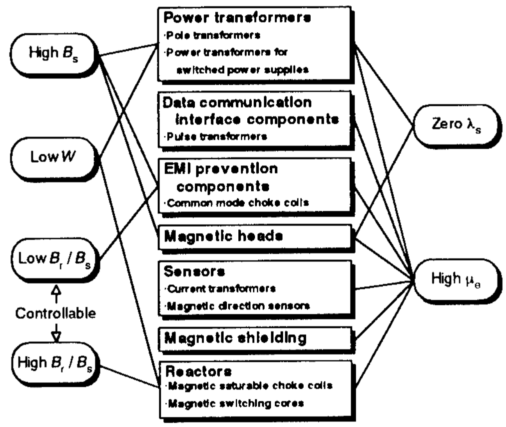

Figure 4. Magnetic characterizations and application fields for Fe-M-B ribbons (NANOPERM®).

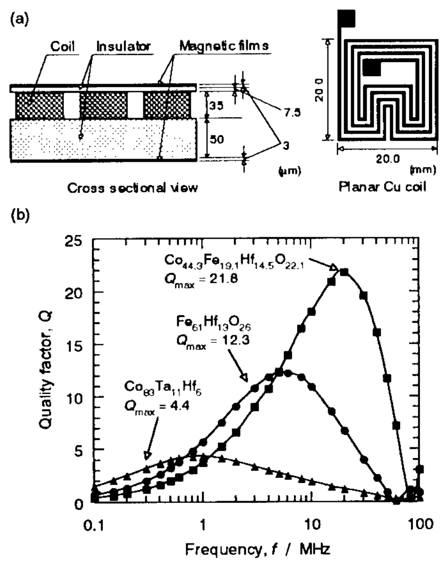

Figure 5. (a) Schematic illustration of planer inductor and (b) frequency dependence of Q of the inductor using Fe-Hf-O, Co-Fe-Hf-O and Co-Ta-Hf amorphous films.

References

1. T. Masumoto, H. Kimura, A. Inoue and Y. Waseda, Mater. Sci. Eng. 23, 141 (1976).
2. Y. Yoshizawa, S. Oguma and K. Yamauchi, J. Appl. Phys. 64, 6044 (1988).
3. A. Makino, K. Suzuki, A. Inoue, Y. Hirotsu and T. Masumoto, J. Magn. Magn. Mater. 133, 329 (1994).
4. A. Makino and Y. Hayakawa, J. Jpn. Inst. Metals 57, 1301 (1993).
5. A. Makino, T. Hatanai, A. Inoue and T. Masumoto, A226-228, 594 (1997).
6. T. Sato, E. Komai, K. Yamasawa, T. Hatanai and A. Makino, IEEE Trans. Magn. 33, 3310 (1997).

Pergamon

NanoStructured Materials, Vol. 12, pp. 829–834, 1999
Elsevier Science Ltd

0965-9773/99/$–see front matter

PII S0965-9773(99)00245-7

BEHAVIOR OF QUASICRYSTAL-REINFORCED $AL_{94}CR_{1}MN_{3}CU_{2}$ UNDER FATIGUE CONDITIONS

Volker Haas[1], Moon Ill Cho[2], Hitoshi Ishii[2], Akihisa Inoue[1]
[1] Institute for Materials Research, Tohoku University, Katahira 2-1-1, Aoba Ku, Sendai 980-8577, Japan
[2] Dept. of Mechanical Engineering, Shizuoka University, Johoku 3-5-1, Hamamatsu 432, Japan

Abstract -- *Their excellent tensile properties make quasicrystal (QC) reinforced aluminum alloys interesting for future structural applications. However, their fatigue behavior, one of the most important design properties, seems not yet to be known. We investigated the fatigue properties by means of a rotating bending test. The fatigue strength at 10^8 cycles was 210 MPa, 30% - 50% higher than conventional Al alloys. The metallographic and fractographic investigation suggested that the fatigue damage developed via slip and subsequent formation of persistent glide bands (PSB) leading to the development of extrusions on the specimen surface. Cracks nucleated at the surface primarily near inclusions present in the material. During growth the crack assumed a tortuous path due to deflection at the quasicrystals. ©1999 Acta Metallurgica Inc.*

INTRODUCTION

Recently, Inoue and his co-workers demonstrated for several QC-forming Al-based alloys (Al > 90 at.%) that embedding nanometre-sized QC at a high volume fraction (70%-80%) in a crystalline matrix improves considerably the strength and the ductility as compared to similar alloys not containing a QC phase (1,2,3,4,5,6,7). For instance, they exhibit tensile strengths, σ_0, of up to 1340 MPa and good bending ductility. Furthermore, their specific strength (up to 4.6×10^5 Nm/kg) is approximately double as large as that of conventional Al alloys. In the mean time, also Al-based bulk materials with similar microstructures produced by gas-atomization and subsequent extrusion are available (8,9,10,11). The mechanical properties are also very good (σ_0 = 500 - 800 MPa, elongations, ε = 5%-30%) indicating the high potential for use in demanding structural applications. While previous studies of bulk QC reinforced materials (8-11) focused on the investigation of the compositional dependence of the phase composition, QC phase morphology and phenomenological tensile properties, important design properties, like the fatigue behavior, seem not yet to be investigated. Therefore, we would like to report on the phenomenological fatigue behavior of a quasicrystal reinforced Al-based alloy.

EXPERIMENTAL

Preliminary studies (12) showed $Al_{94}Cr_1Mn_3Cu_2$ (composition in at.%) to be suited as a model material, since it combines high strength with sufficient ductility, both features beneficial to the fatigue behavior. Specimens were produced by gas-atomizing Al (99.999 at.%), Cr (99.9 at.%), Mn (99.9at.%) and Cu (99.9 at.%) in an Ar gas (99.999 at.%) atmosphere, sieving (mesh < 25 μm) and subsequent extrusion (Temperature 613 K, extrusion ratio 10:1, extrusion speed 1 cm/min). From each of the 3 extruded rods (12 mm ∅ x 60 cm) one tensile specimen was prepared. From the remainder 18 hourglass-type fatigue specimens were machined on a CNC machine and subsequently polished to a mirror-like surface finish.

The extruded material was characterized by intercoupled-plasma (ICP), differential scanning calorimetry (DSC), x-ray diffraction and optical and scanning electron microscopy (SEM). Uniaxial tensile tests were carried out at a strain rate of 1×10^{-3}/s and high-cycle fatigue experiments were conducted on a Shimadzu rotating bending machine (60 Hz) to obtain the stress-life-(S/N) curve. Longitudinal (L-) and transverse (T-) sections were then examined metallographically and the fatigue fracture surface was investigated in the SEM.

RESULTS

The chemical analysis with ICP confirmed the nominal composition within <0.1 at.%. The DSC analysis shows an exothermic peak at an onset temperature of 643 K which was attributed to the decomposition of the QC phase (Fig. 1). The X-ray diffraction pattern confirmed the presence of fcc-Al and the QC phase (Fig. 1). The average of three tensile tests yielded σ_0 = 570 MPa, a yield strength of 460 MPa, ε = 10.3% and a Young's modulus of 89.3 GPa.

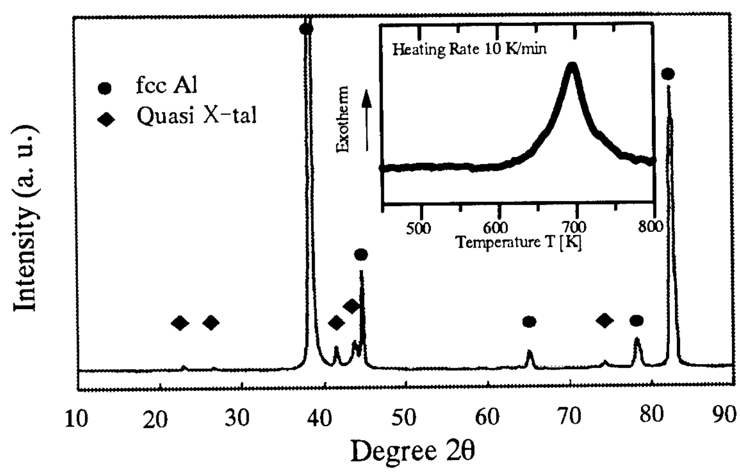

Fig. 1: Diffractogram of as-extruded $Al_{94}Cr_1Mn_3Cu_2$. The inset shows the corresponding DSC trace.

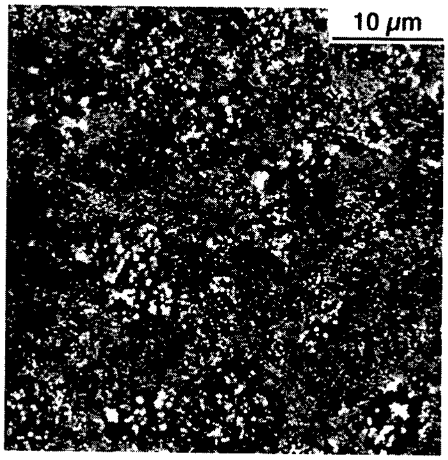

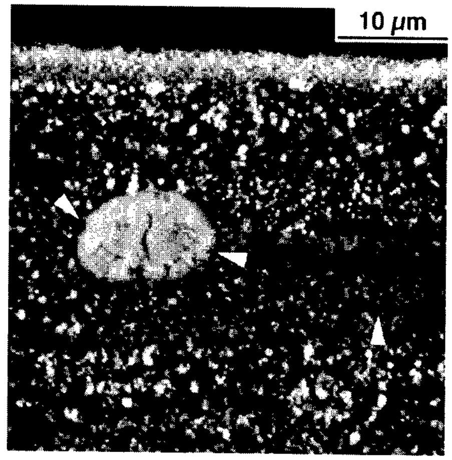

Fig. 2: SEM backscattering images of as-extruded $Al_{94}Cr_1Mn_3Cu_2$. Left: T-direction. Right: L-direction. Note debonding of inclusion and pores (arrows).

The microstructure of the as-extruded alloy (Fig. 2) consisted of elongated grains, the former powder particles, 4 - 12 μm ∅ × 80 - 250 μm in which white precipitates 100 nm - 1 μm ∅ could be seen. Since the QC usually contain a large amount of the heavy alloying elements (13), they should show up brighter in the backscattering image than the matrix phase consisting mainly of Al suggesting that the white precipitates can be identified with the QC phase. Furthermore, the light-gray background found in many grains indicated the presence of nanometer-sized quasicrystals beyond the resolution of the SEM (8). The QC were not uniformly distributed and the morphology depended on the size (< 200 nm round, larger faceted). At the grain-boundaries the material also contained pores (0.5 μm ∅) stemming from incomplete densification. Secondly, inclusions (4 - 15 μm ∅) were present (Fig. 2). Evaluation of an optical micrograph yielded a density of 6×10^{-4} particles/mm^2. The origin of the inclusions was probably the alumina crucible of the gas atomizer.

Fig. 3 depicts the results of the rotating bending fatigue tests. The S/N curve showed type II behavior and, hence, only a fatigue strength, σ_f, could be evaluated. At 10^8 cycles it was estimated to be 210 MPa. Compared with high fatigue strength commercial Al-alloys (14), which vary between 140 MPa (2024-T3) and 160 MPa (7075-T6), the quasicrystal reinforced alloy was 30% to 50% stronger. The metallographic investigation of the fatigued specimens showed no apparent change in the microstructure. Yet, a close inspection of the near surface area of the samples revealed the frequent occurrence of inclusions at a depth of 10 to 30 μm. Besides debonding of the inclusions micro-cracks emanating from the inclusions were observed.

The inspection of the fracture surface showed that fracture seemed to initiate mostly at inclusions at/near the surface of the specimen. Also, the fatigue life was always found to be reduced, when fracture was initiated at an inclusion. The fracture surface consisted of plateaus separated from the surrounding material by tear ridges (Fig. 4). The plateaus appeared to be damaged due to rubbing of the surfaces on each other during the experiment. Since the areas next to a plateau are recessed damage by rubbing is much less likely to occur and, hence, they should be representative

DISCUSSION

The aim of this study was to establish exemplarily the phenomenological high-cycle fatigue behavior of quasicrystalline-reinforced Al alloys. Although the data show some scatter, which may be attributed to the frequent presence of inclusions, the results indicate that QC-reinforced Al alloys can exhibit very high fatigue strengths. Not only is the fatigue strength up to 50% higher than that of commercial alloys, but also the σ_f/σ_0 ratio is with 0.37 about 25% higher (14). Together with the very good static mechanical properties these findings clearly recommend these type of alloys for future demanding structural applications.

As far as the underlying reasons for the observed high σ_f value is concerned it is difficult to draw precise conclusions at that point, since rotating bending tests are not particularly suited for the investigation of fracture mechanisms. Nonetheless, limited understanding can be gained from the metallographic and fractographic examinations. Extrusions are found at the specimen surface. Since they are caused by persistent slip bands (PSB) emanating at the surface, it can be concluded that the initial stages of fatigue proceed via slip and the formation of PSB as found in conventional materials (15). The geometrical dimensions of the extrusions coincide with the dimensions of the grains (approximately 10 μm ∅). Together with the observed absence of intrusions this would suggest, that the PSB are not able to cross the high-angle grain boundaries which were formed between the former powder particles upon extrusion. Furthermore, the protrusions should leave pores in their wake which, judging from the length of the extruded material, may extend almost across the whole diameter of the outermost grain. Such a defect should play a decisive role in crack nucleation. However, in our experiments extrinsic defects, i.e. the inclusions, seemed to be more important. Fractography revealed that they were mostly responsible for crack nucleation and deteriorated the fatigue strength considerably. Given this fact it is desirable to improve process control in order to remove the inclusions and, thus, obtain a material with even more improved fatigue properties. With respect to fatigue crack propagation the irregular fracture surface morphology suggests the following behavior. As the crack propagates it frequently encounters the QC particles. Since none of the particles were found to be cleaved or sheared the crack must be deflected at the particle-matrix interface as evidenced by the numerous QC particles and faceted holes found on the fracture surface. Thus, the QC particles seem to act as an efficient barrier and the crack is forced to assume a tortuous path on a μm-scale. The crack continues to grow until final overload rupture occurs in a ductile manner as also observed in static tensile tests (16).

In conclusion, it can be said, that the QC-reinforced alloy behave like a conventional alloy containing non-shearable particles. However, the QC seem to be particularly effective in strengthening the material. The combination of two mechanisms may be envisaged to be responsible. For one it should be difficult for dislocations to move easily in the matrix because due to the high volume fraction of the QC particles backstresses should build up easily. Thus, crack initiation would be delayed. Secondly, the crack is continuously deflected by the QC and hence, the crack growth rate should decrease yielding the longer fatigue life. In fact, recent measurements of the fatigue crack growth rate (FCGR) showed that QC-reinforced alloys exhibit a higher threshold as well as a reduced FCGR compared to conventional Al alloys (17). The former being around 20 $\mathrm{MPa}\sqrt{m}$ ($\approx$ 4 $\mathrm{MPa}\sqrt{m}$ conventionally) and the latter being approximately 10^2 times smaller at comparable stress concentration ratio ranges.

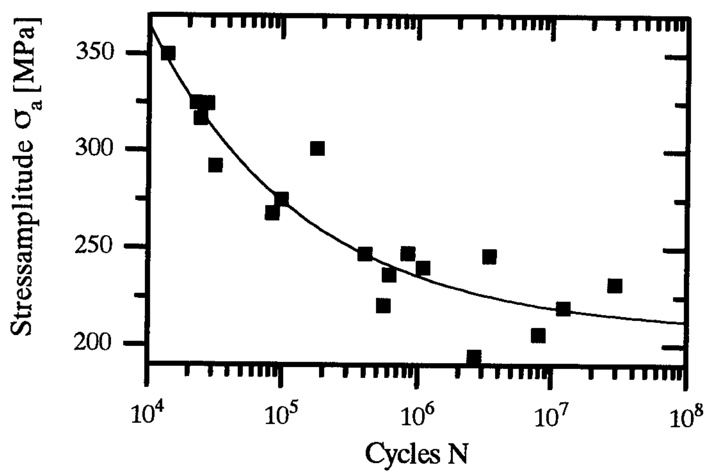

Fig. 3: S/N curve of $Al_{94}Cr_1Mn_3Cu_2$.

for the fatigue fracture surface. No striations could be discerned and instead the surface showed an irregular appearance with many QC sticking out. The QC were never found to be cleaved or sheared. Furthermore, there were many, partly faceted, holes in the surface. The overload area of the fracture was deeply fissured and exhibited very fine dimples (≤1 μm ∅).

On the specimen surface extrusions emanating up to approximately 10 μm from the surface were observed (Fig. 4). They consisted of several plates each 1 μm thick. Their number density and extension from the surface scaled with the cycles, N, and their orientation appeared to be random. Intrusions were not found.

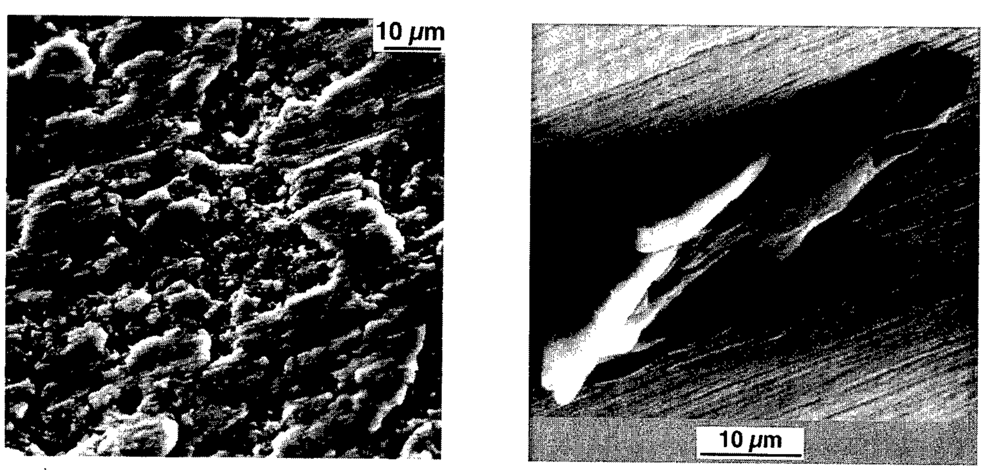

Fig. 4: Left: Damaged plateaus and undamaged fatigue fracture surface with irregular morphology (recesses). Right: Extrusion on specimen surface.

SUMMARY

We studied the phenomenological high-cycle fatigue behavior of a quasicrystal reinforced Al-based alloy of composition $Al_{94}Cr_1Mn_3Cu_2$ by means of a rotating bending fatigue test. The fatigue strength at 10^8 cycles was evaluated to be 210 MPa. This is 30% - 50% higher than that of commercially available alloys making these types of alloys interesting as future structural materials.

From the metallographic and fractographic examination first conclusions regarding fatigue crack nucleation and growth could be drawn. The fatigue damage seems to be initiated by slip and the subsequent formation of persistent glide bands and extrusions. Cracks nucleate at the surface mainly at inclusions and proceeds on a tortuous path through the material whereby the quasicrystalline particles act as effective barriers deflecting the crack.

Acknowledgments: The authors thank YKK corporation for providing the Al alloy and generously allowing the use of their research facilities in Sendai. V. H. thanks the Japan Society for the Promotion of Science (JSPS) for financial support in the framework of the JSPS Postdoctoral Fellowship Program.

REFERENCES

1. A. Inoue, H. Kimura, K. Sasamori, T. Masumoto, *Mater. Trans., JIM*, 1996, 37,1287
2. A. Inoue, H. Kimura, K. Sasamori, T. Masumoto, *Sci. Rep. RITU*, 1996, A42, 165
3. H. Kimura, A. Inoue, K. Sasamori, Y.H. Kim, T. Masumoto, *Mater. Trans., JIM*, 1995, 36, 1004
4. A. Inoue, H. Kimura, K. Sasamori, T. Masumoto, *Mater. Trans., JIM*, 1995, 36,6
5. A. Inoue, H. Kimura, K. Sasamori, T. Masumoto, *Mater. Trans., JIM*, 1995, 35, 85
6. M. Watanabe, A. Inoue, H. Kimura, T. Aiba, T. Masumoto, *Mater. Trans., JIM*, 1993, 34 162
7. A. Inoue, M. Watanabe, H. Kimura, F. Takahashi, A. Nagata, T. Masumoto, *Mater. Trans., JIM*, 1992, 33, 723
8. E.H. Buechler, E. Watanabe, N.S. Kazama, *Intl. J. Non-Equilibrium Process.*, 1997, 10, 35
9. K. Kita, K. Saitoh, A. Inoue, T. Masumoto, *Mater. Sci. Eng.*, 1997, A226-228, 1004-1007
10. A. Inoue, H. M. Kimura, K. Kita, in: A.I. Goldmann, D.J. Sordele, P.A. Thiel, M. Dubois (Eds.), *New Horizons in Quasicrystals*, World Scientific, Singapore, 1997, 256
11. A. Inoue, H.M. Kimura, *Current Opinion in Solid State and Materials Science*, 1997, 2, 305
12. YKK Corporation, Sendai Institute for Materials Science and Technology, unpublished data
13. A. Inoue, H.M. Kimura, K. Sasamori, T. Masumoto, *Intl. J. Rapid. Solid., 1996, 103*
14. American Society for Metals, *Metals Handbook 10th ed. , Vol. 2*, Ohio, 1996, 788
15. S. Suresh, *Fatigue of Materials*, University Press, Cambridge, 1991
16. V. Haas, K. Saitoh, D. Nakasato, A. Inoue, to be published
17. V. Haas, A.T. Yokobori, Jr., A. Inoue, to be published

Pergamon

NanoStructured Materials, Vol. 12, pp. 835–838, 1999
Elsevier Science Ltd

0965-9773/99/$–see front matter

PII S0965-9773(99)00246-9

ON ELECTRON-ELECTRON SCATTERING MECHANISMS IN 2D DEGENERATED SYSTEMS

H.Buhmann*, R.N. Gurzhi+, A.N. Kalinenko+, A.I. Kopeliovich+,
L.W.Molenkamp*, A.V. Yanovsky+
+B.I. Verkin Institute for Low Temperature Physics & Engineering
Academy of Sciences of Ukraine, Lenin Ave. 47, Kharkov 310164, Ukraine
e-mail: kopeliovich@ ilt.kharkov.ua
* II.Physikalisches Institut RWTH Aachen, Templergraben 55,
52056 Aachen, Germany
buhmann@physik.rwth-aachen.de, molenkmp@physik.rwth-aachen.de

Abstract – The detailed quantitative theory of electron-electron scattering processes in 2D electron degenerated systems in GaAs(AlGaAs) heterostructures has been developed on the basis of analytical treatment and numerical calculations. We have found the conditions and intervals of values of the characteristic parameters in which specific properties of 2D relaxation predicted previously on the theoretical level manifest themselves. New effects, i.e. a secondary beam of electrons scattered back and a very narrow beam of holes moving in the direction of injection, have been found. *©1999 Acta Metallurgica Inc.*

As shown by us previously, the processes of momentum relaxation in perfect two-dimensional systems at low temperatures are of qualitatively different character than in an ordinary three-dimensional metal [1-3]. This is connected with the fact that the limitations arising when decreasing dimensionality of space change essentially dynamic properties of degenerate gas of electrons colliding with each other when passing from three to two dimensions. These results are of a general character, i.e. they are related only to the dimensionality of the electron system with the convex and simply connected Fermi surface. The main purpose of this paper is to obtain a detailed picture of electron-electron scattering in the two-dimensional case at different values of a degeneration parameter $T/\varepsilon_F \ll 1$ (T is the temperature, ε_F is the Fermi energy). In a general case instead of T one is to take a characteristic energy of unequilibrium electrons counted off from the Fermi level.

Let f be a nonequilibrium part of the electron distribution. An integral of electron-electron collisions linearized over f may be presented in the form

$$\hat{I}f = -\nu f_{\mathbf{p}} + \int d^2\mathbf{p}' \nu_{\mathbf{p}\mathbf{p}'} f_{\mathbf{p}'}, \quad \nu = \int d^2\mathbf{p}' \nu_{\mathbf{p}'\mathbf{p}}. \tag{1}$$

Note that a kernel $\nu_{\mathbf{p}\mathbf{p}_0}$ has sense of the response function. It describes the change of the number of nonequilibrium quasi-particles in a state $\mathbf{p}$ which is due to the presence

of nonequilibrium electron in a state $\mathbf{p}_0$ (in formula (1) one is to take $f_{\mathbf{p}'} = \delta(\mathbf{p}' - \mathbf{p}_0)$). The response function consists of two parts, i.e. a "hole" part which is negative and describes the appearance of nonequilibrium hole in the state $\mathbf{p}$ and an "electron" part which positive definite:

$$\nu_{\mathbf{p}\mathbf{p}_0} = -\nu^-_{\mathbf{p}\mathbf{p}_0} + \nu^+_{\mathbf{p}\mathbf{p}_0}, \quad \nu^-, \nu^+ > 0 \ . \tag{2}$$

Take for the sake of simplicity that $\varepsilon = \mathbf{p}^2/2m$ (this is a strict law of dispersion for a case of $GaAs/AlGaAs$ heterostructures) and neglect a relatively weak dependence of the squared modulus of the matrix element of interactionon of its variables. (The numerical calculations which we omit here show that the use of a more realistic model does not change essentially the result.) Then we have:

$$\begin{aligned}\nu^-_{\mathbf{p}\mathbf{p}_0} = \frac{n(\varepsilon)}{1-n(\varepsilon_0)} W \int d\varepsilon_2 \, [\varepsilon\varepsilon_0 \sin^2\varphi - (\varepsilon - \varepsilon_0)(\varepsilon_2 - \varepsilon_0)]^{-\frac{1}{2}} \times \\ \times (1 - n(\varepsilon_2))\,(1 - n(\varepsilon_0 + \varepsilon - \varepsilon_2))\,\Theta(\varepsilon + \varepsilon_0 - \varepsilon_2) \times \\ \times \Theta(\,\varepsilon\varepsilon_0 \sin^2\varphi - (\varepsilon - \varepsilon_0)(\varepsilon_2 - \varepsilon_0)\,) \quad ,\end{aligned} \tag{3}$$

$$\begin{aligned}\nu^+_{\mathbf{p}\mathbf{p}_0} = 2W \frac{1-n(\varepsilon)}{1-n(\varepsilon_0)} [\exp(\frac{\varepsilon_0 - \varepsilon}{T}) - 1]^{-1} \times \\ \times \{Li_{\frac{1}{2}}(-\exp(-\frac{\varepsilon - \Delta - \varepsilon_F}{T})) - Li_{\frac{1}{2}}(-\exp(-\frac{\varepsilon_0 - \Delta - \varepsilon_F}{T}))\}.\end{aligned} \tag{4}$$

Here $\varepsilon_0 \equiv \varepsilon_{\mathbf{p}_0}$, φ is the angle between $\mathbf{p}$ and $\mathbf{p}_0$ ("scattering angle"), $n(\varepsilon)$ is the equilibrium Fermi distribution, W is proportional to the squared modulus of the matrix element of interaction, $Li_{\frac{1}{2}}$ is the polylogarithm to the base 1/2, $\Delta = (2m\varepsilon\varepsilon_0 \sin^2\varphi)|\mathbf{p}_0 - \mathbf{p}|^{-2}$.

Fig.1a, 1b presents the dependence of the function $\nu_{\mathbf{p}\mathbf{p}_0}$ on the energy ε and the angle φ calculated by the Eq. (3),(4) for two different values of energy of injected electrons: for Fig.1a $\epsilon \equiv (\varepsilon_0 - \varepsilon_F)/\varepsilon_F = 0.1$ and for Fig.1b $\epsilon = 0.32$ (We supposed that $\varepsilon_0 - \varepsilon_F \gg T$.)

We have received similar results for the relaxation of the termalized distributions and the best coincidence is reached at $T \sim (\varepsilon_0 - \varepsilon_F)/3$.

The one-collision approximation can be also used to treat problems on the change profile of the narrow beam when moving away from the injector at distances which are much less than electron-electron mean free path. However, at the detailed comparison with experiment it is necessary to take into account a whole number of circumstances which are out of the framework of the present paper (in particular, reflection of electrons and holes from boundaries [4]). The results of the preliminary calculations are in qualitative agreement with the experiments [5,6].

Fig.1a

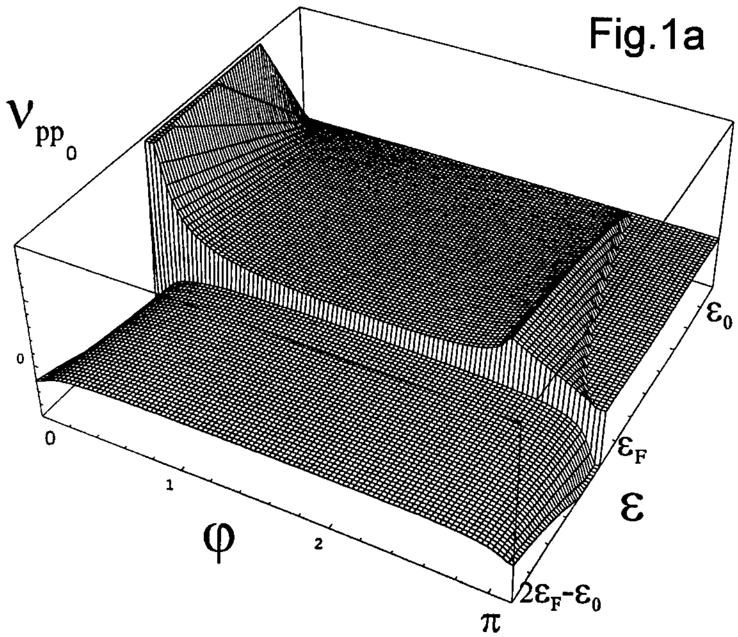

Fig1.b

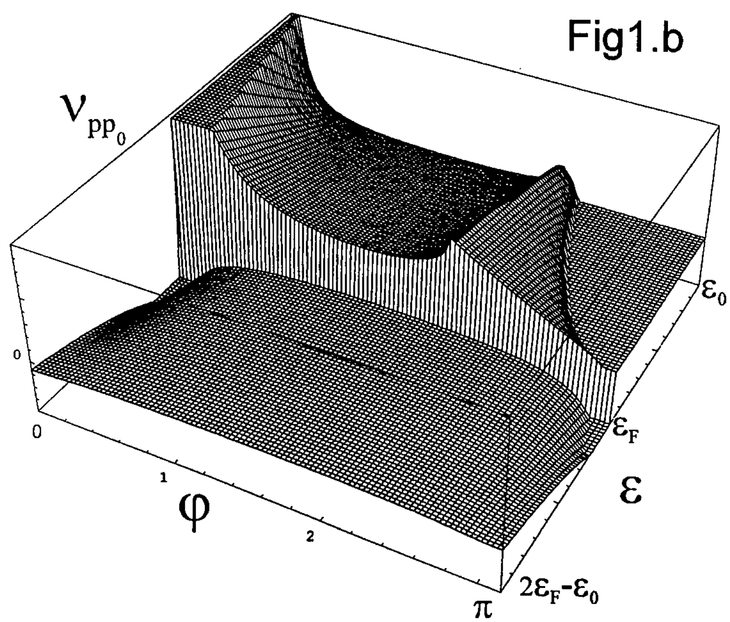

Fig1. Dependence of the response function ν on the energy ε and the angle φ : (a) $\epsilon=0.1$; (b) $\epsilon=0.32$.

In conclusion, let us numbering the principal specific peculiarities of electron-electron relaxation in the 2D electron gas.

1) Weak broadening of the antisymmetric part of a beam; emission of narrow beams of electrons flying almost parallel to the primary beam and holes flying in the opposite direction. These effects manifest themselves well at $\epsilon \leq 0.2$ in the case of high energies or at $T/\varepsilon_F \leq 0.1$ for thermalized distributions. However, they remain noticeable even at $\epsilon \sim T/\varepsilon_F \sim 1$.

2) "Secondary beam" of electrons at the angles which are close to $\pi - 2\sqrt{\epsilon}$. This effect is well-defined at the values of the parameters $3T/\varepsilon_F < \epsilon < 0.2$ or for thermalized distributions at very low temperatures $T/\varepsilon_F < 0.01$.

3) Beam of holes flying forward at the smallest angles ($\varphi < 0.1 \cdot \epsilon^{3/2}$). This effect exists only in high-energy beams if $\epsilon > 3T/\varepsilon_F$.

The research made was possible by partial supports of the "Volkswagen-Stiftung" (Grant I/72 531) and Ministry of Science of Ukraine (Grant 2.4/160).

1. R.N. Gurzhi, A.N. Kalinenko, A.I. Kopeliovich. Phys. Rev. Lett. , **74**, 3872 (1995)

2. R.N. Gurzhi, A.N. Kalinenko, A.I. Kopeliovich. Phys. Rev. B, **52**, 4744 (1996).

3. R.N. Gurzhi, A.N. Kalinenko, A.I. Kopeliovich, Fiz. Nizk. Temp. **23**, 58, (1997).

4. A.S.D. Heindrichs, H. Buhmann, S.F. Godijn and L.W. Molenkamp, Phys. Rev. B, **57**, 3961 (1998).

5. L.W. Molenkamp, M.J.P. Brugmans, H. van Houten, C.T. Foxon, Semicond. Sci. Technol. **7**, B228 (1992).

6. Th. Shäpers, M. Krüger, J. Appenzeller, A.Förster, B. Lengeler, H. Lüth, Appl. Phys. Lett., **66**, 3603, (1995).

Pergamon

NanoStructured Materials, Vol. 12, pp. 839–842, 1999
Elsevier Science Ltd

0965-9773/99/$–see front matter

PII S0965-9773(99)00247-0

STRUCTURE AND MECHANICAL BEHAVIOUR OF AN Al-Mg ALLOY AFTER EQUAL CHANNEL ANGULAR EXTRUSION

M.V.Markushev[1], M.Yu.Murashkin[1], P.B.Prangnell[2], A.Gholinia[2] and O.A.Maiorova[1]
[1]Institute for Metals Superplasticity Problems RAS, Khalturin 39, Ufa 450001, Russia
[2]Manchester Materials Science Centre, Grosvenor Street, Manchester, M1 7HS, UK.

Abstract -- *Equal channel angular extrusion (ECAE) has been used to develop an ultra-fine grain (UFG) structure, with a 0.4μm grain size, in Al-alloy 1560. The structure and mechanical properties, including toughness, have been investigated in the as-deformed condition and after annealing. On annealing in the temperature range 200-350°C abnormal growth of discrete grains to several microns in size occurred, whereas when annealed at higher temperatures the UFG structure coarsened uniformly. The as-deformed and lightly annealed states, both with UFG structures, showed substantially higher strengths, but lower ductility and toughness, compared to UFG material annealed to produce a 5μm grain size.*
©1999 Acta Metallurgica Inc.

INTRODUCTION

There is currently a great deal of interest in ultra-fine grain (UFG) materials (grain size $\leq 1\mu m$). One commercially viable method for their production is the use of severe plastic deformation, in which an UFG structure forms by grain fragmentation and continuous recrystallization (1-3). An UFG structure in Al-alloys can considerably alter their mechanical properties and their behaviour is critically dependent on the specific alloy, the processing conditions and the type of UFG structure formed (1). During annealing the as-deformed UFG material a coarser and more equiaxed grain structure can be formed (2), concurrently there is a sharpening of the grain boundaries (3), a reduction in internal stresses (1,3) and a change in the distribution of boundary misorientations (2). All of these factors would be expected to influence the mechanical behaviour of UFG materials, but their effects are poorly understood.

MATERIAL AND EXPERIMENTAL PROCEDURE

20mm diameter samples of a commercial Al-alloy 1560 (Al-6Mg-0.6Mn) were deformed to a total effective strain of near 9, by Equal Channel Angular Extrusion (ECAE) with a 90^0 angle between the channels in the temperature range 200-400^{0}C. The alloy structure was studied using optical and transmission electron microscopy. The mean grain size (d) and the volume fraction of ultra-fine grains (V_{UFG}) were determined by the linear intercept method. Strength (yield stress, $\sigma_{0.2}$, and tensile stress, σ_t) and ductility (elongation, δ, and reduction in area, ψ) were measured in tension on ∅3x15mm samples. The specific works required for

samples rupture, formation and growth of a crack (a, a_f and a_g) were determined in static bending, on samples 10x10x55mm in dimensions with a U-type lateral notch (as in (4)). Brinnel hardness (HB) was measured using a standard steel ball indentor.

RESULTS AND DISCUSSION

The received UFG structure after ECAE is comprised of grain fragments with a mean high angle boundary separation of d=0.40μm (Fig.1a). The fragments are predominantly asymmetric and the TEM contrast is indicative of a high level of internal stress. After annealing for 1 hour below 200°C, practically no change in structure was detected. Increasing the annealing time at 200°C to 8 hours (Fig. 1b) led to a slight increase in grain size to 0.45μm, with the grains becoming more symmetric, and was accompanied by the formation of stronger extinction contours at grain boundaries. Despite the minimal change in the average grain size, the hardness progressively decreased with annealing time (Fig.2a) suggesting a reduction in internal strain energy and the production of a more equilibrium grain structure. Some decrease in hardness could also be due to coarsening of the secondary precipitates of β (Al_2Mg_3) phase.

On annealing at higher temperatures for one hour significant grain coarsening was observed (Figs.1c and 3). Between 200-350° this occurred inhomogeneously by secondary recrystallization involving the preferential growth of individual grains. After annealing, the size of the abnormal grains was in the range 2-15μm and their volume fraction increased rapidly with temperature. The reason for the abnormal coarsening of some grains may be related to inhomogeneity in the deformed structure and due to inhomogeneous distribution of the alloying elements and second phase particles originating in the initial casting and extrusion. On annealing above 350°C normal grain growth took place. The largest grain size observed after annealing at 300°C, where abnormal grain growth occurred. The change in hardness with annealing temperature closely mirrored the microstructural changes (Fig.2b). Below 200°C there was a slight decrease in hardness due to recovery, whereas above 200°C grain growth

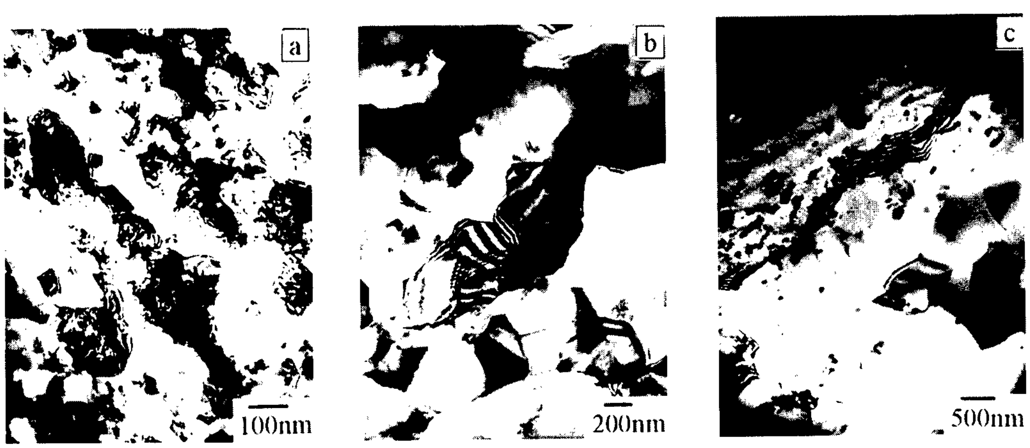

Figure 1. TEM structures of as-deformed by ECAE (a) and further annealed at 200°C for 8 hrs (b) and 300°C for 1hr (c) alloy 1560

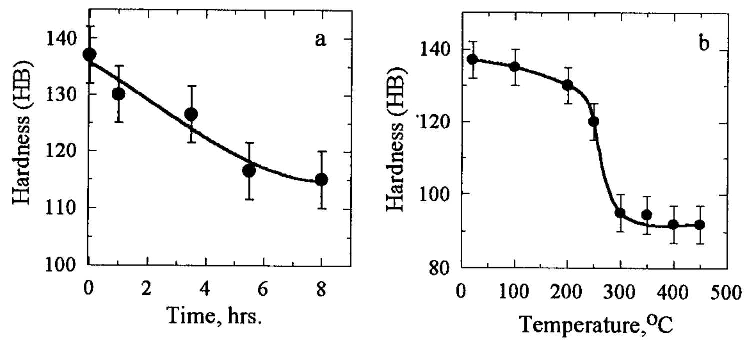

Figure 2. Dependence of hardness on duration of annealing at 200°C (a) and on temperature of 1hr annealing (b) for ECAE processed alloy 1560.

lead to a rapid drop in hardness. Similar behaviour has been observed on annealing other UFG aluminium alloys produced by different deformational methods (1,5).

Three conditions were chosen for tensile and toughness measurements; (A) as ECAE processed, (B) extruded and annealed at 200°C for 8 hours and (C) extruded and annealed for 1 hour at 350°C (Table). The size and the distribution of the primary phases, which play a dominant role in alloy failure, were similar in all states. Surprisingly, transition from the as-deformed (A) to more equilibrium UFG structure (B) led to slight decrease in alloy ductility and toughness. More in line with expectation, the alloy with the fine grain structure showed a large fall in strength combined with a substantial increase in ductility and toughness. In this state the loss of yield strength can be attributed to a relaxation of the internal stresses in the heavily deformed condition and the larger grains size, according to the well known Hall-Petch relation. The behaviour of sample (B) is contrary to work on a 5083 alloy where it was found that there was a recovery in ductility and toughness on slightly annealing the severely strained material (1). The observed effect may be influenced by differences in the processing conditions and the higher Mg level in the 1560 alloy, which could be precipitating predominantly at grain boundaries on annealing. However, more work is required to confirm this explanation.

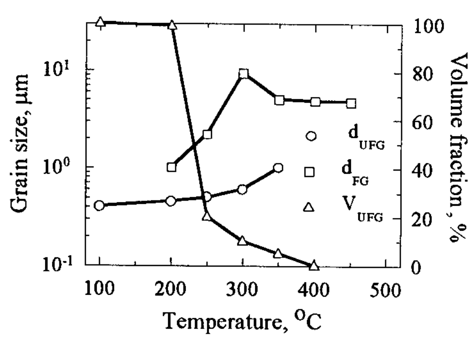

Figure 3. Variation in volume fraction (V) and average size (d) of ultra-fine and fine (UFG and FG) grains with annealing for one hour for the ECAE processed alloy 1560

TABLE
Ambient Temperature Mechanical Properties of 1560 Alloy

State	d, μm	$\sigma_{0,2}$, MPa	σ_t, MPa	δ, %	ψ, %	a, kJ/mm^2	a_f, kJ/mm^2	a_g, kJ/mm^2
A	0.40	355	435	20	42	117	94	23
B	0.45	350	415	17	35	86	70	16
C	4.9	195	380	35	47	361	248	113

Analysis of the lower toughness in UFG states has shown that it is connected not only with a drop in crack growth resistance, which takes place on grain refinement of aluminium alloys (6), but also with a decrease in the resistance to crack formation (Table). The latter effect is unusual and requires further study to understand its physical nature.

CONCLUSIONS

1. In the aluminium alloy 1560 an UFG grain structure with 0.4μm grain size can be produced by severe plastic deformation through equal channel angular extrusion.
2. Heating of the as-deformed UFG alloy above 200°C leads to an increase in grain size by abnormal grain growth and above 350°C by stable grain coarsening.
3. When compared to the alloy with an annealed 5μm grain size the yield stress of UFG as-deformed and annealed states was found to be higher by a factor of 1.8, but both the ductility and the toughness were reduced by more than a half.
4. Decrease in the alloy toughness at UFG structure processing is caused by both drop in the resistance to crack formation and the resistance to crack growth.

ACKNOWLEDGEMENT

M. Markushev is grateful to the Royal Society/Nato Postdoctoral Fellowship Programme for financial support.

REFERENCES

1. Markushev, M.V., Bampton, C.T., Murashkin, M.Yu. and Hardwick, D.A., *Mater. Sci. Eng*, 1997, A234-236, 927.
2. Prangnell P.B., Harris, C. and Roberts, S.M., *Scripta Materialia*, 1997, 37, 983.
3. Valiev, R.Z., Korznikov, A.V. and Muliukov, R.R. *Mat.Sci.Eng.*, 1993, A168, 141.
4. Rabinovich, M.Kh., Markushev, M.V. and Murashkin, M.Y., *Met.Forum,* 1994, 170, 243
5. Gholinia, A., Bowen, J.R., Prangnell, P.B. and Humphreys, F.J., *ICAA-6* (to be published)
6. Rabinovich, M.Kh. and Markushev, M.V., *J.Mat.Sci.*, 1995, 30, 4692 and 1996, 31, 4997

Pergamon

NanoStructured Materials, Vol. 12, pp. 843–846, 1999
Elsevier Science Ltd

0965-9773/99/$–see front matter

PII S0965-9773(99)00248-2

NANOGLASS $Fe_{79}B_{21}$ POWDERS PREPARED BY CHEMICAL REDUCTION: A LOW-TEMPERATURE MöSSBAUER STUDY

G.Y. Wu[1], J.Z. Jiang[2], and X.P. Lin[1]
[1] Jiangsu Institute of Chemical Engineering, Changzhou, Jiangsu, P.R. China.
[2] Department of Physics, Building 307, Technical University of Denmark, DK-2800 Lyngby, Denmark

Abstract--The magnetic behavior of nanoglass $Fe_{79}B_{21}$ powder has been investigated by Mössbauer spectroscopy in a temperature range from 5 to 295 K together with one amorphous $Fe_{80}B_{20}$ ribbon prepared by melt-spinning. It is found that average hyperfine fields for the powder sample are smaller than those for the ribbon sample in the whole temperature range studied. The reduced average hyperfine field of nanoglass $Fe_{79}B_{21}$ powders follows the Bloch's law, $H(T)/H(0)=1-BT^{3/2}$. The B parameters for the powder and the ribbon samples are found to be about 2.8×10^{-5} $K^{-3/2}$ and 2.2×10^{-5} $K^{-3/2}$, respectively, indicating that the degree of local structural disorder in the powder sample is higher than that in the ribbon.

INTRODUCTION

Amorphous metallic materials have many unique and promising properties, such as high strength, high hardness, low magnetic hysteresis, and excellent corrosion resistance. Despite the potential economic benefits, amorphous metallic materials remain largely the subject of laboratory investigation, and only in very few instances they have been employed for commercial applications. The lack of development originates in part from the geometric limitations, i.e., the materials are extremely thin in one dimension. This geometry is not suitable for many engineering applications. However, amorphous alloy powders, because of their nearly spherical geometry, are preferable for the formation of bulk amorphous materials by sintering under static pressure. Thus, the development of new techniques for preparing amorphous alloy powder is desirable. One novel technique is the chemical reduction method which was discovered by Wonterghem et al. (1). There has been considerable interest in this field (2-7) since then. In the present paper we report an on-going project on the low-temperature magnetic behavior of the nanoglass $Fe_{79}B_{21}$ powder prepared by chemical reduction together with the amorphous $Fe_{80}B_{20}$ ribbon prepared by melt-spinning.

EXPERIMENTAL

The nanoglass $Fe_{79}B_{21}$ powders were prepared by chemical reduction of an aqueous $FeSO_4$ solution with a potassium borohydride KBH_4 solution (see Ref. (7) for details). The

amorphous state of the powder samples was checked by their x-ray diffraction pattern. The morphology and average size of the nanoglass particles were examined using transmission electron microscopy. It was found that they have a nearly spherical morphology with diameters ranging from 50 to 500 nm. The boron concentration of the sample was estimated in the following way. The relative amounts of the various crystalline phases (α-Fe and Fe_2B) in the crystallized sample were determined using Mössbauer spectroscopy from the relative areas of their spectral components assuming equal recoil-free fractions. For comparison, the $Fe_{80}B_{20}$ amorphous ribbon was prepared by the melt-spinning. Mössbauer measurements in a temperature range from 5 to 295 K were performed with a conventional constant-acceleration spectrometer in transmission geometry with source of about 25 mCi ^{57}Co in a Rh matrix using a liquid helium cryostat. All isomer shifts are given relative to that of α-Fe at room temperature.

RESULTS AND DISCUSSION

Mössbauer spectra for the nanoglass $Fe_{79}B_{21}$ powder were recorded at various temperatures from 5 to 295 K. It is clear from the broad line widths that these spectra do not represent an unique hyperfine field. This is to be expected from the amorphous state of the sample, in which there are many inequivalent iron sites. We have used two methods to analyse these spectra in order to obtain the average hyperfine field value. The spectra were fitted by the Le Caer program (8) with a hyperfine field distribution. The isomer shift was assumed to be proportional to the hyperfine field. We have also fitted the spectra using Voigtian line profiles whose line positions were constrained to be physically realistic following the method of Lines and Eibschütz (9). All spectra could be fitted using both methods. The average hyperfine field values obtained by the two methods are slightly and consistently different by about 4 %. However, the reduced average hyperfine field values, $H_{eff}(T)/H_{eff}(0)$, are nearly the same, where $H_{eff}(T)$ and $H_{eff}(0)$ are average hyperfine fields at given temperature T and 0 K, respectively. The temperature dependence of the average hyperfine field (obtained by using the Le Caer program (8)) for the nanoglass $Fe_{79}B_{21}$ powder and the $Fe_{80}B_{20}$ ribbon is plotted in Fig. 1 together with the solid lines obtained by fitting the experimental data using the Bloch's law, $H_{eff}(T) = H_{eff}(0)(1-BT^{3/2})$, where B is a coefficient. It is clear that the average hyperfine fields for the powder and ribbon samples are different in the whole temperature range studied and that they are smaller for the powder than those for the ribbon. For the Fe-B alloy system it has been suggested that the hyperfine field is mainly determined by the number of nearest-neighbor boron atoms (11). However, this model can only be considered approximate because other parameters, e.g., the number of nearest-neighbor iron atoms, the iron-iron and iron-boron distances, can also influence the hyperfine interaction of the iron atom in a complex way (12). Their contributions cannot be determined separately. Nevertheless, one may not exclude the possibility that the reduction of average hyperfine field in the powder sample in comparison to the ribbon is the result of an increase in the number of iron atoms having more nearest-neighbor boron atoms. This may result from increasing heterogeneity in the local environment within a powder.

It is established that excitations of long-wavelength spin waves exist in a number of amorphous ferromagnetic alloys prepared by the melt-spinning (12). The good fits using the Bloch's law imply that the long-wavelength spin waves also exists in the nanoglass $Fe_{79}B_{21}$ powders. The coefficient, B, was found to be $2.8 \times 10^{-5}\ K^{-3/2}$ and $2.2 \times 10^{-5}\ K^{-3/2}$ for the powder

and ribbon samples, respectively, which is consistent with data reported by Linderoth (13). One knows that the value of the coefficient B depends on the structure of a ferromagnetic sample. In amorphous ferromagnetic materials, due to the random atomic structure, the value of the coefficient B is several times larger than the values for crystalline ferromagnets, (0.34×10^{-5} $K^{-3/2}$ for α-Fe and 0.75×10^{-5} $K^{-3/2}$ for Ni (12)). Therefore, the slight enhancement of B for the nanoglass $Fe_{79}B_{21}$ powder sample as compared to that for the ribbon sample may indicate that the local structural environments in the powder sample reveals a higher degree of disorder than the ribbon. This is consistent with the reduction of the average hyperfine field in the nanoglass $Fe_{79}B_{21}$ powder sample.

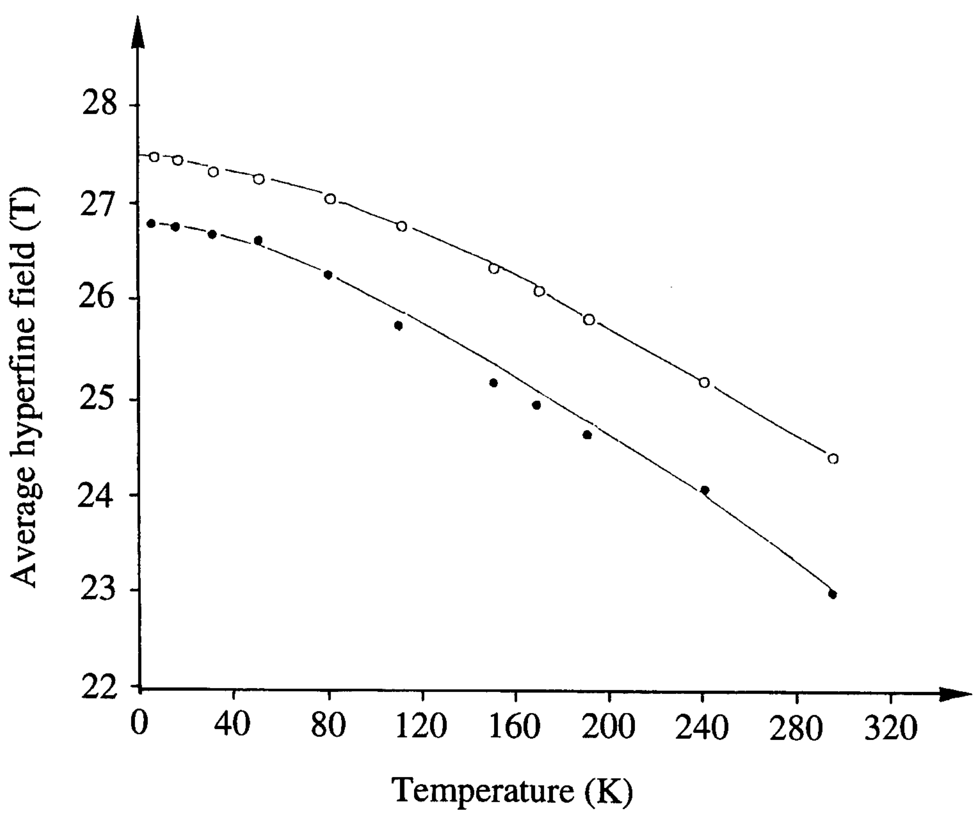

Fig. 1 Temperature dependence of the average hyperfine field (obtained by using Le Caer program (8)) for the nanoglass $Fe_{79}B_{21}$ powder (solid circles) and the $Fe_{80}B_{20}$ ribbon (open circles) together with solid lines obtained by fitting the experimental data using the Bloch's law, $H_{eff}(T)/H_{eff}(0)=1-BT^{3/2}$, where B is a coefficient.

CONCLUSIONS

Nanoglass $Fe_{79}B_{21}$ powders prepared by the chemical reduction method have been investigated by Mössbauer spectroscopy in the temperature range from 5 to 295 K. It is found that the average hyperfine fields of the powder sample are smaller than those of the ribbon in the whole temperature range studied. The reduced average hyperfine field of nanoglass $Fe_{79}B_{21}$ powders follows the Bloch's law, $H(T)/H(0)=1-BT^{3/2}$, indicating excitations of long-wavelength spin waves. The B parameter for the powder is found to be 2.8×10^{-5} $K^{-3/2}$, which is larger than 2.2×10^{-5} $K^{-3/2}$ for the amorphous $Fe_{80}B_{20}$ ribbon. These results infer that the local structural environments in the powder sample reveal higher degree of disorder than in the ribbon.

REFERENCES

[1] J. van Wonterghem, S. Mørup, C.J.W. Koch, S.W. Charles and S. Wells, Nature **322**, 622 (1986).

[2] D. Buchkov, S. Nikolov, I. Dragieva, and M. Slavcheva, J. Magn. Magn. Mater. **62**, 87 (1986).

[3] A. Inoue, J. Saida, and T. Masumoto, Metall. Trans. **19**A, 2315 (1988).

[4] S. Wells, S.W. Charles, S. Mørup, S. Linderoth, J. van Wonterghem, J. Larsen, M.B. Madsen, J. Phys.: Condens. Matter **1**, 8199 (1989); S. Linderoth and S. Mørup, J. Appl. Phys. **69**, 5256 (1991); S. Linderoth and S. Mørup, Physica Scripta **45**, 408 (1992); and S. Linderoth, J. Magn. Magn. Mater. **104-107**, 128 (1992).

[5] L. Yiping G.C. Hadjipanayis, C.M. Sorensen, and K.J. Klabunde, J. Magn. Magn. Mater. **79**, 321 (1989).

[6] J. Jiang, I. Dezsi, U. Gonser, and J. Weissmüller, J. Non-Cryst. Solids **116**, 247 (1990); and J. Jiang, I. Dezsi, U. Gonser, and X.P. Lin, J. Non-Cryst. Solids **124**, 139 (1990).

[7] S. Mørup and S. Linderoth, in Nanophase Materials, eds. G.C. Hadjipanayis and R.W. Siegel, (Kluwer Academic Publishers, Netherlands, 1994), p. 595.

[8] G. Le Caer and J.M. Dubois, J. Phys. E **12**, 1083 (1979).

[9] M.E. Lines and M. Eibschütz, Solid State Commun. **45**, 435 (1983).

[10] J.M. Dubois, G. Le Caer, A. Amomou, and U. Herald, J. Phys. Suppl. **1**, C1-247 (1980).

[11] R.C. O'Handley, J. Appl. Phys. **62**, R15 (1987).

[12] J.Z. Jiang, J. Magn. Magn. Mater. **154**, 375 (1996), and references therein.

[13] S. Linderoth, J. Magn. Magn. Mater. **104-107**, 167 (1992).

Pergamon

NanoStructured Materials, Vol. 12, pp. 847–850, 1999
Elsevier Science Ltd

0965-9773/99/\$–see front matter

PII S0965-9773(99)00249-4

COMPRESSIBILITY OF NANOSTRUCTURED Fe-Cu MATERIALS PREPARED BY MECHANICAL MILLING

J.Z. Jiang[1], J.S. Olsen[2], L. Gerward[1], and S. Mørup[1]

[1] Department of Physics, Building 307, Technical University of Denmark, DK-2800 Lyngby, Denmark.

[2] Niels Bohr Institute, Oersted Laboratory, University of Copenhagen, DK-2100 Copenhagen, Denmark.

Abstract—*The compressibility of nanostructured Fe-Cu materials prepared by mechanical milling has been investigated by in-situ high-pressure x-ray diffraction using synchrotron radiation. It is found that the bulk modulus of both fcc-Cu and bcc-Fe phases decreases with decreasing grain sizes. The unstable ferromagnetic fcc-FeCu solid solution prepared by mechanical alloying has a bulk modulus of about 85 GPa, which is much smaller than the corresponding values for bulk fcc-Cu and bcc-Fe. ©1999 Acta Metallurgica Inc.*

INTRODUCTION

High-energy ball milling is widely used for the preparation of materials, which are far from equilibrium, e.g., nanostructured, amorphous, and supersaturated alloys and ceramics. Using this technique, we have succeeded in alloying immiscible metallic and ceramic systems, such as Fe-Cu (1), Fe_2O_3-Al_2O_3 and Fe_2O_3-SnO_2 (2). In these previous investigations, we have studied the alloying proces, the microstructure and the thermal stability of the metastable alloys, as well as their electrical and magnetic properties. The purpose of the present note is to report some preliminary results on the high-pressure behaviour of mechanically milled Fe-Cu samples. In particular, we want to investigate how the grain size affects the compressibility (bulk modulus) and possible pressure-induced phase transformations in the fcc and bcc phases of the Fe-Cu alloy system. Tentative explanations for the high-pressure behaviour of nanostructured Fe-Cu materials are presented.

EXPERIMENTAL

For the preparation of $Fe_{50}Cu_{50}$ alloys, powders of iron (99.9%) and Cu (99.9%) with particle sizes of approximately 100 μm were milled in Ar atmosphere in a planetary ball mill (Fritsch Pulverisette 5) using hardened stainless steel vial and balls (1). The mechanical milling was interrupted after 0.5, 10, 20, and 30 h, and small amounts of the powder were taken out for analysis. After a milling time of 100 h, the remaining sample consists of pellets of about 0.6 mm diameter and 0.2 mm thickness. Practically all of the original amount of iron was now present in

TABLE 1.

Data for Fe-Cu samples as well as for bulk Fe and Cu.

	fcc-phase				bcc-phase	
Sample, Milling time	Bulk modulus (GPa)	Lattice constant (nm)	Grain size (nm)	Percentage iron present in the fcc phase (%)	Bulk modulus (GPa)	Grain size (nm)
Bulk	151(5)	0.3615	$\approx 10^5$	—	170(5)	$\approx 10^5$
0.5 h	139(9)	0.3615	50(3)	0	163(9)	57(3)
10 h	115(9)	0.3617	21(2)	0	134(9)	22(2)
20 h	129(9)	0.3628	14(2)	5	143(9)	14(2)
30 h	120(9)	0.3634	13(1)	40	—	—
100 h	85(8)	0.3643	17(1)	95	—	—

the fcc phase (Table 1). About 0.9 at.% Fe and 0.3 at.% Cr originated from the abrasion of the vial and balls. High-pressure ($\leq$ 8 GPa) x-ray diffraction measurements were performed using synchrotron radiation and a multi-anvil press, MAX80, at HASYLAB in Hamburg, Germany (3). The pressure was calculated from the lattice constant of NaCl using the Decker equation of state (4).

RESULTS AND DISCUSSION

A summary of the results for the Fe-Cu system is shown in Table 1. No phase transition was observed in any of the samples in the pressure range studied. The bulk modulus, B_0, and its pressure derivative, B_0', were obtained by fitting the Birch equation of state (5) to the experimental pressure-volume data. Using two fitting parameters, a B_0' value in the range 10-40 was found. As it should be close to 4 for most materials, the equation of state was again fitted with the constraint $B_0' = 4$. The resulting fits are good, as exemplified in Fig. 1. Initially, the bulk moduli of the fcc and bcc phases are found to decrease with increasing milling time (Table 1). The data seem to indicate a slight increase after 20 h, although this effect has to be confirmed. No data are available for the bcc phase after 20 h, whereas the bulk modulus of the fcc phase again decreases with increasing milling time. The sample milled for 100 h has a bulk modulus of 85 GPa, which is considerably smaller than the corresponding values for bulk fcc Cu and bcc Fe (6).

In previous studies, it has been found that initially, the only effect of the milling is to reduce the grain size. No detectable alloying occurs before 20 h milling time. Hence, the reduction of the bulk moduli in the samples milled from 0 h to 10 h is presumably correlated with the reduction in grain size for both fcc and bcc phases. A similar grain-size effect on the

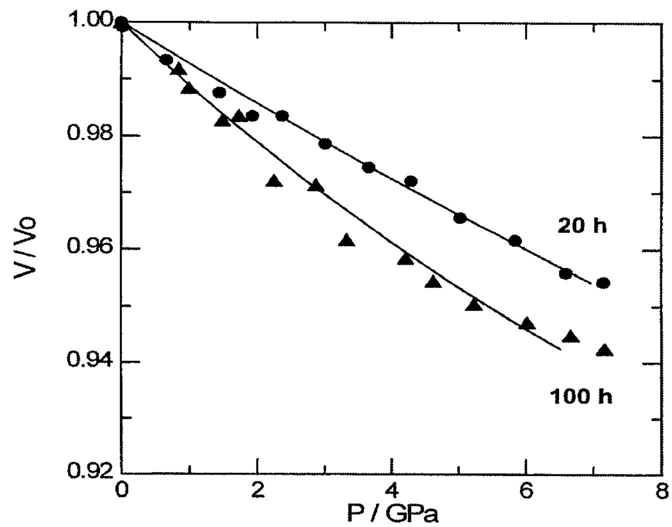

Fig. 1. Compression curves for the fcc phase in Fe-Cu samples milled for 20 h and 100 h, respectively. The full curves are calculated from the equation of state (see text).

bulk modulus was reported for PbS nanoparticles (7), while the opposite result was observed for γ-Fe_2O_3 (8). In contrast, Tolbert *et al.* (9) found the bulk modulus to be independent of grain size for CdSe nanoparticles. The experimental results for different materials seem to indicate that the grain size may affect the bulk modulus in either way, or not at all, depending on the system. It should be noted that the softening of nanocrystalline metals, which has recently been discussed by Schiøtz *et al.* (10) for very small grain sizes, can be explained by grain boundary effects. Thus, it is not directly related to the bulk modulus changes studied in the present work.

In the Fe-Cu sample milled for 20 h, a further reduction of the grain size has occurred, but also a considerable interdiffusion has taken place. The decrease in grain size is expected to lead to a reduction of the bulk modulus. The slight enhancement observed for both phases, if significant, may indicate that the grain size effect is counteracted by a hardening effect for small concentrations of the dopant (*cf.* 11). At this stage, 5% of the original amount of iron is present in the fcc phase (*cf.* Table 1).

On further increasing the milling time, the grain size remains almost unchanged, but the alloying proceeds. The fcc phase becomes ferromagnetic (1,12), which expands the unit-cell volume, as compared to the corresponding paramagnetic material, because of the magneto-volume effect (12). The monotonic reduction of bulk modulus for the fcc phase in the samples milled from 20 to 100 h could be due to alloying with large amounts of iron in the fcc phase and/or a ferromagnetic-to-paramagnetic phase transition of the fcc phase during compression. Work is in progress to examine the latter possibility by *in-situ* high-pressure Mössbauer measurements.

CONCLUSIONS

In conclusion, we have studied the grain size effect on the bulk moduli of fcc-Cu and bcc-Fe samples, as well as fcc-FeCu alloys prepared by mechanical milling. It is found that the bulk moduli of the fcc-Cu and bcc-Fe samples decrease with decreasing the grain size. A small amount of dopants (5%) seems to enhance the bulk moduli of both the fcc and bcc phases. In the ferromagnetic fcc-FeCu solid solution, the value of the bulk modulus is 85 GPa, which is considerably smaller than the corresponding values for the bulk fcc Cu and bcc Fe. This could be due to a ferromagnetic-to-paramagnetic phase transition and/or an alloying effect.

ACKNOWLEDGEMENTS

This work has been supported by the Danish Natural Sciences Research Council through Dansync and by the Danish Technical Research Council. We thank HASYLAB-DESY for permission to use the synchrotron radiation facility. We also wish to thank Dr. P. Zinn, station master of MAX80, for helpful assistance.

REFERENCES

1. J.Z. Jiang, U. Gonser, C. Gente, R. Bormann, Appl. Phys. Lett. 63, 1056 (1993); 63, 2768 (1993); J.Z. Jiang and F.T. Chen, J. Phys. C: 6, L343 (1994); J.Z. Jiang, Q.A. Pankhurst, C.E. Johnson, C. Gente, and R. Bormann, *ibid.* 6, L227 (1994); and J.Z. Jiang, C. Gente, and R. Bormann, Mater. Sci. Eng. A 242, 268 (1998).
2. J.Z. Jiang, S. Mørup, and S. Linderoth, Mater. Sci. Forum 225-227, 489 (1996); J.Z. Jiang, R. Lin, S. Mørup, K. Nielsen, F.W. Poulsen, F.J. Berry, and R. Clausen, Phys. Rev. B 55, 11 (1997); and J.Z. Jiang, R. Lin, K. Nielsen, S. Mørup, D.G. Rickerby and R. Clausen, Phys. Rev. B 55, 14830 (1997).
3. E. Hinze, J. Kremmler and J. Lauterjung, Z. Kristallogr. 196, 117 (1991); and H. Lorenz, I. Orgzall, E. Hinze and J. Kremmler, Scripta Metallurgica et Materialia 27, 993 (1992).
4. D.L. Decker, J. Appl. Phys. 42, 3239 (1971).
5. F. Birch, J. Appl. Phys. 9, 279 (1938).
6. L. Gerward, J. Phys. Chem. Solids 46, 925 (1985).
7. S.B. Qadri, J. Yang, B.R. Ratna, E.F. Skelton, and J.Z. Hu, Appl. Phys. Lett. 69, 2205 (1996).
8. J.Z. Jiang, J. S. Olsen, L. Gerward, and S. Mørup, Europhys. Lett., in the press.
9. S.H. Tolbert and A.P. Alivisatos, Science 265, 373 (1994); and S.H. Tolbert and A.P. Alivisatos, J. Chem. Phys. 102, 4642 (1995).
10. J. Schiøtz , F.D. Di Tolla, and K.W. Jacobsen, Nature 391, 561 (1998).
11. R.E. Schmunk and C.S. Smith, Acta Metall. 8, 396 (1960).
12. C.L. Chien, S.H. Liou, D. Kofalt, W. Yu, T. Egami, T.R. McGuire, Phys. Rev. B 33, 3247 (1986).

Pergamon

NanoStructured Materials, Vol. 12, pp. 851–854, 1999
Elsevier Science Ltd

0965-9773/99/$–see front matter

PII S0965-9773(99)00250-0

IMPROVING THE MAGNETIC PROPERTIES OF NANOCRYSTALLINE $Fe_{73.5}Cu_1Nb_3Si_{13.5}B_9$ BY HEAT TREATMENT OF THE MELT

H.Chiriac, Marilena Tomut and Maria Neagu
National R&D Institute for Technical Physics,
Blv. Mangeron 47, 6600 Iasi 3, Romania

Abstract - *The effect of the heat treatment of the melt on the magnetic properties of the nanocrystalline $Fe_{73.5}Cu_1Nb_3Si_{13.5}B_9$ alloys, obtained by controlled crystallization of rapidly solidified ribbons, was studied by taking into account the inheritance of the short range ordering present in the melt. Previous viscosity measurements on liquid FeSiB alloys and X-ray diffraction results in the literature reveal irreversible changes that take place in the melt during heating. This behavior was assigned to temperature dependence of the short range ordering present in the melt. The crystallization of the amorphous alloy was investigated by DTA and X-ray diffraction. The influence of the melt heat treatment on the magnetic permeability, coercivity and saturation magnetostriction was studied.*

INTRODUCTION

Iron based nanocrystalline materials are obtained by controlled crystallization of the amorphous alloys (1). These materials have a two phase microstructure consisting of b.c.c. Fe(Si) crystals with grain size of nanometer scale embedded in an amorphous phase matrix. The ultrafine structure is due to the combined effect of Cu and Nb additions in the nucleation and growth mechanism, the most known nanocrystalline soft magnetic alloys being $Fe_{73.5}Cu_1Nb_3Si_{13.5}B_9$ with optimized composition. The fine grain size structure averages out the magnetocrystalline anisotropy leading to attractive soft magnetic properties (2).

The role of the precursor amorphous phase on the resulting magnetic properties was previously investigated from the point of view of the degree of structural disorder of the amorphous phase produced with different quenching rates (3). In the present work the influence of the structural features of the amorphous state produced with different heat treatment of the melt before ejection, on the magnetic properties of the nanocrystalline $Fe_{73.5}Cu_1Nb_3Si_{13.5}B_9$ ribbons has been studied. Ejection and overheating temperatures of the molten alloy were chosen by correlating previous measurements on the temperature dependence of the viscosity of liquid FeSiB alloys (4) with XRD data on FeB liquid alloys in the literature (5).

EXPERIMENTAL

Amorphous $Fe_{73,5}Cu_1Nb_3Si_{13,5}B_9$ ribbons were prepared by planar flow casting in the air on a rotating wheel with different heat treatment of the melt and ejection temperatures. The temperature of the melt was measured using a radiation pyrometer. Peripheral velocity of the cooling wheel was kept constant at 35 m/s during the casting experiments. The ejection pressure was modified to ensure equal thickness of the ribbons, and also corresponding quenching rates. Three representative samples 20 μm thick, 1 mm wide were studied. Ribbons A and B were produced by ejecting the molten alloy at 1300°C and 1450°C respectively with no previous overheating. Sample C was quenched by ejecting at 1450°C the molten alloy previously overheated for 3 min. at 1550°C. Samples A and B were maintained at the ejection temperature for 1 min. before quenching. Electromagnetic stirring of the molten alloy was ensured by the heating induction coil fed from a medium frequency generator. The amorphicity of the samples was investigated by X-ray diffraction, XRD.

Crystallization temperatures were evaluated from the DTA curves at a heating rate of 10 °C/min. The amorphous samples were submitted to isothermal annealing in vacuum, for 60 min at different temperatures in the range 425°C-600°C. Phase analysis was performed on nanocrystalline samples by XRD using Co-Kα radiation. The mean grain size for the nanocrystallized samples at 550°C was determined from the full width of the half maximum of the reflections. The magnetic permeability, μ_{rel}, and the coercivity, H_c, of the annealed samples were studied by a fluxmetric setup at 50 Hz. The saturation magnetostriction constant, λ_s, was measured using the small-angle magnetization rotation technique (SAMR).

RESULTS AND DISCUSSION

DTA curves for samples A,B,C are presented in figure 1. Temperatures for the start of the crystallization are 500°C for sample A and 520°C for sample B and C. Amorphous alloy quenched from a lower temperature of the melt is less stable against αFe(Si) crystallization.

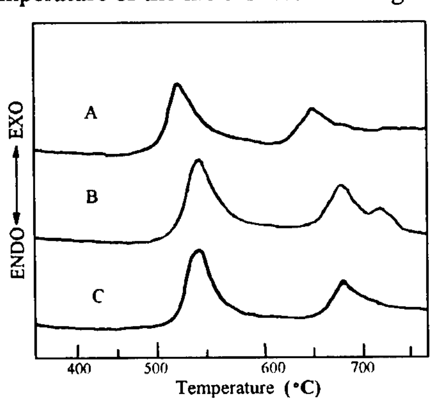

Figure 1. DTA curves at 10 Kmin^{-1} for as cast $Fe_{73,5}Cu_1Nb_3Si_{13,5}B_9$ amorphous ribbons: A- 1300 °C; B- 1450 °C; C- 1450°C with previous overheating at 1550°C

Figure 2 presents the variation of magnetic permeability (a), coercivity (b) and saturation magnetostriction (c) with the annealing temperatures for these samples.

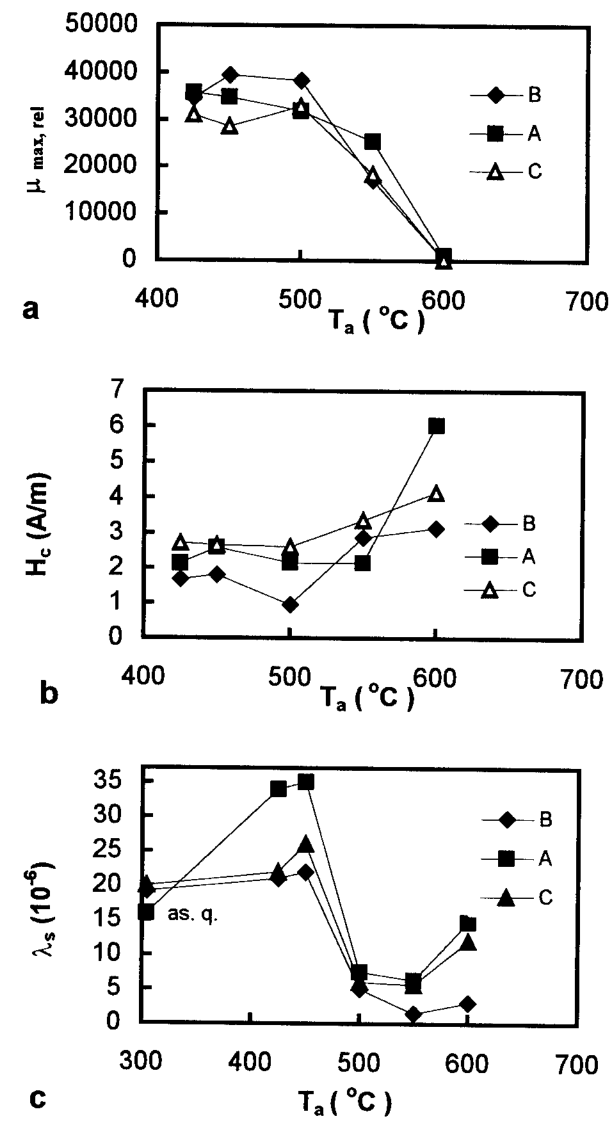

Figure 2. Dependence of the maximum relative permeability (a); coercivity (b); and saturation magnetostriction (c) on the annealing temperature for $Fe_{73,5}Cu_1Nb_3Si_{13,5}B_9$ alloys obtained with different heat treatment of the melt before rapid quenching: A- 1300 °C; B- 1450 °C; C- 1450°C with previous overheating at 1550°C

Samples A and B, that are produced with a heat treatment of the melt below 1500°C show better magnetic properties in the nanocrystalline state. The lowest H_c, λ_s and the highest permeability were found for sample B that was rapid quenched with melt overheating at 1450°C . The optimum annealing temperature range for this sample is 500°C -550°C. At higher temperatures, coercivity of all the samples increase due to the increase of the crystallite size. Sample B annealed at 550°C shows also an optimum grain size of 13nm, compared to larger mean grain size corresponding to sample A-20nm and C-30nm annealed at the same temperature. Correlating the structural model for FeSiB amorphous alloys proposed by Dubois and Le Caer (6) with XRD results on FeB melts (5), a higher quenched-in percentage of αFe like clusters is supposed to be present in amorphous alloys quenched from a temperature lower than 1500°C. Previous viscosity measurements on FeSiB liquid alloys show that irreversible changes take place in the melt heating above 1350°C. These transformations can be assigned to a redistributon of Fe atoms in the Fe_mB compound like clusters in the melt. These results indicate as the optimum heat treatment of the melt for improving the magnetic properties of the nanocrystalline $Fe_{73,5}Cu_1Nb_3Si_{13,5}B_9$ alloys, the intermediate temperature range 1350°C -1500°C. For sample A quenched from a low temperature of the melt, H_c and λ_s in nanocrystalline state increase rapidly due to the increase in the crystallite size at annealling temperature higher than 550°C. The worsening of the magnetic properties of this sample is also caused by a lower Si content of the αFe nanocrystalline phase.

CONCLUSIONS

The influence of the heat treatment of the melt on the magnetic properties of nanocrystallized $Fe_{73,5}Cu_1Nb_3Si_{13,5}B_9$ ribbons was interpreted in the frame of Dubois and Le Caer structural model of FeSiB amorphous alloys, in correlation with previous viscosity measurements and XRD results on these liquid alloys in the literature. Best magnetic properties and mean grain size for nanocrystalline $Fe_{73,5}Cu_1Nb_3Si_{13,5}B_9$ alloys were obtained for the sample produced with a heat treatment of the melt at 1450°C.

REFERENCES

1. Yoshizawa,Y., Oguma, S. and Yamaguchi, K., J.Appl.Phys, 1988, 64, 6044.
2. Herzer, G., IEEE Trans.Mag., 1989, 25, 3327.
3. Allia, P., Tiberto, P., Baricco, M., Knobel, M. and Vinai, F.,IEEE Trans. Mag., 1994, 30, 461.
4. Chiriac, H., Tomut, M., Marinescu, M., and Stantero, A., Rapidly Quenched and Metastable Materials, Supplement, Eds. P.Duhaj, P.Mrafko and P.Svec, Elsevier 1997, p. 132.
5. Mihailova, L.E., Ilinski, A.G., Romanova, A.V. and Hristenko, T. M., Metallofizica, 1990, 12, 52
6. Dubois, J.M. and Le Caer, G., Acta Metall., 1984, 32, 2101.

Pergamon

NanoStructured Materials, Vol. 12, pp. 855–858, 1999
Elsevier Science Ltd

0965-9773/99/$–see front matter

PII S0965-9773(99)00251-2

NANOCRYSTALLINE NH_4MnF_3 WITH CONTROLLED GRAIN SIZE: SYNTHESIS AND ANTIFERROMAGNETISM

M. Roth[1)], R. Hempelmann[1)], O. Borgmeier[2)], T. Eifert[2)] and H. Lueken[2)]
[1)]Universität d. Saarlandes, Physikalische Chemie and SFB277, 66123 Saarbrücken, Germany
[2)]RWTH Aachen, Anorganische Chemie, D-52074 Aachen, Germany

Abstract *Nanocrystalline NH_4MnF_3 was prepared by precipitation in the inverse micelles of w/o-microemulsions using mixtures of ammonium substituted AOT and n-heptane which are able to stabilize large contents of concentrated NH_4F and $Mn(OAc)_2$ aqueous solutions. By appropriate variation of the synthesis parameters the volume averaged crystallite diameter, as measured by X-ray diffraction line shape analysis, can be tuned to values of $10nm \leq D_{Vol} \leq 60nm$. NH_4MnF_3 is antiferromagnetic with a weak canted ferromagnetism below the Néel temperature. Magnetic measurements have been performed using a SQUID magnetometer. For nanocrystalline NH_4MnF_3 we observe the following changes of the magnetic properties with decreasing crystallite size: -the strength of the antiferromagnetic exchange interaction decreases; -the ferromagnetic contribution decreases as can be concluded from the magnetic field dependence of the molar susceptibility below the Néel temperature.*

INTRODUCTION

Preparation of monodisperse, ultrafine particles has been one of the most pursued goals in modern technology, e.g. catalysis, ceramic processing, solar energy conversion processes, pharmaceutical and photographic technology etc.. Water-in-oil microemulsions are ideal systems to perform the controlled production and growth of small particles by precipitation . The solubility of up to now produced precipitates is lower than 10^{-5} mol/l (1,2). In the case of more soluble precipitates one has to deal with many difficulties such as fast agglomeration, low yields and the problem to find a microemulsion system which is able to stabilize highly concentrated salt solutions without salting out (3). The relative high solubility of NH_4MnF_3 (12g in 1l water at room-temperature), the high amount of counter ions, the thermal decomposition at 300 °C and the oxidation to MnO_2 require a novel synthesis route to produce the size modified nanocrystals.

NH_4MnF_3 exhibits a model-like Heisenberg antiferromagnetism (4) with a Néel temperature of 84K for coarse grained material (5). The material in the nanocrystalline form should allow for the study of nano-antiferromagnetism.

TABLE 1: The Synthesis Parameters

sample name	conc. of the NH_4F solution [mol/kg H_2O]	synthesis-temperature	$\Delta t_{M\text{-}C}$ [minutes]	weigt% of aqueous phase
B	3.0	RT	4	10
C	3.0	RT	30	10
D	3.0	RT	1	5
F	1.83	RT	1	9.65

EXPERIMENTAL

The synthesis is explained in detail elsewhere (8). Two AOT-NH_4/n-heptane/water based w/o-microemulsions, one containing NH_4F, the other containing $Mn(OAc)_2$ were mixed under stirring. The salt precipitates according $3NH_4F+Mn(OAc)_2 \rightarrow NH_4MnF_3\downarrow+2NH_4OAc$. By the addition of acetone, the precipitate is coagulated. Boiling the raw product in acetone, the NH_4OAc can be transformed to acetamide and removed by decantation. Soxhlet-extraction cares for the removal of the surfactant. The size-controling parameters are: the period of time between the mixing of the microemulsions and the coagulation, ($\Delta t_{M\text{-}C}$), the content of aqueous phase, the synthesis temperature and the salt content. The synthesis parameters of the the samples investigated by magnetic measurement are given in table 1.
X-ray diffractograms of the powders were measured at room temperature on a Siemens D 500 diffractometer. From the line shape of the peaks the crystallite size and the crystallite size distribution can be determinded by the Warren/Averbach method (7) which we use in a slightly modified version (1).

The magnetic measurements have been performed using a SQUID magnetometer in the temperature range beween 1.7K and 300K at magnetic fields between 0.01 and 5T.

RESULTS

As demonstrated by TEM-micrographs and X-ray diffraction patterns given in (6) the produced crystals consist of pure, partially agglomerated NH_4MnF_3. With longer times $\Delta t_{M\text{-}C}$, decreasing salt content, increasing content of aqueous phase and increasing temperature the crystallite size increases. The volume averaged crystallite sizes and the size distributions of the samples investigated by magnetic measurements are given in Fig. 1.

The magnetic behaviour of *polycrystalline* NH_4MnF_3 (9) (cubic perovskite for T>182K, tetragonally distorted below) can be described by Curie-Weiss laws $\chi_{mol}=C/(T-\theta_p)$ with θ_p around -140K for T>182K and less negative θ_p for 182K>T>130K. The θ_p values correspond to exchange parameters J=-3.27K and -3.10K obtained by the high-temperature susceptibility series expansion method (HTSE).

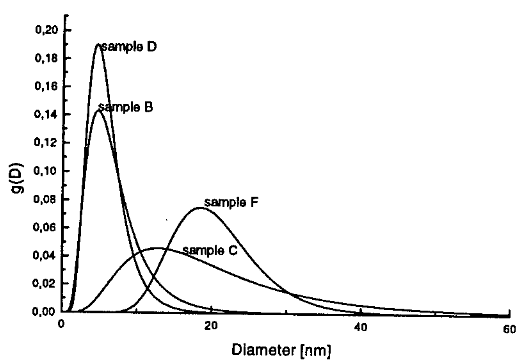

sample	$<D>_{Vol}$	max. of the distribution
D	11nm	4.5nm
B	16nm	4.5nm
F	27nm	18nm
C	56nm	13nm

Figure 1

The Curie constant C correlates with the expected magnetic spin moment, μ=5.92 μ_B. The structural phase transition can be recognised by a slight anomaly in $\chi_{mol}(T)$. Below a broad maximum in $\chi_{mol}(T)$ around $T(\chi_{mol})^{max}\approx 82K$ a small peak at T_N=75K occurs, indicating antiferromagnetic ordering with a weak ferromagnetic contribution on account of the tetragonal distortion.

For *nanocrystalline* NH_4MnF_3, applying μ=5.92μ_B as internal standard, we observe the following changes of the magnetic properties with decreasing particle size: -the characteristic magnetic quantities $|\theta_p|$, T_N, $T(\chi_{mol})^{max}$ decrease, and χ_{mol} increases (see Fig. 2, left).-the ferromagnetic contribution decreases and disappears for $<D_{vol}>$<50nm. -the two large-scale nanocrystalline samples exhibit superparamagnetism. -in the case of the 200nm sample the magnetochemical analysis on the basis of HTSE (see Fig. 2, right) yields J=-2.80 K (cubic phase) and $J_{\parallel}$=-2.38 K, $J_{\perp}$=-2.85 K (tetragonal phase). Obviously in the latter phase the antiferromagnetic coupling is weakened in the direction parallel to the c-axis and enhanced perpendicular to it. This result corresponds nicely to the elongation of the c-axis and contraction of the a-axis with respect to the cubic a-axis (10)

Discussion

A detailed discussion of the size controlling parameters is given in (8). The result of longer times $\Delta t_{M\text{-}C}$ is an increase in the crystallite size due to agglomeration, coalescence and Ostwald ripening as investigated by dynamic light scattering (8). A decrease in the synthesis temperature effects a decrease in the intermicellar exchange by slowing down the Brownian motion. Additionally the agglomeration is retarted. A higer interfacial rigidity effected by a higher salt content means also a decrease of the intermicellar exchange rate. The diminuation of the aqueous phase content decreases the probability for the particles, to come into contact with each other.

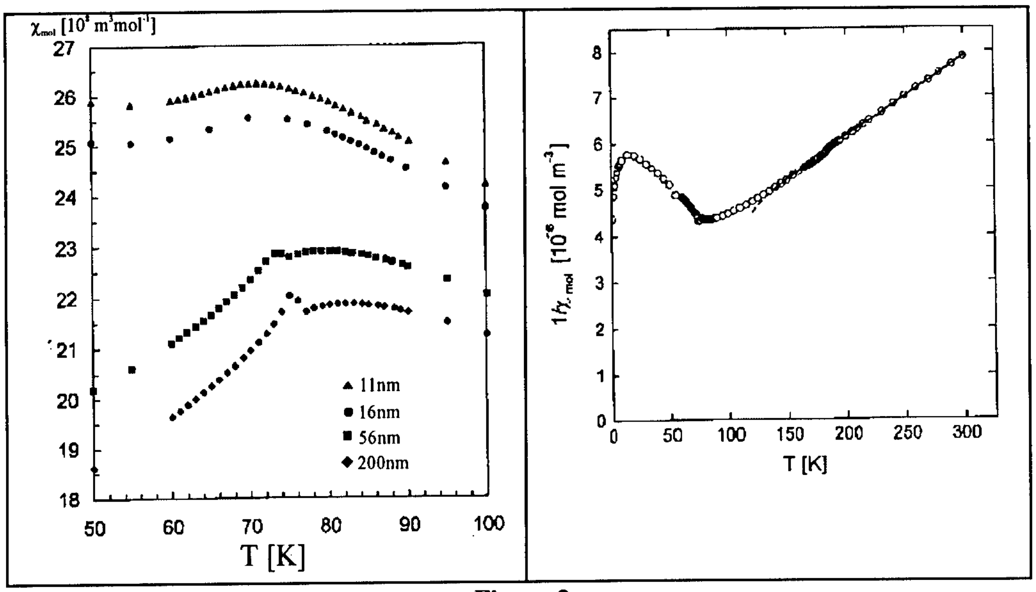

Figure 2

Apart from the weakening of the antiferromagnetic interaction with decresing particle size, caused by increasing surface effects, the magnetochemical investigations show that the *nanocrystalline samples* can be divided in two groups: For $<D_{vol}> > 50$nm superparamagnetism is observed at low temperature. This indicates single domain particles with tetragonal structure. Particles smaller than 50nm, however, are not superparamagnetic. This can be interpreted as a suppresion of the phase transition from cubic to tetragonal below a critical particle size.

REFERENCES

1. Dvolaitzky, M., Ober, R., *Journal of Dispersions Science and Technology*, 1983, 4(1), 29.
2. Qi, L., Ma, J., Cheng, H., Zhao, Z., *Colloids and Surfaces A*, 1996, 108, 117.
3. Beunen, J.A., Ruckenstein, E., *Advances in Colloid and Interface Science*, 1982, 16, 201.
4. Nagamiya, T., Yosida, K., *Antiferromagnetism, Advances in Physics*, 1955, 4,1.
5. Pickart, S.J., Alperin, H.A., Nathans, R., *Journal de Physique* [Paris], 1964, 25, 565.
6. Roth, M. and Hempelmann, R., *Chemistry of Materials*, 1998, 10, 78.
7. Warren, B.E., Averbach, B.L., *Journal of Applied Physics*, 1950, 21, 595.
8. Härtl, W., Beck, Ch., Roth, M., Meyer, F., Hempelmann, R., *Ber. Bunsenges. Phys. Chem.*, 1997, 101 (11), 1714
9. Bartolomé, J. et al., *Physica*, 1983, 115, 190.
10. Helmholdt, R.B et al., *J. Phys. C: Solid State Phys.*, 1980, 13, 5081.

Pergamon

NanoStructured Materials, Vol. 12, pp. 859–862, 1999
Elsevier Science Ltd

0965-9773/99/$–see front matter

PII S0965-9773(99)00252-4

CRITICAL PHENOMENA OF AN IRON-NITRIDE NANOPARTICLE SYSTEM

H. Mamiya and I. Nakatani,
National Research Institute for Metals, Tsukuba 305-0047, JAPAN

Abstract -- *Critical phenomena are studied for the magnetic phase transition of a ferromagnetic nanoparticle system with dipolar interactions and random anisotropy axes. The divergences of the nonlinear susceptibility and the longest relaxation time are observed for a frozen magnetic fluid including uniform iron-nitride particles. These results indicate that the phase transition is similar to the spin glass transition. ©1999 Acta Metallurgica Inc.*

INTRODUCTION

Models for magnetic properties of well-isolated ferromagnetic nanoparticles have been established except for the quantum tunneling of magnetization at very low temperatures (1,2). On the other hand, when the dipolar interactions exist between randomly distributed particles, we observe glassy behavior including irreversibility, nonexponential relaxation, and aging phenomena (3-6). Recently, Djurberg et al. have shown a critical slowing down of the relaxation for Fe-C fine particles at a finite temperature (7). This suggests the existence of a spin-glass like phase transition. It is well-known that the spin glass transition is characterized by the divergences of the nonlinear susceptibility and the longest relaxation time (8). In this paper, such critical phenomena are studied for a frozen magnetic fluid including uniform iron-nitride particles, in order to clarify the phase transition observed for the interacting nanoparticle system.

EXPERIMENTAL

Sample is an iron-nitride ϵ-Fe_3N magnetic fluid prepared by the method of vapor-liquid chemical reaction between iron carbonyl and ammonia (9). The carrier liquid of kerosene has a freezing temperature of about 200 K. Because the measurements were made below 150 K after the sample was cooled in zero field, the particles were randomly fixed in solidified kerosene. Electron microscopy shows that the particles have isotropic shapes and uniform size. The diameters of the particles are about 6 nm. The saturation magnetization is 29.1 emu/cm^3 at 300 K. The temperature dependence of the field cooled magnetization M_{FC} was measured after the sample was cooled from 150 K in various fields H below 6 Oe. The relaxation of the zero field cooled magnetization M_{ZFC} was measured as a function of time t after a field of 1.2 Oe was applied. Before the application of the field the sample was equilibrated at the measurement

temperature during wait time t_w. Ac susceptibility $\chi'+i\chi''$ was measured at frequency f from 12 mHz to 10 kHz, where the magnitude of the ac field is 1.0 Oe.

RESULTS AND DISCUSSION

Figure 1 shows the temperature dependence of M_{FC}/H at $H = 1.2$ Oe. It is found that M_{FC}/H shows a plateau below temperature T_g (~ 70 K), while it decreases with increasing temperature above T_g. In the previous study (10), it has been shown that such a plateau is attributed to a magnetic ordered phase whose transition temperature is T_g. Because a divergence of nonlinear susceptibility χ_2 at T_g has been predicted by a modified local-mean field model: $\chi_2 \propto (T-T_g)^{-3}$ (11), we estimate χ_2 of this sample from M_{FC} at various H by using the following equation:

$$M_{FC} = \chi_0 H + \chi_2 H^3 + \ldots \qquad [1]$$

Figure 2 shows $(-\chi_2)^{-1/3}$ at various temperatures. It is found that $(-\chi_2)^{-1/3}$ has a linear dependence on temperature. The intercept of the temperature axis is about +65 K. In short, χ_2 has a tendency to diverge at T_g, where the critical exponent is almost 3. This result is consistent with that prediction and is similar to the divergence of the nonlinear susceptibility for the spin glass transition.

In-phase component χ' of the ac susceptibility is also shown in Fig. 1. We find that χ' increases as the temperature decreases from 150 K and shows a maximum at temperature T_m. The T_m increases with frequency f. It is considered that the maximum is due to the slowing down of the response for the ac field, because M_{FC}/H, which is almost the same with the equilibrium susceptibility χ_{eq} (10), dose not show the maximum at T_m. However, it is known that T_m does not always give a typical freezing (or blocking) temperature (12). For this reason, we discuss the

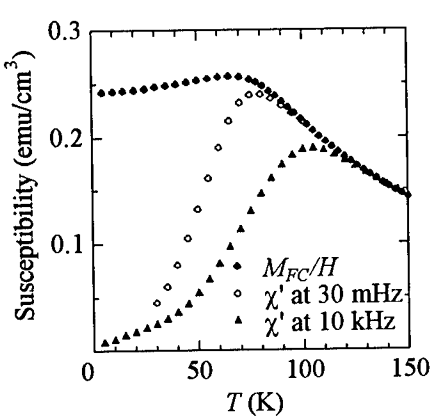

Figure 1. Temperature dependence of the field cooled susceptibility and ac susceptibility.

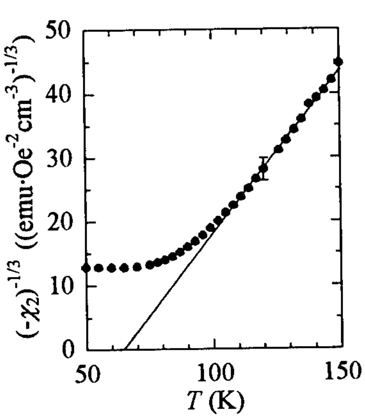

Figure 2. Temperature dependence of $(-\chi_2)^{-1/3}$.

relaxation time distribution g(lnτ) directly, in order to clarify the critical slowing down of the relaxation at T_g. Since out-of-phase component χ" and relaxation rate $S = 1/H \cdot dM_{ZFC}/d\ln t$ are proportional to g(lnτ) with the following relations:

$$g(\ln \tau) = \frac{\chi''}{\chi_{eq}} \cdot \frac{2}{\pi} = \frac{S}{\chi_{eq}}, \qquad [2]$$

where $\tau \approx 1/2\pi f \approx t$, g(ln$\tau$) can be estimated (see Fig. 3). We find that g(lnτ) dramatically broadens with decreasing temperature. At 70 K the tail extends toward longer τ as t_w increases. At 50 K g(lnτ) is distributed over the experimental time window of nine decades, and seems to have a broad peak at $t \sim t_w$. Because the broadened relaxation time distribution and the aging effect are important features of spin glass (13), we corroborate that the dynamics below T_g is also similar to spin glass.

At the spin glass transition temperature, longest relaxation time τ_{max} diverges as the dynamical scaling hypothesis predicts, where its temperature dependence is ruled by the following equation:

$$\tau_{max} = \tau_0 \cdot \left(\frac{T}{T_g} - 1 \right)^{-z\nu}. \qquad [3]$$

Here, τ_0 is the microscopic relaxation time and $z\nu$ is the dynamical exponent. In this paper, τ_{max} is assumed to be τ at g(lnτ) = 0.004, because there is no distribution except for a low tail in the τ range longer than it. We note that τ_{max} at the temperatures near T_g cannot be used for the analysis, since τ_{max} increases with t_w dramatically, as seen at 70 K. The inset of Fig. 3 shows lnτ_{max} above 80 K. It is found that the τ_{max} diverges at almost the same T_g as χ_2. The value of $z\nu$ is 10.5 ± 3, which is similar to the dynamical exponents observed for spin glasses. The value of

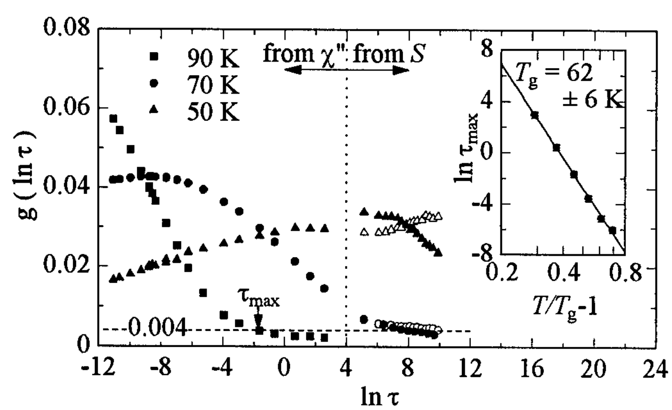

Figure 3. Relaxation time distribution g(lnτ) at various temperatures. Solid symbols show g(lnτ) estimated from χ", or S after $t_w = 6\times10^2$ s, while open symbols show g(lnτ) estimated from S after $t_w = 6\times10^4$ s. The inset shows longest relaxation time τ_{max} vs $T/T_g - 1$, where $T_g = 62 \pm 6$ K.

τ_0 is in the range from 10^{-5} to 10^{-4} s. This is much longer than τ_0 of spin glasses. The reason is that τ_0 of fine particle systems is the relaxation time of the individual particle (7). These are consistent with the results for the relaxation time estimated from χ' of Fe-C particles (7). Therefore, we confirm the existence of a critical slowing down such as observed for spin glasses.

SUMMARY

We find that the nonlinear susceptibility and the longest relaxation time diverge at a finite temperature. The phase transition of the interacting nanoparticle system is similar to the spin glass transition.

ACKNOWLEDGMENT

We wish to express our gratitude to helpful discussions with Dr. T. Furubayashi, Dr. T. Taniyama, and Dr. T. J. Sato.

REFERENCES

1. Jacobs, I.S. and Bean, C.P., *Magnetism III*, Academic Press, New York, 1963, p. 271.
2. Jonsson, T., Mattsson, J., Nordblad, P. and Svedlindh P., *Journal of Magnetism and Magnetic Materials*, 1997, 168, 269.
3. Dormann, J.L., Bessais, L., and Fiorani, D., *Journal of Physics C: Solid State Physics*, 1988, 21, 2015.
4. Chantrell, R.W., El-Hilo, M. and O'Grady, K., IEEE Transactions on Magnetics, 1991, 27, 3570.
5. Luo, W., Nagel, S.R., Rosenbaum, T. F. and Rosensweig, R.E., *Physical Review Letter*, 1991, 67, 2721.
6. Jonsson, T., Nordblad, P. and Svedlindh P., *Physical Review B*, 1998, 57, 497.
7. Djurberg, C., Svedlindh P., Nordblad, P., Hansen, M. F., Bødker, F., and Mørup, S., *Physical Review Letter*, 1997, 79, 5154.
8. Prejean, J.J., Carré, E., Beauvillain, P. and Renard, J.P., *Journal de Physique Colloque*, 1988, 49, C8-995.
9. Nakatani, I., Hijikata, M., and Ozawa, K., *Journal of Magnetism and Magnetic Materials*, 1993, 122, 10.
10. Mamiya, H., Nakatani, I., and Furubayashi, T., *Physical Review Letter*, 1998, 80, 177.
11. Załuska-Kotur, M. A., *Physical Review B*, 1996, 54, 1064.
12. Mamiya, H. and Nakatani, I., *Journal of Magnetism and Magnetic Materials*, 1998, 177-181, 966.
13. Mydosh, J.A. *Spin Glasses: An Experimental Introduction*, Taylor & Francis, London, 1993.

Pergamon

NanoStructured Materials, Vol. 12, pp. 863–866, 1999
Elsevier Science Ltd

0965-9773/99/$–see front matter

PII S0965-9773(99)00253-6

CRYOCHEMICAL SYNTHESIS AND PHYSICAL-CHEMICAL PROPERTIES OF NANO-DISPERSED METALLOPOLYMERS

V.V.Zagorskii, S.V.Ivashko, V.E.Bochenkov, G.B.Sergeev
Department of Chemistry, Moscow State University,119899 Moscow, Russia,
<zagorskii@cryo.chem.msu.su>

Abstract *– New nanodispersed metallopolymer (Ag, Na, Mg, Pb, Mn, Ca, Sm) films have been obtained via low temperature codeposition of metal and reactive para-xylylene monomer vapours at 100 K. Electric conductivity of the films were studied during the components codeposition,upon the samples annealing at 80-300 K and maintaining at constant temperature. With a rise in nanoparticle concentration in the polymer matrix, the conductivity tends to increase. The conductivity may be determined by tunnel transfer of charge carriers from one nanoparticle to another through a thin dielectric layer (up to 50 nm) of polymer matrix.* ©*1999 Acta Metallurgica Inc.*

New nanodispersed metallopolymer films (Ag-, Na-, Mg-, Pb-, Mn-, Ca-, Sm-nanoparticles dispersed in the polymer matrix) have been obtained via low temperature codeposition of metal and reactive para-xylylene monomer vapours at 100 K. It was shown by TEM that metals formed globe-like particles of 5-8 nm size and uniformly distributed in polymer matrix (1). Electric conductivity of the films obtained were studied during the components codeposition, during the sample annealing at 80-300 K and also at constant temperature.

EXPERIMENTAL

The techniques employed, description of apparatus as well as experimental conditions for producing poly-p-xylylene films with encapsulated metallic nanoparticles, have been presented in detail previously (1,2). The samples for electrical studies were prepared by deposition of metal vapours on the poly-p-xylylene film deposited previously on quartz support with platinum contacts. In some experiments plastic support with copper and silver contacts was used. Thus, we have measured the conductivity of an island metal film on polymer insulator.

Two-electrodes measurement circuit with 96V potential were used in electric conductivity experiments.

RESULTS AND DISCUSSION

The results for Ag- and Ca-containing samples on monomer and polymer supports are in accordance with the metal chemical activity (see figures 1 and 2). In the case of chemically inert silver the annealing of the prior insulating film sample at 100 K led to the sharp increase in conductivity values due to rise of silver atoms and clusters mobility. In the case of chemically active Ca annealing of the sample led to sharp decrease in conductivity values . This could be a result of the reaction of Ca-nanoclusters with monomer and guttering effects. Adsorption of residual gases and monomer at the surface of Ca-nanoparticles could cause the decrease of electrical conductivity value. The same results have been obtained for Sm-systems. Pb-poly-para-xylylene systems possess the intermediate electrical conductivity values compared to Ag- and Ca(Sm) -containing systems. More complicated electrical behaviour of Mn-para-xylylene samples is connected with formation of stable π-complexes of metallic Mn with monomer molecules. The existence of stable Mn-para-xylylene π-complexes was shown by reflection IR-spectroscopy.

Electrical-conductivity measurements were made for bimetallic Pb/Sm, Na/Ag and Na/Pb-systems. The resulting curve in bimetallic systems is very similar to the superposition of the electric conductivity curves for the individual metals. The example curve for bimetallic (Pb/Sm) system presented on figure 3. Thus the results obtained show the perspectives of the use of electric conductivity measurements *in-situ* during metal-polymer samples formation for their complex characterisation.

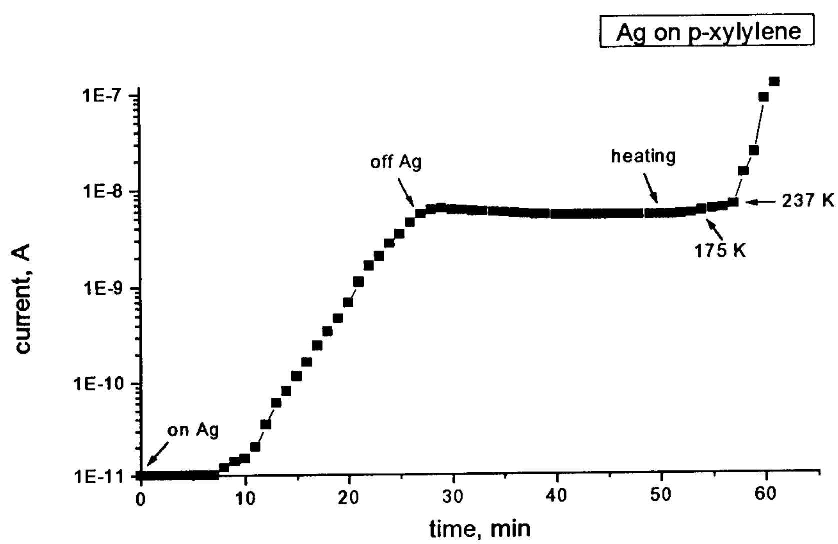

Figure 1. The electric conductivity of Ag-p-xylylene film during the formation and further heating.

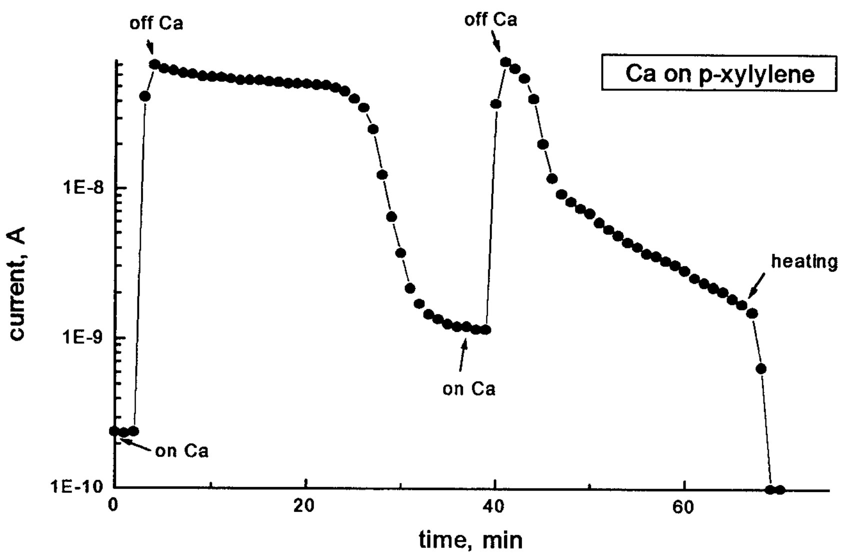

Figure 2. The electric conductivity of Ca-p-xylylene film during the formation, thermostatic control (at 77 K), repeated formation and thermostatic control (at 77K) and further heating.

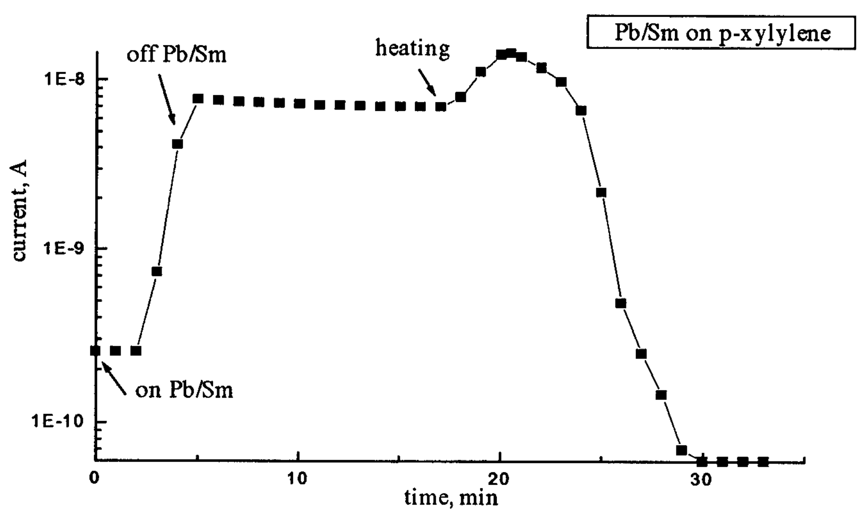

Figure 3. The electric conductivity of bimetallic Pb-Sm-p-xylylene film during the formation, thermostatic control (at 77 K) and further heating.

The conductivity of the island metal film may be determined by tunnel transfer of charge carriers from one nanoparticle to another through a thin dielectric layer (up to 50 nm) of polymer insulator. More comprehensive models are clearly needed both for the theoretical understanding of complex systems such as nanoparticle-polymer materials and for developing fundamental concepts in this area.

CONCLUSION

Thus, the electrical conductivity measurements in similar systems, like one ligand and the row of different metals can provide an additional tool for investigation the difference between reaction mechanisms.

ACKNOWLEDGEMENTS

The work was partially supported by RFBR grant N 96-03-33970a and International OMMEL programme.

REFERENCES

1. Sergeev, G.B., Zagorsky, V.V. and Petrukhina, M.A. *J. Material Chemistry*, 1995, 5(1), p.31-34
2. Zagorsky, V.V., Petrukhina, M.A., Sergeev, G.B., Rosenberg, V.I., and Kharitonov, V.G., Patent RFN 2017547, 15 August 1994.

Pergamon

NanoStructured Materials, Vol. 12, pp. 867–869, 1999
Elsevier Science Ltd

0965-9773/99/$–see front matter

PII S0965-9773(99)00254-8

DEPENDENCE OF MAGNETIC PROPERTIES OF FINEMET ON NANOCRYSTALLISATION CONDITIONS

D. Ramin and W. Riehemann
Institute of Materials Engineering and Technology, Technical University Clausthal,
Agricolastraße 6, D-38678 Clausthal-Zellerfeld, Germany

Abstract *-- Amorphous $Fe_{73.5}Si_{13.5}Cu_1Nb_3B_9$ crystallises at temperatures of about 580° C to a soft magnetic material called FINEMET with superior magnetic properties. Although the nanostructure of FINEMET is very insensible to small variations of annealing parameters some magnetic properties like coercitivity and dynamic power losses vary substantially. Strips of $Fe_{73.5}Si_{13.5}Cu_1Nb_3B_9$ were nanocrystallised under different heat treatment conditions. The annealing temperature, heating and cooling rate were varied. After heat treatment the dynamic hysteresis loops of each specimen were measured with a computer controlled device in the frequency range between 3.2 Hz and 20 kHz at polarisations from 0.6 T to 1.0 T. It was found that a heat treatment with a slow heating rate results in a substantial increase, a slow cooling rate in a moderate increase of the static hysteresis losses compared to a nanocrystallisation with a fast heatup and quenching in water. ©1999 Acta Metallurgica Inc.*

INTRODUCTION

Finemet (1) is a commercially applied nanocrystalline material with excellent soft magnetic properties like very low coercitivity of less than 1 A/m, low AC losses, and high saturation magnetisation compared with soft magnetic amorphous materials. Due to its low frequency dependent dynamic power losses the material has superior properties for high frequency applications. Previous investigations showed variations in the magnetic properties which could be attributed to variations in the material due to the production process (2) but it also indicated that the material's magnetic properties are very sensitive to the nano-crystallisation conditions. In this investigation some dependencies of the magnetic properties on the nanocrystallisation parameters will be shown and discussed.

EXPERIMENTAL

The samples used were strips 110 mm long and 3 mm wide cut from ribbons of amorphous $Fe_{73.5}Si_{13.5}Cu_1Nb_3B_9$ with a thickness of 21 μm provided by Vacuumschmelze, Hanau. All specimens used in this investigation were nanocrystallised in evacuated silica glass tubes at 580° C for one hour. To investigate the effects of heating and cooling rate on the magnetic properties various samples were nanocrystallised with substantially different heating and cooling rates. To obtain rapidly heated samples amorphous ribbons were inserted into a preheated

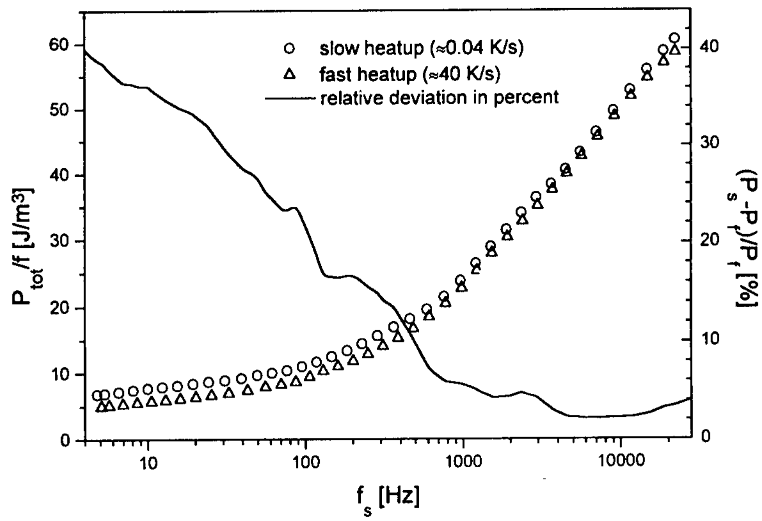

Fig. 1: Power losses of slowly heated (P_s) and of fast heated (P_f) specimen and relative deviation in percent versus frequency at logarithmic scale. Polarisation amplitude: 0.9 T

furnace. To obtain a low heating rate samples were inserted into the cold furnace at room temperature and heated with the maximum heating rate of the furnace of 0.7 K/s. Analogously some samples were quenched in water at room temperature to realise a high cooling rate, others were left in the furnace cooling down at a low rate. The furnace cools down in an exponential decay starting off with -2.2 K/min. Due to the large heat capacity of the furnace the temperature did not significantly change when inserting the silica glass tubes with the samples. The magnetic properties were measured in a frequency range from 3.2 Hz to 20 kHz at different polarisations up to 1 T using a computer controlled digital hysteresis recorder (3). During measurement the earth magnetic field in the sample was compensated by modified Helmholtz coils.

RESULTS

Fig. 1 shows the mean total losses in terms of energy density of 5 samples heated up slowly (≈ 0.04 K/s) in the furnace and of 36 specimens heated to crystallisation temperature with maximum heating rate (≈ 40 K/s) for a polarisation amplitude of 0.9 T versus the frequency corrected to a sinusoidal induction waveform (4) and the relative change of losses in percent. All samples were quenched in cold water after nanocrystallisation. Due to a large variation of the magnetic properties of equally treated samples (2) many samples had to be measured to obtain representative mean values. As seen in Fig. 1 the losses of the slow heated specimens (P_s) at low frequencies were increased by more than 50% compared to fast heated samples (P_f) whereas at higher frequencies the power losses remain practically unchanged. If analogously the power losses of samples fast heated but cooled down slowly in the furnace (P_s) with those of quenched specimens (P_q) are compared higher hysteresis losses of 25% are observed in the slowly cooled specimen (see Fig. 2). If the specimens were both heated up and cooled down at a low rate the results are similar to those of samples which were only heated up slowly but quenched after nanocrystallisation.

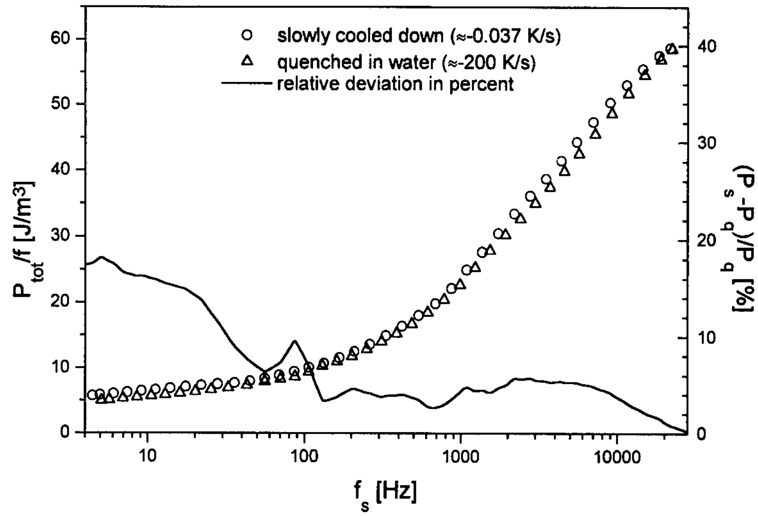

Fig. 2: Power losses of slowly cooled (P_s) and of quenched specimen (P_q) and relative deviation in percent versus the frequency at logarithmic scale. Polarisation amplitude: 0.9 T

CONCLUSIONS

The results show that the heating rate before and the cooling rate after nanocrystallisation are crucial to the soft magnetic properties of Finemet especially for low frequencies namely the hysteresis losses and for the coercitive field. Whereas low heating rates can increase these DC magnetic properties by more than 50% low cooling rates lead to lower increments in the order of 25%. For increasing frequency theses differences decrease and vanish for frequencies higher than 20 kHz. The results indicate that the soft magnetic properties of Finemet could be improved by further increase of the heating and cooling rate. Keeping in mind that time and temperature of the nanocrystallisation treatment is not jet optimised for theses conditions additional improvements should be possible.

ACKNOWLEDGEMENTS

The authors wish to thank Dr. G. Herzer, Vacuumschmelze, Hanau for providing us with amorphous $Fe_{73.5}Si_{13.5}Cu_1Nb_3B_9$ tapes. This work was supported by the Deutsche Forschungsgemeinschaft.

REFERENCES

1. Iuchi, T. et. al., *Journal of Applied. Physics*, 1982, 53, 2410.
2. Ramin, D. and Riehemann, W., *proc. ISEM 8*, Braunschweig 1997, in press.
3. Pott-Langemeyer, M., Riehemann, W., and Heye, W., *Proc. SMM9*, 1989, *Anales de Física B*, 1990, 86, 232.
4. Ramin, D. and Riehemann, W., *proc. MNP*, San Sebastian 1998, accepted for publication.

Pergamon

NanoStructured Materials, Vol. 12, pp. 871–874, 1999
Elsevier Science Ltd

0965-9773/99/$–see front matter

PII S0965-9773(99)00255-X

^{18}O DIFFUSION IN NANOCRYSTALLINE ZrO_2

U. Brossmann[a),c)], U. Södervall[b)], R. Würschum[a)] and H.-E. Schaefer[a)]
[a)]Universität Stuttgart, Institut für Theoretische und Angewandte Physik,
70550 Stuttgart, Germany
[b)]Chalmers University of Technology, Department of Microelectronics and Nanoscience,
41296 Göteborg, Sweden
[c)]now at Max-Planck-Institut für Metallforschung, 70569 Stuttgart, Germany

Abstract– *The diffusion of oxygen in nanocrystalline, undoped monoclinic ZrO_2 was studied using ^{18}O tracer and SIMS profiling. Samples with a mass density of 97 to 99 % and average crystallite sizes of 80 nm and 300 nm were prepared from Zr-metal by DC sputtering, crystallite condensation in an inert-gas atmosphere, oxidation, in-situ consolidation of the n-ZrO_2 powder and subsequent pressureless sintering at 950 or 1050 °C in vacuum. Both volume (V) and interface (B) diffusivities were determined from the depth profiles in the type B regime. The activation energies $Q_V = 2.29$ eV and $Q_B = 1.95$ eV are considerably higher than the values found in Ca- or Y-stabilized ZrO_2. No influence of the crystallize size was observed. ©1999 Acta Metallurgica Inc.*

INTRODUCTION

Diffusion plays a key role in determining technically important properties of oxide ceramic materials, e.g. sintering behavior, ductility and creep resistance. Zirconium dioxide represents a particularly interesting model system due to its polymorphic structure and technical importance as an ionic conductor of oxygen and a structural material for high temperature applications. The tetragonal structure can be stabilized at room temperature as an effect of a small crystallite size, $d \leq 15$ nm [1] or of the addition of subvalent cations, e.g. CaO or Y_2O_3. The latter leads to a strong increase of the oxygen conductivity due to the formation of structural vacancies on the oxygen sublattice.

The present study (for details see [2]) represents the first direct investigation of the oxygen diffusion in interfaces and the crystallites in fully dense, nanocrystalline samples of undoped monoclinic ZrO_2 using ^{18}O as a tracer and secondary ion mass spectroscopy (SIMS) for measuring the diffusion profiles. Until now ^{18}O diffusion studies were limited to gas exchange measurements [3, 4, 5]. The nanocrystalline ZrO_2 samples were prepared by inert-gas condensation, post-oxidation and in-situ consolidation at ambient temperature under a pressure of 1.8 GPa [1]. A relative mass density of about 97 % and an average grain size d of 80 nm were obtained by subsequent pressureless sintering at $T_{\text{sinter}} = 950 - 970$ °C for $2 - 3$ h [2]. Further sintering at 1050 °C for 12 h led to 99 % density and an increase of the grain size to 300 nm.

RESULTS AND DISCUSSION

The shape of the ^{18}O diffusion profiles in n-ZrO_2 (Fig. 1) indicates a concurrent diffusion of ^{18}O in the interfaces and the crystallites of n-ZrO_2 with the ^{16}O - ^{18}O exchange at the surface acting as a constant diffusion source. An analysis of the diffusion profiles in the type-B regime of interface diffusion [6, 7] reveals interface diffusivities D_B, which are 3 - 4 orders of magnitude higher than the volume oxygen diffusivities throughout the temperature range of 450 to 950 °C studied. The volume diffusion coefficients $D_V = (2.5 \pm 1.5) \times 10^{-7} \exp[-(2.29 \pm 0.1)\,\mathrm{eV}/k_B T]\,\mathrm{m}^2/\mathrm{s}$ were determined from the n-ZrO_2 samples with the larger grain size ($T_{\mathrm{sinter}} = 1050\,°\mathrm{C}$) where the surface-near parts of the ^{18}O-diffusion profiles up to depths of several 100 nm are dominated by the diffusion from the surface into the volume of the crystallites. The interface diffusion coefficients $D_B = (3.3 \pm 1.5) \times 10^{-5} \exp[-(1.95 \pm 0.05)\,\mathrm{eV}/k_B T]\,\mathrm{m}^2/\mathrm{s}$ determined from the slopes at deeper penetration are almost identical for both sintering temperatures (Fig. 2) and independent of grain size.

At larger penetration depths a constant ^{18}O background appears (Fig. 1) which increases with temperature and duration of the diffusion anneals. This can be ascribed to ^{18}O penetration through a few residual pores and cracks with subsequent diffusion into the dense agglomerates of crystallites by interface and volume diffusion [2]. Taking into account the crystallite size and the ^{18}O diffusivities D_V and D_B, the size of these agglomerates can be determined to a few tens of a μm. Structures of the same size are confirmed by optical microscopy. The oxygen diffusivities directly determined in the

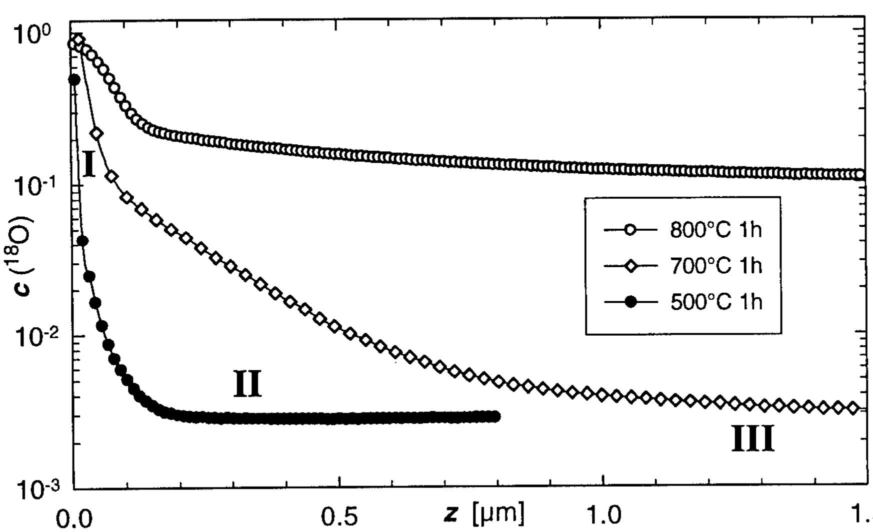

Figure 1: ^{18}O diffusion profiles in nanocrystalline, undoped ZrO_2 sintered at 950 - 970 °C. Temperature and time of diffusion annealing are given in the figure. The ranges of prevailing diffusion from the surface in to the volume (I), via interfaces (II) and into the bulk of the sample (III) due to residual pores are indicated.

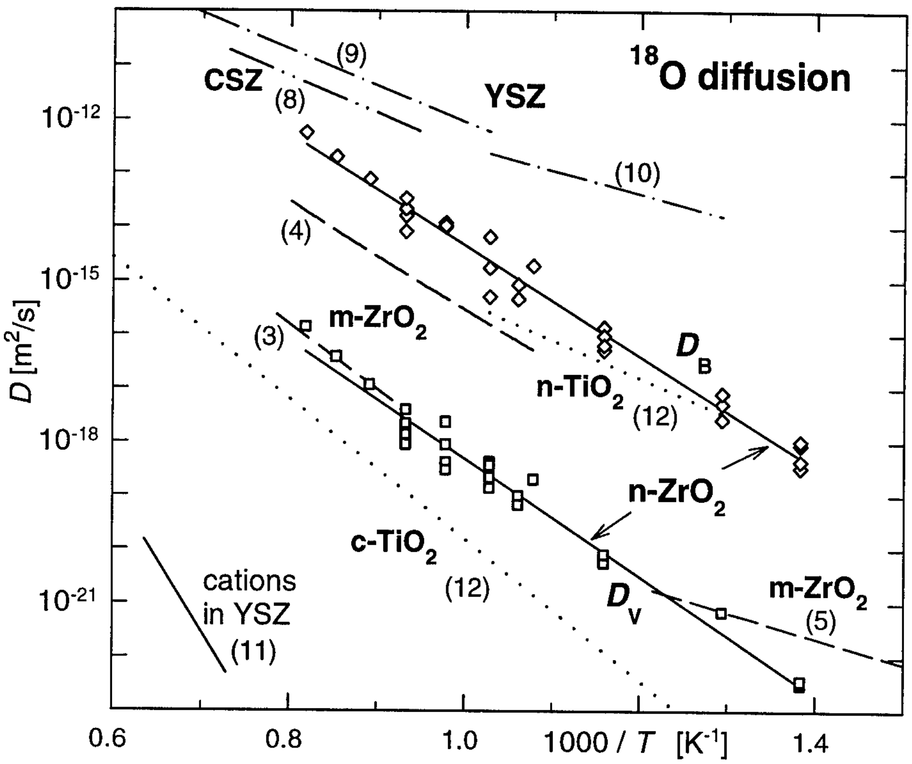

Figure 2: Arrhenius plot of the ^{18}O tracer diffusion coefficients D_V (□) and D_B (◇) measured in undoped, monoclinic n-ZrO_2 with a grain size of 80 to 300 nm and data from literature on diffusion in doped (CSZ, YSZ) and undoped (monoclinic, m) ZrO_2 as well as in both coarse grained (c-) and nanocrystalline (n-) TiO_2.

present studies from diffusion profiles in undoped n-ZrO_2 support earlier results where diffusivities in coarse-grained undoped monoclinic ZrO_2 were indirectly obtained using gas exchange techniques [3, 4] (Fig. 2). The interface diffusion coefficients in n-ZrO_2 are lower than the oxygen diffusivities in Ca- (CSZ) or Y-stabilized zirconia (YSZ) [8, 9, 10] where high volume diffusion coefficients with a low activation energy Q_V = 1.2 - 1.3 eV occur due to a high concentration of structural oxygen vacancies (Fig. 2). This difference may suggest a diffusion mechanism involving the thermal formation of oxygen vacancies in the present case of undoped ZrO_2.

A comparison of the results for ZrO_2 with the chemically related TiO_2 is of particular interest. The diffusion of both oxygen and hafnium was studied in rutile n-TiO_2 [12] with relative densities above 95 % and crystallite sizes $d \simeq 30$ nm after sinter forging at 570 °C and 1.5 GPa. In n-TiO_2 the oxygen diffusivity is much faster ($\simeq 10^5\times$) and the activation energy $Q_B \approx 1.5$ eV [12] much lower than in bulk-TiO_2 (Q_V = 2.58 eV, Fig. 2). Although the differences between the bulk and interface O-diffusion are similar in TiO_2 and ZrO_2, the interface O-diffusion in n-ZrO_2 appears to be much faster than in TiO_2 when these

diffusivities are related to the melting temperatures (Fig. 2).

Regarding the cation self-diffusion in nanocrystalline metal oxides, some information is available from studies of Hf diffusion in n-TiO_2 [12], since Hf as a substitutional cation is considered to reflect the Ti self-diffusion. The Hf diffusivities in n-TiO_2 are similar to extrapolated values for the Ti volume diffusion in TiO_2 based on data of Hoshino et al. [13]. The cationic self-diffusion in rutile is considered to occur via an interstitial mechanism [13, 14]. This view is based on the tendency that TiO_2 exhibits an excess of the metallic constituent [14] and on the observation that the Ti self-diffusivity in rutile increases under reducing conditions due to the formation of Ti interstitials [13]. The results on the Hf diffusion in n-TiO_2 indicate that self-diffusion via self-interstitials in interfaces is not enhanced in comparison to volume diffusion in crystals.

Compared to TiO_2, the cationic self-diffusion in ZrO_2 is characterized by slower bulk diffusivities with a higher activation energy ($4 - 5\,\mathrm{eV}$) as deduced from radio tracer experiments (CSZ, [15]) and the shrinking of dislocation rings (YSZ, [11]). Some indirect information on the cation self-diffusion may also be deduced from sintering processes involving both the cation and the anion diffusion. The onset temperatures of full densification and massive grain growth are substantially higher for n-ZrO_2 [2] than for n-TiO_2 [12]. This again indicates that cation diffusivities in ZrO_2 are lower than in n-TiO_2. On the other hand, the fact that n-ZrO_2 can be sintered to full density at temperatures below $0.45\,T_{\mathrm{m}}$ has to be regarded as evidence that in ZrO_2, in contrast to n-TiO_2, the cation diffusivity in the interfaces is enhanced compared to that in the crystalline state. This may be further clarified by studies of the Zr self-diffusion in fully sintered n-ZrO_2 where both the grain boundary and volume diffusion should be accessible.

This work is supported by the Deutsche Forschungsgemeinschaft.

[1] Soyez, G., Würschum, R. and Schaefer, H.-E. *NanoStruct. Mater.*, 3, 225 (1993)

[2] Brossmann, U., Dissertation, Universität Stuttgart, 1998
Brossmann, U., Würschum, R., Södervall, U. and Schaefer, H-E., to be published

[3] Madeyski, A. and Smeltzer, W.W. *Mat. Res. Bull.*, 3, 369 (1968)

[4] Keneshea, F.J. and Douglas, D.L., *Oxidation of Metals*, 3, 1 (1971)

[5] Ikuma,Y., Komatsu, K. and Komatsu, W. in: *Advances in Ceramics* 24, Science and Technology of Zirconia III, The American Ceramics Society, Columbus (OH), 1988, p. 749

[6] Kaur, I., Mishin, Y. and Gust, W., *Fundamentals of Grain and Interphase Boundary Diffusion*, J. Wiley & Sons, 1997

[7] The conditions of type B kinetics are fullfilled for $T \leq 750°\mathrm{C}$ ($d \approx 80$ nm) and $T \leq 850°\mathrm{C}$ ($d \approx 300$ nm), see [2].

[8] Simpson, L.A. and Carter, R.E., *J. Amer. Ceram. Soc.*, 49, 139 (1966)

[9] Kim, B.K., Park, S.J. and Hamaguchi, H., *J. Amer. Ceram. Soc.*, 76, 2119 (1993)

[10] Tannhauser, D.S. et al., *Nuclear Instruments & Methods*, 281, 504 (1983)

[11] Chien, F. and Heuer, A., *Phil. Mag. A*, 73, 681 (1996)

[12] Höfler, H.J., Dissertation, Universität des Saarlandes, Saarbrücken, 1991

[13] Hoshino, K., Peterson, N.L. and Wiley, C.L., *J. Phys. Chem. Solids*, 4, 1397 (1985)

[14] Atkinson, A. in: *Materials Science and Technolgy*, 11, *Structure and Properties of Ceramics*, Swain, M.V. ed., VCH Weinheim, 1994, p. 299

[15] Rhodes, W.H. and Carter, R.E., *J. Amer. Ceram. Soc.*, 49, 244 (1966)

Pergamon

NanoStructured Materials, Vol. 12, pp. 875–878, 1999
Elsevier Science Ltd

0965-9773/99/$–see front matter

PII S0965-9773(99)00256-1

INTERNAL FRICTION AND THE YOUNG'S MODULUS CHANGE ASSOCIATED WITH AMORPHOUS TO NANOCRYSTALLINE PHASE TRANSITION IN Mg-Ni-Y ALLOY

Y.M.Soifer, N.P.Kobelev[1], I.G.Brodova, A.N.Manukhin[2], E.Korin, L.Soifer[3]

[1] Institute of Solid State Physics, RAC, Chernogolovka 142432, Moscow region, Russia
[2]Institute of Metal Physics, RAC, Kovalevskaya Str., Ekaterinburg 620219, Russia
[3]Department of Chemical Engineering, Ben-Gurion University of the Negev, 84105, Israel

Abstract–*The internal friction and Young's modulus of amorphous $Mg_{84}Ni_{12.5}Y_{3.5}$ alloy obtained by the melt spinning technique have been measured by a vibrating reed method at heating and cooling runs from 300K to 625K. The crystallization kinetics of the alloy was studied by the calorimetric methods. The structure of the samples was determined by the X-ray diffraction technique. The Young's modulus measurements have revealed its significant (up to 50%) irreversible multi-step changes accompanied by the irreversible internal friction peaks. These changes were observed in the same temperature intervals where the anomalies of thermal properties were found out. The results obtained are explained by the structural rearrangement (mainly, a topological ordering and crystallization processes) from amorphous to nanocrystalline state. ©1999 Acta Metallurgica Inc.*

INTRODUCTION

Interest in rapid solidification of magnesium alloys is excited by expectations that the microstructural refinement via this processing and the modification of structure through the formation of nonequilibrium (amorphous, quasicrystalline and nanocrystalline) phases can lead to the development of materials with improved and novel properties (1). Internal friction is known to be a structure-sensitive and has been used to investigate the structural relaxation, the glass transition and crystallization of amorphous alloys. In the present paper, we report the behavior of the internal friction and the Young's modulus of an amorphous Mg-Y-Ni alloy associated with the structural relaxation and crystallization of this alloy.

EXPERIMENTAL

$Mg_{84}Ni_{12.5}Y_{3.5}$ alloy has been prepared by melting the mixture of pure element in the alumina crucible under KCl-NaCl slag-cove at the temperature 1000K. Rapidly quenched alloys have been produced by melt-spinning on the copper drum surface in vacuum. Cooling rates were $5x10^6$ K/s from the temperature 880 K. All the measurements of elastic and dissipative properties were carried out by the vibrating reed method (2) at the frequencies from 200 to 400 Hz in the temperature range from 300K to 625K in the vacuum of 10^{-3} Torr. The specimens cut

from amorphous ribbon of 10x2x0.03 mm^3 in size were usually used. The internal friction Q^{-1} and Young's modulus E were measured during heating and cooling runs (heating rate was about 2 K/min). The structures of the phases were determined by X-ray diffraction technique with Cu-K_α radiation at 298 K after annealing amorphous samples at the certain temperature during 5 min. Differential thermal analysis (DTA) in Ar atmosphere at the heating rate 4 K/min and differential scanning calorimetry (DSC) in nitrogen atmosphere at heating rates from 2 to 120 K/min were used to study crystallization of $Mg_{84}Ni_{12.5}Y_{3.5}$ amorphous samples.

RESULTS AND DISCUSSION

Measurements of the internal friction Q^{-1} and the corresponding Young's modulus change E/E_0 (E_0 is the modulus value of as-cast sample at room temperature) during one cycle heating and cooling in the temperature range from 300K to 625K have shown the complicated nonmonotonic character of temperature dependences observed. In order to clarify the origin of the changes of Q^{-1} and E/E_0, heating and cooling measurements were repeated with rising the upper limit of the heating. The results of such experiments are shown in the Fig.1. The curves manifest multi-stage changes in the Q^{-1} and E/E_0 values occurred during the heating. For the cooling runs there are no practically anomalies in the $Q^{-1}(T)$ and $E/E_0(T)$, therefore one can think that the anomalies observed during the heating runs are associated mainly with irreversible structural changes. The DTA measurements exhibit at least two large (at about 430K and 475K) and one small (at 580K) exothermic peaks (Fig.2). Practically the same stages are revealed by the DSC measurements. According to an analysis of X-ray diffraction patterns of the specimens annealed at various temperatures (Fig.3) the exothermic peaks correspond to the different stages of the crystallization of amorphous $Mg_{84}Ni_{12.5}Y_{3.5}$ alloy. The first stage (430K) is the formation of the $Mg_xNi_yY_z$ (the exact composition have not been determined) metastable crystalline phase, with grains of the mean size of 6 nm. The second one (475K) is a total disintegration of amorphous phase accompanied by the emergence of the nanocrystalline Mg phase and growth of the grain mean size of the $Mg_xNi_yY_z$ phase up to 14 nm. At 580K the transformation occurs from metastable to stable phases.

For convenience of further consideration one can divide the temperature range under investigation to the 3 regions: 1st from 300K to 425K, 2nd region from 425K to 475K and the 3rd region above 475K.

300K-425K. The value E_0 of the Young's modulus of the as-cast specimen at 300K was about 30Gpa. The repeated heating and cooling runs don't lead to the irreversible changes in E/E_0 and Q^{-1} up to the temperatures of about 350K. However, the heating up to 400K leads already to the noticeable (about 4%) variation of E/E_0 and corresponding internal friction alteration. Since according to the X-ray diffraction measurements no crystallization have been found out at these temperatures the observed changes in E/E_0 and Q^{-1} is likely to be associated with the structural rearrangement due to a topological ordering in the amorphous material. The topological ordering occurs at comparatively low temperatures (less than the temperatures of glass transition and crystallization) and leads to a decrease of internal stresses in a sample and to an irreversible increase in E/E_0 and decrease of internal friction. At the same time the cooling ran and repeated heating exhibit a significant reversible rising of Q^{-1} in the temperature interval been considered and a large internal friction peak centered at 425K. We will discuss the possible peak nature when we consider the $Q^{-1}(T)$ behavior in the second temperature range.

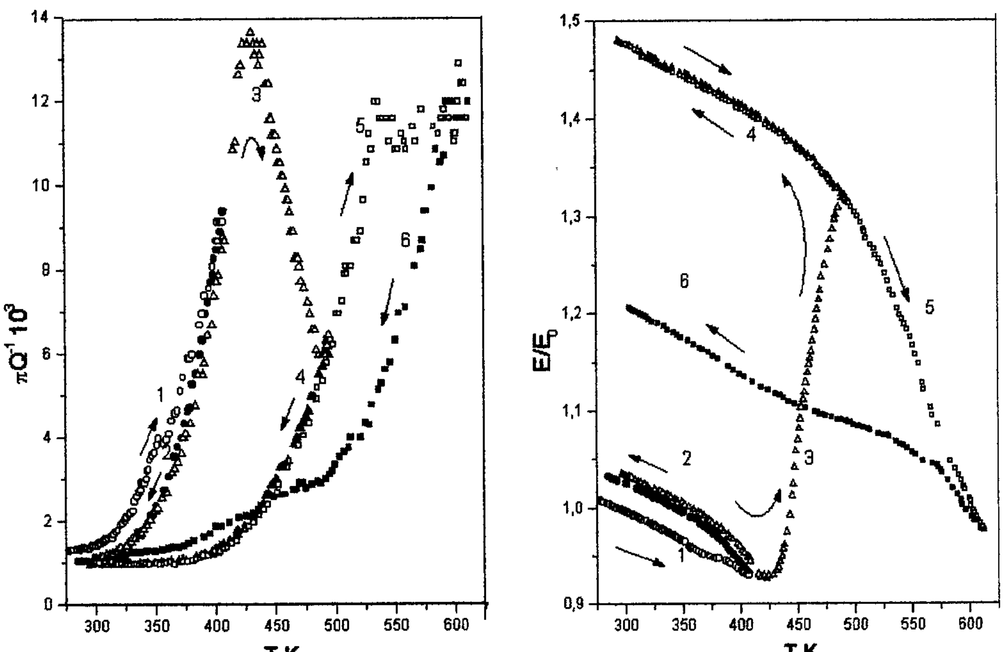

Fig.1. Internal friction (Q^{-1}) and Young's modulus (E/E_0) of Mg-Ni Y alloy measured during the three heating/cooling cycles (up to 400K, 500K and 625K). Open symbols for the heating, solid symbols for the cooling.

425K-475K. The onset of the first stage of crystallization coincides with a beginning of a very significant (by 45%) modulus increase (Fig.1). The increase continues till about 485K. This modulus change is irreversible and the difference in the Young's modulus values of annealed and as-cast specimens achieves 50% at 300K. The internal friction exhibits a large peak centered at 425 K . The high temperature side of the peak ends at 475 K and the new internal friction increase begins. There are no doubts that the irreversible Young's modulus variation is due to crystallization process in the temperature range of 425K to 475K. It is much more difficult to explain the internal friction behavior. The internal friction peak starts from the temperature of 325 K at which no crystallization occurs and ends at the temperature of 475K at which the first stage of crystallization accomplishes. Probably we see the superposition of at least two different processes. The first one is a glass transition in amorphous material (in our case it is about 400K). Such process causes an internal friction peak near the glass transition temperature (3). The second process is the structural rearrangement caused by the crystallization. In the terms of a simple phenomenological consideration the internal friction Q^{-1} is prove to be proportional to the rate of crystallization. Unfortunately the data present do not allow to single out the contribution of each internal friction mechanisms mentioned above. It is necessary more distinct separation of glass transition and crystallization processes.

475K-625K. This temperature range is correspondent to the second stage of crystallization. The Young's modulus increases (Fig.1) up to 490K and then becomes to decrease up to the temperature of 625K (the highest annealing temperature used in our experiments). The modulus decrease is partly irreversible. The Young's modulus value measured at 300K after annealing at

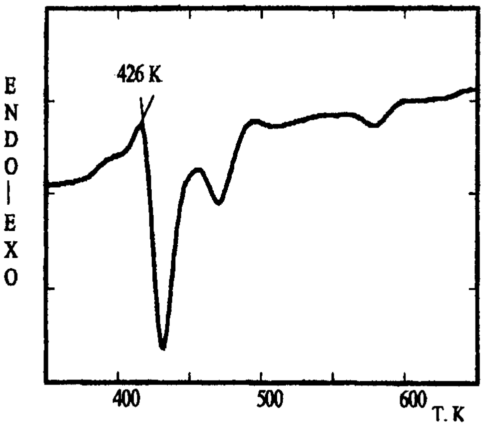

Fig.2. DTA traces of amorphous $Mg_{84}Ni_{12.5}Y_{3.5}$ alloy heating at 4K/min.

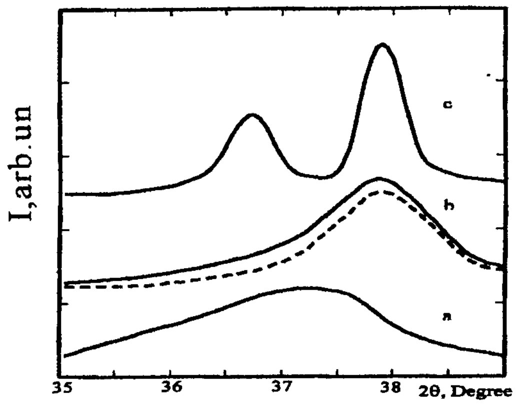

Fig.3. X-ray scattering curves in the field of the first maximum for amorphous $Mg_{84}Ni_{12.5}Y_{3.5}$ alloy: (a) amorphous, (b) annealed at 438K, (c) annealed at 478K. Dotted line corresponds to scattering for nanocrystalline phase. Line $2\theta=36.7^0$ corresponds to (101) α-Mg. Line$2\theta=37.8^0$ corresponds to nanocrystalline $Mg_xNi_yY_z$ phase.

625K is by 25% lower then after annealing at 490K. The result obtained is not much surprising. At the second stage of crystallization the Mg grains appear which are characterized by a low (in compare of Mg compounds) Young's modulus. This result points out that on the one side elastic modulus measurements can be a very good instrument for investigation of crystallization kinetics and on the another side it indicates the possibility to govern by elastic and mechanical properties of Mg-Ni-Y alloys by special kind of heat treatments. The internal friction (Fig.1) demonstrates a complex irreversible peak at about 525K-550K superimposed on the big reversible internal friction background. The irreversible internal friction can be associated with nucleation and growth of Mg grains and with transformation of the metastable $Mg_xNi_yY_z$ phase to stable phase detected by the X-ray measurements. The internal friction background observed is likely to be associated with the grain boundary sliding.

ACKNOWLEDGMENTS

Ya.M.Soifer and N.P.Kobelev acknowledge Russian Foundation for Basic Researches (Grant 98-02-16644 and Grant 95-15-96806) for a partial financial support.

REFERENCES

1. Inoue, A., *Nanostructured Materials*, 1995, 6, 53.
2. Kobelev,N.P., Soifer, Ya.M., Shteinberg,V.G. and Levin, Yu.B., *Phys.Stat.Sol.(a)*, 1987, 102, 773.
3. He, Y. and Li, X..G., *Phys.Stat.Sol.(a)*, 1987, 99, 115.

Pergamon

NanoStructured Materials, Vol. 12, pp. 879–882, 1999
Elsevier Science Ltd

0965-9773/99/$–see front matter

PII S0965-9773(99)00257-3

CHARACTERISTIC FUNCTIONS OF NANOSTRUCTURED MATERIALS

V. Garrido & D. Crespo
Dept. Física Aplicada, Univ. Politècnica de Catalunya, Campus Nord, Modul B4, 08034-Barcelona, SPAIN, e-mail: crespo@benard.upc.es

Abstract -- *Most of the physical properties of systems underlying first order phase transitions, i.e. the scattering properties, can be obtained from the spatial correlation functions. For the case of nucleation and growth kinetics it is possible to obtain all the correlation functions from the particle size distribution. In this paper we obtain the spatial correlation functions corresponding to several kinetics; in particular the correlation functions corresponding to the microstructure developed in partitioning transformations are obtained.*
©1999 Acta Metallurgica Inc.

INTRODUCTION

The spatial correlation functions of a microstructured material give an accurate description of its statistical properties; in particular they are related to the small angel scattering intensity (1). Therefore, its computation is of major interest. An elegant theory that gives exact correlation functions for first order phase transitions - Time Cone method - was developed by Ohta et al. (2). This theory is applicable either to the growth of magnetic domains or to the precipitation of crystals in an undercooled liquid or amorphous matrix. In these systems, the order parameter p stands for the number of distinguishable phases in the transformed phase. However, the method is settled under several hypotheses which heavily restrict its practical applicability to real systems.

The reaction kinetics may be interface controlled, as in the case of crystallization of metals, or diffusion limited, as in the case of primary crystallizations. For both types of kinetics, the transformation may be analysed by the theory of nucleation and growth processes developed in the thirties by Kolmogorov (3), Johnson and Mehl (4), and Avrami (KJMA) (5). The theory is able to evaluate the time dependence of the transformed fraction during the transformation from the knowledge of the kinetic magnitudes, namely nucleation rate, I, and growth rate, G.

An extension of this theory based on a mean field hypothesis - populational KJMA - has been recently derived (6), allowing the evaluation of the particle size population as a function of time. The particle size distributions have already been obtained for interface and diffusion controlled growth processes (6,7), and for the case of a primary precipitation during annealing of a glassy alloy resulting in a nanocrystalline structure (8). This model describes a completely degenerate system, characterized by an order parameter $p\to\infty$, where each individual particle is considered a different phase, thus being distinguishable over the whole transformation. Moreover, it has been shown (9) that the correlation functions of a non degenerate (p=1, i.e. order-disorder

transitions) and partially degenerate ($1<p<\infty$) systems can be expressed in terms of the correlation functions of the completely degenerate ($p\to\infty$) system. Furthermore, this model is less restrictive than the Time-Cone method, and allows evaluation of correlation functions for non-trivial kinetics where the Time-Cone method cannot be applied, i.e. $I(X,t)$ and $G(X,r,t)$, where t is the time, X is the transformed fraction at time t, and r is the individual radius of the growing particles. In this paper the main results of this method are presented and applied to the primary nanocrystallization of a FINEMET amorphous alloy by isothermal annealing.

GENERALIZED CORRELATION FUNCTIONS

The correlation functions are related to the structure developed during the phase transition. Generalizing the conventions used by Sekimoto (10,11) and Ohta et al. (2) we define a phase as the union of all the non-connected particles having the same colour, indicator of a common property such as chemical or crystallographic composition; thus, two particles belonging to the same phase coalesce if they impinge, that is, the boundary between them disappears. The total transformed phase is the union of all phases, which are assumed to be statistically equivalent, and colour 0 is assigned to the untransformed phase.

The phase structure is represented by the following two-valued function:

$$g_i(\vec{r},t)=\begin{cases} 1, & \text{if } \vec{r} \text{ belongs to a grain of the } i\text{-th. phase at time } t \\ 0, & \text{otherwise} \end{cases} \qquad [1]$$

and, in particular, $g_0(\vec{r},t)$ gives the structure of the untransformed phase. The correlation functions are defined as

$$\begin{aligned} &G_0(\vec{r}-\vec{r}',t)=\langle g_0(\vec{r},t)\ g_0(\vec{r}',t)\rangle, && G_1(\vec{r}-\vec{r}',t)=\langle g_i(\vec{r},t)\ g_i(\vec{r}',t)\rangle \\ &H_0(\vec{r}-\vec{r}',t)=\langle g_0(\vec{r},t)\ g_i(\vec{r}',t)\rangle, && H_1(\vec{r}-\vec{r}',t)=\langle g_i(\vec{r},t)\ g_j(\vec{r}',t)\rangle \quad , i\neq j \end{aligned} \qquad [2]$$

where the bracket means the average over the whole volume and all possible i and j values. Therefore, the correlation functions are only functions of $\vec{r}-\vec{r}'$ and t, and we can take $\vec{r}'=0$ without loss of generality. However, the above defined functions are not mutually independent. We have shown (9) that the correlation functions can be written as:

$$\begin{aligned} &G_0(\vec{r},t)=[1-X(t)]^2+[1-X(t)]C_1(\vec{r},t)\ , && G_1(\vec{r},t)=\frac{1}{p^2}\{X^2(t)+[p-X(t)]C_1(\vec{r},t)\}\ , \\ &H_0(\vec{r},t)=\frac{1}{p}[1-X(t)]\{X(t)-C_1(\vec{r},t)\}\ , && H_1(\vec{r},t)=\frac{1}{p^2}X(t)\{X(t)-C_1(\vec{r},t)\}\ . \end{aligned} \qquad [3]$$

Here $C_1(\vec{r},t)$ is the probability of finding, at time t, two points separated by a distance $\vec{r}$ in the same particle. In other words, it is the particle transformed phase self-correlation function averaged for all the particles of the transformed phase. We have postulated (9) that the actual form of $C_1(\vec{r},t)$ for the case of isotropic growth with impingement is

$$C_1(r,t) = X^{-1}(t) \sum_{\gamma} \sum_{\beta} n_\gamma \, n_\beta \, V_\gamma \, V_\beta \, f_0 \left(rL/r_\beta r_\gamma\right) \qquad [4]$$

where $n_\alpha(t)$ is the density of the particles of volume $V_\alpha = \frac{4}{3}\pi r_\alpha^3$, $L(t) = \left(\frac{3\,V(t)}{4\pi\,N(t)}\right)^{1/3}$ is the scaling length, $V(t)$ is the total volume of the transformed phase, $N(t)$ is the total number of droplets and

$$f_0\left(r/r_i\right) = \left[\,1 - \tfrac{3}{4}\left(r/r_i\right) + \tfrac{1}{16}\left(r/r_i\right)^3\,\right] \Theta(2r_i - r) \qquad [5]$$

is the self-correlation function of a sphere, $\Theta(x)$ being the Heaviside function.

RESULTS

Here we show the application of the presented method to the primary crystallization of a FINEMET amorphous alloy of composition $Fe_{73.5}Cu_1Nb_3Si_{17.5}B_5$ by isothermal annealing. The crystallization kinetics of this alloy has been recently described (8,12) by an interface plus diffusion controlled particle growth with soft impingement and a nucleation rate linearly decreasing with the transformed fraction. The corresponding nucleation and growth rates are given by the expressions

$$I(t) = I_0\left[1 - X(t)\right], \qquad G(r) = \begin{cases} G_0 & r < r_T \\ D_0 \left(\dfrac{1 - X(t)/\gamma}{1 - X(t)}\right) \dfrac{1}{r} & r \geq r_T \end{cases} \qquad [6]$$

where D_0 is the diffusion coefficient of the slowest diffusing species and γ is the transformed fraction at the end of the primary crystallization, determined by Mössbauer spectroscopy. The value of the threshold radius r_T at which the growing mechanism is switched is given by

$$r_T = D_0\left(1 - X(t)/\gamma\right) \Big/ G_0\left(1 - X(t)\right) - r^*$$

which ensures that at any time the grain radius is the lowest between the values obtained by pure interface and by pure diffusion growth.

This process is particularly interesting for the present study because the corresponding spatial correlation functions cannot be calculated by the Time-Cone method, because it does not fulfill the restrictions under which it is applicable. Specifically, the growing rate is affected by the environment of the particles and the effect of the nuclei radius cannot be neglected.

Figure 1 shows the particle size distribution obtained by the PKJMA and the corresponding self-correlation functions for isothermal annealing at 490°C (solid lines) and 510°C (dashed lines) respectively. The effect of the increase in the annealing temperature is a significant increase of the particle density and a reduction of the average and maximum particle radius. The main effect in the self-correlation function is a change in the slope, which will be translated in the shape of the corresponding small-angle scattering peak.

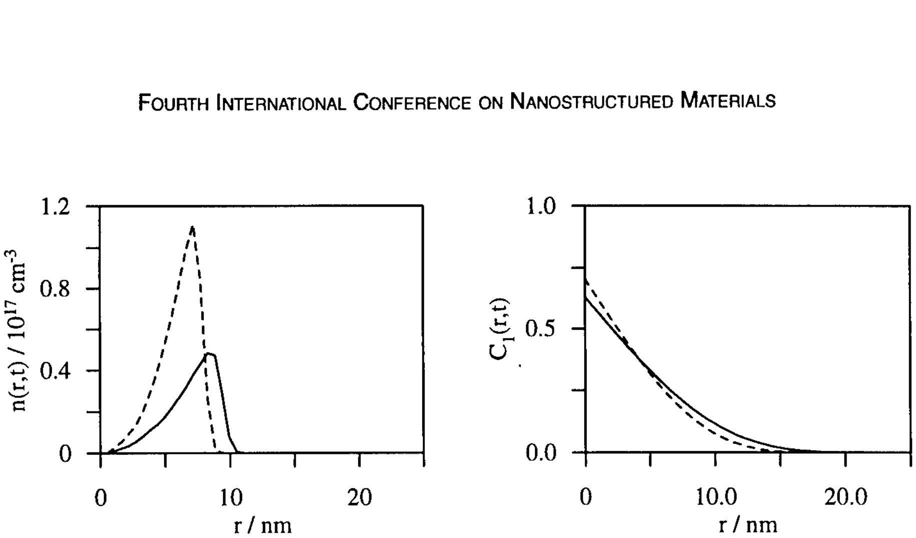

Figure 1 Particle size distributions obtained using the PKJMA model (left), and self-correlation functions computed by the method here presented (right) for the primary crystallization of a FINEMET amorphous alloy, obtained by isothermal annealing at 490 °C (solid line) and 510 °C (dashed line) respectively.

CONCLUSIONS

A method of computing the self-correlation functions in nucleation and growth systems has been developed. It can be applied to situations where the grain growth is affected by the grain environment as, for example, partitioning transformations. Further work will be devoted to the study of the scattering properties of such systems.

Work partially financed by DGICYT, grant PB94-1209, Generalitat de Catalunya 1997SGR 00039 and UPC, grant PR9505.

REFERENCES

1. Guinier, A. and Fournet, G., *Small-angle scattering of X-rays*, John Wiley and Sons, New York, 1955.
2. Ohta, S., Ohta, T. and Kawasaki, K., *Physica*, 1987, 140A, 478
3. Kolmogorov, A. N., *Bull. Acad. Sci. USSR, Phys. Ser.*, 1937, 1, 355
4. Johnson, W.A. and Mehl, P. A., *Trans. Am. Inst. Min. Metall. Pet. Eng.*, 1939, 135, 416
5. Avrami, M., *J. Chem. Phys.*, 1939, 7, 1103; 1940, 8, 212; 1941, 9, 177
6. Crespo, D. and Pradell, T. , *Phys. Rev. B*, 1996, 54, 3101
7. Crespo, D., Pradell, T., Clavaguera-Mora, M. T. and Clavaguera, N. , *Mat. Sci. & Eng A*, 1997, 238, 160
8. Crespo, D., Pradell, T., Clavaguera-Mora, M. T. and Clavaguera, N. , *Phys. Rev. B*, 1997, 55, 3435
9. Garrido, V. and Crespo, D., *Phys. Rev. E*, 1997, 56, 2781
10. Sekimoto, K., *Phys. Lett.*, 1984, 105A, 390
11. Sekimoto, K , *J. Phys. Soc. Jpn.*, 1984, 53, 2545
12. Pradell, T., Crespo, D., Clavaguera, N., Zhu, J. and Clavaguera-Mora, M.T., *NanoStructured Materials*, 1997, 8, 345

Pergamon

NanoStructured Materials, Vol. 12, pp. 883–886, 1999
Elsevier Science Ltd

0965-9773/99/\$–see front matter

PII S0965-9773(99)00258-5

NMR RELAXATION AND LINE SHAPE STUDY ON Li^+ DIFFUSION IN NANOCRYSTALLINE LAYER-STRUCTURED Li_xTiS_2

Rudolf Winter and Paul Heitjans
Institut für Physikalische Chemie und Elektrochemie
Universität Hannover, Callinstr. 3-3A, 30 167 Hannover, Germany

Abstract — *Temperature and frequency dependent* ^{7}Li *spin-lattice relaxation rate measurements on the layer-structured two-dimensional ion conductor* Li_xTiS_2 *in different order states were carried out in the laboratory frame* (T_1^{-1}) *and in the rotating frame* ($T_{1\varrho}^{-1}$). *The activation energies for individual ion hopping, as obtained from these measurements, are about 0.19* eV *for the polycrystalline, 0.16* eV *for the nanocrystalline, and 0.07* eV *for the amorphous material. The frequency dependence of* T_1^{-1} *is sublinear for both disordered modifications. The NMR central transition lines of the nanocrystalline material decompose into a narrow and a broad component in the course of motional narrowing. The relative intensity of the narrow component corresponding to the fraction of highly mobile Li ions increases gradually with temperature, reaching a limiting value of 50% at high temperatures. Hence, we conclude that the interfacial regions are not structurally homogeneous and comprise about half of the atoms of the sample. Contrary to three-dimensional nanocrystals, diffusion in the two-dimensional nanocrystalline material takes place on the grain surfaces rather than within an amorphous interface medium.*

INTRODUCTION

Diffusivity is generally enhanced both in amorphous and nanocrystalline materials, i.e. in systems with homogeneous as well as heterogeneous disorder. On the other hand, even coarse-grained layer-structured materials are generally fast ionic conductors. In this study, we examine the influence of disorder on diffusion in layer-structured, two-dimensional ionic conductors. For this purpose, Li_xTiS_2 has been selected as model compound since it is well-studied due to its relevance as cathode material. It can be prepared in homogeneously (amorphous) as well as in heterogeneously (nanocrystalline) disordered form. The disorder effect is studied by NMR relaxation and line shape measurements.

EXPERIMENTAL

Polycrystalline Li_xTiS_2 ($x \approx 2/3$) samples were prepared by Li intercalation into polycrystalline layer-structured (hexagonal) TiS_2. The intercalation was carried out by stir-

ring the material in a solution of n-butyllithium in hexane [1]. The samples were then heated at 700 K for ten days in order to achieve a homogeneous Li distribution. To obtain nanocrystalline samples, this material was further processed by high-energy ball milling in a SPEX 8 000 mill for 0.5 to 50 hours. In this paper, all data referring to the nanocrystalline material were obtained with samples milled for two hours. The particle size was estimated from X-ray diffraction linewidth measurements performed with a Philips PW 1 710 Bragg-Brentano type diffractometer. The grain size is about 12 nm as derived from the 35° (2Θ) reflection by a Scherrer analysis. The amorphous material was prepared via an organometallic chemical synthesis route by a technique similar to the sol-gel process [2].

For the NMR measurements, a Bruker MSL 100 spectrometer together with an external Kalmus LP 400 HF power amplifier and an Oxford tunable cryomagnet (field max. 7 T) were used. Spin-lattice relaxation rates in the laboratory frame (T_1^{-1}) and NMR line shapes were measured in the temperature range from 140 K to 560 K at several frequencies ranging from 10 MHz to 110 MHz. Additionally, spin-lattice relaxation was measured in the rotating reference frame ($T_{1\varrho}^{-1}$) at 10 kHz.

RESULTS AND DISCUSSION

An overview of the results for amorphous, nano- and polycrystalline Li_xTiS_2 is given in tab. 1. An Arrhenius plot of T_1^{-1} in the three modifications at the resonance frequency $\nu_0 = 24.5$ MHz is displayed in fig. 1. At the lowest temperatures, the curves are characterized by a background relaxation rate, which is only weakly dependent on temperature. The flank of a diffusion-induced peak starts at about 180 K for the amorphous, at 260 K for the nano- and at 300 K for the polycrystalline material. The rate maximum is covered only in the case of the polycrystalline sample since the disordered forms tend to relax structurally during the period of a single measurement at temperatures higher than 550 K. The activation energies E_{nmr}^{lT} obtained from the slopes of these low-temperature flanks are similar in poly- and nanocrystalline Li_xTiS_2, whereas in the amorphous material E_{nmr}^{lT} is about one third the value of the polycrystalline material. A correction of the raw data for the background rate does not change the slope significantly. The frequency dependence of T_1^{-1} in the temperature regime of the diffusion-induced low-temperature flank is described by a power law $T_1^{-1} \propto \nu_0^{-\beta}$ with β significantly below 1, indicating

TABLE 1
Overview of the samples and their properties:
Grain size, activation energy, exponent of frequency dependence, and fraction of nuclei located in interfacial regions

sample	size [nm]	E_{nmr}^{lT} [eV]	β	interface fraction
polycrystalline [3]	≈ 1 000	0.19	1.3	—
nanocrystalline	≈ 12	0.16	0.5	50%
amorphous	—	0.07	0.6	—

the simultaneous occurrence of disorder and correlation of the individual hops (cf. [4]).
The NMR spectra (cf. fig. 2) are Lorentzian-type in the rigid-lattice limit, i.e. at the lowest temperatures. With increasing temperature, the central transition line becomes narrower and –in the case of the nanocrystalline material– tends to decompose into two Lorentzian-type contributions. Closer inspection reveals that the relative intensity of the narrow component increases with increasing temperature until a fraction of 50% is reached. This *gradual* increase reveals the inhomogeneous structure of the interfacial regions: Obviously, not all interface-located Li become mobile at the same temperature. Eventually, the broad component starts narrowing at about 450 K. This decomposition feature is neither observed with the polycrystalline nor the amorphous material. We thus interpret that the 50% intensity of the narrow component corresponds to half of all probe nuclei being located in the interfacial regions.
Since the increase of the intensity of the narrow spectral component is gradual with respect to changing temperature, we conclude that the interfacial regions are not homogeneously disordered. Furthermore, the similar activation energies of nano- and polycrystalline Li_xTiS_2 indicate that diffusion paths in both crystalline forms are similar, and not comparable to those found in the amorphous structure. Therefore, we infer that the fastest paths are located on the grain surfaces, where the structure is still determined by the layer-structured grains while the less dense packing on the interface side already enhances mobility.

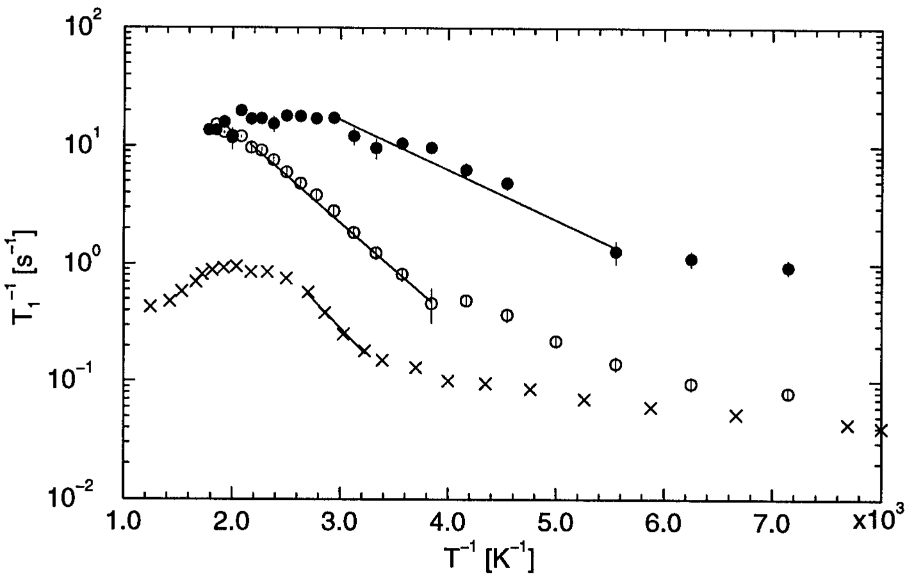

Figure 1: Logarithmic representation of the relaxation rates of ^{7}Li in amorphous (filled circles), nano- (open circles), and polycrystalline (crosses, [3]) Li_xTiS_2 vs. inverse temperature at $\nu_0 = 24.5$ MHz. The lines indicate the fits that are used to estimate the activation energies, respectively.

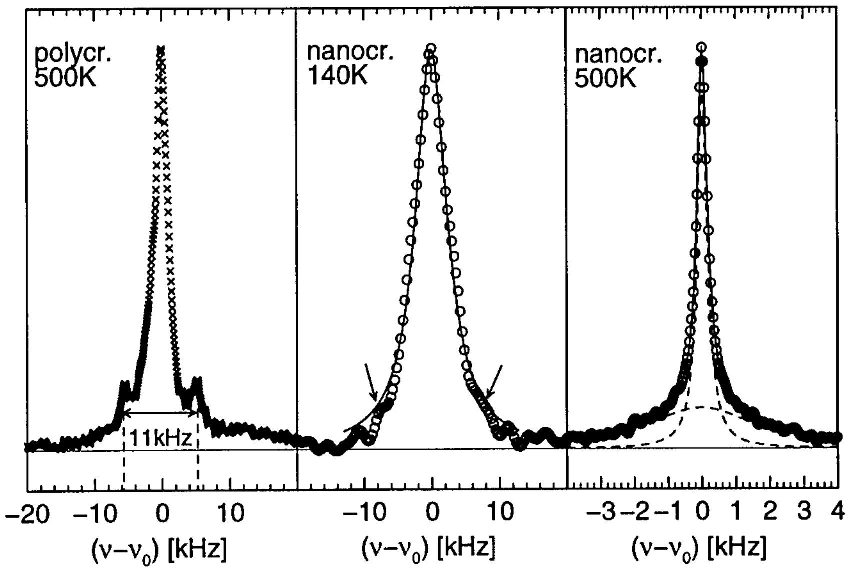

Figure 2: ^{7}Li NMR spectra of poly- and nanocrystalline Li_xTiS_2. Left: slightly motionally narrowed spectrum of polycrystalline material; with quadrupole satellites. Middle: Lorentzian rigid-lattice line of nanocrystalline Li_xTiS_2; with quadrupole shoulders. Right: motionally narrowed spectrum of nanocrystalline Li_xTiS_2. Dashed lines indicate the two Lorentzian fit components interpreted as bulk and interface contributions.

CONCLUSIONS

Li_xTiS_2 is a model compound for the study of the combined effect of disorder and low-dimensional ionic conduction. From the NMR relaxation and line shape data obtained in this study it becomes obvious that, contrary to nanocrystalline three-dimensional ionic conductors (e.g. $LiNbO_3$ [5]), in nanocrystalline two-dimensional conductors diffusion takes place along the surfaces of the grains. The structure of the interfaces does not seem amorphous-like since the NMR relaxation properties of the amorphous modification differ significantly from those of the nanocrystalline material.

Acknowledgment: We would like to thank Roderich Röttger for assistance with X-ray diffraction and the Deutsche Forschungsgemeinschaft (SFB 173) for funding.

REFERENCES

[1] Dines, M.B., Materials Research Bulletin, 1975, 10, 287.
[2] Bensalem, A., Schleich, D.M., Materials Research Bulletin, 1988, 23, 857.
[3] Küchler, W., Heitjans, P., Payer, A., Schöllhorn, R., Solid State Ion., 1994, 70, 434.
[4] Bunde, A., Funke, K., Ingram, M.D., Solid State Ionics, 1996, 86, 1311.
[5] Bork, D., Heitjans, P., in: Smith, M.E., Strange, J.H. (Eds.), XXVIIIth Congress Ampère, Univ. Kent, Canterbury, 1996, p. 418.; J. Phys. Chem., 1998, B102, 7307.

Pergamon

NanoStructured Materials, Vol. 12, pp. 887–890, 1999
Elsevier Science Ltd

0965-9773/99/$–see front matter

PII S0965-9773(99)00259-7

ROOM-TEMPERATURE AGEING EFFECTS ON THE MAGNETIC PROPERTIES OF MECHANICALLY MILLED $SMCO_5$

Diandra L. Leslie-Pelecky and E.M. Kirkpatrick
Department of Physics & Astronomy and Center for Materials Research & Analysis
University of Nebraska, Lincoln NE 68588-0111
R.L. Schalek
Composite Materials and Structures Center, Michigan State University, East Lansing MI 48824-1226

Abstract -- *Mechanical milling of ferromagnetic $SmCo_5$ produces dramatic increases in coercivity or short (15 minutes to 2 hours) milling times. The milled nanostructured material is highly metastable and undergoes room-temperature recovery during the first two weeks after fabrication. Although changes in the coercivity with ageing time are significant, the diffracting crystallite size determined from x-ray diffraction remains constant. We conclude that disorder is a primary determinant of the coercivity of mechanically milled alloys.*

INTRODUCTION

Magnetic nanostructures often exhibit behavior different from bulk materials. Although there are many techniques for fabricating nanostructured materials, mechanical milling has emerged as a unique method of producing disorder in alloys. (1,2) Mechanical milling is a high-energy deformation process that introduces dislocations, vacancies, anti-site defects and strain. $SmCo_5$ was chosen for this study due to its large uniaxial anisotropy, which makes it an important material for permanent magnets and thin-film devices.

EXPERIMENTAL

Commercially purchased $SmCo_5$ powder (-100 mesh) was hermetically sealed in a tungsten-carbide-lined vial and milled in a SPEX 8000 mixer/mill. Milling was stopped every 15 minutes for the first two hours and every hour thereafter to remove a small amount of powder for x-ray diffraction and magnetic measurements, and to break up clumps of powder. All powder handling was performed in an inert-atmosphere glovebox to prevent oxidation.

Magnetic measurements were made using a SQUID. Samples were loaded in paraffin-filled polyethylene bags in the glove box and sealed. The paraffin was melted to immobilize the particles during measurement.

X-ray diffraction (XRD) patterns were obtained using a D-Max-B Rigaku diffractometer with Cu-K_α radiation. XRD is the only technique in which the particles are exposed to the air during measurement. The measured linewidth was Fourier decomposed and compared to a LaB_6 standard to remove instrumental broadening and contributions from the $K_{\alpha 2}$ doublet using the Stokes technique. (3) A single-profile analysis (4) that separates linewidth broadening due to microstrain from broadening due to grain size was applied to the (110) peak to extract the coherent diffracting crystallite size (DCS) and rms (root-mean-squared) microstrain.

DISCUSSION

X-ray diffraction shows that the hcp $SmCo_5$ lines broaden as the milling time increases. After 10 hours, only the (111) peak has appreciable intensity, indicating a nearly amorphous structure. Milling times greater than 25 hours produce precipitation and crystallization of fcc or highly faulted hcp cobalt. No evidence of oxide or tungsten carbide contamination is observed in XRD or energy dispersive x-ray spectra. The DCS decreases exponentially for the first four hours of milling time to a value of about 5 nm. The XRD peaks are too broad for analysis at milling times greater than four hours. Mechanical milling disorders SmCo through the introduction of atomic-level defects that decrease crystallite size and increase dislocation density. The high dislocation density implies a high density of antiphase boundaries. Since the ratio of atoms close to the crystallite interfaces to those within the crystallite is proportional to 1/DCS, the number of atoms located at defect interfaces increases significantly after only short milling times.

Figure 1 summarizes the dependence of the coercivity on milling time. All measurements were made at room temperature. The coercivity increases significantly after short milling times, reaching a maximum value of 16 kOe after 2 hours of milling, then decreases monotonically with continued milling. One possible explanation for the coercivity change is the decrease in the DCS as the powder is milled; however, a study of the room-temperature-ageing behavior of milled material shows that factors other than the DCS can cause significant changes in the coercivity.

Figure 2 shows the coercivity as a function of time after first measurement for a sample milled for 15 minutes. The coercivity of the material at the first measurement is 15 kOe. The coercivity decreases with time, until it stabilizes at 9 kOe after about two weeks. (The data shown in Figure 1 is from a different series of samples and was taken after the coercivity had stabilized at a constant value.)

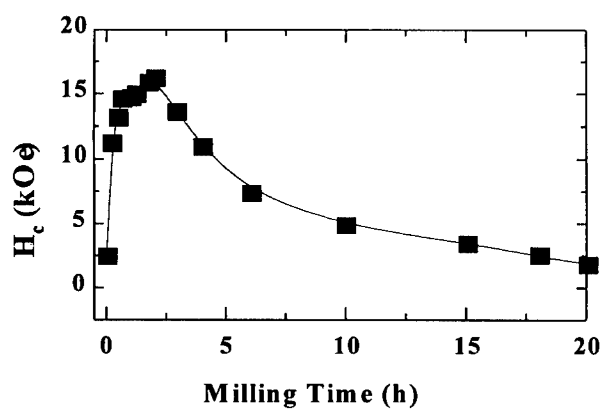

Figure 1: The dependence of the room-temperature coercivity (H_c), on milling time.

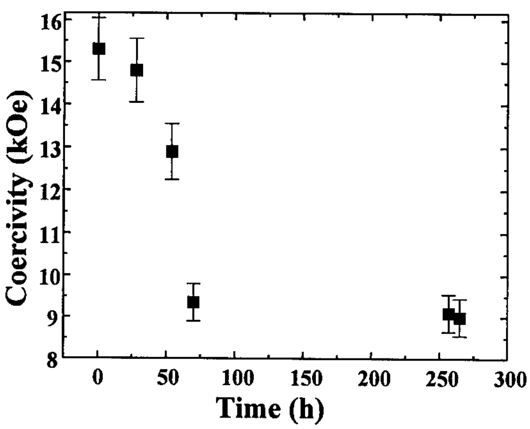

Figure 2: Coercivity as a function of time since first measurement for a $SmCo_5$ sample milled for 15 minutes.

The x-ray diffraction patterns show no change in the linewidth over the two-week period, as shown in Figure 3. The DCS obtained from the (101) peak at 30.5 degrees is 23 (±2) nm and the DCS obtained from the (110) peak at 36.0 degrees is 14 (±1) nm for both patterns. Differential broadening of the XRD peaks is often observed in metastable materials due to large amounts of strain. (5) Strain energy is stored in grain boundaries and other defect regions of the crystallites. (6)

Although most of the mechanical energy in the milling process is converted to heat, some energy is stored in the powder and released by recovery and recrystallization mechanisms. Recrystallization generally occurs at temperatures above 0.5 times the melting temperature (7) and is not expected to occur at room temperature; however, recovery processes occur at much lower temperatures. Recovery at room temperature is accomplished by the removal of point defects such as vacancies, substitutional atoms and antisite atoms. Since the Sm atom is significantly larger than the Co atom, antisite defects produce strains that provide a strong driving force for reordering, even at room temperature.

We thus attribute the changes in coercivity with time to atomic-level reordering after fabrication. The x-ray atomic distribution function of elemental nanophase materials prepared by gas condensation shows that practically all atoms in aged samples are located on crystalline lattice sites. In contrast, about 10% of the atoms in as-fabricated samples are located on non-lattice sites with little or no atomic short-range order. (8) As the amount of disorder can also be varied by milling time, the ageing study suggests that the changes in coercivity with milling time shown in Figure 1 are also a consequence of disorder in the sample.

A simplified depiction of the nanostructure produced by milling is shown in Figure 4. Grey areas represent crystalline $SmCo_5$ and white areas represent disordered Sm-Co.

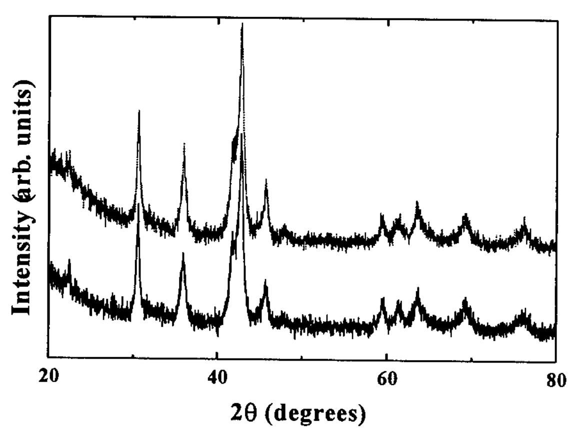

Figure 3: X-ray diffraction patterns for $SmCo_5$ milled for 15 minutes. The upper pattern was taken 400 hours after the lower pattern

Milling increases the volume fraction of glassy interphase. The formation of magnetically glassy materials by mechanical milling has been observed in materials such as $GdAl_2$. (1,9) The low-field susceptibility of milled $SmCo_5$ shows both a ferromagnetic component and the irreversibility expected of a magnetically glassy material. Interpretation of FC/ZFC data is complicated by the ferromagnetic contribution, which dominates the irreversible behavior in large fields.

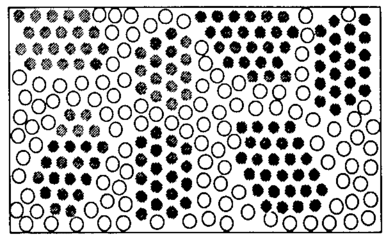

Figure 4: Nanostructure of milled $SmCo_5$. Grey areas represent crystalline $SmCo_5$ regions. White areas represent disordered Sm-Co.

CONCLUSION

Room-temperature ageing causes a decrease in the coercivity of mechanically milled $SmCo_5$ due to atomic-lever reordering. The ageing studies show that changes in coercivity as a function of milling time are correlated to the introduction of disorder and not changing diffracting crystallite size. Further investigation of the relationship between disorder and magnetism is important for fundamental understanding and for applications such as high-energy-product permanent magnetic materials.

ACKNOWLEDGMENTS

This work was supported by NSF grant OSR-925525 and AFOSR grant F49620-98-1-0098. We thank David J. Sellmyer for helpful comments and critical reading of this manuscript.

REFERENCES

1 G. F. Zhou and H. Bakker, Phys. Rev. B (1995) 52, 9437.
2 R. H. Kodama, A. E. Berkowitz, E. J. McNiff, Jr., and S. Foner, Phys. Rev. Lett. (1996) 77, 394.
3 A. R. Stokes, Proc. Phys. Soc. London (1948) 61, 382.
4 P. Ganesan, H. K. Kuo, A. Saavedra, and R. J. DeAngelis, J. Catalysis (1978) 52, 310.
5 D. L. Leslie-Pelecky, M. Bonder, T. Martin, E. M. Kirkpatrick, X. Q. Zhang, S.-H. Kim, and R. D. Rieke, accepted to IEEE Trans. Magn. (1998)
6 E. Hellstern, H. J. Fecht, Z. Fu, and W. L. Johnson, J. Appl. Phys. (1989) 65, 305.
7 R. E. Reed-Hill, *Physical Metallurgy Principles,* D. van Nostrand Company, New York City, NY, 1973).
8 J. Löffler and J. Weissmüller, Phys. Rev. B (1995) 52, 7076.
9 G. F. Zhou and H. Bakker, Phys. Rev. Lett. (1994) 73, 344.

Pergamon

NanoStructured Materials, Vol. 12, pp. 891–894, 1999
Elsevier Science Ltd

0965-9773/99/$–see front matter

PII S0965-9773(99)00260-3

STRUCTURAL CONFIGURATION AND MAGNETIC PROPERTIES OF THE RAPIDLY SOLIDIFIED CuCo ALLOY

E. Bonetti [a], L. Del Bianco [a], L. Savini [a], P. Tiberto [b], F. Vinai [b]

[a] Dipartimento di Fisica, Università di Bologna and Istituto Nazionale per la Fisica della Materia, Viale Berti Pichat 6/2, I-40127 Bologna, Italy

[b] Istituto Elettrotecnico Nazionale Galileo Ferraris and Istituto Nazionale per la Fisica della Materia, I-10125 Torino, Italy

Abstract *- The internal friction as a function of temperature and the giant magnetoresistance for varying magnetic field have been measured on* $Cu_{90}Co_{10}$ *ribbons obtained by planar flow casting with different quenching rate. The results are discussed considering the presence of quenched-in Co precipitates in the Cu matrix of the as-cast ribbons and different levels of dispersion of Co in the Cu matrix in the two cases.*

INTRODUCTION

The granular magnetic systems, consisting of nanometer-sized particles of a magnetic metal (e.g., Fe, Co) dispersed in a non-magnetic metallic matrix (e.g., Ag, Cu), have been extensively investigated in the last few years following the discovery of an effect of giant magnetoresistance (GMR), namely of a large change in the electrical resistance under an external magnetic field (1,2). Rapid solidification techniques have been exploited to produce bulk metastable solid solutions where superparamagnetic and ferromagnetic clusters may be developed by effect of suitable annealing treatments (2). The GMR effect is generally interpreted by the two-current model, based on spin-dependent scattering of conduction electrons at the magnetic/non-magnetic interfaces (3), according to which a homogeneous distribution of fine Co clusters is needed in order to obtain the best response. In this work, the problem of the influence of the synthesis parameters - in particular the quenching rate - on the state of dispersion of Co in Cu, in melt-spun ribbons, has been addressed by performing measurements of internal friction, through acoustic spectroscopy, and of GMR.

EXPERIMENTAL

Rapidly quenched $Cu_{90}Co_{10}$ alloys were obtained in ribbon form by planar flow-casting in a controlled He-atmosphere on a CuZr drum. Two different ribbons have been obtained varying the peripheral wheel velocity (WV) from 12 m/s to 22 m/s to produce samples with

different quenching rate; all other parameters were kept constant (as ejection pressure and crucible-to-wheel distance). The magnetoresistance was measured up to |H| = 20 kOe through a conventional four-contact technique. The magnetic field was applied in the ribbon's plane, perpendicular to the bias current (transverse configuration). The value of GMR for a given value of H was defined as $[(R(H) - R(H = 0))/R(H = 0)] \times 100$. The elastic energy dissipation coefficient (Q^{-1}or internal friction) was measured as a function of temperature on samples, cut from the ribbons in suitable dimensions, using a vibrating reed apparatus operating in the 10^2 - 10^4 Hz frequency range in a vacuum of 10^{-3} mbar (heating rate 3-4 K/min).

RESULTS

In figure 1, the internal friction as a function of temperature of the Cu-Co ribbons obtained with WV = 12 m/s (a) and 22 m/s (b) is shown. Two successive measurements from 300 K up to 850 K (first and second run) have been carried out on each sample. At room temperature, a low Q^{-1}, $(1 \div 3) \times 10^{-3}$, characterises the as-cast ribbons (full circles). A progressive increase of the internal friction with temperature is observed in both samples, but the background damping is remarkably lower in the 22 m/s ribbon. In the curves corresponding to the second runs (open circles), for both samples, the background damping follows a similar trend as in the first measurements. In the second run of the 22 m/s ribbon, a defined peak is well visible at about 570 K, hardly detectable in the first run. As regards the 12 m/s ribbon, only in the second run the presence of a peak is revealed by a slight inflexion of the rising curve starting from about 450 K, but its complete profile is not well defined, probably because of the high background. Representative GMR curves obtained at 300 K on the as-prepared samples are shown in figure 2. It is noteworthy that the two ribbons exhibit significantly different GMR values (2.76 % for the 12 m/s ribbon, 0.72 % for the 22 m/s one).

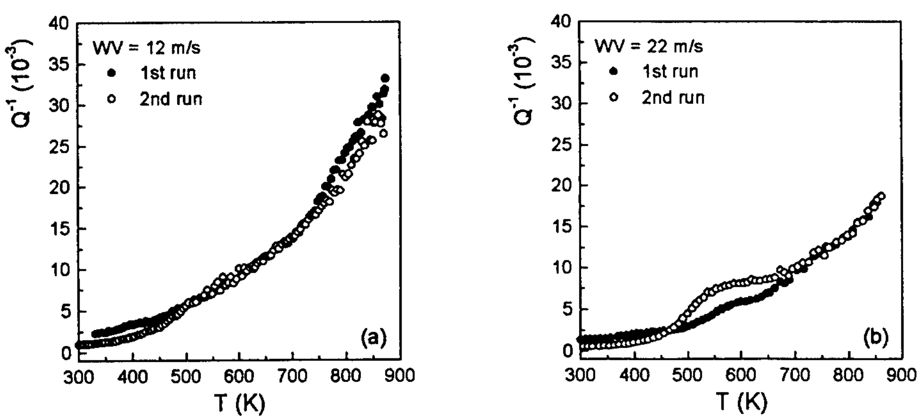

Figure 1. Internal friction (Q-1) as a function of temperature (T) of the CuCo alloys cast with peripheral wheel velocity (WV) of (a) 12 m/s and (b) 22 m/s. For each ribbon, two successive measurements are reported: first run (full circles) and second run (open circles).

DISCUSSION

Generally, in rapidly solidified materials, a very high quenching rate induces in the ribbon a better amorphous state and/or, as in the case of Cu-Co systems, solid solution (4). Actually, the magnetic hysteresis loops, usually measured on the as-cast Cu-Co ribbons (5), exclude that the starting material is an ideal solid solutions (in the sense of a complete atomic dispersion of Co in the Cu matrix) and rather display the coexistence of superparamagnetic and ferromagnetic features (6). In the present case, preliminary observations through transmission electron microscopy techniques indicate that, in the 12 m/s ribbon, a good dispersion of Co has been achieved whereas, in the 22 m/s sample, Co grains of dendritic origin have been found together with a detectable clustering of Co (7). In order to account for these unexpected results, it should be considered that, in some cases, the wheel velocity may act to avoid the ribbon contact with the rotating wheel. As a consequence, depending on the wetting capacity of the melt on the wheel, the sample cast at a lower peripheral velocity can reach a better solid solution state with respect to ribbons produced with higher WV. However, the presented results indicate that in neither case an ideal solid solution has been obtained. Coming to the internal friction results, the peak appearing in the second runs of measurement and only slightly visible (fig. 1b) or practically absent (fig. 1a) in the first runs, has been attributed to the anelastic grain boundary sliding process, in agreement with literature results and taking into account the frequency range we are operating in (8). The reduced peak relaxation strength, compared to polycrystalline Cu (9), may be explained considering the presence of small precipitates, finely distributed at the grain boundaries of the as-cast ribbons, which act as pinning centres against sliding. In fact, the relaxation strength is proportional to the sliding distance along the interfaces, namely to the average distance between the pinning centres. It has been reported that Co precipitates as small as 1 nm in diameter are sufficient to depress drastically the grain boundary peak in the Cu-Co system (10).

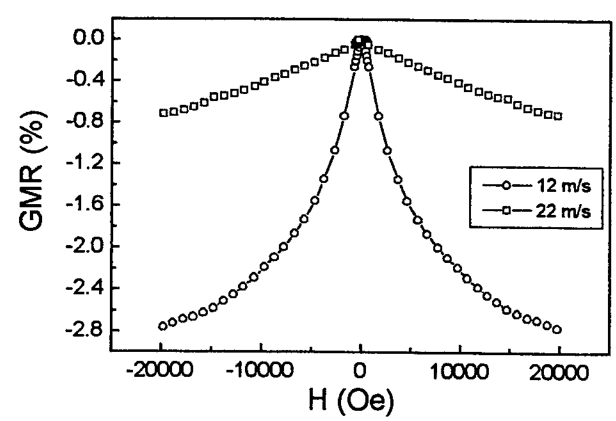

Figure 2. Giant magnetoresistance (GMR) as a function of the applied magnetic field (H) of the CuCo ribbons cast with WV = 12 m/s (circles) and 22 m/s (squares)

The first run of measurement, namely the thermal treatment up to 850 K, induces a coarsening of the Co precipitates at the grain boundaries leading to an increase in the sliding distance and therefore in the peak height, as indeed observed. As regards the background damping, it is generally strictly related to the presence and morphology of the dislocations. In this case, we find that the background is not affected by the thermal treatment, indicating that the dislocations links distribution is not strongly modified by annealing, and we observe a higher background in the 12 m/s ribbon. This last result may be accounted for considering the presence, in the 22 m/s as-cast sample, of Co clusters, actually detected by TEM (7), big enough as to hinder the dislocations movements: this effect results in a reduced elastic energy dissipation at high temperature in the 22 m/s ribbon with respect to the 12 m/s one.

Further evidence that the as-prepared alloys are not ideal solid solutions is provided by the existence, in both systems, of a measurable GMR effect (fig. 2). In particular, the highest GMR value has been observed in the ribbon cast with low WV. This possibly indicates that, in this case, the quenched-in Co particles are of lower mean diameter and are more homogeneously distributed with respect to the 22 m/s ribbon, in agreement with the hypothesis of a better Co dispersion.

In conclusions, the results reveal that a careful control of the synthesis parameters (in the specific case the WV) can lead to the nucleation of Co precipitates during the synthesis procedure and, in turn, to a good GMR value, already in the as-cast alloy. In fact, it is worth pointing out that the GMR measured in the 12 m/s as-cast sample is comparable to the best GMR values (about 4 %) generally obtained, after proper annealing treatments, in the 12 m/s and 22 m/s ribbons as well as in others $Cu_{90}Co_{10}$ alloys cast with intermediate WV (15 and 19 m/s) (5).

This work has been supported by the Consiglio Nazionale delle Ricerche (CNR) national project: "Giant Magnetoresistance in Nanostructured Materials".

REFERENCES

1. Berkowitz, J.R. Mitchell, M.J. Carey, A.P. Young, S. Zhang, F.E. Spada, F.T. Parker, A. Hutten, and G. Thomas, Phys. Rev. Lett. 68, 3745 (1992).
2. J. Wecker, R. von Helmolt, L. Schultz, K. Samwer, Appl. Phys. Lett. 62, 1985 (1993).
3. S. Zhang, Appl. Phys. Lett. 61, 1855 (1992).
4. H.S. Chen in *Amorphous Metallic Alloys* edited by F.E. Luborski (Butterworth, London 1983) p. 172.
5. E. Bonetti, L. Del Bianco, L. Savini, P. Allia, P. Tiberto, F. Vinai, Mater. Science Forum 269-272, 925 (1998).
6. P. Allia, M. Knobel, P. Tiberto, F. Vinai, Phys. Rev. B 52, 15398 (1995).
7. E. Bonetti, M. Vittori, to be published.
8. Nowick, B.S. Berry, *Anelastic Relaxation in Crystalline Solids*, Academic Press, New York, 1972.
9. E. Bonetti, L. Pasquini, E. Sampaolesi, L. Savini, J. Non Crystal. Sol. (1998), in press.
10. D.T. Peters, J.C. Bisseliches, J.W. Spretnak, Trans. AIME 230, 530 (1964).

Pergamon

NanoStructured Materials, Vol. 12, pp. 895–898, 1999
Elsevier Science Ltd

0965-9773/99/$–see front matter

PII S0965-9773(99)00261-5

MECHANICAL BEHAVIOUR OF NIAL AND NI$_3$AL ORDERED COMPOUNDS ENTERING THE NANO-GRAIN SIZE REGIME

E.Bonetti, E.G.Campari, L.Pasquini, E.Sampaolesi, G.Scipione
Dipartimento di Fisica dell'Università di Bologna and Istituto Nazionale per la Fisica della Materia, viale Berti-Pichat 6/2, I-40127 Bologna Italy. E-mail: bonetti@df.unibo.it

Abstract—*The elastic energy dissipation and dynamic modulus of several intermetallic compounds with the NiAl (B2) and Ni$_3$Al (L1$_2$) composition and different grain sizes were measured. The grain dimensions were deduced by XRD data analysis. These alloys exhibit a temperature increasing background damping which raises faster as the grain size enter the nanometric regime. The elastic modulus of out of stoichiometry single crystals increases up to 20 % with temperature in a reproducible manner.* *©1999 Acta Metallurgica Inc.*

INTRODUCTION

Ordered intermetallic Ni-aluminides have stimulated much scientific interest in recent years for their unusual mechanical behavior. Different approaches have been undertaken as regard the possibility to obtain an increase of the low temperature ductility, which limits the technological applications of these compounds (1). Significant improvements in ductility have been attained by alloying with Fe, Hf, Ti and Mo or through the grain refinement (2). By a strong reduction of the grain size and, therefore, reducing dislocation activity and enhancing interface diffusive processes, it is expected that different mechanisms may control the deformation at all regimes from anelastic to viscoplastic.

The present work reports some results regarding a more extensive program aiming to study via mechanical spectroscopy the anelastic and plastic behavior of Ni-Al compounds with different microstructures.

EXPERIMENTALS

Nanocrystalline (n-) compounds were produced by ball-milling (MA) coarse-grained powders of the composition reported in Table 1, while the corresponding single crystals (SC) were grown along the (110) direction in a Bridgman oven. The specimens for anelasticity measurements were obtained, respectively, by cold pressing the milled powders in a constructed die with a rectangular section, while the SC were cut into bars by electroerosion. X Ray Diffraction (XRD) measurements were performed by a Philips PW1710 vertical powder diffractometer, using Cu-Kα radiation and a graphite monochromator in the diffracted beam. The data were analyzed with the Rietveld code GSAS. The internal friction measurements were performed using a vibrating reed apparatus with electrostatic drive and with a resonance

frequency in the $10^2 \div 10^4$ Hz range. The apparatus is equipped with a vacuum system and an oven with the maximum temperature of 1300 K.

RESULTS AND DISCUSSION

In Table I are reported some data regarding two SC (#1, #3), with different compositions and the same kind of structure, and the corresponding mechanical alloyed powders. In this last case, for the composition labeled #2 the Rietveld refinement performed on the XRD spectra shows the development of two different n-Ni(Al) solid solutions (ss), one with equiatomic composition and the other with a higher Ni content. Upon annealing, both ordering and grain growth took place in all the mechanical alloyed powders.

The internal friction exhibited by some representative specimens of various alloys with the Ni_3Al and NiAl ordered structure is shown in figure 1. The alloys investigated are produced out of stoichiometry and contain a variety of other elements, such as Fe, Hf and Ti, usually added with the purpose to improve the mechanical properties of the Ni-Al system. Despite their differences in composition and phases, the elastic energy dissipation behavior of all these alloys can be framed into a general scheme, with a background increasing with the reduction of the grain dimensions from SC to microcrystals and nanocrystals. As reported in figure 1, the n-specimens have an increasing internal friction background, which can be fitted with an exponential. The pure coarse grained Ni_3Al background has a similar trend, with a lower growth rate. This behavior agrees with the results found in pure n-Ni and n-Al.

TABLE 1

Phase analysis performed with Rietveld method for the as-milled powders and for the products after internal friction measurements (#2, #4, #5). The table reports also the data of SC (#1, #3).

Composition (at.%)	Minor elements (at.%)	Synthesis	Phase Analysis (wt.%)		Grain size (nm) MA powders
			As synthesized	After ageing	
#1 $Ni_{54.1}Al_{30.1}Fe_{14.5}$	Hf: 0.5 Al_2O_3: 0.4 Y_2O_3: 0.4	Bridgman oven	NiAl single crystal + precipitates.	NiAl single crystal + precipitates.	
#2 $Ni_{54}Al_{29.5}Fe_{13.3}$	Hf: 1.1 Zr: 0.3 B: 1.4	Mechanical alloying for 30h	Ni(Al) (ss): $Ni_{50}Al_{50}$ 71 ± 5 $Ni_{75}Al_{25}$: 29 ± 5	NiAl: 76 ± 2 Ni_3Al 24 ± 3	NiAl 5-10 Ni_3Al 15-20
#3 $Ni_{56.2}Al_{43.1}Fe_{0.3}$	Ta: 0.3 Mo: 0.1	Bridgman oven	NiAl single crystal + precipitates.	NiAl single crystal + precipitates.	
#4 $Ni_{49}Al_{47.7}Ti_{1.4}$	Mo: 0.6 Al_2O_3: 1.3	Mechanical alloying for 7h	Fcc Ni: 70 ± 1 Fcc Al: 29 ± 1 α-Ti: 1± 0.1	NiAl: 86 ± 1 Ni_3Al: 8 ± 1 Fcc Ni: 4 ± 0.5 α-Ti: 2 ± 0.8	Ni 100-150 Al 300-400
#5 Ni_3Al		Arc oven	Ni_3Al 100	Ni_3Al 100	Ni_3Al ≈ 10^4

A further reduction in the damping occurs in the case of the SC, whose anelastic spectra reveal a peak at 1080 K, which is absent in the n-specimens. This peak is in the temperature range of those observed by other authors in stoichiometric NiAl after deformation (3). It may be tentatively attributed to dislocation-intrinsic point defects relaxation (Snoek-Köster type relaxation), in which costitutional vacancies or antisite atoms pin the dislocations. An explanation for the background damping must take into consideration the grain boundaries, that play an important role, together with other defects such as dislocations, in affecting its trend. When the grain sizes are of the order of nanometers, while dislocations are removed the percentage of grain boundaries increases (as $1/D^2$, with D the grain diameter); therefore the grain boundary mobility become the main dissipation term. Furthermore, it has been found that in n-materials the grain boundary mobility is enhanced with respect to that of ordinary policrystals (4).

All the spectra are reproducible, with the partial exception of the as milled specimens. Due to the milling process, during the first thermal run irreversible relaxation processes occur (5). This is shown for the elastic modulus in figure 2, where the curve for the specimen #4 has an upward trend with the temperature between 700 K and 900 K. As a result of the heating up to 1200 K, which also slightly increases the grain size, this out-of-equilibrium behavior is removed, leaving a monotonous decreasing trend with temperature as shown for the Ni_3Al microcrystalline specimen #5. Moreover, in figure 2 the dynamic modulus trend of the NiAl SC #3 shows an uncommon behavior (also found for the composition #1): its modulus is raising with temperature in all the range explored, with the exception of that including the internal friction peak, where a modulus defect, accompanying the peak of figure 1, occurs.

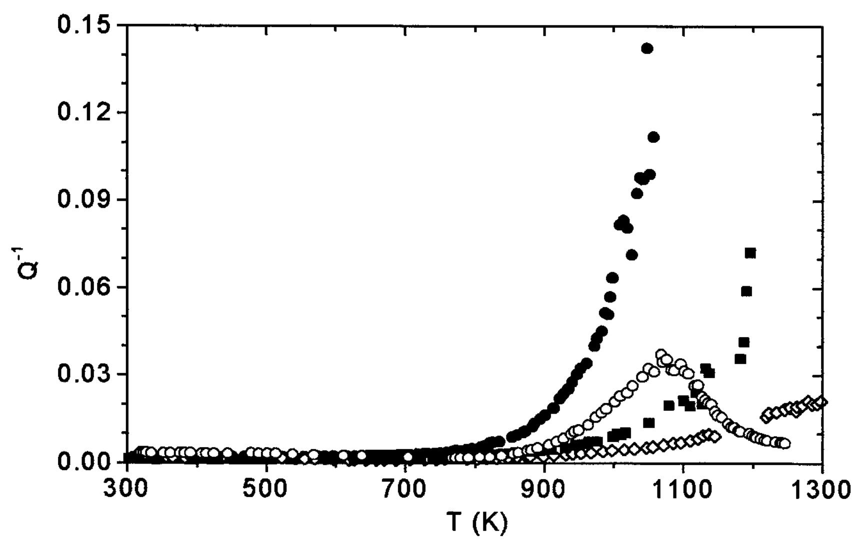

Figure 1 Elastic energy dissipation (Q^{-1}) as a function of temperature of the samples #2 (●),#3 (O),#4 (■), #5 (◊), see Table 1. Resonance frequencies at 300 K: #2, 722 Hz; #4, 2835Hz; #3, 183 Hz; #5, 2845 Hz. Data collected with temperature raising at about 3 K/min.

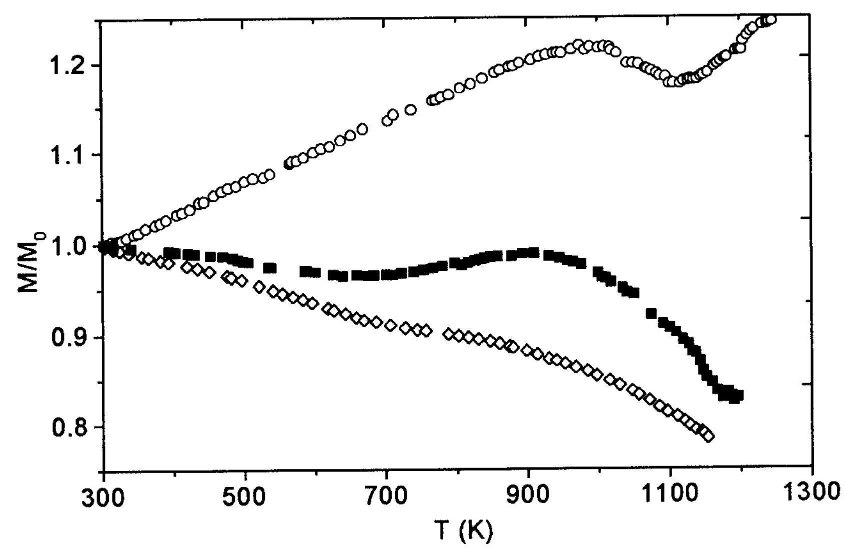

Figure 2 Dynamic Elastic Modulus (M) as a function of temperature of the specimens #3 (O),#4 (■), #5 (◊), in the same experimental conditions reported for figure 1. In all curves the Modulus is normalized to its room temperature value (M_0).

This is a stable feature, which was never observed in stoichiometric ordered NiAl SC. Its origin can be tentatively attributed to the dislocation pinning by defects presents in the out of stoichiometry crystal compositions (6). Work is in progress to better understand this unique behavior. In conclusion, the effects on the mechanical properties of the grain refinement were analyzed and the results seem to indicate an enhancement of the grain boundary mobility in n-intermetallic compounds.

ACKNOWLEDGEMENTS

The authors whish to thank Dott. O. Tassa and C. Testani of centro Sviluppo Materiali for useful discussions and providing the specimens. The author's work was funded in the framework of the MURST Piano Nazionale Materiali – Tema 11.

REFERENCES

(1) R.Darolia, JOM, 1991, 43, 44.
(2) T.Haubold, R.Bohn, R.Birringer and H.Gleiter, Mater. Sci. Eng., 1992, A153, 679.
(3) M.Hirscher, E.Schweizer, M.Weller and H.Kronmüller, Phyl. Mag.Lett., 1996, 74, n.3, 189.
(4) E.Bonetti, G.Scipione, R.Frattini, S.Enzo and L.Schiffini, J. Appl. Phys. 1996, 79, 10, 7537.
(5) E.Bonetti, E.G.Campari, L.Pasquini and E.Sampaolesi: J. Appl. Phys. In press.
(6) S.B.Kustov, S.N.Golyandin, I.Hurtado, J.vanHumbeek and R.de Batist: J. De Physique IV Colloque C8 1996, 6, 389.

Pergamon

NanoStructured Materials, Vol. 12, pp. 899–902, 1999
Elsevier Science Ltd

0965-9773/99/$–see front matter

PII S0965-9773(99)00262-7

MÖSSBAUER STUDY OF THE NANOCRYSTALLINE $Fe_{80}Ti_7B_{12}Cu_1$ ALLOY

A. Grabias, M. Kopcewicz and B. Idzikowski*
Institute of Electronic Materials Technology, Wólczyńska 133, 01-919 Warszawa, Poland
*Institute of Molecular Physics, Polish Academy of Sciences,
M. Smoluchowskiego 17, 60-179 Poznań, Poland

Abstract -- *A combined conversion electron and γ-transmission Mössbauer spectroscopy is applied to investigate the differences in the surface and bulk crystallization of the amorphous $Fe_{80}Ti_7B_{12}Cu_1$ alloy. The radio-frequency (rf) induced effects (rf collapse and sidebands) are used to study the magnetic properties (anisotropy fields, magnetostriction) of the amorphous and nanocrystalline phases. Rf-Mössbauer experiment allowed us to distinguish soft magnetic nanocrystalline bcc-Fe phase from the microcrystalline α-Fe.* ©*1999 Acta Metallurgica Inc.*

INTRODUCTION

The nanocrystalline iron-based ternary alloys have attracted recently a significant attention because of their superior magnetic properties as compared to FINEMET alloys (1). In this study the structure and magnetic properties of the amorphous and nanocrystalline $Fe_{80}Ti_7B_{12}Cu_1$ alloys are investigated by Mössbauer spectroscopy. In order to compare the crystallization induced by annealing in the bulk and at the surface of the sample we used the combined γ-transmission and conversion electron (CEMS) Mössbauer technique (2), which allows the simultaneous study of the bulk and of the surface layer (about 100 nm deep). The magnetic properties have been investigated by an unconventional technique combining the Mössbauer effect with phenomena induced by an external radio-frequency (rf) magnetic field (rf collapse and sidebands) (3). The collapse of the magnetic hyperfine structure occurs due to fast magnetization reversal induced by the rf field, as a result of which the hyperfine field is averaged to zero at the Mössbauer nuclei though the sample remains in the ferromagnetic state. The rf collapse is very sensitive to small changes of the local magnetic anisotropy, allowing the distinction of the soft nanocrystalline bcc-Fe phase from the microcrystalline α-Fe, whose magnetic anisotropy is significantly larger than that of the nanocrystals (4). The rf sideband effect, directly related to magnetostriction, permits the observation of the reduction of magnetostriction, when the nanocrystals are formed (4).

EXPERIMENTAL

The $Fe_{80}Ti_7B_{12}Cu_1$ amorphous ribbon was prepared by the melt-spinning technique in an Ar atmosphere. The ribbons were about 25 μm thick and 3.5 mm wide. In order to obtain the

nanocrystalline structure the amorphous ribbons were annealed for 1 hour at $T_a = 440$, 470, 520, 570 and 620°C. The CEMS and transmission Mössbauer measurements were performed for the as-quenched and annealed samples. The rf-Mössbauer spectra were measured for the $Fe_{80}Ti_7B_{12}Cu_1$ samples exposed to the rf field of 61 MHz with intensities $H_{rf} = 0 \div 12$ Oe.

RESULTS

The Mössbauer transmission and emission (CEMS) spectra recorded for the as-quenched and annealed $Fe_{80}Ti_7B_{12}Cu_1$ alloys are shown in Fig. 1. The spectra of the as-quenched ribbon are typical for ferromagnetic amorphous alloys (Figs. 1a, 1a'). However, there are traces of the crystalline phase at the surface of the as-quenched ribbon (less than 2% of the total spectral area, Fig. 1a'). Both spectra were fitted by the hyperfine field distribution, P(H), method (5). The transmission and CEMS spectra of all annealed samples reveal, in addition to the P(H) component related to the amorphous phase, a discrete spectral component – a sextet with the hyperfine field H_{hf} =32.95 T and isomer shift of 0.00 mm/s, corresponding to the bcc-Fe phase (Figs. 1b-1e, 1b'-1e').

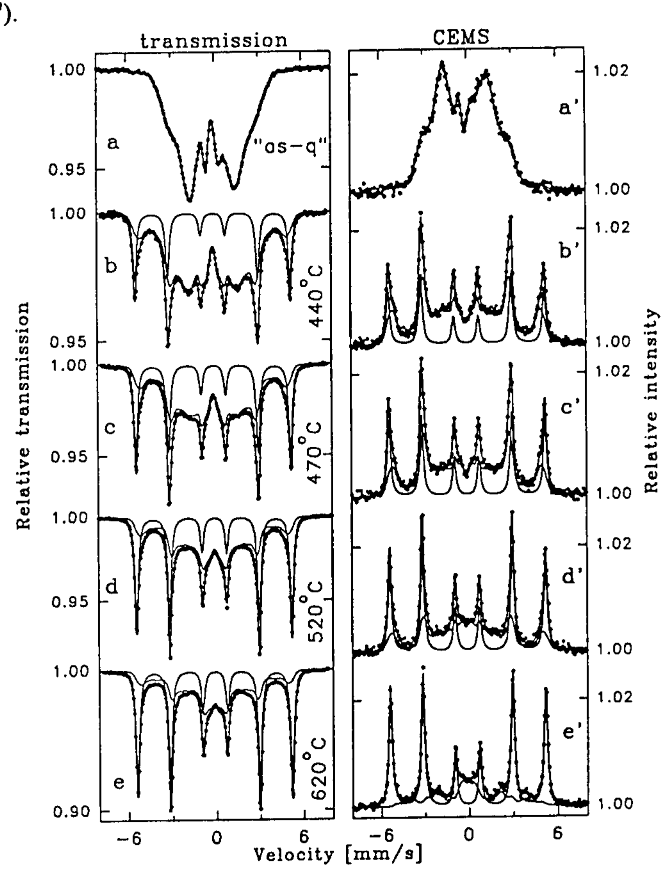

Fig. 1. Mössbauer spectra recorded for the as-quenched and annealed $Fe_{80}Ti_7B_{12}Cu_1$ alloys: (a-e) transmission; (a'-e') CEMS (shiny side of the ribbons).

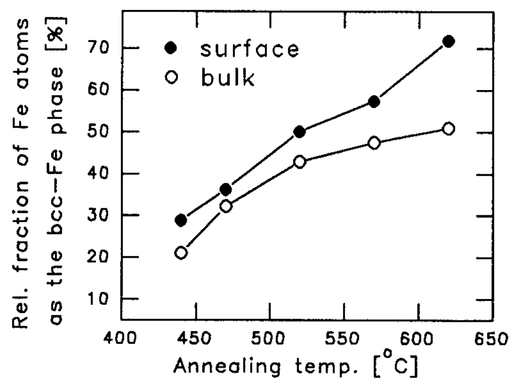

Fig.2. The relative abundance of the bcc-Fe phase in the bulk and at the shiny surface of the $Fe_{80}Ti_7B_{12}Cu_1$ sample.

The relative spectral contribution of this sextet increases with increasing annealing temperature at the expense of the P(H) component, indicating the increase of the volume fraction of the bcc-Fe phase. Transmission spectra of the annealed samples (Figs. 1b-1e) are similar to the corresponding CEMS spectra (Figs. 1b'-1e'). However, by determining the relative abundance of each phase, directly related to the area of a given spectral component, one can see the difference between the amount of the bcc-Fe phase in the bulk and in the surface layer of the sample (Fig. 2). The crystalline phase is more abundant at the surface than in the bulk of the sample at each annealing temperature.

The Mössbauer spectra measured during the exposure of the samples to the 61 MHz field ranging from about 4 to 12 Oe are shown in Fig. 3. A complete collapse of the magnetic hyperfine structure, seen in Fig. 1a, to a quadrupole doublet is observed only for the as-quenched fully amorphous alloy for $H_{rf} \geq 6$ Oe (Figs. 3a-3c). The collapsed doublet broadens markedly at 4 Oe (Fig. 3d), suggesting that the effective magnetic anisotropy of the as-quenched alloy is comparable to 4 Oe. The rf-collapsed central doublet is accompanied by the rf sidebands, what indicates that the as-quenched alloy is magnetostrictive.

The spectra of the nanocrystalline samples recorded at H_{rf} =12 Oe reveal, in addition to the central collapsed quadrupole doublet related to the amorphous matrix, a partly narrowed magnetic component corresponding to the bcc-Fe grains, whose magnetic anisotropy is large enough to partially suppress the rf collapse effect (Figs. 3a', 3a"). The rf induced reduction of the bcc-Fe average hyperfine field, as compared with H_{hf}=32.95 T characteristic of the α-Fe, strongly suggests that the bcc-Fe phase is nanocrystalline with the anisotropy field much smaller than that in the bulk α-Fe, for which such a rf field does not induce any narrowing. The least narrowed magnetic component is observed for the alloy annealed at 440°C (the average $H_{hf} \approx 28$ T, Fig. 3a'). Much larger volume fraction of the bcc-Fe phase formed at higher annealing temperatures (Fig. 2) is reflected in the rf-Mössbauer spectra by the increase of the spectral contribution of the magnetic component (compare Fig. 3a' with Fig. 3a"). The average hyperfine field of the partially collapsed magnetic component decreases to $H_{hf} \approx 25$ T for the sample annealed at 470°C and stabilizes at about 26 T for $T_a \geq 520$°C (e.g. Fig. 3a"). This means that the magnetic anisotropy of the bcc-Fe nanograins formed in the sample at the

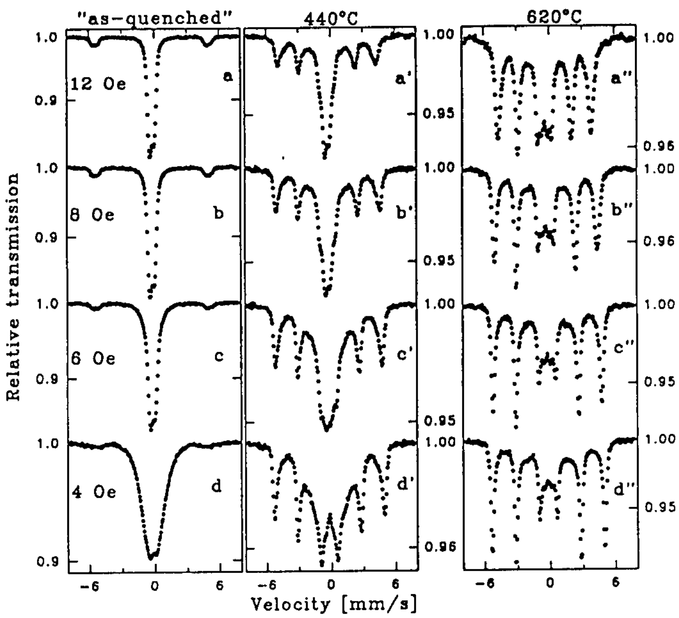

Fig.3. Mössbauer spectra recorded as a function of the rf field intensity for the as-quenched (a-d), annealed at 440°C (a'-d') and 620°C (a"-d") $Fe_{80}Ti_7B_{12}Cu_1$ alloy.

early stage of crystallization (after annealing at 440°C) is somewhat larger than of those formed at $T_a \geq 470°C$. Annealing at $T_a = 520 \div 620°C$ leads to the formation of the bcc-Fe grains with a similar magnetic anisotropies.

The decrease of the rf field intensity causes a gradual broadening of the partially collapsed magnetic component (Figs. 3a'-3c' and 3a"-3c") until the value of 32.95 T is reached for the $H_{rf} = 4$ Oe field (Figs. 3d', 3d"). On the other hand the central collapsed quadrupole doublet related to the retained amorphous phase remains unchanged (Figs. 3a'-c'). Hence, the rf-Mössbauer measurements performed as a function of the rf field intensity reveal significantly larger anisotropy fields in the nanocrystals than in the amorphous matrix. Since the magnetic anisotropy of the bcc-Fe grains is directly related to their sizes, the dependence of the shape of the collapsed spectra on the rf field intensity suggests fairly narrow distribution of the bcc-Fe grain sizes.

ACKNOWLEDGEMENTS

Financial support from the Grant No. KBN 2P03B 068 15 from the Polish Committee of Scientific Research is gratefully acknowledged.

REFERENCES

1. Makino, A., Hatanai, T., Inoue, A., Masumoto, T., Mat. Sci. Eng., 1997, A226-228, 594.
2. Kopcewicz, M. and Grabias, A., J. Appl. Phys., 1996, 80, 3422.
3. Kopcewicz, M., Structural Chem., 1991, 2, 313.
4. Kopcewicz, M., Grabias, A., Williamson, D.L., J. Appl. Phys., 1997, 82, 1747.
5. LeCaer, G. and Dubois, J.M., J. Phys. E, 1979, 12, 1083.

Pergamon

NanoStructured Materials, Vol. 12, pp. 903–906, 1999
Elsevier Science Ltd

0965-9773/99/$–see front matter

PII S0965-9773(99)00263-9

DAMPING FACTORS OF DE HAAS-VAN ALPHEN OSCILLATIONS IN THE VORTEX STATE OF SUPERCONDUCTING MULTILAYERS

V.M.Gvozdikov, M.V. Gvozdikova
Department of Physics, Kharkov State University, 310077, Kharkov, Ukraine

Abstract *-- We have considered microscopically de Haas van Alphen (dHvA) oscillations in a vortex-lattice (VL) state of layered superconductors and shown that factors of damping of these oscillations are: a) additional electron scattering on VL imperfections, resulting in a Dingle-like exponential factor depending on the order parameter and magnetic field, H, b) Landau level broadening into dispersive bands caused by periodic VL, c) the energy gap at the Fermi level, d) the layer-factor, depending on the stacking of the layers. Factors b)-d) damp dHvA amplitudes in a nonexponential fashion. In particular, the factor d) modulating dHvA oscillation due to the layered structure of superconductors is determined by the one-dimensional density of states, g(E), related with the electronic transport across the layers. It is periodic function in 1/H with frequencies depending on location of singularities in g(E) (van Hove singularities and the ones due to the stacking faults).* *©1999 Acta Metallurgica Inc.*

INTRODUCTION

The dHvA effect, have been reported in a number of different types superconductors: the layered, the strongly-coupled *A-15* compounds, the organic molecular, and the high-T_c. Although first observation of the dHvA effect in superconductors was made by Graebner and Robbins in 1976, it took nearly two, decades before undertaking systematic explorations of this phenomenon. Currently, a considerable literature on the theory of this phenomenon exists (see a review (1) for references). All theories, in full accordance with experiments, agree that period of dHvA oscillations below the upper critical field, H_{C2}, does not change. A consent has not been yet achieved about the form and mechanisms of damping of dHvA oscillations because of the rich physics beyond this damping. Recent experiments (2-4) indicate conclusively that dHvA oscillations in superconductors persist in the vortex-state down to surprisingly low fields (equal to $H \approx 0.2H_{C2}$ in borocarbide YNi_2B_2C). The oscillation amplitude is strongly suppressed in a field region immediately below H_{C2} and recover at lower field (3). Such a behavior implies competition between different mechanisms of damping of dHvA oscillations due to VL, layer structure, spatial periodicity of the order parameter, and external magnetic field. To consider the corresponding damping factors and compare results with the recent experiments is the purpose of this paper.

THE FREE ENERGY OSCILLATIONS IN THE VORTEX STATE

The free energy can be calculated with the help of a well-known formula

$$F=\int dr\frac{|\Delta(\vec{r})|^2}{\lambda}-2T\sum_{N,\xi,k}\int_{-\infty}^{\infty}d\omega\rho_{NN}(\omega,\xi,k)\ln\left[2\cosh\left(\frac{\omega}{2T}\right)\right], \qquad [1]$$

Δ is the order parameter, λ is the BCS coupling constant and ρ_{NN} is the spectral density

$$\rho_{NN}(\omega,\xi,k)=\frac{1}{\pi}\left[u_{Nk}^2\frac{\nu}{\nu^2+(\omega+E_N(k,\xi))^2}+v_{Nk}^2\frac{\nu}{\nu^2+(\omega-E_N(k,\xi))^2}\right]. \qquad [2]$$

This quantity is the imaginary part of the diagonal matrix element of the Green function in the Landau-level (LL) basis, where

$$\nu=\hbar/\tau+\hbar/\tau_{\text{int}}(\Delta,\tau)+\hbar/\tau_s(\Delta), \qquad [3]$$

is the LL smearing and $E_N(k,\xi)$ is the energy spectrum within the N-th Landau band. Variable k is the quasi-momentum of the Landau band. u_{Nk} and v_{Nk} are the Bogoliubov-de Gennes functions. These bands appear due to the lift of the LL degeneracy by the VL and other periodic perturbations. ξ is the kinetic energy associated with the electron motion across the layers (i.e. along the external magnetic field). Contrary to the case of periodic VL, which broadens LLs into dispersive Landau bands, pinned and/or melted VL acts as a random factor and smears LLs. This smearing, [3], consists of the three terms caused respectively by the quasiparticle scattering on a crystal lattice, $\hbar/\tau$, on the VL, $\hbar/\tau_s \sim \Delta^2/H^{1/2}$, and the "interference" term, $\hbar/\tau_{int} \sim \Delta^2/H\tau$, which vanishes in the limit $\tau\to\infty$ and when $\Delta=0$.

The quantity $E_N(k)$ generally is very difficult to calculate. In the diagonal approximation, valid near H_{c2}, where $\Delta \ll \hbar\Omega$ (Ω is the cyclotron frequency)

$$E_N(k)=\sqrt{\varepsilon_N^2+\Delta(k)^2}\ . \qquad [4]$$

Here $\varepsilon_N=h\Omega(N+1/2)-\mu$ (μ is the chemical potential) and $\Delta(k)=|F_{NN}(k)|$ stands for the diagonal pairing matrix element of the order parameter in the Landau-Bloch representation. In the case of periodic modulation either Δ or magnetic field in some direction within the planes of a multilayer

$$E_N(k)=\sqrt{\varepsilon_N^2+\Delta^2}+e^{-\frac{H^*}{H}}\left[A_N+B_N\cos(2\pi l_a k)\right]. \qquad [5]$$

The coefficients A_N and B_N depend on Δ and particular choice of periodic perturbations. $H^*=\pi\Phi_0/2a^2$, $l_a=l^2/a$ where l is the magnetic length, and Φ_0 is the flux quantum.

Well below H_m the diagonal approximation breaks down and off-diagonal pairing should be taken into account. Generally, it is yet unresolved problem, but it can be solved within the model approximation implying an exponential decrease of the pairing matrix element

$$\Delta_{nm}=\Delta_0\exp(-\alpha|n-m|), \qquad [6]$$

where α is some positive constant. In the quasiclassical approximation $(2\pi\Delta \gg h\Omega)$ the energy spectrum is

$$E_n(k)=\sqrt{\Delta_0^2+\xi_n^2(k)}, \qquad [7]$$

$$\xi_n(k) = \varepsilon_n + (-1)^n (\hbar\Omega / \pi) \arcsin(\rho \cos ka), \qquad [8]$$

$$\rho = \exp(-2\pi\Delta \tanh \alpha / \hbar\Omega). \qquad [9]$$

After standard calculations of the oscillating part of the free energy [1] with the help of [2], we have

$$F_{osc} = \frac{4\pi T}{\hbar\Omega} \sum_{p=1}^{\infty} (-1)^p \cos\left(2\pi p \frac{\mu}{\hbar\Omega}\right) I_p \Psi(\nu, \Delta, z_p), \qquad [10]$$

$$\Psi(\nu, \Delta, z_p) = g\Psi(\nu, z_p) + \int_{z_p}^{\infty} dz \Psi(\nu, z) \frac{\partial}{\partial z} \sum_k J_0\left(\frac{\Delta(k)}{\hbar\Omega} \sqrt{(z\hbar\Omega)^2 - (2\pi p)^2}\right). \qquad [11]$$

Here $z_p = 2\pi p/\hbar\Omega$, $g = \Phi/\Phi_0$ being the degeneracy factor, (Φ is the flux through a sample)

$$\Psi(\nu, z) = \exp(-\nu z) / z \sinh(\pi T z). \qquad [12]$$

Using the Bessel function relation $dJ_0/dz(z) = J_1(z)$ one can rewrite [11] in the form which explicitly displays the negative sign of the second term in the amplitude $\Psi(\nu,\Delta,z_p)$. This term depends on the order parameter and appears only below H_{c2}. For $H>H_{c2}$ the amplitude [11] reduces to the first term, $g\Psi(\nu,z_p)$, describing the standard picture of dHvA oscillations in normal metals, damped by the Dingle factor $exp(-\nu z_p)$. For fields below H_{c2}, i.e. in the VL state, the amplitudes of oscillations decreases, while the period of dHvA oscillations, in full accordance with the experiments, remains intact. The additional damping in the superconducting state arises owing to the two major contributions from the VL. The first one is due to the additional scattering of electrons on a VL. It acts via the Dingle factor which decreases with the enhancement of Δ. Another mechanism of damping is determined by the last term in [11]. In case [5] an additional factor appears in [11] ($\Psi(\nu,z) \to I^*(z)\ \Psi(\nu,z)$)

$$I^*(z) = J_0\left(Bz \exp(-H^* / H)\right) \cos\left(Az \exp(-H^* / H)\right). \qquad [13]$$

In the case of diagonal approximation [6] we have for the first three harmonics with $p=1,2,3$, we have

$$\hat{I}_1(\rho) = 1 - \rho^2, \qquad \hat{I}_2(\rho) 1 - 4\rho^2 + 3\rho^4, \qquad \hat{I}_3(\rho) = 1 - 9\rho^2 + 18\rho^4 - 10\rho^6. \qquad [14]$$

These factors appear in dHvA oscillation of periodic coherent magnetic breakdown system (5), where $\rho = exp(-H_0/H)$ is the magnetic breakdown probability. In our case the "breakdown field" equals to $H_0 = 2\pi\Delta_0 \tanh \alpha$. We would like to note a remarkable property of the factors [14]: they enhance with the decrease of the field H. Physically this is because Landau bands become narrower when the VL grow thinner.

The dependence of dHvA oscillation amplitudes on the magnetic field in [10] is also related to the factor I_p , This factor is a Fourier transform (on variable z_p) of a 1D density of states, $g(\varepsilon)$, associated with the electron motion along the magnetic field. Thus, any singularity or narrow δ-peak in $g(\varepsilon)$ located at some energy ε_0 makes the factor I_p to be an oscillatory function of the reciprocal field $1/H$. Experimental detection of these oscillations provides a basis for measurements of the ε_0 and thereby to the restoration of the density of states $g(\varepsilon)$. In case of layered sample with a small concentration of stacking faults new oscillations appear.

The frequency of these oscillations depends on the local value of the overlap integral near the stacking fault, σ_f. For small concentrations of stacking faults, c, the factor I_p can be written as

$$I_p = (1-c)J_0(2z_p\sigma) + c\delta I_p, \qquad [15]$$

where δI_p has an exponential Dingle-like form (for $\sigma > \sigma_f$)

$$\delta I_p = \exp\left[-z_p\left(\sigma^2 - \sigma_f^2\right)^{\frac{1}{2}}\right]\cos\left(2\sigma_f z_p\right). \qquad [16]$$

Oscillations of the factor I_p in reciprocal field modulate dHvA oscillations in layered crystals. They are independent of the order parameter and hence survive above T_c in the normal state.

SUMMARY AND CONCLUSIONS

Consider now briefly connection between the results of this paper and current experiments on dHvA effect in the mixed state. The experiments (2-4) show that immediately after crossing H_{c2} there is a region, down to a some field H_m, where dHvA oscillations are damped, but then recover at lower fields $H<<H_m$. In borocarbide YNi_2B_2C at very low temperature $T=0.05K$ damping within the interval $H_{c2}<H<H_m$ is much larger than predicted by any of existing theories (3). We can explain this by noting that according to modern view on the H-T phase diagram in layered systems the VL is melted in the field region $H_{c2}<H<H_{melt}$ immediately below the H_{c2}. In this field interval a "vortex matter" is in the liquid or glassy state so that the most adequate approach to the dHvA effect in this region is the one given by Maki-Stephen, which treat the VL as a random quantity. We can relate the extra damping observed in this region to the interference Dingle factor $exp(-\pi/\Omega\tau_{int})$ calculated above. Further decrease in H recovers a regularity of the VL and switched off the Maki-Stephen mechanism of damping when $H<<H_m$. The periodic VL lifts up the degeneracy of the Landau levels and broad them into the Landau bands. As far as the damping of dHvA amplitudes caused by the Landau bands, [10], is less than Dingle exponent, the corresponding attenuation of oscillations is less than that given by existing theories. Such a crossover from a relatively strong damping just below H_{c2} to a weaker attenuation of dHvA amplitudes have been observed in a number of works (2-4). From all these works, only the most low-temperature measurements made in (3) at $T=0.05K$ show that this crossover is closely related to the vortex pinning. Strong damping below the H_{c2} takes place in the peak-effect-region (with maximal damping at about 6.2 T) while within the interval from 2T to about 4T both pinning and attenuation of dHvA oscillations are relatively small (3). This picture is in a qualitative agreement with our approach.

REFERENCES

1. Wasserman A., Springford M., Advances in Physics, 1996, 45, 471
2. Harrison N., Hayden S., Meeson P., et al., Physical Review B, 1994, 50, 4208
3. T.Terashima, C.Haworth, H.Takeya et al., Physical Review B, 1997, 56, 5120
4. Goll G., Heinke M., Janssen A. et al.,Physical Review B, 1996, 53, 8871
5. Gvozdikov V.M., Fiz. Nizk. Temp., 1986, 12, 705 [Sov.J.Low. Temp Phys., 1986, 12, 399]
6. Gvozdikov V.M., Fiz. Tverd. Tela, 1984, 26, 2574 [Sov. Phys.Solid State, 1986, 26, 1560]

Pergamon

NanoStructured Materials, Vol. 12, pp. 907–910, 1999
Elsevier Science Ltd

0965-9773/99/$–see front matter

PII S0965-9773(99)00264-0

3D TRANSITION FERROMAGNETIC METAL NANO-CRYSTALS PREPARED WITH GAS DEPOSITION METHOD (GDM)

Yuji Sasaki, Manabu Hyakkai, Eiji KITA, Hisanori Tanimoto[a] and Akira Tasaki
Institute of Applied Physics and TARA, University of Tsukuba, Tsukuba 305-8573, JAPAN
[a]Institute of Materials Science and TARA, University of Tsukuba, Tsukuba 305-8573, JAPAN

Abstract -- *The application of gas deposition method (GDM) to the formation of 3d transition metal nano-crystals and their structure is reported. A He circulation system was installed in order to purify the inert gas used during the preparation. The metals of Fe, Co, and Ni were evaporated by RF heating using a ZrO_2 linear set in a tungsten crucible and a carbon crucible. X-ray diffraction study reveals the same crystal structure as those of bulk states for Fe and Ni (bcc and fcc), while the Co nanocrystal has modified structure from the fcc structure. The averaged grain sizes are ranged about 5 nm. The magnetization are more than 95 % of bulk except for samples with loose packing, which were prepared with lower pressure difference between the evaporation and deposition chambers. It is found that oxidization is remarkably suppressed during the fabrication process.*

INTRODUCTION

Gas deposition Method (GDM)(1) is known as a technique to handle ultra fine particle produced with gas evaporation method(2). In this technique, small sized particles are first made similarly to the gas evaporation and are formed into a bulk as in a packing method(3). We have been interested in an aspect of GDM as a novel fabrication way of nano-crystals(4,5). The advantage of this technique is the simple process where the particles are immediately deposited after the formation and the degree of oxidation is considered to be remarkably depressed. To realize it, GDM requires two chambers which are evaporation chamber and a deposition chamber.

Gold nano-crystals made by this method depicted extraordinary mechanical properties such as the enhancement of the mechanical strength(6). This is speculated to be the high density of lattice defects and the mechanism may resemble to that for amorphous materials. On the other hand, transition metal GDM nanocrystals have been investigated in expectation of new electric and magnetic properties. The characteristic feature of the method is the low oxidization rates. Fe nano-crystals were studied with Mössbauer study, X-ray diffraction and magnetometry(5). Each result suggested the low degree of oxidization. The saturation magnetization was almost the same order of that of bulk Fe. To realize such condition, the special attention is paid for the inert gas used during the gas deposition.

In this paper, the fabrication technique of 3d nanocrystal is described and the magnetic properties of Co nanocrystal is mainly reported. 3d ferromagnetic metal nanocrystals are compared.

EXPERIMENTAL PROCEDURE

Figure 1 shows a schematic illustration of the GDM system. The system is almost the same as that described elsewhere(4). A He circulation system is installed because high purity and high rate of He gas supply (40 L/min) are required. To obtain the He gas flow of 40 L/sec with 5 kg/cm^2, two all metal bellows pumps(MBP in Fig.1) are set. He gas used for GD is returned to the circulation system and is purified by two SAES® getter pumps. The oxygen concentration is monitored with a ZrO_2 monitor. The part of oxygen was decreased down to 10^{-7} after 1 hour from the circulation system started to operate.

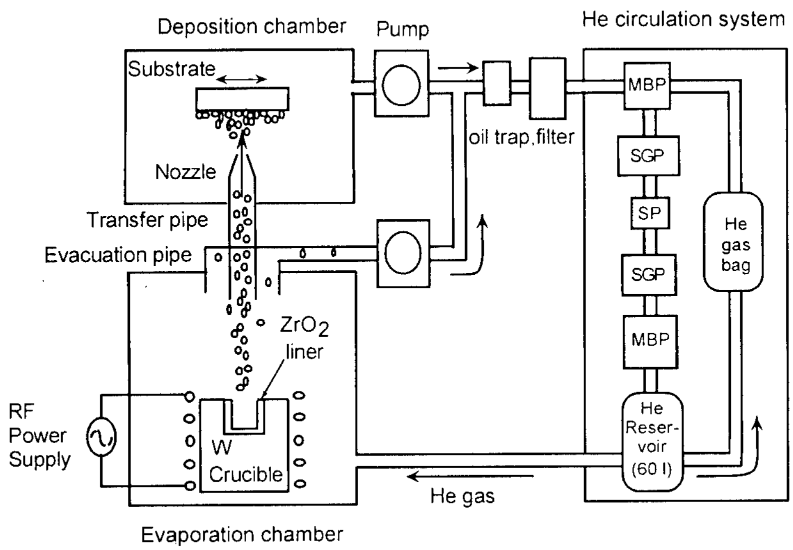

Fig. 1. Schematic illustration of GDM system for the fabrication of 3d transition ferromagnetic nanocrystals. MBP, SGP and SP mean mechanical bellows pumps, SAES getter pump, and a sorption pump.

The pressure difference (Pe) between the evaporation and deposition chambers and the temperature of the hearth (Th) are major factors for the sample fabrication. In this study, Co nano-crystals (n-Co) were produced with changing the pressure difference (Pe). Related to the deposition temperature, the combination of hearth materials and evaporating materials is important. Because the evaporation temperature is needed to elevate over the melting point, alloy formation may take place in some combinations for example Fe versus carbon crucibles and Ni versus W crucibles. The use of ceramics liners such as ZrO_2 and Al_2O_3 can prevent the alloy formation between the metallic crucibles and evaporating materials. We used C crucibles for Ni and a W crucible with ZrO_2 liners for Fe and Co. The substrates for the deposition were Si wafers and polyimide films.

X-ray diffraction study was carried out with using Cu-Kα radiation. Magnetization was measured with a vibrating sample magnetometer at room temperature. The amount of ferromagnetic elements were determined with an inductively coupled plasma (ICP) photo-emission spectroscopy in order to estimate the magnetization per ferromagnetic elements.

RESULTS AND DISCUSSION

Figure 2 shows the X ray diffraction patterns of n-Co prepared with various pressure difference from 500 to 1500 Torr. Strong and broad peaks are seen at around 2 θ=45°. The peaks are considered to be from fcc (111) refrection, however it is difficult to decide because hcp (002) gives almost the same diffraction angle. There are some structure around 50. The particle size was estimated to be around 5 nm from the line width of fcc (220) peaks. Particle sizes slightly decrease with the increase of Pe.

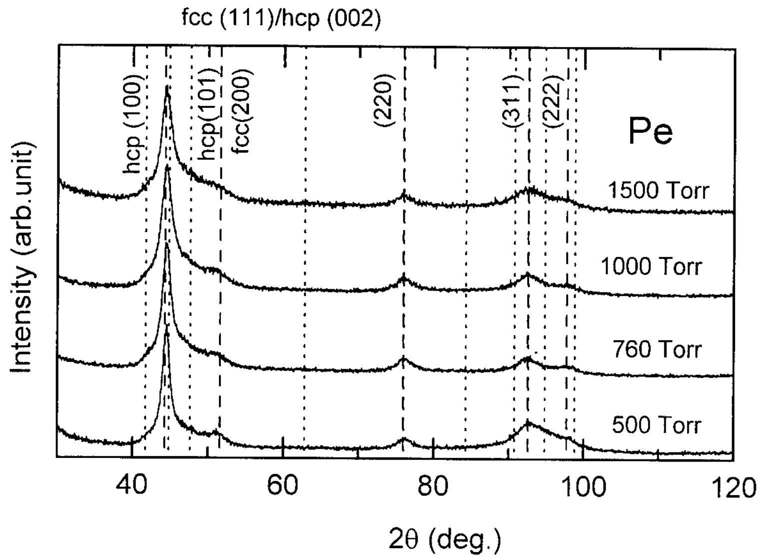

Fig. 2. X-ray patterns of n-Co prepared with Gas-deposition method. The hearth temperature is kept at 1900 °C.

From the magnetization measurements, magnetizations are well saturated at low magnetic field around 100 Oe. The amplitudes of saturation magnetization for n-Fe, n-Ni and n-Co prepared with various Pe are shown in Fig.3(a). The hearth temperature were kept at constant temperatures; 1500 °C for Ni, 1950 °C for Fe and 1900 °C for Co. The difference in the hearth temperatures for Ni and others are due to the difference in the usage of liners. The amplitude were normalized by the value of bulk at room temperature. From the figure, the amplitudes are almost the same as those of bulk. The dependence of magnetization on the Pe seem to be small. In case of n-Co, the magnetization is larger than the bulk value by 5 – 7 %, however, the definite data which prove the enhancement have not been obtained yet.

Figure 3(b) shows the coercivity for the same samples as used in Fig.3(a). Small coercivity is obtained for all nanocrystals, especially about 1 Oe is obtained for n-Co with 1000 Torr of Pe. There are trends to decrease the coercive force as increasing Pe. In the case of n-Co, however, the coercive force raised to 15 Oe. It may be caused by the imperfect crystalline structure of fcc type. As is seen in Fig.2, the main lines are assigned by those of fcc structure and weak reflection lines from hcp are observed around hcp (100), (101) peaks.

Especially for the sample made with the Pe of 1500 Torr, those peaks are more obviously seen. The existence of the hcp phase could be a origin of higher coercive force. When the ultra-fine particles of Co were produce with a gas condensation technique (gas evaporation method), the high temperature phase, the fcc structure, tends to be realized(2). This result suggests a difference in growth process between gas evaporation and gas deposition.

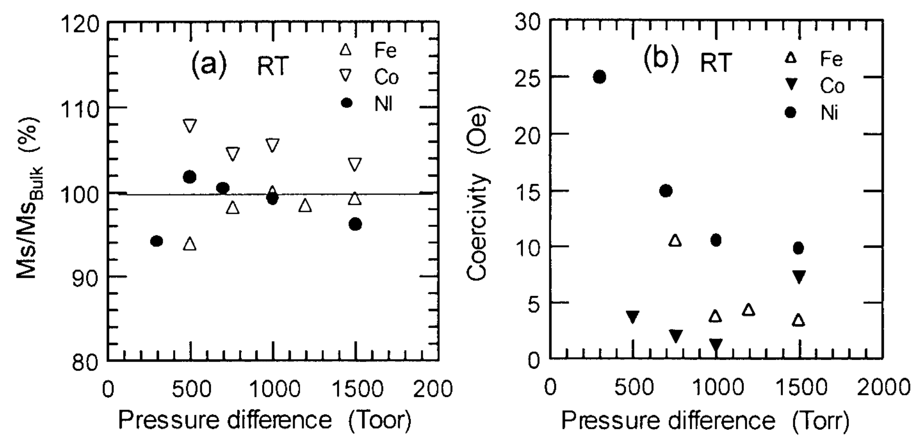

Fig. 3. (a) Saturation magnetization of n-Co, n-Fe and n-Ni versus the pressure difference, Pe. (b) Coercive force of n-Co, n-Fe and n-Ni versus the pressure difference, Pe.

The degree of oxidation in the GDM nanocrystals is concluded to be remarkably small compared with the case of UFP prepared with gas evaporation(7), which are about 70 % of bulk, from the data of magnetization. This is also supported by the result of Mössbauer study for n-Fe prepared with this technique(5). In conclusion, GDM is found to be an appropriate technique to deal with the 3d transition metal UFP preventing surface oxidization.

ACKNOWLEDGEMENTS

The authors express their thanks to Mrs. S.Akao, S.Omiya, T.Sakai and S.Sakai for the help in experiments. This work was partly supported by Grant-in-Aid for Scientific Research (c) (10650647) of the Ministry of Education, Science, Sports and Culture.

REFERENCES

1. Kashu, S., Fuchita, E., Manabe, T. and Hayashi, C., *Jpn. J. Appl. Phys.* 1984. 23. L910.
2. Uyeda, R., *Prog. Mater. Sci.*, 1991. 35. 1.
3. Gleiter, H., *Prog. Mater. Sci.* 1989. 33. 223.
4. Kita, E., Shiozawa, K., Sasaki, Y., Iwamoto, Y. and Tasaki, A., *IEEE Trans. Magn.* 1996. MAG-32. 4487.
5. Sasaki, Y., Hyakkai, M., Kita, E. and Tasaki, A., *J. Appl. Phys.* 1997. 81. 4736.
6. Okuda, S., Tang, F., Tanimoto, H. and Iwamoto, Y., J. Alloys Comp., 1994. 211/212. 494.
7. Tasaki,A., Tomiyama,S., Iida,S., Wada,N. and Uyeda,R., *Jpn. J. Appl. Phys.* 1965.4.707.

Pergamon

NanoStructured Materials, Vol. 12, pp. 911–914, 1999
Elsevier Science Ltd

0965-9773/99/$–see front matter

PII S0965-9773(99)00265-2

DUCTILITY OF NANOCRYSTALLINE ZIRCONIA BASED CERAMICS AT LOW TEMPERATURES

U. Betz, H. Hahn
Darmstadt University of Technology, Department of Materials Science, Thin Films Division, Petersenstr. 23, 64287 Darmstadt, Germany

Abstract -- *The ductile behavior of nanophase yttria doped zirconia ceramics was investigated during low-temperature deformation experiments. Ceramics were produced by following a standard processing route of mechanical compaction of the dispersion mixed nanoparticles synthesised by the inert gas condensation or chemical vapor condensation technique and pressureless sintering. Uniaxial forming in tension has been performed in air at temperatures below 0.5* T_m. *The influence of initial grain size and porosity on strain and strain-rate has been a topic of interest as well as the microstructural evolution during deformation. Constant load tests and tests with stress- and temperature-jumps have been carried out to estimate the thermomechanical parameters, strain-rate-sensitivity exponent, activation energy and grain-size exponent of 10 wt.% yttria partially stabilized zirconia. A maximum elongation of about 60 % has been achieved with a* ZrO_2 *+ 10 wt.%* Y_2O_3 *+ 12 wt.%* A_2O_3 *composite ceramic at 1250 °C. The results were related to a deformation model based on mesoscopic grain boundary sliding. ©1999 Acta Metallurgica Inc.*

INTRODUCTION

The ability of polycrystalline yttria partially stabilized zirconia (Y-PSZ) to exhibit very large elongations has been shown in several high temperature deformation experiments during the last decades [1]. Plastic flow at elevated temperatures is usually expressed by the constitutive creep law

$$d\varepsilon/dt \propto \sigma^n D^{-q} \exp(-Q/RT) \qquad (1)$$

where $d\varepsilon/dt$ is the strain rate, σ is the applied stress with the stress-exponent n, D is the grain size with the grain size-exponent q, T is the temperature, R is the gas constant and Q is the activation energy of the creep process. In order to identify the rate controlling mechanism during superplastic flow it is necessary to combine microstructural analysis with the experimental determination of the thermomechanical parameters n, q and Q. Due to the strong influence of the grain size on the strain rate much efforts were devoted to the synthesis of nanocrystalline materials for applications in superplasticity. While tests in compression of nanophase ceramics have been carried out successfully showing extensive deformability [2]

there is still no evidence for large elongations in tension due to the difficulties in fabricating large ceramic parts which are fully dense and maintain the grain size on the nanoscale.

In this paper emphasis was put on both the synthesis and processing of nanocrystalline zirconia based ceramics and the deformation behavior of these ceramics during low temperature tensile tests.

SYNTHESIS AND PROCESSING

Weakly agglomerated nanocrystalline (n-)yttria and zirconia powders have separately been produced by using the inert gas condensation technique, n-alumina by using the chemical vapor condensation technique [3]. The average crystallite size estimated from X-ray diffraction (XRD) line broadening using the Scherrer-formular was 6 nm for zirconia, 15 nm for yttria and 5 nm for alumina. Specific surface areas calculated from nitrogen adsorption measurements were about 160 m^2/g, 80 m^2/g and 300 m^2/g, respectively. Powders of the desired compositions ZrO_2 + 10 wt.% Y_2O_3 (=5 mol%Y-PSZ) and ZrO_2 + 10 wt.% Y_2O_3 + 12 wt.% Al_2O_3 were mixed and suspended in isopropanol. In order to distribute the particles homogeneously, stirring with a magnetic boat and submitting the suspension to an ultrasonic bath was done simultaneously for 2 hours. Subsequential uniaxial (70 MPa) and isostatic (260 MPa) compaction at room temperature of about 7 g of the dried and crushed powders resulted in relative green densities of approximately 40 %. Sintering in vacuum (2 Pa) has been performed at temperatures between 1050 ° and 1250 °C. The dimensions of the n-ceramic discs ranged from 26 to 30 mm in diameter and 1.5 to 2.5 mm thickness depending on the density.

Fig.1 summarises the results on consolidation of the 5Y-PSZ ceramics concerning the grain sizes (from XRD verified by high resolution scanning electron microscopy HRSEM) and the relative densities measured by the Archimedes' principle. During the intermediate stage of consolidation open porosity is still present and a high densification rate in relation to weak concurrent grain growth results in a steep slope of the graph. Above 90 % of the relative density the pore channels are closing and the elimination of the remaining pores requires higher sintering temperatures which is accompanied by extensive grain growth resulting in a more flat slope in the final stage sintering regime. Log-normal pore size distributions of the n-ceramics have been evaluated using N_2-adsorption measurements for the channel like open porosity [4] and small angle neutron scattering (SANS) experiments to analyse spherical shaped closed porosity [5]. Both methods revealed the same trend of the pore structure evolution in terms of decreasing the total pore volume, shifting the average pore size to higher values and broaden the distribution function with increasing sintering

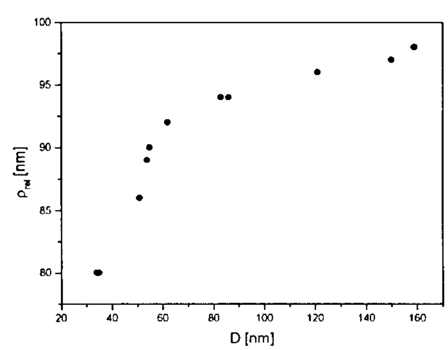

Fig.1: Correlation between the relative density and the grain size of n-5Y-PSZ.

temperature.

It is worth noting that from Fig.1 nearly full density of n-5Y-PSZ could only be achieved with grain sizes above 150 nm. Residual porosity of more than 5 % is present when grain sizes retain below 100 nm. Alternatively, the samples containing the non soluble alumina phase showed promising results yielding densities exceeding 95 % and grain sizes well below 50 nm even after firing at 1250° C.

TENSILE EXPERIMENTS

The deformation behavior of the n-ceramics has been investigated during tensile tests in air at the low-temperature regime (< 0.5 T_m). Different kind of test profiles were selected to determine the thermomechanical parameters of n-5Y-PSZ.

As discussed earlier [6], a creep test was carried out at 1050 °C. By applying a constant stress of 33 MPa during the entire experiment a total elongation of 11 % has been achieved. The true strain rate diminished from $d\varepsilon_{init}/dt = 6.7\times10^{-6}\ s^{-1}$ to $d\varepsilon_{end}/dt = 1.8\times10^{-6}\ s^{-1}$ just prior to cracking. These rates were related to grain sizes of D_{init} = 35 nm and D_{end} = 75 nm, respectively. A value of q = 1.3 was calculated by following equation (1).

True strain as a function of stress has been recorded during a stress-jump test at 1150° C as presented in Fig.2. The initial grain size of the sample was 65 nm. Starting from 10 MPa the stress levels were increased by 5 MPa with sudden jumps after ½ h at the same level. The specimen failed after a total strain of 23 % at a maximum stress of 60 MPa and a strain rate of $2.5\times10^{-5}s^{-1}$. The values $d\varepsilon_1/dt$ at σ_1 before and $d\varepsilon_2/dt$ at σ_2 after each jump were used to determine an average value of n = 3 from 8 jumps by calculating the slopes of the double logarithmic $d\varepsilon/dt$ versus σ plot.

Additionally, the temperature dependence of true strain and strain rates has been studied at constant stress in a temperature-jump test (in detail to be presented elsewhere). The initial grain size of the 5Y-PSZ sample was 35 nm. A constant stress of 20 MPa was established for 1 h at an initial temperature of 1050° C. After rapidly decreasing the stress to zero the temperature was increased by ΔT = 25° C within 10 min, and thereafter the stress of 20 MPa

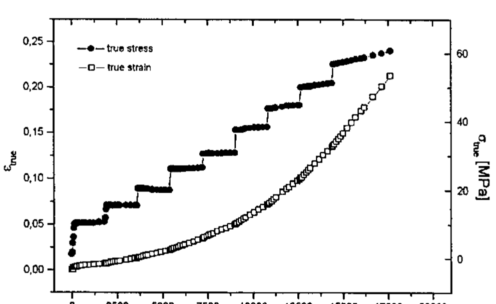

Fig.2: True stress and strain as a function of time in a stress-jump test at 1150 °C.

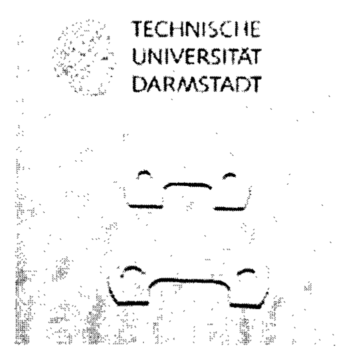

Fig.3: Photograph of an initial and deformed n-5Y-PSZ + 12 wt.% Al_2O_3 tensile specimen.

was reestablished. This procedure was repeated 4 times up to the maximum temperature of 1150° C. Under the assumption that grain growth is negligible during changing the temperature level the value of an average apparent Q of 510 ∓ 33 kJ/mol was estimated from the slopes of the Arrhenius plots of the recorded strain rates $d\varepsilon_1/dt$ and $d\varepsilon_2/dt$, before and after the temperature jump from T_1 to T_2.

Based on the observations made by HRSEM that the grains retain their equiaxed shape after deformation and on the experimentally determined parameters n = 3, q = 1.3 and Q = 510 ∓ 33 kJ/mol which is very close to the value of 506 kJ/mol found for grain boundary diffusion of Zr-cations in 12Ce-TZP [7] the plasticity of nanocrystalline zirconia was attributed to grain boundary sliding due to interface shearing on a mesoscopic scale [8].

In the experiments presented above special attention was put on the fact that the employed 5Y-PSZ samples provided initial grain sizes well below 100 nm. But as illustrated in Fig.1 this is in conjunction with a large volume fraction of pores and therefore large elongations were not expected. Recently remarkable tensile strains were obtained in the composition 5Y-PSZ + 12 wt.% Al_2O_3. Fig. 3 shows a photograph of an initial and a 60 % elongated tensile specimen after pulling at 1250° C. A maximum stress of 47 MPa was applied resulting in a maximum strain rate of $3x10^{-5}s^{-1}$. Extensive concurrent grain growth from 30 nm up to 126 nm occurred during the test while the density decreased from 94 % to 81 %. The origin of failure was detected to be the growth and interlinkage of voids preferred along grinding-lines perpendicular to the tensile axis. The strong curvature of these lines around the voids which partially had a length of several hundred microns gave also evidence for the high ductility of the material.

CONCLUSION

A standard ceramic processing route of mechanical compaction of dry powders followed by pressureless sintering was shown to be applicable to produce large tensile specimen of dense nanocrystalline zirconia based ceramics.

Regardless of porosity the n-ceramics behave very ductile in tension at the low-temperature regime. From the creep parameters of 5Y-PSZ (n = 3, q = 1.3 and Q = 510 ∓ 33 kJ/mol) it is suggest that grain boundary sliding is the rate controlling deformation process. A maximum elongation of 60 % of 5Y-PSZ + 12 wt.% Al_2O_3 with an initial grain size of 30 nm has been achieved at 1250° C.

References

[1] T.G.Nieh, J.Wadsworth, *Mat. Sci. Forum*, 170-172, (1994), p. 359
[2] H.Hahn, R.S. Averback, *J. Am. Cer. Soc.*, 74, (1991), p. 2918
[3] G.Scipione, U.Betz, H.Hahn, *Mat. Sci. Forum*, 269-272, (1998), p. 207
[4] U.Betz, A. Sturm, J.F.Loeffler, W. Wagner, Wiedenmann, H. Hahn, to be published
[5] H.Hahn, *NanoStructured Mat.*, 9, (1997), p. 3
[6] U.Betz, G.Scipione, E.Bonetti, H.Hahn, *NanoStruct. Mat.*, 8, 7, (1997), p. 845
[7] J.A.Allemann, et al., *J. Eur. Ceram. Soc.*, 15, (1995), p. 951
[8] K.A.Padmanabhan, R.Nitsche, H.Hahn, EUROMAT-95

Pergamon

NanoStructured Materials, Vol. 12, pp. 915–918, 1999
Elsevier Science Ltd

0965-9773/99/$–see front matter

PII S0965-9773(99)00266-4

BEHAVIOR AND BONDING MECHANISMS OF ALUMINUM NANOPARTICLES BY ELECTRON BEAM IRRADIATION

BingShe Xu and Shun-ichiro Tanaka
Tanaka Solid Junction Project, ERATO,
Japan Science and Technology Corporation,
1-1-1 Fukuura, Kanazawa-ku, Yokohama 236-0004, Japan

Abstract-- *Activities such as migration, rotation and revolution, and the bonding behavior of aluminum nanoparticles by electron irradiation have been investigated using a high-resolution transmission electron microscope on a stage at room temperature. It was determined that the driving force of the migration, rotation and revolution of the Al nanoparticles was a momentum transfer from spirally trajected electrons and ions inside the pole piece of transmission electron microscope. First, adjacent Al nanoparticles came into contact and bonded via necking between the Al/Al grain boundaries and the twin boundaries migrated to the nanoparticle surface. Finally, these boundaries disappeared, giving rise to a single particle or a single crystal. The driving forces for bonding were the surface energy of the nanoparticles and surface activation by momentum transferred from the high-energy electrons and ions. It is also clear that heating induced by electron irradiation is not a major factor controlling Al nanoparticle activities or the bonding process.*

INTRODUCTION

Nanoscale particle materials are of great interest because of their characteristic physical and chemical properties. Recently, the use of nanoparticles of metals, alloys, semiconductor crystals and ceramics to produce functional materials such as metal or ceramic nanostructured solids in order to obtain superplastic, electronic and catalytic materials, have been the focus of research in this field. However, nanocrystalline materials, such as the nanostructured solid, are prepared using the conventional sintering method. Therefore, the formation mechanisms and the kinetics cannot be directly investigated, and the conventional method does not allow control of material formation at the atomic level. Therefore in order to understand the unusual properties of these nanoparticles, the reaction behavior and the development of processing methods for manufacturing them into a functional material must be investigated. Electron irradiation with *in situ* atomic-scale observation to investigate the behavior and mechanisms of nanoparticle bonding using field control has been reported (1-4). In this study, we present reconfirmation of the behavior and the mechanism of Al nanoparticle activities, such as migration, rotation and revolution. We also discuss the behavior and mechanisms of Al/Al particle bonding, and the mobility of the Al/Al grain boundary (GB) and its internal twin boundary (TB) under electron irradiation, on the basis of *in situ* observation using a high-

resolution transmission electron microscope (HRTEM).

EXPERIMENTAL

Oxide-free Al nanoparticles, with diameters of2~40 nm, were obtained from metastable θ-Al_2O_3 particles by electron irradiation (ESD) (1-5). The Al nanoparticles were placed on an amorphous carbon film with a thickness of approximately 20 nm. The structures and components of Al nanoparticles were confirmed from the extremely fine electron beam diffraction patterns (1-4). These specimens were irradiated at an intensity in the range of $0.3\sim3.3\times10^{20}$e/cm^2•sec using a HRTEM (JEM-2010) on a room-temperature stage to obtain Al/Al bonding. The HRTEM images were recorded using a low-intensity incidence beam to produce high-quality micrographs after the nanoparticles were strongly irradiated.

RESULTS AND DISCUSSIONS

Migration of Al nanoparticles

The phenomena of migration and bonding of several Al nanoparticles upon electron irradiation have been previously reported (2). It is clear that Al nanoparticles undergo clockwise rotation and revolve around the irradiation center, and that the nanoparticle size and shape change, and bonding between adjacent particles occurs. It was also suggested that the driving force of the migration, rotation and revolution of the Al nanoparticles was induced by the Lorenz force which appeared as a momentum transfer from spirally trajected electrons and ions in the magnetic field of the HRTEM pole piece. To confirm these conclusions, we changed the magnetic field direction of the pole piece in the HRTEM. The results are shown in column higher side of Fig.1. When several Al nanoparticles were subjected to electron irradiation of the same intensity (2), they migrated, rotated and revolved. However, movement in the opposite direction, i. e., counterclockwise movement, occurred. This indicates that the driving force of the Al nanoparticle behavior which was transmitted by the electrons was

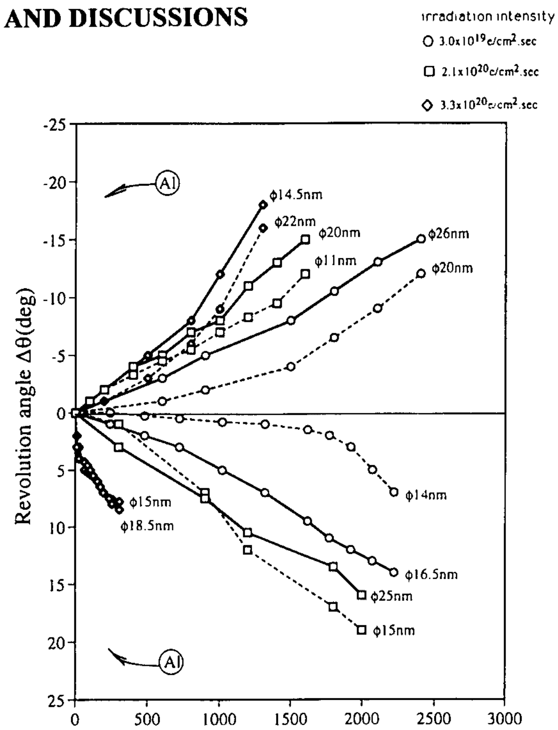

Fig. 1 The clockwise (+) and counterclockwise (-) revolution of Al nanoparticles during electron irradiation in the magnetic field direction, as opposed to the case of clockwise revolution (2,3). ϕ indicates the diameter of the initial Al particle.

in the opposite direction, i. e., counterclockwise movement, occurred. This indicates that the driving force of the Al nanoparticle behavior which was transmitted by the electrons was transferred from the magnetic field in the HRTEM pole piece. On the other hand, we suggest that the behavior of the Al nanoparticles must also be influenced by the extra surface energy.

Formation of Al/Al nanoparticle bonding and the interface structures

The formation of Al/Al particle bonding and alteration of Al/Al GBs were caused by irradiation, as shown in Fig. 2. Figures 2a-d show a sequence of typical micrographs of the bonding processes between two Al nanodecahedra at an irradiation intensity of 3.3×10^{20}e/cm^2•sec for 0 sec (a), 300 sec (b), 900 sec (c), and 2400 sec (d). During the initial irradiation process, the Al nanoparticles migrated, rotated, and revolved around and approached each other, and after 300 sec of irradiation, bonding between two Al nanodecahedra producing a dumbbell-like shape was observed. The remarkable features of the particle bonding behavior are as follows. Al nanoparticles take a predictable path toward each other to form a boundary; for example, on both sides of the Al/Al bonding interface, each {111} plane could come into contact with the other at an angle of approximately 66° to produce a better match. At this stage, the boundary structure corresponding to the Σ3 coincidence boundary is given by the

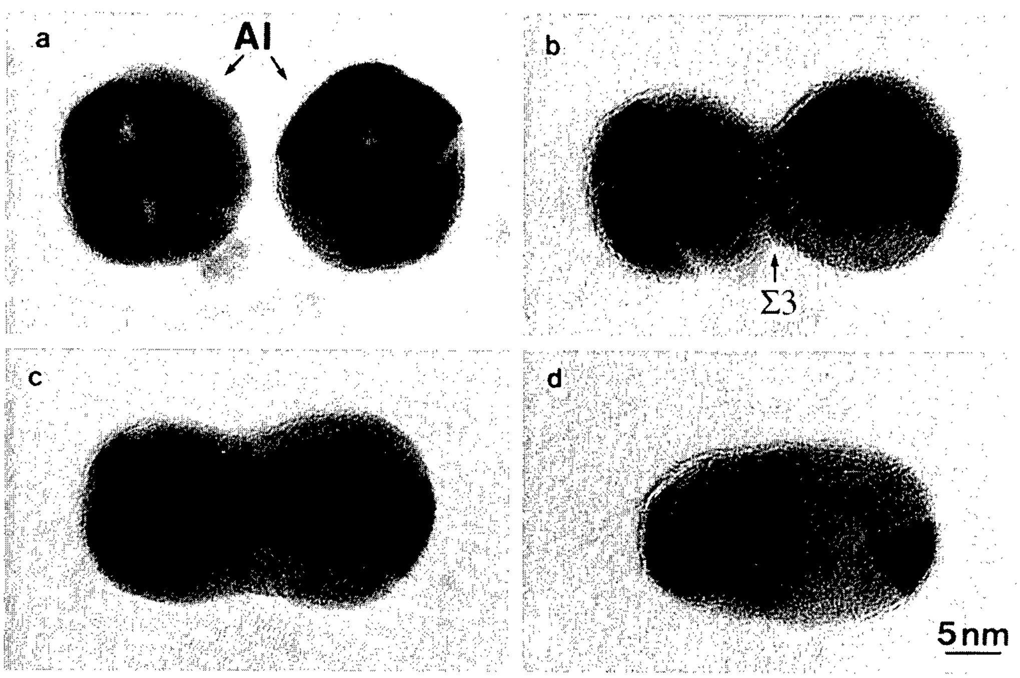

Fig. 2 The sequence of bond formation between two Al nanodecahedra under irradiation at a beam intensity of 3.3×10^{20}e/cm^2•sec, for 0 sec (a), 300 sec (b), 900 sec (c), and 2400 sec (d). (a) and (b): Two Al nanoparticles coming into contact and bonding. The interface is a Σ3 coincidence boundary. (c)-(d): Neck growth, the decrease in distance between the centers of the nanoparticles, and GB and TB migration to the nanoparticle surface producing a single particle or single crystal.

coincidence site lattice theory (CSL) (6). An angular deviation of approximately 5° is noted due to the pentagonal axis of the nanodecahedron on the left side, which is not located perpendicular to the plane of the paper. Figures 2c-d show the Al/Al bonding for an irradiation time of 900~2400 sec. It is clear that Al/Al particle bonding converted two particles into a single particle or into single crystal through a process of neck growth, interface formation (see Figs. 2b, c), and GB and TB migration to the Al nanoparticle surface, and finally, disappearance of the boundary (Figs. 2d). In this case, the change in Al/Al GB nanostructures includes the tendency of {111} crystal planes in Al/Al GB to become parallel, and that the GBs, TBs and defects, such as disclination, move out of the surface of the Al nanoparticles. At present, it is clear that the predominant $\Sigma 3$ CSL boundary is formed due to the low interface energy, similar to Al [110] tilt GBs (7). Furthermore, the phenomenon of two nanoparticles bonding into a single particle or single crystal to form a more stable structure is demonstrated.

Adjacent Al nanoparticles bonded during electron irradiation, causing decrease of free energy. Here, the driving forces for bonding are considered to originate from the Lorentz force and the intrinsic surface energy of the nanoparticles. In the former case, the particle bonding behavior is the same as mentioned above, and in the latter case, it is well known that a nanoparticle possesses greater surface energy than the bulk material due to the large number of surface atoms. When high-energy electrons irradiate the nanoparticles, they lose energy, which can cause an increase in the thickness of the carbon film and nanoparticle temperature through the activation of lattice or plasma vibration. However, the temperature increase of the nanoparticles and substrate due to electron irradiation was estimated to be small, and does not have a major effect on the Al nanoparticle behavior, such as migration, rotation or Al/Al bonding formation (8).

CONCLUSIONS

In this study, we investigated the behavior and bonding mechanisms of Al nanoparticles under electron beam irradiation. It is clear that 1) electron beam irradiation caused migration, rotation and revolution of Al nanoparticles toward the irradiation center before the Al nanoparticles contacted each other, and that the driving force is primarily momentum transfer from the electrons or ions which have a spiral trajectory in the magnetic field of the HRTEM pole piece; 2) adjacent Al nanoparticles came into contact with each other, bonded via necking, and the particle bonding growth was induced by surface diffusion, volume diffusion and viscous flow. Finally the two particles were bonded into a single particle due to GB and TB migration, and 3) heating induced by electron irradiation does not have a major effect on any of these processes.

REFERENCES

1. Xu, B. S. and Tanaka, S.-I., *NanoStructured Materials*, 1995, 6, 727.
2. Xu, B. S. and Tanaka, S.-I., *Materials Science Forum*., 1996, 137, 207.
3. Xu, B. S. and Tanaka, S.-I., *Proc. Int. Conf. JIMIS-8.* , 1996, p.395.
4. Xu, B. S. and Tanaka, S.-I., *NanoStructured Materials*, 1998, 8, 1131.
5. Knotek, M. L., *Rep.Prog.Phys*., 1984, 47, 1499.
6. Brandon, D. G., *Acta Met.*, 1964, 12, 813.
7. Hasson, G., Boos, J.-Y., Herbeuval, I., Biscondi, M. and Goux, C., *Surf. Sci.*, 1972, 31, 115.
8. Xu, B. S. and Tanaka, S.-I., *Mat. Res. Soc. Symp. Proc.*, 1997, 472, 179.

Pergamon

NanoStructured Materials, Vol. 12, pp. 919–922, 1999
Elsevier Science Ltd

0965-9773/99/$–see front matter

PII S0965-9773(99)00267-6

STRUCTURE AND OPTICAL PROPERTIES OF NANOSTRUCTURED GERMANIUM AND SILICON PROCESSED BY SEVERE PLASTIC DEFORMATION

R.K.Islamgaliev[1], R.Kuzel[2], S.N.Mikov[3], E.D.Obraztsova[4], F.Chmelik[2]

[1] Ufa State Aviation Technical University, Ufa 450000, Russia
[2] Charles University, Ke Karlovu 5, 12116 Prague 2, Chech Republic
[3] Uljanovsk State University, Uljanovsk 432000, Russia
[4] General Physics Institute, Russian Academy of Science, Moscow 117942, Russia

Abstract *- The nanostructured Ge and Si processed by severe plastic deformation (SPD) has been studied by various techniques: TEM, XRD, Raman scattering and photoluminescence measurements. The as-prepared samples are characterized by both a small grain size and a specific defect structure of grain boundaries (GB). Microstructural aspects of optical properties in nanostructured Ge and Si are discussed. ©1999 Acta Metallurgica Inc.*

INTRODUCTION

It has been demonstrated recently that nanocrystalline (NC) structures can be successfully introduced into bulk samples of different metals and alloys by SPD [1]. Moreover, the method of SPD was used not only for ductile metals, but also for rather brittle alloys and intermetallics. In this connection, it is of special interest to investigate the features of NC structures in Ge and Si, which can exhibit unusual optical properties [2].

EXPERIMENTAL

In order to fabricate NC structures, Ge and Si single crystals were subjected to torsion straining [1]. The structure of samples was examined by JEM -100B transmission electron microscope. X-ray diffraction (XRD) studies were carried out with Hilger and XRD7 (Seifert-FPM) powder diffractometers. Lattice parameters were evaluated by the Cohen-Wagner extrapolation plot. A mean grain size and elastic strains were evaluated by the Williamson-Hall method. Raman scattering and the photoluminescence measurements were performed at room temperature in a backscattering geometry. The spectra were excited by the 532 nm line of a Nd-ion laser and the 488 nm line of an Ar-ion laser [2,3].

RESULTS AND DISCUSSION

TEM investigations of the as-prepared samples show a very disperse structure characterized by uniform equiaxed grains which are strongly distorted (Fig.1). The histograms of the grain size distribution plotted from a dark field image are described by a lognormal distribution with a mean grain size of 24 nm and 17 nm for Ge and Si, respectively.

The Raman spectra of the as-prepared samples (Fig.2) reveal an increase of the full width at half maximum (FWHM), a decrease of the peak intensity, as well as their asymmetry and shift to lower frequencies. For example, the values of FWHM were equal to 14.0 cm^{-1} and 14.2 cm^{-1} for NC Ge and Si. In addition, a peak shift of 2.0 cm^{-1} and 2.5 cm^{-1} for NC Ge and Si was revealed as well. According to model [4], a better fit of the calculated peaks to the experimental data of Raman scattering (Fig.2) is observed for a mean crystallite size 9 nm and 5.5 nm for NC Ge and Si, respectively. However, there exist extra intensities in the measured spectra. Similar additional peaks were revealed also in thin films of Si [3] processed by evaporation, where they were attributed to the GB defect structure.

The XRD analysis of the as-prepared Ge sample reveals the lines of the phase Fd3m (diamond like) and the tetragonal phase of Ge with the $P4_32_12$ space group. The content of tetragonal phase did not exceed 8 wt%. The additional peaks of tetragonal phase completely disappeared after annealing at 400 °C.

A significant decrease of the intensity of the peaks and their broadening due to both a small grain size and a high level of internal elastic strains (Table) are the features of the XRD pattern for the as-prepared samples (Fig.3).

The lines of cubic phase Fd3m, as well as three strongest lines of cubic phase Ia3 were revealed in the as-prepared Si sample. The value of lattice parameter for the as-prepared sample is 0.5429(1) nm. A mean grain size and a value of elastic strains for the as-prepared samples are of about 7 nm and 0.55%, respectively (Table).

A significant difference of a mean grain size determined by TEM investigations and by XRD and Raman scattering (17 nm, 7 nm, 5.5 nm for Si; 24 nm, 10.4 nm, 9.0 nm for Ge) may be caused by specific defect structure of the as-prepared samples. For instance, HREM studies supply the evidence of the dislocation disturbed structure of GB in NC materials processed by SPD [1], where the extrinsic grain boundary dislocations create long range stress

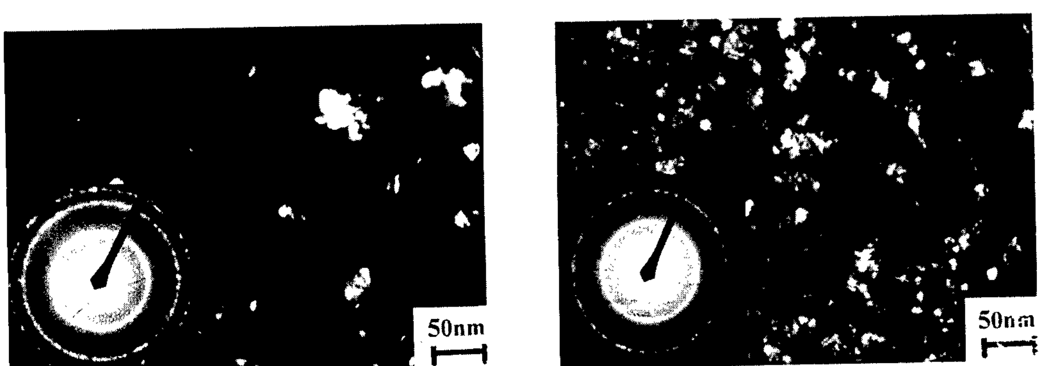

(a) (b)

Fig.1. Structure of the as-prepared samples: a - Ge; b - Si.

TABLE
Lattice Parameter, Strains, Mean Grain Size for Ge and Si

Sample	a (nm)	ε (%)	d (nm)
Ge, as-prepared	0.5657(1)	0.7	10.4
Si, as-prepared	0.5429(1)	0.55	7

fields resulting in the distortions of the crystal lattice near grain boundaries. Moreover, each of structural methods used in this paper may determine the various grain sizes. For example, TEM determines a visible full grain size included the interior with a perfect crystal lattice and the GB defect structure, whereas the data of XRD and Raman scattering allow the calculation of a grain size corresponding to grain interior.

Visible photoluminescence with asymmetrical profile of peak having maximum at 650 nm and FWHM of about 80 cm^{-1} (Fig.4) was revealed in the as-prepared Si sample. This result was obtained in bulk NC Si and it associated only with a small size of grains unlike to porous Si where the role of solution for etching is important as well [5]. The rise of the excitation power leads to the increase of the photoluminescence intensity and does not change the peak position.

According to the theoretical predictions, a visible photoluminescence should be observed after reduction of grain size to the Bohr radius, which is 5 nm in Si [5]. In this case, the visible photoluminescence associates with enlarge of the band gap in nanostructured Si due to quantum confinement and. The interior of grains in NC Si having perfect structure is responsible, obviously, for the observed photoluminescence. The GB defect structure has the distortions of crystal lattice, which are different in various grains and cannot be the basis for emission. The emitted core of grains with a perfect structure should have diameter less than 5 nm that corresponds to a mean size of interior from Raman scattering.

CONCLUSION

The method of SPD has been used to process NC structure in bulk samples of Ge and Si. The as-prepared samples are characterized by a mean grain size less than 25 nm as well as by the GB defect structure associated with high elastic strains and significant microdistortions of crystal lattice. Additional peaks in the Raman spectra, visible photoluminescence for NC Si with maximum at 650 nm, a significant difference of a mean grain size determined by TEM and by XRD and Raman scattering are the unusual features of their structure and optical properties.

REFERENCES

1. R.Z.Valiev. Nanostructured Materials. **6**, 73 (1995).
2. S.N.Mikov, A.V.Igo, V.S.Gorelik, R.K.Islamgaliev. Solid State Physics. 38 (5) (1996) 1635.
3. E.D.Obraztsova. NATO ASI. Series E. 260 (1994) 483.
4. I.H.Campbell, P.M.Fauchet. Solid Stat Commun. 58 (1986) 739.
5. A.G.Cullis, L.T.Canham, D.J.Calcott. J.Appl. Phys. 82(3) (1997) 909.

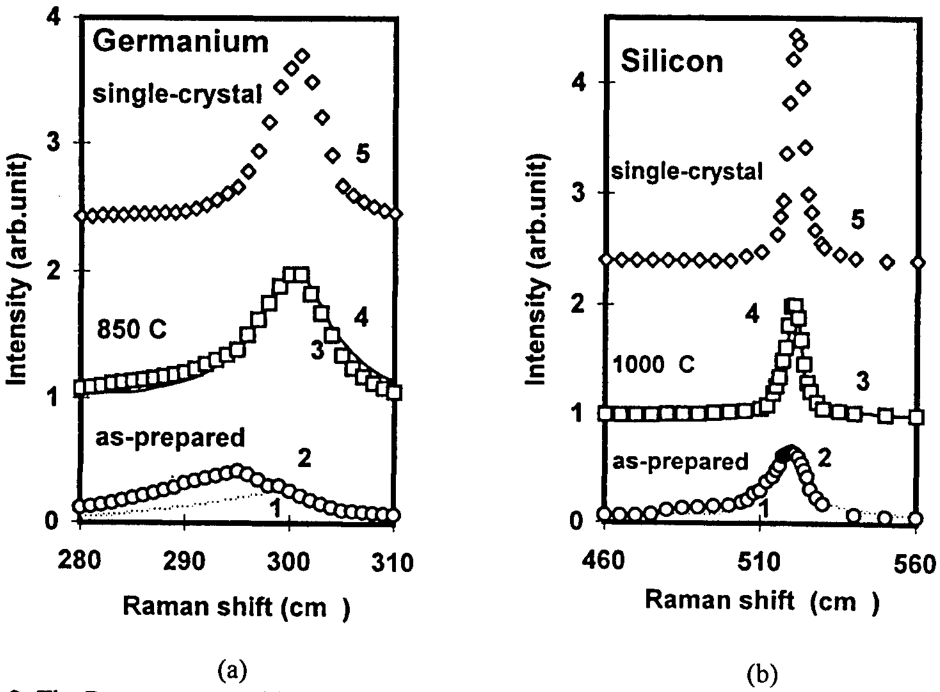

Fig.2. The Raman spectra: (a) - Ge : (1) as-prepared, experiment; (2) as-prepared, calculation; (3) annealed at 850°C, experiment; (4) annealed at 850°C, calculation; (5) single crystal, experiment (b) - Si : (1) as-prepared, experiment; (2) as-prepared, calculation; (3) annealed at 1000°C, experiment; (4) annealed at 1000°C, calculation; (5) single crystal, experiment.

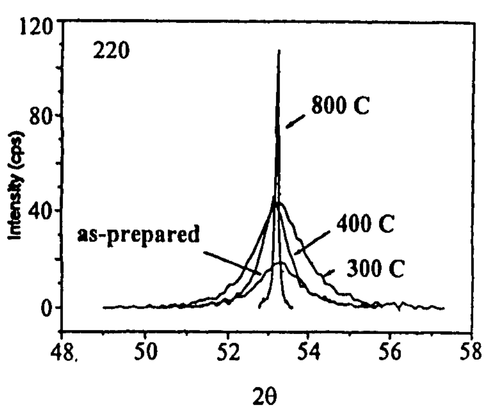

Fig.3. The profiles of the 220 peak in Ge.

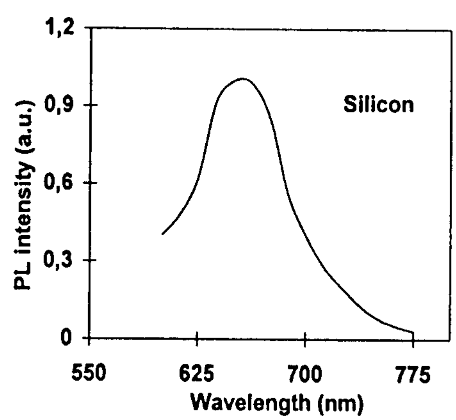

Fig.4. Photoluminescence spectrum in Si.

Pergamon

NanoStructured Materials, Vol. 12, pp. 923–926, 1999
Elsevier Science Ltd

0965-9773/99/$–see front matter

PII S0965-9773(99)00268-8

FORMATION OF METASTABLE STATES IN NANOSTRUCTURED Al- AND Ti -BASED ALLOYS BY THE SPTS TECHNIQUE

V.V. Stolyarov[1], L.O. Shestakova[1], Y.T. Zhu[2] and R.Z. Valiev[1]

[1]Institute of Physics of Advanced Materials, Ufa State Aviation Technical University, Ufa, 450025, Russia,
[2]Los Alamos National Laboratory, Los Alamos, NM 87545,USA

Abstract- *Nanostructured Al and Ti-based alloys have been processed by severe plastic torsion straining (SPTS). It is shown that SPTS under high pressure of these quenched alloys results in refinement of their microstructures to grain sizes of 70-100nm and leads to formation of supersaturated solid solutions. Structural changes during heating of the obtained nanostructured alloys are investigated. ©1999 Acta Metallurgica Inc.*

INTRODUCTION

Nanostructured materials are non-equilibrium systems whose microstructures (grain size, defects, grain boundary state, phase composition [1-3]) and thermodynamic state significantly differ from conventional coarse-grained polycrystalline materials. Recently, a new processing method, SPTS, which induces large plastic strains under high applied pressure at low temperatures, was developed to process bulk nanostructured materials [1]. The advantage of this method is its capability to fabricate bulk samples without pores and impurities. It can also efficiently process multi-phase alloys to obtain non-equilibrium microstructures as well as non-equilibrium phase compositions. The objective of the present paper is to investigate microstructures and phase compositions of two Al and Ti alloys processed by SPTS and subsequent annealing.

EXPERIMENTAL

Two commercial alloys, aluminium alloy 01959 (Al-6%Zn-2.8%Mg-1%Cu-0.37%Zr) and titanium alloy VT6 (Ti-6.1% Al-4.5%V), were used in this study. The as-received alloys had a coarse-grained microstructure with a mean grain size of more than10 μm. Disks of 10 mm in diameter and 0.3 mm thick were cut out from an alloy rod by spark cutting. These disks were quenched and then subjected to SPTS under a pressure of 5 GPa at the room temperature [2].

The logarithmic strain value was e = 5. The samples processed by SPTS were subjected to aging in a temperature range of 20-500 ^{0}C. Differential Scanning Calorimetry (DSC), Transmission Electron Microscopy (TEM) and X-ray analysis were used to investigate the microstructure and properties of these samples. Measurements of microhardness were also conducted.

RESULTS AND DISCUSSION

Aluminium alloy Al-Zn-Mg-Cu-Zr In the quenched state, the alloy consists of_supersaturated Al-based matrix and second-phase particles. After the SPTS, the average grain size of the Al-matrix phase was reduced to 70 nm (Fig. 1a). The Selected Area Diffraction Pattern (SADP) taken from an area of 0.5 μm^2 shows a number of spots arranged in circles, which is typical of nanostructured materials and usually indicates high angle misorientations of neighbouring grains. The second-phase particles are absent in the micrograph, indicating their dissolution during the SPTS process. The bend contours in some grains indicate the presence of high level elastic stress.

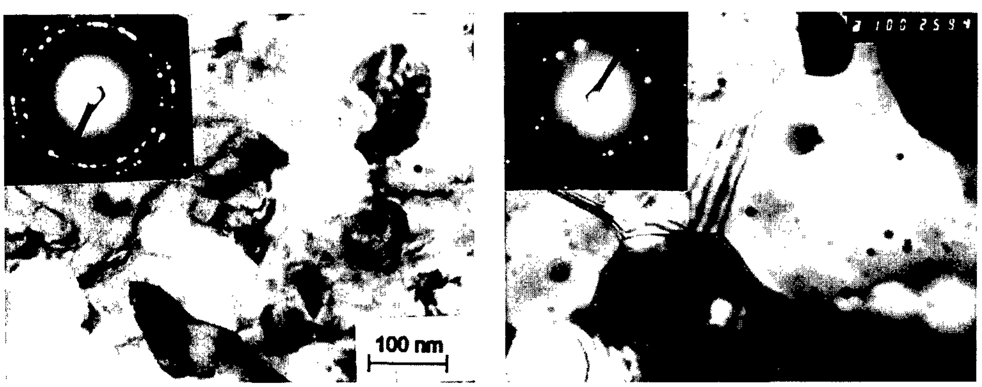

(a) (b)

Figure 1. TEM micrograph and SADP from quenched the Al-alloy 01959, subjected to SPTS (a) and to SPTS + artificial aging , 300 ^{0}C-0.5 h (b)

TABLE 1.
Microhardness (GPa) of the Al-Alloy in Various States (NA means natural aging).

Process	Starting state	Quenching	SPTS	NA	Artificial ageing during 0.5 h at temperature , ^{0}C				
					100	150	200	250	300
As-received	0.75	1.26		1.50	1.25	1.36	1.15	0.96	0.85
SPTS	0.75	1.26	2.24	2.80	2.13	1.96	1.60	1.70	1.22

The microhardness (Table 1) in the as-deformed state is 3 times of that in the as-received state. Natural aging (NA) of the severely deformed alloy at the room temperature for twenty days leads to the precipitation of fine second phase particles of about 10 nm in diameter from the supersaturated solid solution. The grain size of the matrix phase does not change during the NA process. In contrast, artificial aging of the deformed alloy at 300 °C for 0.5 hour leads to growth of both the Al-grains (up to 0.3 μm and larger) and the precipitates (>50 nm) (Fig. 1b). The existence of thickness extinction contours near grain boundaries indicates internal elastic strain relaxation. Compared with the artificial aging, which results in softening of deformed alloy at all selected temperatures, the natural aging for twenty days leads to a significantly higher microhardness of 2.80 GPa.

Titanium alloy Ti-6.1Al-4.5V (VT6). X-ray data (Table 2) show that the as-quenched Ti alloy consists of supersaturated α phase and α'' martensite that agree with [4]. During the SPTS at the room temperature, α'' martensite (rhombic) phase decomposed to form α' martensite (hcp) and metastable β_m-phase. The microstructure and SADP in Fig. 2 (a) attests to the formation of equiaxed grains with high-angle grain boundaries and a mean grain size of 100 nm. The high defect density, diffuse grain boundaries and blurring of reflections suggest the existence of internal stress. Microhardness of the alloy increased by 8% after quenching.

TABLE 2.
Phase Composition, Structure and Microhardness of the VT6 Alloy After Different Treatments

Conditions of the treatment	Phases	Structure and grain size	Hv (GPa)
As-received	$\alpha + \beta$ (5%)	grained, d = 15μk	3.08
Quenching from 900°C	$\alpha + \alpha''$ (20%)	grained + martensite	3.26
Quenching + SPTS (QS)	$\alpha + \alpha' + \beta_m$	high angle GB's , d = 0.1μk	4.70
QS + Aging (300 °C, 0.5 h)	$\alpha + \alpha' + \beta_m$.	high angle GB's, d = 0.1μk	4.43
QS + Aging (500 °C, 0.5 h)	$\alpha + \beta$ (traces)	recrystallizated, d= 1μk	3.62

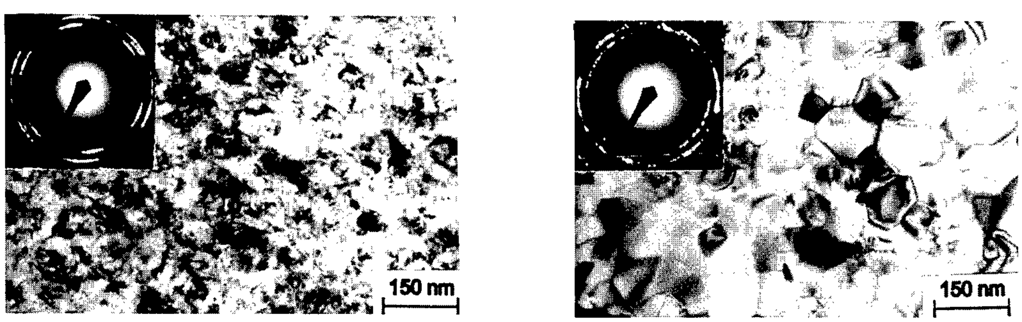

(a) (b)

Figure 2. TEM micrograph and SADP of the quenched Ti-alloy, subjected to SPTS (a) and to SPTS + aging, 300°C – 6 h (b).

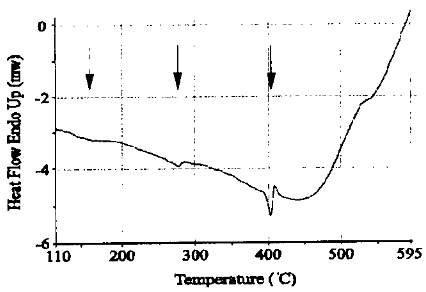

1

Figure 3. DSC curve of nanostructured VT6 alloy, processed by quenched + SPTS at the heating rate of 40 °C/min.

SPTS process increased the microhardness by 44%. Annealing of the deformed alloy leads to the formation of more equilibrium microstructure due to different relaxation processes and structure-phase transformations. DSC measurements of nanostructured VT6 alloy (Fig. 3) show two broad and one strong exothermic peaks (around T=150, 275, 400 °C) during a temperature scan to 590 °C at a heating rate of 40 °C/min. The first two peaks are connected with recovery processes associated with point defect and dislocation density decrease [5], while the last one is associated with recrystallization processes. Note that the recrystallization temperature of the nanostructured Ti alloy decreases by more than 400 °C as compared with its coarse-grained counterpart. Heating at the temperature of 300°C for 0.5 h slightly decreases H_v .Nevertheless, samples aged at 300°C for half hour following the quenching and SPTS show tensile strengths of > 1500 MPa, which is very high for this alloy system.

CONCLUSIONS

Al and Ti alloys with nanostructures and supersaturated solid solutions were processed by SPTS. Changes in microstructure and phase composition caused by annealing were studied. It was found that SPTS promotes the dissolution of second phase particles in the quenched Al-alloy and enhances the subsequent natural aging. For Ti alloy, SPTS at the room temperature resulted in the α'' martensite phase decomposition to form α' martensite and metastable β-phase. The nanostructure in the Ti alloy also leads to a significantly lower recrystallization temperature. Very high tensile strength was obtained after the Ti alloy was subjected to quenching, SPTS and aging. This work demonstrated the potential for significantly improving alloy strength through a combination of SPTS and aging.

REFERENCES

1. Valiev R.Z., Ann. Chim., Mat. Sci., Fr., 21, 6-7 (1996).
2. Stolyarov V.V., Latysh V.V., Shundalov V.A., Salimonenko D.A, Islamgaliev R.K.,Valiev R.Z., Mater. Sci. Eng. A 234-236 (1997) 339-342.
3. Senkov O.N, Froes F.H., Stolyarov V.V., Valiev R.Z. and Liu J., Proc. of 5th Int. Conf. Advanced Particulate Materials and Processes, Eds F.H. Froes and J. Hebeisen, April 1997, West Palm Beach, USA
4. Ilyin A.A., *Mechanism and kinetic of phase and structural transformations in Ti-based alloys,* Nauka, Moscow, 1994, 304
5. Tschope A., Birringer R., Gleiter H., Calorimetric measurements of the thermal relaxation in nanocrystalline platinum, J.Appl.Phys., 71 (11) (1992) 5391-5394

Pergamon

NanoStructured Materials, Vol. 12, pp. 927–930, 1999
Elsevier Science Ltd

0965-9773/99/$–see front matter

PII S0965-9773(99)00269-X

MAGNETIC PROPERTIES AND STRUCTURE OF NANOCRYSTALLINE Fe-Al AND Fe-Ni ALLOYS

E. Jartych[1], J. K. Żurawicz[1], D. Oleszak[2], M. Pękała[3]

1) Department of Experimental Physics, Institute of Physics, Technical University of Lublin, ul. Nadbystrzycka 38, 20-618 Lublin, Poland

2) Department of Materials Science and Engineering, Warsaw University of Technology, ul. Narbutta 85, 02-524 Warsaw, Poland

3) Department of Chemistry, University of Warsaw, Al. Żwirki i Wigury 101, 02-089 Warsaw, Poland

Abstract - *Magnetic and structural properties of nanocrystalline Fe-Al and Fe-Ni alloys were investigated. Alloys were prepared by the mechanical alloying process. The standard X-ray diffraction, Mössbauer and magnetic studies were carried out on the powder samples. The structural investigations proved that in the low-energy mechanical alloying process of Fe and Al the disordered bcc solid solution was formed up to 50 at.% Al. Alloys were amorphous for Al content between 50 and 90 at.%. The final products of milling exhibited interesting magnetic properties different as compared with microcrystalline alloys. In the case of Fe-Ni alloys the bcc solid solution was formed during high- energy ball milling for the composition with 20 at.% Ni, while above 35 at.% Ni the fcc solid solutions were obtained. All mechanically synthesized Fe-Ni alloys were ferromagnetic and no Invar effect was observed for 35 at.% Ni.* ©1999 Acta Metallurgica Inc.

INTRODUCTION

Recently nanocrystalline materials have been intensively investigated because of their outstanding properties (1). Specific magnetic properties of nanocrystals, i.e. saturation magnetization, coercivity, magnetic ordering temperature and hyperfine magnetic field are remarkably different than those of the microcrystalline material. This work is aimed to study structural and magnetic properties of nanocrystalline Fe-Al and Fe-Ni alloys prepared by mechanosynthesis. The obtained results are discussed and compared with the data for microcrystalline alloys with the same compositions. More details were published in (2,3).

EXPERIMENTAL

Powdered Fe, Al and Ni of 99.9 % purity and particle sizes smaller than 100 μm were mixed to get the following compositions: Fe-30, 40, 50 and 75 at.% Al and Fe-20, 35 and 50 at.% Ni. The mechanical alloying process of Fe-Al system was performed in a conventional horizontal low-energy ball mill rotating at a speed of 90 rpm. In the case of Fe-Ni alloys the high-energy mechanosynthesis was performed in the planetary ball mill rotated at a speed of

240 rpm. A stainless-steel vial and balls were used in both cases. All powder handling was performed in a glove-box under an argon atmosphere.

During the studies several standard experimental techniques were applied, i.e. X-ray diffraction, differential scanning calorimetry (DSC), magnetization measurements and Mössbauer spectroscopy (MS). The chemical analysis was made with the relative accuracy up to 3 % and proved that the final composition of obtained Fe-Al and Fe-Ni alloys was the same as the initial proportions of the suitable powders.

RESULTS AND DISCUSSION

The performed studies indicate a strong influence of the mechanical treatment on the magnetic properties of the investigated Fe-Al and Fe-Ni alloys. The analysis shows that milling affects the formation of nanocrystalline phase.

Structure and magnetic properties of Fe-Al alloys

For Al concentrations of 30, 40 and 50 at.% the final products of the milling process were disordered Fe(Al) solid solutions with bcc structure. Above 50 at.% Al the alloys were amorphous up to 90 at.% Al. The lattice constants were 0.2915 nm, 0.2925 nm and 0.2935 nm for 30, 40 and 50 at.% Al, respectively. The crystallite size D and the level of internal strains e obtained by the Williamson-Hall approach were about 4-10 nm and 0.50 %, respectively. DSC measurements and X-ray analysis proved that the phase composition of the mechanically alloyed Fe-30 at.% Al and Fe-40 at.% Al did not change after the heat treatment. In the case of Fe-50 at.% Al and Fe-75 at.% Al alloys ordered FeAl and Fe_2Al_5 intermetallic compounds were formed after heating, respectively (2,3).

Magnetic measurements revealed a strong ferromagnetic interaction, even for 75 at.% Al. During the mechanical alloying process the intermediate phases arose most probably due to the fast diffusion of the Al atoms into the surface layer of nanograins, however they disappeared after 400 h of milling. The final bcc Fe-Al alloys had the magnetic ordering temperature T_c above 1000 K while for the amorphous Fe-75 at.% Al alloy T_c was about 570 K. It is worth emphasizing that T_c of nanocrystalline Fe-Al alloys was significantly larger than that of the microcrystalline alloys (2). The room temperature magnetization σ diminished monotically with the increasing milling periods. For 800 h milled Fe-30 at.% Al and Fe-40 at.% Al alloys the values of σ were about 10 % smaller as compared with the corresponding microcrystalline alloys (2). However, for Fe-50 at.% Al and Fe-75 at.% Al σ reached very large values that was probably caused by traces of still unreacted iron.

Mössbauer spectroscopy provides the information about the local atomic arrangement. Fig.1a) shows the Mössbauer spectra of the mechanically synthesized Fe-Al alloys after 800 h of milling. The fitting by the hyperfine magnetic fields (HMF) distribution was adopted on the Hesse-Rübartsh method. The broad HMF distributions p(B) (Fig. 1b) are result of the high grain boundary density, defects and the relatively high strain level. Only for the Fe-30 at.% Al the local environment model may be applied giving, for magnetic field of about 29 T, three and fewer Al atoms as the nearest neighbourhood of the ^{57}Fe atom. In alloys with 40 and 50 at.% Al any number of Al neighbours might be present. It is known that the hyperfine

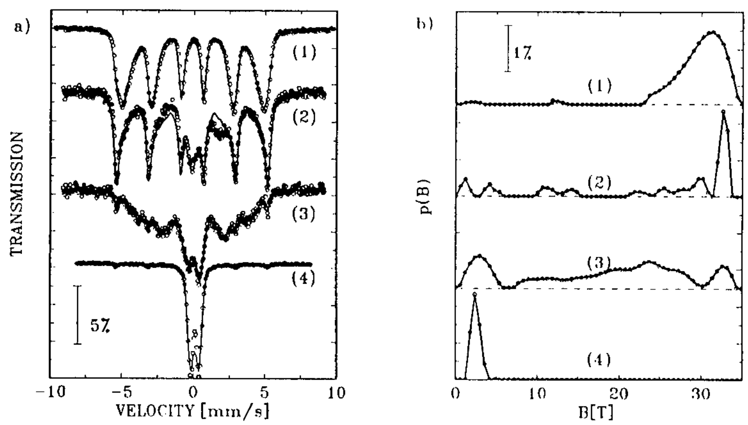

Fig. 1 a) Room temperature Mössbauer spectra and b) HMF distributions for mechanically synthesized 1) Fe-30 at.% Al, 2) Fe-40 at.% Al, 3) Fe-50 at.% Al and 4) Fe-75 at.% Al

magnetic field reaches zero at the concentration of 47.5 at.% Al (4). In our research the Fe-50 at.% Al and Fe-75 at.% Al alloys consisted of two magnetic phases: paramagnetic and ferromagnetic.

Structure and magnetic properties of Fe-Ni alloys

X-ray diffraction studies proved that in the high-energy mechansynthesis of Fe and Ni the bcc solid solution with the lattice parameter of about 0.2869 nm was formed for 20 at.% Ni. Alloys with Ni content between 30 and 40 at.% are known to exhibit a structure phase transition from bcc to fcc and the Invar effect (5). Our X-ray analysis of mechanically synthesized Fe-35 at.% Ni and Fe-50 at.% Ni alloys proved that they had the same fcc structures with lattice parameters of about 0.3591 nm and 0.3594 nm, respectively without any traces of the Invar effect. The average crystallite sizes were 10 nm and the mean level of lattice strain was about 0.50 %.

Magnetic measurements revealed the high values of room temperature magnetization σ being dependent on milling time in opposite manner as compared Fe-Al alloys, i. e. σ increased with the raising milling period. Magnetic ordering temperature diminished with the increasing milling time in the case of Fe-20 at.% Ni and Fe-50 at. % Ni alloys while for Fe-35 at.% Ni T_c is independent on milling period. All values of T_c of 50 h milled Fe-20, 35 and 50 at.% Ni alloys were higher than those of the microcrystalline alloys.

Mössbauer spectra and HMF distributions for 50 h high-energy ball milled Fe-Ni alloys are presented in Fig. 2. The final alloys were ferromagnetic and no Invar effect was observed for Fe-35 at.% Ni. The average values of the hyperfine magnetic fields obtained from HMF distributions were equal to 33.8 T for Fe-20 at.% Ni and 31.5 T for both Fe-35 at.% Ni and Fe-50 at.% Ni alloys. Assuming the local environment model the average number of Ni nearest neighbours of the ^{57}Fe atom might be determined. In Fe-20 at.% Ni alloy the ^{57}Fe atom had one or two Ni atoms in the first coordination sphere while in Fe-35 at.% Ni and Fe-50 at.% Ni alloys at most five Ni atoms were located in the nearest neighbourhood.

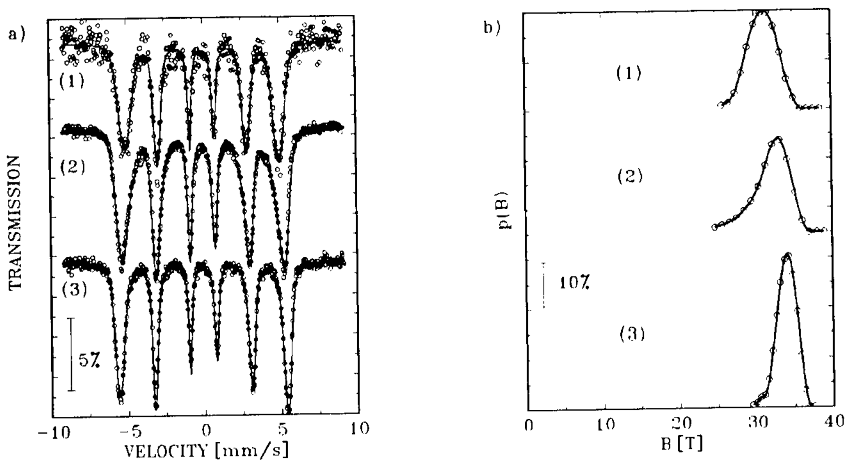

Fig. 2 a) Room temperature Mössbauer spectra and b) HMF distributions for mechanically synthesized 1) Fe-50 at.% Ni, 2) Fe-35 at.% Ni and 3) Fe-20 at.% Ni alloys

CONCLUSIONS

X-ray diffraction studies indicated that the structure of nanocrystalline mechanically synthesized Fe-Al and Fe-Ni alloys was the same as for alloys prepared by other techniques. The magnetic ordering temperature T_c of the nanocrystalline alloys was larger than that of the corresponding alloys on a micrometric scale. The magnetization curves as well as the Mössbauer spectra revealed that the Fe-Al alloys formed during the low-energy ball milling process contained different magnetic phases. High-energy ball milled Fe-Ni alloys were only ferromagnetic. All observed differences between nanocrystalline alloys and adequate microcrystalline alloys seem to be caused by the different density of the grain boundaries.

ACKNOWLEDGMENTS

Financial support of the Science Research Committee under contracts No. 2 P03B 043 11 (E. Jartych), No. 7 T08D 043 10 (D. Oleszak) as well as university grant BST - 592 29 98 (M. Pękała) is gratefully acknowledged. Authors also thank Mrs Lata L and Mr Dobrowolski R for the chemical analysis.

REFERENCES

1. Kurth, C. and Schultz, L., *J. Appl. Phys.* 73 6588 1993
2. Jartych, E., Żurawicz, J. K., Oleszak, D. and Pękała, M., *J. Phys.: Condens. Matter* 10 4929 1998
3. Jartych, E., Żurawicz, J. K., Oleszak, D., Sarzyński, J. and Budzyński, M., *Hyperfine Interact.* 99 389 1996
4. Perez Alcazar, G. A. and Galvao da Silva, E., *J. Phys. F: Met. Phys.* 17 2323 1987
5. Guillaume, Ch. E., *Compt. Rend. Acad. Sci.*, Paris 125 235 1897

Pergamon

NanoStructured Materials, Vol. 12, pp. 931–934, 1999
Elsevier Science Ltd

0965-9773/99/$–see front matter

PII S0965-9773(99)00270-6

INVESTIGATION OF THE SOFT MAGNETIC PROPERTIES OF FeCuNbB ALLOYS

T. Girchardt [1], J. Hesse [1], A. Grabias [2], M. Kopcewicz [2], D. Ramin [3], W. Riehemann [3]
1) Institut für Metallphysik und Nukleare Festkörperphysik, TU Braunschweig, Mendelssohnstr. 3, 38106 Braunschweig, Germany
2) Institute of Electronic Materials Technology, Wolczynska Str. 133, PL-01-919 Warsaw, Poland
3) Institut für Werkstoffkunde und Werkstofftechnik, TU Clausthal, Agricolastr. 6, 38678 Clausthal-Zellerfeld, Germany

Abstract -- *The alloy system of $Fe_{86-x}Cu_1Nb_xB_{13}$ (x=4, 5) was subject to an investigation of its soft magnetic properties.*

The amorphous ribbons were annealed for 1 hour at different temperatures, in order to obtain samples in different crystallisation states, including the nanocrystalline state. After that a phase analysis was done using room temperature Mössbauer spectrometry. The soft magnetic properties were studied using the Mössbauer effect in radio frequency (rf) magnetic fields. We could show that classical measurements, like those of the coercive force H_C, correspond well to the results obtained by our rf Mössbauer measurements.

INTRODUCTION

In order to learn about the soft magnetic properties of $Fe_{86-x}Cu_1Nb_xB_{13}$ (x=4, 5) we investigated the amorphous alloys as well as annealed samples, using "classical" magnetic hysteresis loop measurements and the Mössbauer effect in radio frequency (rf) magnetic fields. The applied rf magnetic field can cause two effects. The first is the sideband effect, which reproduces the Mössbauer spectrum on both sides of the original spectrum. The relative sideband intensity is a measure for the magnetostriction of the sample. The second effect is the rf collapse. If the applied field is strong enough to overcome the anisotropies inside the sample, the typical six line pattern of a Mössbauer spectrum of a ferromagnetic sample collapses to a single line (we will neglect electronic influences like quadrupoles here); intermediate states are possible, too (for details, see (1, 2)).

So the criteria for a soft magnetic state would be a low sideband intensity, meaning only little hysteresis losses due to mechanical work and a - preferably complete - rf collapse indicating low anisotropies.

EXPERIMENTAL, RESULTS AND DISCUSSION

We annealed the amorphous samples for one hour at given temperatures under He atmosphere. We chose 550 °C to obtain samples in a nanocrystalline state, consisting mostly of α-Fe nanograins and a remaining amorphous phase, and 625 °C to achieve a microcrystalline composition with significant amounts of FeB compounds. The samples were then investigated with a magnetometer (3) and with the Mössbauer effect. First spectra were recorded without any applied field at room temperature. By means of these spectra, a phase analysis was done, which confirms the structural composition. Results are not shown here. Then the samples were exposed to an rf field of 60.8 MHz and a strength of 20 Oe. We used a $^{57}Fe(Rh)$ source and a linear velocity.

Tables 1 and 2 show the results of the hysteresis loop measurements. The as quenched amorphous samples are relatively soft magnetic, which is in good accordance with fig. 1. Both samples show a complete rf collapse. Surprisingly the sidebands of the sample with 4 at% Nb are much more intense, which would mean that the sample is less soft, but the complete collapse here only reveals that the rf field strength is higher than the necessary field strength to cause the collapse, but not how much higher.

The samples annealed at 550 °C are still relatively soft, but the collapse in fig. 2 is only partial in both cases, which means that only a portion of the magnetic moments can follow the external field, due to increased anisotropies of the crystalline components. The intensity of the single line in the centre of the spectrum is higher in the lower right spectrum, telling this sample is magnetically softer than the other, which complies well with the values in tables 1 and 2. According to the values of H_C and the losses, the nanocrystalline sample of $Fe_{81}Cu_1Nb_5B_{13}$ should be magnetically softer than the amorphous one, but one should notice that the structural composition is completely different and therefore the rf magnetisation reversal mechanism is different in the amorphous and crystalline state, so the comparability is not complete.

After annealing the amorphous samples at 625 °C things change again. A comparison of fig. 2 and 3 shows (right spectra) a small decrease of the intensity of the centre lines compared with that of the outer lines, indicating further increased anisotropies.

TABLE 1

Coercive Forces

annealing temperature	H_c [A/m] (static, extrapolated to f=0) $Fe_{82}Cu_1Nb_4B_{13}$	H_c [A/m] (static, extrapolated to f=0) $Fe_{81}Cu_1Nb_5B_{13}$
as quenched	2.8	6.6
550 °C	15.7	3.1
625 °C	94.2	6.0

TABLE 2

Losses

annealing temperature	P/f [J/m³] (static, extrapolated to f=0) $Fe_{82}Cu_1Nb_4B_{13}$	P/f [J/m³] (static, extrapolated to f=0) $Fe_{81}Cu_1Nb_5B_{13}$
as quenched	7.0	16.0
550 °C	29.5	7.4
625 °C	160.2	12.0

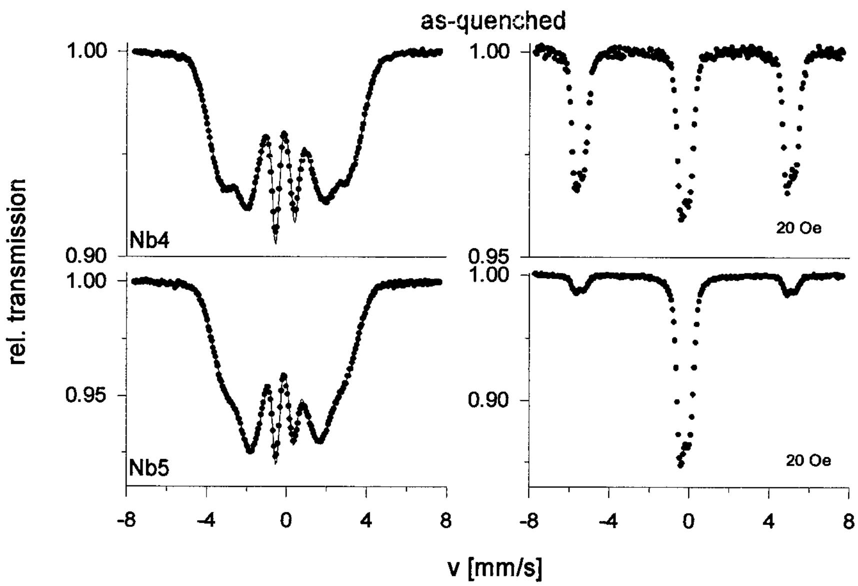

Fig.1 Mössbauer spectra of the amorphous alloys. Left: without rf, right: with rf (20 Oe, 60.8 MHz).

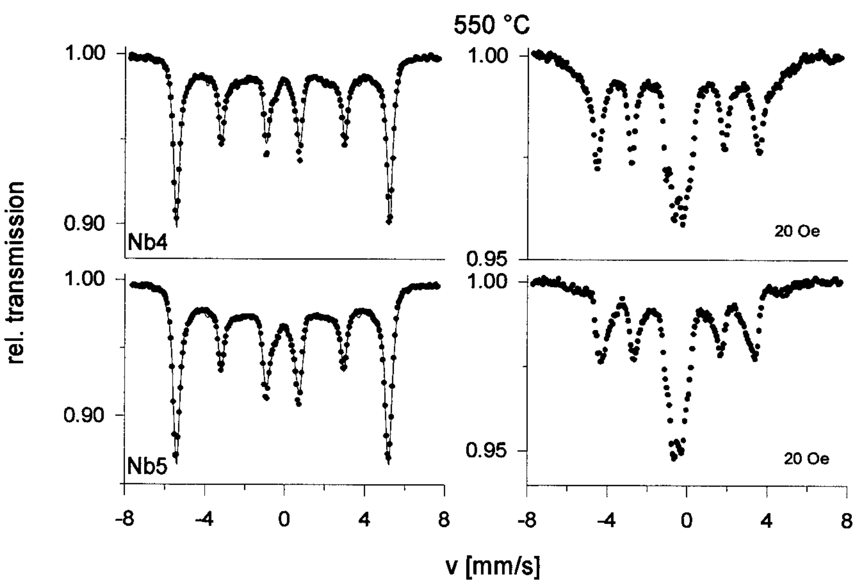

Fig.2 Mössbauer spectra of the samples annealed at 550 °C. Left: without rf, right: with rf (20 Oe, 60.8 MHz).

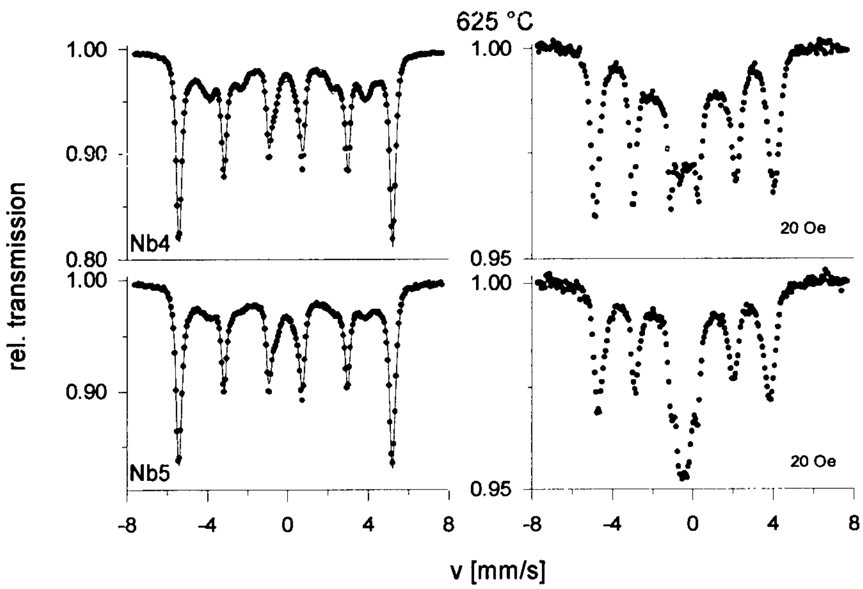

Fig. 3 Mössbauer spectra of the samples annealed at 625 °C. Left: without rf, right: with rf (20 Oe, 60.8 MHz).

ACKNOWLEDGEMENTS

The authors are grateful to Dr. G. Herzer, Vacuumschmelze GmbH, Hanau (Germany) for the amorphous samples. The work was financially supported by the German "Internationales Büro des BMBF", the Deutsche Forschungsgemeinschaft (DFG) and the Polish Committee of Science.

REFERENCES

1. J. Hesse, T. Graf, M. Kopcewicz, A. Afanas'ev, M. Chuev, *Hyperfine Interactions*, in press
2. M. Kopcewicz, *Structural Chemistry* 2, 313, 1991
3. C. Wittwer, W. Riehemann and W. Heye, *J. Magn. Magn. Mat.* 133, 287, 1994

Pergamon

NanoStructured Materials, Vol. 12, pp. 935–938, 1999
Elsevier Science Ltd

0965-9773/99/$–see front matter

PII S0965-9773(99)00271-8

SOFT MAGNETIC PROPERTIES OF Fe(Cu,Nb)SiB ALLOYS EVIDENCED BY MÖSSBAUER EXPERIMENTS IN RADIO FREQUENCY MAGNETIC FIELDS

T. Graf [1), J. Hesse [1) and M. Kopcewicz [2)

1) Institut für Metallphysik und Nukleare Festkörperphysik, Mendelssohnstrasse 3, D-38106 Braunschweig, Germany

2) Institute of Electronic Materials Technology, Wolczynska Str. 133, PL-01-919 Warsaw, Poland

Abstract--*Conventional (transmission) Mössbauer effect investigations on alloys exhibiting a nanostructure deliver valuable information about the alloys' micro structure. The application of a radio frequency (rf) magnetic field parallel to the absorber plain causes the Mössbauer effect to become a very sensitive tool for detecting soft magnetic properties. These features are due to two effects, the appearing of sidebands in the spectra and the collapse of the spectrum. We demonstrate the abilities of this measurement method comparing well- known results about coercivity with the information content of the Mössbauer spectra collected at different compositions of the Fe(Cu,Nb)SiB alloys. ©1999 Acta Metallurgica Inc.*

The experimental method described in this paper is based on two effects discovered by Pfeiffer (1,2) on Mössbauer spectra collected in a radio frequency (rf) magnetic field: the collapse effect and the sideband effect. Collapse means that the well-resolved, magnetically splited spectrum totally collapses to a central line only exhibiting electrical hyperfine interactions like isomer shift and quadrupole splitting (also their distributions). The total collapse of the spectrum appears if the applied rf field strength is high enough and the rf frequency is markedly bigger than the Larmor frequency of the nuclei in the experienced magnetic hyperfine field. Recent investigations of nanostructured soft ferromagnetic alloys in rf fields led to the discovery that the collapse in the Mössbauer spectra can become selective and partial (3). It means that the magnetisation reversal is not fast enough and differs in the various phases of the alloy.

The sideband effect appears if the sample exhibits magnetostriction. Although the magnetostrictive effect changes the sample's dimension in the direction of the applied magnetic field the volume of the sample remains constant. Therefore forced oscillations of the absorber appear (also in the direction of the gamma ray propagation) and reproduce the spectrum as sidebands in equal distances from the main spectrum (determined by the rf frequency).

Since 1988 a new class of very soft magnetic materials has been discovered. First Yoshizawa et al (6,7) reported that after suitable annealing a nanostructured phase can be formed when into a 'classic' amorphous alloy Fe-Si-B, small amounts of Cu and, for example, Nb are added. So the famous FINEMET or VITROPERM alloy $Fe_{73.5}Cu_1Nb_3Si_{13.5}B_9$ was created (very good soft magnetic properties, as high permeability and very low magnetostriction, combined with high saturation magnetisation). These properties occur due to the fact that the nanosized phase consists

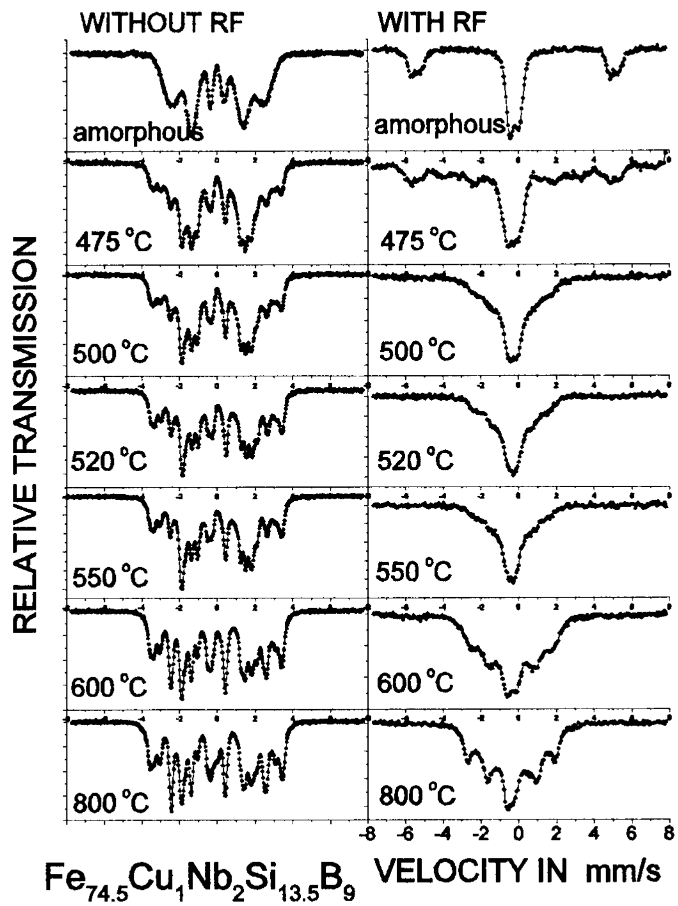

Fig. 1: Mössbauer spectra of the alloy indicated without and with rf. Parameter is the annealing temperature.

of particles with diameters smaller than the magnetic correlation length and exhibits a magnetostriction just opposite to that of the amorphous phase (in this alloy the number and sizes of the nano-particles are so that the magnetostriction of the amorphous phase is compensated).

In rf Mössbauer experiments disappearing sidebands indicate vanishing magnetostriction (4, 5) and therefore the most important condition for achieving the very soft magnetic state. Also the collapse effect can be used to decide either or not the alloy is in an optimum soft magnetic state. To do this we first 'calibrated' the rf field strength performing series of measurements in rf magnetic fields of different strengths on the well-known $Fe_{73.5}Cu_1Nb_3Si_{13.5}B_9$ alloy (3, 5). After that we can start to investigate properties of 'unknown' alloys. We demonstrate the results on two alloy series (which agree with the samples' as reported by Yoshizawa et al (6, 7)) of the composition $Fe\text{-}Cu_{(0,\,0.5,\,1)}\text{-}Nb_3Si_{13.5}B_9$ and $Fe\text{-}Cu_1Nb_{(2,\,3,\,5)}\text{-}Si_{13.5}B_9$ varying the Cu and Nb content vs Fe.

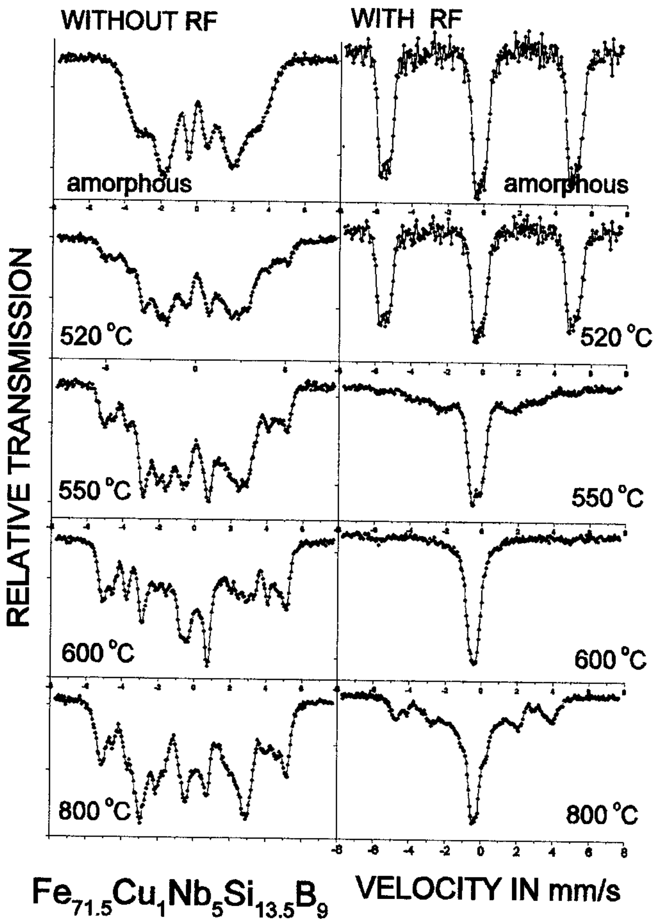

Fig. 2: Mössbauer spectra of the alloy indicated without and with rf. Parameter is the annealing temperature.

In this paper, due to lack of space, only results for the $Fe\text{-}Cu_1Nb_{(2,5)}\text{-}Si_{13.5}B_9$ alloy will be given in the figures.

The melt-spun amorphous ribbons (about 19 μm thick and 15 mm wide) were produced by the Vacuumschmelze GmbH, Hanau, Germany. The one hour anneals were performed in a computer-controlled furnace in a He gas atmosphere. The absorber was exposed to a rf magnetic field (frequency 60.8 MHz, field amplitude about 1600 A/m ≈20 Oe) applied in the plane of the sample. It is a problem to avoid rf heating. Therefore, the absorbers were mounted on a water-cooled sample holder. To all samples the same rf field strength was applied causing the unavoidable heating to be nearly equal for all samples in question.

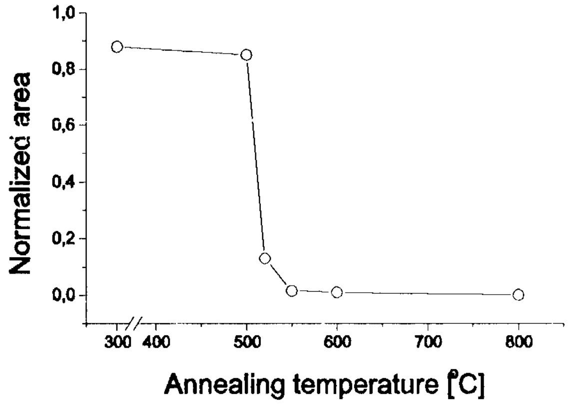

Fig. 3: The relative magnetostriction for the alloy $Fe_{71.5}Cu_1Nb_5Si_{13.5}B_9$ as determined from the sideband area.

In Fig.1 we present (left column) a series of conventional spectra collected after different anneals of the $Fe_{74.5}Cu_1Nb_2Si_{13.5}B_9$ alloy: the as quenched amorphous state, the nanostructured state (achieved after annealing for one hour at 520-550 °C) and the states where micro crystallisation starts (annealing at 600 °C and more). In the right column the spectra collected in the rf field are presented. It can be observed that in no case a total collapse has been reached. This indicates that all these alloys were 'magnetically harder' than the reference alloy $Fe_{73.5}Cu_1Nb_3Si_{13.5}B_9$ which exhibited a totally collapsed spectrum without sidebands.

In Fig. 2 we present a series of spectra collected on differently annealed samples of the $Fe_{71.5}Cu_1Nb_5Si_{13.5}B_9$ alloy. In the right column are the rf spectra. The spectrum corresponding to the alloy annealed at 600 °C indicates that the rf amplitude is large enough to cause the total collapse effect. It can be observed that the sidebands disappear completely. So at this annealing temperature a very soft magnetic state is achieved in complete agreement with measurements of (6, 7). Following the intensity of the side bands vs annealing temperature the relative strength of the samples' magnetostriction can be evaluated (Fig. 3.).

Acknowledgements: The authors are indebted to Dr. G. Herzer, Vacuumschmelze GmbH, for providing the as quenched amorphous ribbons and to the Internationales Büro, (Köln, BMBF) and the Polish Committee of Scientific Research for supporting our collaboration.

References:

1. L. Pfeiffer, J. Appl. Phys. 42, 1725, 1971.
2. L. Pfeiffer, in Mössbauer Effect Methodology, Vol. 7, Plenum Press, New York, 1972 p. 263
3. J. Hesse, T. Graf, M. Kopcewicz, A. Afanas'ev, M. Chuev, Hyperfine Interactions, in press
4. T. Graf, M. Kopcewicz and J. Hesse, J.Magnetism Mag. Mat. 140-144, 423, 1995
5. T. Graf, M. Kopcewicz and J. Hesse, NanoStructured Materials, 6, 937, 1995
6. Y. Yoshizawa, S. Oguma and K. Yamauchi, J.Appl.Phys. 64, 6044, 1988
7. Y. Yoshizawa, K. Yamauchi, J. Japan. Inst. Metals 53, 241, 1989

Pergamon

NanoStructured Materials, Vol. 12, pp. 939–942, 1999
Elsevier Science Ltd

0965-9773/99/$–see front matter

PII S0965-9773(99)00272-X

SIZE AND SHAPE EFFECT ON THE CANTED ANTIFERROMAGNETISM IN α-Fe_2O_3 PARTICLES

D. Fiorani, A.M.Testa, L. Suber
ICMAT, CNR,Area della Ricerca di Roma, CP 10 - 00016 Monterotondo Stazione (Italy),

M. Angiolini, A. Montone
ENEA, INN-NUMA, Casaccia, (Roma)

M . Polichetti
Unita' INFM- Dip Fisica dell'Universita' di Salerno

Abstract The effect of thermal treatments on both the Morin transition and the spin flop field (H_{sf}) of α-Fe_2O_3 acicular particles (major axis:(350 ± 50) nm ; minor axis: (85 ± 15) nm.) has been investigated by means of magnetization vs temperature-magnetic field measurements. Both the Morin transition and the spin flop process have been observed only after an annealing treatment at 500°C. Due to the finite size effect, the values of the Morin temperature and spin-flop field are significantly below the bulk value.

INTRODUCTION

The magnetic properties of antiferromagnetic nanoparticles have been receiving a renewed attention in the last few years because of their potential for exhibiting magnetization reversal by quantum tunneling (1). Moreover, open questions still remain about their magnetic behaviour, the Néel theory having never been carefully verified. The net moment of an antiferromagnetic particle, resulting from the non exact compensation of the two magnetic sublattices, is very sensitive to the particle size and lattice strain and defects . Bulk crystalline α-Fe_2O_3, (T_N = 960 K (2,3)) is an antiferromagnet with spin axis lying along the rhombohedral [111] axis below 263 K (the Morin temperature T_M) (4), and in the (111) plane above T_M. Thus for T< T_M, hematite is an uniaxial AF and spin flopping occurs in high enough fields. Due to the anisotropic superexchange interaction (5,6), spins are slightly canted out of the basal plane (approx. 1°), giving rise to a weak ferromagnetic state (7). In nanoparticles, particle size, lattice strain and defects have a strong influence on both the Morin temperature T_M. and the spin flop field (B_{sf}). So far, these effects have been mainly investigated in spherical particles (8-10). In this context, we have investigated the effect of thermal treatments on both the Morin transition and the spin flop field (B_{sf}) of α-Fe_2O_3 acicular particles by means of magnetization vs temperature-magnetic field measurements

EXPERIMENTAL

α-Fe_2O_3 acicular particles (major axis: (350 ± 50) nm ; minor axis: (85 ± 15) nm.) were prepared by reaction of 2 10^{-2} M $FeCl_3$ and 3.8 10^{-4} M NaH_2PO_4 in H_2O at 100 °C for three days. The precipitate was ultracentrifuged and washed several times with water. The powder was then dried overnight at 50 °C. The thermal treatment was performed by heating the sample at a rate of 3°C min $^{-1}$ to 500 °C for 24 hrs., and subsequent cooling at a rate of 1 °C min $^{-1}$ to room temperature. The size and shape of the particles were determined by Transmission Electron Microscopy (TEM) measurements performed by a a Jeol 4000 FX, operated at 400 kV. The magnetic properties were investigated by means of commercial SQUID and VSM magnetometers (for low field susceptibility and high field magnetization measurements, respectively).

RESULTS AND DISCUSSION

TEM diffraction experiments show the same pattern for the particles both before and after the thermal treatment. In particular, each particle show a single crystal like diffraction pattern; thus the structural differences induced by thermal treatments are not related to any change in the crystallographic structure. Moreover, low resolution - out of focus TEM observations show that the as prepared particles are constituted by small units (size of a few nm) separated by a less dense interlayer, while keeping all the same crystallographic orientation. After the thermal treatment, the structure appears to be compacted, probably by a sintering mechanism, and sherical spots (few nm wide) now appear (11). The less dense interlayer region is probably constituted by water and the thermal treatment induces its condensation in the form of microdrops that on evaporating leave their imprint as spherical empty spaces into the particle. The magnetic behaviour is indeed affected by such structural differences. Before the thermal treatment, the low field zero field cooled susceptibilty is observed to monotically increase with temperature.On the other hand, a sharp increase is observed around 170 K after the annealing (fig.1), signalling the Morin transition accompanied by the appearance of a weak ferromagnetic moment.

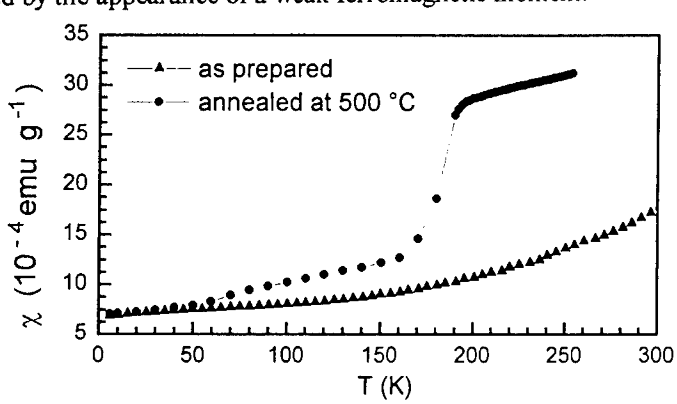

Fig.1 Susceptibility as a function of temperature for the as prepared (triangle) and annealed sample (circle)

The occurrence of weak ferromagnetism is also observed in magnetization vs field measurements. The as prepared sample shows an antiferromagnetic behavior, superimposed to a non compensated moment (fig.2): indeed, data can be described for B_a >1T by a linear law, $m = m_o + \chi_{af} B_a$, being m_0 and the antiferromagnetic susceptibility χ_{af} essentially temperature independent. Conversely, for the annealed sample the magnetization curve displays a "knee" in the field range 2-3 T for temperatures up to 150K (fig.3).

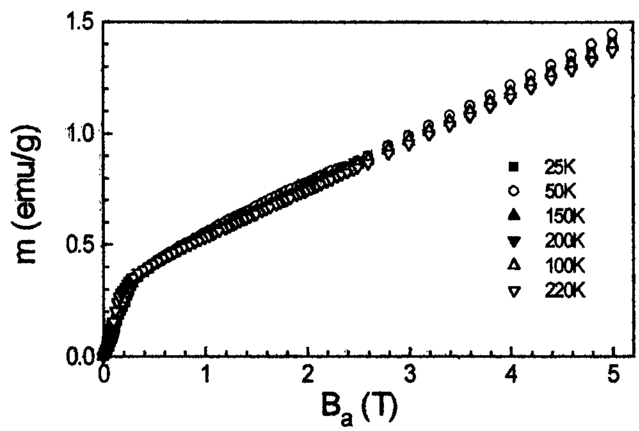

Fig.2 Magnetization vs field at different temperatures for the as prepared sample

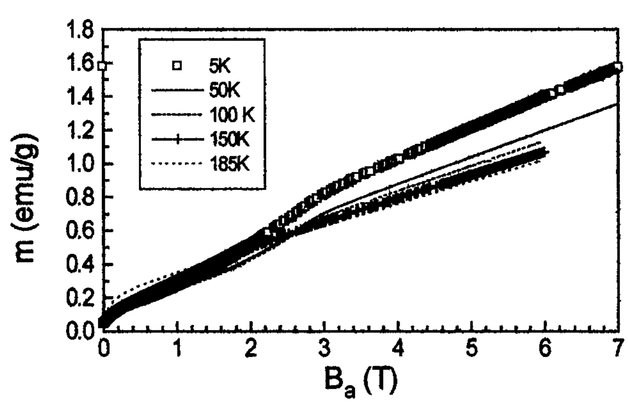

Fig.3 Magnetization vs field at different temperatures for the annealed sample

Such change in the slope of the curve is typical of a "spin flop" process occurring at a temperature dependent field (12), which vanishes at the Morin temperature (fig.4). Furthermore, the use of the linear law in the temperature range 100K-280K yields an intercept which is now temperature dependent, showing an abrupt increase between 150K-

180K (fig.4). Such feature is typical of a weak ferromagnetic behavior: the weak ferromagnetic moment m_0 retains essentially the bulk value, whilst the spin flop field has a value significantly smaller than the bulk (i.e. 6.8 T (12)). The spin-flop field at temperatures well below the Neel point is given approximately by the the geometric mean of the exchange field H_e and the anisotropy field H_a : $H_{sf} \cong (H_e H_a)^{1/2}$, which is reduced in our case by the effect of size confinement

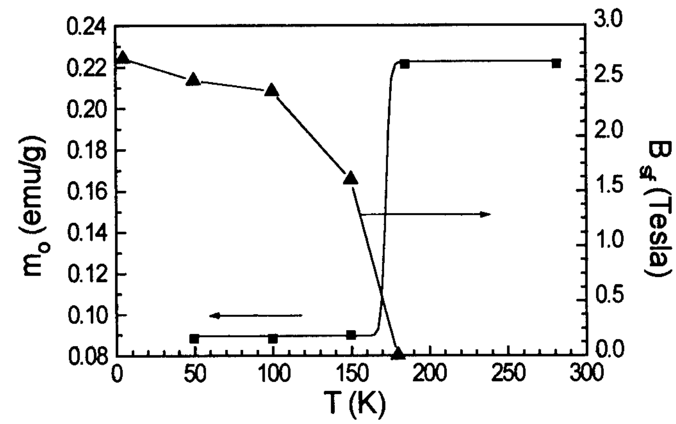

Fig.4 Spin-flop field (triangle) and weak ferromagnetic moment (square) as a function of temperature

In conclusion, the results show that both the Morin transition and the spin flop field strongly decrease with decreasing particle volume and they are strongly affected by microstructural changes induced by thermal treatments

References

1 Ibrahim M. M., Darwish S. and Seehra M., Phys. Rev. B, (1995) 51, 2955
2 Lida S. and Mizeshima K., J. Phys. Soc. Jpn. (1966), 21, 401
3 Besser P. J., Morrish A. M., and. Searle C. W, Phys. Rev. (1967) 153, 632.
4 Morin F. J., Phys. Rev. (1950) 78, 819
5 Dzialoshinskii I. E., J. Phys. Chem. Solids (1958).4, 241
6 Moriya T., Phys. Rev. (1960) 120, 91
7 Shüll C. G.,. Stranser W. A, and. Wollan E. O, Phys. Rev. (1951) 83, 333
8 Yamamoto N., J. Phys. Soc. Jpn. (1968) 24, 23
9 Kündig W.,. Bommel H,. Constabaris G, and. Lindquist R. H, Phys. Rev. (1966) 142, 327.
10. Muench G. J, Arajs S., and. Matijevic E, Phys. Status Solidi A (1985) 92, 187
11 Suber,L., Zysler, R., Garcia Santiago,A., Fiorani, D., Angiolini, M., Montone, A., Dormann, J.L. Materials Science Forum (1998), 269-272, 937
12 Besser, P.T., Morrish A.H. Physics letters (1964) 13, 289

Pergamon

NanoStructured Materials, Vol. 12, pp. 943–946, 1999
Elsevier Science Ltd

0965-9773/99/$–see front matter

PII S0965-9773(99)00273-1

POSITIVE MUONS IN NANOCRYSTALLINE TRANSITION METALS DIFFUSION AND MAGNETIC NANOSTRUCTURE

O.Hartmann, R.Wäppling and M.Ekström
Dept. of Physics, Uppsala University,S-75121 Uppsala, Sweden
B.Heisel, M.Schmelzer, H.Natter and R.Hempelmann,
Physical Chemistry, University Saarbrücken, D-66123 Saarbrücken, Germany

Abstract. *Systematic studies with Muon Spin Rotation (μSR) on nano-Cu and nano-Ni samples produced by pulsed electrodeposition, demonstrates that the diffusion of μ+ in nanocrystalline metals is influenced by the nanostructure. In nano-Cu the mobility of muons is reduced at higher temperatures, where they can reach the grain boundaries. In nano-Ni the appeareance of a longitudinal relaxation is interpreted to be due to muon diffusion to magnetically disordered regions. In the framework of this model, we are able to estimate how the thickness of these magnetically disordered region increases with temperature.*
©1999 Acta Metallurgica Inc.

INTRODUCTION

Positive muons in condensed matter can be considered as hydrogen isotopes with a rich variety of diffusion effects due to their light mass. Furthermore, due to their magnetic moment, positive muons are powerful probes for local magnetic fields. Muon behaviour in bulk metals and compounds have been extensively studied, but only a few attempts have been made to study nanocrystalline materials with μSR. Here we report on systematic studies on nanocrystalline Cu, Ni and Co samples created by pulsed electrodeposition.

EXPERIMENTAL

The nanocrystalline samples were produced by pulsed electrodeposition (1) which results in controlled grain sizes in the range from 10 to 100 nm (volume averaged diameter). The samples are quite dense, with interstitial impurity contents O and N in the order of a few thousand ppm, most likely located in the grain boundaries. More details about sample preparation can be found in (1) and (2).

The μSR experiments performed at ISIS, England, and at PSI, Switzerland. The measurements reported here were made in zero applied field, and in the temperature ranges from 10 K to 320 K obtained in standard cryostats. The muons are implanted in the whole volume of the sample, and their polarization is measured as a function of time after

implantation. The muons will occupy interstitial sites, and are very sensitive probes for any local magnetic field present. The μSR method is used to study local fields and relaxation in magnetic systems, as well as weak nuclear dipole broadening in non-magnetic metals.

RESULTS AND DISCUSSION

Nano-Cu:

Bulk Cu has been extensively studied by μSR, and the muon diffusion behavior, which is observed by means of the dipolar broadening from the Cu nuclear magnetic moments is well understood. Essentially the muons are static during their lifetime (τ_μ = 2.2 μs) at temperatures between T=10 K and T=100 K. Above T=100 K the muon motion increases with an approximate activation energy E_a = 55 meV, and with a low prefactor which implies that the diffusion mechanism for muons is phonon-assisted tunneling.

The temperature dependence of muon depolarization in bulk Cu and nano-Cu in zero field can be seen in Fig 1, which is obtained by fitting the data to a model-independent gaussian function $A(t) = A_o \exp(-\sigma^2 t^2)$. Here A_o is the initially observable polarization, which contains experimental geometry parameters etc. Above 200 K the observed depolarization rates σ in nano-Cu starts to deviate from those in normal bulk Cu. These data can then be interpreted in a model where the randomly implanted muons are able to diffuse inside the grains, but are slowed down and become immobile (trapped) close to the grain boundaries.

In the two-state model used for the final fit (2), one fraction of muons was assumed to start inside the grains, and be able to diffuse. A second small fraction was assumed to start close to or in the grain boundary, and to be in a distorted Cu environment, without possibility to move. Transitions from the first state to the second occur when diffusing muons approach

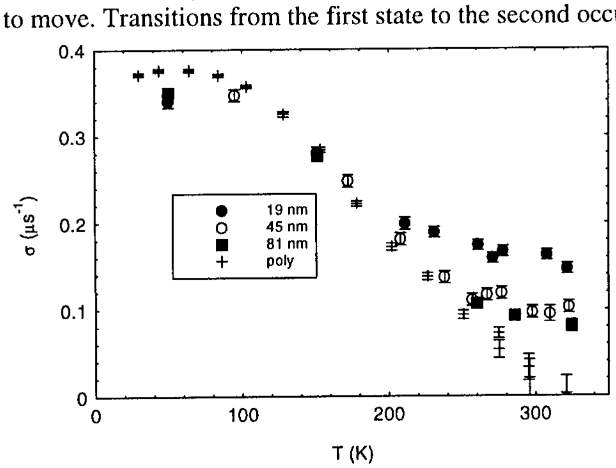

Fig 1. The initial depolarization rates in Cu with various grain sizes, showing the reduced muon mobility above T = 200 K in nano-Cu samples.

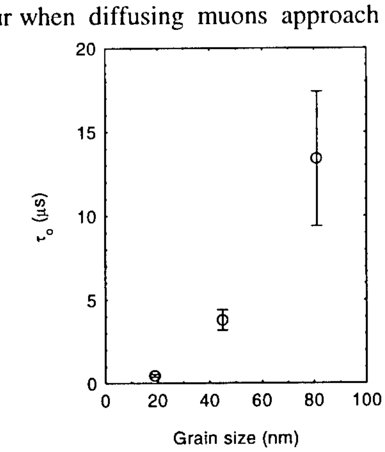

Fig 2. Comparison of times for muons to reach grain boundaries in nano-Cu.

the grain boundaries. The global fits of the data then give the diffusion jump time τ_c in the grains, and the average time τ_f to reach the second state (i.e. become immobilized in the amorphous boundary regions). From these global fits the fraction starting in the boundary regions is found to be small, the jump times τ_c similar to bulk Cu, and the trapping times τ_f = τ_o exp(E_a/kT) approximately proportional to d^2 where d is the average grain size (Fig 2).

Nano-Ni and nano-Co:

In ferromagnetic materials the muon precesses in the local magnetic field and the μSR signal in zero applied field can be written as $A(t) = A_p G_2(t) \cos(\omega t+\phi) + A_{np} G_1(t)$, which in polycrystal samples consists of a precessing part with amplitude $A_p = 2/3\ A_o$ and a non-precessing with $A_{np} = 1/3\ A_o$ The muon precession $\omega = \gamma B_\mu$ depends on the local magnetic field B_μ which is the sum of contact and dipolar fields $B_\mu = B_{cont} + B_d$. The damping or depolarization of this signal $G_2(t) = \exp(-\lambda_2 t)$ can be quite strong due to inhomogeneous distribution of local fields. For pure and well treated samples λ_2 is of the order of 1 μs^{-1} or less. The longitudinal relaxation $G_1(t) = \exp(-\lambda_1 t)$ is very weak in bulk ferromagnets

In nanocrystalline Ni the first observation is that the precessing signal (around 18 MHz at T = 300 K) is strongly damped, but still observable down to the smallest grain size 17 nm (Fig 3). The amplitude A_p of the signal is reduced at the smallest grain sizes, and the damping rate λ_2 increases gradually with decreasing grain size. This can be expected since the dipolar contributions to the local magnetic field at the muon sites close to boundaries can be expected to deviate somewhat from the average value in the interior of the grains. The average frequency of the precessing signal shows no strong deviations from that of bulk Ni.

The second main observation in nano-Ni is the appearance of a longitudinal relaxation time λ_1 which increases with temperature and with decreasing grain size (Fig 4). In the 92 nm ample, and in bulk Ni such relaxation is very weak or absent. Its physical origin must be a variation of he magnetic field components perpendicular to the muon spin direction. We do

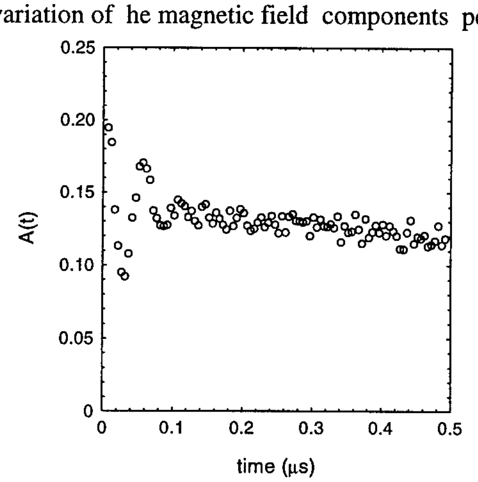

Fig 3. Initial part of μSR spectrum of a 17 nm nano-Ni sample at T=275 K.

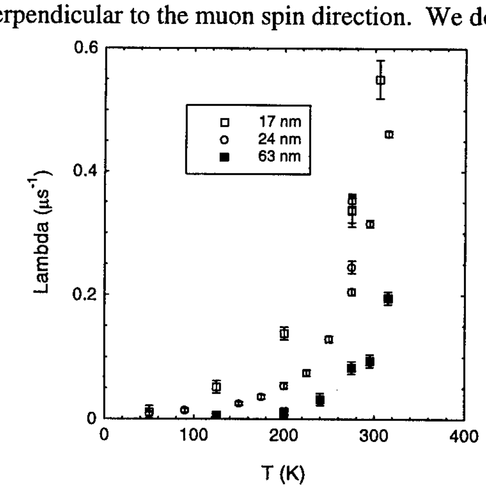

Fig 4. The longitudinal relaxation in nano-Ni for various grain sizes and temperatures.

not expect superparamagnetism in these densely packed samples, and therefore we interpret these data with a diffusion model in analogy with the Cu results.

In the interpretation with a diffusing model, there should be no depolarization λ_l inside the magnetic grains as long as muons jump between sites with the same direction of local field B_μ. A diffusing muon will however would experience a longitudinal depolarization if it moves to a position with different magnetic field direction. We have simulated various situations with M-C techniques, and can reproduce the shape of the depolarization function with a simplified picture starting with randomly implanted muons in spherical grains, and rapid depolarization when reaching boundaries. In this limit a closed formula can be used to obtain the diffusion coefficient D as D/R^2 where R is the average radius of the spheres.

The strong temperature dependence of the obtained D/R^2 obtained from the fits can not be due only to D, but shows that the effective radius R shrinks at elevated temperatures. With reasonable assumptions for D we obtain an approximate temperature dependence for the effective size of the magnetically homogeneous region. For the 17 nm sample this would imply a linear reduction from 17 nm average diameter at 100 K to about 5 nm at T=300 K. We conclude that the particles exhibit an 'effective' size of homogeneous magnetization, which is limited by the extension of the magnetic disorder, that goes together with the structural disorder in the grain boundaries, in accordance with the model of Kronmuller (3).

The μSR studies on nano-Co do not give as clear results as on nano-Ni, but the tendency in the observations is similar. The damping of the precession signal (around 3 MHz) is strong already at grain size 70 nm, and the precession is practically not observable at the smaller grain sizes. A weak longitudinal relaxation is observed at 10 nm particle size, but much weaker than in nano-Ni

CONCLUSION

Systematic μSR studies on nano-Cu as function of grain size shows that the muon diffusion is dependent on the grain size, mainly through limited mobility if the implanted muons can diffuse to boundary regions. In ferromagnetic nano-Ni and nano-Co, studies as function of grain size and temperature give insight into the magnetic nanostructure. The longitudinal depolarization observed in nano-Ni can be interpreted in a model where the muon is able to distinguish between a (narrow) geometrical grain boundary (with topological disorder) and a broad one with magnetic disorder (3). In the framework of this model based on muon diffusion we are able to estimate how the thickness of the magnetically disordered region grows with temperature in nano-Ni.

References

1. Natter,H, Krajewski,T. and Hempelmann, R., *Ber.Bunsenges.Phys.Chem.* 100 1996 55.
2. Soetratmo,M., Natter,H., Hempelmann,R., Hartmann,O., Wäppling, R. and Ekström,M., *Hyperfine Interactions* 105 1997 245.
3. Kronmüller,H., *Basic magnetic properties of nanocrystalline particles and particle ensembles,* in A.Hernando, *Nanomagnetism,* Kluwer Academic Publ., Amsterdam 1993.

Pergamon

NanoStructured Materials, Vol. 12, pp. 947–950, 1999
Elsevier Science Ltd

0965-9773/99/$–see front matter

PII S0965-9773(99)00274-3

INVESTIGATION OF POSSIBILITY TO GET SUPERPLASTIC STATE OF NANOSTRUCTURED COPPER

K.V. Ivanov, I.V. Ratochka, Yu.R. Kolobov.
Institute of Strength Physics and Material Science, RAS.
Pr. Academichesky 2/1,634021 Tomsk, Russia.

Abstract- *The possibility of realisation of superplastic state of nanostructured (NS) copper (grain size 0.1-0.3 μm) produced by equal-channel angular pressing has been studied during creep and tensile tests in vacuum and under the influence of aluminium grain boundary diffusion fluxes from external source (coating). The creep acceleration effect for NS copper under the influence of aluminium grain boundary diffusion fluxes is found. The effect takes place in a lower temperature range as compared with fine-grained copper. It has been established that at 473K strong increase of strain rate sensitivity* ($m=\partial \lg\sigma / \partial \lg\dot{\varepsilon}$) *takes place during deformation of copper under influence of aluminium diffusion fluxes (m=0.5) in comparison with pure copper (m=0.19).* *©1999 Acta Metallurgica Inc.*

INTRODUCTION

Investigations of nanostructured (NS) materials (grain size 0.1-0.3 μm) are intensively developed at present. It is connected with singularity of their physical and mechanical properties. It is known that the transition temperature of NS materials to superplastic state is essentially lower than that of similar but fine-grained (grain size 1-10 μm) superplastic alloys. This difference may be attributed to the higher value of diffusion coefficients in NS materials (1). However earlier investigations of nanostructured materials superplasticity features were carried out only on alloys which display superplastic properties in fine-grained state. Therefore it is interesting to study the possibility to get superplastic state of NS copper which is not superplastic in fine-grained state.

It is known, that grain boundary diffusion fluxes of impurity from an external source (a coating, for example) under specific conditions activate grain boundary sliding (2,3). Herewith in narrow temperature-time interval the strong increase of metal creep rate takes place. In NS materials grain boundary activation and change of mechanical properties caused by it may have their own unique features because of big extension and large non-equilibrium extent of grain boundaries. In particular the increase of diffusion coefficient values in NS materials in comparison with those in fine-grained materials may lead to significant decrease of creep acceleration effect display temperature.

EXPERIMENTAL

Both fine-grained (grain size of 10 μm) and NS (grain size of about 0.3 μm) specimens of copper were investigated. The fine-grained specimens were obtained by rolling reduction up to 90% at room temperature followed by recrystallization during annealing at 873 K, 30 min. The nanostructure was obtained by equal-channel angular pressing method (4). Specimens with dimension $10 \cdot 2.5 \cdot 0.3$ mm^3 were cut out by electro-spark method. The damaged surface layer of the material removed by mechanical grinding and further electrolytic polishing. Then the specimens were coated with aluminium layer of 10 μm in thickness by ion-plasma deposition. Tensile tests were carried out on NS copper in temperature interval of 293-973 K. Creep tests in vacuum and under influence of grain boundary diffusion fluxes of aluminium from the surface were carried out at 373-473K for NS copper and at 573-673 K for fine-grained copper. All tests were performed in vacuum 10^{-2} Pa using PV-3012M machine. The temperature was controlled using a single Pt-Pt(Rh) thermocouple. The temperature drift during testing was less then 1 degree per an hour. The structure of the NS copper at the initial state and the state after annealing at 373K were studied by method of transmission electron microscopy in EM-125 electron microscope at acceleration voltage of 125 kV.

RESULTS AND DISCUSSION

The investigations have shown that the strength of NS copper σ_B = 426.5 MPa and yield strength $\sigma_{0.2}$ =415.5 MPa at room temperature (fig.1). The indicated values σ_B and $\sigma_{0.2}$ exceed appropriate values for coarse-grained copper by approximately two and seven times respectively. σ_B and $\sigma_{0.2}$ monotonously decrease with temperature increase while plasticity enhances from 12% at room temperature up to 48 % at 873 K. At further tests temperature increase plasticity of NS copper begins to decrease again (fig.1). From represented data follow that superplastic state during tensile tests of NS copper (strain rate $\dot{\varepsilon}$ =3.3·10^{-3} s^{-1}) in temperature interval of 293-973K does not realised. Thus the presence of NS structure for indicated conditions is not enough for transition of metal polycrystal to superplastic state at indicated strain rate.

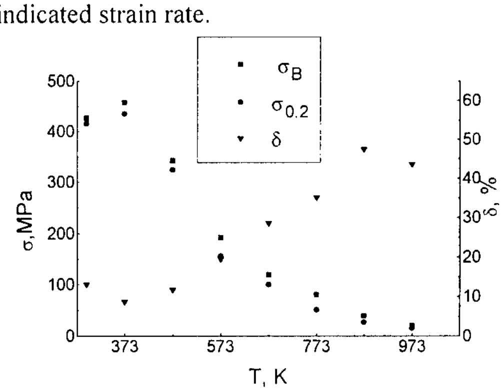

Fig.1. Dependence of strength, yield strength and plasticity on tensile temperature for NS copper.

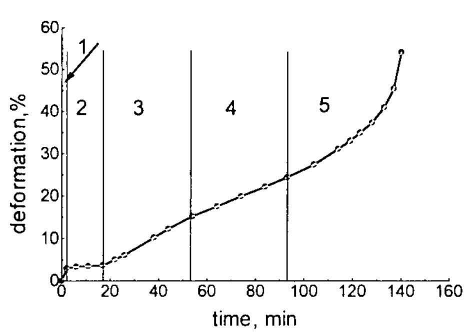

Fig.2. Specimen deformation as a function of time. Creep under σ=127MPa, T=473 K.

It is established that the creep curves of NS copper at 373-473 K have usual three-stage shape characteristic for plastic deformation of polycrystalline materials except the curves at 473K and load less than 140 MPa which have five stages (fig.2). Additional stages 3 and 4 are observed. Herewith plasticity of the copper is risen strongly (from 10 up to 50%). One may assume that such creep character is determined by kinetic singularity of process like dynamic recrystallization development. The characteristic feature of all creep curves at 423-473 K is little stage of steady creep (20-30 min). At the same time at 373 K steady creep occurs during all testing time. Such different character of the creep may be connected apparently with thermostability of the structure formed by equal-channel angular pressing. Electron microscopy studies show that essential changes during annealing at 373 K, 3 hours are not observed. This structure stability of NS copper probably provides the long stage of steady creep at indicated temperature. But at temperatures higher than 423 K the structure of NS copper is supposed to grow non-stabilised which entails the little time steady stage of creep (20-30 min). This is suggested by known literature data on structure stability of NS copper. In (5) is shown that after annealing in temperature interval of 423-448 K the relaxation of internal stresses on grain boundaries begins in NS copper as well as moderate grain growth takes place. However mechanical properties (shear modulus, elastic modulus, microhardness) are still high enough. At annealing temperature above 473 K a strong grain growth begins, considerable relaxation of internal stresses occurs and mechanical properties approach the properties of coarse-grained copper.

The creep acceleration effect determined as the ratio $\dot{\varepsilon}_2/\dot{\varepsilon}_1$($\dot{\varepsilon}_1$- the creep rate of Cu in vacuum; $\dot{\varepsilon}_2$- the creep rate of Cu under conditions of the diffusive contact with Al) for NS copper under the influence of aluminium grain boundary diffusion fluxes takes place at 423-473K. For fine-grained copper the present effect is observed at 573-673K. Thus under the tested condition the creep acceleration effect occurred in considerably lower temperature interval as compared with fine-grained copper. The decrease of the effect display temperature is supposed to be caused by the significant increase of diffusion coefficients of aluminium in NS copper beside fine-grained one. The analogous shift of the creep acceleration effect display temperature for NS nickel as compared with fine-grained one is found recently in (6).

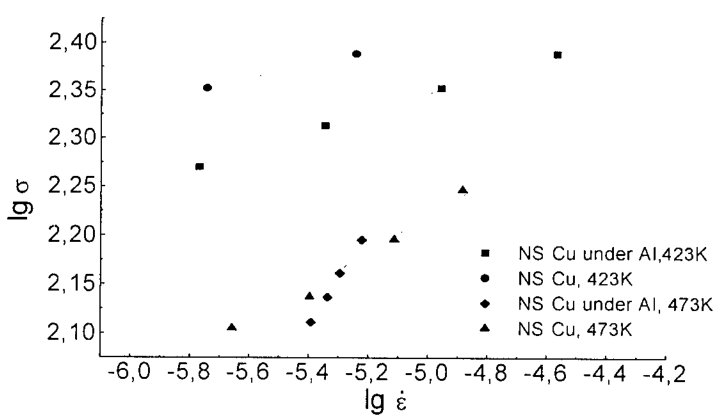

Fig.3. Dependence of flow stress on specimens creep rate

It is shown that the dependence of steady-state creep rate on applied stresses has straight shape in all investigated temperature and creep rate interval both for pure copper and for copper being with diffusion contact with aluminium (fig.3). At 423 K the existence of grain boundary diffusion fluxes from the surface into depth of NS copper leads to increase of the creep rate by approximately five times. Certain increase of strain rate sensitivity m ($m=\partial \lg\sigma / \partial \lg\dot{\varepsilon}$) from 0.08 for pure copper up to 0.1 for copper deformed under influence of the grain boundary diffusion fluxes is observed. Plasticity of NS copper under existence of diffusion fluxes of aluminium does not change and comes to about 10%. More interesting case is at 473 K. Despite the creep acceleration effect of NS copper under influence of grain boundary diffusion fluxes at 473 K is less than at 423 K there is a strong increase of strain rate sensitivity (m=0.5) in comparison with pure copper (m=0.19). Usually one connect such increase of m with change of basic mechanism of deformation from the intragrain dislocation creep to the grain boundary sliding and transit of material to superplastic state. Herewith plasticity of the copper under existence of diffusion fluxes of aluminium does not increase in comparison with the pure copper tested under the same conditions and comes to 40-50%. However the creep curves of NS copper under aluminium coating is three-stage in contradiction to the creep curves of pure copper which as mentioned above have five stage shape. Hence the same value of the copper plasticity may be caused by different reasons. For example plasticity of the pure copper is determined by dynamic recrystallization but plasticity of copper under influence of grain boundary diffusion aluminium fluxes may increase because of increase of grain boundary sliding contribution to total deformation.

CONCLUSIONS

It is shown that superplasticity does not take place during NS copper tensile tests at 293-973K and $\dot{\varepsilon}=3.3\ 10^{-3}\ s^{-1}$. The strong increase of strain rate sensitivity m during creep of NS copper under influence of grain boundary diffusion fluxes of aluminium occurs. However the value of plasticity is not large (about 50%).

ACKNOWLEDGEMENTS

The authors would like to express their gratitude to Prof. R.Z. Valiev (GATU, Ufa, Russia) for supplying materials for the experiments and fruitful discussion as well as Los-Alamos National Laboratory (USA) and Russian Fond of Fundamental Research for financial support of this work.

REFERENCES

1. Valiev R.Z., Korznikov A.V., Mulyukov R.R., Fiz. Met. i Metalloved.,1992, No4,70.
2. Kolobov Yu.R., Trans. Mat. Res. Soc. Jpn, 1994, 16B, 1397.
3. Kolobov Yu.R., Marvin V.B., Ratochka I.V., Korotaev A.D., DAN USSR, 1985,283,605
4. Utyashev F.Z., Enikeev F.U., Latysh V.V., Ann. Chim. Fr., 1996, 21, 379.
5. Korznikov A., Dimitrov O., Korznikova G., Ann. Chim. Fr., 1996, 21, 443.
6. Kolobov Yu.R., Grabovetskaya G.P. et al., Ann. Chim. Fr., 1996, 21,483.

Pergamon

NanoStructured Materials, Vol. 12, pp. 951–954, 1999
Elsevier Science Ltd

0965-9773/99/$–see front matter

PII S0965-9773(99)00275-5

MAGNETIC PROPERTIES OF MECHANICALLY ALLOYED NANOCRYSTALLINE Ni_3Fe

C. N. Chinnasamy, A. Narayanasamy, K. Chattopadhyay[@] and N. Ponpandian
Materials Science Centre, Department of Nuclear Physics,
School of Physical Sciences, University of Madras, Guindy Campus, Madras 600 025, INDIA.
[@]Centre for Advanced Study, Department of Metallurgy
Indian Institute of Science, Bangalore 560 012, INDIA.

Abstract -- *Disordered nanocrystalline Ni_3Fe alloy was prepared by mechanical alloying of elemental powders. X-ray diffractograms show the formation of Ni_3Fe single phase. The chemical composition and morphology of the powder have been obtained by using EDAX and SEM analysis respectively. While the saturation magnetisation decreases with milling time, the coercivity increases. The width of the hyperfine field distributions obtained from Mössbauer studies shows that the alloy is highly disordered. Atomic ordering is found to take place at a faster rate compared to that in the bulk alloy.* ©1999 Acta Metallurgica inc.

INTRODUCTION

Mechanical alloying (MA) is now recognized as a powerful tool for the synthesis of various kinds of materials, such as amorphous alloys, quasicrystalline and nanocrystalline materials. The aim of the present study is to synthesize nanocrystalline Ni_3Fe alloy by MA technique and to study atomic ordering and magnetic properties as a function of grain size.

EXPERIMENTAL

Nickel and iron powders with purities of 99.99% were mixed in the atomic proportion 75:25 and mechanically alloyed in toluene medium in a hardened chromium steel vial using a planetary ball mill (Fritsch Pulverisette P5). The ball to powder ratio was 8:1 and the rotation per minute was 300.

The phase formation was examined by X-ray powder diffraction technique (XRD) using Guinier diffraction geometry with a Huber Diffractis 583 system with Fe $K_{\alpha 1}$ (λ = 0.19373 nm) radiation. Silicon was used as an internal standard. The surface morphology studies and average composition analysis were carried out using a scanning electron microscope (JEOL model JM 840) with EDAX facility. Magnetisation and coercivity of the samples were measured by a vibrating sample magnetometer (PARC model 4500) with a maximum applied field of 7 kOe. ^{57}Fe Mössbauer studies were carried out using a constant acceleration Mössbauer spectrometer (Wissel, Germany, Model No. MDU-1200).

RESULTS AND DISCUSSION

X- ray diffraction

The X- ray powder diffraction patterns of Ni_3Fe for selected milling times are presented in Fig.1(a). The broadening of the diffraction lines increases with milling time due to the reduction in grain size and also because of the increase in the atomic level strain. The average size of the grain was calculated from the full-width at half-maximum of the diffraction peaks using Scherrer equation (1) and is shown in Fig. 1(b) as a function of milling time. Fig. 2 (a) gives the lattice parameter for different milling times of the sample. The abrupt increase in the lattice parameter observed for the sample milled for 20 hours shows the formation of Ni_3Fe alloy. The r.m.s strain increases with milling time and reaches a maximum value of 0.75 as seen from Fig. 2(b).

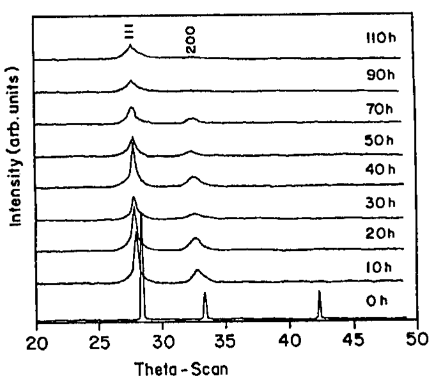

Figure 1. (a) X-ray diffractograms of Ni_3Fe for various milling times.

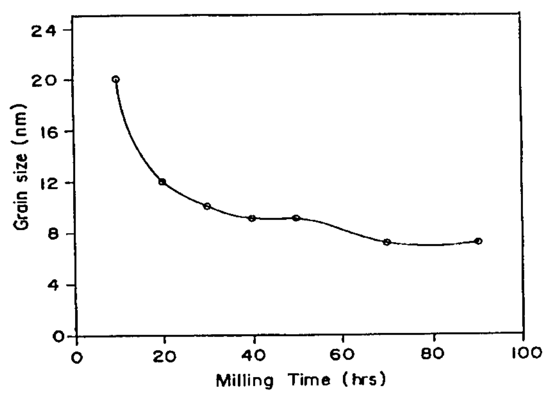

Figure 1. (b) Grain size Vs. milling time.

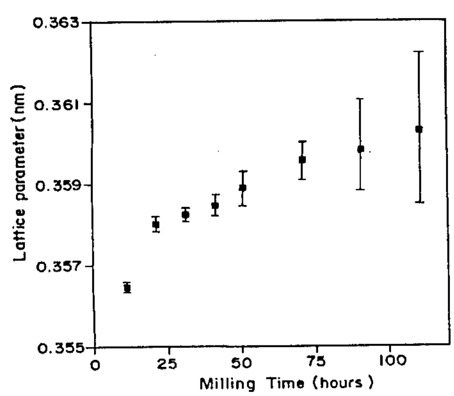

Figure 2. (a) Lattice parameter Vs. milling time.

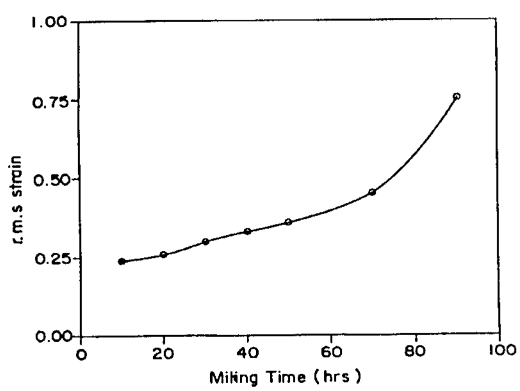

Figure 2. (b) r.m.s. strain Vs. milling time.

Microscopy

SEM micrographs show that the particle size is reduced as milling time is increased. Fig. 3 shows the SEM micrograph of the 50 hours milled sample. The EDAX studies showed that the composition was very close to the stoichiometric value, $Ni_{75}Fe_{25}$ indicating that the contamination due to balls is negligible.

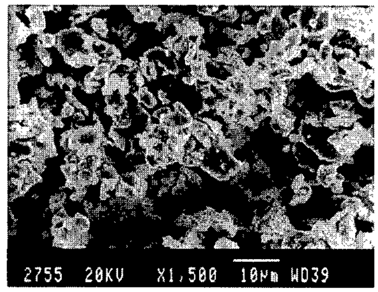

Figure 3. SEM micrograph of the 50 hours milled Ni_3Fe.

Magnetisation and Mössbauer Studies

Figure 4(a) shows the dependence of saturation magnetisation(M_s) on milling time. The decrease in the saturation magnetisation with milling time may be due to dead layers on the surface(2), increase in the volume fraction of superparamagnetic particles (3) and surface oxidation (4). The increase in coercivity with milling time as seen in Fig. 4(b) is due to the reduction of grain size and because of the increase in r.m.s strain (5).

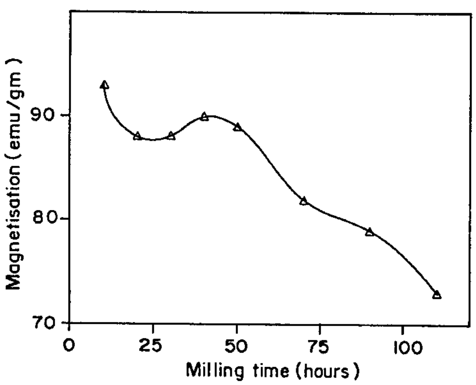

Figure 4. (a) Saturation magnetisation Vs. milling time.

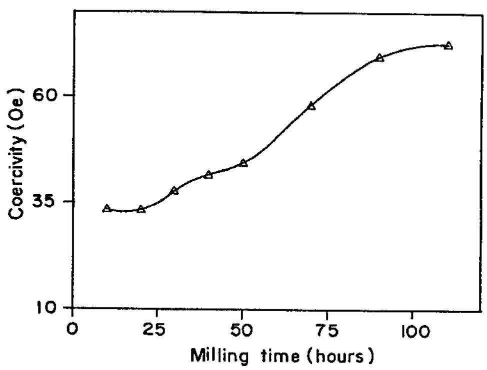

Figure 4. (b) Coercivity Vs. milling time.

Figure 5(a) shows Mössbauer spectra and the corresponding hyperfine field distributions for the Ni_3Fe samples for selected milling times. The spectra were fitted by using Window program (6). The hyperfine field distributions are very broad revealing that the alloy is highly disordered. The average hyperfine field is found to be 290 kOe which agrees well with the value reported in literature(7) for the bulk disordered Ni_3Fe alloy. The width of the P(H) distribution for the 50 hours-milled sample decreased from 65 kOe in the as-milled condition to 42 kOe on annealing at 460°C for an hour as seen in Fig. 5(b) which shows that atomic ordering takes place at a faster rate compared to that in the bulk Ni_3Fe alloy (7).

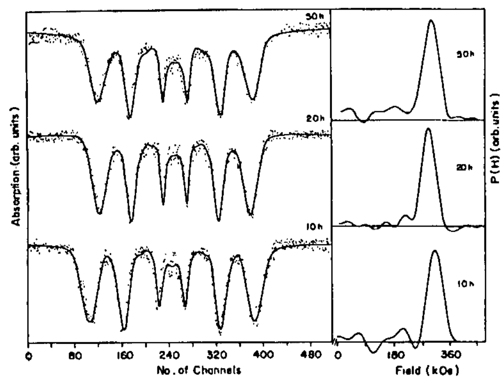

Figure 5. (a) Room temperature Mössbauer spectra and the corresponding hyperfine field distributions of Ni_3Fe for 10, 20 and 50 hours milled samples.

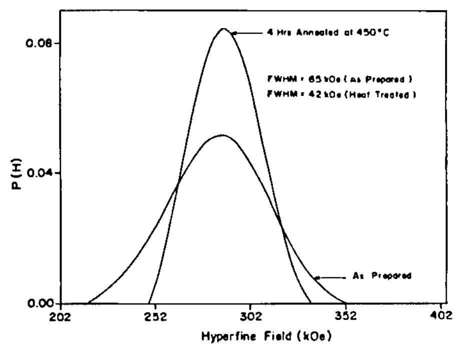

Figure 5. (b) The P(H) distribution of the 50 hours milled Ni_3Fe in the as-prepared and annealed conditions.

CONCLUSIONS

Disordered nanocrystalline Ni_3Fe alloy with a mean grain size of 7 nm has been prepared by mechanical alloying technique. The magnetic properties are found to depend on the grain size. The high coercivity values are due to small grain size and atomic level strain in the as-milled sample. The Mössbauer studies show that atomic ordering takes place at a faster rate in nanocrystalline Ni_3Fe compared to that in the bulk alloy.

ACKNOWLEDGMENTS

The facilities made available under the UGC-COSIST, UGC-SAP, UGC-CAS and DST programmes in both the collaborating institutions are gratefully acknowledged. The authors would like to thank Prof. S. Ranganathan and Prof. P.R. Subramanian for their interest in this work. One of the authors (C.N.C) would like to thank the CSIR, Government of India for the award of Senior Research Fellowship during the course of this work.

REFERENCES

1. Cullity, B.D., *Elements of X-ray Diffraction*, Addison Wesley, New York, 1977, P.102.
2. Li, X.G., Chiba, A., and Takahashi, S., J. Magn.Magn. Mat. 26, 196 (1997).
3. Peter Fulde, A., Luther and Watson, R.E., Phys. Rev. B 8, 440 (1973).
4. Gangopadhyay, S. and Hadjipanayis, G.C., Nanostruc. Mat. 1, 77 (1992).
5. Kuhrt, C. and Schultz, L., J. Appl. Phys. 73, 1221 (1993).
6. Window, B., J. Phys E: Sci. Inst. 4, 401 (1971).
7. Narayanasamy, A., Nagarajan, T., Muthukumarasamy, P., and Radhakrishnan, T.S., J. Phys. F9, 2261 (1979).

Pergamon

NanoStructured Materials, Vol. 12, pp. 955–958, 1999
Elsevier Science Ltd

0965-9773/99/\$–see front matter

PII S0965-9773(99)00276-7

LOCAL MAGNETIC PROPERTIES OF NANOCRYSTALLINE Ni AND Pd-Fe

St. Lauer[1], Z. Guan[1], H. Wolf[1], H. Natter[2], M. Schmelzer[2], R. Hempelmann[2], and Th. Wichert[1]

[1] Technische Physik, [2] Physikalische Chemie, Universität des Saarlandes, Postfach 151150, D-66041 Saarbrücken, Germany

Abstract -- *Ferromagnetic nanocrystalline materials, consisting of Ni and Pd-Fe, are investigated on an atomic scale by perturbed $\gamma\gamma$-angular correlation spectroscopy, complemented by X-ray diffraction and energy dispersive X-ray spectroscopy. Nanocrystalline Ni was produced by pulsed electrodeposition and simultaneously doped with ^{111}In probe atoms. Besides the local magnetic field known from polycrystalline Ni, a second component is detected, which is attributed to a magnetic perturbation due to grain boundaries. During ball-milling of Pd, a $Pd_{0.70}Fe_{0.30}$ solid solution caused by Fe impurities is obtained, which is ferromagnetic at room temperature. Annealing between 600 K and 1000 K transforms this solid solution into the compound γ_2-Pd_3Fe. ©1999 Acta Metallurgica Inc.*

INTRODUCTION

The magnetic properties of nanocrystalline materials are of interest because of their hard-magnetic (1) and soft-magnetic (2) applications. The investigation of macroscopic magnetisation reveals the dependence of the saturation magnetisation and the coercitive field on the grain size (3, 4). The domain structure is analysed e.g. by magneto-optic Kerr-microscopy (3) or small angle neutron scattering (5). In addition, the application of hyperfine techniques, like Mößbauer spectroscopy, muon spin rotation or perturbed $\gamma\gamma$-angular correlation spectroscopy (PAC), detects the local magnetic field at the site of probe atoms or muons. In this paper, nanocrystalline Ni prepared by pulsed electrodeposition (PED) and ferromagnetic Pd-Fe alloys obtained by ball-milling of Pd powder are investigated by PAC experiments.

EXPERIMENTAL DETAILS

The PAC investigations were performed using radioactive ^{111}In, which emits a γ-γ cascade following its decay to the isotope ^{111}Cd. The hyperfine interaction of the ^{111}Cd nucleus with a magnetic field or an electric field gradient (efg) becomes observable by recording the second γ-quantum of the cascade with respect to the first one as a function of the elapsed time t. Due to hyperfine interaction, the PAC time spectrum R(t) is modulated by characteristic frequencies ω_n. In case of pure magnetic dipole interaction, two frequencies $\omega_1 = \omega_L$ (Larmor frequency) and $\omega_2 = 2\,\omega_L$ are observed. Using the relation $\omega_L = (\mu/I)\cdot B_{loc}$ ($\mu = -0.7656\ \mu_N$, $I = 5/2\ \hbar$), the

local magnetic field B_{loc} at the site of the probe nucleus is determined. In case of pure electrical quadrupole interaction and $I = 5/2$, the three frequencies ω_1, ω_2, and $\omega_3 = \omega_1 + \omega_2$ are measured, which allow the characterisation of the traceless efg by the coupling constant $\nu_Q = e \cdot Q \cdot V_{zz}/h$ and the asymmetry parameter $\eta = (V_{xx} - V_{yy}) / V_{zz}$. Slightly different magnetic fields (or efg) at the site of the probe atoms lead to a frequency distribution centred at $\overline{\omega}_L$ (or $\overline{\nu}_Q$) with a width of $\Delta\omega_L$ ($\Delta\nu_Q$). A detailed description of PAC can be found elsewhere (6).

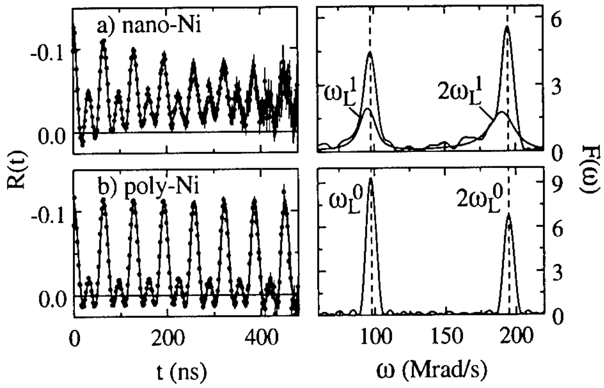

Fig. 1: PAC spectra of nanocrystalline (a) in comparison to polycrystalline Ni (b).

Nanocrystalline Ni was prepared by pulsed electrodeposition (7). Short current pulses with a length of $t_{on} = 2$ ms and a current density of 1 A/cm^2 were applied followed by an off-time of 48 ms. The used electrolyte consisted of Ni(II)sulfate (40 g/l), K,Na-tartrate (120 g/l), and ammonium chloride (40 g/l). The doping of Ni with ^{111}In was achieved during the electrodeposition by adding $^{111}InCl_3$ to the electrolyte. As reference, polycrystalline Ni was doped with ^{111}In by diffusion at 1330 K under vacuum.

Polycrystalline Pd powder was diffused with ^{111}In at 1550 K and was subsequently milled for 40 h in a SPEX 8000 ball-mill. Milling was performed in an Ar atmosphere using non-standard vials. The incorporation of Fe impurities originating from the vials resulted in the formation of an $Pd_{0.70}Fe_{0.30}$ alloy. Its composition was determined by energy dispersive X-ray spectroscopy (EDX).

RESULTS AND DISCUSSION

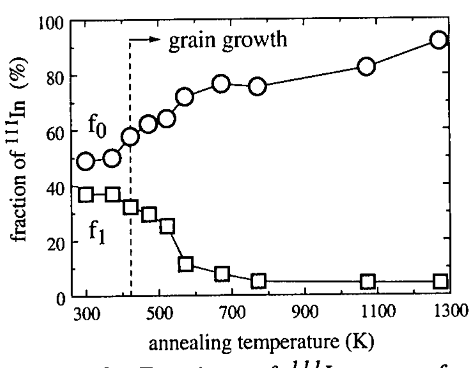

Fig. 2: Fractions of ^{111}In atoms f_0 and f_1 exposed to the two magnetic components.

Nanocrystalline Ni

After deposition of nanocrystalline Ni, analysis by X-ray diffraction (XRD) indicates a mean grain size of 40 nm. The modulation in the PAC spectrum (Fig. 1a) is due to the magnetic dipole interaction of ferromagnetic Ni. The PAC spectrum consists of two components. The Larmor frequency $\omega_L{}^0 = 97.6$ Mrad/s (8) known from polycrystalline Ni (Fig. 1b) without measurable line broadening ($\Delta\omega_L{}^0 = 0$ Mrad/s), and a second, new component, which is shifted to a lower frequency $\omega_L{}^1 = 95.8$ Mrad/s and is significantly broadened ($\Delta\omega_L{}^1 = 6$ Mrad/s).

About $f_0 = 49$ % of the probe atoms measure $\omega_L{}^0$ and $f_1 = 37$ % the shifted frequency $\omega_L{}^1$. The observed shifted and broadened frequency component is similar to the results of PAC experiments, at which the ^{111}In atoms were incorporated one or two monolayers beneath a <111>-surface of Ni (9), or at which the ^{111}In atoms were surrounded by non-magnetic impurities in polycrystalline Ni (10).

The local structure of probe atoms corresponding to f_1 converts to that of f_0, if the sample is annealed for 1 h at temperatures above 423 K (Fig. 2); the fraction f_1 completely disappears at an annealing temperature of 770 K. The temperature of 423 K is in agreement with the temperature, at which grain growth starts as observed by H. Natter and co-workers (7). The component $\omega_L{}^1$, therefore, is obviously characteristic for nanocrystalline Ni and not for impurities, because it is not expected that impurities start to disappear after annealing of the sample at 423 K. It is proposed that the component $\omega_L{}^1$ belongs to lattice sites in the outer part of a crystallite, which is magnetically perturbed by the grain boundaries. The component $\omega_L{}^0$ is measured by the probe atoms in the centre of the crystallites. From the fraction $f_1 = 37$ %, the width of the magnetically perturbed region is estimated to 3 - 4 nm, using the measured grain size of 40 nm and assuming a statistical distribution of the ^{111}In atoms over the whole sample.

Pd-Fe alloy

The experiments at nanocrystalline Pd-Fe alloys start with polycrystalline Pd powder doped with ^{111}In. The PAC spectrum recorded at room temperature indicates no efg (Fig. 3a) showing that the ^{111}In atoms are incorporated on defect-free sites of the Pd lattice. After ball-milling for 40 h, spectrum (Fig. 3b) is recorded yielding that a fraction $f_c = 54$ % of ^{111}In atoms is located still on defect-free lattice sites or is exposed to an efg distribution centred around $\bar{\nu}_Q = 0$ MHz, which is attributed to lattice defects induced by ball-milling. A second fraction $f_d = 39$ % of ^{111}In atoms measures a distribution of Larmor frequencies centred at about $\bar{\omega}_L \approx 110$ Mrad/s, which indicates that the sample became ferromagnetic. The analysis of the composition of the sample by EDX shows an Fe-content of 30 at%. The lattice structure, determined by XRD, is an fcc solid solution having a grain size of about 15 nm. Since ferromagnetism is induced in Pd if the Fe-concentration exceeds 0.01 at% (11), the distribution of Larmor frequencies ($\bar{\omega}_L \approx 110$ Mrad/s) is attributed to the disordered $Pd_{0.70}Fe_{0.30}$ solid solution.

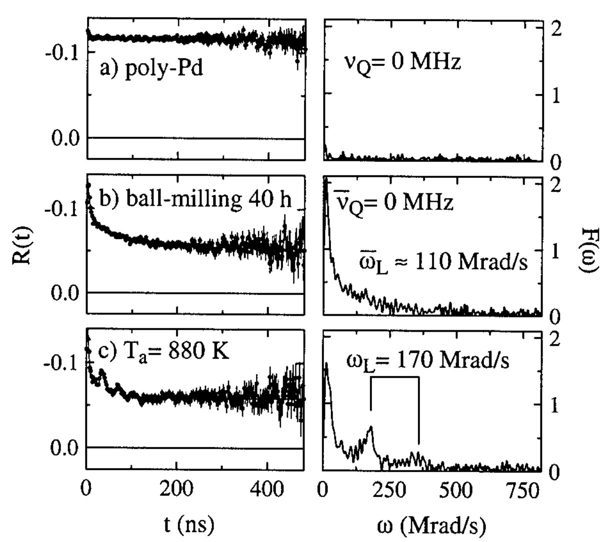

Fig. 3: The PAC spectra of polycrystalline Pd (a) and of the Pd-Fe alloy after ball-milling (b) and annealing (c).

Upon annealing the sample at 880 K, the fraction f_d disappears (Fig. 3c) and is replaced by a local structure characterized by a Larmor frequency of $\omega_L = 170$ Mrad/s ($f_{ord} = 30$ %). XRD analysis at the same time shows the formation of γ_2-Pd_3Fe having an ordered $L1_2$-structure. In contrast to a disordered $Pd_{0.70}Fe_{0.30}$ solid solution, the compound γ_2-Pd_3Fe offers unique sites for the incorporation of ^{111}In resulting in the almost unique Larmor frequency ($\omega_L = 170$ Mrad/s). The conversion of f_d into f_{ord} as a function of annealing temperature is shown in Fig. 4. The fraction f_c of probes, which detect no magnetic interaction, remains almost constant indicating that only a part of the Pd-Fe alloy became ferromagnetic due to Fe impurities. The transformation from disordered $Pd_{0.70}Fe_{0.30}$ to ordered γ_2-Pd_3Fe begins at 600 K and is completed at about 1000 K.

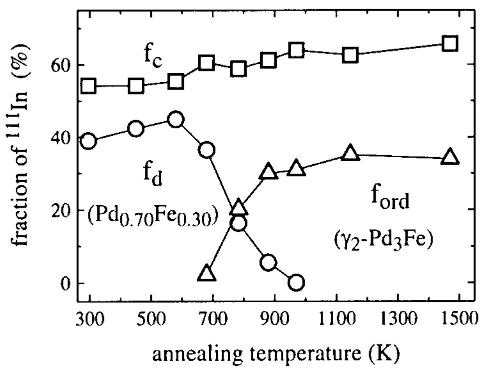

Fig. 4: Fractions of ^{111}In atoms in the Pd-Fe alloy.

ACKNOWLEDGEMENTS

We thank Dr. C.E. Krill and H. Ehrhardt (Lehrstuhl Prof. Birringer, Saarbrücken) for the XRD and EDX analysis of the Pd-Fe samples. The financial support by the Deutsche Forschungsgemeinschaft (SFB 277) is thankfully acknowledged.

REFERENCES

1. H. Kronmüller, Nanostruct. Mater. **6,** 157 (1995)
2. G. Herzer, Scripta Met. et Mat. **33**, 1741 (1995)
3. H. Kisker, T. Gessmann, R. Würschum, H. Kronmüller, and H.-E. Schaefer, Nanostruct. Mater. **6**, 925 (1995)
4. J. Löffler, H. Van Swygenhoven, and W. Wagner, Nanostruct. Mater. **9**, 523 (1997)
5. J. Löffler, W. Wagner, and H. Van Swygenhoven, Nanostruct. Mater. **9**, 331 (1997)
6. Th. Wichert and E. Recknagel, in *Microscopic Methods in Metals*, ed. U. Gonser, Topics in Current Physics **40**, 317 (1986)
7. H. Natter, M. Schmelzer, and R. Hempelmann, J. Mat. Res. to be published Vol. **13** (1998)
8. D.A. Shirley, S.S. Rosenblum, and E. Matthias, Phys. Rev. **170**, 363 (1968)
9. J. Voigt, R. Fink, G. Krausch, B. Luckscheiter, R. Platzer, U. Wöhrmann, X.L. Ding, and G. Schatz, Phys. Rev. Lett. **64**, 2202 (1990)
10. G.S. Collins, Hyp. Int. **9**, 465 (1981)
11. C. Büscher, T. Auerswald, E. Scheer, A. Schröder, H. v.Löhneysen, and H. Claus, Phys. Rev. **B46**, 983 (1992)

Pergamon

NanoStructured Materials, Vol. 12, pp. 959–962, 1999
Elsevier Science Ltd

0965-9773/99/$–see front matter

PII S0965-9773(99)00277-9

THE CONDITIONS FOR EFFECTIVE CLUSTERING IN A PLASMA-DISCHARGE SOURCE IDENTIFIED VIA MONTE-CARLO SIMULATIONS

D.S. Vlachos*, A.C. Xenoulis* and Th. Tsakalakos**
*N.C.S.R. Demokritos, 153 10 Agia Paraskevi, Athens, Greece
**Rutgers University, Piscataway, New Jersey 08855-0909, USA

Abstract – *The assumption that the ionization and coagulation of metal particles in a plasma-generating cluster source can be described by the orbital limited motion theory, examined by Monte Carlo calculations, was found inadequate. That assumption cannot firstly predict the modes of cluster ionization observed experimentally. Secondly, the effectiveness of coagulation was found to depend on the initial size of the condensing particles. Specifically, the coagulation of dust particles proceeds in a satisfactory degree. The coagulation of single atoms in a cluster source, however, saturates at about 140 atoms per cluster, in serious underestimation of relevant experimental data. ©1999 Acta Metallurgica Inc.*

INTRODUCTION

Certain of the most important cluster sources (such as the laser-ablation, the magnetron and the hollow-cathode source) generate plasma during particle coagulation. Nevertheless, clustering under plasma conditions is very poorly studied and understood. On the experimental front, it has been observed that negatively as well as positively ionised clusters coexist during coagulation (1), suggesting that electromagnetic interactions may be responsible for clustering. On the theoretical front, the coagulation of 10 Å-radius dust particles in a steady-state plasma was successfully described in terms of electrostatic and dipole interactions (2). The untested use of this model to describe clustering in a gas-aggregation source, however, is not safe because in the source the coagulation conditions are significantly less favourable than those previously assumed (2). The purpose of the present study is to examine whether or under what conditions the model of Ref. (2) is applicable to a plasma-discharge cluster source. The relevant realistic conditions tested in the present Monte Carlo calculation is that clustering starts from atoms and that the interaction time is about 1 msec (1).

SIMULATION ALGORITHM

A sample volume, 10^{-15} m^3, of the experimental apparatus has been considered with periodic boundary conditions. Monte Carlo calculations take into account the interaction of metal particle with each other and with the plasma components, i.e. electrons and ions. A constant electron density is assumed and the overall neutrality is obtained by adjusting the ion density. All plasma components and metal particles are considered in thermodynamic equilibrium. The scattering rate of a particle with a specific type of scattering center is

calculated using the formulae

$$f_i = \int_0^\infty N(\varepsilon) * v(\varepsilon) * \sigma_i(\varepsilon) * d\varepsilon, \qquad [1]$$

where N is the density of scattering centers, v the relative velocity of the particle and the scattering center and σ the cross section which is calculated in the center of mass reference system. Both coagulation and ionization cross sections are calculated taking into account electrostatic forces. In particular, a neutral particle interacts with a charged particle via a dipole moment induced by the latter to the former. Finally, the temperature of clusters is considered to be size independent, while the density of all plasma components follows a Maxwell-Boltzmann distribution over energy. More details may be found in Ref.(2). The calculations were performed for two kinds of particles, differentiated by their initial size. A radius of 1.5 Å represents Cu atoms, while a radius of 10 Å represents the metal dust particles used in the previous calculation (2).

SIMULATION RESULTS AND DISCUSSION

It may be instructive first to describe qualitatively the evolution of events taking place when Cu atoms (or dust particles) and plasma are mixed. As soon as the interaction is turned on, all the present (initially neutral) Cu atoms are negatively ionized. This happens because the number of collisions with electrons is overwhelming compared to those with Ar^+ ions. As a consequence, a short-lived outburst of clustering observed at the very outset, caused by Cu^0-Cu^- dipole interaction, stops because, as already mentioned, all the particles become negatively charged and repulse each other. Nevertheless, a few dimmers manage to be formed in the mean time. As the particle-plasma interaction continues, some of the negatively charged metal particles will turn to neutral when they collide with Ar^+. These fresh neutrals are very short lived. They almost instantly interact with either other negatively charged Cu particles leading to larger negative clusters, or with electrons reverting to negatively ionized clusters of the same mass. This clustering process, however, soon fades out because the density of scattering centers is reduced due to clustering. Nevertheless, because in the mean time the dimensions of the clusters have increased, a second coagulation stage, supported by multiple ionization, becomes possible. During that stage, the mean negative charge per cluster increases significantly causing a commensurate increase in the strength of the dipole interaction, giving a fresh outburst of clustering events.

In more quantitative terms, Figure 1a shows the evolution in time of the mean number of atoms per cluster and Figure 1b of the mean charge per cluster, for two kinds of particles with initial radius 1.5 Å and 10 Å. The results of Figure 1a clearly demonstrate that the efficiency of coagulation depends significantly on the initial dimensions of the particles involved. In fact, while the 10 Å particles, in agreement with Ref. (2), coagulate efficiently, the coagulation initiated by single atoms stops relatively soon, reaching a plateau at about 140 atoms per clusters. This is a serious size underestimation since the experimental sizes range between 1,000 and 300,0000 atoms per cluster (1).

It should be pointed out that several contradictory effects are competing with each other, and depending on the particular circumstances the one or the other may assume ascendancy. Such a case is, for instance, in the very early stages of clustering, when as Figure 1a reveals single atoms coagulate faster than dust particles. To understand this feature which

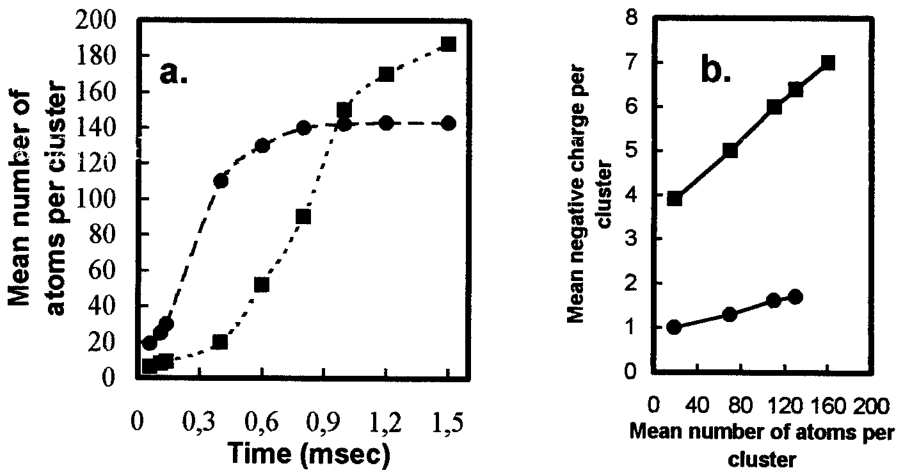

Figure 1. The dependence of mean number of particles per cluster on (a) time and (b) on mean negative charge per cluster for two different atomic radius:(circles 1.5 Å and squares 10 Å).

seems inconsistent with the final outcome, it must be taken into account that, as Figure 1b shows, the small clusters built by atoms sustain smaller negative charge than the clusters composed of dust particles. Consequently, the probability for the former clusters to get neutralized via collisions with Ar^+, and as a consequence to coagulate, is larger than that for the later. This coagulation, however, reduces the number of the atoms and of the atom-composed clusters, leading to the plateau observed in fig. 1a. On the other hand, the charge on the dust-composed clusters, as Figure 1b shows, increases faster with size than on the atom-composed clusters. Apparently, this faster increase is sufficient to compensate for the decreasing number of the dust-composed clusters (see Equation 1), ensuring the unhindered coagulation of these particles.

Let us conclude with a brief demonstration of the effect of various cluster-source conditions on the size of the clusters produced under these conditions. Figure 2 shows the size distribution of dust-composed clusters produced after coagulation of 0.1 msec. Different values of electron temperature, initial particle concentration and electron density are tested. The straight lines obtained indicate that in all cases the calculated cluster-size distribution is in perfect agreement with a lognormal-distribution behavior, previously identified to be associated with neutral particle clustering (3). The present results, however, clearly indicate that particle neutrality is not at all a prerequisite for log-normal clustering behavior. Figure 2 shows, furthermore, that particle coagulation stops when the number of metal particles becomes comparable to the number of electrons. It is interesting to notice that the same effect is produced either by changing the number of metal particles or the number of electrons. Therefore, a very important parameter in plasma clustering is the ratio of the initial number of particles over the number of electrons. Finally, the energy of electrons is also a factor of consequence. Specifically, low energy electrons, being more efficient negative particle ionizers, cause enhanced coagulation.

CONCLUSIONS

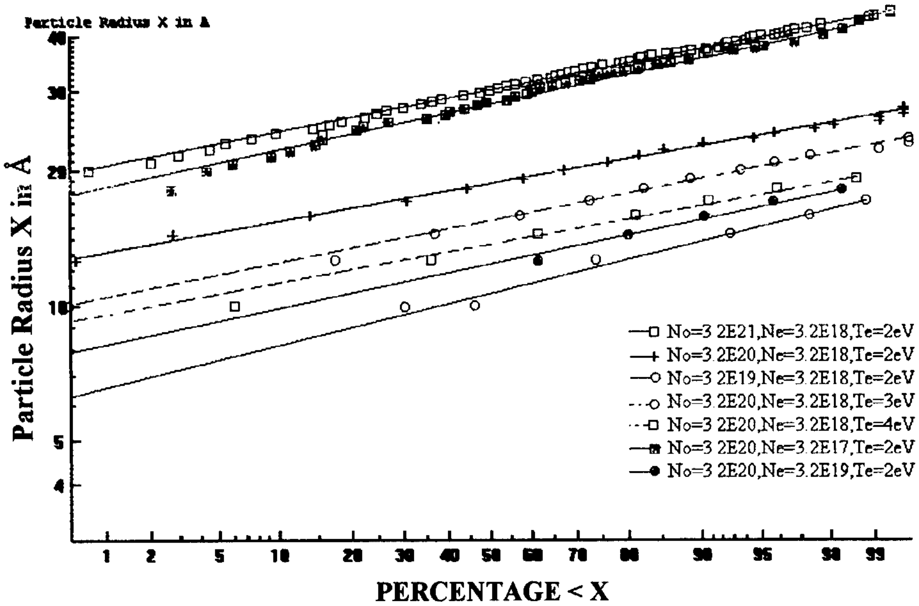

Figure 2. The particle distribution as a function of initial number of particles (No), electron density (Ne) and electron temperature (Te)

A model for particle coagulation in plasma (2) was tested under conditions associated with a plasma-generating, gas-aggregation cluster source. The theoretical calculations reproduced neither the ionization nor the size of the clusters observed experimentally. With respect to the former, while the calculations predict the presence of only negatively charged clusters (and a few virtual neutrals) from the very beginning, the experimental data indicate that negative, positive and neutral clusters coexist during at least the first msec of interaction. In fact, the theoretical underestimation of cluster size, is most probably the consequence of the extremely restricted mode of ionization predicted by the model. Obviously, if positive, negative and neutral particles coexist, their coagulation, via various electrostatic interactions, will be much more efficient and faster than the predictions of the presently tested model (2). It seems, therefore, that the future effort should be directed towards a more realistic description of particle ionization in a plasma-discharge cluster source.

ACKNOWLEDGMENT

This research was supported in part by the Greek Ministry of Development under contract #PENED-1881 and by the International Atomic Energy Agency under contract #9386.

REFERENCES

1. Xenoulis, A.C., Doukelis, G., Tsouris, P., Karydas, A., Potiriadis, C., Katsanos, A.A. and Tsakalakos, Th,. Vacuum, 1998, 50, in press.
2. Schweigert, V.A. and Schweigert, I.V., J. Phys. D: Appl. Phys. 1996,29, 655
3. Granqvist, C.G. and Buhrman, R.A., J. Appl. Phys. 1976 Vol. 47, No. 5, 2200

Pergamon

NanoStructured Materials, Vol. 12, pp. 963–966, 1999
Elsevier Science Ltd

0965-9773/99/$–see front matter

PII S0965-9773(99)00278-0

FERROELECTRIC PHASE TRANSITIONS IN MATERIALS EMBEDDED IN POROUS MEDIA

E.V.Colla, A.V.Fokin, E.Yu.Koroleva, Yu.A.Kumzerov, S.B.Vakhrushev
A.F.Ioffe Physico-Technical Institute, 194021 St.Petersburg, Russia
B.N.Savenko
I.M.Frank Neutron Physics Lab., JINR, 141980 Dubna, Russia

Abstract - *Large quantities of highly dispersed ferroelectric objects were obtained by impregnation of two porous dielectric matrixes (porous glass and artificial opal) with molten ferroelectric materials ($NaNO_2$, KH_2PO_4 (KDP)). The diameters of ferroelectric nanoparticles may be varied from about 100 nm to 3-4 nm. The neutron scattering measurements for $NaNO_2$ particles and low frequency dielectric permittivity measurements for $NaNO_2$, KDP and Rochelle salt particles were performed on such nanosize particles systems. The significant shift of transition temperature from the bulk value for KDP particles as the transition broadening for $NaNO_2$ and KDP particles was observed.* ©1999 Acta Metallurgica Inc.

INTRODUCTION

It is well known that majority of the physical properties of the highly dispersed solids are essentially different from those of the bulk materials. Particularly size effects result in the drastic changes of the phase transition features. The size effect on the ferroelectric phase transitions was first observed as early as in 1950s (1,2) and attracted the attention anew in recent years when it was demonstrated that all practically important characteristics of ferroelectric materials strongly depend on the film thickness or grain size (3). The theoretical considerations (4) on the fine particle's systems based on the Landau phenomenological theory give some predictions for Curie temperature vs characteristic size d (the film thickness, filament or particle's diameter) for both first- and second-order phase transitions cases. The critical value of d_c corresponding to the disappearance of the ferroelectricity was obtained. The main parts of experiments (5-7) whose results were compared with conclusions of the theories were carried out on the microcrystalline samples produced via sol gel process or on some other composite objects. We propose the method that permits to produce the large quantities of ferroelectric nanoparticles with diameters in nanometre scale. It is based on the introduction of studied material into the pores of some artificial or natural matrixes. Advantage of this method is the fact, that excludes any chemical process during the sample preparation and thus provides the possibility to produce the nanoscale fine particle objects by breaking down the bulk solids.

RESULTS AND DISCUSSION

The experiments were performed on $NaNO_2$ embedded into porous glass with pores sizes of about 7 nm (some details about porous glass structure is reported in ref. (8)), and on KDP embedded as in porous glass into the pores of artificial opals (strictly speaking we used not the opals but the pigs designed for jewellery opals production). Opal (about its structure see (9)) is composed of close packed identical amorphous SiO_2 spheres with diameters 250 nm. Such spheres packing produces two kind of «holes» between the spheres. The dominant pores size is about 100 nm and the secondary, 20 nm (9). $NaNO_2$ and KDP salts were introduced into the matrixes from the melt phase. The volume amount of the dispersed salts was about 30% of sample volume.

The low frequency dielectric measurements were carried out on a computer controlled dielectric spectrometer operating in frequency domain mode. The samples for the dielectric studies were the plates of about 10x10x1 mm^3 in size. The neutron scattering measurements on sodium nitrite were performed with the DN-2 time-of-flight diffractometer installed on the IBR2 pulsed reactor. The sample was a rod with square section of 4x4x20 mm^3 in volume.

The widths of the diffraction peaks measured on sodium nitrite in the glass sample were temperature independent and always larger then the widths of the peaks in the reference Al_2O_3 sample. The temperature dependencies of the integrated intensities of the (001) and (020) peaks are presented in Fig.1. Unlike the bulk situation (where T_c=438K) the transition is very broad and in our preliminary measurements reported here we have not reached the end of the transition region. So we can conclude that the width of this region is at least 30-40K. Such large broadening can be related to the effect of fluctuations.

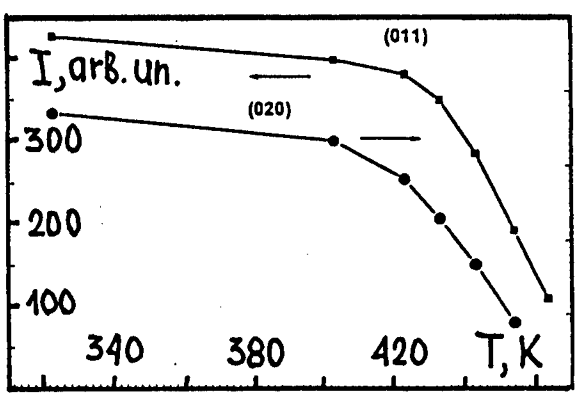

Figure 1. The temperature dependencies of integrated intensities for the (hkl) Bragg reflection peaks (sodium nitrite)

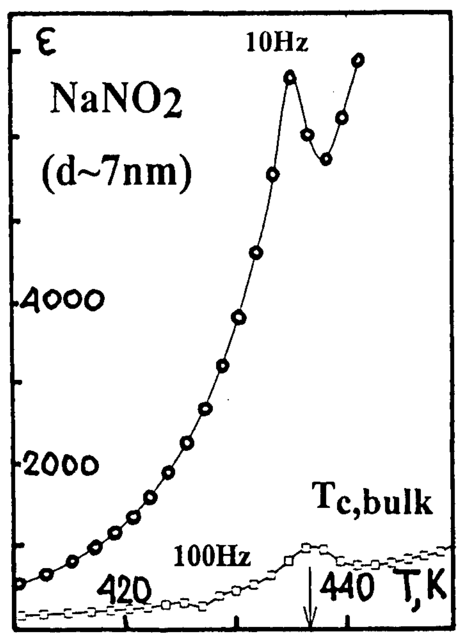

Figure 2. The temperature dependencies of dielectric constant for sodium nitrite

The dielectric measurements for sodium nitrite particles in porous glass are presented in Fig.2. We can clearly see for both measuring frequencies the peculiarities associated with the ferroelectric phase transition (the bulk T_c value is pointed by arrow). The observed shift of T_c in this case is relatively small. Another situation for shift of T_c was observed for KDP particles. In Fig.3 the temperature dependence of dielectric permittivity for KDP fine particles within the opal matrix is presented. For comparison all experimental data obtained both on dispersed and bulk KDP objects (the polycrystalline sample was prepared from bulk KDP remaining after its introducing into the porous media) are reported in this figure. Fig.3 demonstrates a well defined maximum in ε(T) dependence for dispersed KDP. The position of this maximum (T_m=130K) was found to be considerably above Curie temperature for single crystal. The position of maximum ε(T) and its magnitude do not depend on measurement frequency and this ε(T) peak is widely smeared in temperature. For KDP introduced in porous glass (the sizes of the particles are about 7 nm) we have not observed a maximum in ε(T) that can be directly attributed to the ferroelectric phase transition. For T>220K there is a rapid increasing of permittivity with temperature increasing due to ionic current. In the temperature region 170K<T<220K the dependencies become flatter. Starting from T≈170K ε(T) decreases with temperature decreasing. Taking into account such different behavior of ε(T) dependence in temperature regions mentioned above, we can consider the observed dependencies as a result of superposition of two different components. One is ionic current contribution to the complex permittivity and the second one- a broadly smeared in temperature ferroelectric contribution. Following this assumption one can extract this extremely broaden peak caused by the appearance in the system of the ferroelectric ordering. This curve has a maximum at temperature ≈190K that is essentially far from the value of the Curie temperature for the bulk KDP.

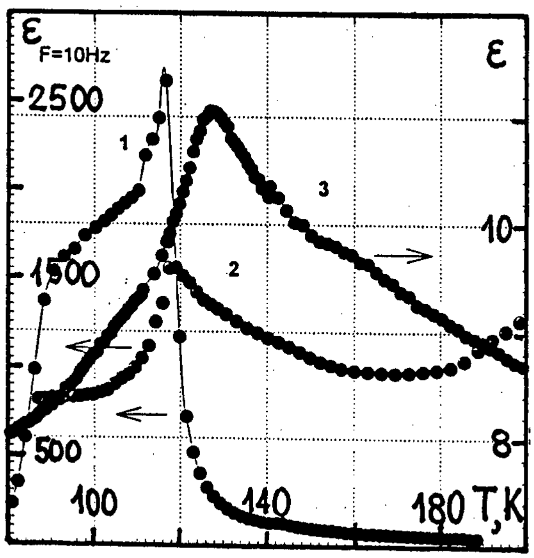

Figure 3. Dielectric permittivity curves obtained on different KDP specimens: 1.KDP single 2. KDP polycrystalline, 3. KDP in opal.

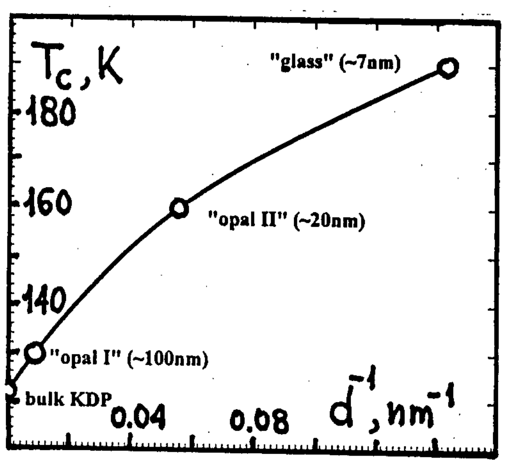

Figure 4. KDP ferroelectric transition temperature dependence on the particle size.

Comparing ε(T) dependence for KDP embedded in opal with the dielectric data obtained on KDP in porous glass , one can suppose that the peculiarity at 160K (Fig.3) could be caused by ferroelectric properties of the second kind KDP particles (an average size of about 20 nm).Taking into account all made assumptions concerning the nature of all observed dielectric peculiarities we have build the dependence of ferroelctric transition temperature on the KDP particle size. It is presented in Fig.4. One can see the large transition temperature increasing with the decreasing of particles size. Such great T_c increasing did not observed in other low dimensional ferroelectric systems. Usually (5, 6, 10, 11) T_c decreases with the decreasing of the characteristic size of the ferroelectric object. Following the phenomenological consideration (4) of the size effect in ferroelctrics one can expect the T_c shift depending on the surface condition and type of media surrounding the ferroelectric small particle. In the case of KDP embedded in glass or opal the matrix due to wetting by KDP melt could have an essential effect on the surface energy.

ACKNOWLEDGEMENTS

The opal matrixes have been kindly presented to us by Dr. S.Romanov. The work was supported by the RFFI Grants N 95-02-04065, N 97-02-18267 and by Grant N 96-2008 of the Programme «Physics of Solid State Nanostructures».

REFERENCES

1. Jaccard J.,Kanzig W.,Peter M., *Helv. Phys. Acta* 1953, 26, 21
2. Anliker K., Brugger H.R., Kanzig W., *Helv. Phys. Acta*, 1954, 27, 99
3. Scott J.F., Pras de Aranjo C.A., *Science*, 1989, 246, 1400
4. Zhong W.L., Wang Y.G., Zhang P.L., Qu B.D., *Phys. Rev.*, 1994,B50, 698
5. Zhong W.L., Jiang B., Zhang V.L., Mat J.M., Cheng H.M., Yang Z.H., Li L.X., *J.Phys:Cond.Matter*, 1993, 5, 2619
6. Uchino K., Sadanaga E., Hirouse T., *J.Am.Ceram.Soc.*, 1989, 72, 1555
7. Marquardt V., Gleiter H., *Phys. Rev. Lett.*, 1982, 48, 1423
8. Wiltzins V., Bates F.S., Dierker S.B., Wignall G.D., *Phys. Rev.*, 1987, A36, 2991
9. Balakirev V., Bogomolov V., Zhuravlev V., Kumzerov Yu., Petranovskii V., Romanov S., Samoilovich L., *Kristallographiya*, 1993, 38, 111
10. Ishikawa K., Yoshikawa K., Okada N., *Phys. Rev.*, 1988, B37, 5852
11. Shih W.Y., Shih W.-H., Aksay I.A., *Phys. Rev.*, 1994, B50, 15575

Pergamon

NanoStructured Materials, Vol. 12, pp. 967–970, 1999
Elsevier Science Ltd

0965-9773/99/$–see front matter

PII S0965-9773(99)00279-2

THERMOELECTROMOTIVE FORCE IN NANOCRYSTALLINE WIRES

F.Barariu, H.Chiriac
National Institute of R&D for Technical Physics,
47 Mangeron Blvd., 6600 Iasi 3, Romania

Abstract – *We present a study of the evolution of the crystallization process from the amorphous through the nanocrystalline to the crystalline state by measuring the temperature dependence of the thermoelectric force supplied by a thermocouple of composition* $Fe_{73.5}Cu_1Nb_3Si_{13.5}B_9$. *The measurements were performed on amorphous wires during the evolution of the crystallization process, one portion of the sample being successively annealed by Joule effect. A comparative study of the evolution of the thermoelectric force for both isochronal and isothermal current annealing and the correlation with the magnetic and electrical resistivity is also presented. The thermoelectric measurements indicate an increase in the value of the thermoelectric force up to a value which corresponds to the complete crystallization.* ©*1999 Acta Metallurgica Inc.*

INTRODUCTION

Nanocrystalline phases, produced by crystallization from amorphous FeCuNbSiB alloys are known to show interesting physical properties. They present excellent soft magnetic properties and interesting electrical properties due to a mixture of very fine bcc Fe grains of nanometric size embedded in an amorphous matrix (1,2).

Although the electrical and magnetic properties of the amorphous and nanocrystalline wires are generally known, there are less information about the thermoelectric properties of these materials. Recently we have reported the appearance of the thermoelectromotive force supplied by an amorphous-crystallized thermocouple for some amorphous and nanocrystalline materials (3,4).

The aim of this paper is to present some results on the thermoelectromotive force (thermo emf) supplied by the junction of a thermocouple which consists of an amorphous wire one half of the wire being kept in the amorphous state and in the other one the nanocrystalline phase have been induced by suitable annealing by Joule effect. This phenomenon has been studied on amorphous $Fe_{73.5}Cu_1Nb_3Si_{13.5}B_9$ wires obtained by us by the in rotating water quenching method. The thermoelectric measurements were correlated with measurements of the magnetic permeability and were explained on the basis of the phases that appear during the crystallization process.

EXPERIMENTAL

We prepared the $Fe_{73.5}Cu_1Nb_3Si_{13.5}B_9$ amorphous wires by the in rotating water quenching technique. The measurements were performed on as-cast wires 560 mm in length, having an uniform cross-section of 1.36×10^{-4} cm^2. The as-cast samples were determined to be amorphous by DTA, X-ray diffraction and thermomagnetic measurements. At the middle of the wire was mechanically connected a platinum wire to give the possibility to heat one portion of the wire by passing a dc current through it to perform crystallization by Joule effect. In this way we obtained three thermocouples: amorphous wire-Pt, crystalline wire-Pt, and amorphous-crystalline wires. The as obtained thermocouple was set in a quartz tube, in vacuum, in order to avoid oxidation of the sample during the current annealing. A small electric furnace was wound on the quartz tube to give the possibility to heat the junction of the thermocouple. The temperature supplied by the furnace was controlled by a chromel-alumel thermocouple set in the vicinity of the amorphous-crystalline one. The free ends of the thermocouples were kept at room temperature during measurements. The whole system was introduced in the magnetic properties measurement system. Using this arrangement we had the possibility to measure the dependence of the electrical resistance on the annealing dc current to control the evolution of the crystallization process and also the magnetic properties after each stage of crystallization by a fluxmetric method. The measurements were performed by coupling the installation with a computer that allowed data acquisition and processing.

RESULTS AND DISCUSSION

In order to determine the appropriate value of the dc current annealing at which to perform the thermo emf measurements we studied the relative variation of the electrical resistance of the wire as a function of the dc annealing current. The electrical resistance shows two peaks of crystallization specific to the nanocrystalline alloys, one (T_{x1}) at corresponding to the nanocrystalline phase and a second one (T_{x2}) corresponding to complete crystallization. The value of 320 mA dc current, at which the annealing was performed, is slightly smaller than the value at which the onset of nanocrystallization takes place.

Figure 1 illustrates the temperature dependence of the thermoelectromotive force supplied by the junction of the amorphous-crystallized FeCuNbSiB thermocouple. The measurements of the thermo emf were carried out after successive isothermal dc current annealing at 320 mA of one portion of the wire thermocouple, in a temperature range between 25°C and 300°C. The results were correlated with measurements of the maximum magnetic permeability (Figure 2), performed after each step of dc current annealing. Up to 5 s annealing time no significant increase in the thermo emf was observed, the annealed portion of the wire being still in the amorphous state. After 10 s total annealing time the thermo emf increases up to 0,3 mV, this value corresponding to the relaxation process. The onset of the nanocrystallization process results in an increase of the thermo emf up to 0,4 mV after a total annealing time of 5 min when an important increase in the permeability can be also observed.

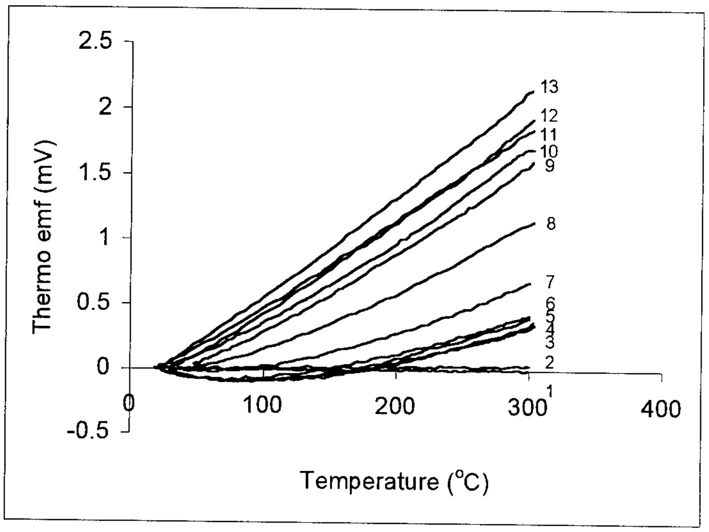

Figure 1. Temperature dependence of the thermo emf .

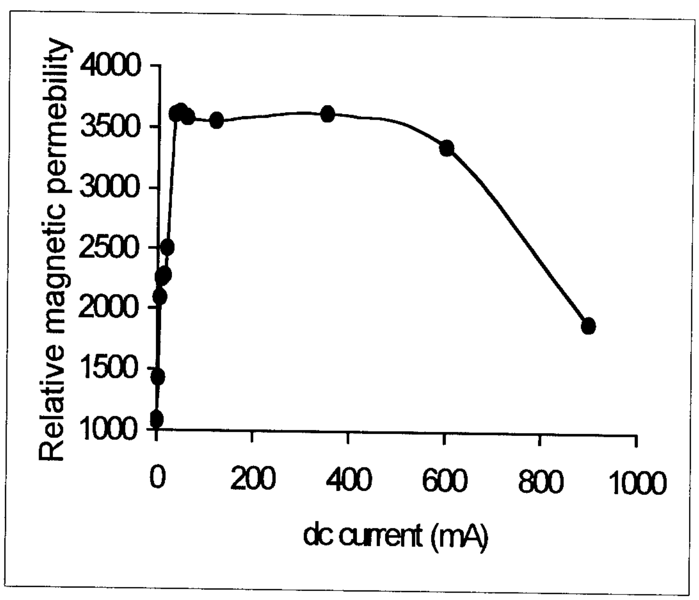

Figure 2. Annealing time dependence of the maximum relative permeability.

Further annealing up to 10 min leads to a slight increase in the thermo emf and an almost constant value of the maximum permeability. In the annealing time range of 10 s up to 10 min it can be observed that the thermo emf takes firstly negative values, than vanishes at different temperatures (depending on the annealing duration), and than changes its sign becoming positive. This behavior can be explained taking into consideration the nature and the volume fractions of the phases that are formed during the crystallization process. The behavior of the thermo emf between 10 s and 10 min annealing time can be attributed to the the formation of the nanocrystalline state consisting of an ultrafine grain structure of bcc FeSi with typical grain sizes of 10-20 nm embedded in a still amorphous matrix. The fact that in this interval the nanocrystalline state is formed is supported by the high values of the permeability and by the electrical resistance behavior. The increase in the annealing time leads to the formation of Fe-borides which deteriorates the magnetic permeability. So we can state that the behavior of the thermoelectromotive force in the mentioned annealing interval is due to the change in the alloy structure i.e.: the enrichment in the nanocrystalline bcc FeSi grains determines negative values in the thermo emf in the 25°C -180°C temperature interval and then the formation of the Fe-borides leads to the change in the sign of thermo emf to positive values.

Increasing the duration of annealing the thermo emf increases continuously up to the maximum of 23 mV, the maximum permeability decreasing down to a value approximately equal to the value of the magnetic permeability in the as-cast state. At this stage the crystallization process is completed. The same behavior of the thermo emf was obtained by isochronal annealing.

CONCLUSIONS

A thermocouple which consists of two parts of an amorphous $Fe_{73.5}Cu_1Nb_3Si_{13.5}B_9$ amorphous wire, an amorphous one and a crystalline one supplies a thermo emf that increases, in absolute value, in two steps: up to a value at which the nanocrystalline structure is formed and then to the complete crystallization of the annealed part. The behavior of the thermo emf is supported by the behavior of electrical resistance and magnetic permeability and can be attributed to the formation of some phases whose thermo emf are different with respect to the amorphous phase.

References

1. Herzer G., *Nanostructured and Non-Crystalline Materials,* World Scientific, Singapore, 1995, p. 449.
2. Herzer G., *IEEE Transactions on Magnetics,* 1989, 25, 3327.
3. Chiriac H., Barariu F., Nagacevschi V., *Journal of Magnetism and Magnetic Materials,* 1996, 160, 239.
4. Chiriac H., Inoue A., Barariu F., Nagacevschi V., *Maerials Science and Engineering:* A, 1996, 226-228, 650.

Pergamon

NanoStructured Materials, Vol. 12, pp. 971–974, 1999
Elsevier Science Ltd

0965-9773/99/$–see front matter

PII S0965-9773(99)00280-9

A GAS-SENSING CoO/SiO_2 NANOCOMPOSITE

Naoto Koshizaki, Katsuya Yasumoto, Takeshi Sasaki

National Institute of Materials and Chemical Research
1-1 Higashi, Tsukuba, Ibaraki, 305-8565 Japan

Abstract — *We developed a gas sensing CoO/SiO_2 nanocomposite which changes its optical transmittance by nitrogen oxide. Films prepared by co-sputtering and sol-gel method showed reversible transmittance change by NO at 350 °C in the wavelength range from 400 to 800 nm. Nano-scale cobalt oxide dots were observed in the CoO/SiO_2 nanocomposite. The sensing properties can be considered to be originated from nanostructures composed of (a) functional CoO nanoparticles whose optical transmittance is changed by nitrogen oxide, (b) nanopores which provide paths for gas molecules, and (c) a transparent SiO_2 matrix which enables us to measure optical transmittance. The octahedral divalent cobalt ions confined at the interface of the composite are inferred to contribute to such transmittance change.*

INTRODUCTION

Nanocomposites dispersed with semiconductor or metal have been extensively studied because of their unique optical properties, such as high third-order nonlinear susceptibility and photoluminescence (1,2). The unique optical properties of these composites result from quantum size effects of the nanoparticles embedded in the matrix. Recently, approaches to utilize the interaction between functional nanoparticles and various kinds of matrices like TiO_2, MgO and ZnO are becoming a new area of interest (3,4). In this case, not only the quantum size effect but also the interface effect between nanoparticles and matrix would occur in the appearance of new and unique function. We developed gas-sensing semiconductor-dispersed nanocomposites whose optical transmittance was changed by exposure to NO using the sol-gel method (5) and the sputtering method (6-8). Although an inert SiO_2 is used as a matrix in this case, the interaction of nanoparticles and matrix at the interface is considered to enhance the sensor functionality. In this paper we discuss the gas-sensing mechanism of CoO-dispersed SiO_2 nanocomposites (CoO/SiO_2) prepared by co-sputtering and sol-gel methods.

EXPERIMENTAL

CoO/SiO_2 nanocomposite films were deposited on quartz glass substrates using co-sputtering method by placing CoO pellets on a SiO_2 glass target. All of the sputter depositions were done in Ar without heating of the substrates. In order to obtain various CoO/SiO_2

nanocomposite films, we changed the number of CoO pellets, the sputtering time and the sputtering pressure (6-8). Pure films were also deposited from CoO targets under the same sputtering conditions. For comparison, the sol-gel method was used for the preparation of CoO/SiO_2 nanocomposite films (5). An ethanol solution of $Si(OC_2H_5)_4$ was mixed with an aqueous solution of $Co(NO_3)_2{\bullet}6H_2O$ and HCl and the mixed solution before gelation was deposited on a SiO_2 glass using a spin coater. The deposited films were pyrolyzed at 400 °C for 2 hours. Thus CoO/SiO_2 composite films with nano-structure similar to the sputter-deposited films were obtained.

The optical transmittance change due to the gas atmosphere was measured in the wavelength range from 400 to 800 nm at 350 °C using a spectrophotometer with a special quartz cell. NO sensitivity is defined as the ratio of transmittance in NO (1%)/N_2 to that in air. Other characterization techniques were the same as described before (5-8).

RESULTS AND DISCUSSION

Figure 1 shows the typical changes in the optical transmittance curves of the CoO/SiO_2 nanocomposite film obtained by sputtering from a SiO_2 target with 4 CoO pellets on at 100 W in 0.27 Pa of Ar atmosphere. The curves were recorded in air and every 8 minutes after the switch of atmosphere from air to 1% of NO. The transmittance increased in the whole wavelength range

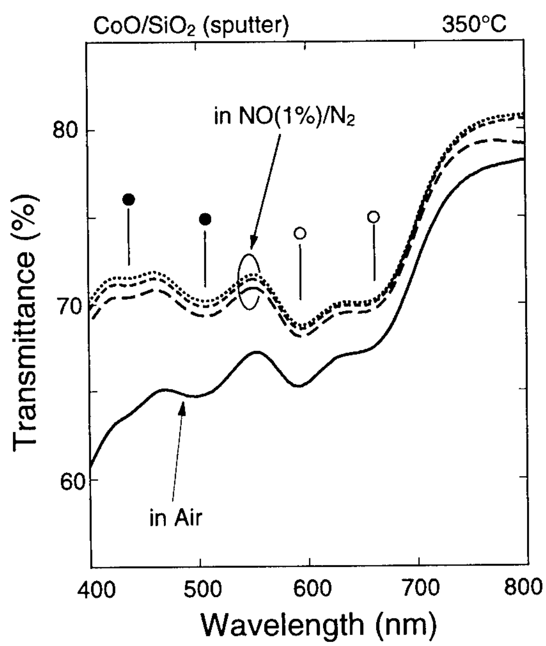

Figure 1. Changes in the optical transmittance curves of the sputter-deposited of CoO/SiO_2 nanocomposite film. Curves from the bottom are recorded in air, and 8, 16 and 24 min after NO(1%)/N_2 exposure. Open and solid circles represent bands from tetrahedral and octahedral divalent cobalt ions, respectively.

with the elapsed time and nearly saturated after 24 min. By the re-exposure to air, the optical transmittance almost reversibly returned to the initial curve. Followings were deduced from the detailed studies on gas sensing characteristics and characterization of the co-sputtered CoO/SiO_2 nanocomposite films (6-8). From the Co concentration dependence of NO sensitivity, the Co component is an active material for transmittance change. XPS analysis revealed that CoO component was present for the samples with high sensitivity. Nanoparticles about 6 nm in diameter embedded in a SiO_2 matrix were clearly observed by TEM. Thus functional CoO nanoparticles is a required component for sensing. From the thickness dependence of NO sensitivity, the sensing process occurred in the interior of the film of about 1 μm. Nanopores are assumed to provide paths for NO to reach the functional CoO nanoparticles inside the film. The transparent matrix of SiO_2 is also important to enable us to measure optical transmittance change.

Several absorption bands were observed for sputter-deposited CoO/SiO_2 nanocomposite as shown in Fig. 1. These bands did not shift with the changes in film thickness, indicating that these structures did not arise from the interference effect of the films. Indeed, such bands were observed in glass dispersed with cobalt ions (9,10). Bands shown as open circles and those as solid circles in Fig. 1 can be assigned to tetrahedral and octahedral divalent cobalt ion, respectively. CoO/SiO_2 nanocomposite obtained by sol-gel method and film sputtered from CoO target also showed similar transmittance change with NO. However, these three films have different cobalt concentration and film thickness. Therefore we should compare the changes not in transmittance but in extinction coefficient by NO exposure to cancel out such differences. The extinction coefficient α can be calculated by the equation, $\alpha = -(\log T)/cl$ where T is transmittance, c is the concentration of cobalt and l is the film thickness. Figure 2 shows a comparison of the difference of extinction coefficients before and after the NO gas introduction for CoO and CoO/SiO_2 films deposited by sputtering and for CoO/SiO_2 film prepared by sol-gel method. The change in extinction coefficient by NO exposure from sputtered CoO film showed

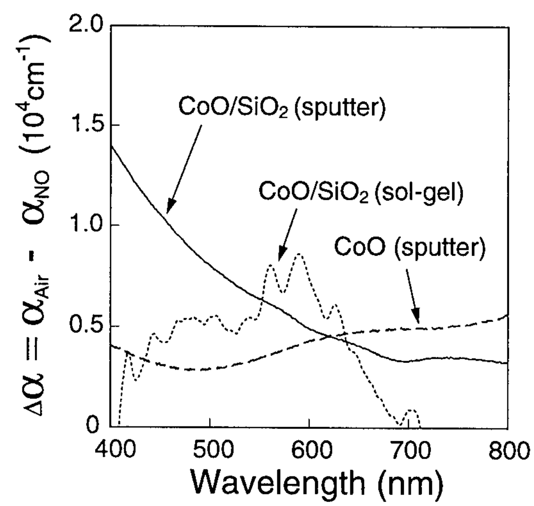

Figure 2. The difference of extinction coefficients before and after the NO gas introduction for CoO and CoO/SiO_2 films deposited by sputtering and for CoO/SiO_2 film prepared by sol-gel method.

small wavelength dependence. In the wavelength range shorter than 600 nm, the α difference in the sputter-deposited CoO/SiO_2 nanocomposite was larger than that in CoO. In this range, the contribution of octahedral Co^{2+} was dominant, as mentioned above. The α difference in the CoO/SiO_2 nanocomposite prepared by sol-gel method was also larger than that in CoO at about 440-630 nm. From these data, the octahedral divalent cobalt ions confined in CoO nanoparticles can be considered to interact effectively with NO, resulted in large transmittance change. Octahedral Co^{2+} should be located mainly on the surface of nanoparticles and take part in the process of transmittance change. Nanoparticle sizes in the nanocomposites prepared by sputtering and sol-gel method were about 6 and 10 nm in diameter, respectively. The wavelength shift of the maximum change by NO exposure might come from this nanoparticle size difference. Thus the high density of interface in the nanocomposite plays a crucial role for such gas sensing characteristics.

SUMMARY

The CoO-doped SiO_2 nanocomposite film prepared by co-sputtering and sol-gel methods showed reversible transmittance changes by exposure to nitrogen oxide. From the comparison of sensitivity data of CoO and CoO/SiO_2 films deposited by sputtering and CoO/SiO_2 film prepared by sol-gel method, the sensing mechanism is inferred that the octahedral divalent cobalt ions confined at the interface effectively interact with NO. This type of material would open up new applications of functional nanocomposites.

REFERENCES

1. Kineri, T., Mori, M., Kadono, K., Sakaguchi, T., Miya, M., Wakabayashi H. and Tsuchiya, T., *Journal of the Ceramic Society of Japan*, 1995, 103, 117.
2. Hayashi, S., Kataoka, M. and Yamamoto K., *Japanese Journal of Applied Physics*, 1993, 32, L274.
3. Sasaki, T., Rozbicki, R., Matsumoto, Y., Koshizaki, N., Terauchi, S. and Umehara, H., *Materials Research Society Symposium Proceedings*, 1997, 457, 425.
4. Koshizaki, N., Umehara, H., Sasaki, T. and Oyama, T., *Nanostructured Materials*, 1998, 8, 1085.
5. Yasumoto, K., Koshizaki, N. and Suga, K., *Sol-Gel Optics II*, SPIE - International Society for Optical Engineering, Bellingham, 1992, p. 604.
6. Koshizaki, N., Yasumoto, K. and Terauchi, S., *Japanese Journal of Applied Physics*, 1995, 34-1, 119.
7. Yasumoto, K. and Koshizaki, N., *Denki Kagaku*, 1996, 64, 1314.
8. Yasumoto, K. and Koshizaki, N., *Journal of Materials Science Letters*, 1997, 16, 215.
9. Duran, A., Fernandez Navarro, J.M., Casariego, P. and Joglar, A., *Journal of Non-Crystalline Solids*, 1986, 82, 391.
10. Boos, A., Pourroy, G., Rehspringer J.L. and Guille, J.L., *Journal of Non-Crystalline Solids*, 1994, 176, 172.

Pergamon

NanoStructured Materials, Vol. 12, pp. 975–978, 1999
Elsevier Science Ltd

0965-9773/99/$–see front matter

PII S0965-9773(99)00281-0

NANOSTRUCTURE AND PHOTOLUMINESCENCE PROPERTY OF Si/MgO AND Si/ZnO CO-SPUTTERED FILMS

Naoto Koshizaki, Hiroyuki Umehara, Takeshi Sasaki, Umapada Pal*, Toshie Oyama

National Institute of Materials and Chemical Research
1-1 Higashi, Tsukuba, Ibaraki 305-8565, JAPAN
*Instituto de Fisica, Universidad Autónoma de Puebla,
Apdo. Postal J 48, Puebla, Pue. 72570, MEXICO

Abstract *— Si/MgO and Si/ZnO films were deposited by placing Si plates on an MgO or ZnO target during sputter deposition. X-ray photoelectron spectroscopic (XPS) analysis revealed that the average Si valency was 3.1 for Si/MgO and 2.6 for Si/ZnO co-sputtered films when Si contents were 20%. Diffraction peaks of not Si-derived but less crystallized matrix were observed at low Si content ranges. Both films are seen to have structures with nanoparticle dispersion from TEM observation. The PL emission observed at 1.7 eV for Si/MgO and at 2.0 eV for Si/ZnO is deduced to arise from the electron-hole recombination mechanism in SiO_x at the interface, which is similar to the Si/SiO_2 co-sputtered film. ©1999 Acta Metallurgica Inc.*

INTRODUCTION

Nano-sized silicons, such as porous silicon and silicon nanoparticles, have attracted much scientific attention because of their photoluminescence (PL) properties (1,2). Si/SiO_2 nanocomposites prepared by co-sputtering and heat treatment have structures embedded with nano-sized silicon (3-6). The photoluminescence of Si nanostructures is considered to originate from the quantum confinement effect of Si nanoparticles and/or the luminescence center at the Si/SiO_2 interface, but the mechanism is still controversial. In order to pursue the possibility of obtaining Si nanoparticles embedded in different matrix materials other than SiO_2, we deposited thin films by sputtering an Al_2O_3, MgO, TiO_2 or ZnO target on which the Si plates are placed (7,8). In this paper, we focus on Si/MgO and Si/ZnO co-sputtered films because these two have interesting nanostructures and PL properties. The correlations between structure, the chemical state of silicon and the PL property of these films are discussed.

EXPERIMENTAL

Co-sputtered films of Si/MgO and Si/ZnO were prepared on SiO_2 substrates using an r.f. sputtering apparatus (Shimadzu HSR-521). Si plates (Osaka Titanium Co. Ltd., n-type) were

symmetrically placed on an MgO or ZnO target 100 mm in diameter for co-sputtering. In order to study the effect of Si addition in small amounts in this paper, the size of the Si plates used was 5 mm × 5 mm, which was a third of the plate size used in the previous experiments (7,8). Thus the content of Si in the films was small even though the number of Si plates were the same as before. The sputtering power, atmosphere and deposition time for Si/MgO and Si/ZnO were 200 W, 0.53 Pa of Ar for 90 min and 100 W, 1.3 Pa of Ar for 60 min, respectively. The thicknesses of the films were approximately 500 nm and 800 nm. Throughout this paper, notations like Si(12)/MgO are used, where the number in parentheses is the number of Si plates placed on the target. Heat treatment was performed for 3 h in a vacuum. The equipment used for characterization and PL measurement was the same as that used in the previous experiments (7,8).

RESULTS AND DISCUSSION

Figure 1 shows the change in Si content of as-deposited Si/MgO and Si/ZnO films with the increase in the number of Si plates which were analyzed by XPS. The content of both films almost linearly increased with the use of up to 12 Si plates, where the atomic concentration of Si was about 20%. Diffusion and reaction of the components occurred by heat treatment above 500 °C for Si/MgO and 600 °C for Si/ZnO in the high Si concentration range. For Si/MgO, the Si component migrated into the interior of the film, resulting in the formation of an MgO layer at the surface. In contrast, the Si component was enriched at the surface for Si/ZnO co-sputtered film.

Figure 2 shows the Si2p XPS spectra of Si(12)/MgO and Si(12)/ZnO co-sputtered films annealed at 400 °C. The same procedure as that described in the previous paper (7) was applied to analyze these data. First, the charge-up shifts of the peaks were calibrated by taking the Mg2p peak from MgO to be 50.8 eV and the Zn2p peak from ZnO to be 1021.8 eV (9). A small metallic Mg peak at 49.0 eV was observed in the Si/MgO film, indicating that Si in a low valency state reduced a small amount of MgO. There was only one component of ZnO in the Zn2p peak from Si/ZnO film. Second, curve fitting calculations were performed for these Si2p peaks, assuming the existence of the following five components: Si metal, Si^{+}, Si^{2+}, Si^{3+}, Si^{4+}, and the binding

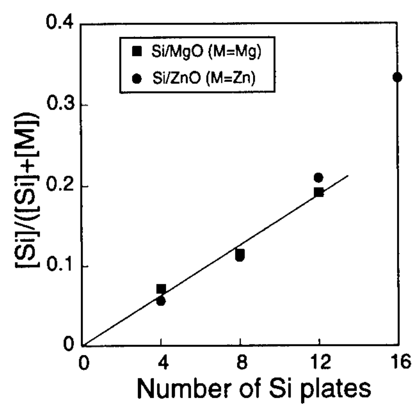

Fig. 1 Changes in Si contents of as-deposited Si/MgO and Si/ZnO co-sputtered films analyzed by XPS.

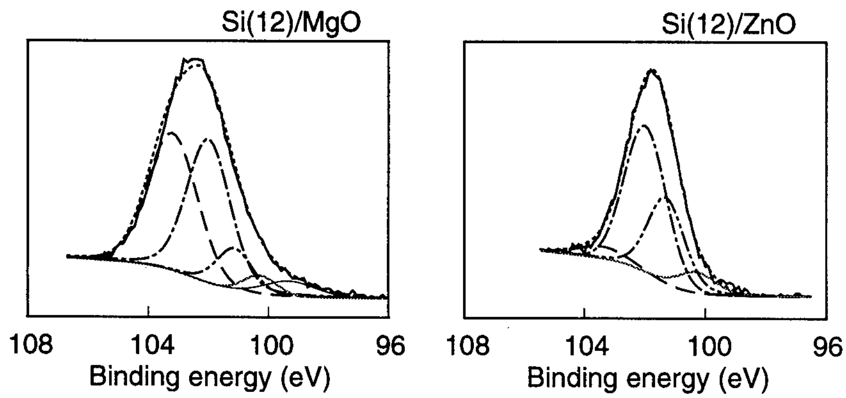

Fig. 2 Si2p XPS spectra of Si(12)/MgO and Si(12)/ZnO co-sputtered films annealed at 400 °C with the results of curve fitting calculations. The band at about 102.3 eV is the Si^{3+} component.

energies and FWHMs of these components. The results of the curve fitting calculations are also shown in Fig. 2. Tri- and tetra- valent silicon was the main component for Si/MgO film, and the tri-valent state was dominant in Si/ZnO film. The average valence of Si/MgO and Si/ZnO was 3.1 and 2.6, respectively.

In the Si(12)/MgO film, a weak and broad MgO(200) peak and no Si-derived peak were observed in the XRD spectra, though a sputtered MgO film showed a strong (200) peak. The shape of the MgO(200) peak did not greatly change even through heat treatment at 900 °C. In the Si/ZnO film, the films sputtered with 4 or 8 Si plates on a ZnO target showed a small and broad ZnO(002) peak, which became sharp by annealing at 600 °C. However, for Si(12)/ZnO film, heat treatment at 400 to 600 °C was required to obtain ZnO(002) orientation. Both Si(12)/MgO and Si(12)/ZnO films are seen to have structures with nanoparticle dispersion from TEM observation.

The PL spectra of MgO and Si(12)/MgO sputtered films are shown in Fig. 3. MgO is known to show PL at 2.0 eV (10). Si(12)/MgO, however, showed stronger PL at 1.8 eV than

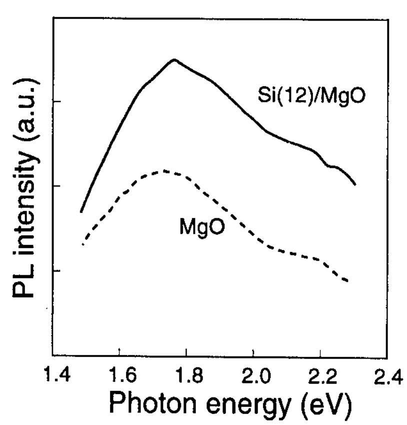

Fig. 3 Photoluminescence spectra of MgO and Si(12)/MgO sputtered films measured at 300K.

MgO as shown in Fig. 3. In our previous paper (7), we studied the relationship of PL and the Si2p XPS spectra of the Si/SiO_2, Si/Al_2O_3 and Si/MgO co-sputtered films, and concluded that the SiO_x ($0<x<2$) content calculated from the XPS spectra is important for the PL emission at 1.7 eV (730 nm) observed in Si/SiO_2 co-sputtered films, because it is thought to be due to the recombination of electrons and holes in the SiO_x region at the interface. In the previous analysis (7), Si/MgO co-sputtered films (Si content: 28%) had quite small PL intensities, because the proportion of the SiO_x component was only about 20% of all Si components, even though the concentration of the metallic Si component was as high as 23%. The 1.7 eV emission was, however, observed through a similar mechanism in this experiment, probably because the proportion of the SiO_x component was high enough at 54%. In contrast, Si(8)/ZnO co-sputtered film annealed at 400 °C had ZnO(002) orientation and similar XPS spectra, and showed PL peaked at about 2.0 eV (610 nm). Although the energy of this PL is slightly large, it can be ascribed to the electron-hole recombination process in SiO_x (11).

SUMMARY

The nanostructure and photoluminescence of Si/MgO and Si/ZnO co-sputtered films, whose Si contents were about 20% were studied. From the XPS analysis, the principal low valency Si state was Si^{3+} for Si/MgO and Si/ZnO at this Si content range. These films had nanocomposite structures. PL emissions at 1.7 eV for Si/MgO and at 2.0eV for Si/ZnO were observed. They can be ascribed to the electron-hole recombination process in SiO_x at the interface.

REFERENCES

1. Canhan, L.T., *Applied Physics Letters*, 1990, 57, 1046.
2. Feng Z.C. and Tsu R. (eds.), *Porous Silicon*, World Scientific, Singapore, 1994.
3. Hayashi S. and Yamamoto K., *Journal of Luminescence*, 1996, 70, 352.
4. Yoshida, S., Hanada, T., Tanabe, S. and Soga, N., *Japanese Journal of Applied Physics.*, 1996, 35, 2694.
5. Shimizu-Iwayama, T., Terao, Y., Kamiya, A., Takeda, M., Nakao, S. and Saitoh, K., *Nanostructured Materials*, 1995, 5, 307.
6. Zhang, Q., Bayliss, S.C. and Hutt, D.A., *Applied Physics Letters*, 1995, 66, 1977.
7. Koshizaki, N., Umehara, H. and Oyama, T., *Thin Solid Films*, 1998, in press.
8. Koshizaki, N., Umehara, H, Sasaki, T. and Oyama, T., *Nanostructured Materials*, 1998, 8, 1085.
9. Moulder, J.F., Stickle, W.F., Sobol, P.E. and Bomben, K.D., *Handbook of X-ray Photoelectron Spectroscopy*, Perkin-Elmer Corporation, Eden Prairie, 1992.
10. Duley, W.W. and Rosatzin, M., *Journal of Physics and Chemisty of Solids*, 1985, 46, 165.
11. Pal, U., Koshizaki, N. and Sasaki, T., *Japanese Journal of Applied Physics*, submitted.

Pergamon

NanoStructured Materials, Vol. 12, pp. 979–982, 1999
Elsevier Science Ltd

0965-9773/99/$–see front matter

PII S0965-9773(99)00282-2

ADSORPTION OF PSEUDOISOCYANINE AND OF A THIACARBOCYANINE DYES ON SILVER HALIDES NANOPARTICLES

L. Jeunieau and J. B. Nagy.

Laboratoire de Résonance Magnétique Nucléaire, Facultés Universitaires Notre-Dame de la Paix, 61,rue de Bruxelles, 5000 Namur, Belgique.

Pseudoisocyanine and a thiacarbocyanine dyes have been adsorbed on silver halides nanoparticles synthesized in a microemulsion system (AOT/heptane/water). The adsorption of pseudoisocyanine leads to the sedimentation of the particles. This can be decreased by adding an appropriate amount of CTAB (cetyltrimethylammonium bromide). The site of adsorption of a thiacarbocyanine has been investigated. The cyanine adsorption is stabilized by an interaction between the sulphur atom and the silver ion on the silver bromide particles and by a coulombic interaction between the nitrogen atom and the chloride ion on the silver chloride particles. ©1999 Acta Metallurgica Inc.

Introduction

Silver halides have an intrinsic absorption in the blue region. In order to spectrally sensitize them to longer wavelengths for photographic purposes, dyes such as the cyanines are generally used [1]. These dyes form aggregates when they are adsorbed on the silver halides nanoparticles. The aggregates are characterized by the position of their absorption band in comparison with the absorption of the adsorbed monomer. The J-aggregates have a bathochromic shift and the H-aggregates have a hypsochromic shift.

Experimental.

The silver bromide particles were synthesized in a microemulsion system : the AOT (sodium bis-(2-ethylhexyl)-sulfosuccinate)/n-heptane/water [2]. The microemulsions were prepared from n-heptane (Aldrich 99+% HPLC Grade), AOT (Sigma 99%) and aqueous solutions of silver nitrate (Jansen Chimica p.a.) and potassium halides (Merk Uvasol spectroscopy) using Millipore water. The solutions concentrations were 0.063M for the silver nitrate and 0.064M for the potassium halides. The microemulsions were prepared with a 0.12M solution of AOT in n-heptane and the aqueous solutions were added in order

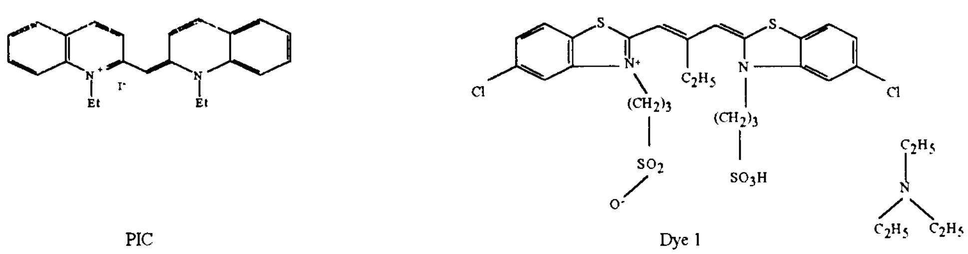

Figure 1 : Structure of the dyes used in this study

to have a ratio $\omega = [H_2O]/[AOT] = 3.1$. 5ml of the microemulsion containing silver nitrate were added to 5ml of the microemulsion containing potassium bromide (or chloride). The average diameter of the particles is equal to 46 Å for the silver bromide particles and 32 Å for the silver chloride particles. The structure of the dyes used is shown in figure 1. For adsorption, 10^{-3}M solutions of dye in methanol were used. The number of dye molecules per particle is equal to 21 for AgBr, and to 8 for AgCl. The method of adsorption is the following : a part of the dye solution corresponding to the required amount of dye is added to 5ml of the AOT solution. This mixture is finally added to the colloidal suspension of silver halide and stirred during 30 minutes. Time zero is taken at the end of the 30 minutes. Uvikon 930 UV-spectrophotometer is used for the UV-visible absorption spectra. The wavelength precision is 0.2nm. The optical path is 1cm. The reference in the absorbance measurement is a 0.12M solution of AOT in heptane. The UV-visible absorption spectra have been spectrally decomposed.

Results and discussions.

Influence of the adsorption of PIC on the stability of the particles.

When PIC is adsorbed on AgBr, both the absorbance of the monomer in solution and of the J-aggregate are decreasing as a function of time (fig.2). This indicates the sedimentation of the particles. At the same time the J-aggregate grows (indicated by an increase of the maximum of absorbance of the J-aggregate). Indeed, the particles are stabilized by the AOT surfactant molecule. However, if PIC is adsorbed, AOT is removed from the surface and the particles are destabilized. The aggregation of the dye molecules decreases the particles stability : the aggregates remove the AOT molecules on a large surface of the particles. The aggregation of the particles is increased by the growth of the J-aggregate with time. A method of stabilisation of the particles is to add a surfactant which is more adsorbed than the AOT.

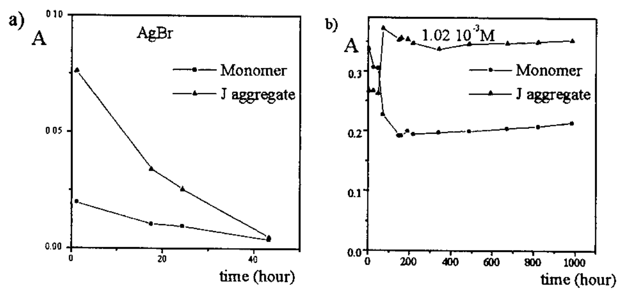

Figure 2 : Variation of the absorbance of the monomer in solution and of the J-aggregate for PIC adsorbed on AgBr without (a) and with (b) a concentration of 1.02 10^{-3} M in CTAB.

For such a surfactant we have used a cationic one, the CTAB (cetyltrimethylammonium bromide). The particles are slightly negative, due to the 3% excess of potassium bromide, and a cationic surfactant is expected to be more adsorbed than an anionic one. For a CTAB concentration of 1.02 10^{-3} M the particles are well stabilized: the absorbance of the monomer in solution decreases while the absorbance of the J-aggregate increases. At the same time the size of the J-aggregate remains constant.

Adsorption of a thiacarbocyanine.

In order to determine the site of adsorption, particles with an excess of 50% in halide or silver are used. If an excess of silver favours the adsorption, we can conclude that the adsorption occurs by an interaction between the sulphur atom and the silver ions. In the opposite case, if an excess of bromide favours the adsorption, the adsorption is favoured by a coulombic interaction between the nitrogen and the halide ions.

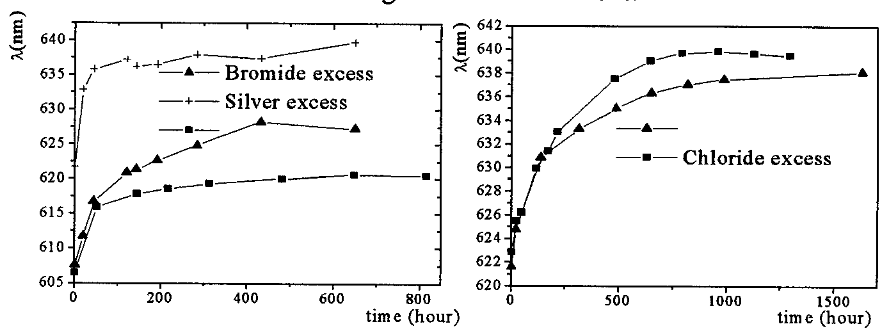

Figure 3 : Variation of the maximum of absorbance of the J-aggregate as a function of time for dye 1 adsorbed on particles of AgBr and AgCl

The J-aggregates are of greater size for the particles of AgBr with an excess of 50% in silver. Oppositely for the particles of AgCl, the size of the J-aggregate is greater in the case of an excess of chloride and no J-aggregates are observed for the particles with an excess of silver (see fig.3). We can thus conclude that the adsorption occurs by an interaction between the silver ion and the sulphur atom for the particles of silver bromide and by a coulombic interaction between the nitrogen atom and the chloride ion for the particles of silver chloride. The difference in the adsorption behaviour on silver bromide and silver chloride can be explained by the difference in the ionicity character of silver chloride and silver bromide. The intercation between sulphur and silver is seen as a soft-soft interaction. This is favoured when the electronic polarizability is greater. The silver electronic polarizability is greater in the AgBr (less ionic) than in AgCl. Oppositely, the interaction between the nitrogen atom and the halide ion can be seen as a hard-hard interaction. This is favoured for more ionic compounds like AgCl.

Conclusions

The adsorption of PIC has a destabilizing effect on the particles of AgBr. However, the particles of AgBr can be stabilized by adding an appropriate amount of CTAB.
A thiacarbocyanine has been adsorbed on silver bromide and silver chloride nanoparticles. The influence of an excess of silver or halides has allowed us to study the adsorption site of the dye. The latter occurs through an interaction between silver and sulphur for the particles of silver bromide and by a coulombic interaction between the nitrogen atom and the chloride ion in the case of silver chloride. This difference has been interpreted as a consequence of the lower ionicity of the silver bromide.

Acknowledgments

Laurence Jeunieau thanks F.R.I.A. for financial help. The authors thank Agfa-Gevaert for providing the dyes.

References

1. Tani, T., *Photoghraphic Sensitivity*, Oxford series on optical imaging science, New York, 1995.
2. Monnoyer, Ph., Fonseca, A, B.Nagy, J, *Colloids and Surfaces*, **1995**, 100, 233

Pergamon

NanoStructured Materials, Vol. 12, pp. 983–986, 1999
Elsevier Science Ltd

0965-9773/99/$–see front matter

PII S0965-9773(99)00283-4

DESIGN AND EVALUATION OF NANOPHASE ALUMINA FOR ORTHOPAEDIC / DENTAL APPLICATIONS

Thomas J. Webster, Richard W. Siegel*, and Rena Bizios
Departments of Biomedical Engineering and *Materials Science and Engineering
Rensselaer Polytechnic Institute, Troy, NY 12180-3590 USA

Abstract –Alumina samples (with a nanophase grain size of 23 nm and a conventional grain size of 177 nm) were synthesized and evaluated for mechanical and cytocompatibility properties. Compared to the 177 nm grain size, the modulus of elasticity of the 23 nm alumina grain size decreased by 70 %; ductility of alumina can, therefore, be controlled and improved through the use of nanophase formulations. Moreover, compared to the 177 nm grain size alumina, osteoblast (the bone forming cells) adhesion on the 23 nm nanomaterial increased by 46 %. The improved mechanical properties of nanomaterials, in addition to the biocompatibility of nanophase ceramics, constitute characteristics that promise improved orthopaedic / dental implant efficacy. ©1999 Acta Metallurgica Inc.

INTRODUCTION

Conventional materials which have been developed for various industrial applications (*e.g.*, in aeronautical or space engineering) have been used as orthopaedic / dental implants as long as they were tolerated by the human body and met certain specifications, such as strength requirements under loading (1). In the course of normal, daily activities, mechanical loads are applied to mammalian bone; for example, jaws sustain 0.25 kN during chewing while hip joints are exposed to 3 – 5 kN during walking (2). In fact, these physiological force requirements have become the primary criterion for selecting materials (such as commercially pure titanium, Ti-6Al-4V and Co-Cr-Mo alloys) for orthopaedic / dental applications. In contrast, ceramics, which have exceptional biocompatibility properties with bone cells and tissues, but are brittle under loading, have experienced limited use in biomedical applications. Unfortunately, conventional metals and metal alloys that meet mechanical requirements for bone-replacement under loading have not produced the "ideal" orthopaedic / dental implant material; in fact, under long-term physiological loading, metal material failures (such as initiation and propagation of cracks) have resulted in clinical complications that necessitated surgical removal of failed bone implants (2).

To date, there have been no diligent, persistent and successful attempts to design and produce a biocompatible substitute which simulates the chemical composition, mechanical

properties and three-dimensional architecture of normal, healthy bone. Bone is a composite material: 30 % of its matrix is organic (consisting of 90 % collagen and 5 % non-collagenous proteins), 65 % inorganic hydroxylapatite and 5 % water (2). Furthermore, the organic and inorganic portion of physiological bone consists of grain sizes in the nanophase regime (2). In addition, conventional orthopaedic and dental implant materials have characteristic grain sizes of several hundred microns (2). Despite their great potential and promise, applications of nanophase materials in the biomedical field (other than drug delivery) have been close to nonexistent. It is, therefore, extremely attractive to ponder whether and how nanomaterials can duplicate bone properties and, thus, become the synthetic biomaterial of the future.

NANOPHASE MATERIALS AS ORTHOPAEDIC AND DENTAL IMPLANTS OF THE FUTURE

With the advent of nanomaterials, it may now be possible to synthesize and process materials for orthopaedic and dental applications which simulate the mechanical properties and chemical characteristics of normal, healthy bone. For example, nanomaterial formulations with improved mechanical properties could replace conventional biomaterials that fail due to crack initiation and propagation during loading. Furthermore, since ductility is enhanced as grain size is reduced (3), nanophase ceramics could be designed and prepared (by selecting processing conditions, such as sinter-forging and, thus, control grain size) to exhibit a wide range of mechanical properties. Most important, future biomaterials consisting of nanophase ceramics could be tailored to meet clinical requirements associated with either anatomical differences or patient age; such requirements arise because, for example, the modulus of elasticity varies by 10 % in bone from the human hip and tibia and by up to 20 % in bone from 20 and 90 year-old humans (2). The chemical characteristics (such as surface properties) of ceramics could also be controlled by decreasing grain size below 100 nm. Nanomaterials with surface properties that both promote swift deposition of new bone on the surface of implants and support bonding of juxtaposed bone could stabilize prostheses *in situ* and, thus, minimize motion-induced damage to surrounding tissues.

DESIGN AND EVALUATION OF NANOPHASE ALUMINA

An example of an effort to design and evaluate nanophase alumina as a biomaterial will be illustrated here. Single-phase alumina samples of 23 nm and 177 nm grain sizes (as determined by the multiple-point BET method) were prepared by compacting 23 nm alumina powder (Nanophase Technologies Corp.) in a tool-steel die *via* a uniaxial pressing cycle. Nanophase alumina compacts were sintered (in air at 10 °C / minute) from room temperature to a final temperature of 1000 °C and maintained at 1000 °C for 2 hours, to obtain 23 nm grain sizes. Conventional alumina samples were sintered (in air at 10 °C / minute) from room temperature to a final temperature of 1200 °C, and maintained at 1200 °C for 2 hours to obtain 177 nm grain sizes. The modulus of elasticity of these alumina samples were determined *via* three-point bending tests. Compared to the 177 nm grain size alumina, the modulus of elasticity of the 23 nm grain size alumina decreased by 70 %. Furthermore, the porosities of nanophase

and conventional alumina were similar. These results provide evidence that the mechanical properties of alumina can be controlled and improved through the use of nanophase formulations.

Materials which are candidates for biomedical applications need to be evaluated in terms of both mechanical properties and biocompatibility. For this reason, *in vitro*, cellular models were utilized to determine the cytocompatibility of nanophase alumina. Numerous rat calvaria osteoblasts (the bone forming cells) adherent on 23 nm grain size alumina exhibited a well-spread cell morphology, which is indicative of increased cellular interaction with a material surface (Figure 1). In contrast, there were mostly rounded (*i.e.*, smaller and not spread) osteoblasts adherent on the 177 nm grain size alumina. Osteoblasts adhesion on the 23 nm grain size alumina was significantly ($p < 0.01$) greater than on borosilicate glass (reference substrate) after 1, 2, and 4 hours (Figure 2). More importantly, osteoblast adhesion increased from 2300 to 3340 cells / cm^2 (after 4 hours) as nanophase alumina grain size decreased from 177 to 23 nm. Compared to the conventional (177 nm) alumina formulation, osteoblast adhesion on the 23 nm nanomaterial increased by 46 %.

The mechanisms of bone cell interactions with nanophase alumina need to be further investigated and elucidated, but, since osteoblast adhesion is the prerequisite to subsequent cell functions (*e.g.*, proliferation, synthesis of extracellular matrix proteins, formation of mineral deposits, *etc.*), enhanced responses could be expected from cells interacting with nanophase ceramics.

177 nm grain size (conventional)

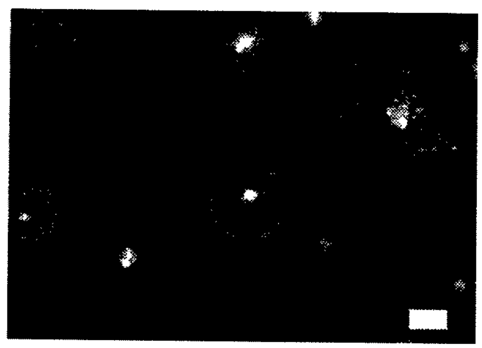

23 nm grain size (nanophase)

Figure 1 : Morphology of Osteoblasts Adherent on Alumina

Representative light micrographs of osteoblasts adherent on alumina for 4 hours. Most of the osteoblasts adherent on the 23 nm grain size alumina were well-spread. In contrast, most of the osteoblasts adherent on the 177 nm grain size alumina were rounded (*i.e.*, smaller and not spread). Stain : rhodamine phalloidin. Bar = 10 μm.

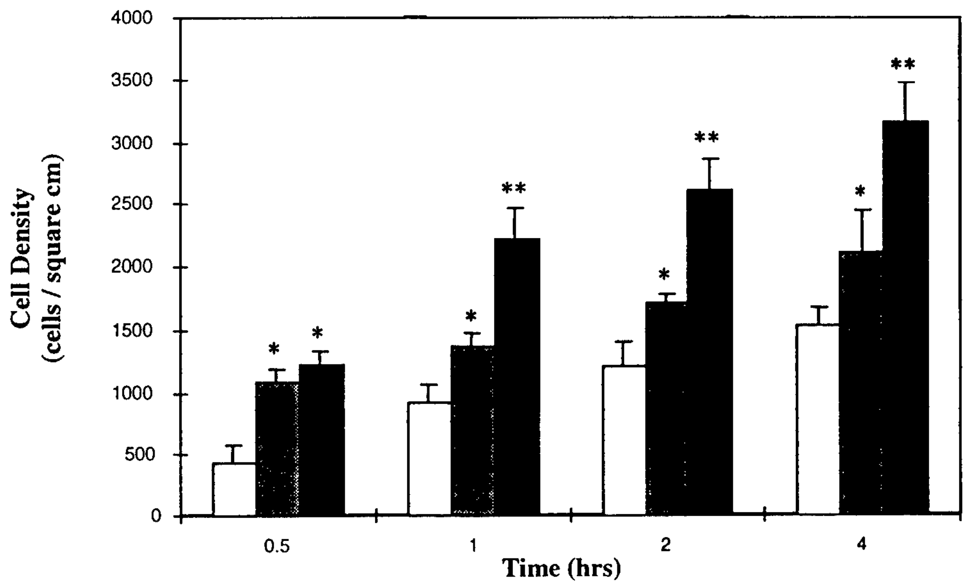

Figure 2 : Time Course of Osteoblast Adhesion

Rat calvarial osteoblasts (3,500 cells / cm^2) in Dulbeccos Modified Eagle Medium containing 10 % serum were seeded on the following substrates :

☐ Borosilicate glass (reference substrate); ■ 177 nm grain size alumina; and ■ 23 nm grain size alumina. Values are mean ± SEM; n = 3; * $p < 0.05$; ** $p < 0.01$ (student t-test to reference substrate).

CONCLUSIONS

Nanostructured ceramics provide as yet unexplored alternatives for orthopaedic / dental implants; the improved mechanical properties of nanomaterials, in addition to the well established biocompatibility of ceramics, constitute characteristics that promise improved orthopaedic / dental implant efficacy.

REFERENCES

1. Ratner, B. *Journal of Biomedical Materials and Research*, 1993, 27, 837.
2. Kaplan, F.S., Hayes, W.C., Keaven, T.M., Boskey, A., Einhorn, T.A. and Iannotti, J.P. *Orthopaedic Basic Science*, American Academy of Orthopaedic Surgeons, Columbus, OH, 1994, p.127.
3. Siegel, R. W. and Fougere, G.E. *Materials Research Society Symposium Proceedings*, 1995, 362, 219.

Pergamon

NanoStructured Materials, Vol. 12, pp. 987–992, 1999
Elsevier Science Ltd

0965-9773/99/$–see front matter

PII S0965-9773(99)00284-6

NANOSINTERING

Joanna R. Groza
Department of Chemical Engineering and Materials Science
University of California, Davis, CA 95616

Abstract - *The aim of this paper is to review the sintering of nanometer size powders (nanosintering). A parallel between nanosintering and densification of regular powders is performed in order to understand the similarities and detect the specifics. Key to nanosintering is to achieve densification with minimal loss (conversion) of initial metastable structure, i.e., by limiting coarsening and undesirable microstructural transformations. Lately, major improvements in the nanopowder synthesis methods and understanding of the densification process (e. g, pore effects and agglomeration) have resulted in fully dense parts by the largest multitude of sintering techniques, including conventional sintering. ©1999 Acta Metallurgica Inc.*

INTRODUCTION

For certain nanomaterial applications, sintering of powders while retaining grain sizes in the nanometer range becomes a critical processing step. Fully dense specimens with nanosize features are most important for structural, magnetic, electric or electronic applications. The main focus in the consolidation of out-of-equilibrium powders has been the retention of the metastable condition of the initial structures. The inevitable coarsening tendency and small specimen size produced by nanopowder densification generated at least some controversies on nanomaterial properties. This paper is devoted to an analysis of the sintering process of powder materials with particle in the nanometer range. Thermodynamic and kinetic aspects of metastable powder densification, sintering mechanisms, and scaling laws applicable to nanopowder sintering are examined. Specific features related to cold compaction, pore size and distribution and their effects on sintering and grain coarsening are addressed. Finally, methods for full densification of metastable powders and their ability to maintain the metastability features are presented.

METASTABILITY AND NANOSINTERING FEATURES

The key feature of nanopowder consolidation is the retention of initial metastable structures. Turnbull divided the metastabilites into three main categories: compositional (extended solution ranges), structural or topological (alternate crystal structure or amorphous phases) and morphological (finely divided structures) (1). In nanopowders, the inherent morphological metastability is associated with topological (e. g., alternate crystal structures than at equilibrium) or compositional (extended solubility or amorphous phases) metastability.

Examples of surface stabilized high pressure nanophases are shown in Table 1. Alternate crystalline structures at large undercoolings were shown in nanocrystalline refractory metals (β-W and β-Ta) (6). Since at least some departure from metastability will occur during sintering, it is important to define the conditions upon which metastability is lost. Some phase transitions in nanomaterials and physical property changes at critical grain sizes are listed in Table 1.

Table 1. Physical and Structural Metastability Ranges.

Material	Critical Grain Size (nm)	Nano Property	Equilibrium Property	Reference
$BaTiO_3$	120	cubic	tetragonal	2
" "	120	drop in T_{curie} *	constant T_{curie}	" "
TiO_2	50	anatase	rutile	3
Y_2O_3	≈13	monoclinic	cubic	4
ZrO_2	8-26	tetragonal	monoclinic	5

*As particle size decreases, the Curie temperature also decreases.

Densification commonly results in grain coarsening. With the exceptions shown in Table 1, a definite threshold value for the grain size to retain the new and unique metastable features has proven difficult to assess. For instance, there is not yet consensus on the strengthening mechanisms or superplasticity benefits in the nanoregime, but a continuous effort is to push the limit toward smallest grain sizes. In this context, an arbitrary limit for the maximum grain size in the dense material still in the nanoregime will be considered ≤ 100 nm.

Nanosintering mechanisms. Consolidation of nanopowders has been summarized in a number of recent reviews (7, 8). Nanosintering presents additional challenges as compared to sintering of regular powders due to particle agglomeration, high reactivity and inherent contamination, grain coarsening and ultimate loss of the nanofeatures. The most recent efforts have been very fruitful in overcoming some of these problems (e. g., agglomeration and grain size control) by major improvements in the nanopowder synthesis methods and understanding of the densification process. For nanopowder consolidation, the critical issue is whether sintering of nanocrystalline materials involves the same mechanisms as conventional ones or some qualitatively new phenomena come into play.

Thermodynamically, powders are unstable due to large surface area. Nanoparticles adopt different surface energies than regular ones, for instance, by a different local atomic arrangement at the surface. TEM studies showed that nanoparticles have a faceted appearance with anisotropic surface energies (e. g., in γ-Al_2O_3 (9)). Kinetically, sintering of nanopowders is significantly enhanced. Therefore, sintering of numerous real nanoparticles indicated depressed sintering onset temperatures (0.2-0.3 T_m) as compared to conventional powders (0.5-0.8 T_m)..

Surface diffusion is expected to be rapid in early sintering stages. In these stages, lower activation energies than for conventional diffusion have been reported in Y-TZP, Al_2O_3, TiO_2 and W (7, 8). For instance, the activation energy (134 kJ/mol) for sintering 40 nm W is lower than the value for volume diffusion (580 kJ/mol) and surface diffusion (~300 kJ/mol) (10). Molecular dynamics (MD) simulations indicated extremely fast sintering of nanoparticles (11). Surface diffusion cannot explain this behavior. Therefore, some other sintering mechanisms have been suggested: dislocation motion, grain rotation, viscous flow, grain

boundary slip. The rapid shrinkage was attributed to fast dislocation activity driven by the contact Hertzian stresses that exceed the ideal shear strength (11). After the neck forms, the adjacent particles rotate to achieve a minimum grain boundary energy. TEM studies of nanoparticles confirmed such a rotation process (12, 13). At this point, the contribution of surface diffusion to nanosintering is not clear. Either a major shift in the contribution of various diffusion mechanisms, or a change in the sintering mechanisms is possible, at least in the initial densification stage.

Scaling Laws. As already mentioned, there is a depression of nanosintering onset. Full densification of nanopowders is completed at temperatures lower than that for conventional powders, as well. To rationalize this decrease in the sintering temperature, different scaling laws have been applied (14, 15). Considering Herring's law, the sintering temperature dependence on the particle size may be calculated. Reasonable agreement of experimental and calculated temperatures was found in TiO_2 and Al_2O_3 assuming certain diffusion mechanisms (16). However, in other cases, departures from the expected sintering mechanisms have been noticed. For instance, data on sintering pure Ni to 60% density (17) resulted in a calculated activation energy value of 239 kJ/mol, closer to volume diffusion (284 kJ/mol) than to expected grain boundary diffusion (115 kJ/mol). This points out to uncertainties in using the scaling law to determine the activation energy values and thus, deduce the sintering mechanisms. The main concern in using Herring's scaling law is a possible change of sintering mechanisms. Next, a careful inspection of the initial assumptions is needed (e. g., the same degree of surface contamination). This is definitely questionable when conventional and nanosize particles are compared since higher contamination has been reported (18). In addition, when sintering occurs at lower temperature, the complete reduction of oxides or hydroxides may be hindered.

PORE EFFECTS AND GRAIN GROWTH

The most common problem in nanosintering is the elimination of large pores that originate from the green compact. The conventional thermodynamic treatment of the pore shrinkage was applied to the nanoceramics sintering by Mayo (7) . The same critical pore-to-size ratio concept applies to nanosintering. Pores smaller than the critical size will shrink, while larger pores undergo the pore-boundary separation. Mayo developed a modified sintering law that directly accounts for pore size effects on densification rate (7):

$$\frac{1}{\rho(1-\rho)}\frac{d\rho}{dt} \propto \frac{1}{d^n}\frac{1}{r}\exp\left(\frac{-Q}{RT}\right)$$

where ρ is density, d is the particle size, n is a constant dependent on the sintering mechanism, r is the pore radius, Q is the activation energy, R is the gas constant and T is the absolute sintering temperature. This equation predicts that the highest densification rate occurs for the finest pore size. A small pore size is also critical in controlling the final grain size based on the pore pinning effect. For these purposes, a small and uniform pore population is desired in the green compact.

Most often, pore distribution is dictated by the green density value. A high green density with a small pore population is easily reached in non- or weakly agglomerated powders. For cold compaction of nanopowders, the use of lubricants, such as in wet processing, tape and

slip casting, osmotic and pressure filtration, or using liquid nitrogen and particle coatings result in higher green density (7, 19). For instance, full densification with 80 nm final grain size after wet compaction is reported by Mayo in ZrO_2-3 mol % Y_2O_3 (7).

The influence of pores on grain coarsening has been well documented theoretically and experimentally, mostly in ceramics. Open pores in nanopowders inhibit grain growth in a similar way that pores prevent grain coarsening in ordinary grain sized ceramics. The pinning action of the pores is, however, difficult to predict. Gupta established an empirical direct relationship between density and grain size in the intermediate stage sintering (20). In a pore controlled grain growth model, Liu and Patterson found a linear relationship between the inverse of grain size and the pore surface area per unit volume (21). This model, similar to Zener's drag effect, is valid only for an immobile pinning phase and was experimentally verified on materials with open pores or dopants that suppress pore breakaway. A further improvement in grain growth predictions may be accomplished if the modeling of pore closure is achieved.

Experimentally, dopants in ceramics have been widely used to suppress grain growth by providing a drag force on the moving boundaries or, forming secondary phase particles. Perhaps one of the most dramatic effect of dopants is the addition of 6% Ca to CeO_2 that retained a 30 nm grain size after full sintering by heating 10 K/min to 1625 K compared to undoped material which resulted in a 400 nm grain size under same sintering conditions (22).

CONSOLIDATION METHODS

When powder particle size decreases below the micron range, the consolidation efforts are faced with additional problems related to powder agglomeration, interparticle friction and contamination. In spite of these new challenges, all known consolidation methods have been applied for full densification of both ceramic and metal nanopowders, including conventional sintering. Examples of dense materials that have retained nanosize grains ≤ 100 nm by conventional sintering are provided in Table 2.

TABLE 2. Densities and Grain Sizes in Selected Nanopowders Densified by Conventional Sintering

		Sintering Parameters:			Final Properties:		
Material:	Init. Gr. Size (nm)	Temp. (K)	Time (hrs)	Atm.	Density (%)	Gr. Size (nm)	Ref.
ZrO_2	6 to 9	1400	1.3	air	full	80	23
ZrO_2-3 mol.% Y_2O_3[1]	<10	1373	1	NR	99.9	80	7
CeO_2-6 at.% Ca	10 to 15	1623	10°C/min.	air	full	30	22
TiO_2[2]	~ 6	873	NR	NR	99	<60	23
TiAl	10-20[3]	723-773	2	vac	>95	15-20	24
Ni	25	1300 [4]	31 K/min.	vac	99	76	25

1. Centrifugally consolidated; 2. Sol-gel prepared; 3. Partial amorphous structure; 4. Rate controlled sintering.

Pressure Sintering. A large variety of pressure assisted methods has been applied for consolidation of nanopowders ranging from low (< 100 MPa) to high preesure methods (>0.5 GPa) such as piston cylinder, diamond anvil, torsion-pressure method (sometimes referred to as

severe plastic deformation consolidation - SPDC). Generally, the capability to collapse the pores in pressure-assisted sintering scales with the shear stress level. A shear stress is also beneficial for the mechanical disruption of surface oxide layers which provides better interparticle bonding. To illustrate the pressure effects, Hahn fully sintered TiO_2 at 725-825 K (~ 0.35 T_m) by applying 1 GPa while retaining the morphologically metastable structure (i. e., with no grain growth) (26). Similarly, Araki et al. densified mechanically alloyed Al-10.7at%Ti powders to 98% under 2 GPa at 573 K with virtually no grain growth and retention of the initial Al supersaturation (27).

Non-Conventional Sintering Methods. The main purpose in using these methods is to enhance densification and prevent grain growth. Some examples include: microwave sintering, shock or dynamic consolidation, field assisted sintering. For instance, field assisted sintering technique (FAST) at 725 K achieved 99% density in nanosize Fe-85% Fe_3C with a final grain size of 45 nm (28). Nanosize grains have been retained by fully sintering mechanically alloyed TiAl powders by spark sintering (29). The very short high temperature exposure in dynamic or shock consolidation provides the best means to retain fine grain size or out of equilibrium conditions such as amorphous structures or supersaturated solid solutions (30, 31).

SUMMARY

Densification of out-of-equilibrium powders presents challenges related to the specific need to retain the metastability of initial microstructures in addition to usual pore elimination into a uniformly dense and sound part. Studies of nanopowder densification have lead to a better understanding of numerous sintering issues such as powder agglomeration, surface condition or contamination, pore role in sintering and grain growth. The resultant control of synthesis (e. g., non-agglomerated nanopowders) and processing has enabled fabrication of fully dense nanocrystalline parts particularly ceramic, even by conventional sintering. Although some distinct differences in the densification of nano- versus micron grained powders seem to emerge and a better understanding of nanosintering has been accomplished, the specific effect of densification variables on final density and properties of nanomaterials is still an area of fruitful future research. More fundamentally, there is a tremendous need for specific materials data in the nanoregime, such as diffusion coefficients and surface energies.

ACKNOWLEDGMENT

The author's research on nanocrystalline materials densification has been supported by National Science Foundation, grants # CTS-9632280 # DMII - 9532072.

REFERENCES

1. Turnbull, D. *Met. Trans.*, 1981,12A, 695.
2. Uchino K., Sadanaga E. and Hirose, T. *J. Am. Ceram. Soc.*, 1989, 72, 1555.
3. Hague, D. C. and Mayo, M. J., *Nanostr. Mater.* 1993, 3, 61.
4. Skandan, G., Foster, C. M., Frase, H., Ali, M. N., Parker, J. C. and Hahn, H. *Nanostr. Mater.* 1992, 1,313.
5. Garvie, R. C. *J. Phy. Chem.* 1978, 82, 218.
6. Krauss, W. and Birringer, R., *Nanostr. Mater.* 1997, 9, 109.

7. Mayo, M., *Int. Mater. Rev.* 1996, 41, 85.
8. Groza, J. R. *Nanostructured Materials: Processing, Properties, and Potential Applications*, ed. C. C. Koch, Noyes Publ. Westwood, NJ, 1998, in print
9. Bonevics, J. E. and Marks, L. D., *J. Mater Res.* 1992, 7, 1489.
10. Trusov, L. I., Lapovok, V. N. and Novikov, V. I., *Science of Sintering,* eds: D. P. Uskokovic, H. Plamour lll, and R. M. Spriggs, Plenum Press, New York, 1989, p. 185.
11. Zhu, H. and Averbach, R. S., *Phil. Mag. Lett.* 1996, 73, 27 and *Mat. Sci. Eng.* 1995, A204, 96.
12. Yeadon, M., Yang, J. C., Ghaly, M., Olynick, D. L., Averbach, R. S., and Gibson, J. M., *Nanophase and Nanocomposite Materials ll* , eds. S. Komarneni, J. C. Parker and H. J. Wollenberger, MRS, Pittsburgh, PA, 1997, p. 179.
13. Rankin, J. and Sheldon, B. W. *Mater. Sci. Eng.* 1995, A204, 48.
14. Alymov, M. I., Maltina, E. I. and Stepanov, Y. N. , *Nanostr. Mat.* 1992, 4, 737.
15. Herring, C., *J. Appl. Phys.* 1950, 21, 301.
16. Messing, G. L. and Kumagai, M., *Am. Ceram. Bull.* 1994, 73, 88.
17. Andrievski, R. A. *Intern. Powder Metall.* 1994, 30,59.
18. Ying, J. Y, *Mechanical Properties and Deformation Behavior of Materials Having Ultra-Fine Microstructures,* eds. M. Nastasi, D. M. Parkin, and H. Gleiter, H., Kluwer Academic Press, Netherlands, 1993, p. 565.
19. Pechenik, A., Piermarini, G. J. and Danforth, S. C., *Nanostr. Mater.* 1993, 2, 479.
20. Gupta, K., *J. Am. Ceram. Soc.* 1972, 55, 276.
21. Liu Y.and Patterson, B. R., *Acta Met. Mater.* 1993, 41, 2651.
22. Rahaman, M. N., *Sintering Technology*, eds. R. M. German, G. L. Messing and R. Cornwall, M. Dekker, NY, 1996, p. 93-100.
23. Skandan, G., *Nanostr. Mater.* 1995, 5, 111.
24. Chang, H., Hofler, J., Altstetter, C. and Averback, R. S., *Mat. Sci. & Eng.* 1992, A153, 676.
25. Ragulya, A. V. and Skorokhod,V. V., *Nanostr. Mater.* 1995, 5, 835.
26. Hahn, H., *Nanostr. Mater.* 1993, 2, 251.
27. Araki, H., Saji, S., Okabe, T., Minamino, Y., Yamane, T. and Miyamoto, Y., *Mat. Trans. JIM*, 1995, 36, 465.
28. Goodwin, T. J., Yoo, S. H., Matteazzi, P. and Groza, J. R., *Nanostr. Mater.* 1997, 8, 559.
29. Kimura, H.and Kobayashi, S., *J. Japan Inst. Met.* 1994, 58, 201
30. Glade, S.C., Thadhani, N.N., *Met.Mater. Trans.* 1995, 26A, 2565.
31. Suryanarayana, C., Korth, G. E. and Froes, F. H., Met. Mater. Trans. 1997, 28A, 293.

Pergamon

NanoStructured Materials, Vol. 12, pp. 993–997, 1999
Elsevier Science Ltd

0965-9773/99/\$–see front matter

PII S0965-9773(99)00285-8

APPLICATIONS OF METAL AND SEMICONDUCTOR NANOCLUSTERS AS THERMAL AND PHOTO-CATALYSTS

J.P. Wilcoxon, T.R. Thurston, and J.E. Martin
Organization 1152, Sandia National Labs, Albuquerque, NM 87185-1421, USA

Abstract-*We discuss studies of photo and thermally driven reactions which illustrate the unique catalytic features of nanoclusters which may be of great technical utility. The application of photocatalysts of nanosize MoS_2 to oxidize organic pollutants to CO_2 is discussed. Nanosize MoS_2 shows improved rates of oxidation of organics such as phenol compared to alternative bulk powders such as TiO_2 or ZnO. Selective hydrogenation of pyrene using both dispersed and supported nanoclusters of Rh, Pt, and Pd is also discussed.*
©1999 Acta Metallurgica Inc.

INTRODUCTION

Dispersed metals have been employed as thermally activated catalysts in the chemical and fuel processing industries from their inception. It has long been recognized that since catalytic activity depends strongly on the number of available surface sites on a catalyst which can interact with a substrate, a given material is most effective if it is in a finely divided form. However, the typical *in situ* preparation methods employed to create highly dispersed catalysts on supports usually give little control over the phase structure and surface morphology of the resulting metal or metal sulfide phase and often it is difficult to study the resulting materials or understand the features of effective heterogeneous catalysts which influence their selectivities and kinetics. Due to these difficulties it would be advantageous to create nanosize metals and metal sufides as fully dispersed solutions whose catalytic behavior, average size, size dispersion, structure, and surface morphologies could be studied both in solution (i.e. acting homogeneously) and also deposited on various common support materials (typically metal oxides such as alumina).

We have undertaken such a program utilizing a versatile approach to the synthesis of nanosize materials-including metals, metal oxides, and sulfides. Since the fully dispersed nanocluster solutions are in organic liquids they can be studied by both traditional surface science techniques such as TEM and also by more exotic approaches such as high pressure liquid chromatography (HPLC) which is usually restricted to organic molecules or polymers. HPLC is a particularly useful approach since a wide variety of chromatography columns with various chemical functionalities are available and their interaction with the nanoclusters gives insights into both size, size dispersion, and nanocluster surface chemistry.

EXPERIMENTAL RESULTS

Destruction of Phenol Using Nanosize MoS_2- The electron-hole pairs generated by solar radiation in semiconducting materials can catalyze redox reactions that destroy organic chemicals, a process with obvious environmental remediation potential. A significant amount

of research on semiconductor catalyzed photo-oxidation of organic chemicals has consequently been done during the past 15 years; reviews of this previous work are given in references [1-2].

Previous investigations of photocatalytic oxidation have focused almost exclusively on TiO_2. Two major disadvantages of TiO_2-based photo-oxidation technology are the lack of adequate fixed bed reactor designs and the large band gap of TiO_2 (~3.2 eV) which means UV light must be used to drive the reaction. We are studying the photocatalytic properties of a possible alternative to TiO_2, nanoscale MoS_2. We chose to investigate this particular material for several reasons inclusing good photostabilty because hole-electron excitation affects only the metal valence d-band electrons, and a size-tunable band gap which is small enough to allow most of the solar spectrum to be harvested. Only nanoscale MoS_2 clusters are photochemically active because these materials have their band gaps shifted by quantum size effects from the bulk value of ~1040 nm to ~550 nm when the cluster size ~4.5 nm [3].

Our metal and metal sulfide nanoclusters were made with an inverse micelle technique.[4] The nanoclusters synthesized in hydrocarbon solvents were purified by extraction against an immiscible polar solvent such as formamide, acetonitrile, or water. Their chemical purity, average size, and size distribution were measured by high pressure liquid chromatography (HPLC)[5]. This technique can also be scaled up to directly purify the nanoclusters. During the chromatography analysis the optical absorbance and/or fluorescent features of the purified nanoclusters were determined using suitable on-line detectors. Possible contaminating inorganic ions were removed by dialysis and their absence verified using an on-line conductivity detector during HPLC. The complete removal of these inorganic by-product ions is the most difficult aspect of the processing and still requires additional refinement.

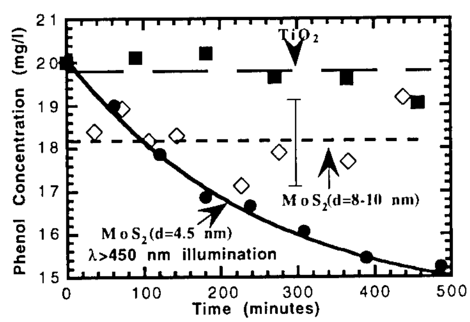

FIG. 1. Phenol destruction as a function of time as determined from HPLC chromatograms.

Our photo-oxidation reactor consisted of a 50 ml Pyrex beaker covered with plastic-wrap (transparent to ~250 nm) and over which was placed either a 365 nm 12 watt lamp or a xenon arc lamp operated at 450 watts with a long-pass (i.e. >450 nm) visible filter in front. Chemical analysis was done using a commerical HPLC instrument equipped with a Hewlett-Packard 1050 diode array detector, and Hewlett-Packard 1046A fluorescence detector. The fluorescence detector allowed detection of phenol to ~10 ppb without preconcentration. Additional details are given elsewhere.[6]

A number of different chemicals were successfully photo-oxidized to CO_2, but most of the work centered on the destruction of phenol. This particular substrate was chosen for its ease of detection and relative resistance to oxidation, and because its photo-oxidation has been studied extensively by many previous researchers. No attempts were made to find the absolute quantum yield of the photo-oxidation process. Rather, following the approach of Serpone *et al.* [7], we compared the relative activity of nanoscale MoS_2 to a well studied photocatalyst, Degussa P25 TiO_2.

In figure 1, we show the phenol concentration as a function of time as determined from HPLC elution peak areas. There is a pronounced decline in the phenol concentration with d=4.5 nm, MoS_2 nanoclusters, a small initial decrease with d=8.0 nm nanoclusters, and no degradation using Degussa P25 TiO_2. Control experiments with either no catalyst, but illumination or illumination without a catalyst showed no decline in the phenol concentration. Thus, oxidation of the phenol is associated with the presence of both MoS_2 catalyst and > 450 nm radiation.

A series of experiments where d= 8 nm MoS_2 nanoclusters were deposited onto commercial semiconductor powders of TiO_2, SnO_2, WO_2, and ZnO were performed. Between 0 and 6 weight percent MoS_2 nanoclusters were deposited on to the support. The only support material with a significant synergistic improvement in activity when combined with nanosize MoS_2 was TiO_2.

The initial destruction rate as a function of MoS_2 loading is shown in figure 2. The destruction rate is enhanced up to a factor of ~2 when the loading is ~2.5 weight percent, and it then decreases with further loading. When d=8 nm MoS_2 is not loaded on to TiO_2, however, the phenol destruction rate is much smaller than the enhancement achieved when it is loaded. These observations strongly suggest that electron or hole transfer is occurring between the TiO_2 powder and d=8 nm MoS_2 clusters. Evidently, the improved charge separation helps the photooxidation process.

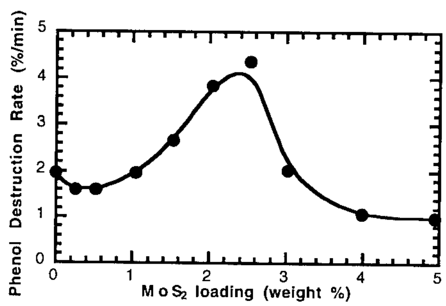

FIG. 2. Dependence of the initial phenol destruction rate on the weight percent loading of d=8 nm, MoS_2 on TiO_2. Irraduated at 365 nm using 12 W lamp.

Hydrogenation of Pyrene- Pyrene is a polycyclic aromatic molecule with four rings which is often employed as a test molecule for hydrogenation catalysts designed for coal liquefaction applications. We have previously reported on direct coal liquefaction using Pd and Fe nanoclusters, in particular finding a very strong nanocluster size effect and have related this behavior to studies using pyrene.[8] Pyrene is very difficult to fully hydrogenate and typical best conversions to the fully hydrogenated 16H-pyrene product reported in the literature using conventional heterogeneous catalysts are ~40% after many hours at high temperatures (~300 ^{o}C) and pressures (1500 psi H_2) .

Our previous experiments on pyrene hydrogenation were exclusively on dispersions of nanoclusters. In these experiments we demonstrated enhanced activity relative to conventional catalysts. Recently, we have deposited nanoclusters of Pd, Pt, and Rh (~2-3 nm in size in each case), on conventional high surface area powders of Al_2O_3 and C. The former support is widely used in industrial hydrogenation catalysts.

Here we report on results of Pd, Pt, and Rh hydrogenation experiments on pyrene. All experiments described here were performed in a stirred batch reactor at 200 ^{o}C, P=1500 psi H_2 with periodic sampling of the liquid phase and analysis by GC/MS to ascertain product distributions and reaction kinetics as a function of time.

Effect of support type on kinetics- The effect of metal type on the rate of disappearance of pyrene is shown in figure 3. The metal nanoclusters were deposited on Al_2O_3. The rates for Pd and Rh were similar with Pt slow by comparison. By comparison, many conventional catalysts show similar rates for hydrogenation by Pt and Rh while Pd is significantly slower. When the same nanocluster metals are loaded onto C the rates for all three metal types increase dramatically (not shown), reaching the levels of conversion shown in figure 3 in less than 2 hours. The relative order of metal activity does not change, however.

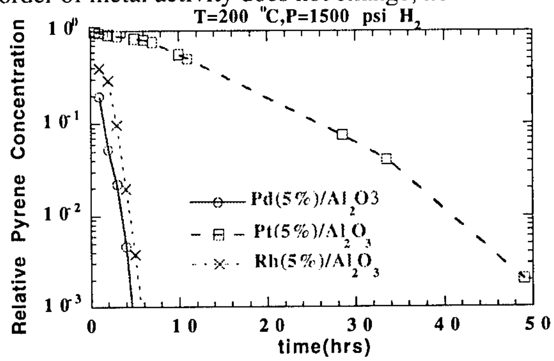

Fig 3. Rate of disappearance of pyrene due to hydrogenation using nanosize metals of Pd, Pt and Rh on a conventional support, Al_2O_3.

Effect of Metal Type on Product Distribution- A wide variety of hydrogenated products result from hydrogenation of a complex aromatic molecule like pyrene. These are often designated by the number of hydrogen atoms added (e.g. 2H-pyrene, 4H-pyrene, 6H-pyrene etc.). We have examined the relative amounts of these products as a function of reaction time, pressure, and temperature. It is possible by variation of the metal type, support, and reaction time to obtain well over 90% of a desired product. For example at t=24 hrs in the experiment shown in figure 3, over 95% of the product is 16H-pyrene for Rh, compared to a 50:50 distribution of 10H- and 16H-pyrene in the case of Pd, while nearly 75% of the product is either 4H- or 6H-pyrene in the case of Pt. This product selectivity also applies to the use of these nanocluster materials in more complex reactions such as direct coal liquefaction-though in this case economic considerations limit the types of feasible materials to base metals such as Fe and Mo.

CONCLUSION

The development of simple synthetic procedures and purification methods for the production of large amounts of nanosize metal and metal sulfide clusters using simple, inexpensive metal salts makes possible the application of these materials as photo- or thermally driven catalysts for a variety of important chemical processes including solar driven photo-oxidation of organic pollutants in water and direct conversion of coal to desired chemicals and fuels. The advantages of using chemically stable inorganic nanoclusters with size-tunable bandgaps was shown for the case of MoS_2. Improvements on the performance of the only other viable material, Degussa P25 TiO_2 powder was demonstrated for both unsupported and supported nanosize MoS_2 photocatalysts. A strong dependence on bandgap was found. Too

small a bandgap, though favorable for light absorbance, provided too small a driving force for hole transfer (oxidation) of the organic.

Studies of the hydrogenation of pyrene were used to show how choice of metal and support material can be used to adjust both the kinetics and the product distribution to achieve desired goals. A surprising observation was the high activity of nanosize Pd relative to Pt and the superior reaction rates of nanoclusters on carbon relative to Al_2O_3. A significant amount of research will be required to sort out the nanocluster structural features responsible for these observations and to elucidate the best methods of deposition of nanoclusters onto supports to increase their activities and selectivities further.

ACKNOWLEDGMENT

This work was supported by the US Department of Energy under contract DE-AC04-AL8500. Sandia is a multiprogram laboratory operated by Sandia Corporation, a Lockheed-Martin Company, for the US Department of Energy.

REFERENCES

[1] M. A. Fox and M. T. Dulay, *Chem. Rev.,* 93, 341, 1993 .

[2] O. Legrini, E. Oliveros, and A. M. Braun, *Chem. Rev.,* 93 , 671, 1993 .

[3] J. P. Wilcoxon and G. A. Samara, *Phys. Rev. B,* 51, 7299, 1995.

[4] J. P. Wilcoxon, *U.S. Patent No. 5,147,841*, 15 September 1992.

[5] J.P. Wilcoxon and S.A. Craft, *NanoStructured Materials*, 9, pp. 85-88, Elesvier Science Ltd, 1997.

[6] T.R. Thurston and J.P. Wilcoxon, submitted to *J. Phys. Chem.*, 1998.

[7] N. Serpone, G. Sauve, R. Koch, H. Tahiri, P. Pichat, P. Piccinini, E. Pelizzetti, and H. Hidaka, *J. Photochem. Photobiol. A: Chem.,* 94 , 191, 1996.

[8] A. Martino, J.P. Wilcoxon, and J. Kawola , *Energy and Fuels*, 8, 1289, 1994.

Pergamon

NanoStructured Materials, Vol. 12, pp. 999–1002, 1999
Elsevier Science Ltd

0965-9773/99/$–see front matter

PII S0965-9773(99)00286-X

NANOSCOPIC TIN OXIDE FILMS ON MESOPOROUS SILICA AS NOVEL CATALYSTS FOR HYDROGEN TRANSFER REACTIONS

S.C.Tsang*, R. Burch, S. Nishiyama, D. Gleeson, N.A. Cruise, A. Glidle and V. Caps

The Catalysis Research Centre,
Department of Chemistry, University of Reading, Reading RG6 6AD, UK

Abstract--*Deposition of tin-oxygen species on mesoporous silica (MCM-41) was achieved via chemical reaction of* $SnEt_4$ *vapour with surface silanol groups followed by heat treatment in air. At low Sn loading, EXAFS studies indicate six Sn-O interactions at an average distance of 2.043 Å and Sn-Si interactions at a distance of 3.791 Å. This suggests that* SnO_6 *octahedra were formed which anchored onto the surface of MCM-41 via Sn-O-Si bonds. At high Sn loading, tin oxide nanocrystallites (*SnO_2*) with rutile structure are evident (TEM, XRD). It was found that these mesoporous-silica supported tin oxides, after* H_2 *pre-treatment, showed higher activity than bulk* SnO_2 *supported on conventional silica in catalysing the hydrogen transfer reaction from a secondary alcohol to an unsaturated aldehyde.*
©1999 Acta Metallurgica Inc.

INTRODUCTION

Recent literature has shown the significance of well-defined nanostructures in new catalyst formulations with improved activity, selectivity and stability. In our laboratory, we are interested in studying mesoporous silicas (with pore sizes between 20- 100 Å) as hosts for guest compound deposition. These silicas are produced by the co-operative assembly of silica and surfactants, which are characterised by larger pores and large internal surface areas. The elongated hexagonally arranged, nanosize channels of the silicas are structurally well defined with a large number of surface hydroxyl groups which can provide reaction or nucleation sites for the entrapment of a wide variety of chemical species [1].

Selective hydrogen transfer using sacrificial alcohol to hydrogenate carbonyl compounds (MPVO: Meerwein-Ponndorf-Verley-Oppenauer reaction) over heterogeneous catalysts has recently received considerable attention [2]. A secondary alcohol such as isopropanol is used to reduce unsaturated aldehydes or ketones over chosen catalysts giving acetone as a by-product. $SnOx/SiO_2$ was reported to be exceptionally selective in a H_2 atmosphere achieving 95% selectivity for crotonaldehyde hydrogenation to crotyl alcohol using 2-butanol as a reaction medium [3]. In this paper we report ultra-thin films containing immobilised nanocrystallites of SnO_2 on mesoporous silica which showed higher catalytic activity than bulk tin oxide for the hydrogenation of crotonaldehyde using isopropanol.

EXPERIMENTAL

Catalyst Preparation

MCM-41 silica was prepared according to a reported method [4] using $C_{16}H_{33}N(CH_3)Br$. 0.5 g MCM-41 silica was mixed with an appropriate amount of $SnEt_4$ (see Table 1), under argon, in a Schlenk tube and heated at 150 °C for 48 h. After cooling to room temperature, the mixture was then evacuated at 80 °C in order to remove any unreacted $SnEt_4$. Finally the material was ramped at 20 °C min^{-1} to 500 °C in flowing air and held for 3 h.

Catalyst Testing

The gas phase MPVO reaction was carried out using a 10 mm i.d. Pyrex tubular reactor packed with 200-250 mg catalyst under 1 atmosphere. The catalyst was heated in air at 500 °C for 1 h followed by reduction in pure H_2 at 400 °C for 1 h prior to testing. A mixture of 0.0397 atm of crotonaldehyde, 0.0431 atm of isopropanol (ratio ≅ 1) balanced with 0.917 atm of nitrogen at the total flow rate of 32.7 cm^3min^{-1} (NTP) was allowed to pass through the catalyst kept at 330 °C. The products were collected and analysed by a PE gas chromatograph.

Catalyst Characterisation

Temperature Programmed Reduction profiles (TPR) were obtained using built in house apparatus. 3d Sn *XPS* spectra of the samples were collected using a SCIENTA ESCA 300 system. EXAFS data were collected for the SnOx/MCM-41 samples at different tin loading (see Table 1). The tin K-Edge X-Ray absorption spectra were recorded over 15 $Å^{-1}$ range on station 9.2 at the Synchrontron Radiation Source (SRS) at the Daresbury Laboratory, UK.

RESULTS

From Table 1, it is interesting to note that the $SnEt_4$ treated MCM samples, after the heat treatment in air, show a decrease in BET surface area with increasing amounts of tin precursor. Powder X-ray Diffraction showed distinctive reflections at high Sn loading (> 0.5 'ML') corresponding to the cassiterite phase SnO_2 (rutile). These intrinsic broad peaks (peak width $2\theta > 3°$) suggest that the tin oxides are in nanoscopic dimensions. All these new features disappeared when the Sn loading was below 0.5 'ML'. Sn K-edge EXAFS spectra from the calcined Sn-MCM samples were analysed (Table 2).

TABLE 1

BET Surface Areas of Various Sn-containing Samples

Material	Vol. of $SnEt_4$ Used /μL	N_2 BET Surface Area/ m^2g^{-1}
2 'ML' Sn-MCM	416	812
1 'ML' Sn-MCM*	208	910
0.5 'ML' Sn-MCM	104	1039
0.25 'ML' Sn-MCM	52	1140
0.1 'ML' Sn-MCM	21	n.d.
$Sn-SiO_2$	52	320
$SnOx/SiO_2$	$SnCl_2$ (wet impregnation)	303

1 'ML' Sn-MCM*: 208 μL $SnEt_4$ is theoretically required to react with all the surface monolayer silanol groups assuming that 1:1 stoichiometry of Sn: silanol is maintained.

No isolated tetrahedral Sn (IV) species were found in these samples. The best fit to the Sn K-edge EXAFS data shows a first shell comprising **six** oxygen atoms which clearly resembles the 6-coordinated tin (IV) ions in the SnO_2 rutile structure. It is interesting to find that at high Sn loading (1 and 2 'ML') there were long range interactions observed at ca. 5 - 7 Å. This suggests there was an extended rutile lattice (3-D stacking of Sn octahedra) in the materials. At ≤ 0.5 'ML' loading, no noticeable interaction was detected at beyond 4 Å inferring that the size of islands/patches were considerably smaller than those for samples of high loading. It is also important to point out that the data fittings were substantially improved when Sn-Si interactions were added. This is attributed to the Sn-O-Si links to the surface with bond distances comparable to those of model systems [2,5]. It is therefore thought that Sn-O-Si was formed *via* the reaction of $SnEt_4$ with silanol group, which may act as nucleation sites for further Sn-oxygen aggregations. TEM confirmed the presence of tin-containing (EDAX) nanoparticles which were present on both inside and outside of the mesoporous channels. This is in good agreement with those observed by Oldroyd et al. [5] over their Ti↑Sn↑MCM.

Catalysis

The results of the hydrogen transfer reaction from isopropanol to crotonaldehyde over a number of hydrogen pre-treated Sn-MCM catalysts with various Sn concentrations are shown in Table 3. It is interesting to find that the two highest loading Sn-MCM samples (1 'ML' and 2 'ML') gave virtually the same catalytic activity as compared with 5%wt $SnOx/SiO_2$ (prepared by $SnCl_2$ wet impregnation on conventional silica). 5% $SnOx/SiO_2$ was prepared by deposition of $SnEt_4$ onto conventional silica, gave only marginally higher catalytic activity for this hydrogen transfer reaction. Thus, the absence of a correlation between the catalytic activity and the apparent surface areas (see Table 1) suggests the bulk species in these samples are unlikely to be the active sites for the catalysis. Interestingly, the catalytic activity increased abruptly at lower Sn loading. Notice that this 0.25 'ML' Sn-MCM catalyst was about more than 5 times more active than the 1 'ML'-Sn-MCM and the $SnOx/SiO_2$ catalysts.

TABLE 2
Structural Data for SnO_2 and Sn-MCM samples

Material	Atom type	Coordination no.	Distance/ Å	Debye-Waller Factor
2'ML'	O	6	2.045(2)	0.0068(2)
Sn-MCM	Sn	1	3.220(2)	0.0028(2)
	Sn	2	3.800(3)	0.009(3)
	Si	4	3.690(15)	0.017(4)
0.5'ML'	O	6	2.043(2)	0.0066(2)
Sn-MCM	Sn	1	3.209(2)	0.0041(3)
	Si	4	3.791(3)	0.0024(4)
SnO_2	O	6	4 x (2.052), 2 x (2.058)	
	Sn	2	3.187	
	O	4	3.591	
	Sn	8	3.710	

TABLE 3

Catalytic Activity of Various Sn-containing Samples

Material	Crotyl Alcohol Formation/ mole/g/g-Sn	Acetone Formation/ mole/g/g-Sn
2 'ML' Sn-MCM	4.07E-3	3.46E-03
1 'ML' Sn-MCM	4.10E-3	4.73E-03
0.5 'ML' Sn-MCM	1.38E-2	1.19E-02
0.25 'ML' Sn-MCM	2.10E-2	1.63E-02
5%Sn/SiO_2	6.32E-3	5.68E-03
5 % SnOx/SiO_2	3.36E-3	2.51E-03

Characterisation

Temperature programmed reduction (TPR) of the Sn-MCM samples was studied in order to reveal the availability and the reactivity of active oxygen in these samples. It is interesting to note that the general TPR profiles of Sn-MCM samples show two distinctive low temperature reduction peaks (maxima at ca.250 °C and 450 °C, respectively) and a large reduction peak at about 600-650 °C (not shown). However, the two low temperature reduction peaks were not seen in the TPR profiles of bulk tin oxide (SnO_2) and supported SnOx/SiO_2. Hence, extensive reduction of bulk SnO_2 cannot occur below 600 °C inferring that trace amounts of tin oxide on the highly unsaturated sites such as corner, edge or step sites, could only be reduced at the hydrogen pre-reduction step. This result strongly suggests that the reactivity of some active oxygen species towards hydrogen in the Sn-MCM samples is much more readily available than the bulk lattice oxygen in SnO_2. There was no high temperature reduction peak corresponding to the bulk SnO_2 reduction for the samples at and below 0.5 'ML' loading, reinforcing the idea that extremely thin 'surface tin-oxygen films' may be initially formed before any further aggregation occurs at high Sn loading. This is also consistent with the XRD data where no bulk SnO_2 peak was detected at the same Sn concentration. These 'surface tin-oxygen films' are thought to be responsible for the catalytic reactions. The nature of the surface tin species was therefore studied by high resolution XPS. Determination and distinction of the Sn^o $3d_{5/2}$ peak using Sn foil (B.E. = 484.8 eV), the Sn^{2+} $3d_{5/2}$ peak using SnO (486.4 eV) and the Sn^{4+} $3d_{5/2}$ peak using SnO_2 (487.1 eV) were all obtained. All the peaks of the Sn-MCM samples are referenced to Si 2p (103.8 eV) which is the major component in these silica-supported samples. It is very interesting to see that there are significant chemical shifts towards the lower binding energy direction when the Sn loading was decreased from 1 'ML' to 0.25 'ML'. Formation of metallic Sn^o was directly excluded because no peak was observed at its corresponding 3 d $_{5/2}$ B.E. region in all the pre-reduced samples. The small chemical shifts are attributed to the differences in relative ratios of Sn^{2+}: Sn^{4+} where a small but sizeable binding energy difference exists between the two Sn ions (0.7 ± 0.05 eV). There were good correlations between catalytic activity and the Sn^{2+}/Sn^{4+} ratios for the samples from 2'ML' to 0.25'ML' inferring that the Sn^{2+} species is involved in the catalysis.

REFERENCES

1. Burch, R. , Cruise, N.A. , Gleeson, D. , Tsang, S.C. ,*J. Mater. Chem*., 8, 1998, 227.
2. Graauw, C.F. de , Peters, J.A. , Bekkum, H. van , Huskens, J. , J. *Synthesis*, Oct. 1994, 1007.
3. Nishiyama, S. , Kubota, T. , Kimura, K. , Tsuruya, S. , Masai, M., *J. of Mol. Catal. A.: Chem*., 120, 1997, L17.
4. Kresge, C.T. , Leonowicz, M.E. , Roth, W.J. , Vartuli J.C. and Beck, J.S. , *Nature (London)*, 1992, 359, 710.
5. Oldroyd, R.D. , Sankar, G. , Thomas J.M. and Ozkaya, D. , *J. Phys. Chem. B* 102, 1998, 1849

Pergamon

NanoStructured Materials, Vol. 12, pp. 1003–1006, 1999
Elsevier Science Ltd

0965-9773/99/$–see front matter

PII S0965-9773(99)00287-1

SYNTHESIS OF β-SiC NANOWIRES WITH SiO_2 WRAPPERS

G.W. Meng[*+], L.D. Zhang[*+], Y. Qin[*+], C.M. Mo[*+] and F. Phillipp[**]

[*] Institute of Solid State Physics, Chinese Academy of Science, Hefei, 230031, China.
[+] Institute of Advanced Study, at USTC, Hefei, 230026, China
[**] MPI fur Metallforschung, Heisenbergstrasse 1, D-70569 Stuttgart, Germany.

Abstract — *β-SiC nanowires with uniform amorphous SiO_2 wrappers have been synthesized by carbothermal reduction of the sol-gel derived silica containing carbon nanoparticles. The product was characterized by IR, TEM, HREM, and EDX. The nanostructures are more than 20μm in length. The diameters of β-SiC nanowires are in the range 10~25 nm, while the outer diameters of the SiO_2 wrappers are between 20 and 70 nm. The formation of β-SiC nanowires is ascribed to the large quantities of SiC nuclei and the nanometer-sized SiC nucleus sites on carbon nanoparticles. The SiO_2 wrappers come from the combination reaction of the SiO vapor and O_2 decomposed from the unreacted SiO_2.*
©1999 Acta Metallurgica Inc.

INTRODUCTION

Since the discovery of carbon nanotubes (1), efforts have been made on the synthesis of one-dimensional nanostructures. These nanostructures have great potential for testing and understanding fundamental concepts about the roles of dimensionality and size in optical, electrical and mechanical properties, and for applications ranging from probe microscopy tips to interconnections in nanoelectronics (2) or quantum devices (3).

As for the synthesis of one-dimensional solid nanostructures, several important new methods have been invented. For example, (i) carbon nanotube-confined reaction method to produce carbides (4) and GaN (5) nanorods; (ii) modified vapor-solid growth process to grow MgO nanorods (6); (iii) combination of laser ablation cluster formation and vapor-liquid-solid growth to synthesize Si and Ge nanowires (2); (iv) selective electroplating method to fabricate a permalloy nanowire (7); (v) DNA molecule template to grow silver nanowire (8). We report here an alternative approach to the synthesis of β-SiC nanowires with SiO_2 wrappers.

EXPERIMENTAL PROCEDURE

Silica sol was prepared with tetraethoxysilane ($(C_2H_5)_4SiO_4$), ethanol and distilled water by sol-gel technique. Saccharose ($C_{12}H_{22}O_{11}$) was dissolved in the sol and used as carbon

source; its quantity was adjusted to obtain a nominal molar ratio C/SiO_2 = 4.1. After gelation the mixture gel was calcined at 700°C for 2 hours in a flowing N_2 atmosphere.

Carbothermal reduction of the silica xerogels containing carbon nanoparticles was performed in a flowing Ar atmosphere. The xerogel granules were heated at 1650°C for 1.5 h, and then at 1800°C for 30 min. After the xerogel granules being taken out, a layer of white product appeared on the xerogel granules.

The white product was characterized by Fourier Transformed Infrared spectrometer (IR) (MAGNA-IR750), transmission electron microscope (TEM) (JEOL, JEM-200CX), high resolution electron microscope (HREM) (JEOL-2010), and energy-dispersed X-ray spectrometer (EDX) (OXFORD, LINK ISIS) attached to the HREM.

RESULTS AND DISCUSSION

The IR spectrum (Figure 1) of the white product shows the β-SiC characteristic absorption band at 789 cm^{-1}, and the SiO_2 characteristic absorption bands at 477 and 1100 cm^{-1} (9). Low-magnification TEM image (Figure 2A) reveals that the white product is composed of nanowires with lengths of typically up to 20 μm. High-magnification TEM image (Figure 2B) shows that every nanowire consists of a thinner nanowire core with an outer wrapper. HREM image (Figure 3A) reveals that the nanowire core is single-crystal, whereas the wrapper is amorphous. Selected area electron diffraction (SAED) pattern (Figure 3B) indicates that the nanowire core has a face-centred cubic structure. Lattice-resolved TEM image (Figure 3A) shows that the distance between parallel fringes is equal to the spacing of the β-SiC (111) atomic planes, confirming that the single-crystal nanowire core is β-SiC. EDX quantitative microanalysis of the nanowire wrapper reveals that it has an approximate composition of SiO_2. Further observations made on TEM and HREM demonstrate that the nanostructures consist of 10-to 25-nm-diameter single-crystal β-SiC nanowire cores surrounded by amorphous SiO_2 wrappers with outer diameters of between 20 and 70 nm.

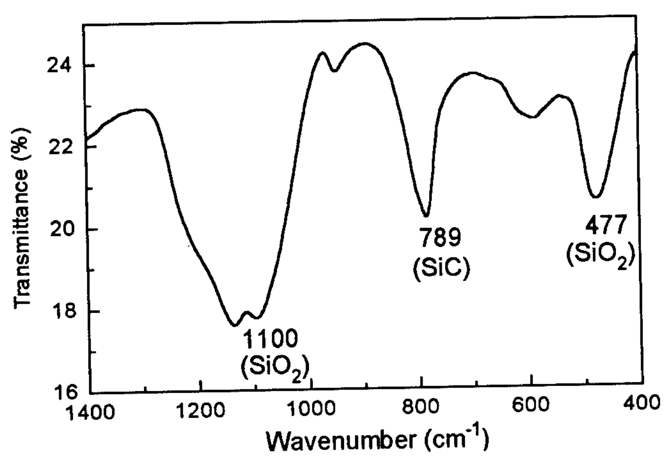

Figure 1. IR spectrum of the as-synthesized product.

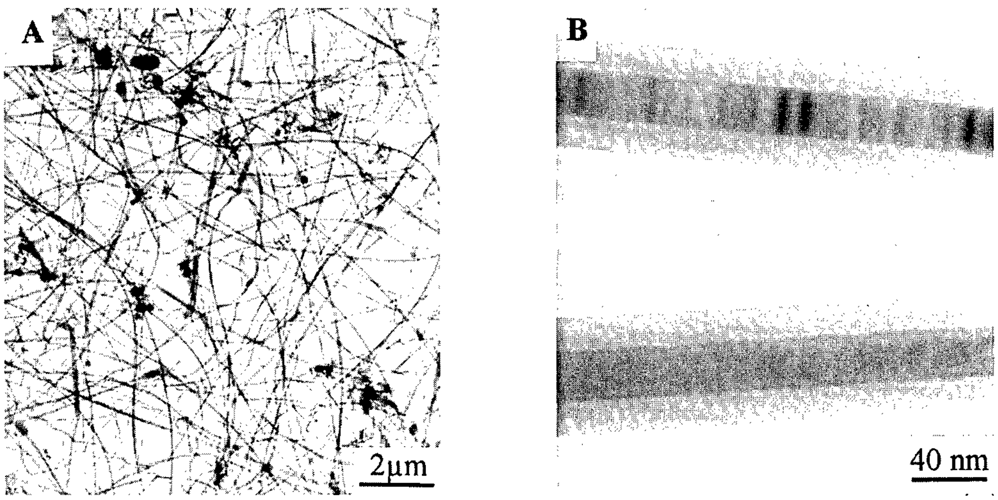

Figure 2. TEM morphology and structure of the as-synthesized product.
(A) Low-magnification TEM image; (B) High-magnification TEM image.

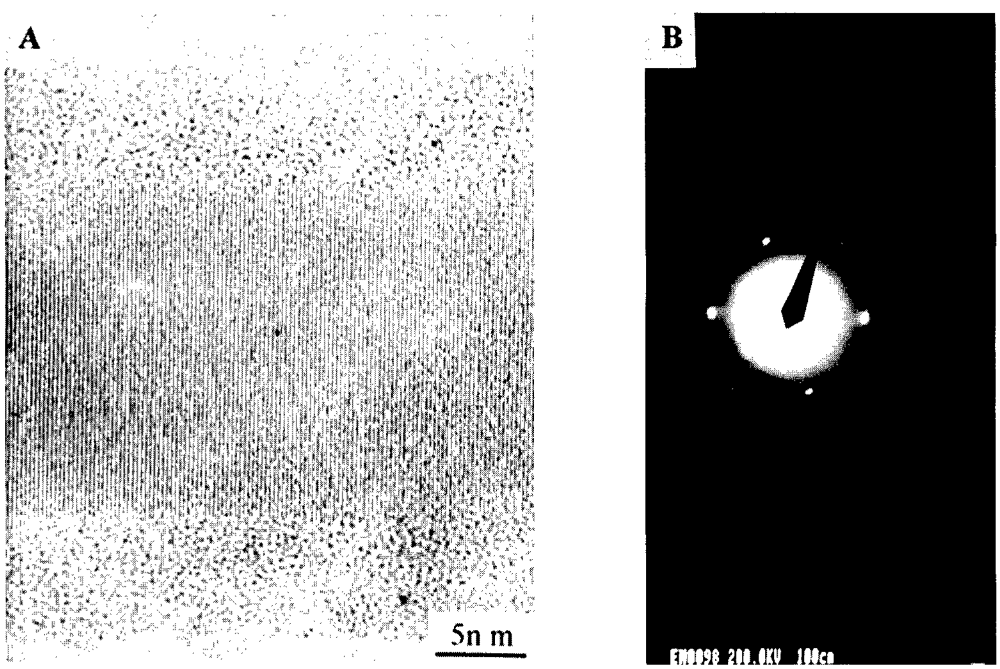

Figure 3. (A) HREM image of a nanowire; (B) SAED pattern of the nanowire core.

During the carbothermal reduction at 1650°C, the following reactions take place (10):

$$SiO\ (v) + 2\ C\ (s) \rightarrow SiC\ (s) + CO\ (v) \quad [1]$$

$$SiO\ (v) + 3\ CO\ (v) \rightarrow SiC\ (s) + 2\ CO_2\ (v) \quad [2]$$

Here v and s refer to the vapor state and the solid state, respectively. SiC nucleates on carbon particles via Reaction 1. Since sol-gel technique makes carbon nanoparticles homogeneously distributed in SiO_2 xerogels, the large number of carbon nanoparticles is beneficial to the formation of large quantities of SiC nuclei. As soon as the SiC nucleus forms, it grows via Reaction 2 to form wirelike β-SiC structure (10). The large quantities of SiC nuclei and the nanometer-sized SiC nucleus sites on carbon nanoparticles are favorable to the formation of nanometer-diameter β-SiC wires. When the temperature is raised from 1650°C to 1800°C and held for 30 min, the unreacted SiO_2 will decompose into SiO vapor and O_2. During cooling, the SiO vapor and O_2 around the β-SiC nanowires combine with each other to form SiO_2, which deposits on the β-SiC nanowires. As a result, every β-SiC nanowire is surrounded by a uniform amorphous SiO_2 wrapper.

CONCLUSION

We have synthesized single-crystal β-SiC nanowires with uniform amorphous SiO_2 wrappers via carbothermal reduction of the sol-gel derived silica containing carbon nanoparticles. The large quantities of SiC nuclei and the nanometer-sized SiC nucleus sites on carbon nanoparticles result in nanometer-diameter β-SiC wires. The formation of SiO_2 wrappers is ascribed to the combination reaction of the SiO vapor and O_2, which come from the decomposition of the unreacted SiO_2 when heated at 1800°C.

REFERENCES

1. Iijima, S., *Nature* 1991, 354, 56.
2. Morales, A.M., Lieber, C.M., *Science* 1998, 279, 208.
3. Fasol, G., *Science* 1998, 280, 545.
4. Dai, H., Wong, E.W., Lu, Y.Z., Fan, S.S., Lieber, C.M., *Nature* 1995, 375, 769.
5. Han, W.Q., Fan, S.S., Li, Q.Q., Hu, Y.D., *Science* 1997, 277, 1287.
6. Yang, P.D., Lieber, C.M., *Science* 1996, 273, 1836.
7. Fasol, G. and Runge, K., *Appl. Phys. Lett.* 1997, 70, 2467.
8. Braun, E., Eichen, Y., Sivan, U., Ben-Yoseph, G., *Nature* 1998, 391, 775.
9. Julre, A., Larbot, A., Guizard, C., Cot, L., *Mat. Res. Bull.* 1990, 25, 601.
10. Wang, L., Wada, H. and Allard, L.F., *J. Mater. Res.* 1992, 7(1), 148.

Pergamon

NanoStructured Materials, Vol. 12, pp. 1007–1010, 1999
Elsevier Science Ltd

0965-9773/99/$–see front matter

PII S0965-9773(99)00288-3

STRUCTURAL AND CATALYTIC PROPERTIES OF Mn OXO-CLUSTERS SUPPORTED ON MESOPOROUS MCM-41

D. Gleeson, R. Burch, N. A. Cruise and S.C. Tsang*

The Catalysis Research Centre,
Department of Chemistry, University of Reading, Reading, RG6 6AD, UK

Abstract--*A novel carbon monoxide oxidation catalyst based on highly dispersed Mn oxo-species grafted onto the internal wall of an MCM-41 material is described. This material is prepared via the chemical reaction of* $Mn_2(CO)_{10}$ *with Si-OH groups on the surface of mesoporous silica, followed by subsequent heat treatment in air. EXAFS studies indicate that this material contains no carbonyl groups but with new Mn-O interactions (three Mn-O at 1.900Å and one MnO at 1.747Å) and a Mn-Si interaction (via Mn-O-Si) at 3.280Å. The best fitted model suggests that the anchored Mn-oxo species has a structure resembling* Mn_2O_7.
©1999 Acta Metallurgica Inc.

Introduction

In 1992, Beck et al [1] of the Mobil Oil Corporation reported the synthesis and characterisation of a new group of silicate/ aluminosilicate materials which they designated M41S. These materials were prepared by the hydrolysis of silicate source in the presence of cationic (alkytrimethylammonium) surfactants, containing regular mesopores, whose size and morphology could be controlled by altering the solution chemistry during preparation. Thus materials with either a hexagonal array of pores (designated MCM-41) or a cubic array (MCM48) were made. The opportunity of using these materials as catalysts or catalyst supports was also recognized at an early stage.

Attempts to prepare catalytically active mesoporous oxides other than silica were frequently made. For example, early attempts to prepare hexagonal and cubic mesoporous transition metal oxides included Mn [2], Sn and Ti [3], however, all these materials were not stable upon removal of the surfactant template, collapsing to give dense, often amorphous phases. The general failure in the preparation of pure mesoporous transition metal oxides other than silica prompts us to investigate the use of silica MCM-41materials as templates for foreign material deposition. The hexagonal nanosize channels of the MCM-41 silica are structurally well defined with a large number of surface hydroxyl groups. It thus should be able to provide a stable and reproducible environment for the deposition of ultra-thin reactive linings of tailored chemical species [4,5].

In this paper, we report the synthesis of Mn-MCM-41 material *via* chemical reaction of $Mn_2(CO)_{10}$ with the surface silanol groups of MCM-41, followed by heat treatment in air. This modified Mn-MCM-41 gave much higher catalytic activity for CO oxidation to carbon dioxide than those displayed by bulk MnOx on conventional silica. Our EXAFS study indicates that novel MCM-41 supported Mn-oxo species structurally resembling Mn_2O_7 were made accordingly.

Experimental

Preparation of MCM-41 anchored Mn-oxo species by chemical vapour deposition

All manipulations were carried out under an inert atmosphere or under vacuum. The MCM-41(pore diameter 30 Å) was prepared according to a previously described method [1]. The MCM-41 was then degassed under a stream of flowing nitrogen for 2 h at 300 °C. The MCM-41 (100 mg) and $Mn_2(CO)_{10}$ (50 mg) were placed in an open-ended tubular silica vessel and a quartz-wool plug was used to separate the two materials. The reactor was inserted into a box furnace was heated to 50 °C. Periodically nitrogen was allowed to flow through the reactor for the even distribution of the manganese species on the MCM material. Finally the treated material was heated in air for 2 h at 300 °C to give an intense brown coloured material.

Preparation of bulk MnOx on MCM-41 by wet impregnation

100 mg of the MCM-41 was added to a cyclohexene solution of $Mn(acac)_3$ with a total volume not less than 1.5 mL. After drying, the material was calcined at 300 °C in air to facilitate the decomposition of the precursor. Transmission Electron Microscopy (TEM) showed that some bulk Mn-oxygen containing particles were found inside and outside the MCM channels. Temperature Programmed Reduction (TPR) suggested that a mixture of MnO_2 and Mn_2O_3 particles were present in the sample. (not shown)

EXAFS Experiment

Manganese K-edge X-ray absorption spectra were recorded over 13.5$Å^{-1}$ k range on Station 7.1 at the Synchrotron Radiation Source (SRS) at the Daresbury Laboratory, UK, operating in transmission mode at 2 GeV and 125 mA. The Si (111) monochromator was adjusted to give 70% harmonic rejection. Samples were finely ground and diluted with BN. Approximately 2 mm thickness of the powder was held in an aluminium holder between sheets of Sellotape. Two scans were recorded for each sample at 77 K.

Results

Figure 1 shows that the Mn-modified MCM-41 (+) prepared via $Mn_2(CO)_{10}$ vapour deposition catalysed the total oxidation of CO to CO_2 in air very effectively as compared with the bulk MnOx oxides on MCM-41 ( ). The onset temperature at which this material catalysed the oxidation of CO was approximately 30 °C lower than that for the bulk MnOx on the MCM.

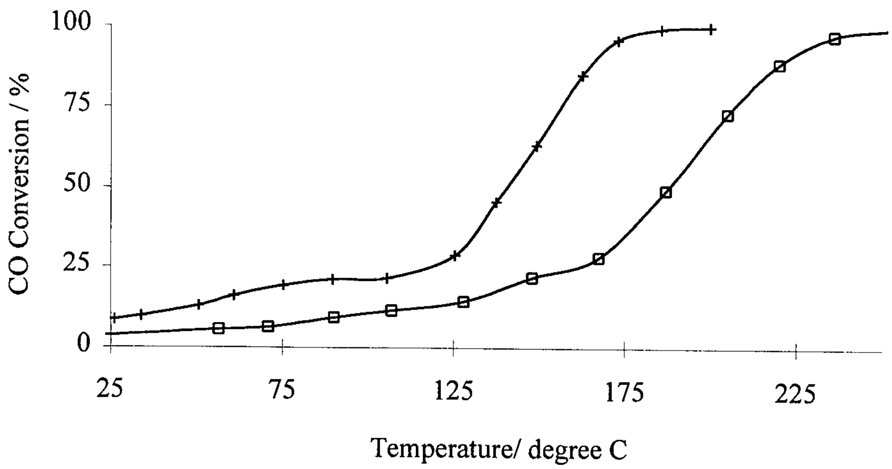

Figure 1: Catalytic Activity for CO Oxidation in Air

TEM study showed the internal walls of MCM channels appeared to be highly corrugated but no bulk particles were observed (not shown). The best EXAFS fitted data are given in Table 1. The overall fits for all the elements and their corresponding distances were obtained, in some cases employing the third and fourth shells. Adding more shells considerably improved the fit of the EXAFS data. Despite the extensive data fitting, the analyses show no Mn-C interaction. This clearly suggests that all the residual carbonyls were either decomposed or detached from the Mn atom during the heat treatment. The best-fitted model suggests three Mn-O distances at 1.900 Å and one Mn-O distances at 1.747Å. The shorter distance at 1.747 Å could be attributed to a Mn=O double bond. Three Mn-O distances of the same value could be the result of averaging three Mn-O single bonds in different chemical environments giving an overall distance of 1.900Å. The Mn-Si interaction with distance of 3.280Å is due to the Mn-O-Si moiety. We propose that at least one of the two remaining single Mn-O bonds is a bridging oxygen formed between the neighboring Mn species. This is supported by the data fit which was improved when a Mn-Mn distance of 2.931 Å was added. If the two bridging oxygens exist between two Mn atoms, this surface anchored molecule is structurally similar to the $[Mn_2O_6]^{-6}$ unit of edge-sharing tetrahedra (oxygen atoms occupy the corner position). It is also possible that one of the single Mn-O bonds comprises Mn-OH resulting from hydrolysis in moist air. Thus, two tetrahedra would be joined, in this case, by corner-sharing oxygen. This structure resembles closely the structure of Mn_2O_7 that can be obtained by the dehydration of two manganoic acid units. It is noted that both of the two possible structures that are given in Scheme 1 can account for the EXAFS data. Unfortunately, EXAFS offers no detection of hydrogen atoms and the difference in the bond distances is too small for their differentiation.

TABLE 1
Structural data for Mn-modified MCM-41

coordination number	atom type	EXAFS distance/ Å	Debye-Waller factor
1	O	1.747(7)	0.005(2)
3	O	1.900(2)	0.002(1)
1	Mn	2.931(9)	0.016(2)
1	Si	3.280(17)	0.012(4)

ef= -5.79(33), R= 27.36, FI= 0.00051

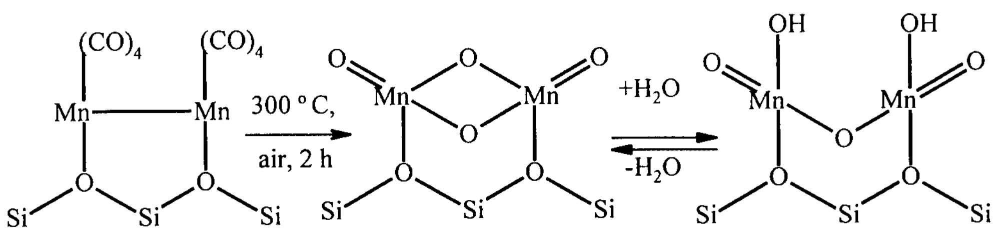

Scheme 1: A Proposed Structure of Mn-Oxo Species On the Walls of MCM-41

Nevertheless, the EXAFS analysis clearly suggests that the surface-anchored Mn species on MCM-41 are structurally very similar to molecular Mn-oxo entities such as MnO_4^-, Mn_2O_7 or $Mn_2O_6^{6-}$ displaying discrete tetrahedra. The nature of these supported Mn-oxo molecular entities is in marked contrast to the three-dimensional repetitive units observed in many manganese oxide lattices where most of the Mn-oxygen ions are buried deep inside the bulk. In many cases, the oxidation rates over the solid materials are limited by the mass transfer of the reactive species. Thus high reaction temperatures are necessary. The mechanism of CO oxidation in air has long been known and, is similar to that seen for the oxidation of hydrocarbons on MnOx. CO is chemisorbed onto the surface were it reacts with lattice oxygen of the reducible oxide CO_2 and is subsequently desorbed as CO_2. Oxygen is then abstracted from the gas stream reoxidising the oxide, and completing the catalytic cycle. The combination of high surface exposure and the molecular nature of anchored Mn species on the MCM-41 makes the resulting solid material catalytically much active than the bulk Mn oxides on the same support.

Reference

1. Kresge, C.T. , Leonowicz, M.E. , Roth, W.J. , Vartuli J.C. and Beck, J.S. , Nature (London), 1992, 359, 710.
2. Liu, j. and Suib, S.L., J. Chem. Sco., Chem Comm., 1997, 1031.
3. Ulagappan, N. and Rao, C.N.R., J. Chem. Sco., Chem Comm., 1996, 1685.
4. Burch, R., Cruise, N.A., Gleeson, D., Tsang, S.C., Chem. Commun, 1996, 951.
5. Burch, R., Cruise, N.A., Gleeson, D., Tsang, S.C., J. Mater. Chem., 1998, 8, 227.

Pergamon

NanoStructured Materials, Vol. 12, pp. 1011–1014, 1999
Elsevier Science Ltd

0965-9773/99/$–see front matter

PII S0965-9773(99)00289-5

STRUCTURAL AND MAGNETIC PROPERTIES OF $(Fe_{100-x}Co_x)_{73.5}Cu_1Nb_3Si_{13.5}B_9$ NANOCRYSTALLINE WIRES

F.Barariu, H.Chiriac, * F.Vinai, I.Murgulescu, * E.Ferrara
National Institute of R&D for Technical Physics,
47 Mangeron Blvd., 6600 Iasi 3, Romania
*** Istituto Elettrotecnico Nazionale "Galileo Ferraris",**
Corso M. D'Azeglio, 42 - 10125 Torino, Italy

Abstract — *Results on the production, structure and magnetic properties of $(Fe_{100-x}Co_x)_{73.5}Cu_1Nb_3Si_{13.5}B_9$ (x = 0, 5, 10, 20) wires obtained by the in rotating water quenching technique, both in the amorphous and nanocrystalline state are reported. The obtained results are compared with that obtained for the FINEMET alloy. The saturation magnetostriction decreases when increasing the Co content in the amorphous wires and also after annealing at 550 °C. The relative magnetic permeability decreases with Co addition and increases after annealing at 550 °C. The magnetic properties of the wires are explained on the basis of the effect of annealing in correlation with the change in the value of the saturation magnetostriction. ©1999 Acta Metallurgica Inc.*

INTRODUCTION

Nanocrystalline structures offer a new opportunity for tailoring the magnetic properties of soft magnetic materials. The most prominent example is the nanocrystalline FeCuNbSiB alloy obtained by devitrification of the amorphous precursor (1). This alloy reveals a homogeneous ultrafine grain structure of bcc FeSi with grain sizes of 10-20 nm and random orientation embedded in a still amorphous matrix. Due to the small size of grains the local magnetocrystalline is randomly averaged out by exchange interactions so that there is only a small anisotropy effect on the magnetization process. The structural phases that are formed lead to low saturation magnetostriction which minimize the magnetoelastic anisotropies. The excellent soft magnetic properties: high saturation induction like iron-based metallic glasses, high permeability like cobalt-based metallic glasses, very small coercive field and low saturation magnetostriction are due to these fine grains of nanometer size which determines a significant decrease of the magnetic anisotropy by averaging out the magnetocrystalline anisotropy (1), and a decrease of the saturation magnetostriction by an order of magnitude after crystallization (2). Many results were reported mainly for alloys with a ribbon shape, the studies being focused on the effect of the annealing conditions (temperature and time) on the magnetic properties of amorphous ribbons, but only few were concentrated on the amorphous wires (4).

The aim of this paper is to present a study on the effect of Fe substitution with Co on the glass-forming ability, and also on the structure and magnetic properties of the FeCuNbSiB in rotating water quenched wires both in amorphous and nanocrystalline state.

EXPERIMENTAL

We prepared $(Fe_{100-x}Co_x)_{73.5}Cu_1Nb_3Si_{13.5}B_9$ (x = 0, 5, 10, 20 at%) amorphous wires with a diameter of 130 μm by the in rotating water spinning method by ejecting the molten alloy, superheated with 200°C, with 8.5 m/s jet velocity under a 53 degrees angle of ejection in a water layer which rotates with a peripheral speed of 9 m/s. The alloy was prepared by induction melting of pure elements in argon atmosphere. The amorphous and the nanocrystalline states were checked by X-ray diffraction, DTA, and thermomagnetic measurements. The DTA measurements were performed with a heating rate of 10°C/min. In order to study the evolution of the magnetic properties during the crystallization process the samples were annealed in a conventional furnace at 500°C, 550°C, and 600°C for 1h, in vacuum. Transient temperature effects were minimized by rapidly inserting and extracting the samples from the special designed furnace. The magnetic measurements were performed by a fluxmetric method at a maximum applied field of 2500 A/m. The saturation magnetostriction of the samples was determined by the SAMR technique.

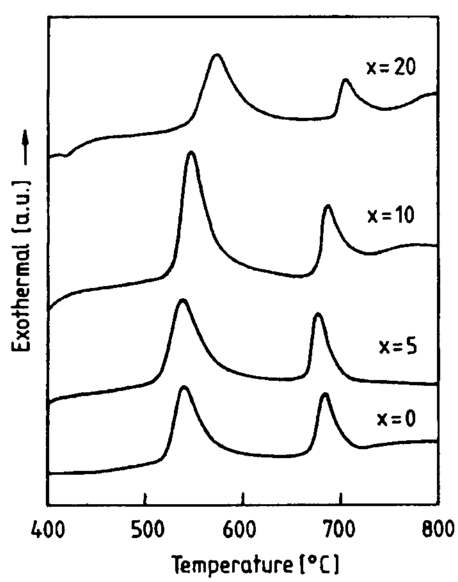

Figure 1. DTA curves for as-cast $(Fe_{100-x}Co_x)_{73.5}Cu_1Nb_3Si_{13.5}B_9$ (x = 0, 5, 10, 20 at%)

RESULTS AND DISCUSSIONS

The substitution of Fe with Co in the FeCuNbSiB alloy leads to an increase in the wire glass-forming ability. Figure 1 illustrates the DTA curves recorded for the amorphous samples.

Two exothermic peaks are seen on the DTA curves for all 4 alloys indicating that these amorphous alloys crystallize through two stages corresponding to the formation of bcc Fe grains and to a still amorphous minority matrix, structure that is specific for the nanocrystalline alloys. The addition of Co shifts the onset of crystallization from 505°C to 535°C and also the first exothermic peak from 540°C to 570°C for x=0 up to x=20 respectively. The temperature at which the crystallization process is completed is not significantly affected.

The saturation magnetostriction studies revealed that in the as-cast state the replacement of Fe with Co leads to a progressive decrease in λ_s for all samples from 23×10^{-6} for x=0 to 13.6×10^{-6} for x=20. All amorphous samples present a large Barkhausen effect (LBE) specific for the high positive amorphous magnetic wires, the magnetic domain structure consisting in an axially magnetized inner core and a radially magnetized outer shell (5). The magnetic behavior of highly positive magnetostrictive amorphous wires is characterized by a rectangular hysterezis loop due to the LBE that occurs at relatively low values of the axial magnetic field. The LBE consists in an abrupt magnetization reversal in the axially magnetized inner core at a well defined value of the applied magnetic field called switching field H*. The value of the remanent magnetization at this field, M*, is very close to that of the saturation magnetization (5).

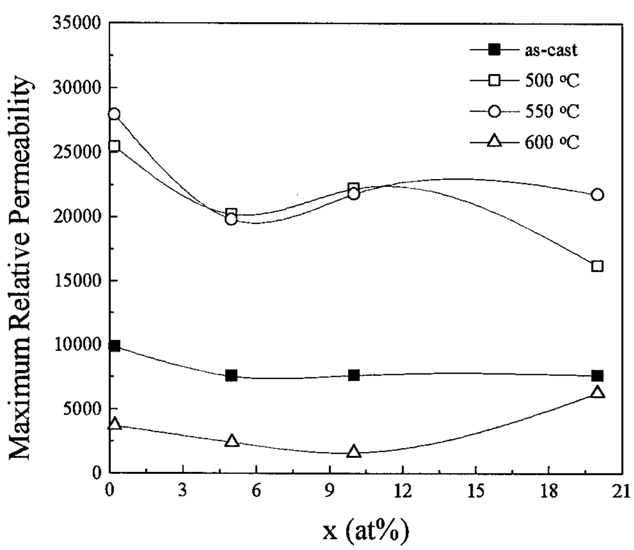

Figure 2. Maximum relative permeability dependence on the Co concentration.

Annealing the samples at the previously mentioned temperatures we noticed a decrease of λ_s for all samples at 550°C when the nanocrystalline phase is formed and then an increase at 600°C. Consequently both H* and M* decreases by increasing the annealing temperature up to 550° when the LBE vanishes. The addition of Co also affects λ_s in the nanocrystalline state as follows: it decreases from 3.3×10^{-6} for x=0 to 1.8×10^{-6} for x=10 and than increases again to 6×10^{-6} for x=20.

Figure 2 presents the dependence of the maximum relative permeability (μ_r) as a function of Co concentration for the as-cast and annealed samples at 500°C, 550°C, and 600°C for 1h. In the as-cast state one can notice a slight decrease of μ_r by increasing the Co content. The 550°C annealing leads to the increase in μ_r for a Co content of 0, 5, 10 at the maximum attained being between about 2 up to 2.5 times higher than in the amorphous state. This behavior is due to the formation of the nanocrystalline state. At 600°C annealing temperature, when the crystallization process is completed (as we observed from the DTA curves recorded on the samples annealed for 1 h at 600°C), μ_r depreciates having smaller values than in the as-cast state.

CONCLUSIONS

The replacement of Fe with Co leads to the improvement in the glass-forming ability of the in rotating water quenched wires. The onset of crystallization as well as the crystallization temperature at which the nanocrystalline state is formed are shifted to higher value. The amorphous wires present LBE. The Co addition leads to a decrease of λ_s by increasing the Co content. Annealing the amorphous wires at 550°C, the optimum temperature for the nanocrystalline phase formation, leads to an improvement of the magnetic properties by achieving small values for λ_s and higher values for μ_r. The LBE effect disappears.

References

1. Herder G., *Nanostructured and Non-Crystalline Materials,* World Scientific, Singapore, 1995, p. 449.
2. Herzer G., *IEEE Transactions on Magnetics,* 1989, 25, 3327.
3. Yoshizawa Y., Yamauchi K., *Materials Transactions JIM*, 1990, 31, 307.
4. Gomez-Polo C., Olofinjana A.O., Marin P., Vazquez M., Davies H.A., *IEEE Transactions on Magnetics*, 1993, 29, 2673.
5. Chiriac H., Ovari T.A., Pop Gh., Barariu F., *Applied Physics*, 1997, 8, 81.

Pergamon

NanoStructured Materials, Vol. 12, pp. 1015–1020, 1999
Elsevier Science Ltd

0965-9773/99/$–see front matter

PII S0965-9773(99)00290-1

NON-LINEAR CONTRIBUTION TO INTENSITY-VOLTAGE CHARACTERISTICS OF GOLD NANOWIRES

A. Correia, J.-L. Costa-Krämer, Y. W. Zhao and N. García.
Laboratorio de Física de Sistemas Pequeños y Nanotecnología, CSIC,
Calle Serrano 144, 28006 Madrid, Spain.

Abstract -- *In this paper, we present experimental results for room temperature (I-V) characteristics of gold nanowires whose zero current conductance is quantized. We have analysed more throroughly the (I-V) characteristics of high stability nanoscopic gold contacts changing several parameters such as the formation technique (MCBJ, nanolithography, STM related technique) or the environment conditions around the nanowire (vacuum, air, polymer, non-conductive substrate). In all these experiments, a faster than linear increase of the current was observed, but at different threshold voltages depending on the situation: 0.1V for "free standing" nanowires (in air or vacuum), 0.2 to 0.5V for non "free standing", i.e., nanowires deposited on a substrate or embedded in a polymer. ©1999 Acta Metallurgica Inc.*

INTRODUCTION

The phenomenom of conductance quantization (CQ) in units of $G_0=2e^2/h$ (where e is the electron charge and h the Planck constant) was first observed at 0.6K in two-dimensional electron gas (2DEG) semiconductor structures (1). After then, CQ in metallic nanowires has constituted a field of increasing interest, the future of communication and information processing technologies depending on the use of nanometric and submicrometer integration as an essential tool (2). Theoretically predicted first as a step-like or oscillatory behavior of conductance in Scanning Tunneling Microscope (STM) calculations (3), it has been observed in wires made of different metals and produced by STM and several related techniques. CQ study was usually performed by driving a STM tip into a metallic sample and then pulling it out. During this process, a nanowire is formed, making it possible to measure both electrical (4,5) and mechanical properties (6,7). Conductance experiments have been also performed with mechanically controllable break junctions (MCBJ) (8-11) and more recently using two macroscopic metallic wires ("Table top experiments") (12). In all these experimental techniques, plateaus appear at quantized values of conductance showing that electron transport through metallic nanowires is ballistic and that the current is carried in quantized modes. However, the individual results are not exactly reproducible: conductance curves measured during the nanowire breaking are not identical due to different dynamical evolutions each breaking process. In order to show that CQ is an actual phenomenon in

metallic nanowires, experiments involving thousands of consecutive measurements without any selection criterium have been performed (13). Studies have been also performed on semi-metals and first experimental evidence of CQ in bismuth at 4K has been recently reported (14). Another interesting subject is the nanowire structural characterization using either scanning (15) or transmission electron microscopy (16).

In this work, we present experimental results for the room temperature I-V characteristics of high stability gold nanowires whose zero current conductance is quantized. In order to analyse more thoroughly the I-V behaviour and its non-linear contribution,several parameters have been changed such as the method for producing nanowires (MCBJ, STM related technique using macroscopic wires, nanolithography) or the conditions around the formed nanowires (vacuum, air, polymer, non conductive substrate). The most representative results for each experiment are displayed in this paper and compared with previous results obtained on I-V characteristics (13,17).

EXPERIMENTAL SET-UP

In order to achieve control, obtain high stability on the formation of nanocontacts and check the influence of several parameters on their electrical properties we used three different approaches. The first one corresponds to a homemade MCBJ set-up where the obtained nanowires are "free standing" (in air or in high vacuum and at room temperature), more details concerning this experimental set-up could be found in reference 18. The second set-up corresponds to a STM related technique. In this configuration, we tried to obtain maximum stability of the formation of the nanowires between two macroscopic gold wires (1/2mm diameter and 99.9% purity) by embedding them with polymer (non "free standing") when CQ was observed. The I-V characteristics were measured in these conditions at room temperature and ambient pressure. Last set-up corresponds to 100nm wide nanowires deposited on a SiO_2 substrate and obtained by nanolithography. Heating the system, we can obtain by diffusion process, in a controllable way, nanowires (non "free standing") whose I-V characteristics are non-linear. In all these experimental set-ups, the current flowing through the nanowire is continously monitored with a current-voltage converter (10^5 gain) connected to a fast digital oscilloscope.

EXPERIMENTAL RESULTS

The study of I-V characteristics behaviour for nanocontacts can only be done in a high stability situation. Using a MCBJ in air and ambient pressure, we observed, once stabilised, a constant current for several minutes (figure 1) (18) corresponding to a metallic nanocontact involving a few conductance levels. This result could be related to previous experiments performed in UHV (13) or in air with macroscopic metallic wires where the stability reached by standard STM techniques (4,5) or MCBJ (19) was improved by more than three orders of magnitude.

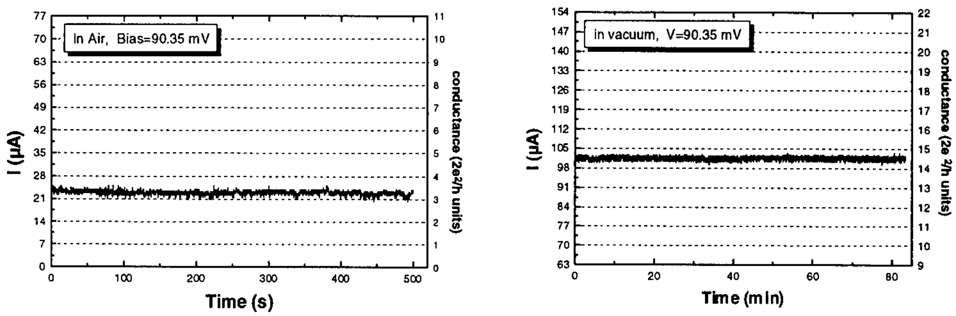

Figure 1: Stability curves obtained with the MCBJ technique in air and in vacuum at RT.

In these conditions of high stability, a triangular potential difference is applied to the contact recording the current simultaneously and we have performed extensive measurements of I-V characteristics (18) (typical results are displayed in figures 2a). We have fitted the measured current dependence on the applied voltage to the expression:

$$I(V) = I_L(V) + I_{NL}(V) = a_1V + a_2V^2 + a_3V^3 \qquad [1]$$

where I(V) is the value of the current in μA, V is the applied voltage in volts and I_L and I_{NL} are the linear and non-linear contributions, respectively. In these experiments, we observe a faster than linear increase of the current at a threshold voltage of ≈0.1V such as in previous results (13). A similar behaviour was obtained using the MCBJ in high vacuum (figure 2b). Thus, it seems that with this experimental set-up the nonlinear character does not depend strongly on the quantum channel (18) and/or on the pressure.

Using the STM related technique, high stability nanocontacts were also obtained and their I-V characteristics behaviour studied. In air and ambient pressure, similar results than above were observed i.e. a characteristic crossover voltage (V_c) to the nonlinear regime at about 0.1V. Considering these experiments, it seems that V_c not depends either on the technique used. Once the current stabilised, we deposit a drop of non conductive glue between the two macroscopic metallic wires and measure the I-V characteristics in these conditions. Obtained I-V curves present a well-defined linear behaviour for contacts having large conductances, whereas for contacts involving only few conductance channels nonlinear effects become evident such as in the previous study. An example of the most representative results concerning the nonlinear component is displayed in figure 3.

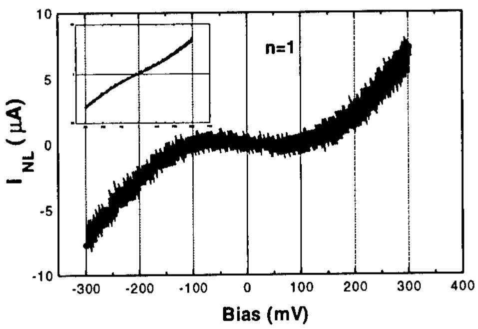

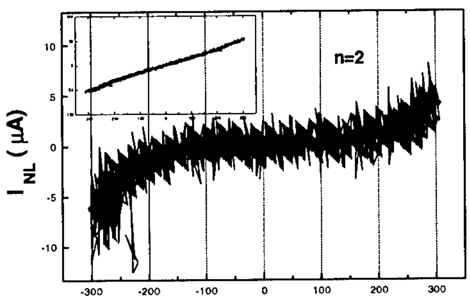

Figure 2: Non linear component of a typical (I-V) characteristic (see inset) obtained using the MCBJ technique; (a) in air (n=1); (b) in vacuum (n=2).

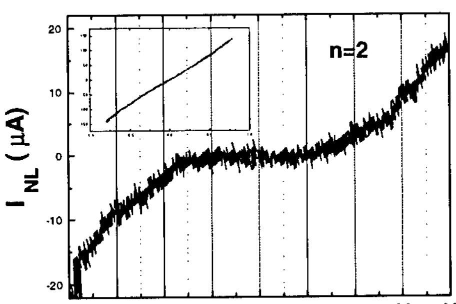

Figure 3: Non linear component of a typical (I-V) characteristic (see inset) obtained using the STM related technique in air (n=2).

We fitted the I-V characteristics with the expression (1) and we observed a faster than linear increase of the current at a different threshold voltage (V_c) than before: from 0.2 to 0.3V.

Another set of experiments have been done in this way with 100nm wide gold nanocontacts obtained by nanolithography on SiO_2 substrate. Next, a monitored current is applied to the nanowire in order to obtain a much smaller one in a controllable way by diffusion process. At the last stage, the nanowire seems broken (i.e we are unable to observe it with our SEM) but a nanocontact remains and I-V characteristics could be measured. In this configuration, the faster than linear increase of the current also appears at a threshold voltage of $\approx$0.5V (see figure 4).

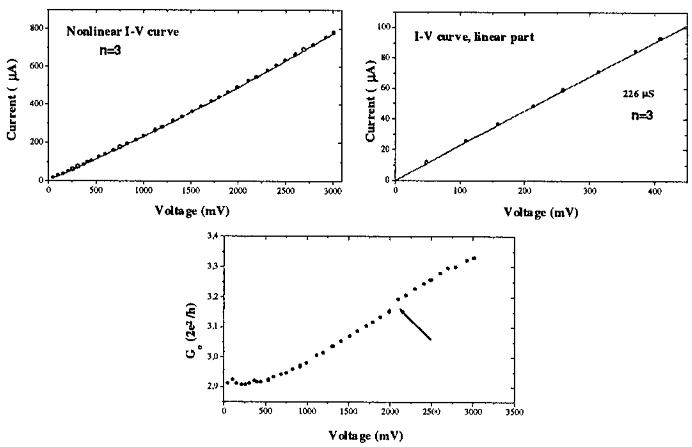

Figure 4: Non linear I-V curve. Notice that the faster than linear increase of the current appears at a threshold voltage of $\approx$0.5V.

CONCLUSION

Summarizing, electrical properties of gold nanocontacts have been studied with different experimental techniques and environment configurations around the nanowire. These nanocontacts exhibit a high stability allowing measurements of currents flowing through nanocontacts, involving few conductance channels, during several minutes. These high-stability features have been used to measure their I-V characteristics showing the importance of nonlinear effects. We observed a faster than linear increase of the current at different threshold voltages depending on the surrounding environment: 0.1V for "free standing" nanowires (in air or vacuum), 0.2 to 0.5V for non "free standing", i.e., nanowires deposited on a substrate or embedded in a polymer. It seems that for "free standing" nanowires this crossover voltage to the nonlinear regime is independent of pressure (air or vacuum) and experimental set-up used in order to measure their I-V characteristics. However, we note an increase of this voltage value when the configuration around the nanowire is

different. The non-conductive material around the nanowire certainly play a role on the nonlinear component of its I-V characteristic.

REFERENCES

1. D. A. Wharam, T. J. Thornton, R. Newbury, M. Pepper, H. Ahmed, J. E. F. Frost, D. G. Hasko, D. C. Peacock, D. A. Ritchie and G.A.C. Jones, J. Phys. **C 21**, L209 (1988).
2. Joint European-American-Japanese Conference on Future Information Technologies, Helsinki, Finland, 1995 (unpublished).
3. N. García and L. Escapa, Appl. Phys. Lett. **54**, 1418 (1989); N. García, STM Workshop Trieste (1987) (unpublished).
4. J. I. Pascual, J. Mendez, J. Gómez-Herrero, A. M. Baró, N. García, and V. T. Binh, Phys. Rev. Lett. **71**, 1852 (1993).
5. L. Olesen, E. Laegsgaard, I. Stensgaard, F. Besenbacher, J. Schiotz, P. Stoltze, K. W. Jacobsen, and J. K. Norskov, Phys. Rev. Lett. **72**, 2251 (1994).
6. N. Agraït, J. G. Rodrigo and S. Vieira, Phys. Rev. B **47**, 12345 (1993).
7. N. Agraït, G. Rubio and S. Vieira, Phys. Rev. Lett. **74**, 3995 (1995).
8. C. J. Muller, J. M. van Ruitenbeek and L. J. de Jongh, Phys. Rev. Lett. **69**,140 (1992).
9. J. M. Krans, C. J. Muller, I. K. Yanson, Th. C. M. Govaert, R. Hesper and J. M. Ruitenbeek, Phys. Rev. B **48**, 14721 (1993).
10. J. M. Krans, C. J. Muller, N. van der Post, F. R. Postma, A. P. Sutton, T. N. Todorov and J. M. Ruitenbeek, Phys. Rev.Lett. **74**, 2146 (1995).
11. J. M. Krans, J. M. van Ruitenbeek, V. V. Fisun, I. K. Yanson and L. J. de Jongh, Nature (London) **375**, 767 (1995).
12. J. L. Costa-Krämer, N. García, P. García-Mochales, and P. A. Serena, Surf. Sci. Lett. **342**, L1144 (1995).
13. J. L. Costa-Krämer, N. García, P. García-Mochales, P. A. Serena, M. I. Marqués and A. Correia, Phys. Rev. B **55**,5416 (1997).
14. J. L. Costa-Krämer, N. García and H. Olin, Phys. Rev. Lett. **78**, 4990 (1997).
15. A. Correia and N. García, Phys. Rev. B **55**, 6689 (1997); A. Correia, M. I. Marqués and N. García, J. Vac. Sci. and Techn. B **15 (3)**, 548 (1997).
16. Y. Kondo and K. Takayanagi, Phys. Rev. Lett. **79**, 3455 (1997)
17. J. L. Costa-Krämer, N. Garcia, I. V. Krive, M. Jonson, H. Olin, P. A. Serena and R. I. Shekhter,NATO ASI Series E, (Kluwer Publishers) **348**, 1 (1998).
18. A. Correia and Y. W. Zhao, submitted to Journal of Vacuum Science and Technology.
19. C. J. Muller, J. M. Krans, T. N. Todorov and M. A. Reed, Phys. Rev. B **53**, 1022 (1996).

Pergamon

NanoStructured Materials, Vol. 12, pp. 1021–1026, 1999
Elsevier Science Ltd

0965-9773/99/$–see front matter

PII S0965-9773(99)00291-3

NANOSTRUCTURED MAGNETIC FILMS FOR EXTREMELY HIGH DENSITY RECORDING

D.J. Sellmyer, M. Yu, and R.D. Kirby
Behlen Laboratory of Physics and Center for Materials Research and Analysis
University of Nebraska
Lincoln, NE 68588-0113

Abstract--*This paper presents recent results on high coercivity, nanocrystalline magnetic films. Elementary models for magnetization decay, thermal stability, and noise are discussed along with requirements on grain size and anisotropy for recording at extremely high areal densities (approaching 100 gigabits per square inch). Characterization of nanocrystalline films by activation-volume measurements and its relationship to nanostructure are emphasized. A number of recently discovered films with high potential for future extremely high density recording are discussed. ©1999 Acta Metallurgica Inc.*

1. INTRODUCTION

The design and fabrication of nanostructured films are playing an increasingly important role in modern science and technology. In the case of nanoscaled magnetic films, a large part of the interest is driven by information storage and magnetoelectronic devices. The areal density for hard disk storage in gigabits per square inch (Gb/in^2) in recent years has been increasing at the rate of about 60% per year (1,2). At present the most advanced systems record at densities of about 3 Gb/in^2 and IBM has demonstrated recording at about 11 Gb/in^2. This remarkable progress naturally raises the question of how far the areal density in conventional longitudinal recording can be increased before fundamental physics limitations begin to predominate. This paper focuses on materials-physics issues in magnetic media for extremely high density recording (EHDR), that is, in the range approaching 100 Gb/in^2 (3).

2. COERCIVITY, NOISE AND THERMAL STABILITY (3,5)

In the last two decades the areal density has increased from about 3 Mb/in^2 to 3 Gb/in^2. Extrapolating this rate of change would suggest in another two decades an areal density of 3 terabits/in^2. But this would require bits of dimensions only tens of atomic diameters. For theoretical and practical reasons this would be extremely difficult to attain. In this section we outline briefly some of the materials limitations in EHDR, focusing especially on coercivity H_c, $M_r\delta$ where M_r is the remanent magnetization and δ the film thickness, and noise.

In the last twenty years H_c has increased in Co-based recording media from about 0.3 kOe to 3 kOe. At the same time $M_r\delta$ decreased from about 2.5 memu/cm^2 to 0.5 memu/cm^2. At present the most advanced media are CoCrPtX alloys where X represents Ta, Nb, ...(4). The

reason for the increase in H_c and decrease in $M_r\delta$ is that the transition parameter (a), which measures the width of the magnetization reversal region between bits, varies approximately as $(M_r\delta/H_c)^{1/2}$. This leads to the clear need for discovery of new media whose H_c values are in the 4-6 kOe region. Similarly $M_r\delta$ must be further decreased although for technical reasons, as δ decreases below about 10 nm, H_c drops which is thus self defeating.

A significant aspect of new media for future EHDR is grain size which controls noise. The signal-to-noise ratio, SNR, is given in dB by 10logN, where N is the total number of grains in the bit. As the bit size decreases, the lateral grain diameter, d, must also decrease since the total number of grains must be in the range 1000 (SNR = 30 dB) to 100 (SNR = 20 dB). The grain size also controls jitter noise which tends to be the dominant source of media noise and which is caused by the fluctuations in bit dimensions due to fluctuations in grain size and arrangement.

Grain size also is important in considering future media because it controls thermal stability. It has been known for many years that the magnetization M often decays with time according to

$$M(t) = M_0 - S\ln t \qquad [1]$$

where S is called the magnetic viscosity. The origin of this effect is thermal activation of the magnetization over energy barriers. The characteristic relaxation time τ for this process is

$$\tau^{-1} = f_0 e^{-E_B/k_B T} \quad , \qquad [2]$$

where E_B is the energy barrier and f_0 an attempt frequency (~10^9 Hz). For independent Stoner-Wohlfarth particles of volume V the energy barrier is

$$E_B = K_u V(1-H/H_A)^{\alpha} \quad , \qquad [3]$$

where K_u is the anisotropy, α is 1.5-2 depending on geometrical and other factors, and H_A is the anisotropy field ($2K_u/M_s$). The grain size, which determines V, plays a crucial role because from Eq. [2], if τ = 100 s which defines the *superparamagnetic limit*, then $K_uV/k_BT \approx 25$. For long-term storage (~ 10 years = 3 x 10^8 s) one must have $K_uV \approx E_B = 40\ k_BT$. Thus the product K_uV is extremely important in designing new high anisotropy, small-grain-size media.

Another manifestation of thermal instability is that the coercivity is a function of measurement time. This can be seen from Eqs. [2] and [3].

$$E_B = K_u V(1-H/H_A)^{\alpha} = k_B T\ln f_0 \tau. \qquad [4]$$

Defining $H_c(\tau_c)$ as the coercivity measured with the characteristic time τ_c leads to

$$H_c(\tau_c) = H_A\{1 - [(k_B T/K_u V)\ln f_0 \tau_c]^{1/\alpha}\} \ . \qquad [5]$$

This implies that the coercivity at writing times (~ 10^{-8} s) can be considerably larger than at measurement times (~ 10 s) or storage times (10^8 s). And the stability parameter K_uV/k_BT controls this variation.

Table I gives simple estimates of requirements on grain size and anisotropy for EHDR. Some assumptions include bit width = W, bit length = B, aspect ratio W/B = 4, $V = d^2\delta$, δ = 10 nm,

TABLE I
Estimates of Grain Size and Anisotropy for EHDR

SNR (dB)	D_A (Gb/in^2)	W (nm)	B (nm)	d (nm)	V ($10^{-18}cm^3$)	K_u ($10^6 erg/cm^3$)
20	10	506	127	25	6	0.3
20	100	160	40	8	0.6	3
20	200	113	28	6	0.3	7
24	10	506	127	16	3	0.8
24	100	160	40	5	0.3	8
24	200	113	28	4	0.1	15

$K_uV/k_BT = 50$, and SNR = 20 or 24 dB. It can be seen that for SNR = 20 dB, for areal density = D_A = 100 Gb/in^2, a grain size of 8 nm and anisotropy of 3×10^6 erg/cm^3 are required. Given that we assume perfectly independent grains, these conditions are stringent but perhaps not completely unrealistic. On the other hand, if a higher SNR (24 dB) is needed, then to attain 100 Gb/in^2, d = 5 nm and $K_u = 8 \times 10^6$ erg/cm^3. Surely such magnetic grains will require altogether new media.

3. CHARACTERIZATION OF NANOCRYSTALLINE FILMS

In the previous section we have presented the most elementary models relating film nanostructure to magnetic properties, especially relating to thermal stability, noise and anisotropy which controls coercivity. We next introduce the concept of an activation volume V^* which is intimately related to magnetic viscosity, coercivity as a function of measuring time, and noise.

The activation volume is related to the field dependence of the energy barrier E_B as shown below. $E_B(H)$ can be expanded in a Taylor series about H_c:

$$\begin{aligned} E_B &\simeq E_B(H_c) + (dE_B(H_c)/dH)(H-H_c) \\ &= \{E_B(H_c) - H_c(dE_B(H_c))/dH\} + (dE_B(H_c)/dH)H \\ &\equiv E_0 + (dE_B(H_c)/dH)H \end{aligned} \qquad [6]$$

V^* is then defined as

$$V^* - (1/M_s)(dE(H_c))/dH \qquad [7]$$

so that

$$E_B = E_0 - M_sV^*H \ . \qquad [8]$$

V^* can be measured in at least two ways. The viscosity S is given by

$$S = |k_B T\chi_{irr}/(dE_B/dH)| , \quad [9]$$

where χ_{irr} is the irreversible susceptibility, $\chi_{irr} = dM_{irr}/dH$.

This leads to

$$V^* = k_B T\chi_{irr}/M_s S . \quad [10]$$

Additionally, it can be shown that (5)

$$H_c = const + (k_B T/M_s V^*)\ln(dH/dt) \quad [11]$$

so that V^* can be measured also from the field sweep-rate dependence of the coercivity.

The relationship between V^* and nanostructure critically depends upon the operative magnetization reversal mechanism. Several $E_B(H)$ functions have been considered including:

$$E_B = E_0 - M_s VH , \quad (linear) \quad [12]$$

$$E_B = \beta(1/H - 1/H_0) , \quad (1/H) \quad [13]$$

where β and H_0 are constants, and the Stoner-Wohlfarth function of Eq.[3].

In the linear dependence (Eq. [12]), Eq. [7] leads to $V^* = V$, where V is assumed to be the volume of magnetization that reverses in a typical Barkhausen jump. On the other hand for the case of independent, coherently rotating Stoner-Wohlfarth particles of volume V, Eqs. [7] and [3] lead (assuming $\alpha = 2$) to $V^* = V(1 - H_c/H_A)$, so that the measured activation volume is dependent on H_c. The H^{-1} dependence of E_B in Eq. [13] has been suggested by Barbara and others as being relevant to incoherent rotation of the magnetization associated with wall displacements(6). It can be seen in this case that the interpretation of V^* via Eqs. [7] and [13] will not be related to a nanostructural parameter in a simple way.

Although most of the theoretical modeling of thermal-instability effects in small-grained recording media has assumed independent Stoner-Wohlfarth "particles", there is evidence we outline below that an incoherent reversal mechanism is relevant to typical media being produced today. For example, Fig. 1 shows the temperature dependence of V^* for CoSm films as reported by Malhotra *et al.* (7), Qualitatively, V^* appears to be proportional to T^2 which is consistent with the 1/H dependence of Eq. [13] as shown by Kirby *et al.*(8). Data of Yu *et al.*(9) are shown in Fig. 2, which exhibits V^* as a function of film thickness δ for a series of CoCrPt alloys. A simple coherently rotating "cylindrical-grain" model would predict $V^* \propto V \propto \delta$ as shown in the dashed line. Again, recent results based on a 1/H dependence of E_B have reproduced the low-thickness upturn seen in Fig. 2. Moreover, similar data have been seen in separate experiments on CoCrTa films by Ross (10) and Zeng *et al.* (11). The physical reason for the apparent "wall-displacement" model may be seen in Fig. 3, which depicts the "domain wall" structure based on detailed TEM and Lorentz-microscopy studies(12,3). It is expected that a similar qualitative picture is relevant to CoCrPt and CoCrTa films, but further data on $V^*(T)$, $V^*(\delta)$ and $H_c(T)$ remain to be taken in order to confirm this.

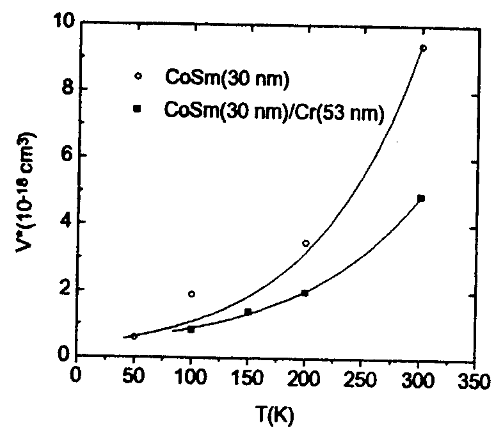

Fig. 1. V^* as a Function of T.

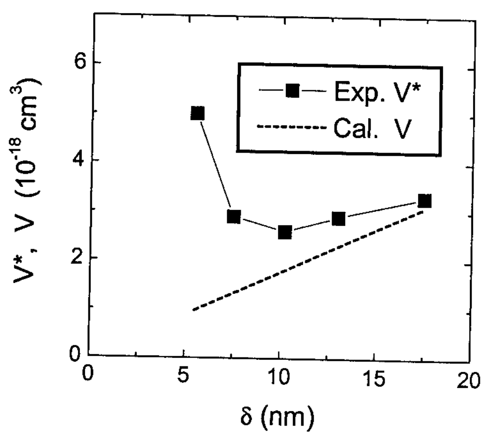

Fig. 2. V* (Experiment) and Grain Volume V (Calculation) vs. CoCrPt Layer Thickness δ.

4. NEW HIGH-ANISOTROPY NANOCRYSTALLINE FILMS

It is clear from the discussion in Section 2 and Table I that an urgent need for future EHDR media is the identification of new compounds or alloys that can be made with high anisotropies, high coercivities, and grain sizes in the 5-10 nm region. Research in our laboratories has, in fact, uncovered several materials with high potential as reviewed recently by Sellmyer *et al.*(3) These materials include CoPr, FePt, CoPt, CoSm, SmFeSiC and SmFeAlC. Coercivities in these films are generally in the range of 5-10 kOe, but higher values also have been obtained. H_c values can be controlled rather easily through composition and thermal processing. The origin of the large H_c values in alloys containing rare earths is generally single-ion anisotropy associated with the rare

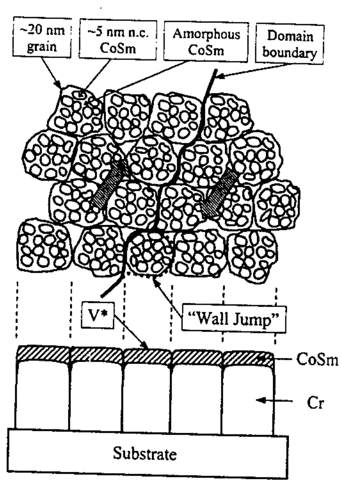

Fig. 3. Nanostructure of CoSm.

earth. In the cases of FePt and CoPt, the $L1_0$ ordered structure, a "natural" multilayered structure plus strong spin-orbit interactions are the sources of the large K_u (and H_c) values. K_u values in these alloys typically are in the range $5 \times 10^6 \leq K_u \leq 5 \times 10^7$ erg/cm^3. Small grain sizes also can be achieved. High resolution TEM results have shown lateral grain sizes in the range $5 \leq d \leq 15$ nm. Activation volume measurements can be used to determine qualitatively a lateral "magnetic cluster" size and these in some cases also are in the sub -10 nm range.

5. SUMMARY AND CONCLUSIONS

We have reviewed research mainly from our laboratories on the topic of nanoscale design of high coercivity, small-grain-size nanocrystalline films with high potential for future magnetic recording at areal densities approaching 100 Gb/in^2. Thermal stability of such media and its relation to the energy barrier and models therefore was emphasized. We have pointed out with several examples that simple models of films based on independent, coherently rotating particles may be inadequate for any present or future media made with conventional fabrication techniques. However, considerable further research is warranted on reversal mechanisms and their relationship to thermal stability.

A brief discussion was given of some of the promising new films investigated in our laboratories. While they have most of the properties needed to increase the areal density by about an order of magnitude, as always it will be necessary to do a large amount of experimentation to produce practical films on a disk that are suitable for recording.

We are indebted for collaboration and many helpful discussions to our colleagues Dr. Mary Doerner of IBM, Dr. Z.S. Shan of HMT Technology, and Mr. Hao Zeng. For financial support we thank the National Science Foundation (DMR-9623992), the National Storage Industry Consortium, and CMRA.

6. REFERENCES

1. Simonds, J.L., *Physics Today*, April, 1995, p. 26.
2. Tristram, C., *Technology Review*, July/Aug., 1998, p. 44.
3. Sellmyer, D.J., Yu, M., Thomas, R.A., Liu, Y. and Kirby, R.D., *Phys. Low-Dim. Struct.*, 1998, 1/2, 155.
4. Lambeth, D. *et al.* in *Magnetic Hysteresis in Novel Magnetic Materials*, ed. G. Hadjipanayis, Kluwer Academic, Dordrecht, 1997, 338, p. 767.
5. Sellmyer, D.J. and Shan, Z.S., in *Magnetic Hysteresis in Novel Magnetic Materials*, ed. G. Hadjipanayis, Kluwer Academic, Dordrecht, 1997, 338, p. 419.
6. Barbara, B., *Proc. Second. Int. Symp. on Coercivity and Anisotropy of Rare Earth-Transition Metal Alloys*, U. of California, San Diego, 1978, p. 178.
7. Malhotra, S.S., Shan, Z.S., Stafford, D.C., Liou, S.H. and Sellmyer, D.J., *IEEE Trans. Mag.*, 1996, 32, p. 4019.
8. Kirby, R.D. *et al.*, to be published.
9. Yu, M., Doerner, M.F. and Sellmyer, D.J., *IEEE Trans. Mag.*, 1998, 34, p. 1534.
10. Ross, C., *IEEE Trans. Mag.*, 1998, 34, p. 282.
11. Zeng, H., Shan, Z.S. and Sellmyer, D.J., to be published.
12. Liu, Y., Shan, Z.S. and Sellmyer, D.J., *IEEE Trans. Mag.*, 1996, 32, p. 3614.

Pergamon

NanoStructured Materials, Vol. 12, pp. 1027–1030, 1999
Elsevier Science Ltd

0965-9773/99/$–see front matter

PII S0965-9773(99)00292-5

NANOSTRUCTURE OF EXCHANGE COUPLED HARD/SOFT FePt COMPOSITE FILMS

Y. Liu*, J. P. Liu** and D. J. Sellmyer**

* Center for Materials Research and Analysis and Department of Mechanical Engineering,
** Center for Materials Research and Analysis and Behlen Laboratory of Physics,
University of Nebraska, Lincoln, NE 68588.

Abstract -- Multilayers of Fe and Pt were deposited by sputtering. The ratio of the thickness of Fe to Pt was adjusted such that stoichiometric FePt and Fe rich films were formed. These films were either annealed at 500°C and above, or processed by rapid thermal annealing (RTA) using a high power lamp. Both the Fe and Pt in the as-deposited films were found to be FCC structure. After heat treatment, $L1_0$ phase (hard phase) and disordered FCC phase (soft phase) were identified in Fe-rich films. Small precipitates of 3-8 nm in the matrix which has larger grains of about 50-200 nm are observed. Perfect coherent interface between the hard phase and soft phase is observed. Processing route, microstructure and properties relation will be discussed.
©1999 Acta Metallurgica Inc.

INTRODUCTION

In the Fe-Pt system several magnetic phases exist. Among these phases, Fe solid solution and Fe_3Pt are soft phases having high magnetization. The $L1_0$ type structure FePt has a layered structure in the [001] direction and a very high anisotropy of 6.6×10^7 ergs/cc [1]. High energy products from 15 MGOe to 30 MGOe have been achieved by several groups [2-4]. Recently, using multi-layer sputtering technique combined with post-annealing and rapid thermal annealing, energy products up to 50 MGOe have been achieved [5,6]. Theoretical calculations showed that when the dimension of the soft phase is smaller than two times the domain wall thickness of the hard phase, effective inter-grain coupling can be achieved [7]. In this paper we present phase identification and volume fraction measurement of the hard phase and soft phase. Their relation with magnetic properties will be discussed.

EXPERIMENTAL PROCEDURE

Multilayers of Fe and Pt were deposited by sputtering. The ratio of the thickness of Fe to Pt was adjusted such that stoichiometric FePt and Fe rich films were formed. One group of these films were then annealed at 500°C and above. Another group of films were processed by rapid thermal annealing (RTA) using a high power lamp. Magnetization loops were measured by a Micromag 2900 alternating gradient force magnetometer. Plan-view transmission electron microscopy (TEM) samples were prepared by dimpling and ion milling process. TEM study was conducted using a JEOL 2010 transmission electron microscope.

RESULT AND DISCUSSION

Figure 1 compares the selected area diffraction (SAD) patterns (a) from an as-deposited film and (b) from an annealed film. Although pure Fe at room temperature is BCC structure, both the Pt and Fe in the as-deposited Pt/Fe multi-layers have the FCC structure as shown in Figure 1 (a). The pattern of the annealed film in Figure 1 (b) can be matched to the $L1_0$ structure. A second phase has been identified by nanodiffraction [8] to be a disordered FCC phase which does not contribute to any additional lines in Figure 1 (b).

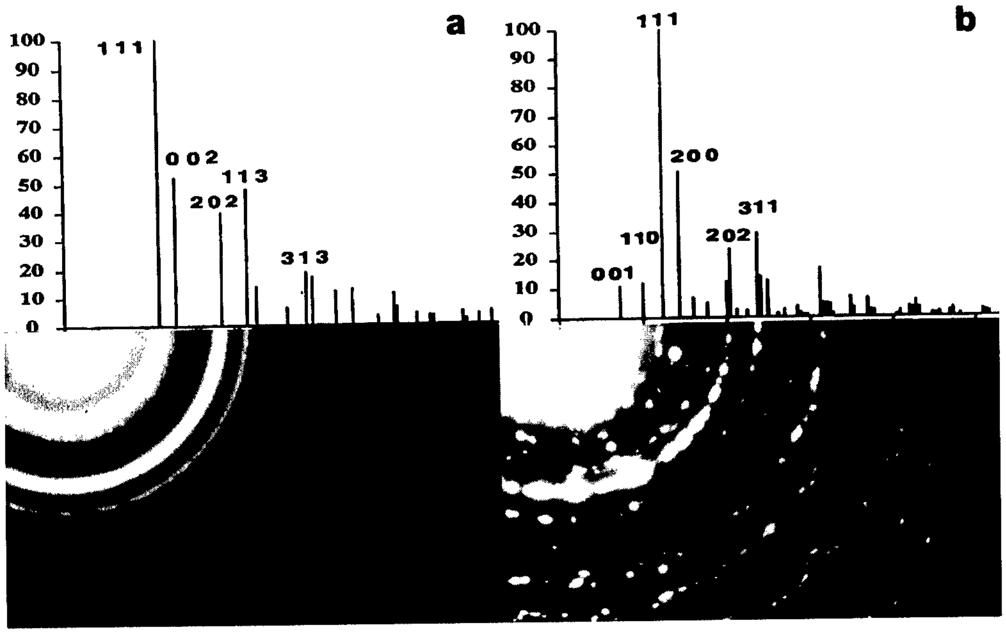

Figure 1. Comparison of SAD patterns (a) from as-deposited film, (b) from annealed film (No2 listed in Table 1).

Figure 2 (a) shows the microstructure of rapid thermal processed film (film No4 in Table 1). The soft phase has the spherical shape and is distributed in the hard phase. High resolution transmission electron microscopy (HRTEM) image in Figure 2 (b) shows that the soft phase and the hard phase have coherent interphase boundary.

The processing route, microstructure and properties relation are summarized in Table 1. Conventional heat treatment results in larger grains of both the soft phase and the hard phase in contrast to the rapid thermal processing. The volume fraction of the soft phase increases with Fe content. However, when the Fe content is close the ratio of Fe/Pt ~ 2/1, the morphology of the soft phase change from smaller spherical shape to grains with the same dimension of the hard phase.

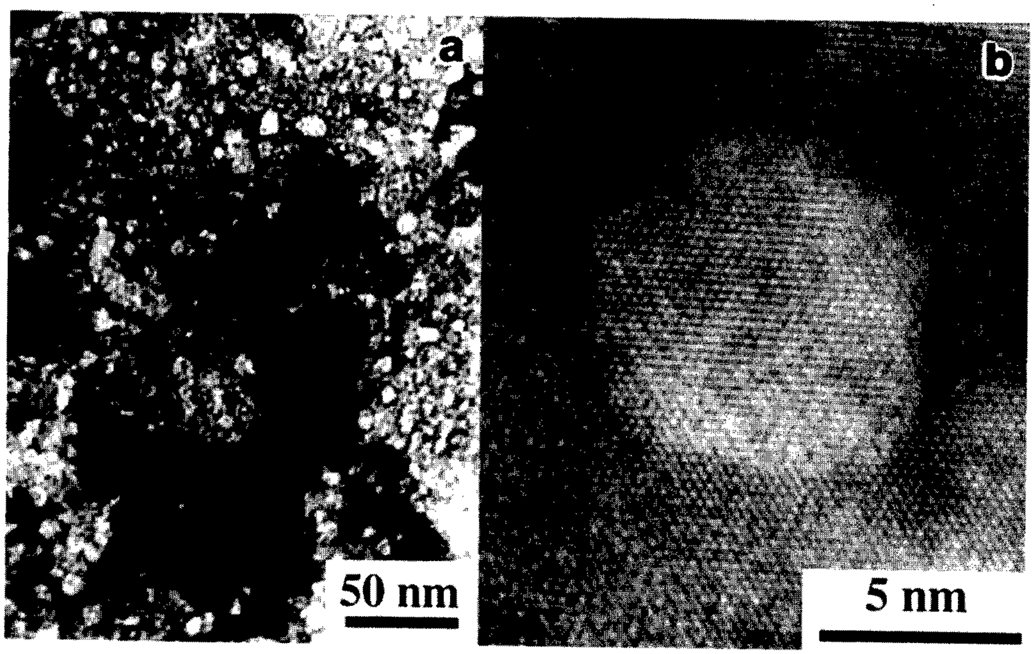

Figure 2 (a) bright field TEM image, (b) HRTEM image. The film is No4 listed in Table 1.

Table 1. Summary of processing, microstructure and magnetic properties of Fe-Pt films.

No	Processing Film configuration Nominal composition Heat treatment	Microstructure Grain size of soft phase Grain size of hard phase Volume fraction S/H	Properties Coercivity Magnetization Energy product
1	(Fe20/Pt13)x16 (Å) Fe-39.4at%Pt 700°C 0.5 hour	not observed 50-200 nm 0	19.1 kOe 1030 emu/cc emu/cc 29.7 MGOe
2	(Fe21/Pt12)x16 (Å) Fe-36.3at%Pt 700°C 0.5 hour	5-20 nm 30-150 nm 4%	15.6 kOe 1120 emu/cc 38.6 MGOe
3	(FePt35/Fe18)x12 (Å) Fe-33.0at%Pt 600°C 10 sec. 700°C 5 sec.	50-150 nm 50-150 nm 13%	11.1 kOe 1260 emu/cc 30.9 MGOe
4	(Fe21/Pt12)x16 (Å) Fe-36.3at%Pt Multi-step at 500°C	3-8 nm 50-100 nm 4%	18.5 kOe 1300 emu/cc 52.8 MGOe

It is known that in the film form several elements exhibit a different structure from the equilibrium phase. Such examples are FCC Co [9], FCC Ti [10] etc. The perfect match of the FCC Fe and Pt lattices favors the low energy state of the interface boundary.

In the equilibrium state, the two phases should be Fe_3Pt and $L1_0$ FePt. The appearance of disordered FCC Fe is associated with the as-deposited state of the film, the insufficient annealing time and the low ordering temperature of the Fe_3Pt phase.

The final morphology of the second phase in the annealed film could be affected by the initial thickness of the Fe layer and Pt layer. It is suggested that initial thinner Fe and Pt layer might facilitate finer grains of the disordered FCC Fe phase.

The grain size of the hard phase is affected by the annealing temperature. Lower annealing temperature resulted in smaller gain size of both the hard phase and the soft phase.

To increase the energy product, coercivity and magnetization must be adjusted to the optimum. Coercivity is strongly affected by the microstructure. Texture which enhance anisotropy of polycrystalline materials is preferred to increase coercivity. The magnetization can be improved by increasing the volume fraction of the soft phase while keeping the grain size of the soft phase unchanged.

CONCLUSIONS

In this paper, we investigated the relation between film composition, processing, microstructure and magnetic properties relation. Two phases: the $L1_0$ FePt phase and disordered FCC Fe phase were identified to be the hard phase and soft phase, respectively. The grain sizes of both the hard phase and soft phase can be controlled by post-thermal processing. The magnetization can be controlled by the Fe content. Maximum energy product was obtained from films with two phases the $L1_0$ phase and the disordered FCC phase generated by rapid thermal processing. Effective coupling between soft phase and hard phase is responsible for the high energy product in this alloy system.

Acknowledgment: Authors wish to thank Xueli Zhao for preparing the TEM samples. This work was performed at the CMRA Central Facility for Electron Microscopy, and supported by Department of Energy, Grant Number DE-FG-02-86ER45262,

References

1. T. Klemmer, D.Hoydick, H.Okumura, B. Zhang, and W.A. Soffa, *Scr. Metall. Mater.* (1995), **33**, 1793.
2. K. Watanabe and H.Masumoto, *J. Jpn,. Insti. Metals* (1984), 48, 930.
3. S. W. Yung, Y.H. Chang, T. J. Lin, and M.P. Hung, *J.Magn. Magn. Mater.* (1992), 116, 411.
4. M. Watanabe and M.Homma, *Jpn. J. Appl. Phys.*, Part 2, (1996), 35, L1264.
5. J. P.Liu, Y. Liu , C. Lou, Z.S. Shan and D.J.Sellmyer, *J. Appl. Phys.*,(1997), 81, 5644.
6. J. P. Liu, C.P. Luo, Y. Liu and D.J. Sellmyer, *Appl. Phys. Let.*, 1998, 72, 483.
7. R. Skomski, and J. M. D. Coey, *Phys. Rev.* B, 1993, 48, 15 812.
8. Y. Liu, J. P. Liu and D. J. Sellmyer, *Electron Microscopy 1998*, Cancun, Mexico, 2, 305.
9. D. Lesley-Pelecky et al. to be published.
10. A.F. Jankowski and M.A. Wall, *NanoStructured Materials*, 1996, 7, 89.

Pergamon

NanoStructured Materials, Vol. 12, pp. 1031–1034, 1999
Elsevier Science Ltd

0965-9773/99/$–see front matter

PII S0965-9773(99)00293-7

WC-Co-DIAMOND NANO-COMPOSITES

Rajendra K. Sadangi, Oleg A. Voronov, Bernard H. Kear*
Diamond Materials Inc., 120 Centennial Avenue, Piscataway, NJ 08854
*Dept. of Ceramic and Materials Engineering, Rutgers University, Piscataway, NJ 08855

Abstract – *Solid state sintering of WC-Co powder compacts at temperatures of 1000 –1200 °C gives a partially sintered material, in which the degree of densification increases with temperature. An important characteristic of these partially sintered materials is that the pores are interconnected in three dimensions. Furthermore, by varying the hold times at the lowest sintering temperature, where solid state diffusion predominates, the pore structure can be coarsened without significant reduction in compact dimensions. Thus materials with precisely controlled pore connectivity and scale can easily be produced. Using a gas phase infiltration technique, we have infiltrated such nanoporous structures with graphitic carbon. After infiltration, the graphite-infiltrated WC-Co preform is transformed to WC-Co-Diamond by a high pressure/high temperature treatment. The resulting superhard material has a characteristic tricontinuous structure, which may or may not be functionally graded, depending on the infiltration technique used. Preliminary results on structural characterization and wear testing of these novel triphasic superhard materials are briefly discussed. ©1999 Acta Metallurgica Inc.*

INTRODUCTION

Various types of synthetic diamond products are used industrially for rock drill bits, mining tools, machine tools, grinding wheels, wire drawing dies, bearing surfaces, and bonded abrasives. Among these applications, polycrystalline diamond compacts (PCDs) are extensively used as drag bit cutters to increase drilling performance and to lower drilling costs. PCD was first introduced in 1972 [1], and consists of a thin layer (0.5 to 1 mm) of sintered polycrystalline diamond bonded to a cemented tungsten carbide substrate. The cutter material is made by sintering diamond powders on to a WC/Co substrate in the temperature range 1500 -2000°C under 5-7 GPa pressure in a High Pressure/ High Temperature (HPHT) apparatus [1,2]. During the cooling phase of the HPHT operation, the differing coefficients of thermal expansion of the materials leave severe residual stresses in the compact. In practice, residual stresses can cause delamination when the PCD cutter is subjected to high impact forces or it can cause chipping or cracking of the cutters. In order to impart toughness to a PCD product, diamond-enhanced inserts have been developed that give greater impact resistance while retaining the wear resistance of the PCD [3,4]. This composite PCD is formed from a graded distribution of diamond crystals and particulates of cemented carbide. The powder mixture is consolidated by the HPHT process used for sintering PCD. Thus, composite layers with varying amount of diamond (100% at surface to 0% at the interior) are bonded to WC/Co

substrate. Since these transition layers create a slowly changing gradient in elastic modulus and coefficient of thermal expansion, residual stresses and spalling are greatly reduced. Such PDC-enhanced inserts [5] have been successfully used in percussion bits and hammer bits.

A variety of polycrystalline diamond-impregnated WC/Co bodies have been developed for use as wear-resistant cutting elements. In one method [6], a powder compact of WC, Co and graphite is formed by cold pressing of a blended mass of the three phases, consolidated by liquid phase sintering, and then subjected to HPHT treatment to transform the graphite into diamond. The particle size of each of the constituent phases in the consolidated material is in the range 0.3-100 microns. The volume fraction of carbon was limited to 10 vol%.

A persistent practical problem has been to uniformly mix the powder constituents prior to HPHT treatment. Typically, the WC and diamond particles experience gross separation because of their widely different densities. Ordinary mixing and blending of powders is difficult to control, especially when the particle size is < 0.1 micron. Moreover, it is important to continuously grade the diamond enhanced insert to improve the performance. We have developed a method for synthesizing a WC-Co-diamond nanocomposite containing a high volume fraction of diamond in a WC-Co matrix. Starting with available nanophase WC-Co powder, the new process [7] involves four sequential steps: (1) partial sintering of a WC-Co powder compact to develop a porous preform, which displays some rigidity and strength, (2) if necessary, machining of the sintered preform to obtain a more complex shape, (3) infiltration of the porous preform with carbon, and (4) HPHT transformation of the carbon-infiltrated WC/Co preform into a fully dense WC-Co-diamond composite.

Though different approaches can be used to infiltrate the porous material with carbon, in this study, we adopted chemical vapor infiltration (CVI). In the CVI process, the kinetics of the carbon deposition may be controlled to develop either an uniform or graded distribution of carbon throughout the porous WC-Co perform. During subsequent HPHT consolidation, the carbon-infiltrated structure transform into a triphasic WC-Co-diamond composite.

EXPERIMENTAL ASPECTS

The multilayered High Pressure Apparatus (HPA) used in this investigation consisted of two shaped anvils of tungsten carbide facing one another, and four supporting steel rings [8]. The anvils compress a container made of lithographic stone. A system of shaped rings and liners are placed around the reaction cell that contains the sample. The reaction cell consists of a graphite crucible, which serves as a heater, graphite washers, filler materials, and sample. Typical performance characteristics of HPHT are pressure of 5-8 GPa at temperatures up to 2000°C in a working volume of $\sim 1\ cm^3$.

Nanophase WC/15 wt.% Co powder from Nanodyne Inc. was uniaxially compacted into 8 mm diameter samples at pressures of 100 MPa and 300 MPa. A floating die configuration was used to minimize density gradients in the green body. The compact was placed in a graphite crucible and inductively heated to 900°C in flowing H_2 to remove surface oxides. Subsequently, the chamber was evacuated and the sample heated to sintering temperature and held for 30 minutes. A higher density compact is obtained at higher temperatures from higher green density compact.

Chemical vapor infiltration (CVI) of the porous compact was carried out in a controlled atmosphere thermal gravimetric analyzer (TGA). The sample was placed on a

platinum boat and supported by a Ni-Cr wire. Weight changes were recorded using a Cahn 1000 micro-balance. The temperature of the furnace was ramped at 15 °C/min up to 900 °C in a flowing gas mixture (100 cc/min) of H_2/CH_4, and held at this temperature for 3 hours. The samples were cooled in flowing hydrogen Figure 3 shows the effect of gas composition on carbon infiltration of the sample. As seen, below 7% CH_4, there is not enough carbon in the gas phase for infiltration into the sample. At higher concentration, the rate of carbon pick up increases. When cooled in hydrogen, carbon is removed by methane gasification reaction. So, in principle, hydrogen can be used as decarburizing gas and a combination of carbon infiltration, and removal can be used to generate various carbon profiles in a sample.

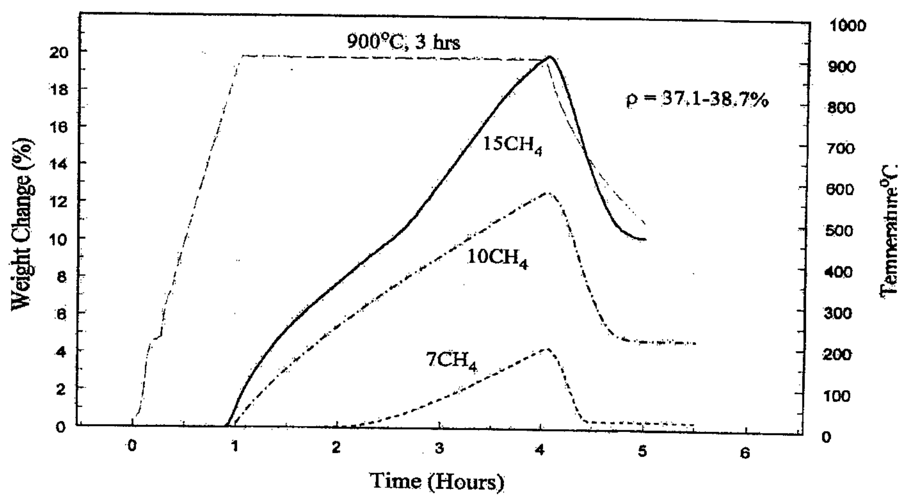

Figure 1 : The effect of gas composition on carbon infiltration in 38% dense samples.

A carbon-infiltrated sample (~ϕ 4mm x height 3mm) containing ~45 vol% carbon was placed in the reaction cell of the HPHT unit. The space between the sample and graphite crucible was packed with hexagonal BN, which acts as an insulator and pressure transmitting medium. The sample was heated in an HPHT apparatus to densify the compact and to fully transform the graphite to diamond. The formation of a relatively high volume fraction of diamond was established by Raman spectroscopy. The Raman spectra was similar in appearance to that found in a CVD-generated microcrystalline diamond film [9]. A typical SEM micrograph of a 3fractured surface, Figure 2, shows bright areas that represent mixtures of WC and Co, and much darker areas that represent diamond. Back-scattered electron imaging confirmed this phase distribution.

The samples were mechanically clamped in a tool holder and granite log tests were carried out under following conditions: feed 0.01"/rev, depth of cut 0.020". Triphasic sample containing ~ 45 vol% diamond had a G ratio (volume of rock cut/diamond wear) of 225,000. Conventional PDCs tested under similar conditions had a G ratio of 400,000.

SUMMARY

We have shown that it is possible to produce a WC-Co-Diamond nanocomposite utilizing nanophase WC-Co as the starting material. Tests have shown that ~45 vol% diamond containing WC-15% Co composite has a wear ratio of 225,000 is about half of conventional PCDs. Carbon deposition by chemical vapor infiltration can be optimized by varying the raw materials and processing conditions. Experiments are underway to synthesize different types of graded composite materials on the basis of WC-Co-diamond composites and evaluate their properties.

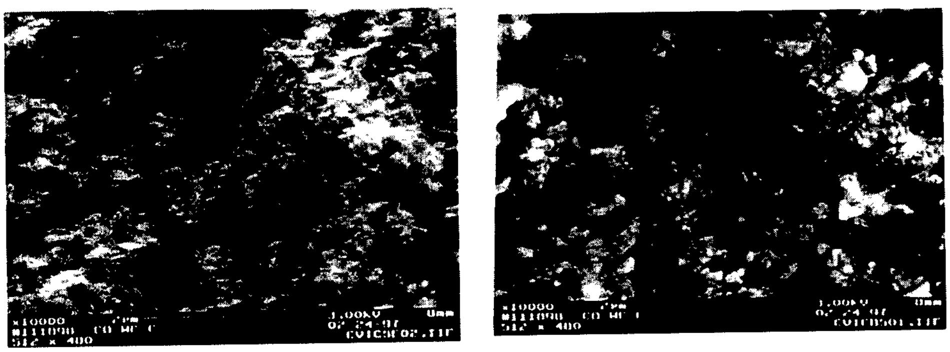

Secondary electron image　　　　Backscattered electron image

Figure 2 . SEM micrograph of fractured surface showing mixtures of WC and Co (bright areas) and diamond (darker areas).

REFERENCES

1. R. H. Wentrof, R. C. DeVries, F. P. Bundy, "Sintered superhard materials," *Science*, 208, pp 873-880 (1980)
2. L.E. Hibbs Jr., R.H. Wentrof, "Borazon and diamond compact tools" *High Temperature and High Pressures*, 6, pp 409-13 (1974)
3. D. R. Hall, "Composite polycrystalline diamond" U. S. Patent no 4,525,178 (1985)
4. D. R. Hall, M.E. Russell, H.T. Hall, Jr., "Composite Polycrystalline Diamond Compact", U.S. Patent No 4, 604, 206 (1986)
5. C.H. Reinsvold et. al., "Diamond-Enhanced hammer bits reduce cost per Foot in Arkoma and Appalachian Basins" paper, SPE 17185 presented at 1988 SPE/IADC drilling Conference, Dallas (Feb. 28 - March 2)
6. M.K. Keshavan, "Diamond Containing Cemented Metal carbide", U.S. Patent No 5, 045, 092 (1991)
7. B.H. Kear, R.K. Sadangi, L.E. McCandlish, O. A. Voronov, "Triphasic diamond composites and method for producing the same" patent pending (1997)
8. O. A. Voronov, "Diamond Ceramics Produced at High Pressure," SAIC report (1995).
9. J. R. Dennison, M. Holtz and G. Swain, "Raman Spectroscopy of Carbon Materials", *Spectroscopy*, 11(8), pp38-46, October 1996

Pergamon

NanoStructured Materials, Vol. 12, pp. 1035–1040, 1999
Elsevier Science Ltd

0965-9773/99/$–see front matter

PII S0965-9773(99)00294-9

PRACTICAL APPLICATIONS FOR ELECTRODEPOSITED NANOCRYSTALLINE MATERIALS

A. Robertson, U. Erb[1] and G. Palumbo
Micro Engineered Materials Department, Ontario Hydro Technologies, 800 Kipling Avenue, Toronto, Canada M8Z 5S4
[1]Department of Metallurgy and Materials Science, University of Toronto, Toronto, Canada M5S 3E4

Abstract *– Electrodeposition provides a cost-effective means of producing fully dense nanocrystalline (10nm-100nm avg. grain size) metals, alloys, and metal-matrix composites as coatings or free-standing forms (foil, sheet, wire, complex shapes). The electrosynthesis approach is highly adaptable to conventional industrial material processes, yielding significant material and process improvements from relatively small capital equipment and process modifications. In this paper, several examples of current and emerging commercial applications for this technology are presented. ©1999 Acta Metallurgica Inc.*

INTRODUCTION

From pioneering efforts in the late 1980's [1], the electrodeposition of nanostructures has advanced rapidly to commercial application as a result of (1) an established industrial infrastructure (i.e., electroplating and electroforming industries), (2) a relatively low cost of application whereby nanomaterials can be produced by simple modification of bath chemistries and electrical parameters used in current plating and electroforming operations, (3) the capability in a single-step process to produce metals, alloys, and metal-matrix composites in various forms (i.e., coatings, free-standing complex shapes), and most importantly (4) the ability to produce fully dense nanostructures free of extraneous porosity.

The importance of the latter cannot be overemphasized with regard to industrial application since many of the extraordinary properties previously attributed to nanostructures (e.g., reduction in elastic modulus, superplasticity in ceramics, reduction in saturation magnetization etc.), have since been demonstrated to be an artifact of residual porosity in these materials. From the outset, the fully dense nanomaterials produced by electrodeposition have displayed predictable material properties based upon their increased content of intercrystalline defects[2]. This 'predictability' in ultimate material performance has accelerated the adoption of nanomaterials by industry, whereby, such extreme grain refinement simply represents another metallurgical tool for microstructural optimization.

In this paper, an overview of some current and emerging practical applications for electrodeposited nanocrystalline materials are presented and discussed in light of the importance of property-specific grain size 'optimization' rather than grain miniaturization for its own sake.

MECHANICAL APPLICATIONS

As would be expected from Hall-Petch considerations, numerous practical applications for nanocrystalline materials are based upon opportunities for high strength coatings and free-standing structural components. The mechanical properties of nanocrystalline nickel (99.99%) with grain size of 10nm and 100nm, in comparison to conventional polycrystalline material, are shown in Table 1. In addition to remarkable increases in hardness, yield strength and ultimate tensile strength with decreasing grain size, it is interesting to note that the work hardening coefficient decreases with decreasing grain size to virtually zero at a grain size of 10nm [3]. The ductility of the material decreases with decreasing grain size from 50% elongation to failure in tension for conventional material to 15% at 100nm grain size and approximately 1% at 10nm grain size. As is also shown in this table, the fatigue performance of the 100nm material is fully consistent with that of the conventional Ni. Compared to conventional polycrystalline Ni, nanocrystalline Ni electrodeposits exhibit drastically reduced wear rates and lower coefficient of friction as determined in dry air pin-on-disc tests [4]. However, contrary to earlier measurements on nanocrystalline materials prepared by consolidation of powders [5-7] nanocrystalline nickel electrodeposits do not show significant reduction in Young's modulus. This result provides further support for earlier findings [8,9], which demonstrated that the previously reported reductions in modulus with nanomaterials produced by powder consolidation, were likely the result of high residual porosity.

The superior mechanical properties of these electrodeposited nanostructures have led to one of their first large scale industrial applications– the Electrosleeve™ process for in-situ repair of nuclear steam generator tubing [10,11]. In this application, nanocrystalline Ni (100nm) is electroformed on the inside surface of steam generator tubes to effect a complete structural repair at sites where the structural integrity of the original tube has been compromised (e.g., corrosion, stress corrosion cracking etc.). Figure 1 shows a cut-away view of an installed Electrosleeve™. The high strength and good ductility of this 100nm grain size material permits the use of a thin 'sleeve' (0.5-1mm) which minimizes the impact on fluid flow and heat transfer in the steam generator.

TABLE 1
Summary of the Mechanical Properties of Conventional and Nanocrystalline Nickel

Property	**Ni 10μm[12]**	**Ni 100nm**	**Ni 10nm**
Yield Strength, MPa (25°C)	103	690	>900
Ultimate Tensile Strength, MPa (25°C)	403	1100	>2000
Tensile Elongation, % (25°C)	50	>15	1
Elongation in Bending, % (25°C)	-	>40	-
Modulus of Elasticity, GPa (25°C)	207	214	204
Vickers Hardness, kg/mm^2	140	300	650
Work Hardening Coefficient	0.4	0.15	0.0
Fatigue Strength, MPa (10^8 cycles/air/25°C)	241	275	-
Wear Rate (dry air pin on disc), $\mu m^3/\mu m$	1330	-	7.9
Coefficient of Friction (dry air pin on disc)	0.9	-	0.5

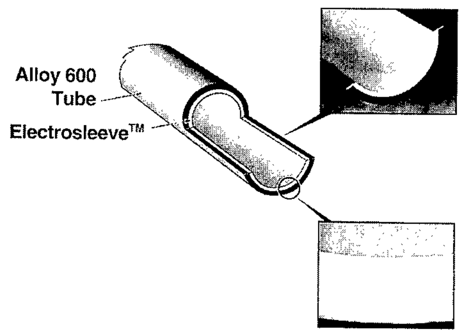

Figure 1. Cut-away view of an installed nano-Ni Electrosleeve™ on a host Alloy 600 nuclear steam generator tube.

Recent geometric models and experimental findings [13,14] have shown that nanostructured materials can also possess a high resistance to intergranular cracking processes, including creep cracking. Several emerging applications for nano-materials possessing high intergranular cracking resistance include, high cycle-life lead-acid battery (positive) grids, and shaped charge liners (Cu, Pb, Ni) for military and industrial applications (e.g., demolition, oil well penetrators etc.) (see Fig.2).

CATALYTIC AND ENERGY STORAGE APPLICATIONS

The high density of intercrystalline defects present within the bulk, and intersecting the free surface of nanostructured materials provides considerable opportunity in catalytic and hydrogen storage applications. Hydrogen transport rates and storage capacity in nanocrystalline Ni have been previously shown to be significantly enhanced over that observed in conventional material [15,16]; six to ten-fold increases in hydrogen diffusivity, and 60-fold increases in hydrogen storage capacity have been determined at room temperature. In addition, a higher electrocatalytic behaviour has been noted with regard to the hydrogen evolution reaction (HER) for alkaline water electrolysis at room temperature [16]. Several applications are being developed for the use of these materials in Nickel Metal Hydride battery systems, and as alkaline fuel cell electrodes.

MAGNETIC AND ELECTRICAL APPLICATIONS

Some of the most promising industrial applications for nanostructured materials are in the area of soft magnets for high efficiency transformers, motors etc. Anticipated reductions in magnetocrystalline anisotropy and coercivity as grain size is reduced below the mean thickness of a magnetic domain wall in conventional materials, have generated considerable development activity in this area. However, many previous studies reported a large reduction in saturation magnetization (up to 40%) with decreasing grain size in nanomaterials produced by powder consolidation [7, 17,18]. In contrast, this detrimental effect has not been observed in nanocrystalline materials produced by electrodeposition [19].

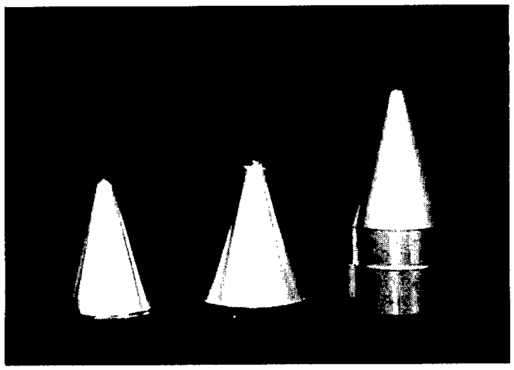

Figure 2. Nanocrystalline -Cu (left), and -Ni (middle) shaped charge liners, electroformed on a Ti mandrel (right).

Theoretical investigation and modeling [20] have shown that grain size should have little effect on magnetic moment; chemical disorder introduced by alloying or impurity elements being a more significant contributor to reductions in saturation magnetization. These electrodeposited nanocrystals can thus provide for soft magnets possessing a low coercivity without compromise of saturation magnetization.

As depicted in Figure 3, the industrial use of these high performance ferromagnetic materials in motor, transformer and shielding applications has been accelerated by the recent development of a drum plating process for cost-effectively producing large quantities of sheet, foil, and wire in nanocrystalline form.

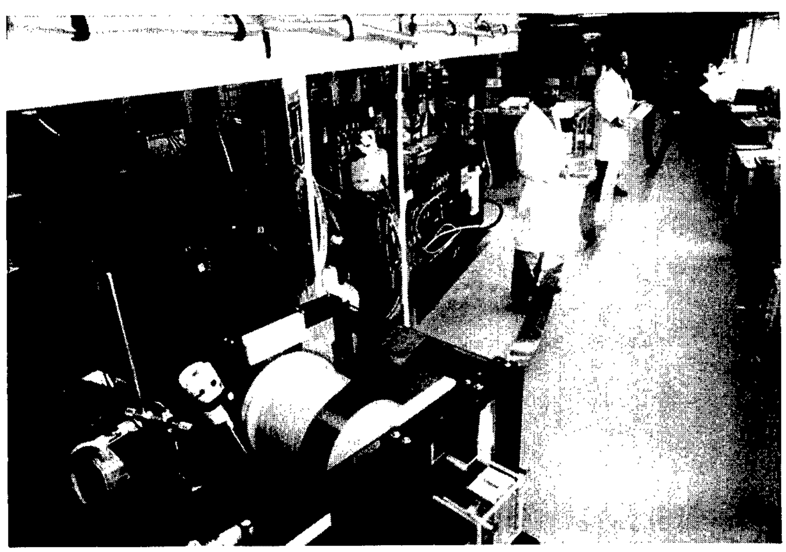

Figure 3. Prototype drum-plater for producing nanocrystalline sheet, foil and wire products.

Another major application for drum-plated nanocrystalline material (as in Fig. 3) is in the production of copper foil for printed circuit boards, where enhanced etching rates and reduced line spacing/pitch can be achieved by reducing grain size. Figure 4 shows a cross-sectional field emission scanning electron micrograph of nanocrystalline Cu foil produced for this application. Grain size has been optimized on the basis of calculated electrical resistivity for nanocrystalline Cu [21] as summarized in Figure 5. A 50nm to 100nm grain size provides optimum etchability while maintaining good electrical conductivity.

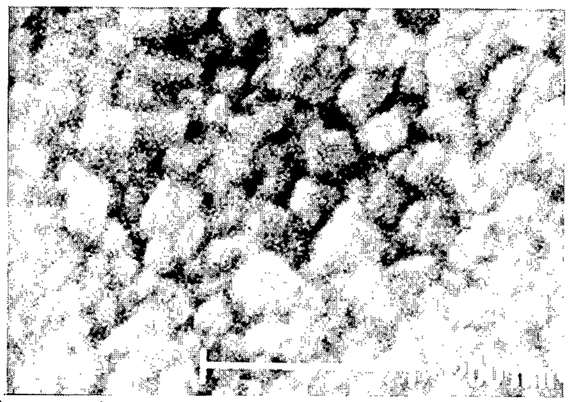

Figure 4. Field emission scanning electron micrograph of electrodeposited nanocrystalline Cu foil having an average grain size of 50nm.

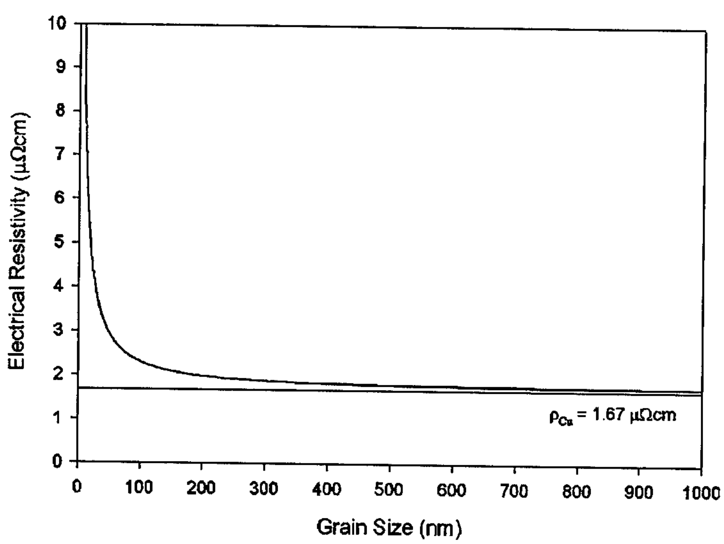

Figure 5. Calculated room temperature electrical resistivity of pure Cu as a function of grain size [21].

SUMMARY

Several current and emerging applications for electrodeposited nanocrystalline materials have been presented. Property-specific optimization of grain size promises to yield new high performance structural and functional materials for a variety of products and industrial applications.

ACKNOWLEDGMENTS

Financial support from Ontario Hydro and the Natural Sciences and Engineering Research Council of Canada is gratefully acknowledged.

REFERENCES

1. Erb, U., El-Sherik, A. M., Palumbo, G. and Aust, K. T., Nanostr. Mat., 2 (1993) 383
2. Palumbo, G., Thorpe, S. J. and Aust, K. T., Scripta Metall. et Mater., 24 (1990) 1347
3. Wang, N., Wang, Z., Aust, K. T. and Erb, U., Mat. Sci. Eng., A237(1997) 150
4. El-Sherik, A. M. and Erb, U., in "Nickel-Cobalt 97-Vol.IV, Applications and Materials Performance, F. N. Smith et al. (eds.), The Metallurgical Society of CIM, Montreal (1997) 257
5. Nieman, G. W., Weertman, J. R. and Siegel, R. W., Scripta Metall. et Mater., 24 (1990) 145
6. Nieman, G. W., Weertman, J. R. and Siegel, R. W., J.Mat.Res., 6 (1991) 1012.
7. Gleiter, H., Progr. Mater. Sci., 33, (1989) 224
8. Krstic, V., Erb, U. and Palumbo, G., Scripta Metall. et Mater., 29 (1993) 1501
9. Zugic, R., Szpunar, B., Krstic, V. and Erb, U., Phil. Mag., A75 (1997) 1041
10. Palumbo, G., Gonzalez, F., Brennenstuhl, A. M., Erb, U., Shmayda, W. and Lichtenberger, P. C., Nanostr. Mat., 9 (1997) 737
11. Gonzalez, F., Brennenstuhl, A.M., Palumbo, G., Erb, U. and Lichtenberger, P.C., Mat. Sci. Forum, 225-227 (1996) 831
12. ASM Metals Handbook, ASM International, Metals Park, OH, Vol. 2, p. 437 (1993).
13. Palumbo, G., King, P.J., Aust, K.T., Erb, U. and Lichtenberger, P.C., Scripta Metall., 25 (1991) 1775
14. Palumbo, G., Lehockey, E.M., Lin, P., Erb, U. and Aust, K.T., Mat. Res. Soc. Symp.Proc. 458 (1997) 273
15. Palumbo, G., Doyle, D. M., El-Sherik, A. M., Erb, U. and Aust, K. T., Scripta Metall. et Mater., 25 (1991) 679
16. Doyle, D. M., Palumbo, G., Aust, K. T., El-Sherik, A. M. and Erb, U., Acta Metall. et Mater., 43 (1995) 3027
17. Gong, W., Li, H., Zhao, Z. and Chen, J., J. Appl. Phys., 69 (1991) 5119.
18. Krill, C.E., Merzoug, F., Krauss, W and Birringer, R., Nanostr. Mat. 9 (1997) 455
19. Aus, M. J., Szpunar, B., El-Sherik, A. M., Erb, U., Palumbo, G. and Aust, K.T., Scripta Metall. et Mater., 27 (1992) 1639
20. Szpunar, B., Erb, U., Palumbo, G., Aust, K. T. and Lewis, L. J., Phys, Rev. B, 53 (1996) 5547
21. McCrea, J., M.A.Sc. Thesis (in progress) Department of Metallurgy and Materials Science, Universiy of Toronto (1998)

Pergamon

NanoStructured Materials, Vol. 12, pp. 1041–1044, 1999
Elsevier Science Ltd

0965-9773/99/$–see front matter

PII S0965-9773(99)00295-0

STABILITY OF ALUMINA CERAMICS BONDED WITH NANOSCALED ALUMINA POWDER

R.J. Hellmig, J.-F. Castagnet, and H. Ferkel
Institut für Werkstoffkunde und Werkstofftechnik, Technical University Clausthal,
Agricolastr. 6, 38678 Clausthal-Zellerfeld, Germany

Abstract -- *Nanoscaled alumina particles were employed for bonding of commerical coarse-grained corundum ceramics. The nanopowder was generated by ablation of solid corundum samples with the pulsed radiation of a Nd:YAG-laser and subsequent condensation of the vapor in a controlled atmosphere. Some of the nanopowder was sandwiched between corundum discs followed by uniaxially hot pressing of the assembly in vacuum at various pressures up to 80 MPa and temperatures up to 1300°C. Some of these specimens were additionally sintered in air at 1500°C without load. In order to determine the structure and the strength of the sample joints HR-SEM investigations and four-point bending tests were carried out.*

INTRODUCTION

In 1993, Cross and Mayo (1) bonded commercial zirconia-3 mol% yttria samples using slurry or presintered Y-TZP interlayers as a joint. They concluded their method as impractical for any but the simplest joint geometry, because of the strong shrinkage void formation with slurry interlayers or the need of preformation of complex sintered interlayers. Three years later, in our laboratories corundum ceramics were successfully bonded with a thin layer of dry alumina nanopowder without formation of large shrinkage voids (2). In particular no coarsening of voids into pores larger than a micron was observed. Furthermore it was found that the weakly agglomerated laser-generated nanoparticles can adapt to surface corrugations of the interface and can easily slide into caves or other voids in the sandwiched powder during compression. However further studies were necessary to test the strength of these joints. The results of these investigations are presented in this work.

EXPERIMENTAL

The nanoscaled powders were generated by ablation of commercial available corundum rods (purity 99.7% Al_2O_3) with the pulsed radiation of a 1 kW Nd:YAG-laser (Rofin Sinar, RSY 1000P) and subsequent condensation of the vapor in a controlled atmosphere. A detailed description of the powder production is given elsewhere (3).

TABLE 1
Preparation Parameters

specimen	pressure	temperature	post-sintered
1	80 MPa	1200°C	yes
2	40 MPa	1200°C	yes
2a	40 MPa	1200°C	no
3	80 MPa	1300°C	yes
3a	80 MPa	1300°C	no
4	40 MPa	1300°C	yes
4a	40 MPa	1300°C	no

The alumina nanopowders are of spherical shape, are crystallized in the γ-phase and their size distribution can be characterized by a logarithmic normal distribution with a median diameter of 14 nm and a geometric standard deviation of 1.6. The unpolished surfaces of two cylindrical corundum discs (ALSINT 99.7, Haldenwanger, α-alumina with a purity of 99.7%) with a diameter of 20 mm were cleaned with ethanol. Between these discs 0.3 g nanoscaled alumina powder was sandwiched and compressed by hand. These sandwiches were placed between the graphite pistons of a hydraulic uniaxially hot press (KCE, HPW 150/400) which allows a maximum load of 100 kN and a maximum process temperature of 1600°C in a vacuum of 10^{-1} Pa.

The bonding experiments were carried out at different temperatures (1200°C and 1300°C) and uniaxial pressures (40 MPa and 80 MPa) to investigate the influence of these parameters on the strength and structure of the joint. Some specimens were additionally sintered after bonding at 1500°C without load in air for 5 hours to investigate the grain growth and accompanied shrinkage void formation in the interlayer. Informations on the specimen preparations are summarized in Table 1.

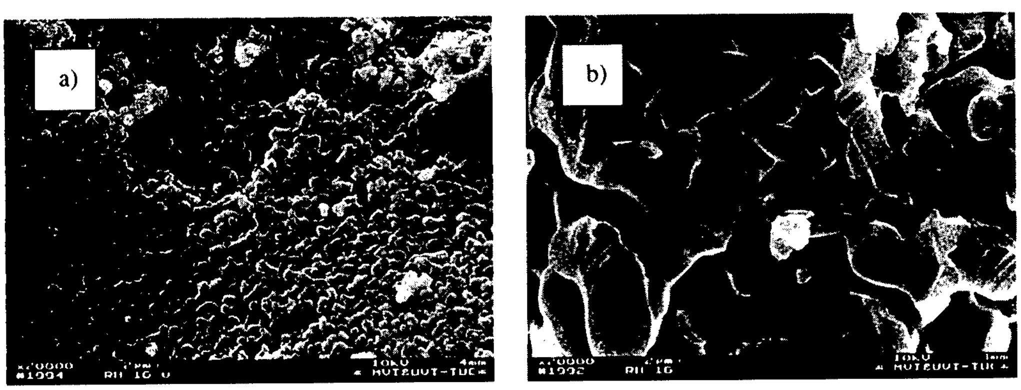

Figure 1: a) HR-SEM picture of the nanostructure in the joint observed directly after hot pressing (sample 3a), b) microstructure after post-sintering (sample 3)

After hot pressing the samples were cut perpendicular to the interface into two pieces to investigate the joint directly and after further sintering. The strength of the joint was examined by four-point bending tests according to the European norm EN 843-1. For the bending tests beams were cut from the bonded samples with the joint being in the middle of the beams. In order to study the microstructure of the joints, high resolution scanning electron microscopy (HR-SEM) investigations were carried out. The density of the material in the interface was determined from the measured volume of the joints and the known weight of the sandwiched nanopowder and was related to the theoretical density of corundum. For comparison beams were also machined from the employed corundum material. The bending strength of these beams was used as a standard.

RESULTS AND DISCUSSION

Figure 1 a) shows a HR-SEM micrograph of the fracture surface of the joint (specimen 3a) tested directly after hot pressing. A homogeneous structure can be observed, the average grain diameter is about 90 nm. No large pores can be seen. This fine structured interlayer has a density of about 0.7 related to the density of ALSINT 99.7. The bonded samples show almost the same bending strengths as the standard bending beams made from the coarse-grained corundum which can be characterized by abending strength of 280 +- 52 Nmm^{-2} averaged from 10 different specimens. It should be mentioned that the bonded specimens not necessarily failed in the joint. Which means that the measured bending strength of specimens which did not fail in the joint is less than the real strength of the joint. These values will lower the average bending strength at the joint from the statistical point of view. As also can be concluded from the table the strength of the joints produced at different conditions without post-sintering is similar for all specimens. Therefore bonding at 40 MPa and 1200°C is already sufficient to achieve a strong connection.

Post-sintering at 1500°C induces no significant increase of the density in the joint (Tab.2). As can be seen in the SEM micrograph of Fig.1 b) (specimen 3), post-sintering changes as expected the structure of the joint drastically. The nanostructure observed directly after hot pressing (Fig.1 a)) has changed into a microscaled porous structure (Fig.1 b)) which looks

TABLE 2
Results

specimen	density	bending strength	number of tests	average grain size
ALSINT 99.7	1	280 +- 52 Nmm^{-2}	10	-
1	0.80	315 +- 46 Nmm^{-2}	3	-
2	0.67	190 +- 31 Nmm^{-2}	5	1.5 μm
2a	0.66	204 +- 57 Nmm^{-2}	2	-
3	0.73	220 +- 62 Nmm^{-2}	3	1.5 μm
3a	0.70	281 +- 35 Nmm^{-2}	3	90 nm
4	0.77	184 +- 84 Nmm^{-2}	2	1.5 μm
4a	0.76	224 Nmm^{-2}	1	100 nm

similar to the structure of sintered γ-alumina nanopowder investigated recently by Wu et al.(4).

In order to achieve a more dense interlayer at the same temperature und pressure conditions, α-alumina nanopowder would probably be a better candidate to form a dense interlayer. However there is still a lack on the production of α-alumina nanoparticles in the size range lower than 20 nm which do not exhibit strong agglomerates or aggregates.

After post-sintering the bending strength of the specimens slightly decreases. According to Figure 1 b) pore sizes larger than 1 μm are present in the post-sintered joint. No coarsening of voids during post-sintering at 1500°C into cavities larger than a few microns can be seen.

Cracks in all joints can be easily blunted by pores. A propagating crack will cleave sinternecks between neighboring grains and its length will increase stepwise by the effective diameter of the corresponding pores. In the nanostructured interlayer the increase of the crack length per pore will be about three orders of magnitude smaller than in the coarse-grained interlayer. However the energy required to cleave a sinterneck in the micrograined material is much higher than in the case of a nanosized sinterneck. On the other hand in the latter case much more sinternecks have to be cleaved to obtain a crack of similar length. Therefore, both considerations have to be taken into account to interpret the measured strength of the joints. However it is conceivable that cracks of a critical length as potential source for material failure are easier formed in the post-sintered layer as can be concluded from the experimental results.

SUMMARY

In summary, the application of laser-generated alumina nanopowders for diffusion bonding of corundum ceramic was demonstrated. The strength of the ceramic joints prepared at different processing conditions were investigated by four-point bending tests and were found to be similar as the bending strength of solid corundum samples nearly independent of the here employed bonding parameters. Bonding of the specimens at 1200°C for one hour at a pressure of 40 MPa was already sufficient to achieve a bond of high strength. When the bonded ceramics were additionally sintered without pressure assistance at 1500°C for 5 hours in air a slight decrease in the bond strength was observed which could be attributed to the formation of microscaled pores in the joint caused by sintering and the γ- to α-phase transition.

REFERENCES

1. Cross, T.H. and Mayo, M.J., Nanostruct. Mater. **3**, 163 (1993)
2. Ferkel, H. and Riehemann, W., Nanostruct. Mater. **7**, 835 (1996)
3. Ferkel, H., Naser, J., and Riehemann, W., Nanostruct. Mater. **8**, 457 (1997)
4. Wu, S.J., de Jonghe, L.C., and Rahaman, M.N., J. Am. Ceram. Soc. **79**, 2207 (1996)

Pergamon

NanoStructured Materials, Vol. 12, pp. 1045–1048, 1999
Elsevier Science Ltd

0965-9773/99/$–see front matter

PII S0965-9773(99)00296-2

HYDROGEN GAS EVOLUTION FROM ALUMINA NANOPARTICLES DISPERSED IN WATER IRRADIATED WITH γ-RAY

T. A. Yamamoto, S. Seino, M. Katsura, K. Okitsu*, R. Oshima† and Y. Nagata†

Department of Nuclear Engineering, Osaka University,
2-1 Yamadaoka, Suita, Osaka, 565-0781 Japan,
*)Department of Materials Science and Engineering, Nagasaki University,
1-14 Bunkyo, Nagasaki 852, Japan,
†)Research Institute for Advanced Science and Technology, Osaka Prefectural University,
Gakuen, Sakai, Osaka 599-8570, Japan.

Abstract -- *Hydrogen gas evolution induced by γ-ray irradiation of nanoparticles dispersed in aqueous solution was studied by measuring hydrogen yields from TiO_2, α- and γ-Al_2O_3 nanoparticles. Hydrogen gas was detected by a gas chromatograph after an irradiation with ^{60}Co γ-ray of the sample solution in a closed vial at room temperature. TiO_2 nanoparticles, a highly photo-catalysis mainly in anatase structure with average diameter of 21 nm, was found to have a relatively low evolution yield, about three times of the back ground hydrogen evolution due to the water radiolysis, while the α- and γ-Al_2O_3 showed a much higher yield, 7 - 8 times of the background, depending on the total dose and dose rate of the γ-ray.*

INTRODUCTION

The target of this work from the technological viewpoint is to make full use of the γ-rays emitted from the spent nuclear fuel assembly or the high level waste given by the fuel reprocessing plant. These γ-rays' energy is now being consumed just in warming up the shielding materials surrounding the nuclear wastes which should be stored for several dozens of years before the geological disposal. A system, which exploits the γ-rays' energy for such a long period on the basis of a simple and stable principle, is desired from viewpoints not only of the energy saving but also of the public acceptance of the total nuclear energy system. The γ-ray is substantially a photon as is the ultraviolet ray or the visible light on which much efforts of the photocatalysis research have been made for utilizing the solar energy by employing semiconductor particles as the catalysis inducing a useful chemical reaction. A similar kind of catalysis effect would be expected, although the γ-ray possesses an energy, from hundreds keV to ca. 1 MeV, far higher than that of the ultraviolet or the visible photons of a few eV. It was indeed reported that semiconductor particles dispersed in water evolve hydrogen gas when irradiated with γ-rays (1). In this work, nanoparticles of alumina usually classified as insulator were submitted to a similar irradiation test in addition to titania which is well known as the highly photocatalysis. Effects of a noble metal, Pt, Pd or Au, which is supported on the

particles by a sonochemical reaction were as well examined.

EXPERIMENTAL

Two type of alumina materials were studied, α-Al_2O_3 in trigonal and γ-Al_2O_3 in cubic spinel structure. The former was purchased as a polishing material with a nominal particle size of 200 nm, the later was supplied from Asahi Chemical Ltd. with a nominal size of 14 nm determined by the BET method. Titania material with a nominal size of 21 nm was supplied by Aerosil Nippon Ltd. (P25), which is almost in anatase structure with a few % of the rutile. Surfaces of these particles were modified with a noble metal, platinum, gold or palladium, by the ultrasonic chemistry method (2) in which these particles were sonicated in an aqueous solution dissolving K_2PtCl_4, $NaAuCl_4$ or $PdCl_2$, respectively. The amount of the noble metal supported was 5wt% of the base nanoparticles. In Figs. 1 and 2, TEM micrographs of the γ-alumina and titania nanoparticles are shown, both of which have been surface modified by sonication in platinum- and palladium-containing solutions, respectively. Note that the γ-alumina material is composed of coalescing primary grains smaller than the nominal size, while titania is in definite grains on which finer palladium grains are visible.

These nanoparticle samples were dispersed in distilled water in a Pyrex-made vial having gas lines through which argon gas purged the air in the free space in the vial and dissolved in the water in advance to γ-ray irradiation. The particles of 0.25 g were dispersed in 75 ml of water. Closing the valves on the gas lines, γ-ray irradiation at room temperature was performed with a ^{60}Co γ-ray source. Dose rate of the γ-ray was set between 0.45 and 3.2 kGy/h, and irradiation time was 18 h. During the irradiation the dispersion has been stirred by a magnetic stirrer. After the irradiation, hydrogen gas, evolved and confined in the free space in the vial, was sampled and analyzed by a gaschromatograph. The amount of hydrogen gas soluble in water was negligible in comparison with the amount detected. Thus detected hydrogen was evaluated by comparing with a background hydrogen level, which is due to the water radiolysis caused by the γ-rays.

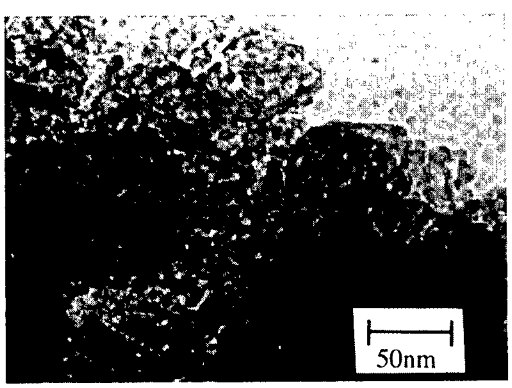

Fig.1 TEM micrograph of γ-Al_2O_3 nanoparticles sonicated with Pd.

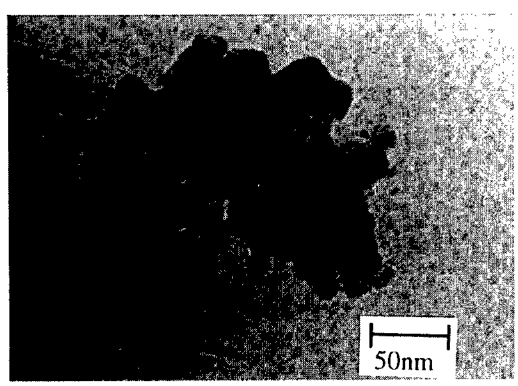

Fig.2 TEM micrograph of TiO_2 nanoparticles sonicated with. Pt.

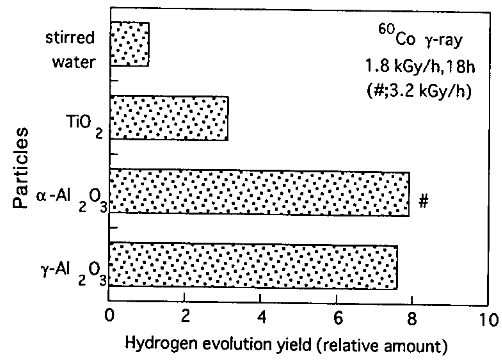

Fig.3 Hydrogen gas evolution yields induced by γ-ray irradiation of titania and alumina nanoparticles dispersed in water, which were normalized to that due to water radiolysis.

RESULTS AND DISCUSSION

Hydrogen gas evolution yields measured with the as-received nanoparticles without any surface modification are shown in Fig.3, in which each value is plotted as a relative value to that measured only with water stirred in a vial placed together with other sample vials. It is noticed that titania and both kinds of alumina have certain effects of enhancement in hydrogen gas evolution, a kind of catalysis induced by the γ-ray. Although titania has been regarded as the best photocatalysis for UV photons, presently observed response to the γ-ray was not so remarkable; only about three times of the water radiolysis, and rather lower than those of both the alumina, 7 - 8 times of the radiolysis. It was confirmed that hydrogen was not evolved only by the dispersion of the alumina particles without γ-rays. The amount of evolved hydrogen gas increased with the total dose irradiated and with the amount of the γ-alumina dispersed in the water, as shown in Table 1. Thus, it is no longer in doubt that both the alumina have a certain catalysis. This γ-ray catalysis effects of the alumina are the first finding, although that of titania has been reported (1). The maximum hydrogen yield in the Fig.3 corresponds to 1.8×10^3 H_2-molecules an incident primary γ-photon. Alumina is a commercially common, cheap and widely used material, but no attention from the photocatalytic research has been paid on it since it is classified usually as an insulator because of its bandgap, ca. 8eV, too wide to be activated by visible or ultraviolet photons. However, energy of the γ-photons is high enough to activate it and create hole-electron pairs even in the "insulator".

Table 1
Hydrogen gas evolution yield at different amount of γ-alumina and at different dose rate, as values normalized to the background

Amount of γ-alumina (mg)	γ-ray dose rate (kGy/h) 1.8	0.45
0	1.0	1.0
50	2.6	1.4
250	7.6	2.3

Table 2

Hydrogen gas evolution yields from surface modified nanoparticles, which were normalized to those without the modification.

Particles	Surface modification None	Pt	Au	Pd	Dose rate (kGy/h)
Titania	1.0	2.2	2.7	----	1.8
α-alumina	1.0	0.71	0.0	----	3.2
γ-alumina	1.0	0.0	0.38	0.0	3.2

Table 2 shows results on the irradiation experiments with the nanoparticles surface modified with the noble metal, in which hydrogen evolution yields are normalized to those without the surface modification. It is clearly shown that the present surface modification has enhanced the γ-ray catalysis of titania, but on the contrary, suppressed those of both kinds of alumina. Especially, in some cases of modified alumina, hydrogen gas evolved was too little to be detected. Hydrogen dissolved into water and/or the noble metal can not quantitatively account for the hydrogen quenching. These facts implies that some kind of reaction occurred to prevent the reduction of hydrogen ion or to get hydrogen gas back to the ion. But there was no definite tendency of combination of metal and kind of alumina giving rise to the quench.

The enhancement found in the titania particles which was surface modified with the noble metal is consistent with results of the photocatalysis studies (3) and even with a study on the γ-ray catalysis (1). Therefore, the response of the dispersed titania to the γ-ray may be explained partially by the mechanism of the photocatalysis or its extrapolation which involves hole-electron pairs. The present results on the alumina are, however, unique and have no counterpart to be compared with. But, it is supposed that the γ-ray catalysis of the alumina would involve mechanisms considerably different from that of the photocatalysis. It is impossible to discuss what it is now and beyond the scope of this paper.

To summarize this work, we irradiated α- and γ-alumina and titania nanoparticles dispersed in water with ^{60}Co γ-rays, and found that both the kinds of alumina enhanced hydrogen generation induced by the irradiation much more than titania. We also found that surface modification with noble metal enhance the catalysis of titania while suppressing those of α- and γ-alumina.

REFERENCES

1. Wada,Y., Kawaguchi,K. and Myochin,M., *Progress in Nuclear Energy*, Suppl. 29, 251 (1995).
2. Okitsu,K., Mizukoshi,Y., Bandow,H., Maeda,Y., Yamamoto,T. and Nagata,Y., *Ultrasonic Sonochemistry*, 3, S249 (1996).
3. Kanno, H., Yamamoto, Y. and Harada, H., *Chem. Phys. Lett.*, 121, 245 (1985).

Pergamon

NanoStructured Materials, Vol. 12, pp. 1049–1052, 1999
Elsevier Science Ltd

0965-9773/99/$–see front matter

PII S0965-9773(99)00297-4

EVALUATION OF MECHANICAL PROPERTIES IN NANOMETER SCALE USING AFM-BASED NANOINDENTATION TESTER

K. Miyahara, N. Nagashima, T. Ohmura, and S. Matsuoka
National Research Institute for Metals
1-2-1 Sengen, Tsukuba-shi, Ibaraki 305-0047, Japan

Abstract *– A nanoindentation hardness tester was developed on the basis of an atomic force microscope (AFM) to evaluate mechanical properties of microstructures. Not only the force – penetration depth curves but the topographic images can be obtained by this tester. One of new features of the developed tester was modified lever design in order to accommodate the Berkovich indenter into the middle of the lever. Furthermore, a piezo-actuator was added to control the applied force and the vertical displacement of the lever was monitored by a laser displacement detector. The diamond tip works as both an AFM tip and indenter.*

Force – penetration depth curves represent mechanical properties of specimens. However, because of indentation size effect, the hardness values obtained by nanoindentation testers are usually greater than the bulk hardness. In this paper several metallic single crystals were used as standard specimens and an empirical model for calculating Vickers hardness from force – penetration depth curves is proposed. Finally, mechanical properties of ferrite in pearlitic steels were obtained using the instrument. ©1999 Acta Metallurgica Inc.

INTRODUCTION

The evaluation of mechanical properties in microstructures becomes much more important as a result of increasing interests in nanostructured materials, semiconductor devices, and structural materials. Nanoindentation hardness testers, which have been developed and studied intensively nowadays (1,2,3), can provide such information. In this paper a new AFM-based nanoindentation tester is introduced and a simple method to evaluate Vickers hardness from force – penetration depth curves is proposed.

AFM-BASED NANOINDENTATION TESTER

Figure 1 shows a diagram of the AFM-based nanoindentation tester and its special lever developed by the authors. The difference from a conventional atomic force microscope is as follows: (a) use of a special lever held on both sides, (b) addition of a piezo-actuator for force control, and (c) measurement of lever displacement instead of its deflection. Further details of this instrument are described elsewhere (1). It should be noted that both force – penetration

depth curves and surface topographic images are easily available with this system.

Indentation experiments were carried out under force control mode. Loading and unloading rate was 10 μN/s for all experiments. AFM images were obtained before and after indentation test in order to choose flat location for hardness test and observe indentation shape. A Berkovich diamond indenter with an apical angle of 60° was used, to obtain sharp AFM images.

In hardness tests, the indentation size effect (ISE) is often observed, i.e., the hardness values obtained by nanoindentation testers are usually greater than the bulk hardness. In order to apply this instrument to material research, it is desirable to measure an 'absolute' hardness value, which is independent of experimental conditions such as curvature radius of indenters and free from the ISE. Empirical methods are necessary for this purpose because whether the ISE is a genuine size effect or not is still under discussion (2) and to estimate effects of indenter roundness and specimen surface analytically and quantitatively is still not easy when penetration depth is as low as 100 nm. Oliver et al. (3) proposed a new technique for determining hardness and elastic modulus by correcting contact area to reduce the indentation size effect. In this work, a simple empirical method for evaluating hardness with reduced indentation size effect is proposed and described in the following section.

EXPERIMENTAL RESULTS AND DISCUSSION

The (100) surfaces of single crystals of tungsten, molybdenum, iron and nickel were used as test specimens. These specimens were polished mechanically and then electrolytically. They are used as standard specimens for determining hardness. The basic idea of hardness determination is to establish the relationship between macroscopic hardness and force – penetration depth curves in nanoindentation. The single crystals were used since they have no grain boundaries or precipitates and therefore the same mechanical properties would be expected in both nanoindentation and macroscopic hardness tests.

Figure 2 shows force – penetration depth curves of the single crystals. It can be seen from Fig. 2 that at the same force level, the depth of indentation decreases as the degree of Vickers hardness increases. This means relative hardness can be compared in any case. Figure 3 shows

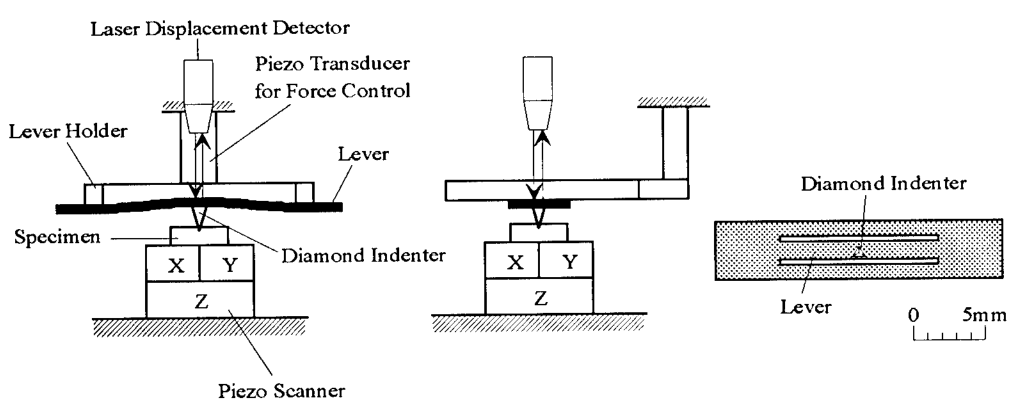

Fig. 1 AFM-based nanoindentation tester and its special lever.

the relationship between force necessary to achieve a certain penetration depth and Vickers hardness obtained by a conventional Vickers hardness tester at 100 gf. Using standard curve fitting technique, a power function model was found to be the best one to describe the relationship. This power function is shown in the following equation:

$$HV = [a(h)\,F]^{\,n} \qquad (h > 100) \qquad [1]$$

where HV is Vickers hardness, F is force in μN, and h is penetration depth in nm. $a(h)$ is h-dependent and n is a constant and $n = 1.214$ in this case. Plotting $F(h)/HV^{1/n}$ against h further and again using curve-fitting for various type of functions, the best fitted one was found as:

$$F(h)\,/\,HV^{1/n} = p\,(h + q)^{2} \qquad (h > 100) \qquad [2]$$

where $p = 5.6634 \times 10^{-3}$ and $q = 122.83$. Subsequently, Eq. [2] can be rewritten in terms of HV as follows:

$$\begin{aligned} HV &= [F\,/\,\{p\,(h + q)^2\}]^{\,n} \\ &= [F\,/\,\{5.6634 \times 10^{-3}\,(h + 122.83)^2\}]^{\,1.214} \qquad (h > 100) \qquad [3] \end{aligned}$$

It should be noted that these parameters may be valid only for the current indenter and their physical meanings are not clear yet. However, a possible hypothesis is that q represents the truncation length of indenter and p and n are related to hardness conversion between 60° indenter and Vickers indenter. Further experiments and discussion will be necessary.

A pearlitic steel was chosen as a test material. The pearlitic steel was etched by 1% nitric acid and 99% alcohol. The microstructure of the pearlitic steel, i.e., ferrite grains and cementite lamellae, is in submicron scale as shown in the AFM image in Fig. 4. The mechanical properties of the microstructure are much of interest in order to establish a model in micromechanics.

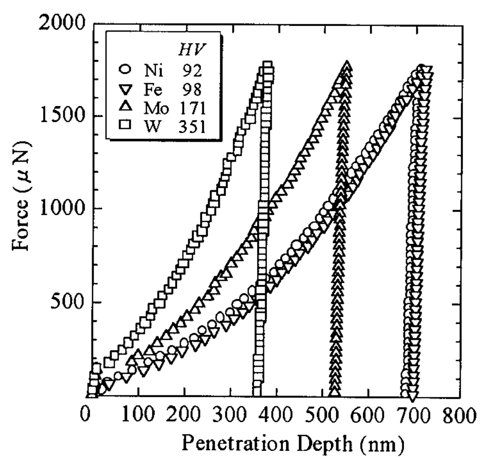

Fig. 2 Force - penetration depth curves of single crystals.

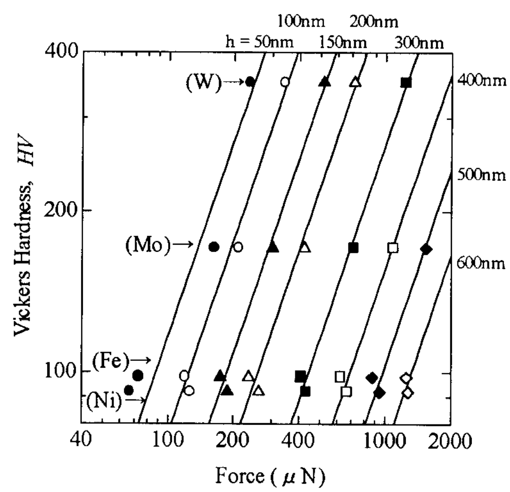

Fig. 3 Relationship between force and Vickers hardness of single crystals

Fig. 4 AFM image of an indentation on ferrite in pearlitic steels

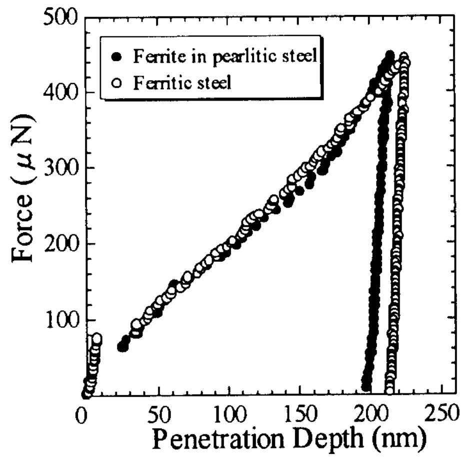

Fig. 5 Force – penetration depth curves of ferrite.

Figure 4 illustrates an indentation on a ferrite grain. Because of imaging capability of the instrument, it is easy to choose a specific location for nanoindentation tests even if a specimen is heterogeneous. Figure 5 shows force – penetration depth curves for both pearlitic and ferritic steels. Both curves showed almost the same properties. A slight difference was observed at 200 nm, which might be due to cementite lamellae. From Fig. 5 and Eq. [3], Vickers hardness is estimated as 160 - 170 and it is greater than 98, which is the value of the iron single crystal. This difference may be due to the effect of dislocations and chemical composition. It's worth noting that there is a discontinuation in force – penetration depth curves shown in Fig. 5. This behavior can be observed in Fig. 2, too. It is considered as a yield point and consistent with the results reported previously (3,4,5).

CONCLUSION

An AFM-based nanoindentation tester was successfully developed, which allows both force – penetration depth curves and AFM topographic images to be obtained. A simple empirical method to evaluate Vickers hardness from force curves was proposed and mechanical properties of pearlitic and ferritic steels were obtained, using the developed tester and proposed method.

REFERENCES

(1) Miyahara, K., Matsuoka, S., Nagashima, N. and Mishima, S., *Trans. Jpn. Soc. Mech. Eng. A*, 61 (1995), pp. 2321-2328.

(2) Tabor, D., *Phil. Mag. A*, 74 (1996), pp. 1207-1212.

(3) Oliver, W. C. and Pharr, G. M., *J. Mater. Res.*, 7 (1992), pp. 1564-1583.

(4) Gerberich, W. W., Nelson, J. C., Lilleodden, E. T., Anderson, P. and Wyrobek, J. T., *Acta metal.*, 44 (1996), pp. 3538-3598.

(5) Miyahara, K., Matsuoka, S and Nagashima, N., *Trans. Jpn. Soc. Mech. Eng. A*, 63 (1997), pp. 2220-2227.

Pergamon

NanoStructured Materials, Vol. 12, pp. 1053–1058, 1999
Elsevier Science Ltd

0965-9773/99/$–see front matter

PII S0965-9773(99)00298-6

ENCAPSULATED IRON, COBALT AND NICKEL NANOCRYSTALS; EFFECT OF COATING MATERIAL (Mg, MgF_2) ON MAGNETIC PROPERTIES

Dajie Zhang, Kenneth J. Klabunde and Christopher M. Sorensen
Departments of Chemistry and Physics, Kansas State University, Manhattan, Kansas 66506
George C. Hadjipanayis
Department of Physics, University of Delaware, Newark, Delaware 19716

Abstract- *Nanometer sized core/shell particles of [Mg]Fe, [MgF_2]Fe, Co, and Ni, where Mg or MgF_2 are the shell materials, have been prepared by a low temperature matrix method. Phase segregation was accomplished within each individual particle by controlled heating to yield the completely oxide free core/shell particles, which were sealed in glass or quartz tubes and studied by SQUID magnetometry. For [Mg]Fe samples with very small Fe crystallites, enhanced anisotropy energies were observed. For core/shell particles, saturation magnetization [Ms] values for Fe, Co, and Ni were found to be both size and temperature dependent. Indeed, M(T) behavior is richly dependent on size in the nanometer range, and on the type of surface interface. Quantitative assessment and discussion of Bloch exponent and Bloch constant variations as iron crystallite size change are discussed.*

INTRODUCTION

The chemistry and physics of nanoscale magnetic particles has been and continues to be an area of great interest [1-4]. From a fundamental perspective the study of nanoparticles sheds light on how bulk properties transform to atomic as size decreases. When nanoscale, the fraction of surface material becomes dominant, hence bulk properties may either give way to surface properties and/or be significantly perturbed by the surface. Moreover, the large surface fraction opens the opportunity for manipulation of properties via interfacial interactions.

In this paper we present experimental data for the magnetization temperature dependence of nanoscale iron particles. Our synthetic technique [5-7] has allowed us to systematically vary the iron particle size. Furthermore, our particles are interfaced with two different materials, hence we study the important interfacial interaction as well. In general for temperatures well below the Curie temperature, the magnetization temperature dependence arises due to spin wave fluctuations as first described by Bloch who found [8]

$$M(T) = M(0)\,(1-BT^b). \tag{1}$$

In Eq.(1), M(T) is the temperature dependent magnetization, B is the Bloch constant

and b is the Bloch exponent. The exponent is given by b = 3/2 for a three dimensional system and has been well verified [8].

The first "non-bulk" theoretical studies of spin waves and M(T) were carried out by Mills and Maradudin [9-11] using calculations and Wildpaner and coworkers [12,13] using simulations. Mills and Maradudin considered surfaces and found the Bloch exponent remained b =3/2 as in the bulk, and $B_{surf} = 2B_{bulk}$. The simulations considered particles of various sizes and found stronger temperature dependencies with decreasing size but did not fit the results to Eq. (1). Furthermore, the spin excitations were not homogenous throughout the particle. More recently, Hendriksen et al.[14] considered the spin wave spectrum of particles by solving the Heisenberg Hamiltonian. Again the excitations were a function of radial position in the particles, and the overall result was a prediction that the exponent b should increase above the bulk value of 3/2 inversely proportional to the particle size.

Experimental investigations of M(T) for nanoparticles yield a mixed story. Pierce et al. [15] studied the magnetization of macroscopic surfaces and found results consistent with Mills and Maradudin. Linderoth et al. [16] followed up their calculations [14] with measurement on Fe-C particles with a diameter of 3.1 nm and found b = 1.9 in qualitative agreement with their theory. Xiao and Chen [17] looked at iron embedded in SiO_2 at ~ 50% volume fraction. The particle size was 2-3 nm. They found b = 3/2 with $B_s \simeq 10B_b$. In previous work involving $MnFe_2O_4$ particles [18], we found b in the range 1.5 to 1.9 for sizes in the range 5 nm to 15 nm. Thus no coherent story is told by the few experiments available, and there is no adequate match with theory.

RESULTS

The core/shell particles were prepared by the Solvated Metal Atom Dispersion (SMAD) method, which involves codeposition of vapors of metal and shell material (Mg or MgF_2) with excess hydrocarbon, followed by warming and heat treatments, see Fig. 1 [6,7].

X-ray diffraction measurements showed the characteristic diffraction pattern of α–Fe for both the as prepared and annealed samples. No evidence for oxides of iron was seen corroborating the air stability of the iron cores of the samples. The breadth of the primary diffraction line of iron near $2\theta = 45^\circ$ was used with the Scherrer formula [19] to estimate the iron crystallite size. Transmission electron microscopy showed roughly spherical iron particles immersed in a matrix which was Mg and MgO for the [Mg]Fe samples or MgF_2 for the [MgF_2]Fe samples.

The SQUID magnetometer was used for magnetic measurements. The saturation magnetization was determined by $H^{-1} \rightarrow 0$ extrapolation using fields of $\underline{H} \leq \underline{.55T}$. Results are shown in Figs. 2 and 3. Figure 3 shows a significant magnetization quench for the [MgF_2]Fe samples, more so for smaller particles. We believe this quench is due to an electron donation from the MgF_2 coating into the unfilled minority d-band of the iron, and a more detailed discussion of this effect will be given in another paper. Regardless of this quench (or lack of it in the [Mg]Fe samples) Figs. 2 and 3 both show increasing temperatures dependencies of Ms with decreasing particle size. In fact, the concave upward dependence of

Figure 1. Schematic of the nano-particle synthesis scheme by the SMAD method.

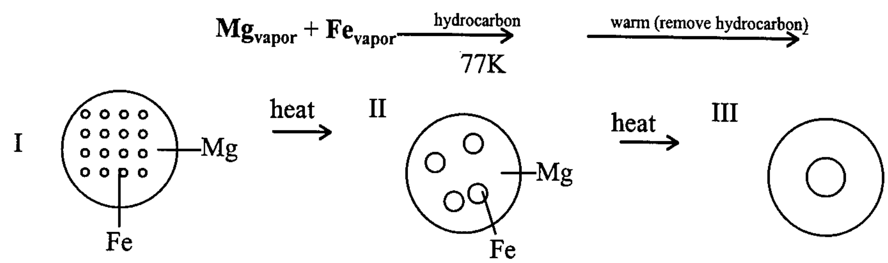

Stage	Temperature
I	-196°C to 25 °C
II	25 °C to 200 °C
III	200 °C to 450 °C

Figure 2. Temperature dependence of magnetization of [Mg]Fe Particles

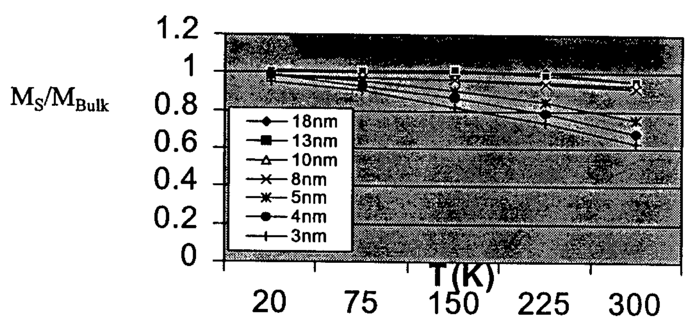

Figure 3. Temperature dependence of magnetization of $[MgF_2]Fe$ Particles

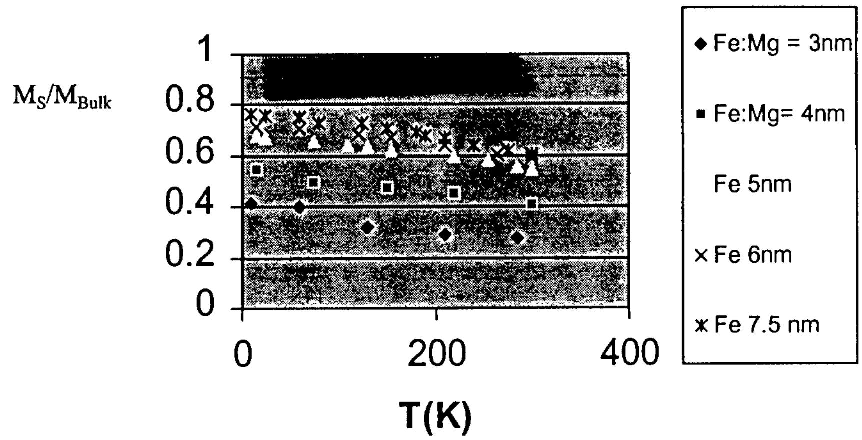

Ms vs. T in Fig. 3 for the dia. = 3nm $[MgF_2]Fe$ sample indicates a Bloch exponent b<1. It is these qualitative observations that represent the main result of this paper, and which we now quantify.

The form of Bloch's Law, Eq.(1), implies that the magnetization depression M(0)-M(T) is a power law with T. Thus a double logarithmic graph of these quantities will yield straight lines, if Bloch's law holds, the slopes of which are the Bloch exponent b and with intercepts related to BM(0). The observed data all fall on the lines to imply Bloch's law holds for our nanoparticles. Again, qualitative comparison of the figures for the two samples shows differences implying that interface as well as size (and magnetic material) is important in determining the M(T) behavior.

Linear fits of Eq.(1) to the data yield the Bloch parameters b and B. Both data sets (for Mg and MgF_2 shell materials) approach the known bulk value for iron as size increases. For all but our largest particles (18 nm) the Bloch constant is significantly greater than the bulk values, increasing by as much as two orders of magnitude. Considering Bloch constants for the two smallest sizes, 3 and 4 nm, for the $[MgF_2]Fe$ system, these sizes yield Bloch constants of $B(3\text{ nm}) = 5\times10^{-2}$ and $B(4\text{nm}) = 2\times10^{-3}$, which are significantly greater than for the corresponding sizes in the [Mg]Fe system.

DISCUSSION AND CONCLUSION

Our results may be summarized as follows: 1)nanoscale particles obey the form of

Bloch's law as written in Eq.(1). 2). With the decreasing size, the Bloch exponent falls from the bulk value of b =3/2 to smaller values. 3) With decreasing size the Bloch constant rises from the bulk values by orders of magnitude. 4) The chemistry of the interface is important in determining the size dependent properties of M(T).

We reviewed previous work on the behavior of M(T) for reduced dimension systems in the Introduction. The qualitative theoretical expectation is that the reduced coordination at the surface will cause the spins at the surface to be more susceptible to thermal excitation which leads to larger magnetization temperature dependencies. This qualitative expectation is borne out by our data. Since reduced coordination is a factor, it follows that the nature of the coordination is also important, and this is also supported by the fact that the [Mg]Fe and [MgF_2]Fe systems show different dependencies of the Bloch parameters with size. Beyond these qualitative comparisons, no quantitative agreement can be made either with theory or past experiment. However, we can conclude that MgF_2 donates electron density to the core Fe crystallite more intensely than Mg. This may be due to a ligand effect where fluoride strongly binds and donates to the iron d-orbital system.

In conclusion it appears that M(T) behavior is richly dependent on size in the nanometer range, and on the type of interface. Despite this complexity, the form of Bloch's law continues to hold. Future work to unravel these dependencies must systematically vary all three parameters.

REFERENCES

1. Magnetic Properties of Fine Particles, edited by J.L. Dormann and D. Fioranni (North-Holland, Amsterdam, 1992).
2. Nanophase Materials, edited by G.C. Hadjipanayis and R.W. Siegel (Kluwer,Dordrecht, 1994)
3. G.C.Hadjipanayis, K.J. Klabunde, and C.M. Sorensen in Nanomaterials: Synthesis, Properties and Applications, edited by A.S. Edelstein and R.C. Commarata (Institute of Physics, Bristol, 1996).
4. D.L. Leslie-Pelecky and R.D. Rieke, Chem. Mater. 8, 1770 (1996).
5. K.J. Klabunde, Free Atoms, Clusters, and Nanoscale Particles (Academic, San Diego, 1994).
6. D. Zhang, G. Glavee, K.J. Klabunde, G.C. Hadjipanayis, and C.M. Sorensen, High Temp. Mater. Sci. 36, 93 (1996).
7. D.Zhang, K.J. Klabunde, C.M. Sorensen, and G.C. Hadjipanaysis, High Temp. Mater, Sci. 36, 135 (1996).
8. B.D. Cullity, in *Introduction to Magnetic Materials* (Addison-Wesley, New York, 1972).
9. D.L. Mills and A.A. Maradudin, J. Phys. Chem. Solids, 28, 1855 (1967).
10. D.L. Mills, Comments Solid State Phys. 4, 28 (1971).
11. D.L. Mills, Comments Solid State Phys. 4, 95 (1972).

12. K. Binder, H. Rauch, and V. Wildpaner, H. Phys. Chem. Solids, 31, 391 (1970).
13. V. Wildpaner, Z. Physik 270, 215 (1974).
14. P.V. Hendriksen, S.Linderoth, and P.A. Lindgard, Phys. Rev.B48, 7259 (1993).
15. D.T. Pierce, R.J. Celotta, J. Unguris, and H.C. Siegmann, Phys. Rev. B26, 2566 (1982).
16. S. Linderoth, L. Balcells, A. Laborta, J. Tejada, P.V. Hendriksen, and S.A. Sethi, J. Mag. Mag. Mater. 124, 269 (1993).
17. G. Xiao and C.L. Chien, J. Appl. Phys. 61, 3308 (1987).
18. J.P. Chen., C.M. Sorensen, K.J. Klabunde, G.C. Hadjipanayis, E. Devlin and A. Kostikas, Phys. Rev. B54, 9288 (1996).
19. B.D. Cullity, Elements of X-Ray Diffraction (Addison-Wesley, New York, 1978).

Pergamon

NanoStructured Materials, Vol. 12, pp. 1059–1062, 1999
Elsevier Science Ltd

0965-9773/99/$–see front matter

PII S0965-9773(99)00299-8

POSITRON ANNIHILATION STUDY OF NANOCRYSTALLINE IRON

D. Segers[1], S. Van Petegem[1], J. F. Löffler[2], H. Van Swygenhoven[2], W. Wagner[2], C. Dauwe[1]

[1]RUG, Department of Subatomic and Radiation Physics, NUMAT, Proeftuinstraat 86, B-9000 Gent, Belgium

[2]Paul Scherrer Institute, CH-5232 Villigen PSI, Switzerland

Abstract *– Positron lifetime measurements on different nanocrystalline iron samples show that the microstructure, with respect to the inherent free volumes in the samples, can be determined. Three distinct defect types can be detected: i) a vacancy-like defect in the interface, ii) a microvoid at the intersection of interfaces and iii) larger free volumes (missing grains) where the annihilation of ortho-positronium is observed. The effect of the crystallite size and preparation conditions of the samples are discussed. ©1999 Acta Metallurgica Inc.*

INTRODUCTION

Positron annihilation is an ideal tool to investigate the microstructure of materials. In iron the positron lifetime varies from the bulk value τ_b =106 ps in defect-free regions to τ_{1V} = 175 ps (1) for the mono-vacancy lifetime up to ~500 ps in multi-vacancy clusters (2). Positrons trapped in even larger cavities can form positronium atoms (Ps), in both the para- (p-Ps) and the ortho-state (o-Ps). The o-Ps gives rise to a long lifetime of the order of nanoseconds.

Schaefer and Würschum (3,4) performed lifetime measurements on nanocrystalline iron and proposed a scheme for analysis based on four possible states of the positron: i) the free positron state (τ_f) ii) a trapped state into a vacancy-like defect in the interface (τ_1) iii) a trapped state into a vacancy cluster at the intersection of interfaces (τ_2) and iv) a state in large free volumes (τ_3) such as missing grains. Similar results were also reported for nanocrystalline Cu and Pd (5)

EXPERIMENTAL

Positron lifetime measurements were carried out with a standard fast-fast lifetime spectrometer with a resolution (FWHM) of 225 ps. The measured lifetime spectra contained at least 5×10^6 counts. They were analyzed with the multi-component pogram LT by Kansy (6).

As a positron source, $^{22}NaCl$ of about 10 μCi was sealed between two kapton foils with a thickness of 7.5 μm, which has to be surrounded by two identical samples in the so called

sandwich configuration. The thickness of the samples varies between 0.15 and 0.43 mm, thick enough to stop all the positrons.

The samples were produced by inert-gas condensation and consolidation in-situ under high vacuum. The characteristics of the samples are summarized in table 1. Unfortunately, the sample processing for the eight samples was different. However we choose sample pairs (table 1: A1+A2, B1+B2, C1+C2, D1+D2) with almost identical grain sizes as determined by the SANS and XRD mean coherence diameter (table 1: D_{SANS} and D_{XRD}).

DISCUSSION

The results of the multi-component analysis, after correction for annihilation in the kapton foils, are summarized in table 2. For the samples A, B and C all the obtained lifetime components are longer than the bulk positron lifetime τ_b in iron (106 ps). For sample D the shortest lifetime τ_f is smaller than τ_b.

In samples A, B and C the crystallite size is much smaller than the positron diffusion length $L_+ \approx 100$ nm measured in crystalline bulk metals (7). This means that in those samples all the positrons thermalized in the crystallites will end up at the traps outside the crystallites and saturation trapping occurs.

Comparing the samples A, B and C, sample A is the only set prepared at room temperature. In sample A the measured lifetime τ_1 is longer than the mono-vacancy lifetime τ_{1V} in iron, whereas for the samples B and C the lifetime τ_1 is shorter than τ_{1V}. We can conclude that in sample A the vacancy-like defects are larger than a mono-vacancy, while in the samples B and C the defects are smaller than a mono-vacancy. This behaviour of τ_1 is inconsistent with the statements of reference (3) and (4) which claims that open spaces smaller than a mono-vacancy are non-effective positron traps. Our measurements clearly show that those open volumes effectively trap positrons. The measured lifetimes τ_2 in the three samples are comparable. The value $\tau_2 \approx 430$ ps corresponds to a microvoid containing about 26

TABLE 1

Characteristics Of The Different Samples

Sample Name	Consolidation Parameters	Sample Processing	Relative Density	D_{SANS} [nm]	D_{XRD} [nm]
A1	2 GPa, RT, 5h	a.p.	n.d.	15	12
A2	2 GPa, RT, 5h	a.p.	n.d.	11	11
B1	2 GPa, RT, 5h	+ ann. 100°C	0.88	15	18
B2	2 GPa, 100°C, 5h	w.c.	0.87	18	21
C1	1.5 GPa, 200°C, 5h	+ ann. 200°C	0.93	63	58
C2	1.5 GPa, 200°C, 5h	+ ann. 300°C	0.94	85	72
D1	1.5 GPa, 200°C, 5h	+ ann. 550°C	0.96	>85	>100
D2	1.5 GPa, 200°C, 14h	+ ann. 400°C	0.94	>85	100

a.p. = as prepared, w.c.= warm compacted, n.d.=not determined

TABLE 2

Summary Of The Multi-component Analysis Results Of The Positron Lifetime Spectra Shown In Figure 1

Sample Name	τ_f (ps)	τ_1 (ps)	τ_2 (ps)	τ_3 (ps)	τ_3' (ps)	I_f (%)	I_1 (%)	I_2 (%)	I_3 (%)	I_4 (%)
A1+A2		193 ± 3	417 ± 9	994 ± 40			48 ± 1	45 ± 1	7 ± 1	
B1+B2		161 ± 1	447 ± 2	1154 ± 14	5491 ± 60		49.5 ± 0.1	43.6 ± 0.1	4.9 ± 0.1	2.0 ± 0.1
C1+C2		157 ± 1	424 ± 3	867 ± 13			70.8 ± 0.2	26.1 ± 0.1	3.1 ± 0.2	
D1+D2	54 ± 1	164 ± 3	369 ± 1	1108 ± 7		24 ± 1	57.8 ± 0.1	16.8 ± 0.1	1.4 ± 0.1	

vacancies (2).

The lifetime spectrum of sample B shows an extra very long component. It could only be analysed with four components, where both τ_3 and τ_3' are to be ascribed to the annihilation of o-Ps from larger free volumes. Normally, positronium cannot exist in metals, because the electron density is much too high. However when the positron is trapped into a very large cavity, the electron density seen by the positron is low enough so that an isolated positron-electron atomic system, called positronium (Ps) can be formed. The natural lifetimes of the two possible states, p-Ps and o-Ps, are respectively 124 ps and 142 ns. In the cavity the o-Ps lifetime is shortened to a few nanoseconds due to frequent collisions of the o-Ps with the inner walls of the free volume.

Although samples B1 and B2 have the same crystallite size, two different o-Ps lifetimes (τ_3 and τ_3') appear. In analogy with the results of the sets A, C and D where only one long lifetime τ_3 is measured, we assume that each sample B1 and B2 gives rise to only one long lifetime (τ_3 or τ_3') and that samples B1 and B2 having the same crystallite sizes (as determined by D_{XRD} and D_{SANS}) have different concentrations and sizes of Ps-trapping holes. So in disagreement with the results of (3) and (4) we do not interpret the results as being a consequence of the presence of a broad lifetime distribution. This is also a strong indication that the sample preparation (consolidation and processing) has a different influence on grain size and free volume.

In sample D, where the crystallite size is of the same order of the positron diffusion length, a very short lifetime $\tau_f = 54$ ps $< \tau_b$ is observed. This is consistent with the trapping model (8, 9). It is known that, for unsaturated trapping of positrons, a number of lifetime components appear, where the shortest is given by $\tau_f = \left(\frac{1}{\tau_b} + \sum_i \kappa_i C_i \right)^{-1}$, with κ_i and C_i respectively the trapping rates and concentration for all possible trapping centres. Whether trapping is saturated or not, the longer lived components ($\tau_i > \tau_b$) are the defect trapped lifetimes. τ_1 is the lifetime of the positrons trapped at vacancy-like defects in the interfaces (smaller than a mono-vacancy), τ_2 is the lifetime in the microvoids, containing about 15 vacancies (2) and τ_3 is again ascribed to the annihilation of o-Ps in larger free volumes. Here

the microvoid lifetime τ_2 is smaller than in the samples A, B and C, indicating that due to crystallite growth (annealing at 400°C and 550°C see table 1) shrinkage of the microvoids is observed.

In order to elucidate more clearly the effects of the different thermal treatments, each sample is being measured individually (10).

CONCLUSIONS

In this work positron lifetime results are presented on nanocrystalline iron samples, not specially prepared for positron annihilation studies. From the measurements, it can be concluded that, in contradiction with the results of reference (3) and (4) : i) open volumes smaller than a mono-vacancy can indeed act as an effective positron trap in n-Fe, and ii) the o-ps lifetime is not distributed according to a very broad lifetime distribution.

It has also been demonstrated that : i) the sample preparation has a different influence on grain size and free volume distribution and ii) that in samples where the grain size is larger than 85 nm effects of delocalized positron states (no saturation trapping) are seen.

The model as proposed in reference (3) and (4), where three different positron trapping states are considered, adequately explains the experimental results for positron localisation in n-Fe.

ACKNOWLEDGEMENTS

This research is supported by the Belgian Federal Government through the office of the prime minister program Interuniversity Attraction Pole IUAP P4/10 and by the Flemish Government program FWO G0006-96.

REFERENCES

1. Vehanen, A., Hautojärvi, P., Johansson, J., Yli-Kauppila, J. and Moser, P., Phys. Rev. B25, 762, 1982
2. Puska, M.J. and Nieminen, R.M., J. Phys. F 13, 333, 1983
3. Schaefer, H.E. and Würschum, R., Phys. Lett. A119, 370, 1987
4. Schaefer, H.E., Würschum, Birringer, R. and Gleiter, H., Phys. Rev. B38, 9545, 1988
5. Würschum, R., Scheytt, M. and Schaefer, H.E., phys. Sta. Sol. (a) 102, 119, 1987
6. Kansy, J., Nucl. Instr. & Meth. 374, 235, 1996
9. Mills, A.P. and Wilson, R.J., Phys. Rev. A26, 490, 1982
8. Bergersen, B. and Stott, M.J., Sol. St. Comm. 7, 1203,1969
9. Connors, D.C. and West, R.N., Phys. Lett. 30A, 24, 1969
10. Van Petegem, S., Segers, D., Löffler, J.F., Van Swygenhoven, H., Wagner, W., Dauwe, C., to be published

Pergamon

NanoStructured Materials, Vol. 12, pp. 1063–1069, 1999
Elsevier Science Ltd

0965-9773/99/$–see front matter

PII S0965-9773(99)00300-1

SYNTHESIS OF MESOPOROUS MATERIALS BASED ON TITANIUM(IV)OXIDE AND TITANIUM NITRIDE

T.V. Anuradha and S. Ranganathan
Department of Metallurgy
Indian Institute of Science, Bangalore - 560 012

Abstract -- *Nanoparticles of titania were obtained by the controlled hydrolysis of $Ti(i\text{-}OC_3H_7)_4$ in the reverse micelles of dodecylamine derived from dodecylamine-isopropanol-water solution (water/oil microemulsion).The mesolamellar phase based on titanium nitride (TiN) was obtained by first decomposing TiN atleast partially using the 1:1 solution of acid mixture (HF and HNO_3 in the ratio of 9:1) in water and then templating onto the cationic surfactant namely, cetyltrimethylammoniumbromide (abbreviated as CTAB) at 80^OC. The synthesis of mesolamellar phase based on TiN involves the charge matched templating approach following the counter-ion mediated pathway. The samples thus obtained were characterized by small angle x-ray diffraction using Cuk_α radiation, scanning electron microscopy and transmission electron microscopy, which indicated some satisfactory results.* ©1999 Acta Metallurgica Inc.

INTRODUCTION

'Meso' is a Greek word which means "in between". These materials have their pore size in the range 20 - 100 A°. They are characterized by their high surface area. Three gms of this material contains as much surface area as a football field. These materials are of very great interest in catalysis because of their large and uniform pore sizes. They are also important because the regular pore structure can serve as support for conductive and magnetic materials, leading to quantum wires for smart electronic devices. Mesoporous materials based on aluminosilicate (MCM-41) were first reported by Mobil in the year 1992. Only recently, this class of materials has been extended to include transition metal oxides (1 – 2). These materials can be synthesized using the template based approach.

The important steps involve in the synthesis of mesoporous materials are as follows:

1. Addition of inorganic analogue to the template.
2. Interaction between the inorganic analogue and the template to result in the formation of composite arrays with structures like hexagonal, lamellar and cubic.
3. Destruction of the template by either heat treatment or solvent extraction.

The methods for the synthesis of mesoporous materials are as follows:

(A) Ligand-assisted templating approach (*involving covalent bond*)
(B) Charge-matched templating approach (*involving couloumbic forces*)
(C) Neutral templating approach (*involving hydrogen bond*)
Thus, basically all the above methods differ from one another in step 2 of the synthesis.

EXPERIMENTAL, RESULTS & DISCUSSION

Mesoporous titania:

We initially attempted to synthesize the mesostructures of titania from dodecylamine and titanium isopropoxide (ligand-assisted templating approach) - (1 to 10), but this was found to result in non-mesoporous and nearly amorphous titania (as confirmed by XRD studies (Fig.1(a) & (b)) with a spherical morphology as shown by SEM studies (Fig.2(a)). Further characterization has been carried out using TEM (Fig.2(b)) wherein it has been observed that the TiO_2 particles aggregated into sols with sizes varying from 50 nm to even 1 μm, eventually forming gelatinous precipitates (11 to 13). We are assuming that the nano particles of TiO_2 are formed by the controlled hydrolyis of titanium isopropoxide in the reverse micelles of dodecylamine in dodecylamine-isopropanol-water solution (water/oil emulsion). There are earlier reports that TiO_2 particles with diameters less than 100 A^{o} can be produced by the controlled hydrolyis of $Ti(i\text{-}OC_3H_7)_4$ in reverse micelles produced in an aerosol OT - hexane - H_2O solution (water/oil emulsion) - (13). In this case, the order of the addition of the reactant materials is found to vary the particle morphology from sphere to something else as indicated by SEM studies (Fig.4), but still the titania obtained here is also amorphous in nature (as confirmed by XRD (Fig.3(a) & (b)) and it is seen here that by changing the order of the addition of the reactant materials, the size of the particle can also be changed (experiment.2). The qualitative and quantitative analysis of the material thus obtained is carried out using X-ray Photoelectron Spectroscopy (XPS) (14 & 15) which showed the Ti - $2p_{3/2}$ signal at 464.872 eV & O - 1s signal at 539.872 eV respectively. Upon the ejection of the photoelectron , the surface of the sample assumes positive charge which therefore affects the K.E. of the ejected photoelectron which gets reflected on its high B.E. Thus the above signal positions have to to be corrected with respect to the C-1s signal to bring them back to their original position. The final peak positions are typical to that of TiO_2. The quantitative analysis of the sample thus obtained indicated the oxygen content to be 64.3%.

Five millilitres of titanium isopropoxide, 1g of dodecylamine, 1ml of isopropanol and 10ml of water were taken. In experiment.1, titanium isopropoxide and isopropanol were added to dodecylamine to result in the pale yellow colored slurry to which 10ml of water was added which was then aged at RT for 18 hours and then it was filtered and dried. The surfactant was best removed by 1:1 of EtOH and HCl mixture. The titania thus obtained was amorphous with a spherical morphology even after its heat treatment at 100^{o}C for 3 days, as indicated by XRD studies.

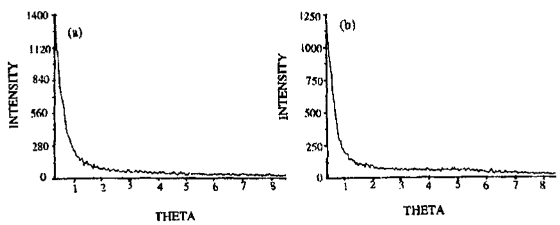

Fig.1 Representative small angle x-ray powder diffraction pattern of titania (a) as obtained (b) after heat treatment (experiment.1)

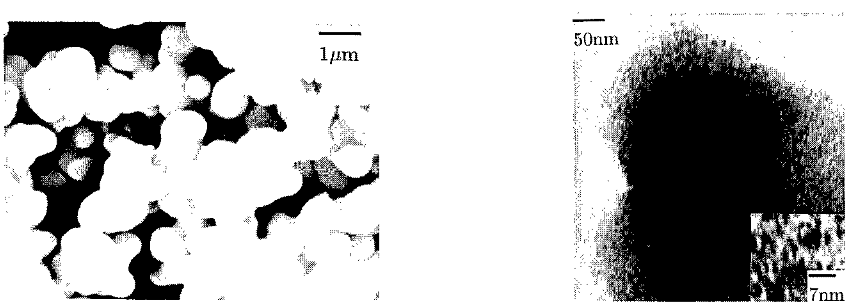

Fig.2 Representative (a) SEM micrograph and (b) TEM micrograph of titania as obtained (experiment.1)

In the experiment.2, titanium(IV)isopropoxide was added to the solution of dodecylamine in isopropanol and water which then resulted in non-mesoporous and amorphous titania (Fig.3) with a morphology different from that of the previous case, as indicated by SEM image (Fig.4).

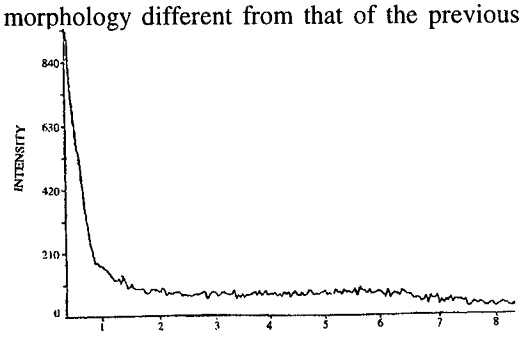

Fig.3 Representative small angle x-ray diffraction pattern of titania obtained after heat treatment (experiment.2)

Fig.4 Representative SEM micrograph of titania (experiment.2)

Mesoporous titanium nitride:

The synthesis of mesoporous TiN is also attempted wherein we used the charge-matching templating approach (method (B)) - (16 to 23). To about two grams of TiN, 1:1 solution of the acid mixture in water is added followed by the addition of an aqueous solution of cetyltrimethylammonium bromide (2 g) in twenty five milliliters of distilled water and then the contents are transferred into a polypropylene bottle and kept in the hot air oven for 3 hrs at 80°C and then kept aside at RT for 24 h to result in the yellow solid which was filtered, washed with distilled water and dried at 100°C. The yellow solid thus obtained was found to be mesoporous with the lamellar structure which has been characterized by small angle XRD (Fig.5 (a) & (b)) and SEM (Fig.6). The high angle XRD has been carried out for the sample obtained, but we could not exactly match the reflections there to any of the phases that are known till date, but the reflections can be indexed to an orthorhombic cell with justification. The qualitative analysis of the material ($C_xH_yN_z(Ti)_pF_qO_r$) was carried out using XPS which showed the Ti - $2p_{3/2}$ signal at 464.872 eV, N -1s signal at 409.872 eV, F -1s signal at 694.872 eV and O -1s signal at 539.872 eV. Thorough quantitative analysis of the elements present in the sample has yet to be carried out. The thermal stability of the sample was studied using 'DSC' analysis in argon atmosphere (Fig.7) which showed a decomposition behavior with three distinct stages of weight losses. The first endothermic weight loss is due to the desorption of water. The second one, exothermic in nature indicates the decompostion of the organic surfactant. But the last two peaks appear in addition to those observed in the case of the lamellar mesophase of silica (containing $C_{20}H_{41}(CH_3)_3N^+$) - (21) and the reasons for the appearance of these additional peaks have to be understood in detail.

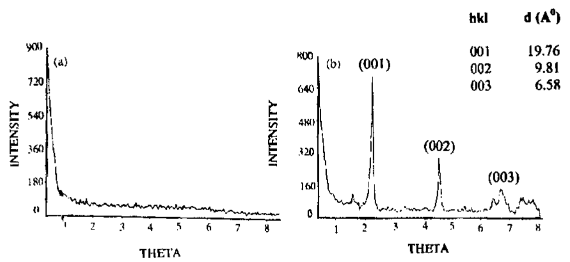

Fig.5 Representative small angle x-ray diffraction pattern of (a) TiN as obtained from the market (b) TiN after treatment with acid mixture as described above followed by templating onto CTAB to result in the mesolamellar composite at 80°C

Fig. 6 Representative SEM micrograph of TiN-based material after templating at 80°C

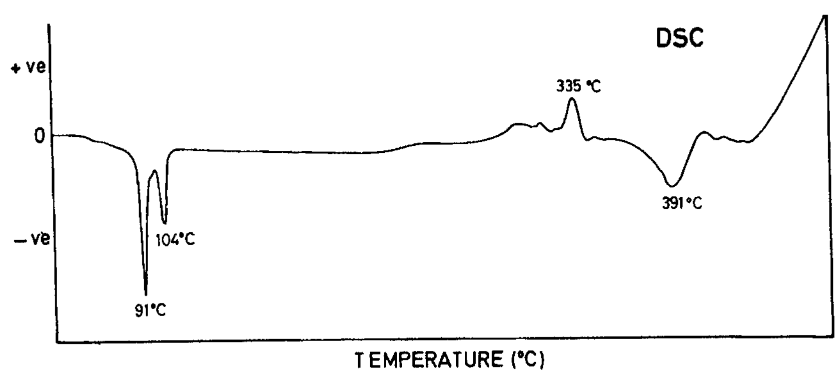

Fig.7 Analysis of thermal stability of lamellar mesophase based on TiN using "DSC"

CONCLUSIONS

1. The nanoparticles of titania were obtained by the controlled hydrolysis of $Ti(i\text{-}OC_3H_7)_4$ in the reverse micelles of dodecylamine produced in an dodecylamine-isopropanol-water solution (water/oil emulsion). Also, the nanoparticles of TiO_2 aggregated into sols with sizes ranging from 50 nm to even 1 μm, eventually forming gelatinous precipitates
2. Mesolamellar phase based on TiN was obtained by templating the inorganic analogue onto the template, cetyltrimethylammoniumbromide (CTAB). The thermal stability of the mesoporous material thus obtained has been studied using DSC analysis. The phase transformations that can be involved here are yet to be studied.

ACKNOWLEDGEMENTS

We wish to thank Prof. K. Chattopadhyay and Ms. Prajina Bhattacharya (IISc, Bangalore, India) for discussions.

REFERENCES

1. David M. Antonelli and Jackie Y.Ying, Current Opinion in Colloid & Interface Science, 1, (1996), 523
2. David M. Antonelli and J.Y. Ying, Angew.Chem.Int.Ed.Engl., 34, (1995), 2014
3. Vittorio Luca, Dugald J. Maclachlan, James M. Hook & Ray Withers, Chem. Mater., 7,, (1995), 2220
4. David M. Antonelli, Atsushi Nakahira and Jackie Y. Ying, Inorg.Chem., 35, (1996), 3126
5. David M. Antonelli and Jackie Y.Ying, Angew. Chem. Int.Ed.Engl.,35, (1996), 426
6. Peter Behrens, Angew.Chem.Int.Ed.Engl., 35, (1996), 515
7. N. Ulagappan and C.N.R. Rao, Chem. Commun., (1996), 1685
8. Peter T.Tanev, Ying Liang & Thomas J. Pinnavaia, J. Am. Chem. Soc., 119, (1997), 8616
9. V. Weidenhof, F. Gropper, U. Muller, L. Marosi, G. Cox, R. Houbertz and U.Hartmann, J.Mater.Res., 12, (1997), 1634
10. R.L. Putnam, N. Nakagawa, K.M. McGrath, N. Yao, I.A. Aksay, S.M. Gruner and A. Navrotsky, Chem. Mater., 9, (1997), 2690
11. Markus Antonietti and Christine Goltner, Angew. Chem. Int. Ed. Engl., 36, (1997), 910
12. Christine G. Goltner & Markus Antonietti, Adv. Mater., 9, (1997), 431
13. David Segal, J. Mater.Chem., (1997), 1297
14. Rahul Sen, B.C. Satish Kumar, A. Govindaraj, K.R. Harikumar, M.K. Renganathan and C.N.R. Rao, J. Mater. Chem., 7, (1997), 2335

15. J.H. Scofield, J.Electron Spectroscop., 8, (1976), 129
16. C.T. Kresge, M.E. Leonowicz, W.J. Roth, J.C. Vartulli and J.S. Beck, Nature, (1992),359
17. Chun-Guey Wu and Thomas Bein, Chem. Commun., (1996), 925
18. S. Ayyappan, N. Ulagappan and C.N.R. Rao, J.Mater. Chem., (1996), 1737
19. Yinhan Huang and Wolfgang M.H. Sachtler, Chem. Commun., (1997), 1181
20. Jian Luo and Steven L. Suib, Chem. Commun., (1997), 1031
21. Qishen Huo, David I. Margolese, Urlike Ciesla, Dirk G. Demuth, Pingyun Feng, Thurman E.Gier, Peter Sieger, Ali Firouzi, Bradley F. Chmelka, Ferdi Schuth and Galen D. Stucky, Chem. Mater., (1994), 1176
22. Pingyun Feng, Yin Xia, Jianglin Feng, Xianhui Bu and Galen D. Stucky, Chem. Commun., (1997), 949
23. G. Pacheco, E. Zhao, A. Garcia, A. Sklyarov and J.J. Fripiat, J. Mater. Chem., (1998), 219

Pergamon

NanoStructured Materials, Vol. 12, pp. 1071–1076, 1999
Elsevier Science Ltd

0965-9773/99/$–see front matter

PII S0965-9773(99)00301-3

EXPERIMENTAL AND COMPUTATIONAL STUDIES OF HETEROFULLERENES

I.M.L. Billas, W. Branz, N. Malinowski, F. Tast, M. Heinebrodt, T.P. Martin, C. Massobrio[†], M. Boero[††] and M. Parrinello.

Max-Planck Institut für Festkörperphysik, Heisenbergstr. 1, 70569 Stuttgart, Germany.

Abstract *- - External doping of fullerenes C_{60} and C_{70} with heteroatoms is performed in a low pressure condensation cell, through the mixing of a vapor of doping material with a vapor made of preformed fullerenes. Mass spectrometric investigations of the resulting cluster distributions of $C_{60}M_x$ and $C_{70}M_x$ clusters are carried out for M = {Fe, Co, Ni, Rh, Ir and Si}. Further laser induced photofragmentation of these $C_{60}M_x$ and $C_{70}M_x$ precursor clusters leads to the production of in-cage doped heterofullerenes with composition $C_{59-2n}M$ and $C_{69-2n}M$. We complement our study with ab-initio calculations of the geometrical and electronic structure of $C_{59}Si$ and $C_{58}Si_2$, obtained within density functional theory by relaxing self-consistently the structures to the local minima. ©1999 Acta Metallurgica Inc.*

INTRODUCTION

Doping the fullerene cage with foreign atoms can alter the properties of these peculiar systems by enhancing their chemical reactivity while maintaining stable closed three dimensional structures. In addition to trapping of heteroatoms inside the hollow fullerene cage (endohedral doping) and to decorating the fullerene surface with heteroatoms (exohedral doping), a third possibility of doping the fullerenes is the substitution of one or more carbon atoms with heteroatoms. The first demonstration of substitutional doping concerned boron-doped fullerenes (1). Different routes to the synthesis of in-cage doped fullerenes have been devised in recent years (2, 3) which have led to the production of macroscopic quantity of B- and N-doped fullerenes. Furthermore, experimental evidence has been reported for the existence of silicon-doped fullerenes (4-7). An interesting way to produce substitutionally doped fullerenes, which differs from the usual fabrication methods, consists in the photofragmentation of exohedral doped fullerenes. In our experiments laser heating of precursor exohedral doped fullerenes $C_{60}M_x$ and $C_{70}M_x$ results in substitutionally doped fullerenes not only for M = Si and B, but also for M = Fe, Co, Ni, Rh, Ir. On the other hand, fullerenes externally doped with materials like Ti, V, Nb, Ta transform, upon laser irradiation, into carbide and carbohedrene clusters (8). Our method therefore provides information on potentially interesting materials for substitutional doping of fullerenes. This might encourage efforts towards the fabrication of macroscopic quantities of these new heterogeneous nanoscale materials. In this framework first principles studies on doped fullerenes can help in predicting and understanding the basic trends and pecularities of these fascinating systems.

EXPERIMENTAL

Clusters of the composition $C_{60}M_x$ and $C_{70}M_x$ (M = Fe, Co, Ni, Rh, Ir and Si) are generated in an inert gas cluster condensation cell filled with about 1 mbar of helium and cooled down at liquid nitrogen temperature (8, 9) . The material M is brought into the vapor phase by laser evaporation of a target located in the condensation cell. This vapor mixes with fullerene vapor (C_{60} or C_{70} vapor) produced from a resistively heated oven and is quenched in the cold helium atmosphere. By monitoring the temperature of the fullerene oven and the power of the vaporization laser it is possible to obtain clusters made almost exclusively of one single fullerene molecule and a various number of atoms of material M. The clusters are transported from the condensation cell through a nozzle and a differential pumping stage into a high vacuum chamber where they are photoionized by a pulsed ArF excimer laser (wavelength 193 nm) and mass analysed in a time-of-flight mass spectrometer.

EXPERIMENTAL STUDIES OF DOPED FULLERENES

At low ionization laser fluences the photoionization mass spectra show a distribution of clusters with composition $C_{60}M_x$ and $C_{70}M_x$(10).When sufficiently high ionizing laser intensities are employed, the fullerene-M (M = Fe, Co, Ni, Rh, Ir, and Si) clusters are simultaneously ionized and heated by the excimer laser pulse up to a temperature at which evaporation and fragmentation processes take place. Mass spectra are shown for C_{60}-Fe (Figs. 1a and 2a), C_{60}-Rh (Fig. 1b) and C_{60}-Si (Fig. 2b) clusters exposed to high excimer laser fluences and for C_{60}-Ir clusters (Fig. 1c) exposed to a moderate laser fluence. As a result of the heating process the externally doped C_{60} or C_{70} molecules evaporate a substantial fraction (if not all) of the atoms at their surface. Furthermore, as shown in Fig. 1, a series of fullerenes smaller than the parent fullerene is observed resulting from the successive evaporation of carbon dimers from the C_{60} or C_{70} molecule and showing the characteristic larger abundances for C_{44} and C_{50} (and C_{60} in case of C_{70} used as parent fullerene), typical of fullerenes. The low mass range of each of the spectra shown in Fig. 1 is very instructive in that it provides numerous indications concerning the fragmentation products of the precusor C_{60}-M clusters. In the case of C_{60}-Fe clusters (Fig.1a), the fragmentation products consist of pure metal and metal carbide clusters of composition Fe_iC_j ($i \approx 1, ...15$ and $j \approx 0, ...6$). A similar observation can be made for C_{60}-Rh clusters (Fig. 1b) with the important difference that the carbon content of the rhodium carbide clusters Rh_iC_j ($j \approx 0, ...2$) is much lower than in the case of iron carbide clusters. In the case of C_{60}-Ir clusters, the low mass range of the spectrum is rather naked, consisting in a few peaks belonging to Ir, Ir_2, Ir_3. No iridium carbide fragment clusters are detected at this specific laser intensity. Other measurements at higher excimer laser fluence (not shown here) indicate the existence of the IrC molecule which could be post-ionized and detected.

Finally and most importantly, the mass spectra of Figs. 1 and 2 indicate that additional fragment products result from the photofragmentation of externally doped fullerenes. Considering first the case of C_{60}-Fe clusters (Fig.1a and 2a), these fragment clusters have the composition $C_{59-2n}Fe$ (n = 0, ...10). In this series, Fig. 2a shows that the species containing a number of total atoms of 44 and 50 are more abundant than the others. On the other hand, when C_{70} is employed, a series of clusters $C_{69-2n}Fe$ (n = 0, ...20) is observed with enhanced abundances for $C_{43}Fe$, $C_{49}Fe$ and $C_{59}Fe$.

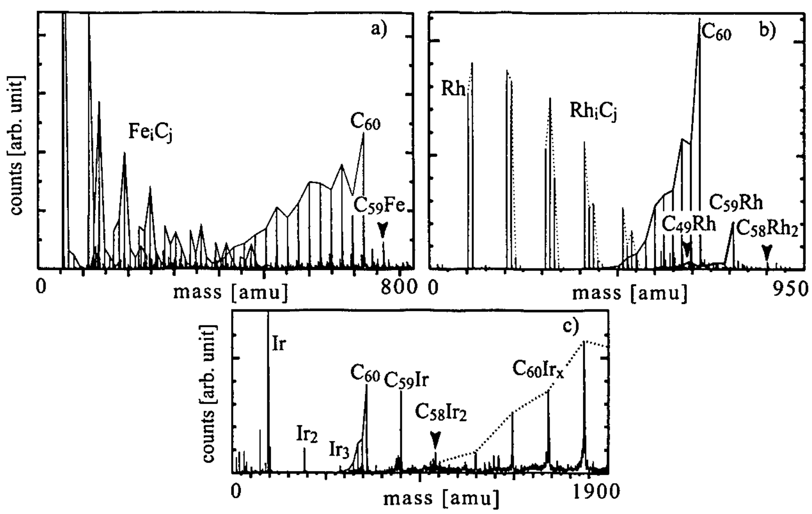

Figure 1. Photoionization mass spectra of (a)$C_{60}Fe_x$, (b) $C_{60}Rh_x$ clusters exposed to high laser fluence and of (b) $C_{60}Ir_x$ clusters irradiated by a moderate laser fluence. A solid line connects fullerene fragments from the C_{60} parent molecule. Solid (a) and dotted (b) connection lines are drawn for each group of carbide clusters containing a fixed number of metal atoms and a varying number of carbon atoms.

Similarily, mass spectrometric measurements indicate the existence of clusters with composition $C_{59-2n}M$ and $C_{69-2n}M$, with M = Co, Ni, Si (Fig.2b) and Rh (Fig. 1b). The same abundance pattern as seen in the case of iron characterizes each of the series $C_{59-2n}M$ and $C_{69-2n}M$ (M = Fe, Co, Ni, Rh and Si) and this abundance pattern is identical to that known for pure fullerenes. Furthermore, we observe that these fragment clusters exist almost exclusively for an even total number of atoms (in the case of Fe, a weak peak corresponding to $C_{58}Fe$ is observed as shown in Fig. 2a). These observations are strong indication that $C_{59-2n}M$ and $C_{69-2n}M$ clusters are substitutionally doped fullerenes where one carbon atom of the pure fullerene cage is substituted by an heteroatom M. In the case of iridium, the $C_{59}Ir$ and $C_{69}Ir$ clusters are the only photofragments observed of composition $C_{59-2n}Ir$ and $C_{69-2n}Ir$. In the absence of other $C_{59-2n}Ir$ and $C_{69-2n}Ir$ clusters, the conclusion that the $C_{59}Ir$ and $C_{69}Ir$ clusters are indeed substitutionally doped fullerenes is drawn from photofragmentation studies of these species (10). With respect to the formation of smaller doped fullerenes $C_{59-2n}M$ and $C_{69-2n}M$ (n>0), the use of complementary photofragmentation mass analysis using a tandem mass spectrometer indicates that they do not originate from the fragmentation of $C_{59}M$ and $C_{69}M$, since these latter first fragment by evaporating a MC molecule (10). However, we observe that the formation of smaller doped fullerenes is related to the release of carbide clusters from the cage. For Fe (Co and Ni), carbide clusters are abundant and their carbon content generous. Accordingly, the $C_{59-2n}Fe$ and $C_{69-2n}Fe$ (n>0) are observed in the mass spectra (Figs. 1a, 2a). For Rh, carbide clusters exist but their carbon content is lower than that of the iron carbide clusters. Accordingly, the relative intensities of the heterofullerenes $C_{59-2n}Rh$ and $C_{69-2n}Rh$ (n>0) are lower than in the case of Fe. For Ir, no carbide clusters, except the molecule IrC, are observed and accordingly, no $C_{59-2n}Ir$ and $C_{69-2n}Ir$ clusters (n>0) are observed. This behavior is related to the natural propensity of the various elements to form metal carbides. While Fe, Co, Ni carbides exist, Rh and Ir possess no stable carbide phase in the bulk.

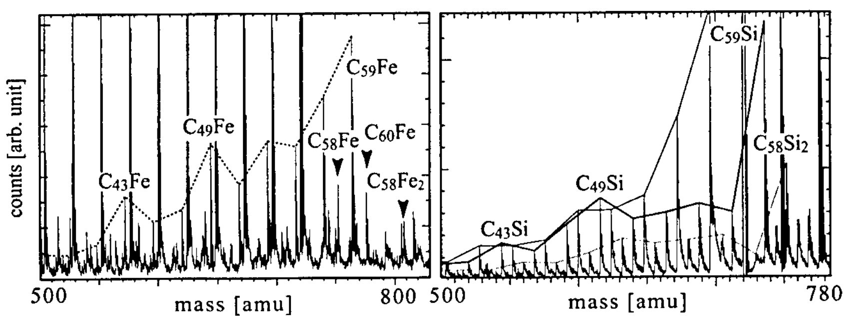

Figure 2. Enlarged view of photoionization mass spectra of (a)$C_{60}Fe_x$, (b) $C_{60}Si_x$ clusters exposed to high laser fluence. Fragment peaks corresponding to (a) $C_{59\text{-}2n}Fe$, (b) $C_{59\text{-}2n}Si$ and $C_{58\text{-}2n}Si_2$ clusters are shown. Notice also the presence of peaks corresponding to the mass of $C_{58}Fe$ and $C_{58}Fe_2$ clusters.

In addition to the the substitutionally doped fullerenes $C_{59\text{-}2n}M$, we observe in the photoionization mass spectrum of C_{60}-M (M = Fe, Rh, Ir, Si) a peak which corresponds to the cluster $C_{58}M_2$ (as indicated in Figs. 1b and 1c for Rh and Ir and in Figs. 2a and 2b for Fe and Si). In the case of silicon, the photoionization mass spectra reveal the existence of peaks belonging to clusters with composition $C_{58\text{-}2n}Si_2$ (n = 0, ...10) with the typical abundance pattern of structures reminiscent of the fullerene geometry, as shown in Fig. 2b. Similar observations of substitutionally doped fullerenes with one and two silicon atoms have also been performed by other groups (4-7).

Similarily, the assignment of the $C_{58}M_2$ (M = Fe, Rh and Ir) to substitutionally doped heterofullerenes would be tempting. However, smaller doped fullerenes with two substituted metal atoms were not observed in our experiments and hence the geometrical structure of $C_{58}M_2$ (M = Fe, Rh and Ir) is uncertain. Similarily it should be noticed that $C_{68}M_2$ clusters are observed if C_{70}-M clusters (M = Fe, Rh, Ir, Si) are used as precursor clusters.

COMPUTATIONAL STUDIES OF $C_{59}Si$ AND $C_{58}Si_2$

We have performed first-principles investigations of in-cage doped fullerenes starting with silicon-doped fullerenes, in particular $C_{59}Si$ and $C_{58}Si_2$, as a first step towards a systematic study of the substitutionally doped fullerenes produced in our experiments. Our calculations have been performed within the framework of the *ab-initio* molecular dynamics introduced by Car and Parrinello (11) by using norm-conserving pseudopotentials of the Trouiller-Martins type (12). The unit cell of our face-centred cubic periodic array has an edge of 21.16 Å, much larger than the diameter of the optimized structures of $C_{59}Si$ and $C_{58}Si_2$. The energy cutoff in the expansion of the Kohn-Sham (KS) orbitals in plane waves is 40 Rydberg. The replacement of a C by a Si atom induces a deformation of the fullerene network which is very localized around the Si site, as shown in Fig. 3a. In $C_{59}Si$, the bond lengths Si-C are 1.85 Å for the carbon atom at the edge hexagon-hexagon and 1.90 Å for the other two carbon atoms at the edge hexagon-pentagon, hence about 30 % larger than the corresponding bond lengths in the C_{60} molecule (13). Typical distances between C and Si in molecules are 1.70 Å for double bonds and 1.88 Å for single bonds. The heterofullerene $C_{58}Si_2$ has been studied for the configurations where the Si atoms are 1st (2 configurations), 2nd (2 configurations) and 3rd

(3 configurations) nearest neighbors (n.n.). One with the Si atoms on opposite sites on the cage has also been considered. The Si-C bond lengths in these structures range from 1.85 Å and 1.93 Å. In all structures considered, the conjugation pattern reflected in the bond length pattern is preserved. The lowest energy configuration is one of the 3rd n.n. configurations where both Si atoms reside on the same hexagon, as shown in Fig. 3b. This latter configuration has been missed in a recent publication (7). Notice that the same arrangement of the two Si atoms is found experimentally in disilabenzene in which two C atoms of the benzene ring are replaced by two Si atoms (14). In our calculations, the energy difference between the two lowest energy configurations is rather small (0.11 eV). Energetically, the relaxed configurations are found to lie within 1 eV with energy differences between next lying configurations of 0.1-0.35 eV. Recent photofragmentation experiments show that the initial fragmentation channel of $C_{58}Si_2$ is the loss of a Si dimer (7). However, as suggested in (7), the photofragmentation process of $C_{58}Si_2$ to C_{58} is complex and the release of a Si dimer from the $C_{58}Si_2$ only implies that the two substituted silicon atoms have to be located not too far apart in the cage network in agreement with our calculations.

The electronic structure of the doped fullerenes $C_{59}Si$ and $C_{58}Si_2$ will be considered on the basis of Kohn-Sham energy level analysis. Only the structure corresponding to the energetically most favorable $C_{58}Si_2$ isomer will be discussed here. A detailed description of the electronic structures of the other isomers will be reported in a forthcoming paper. Comparison of the electronic energy levels of C_{60}, $C_{59}Si$ and $C_{58}Si_2$ as shown in Fig. 3c indicates that the degeneracy of the unoccupied t_{1u} energy levels (LUMO) of C_{60} is partly lifted in $C_{59}Si$ and $C_{58}Si_2$, since one of the t_{1u} levels is shifted to lower energy with respect to the two other levels. The splitting of the highest occupied levels derived from the 5-fold degenerate h_u levels (HOMO) of C_{60} is very small for $C_{59}Si$ while for $C_{58}Si_2$ one of these levels is clearly shifted to higher energy. The HOMO and LUMO energy levels of $C_{59}Si$ and $C_{58}Si_2$ are strongly localized on the Si atoms and on neighboring carbon atoms (15). In the case of $C_{58}Si_2$, a rather strong localization on the Si atoms is also observed for both HOMO-1 and LUMO+1 energy levels. It is interesting to notice that the purely carbon-derived energy levels, i.e. the HOMO-1 and LUMO+1 for $C_{59}Si$ and the HOMO-2 and LUMO+2 for $C_{58}Si_2$ are separated by an energy gap of 1.6 eV reflecting the HOMO-LUMO energy gap of the precursor C_{60} molecule.

a) b) c)

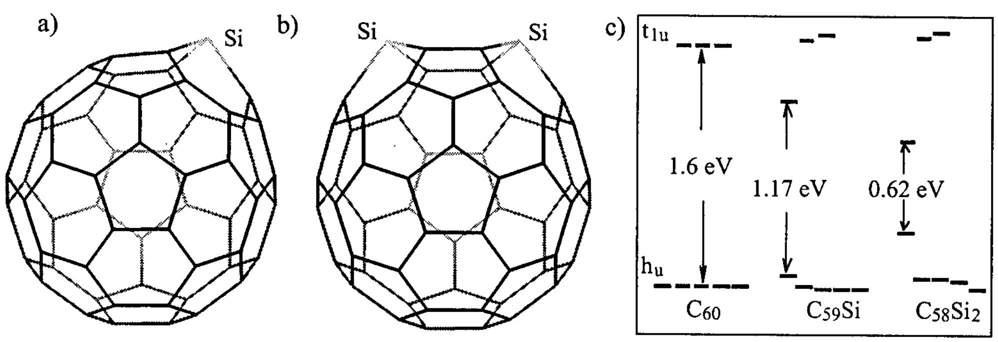

Figure 3. Geometric structure of $C_{59}Si$ (a) and one isomer of $C_{58}Si_2$ (b) together with their corresponding Kohn-Sham energy levels (c) derived from the HOMO and LUMO levels of C_{60}.

The replacement of C atoms by a Si atoms in the fullerene network gives rise to polar bonds between the Si atom and its C neighboring atoms (as measured from example from the Mulliken populations) as expected due to the larger electronegativity of carbon compared to silicon. Further analysis of the electronic structure in terms of localized orbitals (16) and electron localization function (ELF) is underway.

CONCLUSIONS

In conclusion, the new in-cage doped fullerenes synthesized in these experiments appear to be of technological and fundamental interest, due to the richness of their physical and chemical properties. Combined experimental and theoretical effort in his area is currently being pursued on other systems of this family.

ACKNOWLEDGMENT

I.M.L. Billas thanks the European Commission for funding under the TMR program.

† permanent address: IPCMS-GEMME, 23 rue de Loess, F-67037 Strasbourg, France.
†† present address: JRCAT-ATP, 1-1-4 Higashi, Ibaraki 305, Tsukuba-shi , Japan.

1. Guo, T., Jin, C., Smalley, R. E., Journal of Physical Chemistry, 1991, 95, 4948.
2. Muhr, H.-J., Nesper, R., Schmyder, B., Kötz, R., Chemical Physics Letters, 1996, 249, 399.
3. Hummelen, J. C., Knight, B., Pavlovich, J., Gonzalez, R., Wudl, F., Science, 1995, 269, 1554.
4. Kimura, T., Sugai, T., Shinohara, H., Chemical Physics Letters, 1996, 256, 269.
5. Fye, J. L., Jarrold, M. F., Journal of Physical Chemistry A, 1997. 101, 1836.
6. Pellarin, M., Ray, C., Melinon, P., Lerme, J., Vialle, J. L., Keghelian, P., Perez, A., Broyer, M., Chemical Physics Letters, 1997, 277, 96.
7. Ray, C., Pellarin, M., Lermé, J. L., Vialle, J. L., Broyer, M., Blase, X., Mélinon, P., Kéghélian, P., Perez, A., Physical Review Letters, 1998, 80, 5365.
8. Tast, F., Malinowski, N., Frank, S., Heinebrodt, M., Billas, I. M. L., Martin, T. P., Physical Review Letters, 1996, 77, 3529.
9. Zimmermann, U., Malinowski, N., Näher, U., Frank, S., Martin, T. P., Zeitschrift für Physik D, 1994, 31, 85.
10. Branz, W., Billas, I. M. L., Malinowski, N., Tast, F., Heinebrodt, M., Martin, T. P., Journal of Chemical Physics, 1998, 109, 3425.
11. Car, R., Parrinello, M., Physical Review Letters, 1985, 55, 2471.
12. Trouiller, N., Martins, J. L., Physical Review B, 1991, 43, 1993.
13. Feuston, B.P., Andreoni, W., Parrinello, M., Clementi, E., Physical Review B, 1991, 44, 4056.
14. More precisely, in hexamethyl-1,4-disilabenzene, Rich, J. D., West, R., Journal of the American Chemical Society, 1982, 104, 6884.
15. More precisely, for $C_{59}Si$ on the C atom of the edge hexagon-hexagon and for $C_{58}Si_2$ on the neighboring C atoms of the hexagon.
16. Silvestrelli, P. L., Marzari, N., Vanderbilt, D., Parrinello, M., Solid State Communications, 1998, 107, 7.

Pergamon

NanoStructured Materials, Vol. 12, pp. 1077–1080, 1999
Elsevier Science Ltd

0965-9773/99/$–see front matter

PII S0965-9773(99)00302-5

NANO Al_2O_3-Pb AND SiO_2-Pb CERMETS BY SOL-GEL TECHNIQUE AND THE PHASE TRANSFORMATION STUDY OF THE EMBEDDED Pb PARTICLES

P. Bhattacharya and K. Chattopadhyay
Department of Metallurgy, Indian Institute of Science, Bangalore 560 012

Abstract

Sol-gel processing followed by H_2 reduction is used to produce dispersions of nanosized Pb in amorphous SiO_2 and ultrafine γ Al_2O_3 matrices. A depression of 3-5K in Pb melting point is reported. The size and shape of these metastable particles in molten and solid state are discussed in the light of the experimental observations and expectations from the intersection group theory for equilibrium shape. ©1999 Acta Metallurgica Inc.

INTRODUCTION

Dispersion of the nanoscaled metallic particles in the ceramic matrix, known as nanocermets represents an important class of nanomaterials (1). The primary aim of the present investigation is to synthesize nanocermets involving Pb as the metallic dispersion and to explore the behaviour of such particles with reference to a glassy (SiO_2) and nanocrystallline (γ Al_2O_3) matrices. We have adopted the solgel route, which is very effective in synthesizing such composites at low temperatures.

EXPERIMENTAL

The SiO_2 matrix is obtained by using Tetra Ethyl Ortho Silicate (TEOS) as the precursor while Aluminum Sec Butoxide (ASB) is used as the precursor for the synthesis of γ Al_2O_3 matrix. $Pb(NO_3)_2$ is used as the source of Pb. The experimental details are given elsewhere (2,3). For alumina, the gellation yields boehmite, which on heat treatment (873K for 5hr) transforms to ultrafine γ Al_2O_3. In both the cases, Pb appears on hydrogen reduction of the $Pb(NO_3)_2$ following the solgel processing. The samples are characterized by powder x-ray diffraction (Huber G600, JEOL8030), and transmission electron microscope (JEOL 2000FXII) operated at 200 kV.

RESULTS

Figs 1 and 2 show the composite XRD patterns after the reduction treatments to yield SiO_2-Pb and Al_2O_3-Pb. The Pb peaks are sharper with higher reduction temperatures

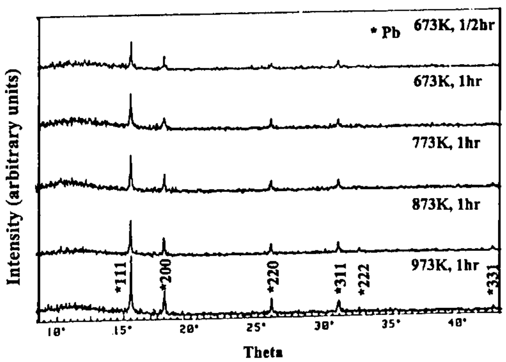

Fig.1 Composite x ray diffraction patterns of SiO_2-Pb reduced at 673K, 773K, 873K 973K for 1hr and at 673K, 1/2 hr.

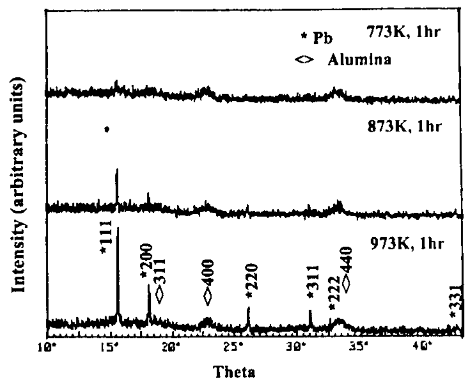

Fig.2 Composite x ray diffraction patterns of Al_2O_3-Pb reduced at 773K, 873K and 973K for 1hr respectively.

while the Al_2O_3 peaks remains diffuse and broad at all temperatures. The particle size of Pb is estimated using the Scherrer formula (Fig. 3). Figure 4a shows a typical microstructure of Pb dispersed in glassy SiO_2 matrix (673K, ½hr). Figure 4b shows the typical microstructure of very fine dispersions of Pb in the γ Al_2O_3 matrix (873K, 1hr). The selected area diffraction patterns are shown in the inset. The faulted and faceted Pb particles in γ Al_2O_3 matrix (~2nm grain size) are shown in Fig. 4c The mean particle size of Pb in γ Al_2O_3 obtained from the electron micrograph (873K, 1hr) is ~15 nm (~21nm from XRD). The Pb particles are highly faceted. The typical shapes corresponding to the sections of cuboctahedron are shown at the bottom of the figure 4. The melting and the solidification behaviour of the Pb particles have been studied under dynamic Ar atmosphere in Perkin Elmer DSC IIC. On heating, melting is seen as sharp endothermic peak. No solidification peak is, however, detectable (Fig. 5).

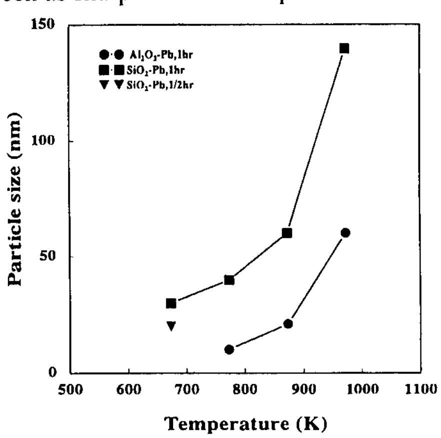

Fig.3 Particle size variation of Pb in SiO_2-Pb and Al_2O_3-Pb under different reduction treatments estimated from the x ray diffraction analysis.

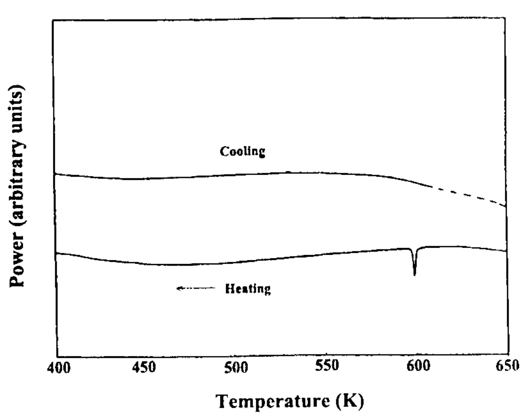

Fig.5 DSC traces in Al_2O_3-Pb samples during the heating and cooling cycles. Melting peak during heating is sharp, but no solidification peak is detectable.

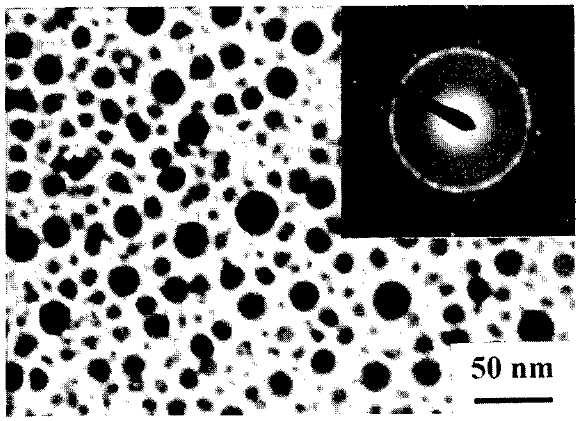

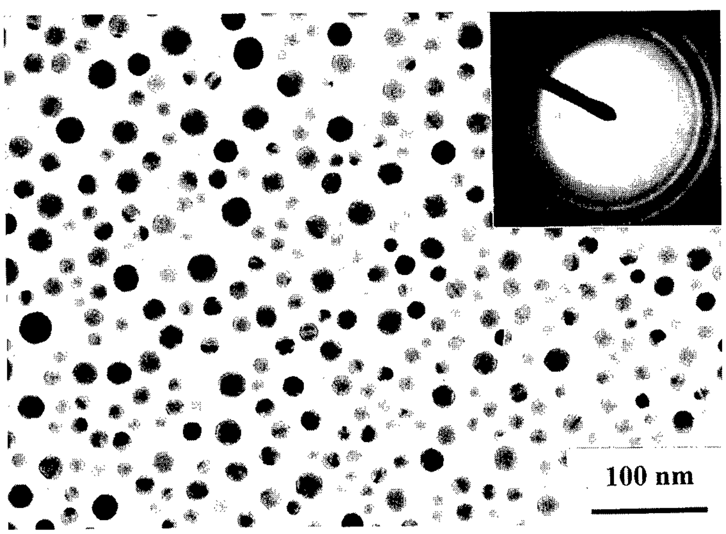

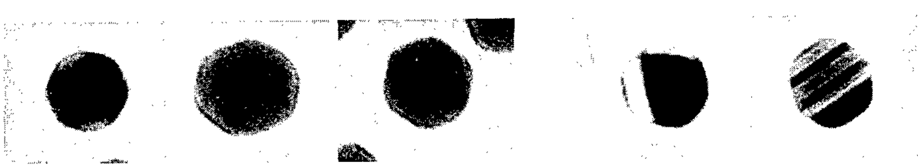

Fig. 4 a) A typical distribution of Pb in glassy SiO_2 matrix. The SAD (inset) shows the rings from Pb. b) The distribution of Pb in the ultrafine γ Al_2O_3 matrix. The inset shows smooth rings from γ Al_2O_3 and Pb. c) The shapes of the Pb particles are shown in the bottom, first two contains defects while the rest shows shapes corresponding to 111, 110 and 100 projections of cuboctahedron.

DISCUSSIONS

The formation and retention of nanosized Pb dispersion instead of it's silicate and aluminate is surprising new result. The melting point of Pb is depressed by 3-5K in the two cases. However, solidification peaks are undetectable and the implication of this is discussed elsewhere (4). In the rest, we shall concentrate on the evolution of the shape of these particles.

A comparison of the Pb particles in the two matrices under identical heat treatment reveals that Pb particles in SiO_2 are larger than that in γ Al_2O_3. Pb dispersed in γ Al_2O_3 is faceted, whereas in SiO_2 they are rounded. At the reduction temperatures, Pb is molten. Equilibrium shape in the embedded case is determined by intersection group (5,6). For Pb in glassy matrix, it will be sphere for the molten Pb and cuboctahedron for solid state. For the nanometric Pb particles embedded in still finer (~2nm) γ Al_2O_3 matrix, situation is more complex. Every Pb particle intersects ~400 γ Al_2O_3 particles. Thus, the matrix symmetry can be approximated to be sphere and the shape should be identical to that expected for SiO_2 .The equilibration time for Pb nanoparticles is of the order of millisecond near the Pb melting point and of the order of second at solid state (about 100K below melting point) (7). Since the samples are furnace cooled from the reduction temperature, the time available for the Pb particles is order of magnitude larger than needed for equilibration. Thus, in both the matrices, faceted cuboctahedral lead is expected. This is validated for ultrafine γ Al_2O_3 matrix, and not for glassy SiO_2 matrix. Clearly there exists kinetic constraint for SiO_2, which tend to retain the liquid shape. This is surprising as kinetic constraint is expected in the crystalline case due to the probability of forming low energy interface between Pb and individual grains of γ Al_2O_3, while the glassy matrix should have behaved isotropically. Further work is in progress in this direction.

ACKNOWLEDGEMENTS

The financial support of the Departments of Science and Technology and Atomic Energy, Govt. of India is gratefully acknowledged. One of us (PB) thanks the Council for Scientific and Industrial Research for the award of research fellowship.

REFERENCES

1. Gleiter, H., *Progress in Materials Science*, 1989, 33, 233.
2. Bhattacharya, P. and Chattopadhyay, K., *Proceedings of the International Conference on Recent Advances in Metallurgical Processes*, Vol II, Bangalore, India, 1997, p. 817.
3. Anushree, Roy. and Sood, Ajay. K., *Pramana - journal of physics*, 1995, 44, 201.
4. Bhattacharya, P. and Chattopadhyay, K., *Materials Transactions, JIM*, 1998, 39, 75 .
5. Cahn, J. W. and Kalonji, G., *Proceedings of an International Conference on Solid-Solid Phase Transformations*, The Metallurgical Society of AIME 1981, p. 3.
6. Moore, K. I. and Chattopadhyay, K. and Cantor, B., *Proceedings of the Royal Society of London*, 1987, A414, 499.
7. Chattopadhyay, K and Bhattacharya, P., *Journal of Electron Microscopy* (communicated)

Pergamon

NanoStructured Materials, Vol. 12, pp. 1081–1084, 1999
Elsevier Science Ltd

0965-9773/99/$–see front matter

PII S0965-9773(99)00303-7

TEM AND HREM STUDY OF THE 3D SUPERLATTICES CONSISTING OF NANOCLUSTERS IN SYNTHETIC OPAL MATRIX

L.M.Sorokin*, V.N.Bogomolov*, J.L.Hutchison, D.A.Kurdyukov*, A.V.Chernyaev* and T.N.Zaslavskaya***

*A.F.Ioffe Physical-technical Institute of the Russian Academy of Sciences, 26 Polytechnicheskaya str., 194021 St.-Petersburg, Russia
**Department of Materials, Oxford University, Oxford, Parks Road, OX1 3PH, UK

Abstract *-- Results of TEM and HREM study of synthetic opals containing different guest materials embedded in their regularly distributed voids either by melt injection or by chemical route are discussed. It was established that in a number of cases (besides HgSe and In as guest materials) one can fabricate rather uniform 3D cluster lattices. Clusters in voids of opal have a single-crystal structure. Structural details of In cluster lattice are shown to result in specific feature of superconducting parameter (critical magnetic field) of In- particle array in the opal matrix.* ©*1999 Acta Metallurgica Inc.*

INTRODUCTION

Further progress in electronics requires the fabrication of the structure with still higher degree of device integration a goal which, in principle, can be achieved by decreasing device size and using the third dimension of object constructed. A fabrication of structures with up 10^{14} active elements per unit volume is possible already with clusters of a submicron size. The dielectric matrix (e.g. synthetic opal) with inserted a semiconductor or metal material in its regularly distributed voids can serve as a novel type of nanocomposites (1). They are so called 3D lattices or cluster crystals. Unusual properties of these nanostructures depend on those of individual clusters, their high concentration and character of the "bridges" between neighbour clusters. To obtain a 3D regular lattice of nanoclusters the silica spheres in initial opal must be regularly stacked in a close-packed cubic or hexagonal array. Thus the opal object manifesting the properties of photonic crystals can be fabricated. The possibility of their production was demostrated in (2). Recent publication on the problem of the 3D cluster lattice construction was dedicated to TEM study of the structural state of different guest materials in opal voids (3). In general it should be clear that the quality of cluster lattice will depend on the perfection of initial single crystal opal but the direct confirmations of this dependence are absent.

In this report new results on structural parameters of opal crystals with guest materials are presented.

EXPERIMENTAL

Synthetic opal crystals were fabricated from aqueous sols of monodisperse spherical SiO_2 particles by technique close to that in (1). Opal crystals were then impregnated by different guest materials (Te, InSb, HgSe- under gas pressure from the melt, In- by chemical route: In compound, decomposition up to In_2O_3 and reduction up to pure In). The specimens under study were cut from bulk samples, polished by dimpling and finally thinned to perforation by Ar^+ ion milling. JEM 4000EX and JEM 2010 electron microscopes were used for observation. EDX study was performed to confirm the composition of silica spheres and clusters after inserting different materials into voids of opal matrix. A few electrophysical measurements were carried out.

RESULTS AND DISCUSSION

Figure1 demostrates opal crystal filled by Te from the melt under high gas pressure. Regularly distributed black spots correspond to cluster lattice in opal matrix (white spots - silica spheres). Serrated behaviour of cluster rows in above image signifies the presence of twin structure in cluster lattice which is due to that in initial opal crystal. It is seen that the guest material occupies almost all pores near the twin boundary of the matrix. That means the twin boundary does not modify the channels between opal voids, i.e. the twin boundary does not interfere with Te to occupy cavities. Quasi-dislocations and stacking faults were revealed

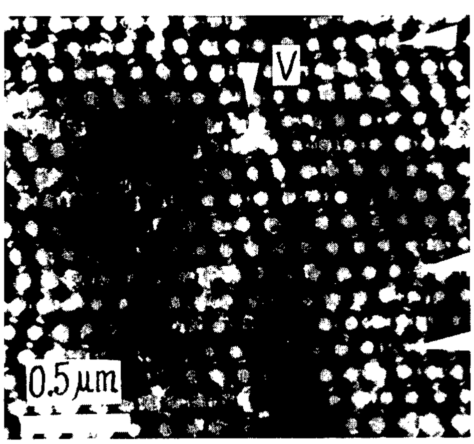

Figure1. (110) projection of 3D lattice of Te clusters in twinned opal matrix.

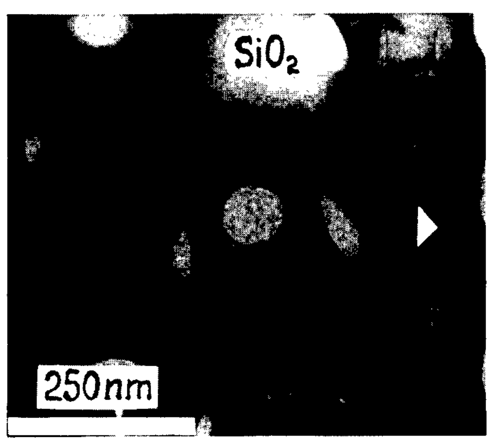

Figure 2. Twinned structure of InSb clusters in cavities of opal crystal.

in initial synthetic opal which also do not effect filling pores in opal. In Figure 1 one can observe isolated pores which are cluster free. They are quasi-vacancies which are probably a result of local sealing channels between voids during growth process.

The projection of the 3D network of linked nodes of InSb clusters is presented in Figure 2. The defect structure in view of ribbon like pattern can be seen. The (110) zone-axis patterns were shown to be consistent with a twinned lattice which extends over several adjacent clusters. It should be proposed that this structure is a result of increasing specific volume of InSb cluster at the transition melt-solid. It was very surprisingly that the guest material in the cavities was single-crystal over large areas.

As against the Te-, GaAs-, and InSb filling the pores of opal, for the HgSe filling the cluster lattice is produced only in local places, not over whole sample of opal crystal. There is no suitable explanation of this observation yet. As to structural state of the HgSe in the pores it is a single crystal type in character (Figure 3).

As mentioned a rather complicated technique was used for filling voids in opal by In material. Figure 4 shows the ununiform distribution of In in opal cavities. Because of the strong difference in electron absorption by the elements contained in the object, the In clusters are seen as dark areas against the background of lighter SiO_2 spheres. In this picture there are areas which are characterized by regularly distributed clusters connected by bridges. Since the In material does not wet the silica surface, on the initial stage of In cluster formation it tends to have the spherical form. This type of clusters of 40-90 nm in size are seen also in Figure 4. The remarkable feature of Figure 4 is the numerous small spherical particles (less 10 nm in size) which cover the surface of silica spheres. Possibly, they are a result of surface chemical reaction between silica and indium oxide.

The magnetic field dependencies of resistivity R(H) for the sample of opal matrix with In (Figure 5a,b) show there are some critical magnetic fields of superconducting transitions corresponding to the presence of In particles of different sizes d: H_a, H_b (T=0.9 K), H_{a1}, H_{b1} (T=0.57 K) correspond to $d<\lambda$ (λ - penetration depth), H_0 (T=0.9 K), H_{01}, H_{02} (T=0.57 K) correspond to $d \sim \lambda$ (for bulk In $H_c(0)$=281.5 Oe, $\lambda(0)$=64 nm (4)).

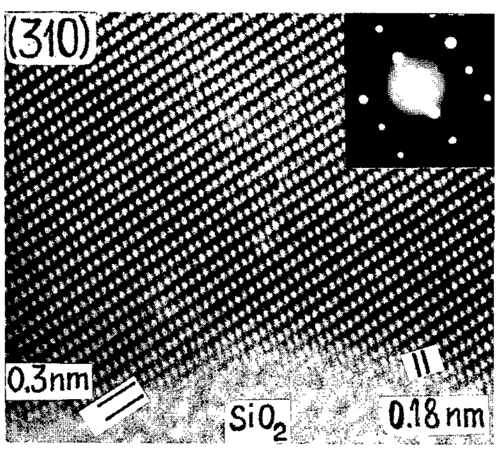

Figure 3. HREM image of cluster in opal crystal filled by HgSe.

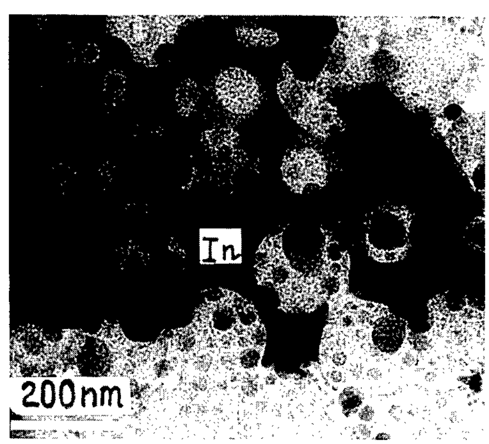

Figure 4. General view of cluster lattice in opal crystal filled by In.

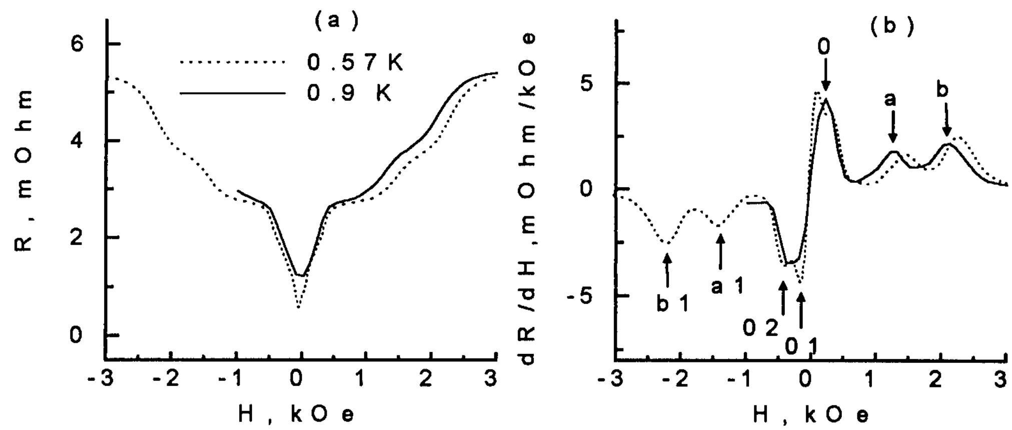

Figure 5. Magnetic field dependencies of the resistivity (a) and derivatives dR/dH (b) of In cluster lattice in opal matrix. H_0 =250 Oe, H_a=1.31 kOe, H_b=2.14 kOe (0.9 K), H_{01}=120 Oe, H_{02}=360 Oe, H_{a1}=1.45 kOe, H_{b1}=2.24 kOe (0.57 K).

CONCLUSION

The growth of opal crystal, similar to atomic crystals, is accompanied by formation of quasi - twins, stacking faults, dislocations and point defects. Most of the defects in opal do not interfere with guest materials to penetrate them into the void sublattice. In this case the cluster lattice reproduces the defect structure of the opal matrix. Internal defect structure of cluster (twinned structure) was revealed only for InSb as a guest material. Neither dislocations nor other lattice defects were detected in single crystal structure of clusters.

ACKNOWLEDGMENT

Partial support of the RFBR (Grants: 96-02-16948-a, 96-02-16852-a) and of the RS of Great Britain is gratefully acknowledged.

REFERENCES

1. Bogomolov V.N., and Pavlova T.M., *Fiz. Tekh. Poluprovodn.*, 1995, 29, 826 [*Semiconductors* 1995, 29, 428].
2. Bogomolov V.N., Kurdyukov D.A., Prokofiev A.V., and Samoilovich S.M., *Pis'ma Zh. Eksp. Teor. Fiz.*, 1996, 63, 496.
3. Bogomolov V.N., Hutchison J.L., Sorokin L.M., Kurdyukov D.A., and Pavlova T.M., *Phys. Sol. State*, 1997, 39, 1869.
4. Roberts B.W., *J.Phys.Chem.Ref.Data*, 1976, 5, 581.

Pergamon

NanoStructured Materials, Vol. 12, pp. 1085–1088, 1999
Elsevier Science Ltd

0965-9773/99/\$–see front matter

PII S0965-9773(99)00304-9

SOL-GEL DERIVED YSTZ -Al_2O_3 AND YSTZ-Al_2O_3-SiO_2 NANOCOMPOSITES

R.N. Viswanath and S. Ramasamy
Department of Nuclear Physics, University of Madras, Guindy Campus,
Chennai - 600 025, INDIA.

Abstract - - *Yttria stabilized tetragonal zirconia (YSTZ) - alumina nanocomposite system has been synthesized by the sol-gel route. Investigations reveal that grain and GB regions are crystallized independently at two different temperatures. The bulk grains are crystallized into tetragonal symmetry above 750°C with an average crystallite size of 10 nm. The GB regions are crystallized above 950°C. These crystallization temperatures increase with Al_2O_3 concentrations. At 1300°C phase transition occurs for specimens with low concentration of Al_2O_3 (less than 10 wt%). With 15 wt% of Al_2O_3, the system remains in tetragonal symmetry even above 1300°C. In order to control the growth rate of the crystallites at high temperatures, the stable composition YSTZ-15wt%Al_2O_3 was dispersed in a SiO_2 glassy matrix. The dispersed product also crystallized with tetragonal symmetry. In addition to the presence of t-ZrO_2, the mullite phase also exists in the dispersed product at 1300°C.* ©*1999 Acta Metallurgica Inc.*

INTRODUCTION

The properties of most of the ceramic polycrystalline products are very much influenced by the arrangement of atoms and its chemical composition at the GB regions. The atomic structure at the GB surfaces can be easily altered by reducing the grain size and by doping (1-3). As the width of the GB regions is large and as the GB structures are probably disordered (4), the GB atoms interact effectively with bulk grains and hence, the "property related GB structures" can be easily tuned. To study this phenomena, ZrO_2 in phase stabilized form was chosen and its GB structure has been modified by doping. Zirconia exists in three distinct polymorphs: monoclinic (m), tetragonal (t) and cubic (c) (5). Tetragonal or cubic ZrO_2 are used for high temperature applications. Yttria has been added to ZrO_2 for stabilizing the tetragonal symmetry at room temperature (6). As Al_2O_3 is one of the promising candidates for high temperature stabilization of tetragonal symmetry (7), Al_2O_3 was added to ZrO_2 in various concentrations (5, 10, and 15 wt%) to prepare a YSTZ-Al_2O_3 nanocomposite. In a separate experiment, YSTZ-Al_2O_3 was dispersed in a SiO_2 glassy matrix by a particle suspension method.

EXPERIMENTAL PROCEDURE

The Sol-gel technique was used to synthesize the YSTZ-Al_2O_3 nanocomposite system. The spectroscopic grade (3 mol%) yttrium nitrate and (97 mol%) zirconium tetrachloride salts

were dissolved in ethylene glycol. The solution was refluxed at 100°C for 12 hours and aluminum chloride salt was added. Again the solution was refluxed at 100°C for the same duration. Water was added into the hot solution (100°C) drop wise. During this period, the alkoxides were hydrolyzed. In this process the alkoxides react with H_2O to form their respective hydroxides. These hydroxides were isolated by filtration and washed with hot water and organic solvents. Finally, on heating at 140°C, the hydroxides decompose and form YSTZ-Al_2O_3. A part of the specimen with the composition YSTZ-15wt%Al_2O_3 was dispersed in tetra ethoxy silane $Si(OEt)_4$ solution to obtain YSTZ-Al_2O_3-SiO_2. Concentrated HCl was used as a catalyst to condense the solution in to a gel. The condensed gel was then heated at 140°C. The structural properties of the synthesized specimens were studied.

RESULTS AND DISCUSSION

The DTA thermogram (Fig. 1) of YSTZ-Al_2O_3 specimen shows two exothermic reaction peaks between 100 and 1300°C. The onset temperatures of the exothermic reactions are 760°C and 960°C respectively for pure YSTZ and the formation of molecular co-ordination in the GBs. These temperatures increase with an increase in concentration of Al_2O_3. XRD patterns are absent up to 750°C. At 750°C, the X-ray reflections start developing. On further increase of the temperature, the peak intensity of the X-ray reflections increases and the FWHM value of the profiles decreases. The profile widths are broad considerably up to 900°C. The typical XRD spectra of a 15wt% Al_2O_3 doped YSTZ specimen heated at 100, 750, 800, 900, 1000 and 1100°C are shown in Fig. 2. Line broadening studies (8) have been carried out to find the FWHM of the XRD profiles. The calculated average crystallite sizes using the Scherrer formula is given in TABLE 1. The table shows that the crystallite size was not increased with temperature up to 900°C. The FT-Raman studies confirmed that the specimens crystallized above 750°C is in tetragonal symmetry. Comparing the DTA results with XRD and FT-Raman spectra, it was concluded that the first exothermic reaction corresponds to the crystallization of the bulk grains. Well defined reflections with resolved line splitting corresponding to the tetragonal symmetry are present for the specimens heated at 1000°C; this temperature is just above the onset temperature of the second exothermic peak. At this temperature, the crystallites start to grow and their sizes increase further with an increase of temperature. As a result, Al_2O_3 at the GB/interface regions co-ordinates with YSTZ and forms a new molecular network. Due to this co-ordination the inter-planar distance (d-spacing) decreases with Al_2O_3 concentration. For example, the difference in d-spacing $d_{(202-220)}$ for the pure YSTZ was approximately 0.02 Å whereas the corresponding value for the 15 wt% doped YSTZ system decreases to 0.01 Å ± 0.002 Å. The inter-planar spacing was

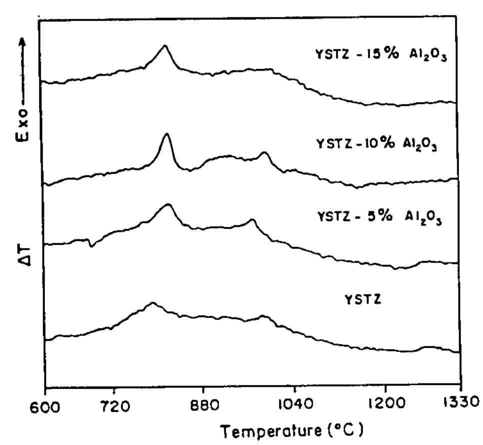

Figure 1. DTA traces of YSTZ-Al_2O_3 nanocomposite system

TABLE 1
Average Crystallite Size of YSTZ - Al_2O_3 and YSTZ - Al_2O_3 - SiO_2 Nanocomposites Heated at Various Temperatures

	Average crystallite size (in nm)				
Specimen	800°C	900°C	1000°C	1100°C	1300°C
YSTZ	10	11	27	47	58
YSTZ-Al_2O_3(5%)	9	11	28	44	55
YSTZ-Al_2O_3(10%)	10	11	32	50	57
YSTZ-Al_2O_3(15%)	9	10	33	50	56
YSTZ-Al_2O_3(15%) - SiO_2	8	9	12	23	30

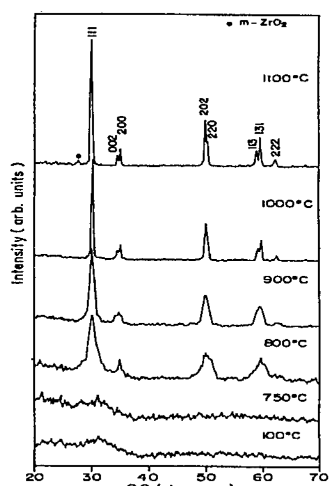

Figure 2. XRD patterns of YZTZ-Al_2O_3 (15 wt%) nanocomposite

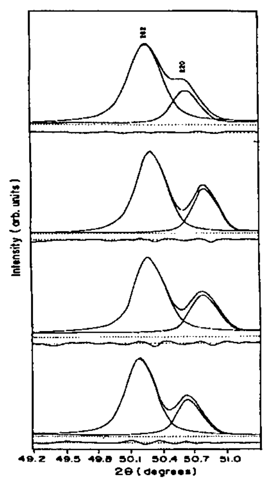

Figure 3. 202 and 220 fitting reflections of (a): pure YSTZ,(b-d):YSTZ-Al_2O_3 (5,10,15 wt%) nanocomposites.

calculated from the fitted XRD profiles. The typical fitted XRD profiles (202) and (220) of the pure and Al_2O_3 doped (5, 10 and 15 wt%) YSTZ specimens heated at 1000°C are given in Fig. 3. The molecular co-ordination in these specimens was confirmed by the FT-IR spectroscopy also (not shown in the text). Hence, it is believed that the second exothermic peak develops due to the co-ordination of GB atoms with the bulk grains.

The phase transition from tetragonal to monoclinic occurs for the specimens 5 and 10 wt% Al_2O_3 doped YSTZ heated at 1300°C. But, the tetragonal symmetry remains stable at 1300°C with the addition of 15 w% Al_2O_3. The bulk density calculated for the sintered specimens increases with sintering temperature and also with Al_2O_3 content. Almost 100% theoretical density was obtained for the15 wt% Al_2O_3 doped YSTZ sintered at 1300°C.

The dispersed product (YSTZ-15wt%Al_2O_3 in a SiO_2 matrix) also crystallizes with tetragonal symmetry. The SEM micrograph (Fig. 4) shows that the particles are almost spherical. As is evident from the XRD patterns, the size of the crystallites increases

with an increase of temperature. However the growth rate of the crystallites was partially controlled due to the dispersion of YSTZ-Al_2O_3 in SiO_2. A maximum crystallite size of 30 nm was obtained for the specimen heated at 1300°C. The SEM picture shows that the particle size is larger than 30 nm implying that each particle is an aggregate of few crystallites. It is important to investigate the composition of the particles looking for SiO_2. At this temperature, in addition to the existence of tetragonal symmetry, a mullite phase also develops. It shows that the dispersed product partially reacts with SiO_2.

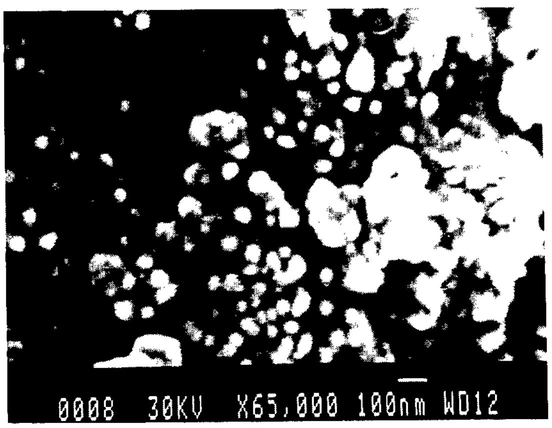

Figure 4.SEM micrograph of YZTZ-Al_2O_3(15%)-SiO_2 heated at 800°C

CONCLUSIONS

The nanocomposite systems YSTZ-Al_2O_3 and YSTZ-Al_2O_3 dispersed in SiO_2 have been successfully synthesized using sol-gel technique. Addition of Al_2O_3 stabilizes the tetragonal symmetry of ZrO_2 even above 1300°C. An almost 100% dense zirconia product has been prepared with the addition of Al_2O_3. Silica acts as an inert barrier between the crystallites and partially controlled the inter-crystallite growth of t-ZrO_2.

ACKNOWLEDGEMENT

The authors thank Prof. P.R. Subramanian, University of Madras, India and Prof. S. Ranganathan, Indian Institute of Science India for their constant support and encouragement. This work was partially supported by DST, UGC-SAP and UGC-COSIST.

REFERENCES

1. Gleiter, H., Progress in Materials Science 33 223 (1989).
2. Suryanarayaana, C., Bulletin of Materials Science 17 307 (1994).
3. Gleiter, H., Nanostructured Materials 6 3 (1995).
4. Birringer, R., Gleiter, H., Klein, H.P., and Marquardt, P., Phys. Letts. 102A 365 (1984).
5. Koji Ishida, Ken Hirota and Osamu Yamaguchi, Hideki Kume, Suguru Inamura and Hiroki Miyamoto, J. Amer. Ceram. Soc. 77 1391 (1994).
6. Ramamoorthy, R., Viswanath, R.N., and Ramasamy, S., Nanostructured Materials, 6 (1995) 337.
7. Prabhu, G.B., and Bourell, D.L., Nanostructured Materials 6 (1995) 361.
8. Benedetti, A., Fagherazzi, G., Enzo, S., and Battagliarin, M., J. Appl. Cryst. 21 (1988) 543.

Pergamon

NanoStructured Materials, Vol. 12, pp. 1089–1095, 1999
Elsevier Science Ltd

0965-9773/99/$–see front matter

PII S0965-9773(99)00305-0

CVD SYNTHESIS OF CARBON-BASED METALLIC PHOTONIC CRYSTALS

Anvar A. Zakhidov*, Ilyas I. Khayrullin, Ray H. Baughman, Zafar Iqbal**
AlliedSignal Inc., Research and Technology, Morristown, NJ 07962-1021, USA
* Department of Thermophysics, Uzbek Academy of Sciences,
Katartal 28, Chilanzar C, Tashkent 700135, Uzbekistan
** New Jersey Institute of Technology, Newark, NJ 07102-1982

Katsumi Yoshino, Yoshiaki Kawagishi, Satoshi Tatsuhara
Department of Electronic Engineering, Faculty of Engineering, Osaka
University, 2-1 Yamada-Oka, Suita, Osaka 565-0871, Japan

Abstract – *Three-dimensionally periodic nanostructures on the scale of hundreds of nanometers, known as photonic crystals, are attracting increasing interest because of a number of exciting predicted properties. In particular, interesting behavior should be obtainable for carbon-based structures having a dimensional scale larger than fullerenes and nanotubes, but smaller than graphitic microfibers. We show here how templating of porous opals by chemical vapor deposition (CVD) allows us to obtain novel types of graphitic nanostructures. We describe the synthesis of new cubic forms of carbon having extended covalent connectivity in three dimensions, which provide high electrical conductivity and unit cell dimensions comparable to optical wavelengths. Such materials are metallic photonic crystals that show intense Bragg diffraction. ©1999 Acta Metallurgica Inc.*

INTRODUCTION

The discovery (1) and upscaled synthesis (2) of fullerenes, which show such interesting phenomena as superconductivity and ferromagnetism, and the more recent discovery and large-scale synthesis of carbon nanotubes (3), has generated considerable interest in carbon-based nanoscale structures. Molecular engineering, using atomic architectures on the scale of 1 to 10 nm and selective chemistry, is expected to create a new generation of molecular electronic devices (4) where the flow of electrons can be modulated by the topology and geometry of the π-π bonds of the carbon structure (5). Although many interesting properties are expected on the scale of 100-500 nm (which corresponds to visible light wavelengths), the synthesis of carbon-based superstructures on this scale has been only recently realized (6). Larger scale carbon structures, of order10 μm in diameter, such as carbon microfibers, have been extensively investigated and are already widely utilized in carbon-carbon composites for various high tech applications..

The purpose of the present work is to bridge the submicron gap between the 10 Å scale of C_{60} and single wall nanotubes (SWNTs) and the 100 Å scale of giant fullerenes and multiwall nanotubes (MWNTs) on one side, and the 10 μm scale of carbon microfibers on the other, by synthesizing periodic conductive carbon structures in the 10 to 100 nm size scale. Carbon-based photonic crystal superlattices would enable wave-guiding much in the same way as electron transport is modulated in nanotube semiconductors (5,6). Such periodic and conductive cubic carbon superlattices may be a good choice of materials for the fabrication of metallic photonic crystals because their electronic and optical properties can be tailored by modifying the degree of π-π conjugation and the geometry of the carbon superstructure.

Photonic bandgap crystals (PCs) (7) having a photonic bandgap (PBG) have attracted considerable interest as the optical analog of semiconductors (8). The PBG plays the role of the forbidden energy gap in semiconductors. To open a wide PBG for a metallic conductor it is necessary, according to theoretical models, to form a metallic mesh with a network topology and very low filling factor (9). Metallic PBG's will then appear below a cut-off frequency that scales as a surface plasmon frequency (10).

In the present work we show how metallic photonic crystals with a network topology and low filling factors can be formed by using face-centered-cubic (fcc) arrays of self-assembled SiO_2 spheres as templates for a nanoscale architecture. This process allows one to fabricate new types of metallic photonic crystals, such as the newly synthesized cubic graphite phase.

PREPARATION OF TEMPLATES

Our process starts with the preparation of a synthetic porous opal matrix by a method which has been employed for several decades by the jewelry industry, and has been more recently described in detail (11). By varying the sizes of the monodispersed SiO_2 spheres between 160 and 300 nm, opal lattices with lattice parameters ranging between 226 and 424 nm were obtained, which were used as templates for the following synthesis. The porous opals were crystallized as fcc crystals with few stacking faults by sedimentation of monodispersed SiO_2 spheres from aqueous colloidal suspensions. The arrays of spheres are polycrystalline, with single crystal domains that are a few centimeters in length in the [111] rapid growth direction and a few millimeters on a side. Mechanical strength was achieved by an annealing process (700-800 °C for several hours), which provided a compressive modulus of 24 GPa, an ultimate strength of 107 MPa, and a failure strain of 0.8% for centimeter-sized blocks cut from the sintered polycrystalline opal. This sintering process causes a small contraction of the interball spacing and the formation of small diameter necks at interball contact points, which are of crucial importance for the following templating process. The interball separations were measured by scanning electron microscopy (12). Such crystallized sphere arrays are similar to gem quality natural opals, except that here the interstitial space between SiO_2 spheres is empty (25 % porosity filled with air), in contrast with the case for natural precious opals.

In the second step of the templating process, the surfaces of the SiO_2 spheres were tiled with carbon layers or the entire void spaces were filled with either CVD-deposited carbon from propylene or methane gas, in the apparatus shown schematically in Fig.1a. Afterwards, the SiO_2 spheres are chemically removed, leaving only a three-dimensionally periodic form of carbon,

which is a type of inverse opal or a 3-dimensional opal-replica. Prior to carbon CVD-infiltration, the bulk opal was cut into plates that were a millimeter thick and approximately 1 cm on a side. The deposition substrate temperature was 750-850 °C and the deposition time varied from 2 to 10 hours. In the third step, the SiO_2 spheres are chemically removed (Fig.1b) - leaving only a three-dimensionally periodic form of carbon, which is a type of inverse opal (also referred to as 3-dimensional opal-replica).

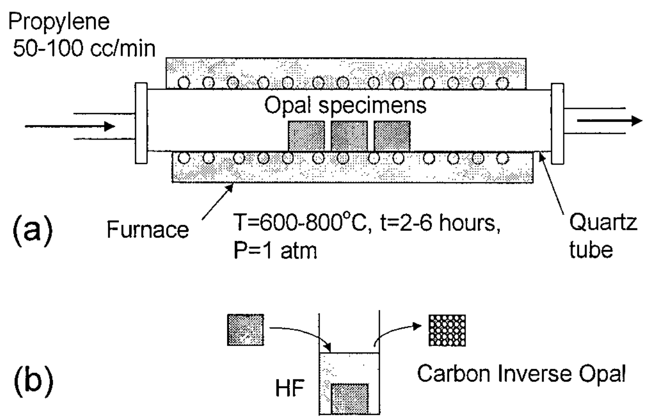

Fig. 1 Schematic diagrams of (a) the apparatus for CVD carbon templating process and (b) etching SiO_2 spheres in aqueous HF.

RESULTS AND DISCUSSION

The void space of the original millimeter thick opal lattice is reliably replicated in the structure of the carbon inverse opal. Figure 2a shows the SEM micrograph of the interconnected octahedral and tetrahedral voids of the starting opal. The SEM image of a sample having complete filling of voids with graphitic carbon is shown in Fig. 2b. When reaction conditions were optimal, we obtained samples that contained only this graphitic-inverse opal phase. The internal surface structure of the original opal was precisely replicated in the carbon phase - indicating that this phase is strong enough to survive the stresses generated during the dissolution of the SiO_2 balls with hydrofluoric acid. Samples that consist of only of this graphitic phase are fairly robust. However, slight variation in reaction conditions results in structural inhomogeneity. In such case the voids of the inner layer are filled with amorphous carbon. The amorphous carbon replica has poor mechanical strength and less accurately replicates the void space of the inverse opal does the graphitic carbon. This disordered carbon phase probably grows deep within the voids. The voids are thus partially filled by non-graphitic material, which loses the orientation of graphitic planes parallel to the surfaces of the spheres. This occurs for the first several layers which were subjected to higher temperatures during deposition. A small channel remains in the center of the void, indicating how the filling process

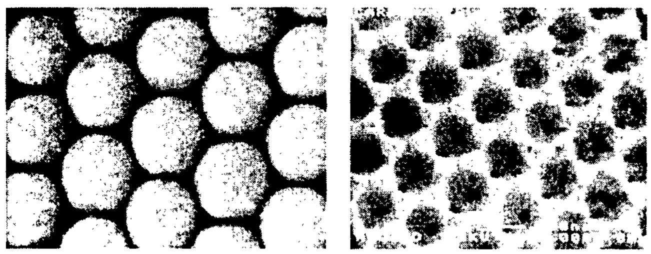

(a) (b)

Fig. 2. (a) The SEM image of parent silica opal before CVD-infiltration (black colored voids are empty). (b) Similar image of the (111) plane of a CVD-carbon inverse opal replica. The silica balls have been removed and voids are now filled with graphitic carbon. This "air-filled" lattice has high porosity (~76 %).

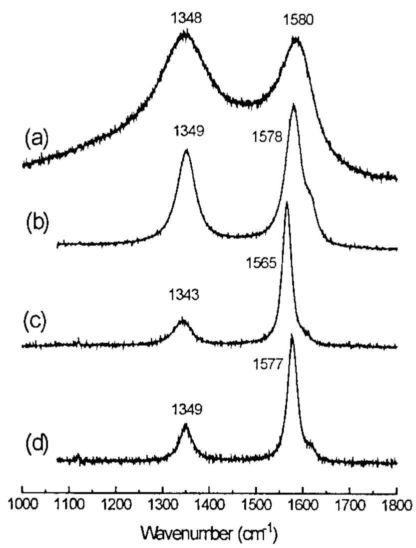

Fig. 3. Raman spectra of (a) CVD opal replica prior to high temperature annealing, (b) the same replica annealed at 2000 °C for 2 h, (c) a graphite film graphite grown on the surface of the sample during the CVD process, (d) a reference pitch fiber sample annealed at 2150 °C.

evolved. This phase shows broad Raman spectra typically associated with disordered microcrystalline carbon. It also demonstrates poor Bragg diffraction coloration, though with more blue and violet hues, due to the higher refractive index **n** of the more conductive carbon. We will not emphasize the properties of this amorphous, poorly conductive-replica phase here.

The micro-Raman spectra from various regions of the CVD graphitic carbon nanostructure are displayed in Fig. 3. The spectra were measured in a back scattering geometry using 1 mW of 514.5 nm laser radiation focused to a 2 μm spot size. The spectrum of the surface film (Fig.

of 514.5 nm laser radiation focused to a 2 μm spot size. The spectrum of the surface film (Fig. 3c) shows two lines at 1565 and 1343 cm^{-1}. The line at 1565 cm^{-1} can be assigned to the E_{2g} C-C stretching mode of graphite at 1582 cm^{-1}, which shows a surprisingly large down-shift in frequency, possibly due to strain in the film. Within the framework of a phonon confinement model, the width of the E_{2g} line corresponds to the lateral size L_a of the graphite nanocrystals in the film, using a correlation obtained by plotting the fitted phonon linewidths and powder x-ray diffraction patterns for single phase carbon standards (13). An average size of 12.6 nm can thus be obtained for the graphite crystallites. The line at 1343 cm^{-1} is associated with a Brillouin zone-boundary (Raman-inactive) mode that is activated by grain boundary disorder due to the finite size of the graphite crystals. The spectrum (and the corresponding L_a) for the surface film is similar to the Raman spectrum for an annealed carbon pitch fiber (Fig. 3d). The spectrum from the replicated nanostructure is shown in Fig. 3a. Here two broad bands at 1580 and 1348 cm^{-1} corresponding to the E_{2g} and the disorder-induced modes of graphite, respectively, are observed. In addition, a relatively strong background associated with a large amorphous carbon component in the structure, is observed. The deconvoluted width of the line at 1580 cm^{-1} is greater than 50 cm^{-1} and corresponds to a crystallite size smaller than 2 nm. The spectrum obtained from the sample annealed at 2000 °C (Fig. 3b) shows a dramatic decrease in scattering from the large amorphous carbon component in the as-prepared nanostructure and a factor of about 4 increase in crystallite size to a value of 7.5 nm.

An electron diffraction pattern from the graphitic inverse replica provides diffraction spacings close to that of ordinary graphite: 3.43 Å for (002), 2.10 Å for (100), 1.72 Å for (004), and 1.23 Å for (110). Only reflections of type (hk0) or (00l) are present, indicating that the carbon layers are not in lateral registry.

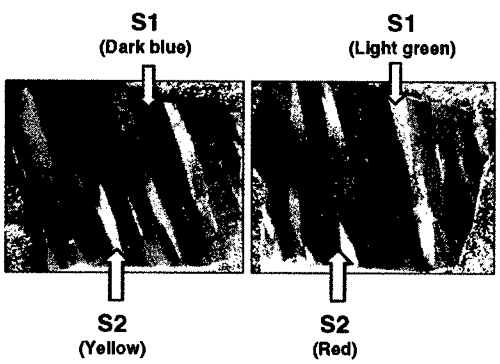

(a)

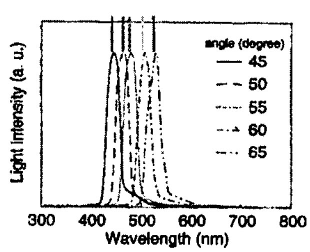

(b)

Fig. 4. (a) Photographs of a graphite inverse opal fabricated by the CVD process. The photographs are shot at two different incident light angles. Intense opalescence is due to Bragg scattering from the three-dimensionally periodic lattice. White arrows show the typical crystallite strips (S1 and S2) that change color on variation of the angle of incidence. The sample size is about 15 mm×20 mm with thickness of about 1 mm. (b) Bragg scattering spectra of one inverse opal crystallite perpendicular to the (111) direction.

A graphitic inverse replica shows colorful iridescence due to strong Bragg diffraction (Fig. 4a). Each color comes from crystallites of about ~ 2 mm to 1 cm in size that are oriented differently around the (111) direction of most rapid growth of the parent opals. The diffracted color shifts on variation of white light incidence angle (Fig. 4b).

The covalent bonding within the graphite sheets should provide high electrical conductivity. This is consistent with measured resistivity of the order of a few μΩ-cm in the carbon opal replicas. Therefore, these carbon replicas will be metallic photonic crystals in the optical region. Metallic PBG structures have been created in the microwave spectral range and the wide band PBG structures were found below $\omega_{cut\text{-}off}$ frequencies (8,9). However, this is the first example of a three-dimensional metallic photonic crystal for the optical region. For opening the metallic-type PBG a very small filling factor is favorable for decreasing the absorption and dissipation, but at the same time high conductivity is desired (10). These are exactly the conditions achievable in our CVD-carbon replicas, since the thickness of the walls, can be made less than 100 Å to provide the smallest filling factor, while three dimensional covalency, even though partially interrupted by short range disorder effects, forms the nanometer scale metallic mesh

One interesting application of the foam-like inverse graphitic carbon is as templates for the assembly of other optical and electronic materials as three-dimensionally periodic solids. Insertion of such materials into the carbon inverse opal can be accomplished by melt, solution, or gas phase infiltration by chemical, electrochemical, or physical deposition processes. While such composites previously made by opal infiltration are less than 24 volume percent of the inserted material, the present process can provide over 76 volume percent filling by the inserted material.

The materials described below contrast with the opal-derived composites of Bogomolov et al. (11c), which are interesting semiconductors, metals, or superconductors consisting predominantly of silica, since SiO_2 was not removed. The important advantage of our highly porous systems is the ability of filling the matrix with functional materials to provide superior performance in targeted applications. For example, we have demonstrated the possibility of enhancing the figure of merit of thermoelectrics by this method (12,14).

SUMMARY

In summary, we would like to stress again that we have obtained for the first time a new periodic and porous conductive carbon nanostructure. This new CVD- carbon nano-network, has interesting topology of covalent bonds, making it a three dimensional low density but highly conductive graphite. It is the first example of a metallic photonic crystal with an expected photonic band gap below a cutoff frequency in IR region. The details of these properties are now under investigation. In the visible optical range these structures show bright Bragg-diffraction induced coloration, which changes significantly with filling of the pores by various liquids.

ACKNOWLEDGMENTS

The authors thank A. Ribaudo and C. Bednarczyk for SEM imaging and N. Jia for measurements of the mechanical properties of the sintered opals. This work has been partially supported by the International NEDO grant on "Tunable Photonic Crystals" and the DARPA grant DAA7-96-J-036.

REFERENCES

1. Kroto, H.W., Heath, J.R., O'Brien, S. C. and Smalley, R. E., Nature, 1985, 318, 162.
2. Kratschmer, W., Lamb, L.D., Fostiropoulos, K. and Huffman, D. R., Nature, 1990, 347, 354.
3. a) Iijima, S. and Ichihashi, T., Nature, 1993, 363, 603; b) Iijima, S., Nature 1991, 354, 56
4. Thess, A., et. al., Science,1996, 273, 483.
5. Bochkrath, M. et. al., Science, 1997, 275,1922.
6. Zakhidov, A. A., Baughman, R. H., Iqbal, Z., Cui, C., Khayrullin, I., Dantas, S. O., Marti, J. and Ralchenko, V. G., Science, 1998, 282, 897.
7. a) Yablonovitch, E., Physical Review Letters, 1989, 57; b) John, S., Physical Review Letters, 1988, 57.
8. a) Sigalas, M. M., Chan, C. T., Ho, K. M., Soukoulis, C. M., Physical Review B: Condensed Matter, 1995, 52, 11744; b) Kuzmiak, V., Maradudin, A. A., Pincemin, F., Physical Review B: Condensed Matter, 1994, 50, 16835; c) Brown, E. R., McMahon, O. B., Applied Physics Letters, 1995, 67, 2138.
9. Fan, Shanhui, Vileneuve, Pierre R., Joannopoulos, J. D., Physical Review B: Condensed Matter, 1996, 54, 11245.
10. Leung, W. Y., Tuttle, G.; Sigalas, M. M.; Biswas, R.; Ho, K. M.; Soukoulis, C. M., Journal of Applied Physics, 1998, 84, 4091.
11. a) Deniskina, N. D., Kalinin, D. V. and Kazantseva, L. K., *Gem quality opals, their synthesis and natural genesi,* Nauka, Novosibirsk, 1988 (in Russian); b) Philips, A. P., Journal Material Science Letters, 1987, 8, 1371; c) Bogomolov, V. N., Kumzerov, Y. A., Romanov, S. G. and Zhuravlev, V. V., Physica C, 1993, 208, 371.
12. Baughman, R. H., Zakhidov, A.A., Khayrullin, I.I., Udod, I.A., Cui, C., Sumanasekera, G.U., Grigorian, L., Eklund, P. C., Browning, V., and Ehrlich, A., *Nanostructured Thermoelectrics Based on Periodic Composites from Opals and Opal Replicas: I. Bi-infiltrated opals.*, Proceedings of XVII International Conference on Thermoelectrics ICT98 (Nagoya Trade & Industry Center, Japan) May 25-28, 1998, 288.
13. Iqbal, Z., Lui, S.C., Zero, K., Murthy, S. and Murdie, N., (to be published).
14. Zakhidov, A., Baughman, R.H., Khayrullin, I., Udod, I., Kozlov, M., Iqbal, Z., Cui, C., Browning, V., Ehlrich., A., Abstracts of Material Society Fall Meeting, Nov. 30- Dec. 4, 1998, Boston, Massachusetts, 488.

Pergamon

NanoStructured Materials, Vol. 12, pp. 1097–1102, 1999
Elsevier Science Ltd

0965-9773/99/$–see front matter

PII S0965-9773(99)00306-2

THE LOW TEMPERATURE DEPENDENCE OF MAGNETIZATION OF AS-DEPOSITED Fe-Hf-C-N NANOCRYSTALLINE THIN FILMS

K.S. Kim, Y.H. Seong, S.C. Yu, S.H. Han* and H.J. Kim*

Department of Physics, Chungbuk National University, Cheongju, 361-763, Korea.
*Thin Film Technology Research Center, Korea Institute of Science and Technology, P.O Box 131, Seoul 130-650, Korea

Abstracts -- We have studied the magnetic properties of as-deposited Fe-Hf-C-N and Fe-Hf-N nanocrystalline thin films with good soft magnetic properties. Thin films have been prepared by a reactive magnetron sputtering method in a nitrogen atmosphere. The as-deposited thin films are fully nanocrystallized during deposition by controlling the composition and sputtering condition. Fe-Hf-C-N and Fe-Hf-N films show good soft magnetic properties of saturation magnetization of about 17 kG and coercivity of 0.5 Oe. In order to investigate the intrinsic magnetic properties, we analyzed the temperature dependence of magnetization. Both of the thin films are composed of finely dispersed Fe(~ 5 nm) and smaller Hf precipitates. It seems that exceptionally small grains and precipitates enhance the soft magnetic properties.
©1999 Acta Metallurgica Inc.

INTRODUCTION

Fe-[Hf,Ta,Zr]-C and Fe-[Hf,Ta,Zr]-N nanocrystalline films are reported to have good soft magnetic properties together with high thermal stability(1,2). A demand for high performances in miniaturized electronic/electrical equipment forces soft magnetic materials to play an important role in micro-magnetic devices including thin film inductors or transformers operating at high frequency. However, the excellent soft magnetic properties of Fe-based thin films are only obtained after post heat treatment. Transition metals carbides or transition metals nitrides formed during the heat treatment are considered to act as nucleation or pinning sites of grain growth, resulting in nanoscale α-Fe grains. The fine grains of α-Fe are regarded as one of the essential factors for magnetic softness. The as-deposited films are applicable to magnetic devices which have not been heat treated, since heat treating deteriorates components and materials that are sensitive to the high temperature exposure. Thin films with higher $4\pi M_s$ are more favorable in practical applications. We already reported that as-deposited Fe-Hf-C-N thin films have nanocrystalline structures and good soft

magnetic properties, coercivity of 0.5 Oe, saturation magnetization of 13 kG, and effective permeability over 3000 up to 100 MHz (3). Thus, the magnetic properties of as-deposited Fe-Hf-C-N thin films are investigated to increase $4\pi M_s$ by controlling the deposition conditions and as-deposited ternary Fe-Hf-N thin films are also investigated for easy fabrication. Moreover, in order to investigate the intrinsic magnetic properties, we analyzed the magnetization behavior. It would be of interest to examine how the resultant magnetic properties change with N_2 partial pressure content in Fe-Hf-C-N alloys.

EXPERIMENTAL

Fe-Hf-C-N and Fe-Hf-N as-deposited thin films have been prepared by a reactive magnetron sputtering method in a nitrogen atmosphere. The pallets of Hf and C are put on the pure Fe target to control thin film compositions. The flow of Ar gas is maintained at 20 sccm, and, N_2 partial pressure is regulated in the range from 0 % to 10 % in order to obtain the films with various nitrogen contents. Both the mixed gases are introduced into the chamber after it has been evacuated to a pressure below 1×10^{-6} Torr. The working pressure is maintained at 1 mTorr. The distance between the target and the water-cooled Si(001) substrate is 6 cm. The RF input power varies from 150 W to 550 W. The film thickness is 1 ± 0.2 μm, measured by a stylus profiler. The compositions and the microstructures of the films are analyzed by X-ray diffraction with Cu $K\alpha$ and transmission electron microscopy(TEM). The temperature dependence of magnetization was measured using a SQUID magnetometer during heating from 5 to 500 K, with an applied field of 20 kOe. The magnetic hysteresis loop are examined by a VSM. The frequency dependence of μ_{eff} is obtained in the hard direction by using an 8-figure coil method. The electrical resistance of the films is measured by a four-point probe method.

RESULTS AND DISCUSSION

Figure 1 represents the temperature dependence of magnetization for the as-deposited Fe-Hf-C-N films as a function of N_2 partial pressure from 5 K to 300 K in field of 20 kOe. It is seen that the magnitude of magnetization decreases monotonically with the increase of temperature. The temperature dependence of magnetization becomes similar to that observed in normal ferromagnets. It is noted that the values of M for the Fe-Hf-C-N thin film without N_2 partial pressure are much smaller than the thin film with N_2 partial pressure. At low temperature, this kind of magnetization M(T) is described in terms of the Bloch's law. The Bloch coefficients B, which is the thermal average of the total contribution arising from spin waves of all wavelengths, is related to the spin wave stiffness D, by the expression (4)

$$D = \zeta(3/2)^{2/3}[g\mu_B/M(0)B]^{2/3}(\kappa_B/4\pi) \qquad [1]$$

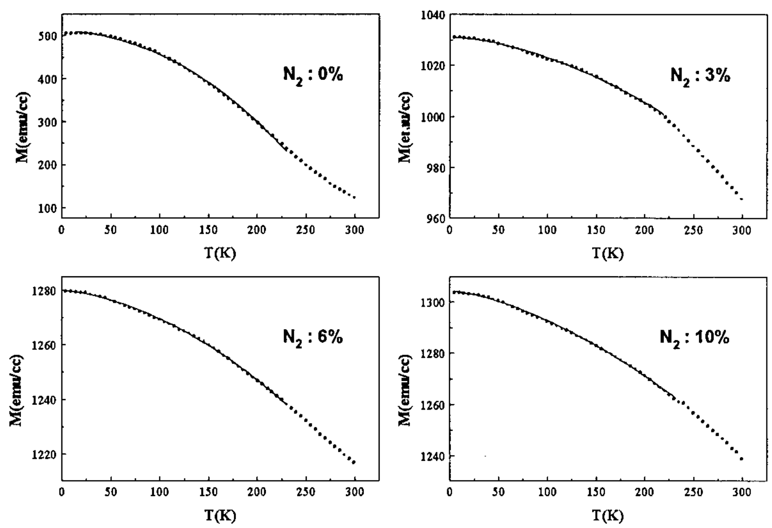

Figure 1. Temperature dependence of magnetization of as-deposited Fe-Hf-C-N thin films as a function of N_2 partial pressure (Solid line gives the results with $T^{3/2}$ fitted curve).

where $\zeta(3/2)$ is the Riemann zeta function and g is the spectroscopic splitting factor. The values of D were determined from a fit to the SQUID magnetic data. It is found that the values of D increase from 140.5 to 197.3 meVÅ^2 with increasing N_2 partial pressure. This may be due to the increasing proportion of positive Fe-Fe and Fe-Hf interactions at short interatomic separations. The larger value of D enhance the exchange energy between atoms. In order to clarify this behavior, we show the effect of N_2 partial pressure on the soft magnetic properties of Fe-Hf-C-N and Fe-Hf-N thin films in Fig. 2. At low N_2 partial pressure (3~4 % and 4~6 %), $4\pi M_s$ are relatively small. Nitrogen, introduced during deposition, enhance the $4\pi M_s$ of the films. The maximum values for both films are ~17.5 kG and ~16.5 kG at 6~8 % and 7~8.5 % of P_{N2}, respectively. The coercivities of both films have a minimum value at 5~6.5 % and 7~8 % of P_{N2}. The minimum coercivities of both films are about 0.5 Oe. Figure 3 shows the effective permeability(μ_{eff}) at 100 MHz with N_2 partial pressure and RF input power. The μ_{eff} of the as-deposited films shows a good flat dependence on frequency, which remains around 3000 up to 100 MHz. As shown in Fig. 3, the μ_{eff} decreases slightly at the input power of 550 W. The best soft magnetic properties are observed at 450 W. The addition of nitrogen strongly affects the μ_{eff} . The μ_{eff} of both films increases with the introduction of nitrogen and reach the maximum of 3000 in the range of 5.5~6 % and 7.5~8 % of P_{N2} for Fe-Hf-C-N and Fe-Hf-N, respectively and remains flat up to 100 MHz without any loss until several 10 MHz. However, excessive N_2 content in the films decreases the μ_{eff} near P_{N2} = 10 %.

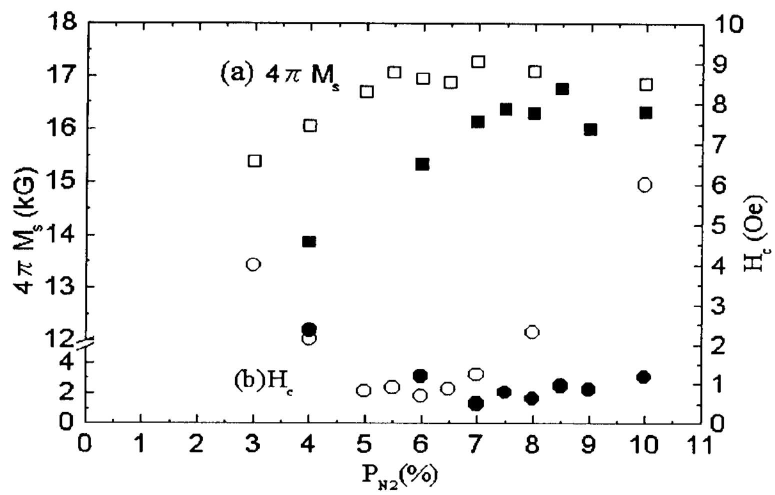

Figure 2. (a) Saturation magnetization ($4\pi M_s$) and (b) coercivity (H_c) as a function of N_2 partial pressure. (an applied field (H_a) of 100 Oe, 4πMs : □ Fe-Hf-C-N ■ Fe-Hf-N, H_c: ○ Fe-Hf-C-N, ● Fe-Hf-N, the error range of data points is $\pm 5\%$)

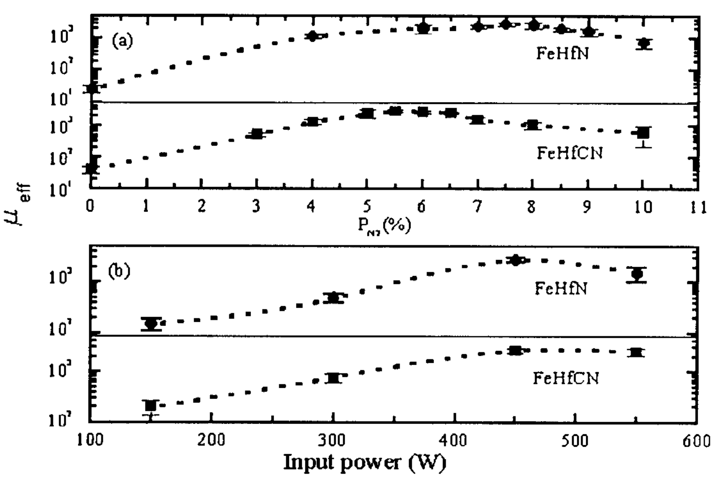

Figure 3. Effective permeability at 100 MHz (measured in the hard direction) with (a) N_2 partial pressure and (b) RF input power. The films show a flat frequency spectrum in optimum condition

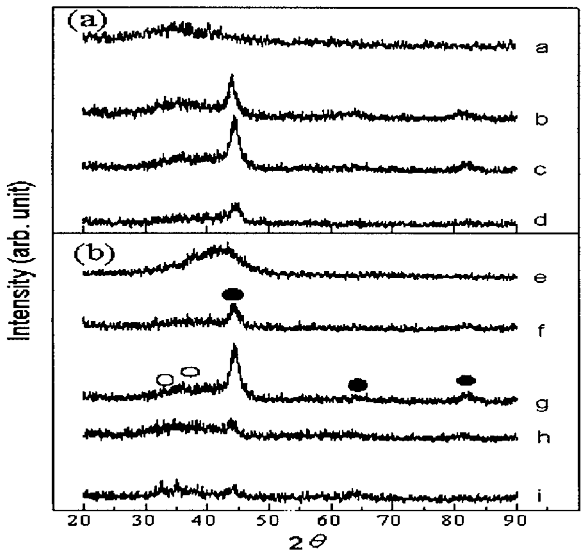

Figure 4. X-ray diffraction patterns ● α-Fe(110), (200), (211) and ○Hf-precipitates (111), (200) of Fe-Hf-C-N thin films with RF input power (a=150 W, b=300 W, c=450 W, d=550 W) and N_2 partial pressure (e=0%, f=3%, g=6%, h=8%, i=10%)

The measured μ_{eff} in the easy direction are not constant and very small (about 10 ~ 100). In order to understand the excellent high frequency permeability, the electrical resistivites of the films are measured. The resistances are around 100 $\mu\Omega$cm which is similar to those of other Fe-nanocrystalline films. This means that the excellent dependence of effective permeability is not mainly due to the decrease of eddy current loss by the decrease of electrical resistivity. The excellent dependency appears when the permeability is measured in the hard direction, which means the existence of in-plane magnetic anisotropy at as-deposited films. A hysteresis loop shows that the frequency dependence of effective permeability is more excellent when the anisotropy is well aligned in the hard direction than widely dispersed (5). This means that the degree of magnetic anisotropy dispersion is related with permeability dependence. However, magneto-crystalline anisotropy is known to be averaged out by the refinement of α-Fe grains (6). The existence of in-plane anisotropy of the films could be due to the stray field from magnetron ring and interstitial insertion of C and N in α-Fe. Due to fast deposition, carbon and nitrogen remain in the octahedral sites of α-Fe lattice, which contributes to uniaxial anisotropy. Even though the uniaxial

anisotropy due to the solute atoms leads to the increase of the net anisotropy, the softness of the films is still maintained.

On the other hand, the variations of X-ray diffraction pattern with the addition of N and RF input power are shown in Fig.. 4. Fig. 4(a) shows that the films deposited at the input power of 150 W are amorphous or mixed phases of amorphous and crystalline states, and that high input power generally crystallizes the films during deposition. Fig. 4(b) shows that nitrogen enhances the crystallization of the films from a mixed phase of crystalline and amorphous states, which is confirmed by TEM analysis. We have already reported the Fe-Hf-C-N films consist of finely grained α-Fe with diameter of ~5nm and Hf(C,N) precipitates of smaller sizes (5). The morphology of exceptionally small grains surrounded by Hf-precipitates contributes to the excellent soft magnetic properties. Thus, as-deposited Fe-Hf-C-N and Fe-Hf-N thin films are completely crystallized in the case where the RF input power and N_2 partial pressure are well controlled.

CONCLUSION

As-deposited $Fe_{79.9\text{-}81.1}Hf_{6.8\text{-}7.2}C_{2.0\text{-}2.5}N_{9.8\text{-}10.8}$ nanocrystalline thin films exhibit excellent soft magnetic properties. The temperature dependence of the magnetization of as-deposited Fe-Hf-C-N thin films approximately follows the prediction of spin wave theory. The spin wave stiffness constant increases with increasing N_2 partial pressure. The addition of nitrogen strongly affects the μ_{eff} and enhances the crystallization of the films from a mixed phase of crystalline and amorphous states. Especially, the small grains and Hf-precipitates enhance the soft magnetic properties.

This research were supported by the Basic Science Research Institute Program, Korean Ministration of Education, 1997, Project No. 2410 and also by the Korean Science and Engineering Foundation under grant No. 96-0702-05-013.

REFERENCES

1. Hasegawa, N. Saito, M. Kojima, A. Makino, A. Misaki, Y. and Watanabe, T., Journal of Magnetic Society of Japan. 14, 319 (1990)
2. Nakanishi, K. Shimizu, O. and Yoshida, S., Journal of Magnetic Society of Japan. 15, 371 (1991).
3. Choi, J.O. Lee, J.J. Han, S.H. Kim, and Kang I.K., Journal of Applied Physics. 75(10), 5785 (1994).
4. Keffer. F., in Encyclopedia of Physics (Springer, Berlin, 1966), Vol. XVII-2.
5. Song, J.Y. Lee, J.J. Han, S.J. Kim, H.J. and Kim, J. Appl. Phys. 83, 6652 (1998)
6. Herzer. G., IEEE Transaction on Magnetics.. 26(11), 1397 (1990)

Pergamon

NanoStructured Materials, Vol. 12, pp. 1103–1108, 1999
Elsevier Science Ltd

0965-9773/99/$–see front matter

PII S0965-9773(99)00307-4

MECHANICAL PROPERTIES OF NANOSTRUCTURED CHROMIUM

V. Provenzano[1], R. Valiev[2], D.G. Rickerby[3], and G. Valdre[4]
[1]Naval Research Laboratory, Washington, DC 20375-5343 USA
[2]Ufa Technical University, Institute of Materials Physics, Ufa, Russia
[3]JRC, Institute of Advanced Materials, I-21020 Ispra (VA), Italy
[4]University of Bologna, Department of Physics, Bologna, Italy

Abstract *- In this paper we present some initial results on pure chromium whose grain structure was refined by severe plastic deformation processing. These results include the microstructural features and the corresponding mechanical properties as a function of severe plastic deformation processing and annealing treatment. They show that severe plastic deformation is quite effective in reducing the grain size down to nanoscale dimensions with an attendant large increase in the hardness value; the hardness data is consistent with Hall-Petch strengthening. The annealing treatment demonstrated that the nanoscale microstructure is retained up to 400°C. Further, the decrease in the hardness value with increasing annealing temperature is quite gradual up to 900°C, suggesting that the microstructure of pure chromium, resulting from the severe deformation is not too unstable, but, it coarsens gradually with increasing temperature. Therefore, in the chromium alloys the deformed microstructure is expected to be even more stable due to the beneficial effect of the alloying additions in pinning the grain boundaries. ©1999 Acta Metallurgica Inc.*

INTRODUCTION

Due to their elevated temperature properties, such as high strength, melting temperature, and oxidation resistance, the chromium-based alloys are potentially very attractive for a variety of structural applications, including their use as low activation materials for fusion reactor components. To date, however, the potential of this class of alloys has not been translated into practice, because, though they are strong and hard, they are inherently brittle. In fact, they exhibit little or no ductility at low temperatures together with an unacceptably high ductile-to-brittle transition temperature (DBTT). The sixties and early seventies, marks the period when the mechanical properties of theses alloys were actively studied, their inherently brittle behavior was amply demonstrated. However, some of the studies, published during this period, appear to suggest that the low temperature ductility and fracture toughness properties could be markedly improved by grain refinement. Among the results reported during this period, are those of Wilcox (1), Gilbert (2), and Wain (3) and their respective co-workers, all of which point to the critical role of grain size on the resulting mechanical properties. For example, Wilcox and co-workers showed that by decreasing the average grain size of chromium, from 37to 2.4 mm by the addition of a few percent of thoria particles, resulted in a significant decrease in DBTT (from 140 to 15°C) together with

significant improvements both in the ductility and strength (1). However, in spite of the promising results reported in the above referenced studies, the overall picture concerning the chromium-based alloys was far from being clear. In fact, data reported by other researchers showed contradictory and confusing trends regarding the beneficial effect of grain refinement on the mechanical properties. Adding to this uncertainty, was the lack of systematic studies. In fact, in a number of studies, the effect of grain size was either masked or not clearly separated from other possible effects, such as solid solution and dispersion strengthening, or prestraining. Finally, no clear consensus was reached among the various researchers concerning the different effects and proposed ductilizing mechanisms.

Although preceded by about a decade of active research, the middle seventies is roughly the time when the interest in the chromium-based alloys for structural applications suddenly declined. This rapid and greatly diminished interest, was most likely caused by the realization that, up to that point, no effective and reliable way was found to significantly improve their ductility and fracture toughness properties. The past few years, however, have seen a renewed interest in high temperature materials that are intrinsically brittle at low and at moderate temperatures, such as the intermetallics and the refractory metals and their alloys. This renewed interest has been partly motivated by the research and development efforts in the area of nanostructured materials.

Nanostructured materials, characterized by small grain sizes (100 nm or less) and large surface to volume ratios, often exhibited unique and novel properties relative to those of the coarse-grained counterparts. Among the novel properties are the mechanical properties of nanocrystalline metals and alloys. For example, Valiev and his co-workers have observed low temperature superplastic behavior in some aluminum alloys and substantial ductility in some intermetallics when the grain size of is reduced to nanoscale dimensions (4, 5, 6). Besides these results, other investigators have reported observing Hall-Petch softening, increased ductility, and the absence of strain hardening in nanocrystalline metals when the grain size falls below some critical dimensions (in the range of 5-15 nm, depending on the metal) (7, 8, 9). The enhanced low temperature ductility observed in nanocrystalline metals has been largely rationalized by the lack dislocation activity at these small grain dimensions and to the onset of creep deformation mechanisms, such as grain boundary sliding (9). The diminishing role of dislocations and the increasing role of grain boundaries in the deformation processes, as the size of the grain becomes very small, are consistent with theoretical results from the modeling studies by Van Swygenhoven and Schiotz and their respective co-workers (10, 11). Taken together, these experimental results and modelling predictions suggest that mechanical properties of intrinsically brittle materials can be significantly improved by refining their microstructure down to nanoscale dimensions.

In this paper we present some initial mechanical property results (Vickers hardness) of pure chromium, whose microstructure was refined by the severe plastic deformation recrystallization (SPDR) method. These results are part of a larger collaborative effort involving our laboratories whose basic objective is the enhancement of the mechanical properties (improved ductility and fracture toughness properties) of high-chromium alloys through grain refinement. Besides the mechanical property results, we also present results form microstructural analysis obtained on chromium samples after grain refinement process and subsequent annealing.

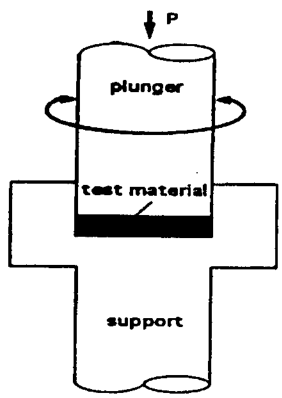

Figure 1. Schematic diagram of torsion straining apparatus used for the severe plastic deformation processing of the chromium samples

EXPERIMENTAL PROCEDURE

As mentioned in the previous section, the process used for refining the microstructure was the SPDR method. Compared to nanostructured materials produced by powder processing techniques, often resulting in samples that are both contaminated and not fully consolidated, the samples produced by SPDR method have two distinct advantages: they are fully consolidated and they preserve the composition of the starting materials. This method was pioneered by Valiev and his co-workers in Ufa, Russia. To obtain the desired nanoscale structure, deformation levels of the order of 4-7 logarithmic strains are used. To reach these high strains and depending on the starting metal or alloys, two different processing routes are employed. They are: torsion under quasi-hydrostatic pressure and equal channel angular pressing, operated in the 400-700°C temperature range.

The results that are presented in this paper refer to those obtained on commercially grade pure chromium that had been severely plastically deformed by torsion straining at room-temperature (torsion apparatus shown schematically in figure 1). The starting material, in form of flat coupons, 99.7% pure chromium and referred as DUCROPUR™, was purchased from Metallwerke Plansee AG, Austria. The coupons had been produced by the company through a proprietary powder processing route. Before the straining, the coupons were machined into thin disk samples of 20 mm in diameter and 2 mm in thickness.

The microstructure of the chromium samples before processing was characterized by optical microscopy, whereas the microstructure after the severe torsion straining and after the deformed samples were given a heat treatment at 400°C for 30 min, was, instead, examined by transmission electron microscopy (TEM). In this initial phase of study, the mechanical properties of the chromium samples as a function of the severe plastic deformation processing and subsequent heat treatment were characterized by hardness measurements.

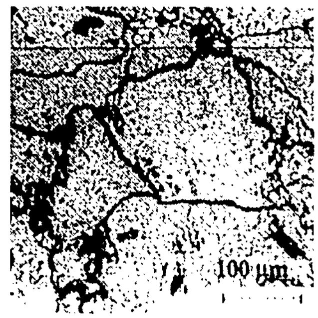

Figure 2. Optical micrograph showing the typical microstrucure of as-received chromium

RESULTS AND DISCUSSION

The optical micrographs presented in Fig. 2 illustrates the typical microstructure of the pure chromium in the as-received condition. The microstructure is characterized by large grains (82 mm average grain size).

The TEM micrographs and the corresponding electron diffraction patterns presented in Fig. 3 typify the microstructural features after the severe plastic deformation (top micrograph) and after the severe plastic deformation and the 400°C annealing treatment (bottom micrograph). With regards these TEM results, it can be concluded that the grain size of the chromium was significantly refined by the severe plastic deformation processing. In fact, the average grain was reduced from close to hundred microns to about 100 nm, representing a reduction in size of the grains of more than two orders of magnitude. Also, the nanoscale grain size was retained after the deformed samples were given the annealing treatment at 400°C. The significant effect of the severe plastic deformation in refining the microstructure is also confirmed by the room temperature Vickers hardness data presented in Fig. 4. Figure 4 (a) shows that greatly reduced grain size produced more than three fold increase in the hardness value (from about one to about 6 GPa) compared to that of the chromium in the as-received condition. Also, the hardness data in Fig. 4 (a) shows there is a small decrease in the hardness value of deformed sample close to the center of the disk where the straining is expected to be somewhat lower. The data presented in Fig. 4 (b) shows the variation of the hardness of the deformed material as a function of annealing temperature (all the samples were annealed for 30 min.). Even for the sample that was annealed at 900°C the hardness value is higher of than that of the as-received condition. This data shows also a gradual decrease in the hardness from room temperature to about 550°C. For higher temperatures, the variation is a little steeper.

Figure 4 (a) shows that greatly reduced grain size produced more than three fold increase in the hardness value (from about one to about 6 GPa) compared to that of the chromium in the as-received condition. Also, the hardness data in Fig. 4 (a) shows there is a small decrease in the hardness value of deformed sample close to the center of the disk where the straining is expected to be somewhat lower. The data presented in Fig. 4 (b) shows the variation of the hardness of the deformed material as a function of annealing temperature (all the samples were annealed for 30 min.). Even for the sample that was annealed at 900°C the hardness value is higher of than that of the as-received condition.

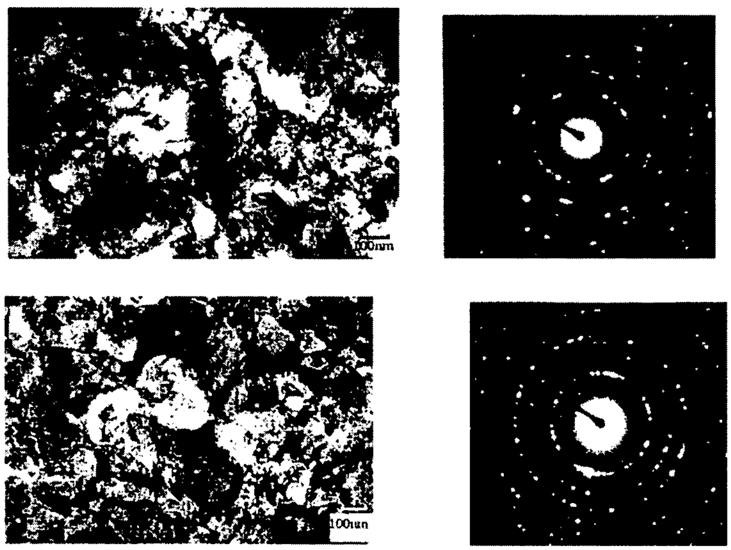

Bright field **SAED**

Figure 3. TEM micrographs and corresponding selected area electron diffraction patterns showing the typical microstructure of chromium after the severe plastic deformation (top panel) and after the deformed specimen was annealed at 400°C for 30 min (bottom panel)

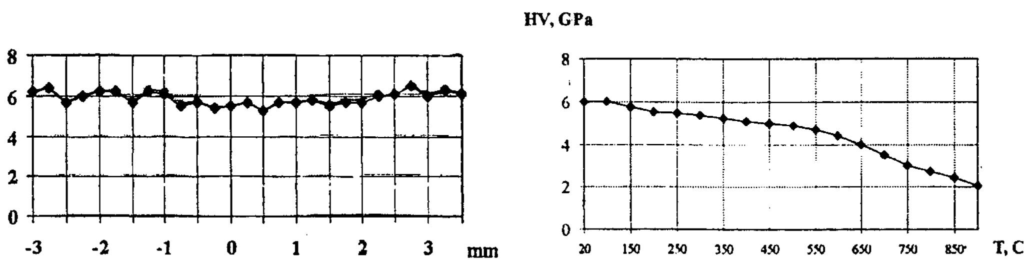

Figure 4. Room temperature Vickers microhardness of deformed chromium along the disk diameter (top panel) and as a function of annealing temperature (bottom panel)

This data shows also a gradual decrease in the hardness from room temperature to about 550°C. For higher temperatures, the variation is a little steeper.

The microstructural features and the hardness data presented in Figs. 3 and 4, lead to the following considerations. First the severe torsion straining, even at room temperature, is quite effective in reducing the grain size of chromium by more than two orders of magnitude. This large reduction in grain size is reflected in the significant increase in the hardness value by more than a factor of three. Secondly, although it is hard to obtain good statistics of grain size from the TEM micrographs shown in Fig. 4, relating to the typical microstructure of the severely deformed chromium samples before and after the annealing treatment, linear intercept analysis yielded the following values for the average grain size: 125 and 170 nm before and after the heat treatment, respectively. Therefore, combining these values to that of 82 μm average grain size of chromium in the as-received condition, the variation of Vickers hardness

with grain size is roughly as follows: 1.2, 5.0, and 6.0 GPa respectively corresponding to: 82, 0.17, and 0.13 μm. Taken together these values show that the hardness of chromium follows the Hall-Petch relation. Finally, the relatively small coarsening of the microstructure of the deformed samples after the 400°C annealing treatment (Fig. 3) together with the gradual decrease in the hardness value with increasing annealing temperature (Fig. 4), suggest a gradual coarsening of the severely deformed microstructure with increasing annealing temperature. This result is somewhat surprising, in consideration of the fact that the microstructure after the severe plastic deformation is heavily worked and thus metastable. Therefore, with regards with microstructural stability, the results obtained on pure chromium are quite promising for the chromium alloys, where it is expected that grain coarsening with temperature will be significantly lower due to the fact that will further stabilize the microstructure by grain boundary pinning.

CONCLUDING REMARKS

As previously stated, the results included in this paper are preliminary. This is mainly due to the fact that they represent the initial results of a collaborative effort that was only started six months ago. Though incomplete, these initial results are encouraging. They clearly indicate that severe plastic deformation method is an effective route for refining the microstructure of chromium, the same is expected for its alloys. Further, the refined microstructure is fairly stable resulting in a significant increase in the harness value when compared to that of the much coarser chromium in the as-received condition. In future, when it is hoped that additional and more complete data will be available, we will be able to report if the refined microstructure and increased hardness observed in the severely deformed pure chromium will translate in improved ductility and fracture toughness properties both of chromium and its alloys when their grain size is refined to the nanoscale dimensions.

References

1. Wilcox, B. A, Veigel, N. D., and Clauer, A. H., Metall. Trans., 3 (1972) 273
2. Gilbert, A, Reid, C. N., and Hahn, G., T, J. Inst. of Metals, 92 (1963) 352
3. Wain, H. L., Jjonhstone, S. T. M., and Henderson, F., J. Inst. Metals, 91 (1962) 41
4. Valiev, R. Z., Ann. de Chem. Fr. 21 des Materaux (1996) 369
5. Valiev, R. Z., Salimonenko, D. A., Tsenev, N. K., Berbon, P. B., and Langdon, T. G., Scripta Materialia, 37, No. 12 (1997) 1945
6. Lian, J., Valiev, R. Z., and Baudelet, B., Acta Metall. Mater., 43, No. 11 (997) 4165
7. Sanders, P. G., Eastman, J. R., and Weertman, J. R., Acta Mater., 45, 10 (1997) 4019
8. Siegel, R. W. and Fouger, G. E., NanoStruct. Mater., 6 (1995) 205
9. Hahn, H. and Padmanabhan, K. A., Phil. Mag. 76, No. 4 (1997) 125
10. Van Swygennhoven, H. and Caro, A., Appl. Phys. Lett. 71 (1997) 12
11. Schiotz, J, Di Tolla, F. D., and Jacobsen, K. W., Nature, 391, No.5 (1998) 561

Pergamon

NanoStructured Materials, Vol. 12, pp. 1109–1112, 1999
Elsevier Science Ltd

0965-9773/99/$–see front matter

PII S0965-9773(99)00308-6

STRUCTURAL DIFFERENCES BETWEEN THE NANOCRYSTALLINE $Fe_{86}Zr_7B_6Cu_1$ AND $Fe_{73.5}Si_{13.5}B_9Nb_3Cu_1$ ALLOYS

Á. Cziráki[1], I. Gerőcs[1], L.K. Varga[2], A Lovas[2,3] and I. Bakonyi[2]

[1]Eötvös University, Dept. of Solid State Physics
H-1088 Budapest, Múzeum krt. 6-8, Hungary

[2]Research Institute for Solid State Physics and Optics, Hungarian Academy of Sciences
H-1525 Budapest, P.O.B. 49, Hungary

[3]Dept. of Mechanical Engineering Tchnology, Technical University of Budapest
H-1111 Budapest, Bertalan L. utca 2, Hungary

Abstract — *The initial permeability, density and microstructure are compared as a function of the annealing temperature for nanocrystalline $Fe_{86}Zr_7B_6Cu_1$ and $Fe_{73.5}Si_{13.5}B_9Nb_3Cu_1$ alloys. In the optimum annealed state where the initial permeability is the maximum, flat disc-shaped bcc-Fe(Zr) grains were observed by transmission electron microscopy in $Fe_{86}Zr_7B_6Cu_1$ in contrast to equiaxed bcc-Fe(Si) grains in $Fe_{73.5}Si_{13.5}B_9Nb_3Cu_1$. X-ray diffraction revealed a preferred orientation of the bcc grains and large internal stresses in the nanocrystalline $Fe_{86}Zr_7B_6Cu_1$ alloy. All these observations may partly contribute to the fact that in the optimum annealed state, the initial permeability is much higher for $Fe_{73.5}Si_{13.5}B_9Nb_3Cu_1$ than for $Fe_{86}Zr_7B_6Cu_1$. ©1999 Acta Metallurgica Inc.*

INTRODUCTION

It has been reported that partial crystallization of amorphous Fe-Z-B-Cu [1] and Fe-Si-B-Nb-Cu [2] ribbons results in nanocrystalline alloys with attractive soft magnetic properties. However, the initial permeability of the two nanostructured alloys differs significantly [1,2]. The aim of this paper is to carry out a detailed investigation of these nanocrystalline alloys as a function of annealing temperature in order to clarify some of the structural reasons of this difference. Besides density measurements, the evolution of structural properties during annealing of these two types of amorphous alloys was investigated by X-ray diffraction (XRD) and transmission electron microscopy (TEM).

EXPERIMENTAL

Amorphous $Fe_{86}Zr_7B_6Cu_1$ and $Fe_{73.5}Si_{13.5}B_9Nb_3Cu_1$ (FINEMET) ribbons of 10 mm wide were prepared by melt-spinning which were subsequently annealed for 1 hour at different temperatures (T_a). The density of the ribbons was measured by the Archimedean method by immersing the sample in toluol and using a Mettler M3 microbalance. The initial permeability was determined from the inductivity of a toroidal ribbon core, measured by a

Hewlett-Packard 7114 type LCR meter at 1 kHz frequency and 0.8 A/m (≈ 10 mOe) exciting field. The structure of the samples was analyzed by a Philips X'Pert type X-ray diffractometer. The grain size and the internal stresses were determined with the help of Williamson-Hall plots, the lattice parameters were deduced for each of the first five reflections of body-centered cubic iron (bcc-Fe) and then extrapolated to the 90° Bragg angle. A direct study of the microstructure formed during annealing in the samples was performed by TEM measurements using a Philips M20 equipment.

RESULTS AND DISCUSSION

The initial permeability values measured on the ribbons annealed at different T_a temperatures for 1 hour are shown in Fig. 1 for the compositions $Fe_{86}Zr_7B_6Cu_1$ and $Fe_{73.5}Si_{13.5}B_9Nb_3Cu_1$ with optimum annealed state at 600 °C and at 550 °C, respectively. In the optimum nanocrystalline state, the FINEMET alloy exhibits a much higher initial permeability than the Fe-Zr-B-Cu alloy.

The density of the annealed samples (Fig. 2) shows a rapid increase at 550°C in the case of the FINEMET alloy whereas it remains almost nearly constant for the Fe-Zr-B-Cu alloy, even after the second crystallization stage.

According to the structural studies performed by XRD and TEM, in the optimum annealed state both alloys exhibit an ultrafine grain structure with an average crystallite size of about 10-20 nm, and the crystallites are embedded in an amorphous matrix. This means that the small grain size is only one of the prerequisites for good soft magnetic behaviour and, therefore, we have to look for further factors to explain the large difference between the soft magnetic properties of the Fe-Zr-B-Cu and Fe-Si-B-Nb-Cu alloys.

For the Fe-Zr-B-Cu alloy, the lattice parameter of the bcc grains is slightly above the value for pure bcc-Fe. On the contrary, the lattice parameters for the nanocrystalline FINEMET samples are well below the pure bcc-Fe value. This can be ascribed to the fact that large Zr and small Si atoms are substitutionally dissolved in the bcc-Fe crystallites in the first and second alloy, respectively.

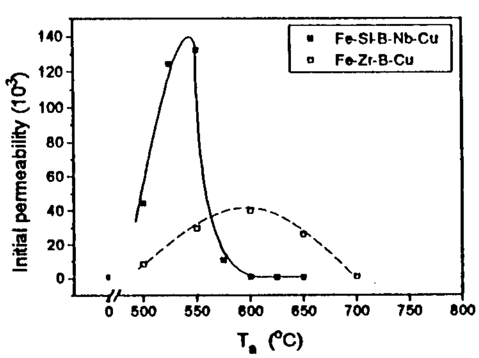

Fig. 1 Initial permeablity as a function of the annealing temperature (T_a)

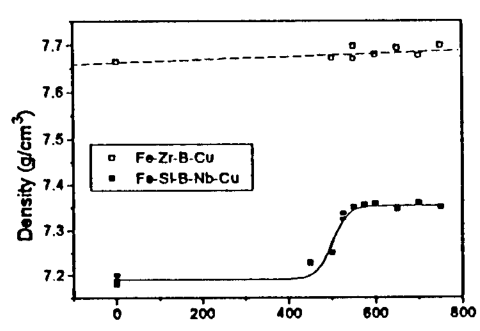

Fig. 2 Initial permeablity as a function of the annealing temperature (T_a)

According to the XRD measurements, the nanocrystalline bcc grains are randomly oriented in the FINEMET samples whereas they have a <110> or a <100> preferred orientation in the Fe-Zr-B-Cu samples.

The TEM studies revealed that the bcc-Fe(Zr) grains have a flat disc-like shape and the disc planes are arranged parallel to each other at a distance of 4 to 5 nm (Fig. 3). This means that they have a relatively large specific surface area (interface with the residual amorphous matrix) with a high level of internal stresses as deduced from XRD measurements. The internal stresses of the ultrafine bcc crystallites are reduced at high annealing temperatures only, beyond the optimum state. On the contrary, the degree of anisotropy in the nanocrystalline FINEMET samples is much smaller since here the bcc grains are equiaxed (Fig. 4), and the bcc-Fe(Si) crystallites have an ordered DO_3 structure as detected by XRD.

For the soft magnetic properties, a further important factor is the relative quantity of the amorphous phase and the nano-grains. The amorphous fraction of both alloys decreases down to below 20 % at the optimum annealing temperature as revealed by both XRD and TEM.

After the second crystallization step occurring at about 650 °C in the Fe-Z-B-Cu and 600 °C in the FINEMET alloy, we could identify the phases $Fe_{23}(Zr,B)_6$ and Fe_3B (with a small amount of the phase $Fe_{3.5}B$ at lower temperatures) which were observed in some previous reports as well [3,4].

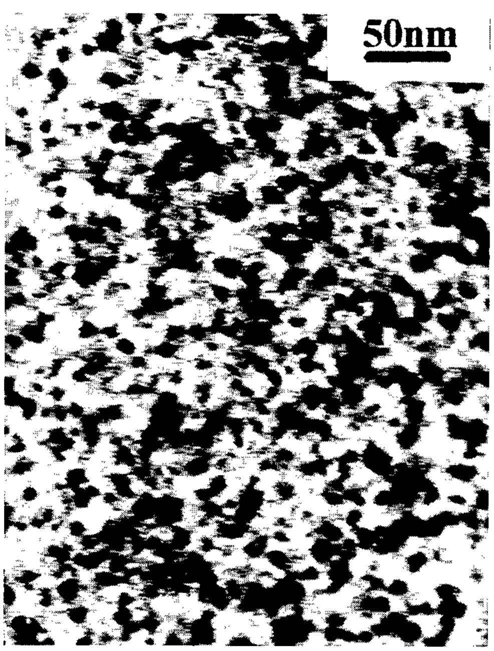

Fig. 3 TEM picture of the Fe-Zr-B-Cu alloy annealed at 600 °C

Fig. 4 TEM picture of the Fe-B-Si-Nb-Cu alloy annealed at 525 °C

Simultaneously to the formation of the $Fe_{23}(Zr,B)_6$ compound phase, an inner diffuse ring also appeared on the corresponding selected area electron diffraction (SAED) patterns, indicating the presence of a residual amorphous phase between the bcc and compound grains. This amorphous phase is completely different from the first residual amorphous matrix coexisting with the bcc-Fe(Zr) phase nucleated at low temperatures after the first crystallization step. It should also be noted that after the second crystallization step, the bcc grains already consist of nearly pure Fe.

The position of the diffuse ring corresponds to about 0.3 nm and it arises from atoms in regions characterized by a very low density. According to the TEM pictures, these areas are very narrow and they contain mainly Zr and B atoms only. At the highest annealing temperature (750 ^{0}C), these areas transform to a Zr_2B phase detected by both XRD and SAED. The presence of these areas with extremely low density helps us to understand why the average density of the Fe-Zr-B-Cu alloy did not change during the crystallization process although an amorphous-crystalline transformation is usually accompanied by a densification as shown also by the FINEMET alloy here (see Fig. 2). Similar effect was detected in other systems, too [5]. In agreement with the results of density measurements, a low-density residual amorphous phase could not been detected in the FINEMET alloy after the second crystallization step.

CONCLUSIONS

In order to trace out the origin of the large difference between the soft magnetic characteristics of $Fe_{86}Zr_7B_6Cu_1$ and $Fe_{73.5}Si_{13.5}B_9Nb_3Cu_1$ nanocrystalline alloys, detailed TEM and X-ray diffraction studies were carried out. The size of the bcc-Fe nanograins embedded in an amorphous matrix was found in the same range for the two alloys in their optimum annealed states. However, the morphology and preferred orientation of the bcc grains are very different for the two alloys due to the differences of the solute elements (Zr and Si) and their concentration in the bcc grains which, on the other hand, have a strong influence on the magnetic properties.

ACKNOWLEDGEMENTS

This work was supported by the Hungarian Scientific Research Fund (OTKA) under grant No. T 022124. The XRD work has been performed on an apparatus purchased by the Eötvös University under grant CEF 1156.

REFERENCES

1. K. Suzuki, A Makino, A. Inoue and T. Masumoto, J. Appl. Phys.. 70, 6232 (1991)
2. K. Yamauchi and Y. Yoshizawa, Nanostruct. Mater. 6, 247 (1995)
3. K. Mahdouk and J.C. Gachon, J. Phase Equil. 17, 218 (1996)
4. W.Z. Chen and P.L. Ryder, Mater. Sci. Eng. B 34, 204 (1995)
5. Á. Cziráki, in: Proc. 7th European Congress on Electron Microscopy (The Hague, 1980). Eds. P. Brederoo and G. Broom (North-Holland, Amsterdam, 1980), Vol. I, p. 280

Pergamon

NanoStructured Materials, Vol. 12, pp. 1113–1116, 1999
Elsevier Science Ltd

0965-9773/99/$–see front matter

PII S0965-9773(99)00309-8

CRYOSYNTHESIS AND PROPERTIES OF METAL-ORGANIC NANOMATERIALS

G.B. Sergeev, A.V.Nemukhin, B.M.Sergeev, T.I.Shabatina, V.V.Zagorskii
Chemistry Department, Moscow State University, Moscow, 119899, Russia

Abstract -- *Materials containing metal nanoparticles have been obtained by co-deposition of metal and organic compound vapors onto a surface at 77 K. A new method to encapsulate the metal nanoparticles and mesogenic cyanobiphenyls in a polymer matrix has been developed. Co-condensates of metal vapors (Ag, Mg, Cd, Zn, Pb, Sm, Mn, Sn) with the p-xylylene monomers lead to the polymers at low temperatures. Globular metal particles of 5-8 nm in size encapsulation polymer films have been obtained. The particles size was estimated by means of transmission electron microscopy (TEM). UV-vis, IR and NMR spectroscopy were used to control the processes of nanomaterial preparation. Bimetallic Ag/Pb cryoorganodispersions with particle size of about 5 nm have been obtained. Properties of bimetallic mixed clusters have been computed by ab initio quantum chemistry techniques.*

INTRODUCTION

The synthesis of metal-organic nanomaterials is of great interest from fundamental and applied viewpoints [1]. Encapsulation and isolation of nanosize metal particles in solid, liquid organic media and polymers allow to obtain materials with novel and unique properties [2].

RESULTS AND DISCUSSION

Materials with metal nanoparticles have been obtained by co-condensation of metal and organic vapors at surfaces cooled at 77 K. Codeposition of vapors of such metals as Ag, Mg, Cd, Zn, Pb, Sm, Sn, Mn with the reactive monomer p-xylylene has been used. Metal vapors were obtained by resistive heating of the bulk metal at 500-1200 °C depending on the volatility. The reactive monomer p-xylylene was prepared by pyrolysis of di-p-xylylene at 550-700 °C in the same vacuum set-up [3]. After codeposition of monomer with metal vapors during 3-30 minutes, the co-condensate was slowly heated up to the room temperatures. The films containing metal particles could be extracted from the vacuum cryostat for further investigations.

The metal-containing poly-p-xylylene films were examined by Transmission Electron Microscopy (TEM). The metal content was determined by means of X-ray fluorescent analysis. It was found, for example that globular Pb particles are rather homogeneously dispersed within poly-p-xylylene at the room temperatures. The size of these particles was found to be 3-8 nm. and is independent of the Pb content in the range 0.1-6,5 wt %. Lead containing poly-p-xylylene material was found to be gas sensitive [4].

TABLE 1.
IR Spectra of Metal - p-xylylene Condensate in Temperature range 80-300K.

Metal	ν (cm^{-1})	Temp. K	Assignment
Zn	855	80	$=CH_2$ def. in π-complex Zn/p-xylylene
	1900 (increase)	120-300	π-comp, Zn/poly-p-xylylene
Cd	855	80	$=CH_2$ def. in π-complex Cd/p-xylylene
	1900 (increase)	120-300	π-comp, Cd/poly-p-xylylene
Pb	865	80	$=CH_2$ def. in π-complex Pb/p-xylylene
	1900 (increase)	120-300	π-comp, Pb/poly-p-xylylene
Ag	865	80	$=CH_2$ def. in π-complex Ag/p-xylylene
	1900 (increase)	120-300	π-comp, Ag/poly-p-xylylene
	1790 (increase)	120-300	π-comp, Ag/poly-p-xylylene
Mg	1500	80	Charge transfer complex Mg/poly-p-xylylene
	1483	80-300	π-comp, Mg/poly-p-xylylene
	1210	80-300	π-comp, Mg/poly-p-xylylene
	740	140-300	σ-comp, Mg/poly-p-xylylene
	720	140-300	σ-comp, Mg/poly-p-xylylene
Mn	1592	80-300	Stable π-comp Mn/p-xylylene
	1578	80-300	Stable π-comp Mn/p-xylylene

Polymerisation of para-xylylene monomer occurs via biradical formation and can be presented by following scheme [5]:

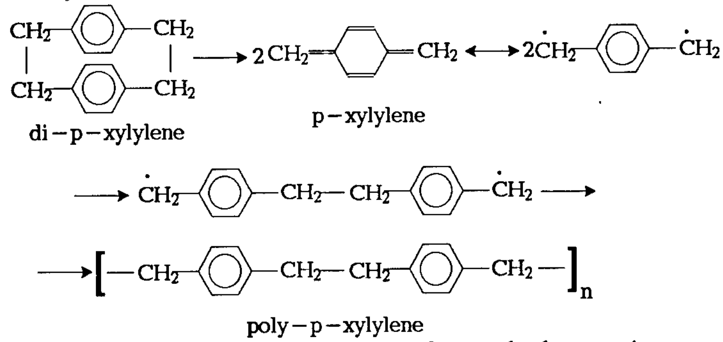

The combination of polymerisation and metal clusters incorporation in the growing polymer matrix takes place during low temperature co-condensation of metal and para-xylylene vapours and following samples annealing. As the result metal-polymeric nanomaterials were formed. Additional information on the process mechanism is available from the IR-spectroscopic studies of metal-poly-para-xylylene interactions. The comparison of the IR-spectra of the neat para-xylylene film and metal-para-xylylene co-condensate films in temperature range 80-300 K and data of the work [6] allowed us to reffer the vibrational bands. The data obtained are presented in Table1.

The data, presented in Table 1, show the fact that less active metals form only π-complexes. In this case we obtained stable samples encapsulated in poly-para-xylylene films. More active metal Mg forms the complexes of two types and stabilisation of metal particles is followed by chemical transformations in the system. In the case of Mn the production of stable complex took place and metal particles stabilisation was not achieved.

TABLE 2.
Low Temperature Vacuum Deposition of Metals and Acrylic Monomers.

Deposed Substances	Deposition Products	Polymer Yield
acrylic acid (AA)	AA	~0 %
Ag/AA	Ag_n/poly(AA) (solid metal-containing polymer film+AA)	≥30-50% (simultaneous co-deposition), ≤5-10% ("layer-by-layer" deposition)
Mn/AA	Mn^{n+}/poly(AA) (solid film+AA)	>50% (simultaneous depos.
methylacrylate (MA)	MA	~0 %
Ag/MA	Ag_n/poly(MA)/MA(organosol) Ag_n/poly(MA) Ag_n-particles <15 nm (TEM data)	~ 1-3 % (in air) ~ 100 % (1-3 days in argon)
Sm/MA	Sm^{n+}/poly(MA)/MA(solid film)	~ 50 %
Mn/MA	Mn^{n+}/poly(MA)	~ 50 %
Sn/MA	Sn^{n+}/poly(MA) (solid film)	~ 50 %
Pb/MA	Pb_n/MA(sol); Pb_n - 5-7nm in size	~ 0 %
(Pb+Ag)/MA	(Pb^{n+}+Ag_n)/MA(sol) (Pb_n/Ag_n)/poly(MA) Pb_n/Ag_n-bimetallic particles 5-7 nm in size (TEM data)	~ 0 % slow polymer. in argon gas
(Ag+Mn)/MA	(Ag_n+Mn_n+Mn^{n+})/poly(MA)	slow polymer. in argon gas
Ag/2-(dimethyl-amino)-ethylmethacrylate (DMAEMA)	Ag_n/poly(DMAEMA)/DMAEMA Ag_n ≤ 25-30nm (TEM data)	~1.5 - 2 %

Our study of cryoorganodispersion formation in different solvents with functional groups C=O, CN etc. led us to a decision to use liquid organic monomers, acrylic derivatives - acrylic acid, methylacrylate and 2-(dimethylamino)ethylmethacrylate for stabilisation of metal nanoparticles in liquid organodispersions and solid polymer films. Main experimental results obtained in this study are presented in Table 2. One can see that the yield of metal-initiated monomer to polymer conversion and oxidation state (Met^{n+}) of the metal depend strongly on the nature of co-deposed components and conditions of cryosynthesis. Therefore, in reactive polymerizing systems stable dispersions containing nanoparticles or metallopolymers could be synthesised only when metals such as silver or lead were chosen.

A typical absorption spectrum of the organosol obtained after melting of the co-condensate has a maximum at 400 nm, that is the characteristic for spherical particles of colloidal silver <20 nm in diameter [7]. The position of the absorption band in the spectrum of organosol is consistent with the results of TEM. The resulting photomicrographs indicate that organosol contains silver particles not exceeding 15 nm in size. The aggregative stability of sols is due to silver-induced polymerization of methylacrylate. Combined condensation of silver, lead and methylacrylate (MA) vapors in vacuum onto a surface cooled by liquid nitrogen followed by heating of the co-condensate results in the formation of organosols consisting of bimetallic particles [8]. The size of the lead and silver/lead particles does not exceed 5 nm i.e. they are smaller then the diameter of silver nanoparticles obtained previously under similar conditions. Absorption spectra of Ag/Pb/MA system show that the silver plasmon absorption band (416-420 nm)

is shifted to the red (λ_{max}=438 nm). The electron microscopy data allow us consider the aggregation of nanoparticles as the main reason of the red shift in an inert environment.

Structures, energies and spectra of homonuclear and mixed binary clusters composed of the metals Ag, Cd, Cu, Mg, Na, Pb, Sn, Zn have been computed by using ab initio quantum chemistry techniques. At most, tetra-atomic clusters have been considered. The calculations have been carried out with the GAMESS programs by using the reliable pseudopotential techniques [9, 10]. For every metal cluster the equilibrium geometry configurations referring to the global minim on the potential energy surface have been found with the Hartree-Fock method and the standard vibrational analysis has been performed. The energies of these geometry configurations have been re-computed with the second order Moller-Plessett perturbation technique. We have found that the binding energies of silver-containing clusters (AgM, AgM_2, Ag_2M) toward various dissociation channels allow one to arrange the elements M by relative their affinities toward Ag as follows: Pb > Sn> (Cu, Mg, Na) > Zn > Cd. Therefore the combinations of Ag with Pb and Sn, are the most promising species for mixed metal clusters.

CONCLUSIONS

We have developed the methods for the preparation of organometal materials with nanosize metal particles and nano-metal organodispersions based on the low temperature codeposition technique. We have shown that these methods are applicable to a number of different metals as well as to bimetallic systems.

ACKNOWLEDGMENTS

This work was partially supported by INTAS grant 94-4229 and RFBR N 96-03-33970

REFERENCES

1. Klabunde, K.J., *Free atoms, clusters and nanoscale particles*, Acad. Press, 1994, p.311.
2. Sergeev, G.B. and Petrukhina, M.A., *Prog. Solid State Chem.,* 1996, 24, 183.
3. Sergeev, G.B., Zagorsky, V.V. and Petrukhina, M.A., *J.Mater.Chem.*, 1995, 5, 31.
4. Sergeev, G.B., Zagorsky, V.V., Petrukhina, M.A., Zav'yalov, S.A., Grigor'ev, E.I. and Trakhtenberg, L.I., *Analyt. Commun.*, 1997, 34, 113.
5. Szwarc, M., *Polym. Eng. Sci.*, 1976, 16, 473.
6. Pebalk, A.V., Kardash, I.E. and Pravednikov A.N., *Vysokomolek. Soed.*, 1980, 23A, 1926.
7. Remer, M.J., *J.Colloid Interface Sci.*, 1985, 107, 297.
8. Sergeev, B.M., Sergeev, G.B. and Prusov, A.N., *Mendeleev Commun.* 1998, 1.
9. Stevens, W.J., Bash, H. and Krauss, M., *J. Chem. Phys.*, 1984, 81, 6026.
10. Ermilov, A.Yu., Nemukhin, A.V. and Sergeev, G.B., *Bull. of the Russian Acad. of Science, Ser. Phys.* 1998, 62, 1169.

Pergamon

NanoStructured Materials, Vol. 12, pp. 1117–1125, 1999
Elsevier Science Ltd

0965-9773/99/$–see front matter

PII S0965-9773(99)00310-4

NANOTECHNOLOGY: A DATA STORAGE PERSPECTIVE

A. K. Menon and B. K. Gupta
Read-Rite Corporation, Fremont, CA 94539, USA

Abstract *-The exponential increase in areal density of recording of magnetic storage devices has reduced the recorded bit size to nano length scale. This has profound implications on all aspects of the storage system including recording device modeling, materials, fabrication, metrology, characterization, and tribology of the head-disk interface. In this paper, the impact of nanotechnology in extending the data storage device storage systems is explored with an emphasis on the fabrication and characterization of nanolayers and structures.* ©*1999 Acta Metallurgica Inc.*

Introduction

With the advent of the information superhighway, high definition television, replacement of chemical photography with digital images, digitization of images (both still and video motion), simulation of engineering designs and events by finite element modeling, enormous amounts of data need to be viewed, manipulated, and stored. A video ROM two-hour recording requires a storage capacity in the 6-8 Gigabytes range. The data storage capacity for future applications is likely to approach tens or hundreds of terabytes. Obviously, the data rate transfer rates need to keep pace with the data storage consumption requirements. For instance, interactive 3-d video
will require an areal density of 10/ $TB.in^{-2}$ and data transfer rates of 100 Gb/sec. The success of the hard disk drives originate from a consistent enhancement in storage capacity and performance combined with significant reductions in price per Gigabyte. In the near future, the demand for the hard drives will grow in the mobile laptops and highend servers market. By year 2001, the revenue of the hard disk drive industries is expected to reach 40 million US dollars. Because of rapid advances in the recording areal density, the average price per megabyte is continuously falling.

Ever shrinking the size of the pole tip structure to nanometer dimensions poses new challenges for the head and media design, characterization of films on nano-scale, deposition of films in the subnanometer range, lithography and patterning sequence, and achieving good tribology performance. In this paper, key issues, challenges, and limitations of the nanotechnology that affect the magnetic performance and the tribology of hard disk drives are discussed.

Areal density growth

The areal density trends of various data storage devices over two decades are shown in Fig. 1. In small personal computers the need for storage is growing from hundreds of megabytes to gigabytes, and in larger systems from tens of gigabytes to terabytes.

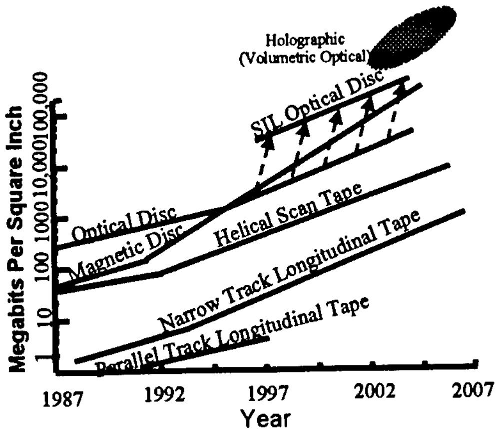

Fig. 1. *Areal density growth of rigid and flexible magnetic media, magneto-optical, and near field optical storage devices.*

Correspondingly, the data rate has increased from hundreds of kilobytes per seconds to megabytes per seconds in PC; and from hundreds of megabytes per seconds to gigabytes per second in larger systems. To achieve high areal densities and data transfer rates at lower cost, commercial market utilizes magnetic hard disc, magnetic flexible tape, and optical disc devices. Although several competing technologies for data storage are available, still magnetic hard disc drives continue to be the primary, high performance storage device of choice. In the past five years, areal density of storage has grown at 60 % annually, Fig. 2. The growth is spurred by the introduction of giant magnetoresistive (GMR) head technology and by proportionately reducing all dimensions. In the hard disc drive storage arena, technologies in all aspects of recording are continuously being stretched to the limit of sustaining the 60 %

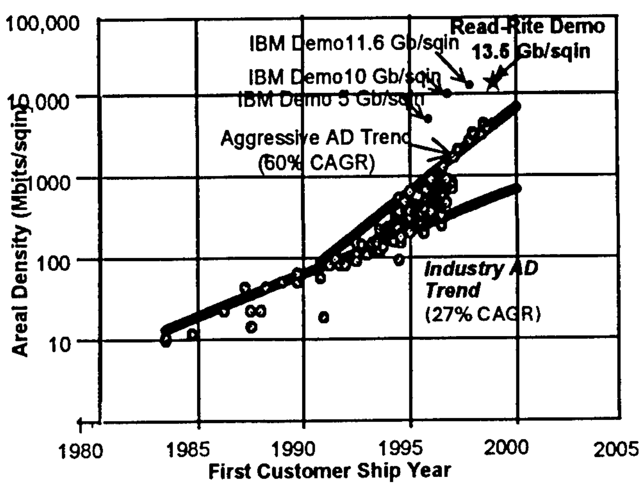

Fig. 2. *The areal density growth for hard disk drives. The cumulative areal density growth rate (CAGR) for hard disc drives is maintained at 60 % since 1990.*

compound annual growth rate (CGR) (Grochowski and Thompson, 1996). Recently, Read-Rite Corporation demonstrated for the first time the feasibility of 13.5 Gb.in^{-2} areal density with the

GMR head. Areal densities of 20 and 40 Gb.in^{-2} are expected in production by year 2002 and 2004, respectively .

The size of the recording bit necessary for higher linear bit and track densities is achieved by scaling down the dimensions of the pole tip structure to nanometer dimensions. The bit aspect ratio reduces from 20 to 4 with an increase in areal density from 0.1 to 100 Gb.in^{-2}. Typical lengths and widths of recording bits in 1, 10, and 100 Gb.in^{-2} areal densities are 3.0 x 0.2 μm, 0.8 x 0.066 μm, and 0.3 x 0.075 μm, respectively. Changes in various head, disc, and interface related parameters to achieve increasing areal densities for hard disc drives are listed in Table 1. The form factor (size) of the recording head shrinks with the areal density. Head design parameters such as read gap, reader track width, and stripe height are also scaled down accordingly to the nanometer dimensions. The magnetic spacing decreases from 75 to 12 nm as areal density increases from 1 to 40 Gb.in^{-2}. Thickness of the wear coatings on head and disc are reduced to zero at 20 Gb.in^{-2} areal density. Key technologies influencing high areal density

Table I. Changes in various head, disc, and hard-disk interface related parameters with increasing areal density For Hard disk drives.

Attribute	Design	1 Gb.in^{-2}	5 Gb.in^{-2}	10 Gb.in^{-2} Projected	20 Gb.in^{-2} Projected	40 Gb.in^{-2} Projected
Projected		1996	1998	2000	2002	2004
Recording Technique	Type	Longitudinal	Longitudinal	Longitudinal	Longitudinal	Longitudinal
	Bit Aspect ratio	15		12		8
	Bit size, μm	3.0 x 0.5		0.8 x 0.066		0.3 x 0.075
Head	Type	Thin film, MR Inductive	MR	Spin Valve GMR	Advanced GMR	Advanced GMR
	Form factor, %	50	30	30	10-15	10-15
	MR Sensitivity, ΔR/R	MR 2%	GMR 8%	GMR 8%	GMR 32%	GMR 32%
	Read gap, nm	250	200	160	140	110
	Read track width, μm	2.7	0.7	0.45	0.30	0.19
	Stripe Height, μm	1	0.5	0.4	0.3	0.2
	Overcoat Thickness, nm	10	6	3	0	0
Media	Substrate	AlNiP-Glass	AlNiP-Glass	Glass, Si	Glass, Si	Glass, Si
	Texturing	Mech/Laser	Ultra-smooth	Ultra-smooth	Ultra-smooth	Ultra-smooth
	Magnetic film Thickness, nm	20-25	14-21	10-15	7-10	5-7
	Overcoat thickness, nm	10-15	10	5	0	0
	Lube	PFPE + Additives	PFPE + Additives	PFPE + Additives	PFPE + Additives	PFPE + Additives
Interface	Mechanics	Flying	Flying	Fly or Prox.	Contact	Contact
	Spinning speed, rpm	7200	10,000	10,000	>10,000	>10,000
	Data rate, MB/s, 65	36-57	105-210	150-300	210-425	300-600
	Magnetic spacing nm	75	40	25	18	12
	Loading mechanism	CSS	CSS dynamic loading	Dynamic loading	Dynamic loading	Dynamic loading

are the new GMR heads, positioning servo-mechanisms for high track densities, low noise magnetic media with high coercivity, and low magnetic spacing head-disc interface for high linear bit densities. Fabrication of GMR heads for high areal density would require the

characterization, deposition, and patterning of nanolayers with controlled thickness in subnanometer range.

GIANT MAGNETO-RESISTIVE (GMR) HEADS

The main emerging technology for the recording head is giant magneto-resistive (GMR) technology, which was unknown until 1988. The GMR heads will enable areal densities to 15 $Gb.in^{-2}$ and beyond. The primary advantage of the GMR head is greater sensitivity to the magnetic field generated by the recorded bit on the disk. The increased sensitivity makes it possible to detect smaller recorded bits and read those at higher data rates. In the GMR head, resistance changes occur in the thin magnetic films separated by a thin conductor. One film has a variable magnetic orientation and is influenced by the disk's magnetic field, the second film has a fixed or pinned orientation.

The GMR structure consists of a multilayer sandwich of CoFe and Cu with a pinned layer (FeMn, NiMn, PtMN, PdPtMn, IrMn, or NiO) at the top. The GMR coefficient of a multilayer structure depends on the thickness of conducting Cu layer and number of the bilayers., In the GMR structure, materials used in the interfacial structure must be immiscible and the interlayer must be thinner than the conduction electron coherence length. The GMR coefficient is strongly influenced by the domain structure, layer thickness, and atomic and mechanical defects in the GMR layers. Symmetric (or dual) GMR structures offer the possibility of achieving large GMR coefficients in the layers which exhibits relatively low saturation fields. The symmetric spin valve (see Egelhof et. Al. 1996), has two pinned layers (NIO) on the top and the bottom. In conventional spin valves, the pinning film of FeMn acts by providing an exchange bias whereas the NiO acts by inducing a very large coercivity in the djacent Co film. In the bottom spin valve, the top Co film is unpinned and is free to switch magnetically at relatively low fields. In symmetric spin valve the top and bottom Co films are pinned and the central Co film is free. The symmetric spin valve structure exhibits higher GMR coefficient of 23.4% as compared to that of bottom structure (17%). The GMR coefficient is significantly increased by reducing the thickness of Cu layer in the symmetric spinvalve structure. The impediment of thinner Cu film is that the ferromagnetic coupling of the central Co film to the top and bottom Co film rises very sharply for Cu thickness less than about 1.8 nm. Future challenges to GMR fabrication involve control of nanometer dimensions and tolerances of ultrathin films, particularly the conducting spacer film which can be only 10-15 atomic layers thick. GMR involves new film materials that require precise process control to assure stability and compositional uniformity to achieve high GMR coefficient at high areal density

SUPERPARAMAGNETIC LIMIT

As the areal density increases astronomically, it is necessary to examine some of the fundamental limits and quasi fundamental limits of magnetic recording. The key fundamental limits of the recording are media noise versus thermal stability of the recorded bit, smallest magnetic spacing achievable, and maximum switching speed of current head/media materials today, 5 $Gb.in^{-2}$ recording heads are in large-scale production. In order to achieve 10 $Gb.in^{-2}$ areal density, it is necessary to have thin film media grain size of roughly 10 nm, magnetic spacing of 30 nm, read gap of 150 nm, and track width of 450 nm. Evolution of grain size and

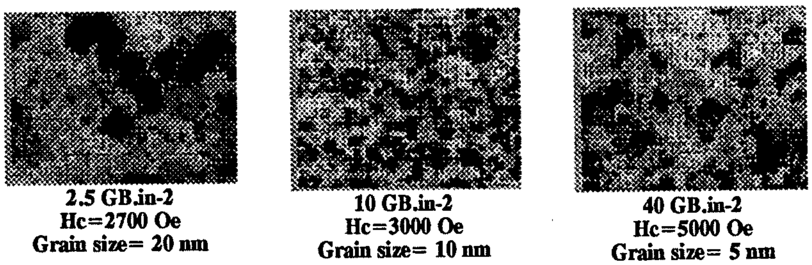

Fig. 3. *Magnetic media parameters evolution with increasing areal density.*

coercivity of magnetic film on the disk with areal density is illustrated in Fig. 3. A system to manufacture 10 Gb.in^{-2} drives is feasible with today's technology and will likely be in production by year 2000. 40 Gb.in^{-2} recording requires sub 5 nm thin film media grain size. Current media materials will not permit stability of the recorded bit while maintaining sufficient signal to noise ratio. Micromagnetic and Monte Carlo analysis showed that transition from stable to unstable bits occurs around 40 Gb.in^{-2} in the current head/media materials for longitudinal recording.

REDUCED MAGNETIC SPACING WITH AREAL DENSITY

The ever increasing demand of high areal density leads to a continuous reduction in the magnetic spacing between the head and media. The areal density (product of bit and track density) of magnetic storage devices is limited by the head width, gap length, and the magnetic /mechanical spacing. The track density depends on the transducer width and bit density depends on the gap length and magnetic spacing. Data rate is determined by the bit density and the disc spinning speed. The spacing loss in a hard disc drive is controlled by reducing the magnetic spacing between the flying head and the spinning disc surface.

Magnetic spacing is decreased by reducing the roughness of head and disc surfaces, thickness of carbon wear coatings on head and disc, thickness of the lubricant, and the mecha-

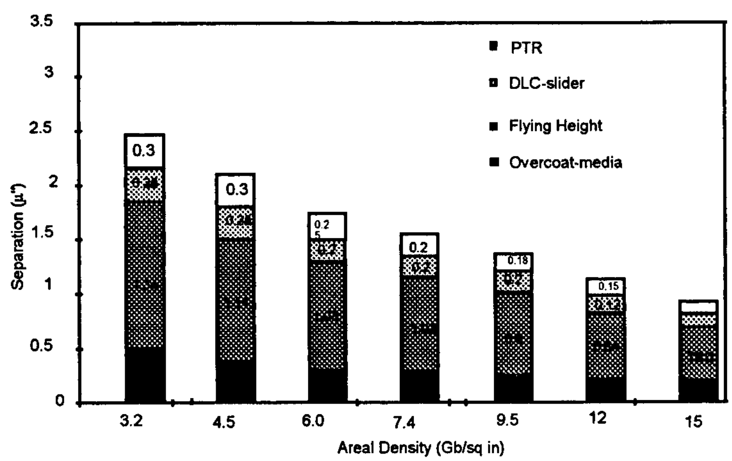

Fig. 4. *Magnetic separation budget with increasing areal density.*

nical spacing between the flying head and disc. Lower mechanical spacing results in ultralow flying of the head over the disc surface. The formation of air bearing between the head and disc takes place when the disc is spinning at full speed. The head-disc spacing budget for increasing areal density is illustrated in Fig. 4. The magnetic spacing for 15 $Gb.in^{-2}$ areal density is in the sub 25 nanometer range. Note that for 15 $Gb.in^{-2}$ areal density, the carbon overcoat thickness on the head and media is about 1 and 2 nm, respectively. The flying height is reduced from 40 nm to 15 nm as the areal density is increased from 1 to 10 $Gb.in^{-2}$. To keep the contribution of head and disk surface roughness in the magnetic spacing budget to minimum, it is essential to achieve the rms roughness of the head and disk surfaces in the subnanometer range. For achieving rms roughness in the subnanometer range, the lapping technology needs dramatic improvements

ULTRATHIN CARBON OVERCOATS

Ultrathin carbon wear coating are applied on head and media to protect the magnetic films against corrosion due to environmental exposure and against mechanical wear due to head dragging over the disc surface prior to take-off and after landing. Currently, a thin nanolayer (5-10 nm thick) of amorphous carbon (also called diamond-like-carbon (dlc)) is applied on the head and media surfaces for improving the tribology of the head-disc interface. Dlc is chosen because of its chemical inertness to environmental exposure, ease of tailoring mechanical and electrical properties, and low cost (Bhushan and Gupta, 1991). Since MR/GMR heads consist of multiple coatings of metals and dielectric materials, high adhesion of dlc on these materials is a primary concern. Any delamination or detachment of coating from any region on the head or disc surface can damage the head-disc interface.

TRIBOLOGY AND CHARACTERIZATION AT THE NANOMETER DIMENSIONS

The reduced flying height necessitates increasingly smoother surfaces for the head and the disk. The smooth surfaces however, give rise to high stiction during the contact start-stop (CSS) operation of the drive. An overcoat of minimum thickness is needed to achieve high readback signal amplitude without sacrificing the friction and wear properties of the head-disk interface. Characterization of the head and disk surfaces at nanometer dimensions is crucial for optimizing the tribological performance (Gupta and Menon, 1999). In this section, techniques for the characterization of the head-disc interface and DLC overcoats at nanometer dimensions are discussed.

Hardness measurements become increasingly difficult when the indentation depths are on the order of a few nanometers. The tip area function that is used to estimate the hardness and elastic modulus, becomes very sensitive to indentation depth at shallower depths. In nanoscratch measurements, a sharp diamond tip (10-50 nm tip diameter) is dragged over the sample surface at constant load or increasing load and the lateral force (friction force) is recorded. Weak coatings are delaminated from the substrates and/or cracked during scratching due to poor adhesion or low fracture toughness. Relatively softer coatings exhibit wide and deep scratches and scooping of the material to one end during scratching. Harder coatings exhibit low friction at the initial stages and an abrupt increase in friction when the normal load exceeds a critical limit known as critical load. The AFM image of a nanoscratch made at increasing load on the air-bearing surface of the 7.5 nm thick DLC coated slider and lateral force and tip penetration depth profile versus normal load plots are shown in Fig.5. The normal

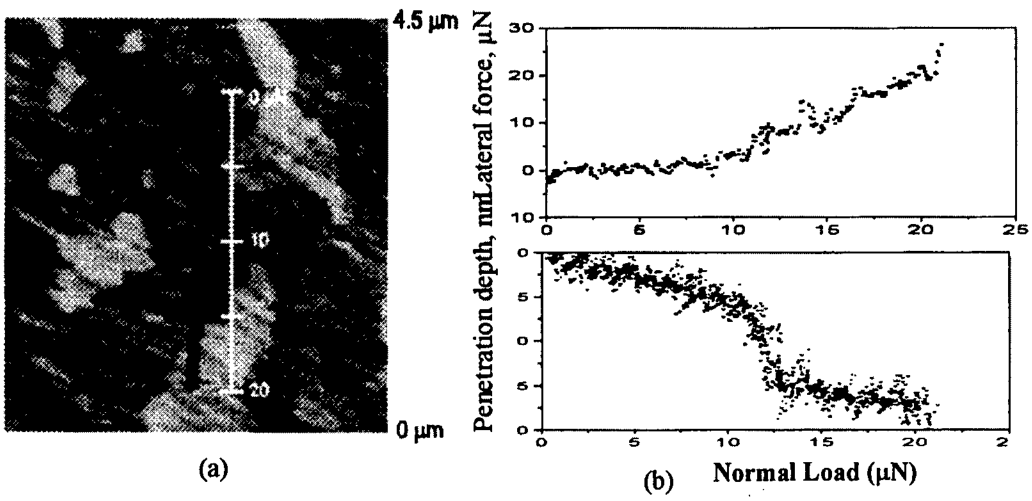

Fig. 5. *(a) The AFM image of a nanoscratch made at increasing load up to 20 µN on the ABS of the 7.5 nm thick dlc coated slider. (b) Lateral force and tip penetration depth profiles (four profiles) versus normal load during nanoscratching at increasing load.*

load corresponding to an abrupt increase in the friction force and tip depth is defined as the critical load. When the normal load exceeds the critical load, the tip penetrates through the coating. The critical load is used to compare the mechanical integrity of the films; higher critical load corresponds to a relatively more mechanically robust coating.

In recent years, STM/AFM/FFM techniques have been used to understand the wear phenomena at an atomic level. With these sophisticated tools, Kaneko et al. [1995] have carried out extensive wear studies of the DLC films and ion-implanted Silicon.

We present a study in which the contact start-stop (CSS) wear performance of the DLC coated sliders is correlated to the nanowear behavior. The DLC coatings are deposited at 50, 100, and 175 V using a direct ion beam technique on the ABS of the MR heads. The nanowear patterns are formed by sliding a cube corner diamond tip over the dlc coated sliders over two passes at 20 µN. The CSS tests are conducted in a clean environment of class 100 at an ambient temperature of 21 °C and a relative humidity of 44%. The AFM images of the wear patterns formed on 7.5 nm thick DLC coatings at 20 µN after sliding over two passes are compared in Fig. 6. Notice that the DLC coating deposited at 175 V exhibits significantly lower wear as compared to that of the 50 V dlc coating.

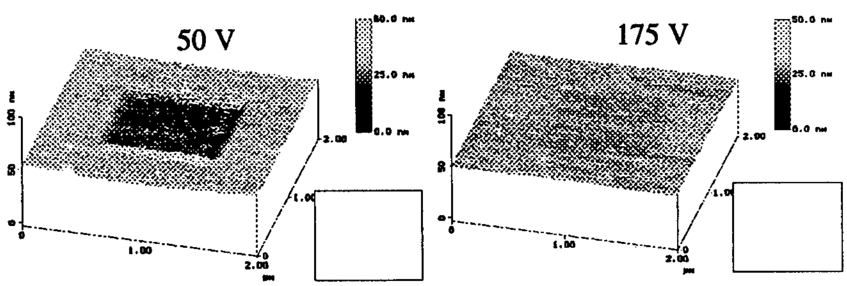

Fig. 6. *AFM images (2 x 2 µm) of nanowear patterns (1 x 1 µm) formed at 20 µN on 7.5 nm thick dlc coatings deposited at 50 and 175 V using a direct ion beam deposition technique.*

The nanowear depths of dlc coatings deposited at 175 V (coating A), 100 V (coating B), and 50 V (coating C) and uncoated Al_2O_3-TiC substrate are compared in Fig. 7. We note that coating A exhibits lower wear depth when compared to coating B followed by coating C. As expected, the wear depth in the uncoated slider is significantly lower because of the higher hardness of the Al_2O_3-TiC substrate. The stiction during the first one-second of a CSS cycle and dynamic friction of various DLC coated sliders and uncoated sliders in ambient environment are compared in Fig. 8. We note that the sliders coated with the DLC coating A exhibits the lowest stiction and friction when compared to the sliders with other dlc coatings. In addition, Head-disk interface with coating A on the head exhibits least amount of wear debris formation during 20,000 CSS cycles. The correlation between the highest nanowear resistance and best CSS performance (low stiction and low wear) of DLC coatings indicates that the wear properties at a nanoscale can be used as an indirect measure of the CSS wear performance of the carbon overcoats.

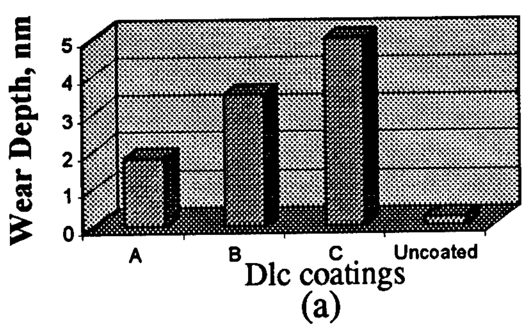

Fig. 7. *Average depth of wear patterns formed at 20 μN on DLC coated and uncoated sliders. The DLC coatings are deposited at 175 V (Coating A), 100 V (Coating B), and 50 V (coating C) using a direct ion beam deposition technique.*

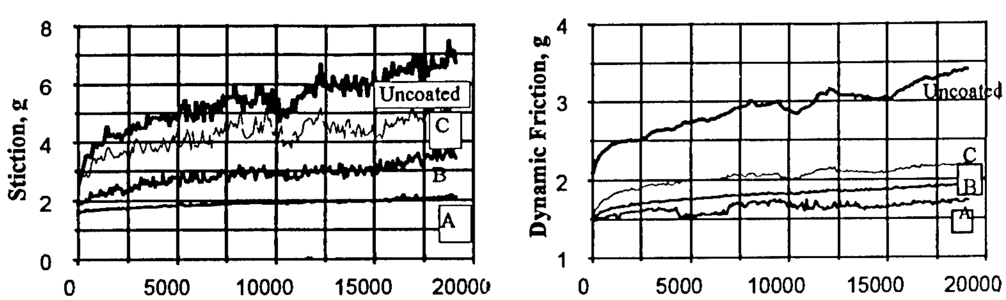

Fig. 8. *Stiction and dynamic friction of dlc coated and uncoated sliders.*

SUMMARY

Areal density of magnetic storage devices is expected to increase at 60 % annual growth rate over next five years. Recording density is expected to increase to 20 GB.in^{-2} in production by year 2002. Advances in nanotechnology with regard to fabrication, characterization, and tribology are essential for sustaining 60 % growth rate. Thickness and composition control on the order of two atomic layers thick films in the GMR structure plays a key role in optimizing the GMR coefficient ($\delta R/R_o$). The reduced track width (200 nm for 40 GB.in^{-2}) poses new challenges for photolithography and patterning sequence. The superparamagnetic limit at 40 GB.in^{-2} requires media magnetic film material for high coercivity with the grain size in the sub five-nanometer range. Reduced magnetic spacing (15 nm at 10 GB.in^{-2}) leads to ultra thin carbon overcoats, smooth head and disk surfaces, and low flying height.

Characterization at the nanometer dimensions is essential to understand the functional CSS performance of the head-disk interface. The mechanical integrity of ultra thin DLC is quantitatively evaluated using nanoscratches in terms of the critical load. In addition, AFM imaging of nanoscratches shed some light on the type of physical damage and adhesion failure of the coating. Nanowear simulates a single asperity contact situation and provides information on the evolution of the wear process. The DLC coating exhibiting the lowest nanowear rate performs best in the CSS test. Based on this data, it appears that nanowear measurements on DLC overcoats can be used as an indirect measure of their CSS performance.

References:

Bhushan, B and Gupta, B. K. *Handbook of Tribology: Materials, Coatings, and Surface Treatments,* McGraw Hill Book Co. NY (1991)

Egelhoff, W. F., Chen, Jr. P. J., Powell C. J., Stiles, M. D., McMichael R. D., Lin, C-L., Sivertsen, J. M., Judy, J. H., Takano K., Berkowitz, A. E., Anthony, T. C., and Brug, J. A. J. Appl. Phys. 79, 5277 (1996).

Grochowski, E., and Thompson, D. A., *IEEE Trans. MAG* 30, 3797 (1994)

Gupta, B. K. And Bhushan, B. *Wear*, 190, 110 (1995).

Gupta, B. K. and Menon, A. K. *IEEE Trans. MAG 35 (1999).*

Kaneko, R., Miyamoto, T., and Hamada, E., *Micro/Nano Tribology*, Ed. Bhushan, CRC Press, Boca Raton, FL., pp. 183 (1995).

Kief, M. T., Bresowar, J., Leng, Q. J. Appl. Phys. 79.8, 4766 (1996).

Neuville S and Matthews, A. *MRS Bulletin*, 22 (9), 22 (1997).

Pergamon

NanoStructured Materials, Vol. 12, pp. 1127–1130, 1999
Elsevier Science Ltd

0965-9773/99/$–see front matter

PII S0965-9773(99)00311-6

DIFFUSION - INDUCED CREEP OF POLYCRYSTALLINE AND NANOSTRUCTURED METALS

Yu.R. Kolobov, G.P. Grabovetskaya, I.V. Ratochka, K.V. Ivanov.

Institute of Strength Physics and Materials Science of RAS,
pr. Akademicheskii, 2/1, Tomsk, Russia, 634021.

Abstract- *Kinetic mechanisms of phenomena to be induced by the diffusion on the grain boundaries in polycrystalline and nanostructured (NS) materials have been analyzed. By way of example of nickel and copper nanostructured (grain size 100÷300 nm) it was shown that the effect of diffusion induced loss of strength by creep was much observed at temperatures low than 400 K in comparison with polycrystalline condition with grain size 20 μm. It was supposed that the physical reason for the decrease in the temperature for the effect to manifest itself is much higher value of diffusion coefficients of impurities in nanostructures.*

INTRODUCTION

An essential change of the grain boundary (GB) state in metals is caused by diffusion fluxes of impurity atoms from an external source (a coating, for example). This effect is seen in diffusion-induced grain boundary migration (DIGM) (1), diffusion-induced recrystallization (DIR) (2) and diffusion-induced activation of GB sliding (DIGBS) (3-6) in polycrystalline materials. The effect of DIGBS is to increase the creep rate and elongation to failure under a given applied load. The effects of DIGM, DIR and DIGBS were shown (4-6) to occur in the B_1 diffusion regime (following the classification proposed by Mishin and Razumovskii in (7)).

According to this classification the diffusion process for immobile grain boundary in a bicrystal may be divided into five diffusion regimes: C, B_1, B_2, B_3, B_4. The names of the regime were chosen with reference to Harrison's well known classification (8). The regime C in Harrison's classification coincides with one in the classification of Mishin and Razumovskii [7]. These authors within the framework of regime B have evolved also four regimes B_1, B_2, B_3, B_4. In the C and B_1 regimes the diffusion is substantially non-stable ($\partial c_b / \partial t \neq 0$, where c_b is the concentration of impurity in GB region). The regime B_2 is characterized by an intensive change of the impurity concentration in the region surrounding the grain boundary ($\partial c_v / \partial t \neq 0$, where c_v is the impurity concentration in the volume). At the same time, the impurity concentration in grain boundary in this regime reaches equilibrium and doesn't change in time ($\partial c_b / \partial t = 0$). The regimes B_3 and B_4 correspond to the volume diffusion.

It would be natural to assume for nanostructured (NS) materials that the effects induced by the influence of diffusion fluxes of impurity atoms on the metal-matrix may have their own unique features. These features may be caused: first, by a large volume fraction of the grain-boundary phase in these polycrystals (up to several percents); and second, by the change of the

diffusion coefficients in NS materials (they may be increased by several orders of magnitude) [9].

Therefore the study of creep acceleration in NS metals under grain-boundary diffusion fluxes of impurity atoms from external sources as compared with coarse-grained materials is of great importance, as well as comparable investigations of the diffusion mobility of atoms in NS and in the coarse-grained materials.

EXPERIMENTAL

Both NS (grain size of 0,3 μm) specimens of nickel and copper (nickel -99, 95, copper - 99, 96) and coarse-grained nickel (grain size of 20 μm) were investigated. The coarse-grained specimens were obtained by rolling reduction of the as-received sheet up to 50% at room temperature followed by recrystallization during annealing at T = 1073 K, for 1 hour. The NS structure was obtained by the method of equal channel angular pressing [9]. Then the specimens were electrolytically coated with a copper layer of 12-15 mm in thickness.

Creep testing was performed at temperatures of 373-573 K (NS nickel and copper) and 773-973 K (coarse grained nickel) under constant loading in vacuum of 10^{-2} Pa, using a PV-3012M testing machine.

To obtain the grain-boundary diffusion coefficients, the coated samples were annealed for 3 h at 398, 423, 443, 573 K (NS nickel) and 423, 573, 773, 823 and 873. The copper concentration in the nickel was measured by the method of second ion mass-spectroscopy (SIMS) using MC-7201 device manufactured in Sumy (Ukraine). An Ar^+ ion beam with an area of 2 mm^2, an energy of 6 keV, and a current density of 0.1 mA/cm^2 was used as an ion probe. Calculation method for grain boundary diffusion coefficients is described particularly in [10].

RESULTS AND DISCUSSION

Curves of temperature dependence of value of creep acceleration in NS (curve 1) and coarse-grained nickel (curve 2) are shown in Fig.1. The magnitude of creep acceleration is indicated by the ratio $\varepsilon_2 / \varepsilon_1$ (ε_1 - the strain rate of the established creep of nickel in vacuum; ε_2 - the rate of the creep of nickel at the conditions of the diffusive contact with copper). Fig. 1. shows that the creep acceleration effect takes place in NS nickel under the grain-boundary diffusion fluxes of copper at the temperatures from 398-473K. Moreover, the maximum value of the effect takes place at 423K. Similar result was found for creep of NS copper under aluminum diffusion from the surface. Under the creep strain rate of NS cooper increase of about 4 times. For coarse grained nickel the creep acceleration effect takes place in interval of higher temperatures of 773-923K which is in a good correspondence with earlier calculated temperature interval of existence of diffusion regime B_1 in nickel - copper system [11].

Thus the temperature interval of creep acceleration effect display in NS nickel under influence of copper diffusion fluxes takes place at more lower temperatures than corresponding for coarse-grained one. It may be attributed to the higher value of diffusion coefficients in NS nickel. In this connection it is interesting to compare diffusion parameters in NS and coarse-grained nickel in temperature interval of 398-573K.

Fig.2 illustrate the concentration profiles of copper penetration into depth of coarse-grained and NS nickel. Derived concentration profiles are used for calculation of copper

diffusion coefficient value in NS and coarse-grained nickel (table 1). Considering that Arrhenius relation for grain boundary diffusion coefficients is true and using experimental data the D_b value was calculated for coarse-grained nickel at 398, 423, 443, 573K (table 1). From table data follow that D_b value of copper in NS nickel is 5-6 order more than in coarse-grained one.

Using table data the activation energies of copper grain boundary diffusion in the coarse-grained and NS nickel were calculated (124,7 kJ/mol and 60,2 kJ/mol respectively).

Thus, as is seen from the above data the diffusion parameters of grain boundaries substantially differ in NS and in coarse-grained nickel. The activation energy for the grain-boundary diffusion of cooper in NS nickel is close to that for the surface self-diffusion in nickel (Q_s = 58 kJ/mol [12]).

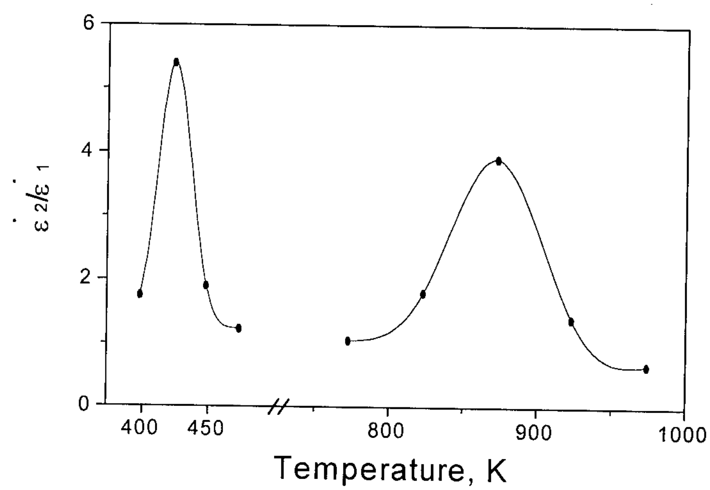

Fig. 1. Dependence of value of creep acceleration on deformation temperature in NS (1) and coarse grained (2) nickel under copper diffusion fluxes from the surface.

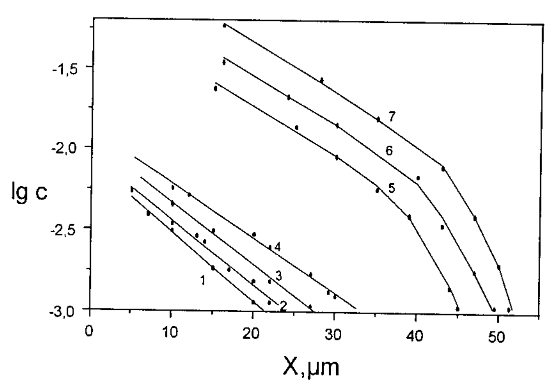

Fig. 2. The copper concentration profiles in NS (curves 1, 2, 3, 4 after annealing at 398, 423, 443 and 573K) and coarse-grained (curves 5, 6, 7 after annealing at 773, 823, 873K) nickel.

TABLE 1

Coefficients for Grain-Boundary Diffusion (D_b) in NS and Coarse- Grained Nickel.

Material	Ni	Ni (NS)
Temperature	D_b, m^2/s	D_b, m^2/s
398	$4,64 \cdot 10^{-21}$ *	$5,06 \cdot 10^{-15}$
423	$4,31 \cdot 10^{-20}$ *	$9,6 \cdot 10^{-15}$
443	$2,14 \cdot 10^{-19}$ *	$2,2 \cdot 10^{-14}$
573	$4,65 \cdot 10^{-16}$ *	$1,4 \cdot 10^{-12}$
773	$4,0 \cdot 10^{-13}$	
823	$1,26 \cdot 10^{-12}$	
873	$3,9 \cdot 10^{-12}$	

(*) The calculated values.

CONCLUSION

The creep acceleration effect of the NS nickel and copper in the presence of grain boundary diffusion fluxes of impurity occurs in lower temperature than one of the coarse-grained materials. The coefficient of grain boundary diffusion of cooper in NS nickel are higher by 5-6 orders of magnitude but the activation energy of grain-boundary diffusion are lower by 2 time than those in coarse-grained nickel. It is Assumed that the reduction of temperature interval of creep acceleration effect of grain-boundary diffusion fluxes can be explained by the higher of the diffusive penetration of grain boundary of NS materials as compared to coarse- grained materials.

Acknowledgements

The authors would like to express their gratitude to Prof. R.Z. Valiev (GATU, Ufa, Russia) for supplying materials for the experiments and fruitful discussions, as well as the Russian Foundation for Basic Research for the financial support for this work.

References

1. King, A.H. Intern., Materials Rev, 1987, 4, 173.
2. Den Broeder, F.J.A.,Klerk, M., Vanderberg, J.M., Hamm, R.A., Acta Met, 1983, B 2, 285.
3.. Kolobov, Yu.R., Marvin, V.B., Ratochka, I.V.,. Korotaev, A.D., Dan Ussr. 1985, 3, 605.
4. Kolobov, Yu.R., Ratochka, I.V., Fiz. Metal. and Metalloved, 1990 8, 185.
5 Kolobov, Yu.R., Trans. Mat. Res. Soc. Jpn., 1994, 16, 1397.
6. Kolobov, Yu.R., Ratochka, I.V., J. Mater Sci. And Technol., 1995, 1, 38.
7. Mishin, Yu.M., Razumovskii, I.M., Scripta Met., 1991, 6, 1375.
8. Harrison, L.G., Trans. Faraday Soc., 1961, B 7, 1191.
9. Valiev, R.Z., Krasilnikov, N.A., Ti.senev, N.K., Mater. Sci. A.Eng., 1991, B 137, 35.
10. Kolobov, Yu.R., Grabovetskaya ,G.P., Ratochka, I.V., at all, Ann. Chim. Fr., 1996, 21, 483.
11. Kolobov, Yu.R., Grabovetskaya, G.P., Ratochka, I.V., at all, , Izv. Vuz. Fiz. 1997, 7, 119.
12. Geguzin, Ya.E., Surface Diffusion and Spreading, Nauka Press,Moscow, 1969, p.273.

Pergamon

NanoStructured Materials, Vol. 12, pp. 1131–1134, 1999
Elsevier Science Ltd

0965-9773/99/$–see front matter

PII S0965-9773(99)00312-8

THE MOLECULAR CLUSTER-MATERIALS FOR NANOELECTRONICS

S.P.Gubin[1], V.V.Kislov[2], V.V.Kolesov[2], E.S.Soldatov[3], A.S.Trifonov[3]
[1]Institute of General and Inorganic Chemistry, Russian Academy of Sciences.
[2]Institute of Radioengineering&Electronics, Russian Academy of Sciences.
[3]Physics Department, Moscow State University.

Abstract *– Complex tunnel nanostructures on the base of atomic and molecular clusters were studied by scanning tunneling microscopy. It was shown that clusters can form an ordered two-dimensional lattice in the monolayer. Electron transport through one- and two-barrier tunnel nanostructures was investigated at room temperature. The decreasing of the Coulomb blockade potential of the tunnel nanostructure with increasing of cluster nuclearity was observed. ©1999 Acta Metallurgica Inc.*

INTRODUCTION

Miniaturization in microelectronics has now reached a point, where further progress depends on the search for alternative technologies, in particular those relying on the properties of isolated molecules. Many advances in this area suggest that novel technologies such as molecular electronics and bioelectronics can be expected to become a reality (1).

Syntheses of cluster materials is already a well developing area of chemical technology. Clusters and cluster molecules differ from other organic and inorganic molecules in that they contain a heavy metallic core, as a rule spherical or almost spherical, surrounded by a ligand shell made up of' light atoms or simple molecules (2). The electronic structure of cluster molecules is characterized by the high density of closely spaced upper filled and lower vacant molecular states, which, on the one hand, result in numerous one-electron reversible redox transitions (3) and, on the other, ensure sufficient stability of the molecular core to the addition or removal of an election (4). Such cluster molecules are often called "electron sources." Therefore, it seems likely that cluster molecules are most probable candidates to be used as the simplest components of future nanostructures in molecular electronics.

The dramatic decrease in the dimensions of electronic structures often gives rise to qualitatively new features of their behavior. For example, in the late 1980s, correlated single-electron tunneling was predicted (5). This effect can be observed in very small tunnel junctions (less than 0.01 μ m^2 in area) at low temperatures, $kT<<e^2/2C$, where e is the electron charge, and C is the junction capacitance. Because of the extremely low capacitance of the tunnel junction, tunneling of even one electron is accompanied by a substantial change in voltage, $\Delta V=e/C$, sufficient to affect subsequent electron tunneling in the system. These interactions give rise to strongly correlated electronic transport.

A fairly promising way to produce tunnel junctions with very small dimensions is by using metalorganic clusters: 1) because these molecular entities are fairly well characterized; 2) because the absorption or removal of one electron causes little changes in cluster structure, thus the clusters may serve as the middle electrode in the tunnel structure; and, 3) because the ligand shell may act as a natural tunnel barrier in the junction. These features are very significant for producing single-electron devices with a narrow spread of parameters, since the tunneling characteristics depend on cluster structure, which is believed to vary only little. Thus cluster is a good candidate on the role of elementary unit for making the one-electronic transition with the small scatter of parameters.

If two tunnel junctions are directly connected in series (single-electronic transistor), conductivity is notably suppressed at low voltages ("Coulomb blockade"), and the I-V curves exhibit periodical step-like features ("Coulomb staircase"), each corresponding to an increase in the charge of the middle electrode by one unit charge.

Further advances can be achieved by creating single-electron junctions from 1 to 10nm in area to ensure correlated single-electron tunneling in the temperature range 4.2-77K and even up to 300K. Based on such nanostructures, it would be possible to develop radically new electronic devices operating under ambient conditions.

EXPERIMENTAL

The objective of this work was to examine the possibility of both attaching separate cluster molecules to a smooth conductive graphite surface and the development tunneling nanostructures with given barrier, to probe the system by methods of scanning tunneling microscopy (STM), and to study electron tunneling through the isolated clusters on a substrate and through nanostructures.

Metal clusters without ligand complexes

Cluster molecules on the surface of highly orientated pyrolytic graphite (HOPG) can be detected by STM. The samples were originally made by the deposition of "naked" silver clusters with average diameter 40±10Å on the freshly prepared HOPG surface. The location of the STM tip above the single cluster allowed the current voltage characteristics (CVC) to be measured. The CVC in this case describes the metallic conductivity of the single tunnel junction "STM tip-conductor" in which the role of the "conductor" is the "naked" metallic cluster deposited on the conductive substrate without any insulation (barrier-free).

After that a substrate, already containing the "naked" silver clusters was treated with a solution of PPh_3 in hexane and then were washed and dried. The topography of the surface did not change but the CVC of the new clusters was considerably affected: the I-V curve has a region of strongly suppressed conductivity. The reason is that an insulating barrier in the form of ligands was formed around the metallic core and as a result single-electron tunneling in the double-junction tunnel system "STM tip-barrier-cluster-barrier-substrate" occurs.

Carbonyl phosphine clusters of platinum and palladium

A cluster with a specified number n of metal atoms owes its stability to the rather subtle balance that exists between the number of intrinsic valence electrons in the metal core, the number of electrons supplied by the ligands. The carbonyl phosphine clusters are typical of Pd and Pt and characterize the ability of these metals to form clusters. On the other hand, heavy-metal clusters must possess a well-developed electron-level structure and can serve as an "electron reservoir" when the transport current passes across a tunnel nanostructure.

The similar results were obtained by using various clusters: $Pd_3(CO)_3(P(C_6H_5)_3)_4$, $Pd_{10}(CO)_{12}(P(C_4H_7)_3)_6$, $Pt_5(CO)_6(PBu_3)_4$, $Pt_{17}(CO)_{12}(PEt_3)_8$, *and* $(Fe_6C(CO)_{16})(NEt_4)$.

Planar nanostructures were formed on the just-cleaved surface of a HOPG substrate. At the first stage, a monomolecular L-B layer of stearic acid, $C_{17}H_{35}COOH$ *(about 24Å), was deposited on the substrate surface. Then, during a single production cycle, a monolayer of the desired cluster substance was formed on the stearic-acid monolayer.*

Thus, a planar two-barrier tunnel structure was produced. As schematically shown at fig.1, it consisted of two unsymmetrical tunnel junctions.

The tunnel transport of electrons across nanostructures was investigated. The CVC curves are almost symmetric and exhibit a characteristic peculiarity near the origin. This peculiarity is results from Coulomb blockade (5) and shows up as a decrease in the conductivity of the tunnel gap and the appearance of a characteristic "step" on the CVC curve. The CVC curves of Langmuir layers formed by cluster molecules without a dielectric sublayer of stearic-acid molecules show an approximately linear behavior near zero.

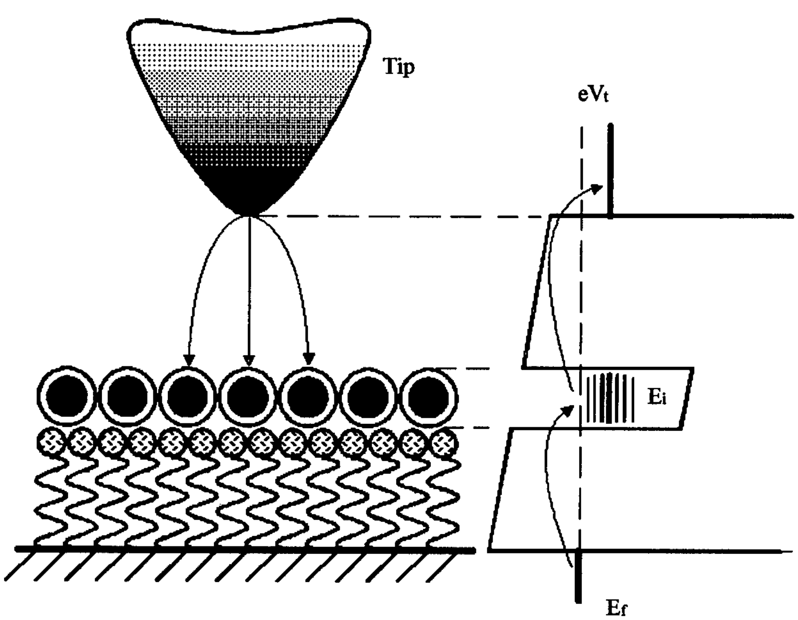

Fig. 1. *The scheme of a experimental double barrier tunnel structure.*

For $Pd_3(CO)_3(PPh_3)_4$ clusters, which have the form of a metal triangle of three palladium atoms, with a side length of about 3 Å, surrounded by ligand groups, the Coulomb barrier potential is anywhere between 460 and 470 mV. For $Pt_5(CO)_6(PEt_3)_4$, clusters, which have the form of a metal pyramid with an additional triangular cantilever of five platinum atoms, surrounded by ligand groups, the Coulomb barrier potential is anywhere between 230 and 240 mV. For $Pd_{10}(CO)_{12}(PBu_3)_6$ clusters, which have the form of built-up metal pyramids with four additional triangular cantilevers of ten palladium atoms, surrounded by ligand groups, the Coulomb barrier potential is anywhere between 270 and 290 mV.

The Coulomb barrier potential, $E_c=e^2/2C$, can be independently estimated for various nanostructures from known geometric dimensions. Considering, the conducting surface by an insulating layer of thickness d and dielectric conductivity ε, the electrostatic capacitance may be written as $C=2\pi\varepsilon\varepsilon_0 r/(1-r/2d)$

Thus noting that, for stearic acid $\varepsilon=2.8$, the molecule length is $d=24$Å and the dimensions of an averaged cluster core $r_1\approx6$Å, $r_2\approx7$Å and $r_3\approx9$Å, the estimations of the Coulomb barrier energy turn out to be $E_{c1}\approx800$ meV, $E_{c2}\approx570$ meV and $E_{c3}\approx440$ meV.

Thus the general trend- a decrease in Coulomb blockade energy with increasing cluster nuclearity- is observed.

It must be noted, that estimations of the electrostatic capacitance are very relative. In the case of organometal clusters, this value has a limited physical meaning: they contain only a few metal atoms, and, therefore, their spectrum of electronic states strongly differs from that of macroscopic metal systems.

CONCLUSIONS

Our experiments have shown the possibility of making reliable reproducible tunnel nanostructures with given complex tunnel barrier on the base of molecular technologies from the organometalic cluster molecules. The effects of correlated electron tunneling in the similar nanostructures and the isolated cluster molecules was studied at the room temperatures.

Further the development of this methods permits to create the element base of nanoelectronics.

References

1. Likharev K.K., *Mikroelektronika*, 1987, 16, 3, p. 195.
2. Gubin, S.P., *Chemistry of Clusters*, Nauka, Moscow, 1987, p.29.
3. Manning M.C. and Trogler W.C., *Coord. Chem. Rev.*, 1981, 38, 2/3, p. 89.
4. Trinh-Toan, Fenhammer W.R, and Dahl L.F., *Am-Chem. Soc.*, 1972, 94, 10, p. 3389.
5. Averin D.V. and Likharev K.K., *Single Electronics: A Correlated Transport of Single Electrons and Cooper Pairs in System of Small Tunnel Junctions, Mesoscopic Phenomena in Solids*, Altshuler B. *et al.*, Eds.,Elsevier, Amsterdam ,1991, p. 173.

Pergamon

NanoStructured Materials, Vol. 12, pp. 1135–1140, 1999
Elsevier Science Ltd

0965-9773/99/$–see front matter

PII S0965-9773(99)00313-X

PRODUCTION OF MAGNETICALLY SOFT MATERIALS BY MECHANICAL MILLING?

Anthony Arrott
Physics Department
Virginia State University, Petersburg, VA, USA 23806

Abstract - - It may be possible to produce a useful magnetically soft material for industrial applications such as high-temperature motors by means of mechanical milling. The complexity of the micromagnetics involved makes it difficult to come to a theoretical conclusions concerning the potential for creating soft magnetic materials with high saturation magnetization and low hysteresis loss from materials with substantial crystalline anisotropy by using the exchange interaction to couple many grains with different anisotropy axes. This should be a tractable experimental problem starting with supermendur (49Fe49Co2V) which has very small anisotropy and then working with less and less Co which increases the saturation magnetization, the magnetic anisotropy and the electrical resistivity while lowering the magnetostriction and the cost. It is argued that this is an interesting problem.

MAGNETICALLY SOFT MATERIALS

Mechanical milling has exhibited accomplishments and potential in many realms of material science. It has been said to be a revolution in metallurgy, permitting the formation of materials not accessible by conventional techniques. In the field of magnetism it is well suited to the production of hard magnetic materials and has found application in heterogeneous systems for permanent magnet materials and particles for magnetic recording. So far there has been no application to the production of soft magnetic materials for motors, generators and transformers. Heterogeneity generally leads to increased hysteresis loss. Typically as the grain size gets smaller, the losses increase. But that is a conclusion reached before the advent of amorphous materials in which the grain size is reduced in some sense to the scale of atoms. Now commercial transformers are being made from amorphous alloys. As a function of grain size, the losses must go through a maximum as the size is decreased from large single crystals to amorphous materials. The length scale for the maximum is set by the parameters of magnetism: the exchange interaction, the magnetostatic interactions, the magnetic crystalline anisotropy and the magnetoelastic coefficients. These lengths are in the range of tens of nanometers.

While it is well established that soft magnetic materials can be made by going all the way to amorphous materials, it is not known in any detail how the soft magnetic properties deteriorate as the grain size is increased in the range 5-20 nm. accessible by mechanical milling. The purpose of this communication is to discuss possible pathways for producing soft magnetic materials by mechanical milling and why one might find it commercially viable to do so.

Particular emphasis is placed on making soft magnetic materials with the compositions of 25 to 50 percent Co in Fe. This composition range has the highest moment per unit mass or volume of any magnetic material.

It is not enough that a soft magnetic material has a high saturation magnetization, it is also necessary that it takes a small internal magnetic field to achieve saturation. The magnetization process in a polycrystalline material is a combination of the motion of domain walls and the rotation of magnetization in the grains. In single crystals the magnetization process can be mostly the motion of domain walls. This is also the case in Fe(Si) wherein metallurgical tricks are used to achieve highly textured grains approximating single crystal behavior. The single crystal like behavior is most useful in transformers. Even in that case there are concerns with the creation of sufficient numbers oft domain walls necessary for easily reversing the magnetization. In motors and generators the magnetization necessarily must rotate in the performance of the required function. Then magnetic anisotropy becomes an important physical quantity for rating the usefulness of the material. The role of anisotropy in determining the magnetization processes in transformers, motors and generators is reasonably well understood: the less of it, the better. If the anisotropy is high and the grain orientation is random, the highest flux available using acceptable driving fields is about 2/3 of the maximum moment per unit volume, and then only if the domain walls move freely.

In addition to high saturation magnetization M_S and low anisotropy K_1, it is important that a soft magnetic material have a low magnetostriction λ. The reasons for this are less well understood. An example of how magnetostriction can give rise to hysteresis is reviewed below. A final important intrinsic physical property is resistivity. The higher the resistivity, the lower the eddy current losses. Eddy current losses are reduced by using thin laminations, insulated from one another. Typically thin means less than 100 μm. As this calls for ductility of the material, metallurgy comes strongly into the picture. Rolling which is used to produce thin sheets can also affect the orientation of the grains as well as the grain size obtained on annealing after rolling.

An over view of magnetic materials must start with an economic fact. Iron in the form of low carbon steel is very inexpensive. Historically it has been cheaper per pound than potatoes on the back of a truck in Idaho. All other soft magnetic materials are more expensive. Low carbon steel accounts for about 96 per cent of the market for soft magnetic materials. Most of the remaining 4 per cent is Fe(Si) for transformers. Everything else falls under the category of specialty materials. These include the permalloys, essentially Ni(Fe) alloys with about 20 per cent Fe and supermendur, 49 Fe 49 Co 2 V. The permalloys are designed to have small anisotropy and small magnetostriction. The saturation magnetization is less than half of that of iron, but all of it is useful. Supermendur has low anisotropy with a saturation magnetization that is greater than that of iron. Supermendur has a very large magnetostriction. The addition of V to supermendur serves to raise the resistivity and to improve the ductility. The resistivity of 50-50 FeCo is actually lower than that of pure iron at room temperature. This reflects the higher Curie temperature of the 50-50 alloy which means that there is less scattering of the conduction electrons by the magnetic excitations. Actually the Curie temperature is virtual because there is a phase transformation from the bcc phase to the fcc phase at 985 C.

Supermendur is useful when there is a premium placed on the weight of an electric motor or generator. Because the anisotropy is low, all of the high magnetic moment per unit volume is useful. The higher induction at saturation means less material for a given application.

This also reduces the mass of the current carriers and the housing of the device. The obvious applications are in airplanes and for devices launched into space. Supermendur has the additional merits that its superior magnetic and mechanical properties are maintained to high temperatures. These attributes sometimes justify the expense of the cobalt, typically 25 US$ per pound. Vanadium is historically cheaper at 10 US$ per pound. Nickel runs about 2 US$ per pound. As iron is only about 0.06 US$ per pound, it is essentially free.

For the applications for which one is willing to pay the premium for supermendur, there are potentially alternative materials that would be cheaper, have higher saturation magnetization, higher resistivity and lower magnetostriction. These are Fe(Co) alloys with 25-40 percent Co plus what ever additives are necessary to make it work. The problem with this material is that the anisotropy is not as low as it is in properly heat treated supermendur. The cubic anisotropy coefficient changes sign with increasing concentration for the Fe(Co) system. The concentration at which this happens is at the 50-50 alloy for FeCo in the fully atomically ordered state. In the fully disordered state the sign changes just below 40 percent Co in Fe(Co). The lower the Co concentration, the lower the magnetostriction, the higher the saturation magnetization and the higher the anisotropy, except that the saturation magnetization goes through a broad maximum near 25 percent Co. There are metallurgical problems with the lower Co alloys, but it is mainly the higher anisotropy that limits the use of the commercially available 27 percent alloy.

The "knee" of a magnetization curve is the point where further magnetization requires too large an internal field to make a motor efficient. This is somewhat beyond the point where the magnetization by domain wall motion is mostly completed and further magnetization is by rotation of the magnetization against the torques arising from the magnetic anisotropy. For typical soft polycrystalline materials the operating field is about 10 Oersted ($\mu_0 H = 1$ mT). If the anisotropy is high the magnetization at the knee is about 2/3 of the saturation magnetization, but as the anisotropy goes to zero the full saturation can be reached in small internal fields, depending on the domain wall motion. For amorphous alloys, the anisotropy is averaged to zero by the exchange coupling among large numbers of atoms each with its own locally preferred direction of magnetization. The effective saturation magnetization is then the saturation magnetization. It is useful to introduce the anisotropy field defined as $H_K \equiv 2K_1/M_s$. If H_K is less than 10 Oe, the anisotropy can be considered low and the effective saturation magnetization will be the saturation magnetization.

MECHANICAL MILLING

The basic question that is being considered here is whether by mechanical milling one can make an Fe(Co) alloy in which the anisotropy is averaged to a small enough number to make it useful for the applications for which supermendur is used, while reducing the amount of Co. The initial question is whether one can recover the properties of supermendur after mechanical milling while retaining the nanocrystalline during processing.

It is known that a material will not be magnetically soft when the grain size is comparable to the width of a domain wall. It is known that a grain size of an atom or a few atoms as in an amorphous material will do the trick. The domain wall width in a grain which is larger than the domain wall width is given by $\sqrt{(A/K_1)}$ where A is the exchange constant in the

continuum model of micromagnetics and K_1 is the cubic anisotropy constant. In large grained materials the structure of domain walls is well understood in terms of the competition between exchange which tends to make the wall as thick as possible and anisotropy that dictates a narrower wall in order to have more of the magnetization along preferred directions. The domain structure in such materials occurs in response to magnetostatic interactions with magnetostriction often playing some role. In amorphous materials the origin and nature of domain walls is not well understood. In the range of grain sizes between the amorphous material and the cases where the walls are comparable to the distances across a grain, not much is known about domains and domain walls either experimentally or theoretically in soft magnetic materials.

In principle, micromagnetics provides all the theory necessary to calculate the properties of magnetic materials as a function of grain size. The limitation of computation power make it difficult to apply the theory to an adequate model of a nanocrystalline material. This leaves the question open to speculation and to experiment. As the experiments have yet to be carried out, the remaining path is that of speculation as to the possibilities of either carrying out meaningful calculations or successful experiments.

The experimental path is reasonably clear. The basic idea in mechanical milling is to use a hammer that delivers a sharp enough blow to result in shear and the pumping of dislocations into particles of size from 10 to 100 μm. The blows must be repeated quickly enough to continue to drive atoms further from their equilibrium positions before they can relax back. Finally the blows must be so many that every atom is displaced many times. A puck and saucer mill meets these requirements, see fig. 1. In addition it can handle kilogram quantities of material making it suitable for producing sufficient material both for characterization and fabrication. The words used to describe the process sometimes sound like science fantasy with dislocations "self-organizing" to form the grain boundaries around dislocation free nanocrystals.

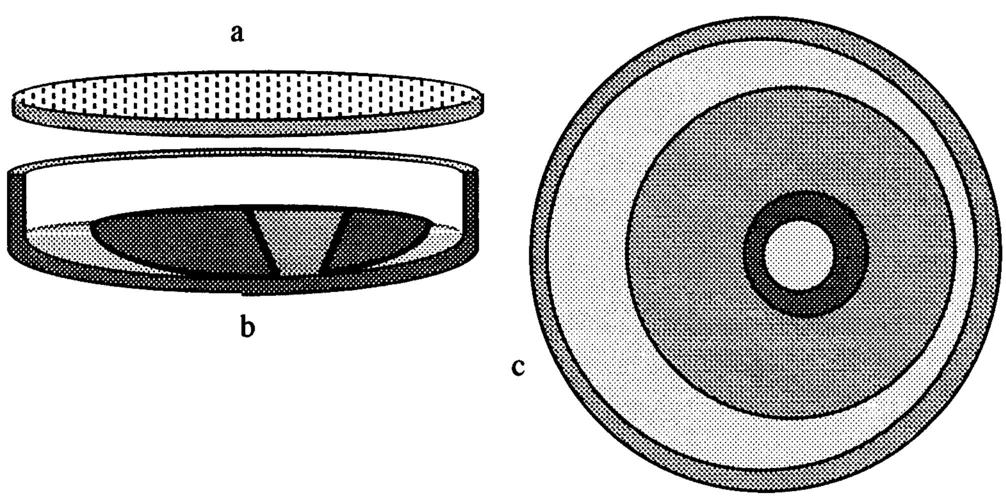

Fig. 1. Puck and saucer mill.
a. The lid for the saucer, shown in b. with puck inside. The hole in the puck facilitates the circulation of the particles. c. Top view of the puck in the saucer, 25 cm in diameter.

If the nanocrystalline grain size can be achieved in the particulate material, the first step is to determine if the individual particles, containing billions of nanocrystals are sufficiently soft. The second step is that of fabrication of laminations suitable for motors. This is likely to be a major part of an experimental investigation. One would have to demonstrate that laminations with full density can be formed by the methods of powdered metallurgy without loss of the nanocrystalline structure by recrystallization and grain growth in the process. Here the speculation is that the use of proper additives can result in the stabilizing of grain boundaries of the nanocrystalline structure to temperatures above those for which the motor is designed to operate and to those necessary for fabrication. The additives might be large atoms (second or third transition series elements) that prefer the grain boundaries during the milling process or migrate to the grain boundaries on annealing. Possibly the proper choice of atmosphere in the milling process could help in stabilizing the nanocrystalline grains.

There is always the possibility that attempts to produce soft magnetic materials could result in the discovery of useful hard magnetic materials. Hitting materials with a hammer has been used for that purpose for centuries.

MICROMAGNETISM AND EXPERIMENT

As mentioned above, it is computationally prohibitive to calculate magnetization patterns in materials with nanocrystalline grain size in particles with dimensions of 100 μm. To describe the variation of the magnetization within the nanocrystals, the grid size for a full micro magnetic calculation should be of the order of 1 nm^3. This would require some 10^{15} cells to describe the particle.

To calculate the approach to saturation, thus determining the effective saturation, one can settle for many fewer elements by choosing a total volume of the order of the exchange length. For a volume of the order of 10^6 nm^3 and a grain size of the order of 10^2 nm^3 the number of elements could be reduced to 10^4. The structure would be generated using random numbers. The calculation should be carried out for a sufficient number of starting seeds to judge the role of fluctuations on the magnetic response. The calculation of the effective anisotropy for the approach to saturation would be straight forward. The calculation of the hysteresis for domain wall motion would be more subtle. Random variations in direction of anisotropy will produce Fourier components of the magnetization pattern with many wavelengths including some well matched to the width of the domain wall. These are the most likely components to produce hysteresis. This is readily demonstrated in models where the anisotropy axis varies only with respect to x with translational invariance in the y and z directions. While keeping all the parameters the same, changing the seed for the generation of the random pattern can sometimes result in several instabilities in the wall motion and sometimes result in no instabilities with hysteresis free motion of the wall through the entire cycle of sweeping the wall back and forth across the region by cycling the field.

The calculation of the effect of magnetostriction on the response of a soft nanocrystalline material is difficult even conceptually. Elastic stresses create very long range effects. One example that illustrates the subtlety of demonstrating hysteresis arising from magnetostriction is shown in the idealized domain pattern in Fig. 2. The periodic pattern shown thas magnetic domains with magnetization along each of three perpendicular axes. A field applied perpendicular to the pattern will cause the domains with square cross section to grow or

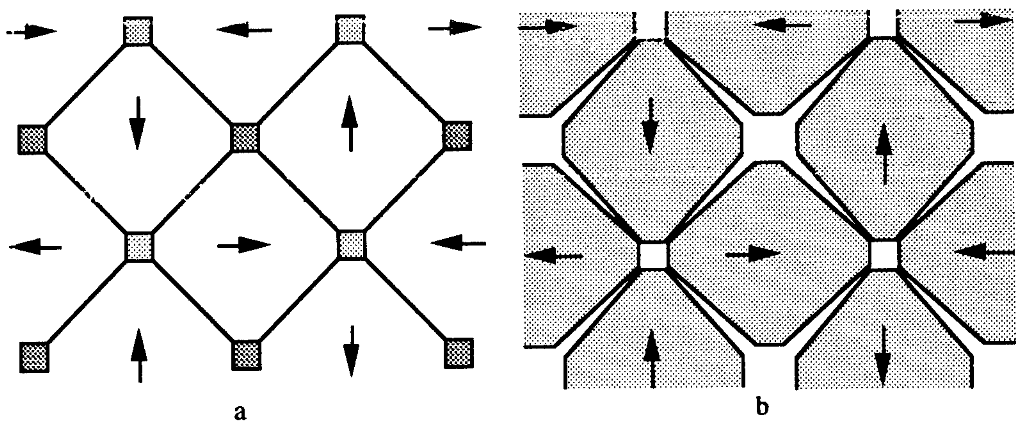

Fig. 2. Role of magnetostriction in hysteresis.
a. Magnetization pattern with six types of domains. The magnetization is either into or out of the plane in the squares. In a given field there can be two different areas of the squares which are stable configurations. b. If the domains were physically separate, the magnetostriction would open gaps between the domains as shown. The elastic stresses must close the gaps.

shrink depending on the sign of the magnetization with respect to the field. For a range of fields there are two different areas for the squares for which the system is stable in a given field, but only if one takes magnetostriction into account. This happens because the elastic energy depends logarithmically on the area of the square for small areas; the core does not shrink to zero. It is important to understand that even a single crystal picture frame is strained by the magnetization being in different directions in each section. It is the change in the direction of the magnetization from domain to domain in the surrounding four domains that strains the crystal. If the crystal expands in the direction of the magnetization, the octagons would each try to separate from its neighbor near the squares about which the magnetization circulates in the positive sense, see Fig. 2b. The growth of the core relieves that strain. At the same time there is an increase in the wall energy as the square grows.

For the foreseeable future, the theory is so intractable that the determination of the role of magnetostriction in the hysteresis of nanocrystalline materials will remain an experimental problem. There seems no way to guess the effects of the atoms in the grain boundaries on the magnitude or even sign of the magnetostriction. Experimentally the fraction of the atoms in the grain boundary can be changed at fixed concentration to investigate this. The temperature dependence of the magnetostriction above ambient has not been reported for these alloys. For the applications to high temperature motors this should be remedied.

Similar comments might be made about the effect of the grain boundaries on the anisotropy in nanocrystalline materials. Yet here theory should be able to make predictions to the extent that single ion anisotropy dominates in the disordered regions with reduced symmetry.

The micromagnetics of magnetically soft nanocrystalline materials appears to be a subject that should attract the attention of both experimentalists and theorists for some time to come. It would be even better if this proves to be of practical use. For now the question mark remains in the title of this paper.

This work is supported by the Air Force Office of Scientific Research.

Pergamon

NanoStructured Materials, Vol. 12, pp. 1141–1144, 1999
Elsevier Science Ltd

0965-9773/99/$–see front matter

PII S0965-9773(99)00314-1

EFFECT OF HIGH HYDROSTATIC PRESSURE ON THE FERROELECTRIC PROPERTIES OF EPITAXIAL $Nb:Pb(Zr_{0.52}Ti_{0.48})O_3/YBa_2Cu_3O_{7-x}$ NANOSTRUCTURES

A.M. Grishin, S.I. Khartsev*, P. Johnsson, K.V. Rao
Department of Condensed Matter Physics, Royal Institute of Technology
S-100 44 Stockholm, Sweden

Abstract--*The dielectric permittivity, loss tan δ, and polarization P-E loop in epitaxial pulsed laser deposited $Nb:Pb(Zr_{0.52}Ti_{0.48})O_3$ (600 nm)/$YBa_2Cu_3O_{7-x}$(200 nm)/$LaAlO_3$ heterostructures have been measured at high pressures of Gpa range. Remnant polarization has been found to decrease monotonously while the dielectric permittivity increases 1.5 times with the hydrostatic pressure increase up to 1 GPa. Superlinear pressure dependence of polarization has been found and explained in terms of mismatch stress which prevails in the low pressure range and is prominent in nanostructured ferroelectric layers. This effect also corresponds to recently observed correlation between the ferroelectric and nanocrystalline structure of highly c-axis oriented thin ferroelectric films.* ©*1999 Acta Metallurgica Inc.*

INTRODUCTION

Last years ferroelectric thin films have attracted much attention both in fundamental studies and for the purpose of applying them to nonvolatile memory, IR-detection, etc. Although tremendous breakthrough has been achieved in epitaxial ferroelectric film processing technique, to the best of our knowledge no study of ferroelectric thin film properties under high hydrostatic pressure has yet been done. This paper present experimental results on the ferroelectric properties of thin PNZT films under high pressure and theoretical modeling of mismatch stress that explains these effects in terms of the nanostructured crystallites that the film is made of.

EXPERIMENTAL

A doped PZT target of the following composition $[Pb(Zr_{0.52}Ti_{0.48})O_3 + 1\%Nb_2O_5]$, hereafter referred to as PNZT, was used for the preparation of *in situ* PNZT/YBCO thin film heterostructures on single crystal $LaAlO_3$ substrates by using a Nd:YAG pulsed laser deposition. The details on film processing and ferroelectric characterization have been previously de

* Also at Donetsk Institute for Physics and Engineering, 340114 Donetsk, Ukraine

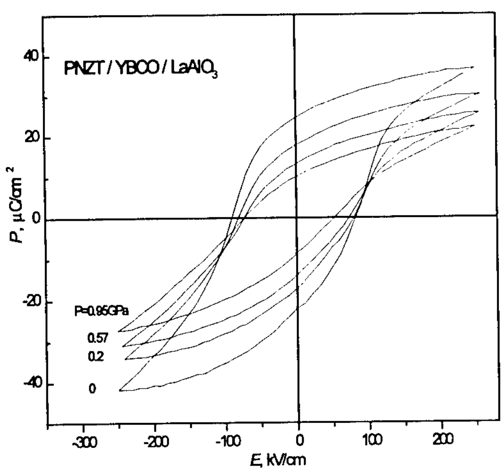

Fig.1 Polarization of ferroelectric PNZT film vs. applied electric field measured at different pressures applied to the PNZT/YBCO/$LaAlO_3$ structure.

scribed elsewhere (1,2). In brief, a 10 ns pulse width Nd:YAG laser (355-nm, tripled mode, 10-Hz, energy density of 3-4 J/cm^2, a distance between target and substrate of 95 mm) beam ablates rotating stoichiometric targets of YBCO and PNZT. The deposition is carried out in an oxygen pressure of about 200-300 mTorr. The YBCO underlayer is grown at a substrate temperature of 760 °C and the deposition is followed by annealing in 850 mbar of oxygen pressure at 450 °C. After this, deposition of the PNZT layer is done at a substrate heater temperature of 575 °C and finally the whole heterostructure is annealed in an oxygen pressure of 800 mbar at 400 °C and then cooled to room temperature.

X-ray θ-2θ diffraction pattern for the PNZT/YBCO/$LaAlO_3$ heterostructures exhibits only the narrow (00*l*) PNZT and YBCO reflections indicating high degree of *c*-axis orientation in both PNZT and YBCO layers (2). This is also suggested by the narrow rocking curves which full width at half maximum (FWHM) has been found to be 1.73°, 1.07°, and 0.34° for PNZT, YBCO, and $LaAlO_3$, respectively. The PNZT/ YBCO/$LaAlO_3$ heterostructures have also been found to possess high texturing in the ***a-b*** plane. The perfect crystalline matching of PNZT and YBCO layers with each other and with single crystal $LaAlO_3$ substrate is exhibited by four-fold symmetry showed by a φ-scan of the YBCO (0110), PNZT (113) and $LaAlO_3$ (128) reflections (3).

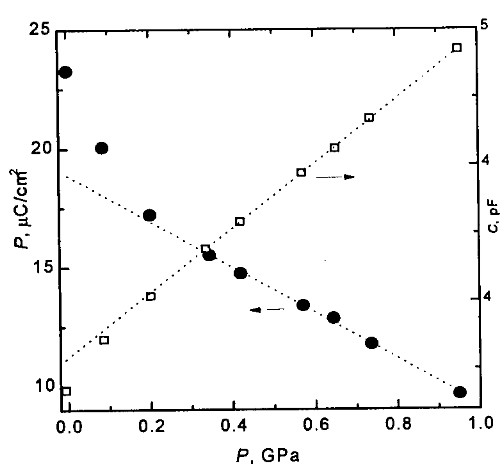

Fig. 2 Remnant polarization and dielectric permittivity of ferroelectric PNZT film vs. pressure applied to the PNZT/YBCO/$LaAlO_3$ structure.

Dielectric permittivity ε and loss *tan* δ measured using a RCL meter at 100 Hz have been found to be 310 and 0.023 correspondingly. Ferroelectric hysteretic *P-E* curves have been measured in the pulse regime by RT66A (Radiant Technologies) testing setup and are shown in Fig.1 at various hydrostatic pressures. To measure ε and the polarization loops a high-pressure vessel of "piston-clamp"-type (4) was used. Polyethylensilocsan (PES-5) was used as a pressure transmitting medium. The lead wires were led out of the

high pressure vessel through a conical hole sealed by epoxy resin. The pressure was measured by a calibrated manganin resistance probe with the accuracy of $\pm$ 0.025 GPa.

Remnant polarization decreases monotonously while the dielectric permittivity increases almost 1.5 times with a hydrostatic pressure increase up to 1 GPa (see Fig. 2). At high pressure both dielectric permittivity as well as remnant polarization vs. pressure curves fit nicely by the linear pressure dependence while superlinear deviations are clearly observed at low pressures (below 0.2 GPa).

DISCUSSION

The model of compression anisotropy can be put forward to explain the observed features. At high pressure the linear reduction of the remnant polarization P_r is in accordance with the isotropic compressibility of a ferroelectric immersed in a hydrostatically compressed medium: the conditions of the hydrostatic compression is fulfilled, tetragonal distortions in PNZT unit cell remains constant while the unit cell parameters decrease with pressure increase. At this range pressure induced strain prevails over film "growth" strain caused by substrate/film lattice parameters mismatch. At lower pressure the external pressure results in strain which is comparable or even less than the mismatch strain. At these deformations film clamping on the substrate introduces *compression anisotropy* which should be taken into consideration. To calculate the "critical" pressure p_{cr} when the external load reaches the mismatch stress a simple model of force balance can be introduced. We assume that this critical load corresponds to the condition of equality of the two forces applied to the given crystallite: the force from the external pressure and the force from the film/substrate interface. External pressure p induces the force proportional to the surface of the crystallite:

$$f_{ex} = p \cdot 2\pi r \cdot h, \qquad [1]$$

where r and h are the characteristic crystallite radius and height. The force acting from the substrate to the crystallite is caused by a substrate/film mismatch can be estimated as the product of a characteristic mismatch stress times the area of to which this stress is applied. The mismatch stress is proportional to Young's modulus, C, times the substrate/film mismatch, $\Delta a/a$, while the area can be estimated approximately as a product of the perimeter of a cylindrical crystallite, $2\pi r$ times characteristic length l. l is the length of spatial decay of the elastic mismatch strain. Due to the long-range character of elastic interactions there is no other parameter with the dimension of length except $l \approx r$. As a result we get the following expression for the mismatch force:

$$f_m = C \cdot \frac{\Delta a}{a} \cdot 2\pi r^2 . \qquad [2]$$

The condition of the balance between these two forces brings us to the following expression for the critical pressure:

$$p_{cr} = C \cdot \frac{\Delta a}{a} \cdot \frac{r}{h}, \qquad [3]$$

At high pressures exceeding p_{cr} the strain is caused by the external load hence it has isotropic character and both polarization and dielectric permittivity depend linearly on the applied pressure. At lower pressure $p < p_{cr}$ the existence of mismatch stress violates Hooke's law and results in nonlinear dependence and higher sensitivity of electrical properties of PNZT film on the external load than at the linear regime.

The column-like growth of highly *c*-oriented ferroelectric films is well known from electron microscope observations. Also, the small depolarizing coefficient N in epitaxial PZT/YBCO heterostructures has recently been found to be $2.37 \cdot 10^{-4}$ (5) and corresponds to prolate ellipsoidal shaped crystallites with a length-to-diameter ratio of 140. Taking this into account we assume ferroelectric film consists of column-shaped nanocrystallites elongated parallel to the film normal. Since the mismatch stress is applied on the substrate/film interface at the crystallite foot while the entire crystallite surface is affected by external pressure the crystallite radius-to-length ratio appears in the Eq. 3. This small parameter $r/h \sim 10^{-2}$ leads to a significant reduction of the value p_{cr} and makes the mismatch stress inefficient. The typical values $C \sim 5 \cdot 10^{11}$ J/m^3 and $\Delta a/a \sim 2\%$ gives us $p_{cr} \sim 0.1$ Gpa which is in nice correspondence with the critical pressure observed in our experiment.

CONCLUSION

In conclusion, the ferroelectric properties of epitaxial PNZT/YBCO/$LaAlO_3$ heterostructures have been measured at various hydrostatic pressures up to 1GPa for the first time. Superlinear pressure dependence of remnant polarization and dielectric permittivity has been observed at low pressures and explained in the model of compression anisotropy of nanostructured crystallites. The pressure sensitivity of the ferroelectric film, 140% Gpa^{-1}, has been found very promising for sensor applications. It is illuminating to compare this with the sensitivity of the manganin resistance probe used in our experiment: 2.4% Gpa^{-1}. Nanometer thick films consisting of isometric nanocrystallites with $r/h \sim 1$ are the best candidates for functional ferroelectric structures possessing prominent nonlinear pressure dependent properties.

REFERENCES

1. Björmander, C., Grishin, A.M., Moon, B.M., Lee, J., Rao, K.V., Appl. Phys. Lett., 1994, 64, 3646.
2. Björmander, C., Sreenivas, K., Duan, M., Grishin, A.M., Rao, K.V., Appl. Phys. Lett., 1995, 66, 2493.
3. Björmander, C., Sreenivas, K., Duan, M., Grishin, A.M., Rao, K.V., Microelectronic Engineering, 1995, 29, 111.
4. Uehara, H., Komukae, M., Oishi, K., Osaka, T., Makita, Y., J. Phys. Soc. of Japan. 1996, 65, 3094.
5. Grishin, A.M., Yamazato, M., Yamagata, Y., Ebihara, K., Appl. Phys. Lett., 1998, 71, 620.

Pergamon

NanoStructured Materials, Vol. 12, pp. 1145–1148, 1999
Elsevier Science Ltd

0965-9773/99/$–see front matter

PII S0965-9773(99)00315-3

THE SOLID STATE THERMAL TRANSFORMATION OF THE METAL CARBOXYLATES AS A SOURCE OF FORMATION OF NANOSIZED STABILIZED PARTICLES

A.S. Rozenberg, and A.D. Pomogailo
Institute of Chemical Physics Research Russian Academy of Sciences
142432 Chernogolovka, Moscow Region, Russian Federation

Abstract – *In the self-generated atmosphere the kinetics, topography and composition of products of the thermal transformations of the formates Fe(II,III), Ni(II), Cu(II), Pb(II), oxalates Fe(III), metal containing monomers – acrylates of simple and cluster cations* $M(CH_2{=}CHCOO)_n{\cdot}mH_2O$ *(*$MAcr_n$*, M = Co(II), Ni(II), Cu(II), Fe(III)), maleate Co(II) as well as (co)crystallizates of* $FeAcr_3$ *and* $CoAcr_2$ *(1:1, 2:1) have been studied. Influence of different factors both on the thermolysis kinetics and on reached product dispersion have been studied. The correlation between the formed metal containing product dispersion and the kinetic parameters of thermolysis process are ascertained. It was shown that the synthesis of nanosized metal-containing particles and their stabilization in polymer matrix during the thermal transformation of the carboxylates of the unsaturated acids can be realized simultaneously. The problems of the products dispersion control by the solid state reactions are discussed. ©1999 Acta Metallurgica Inc.*

INTRODUCTION

The materials based on nanoparticles have found various, at times unexpected, applications in chemistry, physics, and biology, stimulating research on various theoretical and practical problems. These problems are primary associated with synthesis control and the stabilization of highly reactive energy-saturated nanoparticles (NP) synthesized by solid phase reactions. The formation and stabilization of the synthesized by solid-phases processes high-reactive NP, and the search for efficient ways for their chemical passivation are rather challenging problems. There are principally two approachs for the matrix isolation of NP. The first consists of the mere addition of a powder, suspension, or solution of a polymeric stabilizer to an as-prepared nanoparticle dispersion. The second approach involves the preparation of NP in the presence of a stabilizer or preparation of the stabilizer from its precursor in the presence of already prepared NP. One of the promising approachs of this last method is solid-phase conversions of saturated (formates, oxalates) or unsaturated (acrylates, metacrylates, maleates) carboxylates of transition or heavy metals. This work was concerned with this method.

EXPERIMENTAL

Crystallized industrial powders of metal formates and oxalates were used for the investigation. The metal acrylates and maleates were obtained according to a method (1). Cocrystallites were prepared by coprecipitation of salts from an alcoholic solution. The sample thermolysis was carried out in the isothermal regim in a non-isothermal reactor (at experimental temperature, T_{exp}), the heated volume of the compound was 0.03V (V is the reaction vessel volume; the basic part of the vessel was at room temperature, T_r). The kinetics of gas evolution was recorded using a membrane zero-manometer. The mass loss of the sample and total amounts of gaseous products at T_r were determined at the end of the experiments. The low-temperature fractionation of gaseous products was carried out at 77K.

The specific surface areas, S_{sp}, of the initial samples and of the solid-phase products after their thermal transformation were determined by the low-temperature nitrogen adsorption method (method BET (2)). Optical microscopic observations were performed in transmitted light on a MBI-15 Leitz Metalloplan instrument. An IEM-1200Ex instrument (accelerating voltage 120 kV) was used for electron microscopic studies. Mass spectral analysis was performed with a MS 3702 quadruple mass spectrometer.

DISCUSSION

The preparation of ultrafine metals and/or their oxides in solid phase by thermal decomposition of salts of organic acids, such as formates, acetates, and oxalates has long been known and is currently used. Meanwhile, most research sets aside relations between kinetic parameters of the solid-phase reaction and the particle size of products, i.e. the limits of particle size control. The most comprehensive information about the effects of various factors on the kinetics of thermal transformations and the product particle size is deduced from investigating thermolysis in a self-generated ambient (SGA) atmosphere at a constant temperature. Previous complex studies (3-7) on the kinetics and topography of thermolysis of crystalline powders of Fe(II), Fe(III), Ni(II), Pb(II), and Cu(II) formates and Fe(III) oxalate allow the inference that thermal transformation of these compounds increases during decay process. Conversion versus time curve is S-shaped, characteristic of solid-state chemical processes. The initial conversion rate W_0 is related to the rate of generation of decay centres (nucleation of a new phase), as shown by the evolution of the topography of the decomposition of crystals. The rate of these processes (growth of nuclei) is controlled by the conversion rate in the acceleration period, including the maximum conversion rate W_{max}. The ratio $\Psi = W_{max}/W_0$ is the measure of process acceleration.

Electron microscopic examination of solid decomposition products revealed some common features in product morphology. All products consist of like-spherical electron-contrasting NP of near-spherical and have fairly narrow near log-normal partical-size distributions. We compared the mean particle-size at the end of decomposition determined by electron microscopic examination, $\bar{d}_{f,\,EM}$, with the values calculated from S_{sp}, $\bar{d}_{f,S}$, assuming the spherical share of particles. The compared values were close (Table) and enabled us to consider the particle as compact and nonporous.

TABLE
Mean particle size of products from electron microscopy examination

Compound	T_{ex}, °C	$\bar{d}_{f,S}$, nm	$\bar{d}_{f,EM}$, nm	$\bar{L}_{coat}$*, nm	Product**
$Fe(HCOO)_2.2H_2O$	270	27.0	20.0	3 – 5	Fe_3O_4
$Fe(HCOO)_3$	270	25.0	–	–	Fe_3O_4
$Ni(HCOO)_2.2H_2O$	210	30.0	50.0	~ 4.0	Ni
$Cu(HCOO)_2$	140	30.0	~ 30.0	–	Cu
$Fe_2(C_2O_4)_3.5H_2O$	310	35.0	30.0	–	Fe_3O_4
* The thickness of a polymer coat; ** The results of electron diffraction.					

The general condition determining whether ultrafine materials will form or not is the competition of rates of nucleation (W_N) and growth (W_G) of the new phase. In the general case, the mean particle size of products of a solid-phase reaction is depended on the ratio W_G/W_N : $\bar{d}_{f,p} \approx (W_G)^a/(W_N)^b$, where the exponents a and b depend on the geometry of nuclei (8). Obviously, $W_{max}/W_0 \sim W_G/W_N$ and, consequently, $\bar{d}_{f,p} = \bar{d}_{f,S} \sim \Psi$. Then, the $\bar{d}_{f,S}$ value should increase with increasing the Ψ value. In fact, a correlation between $\bar{d}_{f,S}$ and Ψ does occur, as calculated from the thermolysis kinetics at various T_{exp}. This fact points to reciprocal relations between the thermolysis kinetics and the product particle size.

Our exploration of factors that influence the kinetics parameters of decomposition and the product particle size revealed a few common trends. An increase in T_{exp}, in m_0/V ratio (m_0 is the initial weight of the sample, V is the overall reactor volume), and in defects of adducts crystall structure influenced on the decomposition rate and on the product particle size. The effects of the thermolysis gaseous products on $W_{max} \leftrightarrow W_G$ and $W_0 \leftrightarrow W_N$ are similar to those of the m_0/V ratio. In experiments at a constant temperature and in SGA, all the above-specified factors can be quantitatively accounted for either to the initial parameters of decomposition process, or to standardized kinetic parameters of conversion that allows to control the particle sizes.

An additional factor influencing on the product particle size is self-conservation. This phenomenon was observed in decomposition of Fe(II), Fe(III), Ni(II), and Cu(II) formates: C-H-O products of decomposition undergo catalytic transformations to form a carboxylate-type polymer film covering the surface of newly formed ultrafine particles; the composition of this film is supposedly $-[-CH_2O-]_k-[-CH(COOH)O-]_s-$ ($k >> s$). The film thickness $\bar{L}_{cont}$ ranges between 3.0 and 5.0 nm (Table). The observed accumulation of the polymeric product at the end of conversion correlates with the increasing fineness of solid state product.

From the fact that a polymeric film can form on ultrafine thermolysis products of some saturated transition metal carboxylates, we inferred that systems for which a combination of synthesis of metal-containing phase and polymerization of C-H-O conversion products is possible, are expected to yield stabilized ultrafine products. These systems were transition metal carboxylates of unsaturated mono- and dicarboxylic acids, such as acrylates, maleates, and fumarates of simple and cluster cations; all these compounds are metal containing monomers. The thermal transformations of acrylates $M(CH_2{=}CHCOO)_n.mH_2O$ (M = Co(II), Ni(II), Cu(II), Fe(III)), cobalt maleate $Co(OOCH{=}CHCOO).2H_2O$ and (co)crystallizates of $FeAcr_3$ and $CoAcr_2$ (1:1, 2:1) (7, 9, 10) are a multistage process. This process involves the following three major macroscopic stages: (i) dehydration of the starting monomeric crystal

hydrate; (ii) (co)polymerization of the dehydrated monomers; and (iii) decarboxylation of metal containing groups of the polymer to form a metal-containing phase including mixed oxides, and a decarboxylated polymeric matrix. The final empirical composition of resulting polymer which contains metal-containing both carboxylate and non-carboxylate fragments, can be described by the general formula $(CoC_6H_6O_4)_{p-x}(C_4H_6)_x(CoC_6H_4O_4)_{q-y}(C_4H_4)_y(C_6H_8O_4)_{1-z}(C_4H_8)_z$, $x \leq p$, $y \leq q$, $z \leq 1$ (an example formula for $CoAcr_2$).

The solid-phase reaction products show similar topographies when examined by electron microscopy. We observed electron-contrasting metal- containing particles of near-spherical shape, which are distributed fairly uniformly over the volume of the less electron-contrasting polymer matrix (the observed average particle - particle distance is 8.0 - 10.0 nm). These particles have rather narrow size distribution. The mean particle diameter was $\bar{d}$ = 5.0 - 9.0 nm, which is smaller than the value determined for the transformation products of saturated metal carboxylates (Table).

SUMMARY

The aforementioned features on thermal coversions in metal carboxylates demonstrate the possibility to prepare polymer-immoilized nano-sized and cluster particles of metal and metal oxides of desirable particle-size distribution.

ACKNOWLEDGMENTS

The work was financially supported by the Russian Foundation for Basic Research (Project No 98-03-32353).

REFERENCES

1. Dzhardimalieva, G.I., Pomogailo, A.D., Ponomarev, V.I., Atovmyan, L.O., Shulga, Yu.M., and Starikov, A.G., *Izv. Acad. Nauk USSR, Ser. Khim.*, 1988, 1525.
2. Gregg, S.J., and Sing, K.S., *Adsorption,Surface Area and Porosity*, Academic Press, New York, 1967.
3. Alexandrova, E.I., Raevskii, A.V., Rozenberg, A.S., and Titkov, A.N., *Khim. Fiz.*, 1989, vol. 8, 1630; 1990, vol. 9, 1244.
4. Rozenberg, A.S., and Titkov, A.N., *Poroshk. Metall.* (Kiev), 1990, No 10, 58.
5. Alexandrova, E.I., Rozenberg, A.S., and Titkov, A.N., *Khim. Fiz.*, 1994, vol. 13, No 7, 50.
6. Rozenberg, A.S., and Alexandrova, E.I., *Izv. Acad. Nauk, Ser. Khim.*, 1996, 72.
7. Rozeberg, A.S., Dzhardimalieva, G.I., and Pomogailo, A.D., *Doklady Physical Chemistry*, 1997, Vol. 356, Nos. 1-3, 294.
8. Morokhov, I.D., Trusov, L.I., and Chizhik, S.P., *Ul'tradispersnye metallicheskie sredy* (Ultra-dispersion metallic environments), Moscow: Atomizdat, 1977.

Pergamon

NanoStructured Materials, Vol. 12, pp. 1149–1152, 1999
Elsevier Science Ltd

0965-9773/99/$–see front matter

PII S0965-9773(99)00316-5

MAGNETIZATION REVERSAL OBSERVATION AND MANIPULATION OF CHAINS OF NANOSCALE MAGNETIC PARTICLES USING THE MAGNETIC FORCE MICROSCOPE

J. Wittborn, K.V. Rao, R. Proksch[+*++], I. Revenko[+*], E.D. Dahlberg[++] and D.A. Bazylinski[+++]

Dept. of Condensed Matter Physics, KTH, Teknikringen 14, SE-10044 Stockholm, Sweden. [+]Dept. of Physics, St. Olaf College. [++]Magnetic Microscopy Center, School of Physics and Astronomy, University of Minnesota, Minneapolis, MN 55455, USA. [+++]Dept. of Microbiology, Immunology and Preventive Medicine. Iowa State University, Ames, Iowa, USA.
* Present address: Digital Instruments, Santa Barbara, CA 93117, USA.

Abstract *– The magnetization reversal of chains of 40-50 nanometer, magnetic particles has been studied using Magnetic Force Microscopy (MFM) in an applied field. The field was stepwise increased and decreased in order to make hysteresis loops for the chains. The magnetic particles, magnetosomes biomineralized by magnetotactic bacteria, are single crystal* Fe_3O_4 *with a narrow size distribution. A method for extracting Switching Field Distributions (SFD's) from sets of MFM images of such chains was developed. The coercivity was found to increase with the number of particles in a chain up to 7 or 8 particles and then decrease with increasing number of magnetosomes. After the initial reversal observations, one of the chains was cut into smaller pieces using the MFM-tip, thus producing separated chain segments, which resulted in altered inter-particle interactions. Additionally, multiple hysteresis loops were made for the same chain, showing that the field from the tip affects the sample magnetization.* ©*1999 Acta Metallurgica Inc.*

The effects of magnetostatic interactions on the magnetic reversal of single domain magnetic particles are important to understand from both a pure and an applied viewpoint. In this work, chains of 40-50 nanometer, magnetite (Fe_3O_4) particles, bio-mineralized by magnetotactic bacteria (1,2) have been studied and manipulated using a Magnetic Force Microscope (MFM) in an applied magnetic field. These particles (called magnetosomes) have a species-specific morphology. For the *Aquaspirillum magnetotacticum* of strain MS-1, which we have used, they consist ideally of octahedral prisms of {111} faces truncated by {100} faces (3). They are single crystal particles with the cubic inverse spinel crystal structure of magnetite with [111] easy axes directions. In the bacteria the magnetosomes are preferentially aligned with the [111] direction parallel to the long axis of the chain (3), thus creating a maximum magnetic moment. These particles make ideal samples for studying the collective behavior of single domain particles as they have an extremely narrow size and shape distribution.

Extracted magnetosome chains were deposited on cleaved mica and left to dry in a magnetic field in order to self assemble into chains oriented along the field (three chains of 35 to 83 magnetosomes were studied). The magnetosome chains were imaged (both AFM and MFM), using a D3000 Nanoscope from Digital Instruments. The chains, such as the one shown in fig. 1, were imaged in various applied fields. The magnetization of the chain was first saturated in an applied field of about 1 kOe. The applied field was next decreased to 0 Oe and then stepwise increased in the opposite direction until the MFM image showed the moment of all particles in the chain were reversed, the field was then stepwise decreased to 0 again and then stepwise increased until the moment of all particles in the chain were reversed again, finally the field was stepwise decreased to zero again, thus completing the hysteresis loop for the chain. After the initial study, the MFM-tip was used to cut the chain shown in fig. 1 into smaller pieces. The resulting shorter chains (see fig 2) were studied the same way as the original chain.

Fig 1) A magnetosome chain. a) topography of the sample. b) magnetic structure of the sample.

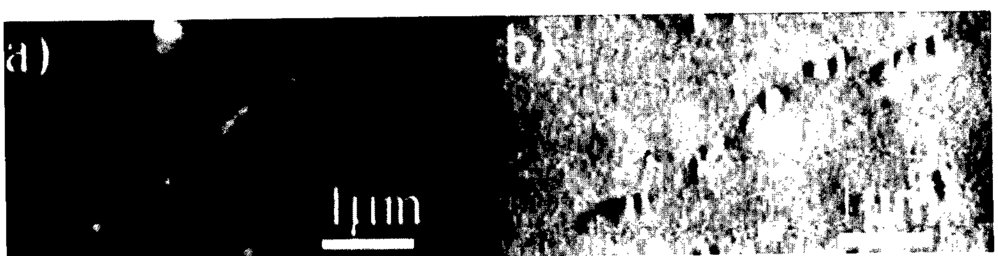

Fig 2) The same magnetosome chain as in fig 1 after being segmented into smaller pieces using the MFM-tip. a) topography of the sample. b) magnetic structure of the sample.

In order to characterize the measurements the consecutive images were subtracted, resulting in a series of images showing the change in sample magnetization between the incremented fields (see fig. 3). The magnetization change was quantified by numerically integrating over these images in order to get the switching field distribution (SFD). The switching field, H_s, was defined as the average of the two field values in between which the largest change in magnetization occurred. We defined the coercivity, H_c, as the average of the absolute value of the two switching fields.

The resulting SFD for the whole chain shown in fig. 1 is shown in fig. 4a. This SFD appear to consist of a number of sharp peaks. The reason being this apparently continuous chain has small kinks and separations between some magnetosomes causing parts of the chain to

reverse more or less independently. Digitally masking all but smaller sections of the chains which appear to act as single units, and calculating the SFD shows they consist of only two peaks (See fig. 4b), i.e. there are two well defined (within experimental error) switching fields, which means that all the moments of the magnetosomes in these segments of the chain reverses together.

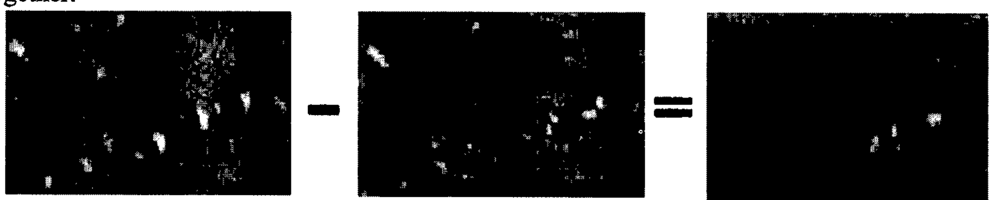

Fig 3) Subtraction of two consecutive MFM images, made at 100.0 and 127.4 Oe respectively, resulting in a "difference image" where the features of the image represent the amount of change in magnetization between the two MFM images.

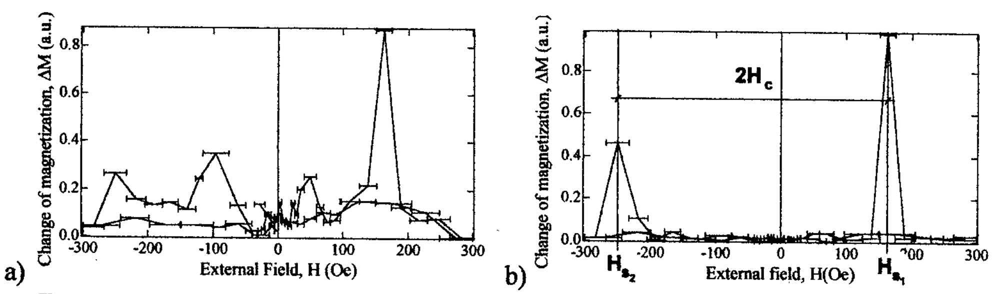

Fig 4) Switching Field Distribution for a) the chain shown in fig. 1, and b) for a digitally masked segment of the same chain, with the switching fields, H_s, and the coercivity, H_c, for that segment marked in the figure.

It appears that independent of the measurements on the segmented or unsegmented magnetosome chain that the highest coercivities occur in the middle of a magnetosome chain. Also, it was found that the segments of the chains behaved as if they had only a weak magnetostatic interaction. The measurements of the hysteresis loops for the magnetosome chains were made as a function of the number of magnetosomes in the chain segments. The coercivity of the chain segments increases with the number of particles in a manner consistent with both the coherent rotation (4) and fanning (5) models up to 7 or 8 particles. For longer chains the coercivity decreases, which may indicate a transition to a mode of magnetization reversal of a less uniform nature. In fig 5 is shown the coercivity as a function of number of particles for the same chain segments before and after cutting the chain apart using the MFM tip. In this plot we have normalized the coercivities with respect to the small lonely chain seen at the top of fig 1 and 2, which is presumed to be unaltered by the cutting procedure. Additionally, we plotted the coercivities given by the fanning model.

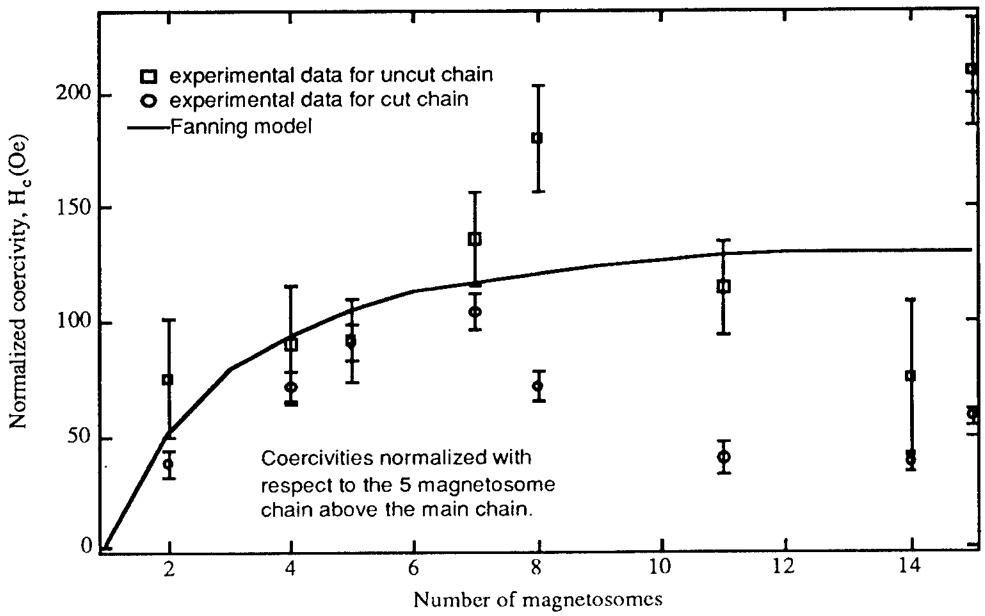

Fig 5) The coercivity, $H_c(Oe)$, plotted against the number of magnetosomes in the segments of the chains shown in figs. 1 and 2. For comparison, the coercivities given by the fanning model are shown.

In conclusion, we have measured the coercive field of three isolated chains of octahedral shaped magnetite particles with an approximate size of 40-50 nm produced by magnetotactic bacteria. We show that it is possible to calculate Switching Field Distributions (SFD's) for series of images obtained by Magnetic Force Microscopy of single magnetic domain particles. We find the chain segments of magnetosomes appear to reverse their magnetization in a manner consistent with the chain of spheres fanning model for up to 7 or 8 particles, with a decrease in the coercivity for longer chains. It may be for these longer chains a more collective reversal mechanism, akin to a domain wall, dominates.

This research was supported by the Swedish National Board for Technical and Industrial Development, NUTEK and the U.S. Office of Naval Research. One of us (JW) acknowledges travel grants from the Royal Institute of Technology and The Royal Swedish Academy of Sciences, which made possible visits to the Magnetic Microscopy Center at the University of Minnesota for carrying out a part of this work.

REFERENCES

1 Blakemore, R.P., *Science*, 1975, 190, 377.

2 Blakemore, R.P. *Annual Review of Microbiology*, 1982, 36, 217.

3 Mann, S., Frankel, R.B. and Blakemore, R.P., *Nature*, 1984, 310, 405.

4 Stoner, E.C. and Wohlfart, E.P., *Philosophical Transactions of the Royal Society*, 1948, A-240, 599.

5 Jacobs, I. S. and Bean, C. P., *Physical Review*, 1955, 100, 1060.

Pergamon

NanoStructured Materials, Vol. 12, pp. 1153–1156, 1999
Elsevier Science Ltd

0965-9773/99/$–see front matter

PII S0965-9773(99)00317-7

STRUCTURAL CHARACTERIZATION OF ULTRA DISPERSED (NANO-) MATERIALS AS INTERMEDIATE BETWEEN AMORPHOUS AND CRYSTALLINE STATES

V.F.Petrunin

Moscow Engineering Physics Institute, Moscow, 115409, Russia
Tel: +07-095-323-9333 Fax: +07-095-324-2111 email: petrunin@atomic.mephi.ru

Abstract *-Ultra dispersed materials (UDM) such as thin films, thin whiskers, fine powders, nanocrystals (NCs) have been designed. Calculated values of interatomic distances along various crystallographic directions are found to essentially decrease at the centre of the particle and much more reduced as the surface is approached. Similar changes of interplanar distances corresponding to an inhomogeneous distortion in UDM are confirmed experimentally, mainly by neutron diffraction. ©1999 Acta Metallurgica Inc.*

INTRODUCTION

When the size of condensed matter morphological elements (small particles, crystallites, etc.) becomes comparable with a characteristic distance of some physical phenomenon (size of domain, length of phonon or electron free path, the dimension of defects, etc.), then various dimensional effects can occur [1]. To this class of materials may be assigned thin films, thin whiskers, fine powders, high porous materials, etc. Ncs [2] are compact UDMs by this definition. UDMs have significant energy due to their large surface areas and they are usually prepared under extreme conditions (high temperatures, rapid processes) so that they are non-equilibrium systems. Research on materials in the ultra dispersed state has been going on for 50 years behind closed door in the USSR and latter in the FSU [3,4]. Although many examples of UDMs have been studied by a variety of physical techniques and information on the peculiarities of their structure and properties have been obtained [5], a great deal of UDMs specific atomic arrangement should be further investigated. In particular, the question of availability and character of atomic structure difference between ultra dispersed and massive crystalline state of material is investigated in this work.

COMPUTATIONAL PROCEDURE

Model computations concerning the atomic arrangement in small particles have been undertaken using the classical methods of molecular dynamics [5,6]. Calculations were made for two small particles: one of 736 nickel and other of 1047 gold atoms. The interatomic interactions with the nearest neighbours in two coordination shells were taken into account by means of an effective pair potential. In both cases the calculated values of interatomic distances along various crystallographic directions are essentially decreased at the centre of the particle and also much reduced as the

surface is approached in all directions, less in compacted and more in crumbly ones (Fig.1). Such changes of interatomic separation correspond to an inhomogeneous distortion.

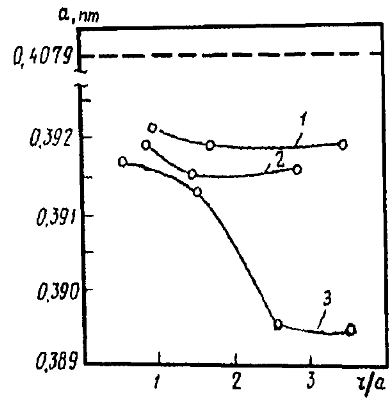

Fig 1. Calculated values of interatomic distances for small (1047 atoms) gold particle along various crystallographic directions: 1-[111];2-[110];3-[200]

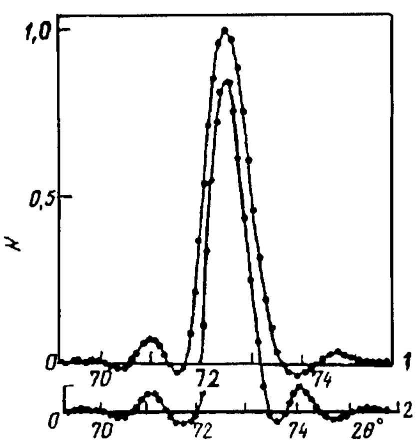

Fig.2. Physical profiles of neutron diffraction peaks (400) for massive and ultradispersed powder TiN L=16 nm), calculated by means of harmonic analysis. Asymmetry for ultradispersed sample is saw.

Theoretical treatment of the impurity atoms distribution inside the small particle also show its nonequiparticle character along the radius[5]. Thermodynamic analysis of the interstitial solid solution in the small particle allows us to determine four types of equilibrium concentration profiles, depending on the atomic radii ratio of the components and the interatomic binding,. However, in all cases they correspond to the solution decay and to depletion or to enrichment of surface.

RESULTS

Electron, X-Ray and mainly neutron diffraction experiments have been carried out to estimate the validity of the above model. Of the three direct methods of structure analyses the neutron diffraction provides fuller and sometimes unique information about UDM. Neutron method permits to measure more accurately a diffraction maxima intensity since an amplitude of coherent scattering has no angular dependence. The neutron amplitude of the light atoms H, C, N, and O are more significant and allow their positions to be determined, since these elements frequently occur in binary UDM or as impurities. Additionally, it is easy to study UDM inside sealed air-tight containers without much loss of intensity and to obtain average information from the whole volume.

Although MEPI neutron difractometer resolution is not very high, significant diffraction pattern can be observed and its asymmetry can be exposed by mathematical harmonic analysis (Fig.2). For the Ni fine powder sample (with 16 nm medium size of particles) immediately after preparing the microdistortions calculated from Fourier coefficients, it was found that $\Delta L/L=0{,}235$ %. The FCC crystalline lattice period

determined by X-Ray diffraction analysis found to be 0,3523 nm, is less than that for the bulk Ni sample (0,3542 nm). The static and dynamic mean square root values for the atomic displacement determined by additional neutron diffraction measurements at liquid helium temperature were 0,0083 nm and 0,0114 nm resp., which is larger than 0,0069 nm and 0,0092 nm for bulk Ni. No peaks of oxide phase were detected for the fresh sample. After a 6 months storage of this sample in air nickel oxide NiO phase was found at an impurity level 7%. Thus fresh Ni small particle is characterised by a spatially inhomogeneous concentration distribution of oxygen atoms manifested in an inhomogeneous extension of the lattice and with an increase in the mean square atomic displacements.

Lattice constants of some metallic and compound's UDM were precisely determined using X-ray diffraction technique with silicon internal standard. These values for Cu, Al, Be ultra fine powders were also found to be less than that of a bulk samples, but the difference (less than 0,1 %) is within the experimental error and the value for Be could not be decreased because of large value of diffraction maxima width. The high resolution electron images of small gold particles (about 2 nm) are found qualitatively agree with the monotonical decrease of interplanar distances near the surface.

Neutron and X-Ray analysis of ultra fine TiN and ZrN powders establish that their particles size diminution leads to a regular decrease of the lattice constant (up to 0,3 %) and the increase of the root-mean square atom displacements (up to 20 %). It is found simultaneously that composition of ultra fine nitrides is not stoihiometric and depends from the particle size. Considerable microdistortion of ultra dispersed ZrN crystal lattice was discovered by means of harmonic analysis of asymmetrical peaks profiles (Fig.3). It was found that a part of oxygen-impurity atoms could penetrate into the nitride lattice replacing mainly nitrogen atoms.

Neutron diffraction patterns of ultra dispersed powders NbN, prepared by different methods show the gradual change of atomic ordering from crystalline- to amorphous-like, with a reduction temperature of synthesis from 5270 to 770 K and crystallite size from 80 to 5 nm (Fig.4).

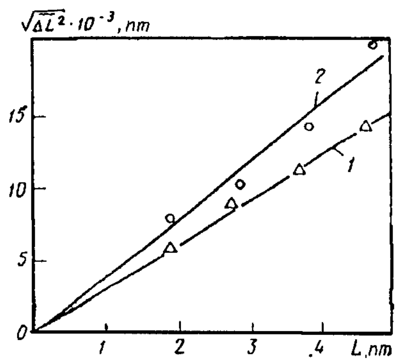

Fig.3. Microdistortion of ultradispersed powder (L=66 nm) ZrN lattice along directions : 1-[110];2-[200]

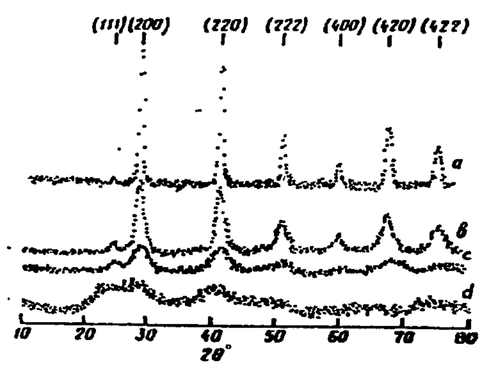

Fig.4. Neutron diffraction patterns of ultradispersed powders
NbN, preparing at different temperature: a-5270,b-1270,c-1070, d-770 K.

DISCUSSION

Theoretical estimates in this work show that usual bulk crystalline lattice does not correspond to atomic arrangement of small particle from energy minimum point of view. The interatomic distances would be changed, mainly on the surface and near surface layers. Experimental neutron, X-Ray and electron diffraction data for metals and nitrides UDM reveal the interplaner distances decrease, the static and dynamic atomic displacement increase, small particle microdistortion and amorphous-like disorder at the size of particle decrease. All these results can be explained by the model of inhomogeneous distortion of UDMs small particle.

CONCLUSION

A generalization of all theoretical and experimental results allows to suggest model of UDMs atomic arrangement which illustrates the possibility of transition from crystalline to amorphous state through an ultra dispersed state (Fig.5). Inhomogeneous distortion of small particle provokes a atomic density distribution which is different from crystalline and the amorphous ones. The atomic ordering in crystals is found to be present at very large distances (more 100 *a*), in amorphous materials only at short distances (less 100 *a*), and in UDM at interemediate distances (10-100 *a*). So UDM atomic structure is peculiarly intermediate between the crystalline and amorphous states. The reasons for the pecularity of UDM atomic structure is the significant surface energy, small size of crystallite and extreme conditions of preparation.

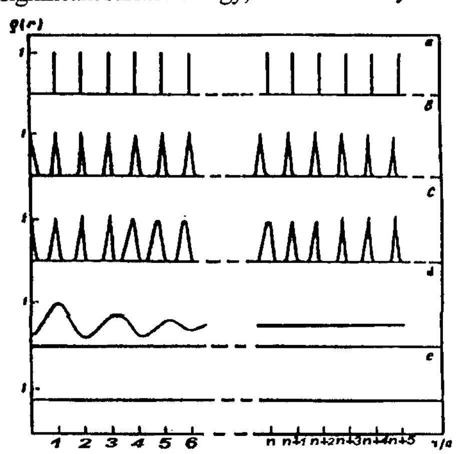

Fig.5 Atomic density function for solid wit different atomic ordering:
a-ideal crystal, b- real crystal, c-ultradisperse material,
d-amorphic material, e-ideal amorphi substance.

REFERENCE

[1] I.DMorokhov, V.I. Petinov, L.I. Trusov, V.F. Petrunin, Sov. Phys. Usp. 24 (4) (1981) 295.
[2] H. Gleiter, Nanostructured Mater. 1 (1992) 1.
[3] G.M. Gryznov, V.F. Petrunin, Conversion in Machine Building of Russia 1 (4) (1992) 24.
[4] M.I. Alymov, O.N. Leontieva, Nanostructured Mater. 6 (1995) 393.
[5] V.F. Petrunin, J. Mendeleev Chem. Soc. (in Russian) 7 (2) (1991) 146.
[6] D. Timpel, K. Scheerschmidt, I. Non-cryst. Solids, accepted for publication.

Pergamon

NanoStructured Materials, Vol. 12, pp. 1157–1160, 1999
Elsevier Science Ltd

0965-9773/99/$–see front matter

PII S0965-9773(99)00318-9

THERMOMAGNETIC STUDY OF METASTABLE NANOGRAINS IN SOFT MAGNETIC NANOCRYSTALLINE ALLOYS

L.K. Varga [1] and K.V. Rao[2]

[1] Research. Institute. for Solid State Physics, 1525 Budapest P.O.B. 49, Hungary
[2] Department. of Condensed Matter Physics The Royal Institute of Technology, Stockholm

Abstract *– The magnetic decoupling and the transformation temperatures of metastable nanophases have been investigated as a function of annealing temperature in partially crystallized $Fe_{73.5}Si_{13.5}B_9Nb_3Cu_1$ (Finemet) and $Fe_{92-x}B_xZr_{7-y}Nb_yCu_1$, with x = 2,4,6,8,10,12 and y = 0, 3.5 at% (Nanoperm) type nanostructured soft magnetic alloys. By comparative initial permeability (μ_i) and low field dc magnetization (M_s) measurements it is demonstrated that the nanograins show a superferro-superpara- and a superpara-para-magnetic transition at high temperatures, between the Curie points belonging to the starting amorphous and equilibrium bcc phases respectively, in both type of nanocrystalline alloys. We find that these transition temperatures depend on the annealing conditions. ©1999 Acta Metallurgica Inc.*

Introduction

At present, the best known soft magnetic materials around room temperature are the nanocrystalline alloys obtained from amorphous precursors containing small amount of nucleating (Cu) and grain growth inhibiting (Nb, Zr, or other early transitions) elements. The most successful compositions are the Fe-Si-B (Finemet) and Fe-Zr(Nb)-B (Nanoperm) based alloys. A disappointing feature of them is that they loose their good magnetic properties several ten degrees above room temperature. This behavior is due to the magnetic decoupling with increasing temperature of the bcc nanocrystals with high Curie temperature (T_c) embedded in the remaining amorphous matrix with low T_c.

Various authors have shown how that magnetic investigations at high temperature could provide information's about the behavior of two-phase nanostructured systems [1]. In the present work, the magnetic behavior at high temperature is studied in a wide range of temperatures (from 77 to 900 K) by initial permeability and low field (40 Oe) saturation magnetization measurements. Special attention is devoted to the magnetic transformation sequences, common in all the three family of alloys: strongly and weakly coupled ferromagnet, superferromagnet and superparamagnet.

Experimental

The initial permeability is measured as a function of temperature in a home built tubular furnace in He protective atmosphere at 1 kHz and H_m = 0.8 A/m on toroidal samples of 15mm average diameter using a computer controlled Hewlett Packard 7114 A type LCR meter. The heating rate was 10 K/min in the temperature range from liquid nitrogen to 750 °C.

The magnetization was measured in a thermally controlled microbalance (thermogravimetry analyzer type TGS- Pelkin-Elmer). In this system the probe reacts to the weak dc magnetic

field generated by a small external permanent magnet permitting the determination of the thermomagnetic curve in a large range of heating rates (5-160 K/min). In this work all the measurements have been done in H_{dc}=40 Oe and the heating rate was v_h=20 K/min.

Results and Discussion

Optimal annealed Finemet samples. In Fig.1 the partition of the temperature range from room temperature to the Curie temperature of the bcc phase is shown for the optimal annealed Finemet sample. While small changes in K is hardly observable in $M_s(T)$, the initial permeability shows a characteristic Hopkinson peak whenever the material becomes extremely soft. This happens at two temperatures in this two-phase material. In the coupled ferromagnetic state this maximum of μ_i occurs at the T_c of one of the component with lower T_c (the amorphous phase). The peak at T_c in any material is due to the proportionality of μ_i to $Ms^2/\langle K\rangle^n$ where n=1/2 for domain wall displacement and n=1 for domain rotation mechanism of magnetization. Since the anisotropy decreases faster than magnetization on heating, the initial permeability is expected to increase with temperature, tend to infinity just below the Curie point and then drop to ~1 for the paramagnetic phase. In the case of partially crystallized nanophased material however a round shape Hopkinson peak is observed at T_c^{am}, with the maximum shifted towards the room temperature. This phenomenon occurs presumably by producing composition gradients within the remaining amorphous phase, in such a way that there is no longer a unique Curie temperature, but a distribution of T_c, consequently instead of a single $\mu_i(T)$ curve, the combination of a family of curves is obtained. Above the first Hopkinson peak the bcc nanograins are gradually decoupled as the increasing temperature gradually surpass the T_c's of all the coupling amorphous spacers with slightly different chemical compositions. The weakened coupling results in an increase of the effective crystalline anisotropy, i.e. the domain structure changes from wide domains to a pattern of small irregular domains [2] . The coercive field starts also to increase with temperature but just before the $T_c^{am.}$ only [3], showing a smaller sensitivity to the partially decoupled ferromagnetic state than the initial permeability.

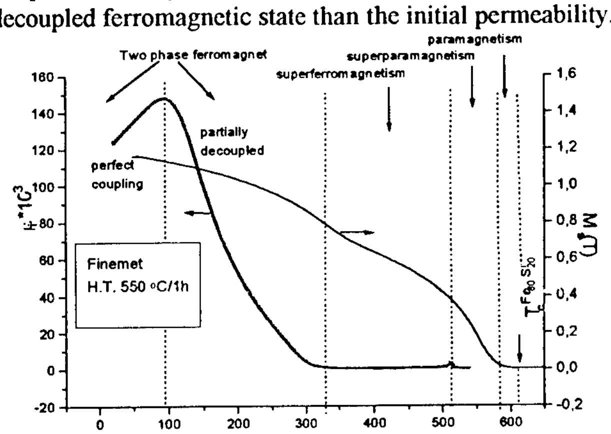

Fig.1 The magnetic transition sequences in a two phase nanocrystalline material

The coupling between nanograins is not completely interrupted at T_c^{am} but still persist to the next temperature interval characterized by superferromagnetic state. In this state a residual coupling, exchange or dipolar or both, depends sensitively on the annealing conditions, i.e. on

the crystalline fraction. We can hardly obtain a noninteracting monodomain particle system characterized with $H_{c,o}= 2K_1/M_s$. At a given fraction, i.e. at a given distance between the grains, the strength of the interaction decreases with increasing temperature due to the simultaneous decrease of magnetization in the bcc nanograins until thermal energy dominates and the magnetization state gets superparamagnetic. At this transition (T_{sf}) the system is again soft magnetic and a second peak at the initial permeability thermogram (measured with 10 mOe only!) can be observed. The magnetization however, is still dependent on the measuring field amplitude. The lower the measuring field the lower will be the transition temperature from superpara- to paramagnetic transition. Comparison of this T_{sp} temperatures obtained in different laboratories can be made when the measuring field is also specified along with the structural characteristics.

Annealing at different temperatures. In Fig. 2a the high temperature ranges of the $\mu_i(T)$ and $M^3_s(T)$ curves are shown for the Finemet alloy, indicating the sf-sp transition peaks of initial permeability's and the sp-p transition of M_s.

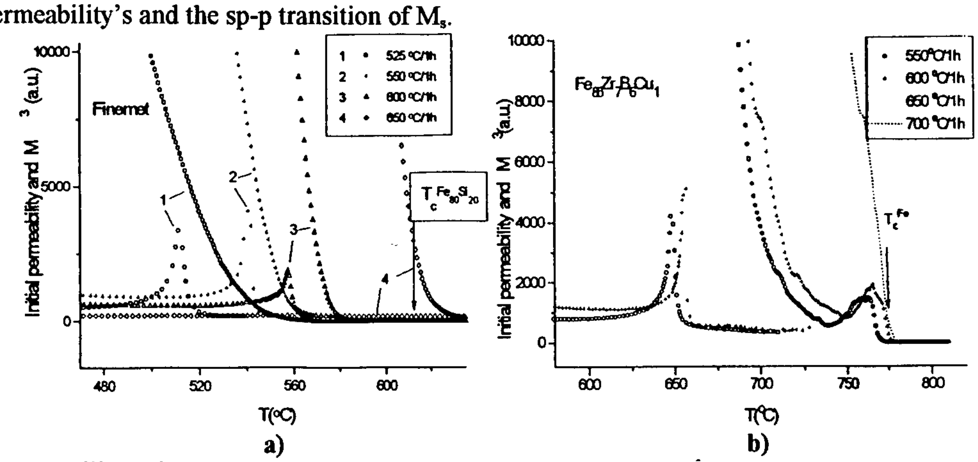

Fig.2 The second peak in μ_i (T) thermogram and the end of M^3(T) curves showing the superferro-superpara (T_{sf}) and superpara-paramagnetic (T_{sp}) transitions respectively for Finemet (a) and $Fe_{86}Zr_7B_6Cu_1$(b) alloys annealed between the two crystallization steps.

The second peak of μ_i (T) thermogram is systematically lower than the linear extrapolation of the end of the M^3(T) curves. For example, for three selected annealing temperatures: 525, 550, and 660 °C the T_{sf}= 511, 541 and 557 °C and T_{sp}= 533, 553 and 572 °C respectively. Note, that these transition temperatures are all bellow the corresponding annealing temperatures, so they are reproducible providing the measuring time is short enough to minimize further structural changes. For T_a= 650 °C we have got no second μ_i (T) peak and the magnetization curve extrapolates to the expected Curie temperature of the bcc $Fe_{80}Si_{20}$ phase (610 °C) indicating that the material has lost its monodomain particle behavior. At this heat treatment different hard magnetic compound phases (Fe_2B) appears also.

Annealing of Fe-Zr(Nb)-B-Cu samples. Such reproducible transitions between different magnetic states can hardly be obtained with FeZrBCu based alloys where the T_{sf} and T_{sp} transition temperatures are above the annealing temperatures, so further structural transformation during the measurements can not be excluded. Nevertheless we present in Fig.2b the comparative transition temperatures obtained at different annealing temperatures around the optimal one (600 °C/1h), for $Fe_{86}Zr_7B_6Cu_1$, the most studied FeZrB based alloy.

Compared to Finemet however, these transition temperatures are all above the annealing ones, consequently these transitions are not reproducible.

Increasing the B content from 6 to 12 at% the superparamagnetic transition could be reduced about 200 degree (Fig.3a) applying the same heat treatment (550 °C/15 min.) showing that finer precipitates have been produced with a larger distance between them which result in a smaller intergrain interactions.

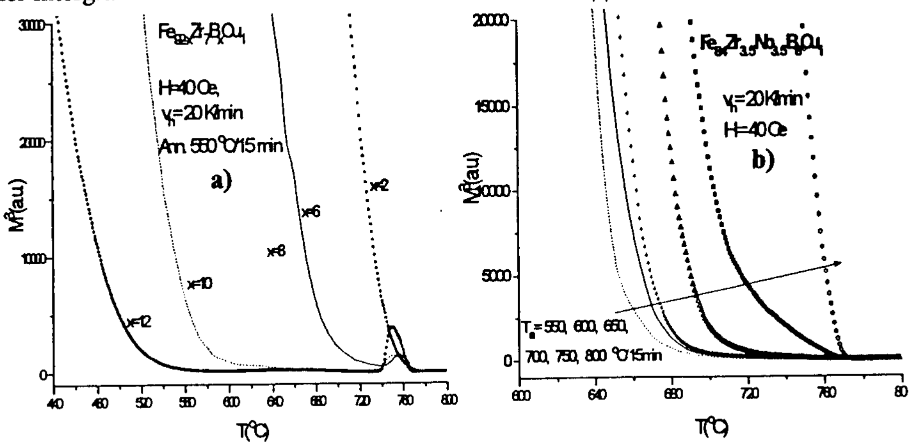

Fig.3 The high temperature part of $M^3(T)$ curves for annealed $Fe_{92-x}Zr_7B_xCu_1$ (a) and Nanoperm (b) alloys indicating the superpara-para-magnetic transitions.

Changing half of the Zr with Nb (Nanoperm) improves the magnetic properties by increasing the initial permeability at room temperature more than twice compared to the Nb free alloy. The effect of Nb is reflected in the magnetization curves also (Fig.3b). Even the heating velocity of v_h=20 K/min is high enough to not be observed the magnetization upraise due to the second crystallization step. The T_{sp} temperatures are also smaller than in the corresponding Nb free alloy.

Summary

We have found clear evidences for a series of magnetic transformations in the biphasic nanocrystalline alloys in all the compositions discussed here. The common feature of these soft magnetic materials is that they loose their softness several degrees above the room temperature. With increasing temperature, above the T_c of remaining amorphous phase, the magnetic state transforms through superferromagnetic in superparamagnetic and then in paramagnetic states. The T_{sf} and T_{sp} transition temperatures sensitively depends on the composition and on the annealing conditions and T_{sp} depends also on the measuring field amplitude. Tailoring of new biphased nanocrystalline materials is necessary to increase the T_c of matrix responsable for the ferromagnetic coupling between the bcc nanoparticles and to prepare in this way a soft magnetic material applicable at high temperatures as well.

References

1. Hernando A., Vazquez M., Kulik T., Prados C., *Phys. Rev.* **B 51** (1995) 3581.
2. Scheffer R., Hubert A. and Herzer G., J. Appl. Phys. **69** (1991) 5325.
3. Mazaleyrat F., " Contribution a l'etude de rubans ferromagnetique nanocristallins" These de Doctorat de l'Universite Paris 6 (1996).

Pergamon

NanoStructured Materials, Vol. 12, pp. 1161–1166, 1999
Elsevier Science Ltd

0965-9773/99/$–see front matter

PII S0965-9773(99)00319-0

NANOCRYSTALLINE Sm-Co-Cu(Ni) THIN FILMS WITH GIANT COERCIVITY

G. C. Hadjipanayis[1], C. Prados[1,2], A. Hernando[2]
(1) Dept. of Physics and Astronomy. University of Delaware, Newark, DE 19716, USA.
(2) Instituto de Magnetismo Aplicado. RENFE-UCM.P. O. Box 155 28230 Las Rozas, Madrid, Spain

Abstract -Nanostructured Srn-Co, Sm-Co-C;u, Sm-Co-Ni thin films have been obtained by crystallizing the as-deposited amorphous films which were sputtered onto Cr buffer layers. Room temperature coercivity increases from less than 100 Oe in the amorphous state up to 42 kOe in a $SmCo_2Cu_3$ Sample annealed 30 min. at 550°C. Initial magnetization curves showed a behavior characteristic of uniform domain wall pining. Magnetic viscosity measurements indicated that the switching volume is of the same order as the $Sm(Co,Cu)_5$ crystallites size. Remanence Measuremcnts showed that interparticulate interactions were magnetizing and rather independent of the crystallization static. These data pointed to domain wall pinning at the high anisotropy Sm-C'.o precipitatcs as the origin of the huge coercivity in the annealed films.

INTRODUCTION

The magnetic properties of rare earth-transition metals (RE-TM) with $CaCu_5$ structure have been extensively studied since the seventies. The most outstanding property exhibited by some of these compounds is the presence of the so-called giant intrinsic magnetic hardness [1], where anisotropy fields of the order of 100 T and coercivities larger than 20 T have been reported at cryogenic temperatures in $Sm(Co\text{-}Ni)_5$ and $Sm(Co\text{-}Cu)_5$ alloys. The large magnetic anisotropy exhibited by the RE-TM alloys makes them the best candidates for hard high strength permanent magnets; Sm_2Co_{17} and $SmCo_5$ are currently being used as the basic compounds in the latest generations of advanced permanent magnets. On the other hand, the technological advances in computation have provided an insatiable demand for larger area recording density in magnetic storage devices. Two of the conditions that the longitudinal recording media have to fulfill in order to satisfy future requirements are to consist of small magnetic particles which exhibit large coercivity [2]. The reason for these requirements is to minimize the transition length between consecutive flux reversal regions and hence allow higher linear bit densities. In order to achieve larger coercivities than those obtained by the traditional Co-Cr-Pt alloys, RE-TM compounds and mainly $SmCo_5$, have been studied by a number of authors. Most of these previous investigations have shown that an underlayer of polycrystalline Cr controls the grain size and structural morphology, increasing thus the coercivity, and also it provides an appropriate crystallographic texture improving the in-plane anisotropy [3].

In this work, the structural and magnetic properties of $SmCo_5$, $SmCo_2Cu_3$ and $SmCo_2Ni_3$ thin films deposited by dc sputtering on a Cr underlayer are studied in the in the as-deposited and crystallized states obtained by a *ex-situ* annealing at different temperatures. The

different microstructures obtained in these compounds lead to a range of coercivity values extended over more than three orders of magnitude at room temperature (from 100 Oe in the amorphous as-deposited state to more than 40 kOe in the crystallized state). To understand the origin of large coercivity, magnetic viscosity and remanence measurements have been made to determine magnetic switching volumes, intergrain interactions and their relation to microstructure and hysteresis.

EXPERIMENTAL

The Cr buffer layers have been deposited from a pure (99.9 %) solid Cr target onto room temperature water cooled Si substrates. The Sm-Co-Cu(Ni) films were subsequently deposited also at room temperature from pressed powder targets with nominal compositions $SmCo_5$, $SmCo_2Cu_3$ and $SmCo_2Ni_3$. The discharge gas used was Ar at 5 mtorr. The deposition rates were approximately 1.2 A/s and 6 A/s, and the layer thickness 300 and 500 nm for the Cr and Sm-Co-Cu(Ni) films, respectively. The bilayers were annealed in vacuum for 30 min. at temperatures ranging from 400 to 640°C. The film structure was studied by x-ray diffraction (XRD) and by planar and cross-sectional transmission electron microscopy (TEM). The magnetic properties were measured at room temperature with a Quantum Design dc SQUID magnetometer and an Oxford Instruments vibrating sample magnetometer (VSM). Magnetic characterization included initial curves, coercivity measurements from the correspoding hysteresis loops, evolution of magnetization with time, which allows to determine the magnetization switching volume, and remanence curves to estimate the interactions between the magnetic particles.

RESULTS AND DISCUSSION

High angle XRD patterns indicates that the Cr buffer layers have grown with a (110) texture perpendicular to the film plane (Fig. 1). The Sm(Co, Cu, Ni) films were amorphous in the as-deposited state. After annealing, the appearance of a broad crystalline peak near of the $SmCo_5$ (111) line indicated that a nanocrystalline structure has been developed with the annealing heat treatment. Shown in figure 2 are the Sm-Co-Cu(Ni) crystalline grain size along the perpendicular direction to the film plane for the films with compositions SmCo2Cu3 and SmCo2Ni3 for different annealing temperatures. Grain sizes have been determined from the full-width at half-maximum (FWHM) by using Scherrer's formula. The values of the grain sizes were around 20 nm for $SmCo_2Ni_3$and 10 nm for $SmCo_2Cu_3$. In the case of $SmCo_5$, the grain size was estimated to be in the order of 5 nm for all the annealing temperatures, in the limit of the fitting procedure. The evolution of the intensity in the Sm-Co diffraction patterns indicates that the crystallized fraction, rather that the grain size was growing with the increasing of annealing temperature. Preliminary TEM studies showed that the nanocrystallites were embedded in a residual amorphous matrix (Fig 3) The cross-sectional TEM micrograph shows the columnar structure caused by the Cr buffer layer. The size of the crystallites determined by TEM is comparable to thet estimated from XRD.

Typical hysteresis loops in the various stages of annealing are shown in Fig 4a, b together the initial magnetization curve. The shape of the initial curve is characteristic of domain wall pinning-type materials. Figure 5 shows the evolution of coercivity and remanence with annealing temperature for the three compositions studied (note the logarithmic scale inordinates axis for coercivity). Coercivity values have been determined from room temperature

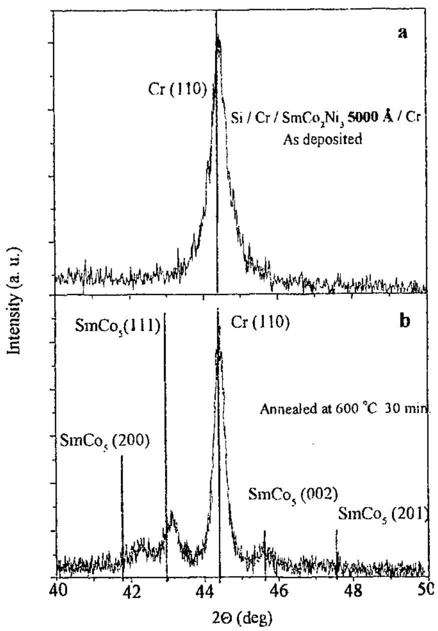

Fig. 1. XRD patterns of as-deposited (a) and annealed (b) Si/Cr/SmCo2Ni3 5000A/Cr films.

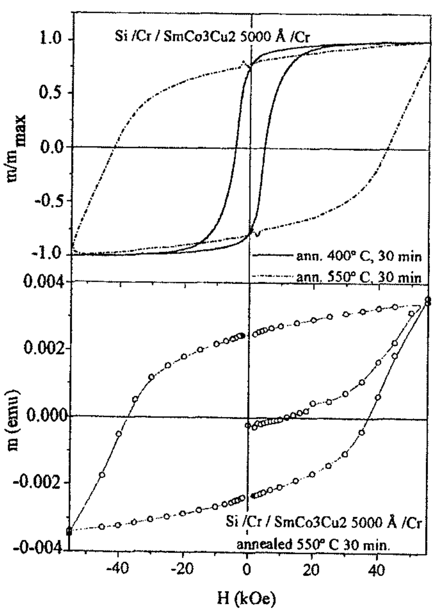

Fig. 4. (a) Typical toom temperature hysteresis loops obtained in Si/Cr/SmCo2Cu3 5000A/Cr annealed at 400oC and 550oC

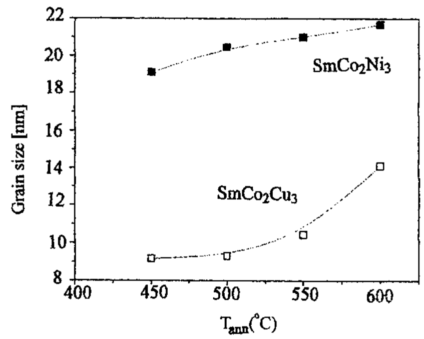

Fig. 2. Grain size of the layers of compositions SmCo2Cu3 and SmCoNi3 films as a function of the annealing temperature. Grain size has been determined from width of the (111) SmCo5 line using the Scherrer's formula.

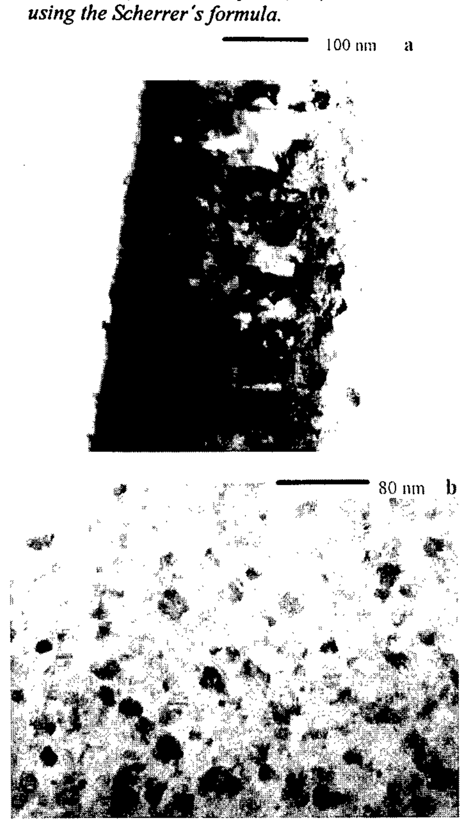

Fig. 3. TEM microstructure measurements.
(a) Cross-sectional micrograph showing the different layers and columnar structure caused by the Cr buffer layer (Si/Cr/SmCo2Cu3 5000A/Cr film ann. 600oC).
(b) Planar view showing the Sm-Co-Cu crystals. (Si/Cr/SmCo2Cu3 5000 A/Cr film ann. 550oC)

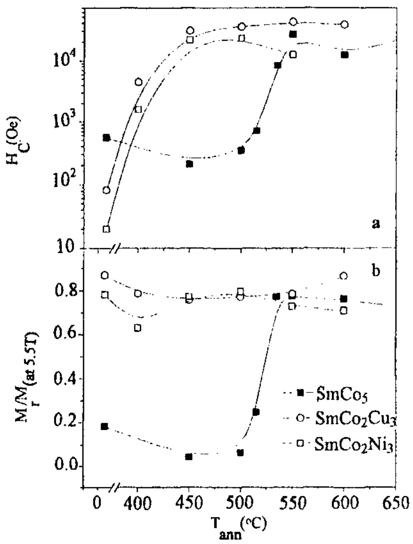

Fig. 5. Evolution of coercivity (a) and remanence (b) with the annealing temperature in the films SmCo2Cu3, SmCo2Ni3 and SmCo5. Coercivity has been obtained measuring hysteresis loops with a maximum applied field of 55 kOe.
Note the logarithmic scale in ordinates.

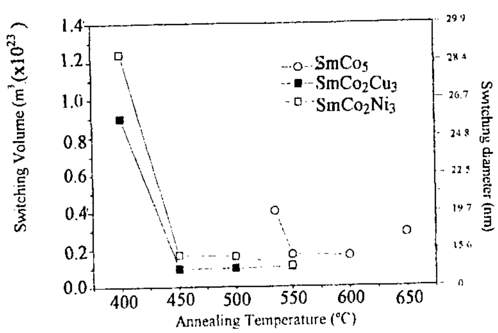

Fig. 6. Switching volume and size in the films SmCo2Cu3, SmCo2Ni3 and SmCo5 as a function of the annealing temperature.

hysteresis loops measured with a maximum applied field of 55 kOe. The films exhibit low coercivity in the amorphous as-deposited state, which is increasing as the nanocrystalline structure develops. In the case of $SmCo_5$ magnetic hardening starts around 515°C for $SmCo_2Cu_3$ and $SmCo_2Ni_3$. The maximum coercivity has been as large as 42 kOe in the case of $SmCo_2Cu_3$ annealed 30 min. at 550°C. These values of coercivity are comparable and even much larger than those recently reported in expitaxial oriented Sm-Co films measured along their hard axis [4].

The origin of the high coercivities has been investigated using magnetic viscosity, $M(H,t)$, and remanence measurements. By measuring the time dependence of magnetizatiion and the irreversible susceptibility, the switching volume of magnetic reversal was estimated. Following the refernence [5,6], near the coercive field, the change in magentization with time follows the relation

$$M(H,t) = \mathrm{M(H,i)+S(H)ln(r)} \qquad \text{(I)}$$

where M is the magnetization, S the viscosity coefficient and t the time elapsed since the last field change at t_o. The time dependence of the magnetization is originated by thermally activated transitions (through domain wall motion or magnetization rotation) over anisotropy energy barriers. A measure of the energy barriers distribution is the irreversible susceptibility χ_i. Near the coercive field, S and χ_I, take the maximum values, indicating that the coercivity characterizes the switching of the most typical magnetic grains of the sample. The switching volume V can be related to the maximum values of S and g; through the expression [5, 7]:

$$\frac{S}{\chi_i} = \frac{K_B T}{\mu_0 M_S V} \qquad [2]$$

where M_s, is the saturation magnetization, and k_B the Boltzmann constant.

Figure 6 shows the evolution of the switching volume with the annealing temperature for the three compositions studied. If we consider V to be spherical, it would be possible to define the 'switching size', d_s as the diameter of the switching volume, $V=4/3\pi(d_{s/2})^2$. This definition allow us to compare V with the evolution of the grain size shown in figure 2. The typical values of d_s for the annealing temperatures in which the largest coercivity is achieved are around 15 nm for $SmCo_5$ and $SmCo_2Ni_3$, and 12 nm for $SmCo_2Cu_3$ films. It is worth noting that these values are close to those of the grain sizes estimated from XRD patterns. This is indicating that the crystalline precipitates are one of the determining factors in the coercivity enhancement and in the control of the magnetization reversal.

Remanence curves and δM plots are extensively used to analyze the intergranular magnetic interactions between particles in granular systems [8]. The δM is defined from the normalized isothermal magnetization remanence $M_r(H)$, and the normalized dc demagnetization remanence $M_d(H)$ as

$$\delta M = M_d - (I - 2M_r) \qquad [3]$$

Precise definition of these principal remanence curves are given, for instance, in reference [9].

Non-interacting particles follow the Wohlfarth relation in which δM equals zero.

Negative δM values are interpreted as demagnetizing interactions while positive δM is taken to indicate magnetizing interactions, that is, exchange coupling. δM plots for the three compositions at two representative annealing conditions are plotted in figure 7. δM is positive in all the cases, and the maximum values do not change substantially with the annealing temperature and even are quite similar for the three different compositions, despite of the huge change in coercivity. Intergrain interactions are always magnetizing and of the same order for the diferent crystallization stages studied. This is indicating that interaction between particles is not playing a definitive role in the coercivity enhancement.

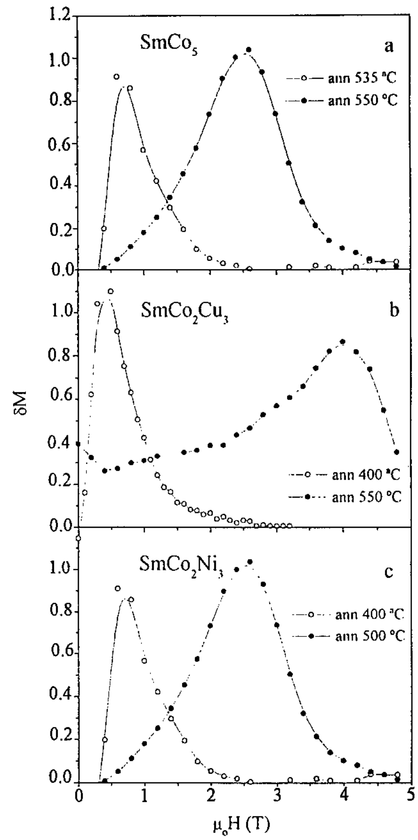

Fig. 7. σM plots for the samples films SmCoCu3, SmCoNi3, and SmCo5 as SmCo5 at two representative annealing conditions corresponding to low and high coercivity stages.

In the as-deposited state and after

Low temperature heat treatments the film structure remains amorphous and the coercivity is of the order of 100 Oe. After higher temperature annealing, when a nanocrystalline structure of high anisotropy Sm-Co-Cu(Ni) particles embedded in an amorphous matrix is developed, the coercivity increases by more than two orders of magnitude. Magnetic viscosity measurements indicate that the reversal switching volume is comparable to the precipitates size. On the other hand, the remanence behavior of the samples points towards the presence of a magnetizing (exchange) interaction between particles rather independent on the annealing temperature, and hence on the crystallization stage. Therefore the huge increasing on coercivity seems to be associated with the hindrance to the magnetization reversal due to domain walls pinning at the high anisotropy Sm-Co precipitates, rather than to the grain isolation described in precedent works. The pinning effectiveness improves with the density of crystallites reaching the optimum level at annealing temperatures around 500-550 °C.

CONCLUSION

In summary, we have fabricated Sm-Co-Cu(Ni)/Cr bilayers by dc sputtering deposition. Films are initially amorphous and relatively soft. A nanocrystalline structure is developed after annealing giving rise to a huge enhancement in coercivity. Structural and room temperature magnetic characterization (initial magnetization curve, hysteresis loops, viscosity and remanence) indicate that domain wall pinning at the high anistropy precipitates is in the origin of the huge coercivity. The possibility of tuning the coercivity along more than two orders of mahnitude through the annealing conditions, makes this kind of thin films compounds suitable for a wide variety of applications, from longitudal recording media to thin film permanent magnet.

ACKNOWLEDGMENTS

This work was supported by NSF Grant No. DMR-9307676. C. P. gives thanks to Programa Cientifico la OTAN for financial support.

References

[1] S. Foner, E. J. McNiff H. Oesterreicher, F. T. Parker and M. Misroch, J. Appl. Phys. 49 2061 (1979). H. Oesterricher, F. T. Parker and M Misroch, J. Appl. Phys. 50, 4273 (1979)
[2] D. N. Lambeth, D. E. Laughlin, S Charap, L. -L. Lee, P. Harllee and L. Tang, *Nanomagnelism,* Ed by G. C. Hadjipanayis (1996), pp 767
[3] E. M. T. Veiu and D. N. Lambeth, IEEE Trans. Mag., MAG-28, 3949 (1992). Y. Liu, D. J. Sellmyer, B. W. Robertson, S. S. Shan and S. H. Liou, IEEE Trans. Mag. MAG-3 l, 2740, (1995)
[4] E. Fullerton, J. S. Jiang, C. Rehm, C. H. Sowers, S. D. Bader, J. B. Patel and X. Z. Wu, Appl. Phys. Lett. 71(11), 1579 (1997)
[5] E. W. Singleton, Z. S. Shan, Y. S. Jeong and D. J. Sellmyer. IEEE Trans. Mag.,31, 2743 (1995)
[6] R. Street and J. C. Woolley, Proc. Phys. Soc. Sect. A. 62, 562 (1 949)
[7] E. P. Wohlfarth, J. Phys. F: Met. Phys. 14, 155 (1984)
[8] P.Y. Mayo, K.O'Grady, P.E. Kelly, J. Cambridge, Y.L. Sanders, T. Yogi and R.W.Chantrell. J. Appl. Phys. 69, 4733 (1991)
[9] R.W.Chantrell, *Nanomagnetism*, Ed. By G.C. Hadjipanayis (1996), pp 21

Pergamon

NanoStructured Materials, Vol. 12, pp. 1167–1171, 1999
Elsevier Science Ltd

0965-9773/99/$–see front matter

PII S0965-9773(99)00320-7

SYNTHESIS AND PROPERTIES OF NANOFUNCTIONALIZED PARTICULATE MATERIALS

J. Fitz-Gerald, S. Pennycook, H. Gao and R. K. Singh

Department of Materials Science and Engineering,
University of Florida, Gainesville, Florida, 32611

Abstract -- *A wide range of advanced technology for existing and emerging products based on high temperature metal-ceramic composites used in aircrafts, cutting tools, lithium-ion based rechargeable batteries, superconductors, field emission based flat-panel displays, etc. employ micron to submicron sized (0.1 -10 microns) particulate precursors in their manufacturing process. Although there has been a significant emphasis given to control of the particle characteristics (shape, size, surface chemistry, adsorption, etc.), relatively little or no attention has been paid to concomitant designing desirable surface and bulk properties at the particulate level, which can ultimately lead to enhanced properties of the product. By attaching atomic to nano-sized inorganic, multi-elemental clusters either in discrete or continuous form onto the surface of the core particles, i.e nano-functionalization of the particulate surface, materials and products with significantly enhanced properties can be obtained. In this paper, we demonstrate the synthesis of artificially structured, nano-functionalized particulate materials with unique optical, cathodoluminescent, superconducting and electrical properties. In this paper, we show the feasibility of the pulsed laser ablation technique to make very thin, uniformly distributed and discrete coatings in particulate systems so that the properties of the core particles can be suitably modified. Experiments were conducted for laser deposition on Al_2O_3, SiO_2, core particles by pulsed excimer laser (wavelength = 248 nm and pulse duration = 25 nanosecond) by irradiation of a Ag and Y_2O_3:Eu^{3+} targets. ©1999 Acta Metallurgica Inc.*

INTRODUCTION

Sub-micron to micron sized metallic and ceramic particles (100 nm to 10 microns) act at principal precursor materials for a wide range of existing and emerging products involving advanced ceramics, metals, composites which spans several industries such as aerospace, automobile, machining, vacuum electronics, batteries, data storage, catalysis, etc [1-2]. Particulate materials, as core technologies impact over 1 trillion dollar yearly on a worldwide basis [3]. To achieve desirable properties in the final product, typically the properties of the particles such as shape, size, composition, surface charge, flowability, etc., have been controlled. These characteristics play an important role in determining the final microstructure, and thus the product's properties. However with the rapid advancements in non-particulate technologies such as computers, telecommunications and electronics, there is a strong need to develop novel particulate systems which can result in value-added products [4].

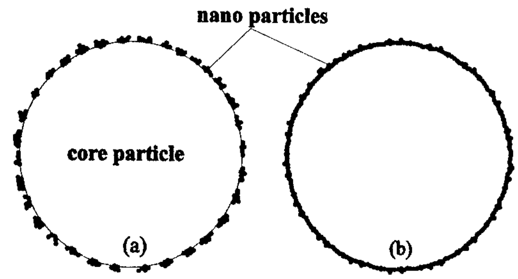

Figure 1. Schematic diagram of a nanofunctional particulate consisting of a core particle coated with nanoparticles

Increasing interest in the recent years has been focused on a wide variety of nanostructured materials, which possess grain or phase structures modulated on a length scale of less than 100 nm, because it is anticipated that their properties will be different from and often superior to conventional materials that have phase or grain boundaries over a coarser size scale [5-6]. Using artificial engineered nanostructured materials, it may also be possible to engineer the properties by controlling the size of the constituent domains and the manner in which they are assembled. Some of the recent efforts have been focused on synthesizing atomic clusters, zero dimensionality quantum well structures, one dimensional modulated multilayered materials, and three dimensional modulated nanophase materials and nanocomposite materials [3-7]. Although the synthesis of nanofunctionalized particulates is highly desirable from both fundamental and technological viewpoint, significant progress has not been made in this field due to several complicating factors [11-13]. Some of the cluster materials are in the form of multicomponent stochiometric materials such as phosphorescent materials (e.g, Eu doped yttrium oxide, sulphide). This complicates the uniformly deposition of these species onto the core particle [9-10]. In addition, the functionalized surface should typically have nanometric dimensionality control for optimum interaction between bulk and surface properties. Techniques presently used in the literature such as fluidized bed coating, powder blending, mechanofusion processing, chemical precipitation and chemical vapor phase condensation are not capable of overcoming the above mentioned barriers [11-13].

EXPERIMENTAL

In this paper, we show the feasibility of the pulsed laser ablation technique to form discrete Ag nano particle coatings on core particles of Al_2O_3 and SiO_2. A schematic diagram of two types of nano-functionalized particulate materials is shown in Fig. 1. This schematic shows both discrete and continuous nano-functionalized layers onto core particles.

Fig. 2 shows a schematic diagram of the experimental setup to fabricate the particulate coatings. An excimer laser irradiates the target material through the ultraviolet transparent quartz window. Typical energy densities employed in the experiments were approximately 2-3 J/cm^2. The laser plume is directed perpendicular to the target material to an agitated bed of core particles. The core particles are suspended in the system by a mechanical agitation method. The thickness and surface coverage of the coating is controlled primarily by the repetition rate of the laser and the residence time of the suspension. By controlling the energy as well as the background pressure in the system, the composition and size of the nano particles can be controlled. Earlier work has shown a correlation between the cluster size and the background gas pressure [14-15]. When the background gas pressure is increased, the cluster size changes from a few atoms to nanometer dimensions. The experiments have been conducted using Al_2O_3

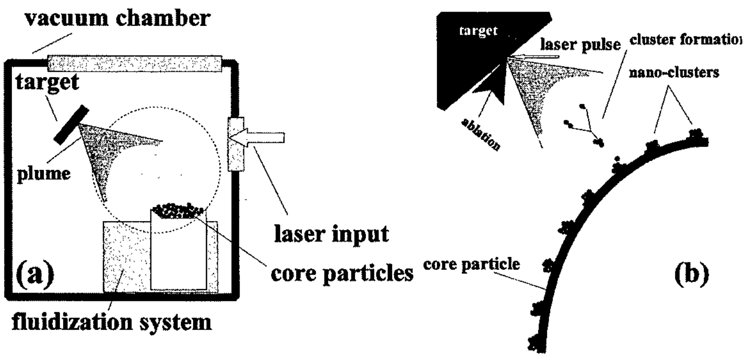

Figure 2. Schematic diagram of the system employed to synthesize nano-cluster coatings

and SiO_2 core particles with a high purity Ag , Y_2O_3:Eu^{3+}, and $TaSi_2$ targets as sources.

RESULTS AND DISCUSSION

Due to the fact that the size of the ablated nano particles is below the resolution of the SEM, the presence of the coating on the surface was determined by chemical analysis.

Figures 3 (a), (b), respectively show SEM and Ag chemical images of Ag/Al_2O_3 composite particles synthesized by the laser ablation process. The SEM micrograph shows approximately 18 μm faceted alumina particles, however it does not reveal the presence of a nano particle film on the surface. From the WDX Ag chemical map shown in figure 3(b), it appears that the Ag is distributed uniformly on the surface of the Al_2O_3 particles.

Fig. 3(c) shows a Z-contrast scanning transmission electron micrograph (STEM-Z) image of the Ag nanoparticles on the Al_2O_3 core particle substrate. The image shows a discrete coating of Ag nanoparticles, polycrystalline, ranging in size depending on process parameters from 4.5-33 nm [16].

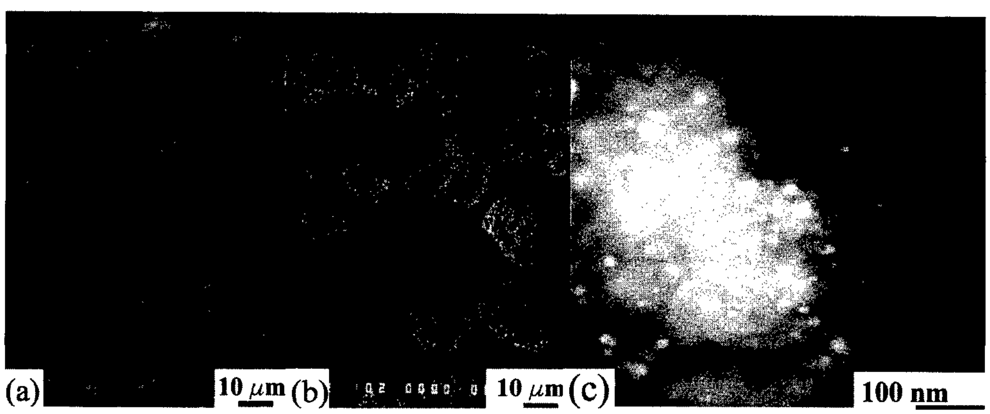

Figure 3. Imaging of nanoparticle coatings.

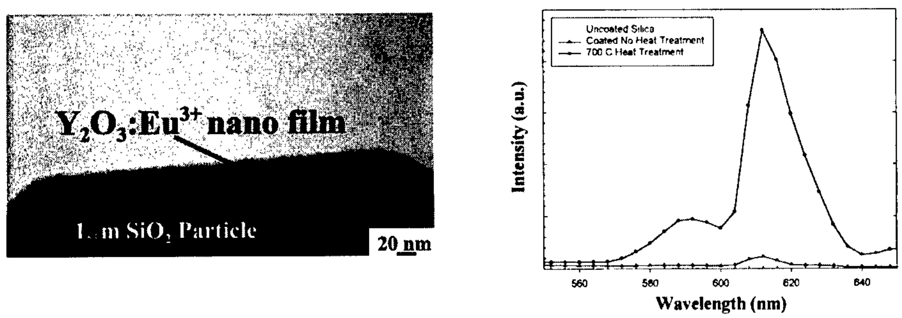

(a) (b)

Figure (4) (a) TEM image showing a continuous thin film of Y_2O_3:Eu^{3+} deposited on the core particle, (b) PL spectra from coated core particles showing the standard Eu peak at 611 nm.

Nano-functional particulate materials can be designed to achieve properties which cannot be obtained with existing particulate materials. An example of this is shown for particulate requirements for field emission based flat panel display applications [8]. This emerging technology has several advantages in terms of low power consumption, high brightness, large viewing angle and is expected to replace liquid based crystal technology in specific applications [8]. In this application, the multiple field emission electron beam sources directly strike a phosphor particulate based screens possessing red blue or green activators to produce light which is emitted out of the surface.

The phosphor screens are typically made from powder materials which exhibit a multitude of shapes and sizes distributions, thus causing non-uniformity in the thick film microstructure. Additionally, upon continuous irradiation with intense electron beams, the brightness of the screens degrade thus limiting its usefulness and have become a major impediment for commercialization [8]. Figure 4(a) shows a TEM micrograph in cross section of a Y_2O_3:Eu^{3+} luminescent (611 nm emission) nano coating on 1 μm spherical SiO_2 core particles revealing important microstructural characteristics of the 25 nm Y_2O_3:Eu^{3+} layer. It can be readily observed that the deposited layer is continuous over the perimeter of the curved surface of the 1 μm core SiO_2 particles. More studies are presently being conducted to understand the nature of layer growth on curved interfaces. These nano-functionalized particulates were heat treated at 700°C for 1 hr. in oxygen to activate the phosphor layer. Fig. 4(b) shows the typical photoluminesence spectrum obtained from Y_2O_3:Eu^{3+}/SiO_2 nano-functionalized particles. The figure show that the particles yield a dominant red light emission peak at 611 nm due to $^5D_0$-$^7F_2$ transition. Due to shielding effects of $4f^6$ electrons by $5s^2$ and $5p^6$ electrons in outer shells of Eu ion, one expects a sharp emission within Eu ions. The photoluminesence brightness was significantly higher when the samples were annealed in oxygen at 700°C for 1 hour.

CONCLUSIONS

A novel technique using pulsed laser ablation to synthesize engineered particulate materials has been presented. TEM observations have shown that the backfill gas pressure and molecular weight have significant effects on Ag nano particle formation during ablation. Further

STEM characterization of the interfaces is presently underway.

In short, it is felt that PLD method represents a viable method to surface modify particulate systems, which are required for a wide variety of current and future applications.

ACKNOWLEDGEMENTS

Part of this research is sponsored by the National Science Foundation funded Engineering Research Center on Particle Science and Technology via grant #ERC 94-0929. The authors would like to thank Kyu-Gong Cho for optical emission measurements.

REFERENCES

1. Tom Forester, The Materials Revolution, MIT Press (1988).
2. Materials Science & Engineering for the 1990s, National Academy Press, Washington DC 1990.
3. U. S Department of Commerce Annual Report, 1992.
4. Scientific American, May, 1997 pg. 38-39.
5. H. Glieter, Advanced Materials, 4, 474 (1992).
6. R. W. Seigel, Nanostructured Materials, 4, 121 (1994).
7. See for example, E. Gonsalves, J. Baraton, R. K. Singh, H. Hofmann, J. Akarra,
8. editors,"Surface Modification of Nanomaterials for Value of Added Application",
9. Proceedings of the November, 1997 Materials Research Society , Fall Meeting (1998).
10. J. Fitz-Gerald, R.K. Singh, T. Trottier and P. H. Holloway, App. Phys. Lett, Vol 72, 15 (1998).
11. Y. Kousaka, Y. Endo, M. Alonso, H. Ichitoubo, A. Fukui, Advanced Powder Tech., 6, 11 (1995).
12. I. Saito, M. Senna, Kona, 13, 191 (1993).
13. K. Higashitani, T. Yamamura, Y. Ishiki, A. kage, A. Kondo, Kona 12, 119 (1994).
14. S. Jin, T. H. Tifel, M. McCormack, R. A Fastnatch, R. Romish, and L. H. Chen,Science, 264 413 (1994).
15. See for example, " Pulsed Laser Processing of Materials : Fundamentals and Applications", Editors R. K. Singh, D. P. Norton, J. Narayan, M. Hanabusa, Materials Research Society Proceedings, Vol 347 (1997).
16. K.D. Rinnen, K.D. Kolenbrabder, A.M. DeSantioolo, M.L. Mandich, J.Chem Phy. 96, 4088 (1992).
17. T. Yoshida, S. Takeyama, Y. Yamada, K. Mutoh, Appl. Phys. Lett, 68, 772 (1996).
16. J. Fitz-Gerald, R. K. Singh, KONA, (in press), (1998).

Pergamon

NanoStructured Materials, Vol. 12, pp. 1173–1182, 1999
Elsevier Science Ltd

0965-9773/99/$–see front matter

PII S0965-9773(99)00327-X

AUTHOR INDEX VOLUME 12, 1999

Pergamon

NanoStructured Materials, Vol. 12, pp. 1183–1188, 1999
Elsevier Science Ltd

0965-9773/99/$–see front matter

PII S0965-9773(99)00328-1

SUBJECT INDEX VOLUME 12, 1999

Notes for the Guidance of Authors
NanoStructured Materials

Manuscripts will be considered for publication which are short papers of new work or discussions of work already published. Papers should address the aspects of nanostructured materials defined in the Aims and Scope statement. Manuscripts must be submitted in English *only* and it is the responsibility of *authors* to see that proper use of English and style is maintained. Poorly written papers will be returned to authors, thus delaying publication.

Submission of Papers: An original and one copy, **both containing original micrographs**, plus one diskette copy of manuscripts should be submitted. Manuscripts should be submitted directly to: Editorial Office, Professor Thomas Tsakalakos, Nanostructured Materials, College of Engineering, Rutgers University, 98 Brett Road, Piscataway, NJ 08854-8058, USA. Tel: +1 732-445-2888; Fax: +1 732-445-3229; Email: nanostru@rci.rutgers.edu or tsakalak@rci.rutgers.edu
Please note that email submissions are not accepted. Authors of multiple-authored papers must sign a statement to the Principal Editor that all authors have agreed to the submission of the paper.

Acceptance of Papers: The Editors and competent referees will decide whether a paper is to be accepted or not. This procedure is designed to ensure that decisions are reached in the minimum possible time.

Format and Layout: Manuscripts should be typed single spaced on sheets of 8.5" × 11" (21.6 × 27.94 cm) (A4) paper, leaving a space of 8.5" × 4.5" (21.6 × 11.43 cm) on top of the first page for printing the title, authors' affiliations and received/accepted dates. Articles should include an abstract of approximately 100–150 words. Appropriate blank space should be left within the text for the positioning of figures and tables.

Authors should send figures that need little or no reduction for printing. The figures should be no more than 5.67" (14.4 cm) wide. Depths may vary, but one third of the text page, i.e. 2.5" (6.35 cm), would be ideal. Halftone micrographs are reduced on average by 25% and line art may be reduced by 25% to 50% to fit the page. Because of the reduction of the micrographs, magnifications should be indicated by nm, μm, and mm markers. Markers and other lettering should be placed 3 mm from the edge of the micrograph.

References should be indicated in the text by consecutive numbers in parentheses, e.g. (1,2), as part of the text, not raised above it, the full reference being cited in a numbered list at the end of the text. References should contain the names of the authors together with their initials, the title of the journal, volume number, first page number, and year, as illustrated below. References to books should contain the publisher's name and location. Use single spacing between references.

[1] Sack HS, Moriarity MC. Solid State Comm. 1955;3:93.

[2] Rosenberg HS, Low Temperature Solid State Physics. Oxford: Clarendon Press, 1963:210.

SI units must be used exclusively. Use only standard SI symbols and abbreviations in text and illustrations.

Computer Disks: In order to speed publication and ensure accuracy, authors are required to submit a computer disk (5.25" or 3.5" HD/DD disk) containing their paper along with the manuscript to the Editorial Office. Please observe the following criteria: (1) Send a hard copy and computer disk when first submitting your paper. (2) When your paper has been refereed, revised if necessary and accepted, send a disk containing the *final* version with the *final* hard copy. **Make sure that the disk and hard copy match exactly**. (3) Specify what software was used, including which release (e.g., WordPerfect 6.0). (4) Specify what computer was used (either IBM compatible PC or Apple Macintosh). (5) Include both the text file and ASCII file, and separate table and illustration files, if available. (6) The file should follow the general instructions on style/arrangement and, in particular, the reference style of this journal as given in the Notes for the Guidance of Authors. (7) The file should be single-spaced and the wrap-around end-of-line feature should be used (i.e., no returns at the end of each line). All textual elements should begin flush left, with no paragraph indents. Place two returns after every element such as title, headings, paragraphs, figure and table callouts, etc. (8) Keep a backup disk for reference and safety.

Color: Figures can be reproduced in full color, however, the author or institution will be expected to contribute towards the costs involved. For 1999, the cost of printing in color will be US$650.00 per printed color page.

Copyright Agreements: Since the enactment of U.S. Copyright laws on January 1, 1978, a Transfer of Copyright Agreement is required by the publisher to accompany every article accepted for publication. Upon acceptance for publication, the corresponding author of each manuscript will be sent an agreement to be completed prior to preparation for publication.

Reprints and copies of the issue (at a specially reduced rate) can be ordered on the form which accompanies the letter of acceptance. This along with the Transfer of Copyright Form should be returned to: Elsevier Science, Inc., 655 Avenue of the Americas, New York, NY 10010 at your earliest convenience.